



# Results of Aero/Acoustic Tests and Analytical Studies of a Two-Dimensional Eight-Lobe Mixer-Ejector Exhaust Nozzle at Takeoff Conditions

P. Schweiger, A. Stern, and E. Gamble  
Pratt & Whitney, East Hartford, Connecticut

T. Barber, L. Chiappetta, and R. LaBarre  
United Technologies Research Center, East Hartford, Connecticut

M. Salikuddin, H. Shin, and R. Majjigi  
General Electric Aircraft Engines, Cincinnati, Ohio

## The NASA STI Program Office . . . in Profile

Since its founding, NASA has been dedicated to the advancement of aeronautics and space science. The NASA Scientific and Technical Information (STI) Program Office plays a key part in helping NASA maintain this important role.

The NASA STI Program Office is operated by Langley Research Center, the Lead Center for NASA's scientific and technical information. The NASA STI Program Office provides access to the NASA STI Database, the largest collection of aeronautical and space science STI in the world. The Program Office is also NASA's institutional mechanism for disseminating the results of its research and development activities. These results are published by NASA in the NASA STI Report Series, which includes the following report types:

- **TECHNICAL PUBLICATION.** Reports of completed research or a major significant phase of research that present the results of NASA programs and include extensive data or theoretical analysis. Includes compilations of significant scientific and technical data and information deemed to be of continuing reference value. NASA's counterpart of peer-reviewed formal professional papers but has less stringent limitations on manuscript length and extent of graphic presentations.
- **TECHNICAL MEMORANDUM.** Scientific and technical findings that are preliminary or of specialized interest, e.g., quick release reports, working papers, and bibliographies that contain minimal annotation. Does not contain extensive analysis.
- **CONTRACTOR REPORT.** Scientific and technical findings by NASA-sponsored contractors and grantees.

- **CONFERENCE PUBLICATION.** Collected papers from scientific and technical conferences, symposia, seminars, or other meetings sponsored or cosponsored by NASA.
- **SPECIAL PUBLICATION.** Scientific, technical, or historical information from NASA programs, projects, and missions, often concerned with subjects having substantial public interest.
- **TECHNICAL TRANSLATION.** English-language translations of foreign scientific and technical material pertinent to NASA's mission.

Specialized services that complement the STI Program Office's diverse offerings include creating custom thesauri, building customized databases, organizing and publishing research results . . . even providing videos.

For more information about the NASA STI Program Office, see the following:

- Access the NASA STI Program Home Page at <http://www.sti.nasa.gov>
- E-mail your question via the Internet to [help@sti.nasa.gov](mailto:help@sti.nasa.gov)
- Fax your question to the NASA Access Help Desk at 301-621-0134
- Telephone the NASA Access Help Desk at 301-621-0390
- Write to:  
NASA Access Help Desk  
NASA Center for Aerospace Information  
7121 Standard Drive  
Hanover, MD 21076





# Results of Aero/Acoustic Tests and Analytical Studies of a Two-Dimensional Eight-Lobe Mixer-Ejector Exhaust Nozzle at Takeoff Conditions

P. Schweiger, A. Stern, and E. Gamble  
Pratt & Whitney, East Hartford, Connecticut

T. Barber, L. Chiappetta, and R. LaBarre  
United Technologies Research Center, East Hartford, Connecticut

M. Salikuddin, H. Shin, and R. Majjigi  
General Electric Aircraft Engines, Cincinnati, Ohio

Prepared under Contract NAS3-26618

National Aeronautics and  
Space Administration

Glenn Research Center

## **Acknowledgments**

Acknowledgment is given to General Electric Aircraft Engines for their efforts in conducting the test portions of the program and data reduction.

## **Document History**

This research was originally published internally as HSR042 in September 1996.

Note that at the time of research, the NASA Lewis Research Center was undergoing a name change to the NASA John H. Glenn Research Center at Lewis Field. Both names may appear in this report.

Available from

NASA Center for Aerospace Information  
7121 Standard Drive  
Hanover, MD 21076

National Technical Information Service  
5285 Port Royal Road  
Springfield, VA 22100

Available electronically at <http://gltrs.grc.nasa.gov>

## FOREWORD

This report presents the results of aero-acoustic testing and analytical studies conducted to investigate the noise generated by various two-dimensional shrouded mixer-ejector exhaust nozzle designs. The testing was conducted for NASA by Pratt & Whitney (P&W) and General Electric Aircraft Engines (GEAE) in a joint program under their respective contracts, (P&W) NAS3-26618 (Large Engine Technology (LET)) Task Order 8, and (GEAE) NAS3-26617, Task Order 9, both under the direction of Mr. Frank Humenik, NASA Program Manager.

The NASA Task Manager for both tasks is Mr. Douglas Harrington. Mr. Alfred N. Stern served as Task Manager for P&W and Dr. M. Salikuddin served as Task Manager for GEAE.



## CONTENTS

<i>Section</i>	<i>Page</i>
1. SUMMARY.....	1
2. INTRODUCTION.....	3
2.1 BACKGROUND.....	3
2.2 OBJECTIVES.....	3
3. TEST APPARATUS.....	5
3.1 ACOUSTIC TEST FACILITY.....	5
3.1.1 Facility Instrumentation and Model Orientation.....	5
3.1.2 Data Acquisition.....	6
3.1.3 Laser Doppler Velocimeter Test Capability.....	6
3.2 HARDWARE.....	7
3.2.1 Pratt & Whitney Baseline Round Convergent Nozzle.....	7
3.2.2 Pratt & Whitney 2D Mixer-Ejector Nozzles.....	7
3.2.3 Model Instrumentation.....	10
3.3 TEST PROGRAM.....	11
3.3.1 Model Configurations.....	11
3.3.2 Test Plan.....	11
4. RESULTS AND DISCUSSION.....	33
4.1 ACOUSTIC ANALYSIS AND TEST RESULTS.....	33
4.1.1 Description of Analysis Steps Used by P&W and GEAE.....	33
4.2 ACOUSTIC TEST RESULTS.....	34
4.2.1 Baseline Round Convergent Nozzle Results.....	34
4.2.2 Effect of Mixer Area Ratio (MAR).....	37
4.2.3 Effect of Shroud Area Ratio (SAR).....	38
4.2.4 Mixer Comparison.....	38
4.2.5 Effect of Treatment and Liner Deterioration.....	39
4.2.6 Azimuthal Variation of Noise Level.....	40
4.2.7 Effect of Ejector-Shroud Length.....	41
4.2.8 Flight Effects.....	41
4.2.9 Effect of Aerodynamic Hysteresis on Noise Level.....	42
4.2.10 Effect of Operating Off the LIM Throttle Line.....	42
4.2.11 Comparison to NASA-LeRC Results (NAS3-2595 APT Task 11).....	43
4.3 AERODYNAMIC TEST RESULTS AND ANALYSIS.....	44
4.3.1 Vortical Mixer-Ejector Nozzle Configurations.....	45
4.3.2 Axial Mixer-Ejector Nozzle Configurations.....	49
4.3.3 Mode Switch Phenomena and Control.....	51

4.4	LASER TWO-DIMENSIONAL FIBER OPTICS FLOWFIELD MEASUREMENT .....	52
4.4.1	Laser Doppler Velocimeter Test Results for External Plume .....	53
4.4.2	Laser Doppler Velocimeter Test Results for Internal to Ejector Flowfield .....	60
4.5	COMPUTATIONAL STUDIES OF PRATT & WHITNEY MIXER-EJECTOR EXHAUST NOZZLE CONCEPTS WITH COMPARISONS TO GEAE CELL 41 EXPERIMENTAL DATA .....	63
4.5.1	Geometry .....	63
4.5.2	Grid Generation .....	63
4.5.3	Flowfield Modeling .....	66
4.5.4	Mixing Effectiveness Measures .....	67
4.5.5	Computational Fluid Dynamics Background .....	67
4.5.6	Discussion Of Results .....	69
5.	CONCLUSIONS .....	73
6.	REFERENCES .....	75
	ATTACHMENT 1 — ILLUSTRATIONS FOR SECTION 4.....	77
	APPENDIX A — LIST OF SYMBOLS.....	425
	APPENDIX B — ACOUSTIC TEST RUN SCHEDULE.....	429
	APPENDIX C — COMPARISON OF GEAE AND P&W EPNL RESULTS .....	443
	APPENDIX D — MODEL SCALE EFFECTS.....	447
	APPENDIX E — LIST OF TABLES .....	457
	APPENDIX F — LIST OF ILLUSTRATIONS .....	459

## 1. SUMMARY

This report summarizes the results of hot flow aero-acoustic tests conducted for NASA, with Pratt & Whitney (P&W) High-Flow Two-Dimensional (2D) Exhaust Nozzles, by General Electric Aircraft Engines (GEAE) in the GEAE Anechoic Freejet Jet Noise Facility (Cell 41) located in Evendale, Ohio. The test planning, test execution, data reduction, and analysis were jointly performed by P&W, under Contract NAS3-26618 (LET), Task Order 8, and GEAE, under Contract NAS3-26617 (LET) Task Order 9. The tests evaluated the impact of various geometric and design parameters on the noise generated by a 2D, shrouded, eight lobe, mixer-ejector exhaust nozzle. The shrouded mixer-ejector provides noise suppression by mixing relatively low energy ambient air with the hot, high-speed primary exhaust jet. Additional attenuation was obtained by lining the shroud internal walls with acoustic panels to absorb acoustic energy generated during the mixing process. Two mixer designs were investigated, high mixing vortical and aligned flow axial, along with variations in shroud internal mixing area ratios and shroud length. The shrouds were tested as hardwall or lined with acoustic panels packed with a bulk absorber. A total of 21 model configurations at 1:11.47 scale were tested. The models were tested over a range of primary nozzle pressure ratios and primary exhaust temperatures representative of typical High Speed Civil Transport (HSCT) aerothermodynamic cycles. Static and flight-simulated data were acquired during testing. A round, convergent, unshrouded nozzle was tested to provide an acoustic baseline for comparison with the test configurations. Comparisons were made to previous test results obtained with this hardware at the NASA-Lewis Research Center (LeRC) 9 ft x 15 ft Low-Speed Wind Tunnel (LSWT). A significant reduction in exhaust system noise was demonstrated with the 2D shrouded nozzle designs.

Computational fluid dynamics (CFD) analysis using the P&W NASTAR Navier-Stokes code was developed for both P&W-designed mixer-ejector configurations, nominally operating at a nozzle pressure ratio (NPR) of 3.5 and a primary jet total temperature of 1275°F. Comparisons were made with experimental data obtained in the GEAE Cell 41 facility. Many of the observed physical trends were reproduced by the calculations.

### Major Results and Conclusions

- Caution should be used when acoustic testing is performed with scale models less than 1/10 scale because difficulties with data reduction can arise due to large atmospheric attenuation corrections.
- The vortical mixer design with the long (216 inches full scale) acoustically treated shroud (SAR=4.9, MAR=0.97) provided the largest sideline flight ( $V_{\text{fl}}=357$  ft/sec) noise reduction, better than 15 EPNdB below the reference convergent nozzle at 2400 ft/sec unsuppressed primary jet velocity. (SAR is defined as the ratio of mixing plane area at the mixer exit to primary mixer throat area. MAR is defined as the ratio of shroud exit area to mixing plane area at the mixer exit plane.)
- The vortical mixer with the long shroud (SAR=4.9, MAR=0.97), and perforated plate over honeycomb acoustic treatment packed with a bulk absorber, demonstrated a 5-8 EPNdB sideline noise reduction below the long hardwall shroud at  $M_n=0.32$  ( $V_{\text{fl}}=357$  ft/sec) over the entire range of unsuppressed primary jet velocity tested.
- The vortical mixer design with the long acoustically treated shroud (SAR=4.9, MAR=0.97) showed a 1 to 2 EPNdB sideline flight ( $V_{\text{fl}}=357$  ft/sec) noise reduction relative to the axial mixer design with the long treated shroud (SAR=4.9, MAR=0.97) at unsuppressed primary jet velocity greater than 2200 ft/sec.
- The long 2D mixer-ejector designs with both treated and hardwall shroud (SAR=4.9, MAR=0.97) exhibited a 2-3 EPNdB azimuthal noise increase from the sideline to community (overhead) position over the range of unsuppressed primary jet velocity tested at  $V_{\text{fl}}=357$  ft/sec.

- Flight effects at  $V_{fl}=357$  ft/sec accounted for approximately 2-3 EPNdB reduction in the sideline noise for the long treated configurations: 3 (vortical mixer, SAR=4.9, MAR=0.97), 5R (vortical mixer, SAR=4.4, MAR=0.97) and 13 (axial mixer, SAR=4.9, MAR=0.97).
- Acoustic data were obtained with the baseline round convergent nozzle and configuration 3 (vortical mixer, long treated shroud, SAR=4.9, MAR=0.97) while holding various conditions constant. Data was measured at constant jet velocity, turbine exit total temperature, and nozzle pressure ratio. The results show that the long treated mixer-ejector was more sensitive (larger noise increase) to changes in the throttle line than the baseline round convergent nozzle.
- The EPNL reductions from Cell 41 are similar to those obtained in the NASA-LeRC LSWT, although spectral data show differences. The comparisons confirm technical concerns related to nearfield measurements and facility noise in the NASA-LeRC LSWT.
- An aerodynamic mode switch from compound-compressible subsonic to compound-compressible sonic flow within the ejector shroud was observed with both mixer designs. This phenomenon occurred during testing with ambient temperature primary flow and at high NPR (greater than 4.5). The mode switch was very gradual such that definition of the nozzle pressure ratio at which the switch occurred was subject to interpretation. The mode switch with the axial mixer was more subtle than that seen with the vortical mixer. The mode switch could be controlled at NPR values less than 4.5 by using a short ejector shroud (120 inches full scale) and/or low MAR.
- External plume laser Doppler velocimetry (LDV) measurements of the vortical mixer-ejector with long shroud show an effect of ejector acoustic treatment on the ejector external velocity profiles. This effect was observed with a diffusing mixing region (MAR=1.18, SAR=4.9). Axial velocities at the ejector centerline were nearly identical for both treated and hardwall ejectors, whereas, axial velocities between the ejector centerline and ejector walls were higher (100 ft/sec) for the treated configurations than for the hardwall ejector at flight-simulated conditions. Possible explanations for this are increased treated ejector wall boundary layer blockage and effect of the thicker treated ejector boundary layer on internal ejector shock structure.
- Vortical nozzle calculations of shroud pressure loading produce reasonable agreement with measured data. Predictions show: reduction in ram drag with lower flight Mach number, positive effect of flight Mach number on thrust coefficient, and increased shroud loading with increased nozzle pressure ratio. Specific operating points predict the presence of a strong shock in the shroud mixing region.
- Experimental LDV measurements show that the sidewalls have an effect on the internal mixing region flowfield, at least near the ejector exit plane. However, away from the sidewall, the vortical nozzle calculations, which modeled one half of a mixer lobe, produced velocity profiles that were in reasonable agreement with LDV measured sidewall-to-sidewall axial velocity profiles. This geometry modeling scheme would become more appropriate if the number of mixer lobes were increased, reducing the significance of sidewall interactions on the mixing region flowfield.
- Calculations of the shroud static pressure loading and plume axial velocity field for the axial mixer-nozzle configurations are in poor agreement with measured LDV and static pressure data. The calculated pressure recovery is dominated by a large scale zone of separation on the shroud surface, apparently induced by the lip shock/boundary layer interaction.



## 2. INTRODUCTION

### 2.1 BACKGROUND

With the renewed national interest in developing a High Speed Civil Transport (HSCT), there is increasing concern regarding two significant environmental issues that arise from such an aircraft system: airport community noise and engine emissions (ozone depletion). The present effort describes the analysis of a two-dimensional (2D), or planar, mixer-ejector exhaust nozzle to achieve the Federal Aviation Regulation 36 Stage III noise goals. An ejector is a fluid dynamic pump that provides a means for pumping low energy (velocity or temperature) secondary fluid using the kinetic energy of the primary stream. The fundamental principles of an ejector, first suggested by von Karman, are based on increasing the thrust of the primary propulsive nozzle and mixing the high-temperature exhaust flow with ambient air to lower jet noise. Whether acting as a pump or used to lower jet noise, the key mechanism for the operation of the ejector is energy transfer from the primary to the secondary fluid stream through viscous mixing. Common ejectors require long mixing ducts to entrain and mix primary and secondary flows. Long mixing ducts result in increased wall friction losses, extra weight, and higher costs. By incorporating a forced mixer, energy can be transmitted from the engine stream to the fan stream in an efficient manner. This means that significant thrust gains can be obtained for many turbofan cycles, and jet exhaust noise reduction benefits may be obtained with minimal engine performance penalties. Forced mixing is dominated by large-scale secondary flows, not viscous diffusion, and is, therefore, an efficient mixing process. A key benefit of mixer-ejectors, relative to conventional ejectors, is that good pumping and effective mixing can be achieved over very short mixing duct lengths. Shortening of the ejector mixing duct in aircraft exhaust systems reduces weight and fabrication costs. Typical mixer-ejectors show well-mixed shroud exit flows occurring in one- to two-mixing duct diameters, as opposed to conventional ejectors, which require lengths of five to seven duct diameters.

Supersonic mixer-nozzle and mixer-ejector concepts for aerodynamic mixing enhancement were first developed at United Technologies Research Center (UTRC) under Naval Air Systems Command support (Contract N00014-85-C-0506). These concepts were verified in the UTRC Acoustic Research Tunnel, and in computational studies during the late 1980s. The tests conducted under Contract NAS3-22618, Large Engine Technology (LET), Task 8, continue acoustic and aerodynamic investigations of the Pratt & Whitney high-flow 2D exhaust nozzle previously tested under Contract NAS3-25952, Aero Propulsion Technology, Task 11, in the NASA Lewis Research Center (NASA-LeRC) 9 ft x 15 ft Low Speed Wind Tunnel (LSWT) in 1991.

### 2.2 OBJECTIVES

The acoustic test program had two main objectives: first, the investigation of various 2D nozzle geometric and design variations, and their impact on exhaust system noise; and second, a comparison of the GEAE Cell 41 facility to the NASA-LeRC LSWT, and verification of previous test results. The task also provides data that can be compared to future results in the NASA-LeRC Nozzle Acoustic Test Rig (NATR) facility. Aerodynamic and laser Doppler velocimetry (LDV) data were to be obtained to support the acoustic investigation and provide data for comparisons to planned computational fluid dynamics (CFD) studies. Figure 1 shows the model mounted in the GEAE Cell 41 test facility.

The three nozzle geometric variations were: 1) mixing area ratio (MAR), which is the ratio of shroud exit area ( $A_{exit}$ ) to internal mixing plane area ( $A_{mix}$ ); 2) shroud area ratio (SAR), which is the ratio of internal mixing plane area ( $A_{mix}$ ) to primary throat area ( $A_{g*}$ ); and 3) shroud length. Two mixer design variations were investigated: a compact vortical mixer and a longer axial mixer. Also, the effect of an acoustically treated shroud was evaluated by comparison to a hardwall shroud.

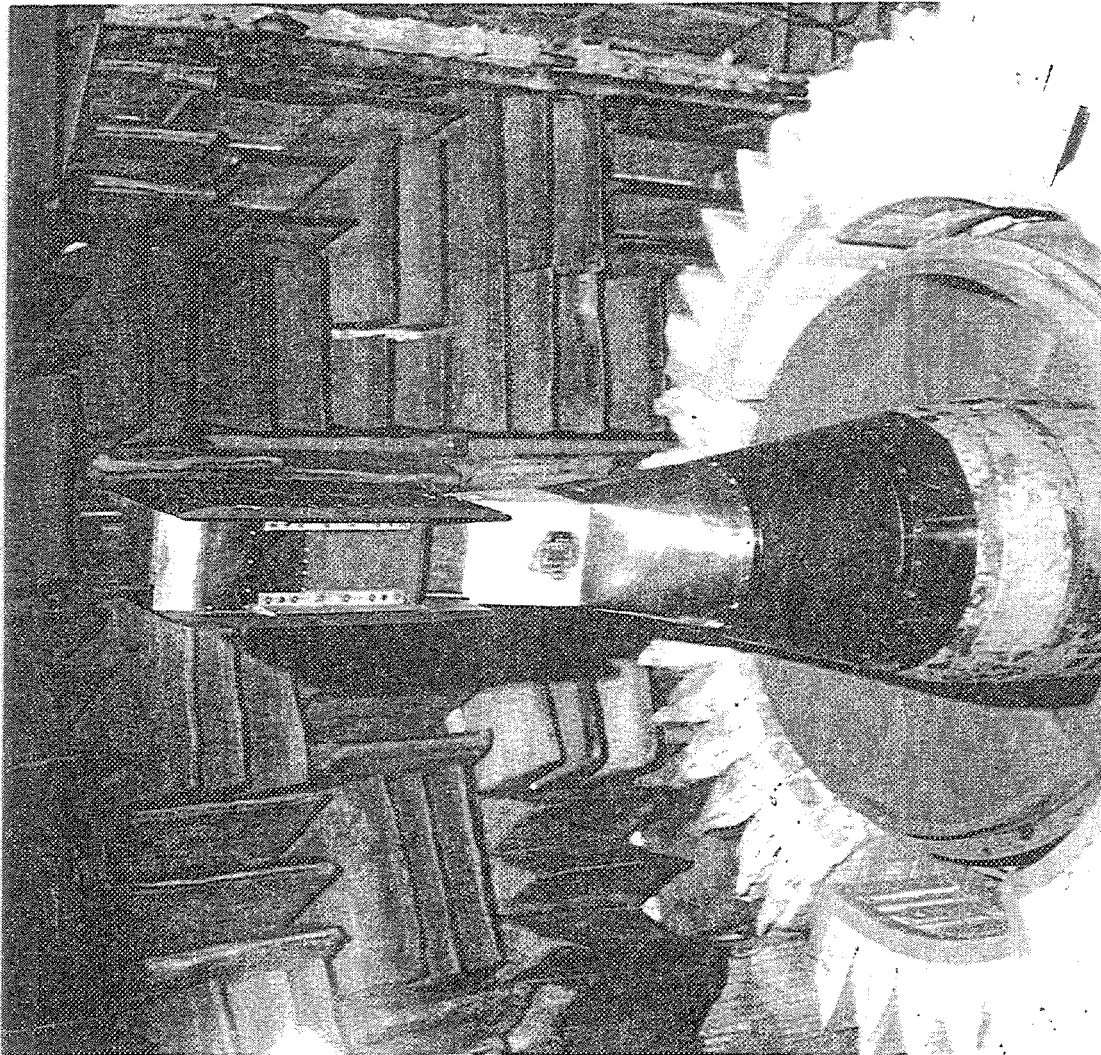
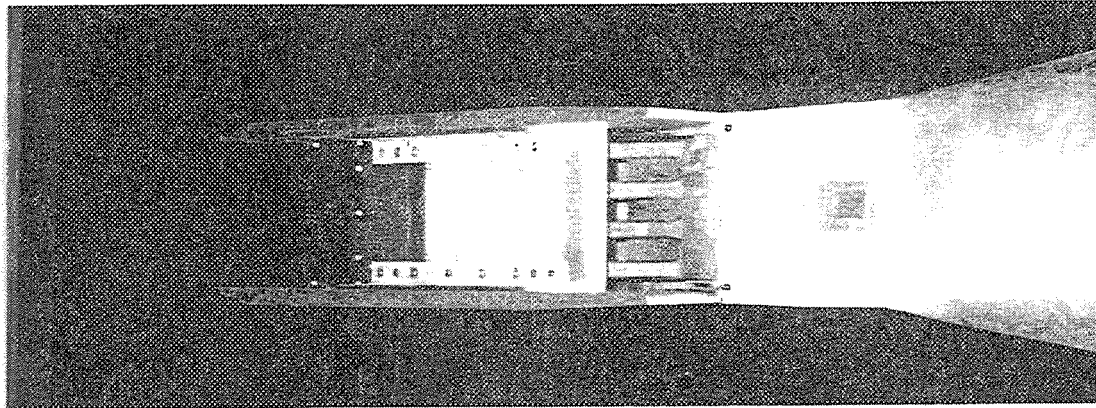


*Figure 1. Mixer-Ejector Model Mounted in Acoustic Test Facility*

### 3. TEST APPARATUS

#### 3.1 ACOUSTIC TEST FACILITY

The General Electric Aircraft Engines (GEAE) anechoic free-jet noise facility, shown in Figure 2, is a cylindrical chamber 43 ft (13.1 m) in diameter and 72 ft (21.95 m) in height. To render the facility anechoic above 220 Hz, the inner surfaces of the chamber are lined with wedges of fiberglass wool. The facility can accommodate model configurations up to 5.3 in. (13.5 cm) and 5.5 in. (14.0 cm) equivalent flow diameter in the inner and outer flow streams, respectively. The corresponding throat areas for these streams are 22 in<sup>2</sup> and 24 in<sup>2</sup>. The streams of heated air for the dual-flow arrangement, produced by two separate natural gas burners, flow through silencers and plenum chambers before entering the test nozzle. The operating domain of the facility in terms of total temperature, pressure ratio, mass flowrate, and jet velocity is indicated in Figure 3 for single-flow and dual-flow operation under static and simulated flight operation. Each stream can be heated to a maximum of 1960°R with the nozzle pressure ratio (NPR) as high as 5.5, resulting in a maximum jet velocity of 3000 ft/sec. Since the nozzle configurations have a single stream in the present program, the flow was provided through the core burner/flow delivery plenum system.

The tertiary air stream system consists of a 250,000 scfm (at 50 in. of water column static pressure) fan and a 3500 horsepower electric motor. The transition duct work and silencer route the air from the discharge through the 48-in. (1.2-m) diameter free-jet exhaust. The silencer reduces the fan noise by 30 to 50 dB. Tertiary flow, at its maximum, permits simulation up to a Mach number (Mn) of 0.4. Mach number variation is achieved by adjusting the fan inlet vanes. The combined model and free-jet airflow is exhausted through a T-stack silencer directly over the models in the ceiling of the chamber. The T-stack is acoustically treated to prevent high-level noise transmission to the surrounding community.

##### 3.1.1 Facility Instrumentation and Model Orientation

Figure 2 shows the facility is equipped with two systems of arrayed microphones to measure the acoustic characteristics of the test models in the far field: a fixed array of microphones, and an array on a traversing tower. The fixed array has 17 microphones mounted from the false floor, the wall, and the ceiling of the test cell. These microphones provide measurements at a minimum distance of 26.75 ft (8.15 m) from the nozzle reference location, covering the polar angle ( $\theta$ ) range from 50 to 155 degrees. The traversing tower contains 13 microphones mounted at polar angles ranging from 45 to 155 degrees. The tower-mounted microphones provide measurements at a distance of 22 ft (6.7m) from the nozzle reference location. The traversing tower can be positioned at any azimuthal angle ( $\psi$ ) between +55 and -55 degrees with respect to the fixed microphone array.

The Pratt & Whitney (P&W) two-dimensional (2D) mixer-ejector nozzles were assembled in the orientation shown in Figure 4. The nozzle major axis was rotated 30 degrees from the north-south facility center line. Community noise measurements were acquired along the nozzle minor axis with the traversing tower at  $\psi = 75$  degrees. The sideline noise measurement location was defined as 25 degrees below the nozzle major axis (determined from the nominal aircraft altitude of 689 ft and a 1476-ft sideline distance), corresponding to a tower position of  $\psi = 10$  degrees. The fixed microphones acquired data at  $\psi = 45$  degrees. Table 1 describes the relationship between the test facility tower position and the angle relative to the engine major axis.

Table 1. Microphone Positions

<i>Position</i>	<i>Sideline (deg)</i>	<i>Fixed Microphones (deg)</i>	<i>Community (Overhead) (deg)</i>
Facility Tower Position ( $\psi$ )	10	45	75
Angle Relative to Engine Major Axis	25	60	90

### 3.1.2 Data Acquisition

The test facility is supported by well-calibrated acoustic and aerodynamic data acquisition systems. Acoustic data measured by both microphone arrays is analyzed by the online system. The online system computes 1/3-octave band data for the model scale at a 40-ft arc, corrected to standard day conditions (59°F, 70 percent relative humidity (PRH)). Narrowband data is measured and recorded on magnetic tapes for postprocessing. All static and total pressures (including model surface pressures) are measured using an aerodynamic data acquisition system. This system consists of multiport scanivalve-contained pressure transducers, signal conditioner, and analog/digital converters. Pressure signals are supplied to a MicroVAX computer system for analysis, or for downloading to the mainframe computer system. Concurrently, a front-end computer with touch screen application is used for signal and facility control, and for real-time data monitoring. Temperature data (thermocouple signals) are fed directly to the front-end computer.

### 3.1.3 Laser Doppler Velocimeter Test Capability

The test facility is equipped with a laser doppler velocimeter (LDV) system (i.e., a three dimensional laser fiber flow system) that was used in the 2D mode to obtain axial and shroud-to-shroud flow velocity component information (Figure 5). The optical system consists of a 60-mm diameter fiber optic probe, a 1.9X beam expander, and a 1.5X beam expander with 140-mm diameter front lens. The focal length of this lens is 200 mm. The optical system has a 3.27234-degree beam angle, a 114.2572 mm-beam distance, 36 fringes, and a 9.0096-micron fringe spacing. The laser doppler anemometer system is modified to obtain online data from a counter processor with an x-y plotter using a Fluke 172A computer. The seeding of each flow stream is provided by individual 100-psi vacuum pumps. For high-temperature flow, 1-micron alumina powder is used for seeding.

The flow velocity is obtained from a counter/processor through a digital/analog converter that provides a voltage-related Doppler frequency and a Bragg cell frequency of 40 MHz. The measured voltage is converted to flow velocity (meters/second) using the following:

$$\text{Flow Velocity (m/sec)} = [(\text{Voltage} \times \text{Amplification Factor}) - 40 \text{ MHz}] \times \text{fringe spacing (microns)}$$

The amplification factor for the present system is 100 with a 9.0096-micron fringe spacing. While instantaneous data were plotted on the x-y plotter, the measured data and the corresponding laser locations were digitized simultaneously, averaged with 20 readings, and stored in the Fluke computer.

## 3.2 HARDWARE

### 3.2.1 Pratt & Whitney Baseline Round Convergent Nozzle

A round, convergent, unshrouded nozzle was used as the acoustic baseline for testing. The baseline nozzle, designed by NASA Langley Research Center, has a throat area that is equal to the nominal mixer-ejector primary nozzle throat area ( $8.25 \text{ in}^2$ ) (Figure 6).

### 3.2.2 Pratt & Whitney 2D Mixer-Ejector Nozzles

The P&W 2D High-Speed Civil Transport (HSCT) mixer-ejector nozzle models consisted of a mixer and an ejector shroud formed by two parallel flat sidewalls held nominally 6.8-in. apart. Two adjustable flaps or shrouds completed the ejector assembly. Figures 7, 8, and 9 describe the hardware. The mixer exit plane was axially located at the minimum shroud area. Two different length ejector shrouds were tested: short [10.46 in. (120 in. full scale)], and long [18.85 in. (216 in. full scale)]. For each ejector length, two types of internal wall treatment were tested: 1) hardwall, and 2) treated, using bulk absorber filled honeycomb acoustic panels. The acoustic panels covered the interior surfaces of the long and short ejector shrouds from the shroud throat to 2.58 in. (model scale) from the shroud exit.

#### 3.2.2.1 Variation of Shroud and Mixing Area Ratios

The movable shrouds allowed variation of the two principle area ratios used to describe the test configurations. Figure 8 describes these ratios. The shrouds were moved parallel to each other to adjust the shroud area ratio (SAR), effectively changing the shroud throat height and area. The SAR is the ratio of the total shroud cross-sectional area at the mixer exit ( $A_{\text{mix}}$ ) to the throat area of the primary mixer ( $A_{g*}$ ). The nominal shroud throat height was set to 6.0 in. or 5.4 in., with a fixed shroud width of 6.8 in., yielding nominal SARs of 4.9 and 4.4, respectively. The mixing area ratio (MAR) was changed by installing angled brackets to hold the shroud flaps. (The MAR is the ratio of the total shroud exit area ( $A_{\text{exit}}$ ) to total shroud cross-sectional area at  $A_{\text{mix}}$ .) Brackets were designed to give nominal MARs of 1.19, 0.97, and 0.88. A MAR greater than 1.0 denotes a diverging shroud mixing region, and a MAR less than 1.0 denotes a convergent mixing region. The shrouds were always adjusted symmetrically to produce an axial thrust vector.

The cold-inspected model dimensions, areas, and area ratios for the P&W 2D mixer-ejector acoustic and hard-wall models are shown in Tables 2 and 3, respectively. Configurations 19 through 21 were inspected near the end of the test program. The inspections show that the sidewalls of the long ejector had spread apart approximately 0.050 in. at the shroud exit. The brackets that hold the shroud to the sidewalls did not extend to the end of the shroud, but ended about 7.6 in. forward of the shroud exit. This spreading was attributed to the unconstrained thermal growth of the hot interior surface of the shroud aft of the bracket ends. The effect of the sidewall spreading on the final model area ratios and test results was considered minimal.

Table 2. Acoustic (i.e., Treated) Configurations --- Cold Inspected Model Dimensions

Configuration/ Mixer (V=Vortical A=Axial)	Shroud Length/ SAR/MAR	Shroud Throat Width (Wm) (in.)	Shroud Exit Width (We) (in.)	Shroud Throat Height (Hm) (in.)	Shroud Exit Height (in.)	$A_{mix}$ (Wm x Hm) (in <sup>2</sup> )	$A_{exit}$ (We x He) (in <sup>2</sup> )	SAR ( $A_{mix}/A_{g*ave}$ ) $A_{g*ave}=8.33 \text{ in}^2$	MAR ( $A_{exit}/A_{mix}$ )
2/V	Lng/4.9/1.18	6.803	6.803	5.980	7.120	40.68	48.44	4.88	1.19
3/V, 13/A	Lng/4.9/0.97	6.803	6.803	6.000	5.843	40.82	39.75	4.90	0.97
4/V	Lng/4.9/0.88	6.803	6.803	6.000	5.300	40.82	36.06	4.90	0.88
21/A	Lng/4.9/0.88	6.800	6.853	6.094	5.200	41.44	35.64	4.97	0.86
5/V	Lng/4.4/0.97	6.803	6.803	5.395	5.237	36.70	35.63	4.41	0.97
6/V	Lng/4.4/0.88	6.803	6.803	5.394	4.695	36.70	31.94	4.41	0.87
7/V	Lng/4.4/1.18	6.803	6.803	5.387	6.508	36.65	44.27	4.40	1.20
18/V	Shrt/4.4/1.185	6.802	6.802	5.392	6.492	36.68	44.16	4.40	1.20

Table 3. Hardwall Configurations --- Cold Inspected Model Dimensions

Configuration/ Mixer (V=Vortical A=Axial)	Shroud Length/ SAR/MAR <sup>1</sup>	Shroud Throat Width (Wm) (in.)	Shroud Exit Width (We) (in.)	Shroud Throat Height (Hm) (in.)	Shroud Exit Height (in.)	$A_{mix}$ (Wm x Hm) (in <sup>2</sup> )	$A_{exit}$ (We x He) (in <sup>2</sup> )	SAR ( $A_{mix}/A_{g*ave}$ ) $A_{g*ave}=8.33 \text{ in}^2$	MAR ( $A_{exit}/A_{mix}$ )
8/V/14V	Lng/4.9/1.18	6.800	6.800	5.982	7.040	40.68	47.87	4.88	1.18
9/V	Lng/4.9/0.97	6.800	6.800	5.990	5.731	40.73	38.97	4.89	0.96
19/A	Lng/4.9/0.97	6.800	6.854	5.990	5.731	40.73	39.28	4.89	0.96
20/A	Lng/4.9/0.88	6.800	6.853	6.094	5.200	41.44	35.64	4.97	0.86
10/V	Lng/4.4/1.18	6.800	6.800	5.380	6.436	36.68	43.76	4.39	1.19
11/V	Lng/4.4/0.97	6.800	6.800	5.395	5.128	36.69	34.87	4.40	0.95
12/V	Lng/4.4/0.88	6.800	6.800	5.394	4.617	36.68	31.40	4.40	0.86
15/V, 16A	Shrt/4.9/1.185	6.802	6.806	5.997	7.093	40.79	48.27	4.90	1.18
17/V	Shrt/4.4/1.20	6.802	6.806	5.424	6.508	36.89	44.27	4.43	1.20

<sup>1</sup> Note: long shroud length = 18.85 in.; short shroud length = 10.46 in.



### 3.2.2.2 Mixer Design

Two mixer nozzles were tested. Both mixers were convergent-divergent type with an inspected core expansion area ratio (CER) of 1.422 to 1.427. The nozzles were the result of an intensive computational fluid dynamics (CFD) study that optimized lobe geometry to establish the best-mixing nozzles within the constraints of the existing geometry. The cold-inspected areas for the two mixers are shown in Table 4.

Table 4. Cold-Inspected Mixer Areas

Mixer	Throat Area ( $A_{g*}$ ) ( $\text{in}^2$ )	Exit Area ( $A_g$ ) ( $\text{in}^2$ )	Core Expansion Area Ratio (CER) ( $A_g/A_{g*}$ )
Vortical	8.31	11.86	1.427
Axial	8.35	11.87	1.422
Average Mixer Throat Area ( $A_{g*ave}$ )	8.33		

#### 3.2.2.2.1 Vortical Mixer

The nozzle is roughly rectangular with four lobes on each side (Figure 10). The design is intended to be shock-free at a design condition of  $\text{NPR} = 4.5$  and total temperature ( $T_t$ ) = 2100°R. The vortical mixer nozzle has an  $A_{g*}$  of 8.31  $\text{in}^2$  and a measured exit area of 11.86  $\text{in}^2$ . The vortical mixer nozzle is named for the large-scale vorticity it generates, leading to rapid mixing. The design is inherently more compact, generating relatively low wetted-area loss.

#### 3.2.2.2.2 Axial Mixer

In an axial mixer, the hot primary flow is turned axially before it exits the four rectangular lobes (Figure 11). There is no gap between the valleys of the lobes to avoid the expected hot region found in earlier designs with this gap. The nozzle was designed to be shockfree at the design condition of  $\text{NPR} = 4.5$  and  $T_t = 2100^\circ\text{R}$ . The mixer nozzle has an  $A_{g*}$  of 8.35  $\text{in}^2$  and a measured exit area of 11.87  $\text{in}^2$ . The axial mixer nozzle mixes primarily by using large amounts of shear layer. The axial nature of its discharge generates less thrust loss than the vortical mixer nozzle. However, this longer, less compact nozzle should provide less rapid mixing and a higher frictional loss due to its larger size.

#### 3.2.2.2.3 Mixer Penetration

Mixer penetration (PEN) is defined as the ratio of the maximum mixer exit height ( $H_{mxe}$ ) divided by the shroud throat height ( $H_m$ ). Figures 10 and 11 show the maximum exit heights for the vortical mixer ( $H_{mxe}=3.930$  in.) and axial mixer ( $H_{mxe}=5.460$  in.). With  $\text{SAR}=4.9$  ( $H_m=6.0$ ), the vortical and axial mixers were nominally 65 percent and 90 percent penetrated, respectively. With  $\text{SAR}=4.4$  ( $H_m=5.4$ ), the vortical mixer penetration increased to 73 percent. The axial mixer was not tested with  $\text{SAR}=4.4$  because of mixer-shroud interference.

### 3.2.2.3 Ejector Shroud Liner Design

The walls of the ejector shroud were designed to hold acoustic panels on all four interior surfaces. Test results under Task 11 of the Aeropropulsion Technology contract (NAS3-25952) indicated superior acoustic performance was provided by the honeycomb and perforated plate acoustic panel with bulk absorber. The bulk absorber panels provide broad spectrum sound attenuation and are relatively insensitive to scaling and noise source uncertainties. Due to durability concerns, the bulk absorber panel is not realistic for production use; however, the acoustic perfor-

mance of the panels is representative of good design. Programs are underway to develop a design system for realistic production acoustic treatments that provide similar acoustic performance.

The shroud length-to-diameter ratio ( $L/D$ ) for the acoustically treated configurations is shown in Table 5. The parameter was calculated for the P&W 2D mixer-ejector shroud using the following equation:

$$L/D = 1/4 (A_{\text{treated}}/A_{\text{cross average}})$$

where  $A_{\text{treated}}$  is the effective acoustically treated surface area inside the ejector shroud, and 'across average' is the average cross-sectional flow area of the shroud. The  $A_{\text{treated}}$  term does not include the acoustic treatment area within five lobe widths of the mixer exit. This area was assumed to be ineffective because of the high mixing rate within this region.

*Table 5. Pratt & Whitney 2D Mixer-Ejector L/D*

<i>Treated Shroud</i>	<i>SAR</i>	
	<i>4.4</i>	<i>4.9</i>
Long	2.2	2.1
Short	0.81	0.77

The acoustic panels were constructed by packing a fibrous Kevlar material (Astroquartz) into stainless steel honeycomb, backed by a 0.010-in. thick stainless steel plate, to a density of 4.5 lb/ft<sup>3</sup>. The honeycomb was 0.5-in. deep with 0.375-in. cell width, and 0.010-in. cell wall thickness. The packed honeycomb was covered with a 0.025-in. thick, 34-percent open porous stainless steel plate.

#### **3.2.2.3.1 Liner Deterioration During Testing**

The acoustic panels began to show deterioration following testing of the vortical mixer with SAR = 4.4, after approximately 120 hours of testing with hot primary flow (Figure 12). Previous tests with this liner (Astroquartz bulk material packed in a honeycomb matrix) had shown good durability; however, testing was generally of a shorter duration. With the lower SAR, the ejector walls were positioned inward, closer to the mixer exit. This subjected the bulk material to more hot flow impingement, and allowed the hot flow to attach to the ejector walls. This positioning is believed to contribute to the deterioration. The binding agent that holds the Astroquartz fibers appeared to evaporate after extended high-temperature testing, allowing the fibers to be blown out of the panels through the porous plate. The availability of replacement panels facilitated evaluation of the effect of the panel degradation. Vortical mixer Configurations 5 and 7 with SAR = 4.4 were run with the deteriorated panels; configurations 5R and 7R are those same configurations retested with undamaged panels.

#### **3.2.3 Model Instrumentation**

Figures 13 and 14 show the instrumentation positions on the mixer models. Ten pressure taps and four thermocouples were placed on each mixer model. Five pressure taps and two thermocouples faced the hot primary flow, with the remaining five pressure taps and two thermocouples facing the cool secondary or entrained flowpath. There were 20 static pressure taps installed on the internal surfaces of the long and short hardwall ejector shrouds. Figure 15 describes the locations of the upper ejector shroud pressure taps. The taps are located along the shroud centerline. There were no taps on the lower shroud.



### 3.3 TEST PROGRAM

#### 3.3.1 Model Configurations

The configurations were selected based on joint discussions among NASA Lewis Research Center (NASA-LeRC), P&W, and GEAE to investigate the effects of mixer design, shroud length, flowpath area ratios, and shroud treatment. All configurations were tested for noise. Aerodynamic data were obtained during noise testing of the hardwall configurations, which were instrumented with static pressure taps on the internal shroud walls. Selected configurations were tested with LDV to map the velocity fields inside the shroud, and externally downstream of the nozzle exit. Table 6 describes the configurations tested.

#### 3.3.2 Test Plan

##### 3.3.2.1 Test Point Matrix

The test point matrix is constructed around the GE21/F14 LIM cycle for the 2.4-Mn HSCT. This cycle matches the other major engine cycles under current consideration up to maximum dry setting (Power Code 50). Figure 16 compares GEAE's VCE LIM, mixed flow turbfans (MFTFs) A-5, A-17, and A-23, and P&W's STJ989 TBE cycles with plots of NPR and  $T_{18}$  versus nozzle ideal velocity. Figure 17 shows the cycles represented as a NPR versus  $T_{18}$  plot. Also shown are the cycle conditions of currently operational standard F404-400 engines up to maximum dry, which is a representative MFTF, and the prime candidate test bed engine for the planned HSCT Critical Propulsion Component Program. The GE LIM, A-5, A-17, and A-23 cycles are essentially the same for operation from idle to maximum dry. They differ from each other as the afterburner (A/B) is ignited. The NPR lines flatten at about 3 to 4 for all these cycles as A/B is introduced, and the  $T_{18}$  lines quickly rise away from the clustered cycles as A/B is introduced. The F404 cycle has higher  $T_{18}$  at lower jet velocities (and NPRs) up to about 1500 ft/sec (and NPR = 2). At higher jet velocities, this cycle is very close to the LIM cycle. The STJ989 cycle has slightly higher  $T_{18}$  for the entire jet velocity range.

Table 7 shows the 17 points run during the testing. The points are defined by the primary (core) stream nozzle pressure ratio based on ambient pressure, turbine exit total temperature, and the resulting unmixed, ideally expanded, primary jet velocity. Figure 18 illustrates the locations of these points on an NPR versus  $T_{18}$  format. Points 1 through 7 are on the LIM cycle line. Point 8 is also on the LIM line but beyond the initiation of A/B. Point 9 is on the F404-400 cycle and was chosen for future comparison with the F404-400. Point 10 was selected to compare the LDV data and CFD predictions. Points 12 and 13, along with point 5, create a constant velocity line at about  $V_{jet} = 2384$  ft/sec. Points 14 and 15, along with points 6 and 10, form another constant velocity line at about 2520 ft/sec. Point 11, along with points 5, 14, 7, 10, and 12, form two isothermal lines at 1590°R and 1735°R, respectively. Points 4, 11, 12, as well as points 7, 13, and 14, form two iso-pressure-ratio lines at 3 and 4, respectively. Points 16 and 17 were selected to match the test conditions of NASA-LeRC LSWT tests of the same nozzles.

##### 3.3.2.2 Test Conditions

Testing was conducted at Mn=0.0 and Mn=0.32 for all configurations. The first four configurations were also run at Mn=0.36. The first seven configurations were run at Mn=0.30 for test point 5 only. Configurations 1, 2, 8, and 15 were tested at Mn=0.20 for selected points for comparison to data obtained in the NASA-LeRC LSWT. Appendix B shows the acoustic test run schedule for each configuration. Points with  $T_{18}$  labeled hot were run at temperatures similar to the LIM throttle line

Table 6. Pratt & Whitney Two-Dimensional Mixer-Ejector Exhaust Nozzle Configurations

Configurat ion Number	Mixer Type	Shroud Length	Treatment	SAR ( $A_{mix}/A_{g*}$ )	MAR ( $A_{exit}/A_{mix}$ )	Test Type
1	Baseline: 3.241-in. Diameter, Round, Convergent Nozzle					Noise
2	Vortical	Long	Treated	4.9	1.19	Noise
3	Vortical	Long	Treated	4.9	0.97	Noise
4	Vortical	Long	Treated	4.9	0.88	Noise
5	Vortical	Long	Treated	4.4	0.97	Noise
5R (Repeat)	Vortical	Long	Treated	4.4	0.97	Noise
6	Vortical	Long	Treated	4.4	0.87	Noise
7	Vortical	Long	Treated	4.4	1.19	Noise
7R (Repeat)	Vortical	Long	Treated	4.4	1.19	Noise
8	Vortical	Long	Hardwall	4.9	1.18	Noise; Flap Static Pressures; Ext. LDV
9	Vortical	Long	Hardwall	4.9	0.97	Noise; Flap Static Pressures
10	Vortical	Long	Hardwall	4.4	1.18	Noise; Flap Static Pressures
11	Vortical	Long	Hardwall	4.4	0.97	Noise; Flap Static Pressures
12	Vortical	Long	Hardwall	4.4	0.88	Noise; Flap Static Pressures
13	Axial	Long	Treated	4.9	0.97	Noise
14	Axial	Long	Hardwall	4.9	1.18	Noise; Flap Static Pressures; Ext. LDV
15	Vortical	Short	Hardwall	4.9	1.185	Noise; Flap Static Pressures; Ext. LDV; Int. LDV
16	Axial	Short	Hardwall	4.9	1.185	Noise; Flap Static Pressures; Ext. LDV; Int. LDV
17	Vortical	Short	Hardwall	4.4	1.20	Noise; Flap Static Pressures
18	Vortical	Short	Treated	4.4	1.185	Noise
19	Axial	Long	Hardwall	4.9	0.97	Noise; Flap Static Pressures
20	Axial	Long	Hardwall	4.9	0.88	Noise; Flap Static Pressures
21	Axial	Long	Treated	4.9	0.88	Noise

### 3.3.2.3 Aerodynamic Test

Aerodynamic data were obtained for all the hardwall configurations. These data consisted of static pressure distributions along the inner wall of the upper shroud surface from forward of the shroud throat to a point near the shroud exit. The tests were run to investigate the internal shroud flowfield change from subsonic to supersonic as the nozzle was run along the LIM cycle line. All the hardwall configurations were run along the LIM cycle line (hot) at  $Mn=0.0$  and  $Mn=0.32$ , and with ambient temperature at  $Mn=0.0$ . Configurations 14, 15, 17, 19, and 20 were run at  $Mn=0.0$  with warm conditions of  $860^{\circ}R$ . Some tests were run with small changes in NPR and  $T_{t8}$  to capture the point of transition from subsonic to supersonic flow. A check on hysteresis during the change from subsonic to supersonic and back was investigated by increasing NPR and  $T_{t8}$  in small steps to a maximum; then NPR and  $T_{t8}$  were incrementally decreased, repeating the same conditions. The results of this testing are presented and discussed in Section 4.3 of this report.

Table 7. Test Point Definition

Test Point	NPR	$T_{t8}$ ( $^{\circ}R$ )	$V_{jet_{ideal}}$ (ft/sec)
1	1.5	1000	1147
2	2.0	1175	1595
3	2.5	1325	1919
4	3.0	1485	2200
5	3.4	1590	2384
6	3.7	1673	2520
7	4.0	1750	2637
8	4.5	1860	2812
9	3.4	1645	2426
10	3.5	1735	2518
11	3.0	1590	2278
12	3.0	1735	2382
13	4.0	1435	2382
14	4.0	1590	2510
15	4.5	1490	2509
16	3.0	1560	2256
17	4.0	1960	2796

### 3.3.2.4 Laser Doppler Velocimeter Test

The LDV tests were run primarily at  $Mn=0.32$ . Some static data were obtained for selected configurations. Points 3, 8, and 10 (Table 7) were run to obtain LDV velocity data. Point 3 was chosen because of the lower

primary NPR and temperature, which would provide lower internal velocities to facilitate the internal shroud LDV measurements. Table 8 defines the LDV run schedule. Section 4.4 describes the results of the LDV tests.

*Table 8. Laser Doppler Velocimeter Run Schedule*

<i>Mixer</i>	<i>Hardwall Shroud Length</i>	<i>Primary Nozzle Pressure Ratio (NPR)</i>	<i>Primary Total Temperature (°R)</i>	<i>Mach Number (Mn)</i>	<i>Comments</i>
Axial	Short	3.5	1735	0.32	External Plume Survey
		2.5	1325	0.32	
	Long	2.5	1325	0.32	
		3.5	1735	0.32	
				0.0	
		4.5	1860	0.32	
Vortical	Long	2.5	1325	0.32	
		3.5	1735	0.32	
				0.0	
		4.5	1860	0.32	
	Short	2.5	1325	0.32	
		3.5	1735	0.32	
				0.0	
		4.5	1860	0.32	
		3.5	1735	0.32	
				0.0	
		2.5	1325	0.32	
		3.5	1735	0.32	Internal Survey
				0.0	
		2.5	1325	0.32	
		3.5	1735	0.32	
	Long	3.5	1735	0.32	External Plume Survey; Treated Shroud
Axial	Short	3.5	1735	0.32	Internal Survey
		2.5	1325	0.32	
		3.5	1735	0.0	

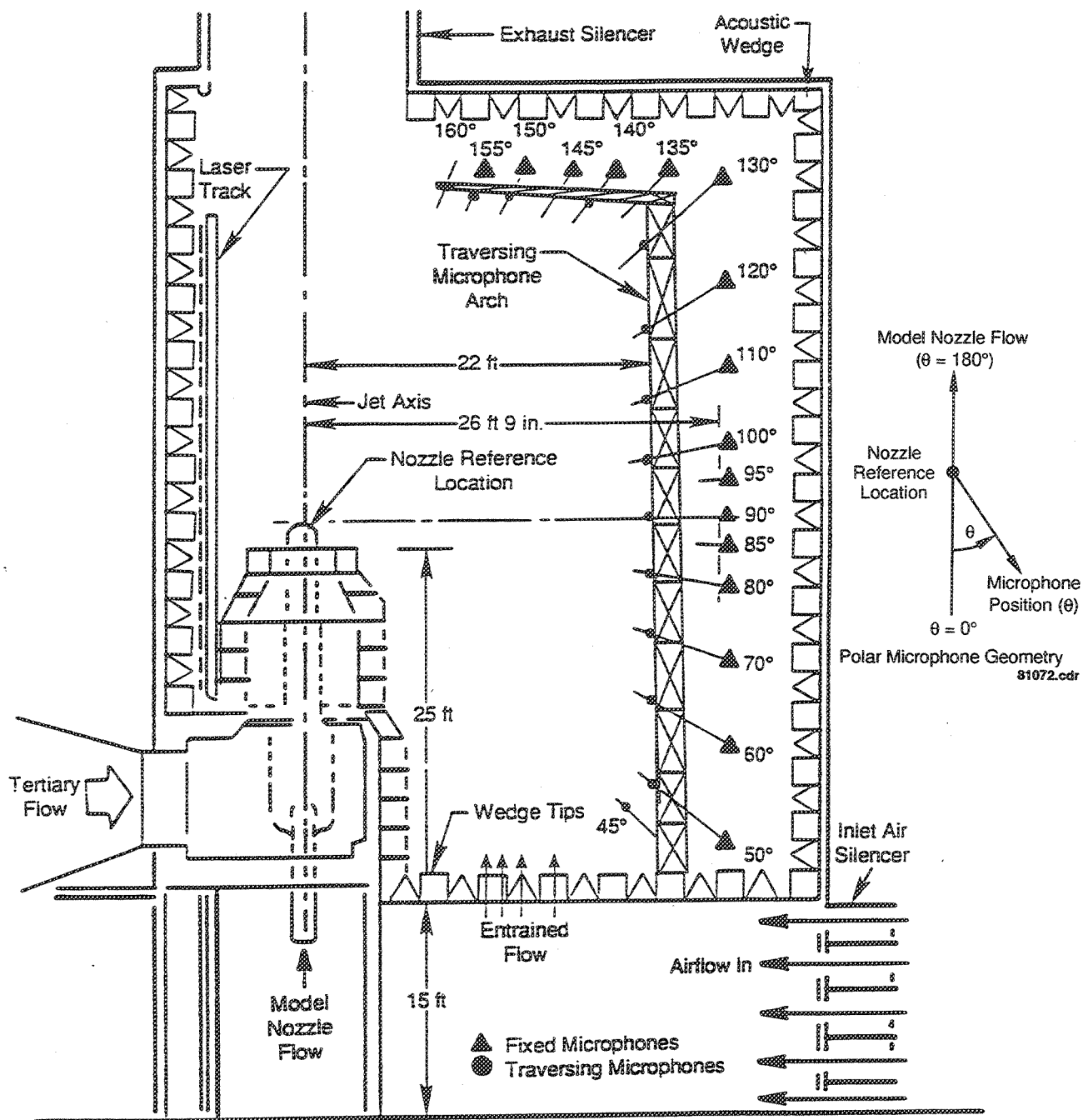


Figure 2. Side View of Cell 41 Anechoic Free-Jet Facility

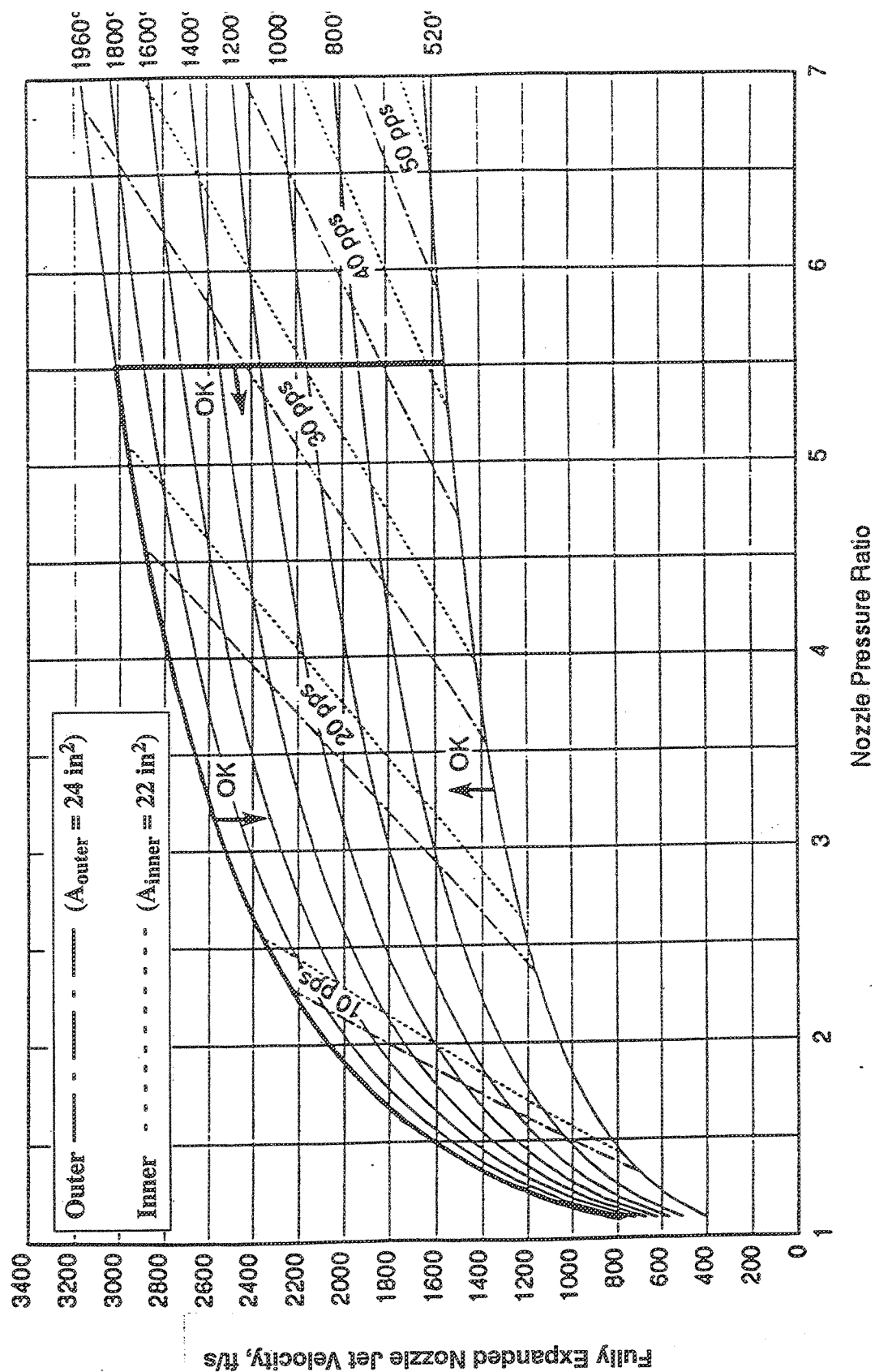


Figure 3. Operating Domain of Cell 41 Anechoic Free Jet Facility

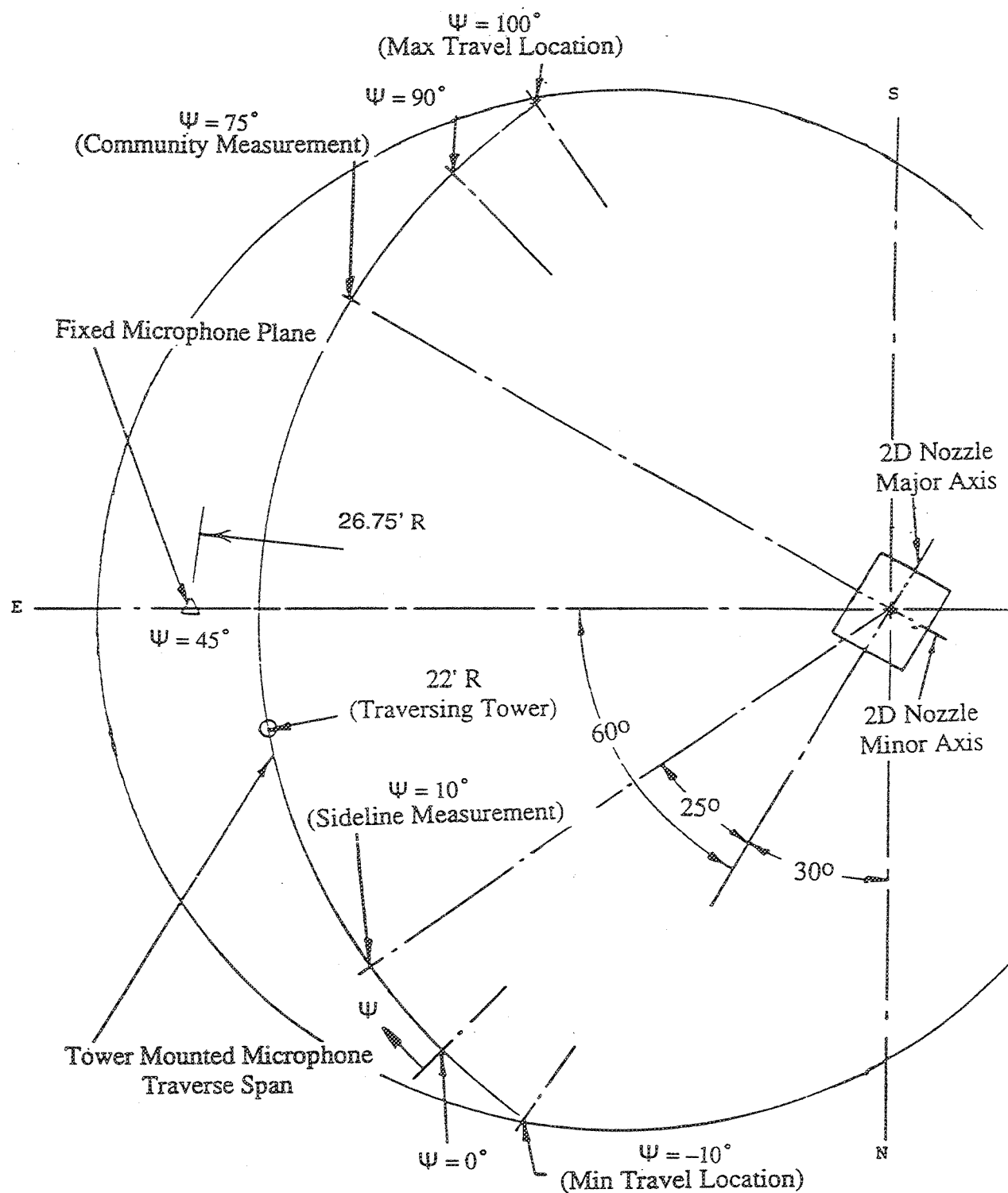


Figure 4. Plane View of Cell 41 Anechoic Free Jet Facility Showing 2D Nozzle Orientation for Acoustic and LV Tests

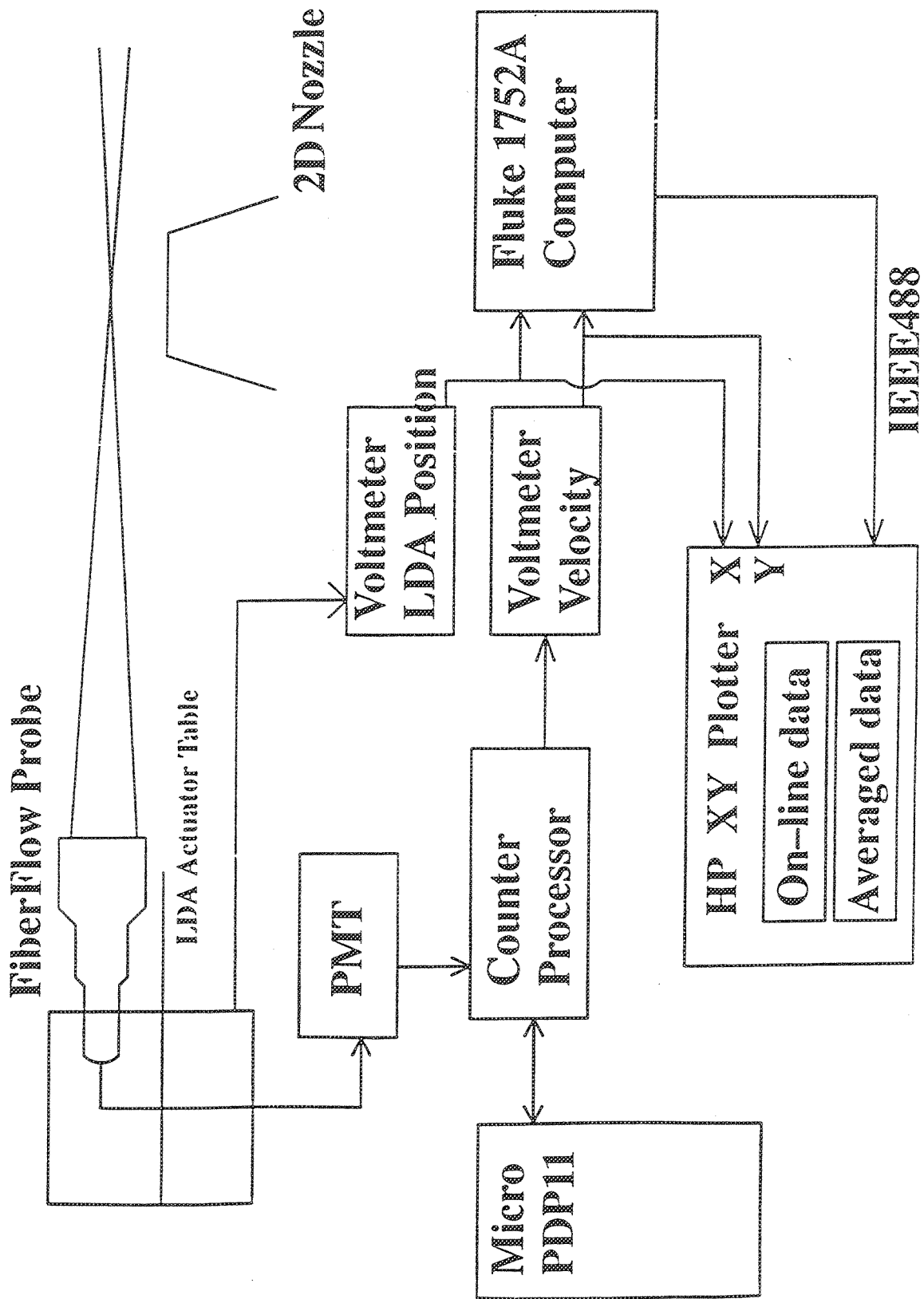
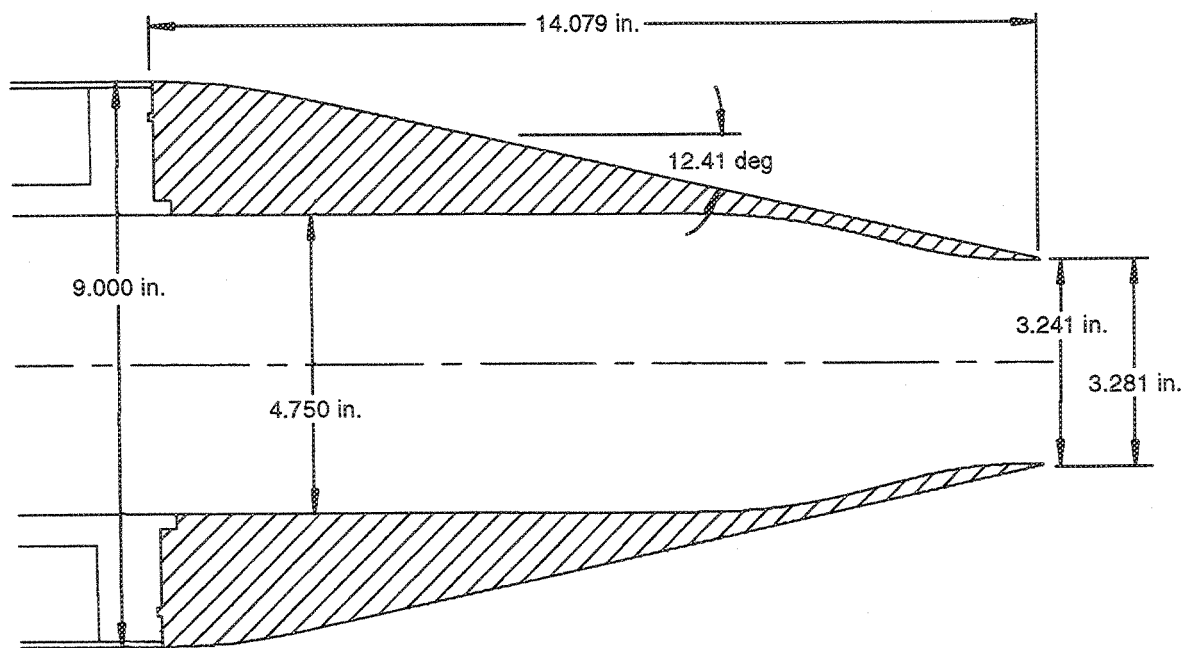


Figure 5. Laser Doppler Velocimeter System





49668

*Figure 6. P&W Baseline Round Convergent Nozzle*

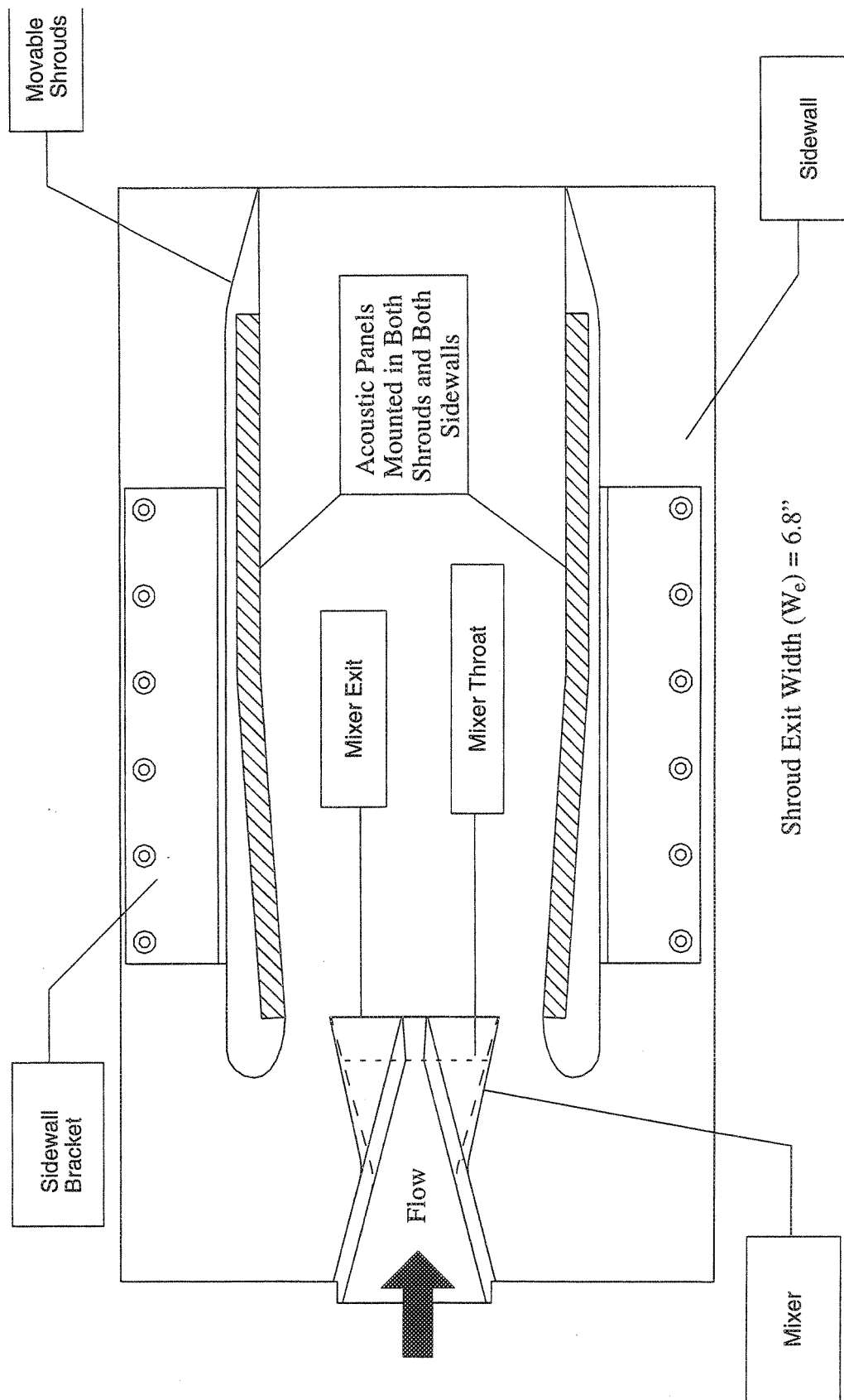
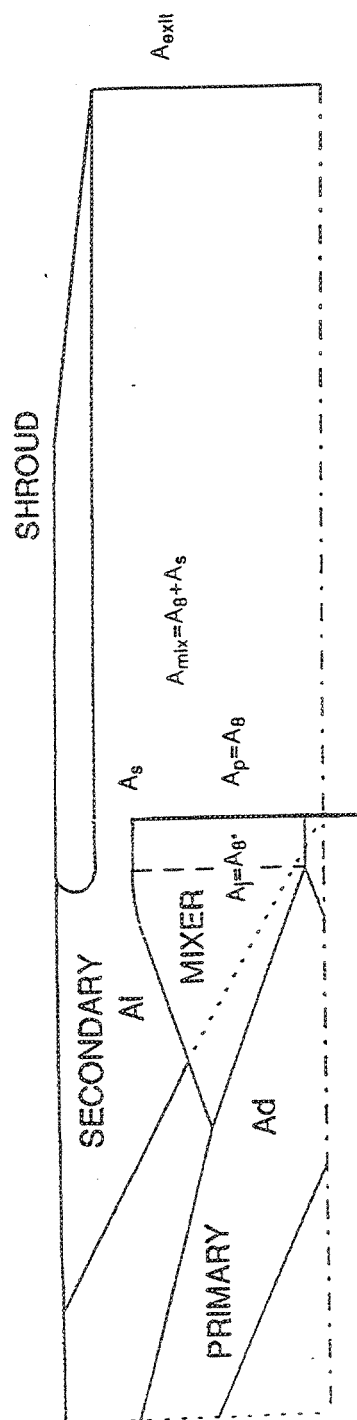


Figure 7. Assembly Drawing for P & W 2D Mixer-Ejector Nozzle



Shroud Throat at Mixer Exit

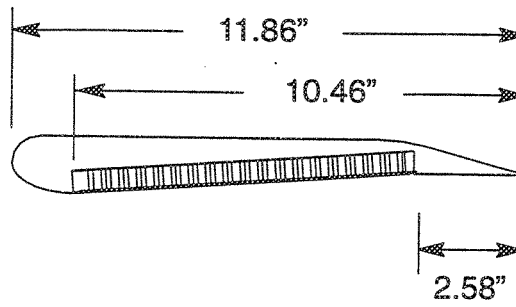
SUBSCRIPTS

Shroud Exit..... exit  
 Secondary Flow Inlet..... i  
 Primary Nozzle Throat..... j or 8\*  
 Mixing Plane..... mix  
 Primary Nozzle Exit..... p or 8  
 Secondary Stream..... s  
 Transition Duct..... d

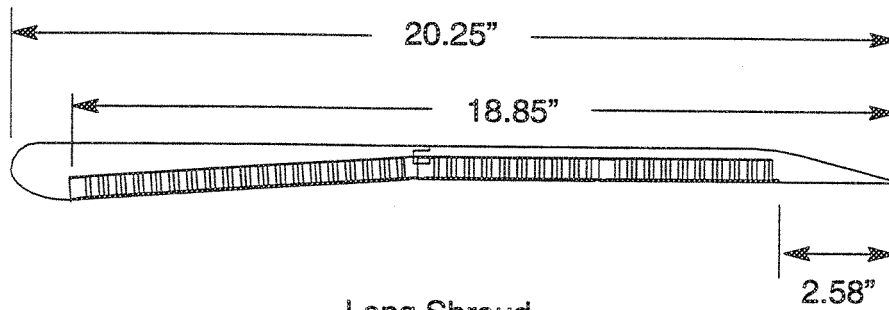
RATIOS

Primary Area Ratio.....  $A_g/A_{g^*}$  CER  
 Shroud Area Ratio.....  $A_{mix}/A_{g^*}$  SAR  
 Mixer Area Ratio.....  $A_{exit}/A_{mix}$  MAR

Figure 8. Mixer/Ejector Nomenclature



Short Shroud



Long Shroud

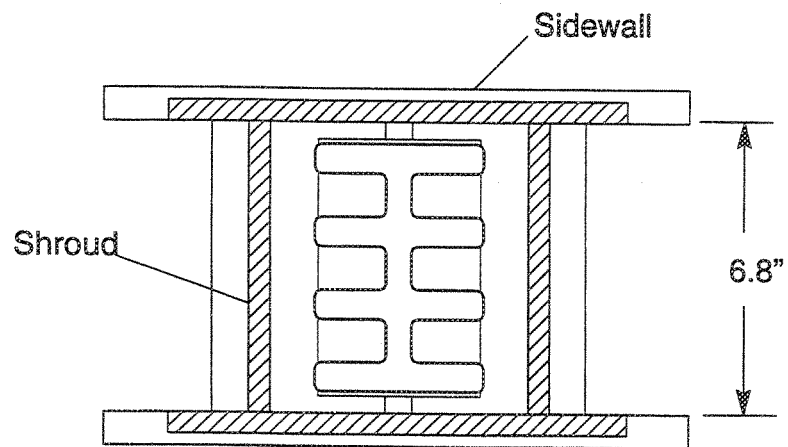
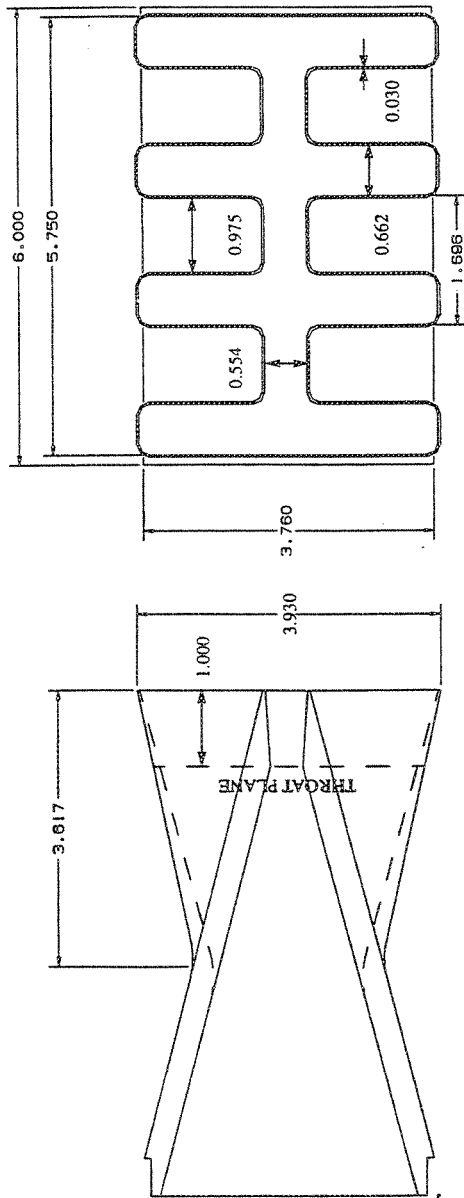
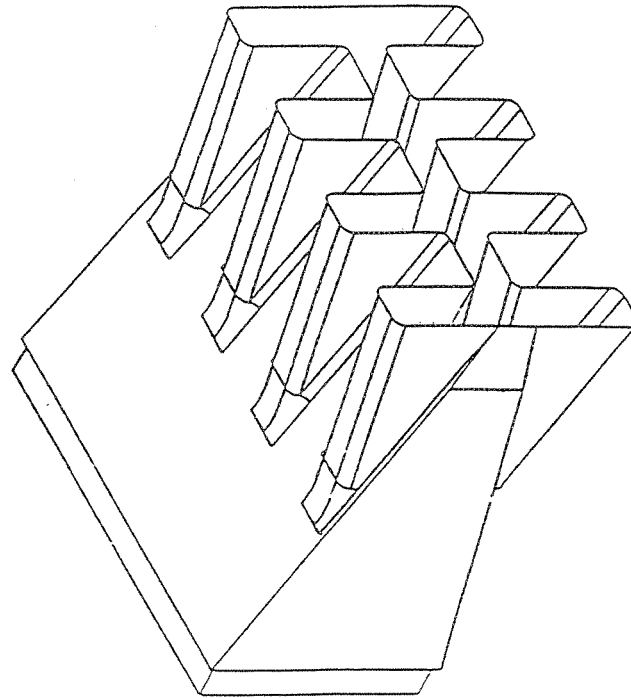


Figure 9. Lined Mixer-Ejector Configuration



View Looking Forward at Mixer Exit



ISOMETRIC VIEW

Figure 10. Geometry of 2D Vortical Mixer Nozzle (All Dimensions in Inches)

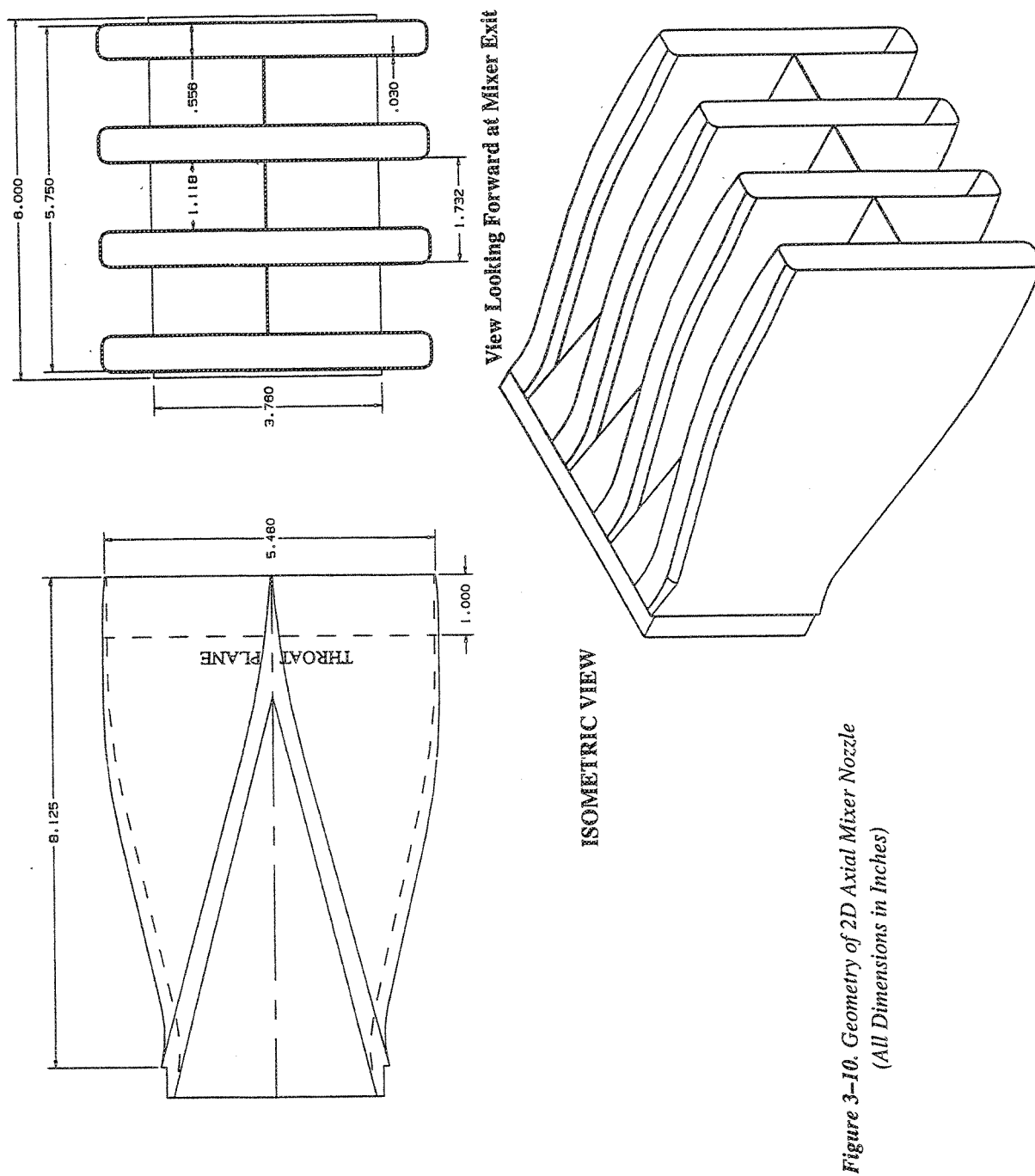
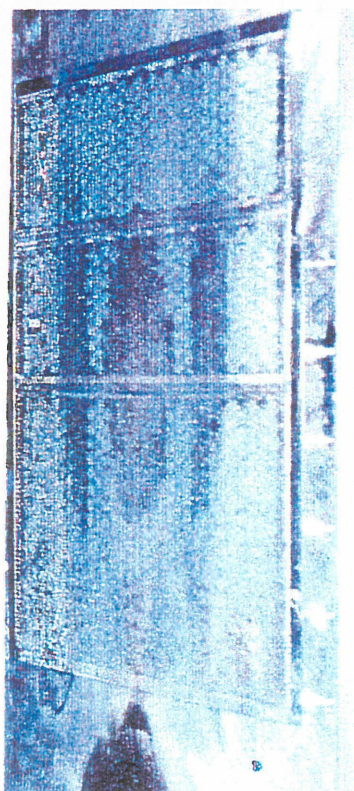
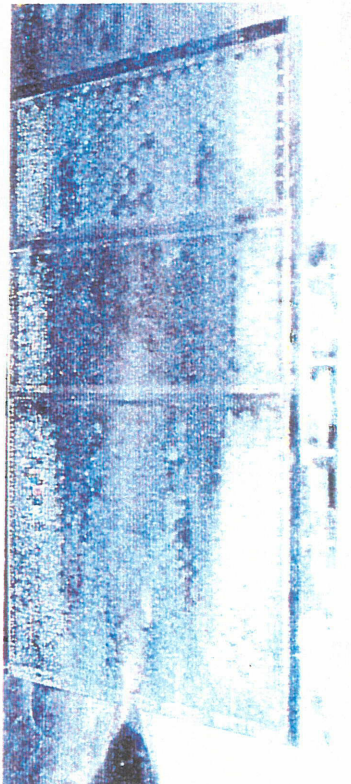


Figure 3-10. Geometry of 2D Axial Mixer Nozzle  
(All Dimensions in Inches)

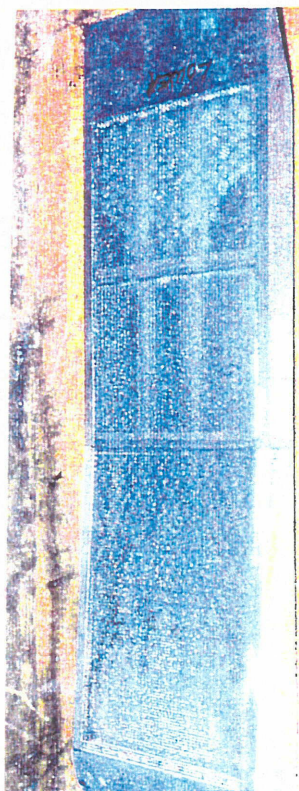
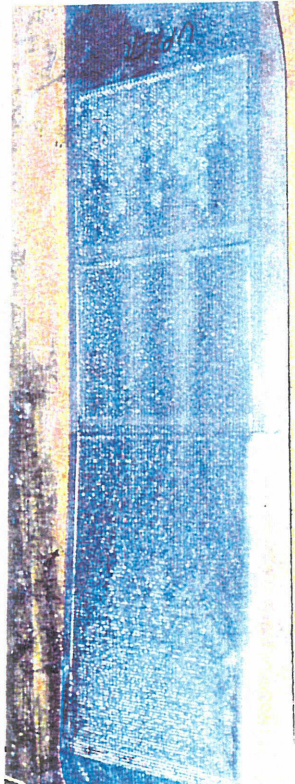
Figure 11. Geometry of 2D Axial Mixer Nozzle (All Dimensions in Inches)

# PW 2D Model : Astroquartz Degradation

Side Panels



Upper/Lower Panels



Flow ⇒

Figure 12. P & W 2D Model – Astroquartz Degradation

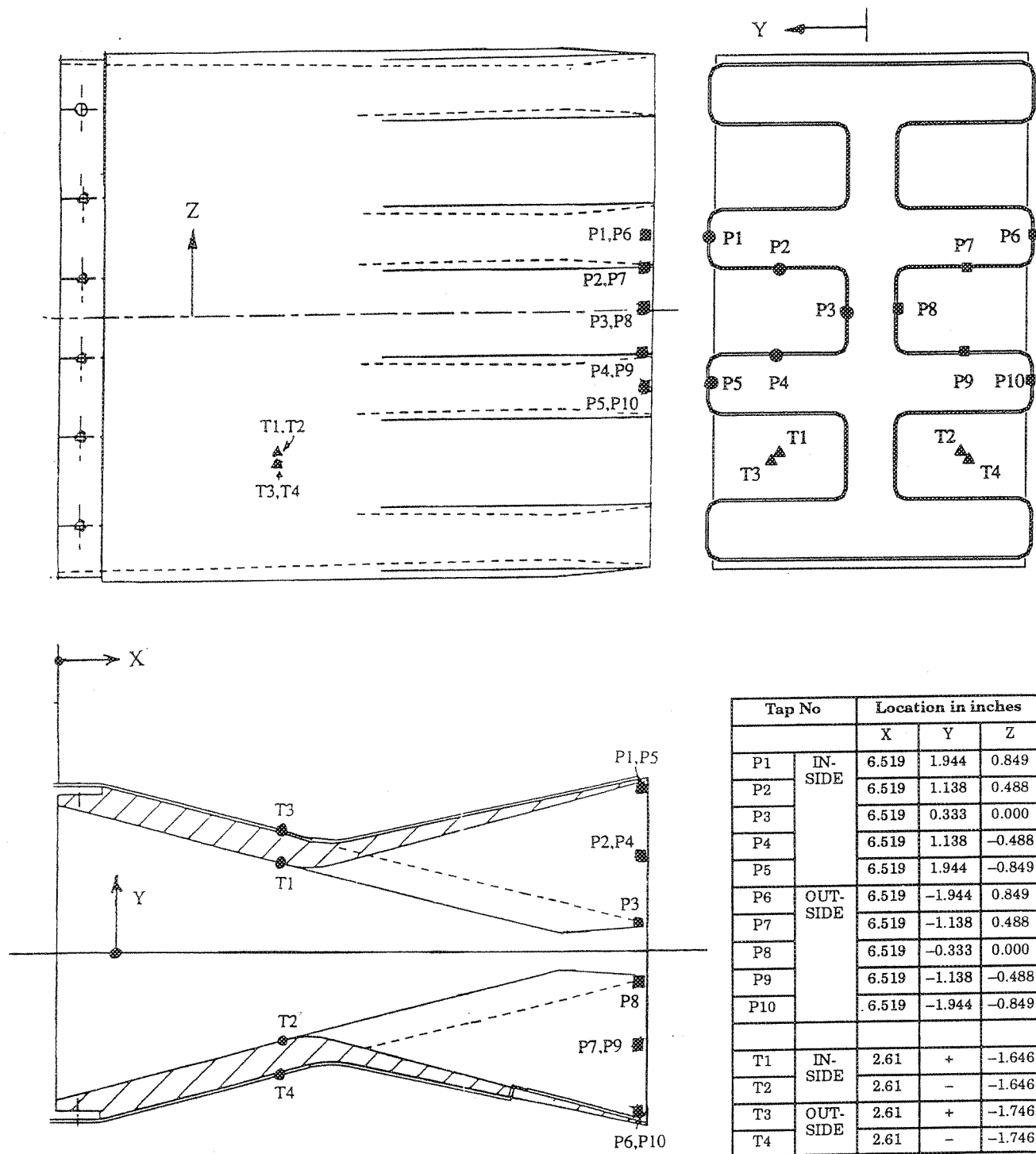


Figure 13. Static Pressure and Thermocouple Instrumentation for Vortical Mixer Nozzle



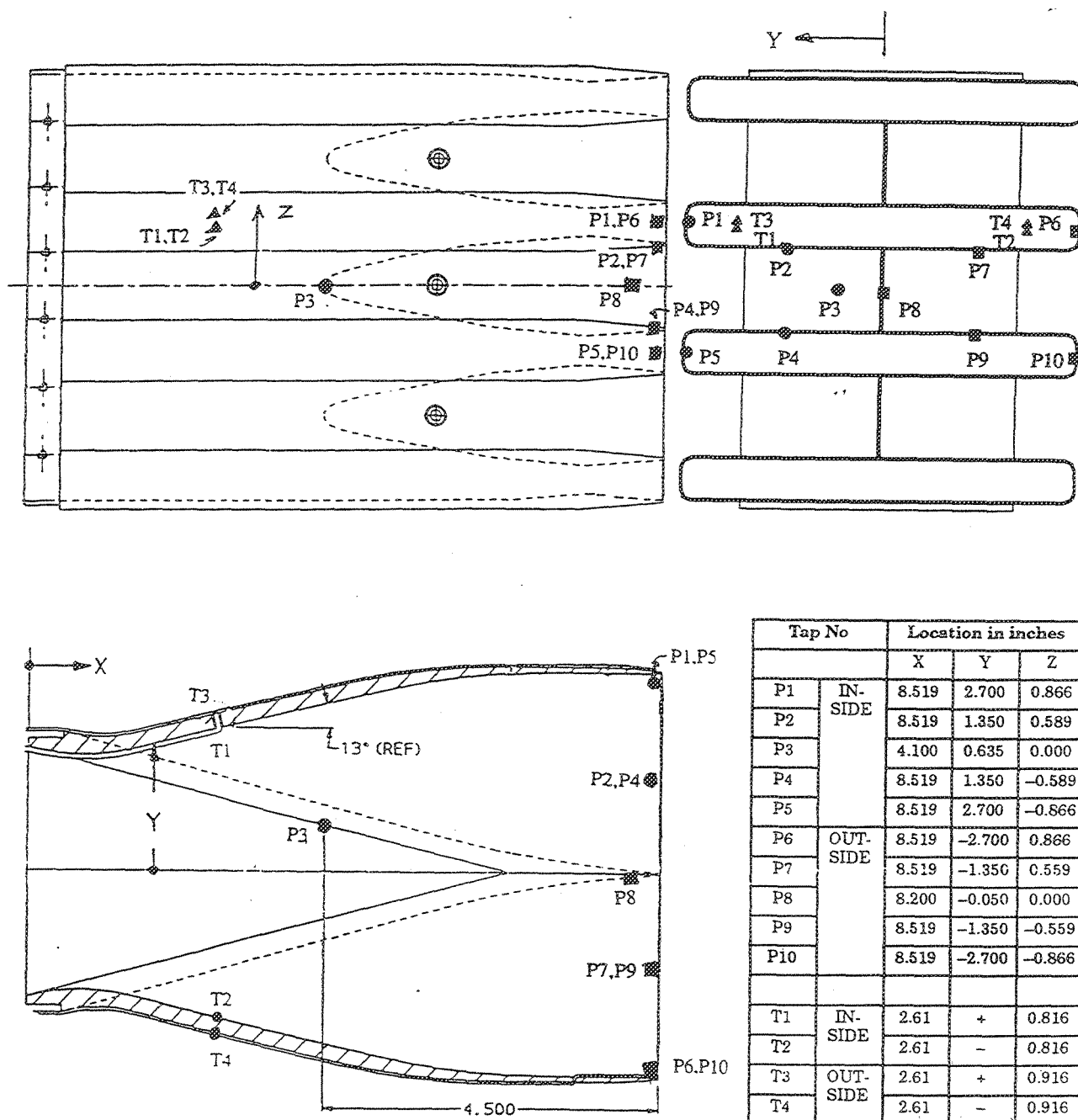


Figure 14. Static Pressure and Thermocouple Instrumentation for Axial Mixer Nozzle

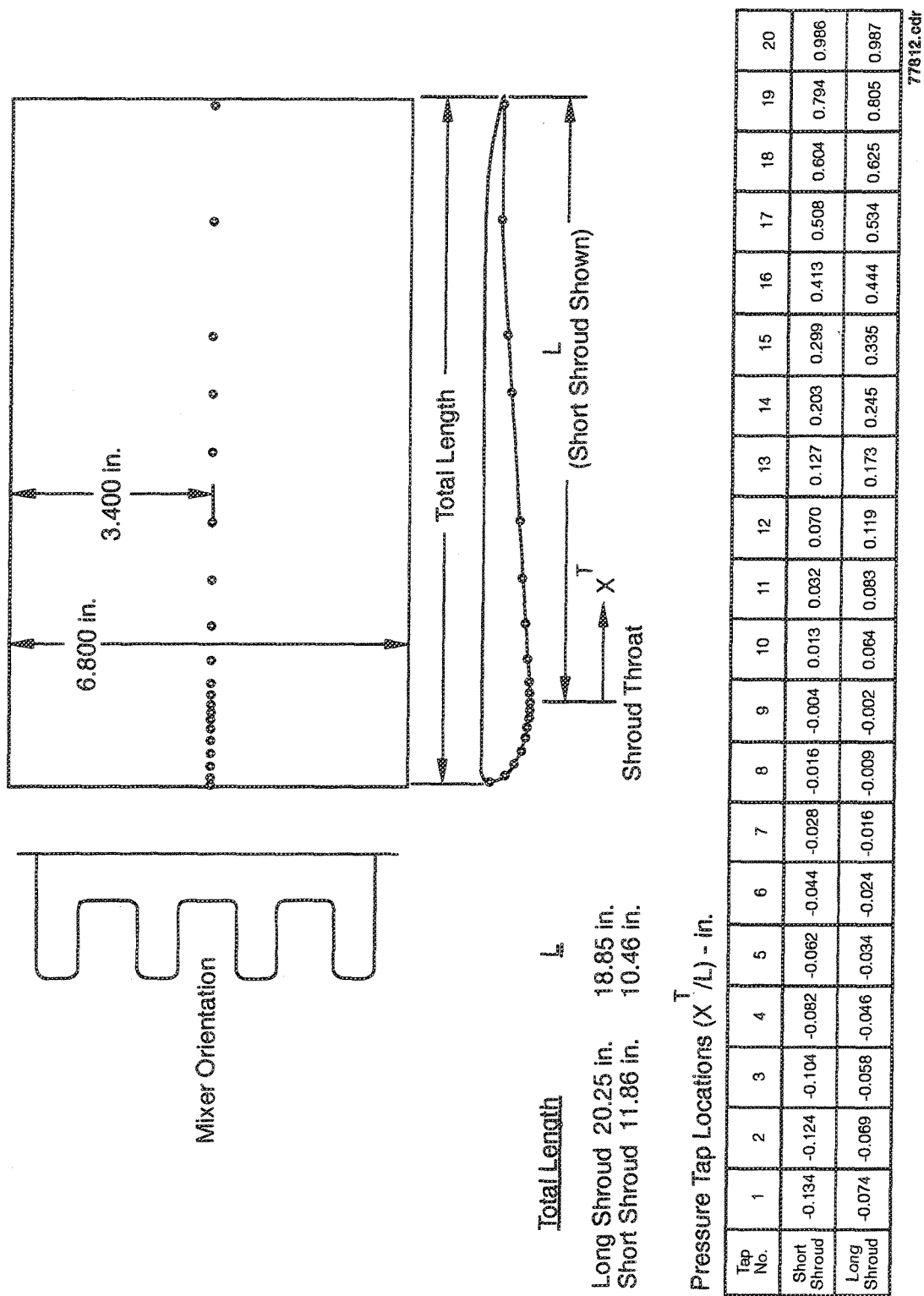


Figure 15. Static Pressure Instrumentation for P&amp;W Two-Dimensional Hardwall Shrouds

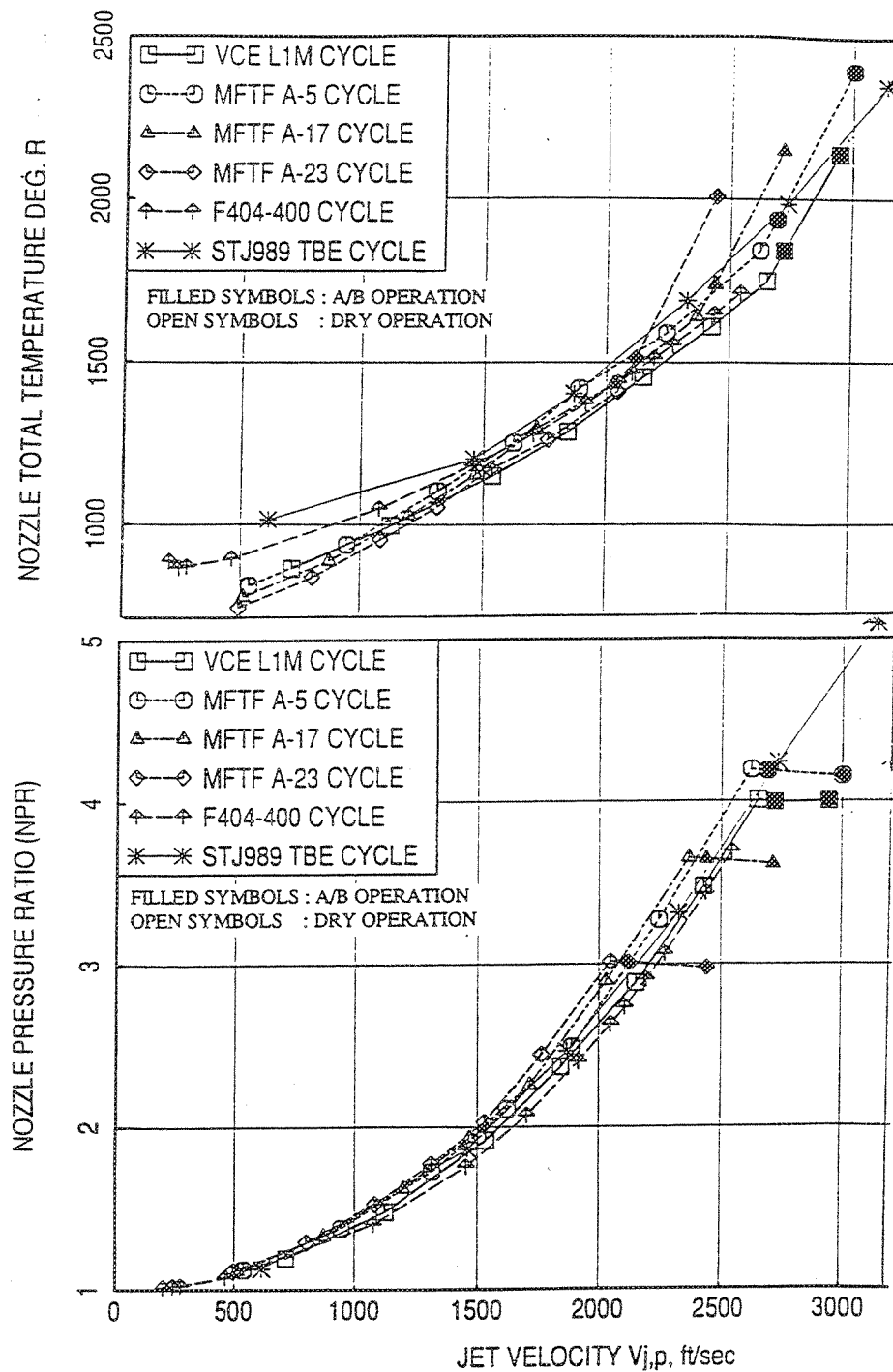


Figure 16. Comparison of Exhaust Nozzle Pressure Ratio and Total Temperature Versus Ideal Jet Velocity for Cycles Currently Under Consideration for HSCT Propulsion

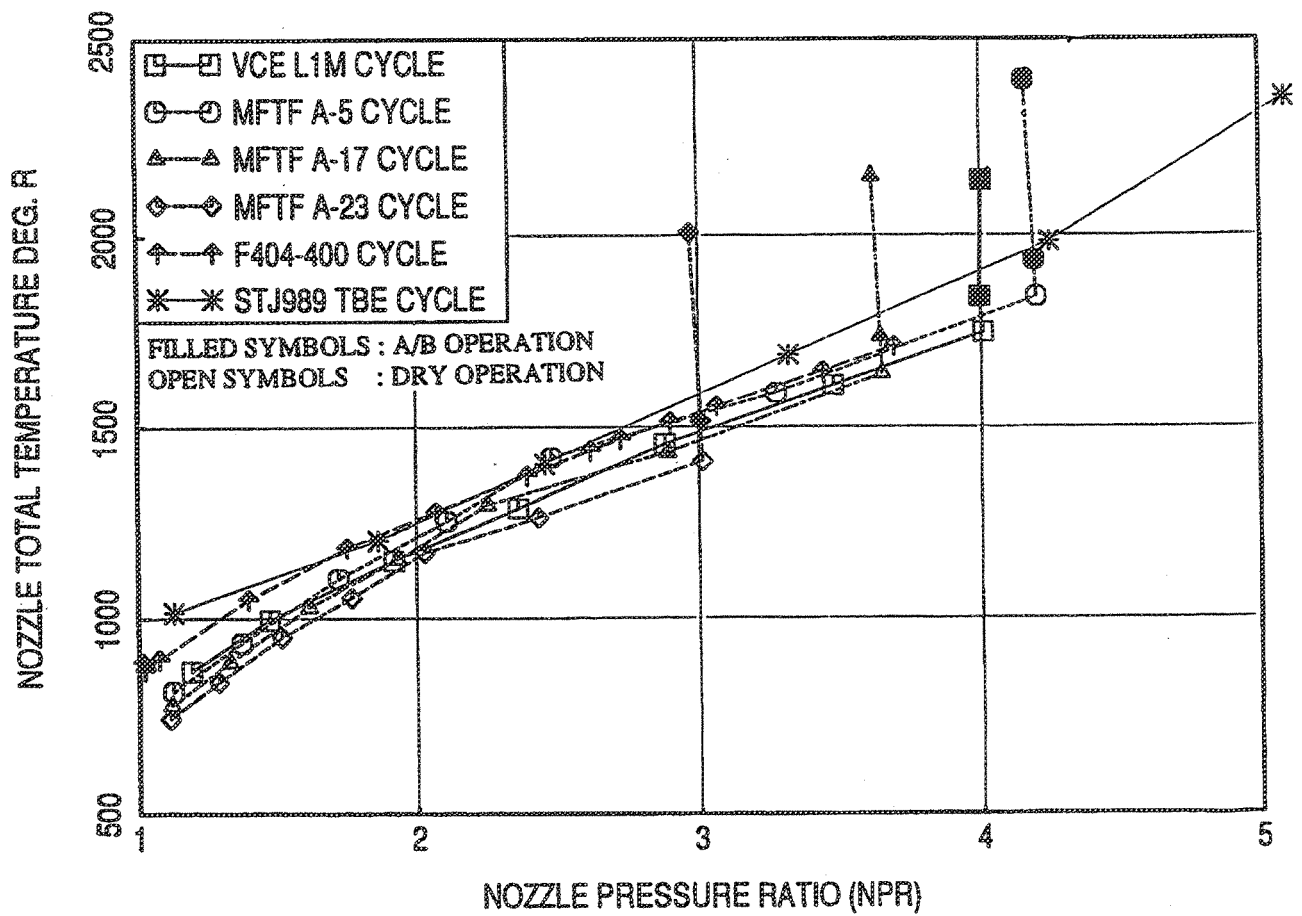


Figure 17. Comparison of Exhaust Nozzle Pressure Ratio With Respect to Total Temperature for Cycles Currently Under Consideration for HSCT Propulsion

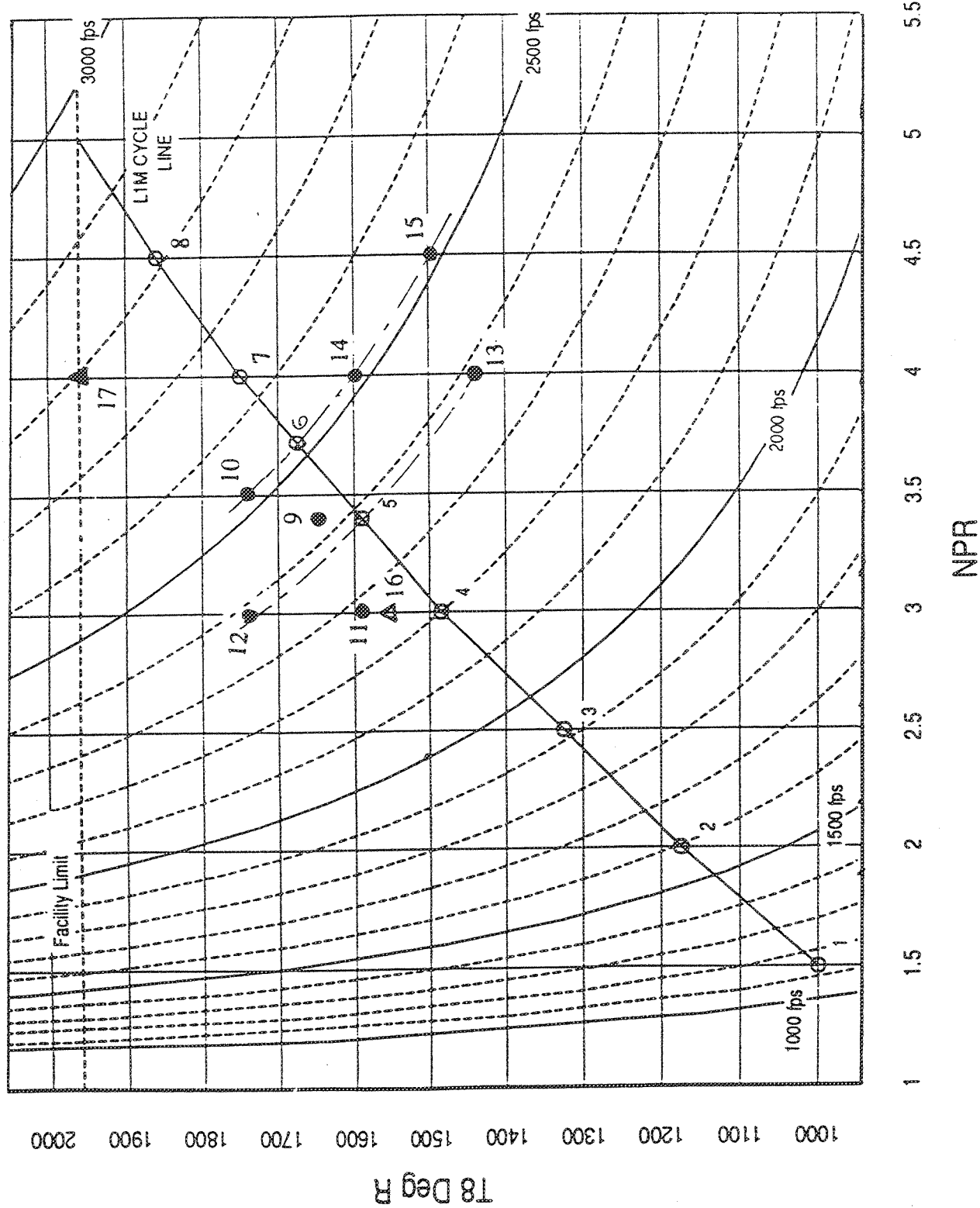


Figure 18. Acoustic Test Points for Pratt & Whitney Mixer-Ejector Nozzles in Terms of Nozzle Pressure Ratio Versus Total Temperature With Iso-Jet Velocity Lines

This page intentionally left blank.

## 4. RESULTS AND DISCUSSION

### 4.1 ACOUSTIC ANALYSIS AND TEST RESULTS

#### 4.1.1 Description of Analysis Steps Used by P&W and GEAE

##### 4.1.1.1 GEAE Acoustic Data Processing

The farfield data measured by both arrays of microphones are analyzed by the on-line system. This system computes 1/3-octave band data for the model scale at a 40-ft arc corrected to standard day conditions (59°F and 70 percent relative humidity [PRH]), and narrow-band data as measured. These data are further processed to generate various acoustic parameters for a full scale nozzle ( $A_8=1086 \text{ in}^2$ ) at a sideline location (distance=1629 ft, based on 689-ft altitude and 1476-ft sideline) with standard day conditions. These parameters include sound pressure level (SPL), sound power level (PWL), overall sound pressure level (OASPL), perceived noise level (PNL), tone-corrected perceived noise level (PNLT), and effective tone-corrected perceived noise level (EPNL).

The acoustic data processing is illustrated in the flowchart of Figure 19. The background correction and flight transformation processes are applied to the data with flight simulation. The flight transformation procedure (developed by R. Mani [Ref. 15]) transforms the free jet noise into flight noise. The method uses the measured free jet data, and extracts from it a basic directivity. (That directivity is what sources associated with the primary nozzle plume would create if they were to radiate into a static rather than free-jet environment.) The directivity pattern is used to estimate what the noise in flight would be. It is done by applying analytically derived flight effects on monopole, dipole, and quadrupole sources. The EPNL is calculated on the basis of PNLT directivity with the duration correction for the simulated flight velocity. The static condition EPNL is computed using the PNLT values, and is termed 'pseudo EPNL' (assuming a flight velocity of 360 ft/sec [ $M_n=0.32$ ]).

For Pratt & Whitney (P&W) requirements, the on-line 1/3-octave-band data is processed to calculate SPL, OASPL, PNL, PNLT, and PWL at an arc of 150 ft for standard day conditions of 77°F and 70 PRH. Flight transformation is applied to the flight simulated data. These data are used by P&W to compute EPNL.

##### 4.1.1.2 P&W Acoustic Data Processing

Acoustic data received from the test facility were scaled to a primary (core) nozzle throat area ( $A_{8*}$ ) of  $1086 \text{ in}^2$ , covering the polar angles ( $\theta$ ) from 50 to 150 degrees. The data had been adjusted to a 150 ft arc at the Federal Aviation Administration (FAA) standard day (77°F, 70 PRH). Data for the forward polar angles were developed by assuming the 50 degree, 150 ft arc, spectra data forward of 50 degrees.

Pratt & Whitney flight EPNL data were calculated by extrapolating the information to the Boeing aircraft flight path of 689 ft altitude, 1476 ft sideline distance (1629 ft hypotenuse), and 5.5 degree aircraft climb angle with 13.2 degree aircraft pitch angle. A four-engine aircraft was assumed flying over grass with extra ground attenuation (EGA) and adjacent engine exhaust shielding. The modified FAA tone corrections with Amendment 15 (dated April 5, 1988) for 800 to 10,000 Hz were used. The flight Mach number ( $M_n$ ) was set to that tested in the facility. Static acoustic results were calculated by assuming a flight velocity of 357 ft/sec ( $M_n=0.32$ ) to provide a time scale for the duration portion of the EPNL calculation. Results in the form of tone-corrected PNLT directivity and SPL spectra were extrapolated to the 1629 ft sideline position for a single engine, and presented free field for clearer comparisons.

Some acoustic results (EPNL) provided by General Electric Aircraft Engines (GEAE) were calculated assuming a single engine at free field, at standard day conditions of 59°F/70 PRH, flying a flat flight path at 689 ft altitude and 1476 ft sideline distance (1629 ft hypotenuse).

## 4.2 ACOUSTIC TEST RESULTS

Except where noted, acoustic results in the form of EPNL were calculated with the P&W assumptions defined in Section 4.1.1.2. Caution should be used when comparing P&W and GEAE derived acoustic results because of differences in the data reduction. All EPNL results are plotted and contrasted to the calculated ideally expanded, unsuppressed primary jet velocity ( $V_{j,p}$ ).

### 4.2.1 Baseline Round Convergent Nozzle Results

#### 4.2.1.1 Comparison of Pratt & Whitney, General Electric Aircraft Engines, and Boeing Round Convergent Results

The P&W round convergent nozzle with 8.25 in<sup>2</sup> throat area was tested in Cell 41 to establish a reference to evaluate the acoustic benefit of the different mixer-ejector nozzles. The acoustic results of this nozzle are presented in this section in a comparative manner, in which the acoustic data for two other round convergent nozzles, a GEAE design and a Boeing design, tested in Cell 41, are compared with P&W nozzle data. The shape and size of these three nozzles are different. The throat areas (i.e., same as exit area) for GE, Boeing, and P&W nozzles are 20.43 in<sup>2</sup>, 13.2 in<sup>2</sup>, and 8.25 in<sup>2</sup>, respectively. The nozzle interior shapes and lip thicknesses are significantly different for these nozzles (Figure 20).

The farfield noise data for all three nozzles are corrected to the standard day conditions (59°F, 70 PRH), extrapolated to 1629-ft distance, scaled to 1086-in<sup>2</sup> area, and expressed in terms of sound power level (PWL), overall sound pressure level (OASPL), perceived noise level (PNL), tone-corrected perceived noise level (PNLT), effective perceived noise level (EPNL), and sound pressure level (SPL), which are presented as functions of jet velocity ( $V_j$ ), frequency ( $f$ ), and angle-to-inlet ( $\theta$ ).

##### 4.2.1.1.1 Static Data

Figure 21 shows the pseudo EPNL, PNLT at different polar angles ( $\theta$ ), and peak PNLT comparisons between these three nozzles at static condition. The P&W conic nozzle data is higher at jet velocities of 2200, 2384 and 2520 ft/sec compared to Boeing conic nozzle data. The GEAE nozzle data agrees with P&W nozzle data at 2384 ft/sec. The higher levels for the P&W nozzle at 2200, 2384, and 2520 ft/sec and the GE nozzle at 2384 ft/sec, relative to Boeing conic nozzle data, are due to noted screech phenomena in the P&W conic nozzle and, to some extent, in the GE conic nozzle, which will be discussed later.

To examine the difference of acoustic characteristics between the three nozzles, OASPL, PNL, and PNLT directivities, and PWL and SPL spectra for four different VJ are examined. The nominal velocities and cycle condition definitions are shown in Table 9.



Table 9. Nominal Velocities and Cycle Conditions

$V_j$ (ft/sec)	NPR	$T_8$ (°R)
1147	1.5	1000
1919	2.5	1325
2384	3.4	1590
2812	4.5	1860

Figures 22 and 23 show the OASPL, PNL, and PNLT directivities and PWL and SPL spectra, respectively, at  $V_j=1147$  ft/sec. Figure 22 shows relatively higher levels of OASPL, PNL, and PNLT at the forward arc compared to the other two angles. Figure 23 indicates good agreement of PWL, as well as SPL, at various polar angles up to about 4 kHz. Above 4 kHz, the levels for P&W nozzle are higher compared to the other two nozzles. Similar results for the other three velocities are plotted in Figures 24 through 29. With increasing velocity, the PWL and SPL levels for P&W nozzle becomes much higher compared to GE nozzle at higher frequencies. The Boeing nozzle data lies between the GE and P&W nozzle results, indicating a uniform trend with respect to increasing throat area.

Figure 27 shows the spectral comparisons of PWL and SPLs between the three nozzles at  $V_j=2384$  ft/sec. Strong tones are observed at 160 Hz for P&W and GE nozzle cases. These tones are caused by screech phenomena, which influences the EPNL and PNLT levels, observed earlier in Figure 21. Screech is an instability phenomenon which depends on feedback mechanism with plume shock structure and nozzle lip. Minor configurational and flow field differences can influence the occurrence of screech.

#### 4.2.1.1.2 Flight Data

Results presented under flight are evaluated using the test data with a simulated flight Mach number (Mn) of 0.32 ( $V_\infty=360$  ft/sec). Figure 30 shows the EPNL and PNLT at different  $\theta$ , and peak PNLT comparisons between these three nozzles with flight simulation. Unlike the static case, the P&W nozzle data is slightly higher compared to other two cases between 2200 and 2800 ft/sec.

Figures 31 and 32 show the OASPL, PNL, and PNLT directivities and PWL and SPL spectra, respectively, at  $V_j=1147$  ft/sec. Figure 31 shows relatively higher levels of OASPL at the forward arc compared to the other two angles. Figure 32 indicates good agreement of SPL at higher polar angles and some level of difference in the forward arc and PWL up to about 4 kHz. Above 4 kHz the levels for the P&W nozzle are higher compared to the other two nozzles. Similar results for the other three velocities are plotted in Figures 33 through 38. With increasing velocity, the PWL and SPL levels for the P&W nozzle become much higher compared to the GE nozzle at higher frequencies. The Boeing nozzle data lies in-between the GE and P&W nozzle results, indicating a uniform trend with respect to increasing throat areas. For flight condition screech did not occur for any of the three nozzles, as indicated in Figure 36, at  $V_j=2384$  ft/sec.

#### 4.2.1.1.3 Conclusions

As a general observation, the SPL and PWL data for these three nozzles exhibited significant differences at high frequencies. The SPL and PWL levels seem to increase with decreasing model scale nozzle size at higher frequencies. Two possible reasons may be the cause for such data trends. The shape of the nozzles (e.g., internal contour, convergence angle, lip thickness, and external closure shape) could be a contributing factor for the observed

differences. However, in our opinion, this does not seem to be the dominant factor to cause the systematic trend of increasing level with decreasing nozzle size. The other reason, which we believe the dominant cause for such behavior, is the uncertainty in the atmospheric absorption corrections applied to the measured data at high frequencies during scaling, extrapolating, and standard day conversion processes. The variation in the geometrical shape between the nozzles may have some effect on the acoustic data. However, this effect is relatively small and is not necessarily expected at only high frequencies. Geometric differences could result in plume differences, which in turn may affect low and high frequency noise levels. The data, however, show a definite trend at high frequencies with model size.

To obtain an exact quantitative assessment and sort out these two factors, several nozzles of exactly the same geometry, but with different sizes, need to be tested. Since such an effort is not possible in the foreseeable future, we analyzed the existing data and assessed the trends which could provide credence to our hypothesis. Data at four test conditions, the same as those listed under static data, are processed in a way to study the data at intermediate steps. Table 10 lists the actual test conditions for each of the three nozzles. The data processing uses (a) the spectral data as measured for the model scale at the microphone location to generate (b) lossless data for the model scale, which is (c) scaled to a full-size nozzle ( $A_{8*}=1086 \text{ in}^2$ ). Finally, the lossless full scale nozzle data are (d) extrapolated to a fixed sideline distance (1629 ft) and corrected to the standard day condition (59°F, 70 PRH). In the present exercise, the as-measured data of step (a) are also scaled to the full scale nozzle without applying any correction. This step is marked as (b'), which is not required for regular data processing. However, this set of data will be useful to explain the data trend. As a typical example, the data at various stages of processing are shown in Figures 39 through 41 for one test condition ( $V_j=2812 \text{ ft/sec}$ ,  $\text{NPR}=4.5$ ,  $T_8=1860^\circ\text{R}$ ) at three polar angles.

Table 10. Conic Nozzle Test Conditions

NPR	$T_t$ (°R)	$V_j$ (ft/sec)	GE				Boeing				Pratt & Whitney			
			Run No.	PRH	$T_{amb}$ (°F)	$P_{amb}$ (inHg)	Run No.	PRH	$T_{amb}$ (°F)	$P_{amb}$ (inHg)	Run No.	PRH	$T_{amb}$ (°F)	$P_{amb}$ (inHg)
4.5	1860	2812	861	90	44.5	29.2	22	68	68.0	29.3	22	49	82.0	29.4
3.4	1590	2384	852	61	57.2	29.4	14	80	66.6	29.3	13	56	76.9	29.4
2.5	1325	1920	854	61	58.0	29.4	8	84	65.8	29.3	9	56	75.9	29.4
1.5	1000	1147	855	61	58.4	29.4	2	85	62.9	29.3	7	59	74.9	29.4

The as-measured data show systematic trends spectrally due to nozzle size variation, as shown in Figures 39(a), 40(a), and 41(a) for  $\theta=60$  and  $130$ , respectively, for the nominal  $V_j=2812 \text{ ft/sec}$ . As expected, the noise levels are proportional to the nozzle size with appropriate peak frequency shift. However, flowpath variations in the nozzle do not seem to influence the data trend significantly. Next, the as-measured data are scaled to a size of  $1086 \text{ in}^2$  without applying atmospheric correction. As shown in Figures 39(b'), 40(b'), and 41(b'), the noise levels collapse reasonably well in the low frequency range at all angles. At higher frequencies, the noise level decreases with decreasing nozzle size and the relative noise level differences between the nozzles increases with frequency, mostly in the forward arc.

Next, the as-measured data are corrected to standard day, projected to full scale ( $A_{8*}=1086 \text{ in}^2$ ), and extrapolated to 1629 ft sideline. In this process, the as-measured data for the model scale nozzles are first converted to

lossless by adding atmospheric attenuation suffered in the scale model size. The low frequency results do not show much change compared to the corresponding as-measured data as they suffer much less attenuation (Figures 39(b), 40(b), and 41(b)). However, in high frequency range, where, the atmospheric corrections are fairly large, the noise levels show significant differences. In the rear arc, the noise levels increase significantly and the increase in levels is monotonically increasing as nozzle size decreases. This is a combined effect of atmospheric correction and nozzle geometry. Then, the model scale lossless data are scaled to  $1086 \text{ in}^2$ . The noise levels collapse reasonably well in the low frequency range at all angles, similar to the as-measured full scale results. However, at higher frequencies, the noise level increases with decreasing nozzle size and the relative noise level differences between the nozzles increases with frequency (Figures 39(c), 40(c), and 41(c)). The final process of extrapolation to 1629 ft and conversion of extrapolated data to standard day condition does not alter the relative spectral differences between the three nozzles noted on the full-scale lossless basis, as shown in Figures 39(d), 40(d), and 41(d).

The full scale SPL data for a smaller size nozzle comes from corresponding higher frequency in the scale model size compared to a larger size nozzle. For example, SPL at 4-kHz frequency on the full scale comes from about 46 kHz for the P&W nozzle ( $A_{g*}=8.3 \text{ in}^2$ ), whereas, it comes from about 30 kHz for the GE nozzle ( $A_{g*}=20 \text{ in}^2$ ). The acoustic data at high frequencies is subject to significant uncertainties in the atmospheric attenuation model as well as atmospheric variation (especially, relative humidity) during the test conduct. In our studies of these three nozzles, the smallest nozzle showed significant high frequency contribution on a full scale basis compared to other nozzles, and deviates from classical conic nozzle spectrum based on historic data on model scale and full scale engines. However, on the as-measured scale model basis, the spectral features between the three nozzles are not significantly different, indicating geometric differences (lip shape, contours, etc.) are not as significant as the uncertainties associated with atmospheric attenuation corrections applied at very high frequencies (typically, 32 kHz and higher).

For complex nozzles, whose expected spectral content is not known a priori, and wherein high-frequency spectral content is likely to be the dominant portion of the total spectrum (typically, greater than 30 kHz), it is important to minimize the impact on test results of modeling uncertainties of atmospheric attenuation, as well as uncertainty of exact knowledge of ambient conditions in the test chamber. Also, in the context of multi-element nozzles, individual jets have small characteristic dimensions. In addition, metal thickness does not scale down proportionately from full size. To minimize the impact of these two effects in scale model tests, it is preferable to test as large a model as possible.

#### 4.2.2 Effect of Mixer Area Ratio (MAR)

The ejector shrouds were rotated by installation of angled support brackets to vary the mixing area ratio (MAR). The MAR is the ratio of the total shroud exit area ( $A_{\text{exit}}$ ) to total shroud cross-sectional area at the mixer exit ( $A_{\text{mix}}$ ) (Figure 8). A MAR greater than 1.0 denotes a diverging shroud mixing region; a MAR less than 1.0 denotes a convergent mixing region.

Figure 42 shows the results of an ideal (lossless) one-dimensional momentum-based calculation for a SAR of 4.9. The calculation provided an estimate of the ideal pumping ability of the shrouded mixer-ejector nozzle, assuming 100-percent mixing. The flow conditions entering the mixing region were estimated by assuming two-percent total pressure loss through the primary nozzle, and NASA 12-21-58L to calculate the secondary inlet pressure loss and scrubbing losses on the mixer surface. The results are shown as the ratio of the secondary mass flow ( $W_s$ ) to primary nozzle mass flow ( $W_p$ ). The dashed line shows the estimated pumping ratio for SAR=4.9 and MAR=1.19

based on the ideal calculation and results from the 1991 NASA-LeRC 9 ft x 15 ft tests under Task 11 of the Aero-propulsion Technology contract (NAS3-25952).

Figures 43 and 44 show the static and flight-simulated results of the treated shroud with vortical mixer. The MAR was varied at a constant SAR of 4.9. The vortical mixer design with the long (216-in. full scale) acoustically treated shroud (MAR=0.97, SAR=4.9) provided the largest sideline flight ( $V_{\text{fl}}=357$  ft/sec) noise reduction of better than 15 EPNdB below the reference convergent nozzle at 2400 ft/sec unsuppressed primary jet velocity. Figures 45 through 50 compare the flight-simulated PNLT directivity and noise spectra for the three MARs at various jet velocities.

Figures 51 and 52 show the static and flight-simulated results at SAR of 4.4. The results show that for SAR of 4.4, the MAR of 0.97 and 0.88 gave very similar results at the higher primary jet velocities, whereas at the lower primary jet velocities, the MAR of 0.97 again provided the lower sideline noise. Figures 53 through 58 compare the flight-simulated PNLT directivity and noise spectra for the three MARs at various jet velocities.

Figures 59 and 60 show the static and flight-simulated results of the treated shroud with axial mixer. The MAR of 0.88 produced a lower sideline noise level compared to the MAR of 0.97. Figures 61 through Figures 66 compare the flight-simulated PNLT directivity and noise spectra for the two MARs at various jet velocities.

#### 4.2.3 Effect of Shroud Area Ratio (SAR)

The shrouds were moved outward from the model centerline, parallel to each other, to adjust the SAR, effectively changing the shroud throat height and area. The SAR is the ratio of the total shroud cross-sectional area at  $A_{\text{mix}}$  to the throat area of the primary mixer ( $A_{g*}$ ) (Figure 8). The nominal shroud throat height was set to 6.0 in. or 5.4 in., yielding nominal SARs of 4.9 and 4.4, respectively.

Figures 67 and 68 show the static and flight-simulated acoustic results of the treated shroud with the vortical mixer, comparing the two SARs of 4.9 and 4.4. At unsuppressed primary jet velocities less than 2400 ft/sec, the vortical mixer and long, acoustically treated shroud with SAR=4.4 and MAR=0.97 provided an additional 1–2 EPNdB sideline flight noise reduction below the SAR=4.9 results. This reduction occurred at both static and flight-simulated conditions of  $M_n=0.32$  ( $V_{\text{fl}}=357$  ft/sec). Above 2400 ft/sec, the two SARs produce very similar results. Figures 69 through 74 compare the flight-simulated PNLT directivity and noise spectra for the two SARs at MAR=0.97 over various jet velocities.

#### 4.2.4 Mixer Comparison

Two mixer designs were tested. These were referred to as the vortical and axial mixers. The axial mixer was designed to provide axial flow from the hot lobes to maximize velocity (thrust) vectors and minimize momentum losses due to high vorticity. The vortical mixer introduced vertical shears to increase vorticity and accelerate mixing along the shear path. The vortical mixer is shorter and requires less penetration of the mixer lobes to promote mixing.

Figures 75 and 76 compare the static and flight-simulated ( $M_n=0.32$ ,  $V_{\text{fl}}=357$  ft/sec) acoustic results of the two mixers when tested with the fully treated ejector and the hardwall ejector. At unsuppressed primary jet velocity greater than 2200 ft/sec, the vortical mixer design with the long, acoustically treated shroud (SAR=4.9, MAR=0.97) showed a 1 to 2 EPNdB sideline flight ( $V_{\text{fl}}=357$  ft/sec) noise reduction relative to the axial mixer design with the long treated shroud (SAR=4.9, MAR=0.97). Figures 77 and 78 compare the acoustic results with

MAR=0.88 for the fully treated ejector only. At jet velocities greater than 2200 ft/sec, the vortical mixer showed superior noise reduction. The flight-simulated tone corrected perceived noise level (PNLT) directivity plots (Figures 79 and 80) show that the two mixers performed similarly when tested with the hardwall ejector. When the ejector was fully treated, the vortical mixer provided broader attenuation in the aft region reducing the peak PNLT compared to the axial mixer.

Figures 81 and 82 compare the noise spectra from the two mixers at a relatively low primary exit jet velocity and near the expected takeoff primary exit jet velocity. The plots show an overall reduction in the aft noise for the vortical mixer over the axial mixer at the higher jet velocity. This is consistent with the higher mixing ability of the vortical mixer which provides a longer mixing region within the treated ejector.

#### 4.2.5 Effect of Treatment and Liner Deterioration

A number of geometries were tested with both the hardwall and fully treated ejector. The fully treated ejector with the bulk absorber was highly effective in reducing the noise of the P&W 2-D mixer-ejector.

Figures 83 through 88 compare the sideline noise results of the vortical mixer configurations at both static and flight-simulated conditions. The vortical mixer with the long shroud (SAR=4.9, MAR=0.97), and perforated plate over honeycomb acoustic treatment packed with a bulk absorber, demonstrated a 5–8 EPNdB sideline noise reduction below the long hardwall shroud at  $M_n=0.32$  ( $V_{fl}=357$  ft/sec) over the entire range of unsuppressed primary jet velocities tested. Figures 89 through 91 show the flight-simulated PNLT directivity plots, comparing the treated (configuration 3) and hardwalled (configuration 9) ejectors. Figures 92 through 94 show the noise spectra at selected polar angles.

Figures 95 and 96 compare Configurations 13 and 19 (SAR=4.9, MAR=0.97), showing the benefit of the treated ejector when tested with the axial mixer. Figures 97 through 99 show the PNLT directivity plots comparing configurations 13 and 19. Figures 100 through 102 show the noise spectra at selected polar angles.

Figure 103 shows a comparison of the liner effectiveness of the vortical and axial mixers with flight simulation. The effectiveness is the difference in EPNL (EPNdB) between the hardwall and fully treated ejectors. The superior mixing of the vortical mixer produced more internal noise than the axial mixer. As a result, the treated ejector was more effective with the vortical mixer (configuration 3) than with the axial mixer (configuration 13) at all the primary jet velocities tested.

Figure 104 shows the liner attenuation results for the vortical mixer with SAR=4.9, MAR=0.97, and primary jet velocity of 2384 ft/sec. The liner attenuation was obtained by arithmetically subtracting the treated noise spectra from the hardwall noise spectra at selected polar angles. This computation gives an indication of the noise reduction provided by the acoustic treatment. Figure 105 compares the perceived annoyance (NOY) spectra at selected polar angles. Comparing Figures 104 and 105 shows that the peak liner attenuation occurs at a lower frequency (500 to 1000 Hz) than the peak annoyance (2000 to 3000 Hz). This indicates that additional liner attenuation could possibly be obtained by adjusting the depth of the treatment to shift peak attenuation to a higher frequency. Figures 106 and 107 show similar results for the vortical mixer at SAR=4.4 and MAR=0.97. Figures 108 and 109 show the results from the axial mixer with SAR=4.9 and MAR=0.97. The attenuation plot (Figures 108) shows that the axial mixer achieved lower noise reduction with the treated ejector than did the vortical mixer (Figure 104). The perceived NOY spectra show a similar miss in liner depth as seen with the vortical mixer.

Ejector liner deterioration was visually detected following testing of the vortical mixer with SAR=4.4, after approximately 120 hr of hot test time. Previous tests with this liner, Astroquartz bulk material packed in a honey-

comb matrix, had shown good durability; however, earlier testing was generally of a shorter duration. With the lower SAR, the ejector walls were positioned inward, closer to the mixer exit, subjecting the bulk material to more hot flow impingement as well as allowing the hot flow to attach to the ejector walls. This positioning is believed to contribute to the deterioration. Figure 110 illustrates the loss of bulk absorber material from the acoustic panels. The deteriorated acoustic panels in the ejector were replaced with fully treated panels, and two configurations were retested. Figures 111 through 114 compare the static and flight-simulated sideline noise results of the hardwall, deteriorated treated, and fully treated ejectors for MAR=0.97 and MAR=1.19, respectively. Despite the loss of the bulk absorber and oversized face sheet open area (34 percent POA), the panels still provided reasonable acoustic performance. The deteriorated treatment had reduced the liner effectiveness, approximately 1 to 2 EPNdB across the range of primary jet velocities tested. This reduction may be attributed to the high, local, internal Mach numbers over the face sheet inside the ejector. A better understanding of the effect of local flow conditions on liner impedance is needed to best achieve the potential for improved liner attenuation performance described here. Figures 115 through 119 show the flight-simulated PNLT directivity plots comparing configurations 11, 5, and 5R at MAR of 0.97 and configurations 10, 7, and 7R at MAR of 1.19. Figures 120 through 124 show the noise spectra at selected polar angles.

#### 4.2.6 Azimuthal Variation of Noise Level

The acoustic test facility was equipped with two systems of microphone arrays, positioned along lines parallel to the model centerline, to measure the acoustic characteristics of the test models in the farfield. One array was mounted on a traversing tower which was rotated about the centerline of the nozzle model and was used to obtain acoustic data at two azimuthal locations corresponding to sideline (25 degrees from the nozzle major axis), and community or overhead (90 degrees from the nozzle major axis). The second array of microphones was stationary and positioned 60 degrees from the nozzle major axis.

The acoustic data from all three positions were reduced as if at the same position of 689-ft altitude and 1476-ft sideline (1629-ft direct distance) for comparison. Figures 125 and 126 show the results of testing for the vortical and axial mixers, respectively. The long 2D mixer-ejector designs with both treated and hardwall shroud (SAR=4.9, MAR=0.97) exhibited a 2–3 EPNdB azimuthal noise increase from the sideline to community (overhead) position over the range of unsuppressed primary jet velocity tested at  $V_{\text{eff}}=357$  ft/sec.

Figures 127 through 129 compare PNLT at three different primary jet velocities for the vortical mixer. The figures show the dominance of the community noise over the other two microphone positions. Figures 130 through 132 show the PNLT for the axial mixer at the same primary jet velocities with the community microphone position also giving the highest noise.

Figures 133 and 134 show the spectral data for the treated ejector at 2384 ft/sec unsuppressed primary jet velocity with the vortical and axial mixer, respectively. Figures 135 and 136 show the spectral data for the hardwall ejector at 2384 ft/sec unsuppressed primary jet velocity with the vortical and axial mixer, respectively. The major source of the azimuthal variation occurs in the internal mixing noise at the middle to high frequencies. This difference is especially evident at the polar angle ( $\theta$ ) of 120 degrees, where the internal noise exhibits a strong azimuthal variation.

Two possible explanations for the azimuthal noise variation are: (1) an internal mixer lobe-to-mixer lobe shielding effect in the direction aligned with the lobe rows, along the nozzle major axis, and/or (2) a difference in the axial velocity profile between the shroud-to-shroud direction, corresponding to the community position and sidewall-to-sidewall direction.

#### 4.2.7 Effect of Ejector-Shroud Length

The long shroud provided more noise attenuation than the short shroud along the entire LIM throttle line. Figures 137 and 138 show the sideline acoustic results at static conditions and  $Mn=0.32$  ( $V_{\text{jet}}=357$  ft/sec), respectively, for the vortical mixer with the short and long shrouds, both in the hardwall and fully treated condition. The  $SAR=4.4$  and  $MAR=1.19$  combination was the only geometry available for this comparison. The long hardwall shroud provided a 1–2 EPNdB reduction in sideline noise below the short hardwall shroud with the vortical mixer ( $SAR=4.4$ ,  $MAR=1.9$ ), both statically and at  $Mn=0.32$  ( $V_{\text{jet}}=357$  ft/sec). The addition of the treatment to the long shroud provided an additional 6–7 EPNdB reduction, showing that the majority of the noise reduction due to the long treated shroud was provided by the acoustic treatment on the shroud inner surface area.

Figures 139 and 140 compare the flight-simulated PNL directivity and noise spectra at a jet velocity of 2384 ft/sec. The spectra show that the long hardwall shroud alone tends to reduce the lower frequency noise when compared with the short hardwall shroud. Comparing the long hardwall and long treated shrouds show that the largest noise reduction occurs in the middle frequency range of 500–4000 Hz.

Figures 141 through 144 compare the acoustic results from the other geometries tested with both long and short hardwall shrouds. The results show that the 1 to 2 EPNdB advantage of the long hardwall shroud over the short hardwall shroud was consistently demonstrated with both the vortical and axial mixers.

#### 4.2.8 Flight Effects

##### 4.2.8.1 Effect of Simulated Mach Number Error on Test Results

Due to undetected acoustic facility instrumentation problems early in the test, the baseline round convergent nozzle and configuration 2 (vortical mixer/long treated shroud/ $SAR=4.9/MAR=1.19$ ) were unknowingly tested with flight simulation at  $Mn=0.36$  and not the planned  $Mn=0.32$ . Configurations 3 and 4 (vortical mixer, long treated shroud,  $SAR=4.9$ ,  $MAR=0.97$  and  $0.88$  respectively) were tested at both  $Mn=0.36$  and  $0.32$  once the problem had been discovered and resolved. All subsequent configurations were tested at static and  $Mn=0.32$  conditions.

Figure 145 shows the EPNL results from configurations 3 and 4. The data from configurations 3 and 4 were processed at the same flight Mach number as that simulated during testing. The variation in test Mach number ( $Mn=0.32$  to  $0.36$ ) changed the EPNL results less than 1.0 EPNdB. Figures 146 and 147 show the results from the baseline round convergent nozzle and configuration 2 tested at  $Mn=0.36$ , and processed at  $Mn=0.36$  and  $0.32$ . Processing the  $Mn=0.36$  data at  $Mn=0.32$  produced a similar change in EPNL demonstrated by the tests of configurations 3 and 4. Based on this study, retesting of the baseline round convergent nozzle and configuration 2 at  $Mn=0.32$  were considered unnecessary. Note that any flight-simulated PNL and noise spectra data from the baseline round convergent nozzle and configuration 2 reflect the flight effects at  $Mn=0.36$ .

##### 4.2.8.2 Flight Simulated Results

Figures 148 through 151 compare the flight effects on the baseline round convergent nozzle and on selected mixer-ejector configurations. Flight effects at  $V_{\text{jet}}=357$  ft/sec accounted for approximately 2–3 EPNdB reduction in the sideline noise for the long treated configurations 3 (vortical mixer,  $SAR=4.9$ ,  $MAR=0.97$ ), 5R (vortical mixer,  $SAR=4.4$ ,  $MAR=0.97$ ), and 13 (axial mixer,  $SAR=4.9$ ,  $MAR=0.97$ ).

Figures 148 through 151 show that flight effects were more significant for the baseline round convergent nozzle than the mixer-ejector nozzles. This is explained by the dominance of jet noise in the convergent nozzle noise. The ejector nozzle noise was internal noise dominated so that external flight effects were less significant.



Figures 152 through 155 compare the baseline round convergent nozzle with configuration 3 (vortical mixer, long treated shroud, SAR=4.9, MAR=0.97). Figures 156 through 159 compare the baseline round convergent nozzle with configuration 9 (vortical mixer, long hardwall shroud, SAR=4.9, MAR=0.97). The figures show the PNLT directivity at selected primary jet velocities and noise spectra at  $V_{jet}=2384$  ft/sec. The spectra show a large reduction in the low frequency noise with flight simulation.

Configuration 9 (Figure 149) showed a reduction in flight effects with increasing primary jet velocity. The PNLT (Figures 156 through 158) for the hardwall configuration 9 show evidence of forward lift of the dominating internal noise. Figure 159 shows this as an increase in the measured noise in the forward arc (60 degrees) with flight simulation. This same trend occurred with configuration 3 (Figures 152 through 154), but attenuation of the internal noise by the treated ejector overwhelmed any effect of the forward lift (Figure 155).

#### **4.2.9 Effect of Aerodynamic Hysteresis on Noise Level**

Tests were run with selected configurations with the long hardwall ejector to investigate hysteresis in the shroud internal flow field. The hysteresis was seen as a shift in the conditions at which the shroud internal flow field switched from predominantly subsonic to supersonic. Static pressure taps on the shroud internal walls were used to monitor the flowfield. These tests were run at ambient, warm (860°R), and hot (L1M throttle line) primary stream temperatures.

Acoustic hysteresis data were also obtained during these tests. The hot tests were checked for acoustic hysteresis because the high jet velocities produce the best potential for measuring a change in the noise levels. The acoustic hysteresis was investigated by increasing NPR and  $T_{t8}$  in small steps to a maximum, then NPR and  $T_{t8}$  were incrementally decreased repeating the same conditions.

Figures 160 through 167 show the results of static and flight-simulated acoustic hysteresis studies for a number of configurations. The EPNL plots show that over the range of NPR and  $T_{t8}$  investigated, none of the configurations showed significant hysteresis in the acoustic data obtained. The acoustic data were insensitive to the direction a particular test point was approached in terms of NPR and  $T_{t8}$ . The data also show good repeatability with the L1M cycle data taken early in the testing of each configuration.

Figures 168 through 170 show the PNLT directivity for selected points from the long hardwall ejector: configuration 8 (vortical mixer, SAR=4.9, MAR=1.19), configuration 14 (axial mixer, SAR=4.9, MAR=1.19), and configuration 19 (axial mixer, SAR=4.9, MAR=0.97). Figures 171 through 173 show the noise spectra for these same points. The plots confirm the repeatability of the acoustic data.

#### **4.2.10 Effect of Operating Off the L1M Throttle Line**

Points were added to the test matrix to explore the acoustic performance of certain configurations off the L1M throttle line. The acoustic data from these points give results along lines of constant primary jet velocity, NPR, and  $T_{t8}$ . The acoustic results were well ordered and showed the expected relationships to one another.

Figures 174 and 175 show the off-throttle line acoustic results for the baseline round convergent nozzle and configuration 3 (vortical mixer, long treated shroud, SAR=4.9, MAR=0.97). Lines of constant jet velocity, turbine exit total temperature, and NPR are noted on the plots. Noise results were sensitive to changes in the simulated engine thermodynamic cycle. The long, treated mixer ejector was more sensitive to changes in the throttle line than



the baseline round convergent nozzle. The sideline noise increased more for configuration 3 than the baseline round convergent nozzle over the same increase in NPR. This is especially evident along the  $V_{jet}=2520$  ft/sec line.

Figures 176 and 177 describe the constant primary jet velocity line at approximately 2384 ft/sec. This line is made up of test points 12, 5 and 13 (see Table 7). The primary jet velocity is held constant for the points by raising NPR while  $T_{t8}$  was lowered. Figure 178 shows that noise increased as NPR was increased and  $T_{t8}$  was decreased. Increasing NPR increases shock noise when present, and lowering  $T_{t8}$  increases the flow density, which also contributes to increased noise. Figures 179 through 182 show PNLT directivity and noise spectra for the baseline round convergent nozzle and configuration 3 for the three constant velocity points. Figure 179 shows that, at constant  $V_j$ , shock noise in the forward arc is the main reason for increased noise for the round convergent nozzle. The noise spectra for the ejector shows that, despite the lack of shock noise, the ejector is more sensitive to changes in  $T_{t8}$  because of density effects increasing ejector internal mixing noise. The internal mixing noise tends to be the source of peak PNL for the mixer-ejector nozzles and is an important contributor to the increased EPNL level.

Figures 183 and 184 describe the constant primary jet velocity line at approximately 2520 ft/sec. This line is made up of test points 10, 6, 14, and 15. The results are similar to those seen at 2384 ft/sec. At the higher jet velocity, the long, treated mixer-ejector nozzle was more sensitive to the change in pressure ratio than the baseline round convergent nozzle. Figure 185 shows that the increase in sideline noise was greater for configuration 3 over the same change in NPR. Figures 186 through 189 show PNLT directivity and noise spectra for the baseline round convergent nozzle and configuration 3 for the four constant velocity points.

Figures 190 and 191 describe the constant  $T_{t8}$  line at 1590°R. This line is made up of test points 11, 5 and 14 with increasing  $V_j$  and NPR. Figure 192 shows that the configurations performed as expected with the sideline noise increasing with increasing  $V_j$  and NPR. Figure 192 also shows the increase in sideline noise was greater for the long, treated mixer ejector nozzle (configuration 3) over the same change in jet velocity. This difference between the unsuppressed convergent nozzle and suppressed ejector nozzle can be explained by the change in noise sensitivity to jet velocity. The change in noise for a given change in jet velocity is greater for the lower suppressed jet velocity of the ejector nozzle than the relatively high unsuppressed jet velocity of the convergent nozzle. Figures 193 through 196 show PNLT directivity and noise spectra for the baseline round convergent nozzle and configuration 3 for three constant turbine exit temperature points.

Figures 197 and 198 describe the constant NPR line at 3.0, which is made up of test points 4, 11 and 12. Figure 199 shows relatively small changes in sideline noise were produced when NPR was held constant and the turbine exit total temperature was increased to raise the primary jet velocity. With the contribution of shock noise held constant by the constant NPR, the increased jet noise caused by raising the jet velocity was partially offset by the reduced flow density at the higher  $T_{t8}$ . Figures 200 through 203 show PNLT directivity and noise spectra for the baseline round convergent nozzle and configuration 3 for the three constant primary NPR points.

#### **4.2.11 Comparison to NASA-LeRC Results (NAS3-2595 APT Task 11)**

Acoustic data were obtained for a number of points to compare the acoustic results to those obtained at NASA-Lewis Research Center (LeRC) 9 ft x 15 ft low speed wind tunnel (LSWT) in 1991 under Contract NAS3-25952, Aeropropulsion Technology (APT), Task 11. Two separate issues were suspected of compromising the validity of the NASA-LeRC results. These were: 1) the aft noise in the baseline round convergent nozzle was not measured, and 2) contamination of the hardwall and treated ejector acoustic results by facility noise. The NASA-LeRC model acoustic data obtained under APT Task 11 were originally scaled to a mixer throat area of 860 in<sup>2</sup> from the nominal

model mixer throat area (10.2:1). The NASA-LeRC data were rescaled to 1086 in<sup>2</sup> (11.47:1) for comparison to the GEAE Cell 41 results. Figure 204 compares the results obtained at GEAE Cell 41 to those obtained at the NASA-LeRC LSWT facility. The EPNL reductions from Cell 41 are similar to those obtained in the NASA-LeRC LSWT, although spectral data show differences. A noise prediction for the round convergent nozzle is also included. Comparisons confirm technical concerns related to nearfield measurements and facility noise in the NASA-LeRC LSWT.

Figures 205 and 206 compare the test results for the baseline round convergent nozzle at the nominal condition of NPR=3.5 and  $T_{t8}=1735^{\circ}\text{R}$ . Figure 205 shows a comparison of the PNL directivity from the NASA-LeRC results, those obtained at the GEAE Cell 41 facility, and a convergent nozzle noise prediction using SAE jet mixing (ARP876), and SAE shock (Harper-Bourne & Fisher) predictions. The PNL directivity shows that the radiated jet mixing noise aft of approximately 120 degrees was not measured. The spectra shown in Figure 206 confirm this observation. The suspected reason for this was that the microphones were mounted in the NASA-LeRC tunnel too close to the model centerline. This allowed the aft radiating energy to be convected past the microphones. The microphones in the GEAE Acoustic Facility (Cell 41) were mounted a minimum of 22 ft from the model centerline.

Figures 207 and 208 compare the test results for configuration 2 at the nominal condition of NPR=3.5 and  $T_{t8}=1735^{\circ}\text{R}$ . Configuration 2 had the long, fully treated shroud with the bulk absorber, SAR=4.9 and MAR=1.19. The PNL directivity (Figure 207) shows the NASA-LeRC results to be louder than the results from the GEAE Cell 41 facility aft of the shroud exit. The spectra (Figure 208) show that the NASA-LeRC results were contaminated by facility internal noise. The contamination is especially evident at the lowest frequency and 1000–2000 Hz bands.

Figures 209 and 210 compare the test results for configuration 8. Configuration 8 had the long, hardwall shroud, SAR=4.9 and MAR=1.19. The test results from NASA-LeRC for this configuration also show indications of contamination by test facility noise. However, PNL directivity shows that facility noise had a lesser effect on the hardwall (Figure 209) compared to the fully treated (Figure 207) ejector. This was expected because of the higher noise levels of the hardwall configuration. The spectra (Figure 210) show that facility noise was most apparent in the aft arc region.

### 4.3 AERODYNAMIC TEST RESULTS AND ANALYSIS

Based on one-dimensional ideal ejector analysis and available results of static pressure distribution on shroud surfaces for mixer-ejector nozzles, it has been observed that an ejector may be operating in either a subsonic mode or supersonic mode and that this switching of modes from one to the other occurs at a particular NPR, termed the critical NPR or  $\text{NPR}_{\text{cr}}$ . This phenomenon is dependent on NPR, MAR, total temperature, SAR, and direction of NPR variation. A typical example of mode switch is shown in Figure 211(a). The mode switch seems to occur at different values of  $\text{NPR}_{\text{cr}}$  based on whether the NPR is gradually increased from below its critical value or is gradually decreased from above its critical value, for the same geometry and temperature conditions (hysteresis phenomenon). This is qualitatively demonstrated in Figure 211(b) by plotting NPR with respect to the normalized shroud force defined in Section 4.3.1.1.

Mode switch has significant impact on nozzle thrust coefficient, as well as dynamic stability, as noted in performance tests in the NASA Langley 16 ft transonic tunnel (NAS3-26617, Large Engine Technology Task Order 19). For the mixer-ejector nozzles under consideration, it is very difficult to accurately predict the mode switch phenomenon and its impact on performance, since it involves complex geometries and three-dimensional unsteady flowfields in the ejector. For such cases, it is necessary to experimentally evaluate the mode switch characteristics

of the nozzle with respect to NPR, temperature, and mixer-ejector geometry. Such assessments are critical to nozzle design and operation. With this motivation, several P&W mixer-ejector nozzles were tested to evaluate their mode switch characteristics in terms of static pressure and acoustics in the Cell 41 test program.

Tests were conducted in Cell 41 for P&W mixer-ejector nozzles to study their mode switch characteristics by measuring the static pressures at twenty axial locations on the shroud centerline (i.e., along the secondary flow) from mixer exit to the ejector exit. The locations of these pressure taps are shown in Figure 212. Only hardwall configurations were tested for this study, since static pressure instrumentation was not available for the treated ejector configurations.

#### 4.3.1 Vortical Mixer-Ejector Nozzle Configurations

##### 4.3.1.1 Effect of Temperature and Flight Simulation with Long Shroud (SAR=4.4, MAR=1.18)

Typical axial static pressure distributions on the shroud centerline for the vortical mixer configuration at ambient temperature and for LIM cycle conditions, with and without flight simulation, are shown in Figure 213. For all cases, the static pressure distributions with respect to NPRs are qualitatively similar, in that with increasing NPR, the flow gradually changes from subsonic mode to supersonic mode, and the axial extent over which the static pressures are below the choking pressure ratio increases with NPR. For specific heat ratio of 1.4, the choking pressure ratio ( $P_s/P_{amb}$ ) is about 0.528. The axial extent over which static pressures are below the critical limit are interpreted as being in the supersonic mode for ejector operation. For this configuration, the static pressure distribution change with NPR is more gradual. Location  $X/L=0$  along the axial distance corresponds to the mixer exit plane. The ejector inlet lip static pressure distribution indicates a rapid acceleration, making static pressure lower than needed for sonic velocity near the chute exit plane for NPR above 2.5. This probably indicates a locally supersonic, secondary stream. The transition or mode switch occurred for all three cases. Qualitatively the effect of flight simulation on static pressure distributions, as observed in Figure 213, between examples (b) and (c), is minor.

The differences in axial static pressure distribution between increasing and decreasing directions of NPR, at NPR levels close to mode switch region, are shown in Figures 214 through 216, at ambient temperature and for LIM cycle conditions, without and with flight simulation. Small difference in pressure distribution is observed indicating that the static pressure levels are relatively lower for the same NPR during the decreasing direction of pressure setting. However, the effect is relatively smaller with flight simulation. The hysteresis phenomenon is stronger if the static pressure distribution differences are significantly higher.

To assess the impact of mode switch on the shroud loads and to develop criteria to establish critical NPR at which mode switch occurs, static pressure distributions along the shroud were integrated to provide a pressure load and moment. These parameters are expressed below.

$$\text{Normalized Shroud Force} = 1 - \left[ \frac{1}{L} \sum_{i=1}^{20} \left( \frac{P_s}{P_{amb}} \right) \Delta X \right]$$

$$\text{Normalized Moment of the Force} = 1 - \left[ \frac{1}{L^2} \sum_{i=1}^{20} \left( \frac{P_s}{P_{amb}} \right) X^T \Delta X \right]$$

These parameters are plotted with respect to NPR for all the configurations at different test conditions (Figure 212). The characteristics of these plots with respect to the force are similar to those with respect to the moment of the force. Hence, the plots with respect to the normalized force due to shroud only are presented here.

The normalized force parameters for the above mentioned vortical mixer-ejector configuration are plotted with respect to NPR in Figure 217 to show the effect of temperature (Figure 217(a)) and flight (Figure 217(b)) on mode switch phenomenon. The normalized forces for decreasing NPR are shown by filled symbols. Thus, the hysteresis loop is contained within the empty and filled symbols. The hysteresis is relatively small for all the conditions (Figure 217). Critical NPR seems to be unaffected by flight simulation, however, the hysteresis loop is relatively less prominent with flight simulation (Figure 217(b)).

#### **4.3.1.2 Effect of MAR with Long Shroud (SAR=4.4)**

Axial static pressure distributions on the shroud centerline for vortical mixer configurations of different MAR at ambient temperature and for LIM cycle conditions, with and without flight simulation, are shown in Figures 218 through 220. The transition or mode switch occurred for all three configurations at ambient temperature conditions (Figure 218). The transition is very gradual for MAR=1.18 and abrupt for MAR=0.97. For MAR=0.88, the transition is barely initiated at NPR=5.6. A complete transition might have occurred at a much higher NPR. For LIM cycle conditions, without and with flight simulation, the transition took place only for MAR=1.18 and the subsonic mode persisted at other two MAR up to NPR=4.5 (Figures 219 and 220).

The effect of flight simulation on shroud static pressure distribution for all the configurations with different MAR seems to be insignificant as observed in Figures 219 and 220. This is further examined in Figure 221 by comparing the shroud static pressure distributions between static and flight simulation conditions for the same test condition. Static pressure decreases with flight on the shroud surface for MAR=1.18. For lower MAR settings the effect due to flight is insignificant.

The differences in axial static pressure distribution between increasing and decreasing directions of NPR, at NPR levels close to mode switch region, are shown in Figures 222 and 223, at ambient temperature for MAR=0.97 at static condition. While small difference in pressure distribution is observed at NPR=4.0, drastic differences are seen at NPR of 4.2, 4.3, and 4.4. In fact, while the subsonic mode existed at these conditions during increasing direction of NPR, the flow remained in supersonic mode during decreasing direction of NPR, indicating strong hysteresis on mode switch.

The hysteresis is further examined in Figure 224 by plotting shroud pressure parameter with respect to NPR for all three MAR configurations. The transition or mode switch occurred for MAR=1.18 at ambient temperature and LIM cycle conditions, with and without flight simulation. The hysteresis is small for all these cases as denoted by shaded areas. The hysteresis loop seems to be more prominent at static condition relative to flight simulation. For MAR=0.97, mode switch occurred only at ambient temperature condition. Apparently, the strongest hysteresis is observed for this configuration at ambient temperature condition. Mode switch did not occur for MAR=0.88 at any condition lower than NPR=5. One also notes the relative low values of shroud loads as static pressures were close to ambient when the nozzle was in the subsonic modes. The shroud loads increase substantially in the supersonic mode. Critical NPR increases with decreasing MAR and increasing temperature. It should be noted that the sign of load changes for MAR=0.88 indicates that the shroud static pressure becomes higher than atmospheric pressure over most of the shroud length.

It should be noted that a strong hysteresis occurs only when the mode switch is abrupt. For gradual transition from subsonic to supersonic modes, hysteresis with respect to NPR is small.

#### **4.3.1.3 Effect of MAR with Long Shroud (SAR=4.9)**

Axial static pressure distributions on the shroud centerline for vortical mixer configurations with MAR settings of 1.18 and 0.97 at ambient temperature and for LIM cycle conditions, with and without flight simulation, are shown in Figures 225 and 226. The transition or mode switch occurred for all three conditions for MAR=1.18 (Figure 225), whereas, for MAR=0.97, the transition occurred only at ambient condition within the NPR limit. The transition is relatively gradual for MAR=1.18 compared to MAR=0.97 (Figure 226).

The effect of flight simulation on shroud static pressure distribution for both configurations is examined in Figure 227. The shroud static pressure distributions between static and flight simulation are compared for NPR=3.4 and  $T_t=1645^\circ\text{R}$ . The static pressure decreases with flight on some portions of the shroud surface for MAR=1.18. The effect due to flight is insignificant for MAR=0.97.

The differences in axial static pressure distribution between increasing and decreasing directions of NPR, at NPR levels close to mode switch region, are shown in Figure 228, at ambient temperature for MAR=0.97 at static condition. Hardly any difference in pressure distribution is observed, indicating the absence of hysteresis on mode switch. This is further examined in Figure 229 by plotting shroud pressure parameter with respect to NPR for both MAR configurations. It should be noted that the decreasing NPR tests are not done for MAR=1.18 at ambient condition. The hysteresis diminishes with flight compared to static condition as observed in Figures 229(b) and 229(c) for MAR=1.18.

#### **4.3.1.4 Effect of SAR with Long Shroud**

The normalized force parameters for the vortical mixer-ejector configurations for two different SARs with fixed MAR settings of 1.18 and 0.97 are plotted with respect to NPR for ambient and LIM cycle conditions, with and without flight simulation in Figures 230 and 231. The transition or mode switch occurred for both SAR configurations with MAR=1.18 at all three temperature conditions. The hysteresis is small for these configurations as denoted by the shaded areas. However, the hysteresis loop seems to be more prominent at static condition compared to flight simulation. Critical NPR seems to increase with increasing SAR (Figure 230). For MAR=0.97, the mode switch occurred only for ambient temperature condition (Figure 229). At this condition, the configuration with SAR=4.4 exhibits a very strong hysteresis compared to the configuration with SAR=4.9. The shroud load increases abruptly during the mode switch for MAR=0.97 compared to configurations with MAR=1.18 (Figure 228).

#### **4.3.1.5 Effect of SAR with Short Shroud (MAR=1.18)**

Axial static pressure distributions on the shroud centerline for vortical mixer configurations of SAR=4.9 and 4.4 at ambient temperature,  $400^\circ\text{F}$ , and for LIM cycle conditions, with and without flight simulation, are shown in Figures 232 through 235. The transition or mode switch did not occur for any of the four conditions for SAR=4.9. However, for SAR=4.4 the transition occurred for all four conditions. The transition is relatively gradual for this configuration.

The effect of flight simulation on shroud static pressure distribution for both the configurations is examined in Figure 236 by comparing the shroud static pressure distributions between static and flight simulation conditions for NPR=3.4 and  $T_t=1645^\circ\text{R}$ . Static pressure decreases with flight over certain portions of the shroud surface, especially for SAR=4.4.

The normalized force parameters for the mixer-ejector configuration with SAR=4.4 are plotted with respect to NPR in Figure 235 to show the effect of temperature (Figure 237(a)) and flight (Figure 237(b)) on mode switch

phenomenon. The normalized forces for decreasing NPR are shown by filled symbols. Thus, the hysteresis loop is contained within the empty and filled symbols. The hysteresis is relatively small for all the conditions (Figure 237). The critical NPR is higher for the LIM cycle compared to ambient or 400°F temperature conditions (Figure 237(a)), indicating that the critical NPR increases with increasing temperature. The critical NPR seems to be lower with flight simulation compared to static condition and the hysteresis loop is relatively less prominent with flight simulation (Figure 237(b)).

#### **4.3.1.6 Effect of Shroud Length (SAR=4.4, MAR=1.18)**

The effect of shroud length on mode switch is examined for vortical mixer-ejector configurations of two different shroud lengths (18.85 in. and 10.46 in.) with SAR=4.4 and MAR=1.18 by plotting shroud pressure parameter with respect to NPR in Figure 238. Again, the hysteresis seems to be small for both the configurations at all the three conditions. However, the hysteresis loop is relatively more significant and critical NPR is relatively higher for the long shroud configuration compared to the short shroud configuration. Again, the hysteresis diminishes by flight simulation for both the configurations.

#### **4.3.1.7 Impact of Mode Switch and Hysteresis on Farfield Noise**

The mode switch occurs in two specific manners, one, a gradual transition and second, an abrupt change from subsonic to supersonic mode. For gradual transition, the hysteresis is minimal, whereas, for abrupt mode switch, strong hysteresis is observed. The impact of mode switch and hysteresis on farfield noise for gradual transition cases is examined in Figure 239 for a vortical mixer-ejector configuration with SAR=4.4, MAR=1.18, and long shroud. In this figure, the normalized shroud force, and the corresponding EPNL levels, are plotted with respect to ideal jet velocity for ambient and LIM cycle conditions, with and without flight simulation, close to mode switch region. The impact of mode switch on farfield noise is gradual EPNL increase with increasing velocity (or NPR). The hysteresis for this configuration is insignificant for all three conditions. In general, very little change in EPNL is observed due to hysteresis. The PNLT directivities and SPL spectra for these cases (results not shown here) do not show any significant effect of hysteresis loop.

It is also necessary to examine a case with abrupt mode switch and strong hysteresis. Hence, the shroud force parameters and the corresponding EPNL values are plotted with respect to ideal jet velocity in Figure 240 for vortical mixer-ejector configurations with SAR=4.4 and long shroud at ambient temperature conditions for two different MAR settings: one with abrupt mode switch and strong hysteresis at MAR=0.97, and the other with gradual transition and small hysteresis at MAR=1.18. A strong hysteresis exists for MAR=0.97 compared to MAR=1.18, for three velocity points, namely, 1490, 1498, and 1508 ft/sec (corresponding NPR of 4.2, 4.3, and 4.4) as observed in Figure 240. Note that all these points correspond to ambient temperatures in the core stream. The EPNL values are also significantly different for two of the same jet velocity points, namely, 1498 and 1508 ft/sec, between subsonic and supersonic modes for MAR=0.97. For the velocity point 1490 ft/sec (NPR=4.2), even though the shroud force parameter shows significant hysteresis, the EPNL does not indicate such phenomenon. This could be explained on the basis of the sensitivity of hysteresis. This point is close to the end of hysteresis loop towards subsonic mode. Hence, slight reduction on NPR could close the loop and bring back the flow from supersonic to subsonic mode.

Figure 241 shows PNLT at a number of polar angles and peak PNLT values with respect to jet velocity. The PNLT values are significantly increased at the same velocity points of 1498 and 1508 ft/sec between subsonic and supersonic modes. The PNLT directivities at these velocities are shown in Figure 242. A substantial increase in PNLT levels is observed at all angles. Spectral plots of SPL for the two cases are shown in Figures 243 and 244. Significant SPL increase is observed for the entire frequency range at all polar angles. In the forward quadrant, as shown for 60 degrees, an SPL hump with a peak at about 1 kHz (i.e., about 11 kHz for model scale) is observed for



supersonic mode. This could be the shock noise due to the possible strong shock close to the ejector exit (see Figures 222 and 223 for static pressure distribution). The noise increase between subsonic and supersonic modes is due to shock associated noise. Since the mode switch is abrupt, the shock-associated noise component becomes prominent compared to a gradual transition case.

At low temperature and high supersonic NPR conditions, the relative contribution of shock-associated noise tends to be significantly higher compared to jet-mixing noise. Based on past experience with round supersonic cold jets, shock noise of such configurations dominates at all observer angles and the spectral shapes maintain characteristics associated with shock broadband noise. For the case of supersonic mode operation, a significant portion of the ejector flow is supersonic, and static pressure equalization to ambient pressure occurs through a strong shock near the ejector-shroud trailing edge. The interaction of flow turbulence with this strong shock is probably the significant contributor to the noted increase in noise levels compared to the subsonic mode.

In the case of subsonic ejector operation, shock structures, if any, are fairly close to the mixer exit plane and the shock-associated noise of such configurations is relatively weak. During supersonic operation, the shock is close to the ejector exit plane and can effectively radiate noise to the farfield. Also to be noted is the increase in SPL at almost all frequencies. This indicates the possibility of a very different plume structure with higher turbulence levels for the supersonic mode under ambient temperature conditions. No LDV plume data was taken at these conditions to check the above hypothesis.

However, as noted from data shown before, the mode switch phenomenon is gradual and has very little hysteresis at elevated temperatures representative of cycle simulation. Higher temperature dampens hysteresis phenomena. Also, as temperature increases, relative contribution of jet-mixing noise compared to shock-associated noise increases at a given NPR. Hence, any increase in shock noise associated with a shock near the trailing edge of ejector would be less dominant due to increased domination of jet-mixing noise. If there were a strong hysteresis at higher temperature condition, for which the ejector flow would have been in subsonic mode during increasing NPR and supersonic mode during decreasing NPR for the same NPR, the impact on noise would have been minimal based on the above argument. However, in the present situation, the above explanation can be applied to the mode switch itself, where the subsonic and supersonic modes are present at two different values of NPR, which are close to each other. If the shock-associated noise had been dominant over the jet-mixing component, then significant noise increase might have been observed from subsonic to supersonic modes. However, the noise increase is relatively small (Figure 239) for LIM cycle cases compared to the ambient temperature case, which is due to dominant jet-mixing noise at elevated temperature. The noise increase between subsonic and supersonic modes for high temperature situations is mostly due to the increase in jet-mixing noise because of jet velocity increase associated with NPR change.

#### **4.3.2 Axial Mixer-Ejector Nozzle Configurations**

##### **4.3.2.1 Effect of Temperature and Flight Simulation with Long Shroud (SAR=4.9, MAR=1.18)**

Typical axial static pressure distributions on the shroud centerline for an axial mixer configuration at ambient temperature and at slightly heated condition (400°F) are shown in Figure 245. For both cases, the static pressure distributions with respect to NPRs are qualitatively similar; with increasing NPR, the flow gradually changes from subsonic mode to supersonic mode and the axial extent over which the static pressures are below the choking pressure ratio increases with NPR. Figure 246 shows the similar results for the same axial nozzle for LIM cycle conditions. The static pressure distributions are presented in this figure with and without flight simulation. Qualitatively, the effect of flight simulation on static pressure distributions is minor. This is further illustrated in Figure 247 by comparing axial static pressure distributions between static and flight simulation conditions at a number of aero-

thermodynamic conditions. Apparently, flight simulation slightly enhances the mode switch from subsonic to supersonic cases.

The differences in axial static pressure distribution between increasing and decreasing directions of NPR, close to mode switch region ( $\text{NPR}=4$ ), are shown in Figure 248 at ambient temperature and for LIM cycle condition, without and with flight simulation. The static pressure levels are slightly lower for the same NPR during the decreasing direction of pressure setting for flight simulation condition. The hysteresis phenomenon is stronger if the static pressure distribution differences are significantly higher.

The normalized force parameters for the above mentioned axial mixer-ejector configuration are plotted with respect to NPR in Figure 249 to show the effect of temperature (Figure 249(a)) and flight (Figure 249(b)) on mode switch phenomenon. The critical NPR is slightly higher for the LIM cycle compared to ambient and 400°F temperature conditions, showing that the critical NPR seems to increase with increasing temperature. The critical NPR seems to be unaffected by flight simulation.

#### **4.3.2.2 Effect of MAR with Long Shroud ( $\text{SAR}=4.9$ )**

Axial static pressure distributions on the shroud centerline for axial mixer configurations of different MAR at ambient temperature, 400°F, and for LIM cycle conditions, with and without flight simulation, are shown in Figure 250 through 253. The transition or mode switch occurred for all three configurations at ambient and 400°F temperature conditions (Figures 250 and 251). The transition is very gradual for  $\text{MAR}=1.18$  and abrupt for  $\text{MAR}=0.97$ . For  $\text{MAR}=0.88$ , the transition is barely initiated at  $\text{NPR}=5.5$  for ambient condition, but almost complete for the 400°F case at  $\text{NPR}=5.4$ . A complete transition at ambient condition might have occurred at a much higher NPR. For LIM cycle conditions, with and without flight simulation, the transition took place for  $\text{MAR}=1.18$  and 0.97 and the subsonic mode persisted at  $\text{MAR}=0.88$  up to  $\text{NPR}=5.0$  (Figures 252 and 253).

Axial static pressure distributions on the shroud centerline for axial mixer configurations of different MAR are compared at a number of NPR values close to the transition level at ambient temperature, 400°F, and LIM cycle conditions, with and without flight simulation, in Figures 254 through 257. Early transition with respect to NPR occurs for higher MAR.

The normalized force parameters for the axial mixer-ejector configurations with three different MAR values are plotted with respect to NPR for ambient and 400°F conditions (Figure 258). The transition or mode switch occurred for all three MARs at both the temperature conditions. The hysteresis is small for these configurations as denoted by shaded areas. However, the hysteresis loop seems to be more prominent at 400°F relative to ambient temperature and for decreasing MAR. Figure 259 shows similar plots for the axial mixer-ejector configurations for LIM cycle conditions, with and without flight simulation. The mode switch did not occur for  $\text{MAR}=0.88$  at these temperature conditions up to  $\text{NPR}=5$ . Also noted are the relative low values of shroud loads as static pressures were close to ambient when the nozzle was in the subsonic modes. Figures 258 and 259 indicate that the critical NPR increases with decreasing MAR up to about 0.9 and with increasing temperature.

The impact of hysteresis is further illustrated by plotting the differences in axial static pressure distribution between increasing and decreasing directions of NPR, at NPR levels close to mode switch region, in Figures 260 and 261, at ambient and 400°F temperature conditions for  $\text{MAR}=0.97$  at static condition. Small difference in pressure distribution is observed for all nozzle pressure conditions. Similar results for  $\text{MAR}=0.88$  at 400°F condition, where significant hysteresis is observed (Figure 258), are plotted in Figures 262 and 263. While, small difference in pressure distribution is observed at  $\text{NPR}=5.0$ , drastic differences are seen at NPR values of 5.2 and 5.3. In fact, while the subsonic mode existed at these conditions during increasing direction of NPR, the flow remained in the



supersonic mode during decreasing direction of NPR, indicating strong hysteresis on mode switch. At  $MAR=0.88$ , stronger hysteresis was expected at ambient condition compared to  $400^{\circ}F$ . In order to capture the hysteresis as the NPR is reduced, the NPR must first be raised high enough so that the flowfield completely transitions to supersonic conditions. For the ambient temperature condition at  $MAR=0.88$ , the transition was not completed at  $NPR=5.5$ . Perhaps a higher NPR would have resulted in a complete transition.

#### **4.3.2.3 Impact of Mode Switch and Hysteresis on Farfield Noise**

The mode switch occurs in two specific manners: a gradual transition or an abrupt change from subsonic to supersonic mode. For gradual transition, the hysteresis is minimal, whereas, for abrupt mode switch a strong hysteresis is observed. The impact of mode switch and hysteresis on farfield noise for gradual transition cases is examined in Figure 264 where noise levels for increasing as well as decreasing NPR are plotted at the same NPR, for an axial mixer configuration with  $MAR=1.18$ . Based on Figure 264, the impact of hysteresis seems to be insignificant on noise levels for this configuration. Whether significant hysteresis, which keeps the modes subsonic during increasing NPR and supersonic during decreasing NPR at the same condition, would impact on farfield noise, is examined for the axial mixer configuration with  $MAR=0.88$  at  $400^{\circ}F$  condition in the following section.

The shroud force parameter and the corresponding EPNL, peak PNLT, and PNLT at various polar angles are plotted with respect to NPR in Figure 265 for an axial mixer-ejector configuration with  $SAR=4.9$  and with long shroud at  $400^{\circ}F$  temperature conditions. Figure 265 shows an abrupt mode switch and strong hysteresis occurred with  $MAR=0.88$  for three NPR values, 5.2, 5.3, and 5.4. The EPNL levels are also different for  $NPR=5.2$  and  $NPR=5.3$ , between subsonic and supersonic modes. The PNLT values are significantly increased at  $NPR=5.2$  and 5.3 between subsonic and supersonic modes. For  $NPR=5.1$ , even though the shroud force parameter shows significant hysteresis, the EPNL and PNLT values do not indicate such phenomenon. This can be explained on the basis of the sensitivity of hysteresis. This point is close to the end of hysteresis loop towards subsonic mode. Hence, slight reduction of NPR could close the loop and bring back the flow from supersonic to subsonic mode.

The PNLT directivities at NPR values of 5.0, 5.1, 5.2, 5.3, and 5.4 are shown in Figure 266. Substantial increase in PNLT is observed at aft angles for NPR levels of 5.2 and 5.3. Spectral plots of SPL for  $NPR=5.0$ , 5.2, 5.3, and 5.4 are shown in Figures 267 through 270. Significant SPL increase is observed for the entire frequency range at aft polar angles.

#### **4.3.3 Mode Switch Phenomena and Control**

The aerodynamic testing and data analyses during this program were principally conducted to aid in understanding mixing duct transition from compound compressible subsonic to compound compressible sonic flow. For the geometries evaluated in this program, strong evidence of mode switch and hysteresis was not always evident. This may, in part, be due to the lower penetration of the mixer hot lobes (65 percent penetration for the vortical mixer and 90 percent for the axial mixer) which provided a shielding or buffering flow along the shroud walls (see Section 3.2.2.2.3). It is possible that stronger shocks existed at center stream and the buffering flow prevented the attendant axial pressure gradients from being measured at the shroud wall. It is also conceivable that the buffering flow could modify the internal shock structures, spreading these gradients. Either scenario, however, can only be conjecture at this point as the data does not allow better definition.

The major concern with mode shift in a mixer-ejector nozzle is the associated sudden change in static pressures and loads in the mixing duct and the attendant shift in shroud loading (forces). Another concern, not measured here, would be any sudden shift in thrust performance as NPR increases (and decreases). During this program, a sudden shift in loading was only observed for ambient temperature and at high NPR (4.5 or greater).

The axial mixer reduced the severity of the mode shift. With short shrouds and/or low MAR, the mode switch can be eliminated from the operating regime. Even if mode switch does occur, the associated change in mixing duct pressures is gradual and is not characterized by sudden shifts in static pressure.

The strongest influence on mode switch was found to be the MAR, as shown in Figure 271, which gives the critical NPR (for mode switch) for the long shroud configurations. Based on this relationship, a MAR of 0.92 (or less) would prevent mode switch when operating at NPRs less than 4.5 for both the vortical and axial mixers operating at takeoff flight Mach numbers.

#### 4.4 LASER TWO-DIMENSIONAL FIBER OPTICS FLOWFIELD MEASUREMENT

Laser Doppler velocimeter (LDV) measurements have been made on several vortical and axial mixer-ejector configurations in Cell 41 for external plume survey and the survey of flowfield internal to the ejector. Figure 272 shows the fiber optics LDV system (operated in a two-velocity component mode with four beams) and an axial mixer-ejector nozzle configuration, mounted in the anechoic chamber. For each configuration, data is acquired at different nozzle flow conditions, with and without flight simulation. In addition, the effects of shroud length and acoustic treatment on plume flowfield are studied. The LDV system is used in a two-dimensional mode in the current series of tests; the X- (axial) and Y- (vertical) components of velocity and turbulent intensity are acquired in all traverses.

The LDV measurements are made in two different ways: 1) by continuously traversing the laser, and 2) acquiring about 2000 data samples at a single location. For continuous survey, 50 data points within a short duration are averaged, and the averaged velocity components are assigned to the mid-location of the distance traversed within the duration. Approximately 20 averaged data points are obtained per inch along spanwise and vertical traverse directions during continuous traverse. Along the axial (X) direction in the external plume, the traverse speed is much higher and approximately one averaged data point is obtained per inch. Velocity obtained in this way is termed the running average velocity. In the second method, all the data samples (about 2000 data samples) are averaged to obtain the velocity components. Using these data samples, the relative turbulence intensity along X-direction ( $TI_x$ ) in percent is computed as follows:

$$TI_x = 100 \frac{\sqrt{\frac{\sum_{i=1}^N (V_{x,ave} - V_{x,i})^2}{N}}}{V_{x,ave}}$$

where  $N=2000$ ,  $V_{x,ave}$ =average velocity component along the X-direction,  $V_{x,i}$ =instantaneous (sample) velocity component along the X-direction.

Taking 2000 data samples for every location gives statistically more accurate results compared to the continuously traversed results. However, the continuous traversing method is much faster and reasonably adequate to get an estimate of mean velocity. Most of the measurements are made using the running average method in the current program to understand mean flowfield distributions and for comparison with CFD predictions. Limited amounts of measurements are made with 2000 data samples per location to validate the running average data and to obtain sta-

tistically more accurate turbulence intensity results. The validity of running average results will be shown later by comparison with averaging of 2000 data samples.

Laser doppler velocimeter tests are conducted to study the effects of mixer design and ejector length on mean velocity and relative turbulence intensity profiles at the ejector exit plane, and the plume decay rates aft of the ejector exit. Plume decay is evaluated by LDV traverses along major and minor axes at several axial locations from the ejector exit. Typical traverse locations are shown in Figure 273(a). The ejector exit plane mean and turbulent velocity profiles are measured along the spanwise direction (Z-direction) at every 0.5-in. interval, starting at  $Y=0$ . In addition, measurements are made at four spanwise traverses and two vertical (Y-direction) traverses, as shown in Figure 273(b). The coordinates for traverse locations are also normalized with respect to the width of the ejector,  $We$ , which is 6.8 in. for all configurations (Figure 273).

#### 4.4.1 Laser Doppler Velocimeter Test Results for External Plume

##### 4.4.1.1 Axial Mixer-Ejector Configurations

Figure 274 shows an isometric view of an axial mixer-ejector configuration. In addition, the axial (X), vertical (Y), and spanwise (Z) traverse directions are shown in this figure. Two configurations of axial mixer-ejector nozzle are tested, one with short hardwall shroud ( $L_{EJ}=10.46$  in.) and the other with long hardwall shroud ( $L_{EJ}=18.85$  in.). The shroud area ratio (SAR) and mixing area ratio (MAR) are kept at 4.9 and 1.18, respectively, for both these configurations.

Figure 275 shows a comparison, conducted with the axial mixer-ejector and the long hardwall shroud, between running average axial velocity ( $V_x$ ) and the axial velocity from averaging 2000 data samples along X-, Y-, and Z-directions. The corresponding relative turbulence intensity results are also plotted. The comparisons indicate very good agreement between the running average and 2000 data sample-averaged velocities. Hence, the running average mean velocities are presented in the remaining portion of this section. Relative turbulence intensities close to the ejector exit plane ( $X=0.65$  in.) are about 16 to 18 percent (note that turbulence intensity is relative because is normalized by the local mean velocity). Along the axial direction, the relative turbulence intensity decreases with respect to X to about 10 percent at  $X=35$  in. and then increases with X due to a reduction in mean velocity. These high levels of relative turbulence intensity indicate significant mixing processes are still occurring, and it is quite evident that there is no potential core in the exit plume. This point needs to be kept in mind in estimating external plume noise using existing semi-empirical jet noise prediction methods, such as the SAE method which is based on round jets with well defined potential cores.

Figure 276 shows the axial ( $V_x$ ) and vertical ( $V_y$ ) velocity distributions along Y- and Z-directions for the axial mixer-ejector nozzle with short hardwall shroud at close vicinity of the ejector exit plane. The spanwise distribution of axial velocity clearly indicates the crests and troughs due to the individual chutes, with a variation of about 500 ft/sec. This data is indicative of lack of efficient mixing of primary and secondary streams in the ejector. The vertical distribution of axial velocity shows a dip at the center, indicating possible secondary flow migration towards nozzle centerline. The vertical velocity along spanwise and vertical directions show a small variation and the mean value is very close to zero. The external flow is predominately in the axial direction. In subsequent results, only the axial velocity component will be shown.

Spanwise and vertical distributions of axial velocity along X-direction for the axial mixer-ejector-nozzle with short hardwall shroud are examined in Figure 277. The axial velocity difference, between the crests and troughs due to individual chutes along spanwise direction, gradually diminishes with increasing axial distance due to mixing. At about one nozzle width ( $X=6.8$  in.) downstream of the ejector exit plane, the velocity profiles are more uni-

form. The velocity dip at the center along vertical direction gradually reduces with  $X$ , but still persists at  $X=6.8$  in. Comparison of axial velocity distributions between spanwise and vertical directions at 10 axial locations are shown in Figure 278 for axial mixer-ejector configurations with short and long hardwall shrouds. Closer to the exit plane, significant difference is observed between spanwise and vertical velocity distributions. However, with increasing  $X$ , the velocity distribution differences between the axes diminish, and both the profiles look very similar beyond  $X=40$  in.

#### 4.4.1.1.1 *Effect of Nozzle Pressure Ratio (NPR)*

Figure 279 shows the comparison of velocity variations along the vertical direction between the center of hot and cold chute flow regions close to the ejector exit plane at two NPRs. A dip in velocity at the center of the nozzle ( $Y=0$ ) is noted as before. However, the magnitude of the velocity dip is smaller at the center of hot flow region compared to the center of the chute. The velocity minima values do not change significantly by changing the NPR and total temperature, indicating entrained secondary flow is not being efficiently mixed with primary. However, the velocity distributions away from the center are lower for  $NPR=2.5$  compared to  $NPR=3.5$ , indicating that the flow away from nozzle vertical and spanwise centerlines is dominated by the primary stream.

The effect of NPR is examined in Figure 280 by comparing the spanwise and vertical velocity and relative turbulence intensity distributions between two flow conditions close to the ejector exit plane. The spanwise velocity distribution clearly indicates the crests and troughs due to individual chutes for both the conditions. However, the magnitudes of the axial velocity and the velocity difference between the crest and trough are higher for the higher NPR, which is due to higher convection Mach numbers as NPR is increased and reduced lower levels of mixing. The velocity distributions in the vertical direction for the two NPRs are very close to each other at the center and up to about mid way from the center to the shroud. Again, the velocity at  $Y=0$  is predominantly entrained flow, which stays at about same value irrespective of primary stream NPR. Closer to the shroud, the axial velocity increases towards the shroud for  $NPR=3.5$ , whereas, the velocity gradually decreases for  $NPR=2.5$ , indicating the predominance of the primary stream towards the shroud. We do not see much variation of relative turbulence intensity between the trough and crest along the  $Z$ -direction. Apparently, the relative turbulence intensity is slightly higher for lower jet velocity (i.e., for lower NPR) and is in the range of 20 percent.

The axial velocity distributions between two nozzle aerothermodynamic conditions are further compared at 10 axial locations in Figure 281. The velocity levels for  $NPR=3.5$  are higher compared to  $NPR=2.5$  with respect to  $Y$  as well as  $Z$  directions for all the  $X$  locations, up to  $X=68$  in. (i.e., 10 ejector widths from the exit plane).

The axial evolution of the external plume and the relative turbulence intensity variations along  $X$  are shown in Figure 282. For  $NPR=3.5$  the axial velocity increases along  $X$  up to about 3 ejector widths ( $X=20$  in.), remains constant up to about  $X=50$  in., and then decreases. However, for  $NPR=2.5$ , the velocity increases gradually, attains a constant level at about two widths from the ejector exit, and remains constant further downstream. The relatively higher value reached for  $NPR=3.5$  at nozzle centerline is due to further acceleration of the flow at the nozzle centerline by the high velocity regions. It should be noted that the velocity at the exit plane is about the same for both NPRs, which is due to the unmixed secondary flow. Relative turbulence intensity, as also observed in Figure 280, is slightly lower for  $NPR=3.5$  at the exit plane compared to  $NPR=2.5$  and is about the same slightly downstream. The relative turbulence intensity is slightly higher for  $NPR=3.5$  in the plume beyond  $X=20$  in. The relative turbulence intensity levels are indicative of a very turbulent plume for the axial mixer-ejector configuration compared to the potential core of a round convergent nozzle, which typically has 2 to 3 percent relative turbulence intensities in the potential core.

The effect of NPR on axial velocity and relative turbulence intensity distributions, along spanwise and axial directions, for the axial mixer-ejector nozzle configuration with long hardwall shroud, is examined in Figure 283. The spanwise velocity distributions for three NPRs (2.5, 3.5, and 4.5) show no crest and trough corresponding to the chutes, indicating almost complete mixing within the ejector. The spanwise velocity variation is relatively small for each of the NPR and the average value increases with NPR. The velocity variation along the X-direction shows gradual increase, followed by a plateau, and then a decrease. The velocity decay is much steeper for NPR=4.5. The relative turbulence intensity levels are slightly lower for NPR=2.5 along the Z-direction compared to NPR=3.5. Along the X-direction, the relative turbulence intensity levels reach a minimum of about 10 percent for both the flow conditions at X=30 in. and then start increasing with increasing X.

The axial velocity distributions between two nozzle aerothermodynamic conditions are further compared at 10 axial locations in Figure 284 for the long shroud mixer-ejector configuration. As expected, the velocities for NPR=3.5 are higher compared to NPR=2.5 with respect to Y- as well as Z-directions for all the X locations, up to X=68 in. (10 ejector widths from the exit plane).

#### 4.4.1.1.2 *Effect of Shroud Length*

Effect of shroud length on spanwise velocity and relative turbulence intensity distributions are examined in Figure 285. While the crests and troughs are prominently observed for short shroud configuration ( $L_{EJ}=10.46$  in.), the mean velocity is relatively uniform for long shroud configuration ( $L_{EJ}=18.85$  in.) without any distinct crest and trough. The turbulent intensity levels are relatively lower for the long shroud configuration along spanwise and vertical directions, which is another indication of better mixing for the longer shroud. The velocity profiles for short and long shrouds are compared at a number of axial locations in Figure 286. The nonuniformity of velocity distribution along the Z-direction for the short shroud configuration diminishes with increasing X, and becomes uniform at X=20 in. (about three widths downstream of the ejector exit). Along the Y-direction, the velocity dip at the center decreases with increasing X, and the profile becomes uniform at about X=40 in. for both shroud configurations. Figure 287 shows the effect of shroud length on velocity and relative turbulence distributions along the X-direction at the ejector centerline ( $Y=Z=0$ ). The velocity for the short shroud case is much lower compared to that for the long shroud at the ejector exit plane, indicating poorer internal mixing for the short shroud configuration. The relative turbulence intensity levels are slightly higher for the short shroud configuration compared to the long shroud case. Relative turbulence intensity decreases with respect to X, reaches a minimum (about 10 percent) at about 30 in. downstream of the ejector exit, and then increases with increasing X.

#### 4.4.1.1.3 *Effect of Flight Simulation*

The effect of flight simulation on velocity and relative turbulence intensity distributions along the axial direction are shown in Figure 288 for the long shroud configuration. The effect of freestream Mach number is very prominent on velocity decay along the X-direction. The velocity at the ejector exit plane is lower with flight simulation than the static case. This is probably caused by reduced internal mixing for the flight case due to increased secondary flow entrainment relative to the static case. However, the velocity decay along X-direction is much faster for the static case compared to flight case, which is due to reduced mean shear in the flight case. The relative turbulence intensity levels are very close to each other, with and without flight, closer to the ejector exit up to about X=30 in. Further downstream, at higher axial locations in the plume, the relative turbulence intensity is higher at static condition compared to flight simulation. The effect of flight on velocity distributions along spanwise and vertical directions are shown in Figure 289 and 290, respectively, for axial locations of 0.65 in. and 6.8 in. The effect of flight seems to be minimal along Y and Z, closer to the ejector exit, since the full effect of mean shear reduction due to freestream is not felt by the plume at distances close to the exit plane. This is further illustrated in Figure 291 by comparing the velocity profiles, with and without flight simulation, at a number of axial locations.

#### 4.4.1.2 Vortical Mixer-Ejector Configurations

Typical LDV results in the external plume for vortical mixer-ejector configurations are presented in this section. Figure 292 is an isometric view of a vortical mixer-ejector configuration, showing the axial (X), vertical (Y), and spanwise (Z) traverse directions. Two configurations of vortical mixer-ejector nozzle, one with short hardwall shroud ( $L_{EJ}=10.46$  in.) and the other with long hardwall shroud ( $L_{EJ}=18.85$  in.), are tested. The shroud area ratio, SAR, and mixing area ratio, MAR, are kept 4.9 and 1.18, respectively, for both configurations.

Figure 293 shows the comparison of axial velocity variations along the vertical direction between the centers of hot and cold chute flow regions close to the ejector exit plane for long and short shroud configurations. The velocity level at  $Y=0$  is higher at the center of the hot flow region compared to the center of the chute for both the configurations. However, the velocity difference between these two points is much smaller for the long shroud configuration. Axial velocity distributions for the short shroud configuration have velocity variation of about 500 ft/sec for hot and about 250 ft/sec for cold chute flow regions indicating lack of good mixing within the length of ejector. However, the velocity variations for the long shroud configuration are much smaller indicating that almost complete mixing occurs by the end of long ejector.

The axial velocity profile variations along the axial direction are further examined in Figure 294 by comparing velocity profiles between spanwise and vertical directions at a number of axial locations. For the short shroud configuration, the profiles are very nonuniform and different between spanwise and vertical directions closer to the exit up to about 4 to 5 widths ( $X=27$  in.). At axial locations further downstream, the velocity profiles are closer to each other and relatively more uniform. The velocity profiles along the vertical direction are relatively wider at these locations. For the long shroud configuration, the velocity profiles are relatively more uniform. The velocity profiles between spanwise and vertical directions are similar to each other from about the 3-width position ( $X=20$  in.), which is indicative of better mixing for the longer shroud configuration.

##### 4.4.1.2.1 Effect of Nozzle Pressure Ratio (NPR)

The axial decay of the external plume along the nozzle centerline ( $Y=Z=0$ ) is shown in Figure 295 for three different aerothermodynamic conditions, for short and long shroud configurations. Except for  $NPR=2.5$ , the axial velocity remains constant for up to about five ejector widths ( $X=34$  in.) and then starts decaying. For  $NPR=2.5$ , the velocity increases gradually, attains a maximum level at about six widths from the ejector exit, and then decreases. For the short shroud configuration, at  $NPR=2.5$ , the initial velocity is lower compared to long shroud configuration and, hence, the velocity rise is relatively higher compared to long shroud configuration, even though the peak level is the same for the both cases. The axial mean velocity variation exhibits typical subsonic jet characteristics, in that the velocity decay is approximately proportional to  $1/X$  after about seven widths from the ejector exit plane (about 50 in.). However, turbulent intensity distributions need to be analyzed to interpret the plume decay features.

Vertical distributions of axial velocity at two axial (X) locations for long and short shroud vortical mixer configurations are examined in Figure 296 under three different aerothermodynamic conditions. Close to the ejector exit plane, three velocity peaks are observed along the Y-direction, including one at the center of the cold chute ( $Y=0$ ) for short and long shroud configurations at NPR values of 3.5 and 4.5. For  $NPR=2.5$ , a valley is observed at the center as opposed to a peak for higher NPRs. The difference between the peaks and the dips is relatively higher for the short shroud configuration compared to the long shroud case. However, with increasing X, the velocity variation along Y reduces and becomes relatively flatter, as observed in Figure 296(c) and Figure 296(d) at  $X=13.6$  in.

Figure 297 shows the axial velocity distributions along the spanwise (Z) direction for the cases shown in Figure 296. Close to the ejector exit plane ( $X=0.65$  in.), chute to chute variations are clearly identifiable in the

velocity distributions. The spanwise velocity distribution clearly indicates the crests and troughs due to individual chutes for short shroud configuration. The magnitudes of the axial velocity, and the velocity difference between the crest and trough, increase with increasing NPR, which is due to higher convection Mach numbers as NPR is increased, and results in a lower level of mixing. However, for the long shroud configuration, the velocity variation between primary and secondary flow regions is much smaller compared to the short shroud case, which is indicative of better mixing for the longer shroud. With increasing X, the velocity profiles become more uniform for both the configurations at all three flow conditions. As shown in Figure 297(c) and Figure 297(d), the velocity profiles along the Z-direction are uniform and resemble single flow nozzle profiles at  $X=13.6$  in.

Axial velocity profiles for  $NPR=2.5$  are compared with those for  $NPR=3.5$  along spanwise and vertical directions at a number of axial locations up to ten widths from the exit plane, for short and long shroud configurations (Figures 298 and 299). As expected, the peak velocities for  $NPR=3.5$  are higher compared to those for  $NPR=2.5$  for both shroud configurations. However, the velocity profiles are more uniform close to ejector exit for the long shroud configuration, indicating better mixing in the ejector.

The effect of NPR on relative axial turbulence intensity distributions for short and long shroud configurations is shown in Figure 300. In general, the relative turbulence intensity levels are about 20 percent at the ejector exit for the short shroud configuration. These levels are about 15 percent for long shroud configuration. Axially, for both configurations, the relative turbulence intensity decreases with X, reaches a minimum at about 30 in. from the exit plane, and then increases for higher X. The minimum level is about 10 percent. The effect of NPR on relative turbulence intensity is insignificant at the ejector exit. However, these levels are higher for  $NPR=3.5$  compared to  $NPR=2.5$  along axial direction. The effect is significant for the short shroud configuration. Based on the magnitude of relative turbulence intensity, the external plume flow appears to be highly turbulent. Hence, it is incorrect to assume the externally generated noise to be similar to a reference conic nozzle.

#### *4.4.1.2.2 Effect of Shroud Length*

The effect of shroud length on external plume velocity distributions is further examined in Figure 301. Velocity distributions along the X-direction at  $Y=Z=0$  show very little effect of ejector length. With respect to spanwise velocity distribution, while the crests and troughs are prominently observed for the short shroud configuration ( $L_{EJ}=10.46$  in.), the velocity is relatively uniform for the long shroud configuration ( $L_{EJ}=18.85$  in.) without any distinct crest and trough (Figure 301(b)). Velocity distributions along the Y-direction also indicate uniform profile for the long shroud compared to the short shroud configuration. This is further demonstrated in Figure 302 by comparing the spanwise and vertical velocity profiles between short and long shroud configurations at a number of axial locations up to about ten widths from ejector exit plane.

#### *4.4.1.2.3 Effect of Flight Simulation*

The effect of flight simulation on velocity distributions along the three axes are examined in Figures 303 through 306 for the vortical mixer-ejector nozzle with long and short hardwall shroud configurations. The effect of freestream Mach number is minimal on nozzle centerline velocity distribution for about three to four times of ejector width. In this region, the velocities with and without flight simulation are of the same level and remain the same with respect to X. Further downstream, the velocity decay along the X-direction is much faster for the static case than the flight case, which is due to reduced mean shear in the flight case. These effects are quite similar for short and long shroud configurations. The effect of flight seems to be minimal along Y and Z for long and short shroud configurations near the ejector exit plane, since the mean shear reduction due to freestream has not yet impacted the internal regions of the plume close to the exit plane. However, further downstream, as observed in Figures 304 and 306, the velocity profiles show significantly more decay for static condition than those with flight simulation.



The impacts of shroud length and flight simulation on axial variation of relative turbulence intensity are shown in Figure 307. For the static condition, the relative turbulence intensity is higher for the short shroud configuration compared to long shroud. However, this difference is negligible with flight simulation at large distances from the exit. Closer to the ejector exit, the relative turbulence intensity is still higher for the short shroud configuration. The relative turbulence intensity is higher for static condition compared to flight simulation downstream of the ejector exit plane. This effect is more noticeable for the short shroud configuration compared to long shroud.

#### 4.4.1.2.4 Effect of Acoustic Treatment

The effect of acoustic treatment on the external velocity profiles are examined for a vortical mixer-ejector nozzle with long shroud ( $L_{EJ}=18.85$  in.). All the LDV measurements were taken at a fixed aerothermodynamic condition of  $NPR=3.5$ ,  $T_t=1735R$ , and  $V_j=2518$  ft/sec.

Figure 308 shows the axial ( $V_x$ ) velocity distributions along Y- and Z-directions at three axial (X) locations downstream from the ejector exit plane with flight simulation ( $Mn=0.32$ ). Contrary to physical intuition, the axial velocity with acoustic treatment seems to be slightly higher (about 100 ft/sec) compared to the hardwall configuration at both Y- and Z-directions for all three axial locations. At and near the centerline ( $Y=Z=0$ ), the velocities with and without treatment are almost equal. Figure 309 shows similar results at two axial locations at static condition. In this case, the axial velocities are lower with treatment at and close to the centerline, but remain higher away from the center, compared to the hardwall configuration. Apparently, the axial velocity increase due to treatment is relatively lower for static condition compared to the flight simulation case.

Figure 310 shows the effect of treatment on axial velocity distributions along vertical direction (Y) at the center of hot and cold chute flow regions close to the ejector exit plane ( $X=0.65$  in.) with flight simulation. Again, the velocities with treatment are higher away from the centerline and almost equal near the centerline, compared to the hardwall configuration, at hot and cold chute flow regions.

Figure 311 shows the effect of treatment on axial velocity distributions along spanwise directions (Z) at various Y locations close to the ejector exit plane ( $X=0.65$  in.) with flight simulation. At  $Y=1.0$  in., the entire velocity profile with treatment is about 100 ft/sec higher compared to the hardwall configuration. With increasing height (Y), the velocities for the treated configuration become lower compared to the hardwall configuration close to the ejector wall, and the trend is reversed near the centerline.

Two hypotheses are proposed to explain the velocity increase due to ejector treatment. First, the boundary layer thickness might have increased due to increased the roughness of the treatment, which would cause a reduction in the ejector cross-sectional area. Hence, the overall velocity with treatment might have gone up for the same amount of mass flow rate. The assumption of same amount of mass flow rate with and without treatment is based on static pressure distribution, shown in Figure 312, which indicates secondary stream choking ( $P_s < P_{cr}$ ) and, hence, one may assume primary and secondary mass flow rates stayed the same for hard and treated cases. Unfortunately, there was no static pressure instrumentation for the treated configurations. However, it is conceivable that the secondary flow is compound choked for this condition, based on the static pressure distribution in Figure 312. It should be pointed out that, for turbulent boundary layers, roughness has minimal effect, and the wall is hydraulically smooth, if all protuberances are contained within the laminar sublayer, or the dimensionless roughness is less than 5 (Ref.: Boundary Layer Theory by Schlichting). For the present case, our explanations are based on the assumption that the treatment roughness is high enough to effect the boundary layer.



Secondly, based on the static pressure distributions on the hardwall shroud surface (Figure 312), a relatively strong static pressure gradient is present in the ejector slightly downstream of the mixer exit plane. The steeper static pressure rise probably represents a shock structure whose strength might have been reduced for the treated ejector (no pressure data available for the treated configuration) and, hence, the pressure rise across the shock might have been lower compared to the hardwall configuration. This might have caused a higher flow velocity for the treated configuration. This is a conjecture due to lack of static pressure data for the treated configuration.

Both these effects might have contributed to the velocity increase for the treated configuration compared to the hardwall case as observed in Figures 308, 310, and 311. The treatment roughness could make the velocity gradient less steep than that near a smooth one, as can be seen in Figure 311, especially at higher Y locations. Due to effectively thicker boundary layer for the treated case, close to the shroud (higher Y), the treated configuration exhibits slightly lower velocities near the sidewalls, and slightly higher velocities in the interior of the nozzle to satisfy mass flow continuity. For static condition, the velocity increase due to treatment is relatively small (Figure 308), which might have been caused due to the weaker shock, as indicated by shroud surface pressure distribution in Figure 312. Since the shock strength for static condition is small for hardwall, the treatment might not have impacted on its strength as much and, hence, the velocity increase might have been caused only by change in boundary layer due to treatment.

In future tests, it would be advisable to make LDV measurements of the treated as well as hardwall configurations, along with static pressure distribution measurements to understand and interpret the effect of treatment on performance and mixing.

#### **4.4.1.3 Effect of Mixer Design (Axial Versus Vortical)**

It is important to examine the effect of mixer design on velocity and relative turbulence intensity distributions, since the axial and vortical mixers are quite different in their designs. Figure 313 shows the axial, vertical, and spanwise velocity distribution comparisons between axial and vortical mixers with short shroud. As can be seen, the velocity profiles are drastically different between the axial and vortical configurations. At the center of the exit plane, the axial velocity is very low for the axial mixer compared to the vortical configuration. The centerline velocities are closer for the two mixers after about ten widths ( $X=70$  in.) from the ejector exit. Velocity distributions along spanwise and vertical directions close to the ejector exit are significantly different between the two mixer designs. The velocity comparisons between the two mixers along the axial direction are shown in Figure 314 for  $NPR=3.5$ . Similar characteristics are still observed for lower  $NPR$  ( $NPR=2.5$ ) conditions, as shown in Figure 315. The lower velocity levels for the axial mixer indicate more ambient entrainment in the ejector compared to the vortical configuration.

Similar results with the long shroud are shown in Figures 316 and 317. In this case, the velocity profiles along the spanwise direction are more uniform for both designs compared to short shroud profiles. This is indicative of better mixing. However, the velocity distribution in the vertical direction for the axial mixer shows large variation compared to the vortical mixer. Velocity distributions along the X-direction show lower levels for the axial mixer at the centerline for the entire distance of the traverse ( $X=75$  in.). Similar results with the long shroud at static condition are shown in Figures 318 and 319.

Relative turbulence intensity distributions between the axial and vortical mixer configurations are shown in Figure 320. Close to the ejector exit plane, the relative turbulence intensity levels are slightly higher for the axial mixer compared to the vortical configuration, due to lower mean velocity for the axial mixer. However, the distributions along the X-direction indicate very little difference in relative turbulence intensity between the mixer designs beyond 2–3 widths from the exit.

#### 4.4.1.3.1 Axial Velocity Contours Close to Ejector Exit Plane

Laser doppler velocimetry traverses along Z-directions were made at  $X=0.65$  in., at different Y, with a step of  $Y=0.5$  in. Seventeen such traverses were made for both mixer configurations at this plane, and utilizing these data, axial velocity contour plots were generated. Typical contour plots with flight simulation ( $Mn=0.32$ ) are presented in this report to show mixing characteristics with respect to ejector length and mixer design. Short ( $L_{EJ}=10.46$  in.) and long ( $L_{EJ}=18.85$  in.) hard wall shrouds were used for both vortical and axial mixer configurations. For all the configurations, the same SAR of 4.9 and MAR of 1.18 were maintained.

Figure 321 shows the axial velocity contours for vortical mixer-ejector configurations with short and long shrouds for  $NPR=2.5$ ,  $T_t=1325^\circ R$ , and  $V_j=1919$  ft/sec. For the long shroud configuration, the velocity distribution indicates more flow uniformity compared to the short shroud configuration. This indicates relatively better mixing for the long shroud ejector. Similar results for axial mixer configurations are shown in Figure 322. Again, the results indicate more velocity uniformity for long shroud configuration compared to short shroud case. Comparing the results for the two mixer designs for long shroud configurations (Figure 321(b) and Figure 322(b)), more velocity uniformity is observed for axial mixer-ejector nozzle.

Similar results for vortical and axial mixer-ejector configurations for a higher nozzle pressure condition ( $NPR=3.5$ ,  $T_t=1735^\circ R$ ,  $V_j=2518$  ft/sec) are plotted in Figures 323 and 324, respectively. The general behavior with respect to velocity uniformity is similar to what is observed in Figures 321 and 322 for  $NPR=2.5$ ,  $T_t=1325^\circ R$ ,  $V_j=1919$  ft/sec. However, relatively higher level velocity contours are observed for  $NPR=3.5$ ,  $T_t=1735^\circ R$ ,  $V_j=2518$  ft/sec. The significant differences in the velocity distribution of axial and vortical mixer designs for both ejector lengths are due to differences in mixer designs. The axial mixer design shows vertical strips whereas the vortical mixer shows more uniform mixing with concentrated high velocity peaks in the center. This is particularly evident for the short ejector configurations.

#### 4.4.2 Laser Doppler Velocimeter Test Results for Internal to Ejector Flowfield

Only the short hardwall shroud configurations ( $L_{EJ}=10.46$  in.) were tested for the internal ejector flowfield. Glass windows (8 in. x 7 in.) were used on the sidewalls to cover the entire width (Y) and extend from the exit of the mixer to about 2.5 in. upstream of the ejector exit plane, along the length (X) of the side walls. Figure 325 shows the laser beams of the fiber optics LDV system (operated in a two-velocity component mode with four beams) passing through the sidewall glass windows of a mixer-ejector nozzle configuration, mounted in the anechoic chamber.

Laser Doppler velocimetry tests for internal flowfield survey are conducted to study the effects of mixer design and flow conditions on mean velocity and relative turbulence velocity profiles internal to the ejector. Laser Doppler velocimetry traverses are made at a number of locations along axial (X), vertical (Y), and spanwise (Z) directions. The coordinates for traverse locations are shown in Figure 326 and are quantified in inches as well as in a normalized parameter with respect to the width, W of the ejector, which is 6.8" for all configurations.

The mean and turbulent velocity profiles along the axial (X) direction are measured at three locations, 1, 2, and 3 (Figure 326), covering the entire glass window length from the mixer exit to approximately 2.5 in. upstream of the ejector exit. Locations 1, 2, and 3 correspond to the midpoint of the core or hot flow, the center of the core or hot flow at nozzle centerline, and the center of the secondary or cold flow, respectively. Traverses along vertical (Y) and spanwise (Z) directions are made at three axial locations,  $X=-9.4$  in.,  $X=-6.4$  in., and  $X=-3.4$  in. At each axial location, two vertical (Y) and four spanwise (Z) surveys (Figure 326) are made.

#### 4.4.2.1 Axial Mixer-Ejector Configuration

The spanwise traverses at two Y locations (i.e., Y=0.85 in. and 2.55 in.) out of four are isometrically illustrated in Figure 327 for the axial mixer-ejector configuration.

Spanwise distributions of axial velocity at (a) Y=0 (centerline plane), (b) Y=0.85 in., (c) Y=1.7 in., and (d) Y=2.55 in. (close to shroud), for three axial locations, are shown in Figure 328. At Y=0 (Figure 328(a)), the axial velocity difference between the crests and troughs, due to individual chutes along the spanwise direction, diminishes rapidly with increasing X due to mixing. At Y=0.85 in. and 1.7 in. (Figure 328(b) and (c)), the axial velocity crests are much higher at X=-6.4 in. and -3.4 in. compared to those levels at Y=0. The velocity distributions at different axial locations are further diminished at Y=2.55 in. They are significantly influenced by the entrained secondary flow. These results are replotted in Figure 329 comparing the spanwise velocity distributions at different Y locations at three axial positions. Close to the mixer exit (X=-9.4 in.), the velocity distributions show reasonably distinct (unmixed) primary and secondary streams to about Y=1.7 in. However, at Y=2.55 in., the velocity levels are much lower at the trough and at the crest compared to those at lower Y locations. This is due to the unmixed, entrained, secondary flow close to the ejector shroud. At axial locations downstream, the crest velocity levels at Y=0 are lower, indicating primary flow migration from the center plane of the ejector.

The effect of NPR on spanwise velocity distributions is shown in Figure 330 at X=-3.4 in. At Y=0, the velocity levels are higher for higher NPR. However, such a distinct trend is not observed with increasing Y, which is caused by the mixing of the hot primary stream with secondary flow.

The effect of simulated flight on the spanwise velocity distributions is shown in Figure 331. The peak velocity levels decrease with flight simulation, mostly away from the center plane (Y=0). This is possibly caused by increased entrainment due to flight leading to a reduction of axial velocity levels.

Limited internal LDV measurements were acquired for the axial mixer configuration. Utilizing these data, axial velocity and relative turbulence intensity distributions along the X-direction are obtained and are shown in Figure 332. The axial distributions are acquired at the center plane (Y=0) and at chute mid-height plane (Y=1.35 in.), along the cold stream (Z=0) and hot stream (Z=0.97 in.). The hot stream velocity distributions between Z=0 and Z=0.87 in. are significantly different, whereas, similar results along the cold stream are almost identical for most of the ejector length away from the mixer exit. Note that the mean velocity measured at X=-9.4 in. is close to ideally expanded jet velocity. Cold flow has been accelerated from about 360 ft/sec in freestream to about 650 to 700 ft/sec at X=-9.4 in. The relative turbulence intensity levels vary between 10 to 20 percent, and the levels along the cold streams seem to be higher compared to hot stream. These levels are comparable to what is measured external to the ejector.

#### 4.4.2.2 Vortical Mixer-Ejector Configuration

The axial (X) and vertical (Y) traverse locations for the vortical mixer are illustrated in Figure 333. The spanwise traverses at Y=0.85 in. and Y=2.55 in. are isometrically illustrated in Figure 334.

The axial velocity and relative turbulence intensity distributions along the X-direction, internal to the ejector, are shown in Figure 335 for NPR=2.5 and total temperature of 1325°R. The corresponding ideal velocity,  $V_j$ , is 1919 ft/sec. Velocity distributions along traverses 1 and 2, which are at the center of the primary jet at two different heights (Y=1.1 in. and Y=0), are almost identical to about X=-7.5 in., and are much higher compared to that along the center of secondary flow (along traverse 3), indicating relatively little spanwise mixing between primary and secondary streams. Downstream of X=-7.5 in., the core velocity drops drastically, while the secondary flow velocity increases slowly, indicating occurrence of mixing between core and secondary flows. Velocity decrease at the

middle of core jet away from the nozzle centerline is faster compared to that at the middle of core jet at the nozzle centerline. Primary jet at nozzle centerline is relatively isolated from secondary jet. Spanwise mixing is relatively poor, even at  $X=-4$ , since the velocities along 1, 2, and 3 are not the same. The relative turbulence intensity distribution, shown in Figure 335, is measured along traverse 2 ( $Y=0$ ,  $Z=0.85$  in.), which is along the hot stream. The relative turbulence intensity level is lowest close to the mixer exit at is about 10 percent. The level increases with increasing  $X$ .

Spanwise distributions of axial velocity, at  $Y=0.85$  in. (mid-lobe height) and at  $Y=2.55$  in. (close to shroud), are shown in Figure 336. At  $Y=0.85$  in., the axial velocity difference between the crests and troughs, due to individual chutes along spanwise direction, gradually diminishes with increasing  $X$  due to mixing (Figure 336(a)). However, at  $Y=2.55$  in., the traverse locations lie in the gap between the mixer and the shroud. Therefore, the velocity distribution about 1 in. downstream of the mixer exit ( $X=-9.4$  in.) basically shows the uniform secondary flow velocity of about 650 ft/sec (Figure 336(b)). With the gradual mixing between core and secondary flows along increasing  $X$  (particularly due to vectoring of hot flow for the vortical mixer), crests and troughs due to individual chutes are noted along spanwise velocity distributions. The velocity difference between the crests and troughs increases considerably downstream due to dominant migration of primary stream towards the shroud for the vortical mixer.

The effect of NPR on axial and spanwise velocity distributions are described in Figure 337. Axial velocity distributions occur in the middle of secondary flow (along the traverse 3 at  $Y=1.10$  in. and  $Z=0$ , Figure 337(a)). The secondary flow velocity near the mixer exit for  $NPR=3.5$  is distinctly higher compared to that for  $NPR=2.5$ . Further downstream, the velocity distributions are somewhat similar, but at large distances downstream, higher NPR results in a larger velocity (Figure 337(a)). The spanwise velocity distribution at  $X=-3.4$  in. and  $Y=0$  shows higher velocity levels for  $NPR=3.5$  compared to that for  $NPR=2.5$  across the entire span (Figure 337(b)). Also note the relative level of unmixedness at this downstream distance for both NPR.

The effect of flight simulation on velocity distributions along axial and spanwise directions for  $NPR=3.5$  are shown in Figure 338. Velocity distributions along the  $X$ -direction are taken along the secondary flow at  $Y=1.10$  in. and  $Z=0$  (along point 3 of Figure 333). Close to the mixer exit, the velocity increases with flight and the trend is reversed beyond  $X=-7.5$  in. (Figure 338(a)). The effect of flight is to initially increase secondary flow entrained velocity. However, because of reduced shear, secondary flow velocity does not increase as quickly for the flight situation as for the static case. Spanwise distribution at  $X=-3.4$  in. shows that the peak velocities of the primary jet remain higher for flight case due to reduced shear (Figure 338(b)).

#### **4.4.2.3 Effect of Mixer Design (Axial Vs Vortical)**

Some of the internal LDV results for the axial mixer configuration are compared with those for a vortical mixer-ejector configuration to show the effect of mixer design on velocity distributions internal to the ejector. Comparison of spanwise velocity distributions between vortical and axial mixer-ejector configurations, at  $X=-9.4$  in. (close to mixer exit), for several vertical locations ( $Y$ ), is shown in Figure 339. For both mixer-ejector configurations, the velocity at the crests is reasonably the same at  $Y=0$  and  $Y=0.85$  in. However, the crest velocity level significantly diminishes for the vortical mixer configuration with increasing vertical positions greater than 0.85 in. At  $Y=2.55$  in., the velocity distribution basically shows uniform secondary flow velocity of about 650 ft/sec (Figure 339(d)) for the vortical mixer, since the traverse locations lie in the gap between the mixer and the shroud. There is no appreciable gap between the mixer and the shroud for the axial configuration. Hence, the influence of primary stream is retained at higher vertical locations, including at  $Y=2.55$  in., for the axial mixer-ejector configuration. The velocity at the crest with increasing  $Y$  remains the same for a certain height and then decreases rapidly for the vortical mixer configuration. However, for the axial mixer configuration, the crest velocity level increases

and then slowly decreases with increasing  $Y$ . The trough velocity for the vortical mixer decreases with increasing  $Y$  up to  $Y=0.85$  in., and then remains more or less the same for the rest of the ejector height. For the axial mixer-ejector, the trough velocity remains reasonably the same with increasing  $Y$  to about  $Y=1.7$  in., and then decreases rapidly from about 700 ft/sec to about 200 ft/sec between  $Y=1.7$  in. and  $Y=2.55$  in.

Comparison of spanwise velocity distributions between vortical and axial mixer-ejector configurations, at  $Y=0$ , for several axial locations ( $X$ ), is shown in Figure 340. For both mixer-ejector configurations, the axial velocity difference between the crests and troughs, due to individual chutes along spanwise direction, gradually diminishes with increasing  $X$  due to mixing. At  $X=-9.4$  in., the peak velocity levels due to core flow are nearly the same for both mixers. However, the velocity at the trough is much higher for the vortical mixer compared to the axial configuration. With increasing  $X$ , the velocities at the crest and at the trough are higher for the vortical mixer compared to the axial configuration, indicating that additional spanwise vorticity induced by the vortical mixer is not effective in improving mixing relative to the axial mixer.

Comparisons of spanwise velocity distributions between vortical and axial mixer-ejector configurations, at  $X=-3.4$  and  $Y=0$ , for two different nozzle aerothermodynamic conditions are shown in Figure 341. For both mixer-ejector configurations, the entire spanwise velocity distributions increase with increasing NPR. However, the velocity distributions for the vortical mixer are higher compared to the axial configuration for both nozzle conditions.

These sets of extensive LDV data could be used for further CFD validation, internal ejector noise modeling, and understanding the physics of mixing in high speed ejectors.

## **4.5 COMPUTATIONAL STUDIES OF PRATT & WHITNEY MIXER-EJECTOR EXHAUST NOZZLE CONCEPTS WITH COMPARISONS TO GEAE CELL 41 EXPERIMENTAL DATA**

### **4.5.1 Geometry**

The exhaust system consists of a primary nozzle and a flight-type ejector. The primary nozzles are two-dimensional (2-D), having identical symmetric (opposed) lobes, as shown in Figure 342. The area ratio of both nozzles,  $A_8/A_{8^*}$ , is 1.45. The lobes of the vortical nozzle have a constant ramp angle of 15 degrees, and a lobe aspect ratio of 2.52. The nozzle is mounted within and to the ejector such that the secondary to primary area ratio,  $A_9/A_p$ , is 2.274. The surface geometry was received from P&W in three files in SPEC395 format. One file was received for the internal hot flow mixer surface, one for the cold flow external mixer surface, and one for the ejector shroud. The axial nozzle nominally has the same exit area ratio as the vortical nozzle; however, the lobe's initial ramp angle of about 12 degrees is turned back to horizontal at the exit plane. The surface geometry was received from P&W as an ICGM IGES file. The geometry for both mixer-ejector exhaust systems can be characterized numerically by the information found in Table 11.

### **4.5.2 Grid Generation**

#### **4.5.2.1 Background**

With interest now focusing on real world three-dimensional (3D) problems, and the desire to accurately predict or model complex physics, grid generation has become a pacing issue. Techniques for generating structured grids include elliptic grid generators, hyperbolic generators, algebraic methods, transfinite interpolation techniques, and conformal mapping. A previous mixer-ejector design was meshed at P&W using the conformal mapping technique of Ives and Zacharias (1). An alternative approach is used for the current analysis efforts. Since the production version of the NASTAR flow solver code required a structured, single block grid, it was determined that the full 3D grid could be generated by defining 2D cross-sectional grids at predefined axial stations, and then stacking these

together to define the 3D grid. This approach (called dimension reduction) redefines the grid generation task into two separate efforts. The second stage of the mesh generation process involves stacking the cross-sectional grids to form a 3D mesh.

*Table 11. High Speed Civil Transport Mixer-Ejector Exhaust Nozzle System Geometries*

	<i>Vortical</i>	<i>Axial</i>
Ramp Angle (Degrees)	15	12 <sup>1</sup>
Outer Aspect Ratio (Crest-to-Trough Height/Crest Width)	2.52	4.36
Mixer Lobe Trailing edge Information:		
Crest-to-Trough Height (in.)	1.65	2.44
Crest Width (in.)	0.655	0.56
Trough Width (in.)	1.025	0.92
Characteristic Length:		
Hot Passage Mixer Length (From Onset of Geometry (in.))	3.725	5.865
Hot Passage Mixer Length (From Entrance Plane (in.))	6.115	6.115
Cold Passage Mixer Length (From Onset of Geometry (in.))	3.525	5.615
Cold Passage Mixer Length (From Entrance Plane (in.))	6.115	6.115
	Short (in.)	Long (in.)
Shroud	11.86	19.996 <sup>2</sup>
Mixer Trailing Edge	10.46	18.596 <sup>3</sup>
Shroud Trailing Edge to Computational Exit Plane	12.915	9.779
Shroud Height (Centerline to Chord Trailing Edge)	3.55	3.55
Far Field Boundary (Approximately 25 Shroud Heights)	92.5	92.5
Mixer Thickness at Entrance Plane	0.34	0.34
Mixer Thickness at Trailing Edge	0.03	0.03

<sup>1</sup> Approximate

<sup>2</sup> Actual Long Shroud Model Chord Length = 20.250 in.

<sup>3</sup> Actual Length = 18.850 in.

#### **4.5.2.2 Grid Generation**

An ideal grid generation process is one that is rapid, produces grids with little skewness, and has clustering control. Since the overall grid was 3D, judicious choices of the axial stations were required. An alternative 2D grid-ding technique using EXTOP2 was proposed. The EXTOP2 is a knowledge-base expert system multiblock grid-ding code developed by J.F. Dannenhoffer (2,3). Although the code has multiblock capabilities, a single block grid was generated. The power of this structured grid technique is that only boundary definitions are needed; grid

smoothing and stretching are functionally controlled (instead of only manually controlled) by the user; and a knowledge base that can be used for additional or alternative axial cuts is maintained.

The process of generating the grid consists of a number of separate tasks. First, the vortical nozzle surface geometry files, received from P&W in SPEC395 format, were converted to PLOT3D format and read into the FIELDVIEW (4) visualization code. Axial cutting planes were prescribed (via an input file) and boundary data corresponding to the intersection of the cutting plane and the surface geometry were written to a separate file. For the axial nozzle, the surface geometry obtained from the ICEM IGES file was sliced axially using the ICEM cutting plane option. The resulting files, now containing intersections of cutting planes with all three geometric surfaces, were postprocessed to give individual cut boundaries.

The determination of the axial cut locations was driven by two competing forces. Definition was needed near the leading edge of the shroud, the trailing edge of the mixer, the onset of the mixer geometry, and the trailing edge of the shroud. However, too many axial locations would cause the grid to grow rapidly in size. (Each axial station introduced  $90 \times 35 = 3150$  grid points.) There were also grid concerns near the leading edge of the ejector shroud (5). A sheared H-grid is used here because of the requirement that the grid be a single block. This form can result in numerical problems, reflected as a loss in total pressure in inviscid regions of the flow, if the grid cells exhibit too much skewness or large aspect ratios, since control volumes with large skew have large flux balance errors (truncation error). In the ejector calculation, this error manifests itself via the entrained air between the ejector and the nozzle having insufficient total pressure, thus effecting the predicted mixing capability of the ejector. With these considerations in mind, Figures 343 and 344 show the  $90 \times 35$  axial grid, somewhat truncated above the shroud, along the crest and trough cuts of the vortical and axial mixer nozzles in a short and long shrouded ejector.

The next major step in the grid generation process was to generate the 2D cross-sectional grids at each axial station. In some regions, this was a trivial task, particularly before the onset of the mixer geometry and after the trailing edge of the shroud. The only requirements were that the three separate grid portions (the hot flow internal passage, the cold flow external passage, and the freestream passage) match at grid interfaces, and that viscous stretching be applied at the grid interface prior to the leading and trailing edges of the shroud to capture any shear layer that might develop. The 3D grid was generated cross section by cross section, and not as three passage grids that were eventually tied together. Therefore, it was necessary to have the cross-sectional grids vary smoothly in the axial direction since the 3D stacking process would necessarily identify corresponding triples as grid neighbors (i, j, k). This was especially important along the mixer surface. The generation of the cross-sectional grids from the onset of the mixer geometry to the trailing edge of the shroud was accomplished using the functionality of the knowledge base available in EXTOP2. In this region, grid lines needed to be blended from horizontal to vertical and back to horizontal with a single block grid, particularly near the trailing edge of the mixer lobe. This necessarily implies that grid cells will have a wide range of skewness. To handle this sudden change in geometry, the stack language available in EXTOP2 was used to determine the number of grid points to use in each segment of the mixer surface (i.e., how many points along the crest, across the rise, and along the trough). This determination was made as a function of axial location. Viscous stretching to the mixer surface, as well as to the lower surface of the shroud, was also accomplished in this way. To reduce both the number and the effect of the highly skewed cells induced by the severe crest to trough geometry, the EXTOP2 system was used to blend the mixer trailing edge to a benign straight segment at the shroud trailing edge. This eliminated the viscous stretching, necessary along the mixer surface, that is no longer aligned to the nozzle shear layer wake. Consequently, an unstretching operation allows a more efficient use of the grid lines, and a blending of the grid from the mixer trailing edge to the shroud trailing edge was introduced. Some cross-sectional grids are shown in Figure 345 (not all axial stations are shown).



Cross-sectional grids include:

- The grid prior to the onset of the mixer geometry
- Grids up to the trailing edge of the mixer, including the leading edge of the shroud and the mixer lobe trailing edge
- The nonlinear blending from the mixer trailing edge to the shroud trailing edge
- Representative grids from the shroud trailing edge to the exit of the computational domain.

#### 4.5.3 Flowfield Modeling

In this section, the computational fluid dynamics (CFD) analysis approach for modeling the mixer-ejector flowfield is described. First, a brief description of the NASTAR code used, boundary conditions employed in the simulation, and operation of the code is presented. A brief description of some recent analytical studies is also included.

##### 4.5.3.1 NASTAR Navier-Stokes Analysis

The viscous analysis used was the P&W NASTAR code. This NASTAR code solves the Reynolds-averaged form of the governing equations for steady, 3D flows including the effects of turbulence and heat release due to chemical reaction. The code was developed at P&W and is based on the method due to Rhie (6). The NASTAR code represents a significant extension of the pressure-correction methodology used in the TEACH family of codes (7). The governing equations are approximated using a finite-volume method. The discretized continuity and momentum equations are used to derive a pressure-correction equation used in place of the continuity equation. Rhie's method provides a single-cell, generally curvilinear coordinate, procedure that is applicable for Mach numbers ranging from incompressible flow to hypersonic flow. The results described in the current study were obtained using the two equation ( $k - \epsilon$ ) model for turbulence developed by Jones and Launder (8). Boundary conditions for the NASTAR analysis entailed specifying the total pressure and total temperature at the entrance to the mixer nozzle (i.e., upstream of the throat), and at the upstream end of the domain for the external flow. A constant value for freestream static pressure was prescribed along both the upper boundary and downstream end of the domain. The baseline flow conditions are listed in Table 12. The upper boundary was located approximately 92 in. above the centerline of the nozzle to ensure that the near-region flow was not affected by the location of this boundary. Planes of symmetry defined the lateral extent of the domain, and passed through the crest/peak and trough/valley of the mixer. Finally, the lower boundary of the computational domain was also represented as a plane of symmetry.

Table 12. Baseline Flow Conditions for CFD Analysis

Parameter	Symbol	Value
Ejector Back (Free Stream) Pressure	P	14.5 psi
Free Stream Total Temperature	$T_0$	530°R
Nozzle Pressure Ratio	NPR ( $P_{op}/P$ )	3.5
Primary Total Temperature	$T_{op}$	1275°F

The calculations were initialized using the freestream velocity everywhere except within the mixer nozzle, where the velocity was set to one corresponding to a Mach number of 0.1 at the entrance stagnation temperature. In the mixer, the static pressure was varied linearly from the entrance (total) value to the freestream static pressure at



the end of the mixer, thereby avoiding sharp discontinuities in static pressure at the mixer exit. This is the recommended method for initializing the flowfield for NASTAR when large pressure differences exist at the boundaries, such as those that occur across a choked, underexpanded nozzle. The algorithm used in NASTAR provides for a controlled amount of numerical damping to be added to the calculation. The amount of damping is determined from the local cell Reynolds number. For values of local cell Reynolds number greater than a user-specified maximum, sufficient dissipation is added to promote numerical stability. Generally (and in the present case), the user-specified maximum cell Reynolds number was increased during the iteration to the recommended upper (minimum added dissipation) limit. Various measures were used to determine whether the computation was converged sufficiently. As with most CFD codes, NASTAR provides the user with periodic reports of the level of residual errors that represent the extent to which the discrete form of the governing equations are in balance. In addition to the residual history, selected integral measures were also monitored as the iteration proceeded. For example, the pumping ratio (the ratio of secondary to primary mass flow rates at the mixer exit) was computed. This ratio approached an asymptotic value, indicating that the iteration had essentially converged (see below). Also, mass conservation requires that the flow rate within the shroud be constant from one axial position to another. An integral measure of total enthalpy within the shroud was also monitored. Other applications of NASTAR to similar geometries are described in Ref. 6.

#### 4.5.4 Mixing Effectiveness Measures

There are presently no reliable flowfield-based parameters to assess jet noise penalties or improvements. Consistent with previous CFD studies, the quantities examined included:

- Shroud static pressure loading
- Contours of stagnation temperature ( $T_0$ ) at the mixing duct exit plane
- Vertical (trough-cut) profiles of axial velocity ( $U$ ), downstream of the mixing duct exit
- Pumping or aspiration ratio ( $\omega = m_s/m_p$ )
- Gross thrust coefficient ( $C_{vg}$ )
- A mixedness parameter ( $\eta[x]$ ) based on the axial distribution of mass-averaged  $T_0$ .

$$\eta(x) = 100 \left( 1.0 - \frac{\int \rho u |T_{0x} - T_{0m}| dA}{\int \rho u |T_{0i} - T_{0m}| dA} \right)$$

where the subscripts x refers to the local axial plane, i to the initial axial plane in the mixing duct, and m to the fully mixed-out plane.

#### 4.5.5 Computational Fluid Dynamics Background

Pratt & Whitney and United Technologies Research Center (UTRC) have an extensive history of applying the NASTAR Navier-Stokes analysis to axisymmetric mixer nozzles and planar mixer-ejector exhaust systems. Most recently, calculations (9) have been presented with comparisons to experimental data for the P&W GEN 1 (APT) vortical mixer-ejector exhaust system. More extensive use of this computational resource has been limited by two principal factors: grid generation time, and net solution CPU time. Turn-around time for parametric designs is strongly influenced by the time needed to go from a given CAD file for a lobe surface to a satisfactory grid, especially for single block grids. Recent experience indicates that viscous driven problems (like ejectors) require long

CPU times to converge on pumping level and thrust coefficient performance parameters. For example, a 200K grid point fan problem requires about 1000 NASTAR iterations, while an equivalently sized mixer-ejector problem requires 4000 to 8000 iterations. At the request of P&W, UTRC recently assessed (10) an alternative computational approach using the multi-block GASP code in a Euler mode (LET 26) for flow in a lobed-mixer exhaust system operating at a NPR of four. The general idea for using GASP in the Euler mode is to reduce computational time so that computational fluid dynamics (CFD) can be used to rapidly assess alternative designs. The GASP code, with its multiple-region grids, can also simplify grid generation. The GASP calculations were made assuming that the flow is rotational but inviscid; that is, the code was operated in the Euler mode. The NASTAR computations were made assuming fully viscous, turbulent flow. Comparison of the results shows, as expected, that the flow fields differ significantly, and, therefore, the Euler analysis can not be used to model mixer-ejector problems. Although the pumping ratios computed by the two codes are similar, this agreement is considered to be fortuitous because the mixer system operates differently with respect to entrainment of freestream air in the experiment (as opposed to on the wing). Additional CFD studies (11) were recently performed to determine whether one can decouple the mixer nozzle calculation from the mixing duct/secondary flow stream calculation. The motivation for such a calculation is to simplify the use of the NASTAR single-block code, and eliminate the need to preserve grid continuity between the nozzle and external flow regions. Such a calculation is predicated on a choked mixer nozzle, and little or no upstream influence is expected. Results obtained by Chiappetta for the GEN 1 vortical nozzle single-zone and dual-zone calculation demonstrate some measurable differences, especially in shroud loading, mixing efficiency ( $\eta$ ), pumping level and thrust coefficient (Ref. 4). These calculations, however, indicate that the mixing patterns at the ejector exit are qualitatively equal. Parametric studies of the GEN 1 vortical nozzle have also been completed (LET 26) using a simplified definition of the nozzle geometry, i.e. the lobes, or chutes, have been represented as rectangular, cross-sectional lobes having the equivalent area as the base or actual lobe. This approximation simplifies the grid generation process, and eliminates the need for continuous interaction with CAD-CAM files. Comparison calculations for the GEN 1 nozzle, using the complete lobe definition and the rectangularized surface, demonstrate that the approximate geometry resulted in somewhat lower levels of secondary flow pumping and thrust coefficient (Table 13) due to cross flow separation around the lobe's sharp corner. Both lobes produce the same flowfield. These calculations showed that mixing results obtained using the same level of geometrical approximation are comparable. Figure 346 shows the geometry and shroud loading distribution for the actual (baseline) and squared (generic) mixer nozzles. Two solutions corresponding to the crest and trough distributions are shown for each computed case. Figure 347 illustrates that the mixing duct exit plane total temperature distributions are largely identical.

*Table 13. Squared Lobes Effect (Vortical Mixer, Short Shroud)*

<i>Case</i>	<i>MAR</i>	<i>NPR</i>	<i>T<sub>op</sub> (°F)</i>	<i>M</i>	$\omega$	$\eta$ (%)	<i>C<sub>vg</sub></i>
3: Base	1.18	4.0	1500	0.2	1.46	80.1	0.954
9206: Squared	1.18	4.0	1500	0.2	1.40	80.7	0.888

New configurations using this grid generation approach can produce practical grids in a matter of hours. Results of NASTAR calculations that have been performed using this approach are presented on Table 14. The results obtained for two different MAR values indicate that while increased lobe count improves flow mixedness ( $\eta$ ), nozzle loss also increases. Doubling the lobe count substantially improves the mixedness of the flowfield for

MAR=1.18 (Figure 347), the thrust coefficient increases substantially, and the mixedness ( $\eta$ ) decreases as MAR approaches one.

Table 14. Parametrics with Squared Lobes (Vortical Mixer, Short Shroud)

Case	MAR	NPR	Number of Lobes	$T_{op}$ (°F)	M	$\omega$	$\eta$ (%)	$C_{vg}$
9302	1.18	3.5	8	1500	0.2	1.68	90.1	0.884
9323	1.18	3.5	16	1500	0.2	1.59	93.5	0.798
9210	1.00	4.0	8	1500	0.2	1.28	82.4	0.949
9303	1.00	4.0	16	1500	0.2	1.28	84.5	0.939

These trade-offs of  $C_{vg}$  are somewhat similar to those obtained by Boeing (12) using the Compound Flow Analysis (CFA93). This one-dimensional Navier-Stokes analysis uses specified mixing duct inlet flow conditions and duct geometry to parametrically assess mixer-ejector system performance. The results indicate that vortical mixers, with a slightly divergent mixing duct (MAR>1), have a greater primary flowpath pressure loss than an axial mixer; however the enhanced mixing and more rapid pressure rise for the vortical mixers more than compensate for these losses. Increasing lobe count escalates the pumping ratio without significantly effecting the gross thrust performance (contrary to the results of the NASTAR calculations). Apparently, the increased lobe count induces additional mixing losses which overcome any additional momentum transfer benefit.

United Technologies Research Center has also completed an analysis of GEN 1.5 mixer-ejector exhaust nozzle concepts (13) using the P&W NASTAR Navier-Stokes code. The configurations selected for analysis were established using baseline configurations proposed by P&W and GEAE. Parametric studies were also performed to assess the performance of designs based on vorticity concepts that have evolved through work conducted at UTRC, GEAE and the Massachusetts Institute of Technology (MIT). The primary results of these computational studies show that high aspect ratio chute nozzles (4.0) are largely dominated by viscous-driven mixing, not vorticity-driven mixing. The mixedness parameter for the various nozzle designs is displayed on Figure 348. Two distinct mixing rate regions are seen. In earlier work at MIT, researchers also cited this behavior and related it to the initial sharp rise due to stirring, or vortically driven mixing, with a subsequently slower mixing growth rate attributed to shear-layer effects. In the designs considered, the mixing is almost entirely due to shear layer effects (Figure 349). The initial rise appears to be a result of the growth of the almost two-dimensional shear layer on the chute side-walls, while the later slower growth rate arises from the merging of these shear layers into the stratified flow. Other results obtained from this study were:

- Mode switching may be a manifestation, on the shroud loading, of different types of normal shock wave interaction with the secondary flow stream.
- High penetration chutes (100 percent) impose a high temperature layer on the shroud surface that persists for the entire mixing duct length.

#### 4.5.6 Discussion Of Results

NASTAR calculations have been performed for both the vortical and axial mixer nozzles in the short-shrouded and long-shrouded ejector system. Calculations were performed for nozzles operating at a NPR of 3.5, and a primary flow total temperature of 1275°F (1735°R). Calculations were also run at slightly different flow conditions to facilitate comparison with experimental data measured at the GEAE Cell 41 facility. The flowfield experimental

data consisted of static pressure loading measured along the shroud mixing duct surfaces, and two-component velocity measurements (axial U, vertical W) obtained using laser Doppler velocimetry (LDV). Table 15 provides a matrix of the NASTAR calculations, flow conditions, and calculated performance characteristics (i.e.  $\omega$ ,  $\eta$ ,  $C_{vg}$ ).

Table 15. Cell 41 Mixer Nozzle Analyses

Case	Mixer	Shroud	NPR	$T_{op}$ (°R)	$M_\infty$	$\omega$	$\eta$ (%)	$C_{vg}$	Comments
9322	V	S	3.5	1735	0.32	1.64	80	0.815	Baseline
9405	V	S	3.5	1960	0.32	1.75	81	0.832	$T_0$ Effect
9301	V	S	3.5	1960	0.20	1.70	81	0.940	$T_0$ , $M_\infty$ Effect
9320	V	L	3.5	1735	0.32	1.66	91	0.831	Baseline
9402	V	L	3.8	1735	0.32	1.52	90	0.827	NPR Effect
9403	V	L	3.5	1635	0.32	1.60	90	0.827	$T_0$ Effect
9302	V	L	3.5	1960	0.20	1.57	94	0.897	$T_0$ , $M_\infty$ Effect
9401	A	S	3.5	1735	0.32	1.58	74		Baseline
9404	A	S	4.0	1960	0.32	1.36	76		$T_0$ , NPR Effect
9406	A	S	3.5	1960	0.32	1.68	76		$T_0$ Effect
9312	A	S	3.5	1960	0.20	1.30	76		$T_0$ , $M_\infty$ Effect

#### 4.5.6.1 Vortical Mixer Nozzle Comparisons

Calculations were performed for a vortical mixer nozzle/short shrouded ejector configuration operating at a nominal test point of NPR=3.5 and  $T_{op}$ =1735°R (denoted as case 9322), and compared to experimental test points 868/871. The predicted static pressure loading on the shroud inside surface is only in fair agreement with the measured data (Figure 350). The leading edge suction effect is accurately modeled while the recovery to freestream static is less so. To examine solution sensitivity to input flow conditions, the effects of higher primary total temperature (9405) and lower flight Mach number (9301) was examined. The effect of increased total temperature has substantially improved the agreement in the pressure recovery region. Table 15 illustrates the effect of lower ram drag, i.e. improved  $C_{vg}$ , with lower flight Mach number. Mach number distributions (Figure 351) indicate the presence of a fairly strong shock midway down the mixing duct in the trough cut plane (9322) that is not present in the higher primary temperature case (9405). Comparisons have also been made for the axial velocity field in the exhaust plume from the ejector. The experimental axial velocity data, obtained from vertical plane LDV traverses aligned to the trough plane, have been compared to the baseline 9322 case. A schematic diagram of the mixer-ejector geometry, the reference Cartesian directions, and the axial location of external and internal LDV traverse planes are shown on Figure 352. Figure 353 shows a vertical direction trough cut comparison of the baseline 9322 case with experimental traverse data. The experimental data, which consisted of a complete vertical run from below the mixer to above the mixer, have been reflected about the nozzle symmetry axis. Little asymmetry about the axis is seen. While the calculation predicts a centerline level approximately 10 percent lower than the observed experimental data, the vertical distribution is in close agreement. A similar comparison in the horizontal or lateral center-axis plane is shown on Figure 354. The computational solution has been replicated four times to illustrate an equiv-

alent nozzle quadrant. The effect of the sidewall shear layer, clearly visible in the experimental data, is not modeled in the calculation. A color contour plot of the calculated axial velocity field, replicated eight times to illustrate the effective nozzle pattern at the ejector exit plane (Figure 355) with the corresponding nozzle exit plane exit for reference.

Equivalent computational studies have been performed for the vortical nozzle with a long shrouded ejector. A baseline (9320) solution has been compared to experimental data obtained at different NPR and  $T_{op}$  operating points. Additional cases at a higher NPR (9402), and at a lower total temperature (9403), have also been calculated. These solutions are compared to the measured shroud static pressure loading on Figure 356. The loading agreement is quite good, with the computed solutions illustrating the observed effect of increased loading with increased NPR, as well as an increased degree of nonmonotonic recompression. The effect of flight Mach number (9302) again illustrates the positive effect on gross thrust coefficient (Table 15). The calculated Mach number distributions shown on Figure 357 indicate that, while both solutions predict a strong mid-duct shock in the trough plane, the higher NPR case shock appears to be stronger. Figure 358 presents a comparison of the axial velocity field at three axial planes in the plume. The agreement is similar to that observed in Figure 353 for the short shrouded installation, with the same degree of mismatch along the centerline. The long shroud case calculated centerline velocity appears in both cases to be approximately 10 percent lower than the short shroud case results. Figure 359 presents a color representation of the replicated exit plane axial velocity field. The previously cited observation of a lower level of axial velocity is corroborated by the basic shift of the color field to the green portion of the color spectrum.

Figure 360 illustrates a comparison of the computed exit plane total temperature distributions, as well as the distribution in the long duct at an axial plane ( $x=-7.28$  in.) equivalent to the short duct exit. Although the flow in the long duct case is more mixed, the solutions at the same axial plane appear almost identical. The added mixing, therefore, is due largely to the extra length and additional viscous forces. The calculated mixedness,  $\eta$  (Table 15), also shows the long duct case is more mixed. No clear pattern emerges in the calculated values of pumping ratio  $\omega$ , or gross thrust coefficient  $C_{vg}$ .

#### **4.5.6.2 Axial Mixer Nozzle Comparisons**

Calculations were performed for an axial mixer nozzle/short shrouded ejector configuration operating at a nominal test point of NPR=3.5 and  $T_{op}=1735^{\circ}\text{R}$  (denoted as case 9401), and compared to experimental test points 1513/1512/1516. The predicted static pressure loading on the shroud inside surface is in poor agreement with the measured data (Figure 361). The leading edge suction effect is accurately modeled, while the recovery to freestream static appears to be dominated by a shock-driven pressure recovery process. Sensitivity to input flow conditions by the solution was investigated. The effect of higher primary total temperature (9312), lower flight Mach number (9301), and higher NPR (9404) were calculated, with little improvement over the baseline results. A closer look at the mixing duct Mach number distributions (Figure 362) indicates the presence of a fairly strong transonic region on the shroud lip in the trough cut plane. The bubble terminates in a shock which causes the wall boundary layer to separate over most of the shroud length. Comparisons have also been made for the axial velocity field in the exhaust plume from the ejector. The experimental axial velocity data, obtained from vertical plane LDV traverses aligned to the trough plane, have been compared to the baseline 9401 case. Figure 363 shows a comparison of the baseline 9401 case with experimental vertical traverse data. The experimental data has again been reflected about the nozzle symmetry plane. The calculation predicts a significantly different near-centerline behavior than observed in the experimental data. The data seem to exhibit a shear layer-like behavior, while the calculation is much more uniform. A similar comparison in the horizontal or lateral center-axis plane is shown for completeness (axial change: Figure 364, vertical change: Figure 365). The computational solution has been repli-

cated four times to illustrate an equivalent nozzle quadrant. The effect of the sidewall shear layer, clearly visible in the experimental data, is not modeled in the calculation.

An equivalent computational study has been performed for the axial nozzle with a long shrouded ejector. A baseline (9311) solution has been compared to experimental data obtained at different NPR and  $T_{op}$  operating points. As above, the loading agreement shown in Figure 366 is not good, with the computed solutions illustrating a much more rapid recompression to ambient.

#### **4.5.6.3 Vertical Velocity ( $W$ ) Data**

Vertical velocity traverse data are shown in Figure 367 at a position approximately 3.4-in. downstream of the trailing edge of the shroud. Note that the velocity is designated as the  $W$ -component for the NASTAR computations and corresponds to the  $Y$ -component in the test program. The data are acquired in a traverse that is made from below (above) to above (below) the plane of symmetry across the lobes; the data for  $Y < 0$  have been restated to the positive  $Y$ -axis. In contrast to the level of agreement between the predicted and measured axial components, the agreement between the predicted and measured vertical component is quite poor. These discrepancies persist at all downstream locations. It has been concluded that the data are unreliable for present purposes for the following reasons:

- The allowable test time for acquiring the LDV data was shorter than desired. For example, each data point shown represents the average of approximately 50 samples acquired in a single burst of the data acquisition system. Experience in making measurements in complex flows suggests that more reliable measurements can be made by acquiring 2000 samples per data point. While the same problem occurs for all of the components measured, the magnitude of the axial velocity is large enough that these sampling errors are relatively small; thus, for the axial component of velocity, the effects of the small sample size are relatively unimportant in determining the mean value of this component.
- The data recorded actually represent the magnitude of the velocity vector and a procedure is used to determine the three Cartesian components. Errors associated with the small sample size have a greater impact on the accuracy of the cross-stream components than on that of the axial component.

The accuracy problem can be made worse due to slight misalignments or imperfections in the model. The NASTAR results were obtained by assuming that a plane of symmetry exists in the plane of the crest and trough (the results shown above are for the trough location). It is difficult to guarantee that the data were acquired in the plane of symmetry through the trough. The measured vertical component of velocity does not vanish on the horizontal plane of symmetry across the lobes at  $Y=0$  (Figure 367). Small shifts in the aerodynamic plane of symmetry from the assumed geometric plane of symmetry can account for this discrepancy. The data show that the vertical component does vanish on average at  $Y=0$ . It is possible that the vertical component would vanish there if larger sample sizes were obtained.

## 5. CONCLUSIONS

A hot flow aero-acoustic test was conducted to evaluate the impact of various geometric and design parameters on the noise generated by a two-dimensional (2D) shrouded, eight lobe, mixer-ejector exhaust nozzle. Noise attenuation was enhanced by lining the shroud internal walls with acoustic panels which absorb acoustic energy generated during the mixing process. A total of 21 model configurations at 1:11.47 scale were tested. Two mixer designs were investigated, the high-mixing vortical and aligned-flow axial, along with variations in the shroud internal mixing area ratios and shroud length. The shrouds were tested as hardwall or lined with acoustic panels packed with a bulk absorber. The models were tested over a range of primary nozzle pressure ratios and primary exhaust temperatures representative of typical High-Speed Civil Transport (HSCT) aerothermodynamic cycles. Static and flight-simulated data were acquired during testing. A round convergent unshrouded nozzle was tested to provide an acoustic baseline for comparison to the test configurations.

1. Caution should be used when acoustic testing with scale models less than 1/10 scale because difficulties with data reduction can arise due to large atmospheric attenuation corrections.
2. The vortical mixer design with the long (216 inches full scale) acoustically treated shroud (MAR=0.97, SAR=4.9) provided the largest sideline flight ( $V_{fl}=357$  ft/sec) noise reduction of better than 15 EPNdB below the reference convergent nozzle at 2400 ft/sec unsuppressed primary jet velocity. (MAR is defined as the ratio of shroud exit area to mixing plane area at the mixer exit plane. SAR is defined as the ratio of mixing plane area at the mixer exit to primary mixer throat area.)
3. At unsuppressed primary jet velocities less than 2400 ft/sec, the vortical mixer with long acoustically treated shroud with SAR=4.4 and MAR=0.97 provided an additional 1-2 EPNdB sideline flight noise reduction below the SAR=4.9 results. This reduction occurred at both static and flight-simulated conditions ( $M_n=0.32$ ,  $V_{fl}=357$  ft/sec).
4. The vortical mixer design with the long acoustically treated shroud (SAR=4.9, MAR=0.97) showed a 1 to 2 EPNdB sideline flight ( $V_{fl}=357$  ft/sec) noise reduction relative to the axial mixer design with the long treated shroud (SAR=4.9, MAR=0.97) at unsuppressed primary jet velocity greater than 2200 ft/sec.
5. The vortical mixer with the long shroud (MAR=0.97 and SAR=4.9) and perforated plate over honeycomb acoustic treatment packed with a bulk absorber demonstrated a 5-8 EPNdB sideline noise reduction below the long hardwall shroud at  $M_n=0.32$  ( $V_{fl}=357$  ft/sec) over the entire range of unsuppressed primary jet velocity tested.
6. The long 2D mixer-ejector designs with both treated and hardwall shroud (SAR=4.9, MAR=0.97) exhibited a 2-3 EPNdB azimuthal noise increase from the sideline to community (overhead) position over the range of unsuppressed primary jet velocity tested at  $V_{fl}=357$  ft/sec.
7. The long hardwall shroud provided a 1-2 EPNdB reduction in sideline noise below the short hardwall shroud with the vortical mixer (MAR=1.19, SAR=4.4) statically and at  $M_n=0.32$  ( $V_{fl}=357$  ft/sec).
8. Flight effects at  $V_{fl}=357$  ft/sec accounted for approximately 2-3 EPNdB reduction in the sideline noise for the long treated configurations 3 (vortical mixer/SAR=4.9/MAR=0.97), 5R (vortical mixer/SAR=4.4/MAR=0.97) and 13 (axial mixer/SAR=4.9/MAR=0.97).



9. Acoustic data were obtained with the baseline round convergent nozzle and configuration 3 (vortical mixer/long treated shroud/SAR=4.9/MAR=0.97) while holding various conditions constant. Data was measured at constant jet velocity, turbine exit total temperature, and nozzle pressure ratio. The results show that the long, treated mixer-ejector was more sensitive (larger noise increase) to changes in the throttle line than the baseline round convergent nozzle.
10. The EPNL reductions from Cell 41 are similar to those obtained in the NASA-LeRC 9x15 LSWT although spectral data show differences. The comparisons confirm technical concerns related to nearfield measurements and facility noise in the NASA-LeRC 9x15 low speed wind tunnel (LSWT).
11. An aerodynamic mode switch from compound-compressible subsonic to compound-compressible sonic flow within the ejector shroud was observed with both mixer designs. This phenomenon occurred during testing with ambient temperature primary flow and at high NPR (<4.5). The mode switch was very gradual such that definition of the nozzle pressure ratio at which the switch occurred was subject to interpretation. The mode switch with the axial mixer was more subtle than that seen with the vortical mixer. The mode switch could be controlled at nozzle pressure ratios less than 4.5, by using a short ejector (i.e. 120 inches full scale) shroud and/or low mixing area ratio (MAR).
12. External plume laser Doppler velocimetry (LDV) measurements of the vortical mixer-ejector with long shroud show an effect of ejector acoustic treatment on the ejector external velocity profiles. This effect was observed with a diffusing mixing region (MAR=1.18 and SAR=4.9). Axial velocities at the ejector centerline were nearly identical for both treated and hardwall ejectors. Axial velocities between the ejector centerline and ejector walls were higher (100 ft/sec) for the treated configurations as compared to the hardwall ejector at flight-simulated conditions. Possible explanations for this are increased treated ejector wall boundary layer blockage and effects of the thicker treated ejector boundary layer on internal ejector shock structure.
13. Vortical nozzle calculations of shroud pressure loading produce reasonable agreement with measured data. Predictions show: reduction in ram drag with lower flight Mach number, positive effect of flight Mach number on thrust coefficient, and increased shroud loading with increased nozzle pressure ratio. Specific operating points predict the presence of a strong shock in the shroud mixing region.
14. Experimental LDV measurements show that the sidewalls have an effect on the internal mixing region flow-field at least near the ejector exit plane. However, away from the sidewall, the vortical nozzle calculations, which modeled one-half of a mixer lobe, produced velocity profiles which were in reasonable agreement with LDV measured sidewall-to-sidewall axial velocity profiles. This geometry modeling scheme would become more appropriate if the number of mixer lobes were increased reducing the significance of sidewall interactions on the mixing region flowfield.
15. Calculations of the shroud static pressure loading and plume axial velocity field for the axial mixer nozzle configurations are in poor agreement with measured LDV and static pressure data. The calculated pressure recovery is dominated by a large scale zone of separation on the shroud surface, apparently induced by the lip shock/boundary layer interaction.
16. Future Computational Fluid Dynamics studies should address possible grid sensitivity issues by axially redistributing the computational mesh in the mixing duct region.

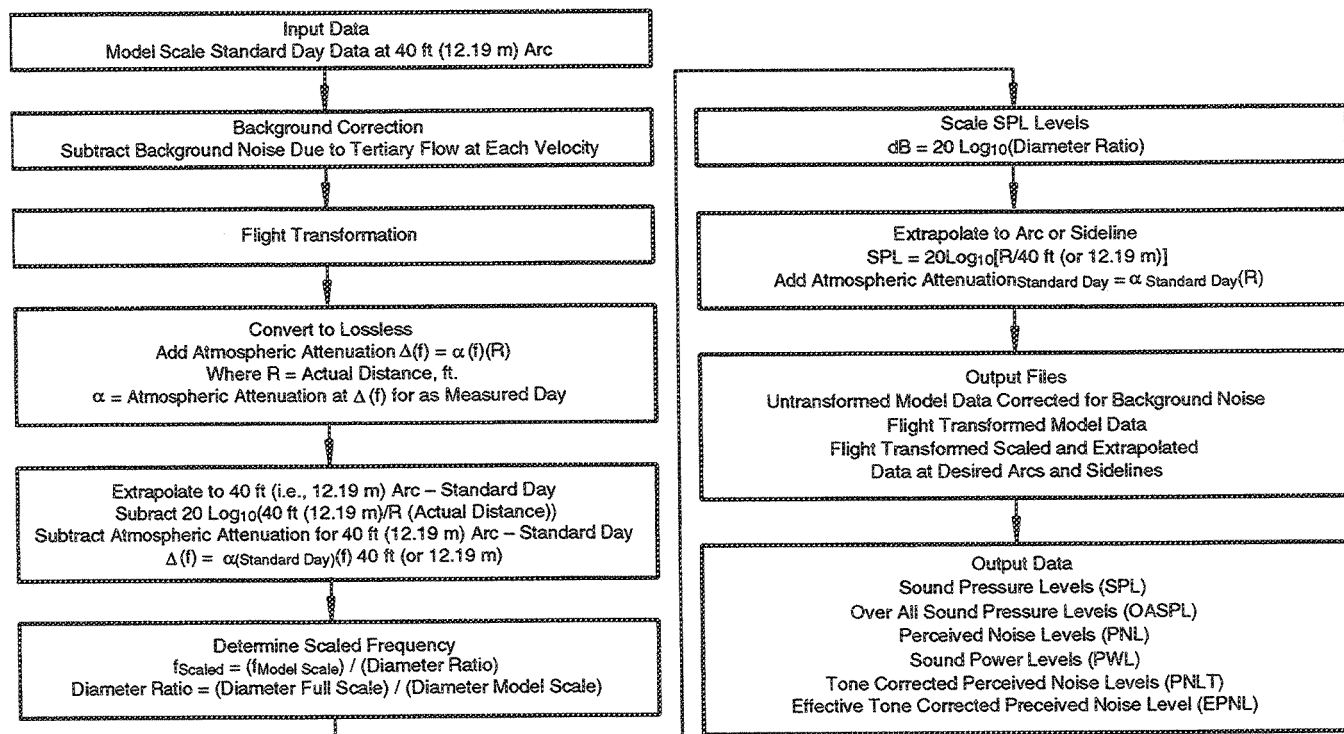


## 6. REFERENCES

1. Ives, D. C. and Zacharias, R. M., Conformal Mapping and Orthogonal Grid Generation, AIAA 87-2057, AIAA/SAE/ASME/ASEE 23rd Joint Propulsion Conference, San Diego, CA, June 1987.
2. Dannenhoffer, J. F. III, Computer-Aided Block-Structuring Through the Use of Optimization and Expert System Techniques, AIAA 91-1585, AIAA 10th Computational Fluid Dynamics Conference, Honolulu, Hawaii, June 1991.
3. \_\_\_\_\_ A Block-Structuring Technique for General Geometries, AIAA 91-0145, AIAA 29th Aerospace Sciences Meeting, Reno, NV, January 1991.
4. Miller, S. L., and Edwards, D. E., VISA: An Interactive Graphics System for Scientific Visualization, AIAA 91-0795, AIAA 29th Aerospace Sciences Meeting, Reno, NV, January 1991.
5. Malecki, R., Mityas, S., & Lord, W., Navier-Stokes Analysis of an Ejector and Mixer-Ejector Operating at Pressure Ratios in the Range 2-4, AIAA 90-2730, AIAA/SAE/ASME/ASEE 26th Joint Propulsion Conference, Orlando, FL, July 1990.
6. Rhie, C. M. & Chow, W. L., Numerical Study of the Turbulent Flow Past an Airfoil with Trailing Edge Separation, AIAA J., Vol. 21, No. 11, November 1983, pp. 1525-1532.
7. Patankar, S. V., Numerical Heat Transfer and Fluid Flow, (New York), Hemisphere Publishing, 1980.
8. Jones, W. P. and Launder, B. E., The Prediction of Laminarization With a Two-Equation Model of Turbulence, Int. J. Heat and Mass Transfer, Vol. 15, 1972, pp. 301.
9. Barber, T. J., LaBarre, R. E., and Chiappetta, L. M., Analysis of Second Generation High Speed Civil Transport Mixer-Ejector Exhaust System, UTRC 92-6, April 1992.
10. Chiappetta, L. M., Comparison of GASP and NASTAR Calculations, memorandum to T. J. Barber and L. Porter, November 11, 1993.
11. \_\_\_\_\_ Using Nozzle Results as Boundary Conditions for Lobed Mixer Calculations, memorandum to T. J. Barber and L. Porter, December 14, 1993.
12. Henke, R. K., and Lidstone, G. L., Analytical Evaluation of Generation 1.5 Nozzle Concepts for the High-Speed Civil Transport, NASA CR-xxxx, March 1994.
13. Barber, T. J., Chiappetta, L., & Hendricks, G., Parametric Analyses of Mixer-Ejector Exhaust Systems for HSCT Applications, memorandum to A. Stern, January 31, 1993.
14. Lord, W.K., Jones, C.W., and Stern, A.M., Mixer Ejector Nozzle for Jet Noise Suppression, AIAA-90-1909, AIAA/SAE/ASME/ASEE 26th Joint Propulsion Conference, Orlando, FL, July 1990.
15. Clapper, W.S., et al., High Velocity Jet Noise Source Location and Reduction; Task 4 --- Development/Evaluation of Techniques for Inflight Investigation. FAA-RD-76-79, IV, R77AEG189.1977.

This page intentionally left blank.

## **ATTACHMENT 1 — ILLUSTRATIONS FOR SECTION 4**



56393

Figure 19. Acoustic Data Processing Flowchart

All dimensions in inches  
Sketches not to scale

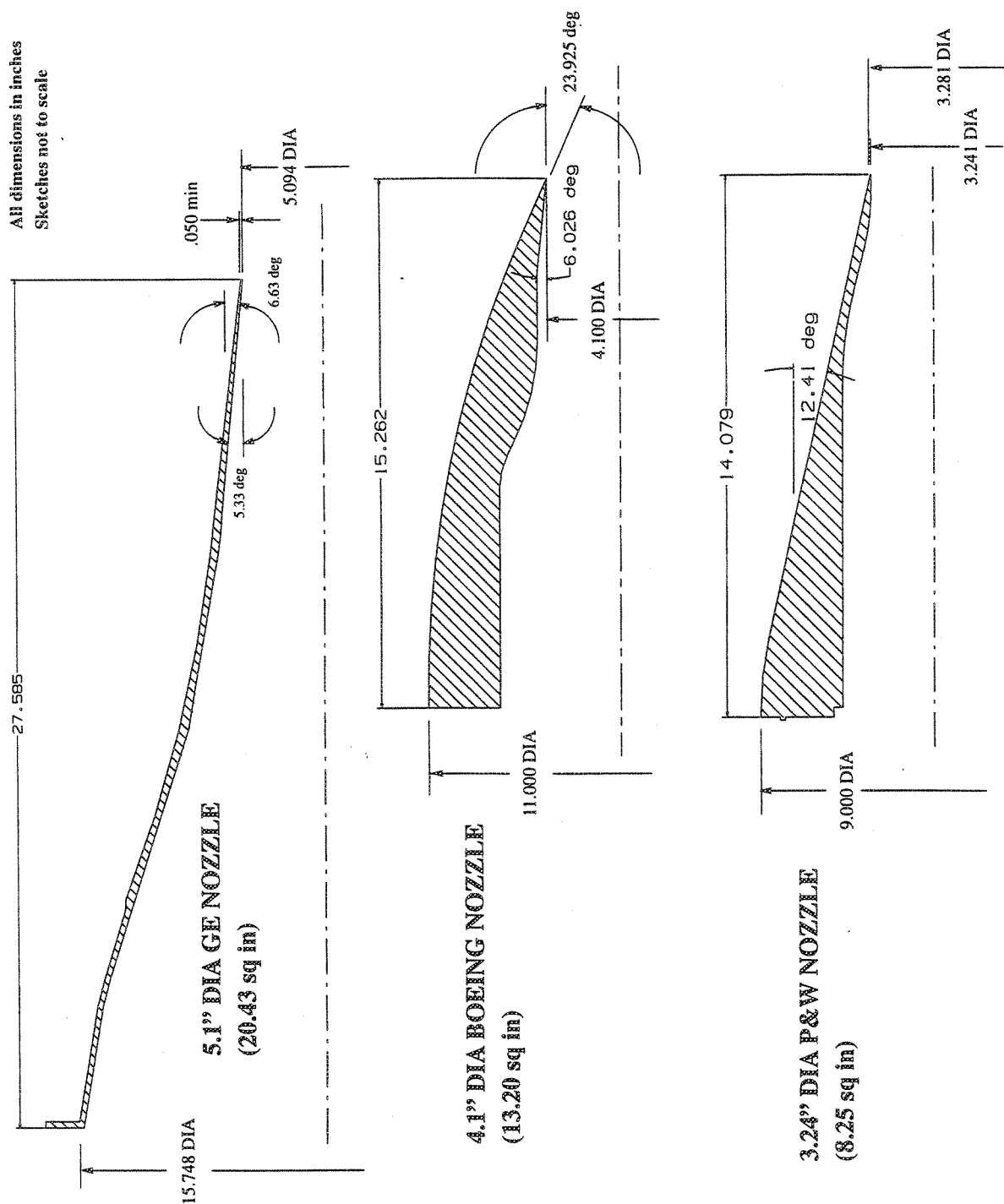


Figure 20. Cross-Sectional Views of Three Different Size Round Convergent Nozzles Tested in Cell 41

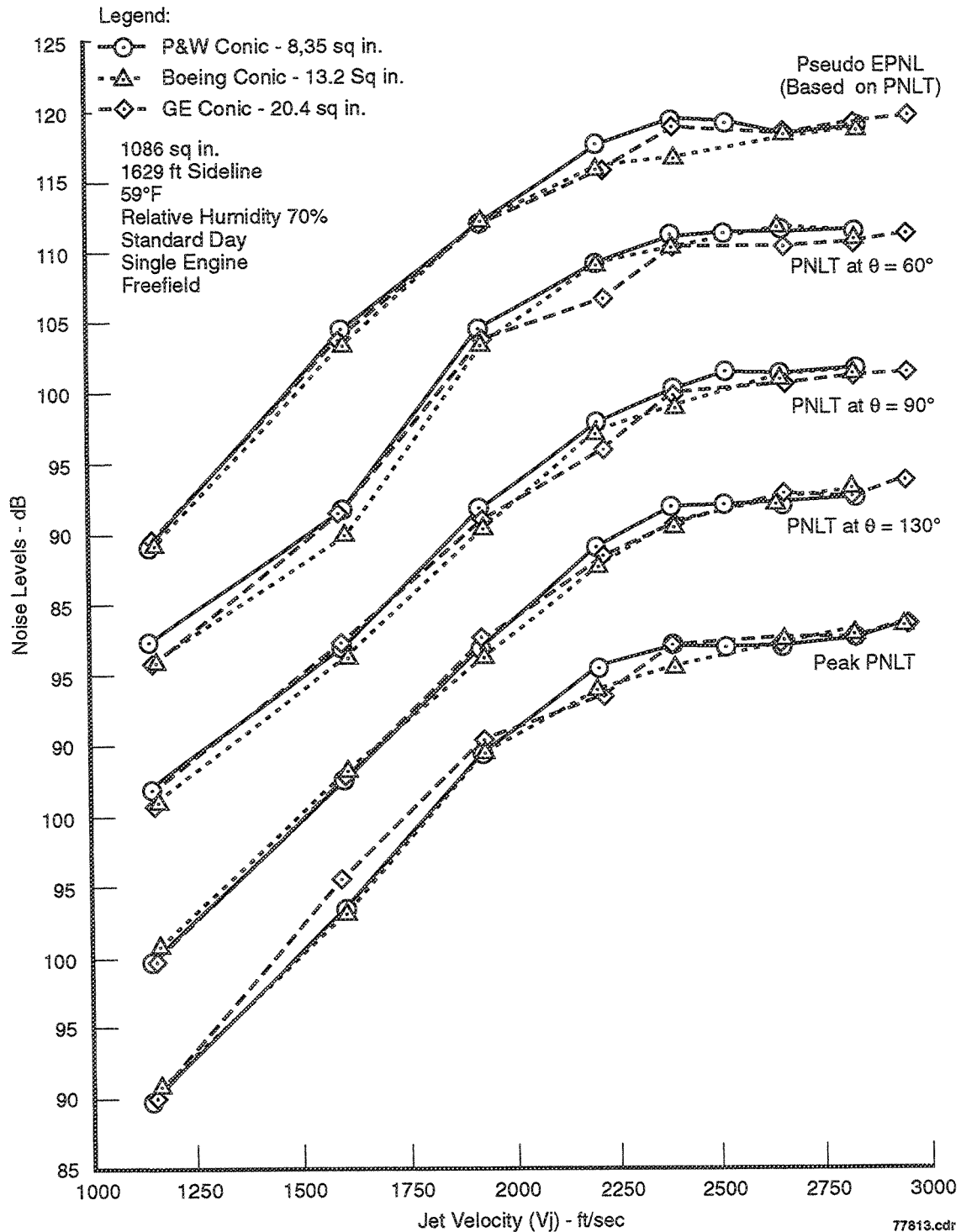


Figure 21. Comparison of Pseudo-EPNL, PNLT at Various Polar Angles ( $\theta$ ) and Peak PNLT Data as a Function of Jet Velocity Between Three Different Size Conical Nozzles at Static Condition

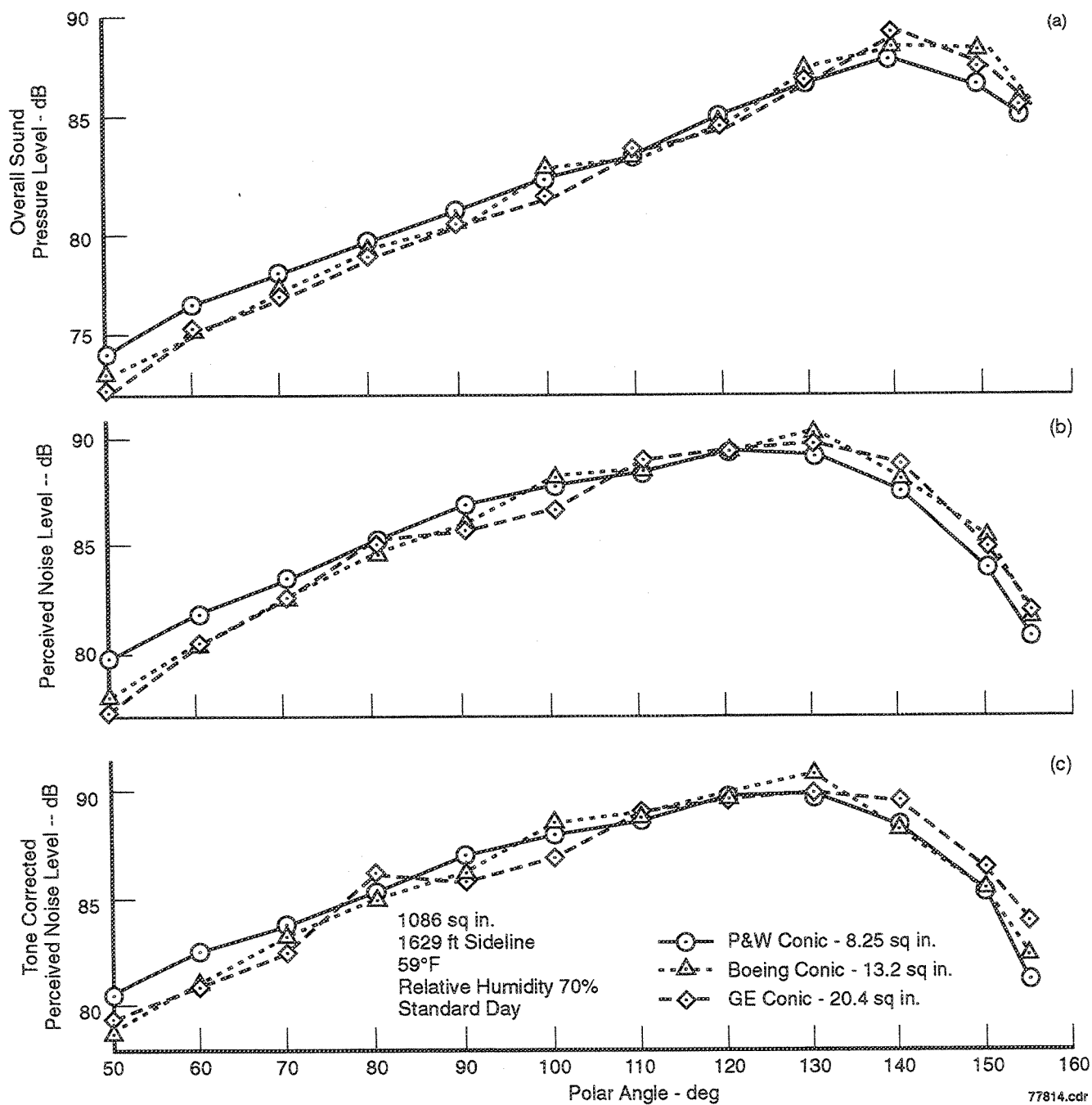


Figure 22. Comparison of: (a) OASP, (b) PNL, and (c) PNLT Directivities at  $V_j=1147$  ft/sec,  $NPR=1.5$ ,  $T_8=1000^\circ R$  Between Three Different Size Conical Nozzles at Static Conditions

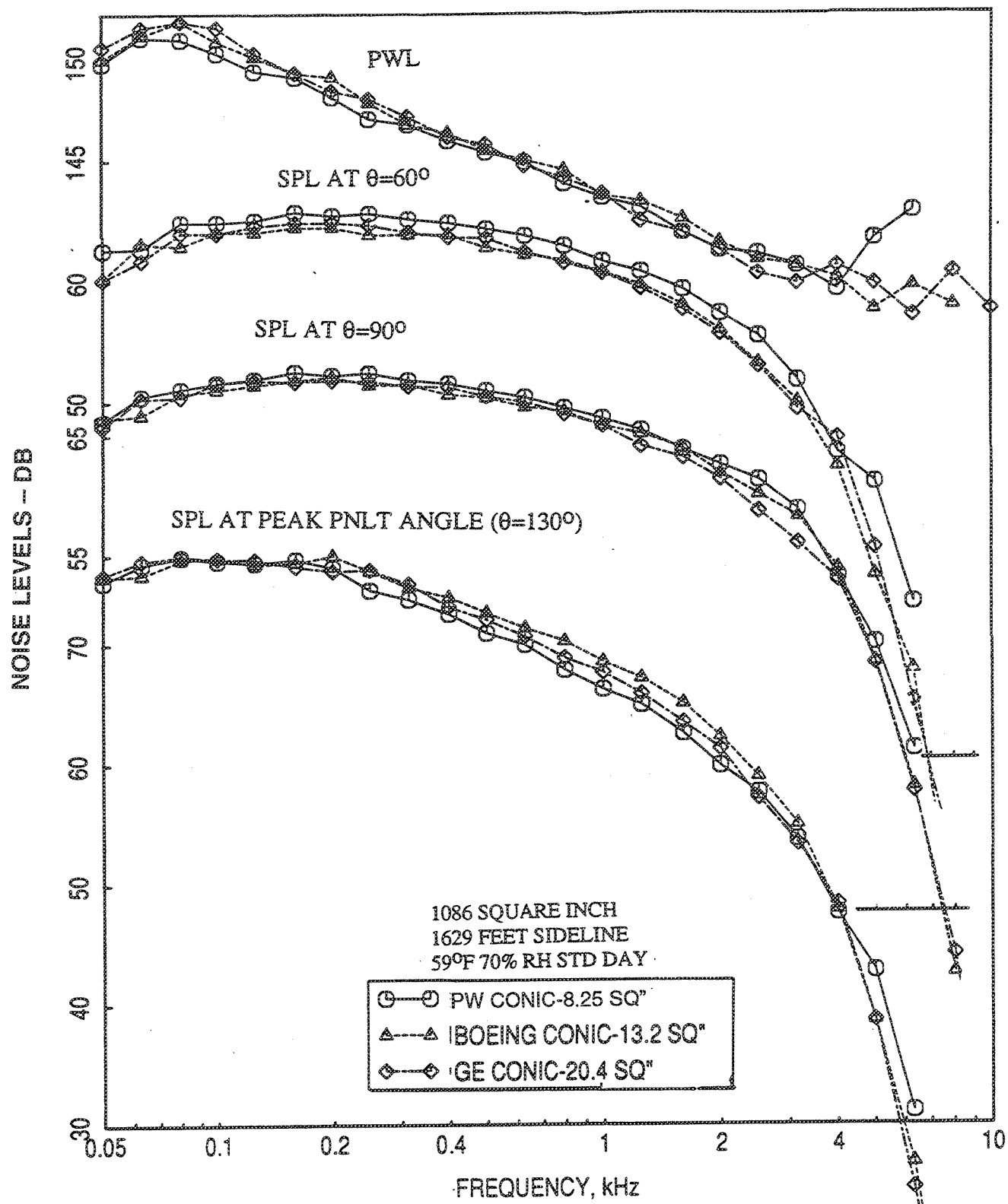


Figure 23. Comparison of PWL Spectra and SPL Spectra at Various Polar Angles ( $\theta$ ) at  $V_j=1147$  ft/sec,  $NPR=1.5$ ,  $T_8=1000^\circ R$  Between Three Different Size Conical Nozzles at Static Condition



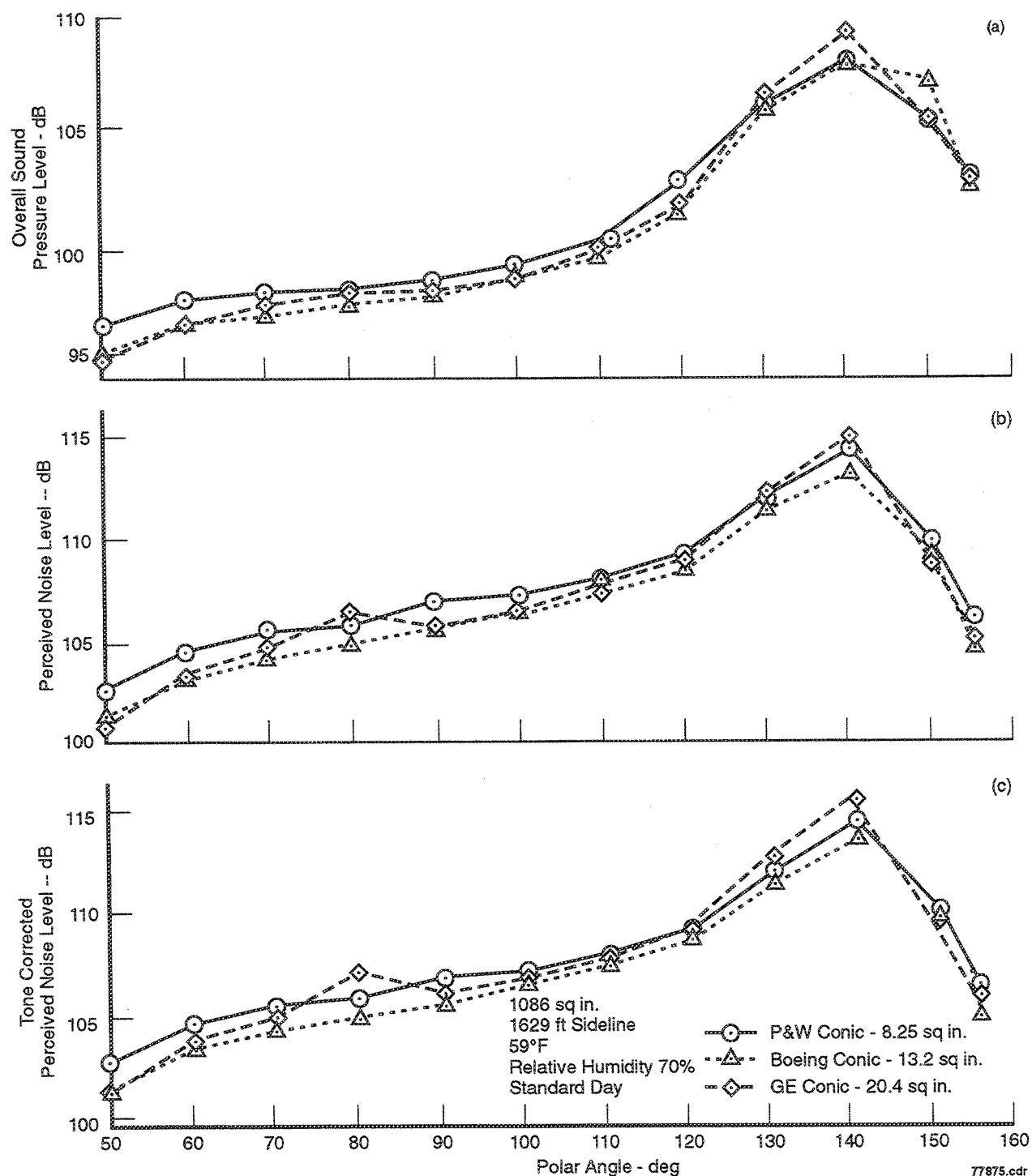


Figure 24. Comparison of: (a) OASP, (b) PNL, and (c) PNLT Directivities at  $V_j=1919$  ft/sec,  $NPR=2.5$ ,  $T_8=1325^\circ R$  Between Three Different Size Conical Nozzles at Static Conditions

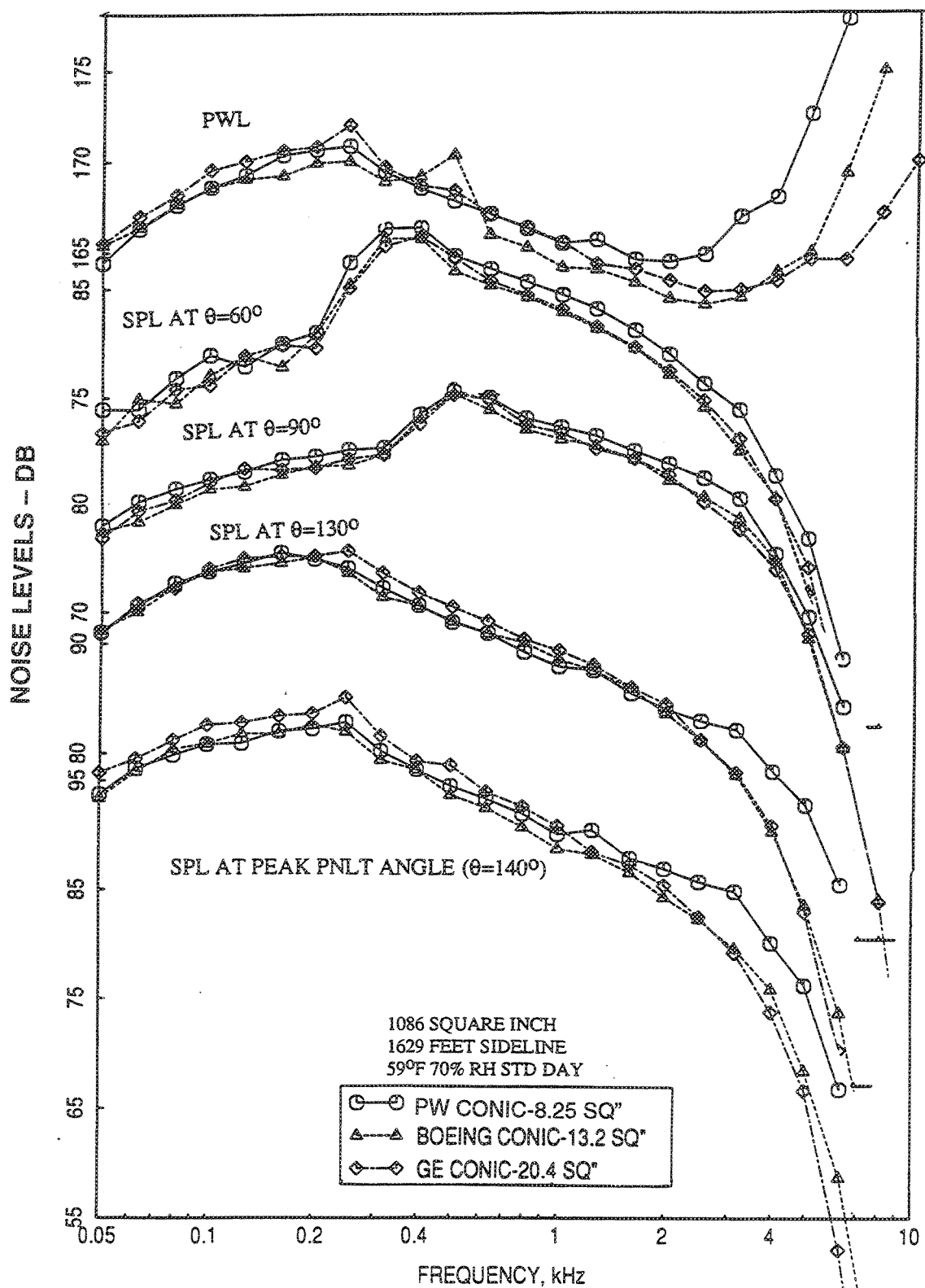


Figure 25. Comparison of PWL Spectra and SPL Spectra at Various Polar Angles ( $\theta$ ) at  $V_j=1919$  ft/sec,  $NPR=2.5$ ,  $T_8=1325^\circ R$  Between Three Different Size Conical Nozzles at Static Condition

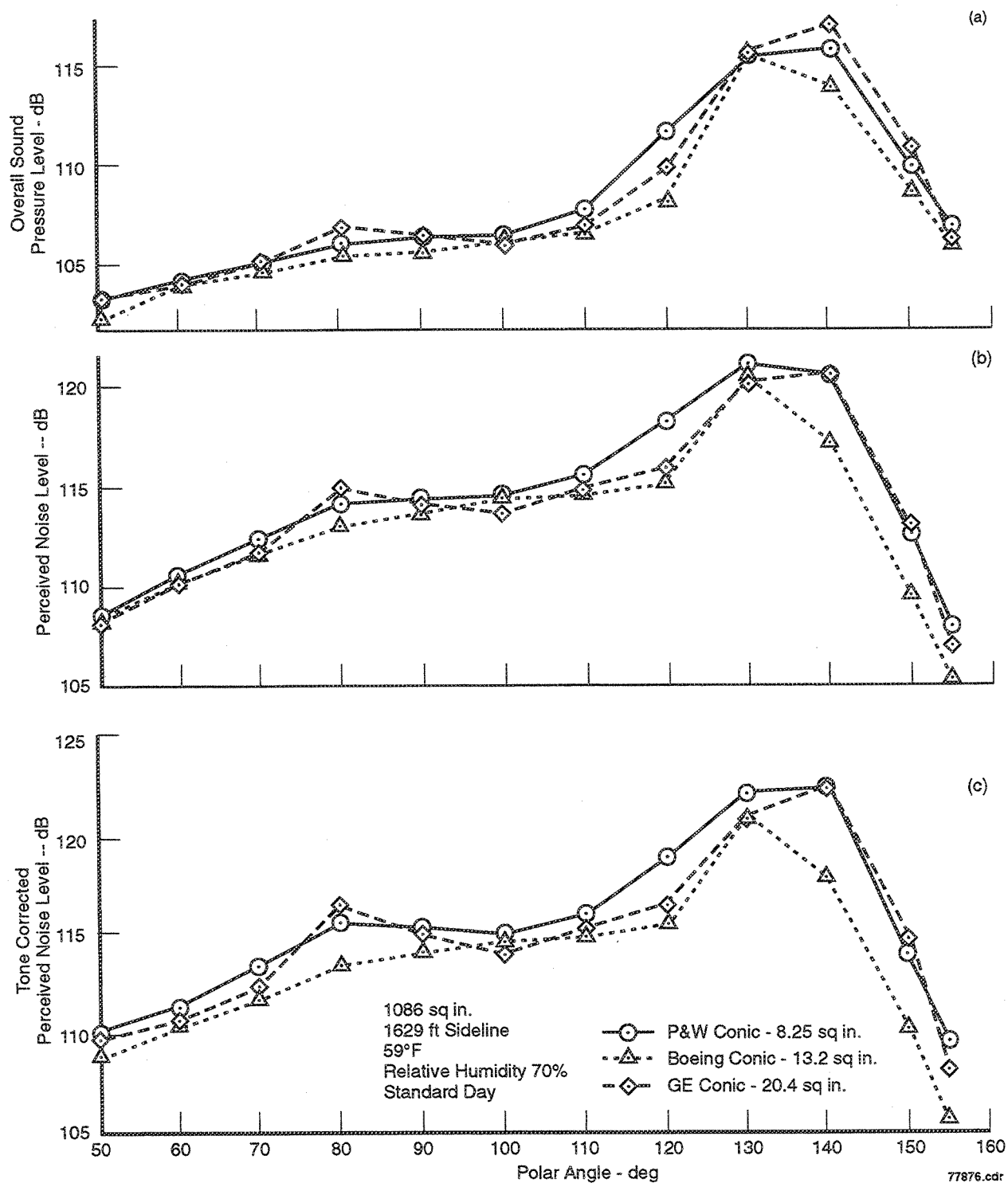


Figure 26. Comparison of: (a) OASP, (b) PNL, and (c) PNLT Directivities at  $V_j=2384$  ft/sec,  $NPR=3.4$ ,  $T_8=1590^\circ R$  Between Three Different Size Conical Nozzles at Static Conditions

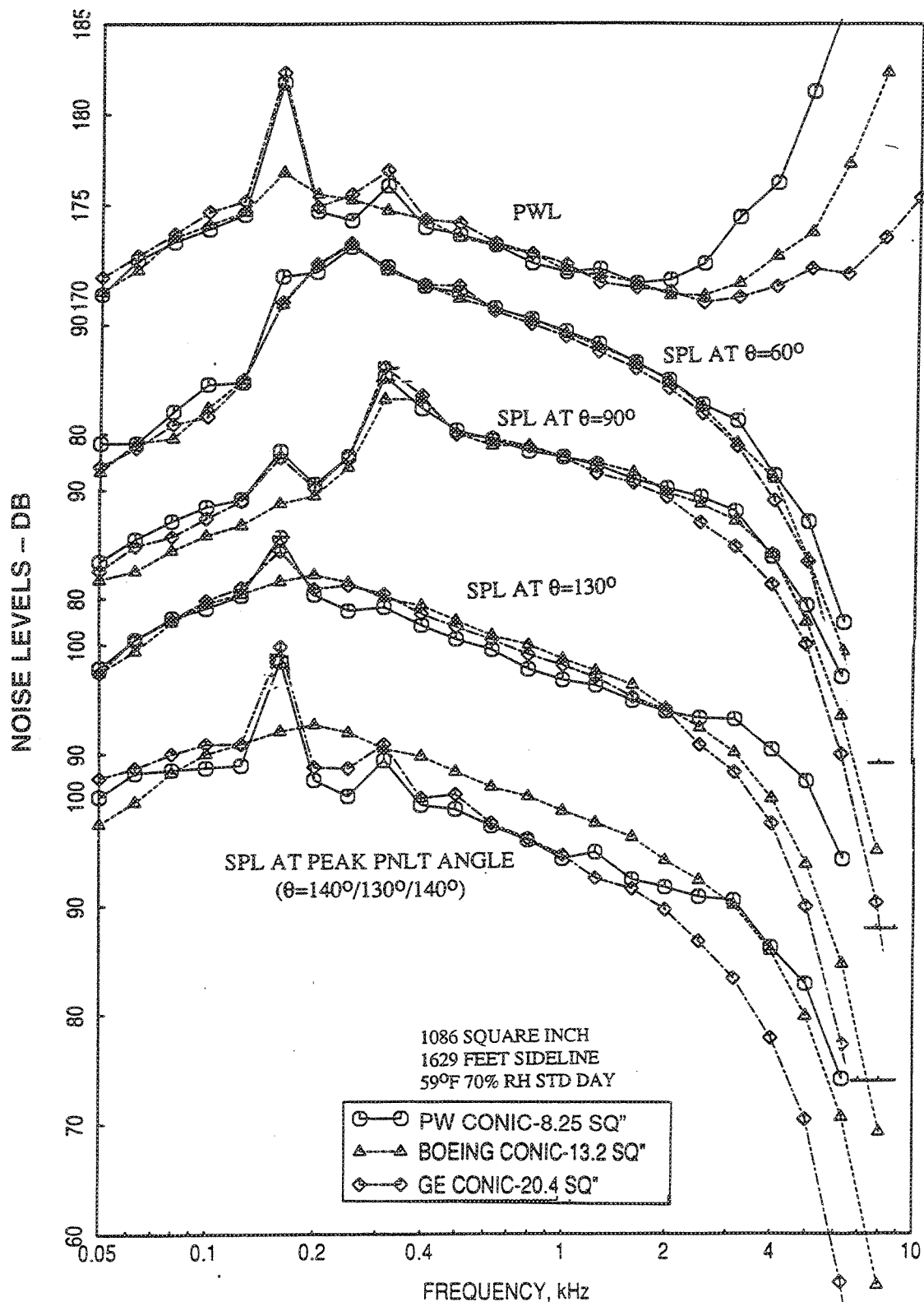


Figure 27. Comparison of PWL Spectra and SPL Spectra at Various Polar Angles ( $\theta$ ) at  $V_j=2384$  ft/sec,  $NPR=3.4$ ,  $T_8=1590^\circ R$  Between Three Different Size Conical Nozzles at Static Condition

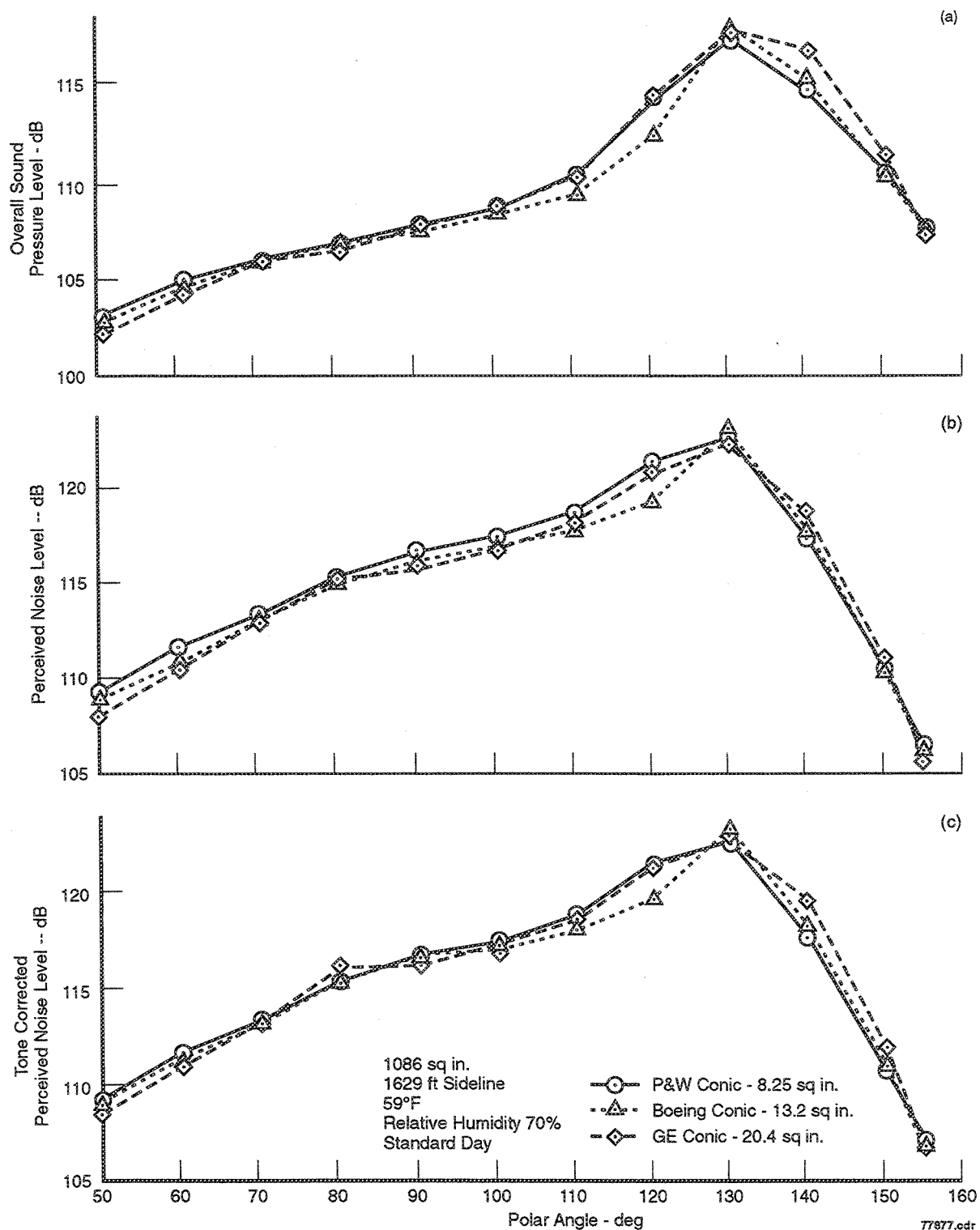


Figure 28. Comparison of: (a) OASP, (b) PNL, and (c) PNLT Directivities at  $V_j=2812$  ft/sec,  $NPR=4.5$ ,  $T_8=1860^\circ R$  Between Three Different Size Conical Nozzles at Static Conditions

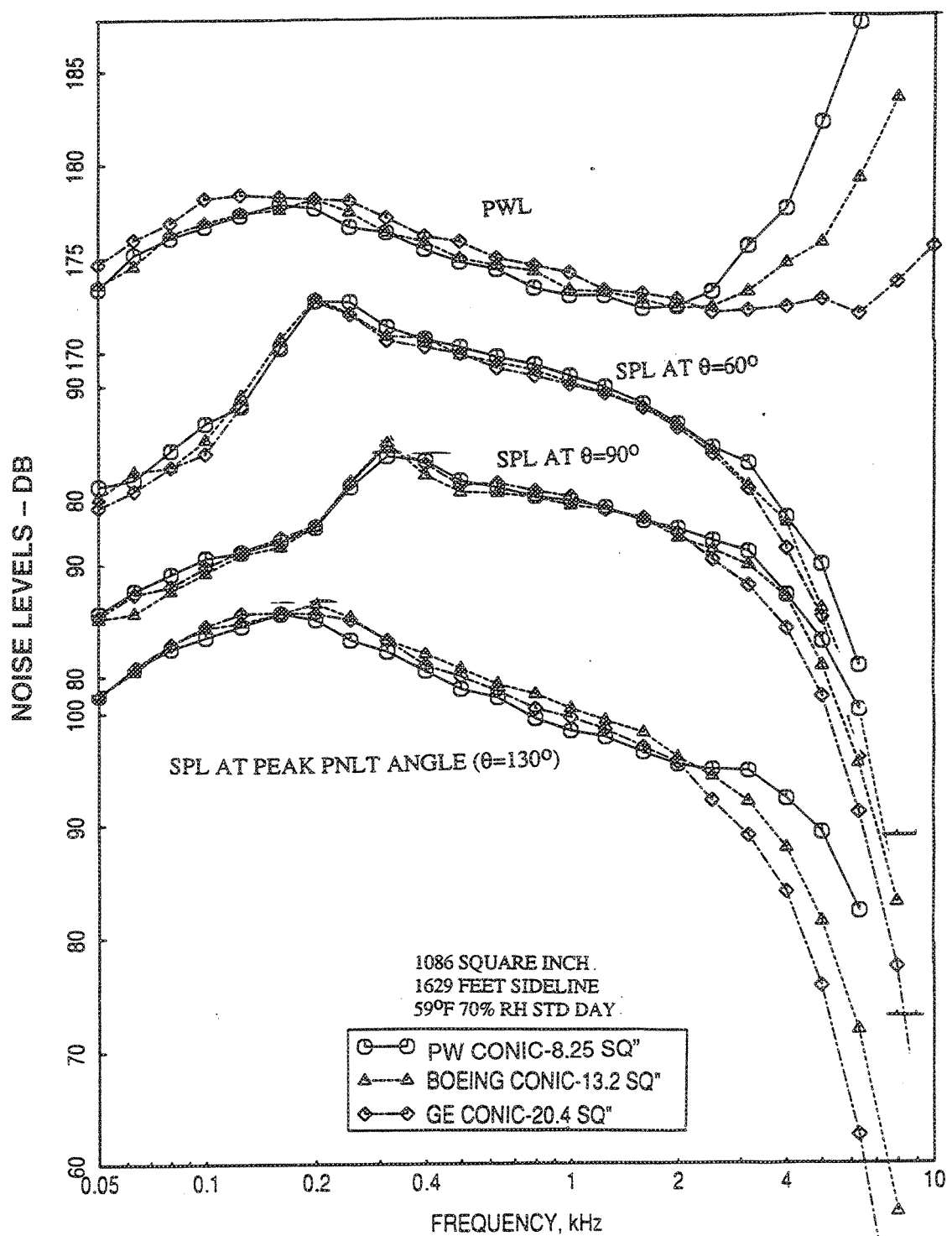


Figure 29. Comparison of PWL Spectra and SPL Spectra at Various Polar Angles ( $\theta$ ) at  $V_j=2812$  ft/sec,  $NPR=4.5$ ,  $T_8=1860^\circ R$  Between Three Different Size Conical Nozzles at Static Condition

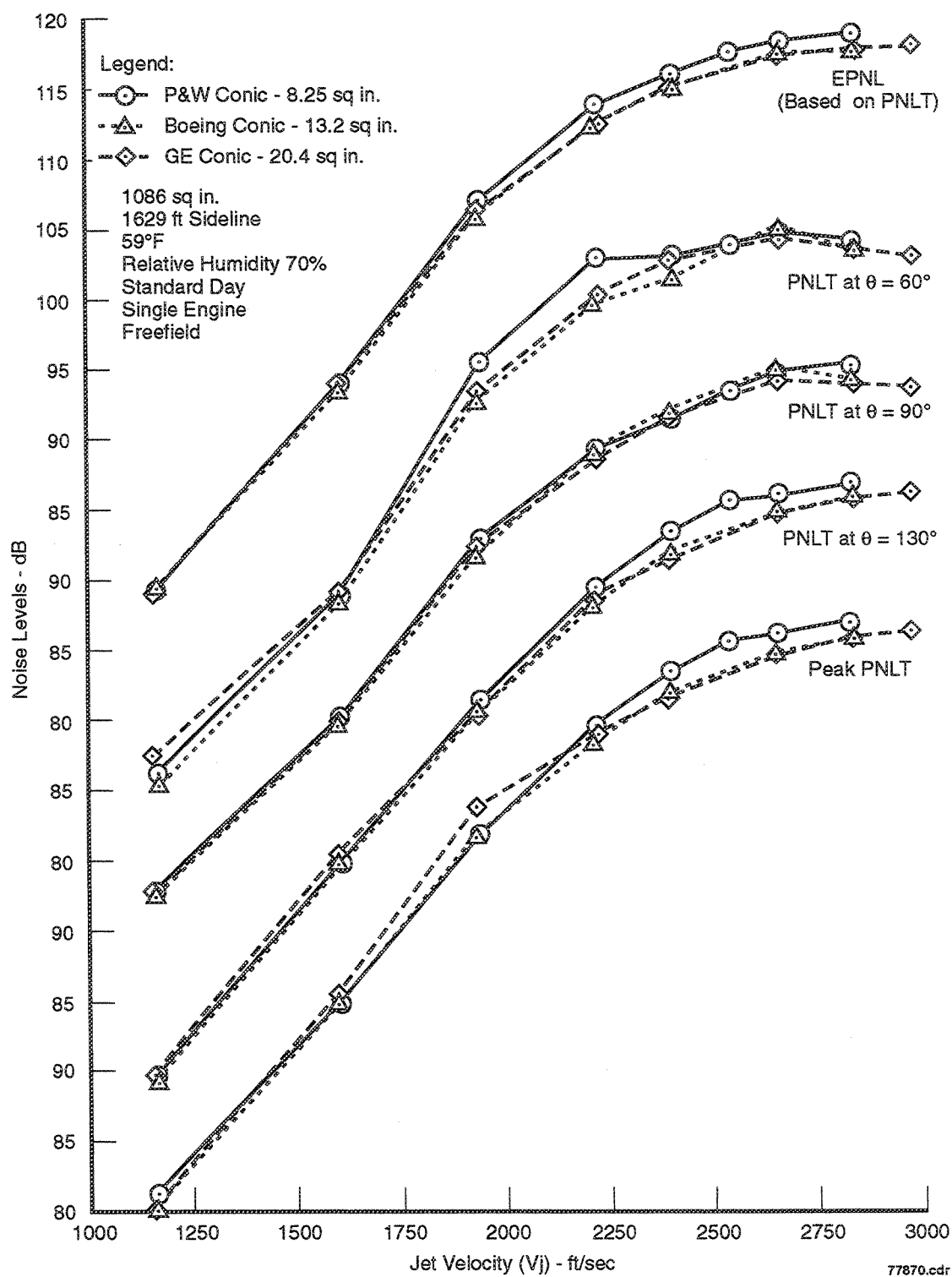


Figure 30. Comparison of Pseudo-EPNL, PNLT at Various Polar Angles ( $\theta$ ) and Peak PNLT Data as a Function of Jet Velocity Between Three Different Size Conical Nozzles With Flight Simulation ( $M_n=0.32$ )

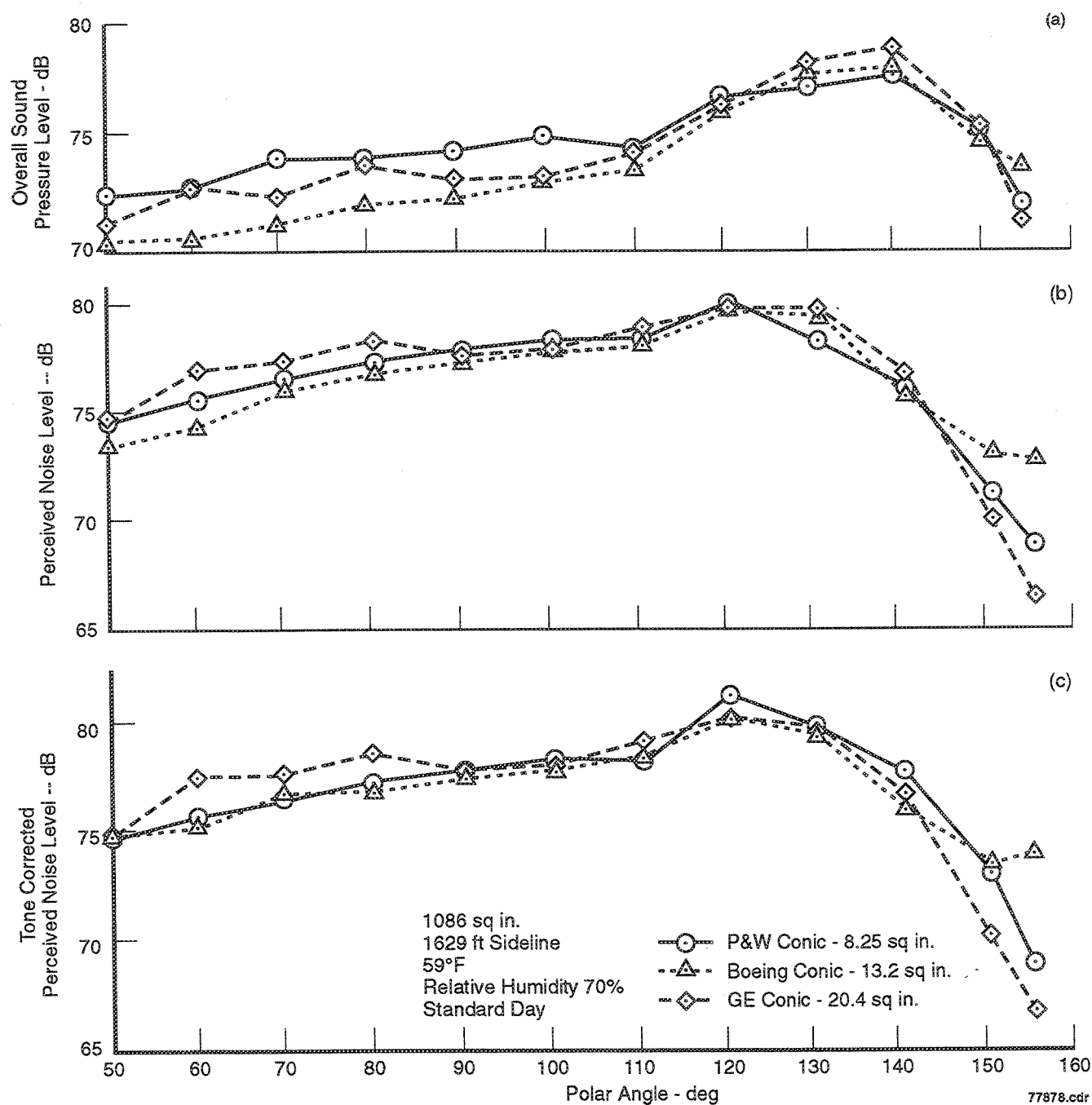


Figure 31. Comparison of: (a) OASP, (b) PNL, and (c) PNLT Directivities at  $V_j=1147$  ft/sec,  $NPR=1.5$ ,  $T_8=1000^\circ R$  Between Three Different Size Conical Nozzles With Flight Simulation ( $Mn=0.32$ )



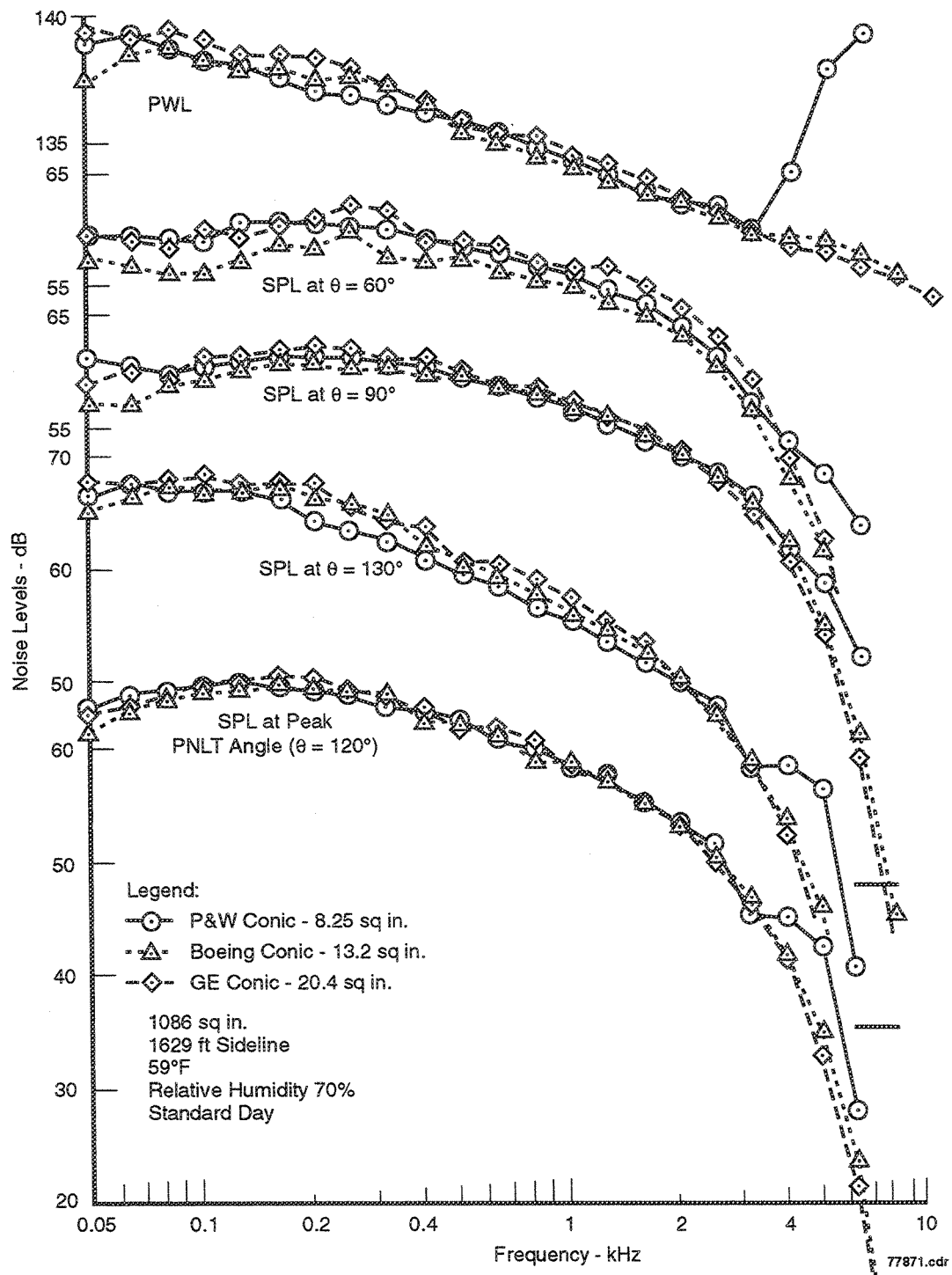


Figure 32. Comparison of PWL Spectra and SPL Spectra at Various Polar Angles ( $\theta$ ) at  $V_j=1147$  ft/sec,  $NPR=1.5$ ,  $T_8=1000^\circ R$  Between Three Different Size Conical Nozzles With Flight Simulation ( $M_n=0.32$ )

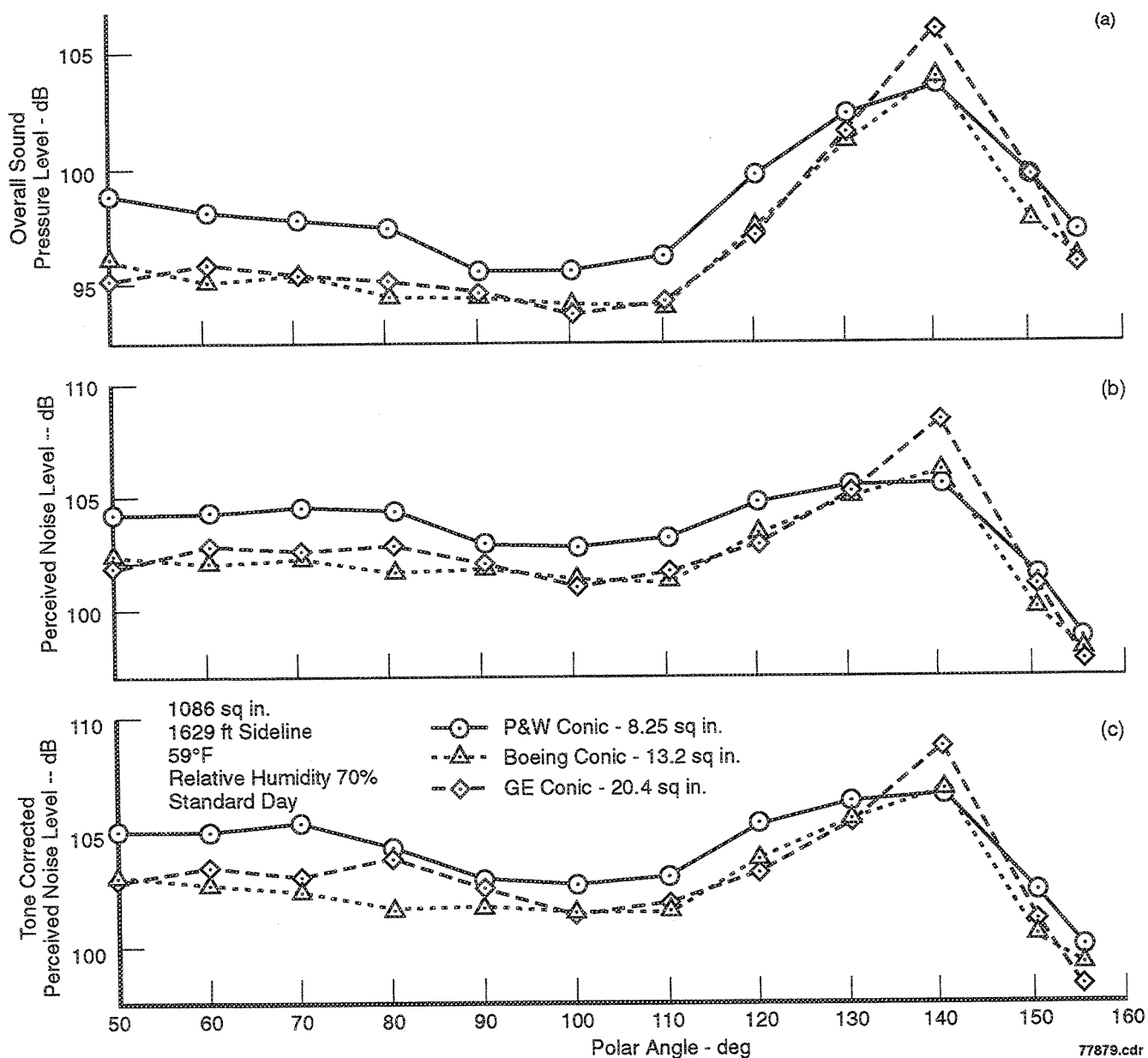


Figure 33. Comparison of: (a) OASP, (b) PNL, and (c) PNLT Directivities at  $V_j=1919$  ft/sec,  $NPR=2.5$ ,  $T_8=1325^\circ R$  Between Three Different Size Conical Nozzles With Flight Simulation ( $M_n=0.32$ )

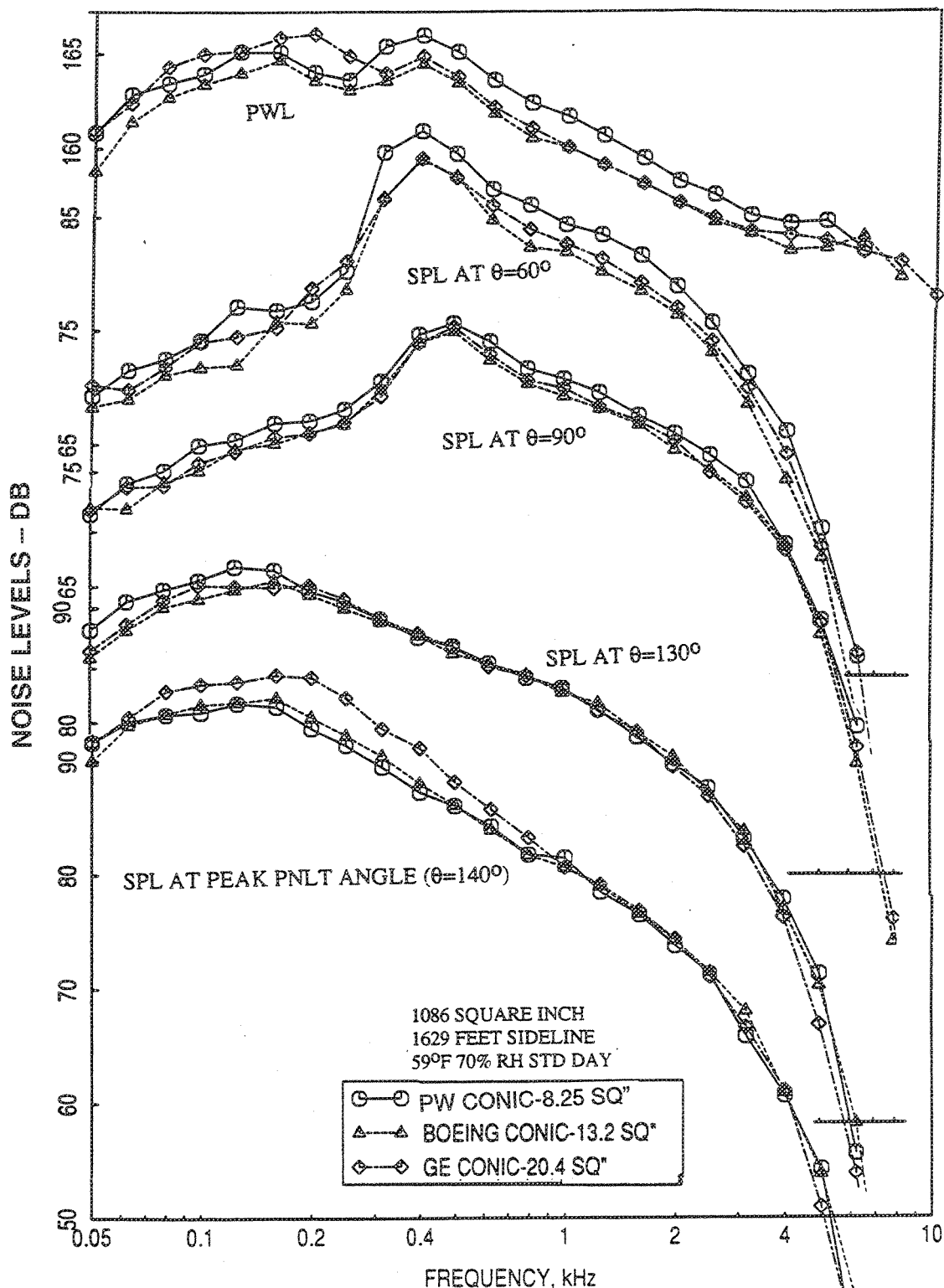


Figure 34. Comparison of PWL Spectra and SPL Spectra at Various Polar Angles ( $\theta$ ) at  $V_j=1919$  ft/sec,  $NPR=2.5$ ,  $T_g=1325^\circ R$  Between Three Different Size Conical Nozzles With Flight Simulation ( $M_n=0.32$ )

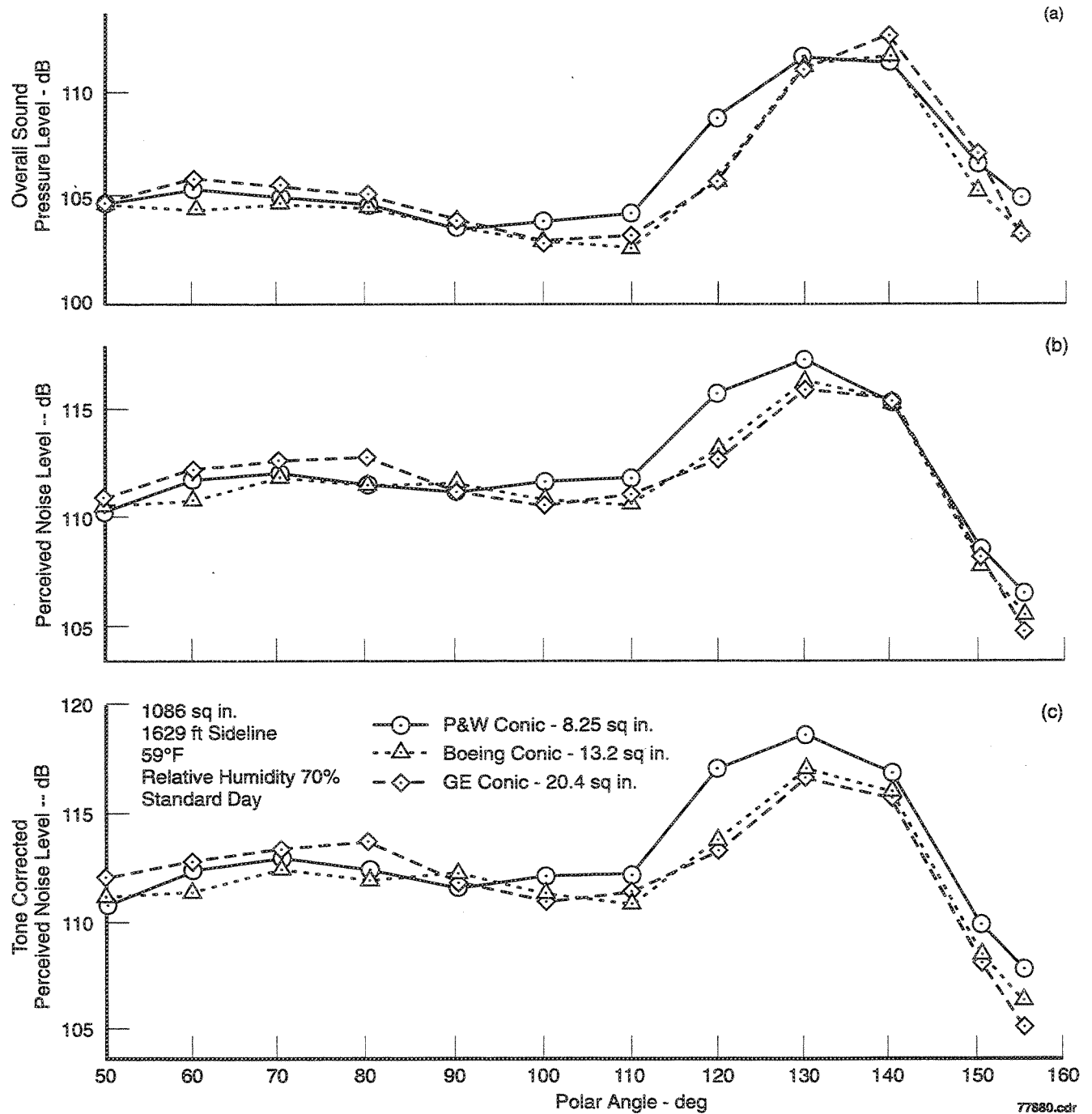


Figure 35. Comparison of: (a) OASP, (b) PNL, and (c) PNLT Directivities at  $V_j=2384$  ft/sec,  $NPR=3.4$ ,  $T_8=1590^\circ R$  Between Three Different Size Conical Nozzles With Flight Simulation ( $M_n=0.32$ )

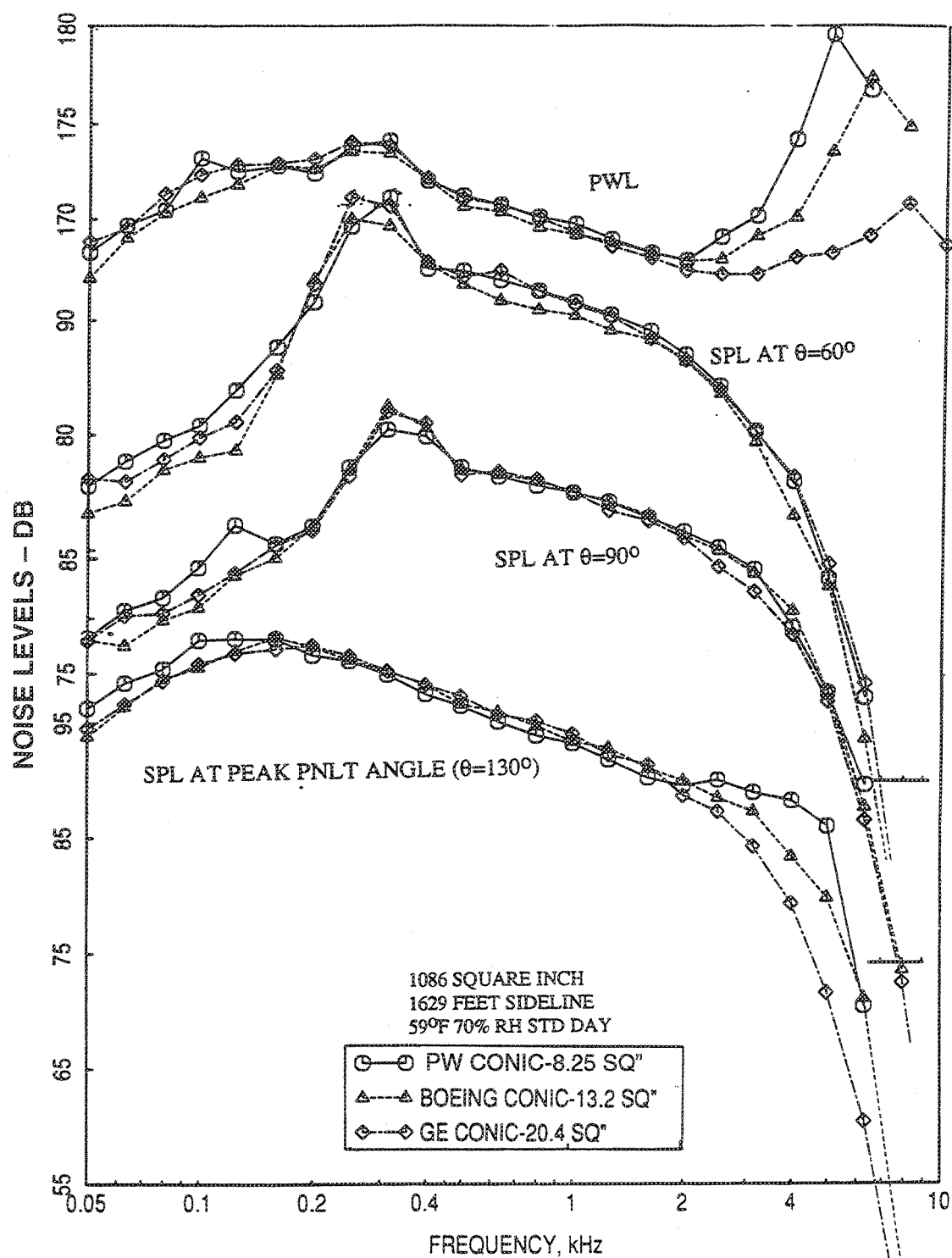


Figure 36. Comparison of PWL Spectra and SPL Spectra at Various Polar Angles ( $\theta$ ) at  $V_j=2384$  ft/sec,  $NPR=3.4$ ,  $T_g=1590^\circ R$  Between Three Different Size Conical Nozzles With Flight Simulation ( $M_n=0.32$ )

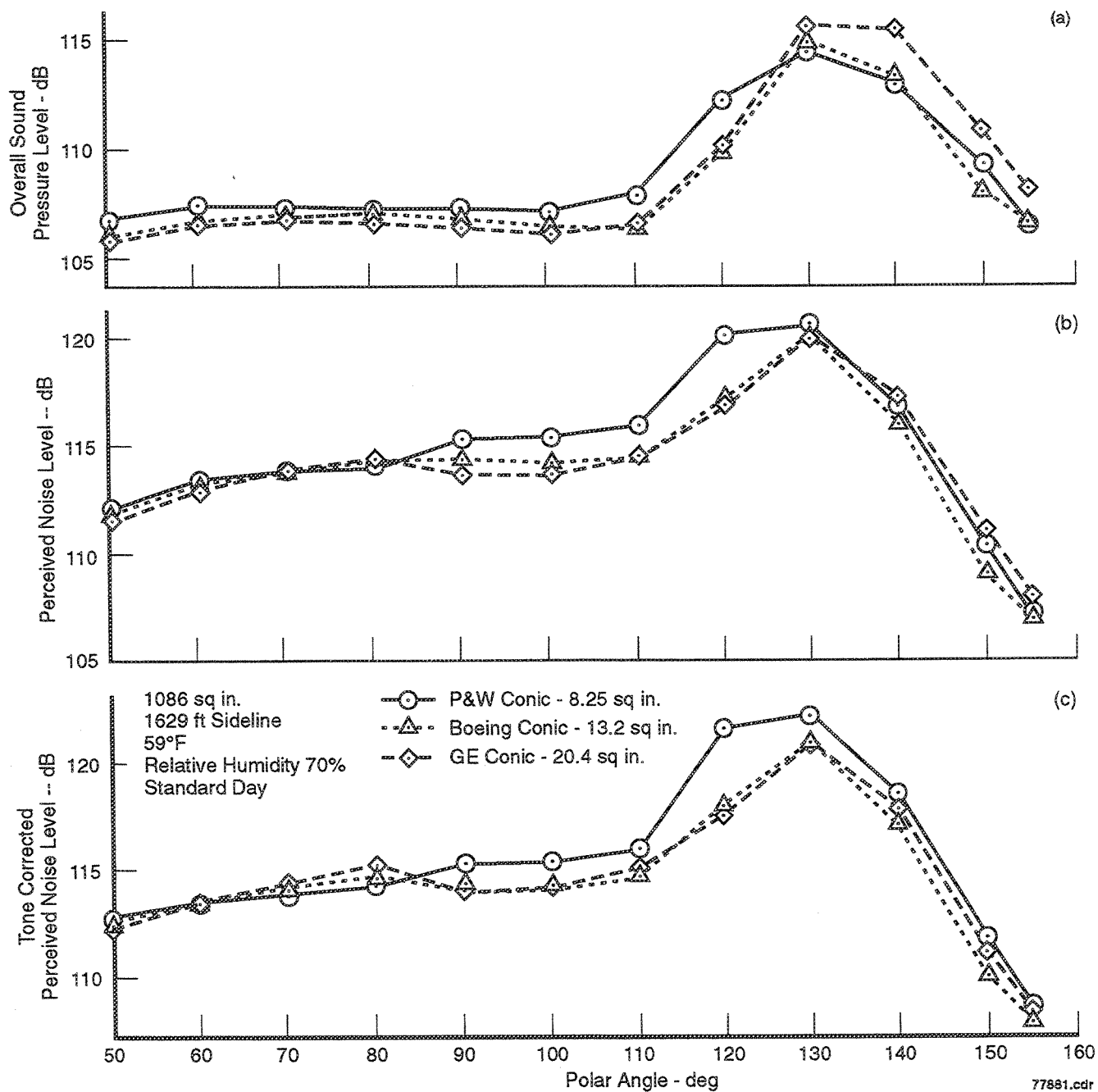


Figure 37. Comparison of: (a) OASP, (b) PNL, and (c) PNLT Directivities at  $V_j=2812$  ft/sec,  $NPR=4.5$ ,  $T_8=1860^\circ R$  Between Three Different Size Conical Nozzles With Flight Simulation ( $Mn=0.32$ )

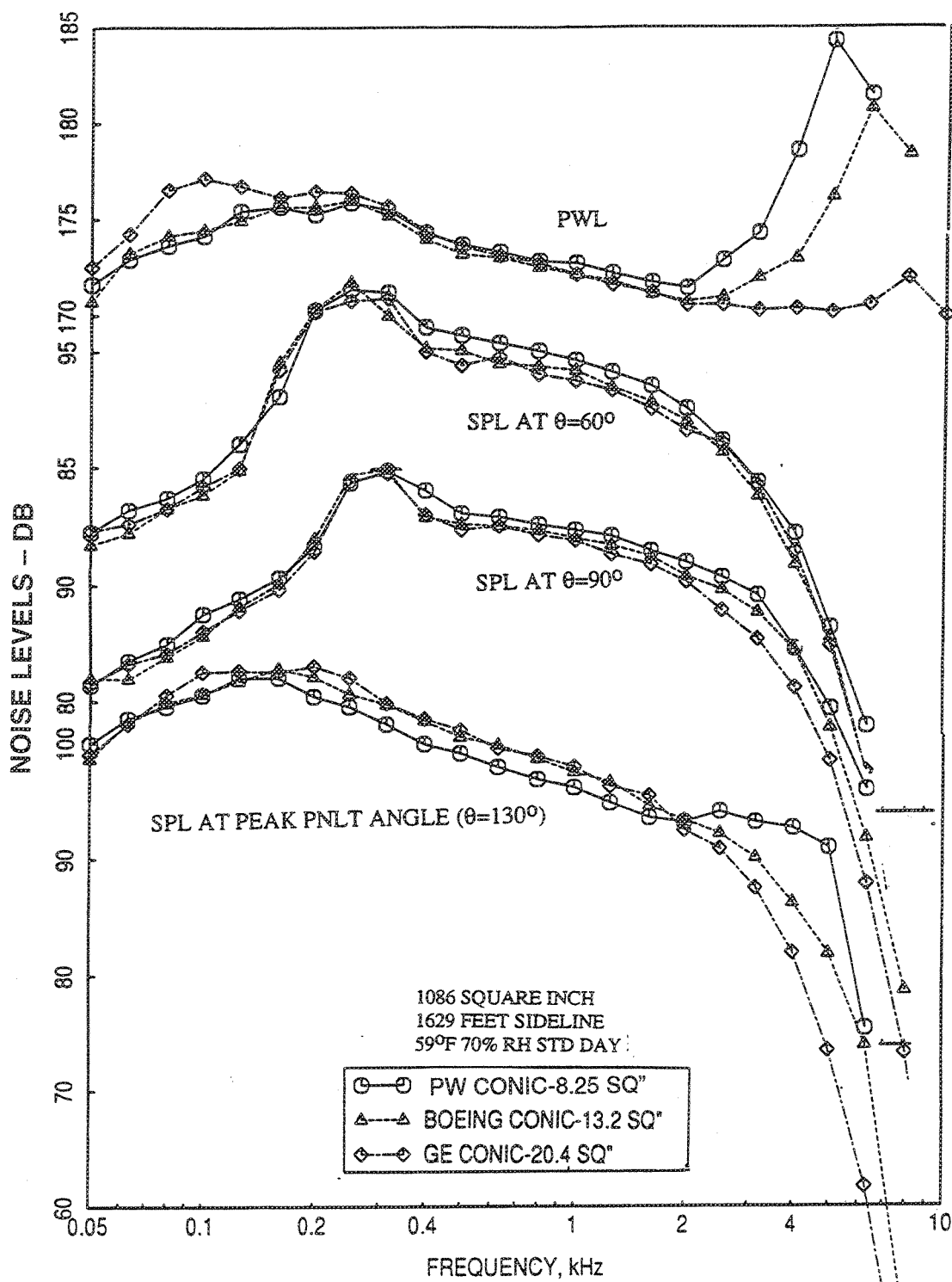


Figure 38. Comparison of PWL Spectra and SPL Spectra at Various Polar Angles ( $\theta$ ) at  $V_j=2812$  ft/sec,  $NPR=4.5$ ,  $T_8=1860^\circ R$  Between Three Different Size Conical Nozzles With Flight Simulation ( $M_n=0.32$ )

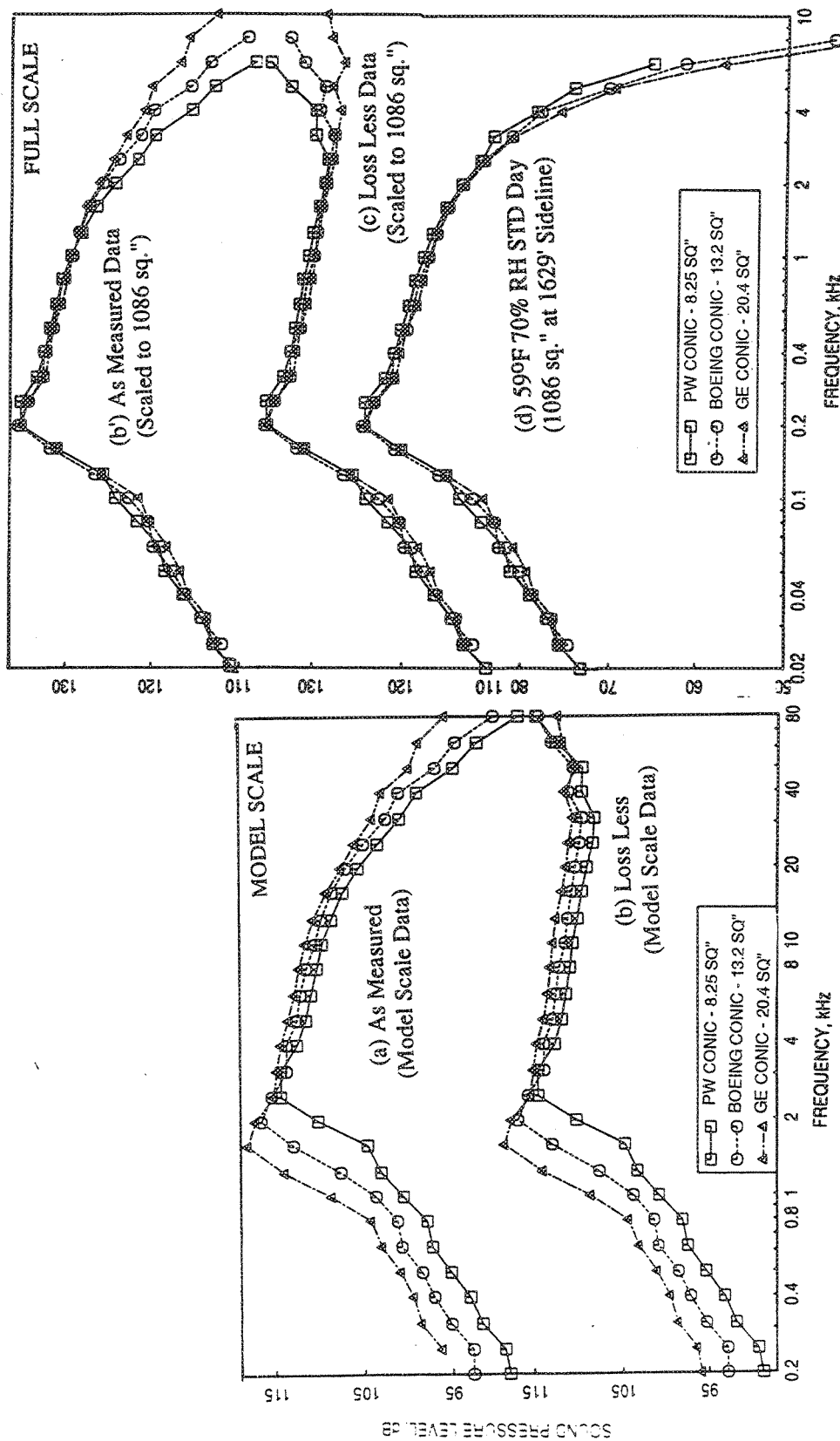


Figure 39. Comparison of SPL Spectra at Polar Angle ( $\theta$ )=60°,  $V_j$ =2812 ft/sec, NPR=4.5, and  $T_8$ =1860°R Between Three Different Size Conical Nozzles at Static Condition



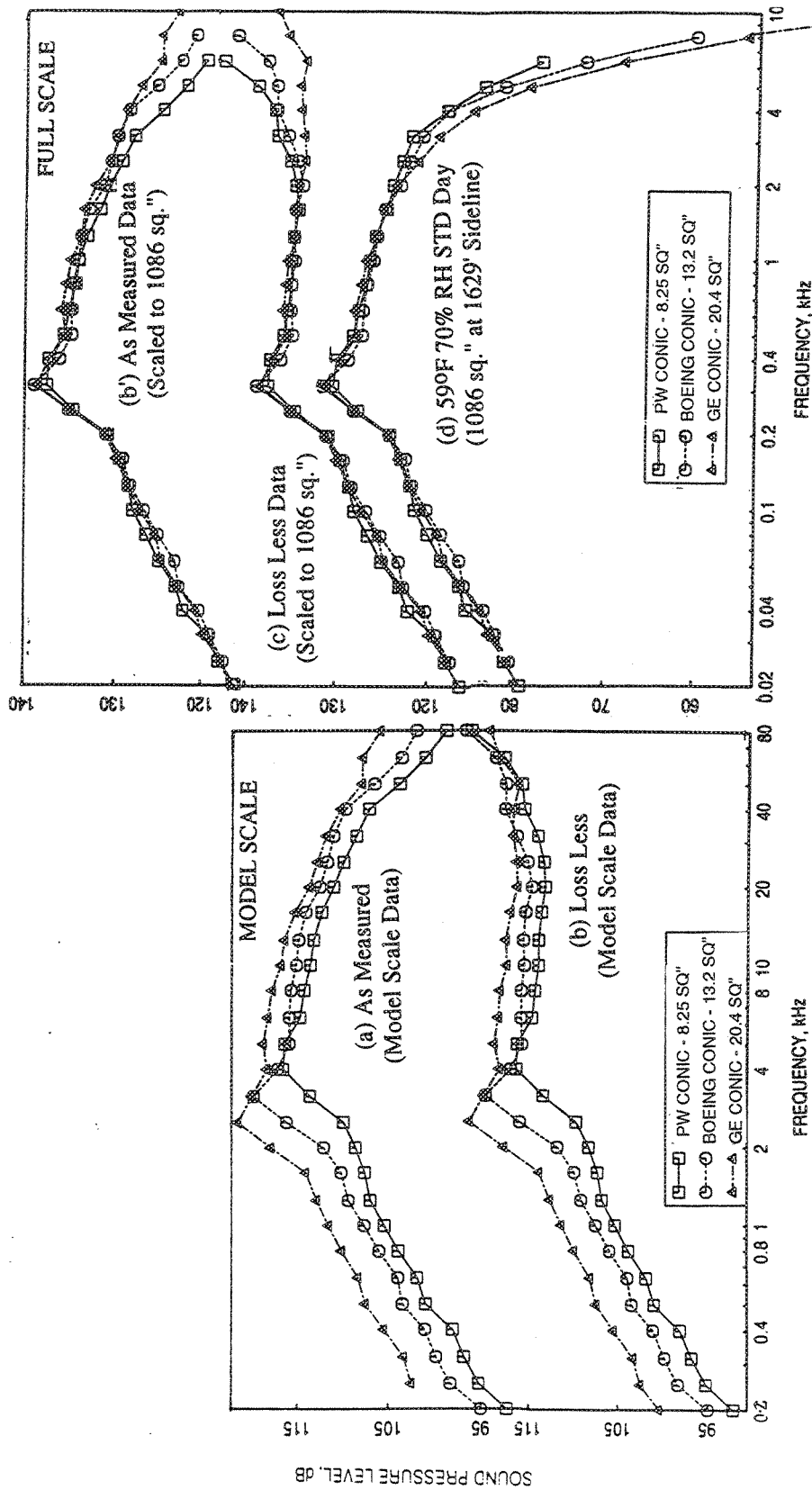


Figure 40. Comparison of SPL Spectra at Polar Angle  $(\theta)=90^\circ$ ,  $V_j=2812$  ft/sec,  $NPR=4.5$ , and  $T_8=1860^\circ R$  Between Three Different Size Conical Nozzles at Static Condition

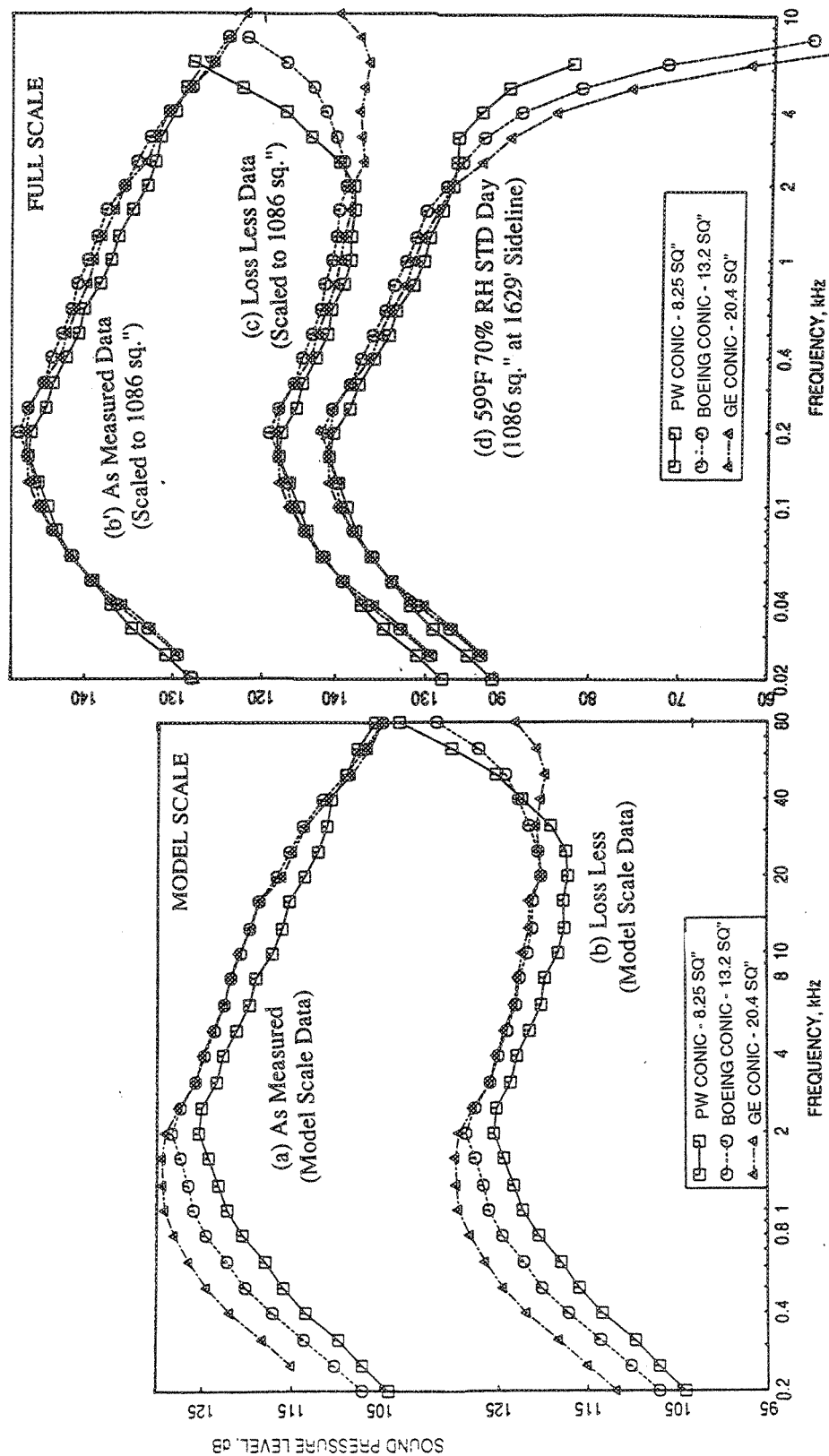


Figure 41. Comparison of SPL Spectra at Polar Angle ( $\theta$ )=130°,  $V_j$ =2812 ft/sec, NPR=4.5, and  $T_g$ =1860°R Between Three Different Size Conical Nozzles at Static Condition

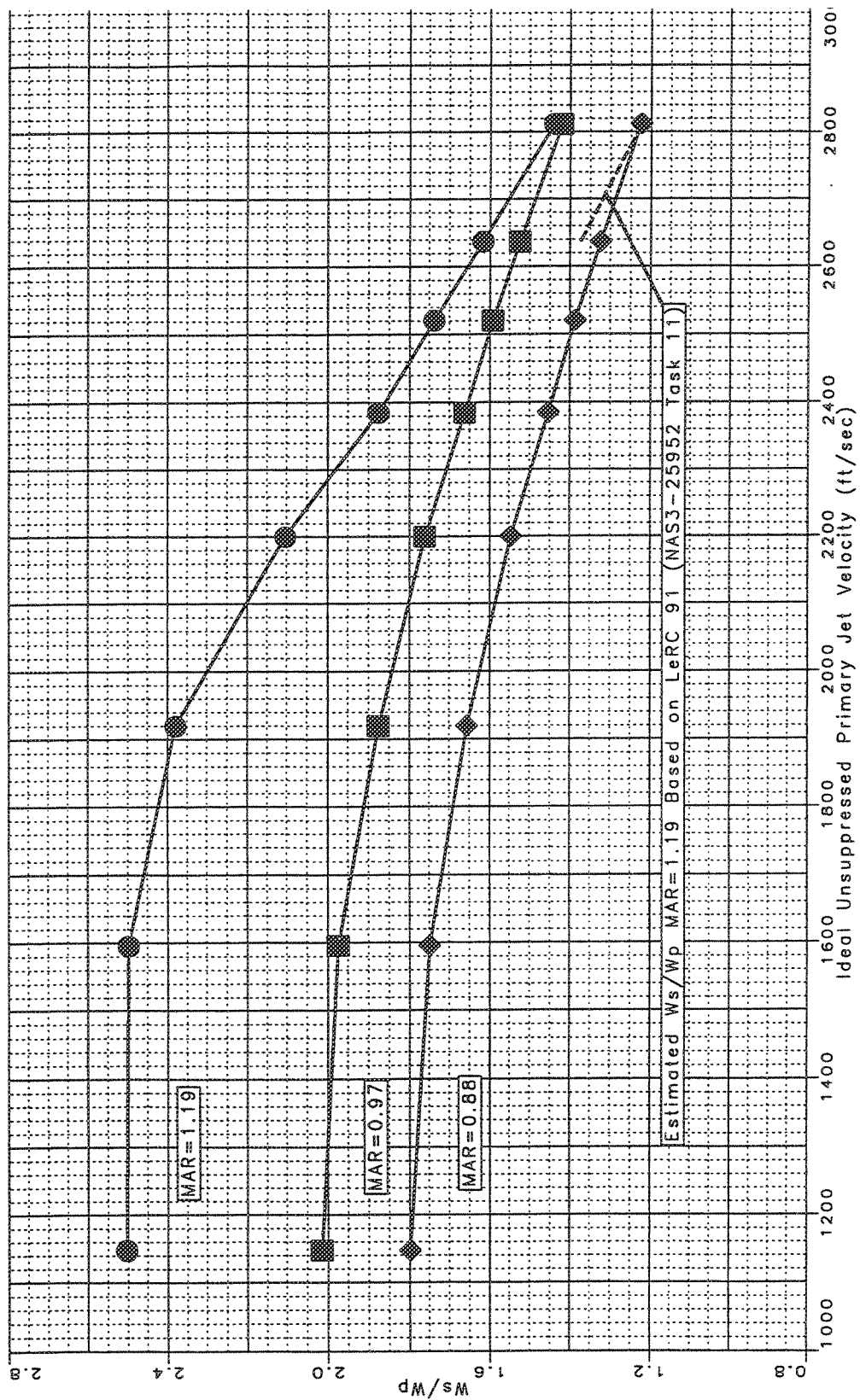


Figure 42. Ideal One-Dimensional Ejector Pumping Estimate (SAR=4.9, Altitude=689 ft,  $M_n=0.32$ )

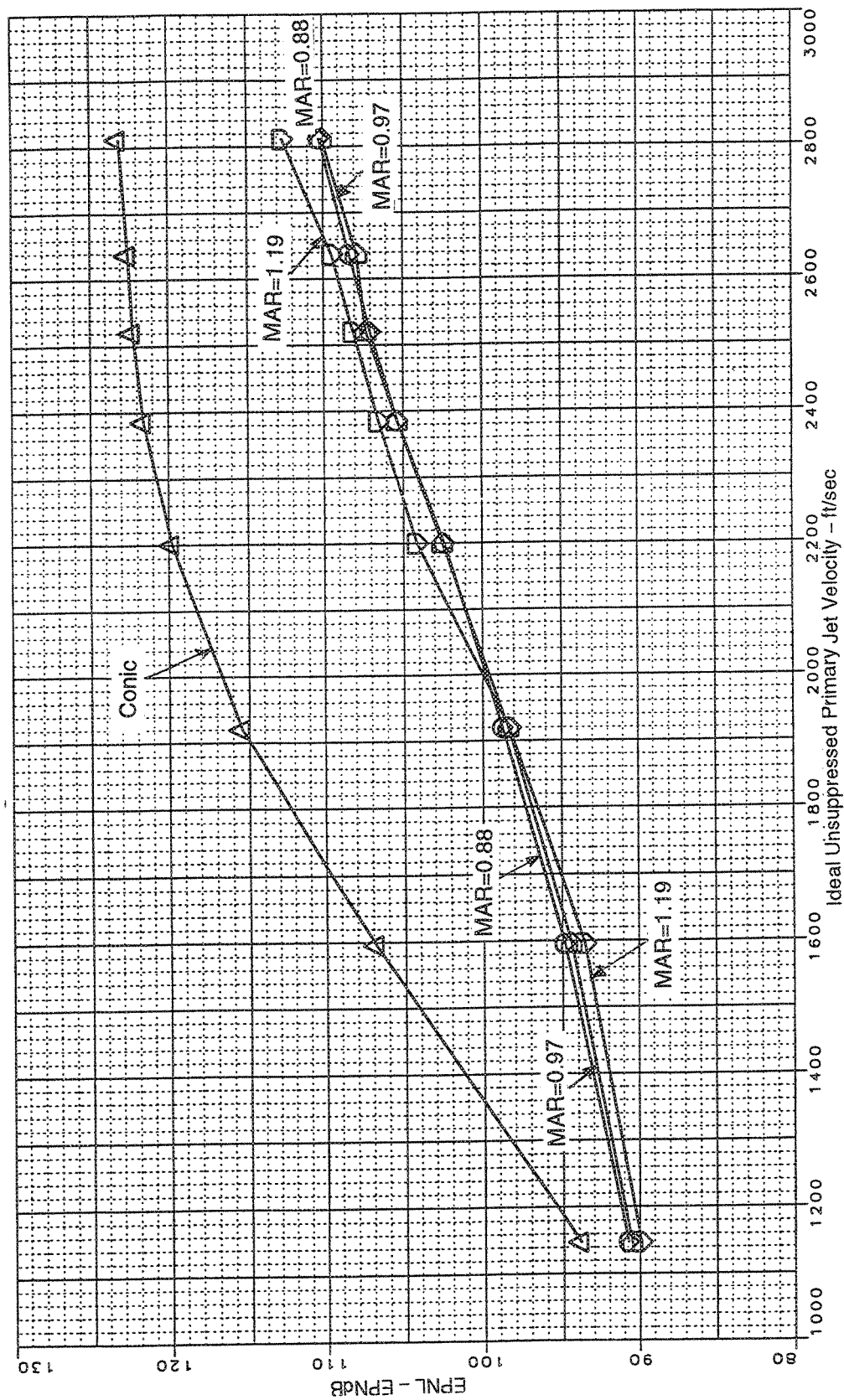


Figure 43. Effect of MAR ( $A_{\text{exit}}/A_{\text{mix}}$ ) on Sideline Noise, Vortical Mixer, Long Treated Shroud  
( $SAR=4.9$ ,  $A_{g*}=1086 \text{ in}^2$ ,  $SL=1629 \text{ ft}$ , Static)

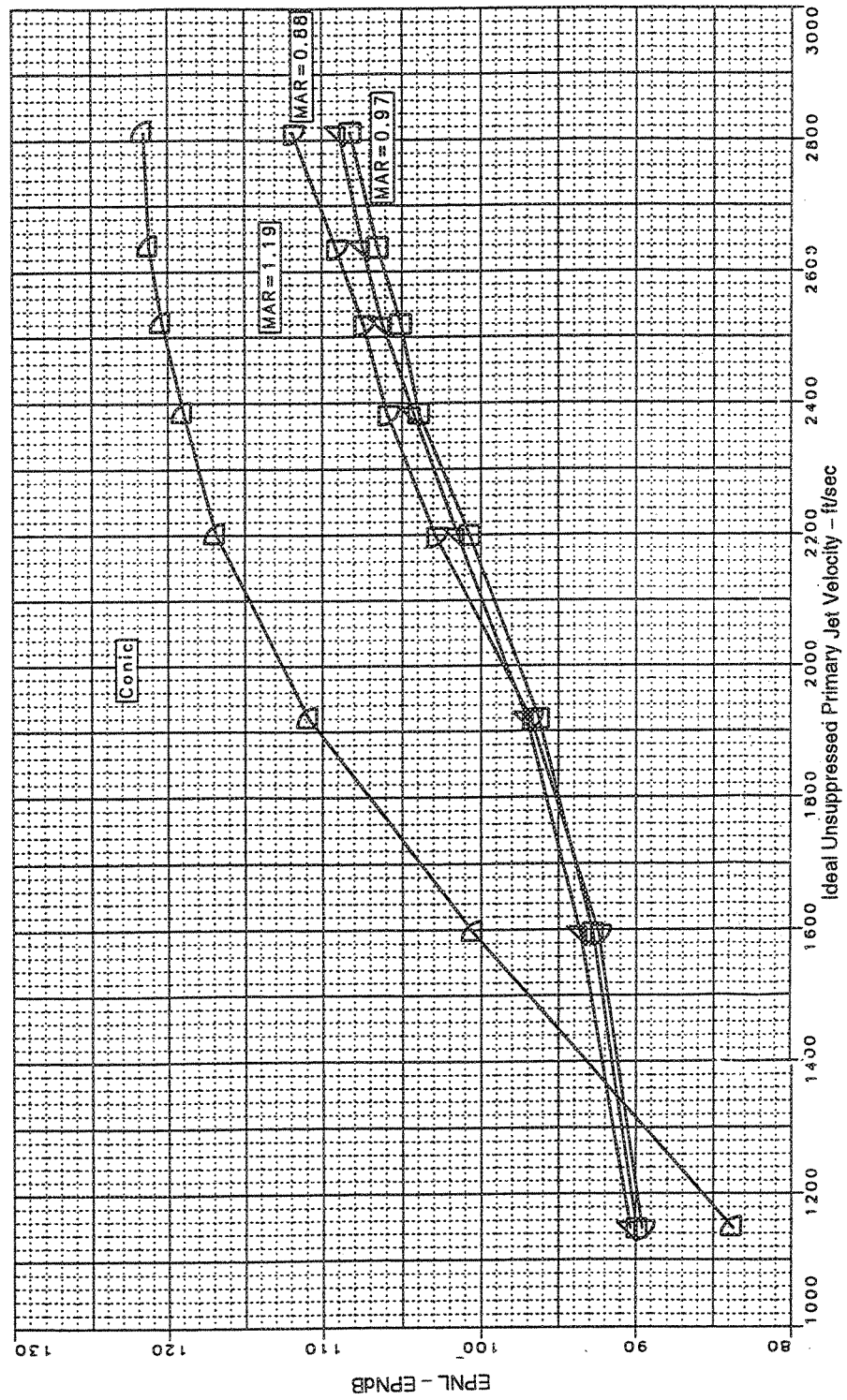


Figure 44. Effect of MAR ( $A_{exit}/A_{mix}$ ) on Sideline Noise, Vortical Mixer, Long Treated Shroud  
 (SAR=4.9,  $A_{g*}=1086 \text{ in}^2$ , SL=1629 ft,  $Mn=0.32$ ,  $V_{\eta}=357 \text{ ft/sec}$ )

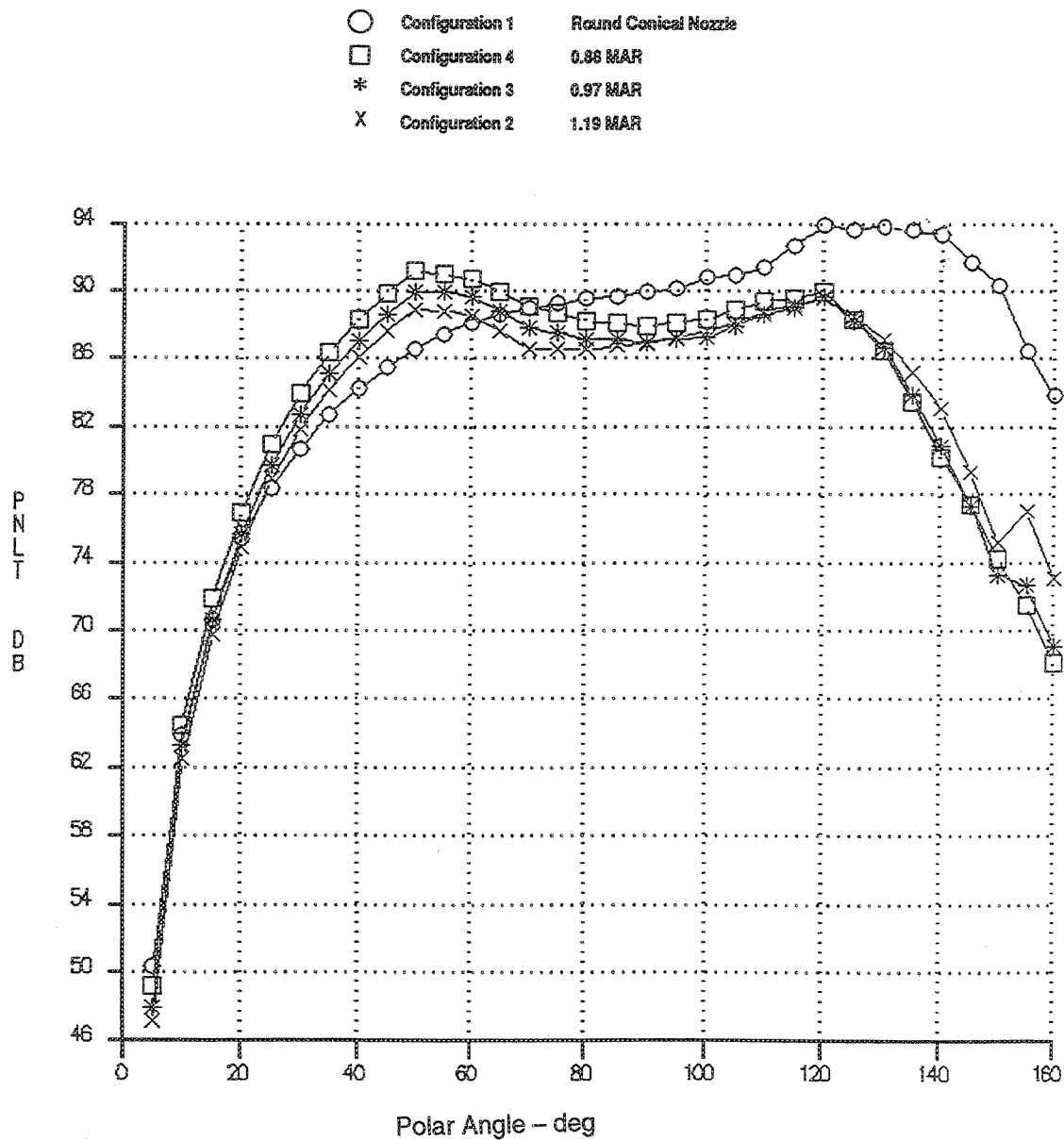


Figure 45. Effect of MAR on PNL T vs. Angle — Ideal Unsuppressed Primary Jet Velocity=1595 ft/sec  
 Vortical Mixer, Long Treated Shroud  
 (Sideline=1629 ft,  $A_{g*}=1086 \text{ in}^2$ , SAR=4.9,  $V_{\Pi}=357 \text{ ft/sec}$ )

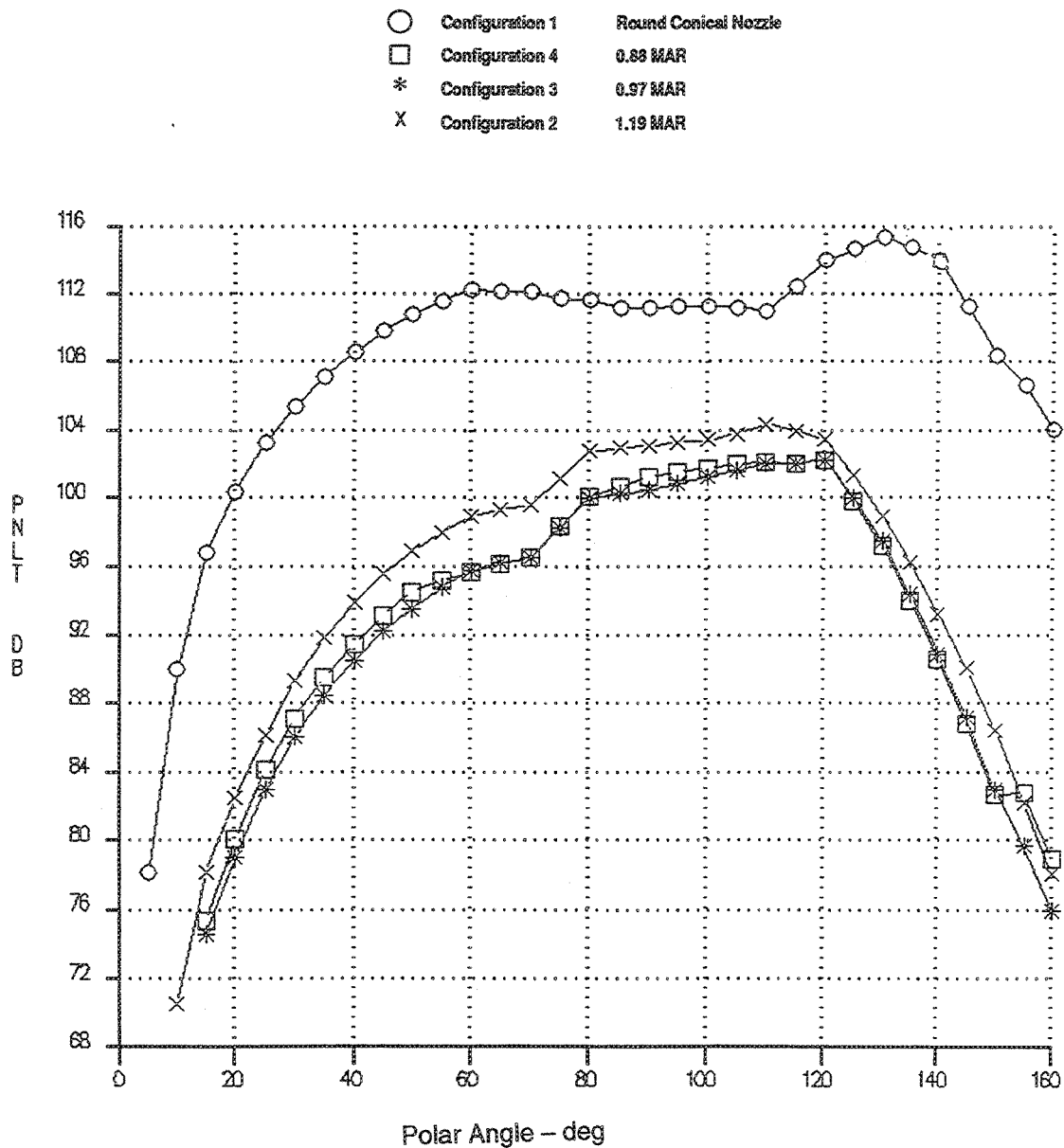


Figure 46. Effect of MAR on PNLT vs. Angle — Ideal Unsuppressed Primary Jet Velocity=2384 ft/sec  
Vortical Mixer, Long Treated Shroud  
(Sideline=1629 ft,  $A_{g*}=1086 \text{ in}^2$ , SAR=4.9,  $V_{fl}=357 \text{ ft/sec}$ )

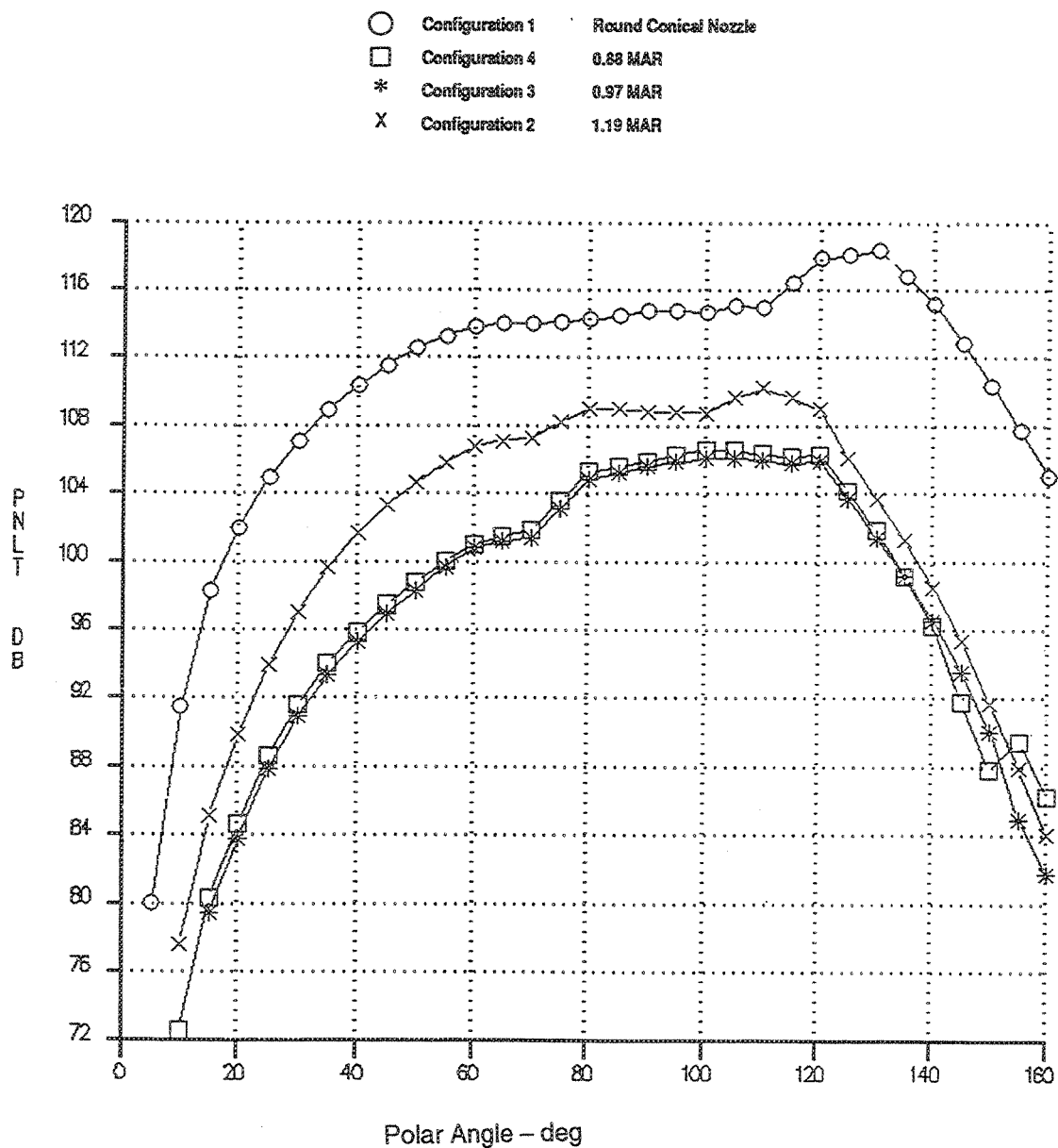


Figure 47. Effect of MAR on PNLT vs. Angle — Ideal Unsuppressed Primary Jet Velocity=2812 ft/sec  
 Vortical Mixer, Long Treated Shroud  
 (Sideline=1629 ft,  $A_{g*}=1086 \text{ in}^2$ , SAR=4.9,  $V_{fl}=357 \text{ ft/sec}$ )



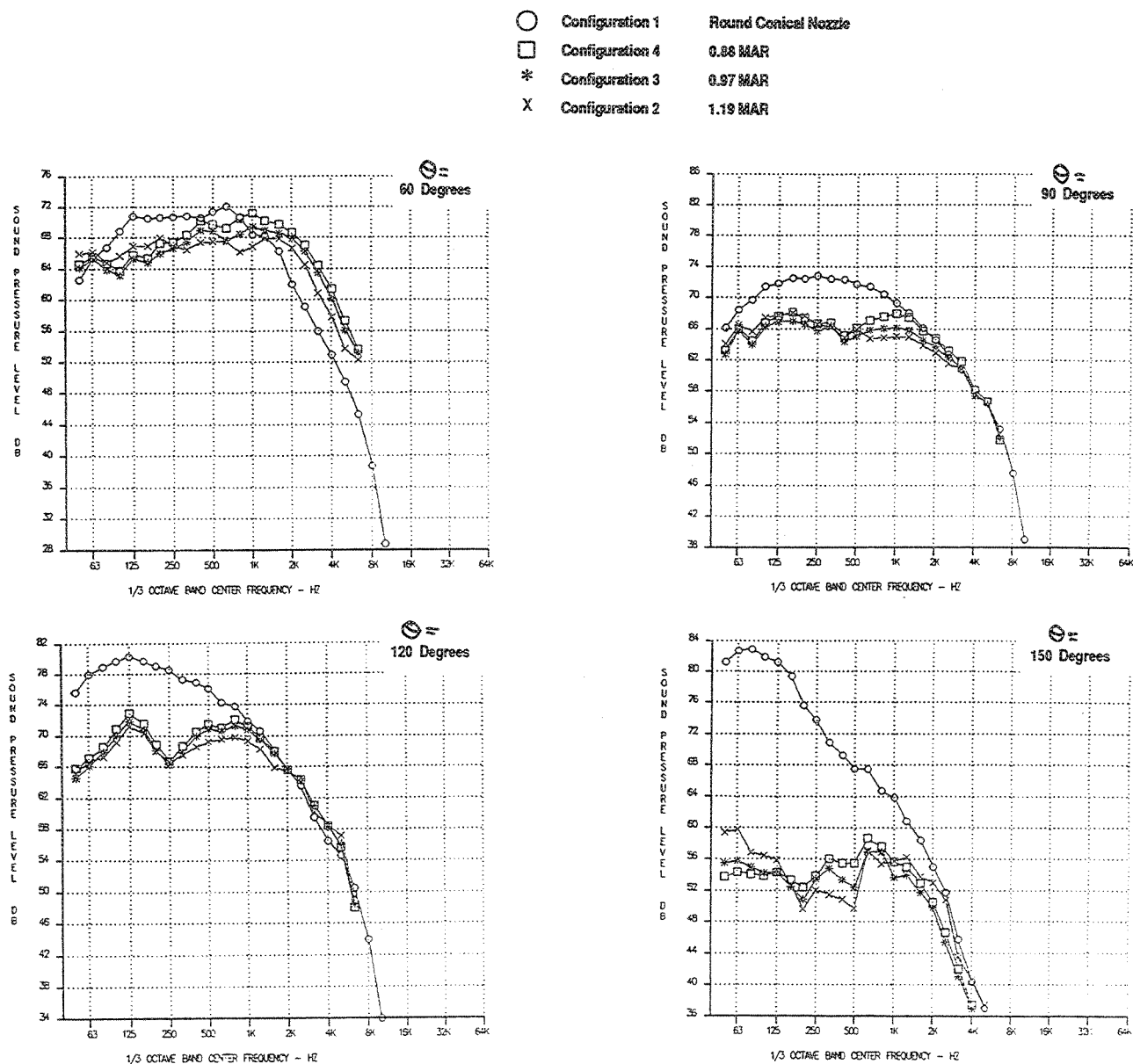


Figure 48. Effect of MAR on SPL Versus Frequency — Ideal Unsuppressed Primary Jet Velocity=1595 ft/sec  
 Vortical Mixer, Long Treated Shroud  
 (Sideline=1629 ft,  $A_{g*}=1086 \text{ in}^2$ , SAR=4.9,  $M_n=0.32$ ,  $V_{fl}=357 \text{ ft/sec}$ )

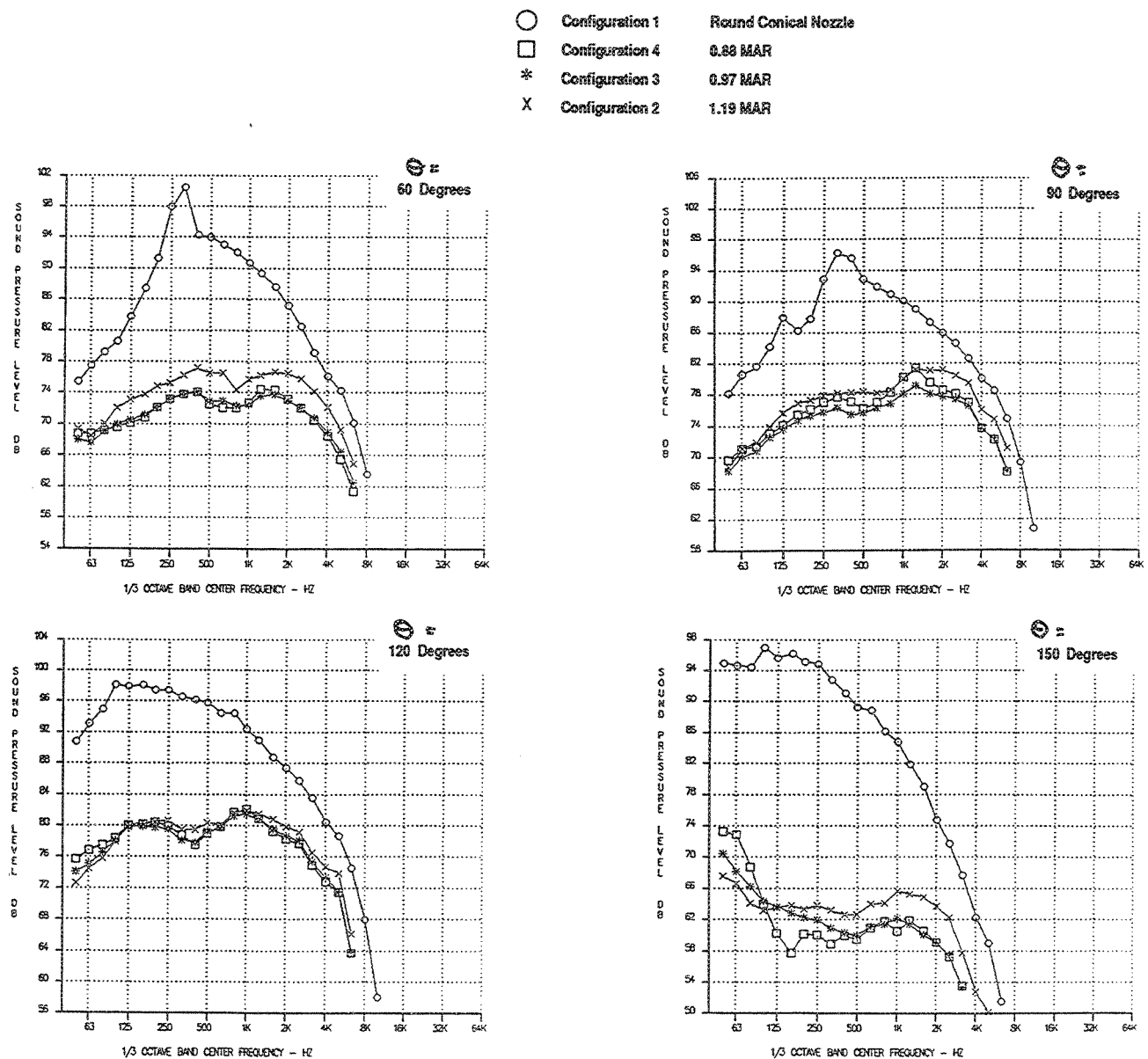


Figure 49. Effect of MAR on SPL Versus Frequency — Ideal Unsuppressed Primary Jet Velocity=2384 ft/sec  
 Vortical Mixer, Long Treated Shroud  
 (Sideline=1629 ft,  $A_{g*}=1086 \text{ in}^2$ , SAR=4.9, Mn=0.32,  $V_{\Pi}=357 \text{ ft/sec}$ )

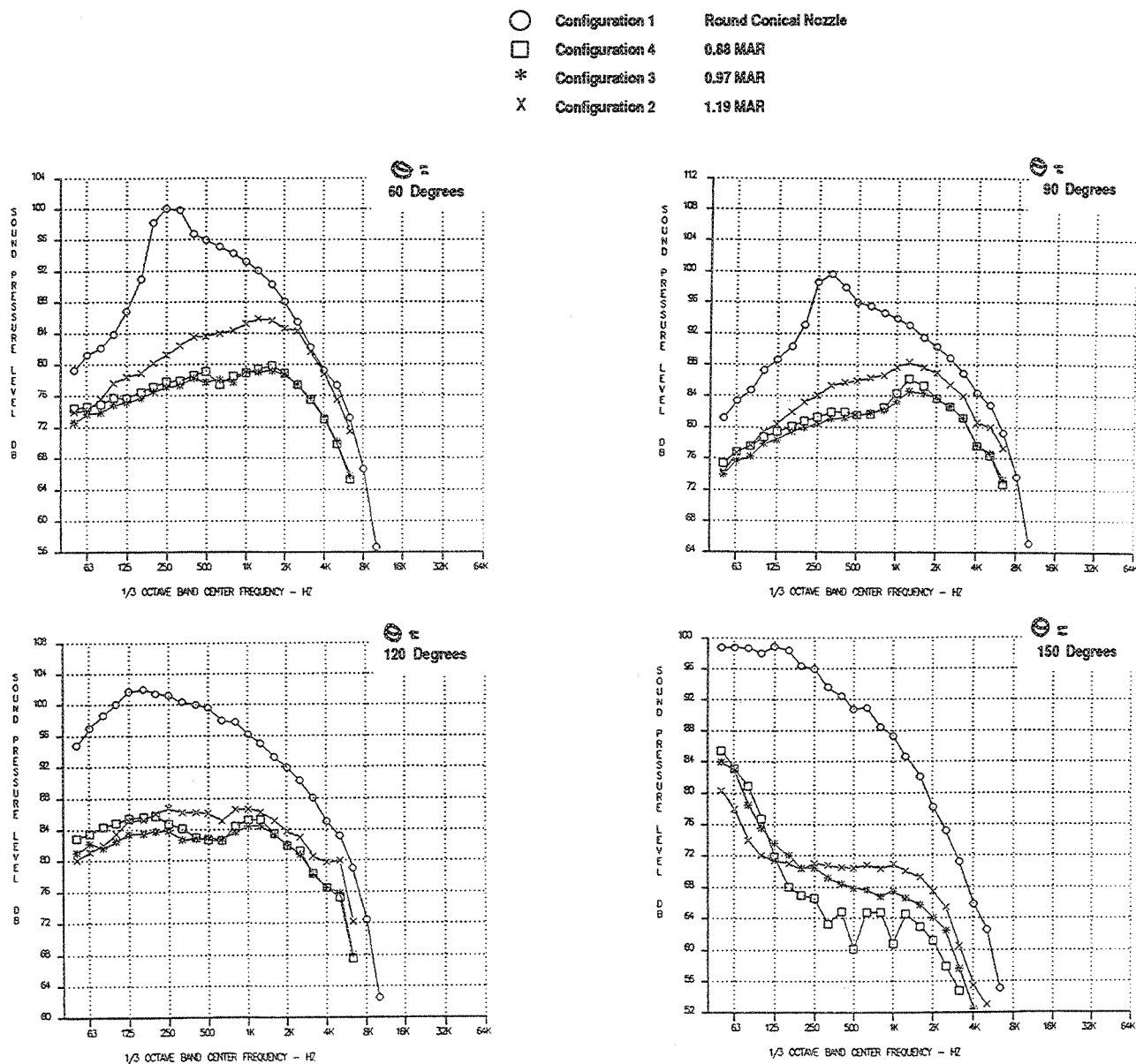
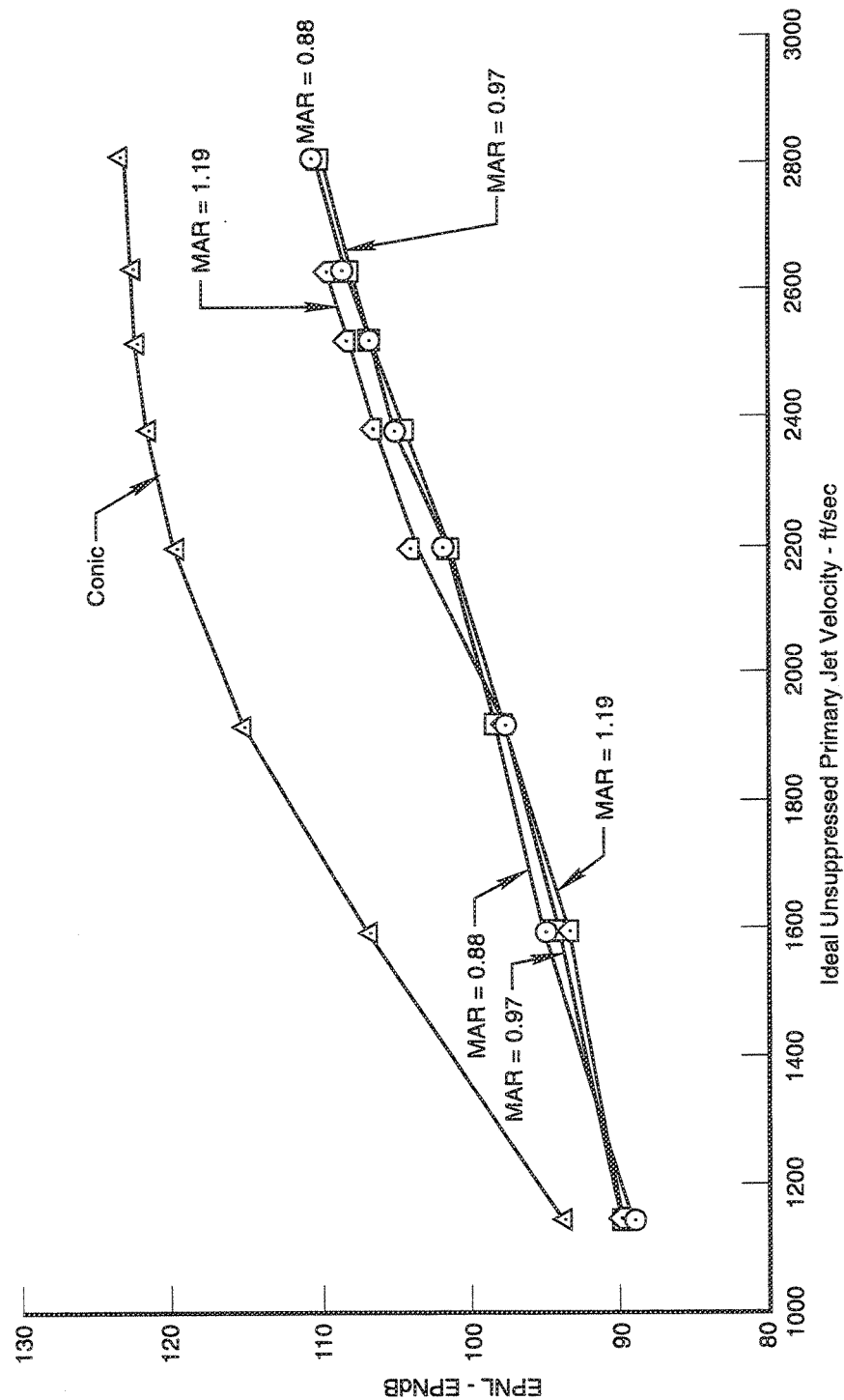
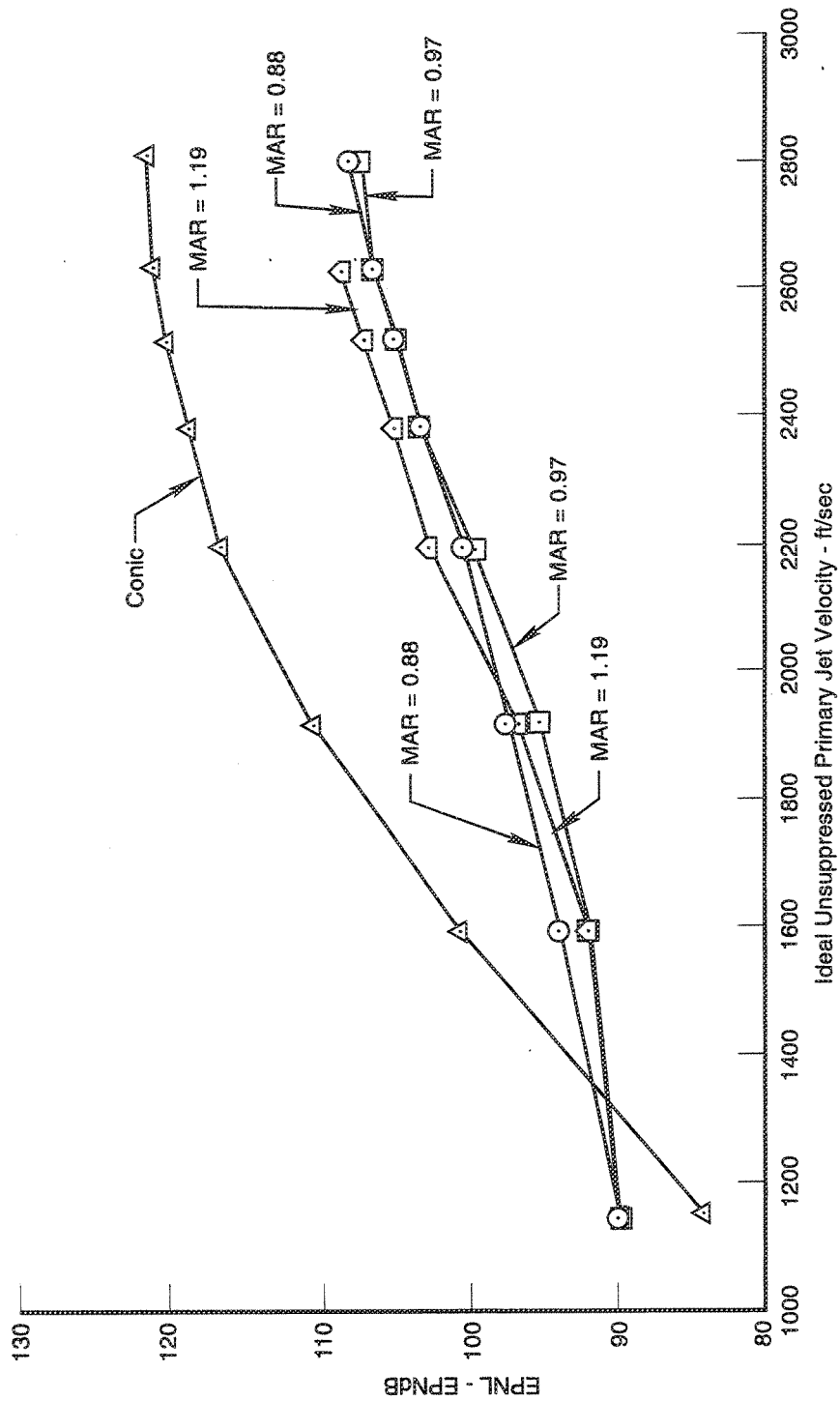


Figure 50. Effect of MAR on SPL Versus Frequency — Ideal Unsuppressed Primary Jet Velocity=2812 ft/sec  
Vortical Mixer, Long Treated Shroud  
(Sideline=1629 ft,  $A_{g*}=1086 \text{ in}^2$ , SAR=4.9,  $Mn=0.32$ ,  $V_{fl}=357 \text{ ft/sec}$ )



77685.cdr

Figure 51. Effect of MAR (Aexit/Amix) on Sideline Noise, Vortical Mixer, Long Treated Shroud  
(Sideline=1627 ft, SAR=4.4, Ag\*=1086 in<sup>2</sup>, Static)



77886.cdr

Figure 52. Effect of MAR (Aexit/Amix) on Sideline Noise, Vortical Mixer, Long Treated Shroud  
(Sideline=1629 ft, SAR=4.4,  $A_{g*}=1086$  in<sup>2</sup>,  $M_n=0.32$ ,  $V_{\eta}=357$  ft/sec)

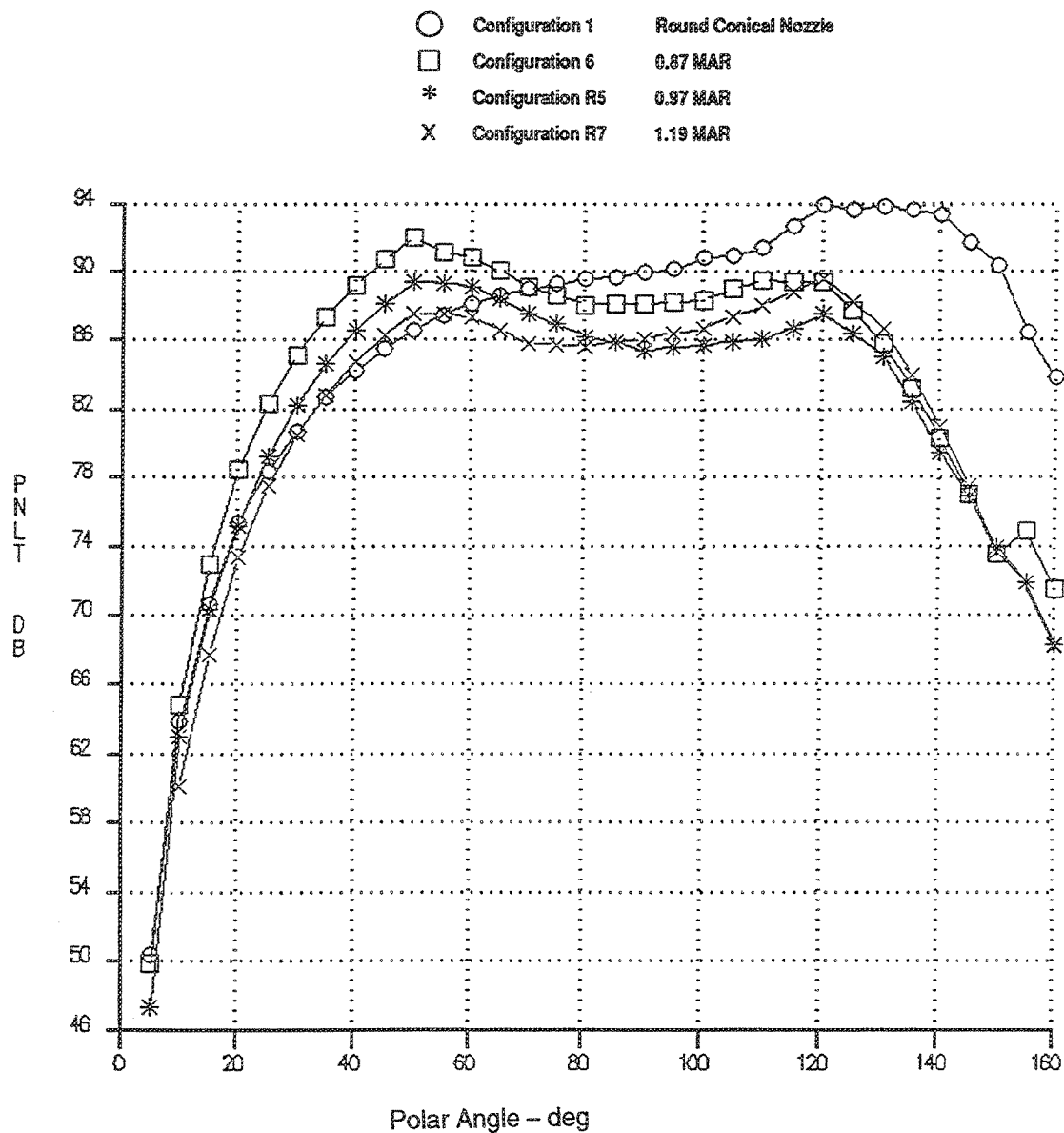


Figure 53. Effect of MAR, PNLT Versus Angle — Ideal Unsuppressed Primary Jet Velocity=1595 ft/sec  
 Vortical Mixer, Long Treated Shroud  
 (Sideline=1629 ft,  $A_{g*}=1086 \text{ in}^2$ , SAR=4.4,  $M_n=0.32$ ,  $V_{\Pi}=357 \text{ ft/sec}$ )

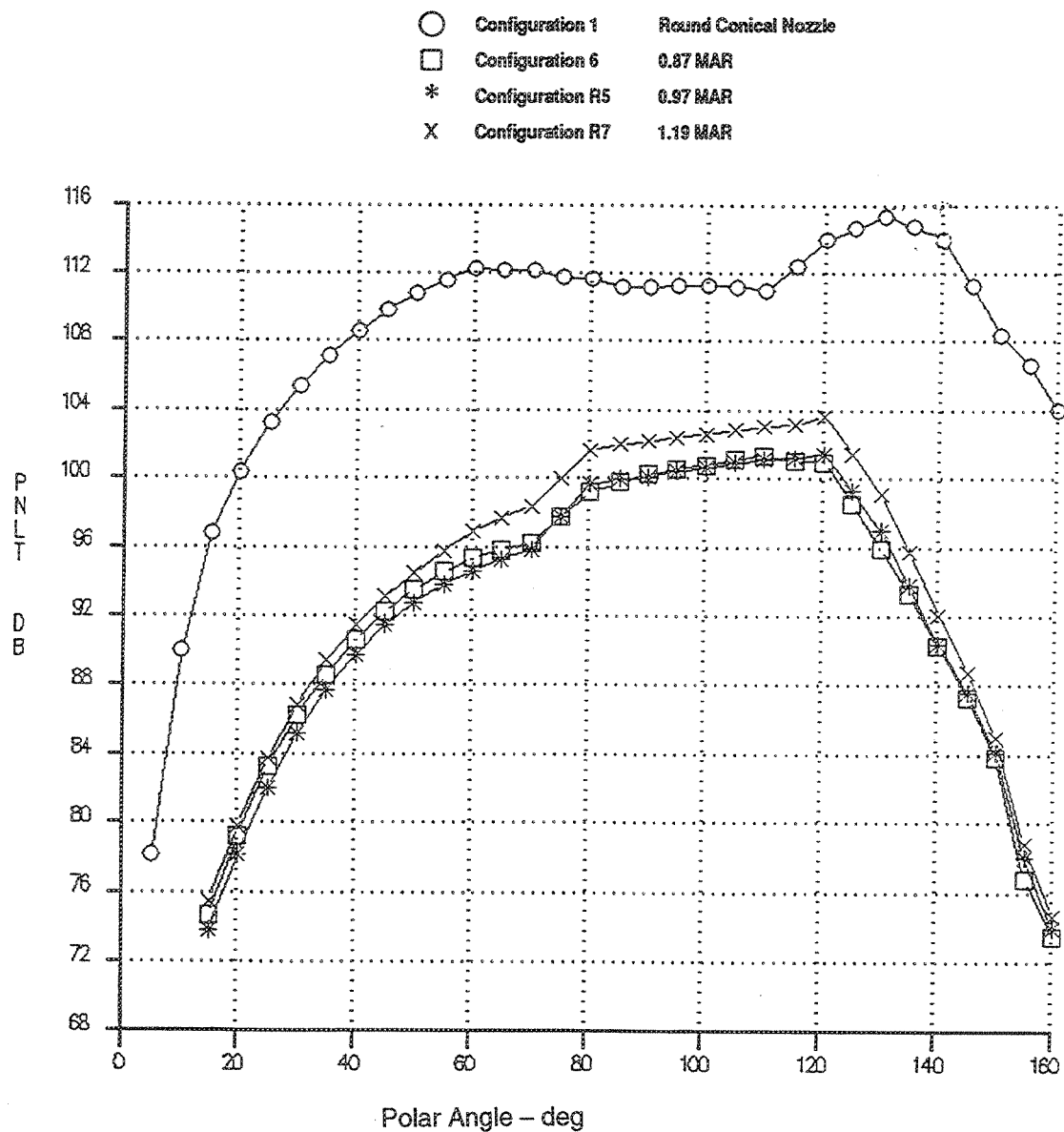


Figure 54. Effect of MAR, PNLT Versus Angle — Ideal Unsuppressed Primary Jet Velocity=2384 ft/sec  
Vortical Mixer, Long Treated Shroud  
(Sideline=1629 ft,  $A_{g*}=1086 \text{ in}^2$ , SAR=4.4, Mn=0.32,  $V_{fl}=357 \text{ ft/sec}$ )

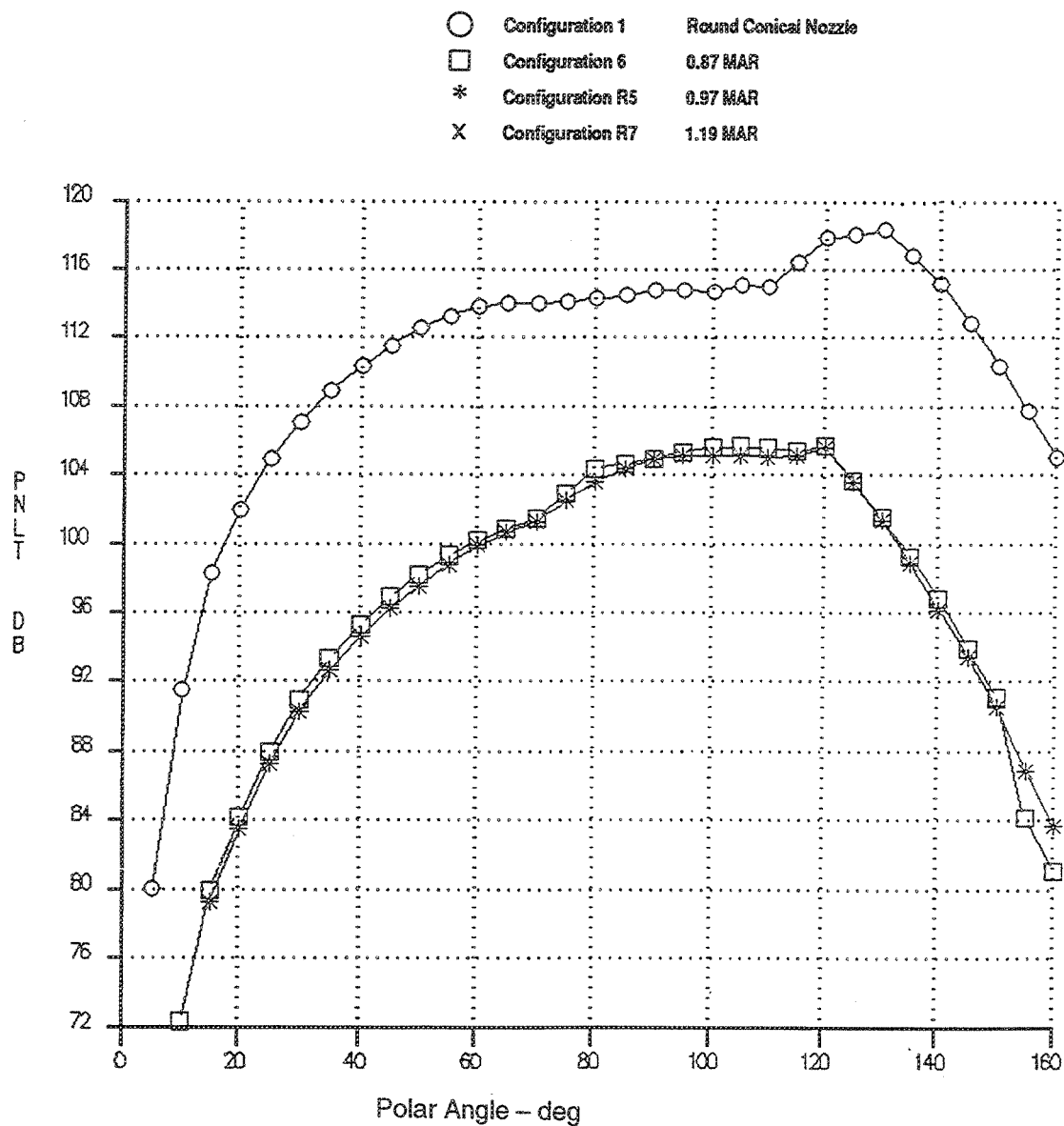


Figure 55. Effect of MAR, PNLT Versus Angle — Ideal Unsuppressed Primary Jet Velocity=2812 ft/sec  
 Vortical Mixer, Long Treated Shroud  
 (Sideline=1629 ft,  $A_{g*}=1086 \text{ in}^2$ , SAR=4.4,  $M_n=0.32$ ,  $V_{\Pi}=357 \text{ ft/sec}$ )



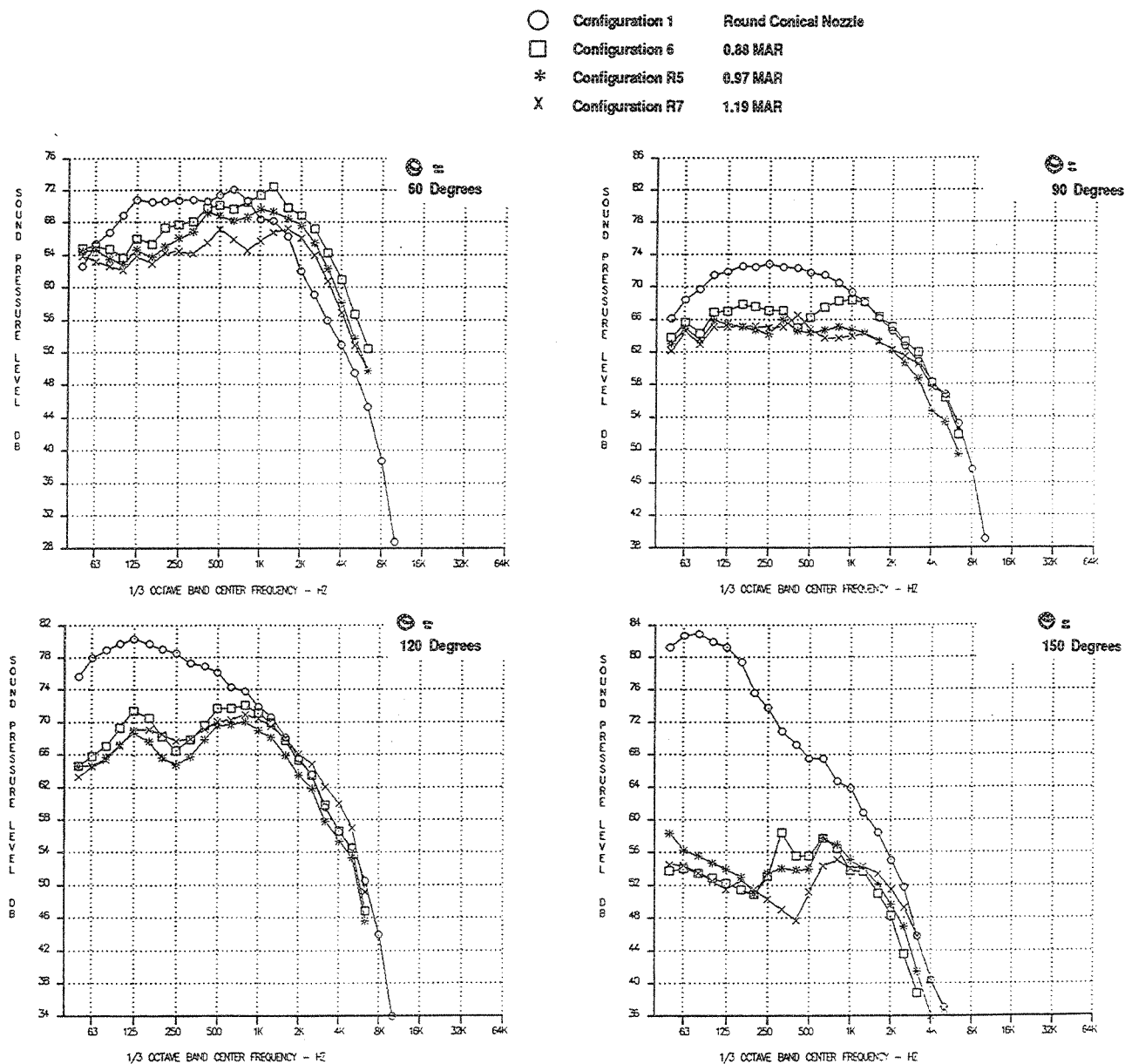


Figure 56. Effect of MAR, SPL Versus Frequency — Ideal Unsuppressed Primary Jet Velocity=1595 ft/sec  
 Vortical Mixer, Long Treated Shroud  
 (Sideline=1629 ft,  $A_{8*}=1086 \text{ in}^2$ , SAR=4.4, Mn=0.32,  $V_{\Pi}=357 \text{ ft/sec}$ )

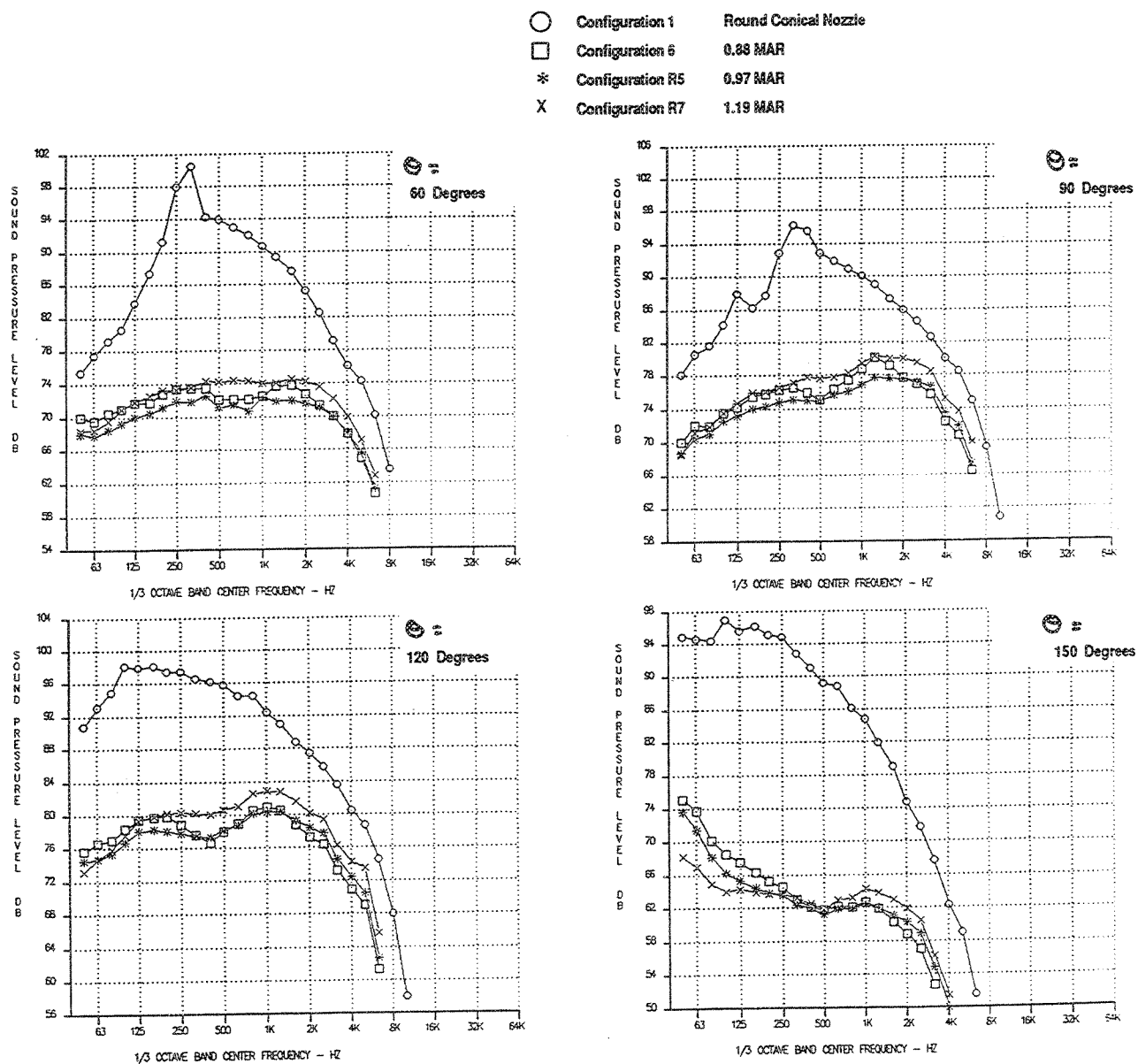


Figure 57. Effect of MAR, SPL Versus Frequency — Ideal Unsuppressed Primary Jet Velocity=2384 ft/sec  
 Vortical Mixer, Long Treated Shroud  
 (Sideline=1629 ft,  $A_{g*}=1086 \text{ in}^2$ , SAR=4.4, Mn=0.32,  $V_{fl}=357 \text{ ft/sec}$ )

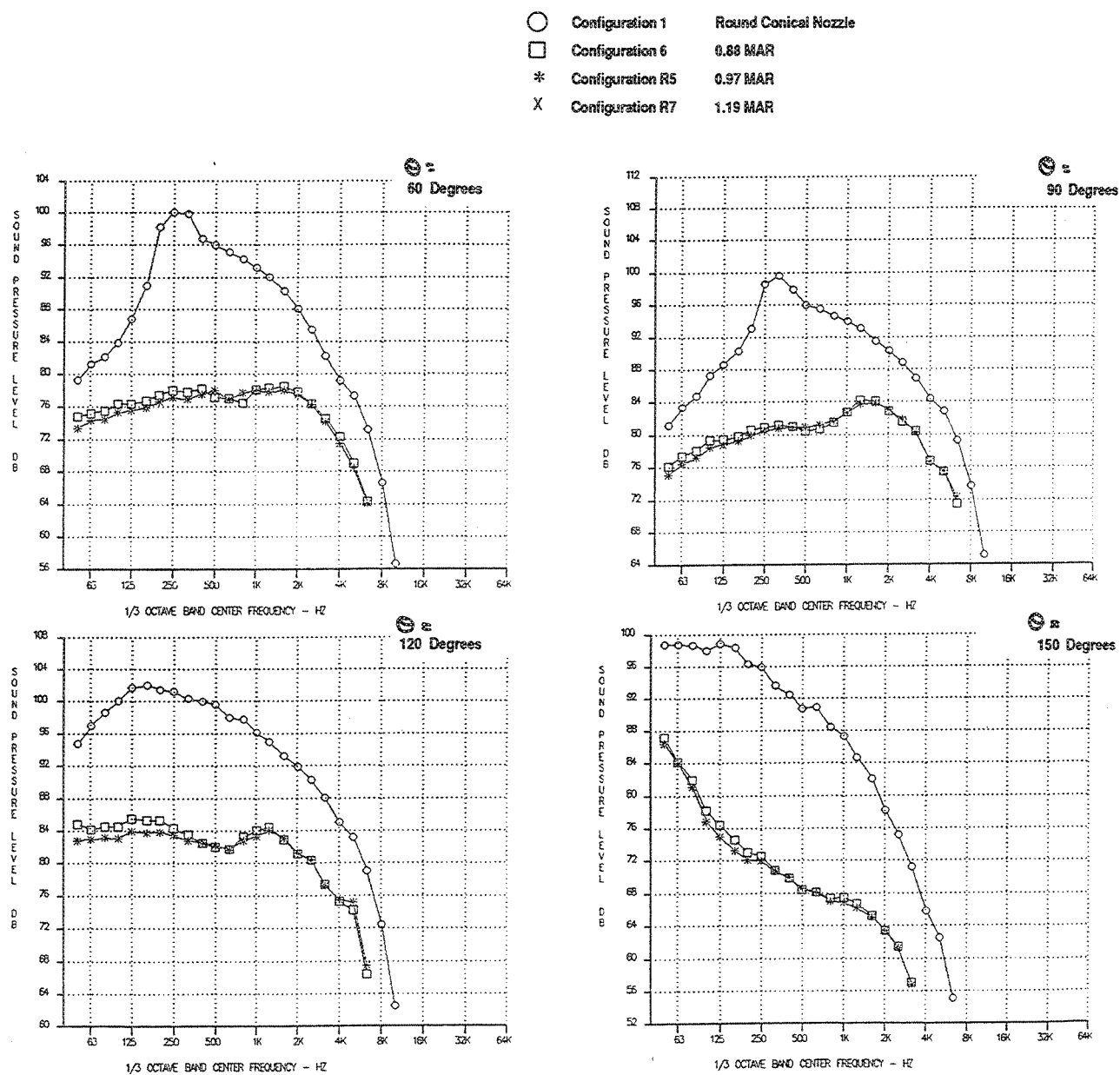


Figure 58. Effect of MAR, SPL Versus Frequency — Ideal Unsuppressed Primary Jet Velocity=2812 ft/sec  
 Vortical Mixer, Long Treated Shroud  
 (Sideline=1629 ft,  $A_{g*}=1086 \text{ in}^2$ , SAR=4.4,  $M_n=0.32$ ,  $V_{fl}=357 \text{ ft/sec}$ )

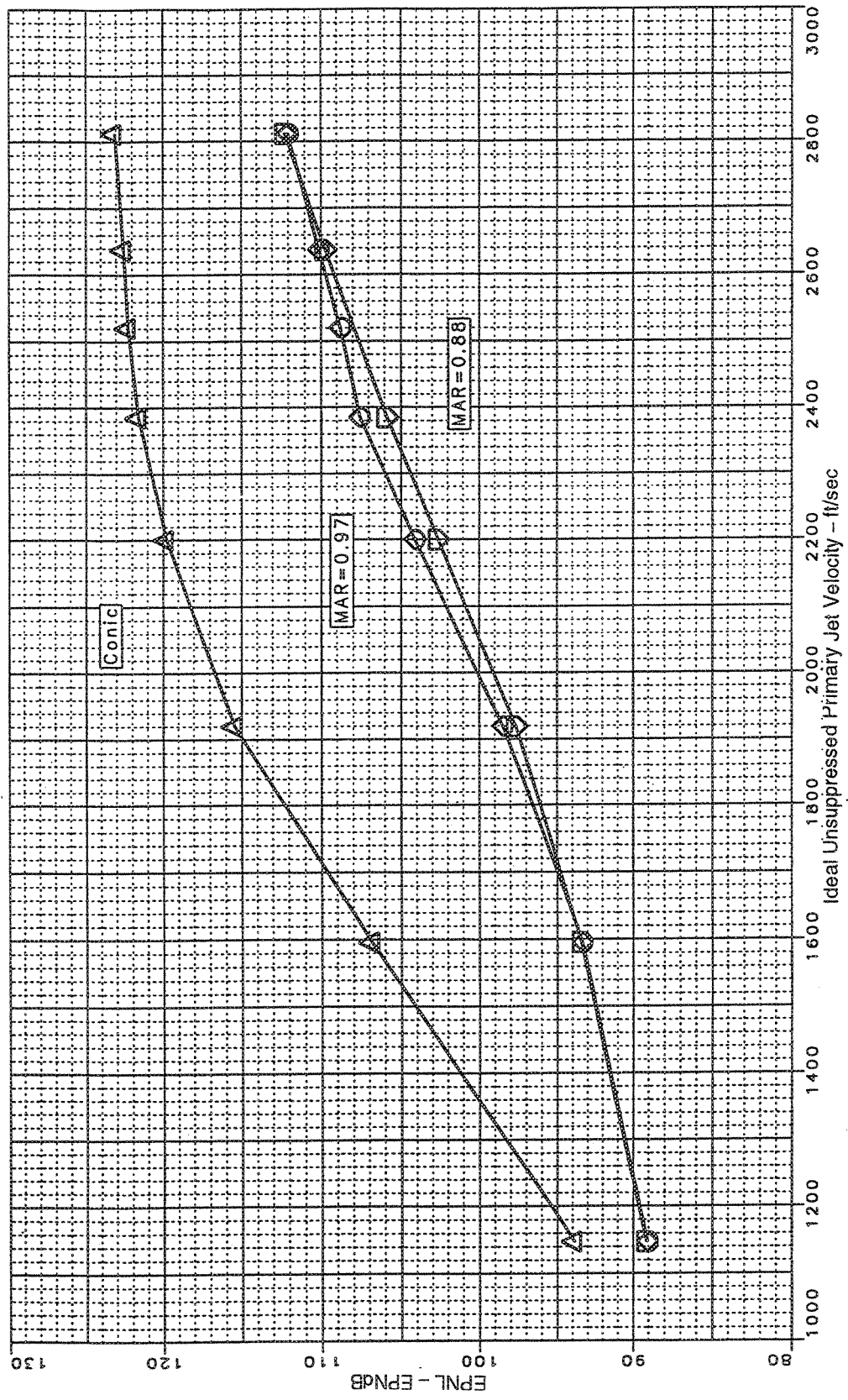


Figure 59. Effect of MAR ( $A_{\text{exit}}/A_{\text{mix}}$ ) on Sideline Noise, Axial Mixer, Long Treated Shroud  
(Sideline=1629 ft, SAR=4.9,  $A_{\text{R}}=1086 \text{ in}^2$ , Static)

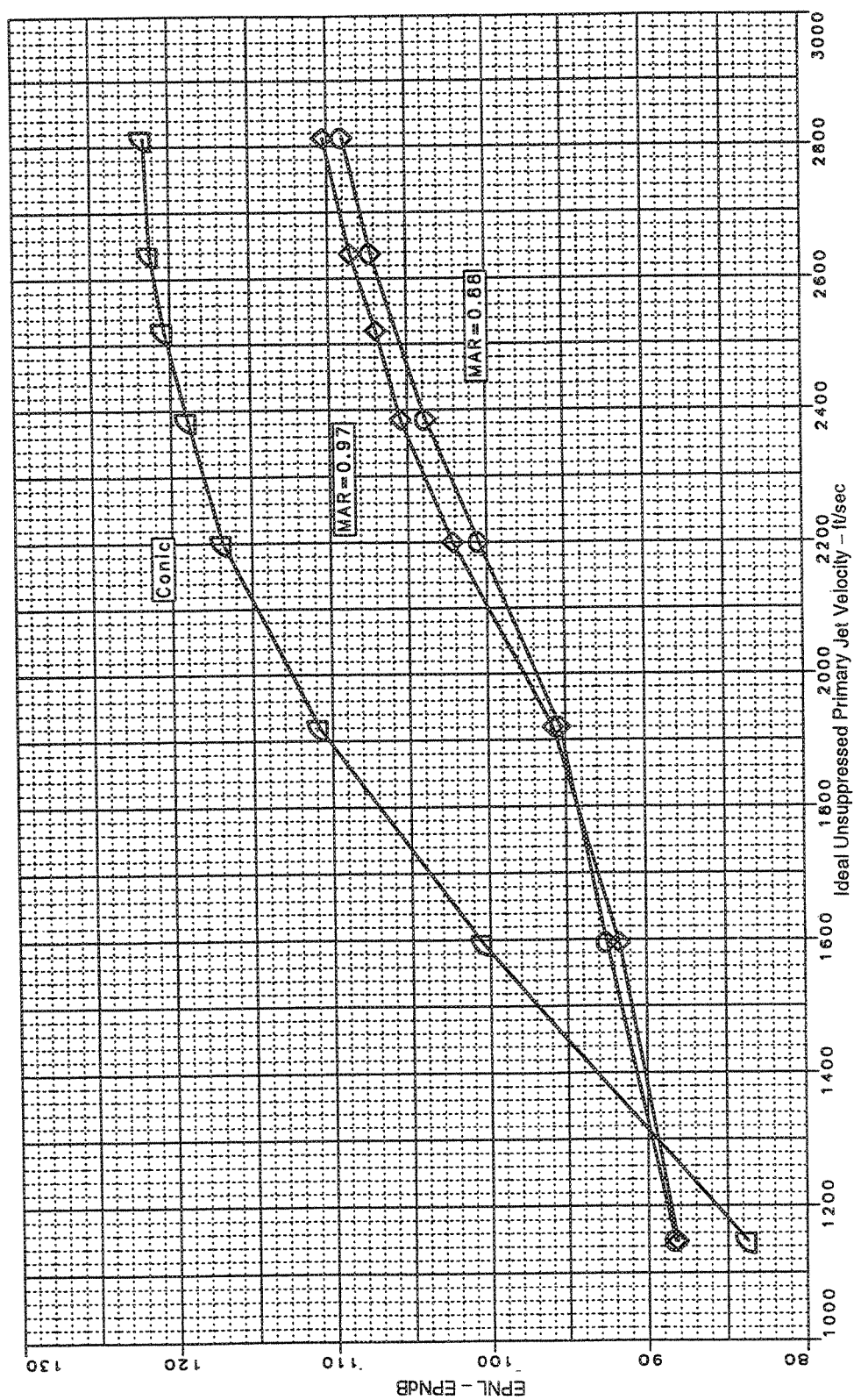


Figure 60. Effect of MAR ( $A_{\text{exit}}/A_{\text{mix}}$ ) on Sideline Noise, Axial Mixer, Long Treated Shroud  
(Sideline=1629 ft, SAR=4.9,  $A_{g*}=1086 \text{ in}^2$ ,  $M_n=0.32$ ,  $V_{\eta}=357 \text{ ft/sec}$ )

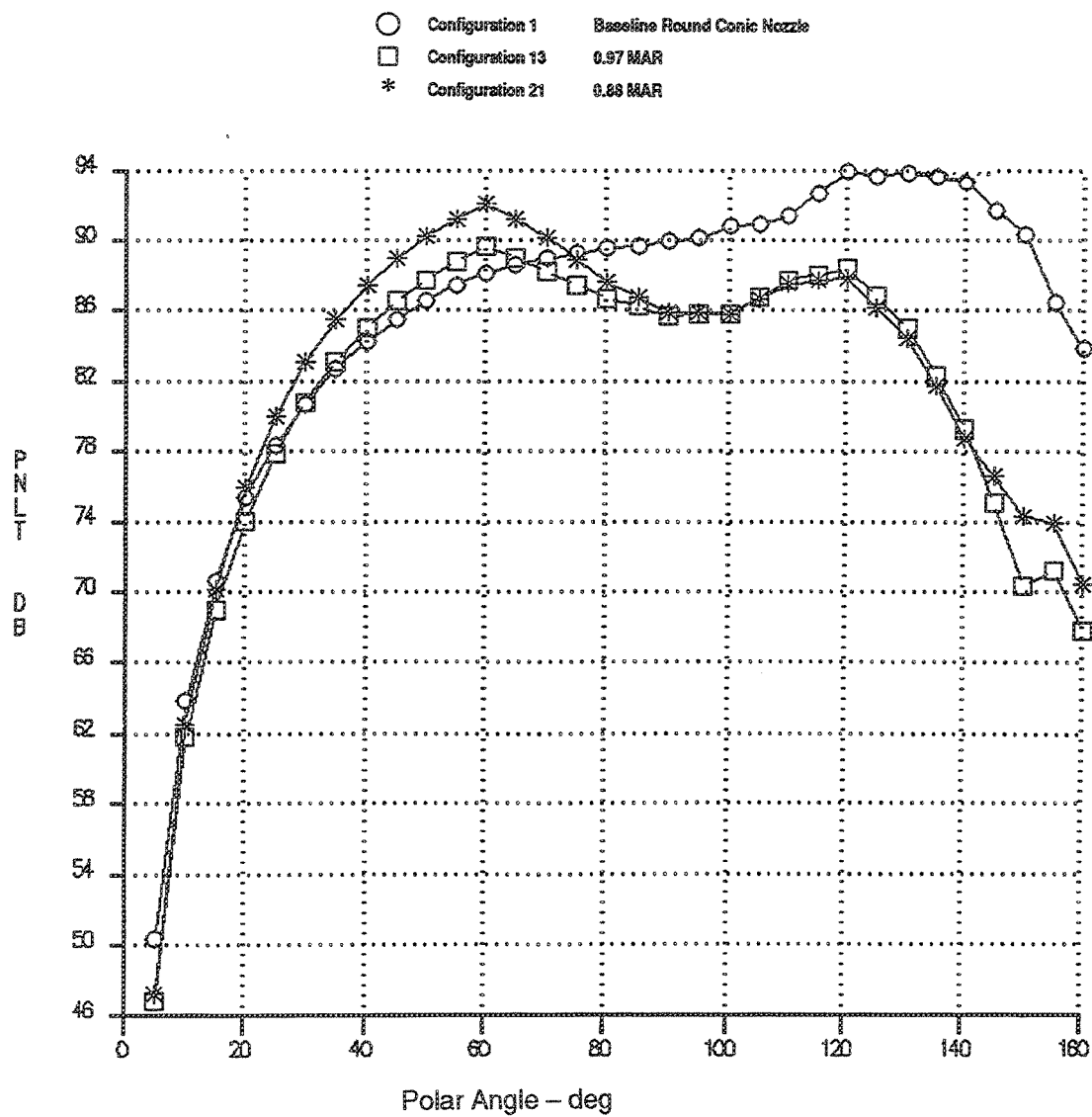


Figure 61. Effect of MAR, PNLT Versus Angle — Ideal Unsuppressed Primary Jet Velocity=1595 ft/sec  
 Axial Mixer, Long Treated Shroud  
 (Sideline=1629 ft,  $A_{g*}=1086 \text{ in}^2$ , SAR=4.9,  $M_n=0.32$ ,  $V_{fl}=357 \text{ ft/sec}$ )

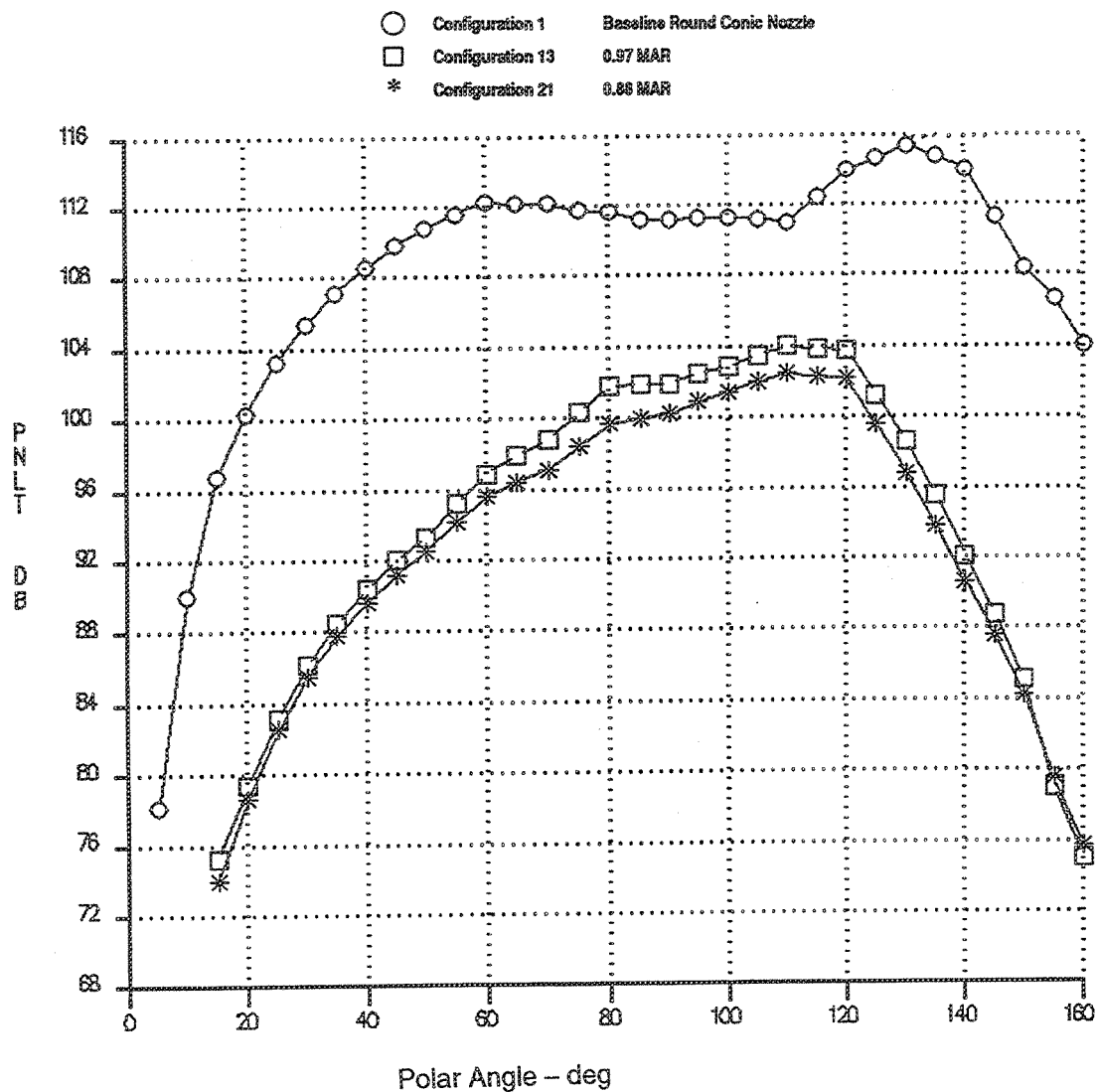


Figure 62. Effect of MAR, PNLT Versus Angle — Ideal Unsuppressed Primary Jet Velocity=2384 ft/sec  
 Axial Mixer, Long Treated Shroud  
 (Sideline=1629 ft,  $A_{g*}=1086 \text{ in}^2$ , SAR=4.9,  $M_n=0.32$ ,  $V_{fl}=357 \text{ ft/sec}$ )

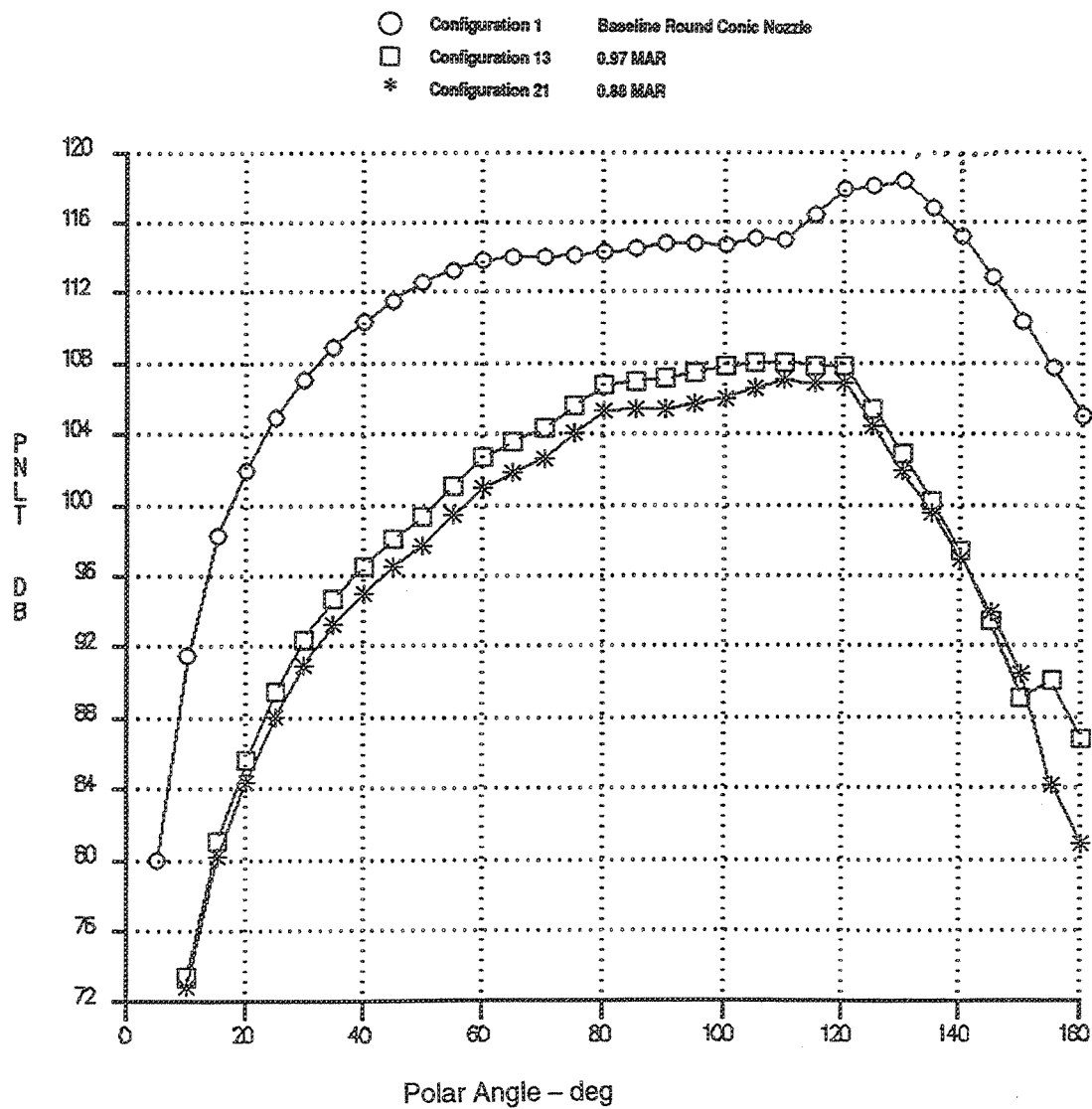


Figure 63. Effect of MAR, PNLT Versus Angle — Ideal Unsuppressed Primary Jet Velocity=2812 ft/sec  
 Axial Mixer, Long Treated Shroud  
 (Sideline=1629 ft,  $A_{g*}=1086 \text{ in}^2$ , SAR=4.9,  $M_n=0.32$ ,  $V_{\text{fl}}=357 \text{ ft/sec}$ )



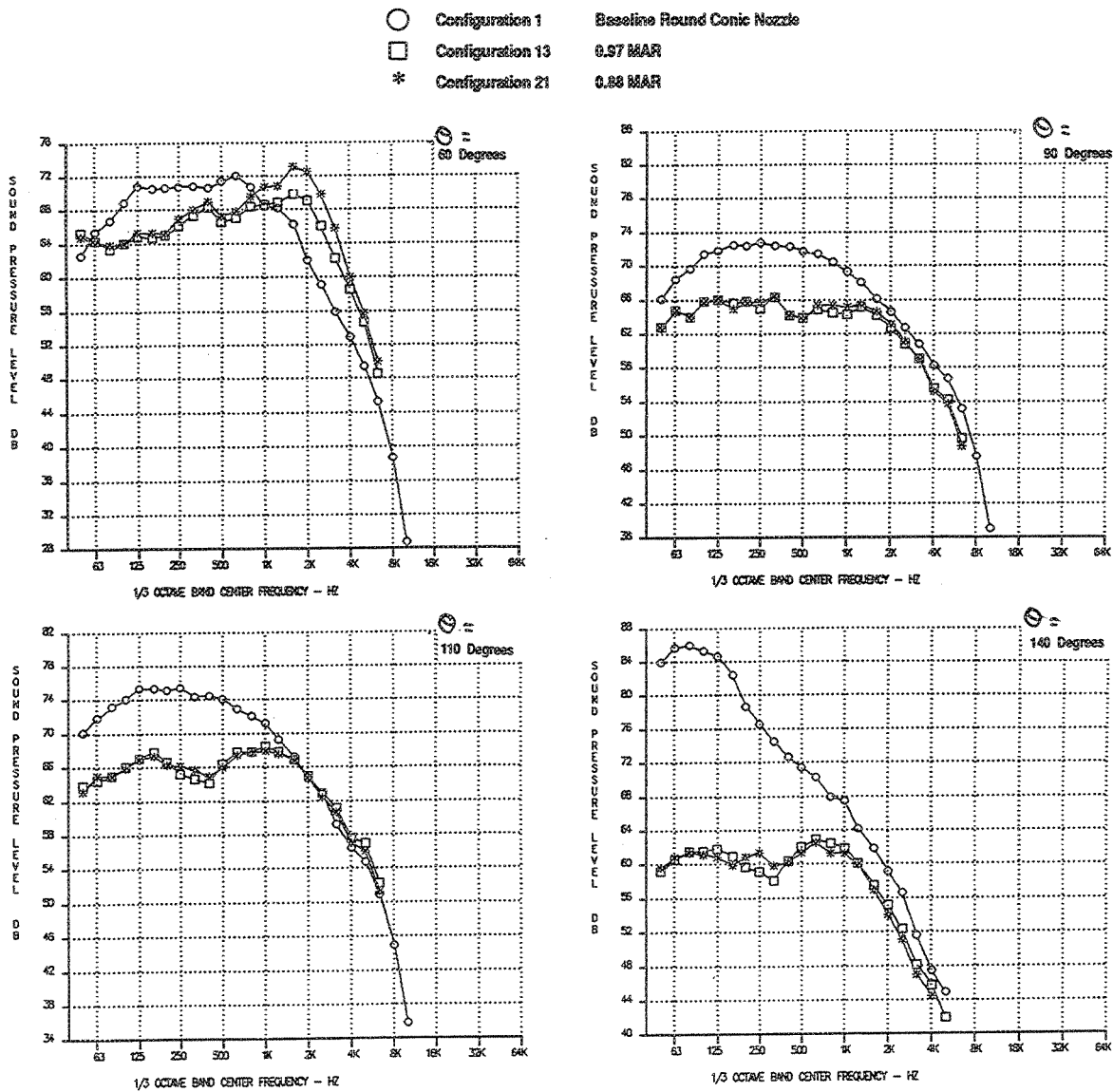


Figure 64. Effect of MAR, SPL Versus Frequency — Ideal Unsuppressed Primary Jet Velocity=1595 ft/sec  
 Axial Mixer, Long Treated Shroud  
 (Sideline=1629 ft,  $A_{8*}=1086 \text{ in}^2$ , SAR=4.9,  $M_n=0.32$ ,  $V_{\Pi}=357 \text{ ft/sec}$ )

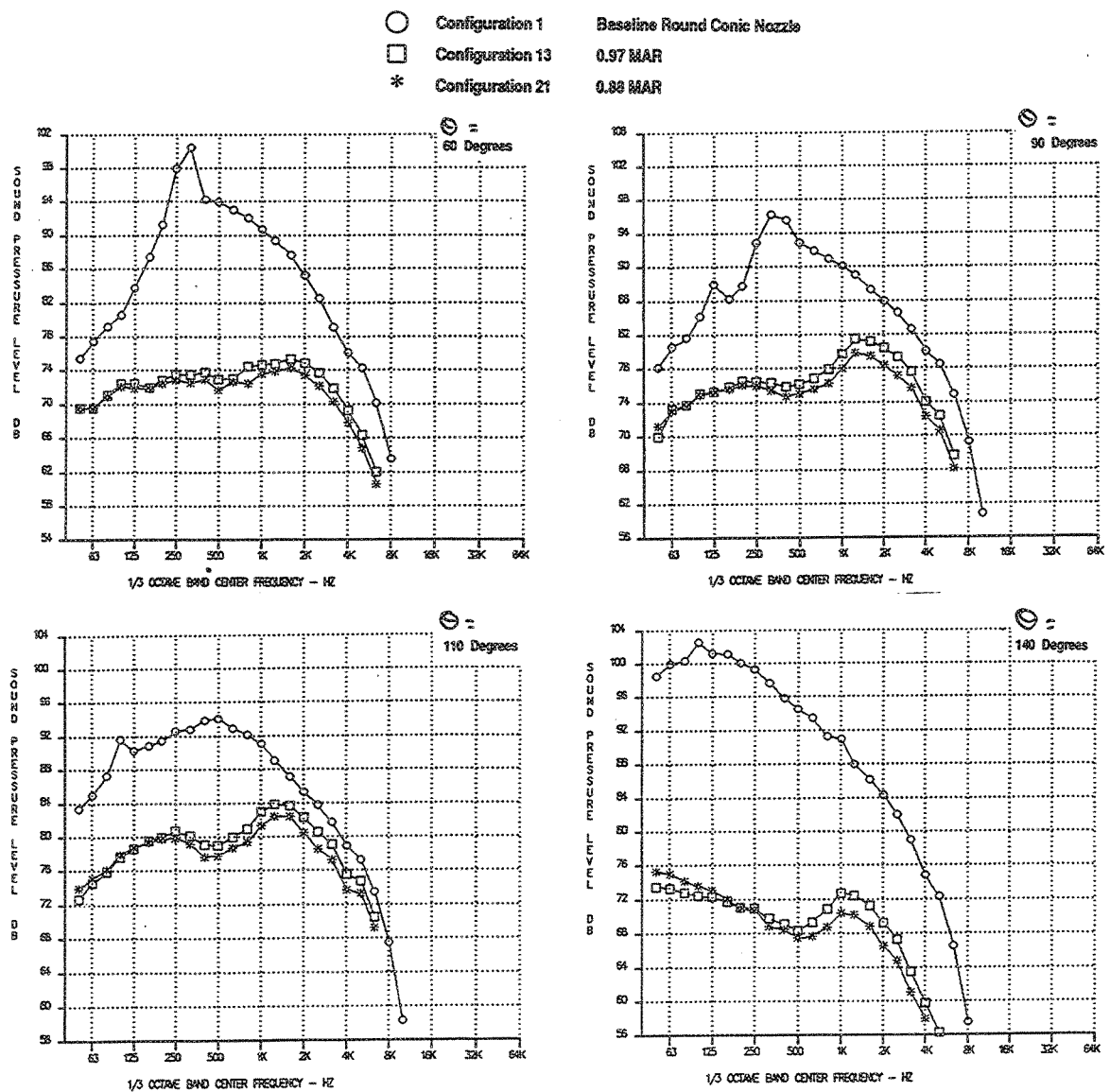


Figure 65. Effect of MAR, SPL Versus Frequency — Ideal Unsuppressed Primary Jet Velocity=2384 ft/sec  
 Axial Mixer, Long Treated Shroud  
 (Sideline=1629 ft,  $A_{g*}=1086 \text{ in}^2$ , SAR=4.9,  $M_n=0.32$ ,  $V_{\text{fl}}=357 \text{ ft/sec}$ )

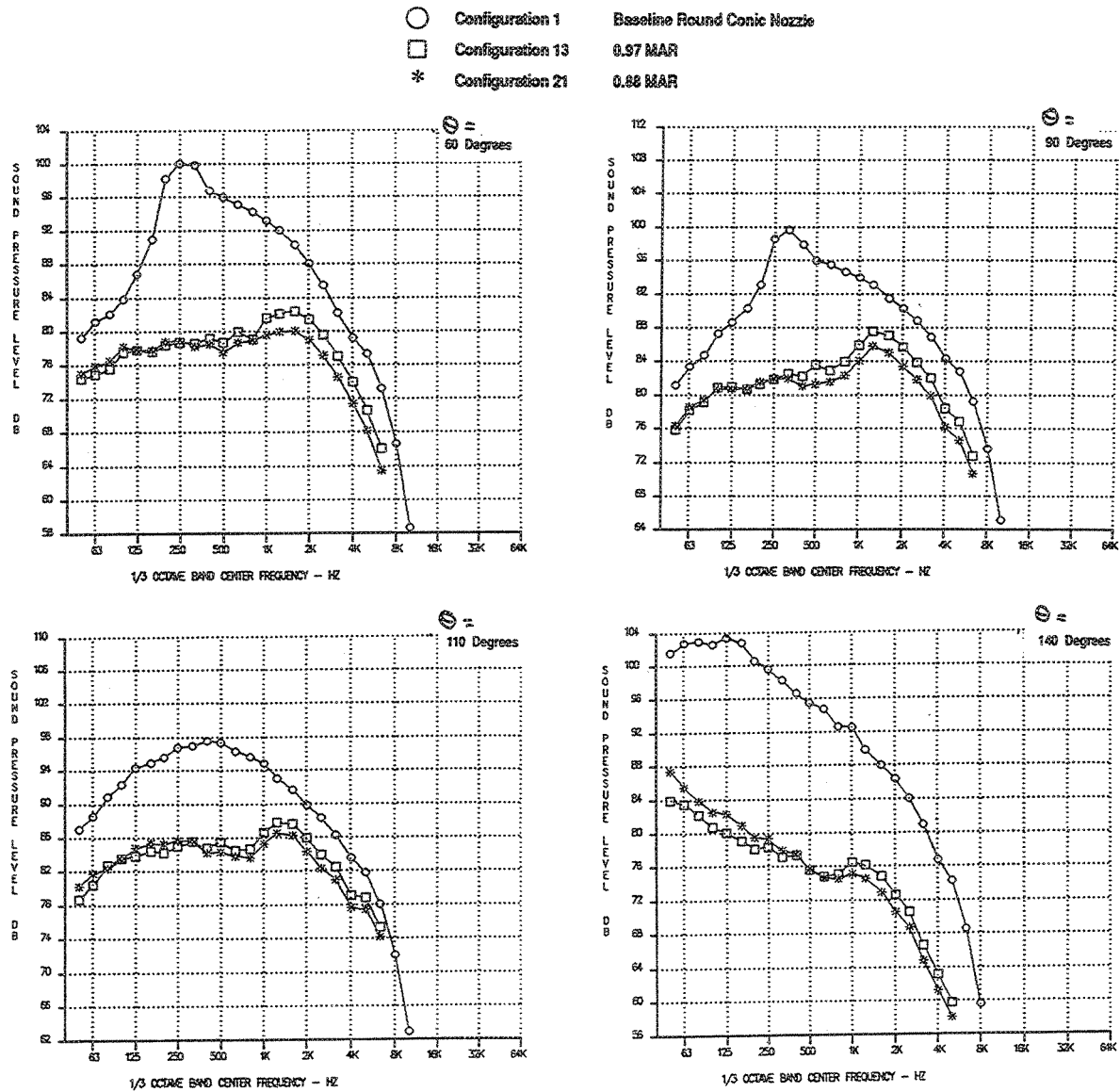


Figure 66. Effect of MAR, SPL Versus Frequency — Ideal Unsuppressed Primary Jet Velocity=2812 ft/sec  
 Axial Mixer, Long Treated Shroud  
 (Sideline=1629 ft,  $A_{g*}=1086 \text{ in}^2$ , SAR=4.9,  $M_n=0.32$ ,  $V_{fl}=357 \text{ ft/sec}$ )

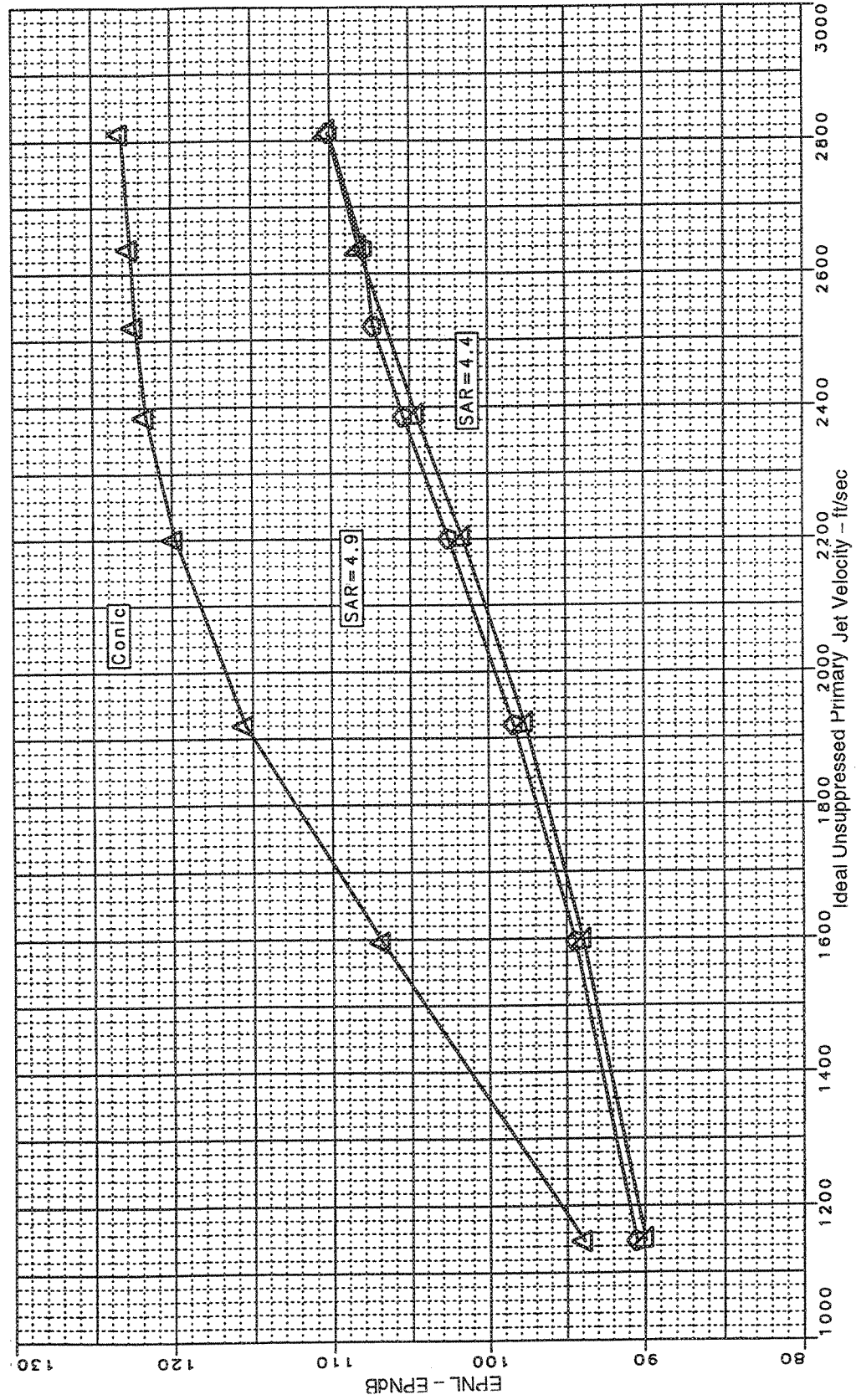


Figure 67. Effect of SAR ( $A_{mix}/A_{g*}$ ) on Sideline Noise, Vortical Mixer, Long Treated Shroud  
(Sideline=1629 ft, MAR=0.97,  $A_{g*}=1086 \text{ in}^2$ , Static)

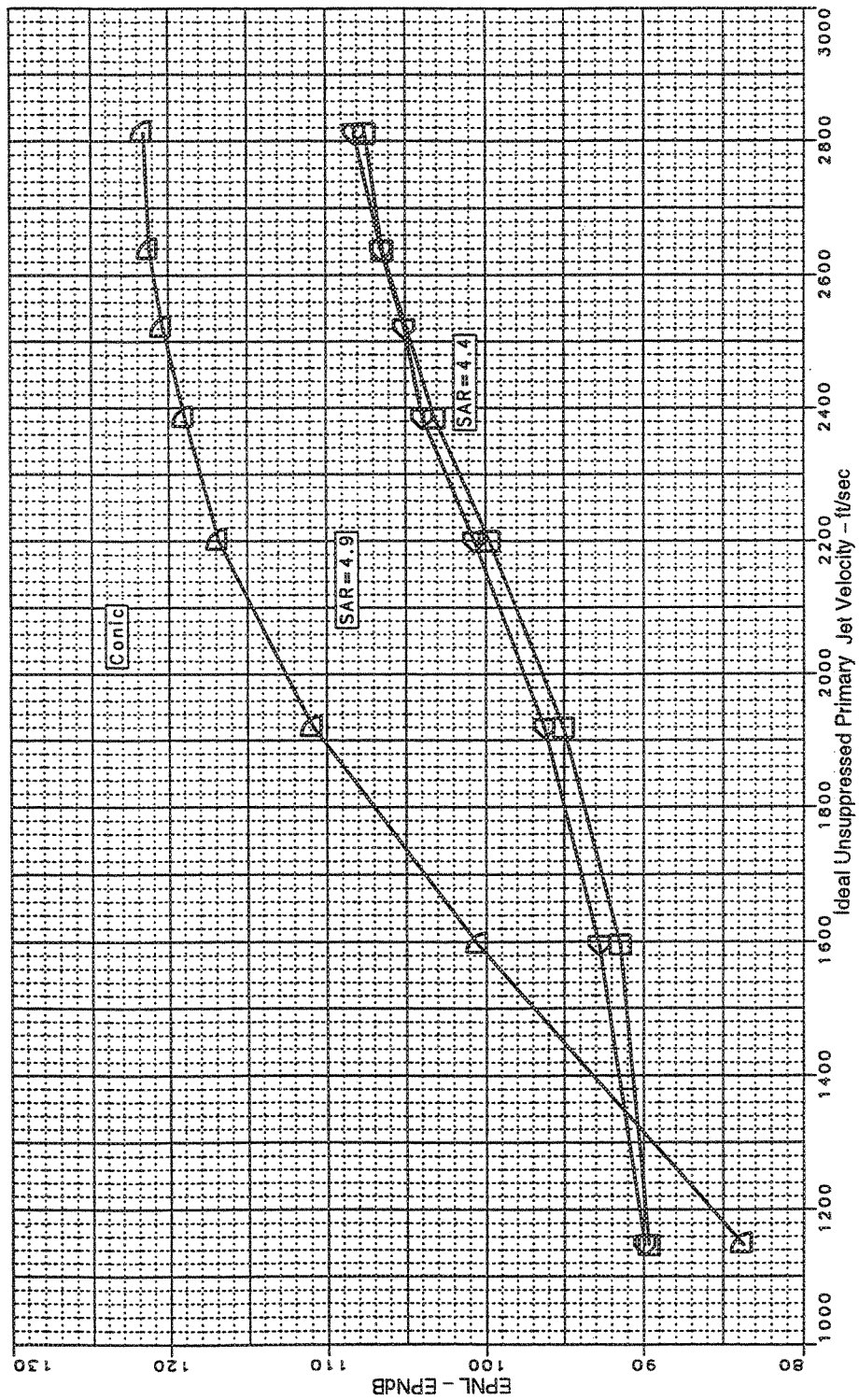


Figure 68. Effect of SAR ( $A_{mix}/A_{g*}$ ) on Sideline Noise, Vortical Mixer, Long Treated Shroud  
 (Sideline=1629 ft,  $MAR=0.97$ ,  $A_{g*}=1086 \text{ in}^2$ ,  $Mn=0.32$ ,  $V_{f1}=357 \text{ ft/sec}$ )

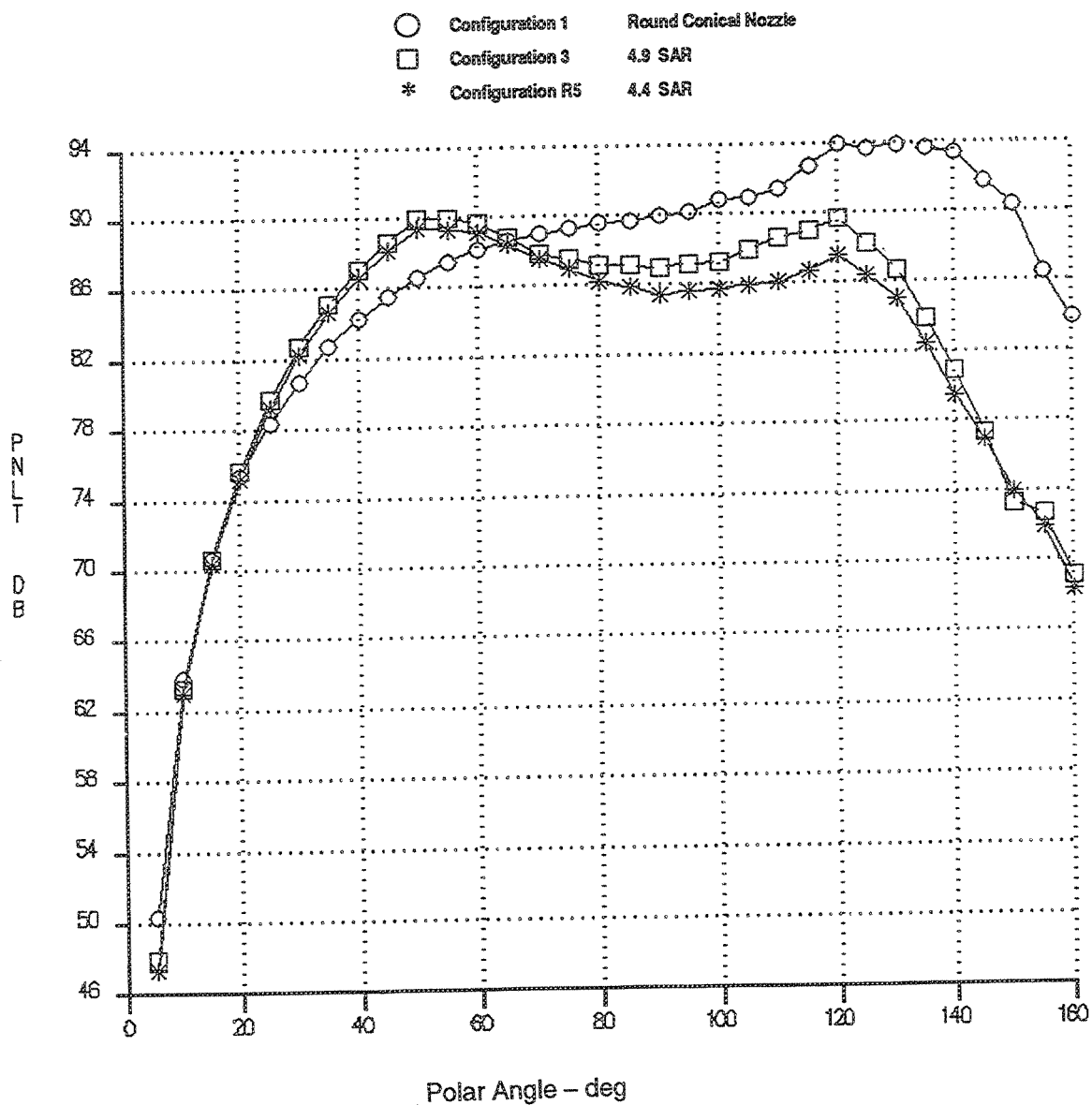


Figure 69. Effect of SAR, PNLT Versus Angle — Ideal Unsuppressed Primary Jet Velocity=1595 ft/sec  
 Vortical Mixer, Long Treated Shroud  
 (Sideline=1629 ft,  $A_{g*}=1086 \text{ in}^2$ ,  $MAR=0.97$ ,  $Mn=0.32$ ,  $V_{fl}=357 \text{ ft/sec}$ )

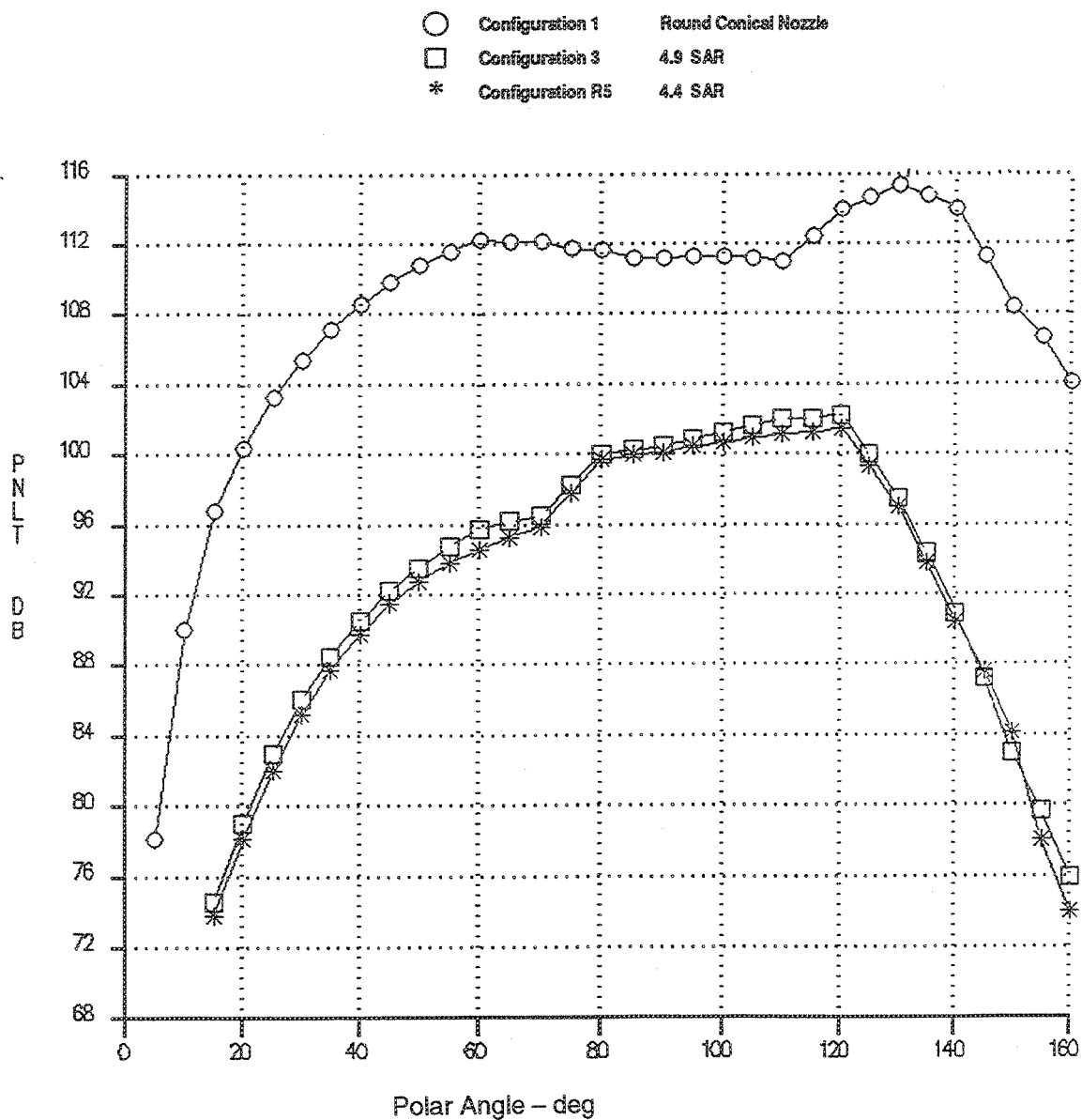


Figure 70. Effect of SAR, PNL T Versus Angle — Ideal Unsuppressed Primary Jet Velocity=2384 ft/sec  
 Vortical Mixer, Long Treated Shroud  
 (Sideline=1629 ft,  $A_{g*}=1086 \text{ in}^2$ ,  $MAR=0.97$ ,  $Mn=0.32$ ,  $V_{fl}=357 \text{ ft/sec}$ )

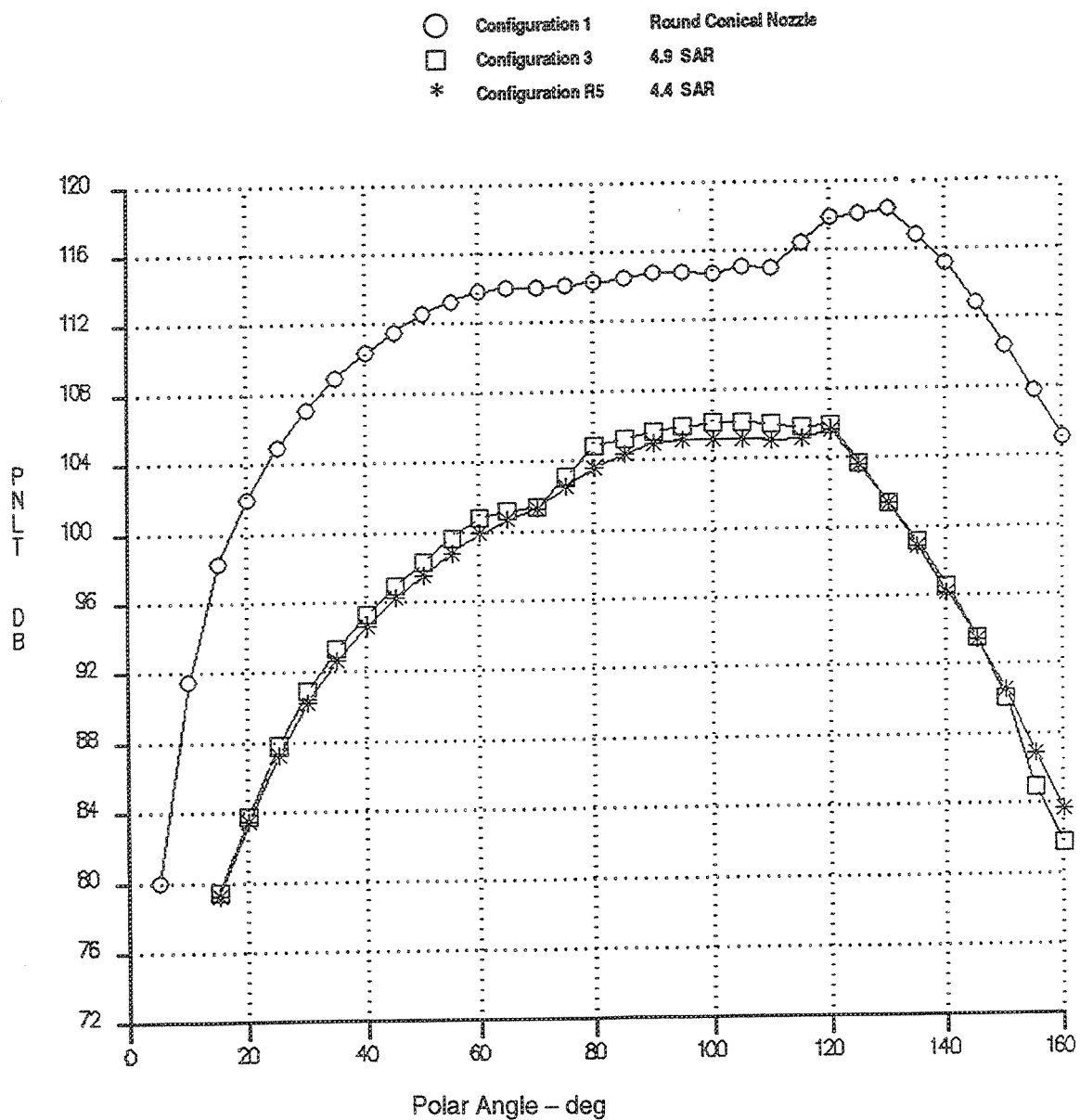


Figure 71. Effect of SAR, PNL T Versus Angle — Ideal Unsuppressed Primary Jet Velocity=2812 ft/sec  
 Vortical Mixer, Long Treated Shroud  
 (Sideline=1629 ft,  $A_{g*}=1086 \text{ in}^2$ ,  $MAR=0.97$ ,  $Mn=0.32$ ,  $V_H=357 \text{ ft/sec}$ )



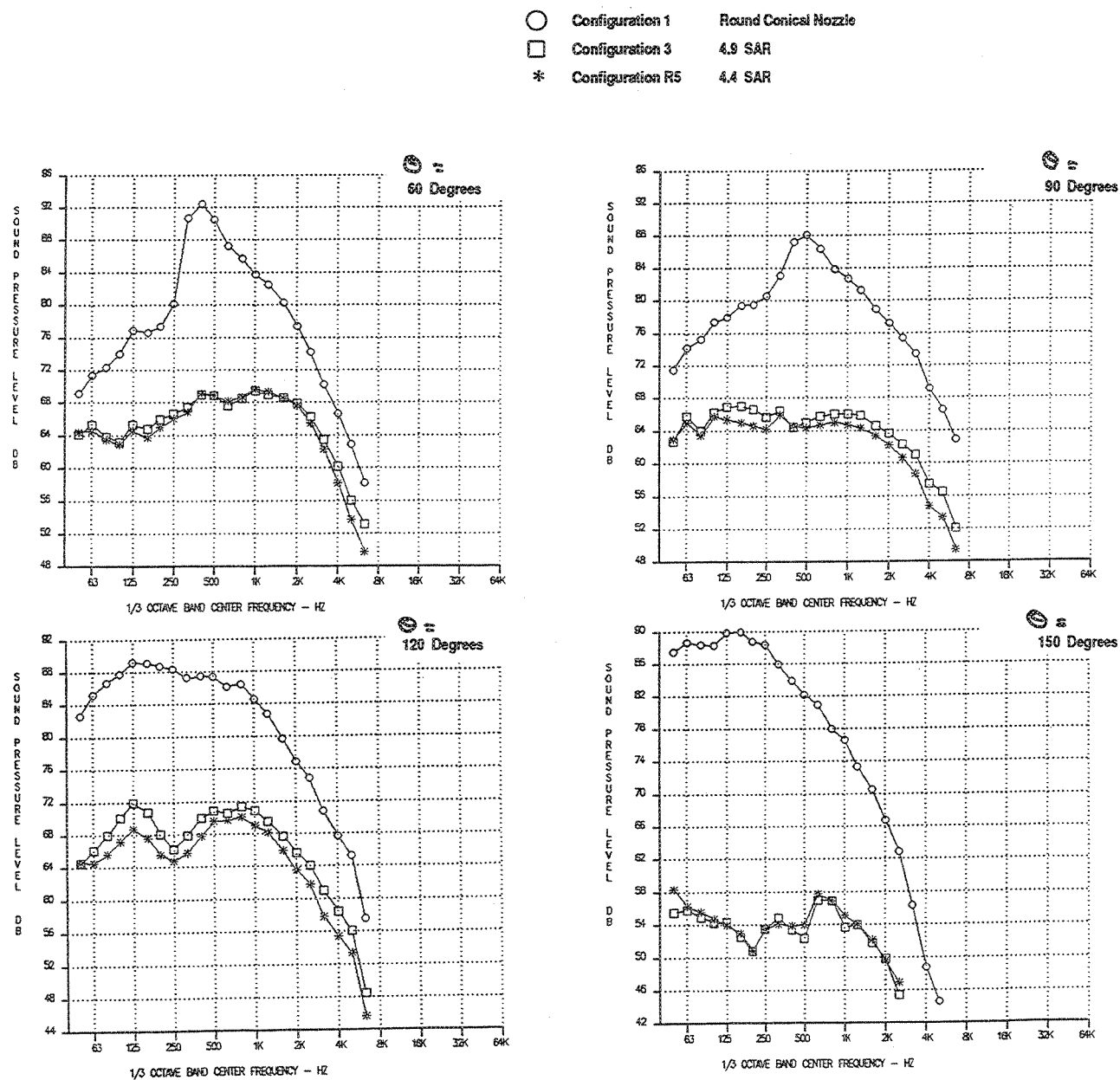


Figure 72. Effect of SAR, SPL Versus Frequency — Ideal Unsuppressed Primary Jet Velocity=1595 ft/sec  
 Vortical Mixer, Long Treated Shroud  
 (Sideline=1629 ft,  $A_{g*}=1086 \text{ in}^2$ ,  $MAR=0.97$ ,  $Mn=0.32$ ,  $V_{fl}=357 \text{ ft/sec}$ )

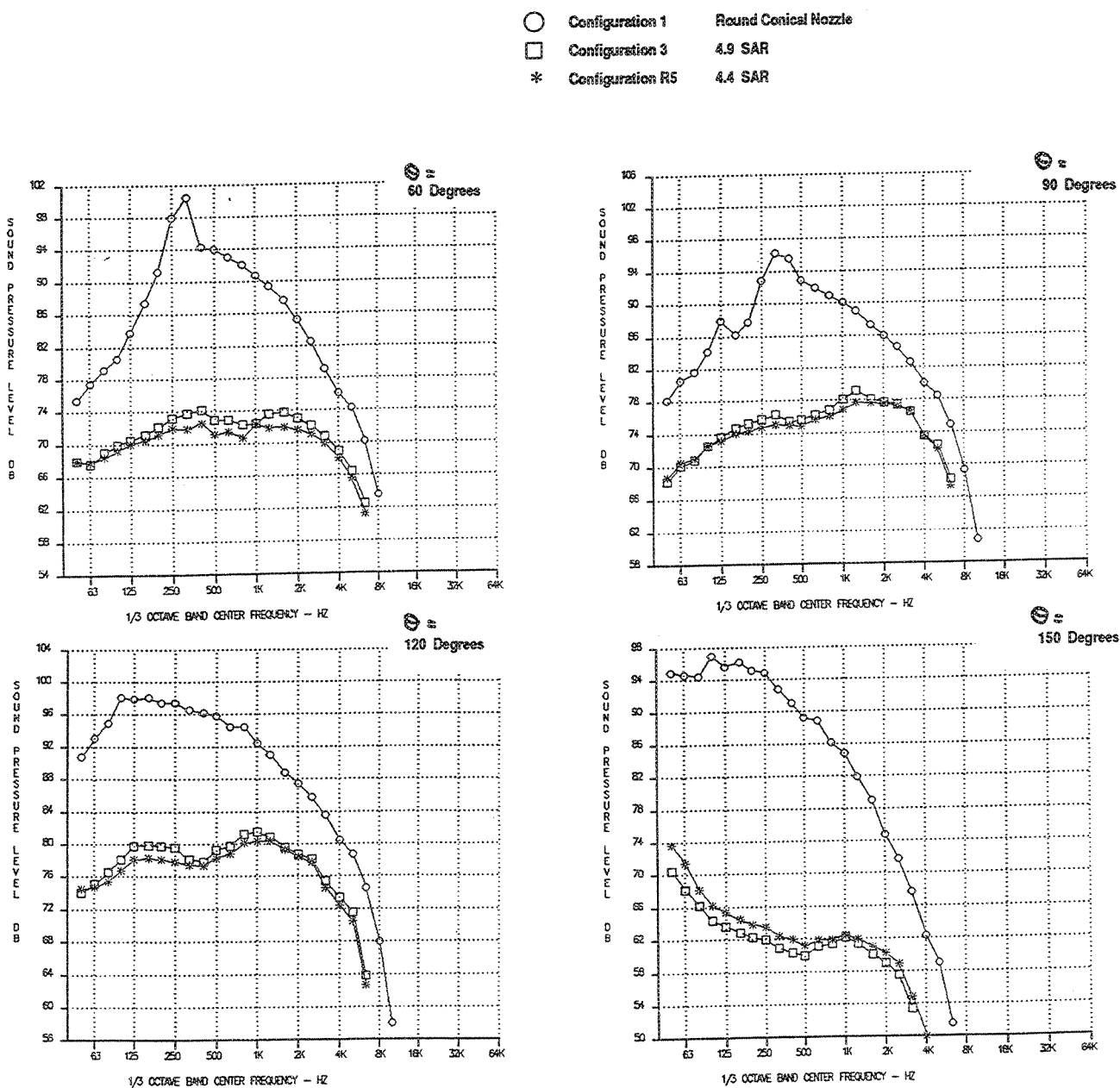


Figure 73. Effect of SAR, SPL Versus Frequency — Ideal Unsuppressed Primary Jet Velocity=2384 ft/sec  
 Vortical Mixer, Long Treated Shroud  
 (Sideline=1629 ft,  $A_{g*}=1086 \text{ in}^2$ ,  $MAR=0.97$ ,  $Mn=0.32$ ,  $V_{f1}=357 \text{ ft/sec}$ )

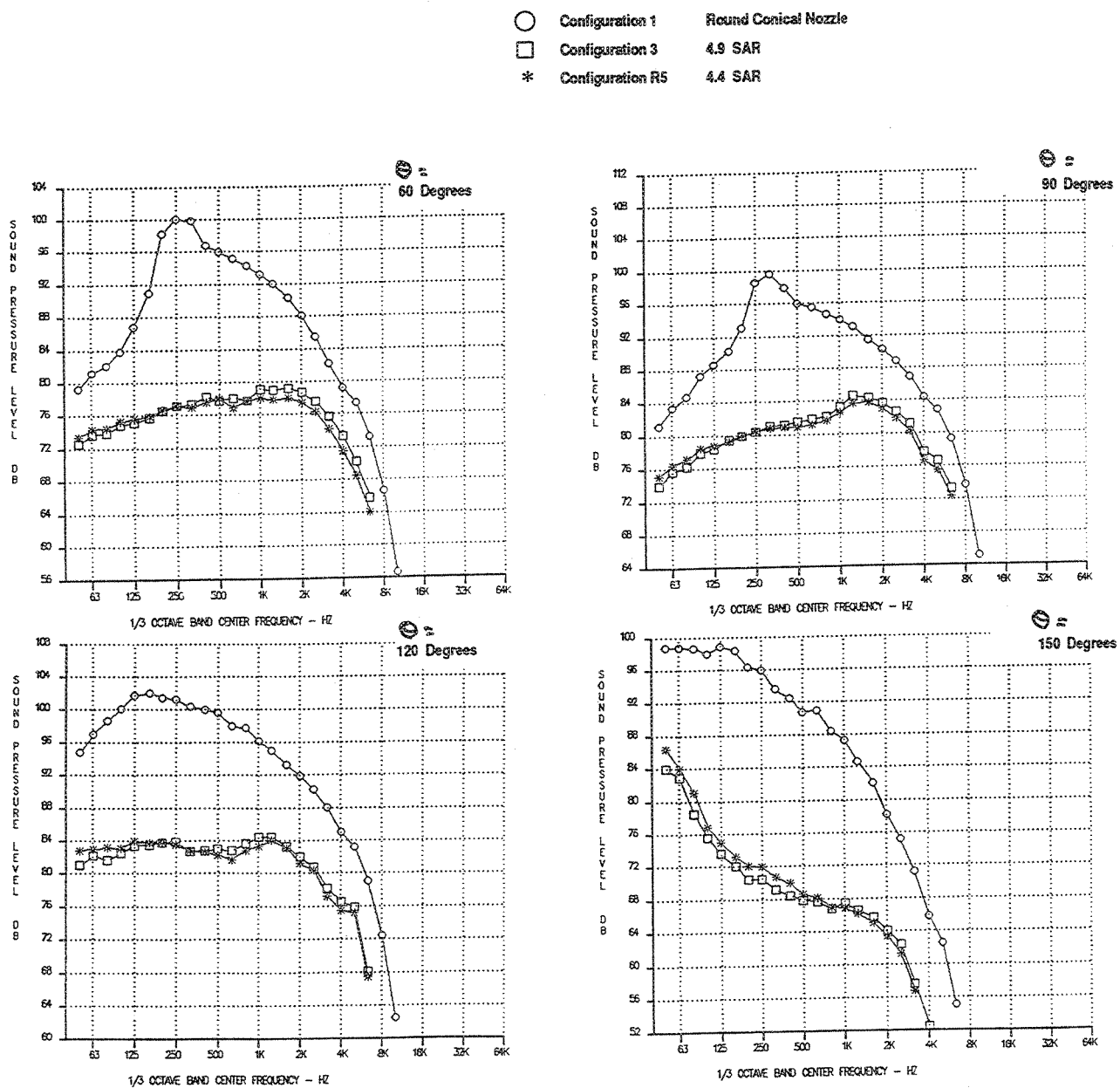


Figure 74. Effect of SAR, SPL Versus Frequency — Ideal Unsuppressed Primary Jet Velocity=2812 ft/sec  
 Vortical Mixer, Long Treated Shroud  
 (Sideline=1629 ft,  $A_{g*}=1086 \text{ in}^2$ ,  $MAR=0.97$ ,  $Mn=0.32$ ,  $V_{fl}=357 \text{ ft/sec}$ )

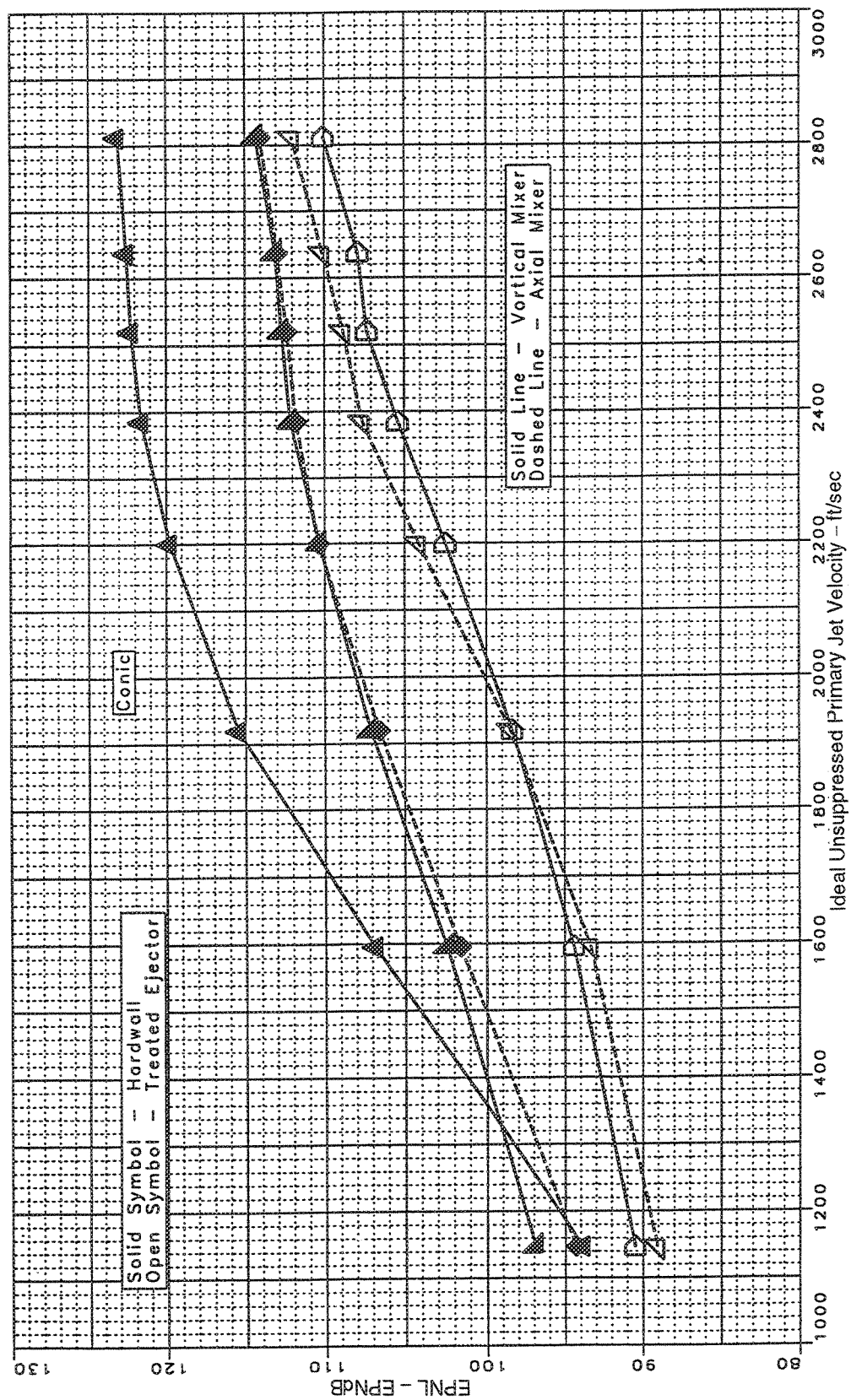


Figure 75. Mixer Comparison Long Shroud (Sideline=1629 ft, SAR=4.9, MAR=0.97,  $A_{g*}=1086 \text{ in}^2$ , Static)

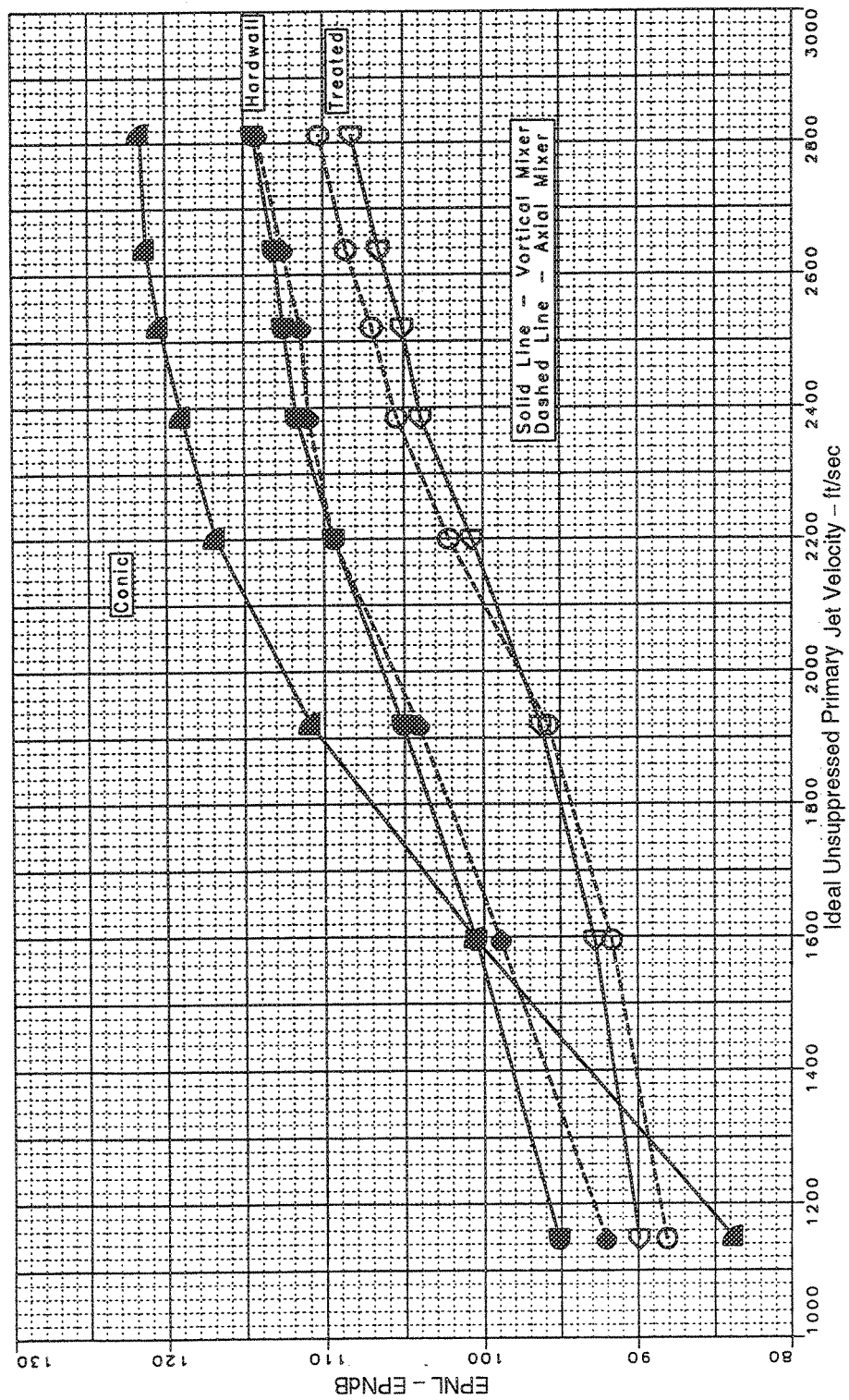


Figure 76. Mixer Comparison Long Shroud (Sideline=1629 ft, SAR=4.9, MAR=0.97,  $A_{gs}=1086 \text{ in}^2$ ,  $Mn=0.32$ ,  $V_{\eta}=357 \text{ ft/sec}$ )

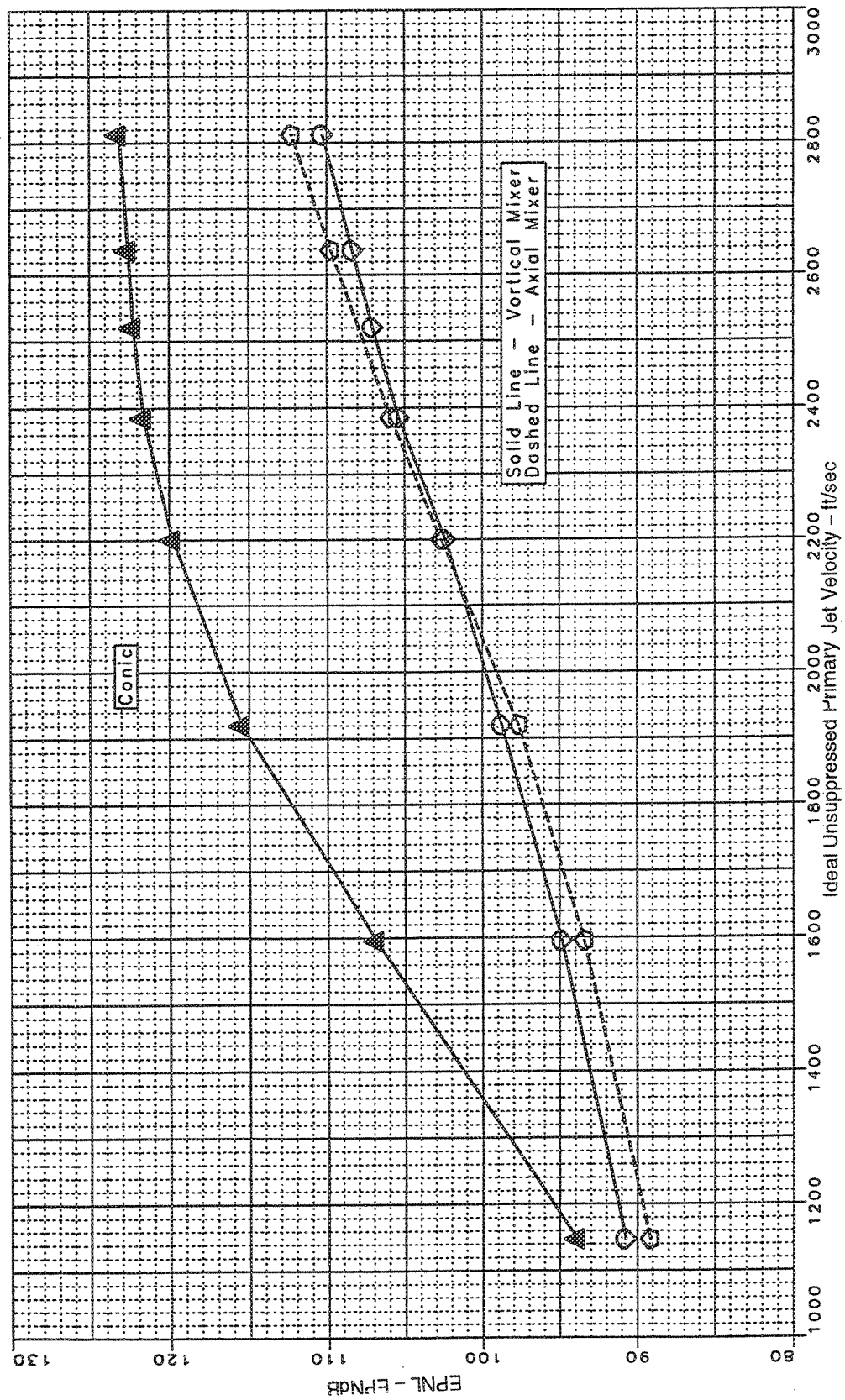


Figure 77. Mixer Comparison Long Shroud (Sideline=1629 ft, SAR=4.9, MAR=0.88,  $A_{g*}=1086 \text{ in}^2$ , Static)

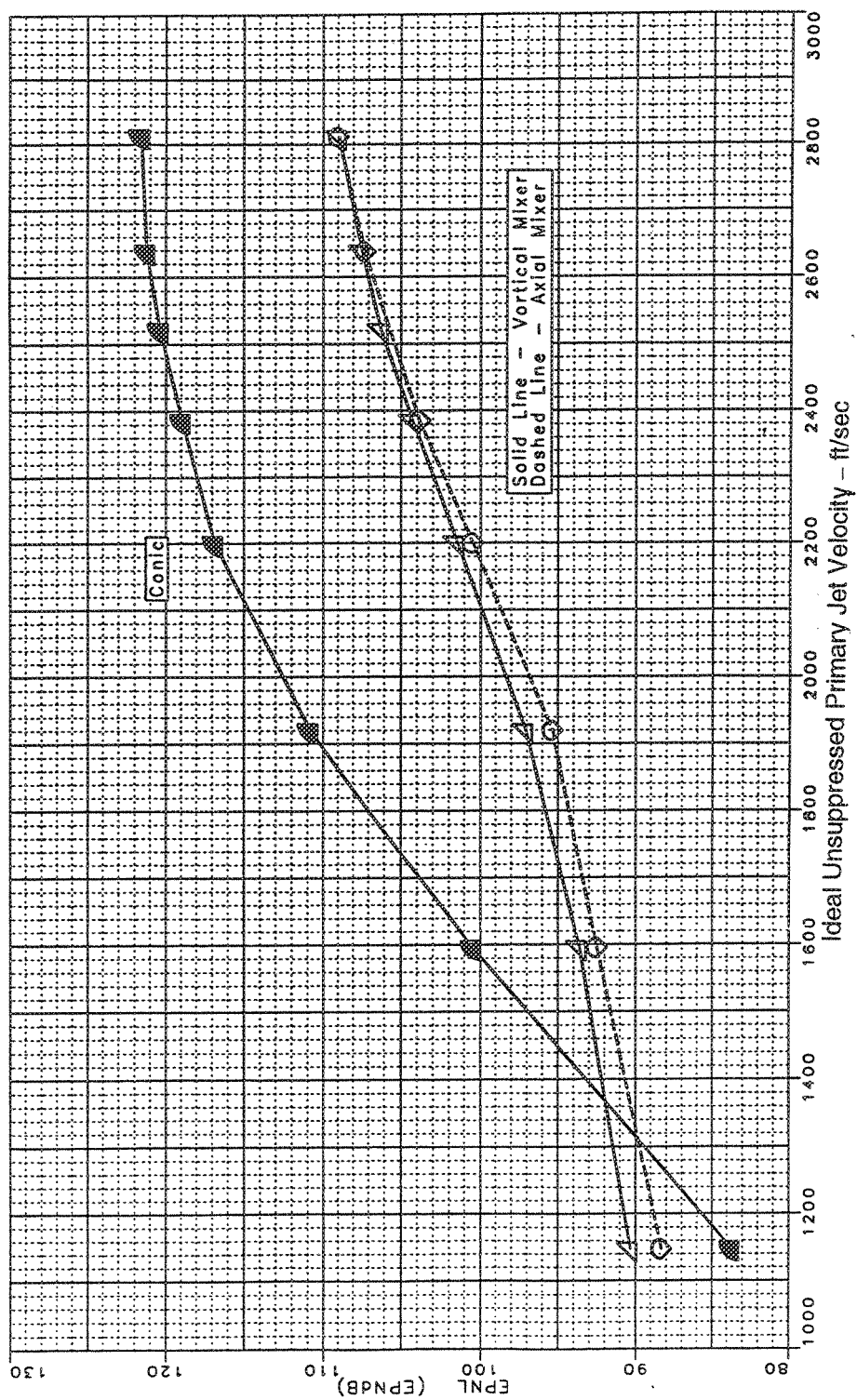


Figure 78. Mixer Comparison Long Shroud (Sideline=1629 ft, SAR=4.9, MAR=0.88,  $A_{g*}=1086 \text{ in}^2$ ,  $Mn=0.32$ ,  $V_{\eta}=357 \text{ ft/sec}$ )

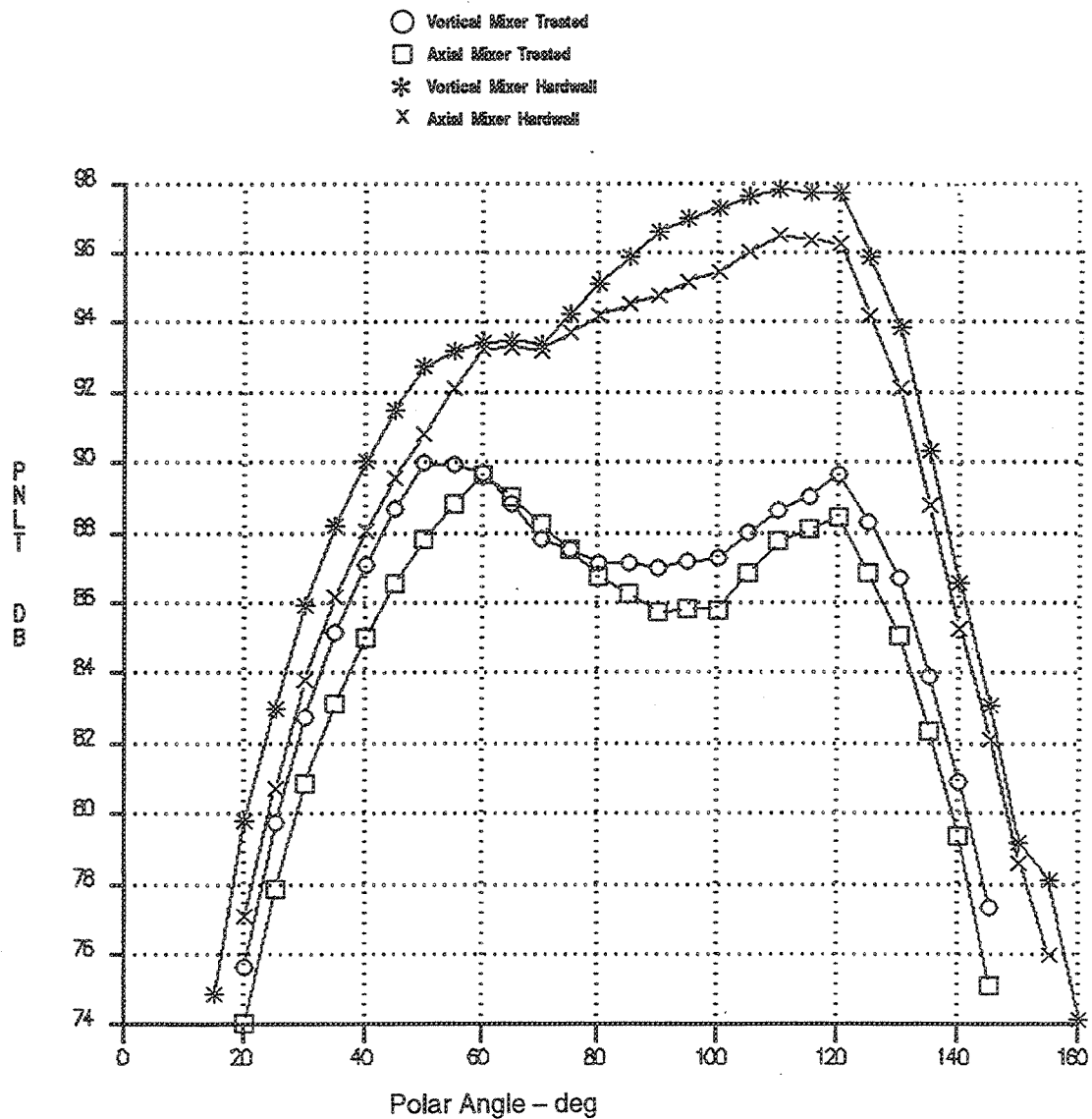


Figure 79. Mixer Comparison, PNLT Versus Angle — Ideal Unsuppressed Primary Jet Velocity=1595 ft/sec  
Long Shroud

(Sideline=1629 ft, SAR=4.9, MAR=0.97,  $A_{g*}=1086 \text{ in}^2$ ,  $M_n=0.32$ ,  $V_{fl}=357 \text{ ft/sec}$ )



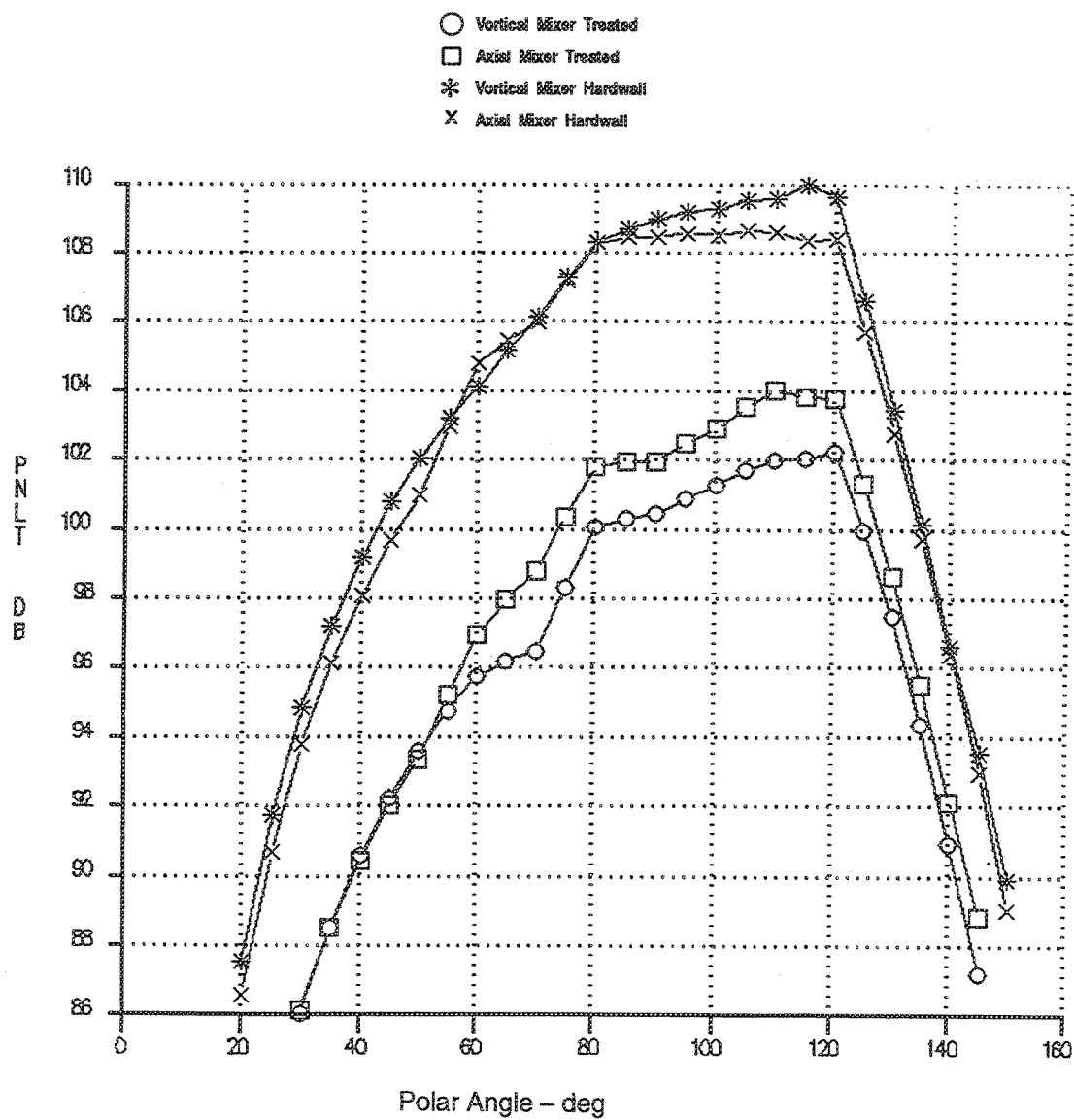


Figure 80. Mixer Comparison, PNLT Versus Angle — Ideal Unsuppressed Primary Jet Velocity=2384 ft/sec  
Long Shroud

(Sideline=1629 ft, SAR=4.9, MAR=0.97,  $A_{g*}=1086 \text{ in}^2$ ,  $Mn=0.32$ ,  $V_{\text{fl}}=357 \text{ ft/sec}$ )

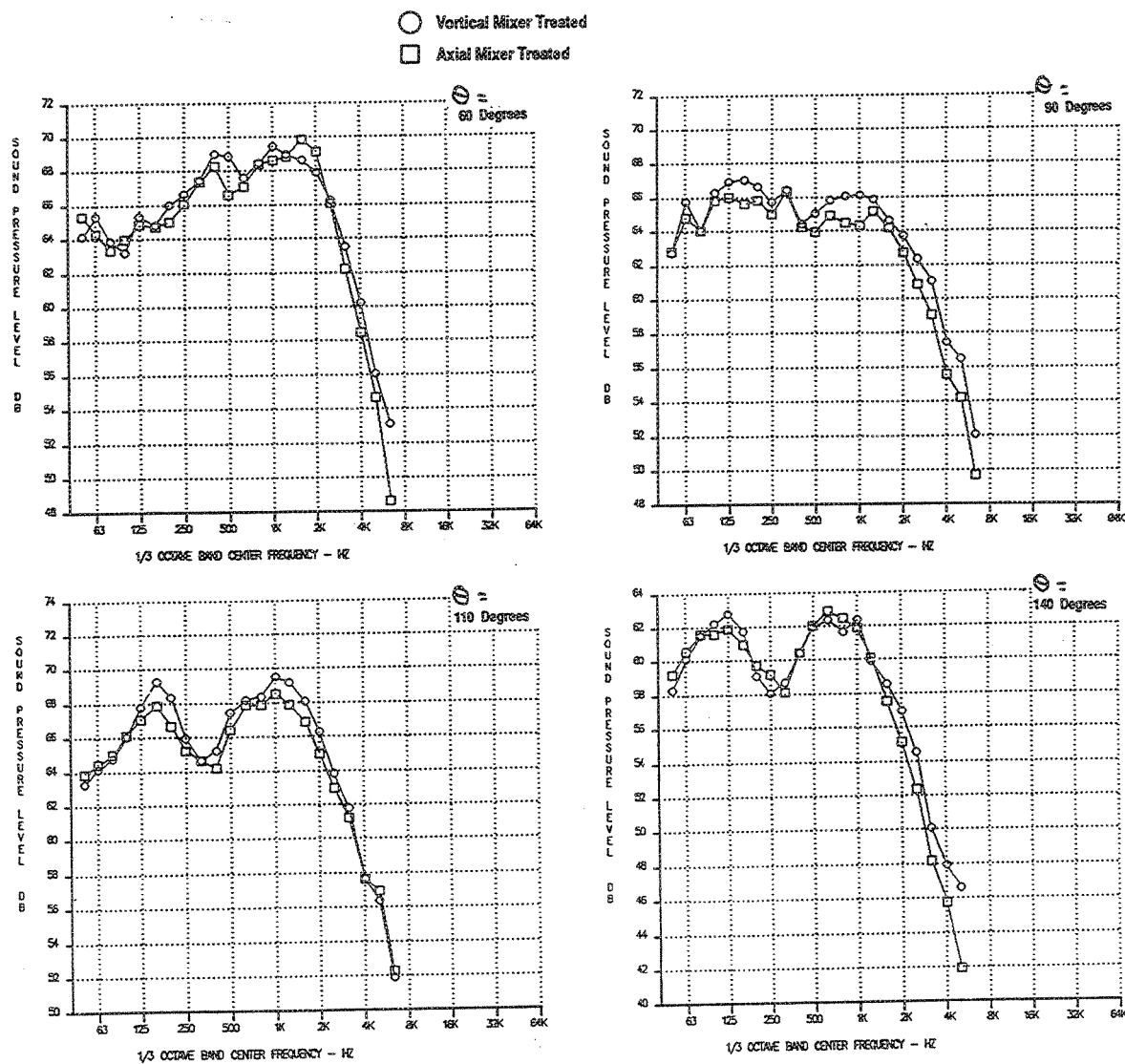


Figure 81. Mixer Comparison, SPL Versus Frequency — Ideal Unsuppressed Primary Jet Velocity=1595 ft/sec Long Shroud

(Sideline=1629 ft, SAR=4.9, MAR=0.97,  $A_{g*}=1086 \text{ in}^2$ ,  $M_n=0.32$ ,  $V_{fl}=357 \text{ ft/sec}$ )

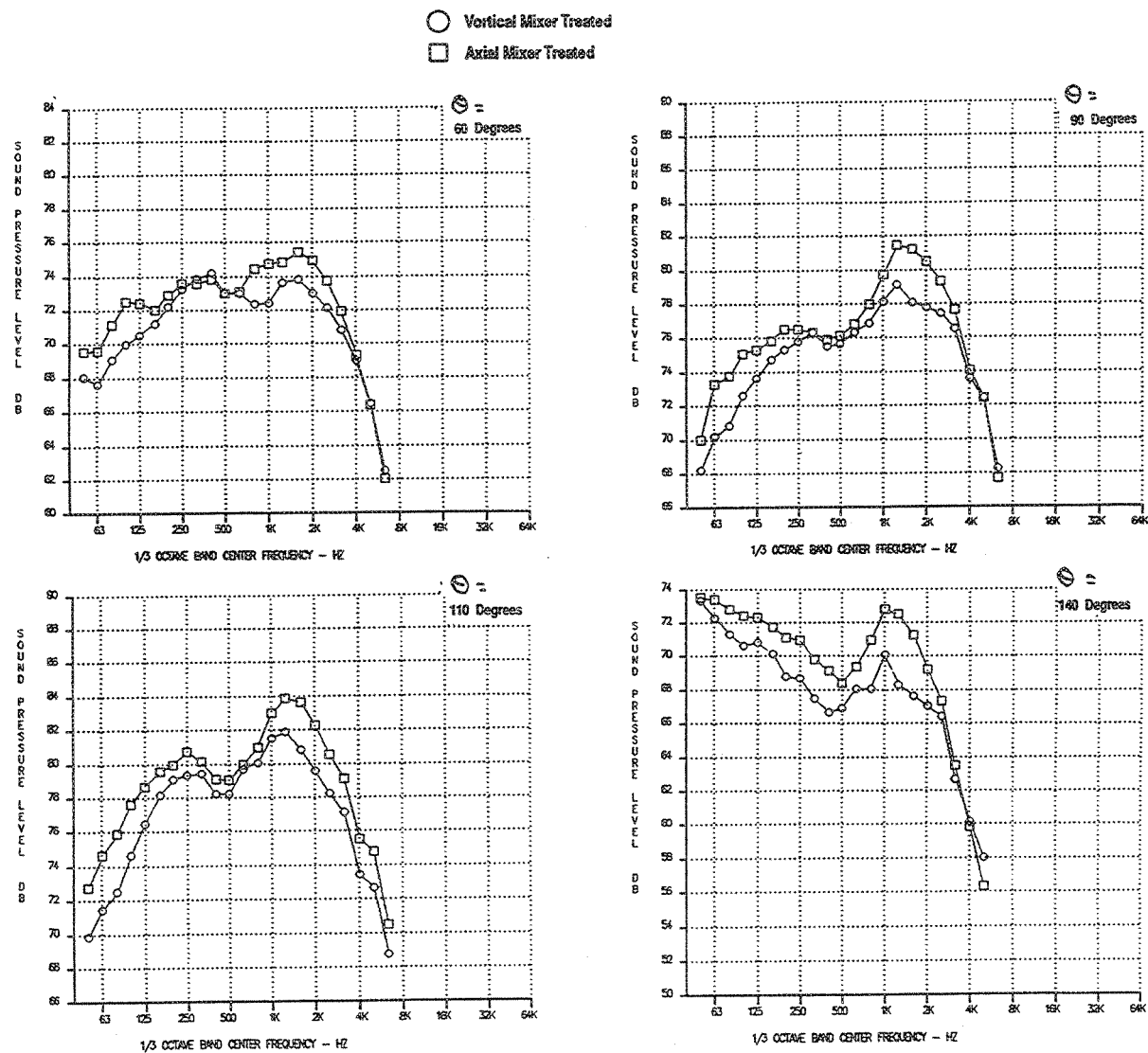


Figure 82. Mixer Comparison, SPL Versus Frequency — Ideal Unsuppressed Primary Jet Velocity=2384 ft/sec  
 Long Shroud

(Sideline=1629 ft, SAR=4.9, MAR=0.97,  $A_{g*}=1086 \text{ in}^2$ ,  $M_n=0.32$ ,  $V_{\text{in}}=357 \text{ ft/sec}$ )

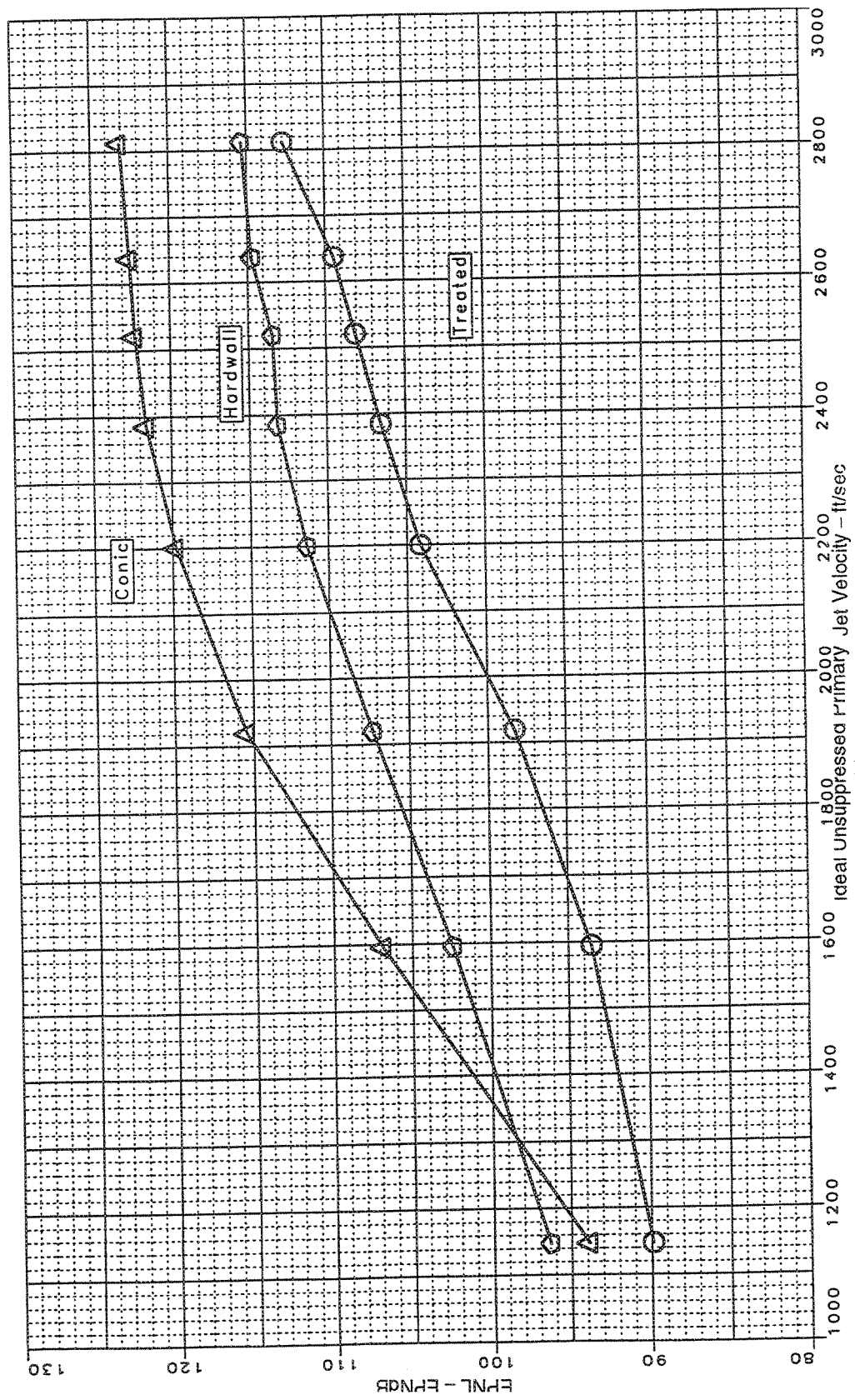


Figure 83. Effect of Treatment on Sideline Noise, Vortical Mixer, Long Shroud  
(Sideline=1629 ft, SAR=4.9, MAR=1.19,  $A_{g*}=1086 \text{ in}^2$ , Static)

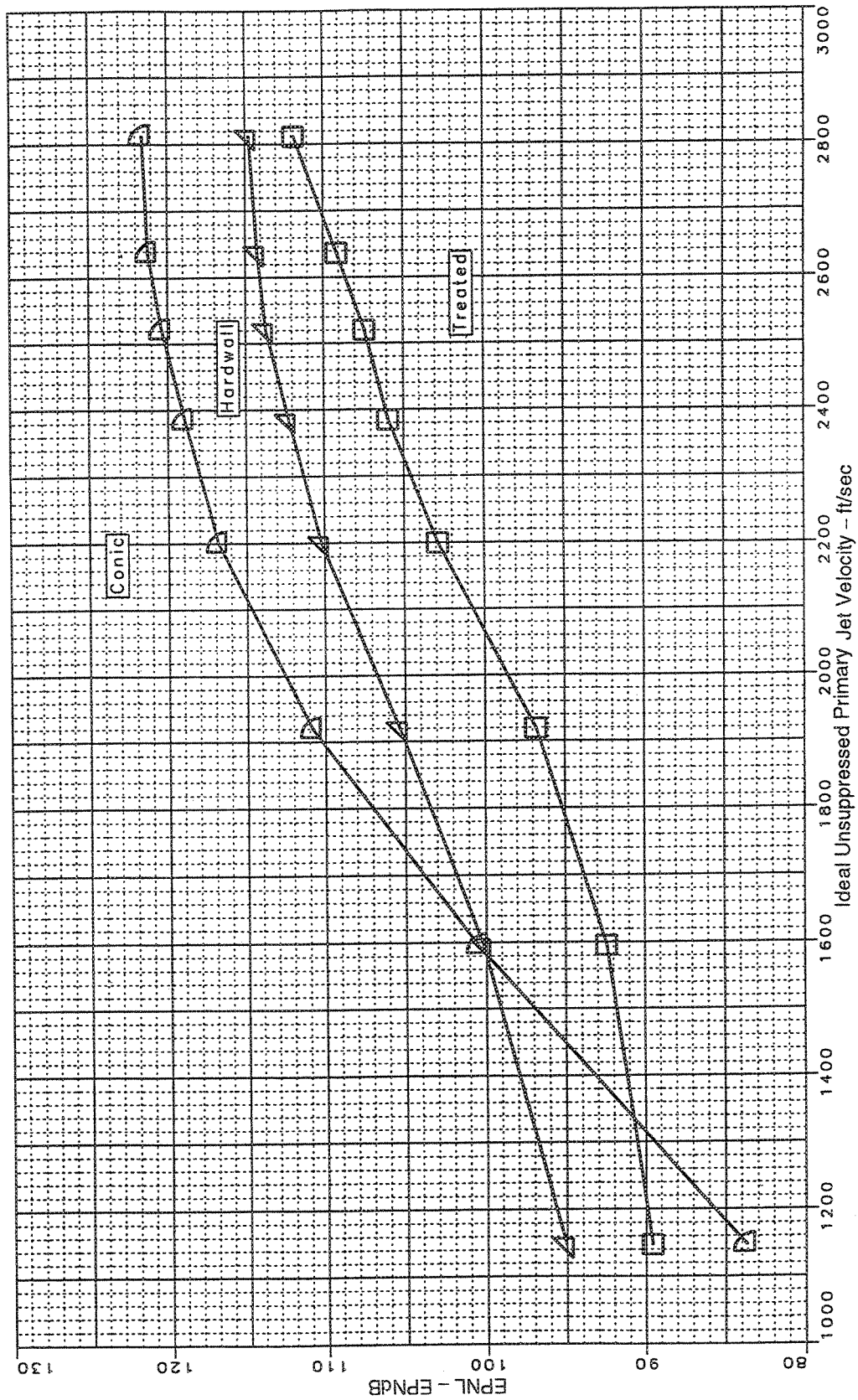


Figure 84. Effect of Treatment on Sideline Noise, Vortical Mixer, Long Shroud  
(Sideline=1629 ft, SAR=4.9, MAR=1.19,  $A_{g*}=1086 \text{ in}^2$ ,  $Mn=0.32$ ,  $V_{\eta}=357 \text{ ft/sec}$ )

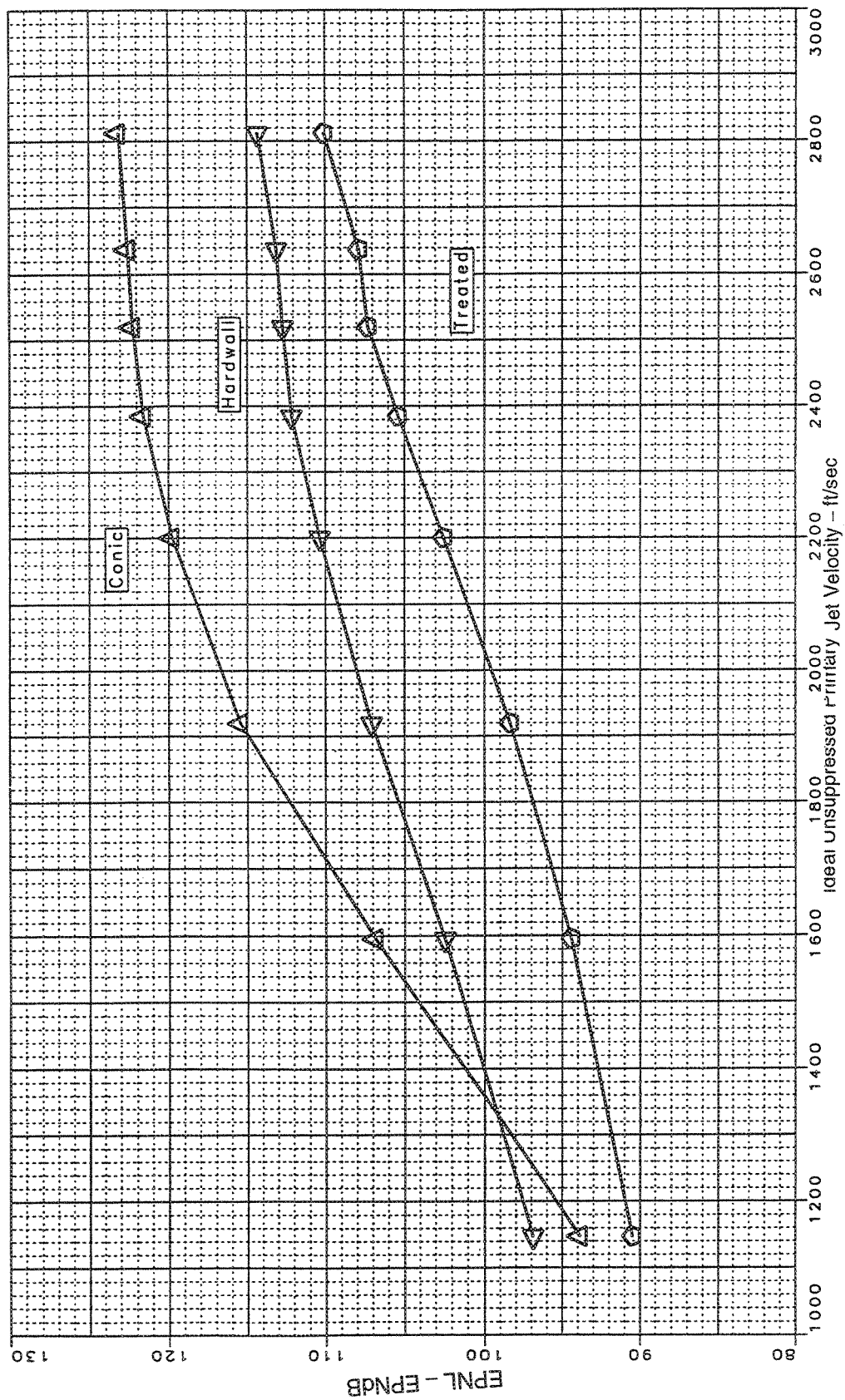


Figure 85. Effect of Treatment on Sideline Noise, Vortical Mixer; Long Shroud  
(Sideline=1629 ft, SAR=4.9, MAR=0.97,  $A_{g*}=1086 \text{ in}^2$ , Static)

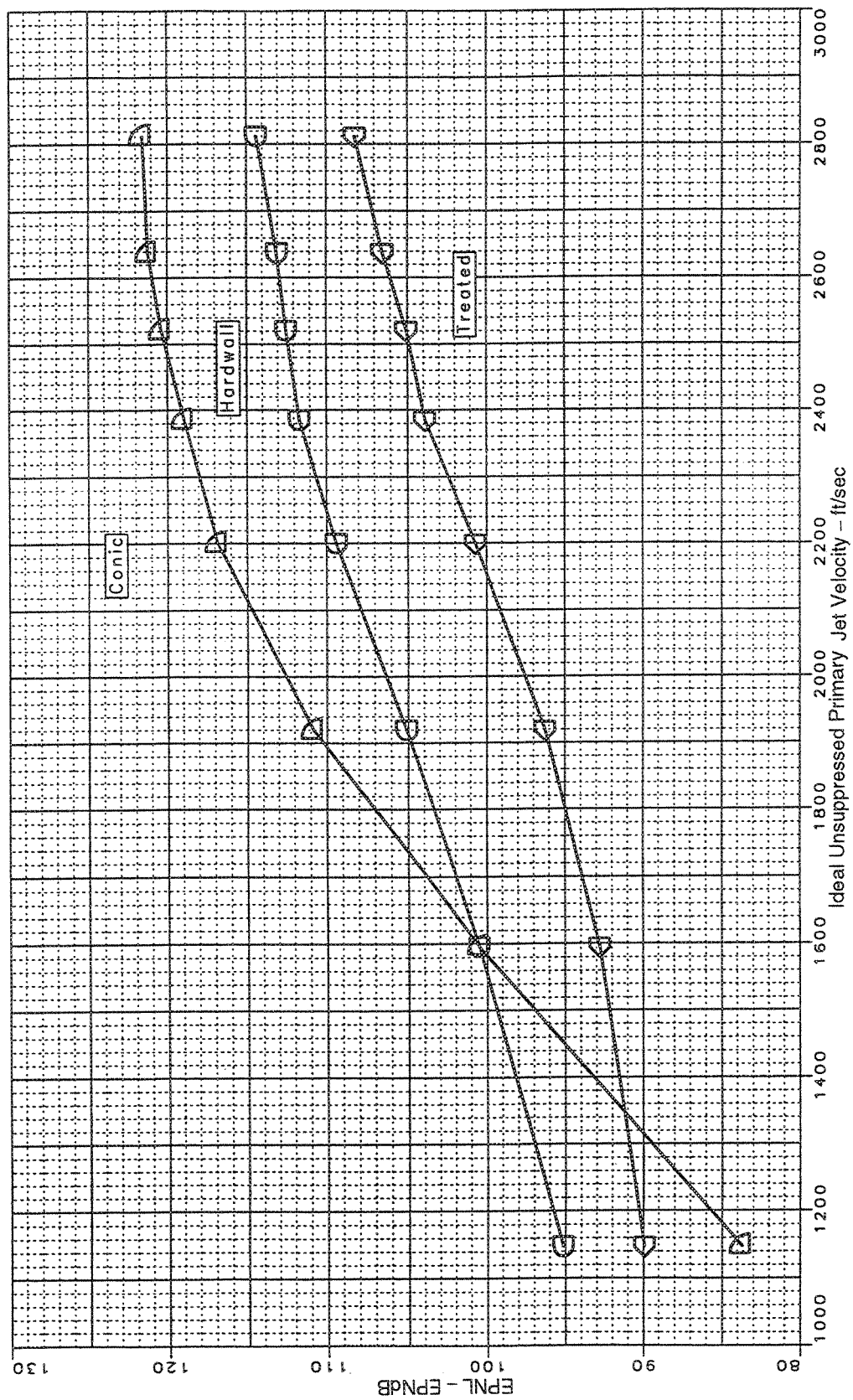


Figure 86. Effect of Treatment on Sideline Noise, Vortical Mixer, Long Shroud  
(Sideline=1629 ft, SAR=4.9, MAR=0.97,  $A_{g*}=1086 \text{ in}^2$ ,  $M_n=0.32$ ,  $V_{ft}=357 \text{ ft/sec}$ )

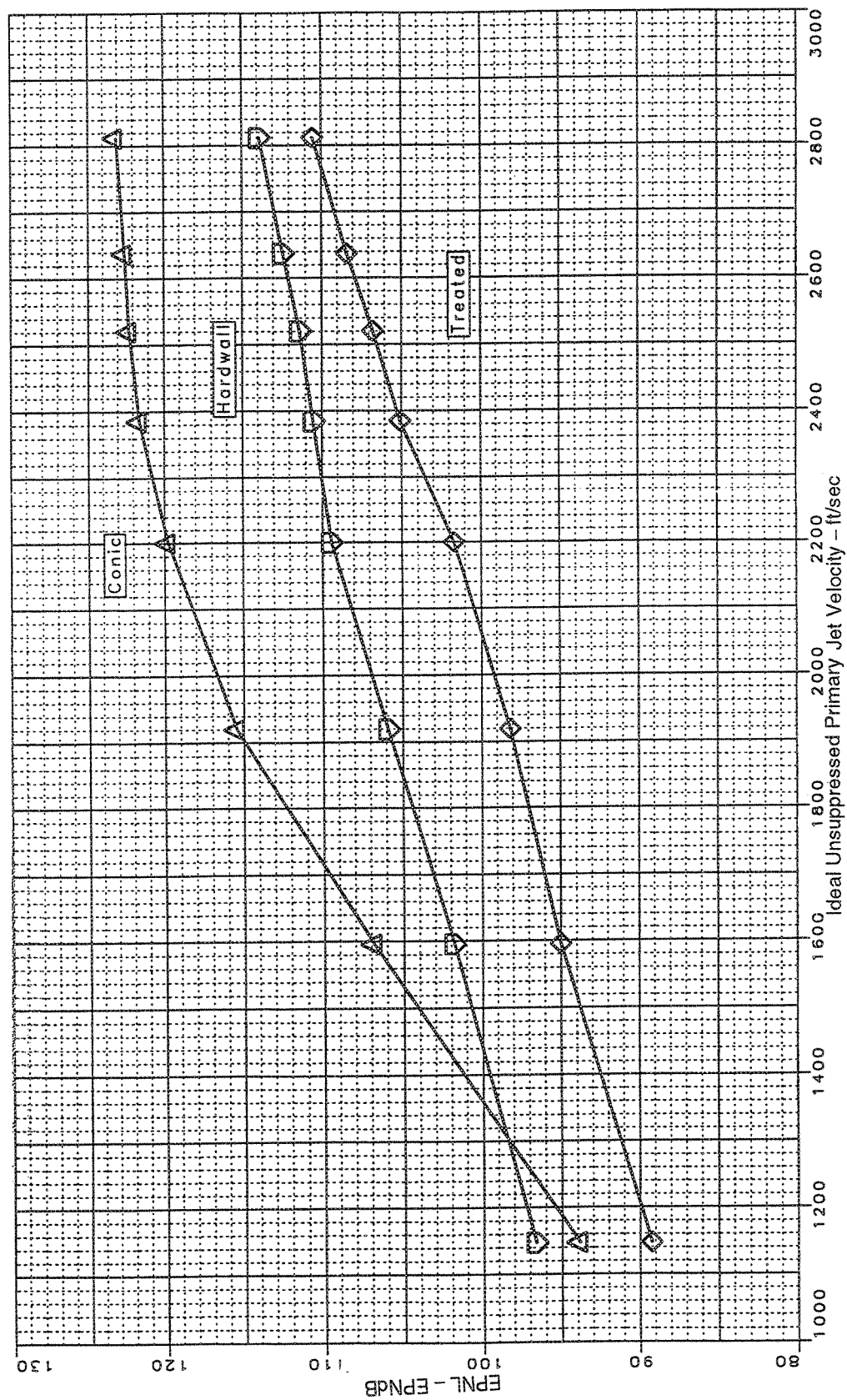


Figure 87. Effect of Treatment on Sideline Noise, Vortical Mixer, Long Shroud  
(Sideline = 1629 ft, SAR=4.4, MAR=0.88,  $A_{g*}=1086 \text{ in}^2$ , Static)



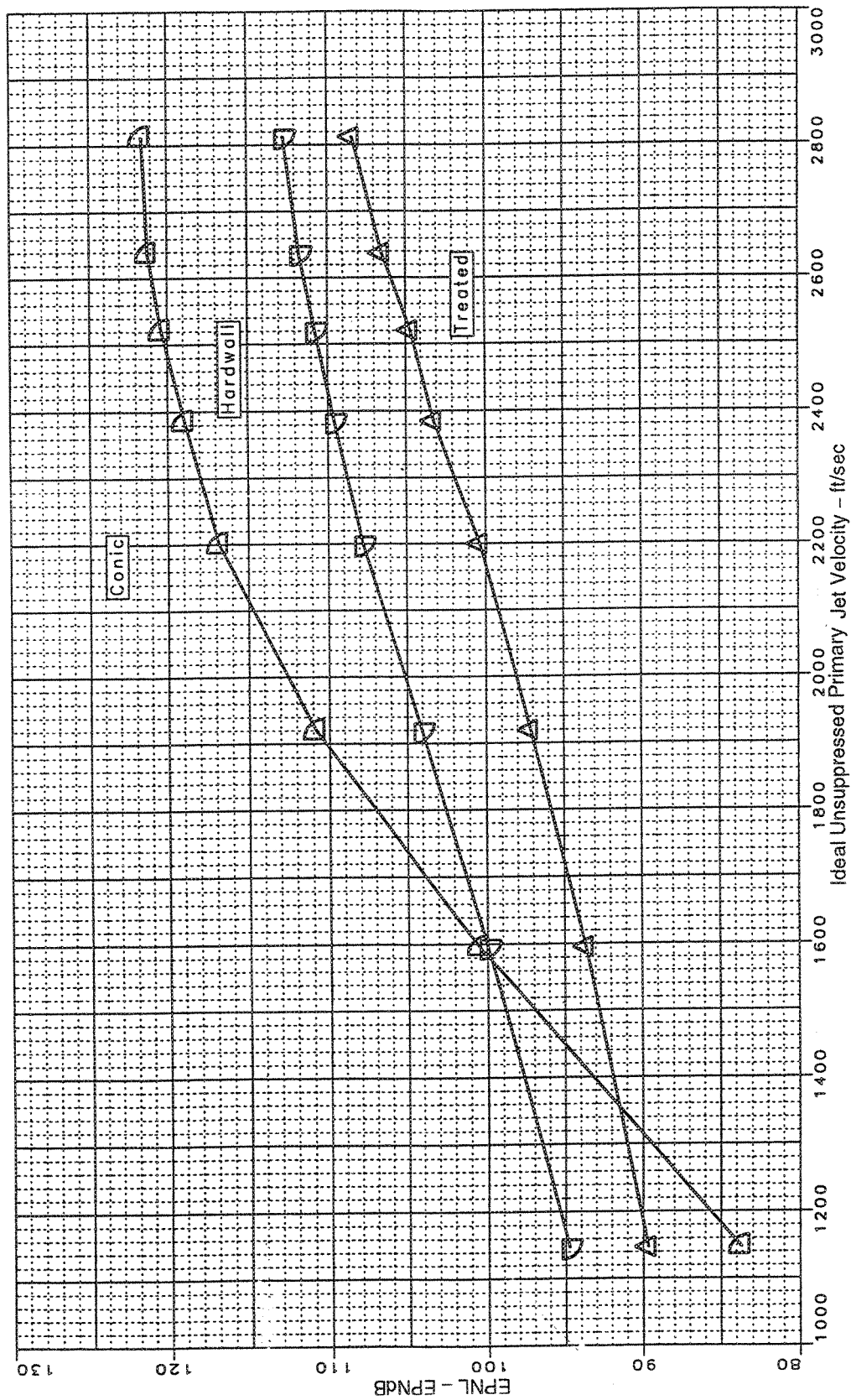


Figure 88. Effect of Treatment on Sideline Noise, Vortical Mixer, Long Shroud  
(Sideline=1629 ft, SAR=4.4, MAR=0.88,  $A_{g*}=1086 \text{ in}^2$ ,  $Mn=0.32$ ,  $V_{\eta}=357 \text{ ft/sec}$ )

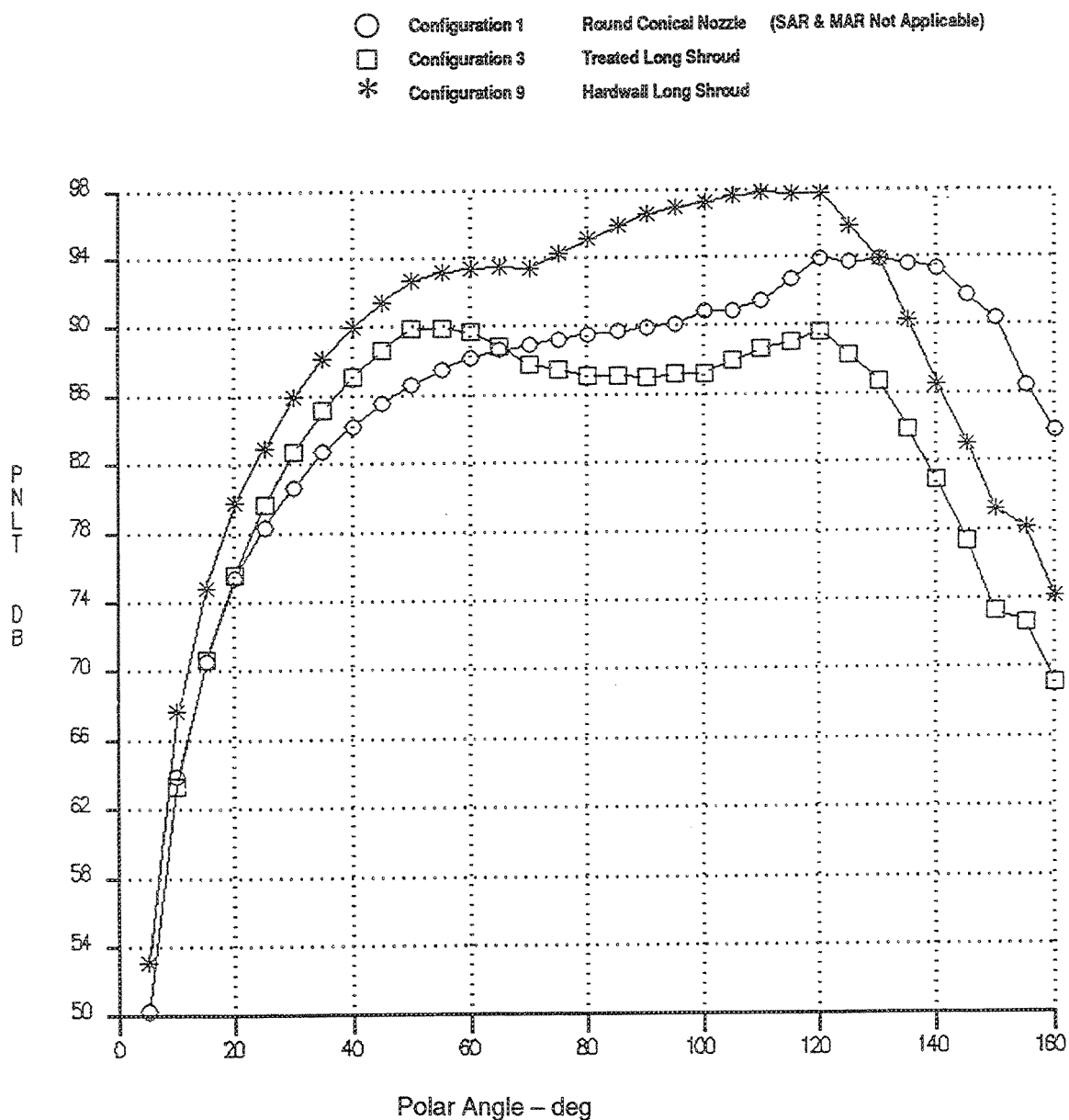


Figure 89. Effect of Treatment on Noise, PNL T Versus Angle  
 — Ideal Unsuppressed Primary Jet Velocity=1595 ft/sec, Vortical Mixer, Long Shroud  
 (Sideline=1629 ft, SAR=4.9, MAR=0.97,  $A_{g*}=1086 \text{ in}^2$ ,  $M_n=0.32$ ,  $V_{fl}=357 \text{ ft/sec}$ )

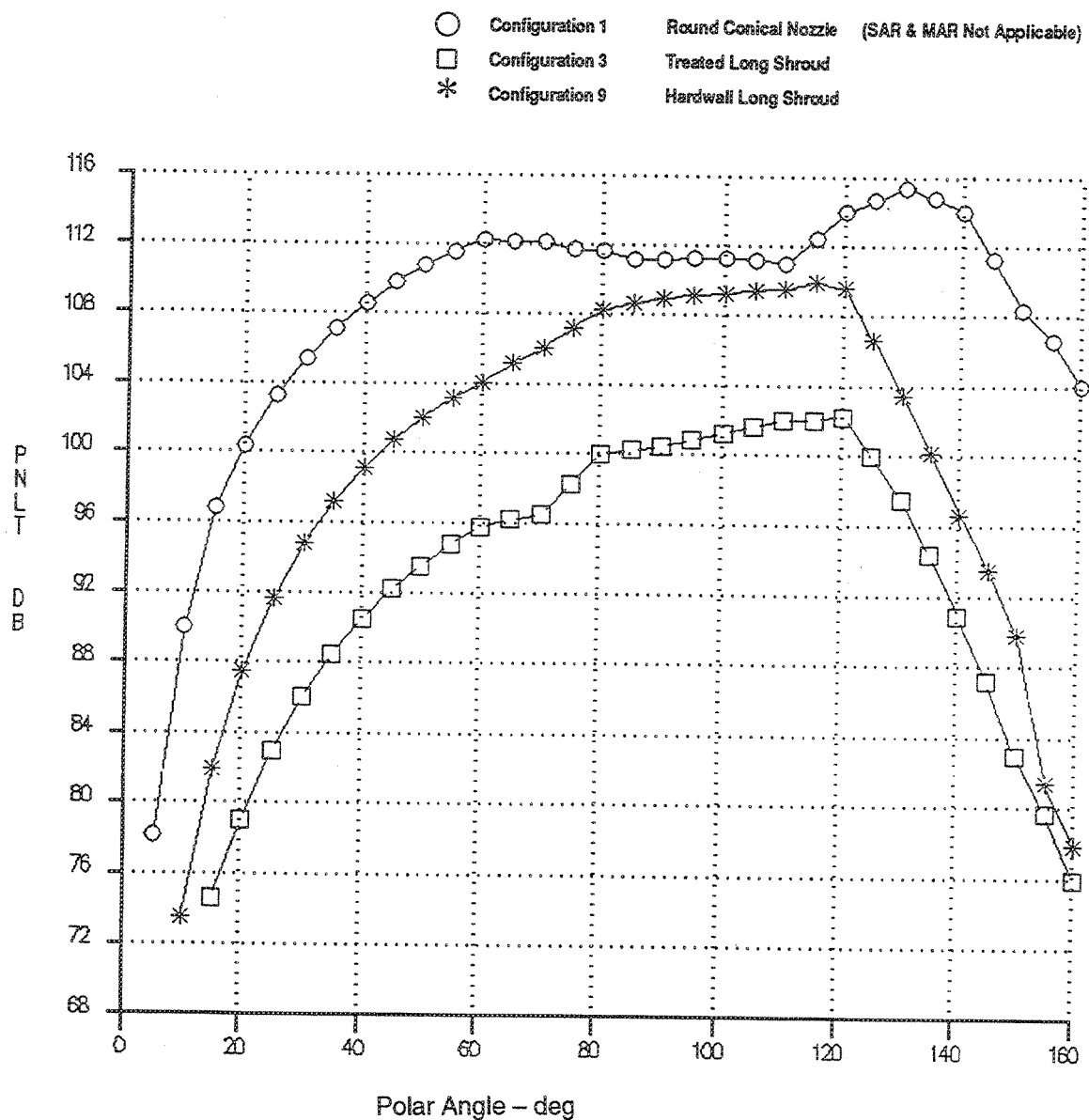
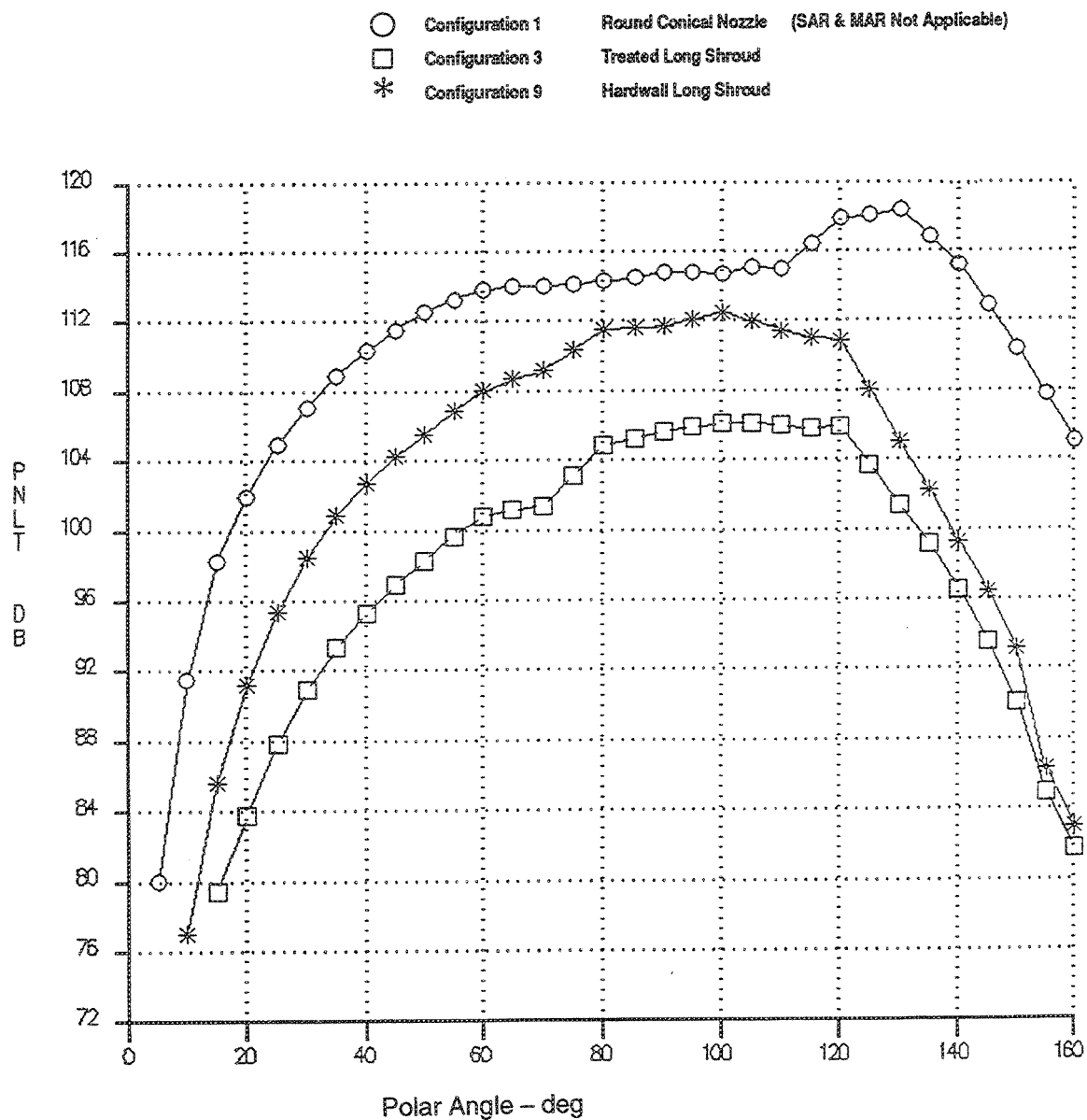


Figure 90. Effect of Treatment on Noise, PNL T Versus Angle  
 — Ideal Unsuppressed Primary Jet Velocity=2394 ft/sec, Vortical Mixer, Long Shroud  
 (Sideline=1629 ft, SAR=4.9, MAR=0.97,  $A_{g*}=1086 \text{ in}^2$ ,  $Mn=0.32$ ,  $V_{fl}=357 \text{ ft/sec}$ )



*Figure 91. Effect of Treatment on Noise, PNLT Versus Angle*  
 — Ideal Unsuppressed Primary Jet Velocity=2812 ft/sec, Vortical Mixer, Long Shroud  
 (Sideline=1629 ft, SAR=4.9, MAR=0.97,  $A_{g*}=1086 \text{ in}^2$ ,  $M_n=0.32$ ,  $V_{fl}=357 \text{ ft/sec}$ )

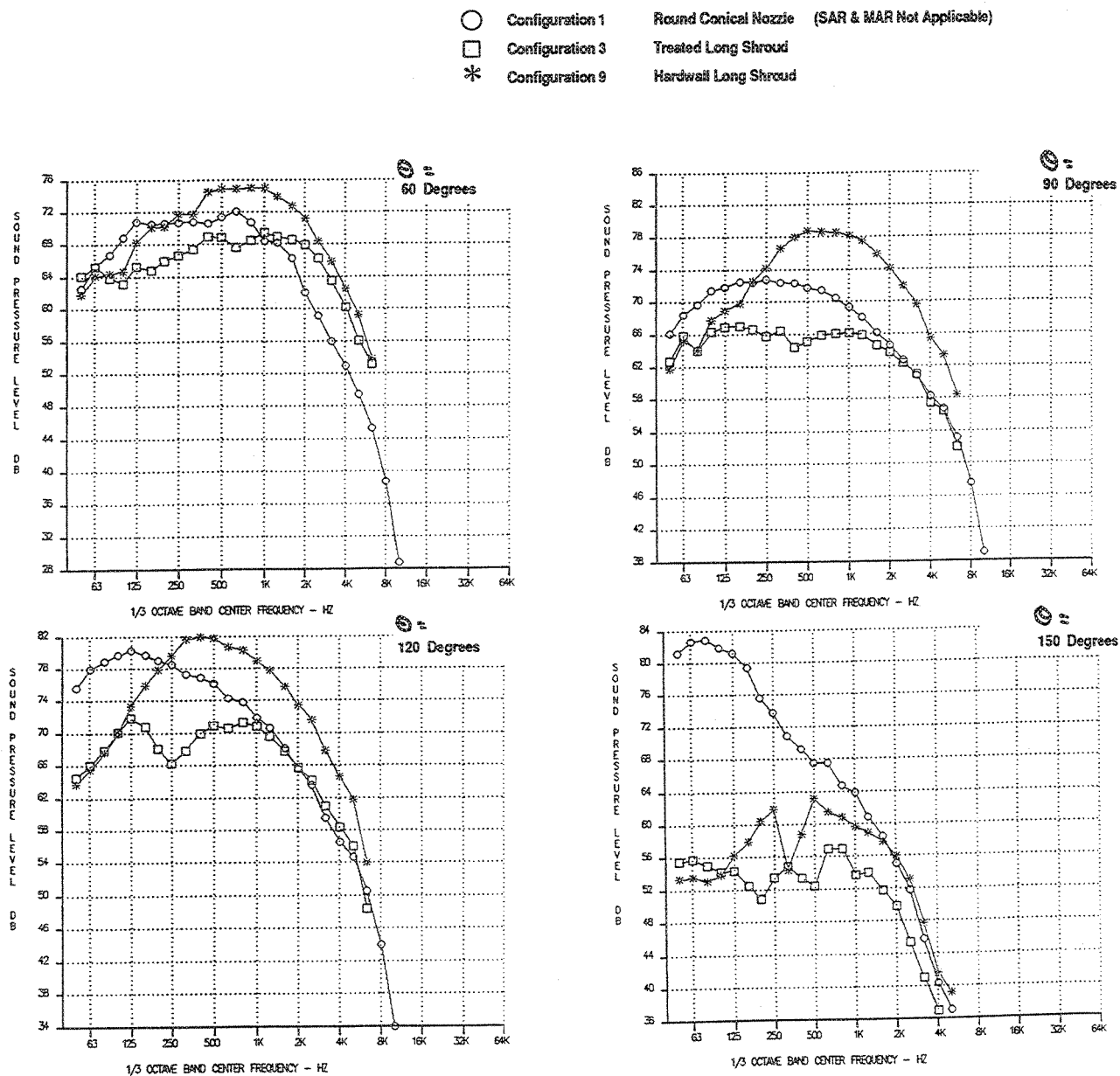


Figure 92. Effect of Treatment on Noise, SPL Versus Frequency  
 — Ideal Unsuppressed Primary Jet Velocity=1595 ft/sec, Vortical Mixer, Long Shroud  
 (Sideline=1629 ft, SAR=4.9, MAR=0.97,  $A_{g*}=1086 \text{ in}^2$ ,  $M_n=0.32$ ,  $V_{fl}=357 \text{ ft/sec}$ )

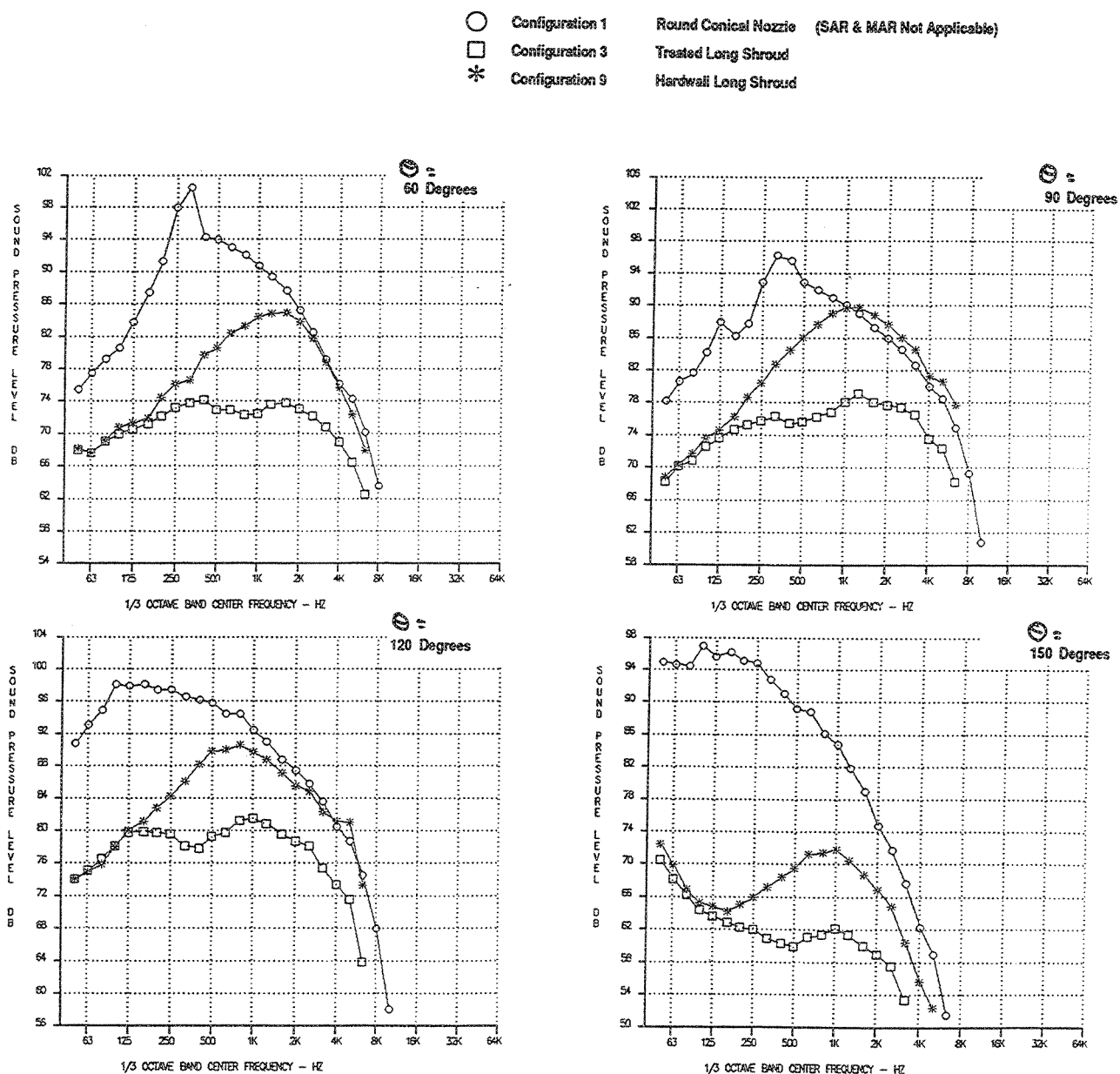


Figure 93. Effect of Treatment on Noise, SPL Versus Frequency  
 — Ideal Unsuppressed Primary Jet Velocity=2384 ft/sec, Vortical Mixer, Long Shroud  
 (Sideline=1629 ft, SAR=4.9, MAR=0.97,  $A_{g*}=1086 \text{ in}^2$ ,  $M_n=0.32$ ,  $V_{fl}=357 \text{ ft/sec}$ )

- Configuration 1 Round Conical Nozzle (SAR & MAR Not Applicable)
- Configuration 3 Treated Long Shroud
- \* Configuration 9 Hardwall Long Shroud

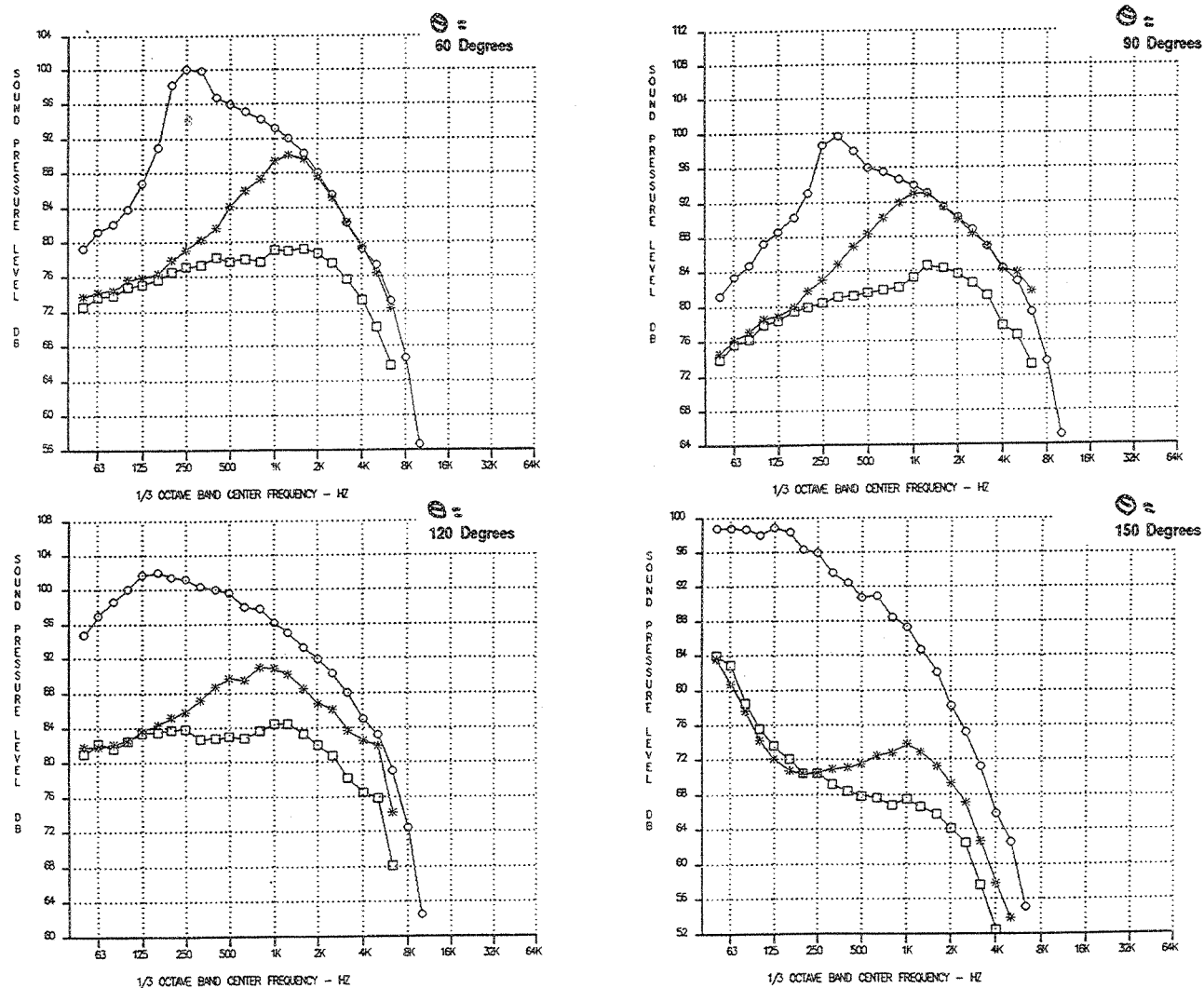


Figure 94. Effect of Treatment on Noise, PNLT Versus Angle  
 — Ideal Unsuppressed Primary Jet Velocity=2812 ft/sec, Vortical Mixer, Long Shroud  
 (Sideline=1629 ft, SAR=4.9, MAR=0.97,  $A_{g*}=1086 \text{ in}^2$ ,  $M_n=0.32$ ,  $V_{\Pi}=357 \text{ ft/sec}$ )

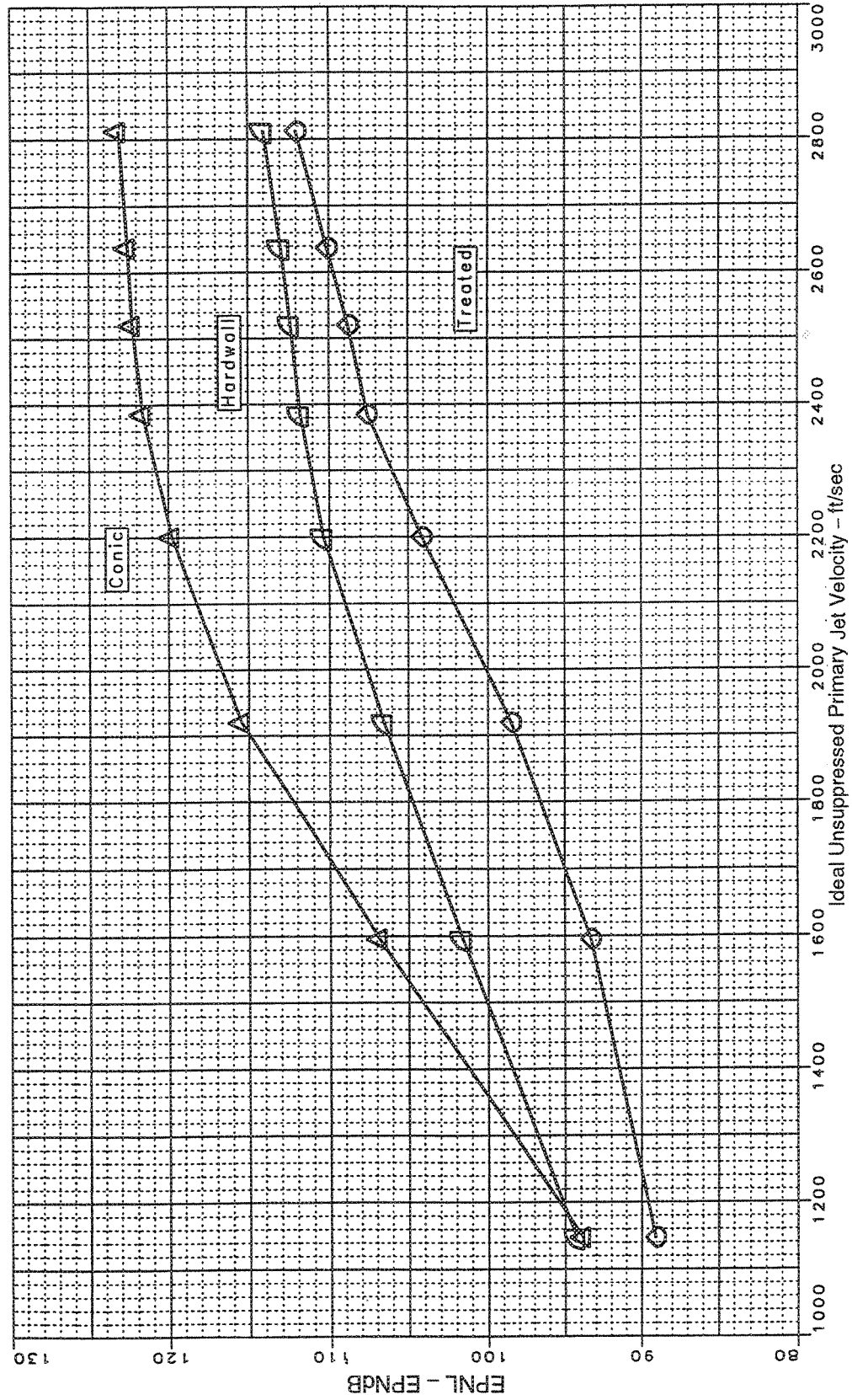


Figure 95. Effect of Treatment on Sideline Noise, Axial Mixer, Long Shroud  
 (Sideline=1629 ft, SAR=4.9, MAR=0.97,  $A_{g*}=1086 \text{ in}^2$ , Static)



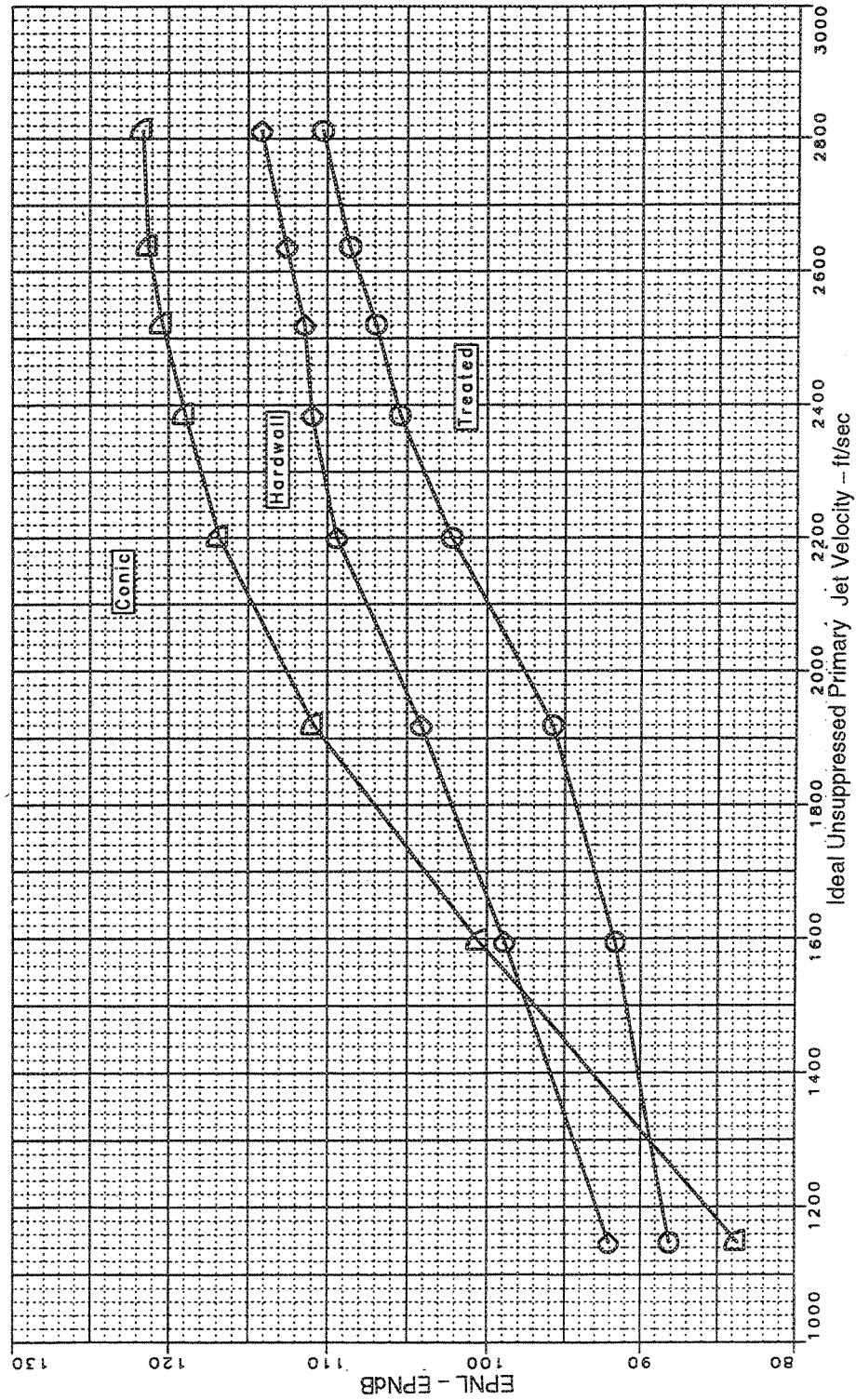


Figure 96. Effect of Treatment on Sideline Noise, Axial Mixer, Long Shroud  
 (Sideline=1629 ft, SAR=4.9, MAR=0.97,  $A_{g*}=1086 \text{ in}^2$ ,  $M_n=0.32$ ,  $V_n=357 \text{ ft/sec}$ )

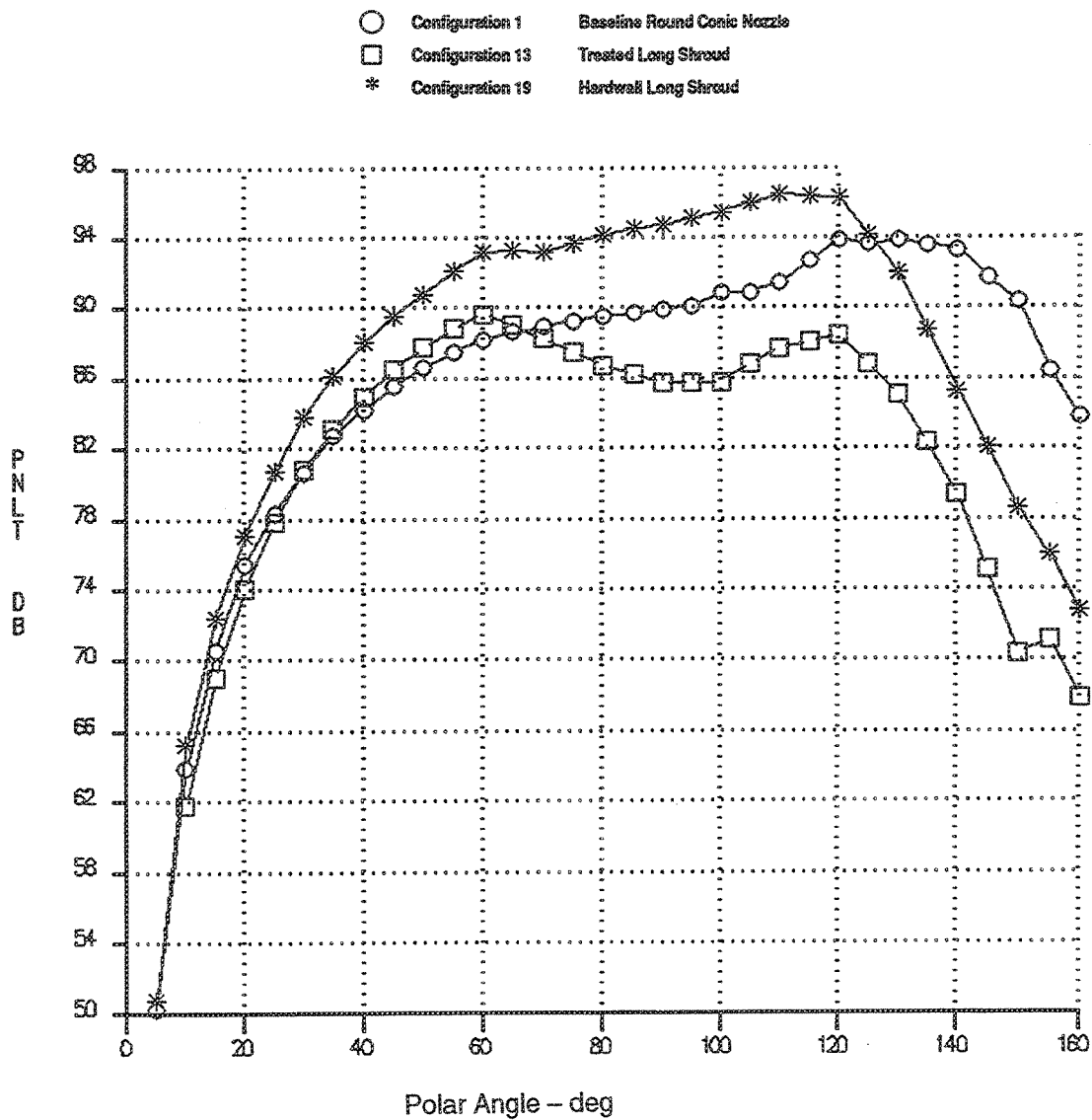


Figure 97. Effect of Treatment on Noise, PNLT Versus Angle  
 — Ideal Unsuppressed Primary Jet Velocity=1595 ft/sec, Axial Mixer, Long Shroud  
 (Sideline=1629 ft, SAR=4.9, MAR=0.97,  $A_{g*}=1086 \text{ in}^2$ ,  $M_n=0.32$ ,  $V_{fl}=357 \text{ ft/sec}$ )

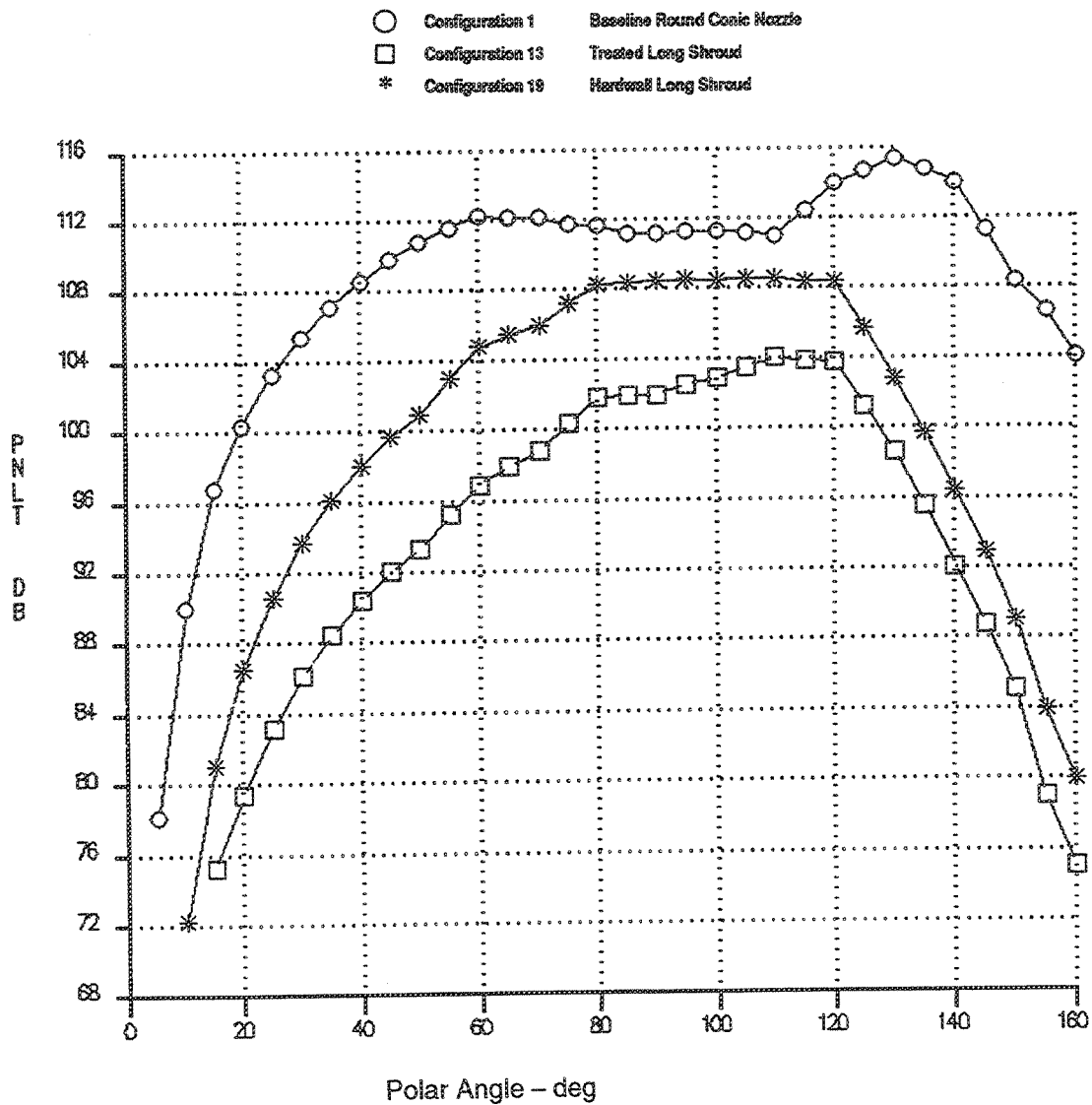


Figure 98. Effect of Treatment on Noise, PNLT Versus Angle  
 — Ideal Unsuppressed Primary Jet Velocity=2384 ft/sec, Axial Mixer, Long Shroud  
 (Sideline=1629 ft, SAR=4.9, MAR=0.97,  $A_{g*}=1086 \text{ in}^2$ ,  $M_n=0.32$ ,  $V_{fl}=357 \text{ ft/sec}$ )

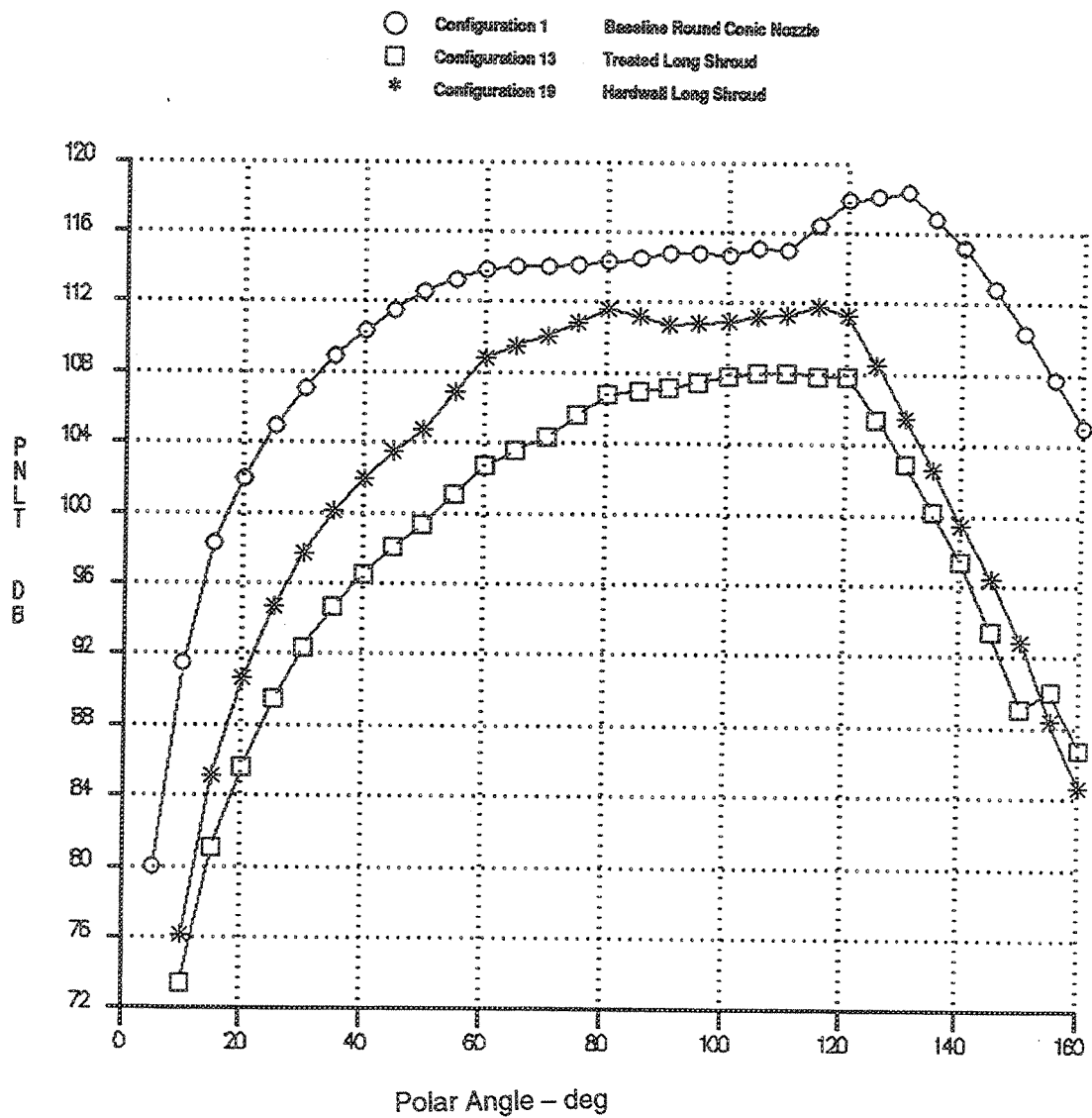


Figure 99. Effect of Treatment on Noise, PNLT Versus Angle  
 — Ideal Unsuppressed Primary Jet Velocity=2812 ft/sec, Axial Mixer, Long Shroud  
 (Sideline=1629 ft, SAR=4.9, MAR=0.97,  $A_{g*}=1086 \text{ in}^2$ ,  $M_n=0.32$ ,  $V_{fl}=357 \text{ ft/sec}$ )

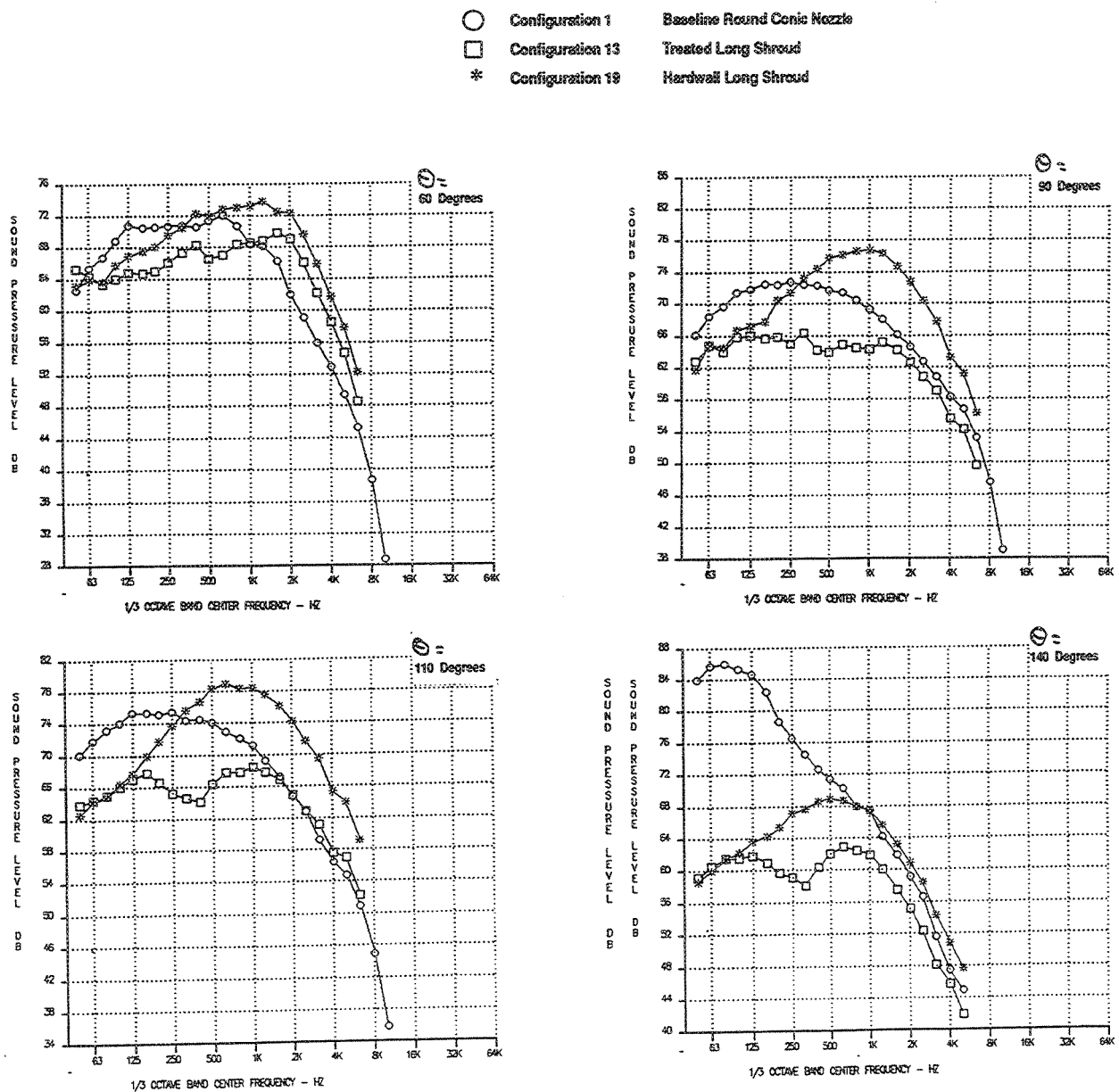


Figure 100. Effect of Treatment on Noise, SPL Versus Angle  
 — Ideal Unsuppressed Primary Jet Velocity=1595 ft/sec, Axial Mixer, Long Shroud  
 (Sideline=1629 ft, SAR=4.9, MAR=0.97,  $A_{g*}=1086 \text{ in}^2$ ,  $Mn=0.32$ ,  $V_{fl}=357 \text{ ft/sec}$ )

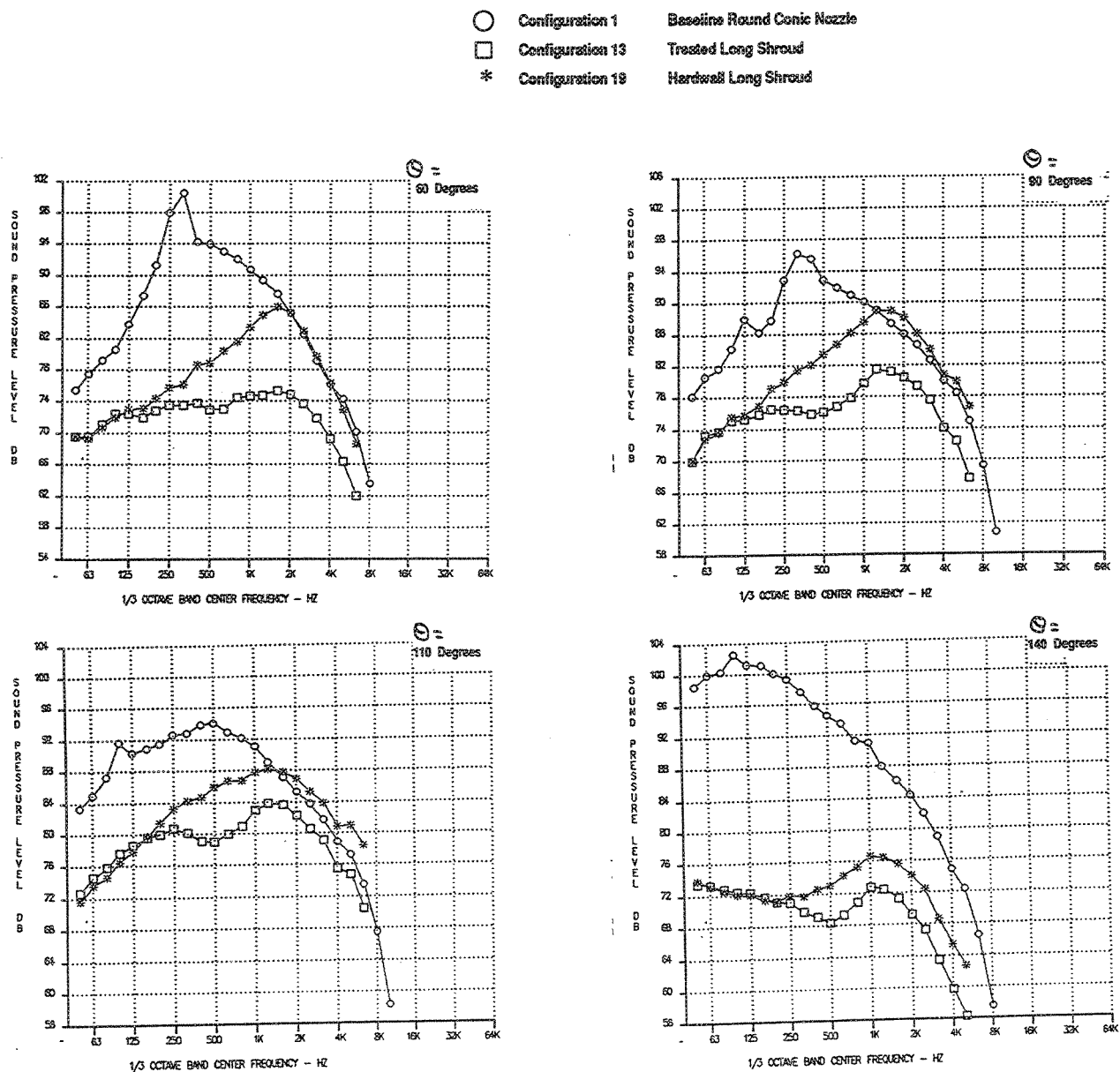


Figure 101. Effect of Treatment on Noise, SPL Versus Angle  
 — Ideal Unsuppressed Primary Jet Velocity=2384 ft/sec, Axial Mixer, Long Shroud  
 (Sideline=1629 ft, SAR=4.9, MAR=0.97,  $A_{g*}=1086 \text{ in}^2$ ,  $M_n=0.32$ ,  $V_{f1}=357 \text{ ft/sec}$ )

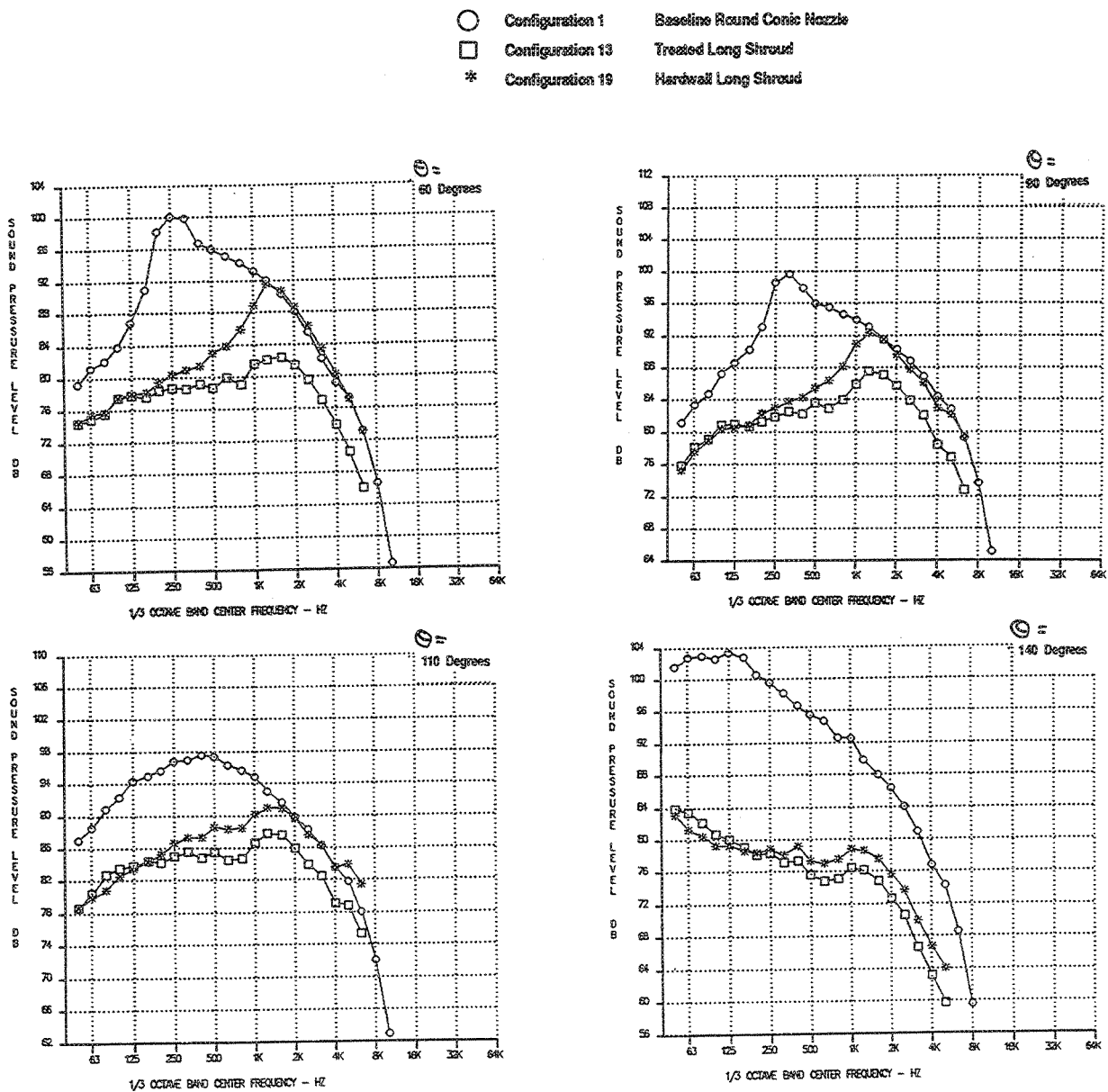


Figure 102. Effect of Treatment on Noise, SPL Versus Angle  
 — Ideal Unsuppressed Primary Jet Velocity=2812 ft/sec, Axial Mixer, Long Shroud  
 (Sideline=1629 ft, SAR=4.9, MAR=0.97,  $A_{g*}=1086 \text{ in}^2$ ,  $M_n=0.32$ ,  $V_{fl}=357 \text{ ft/sec}$ )

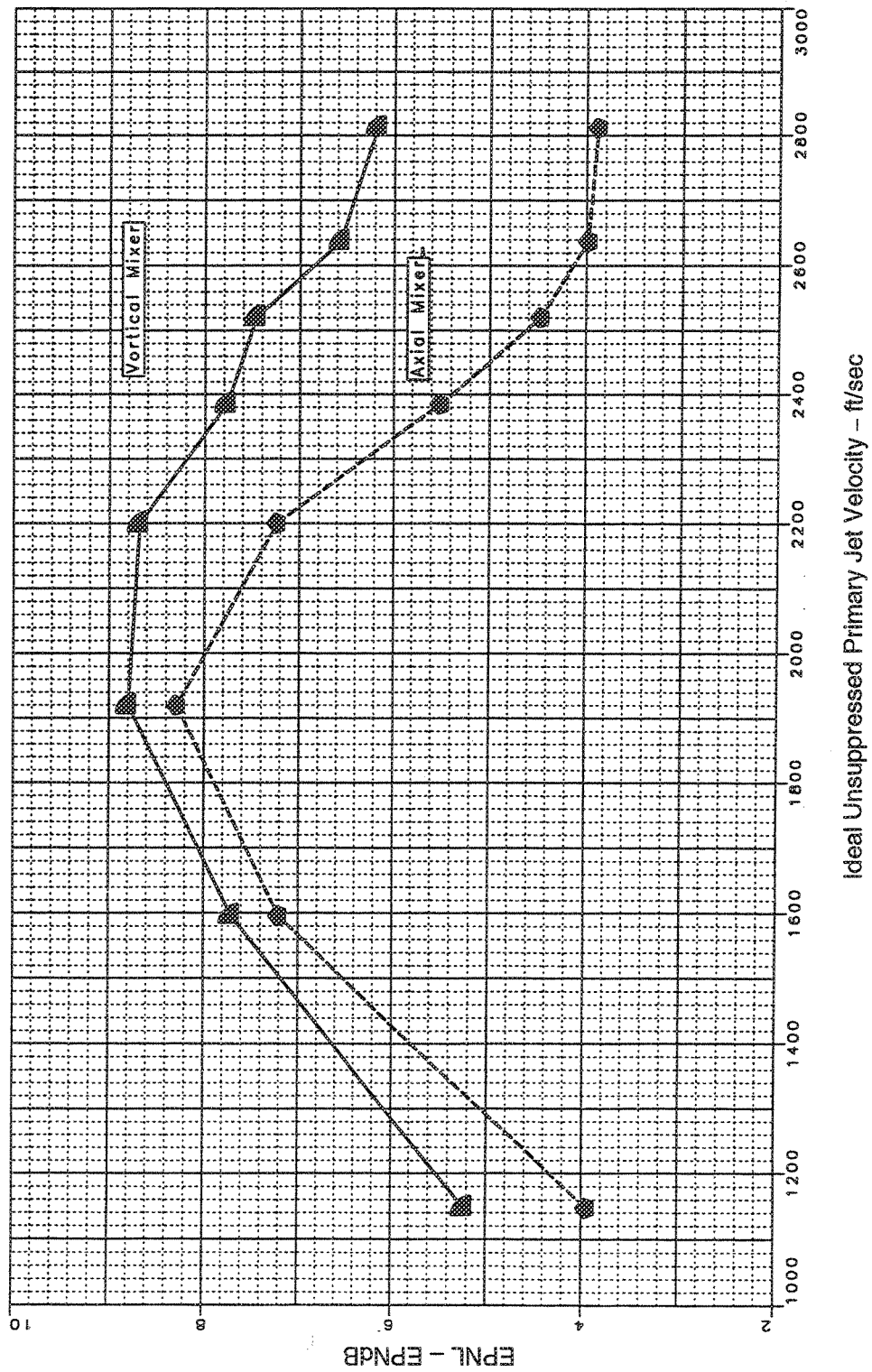


Figure 103. Comparison of Liner Effectiveness — Hardwall-Treated Vortical and Axial Mixers, Long Shroud  
(Sideline=1629 ft, SAR=4.9, MAR=0.97,  $A_{gs}=1086 \text{ in}^2$ ,  $Mn=0.32$ ,  $V_{\bar{u}}=357 \text{ ft/sec}$ )



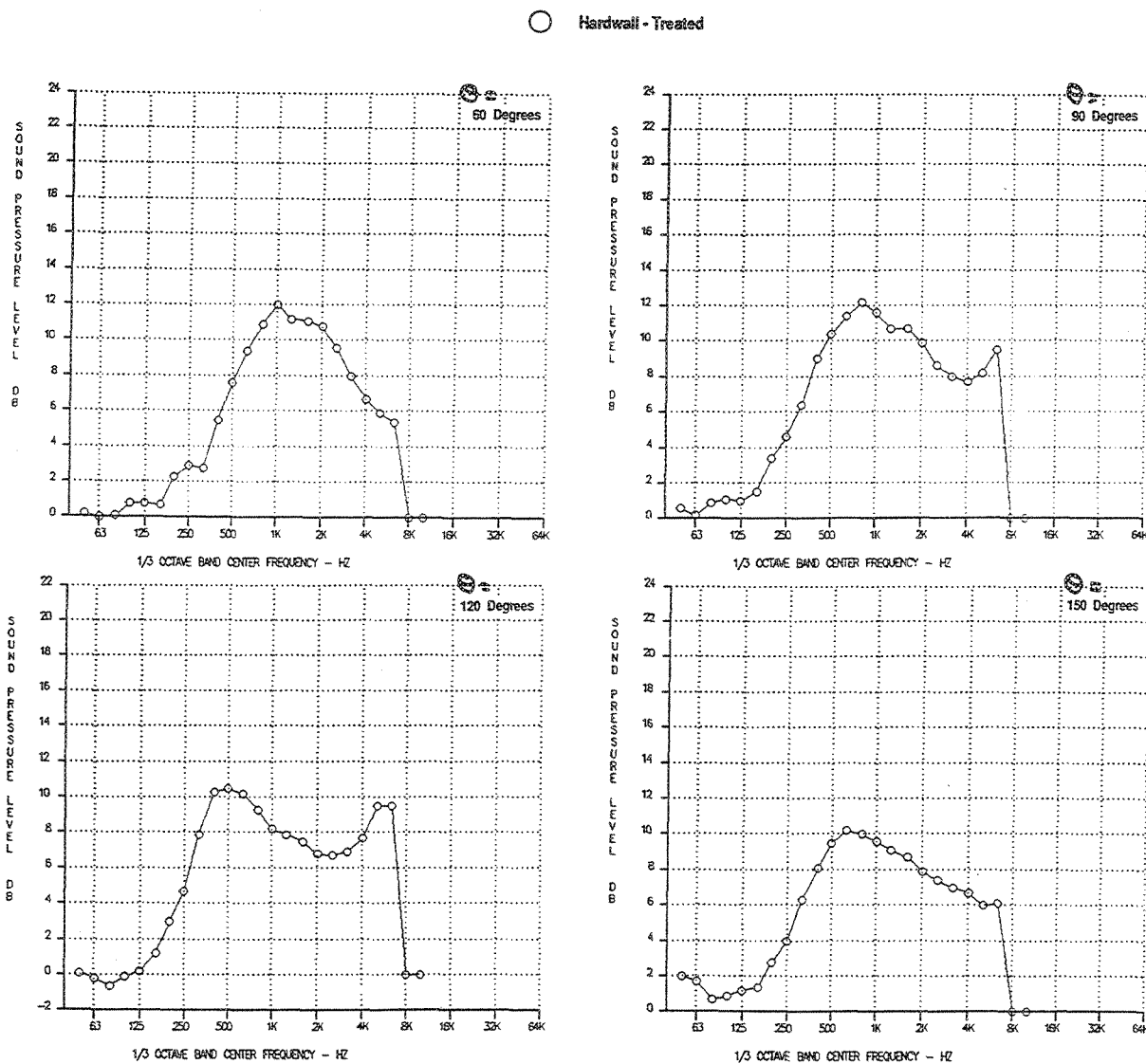


Figure 104. Linear Attenuation, SPL Versus Frequency — Ideal Unsuppressed Primary Jet Velocity=2384 ft/sec  
Vortical Mixer, Long Shroud  
(Sideline=1629 ft, SAR=4.9, MAR=0.97,  $A_{8*}=1086 \text{ in}^2$ ,  $M_n=0.32$ ,  $V_{\Pi}=357 \text{ ft/sec}$ )

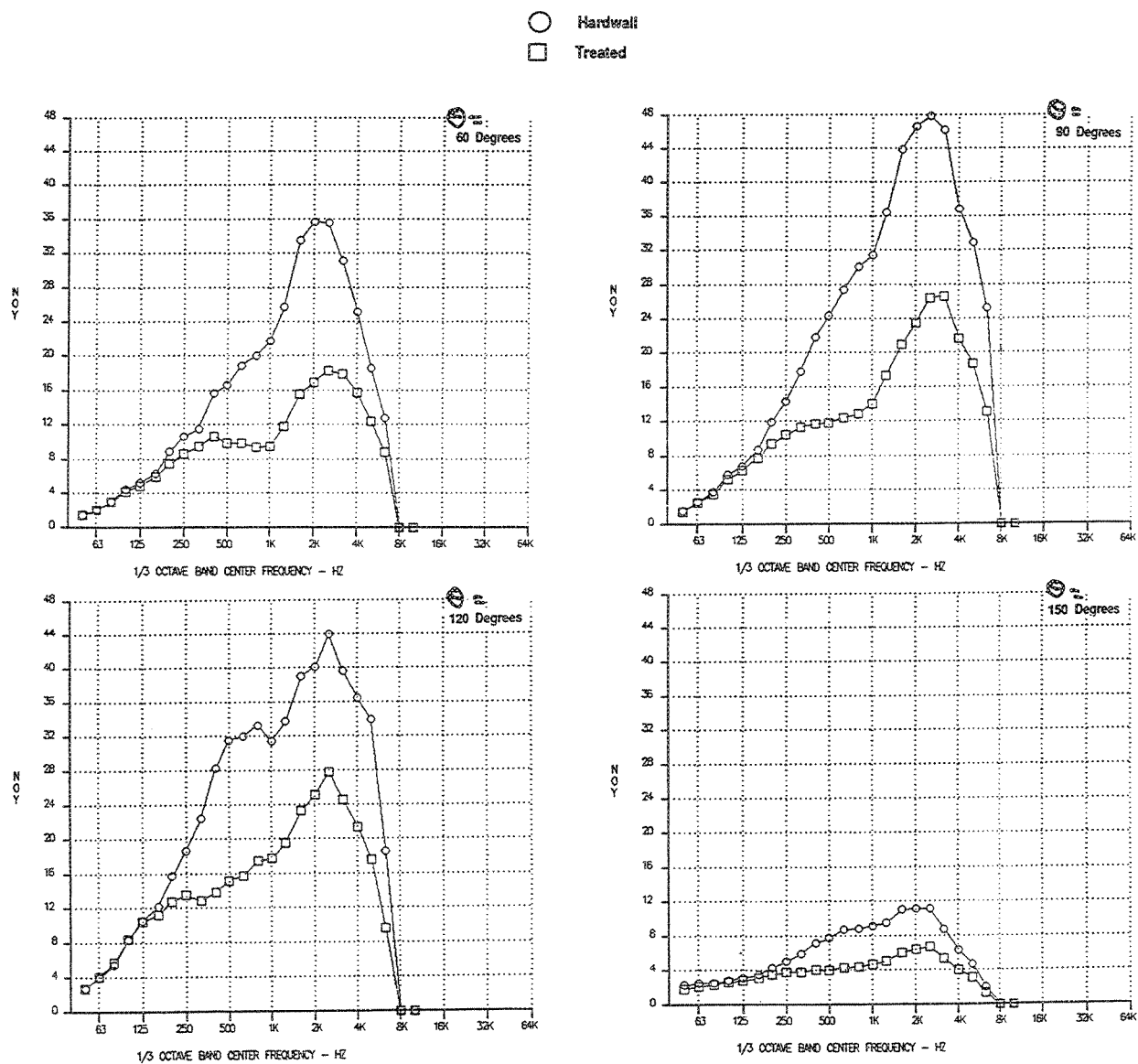


Figure 105. Liner Attenuation, NOY Versus Frequency — Ideal Unsuppressed Primary Jet Velocity=2384 ft/sec  
Vortical Mixer, Long Shroud  
(Sideline=1629 ft, SAR=4.9, MAR=0.97,  $A_8=1086 \text{ in}^2$ ,  $M_n=0.32$ ,  $V_H=357 \text{ ft/sec}$ )

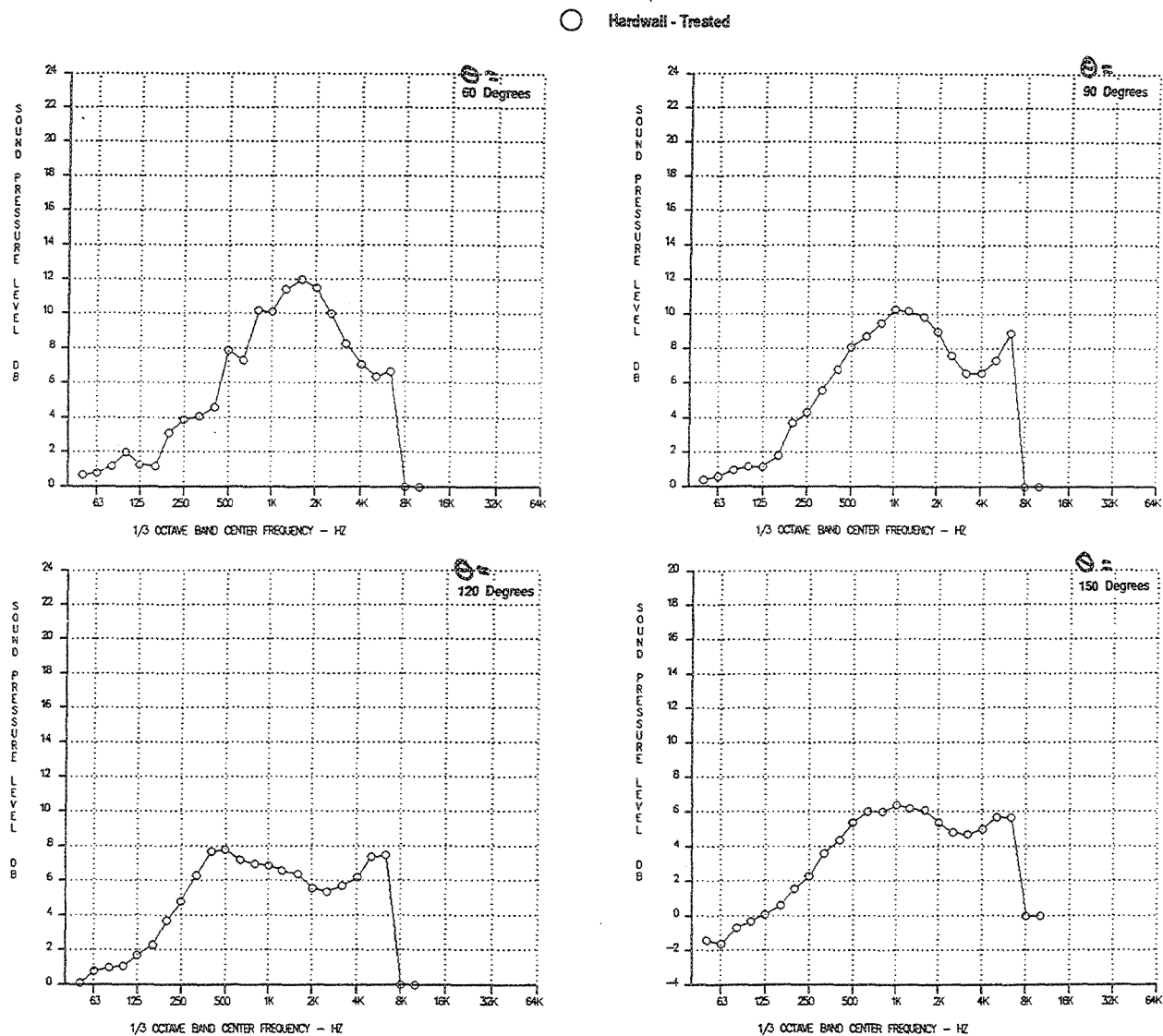


Figure 106. Liner Attenuation, SPL Versus Frequency — Ideal Unsuppressed Primary Jet Velocity=2384 ft/sec  
Vortical Mixer, Long Shroud  
(Sideline=1629 ft, SAR=4.4, MAR=0.97,  $A_8=1086 \text{ in}^2$ ,  $M_n=0.32$ ,  $V_{H1}=357 \text{ ft/sec}$ )

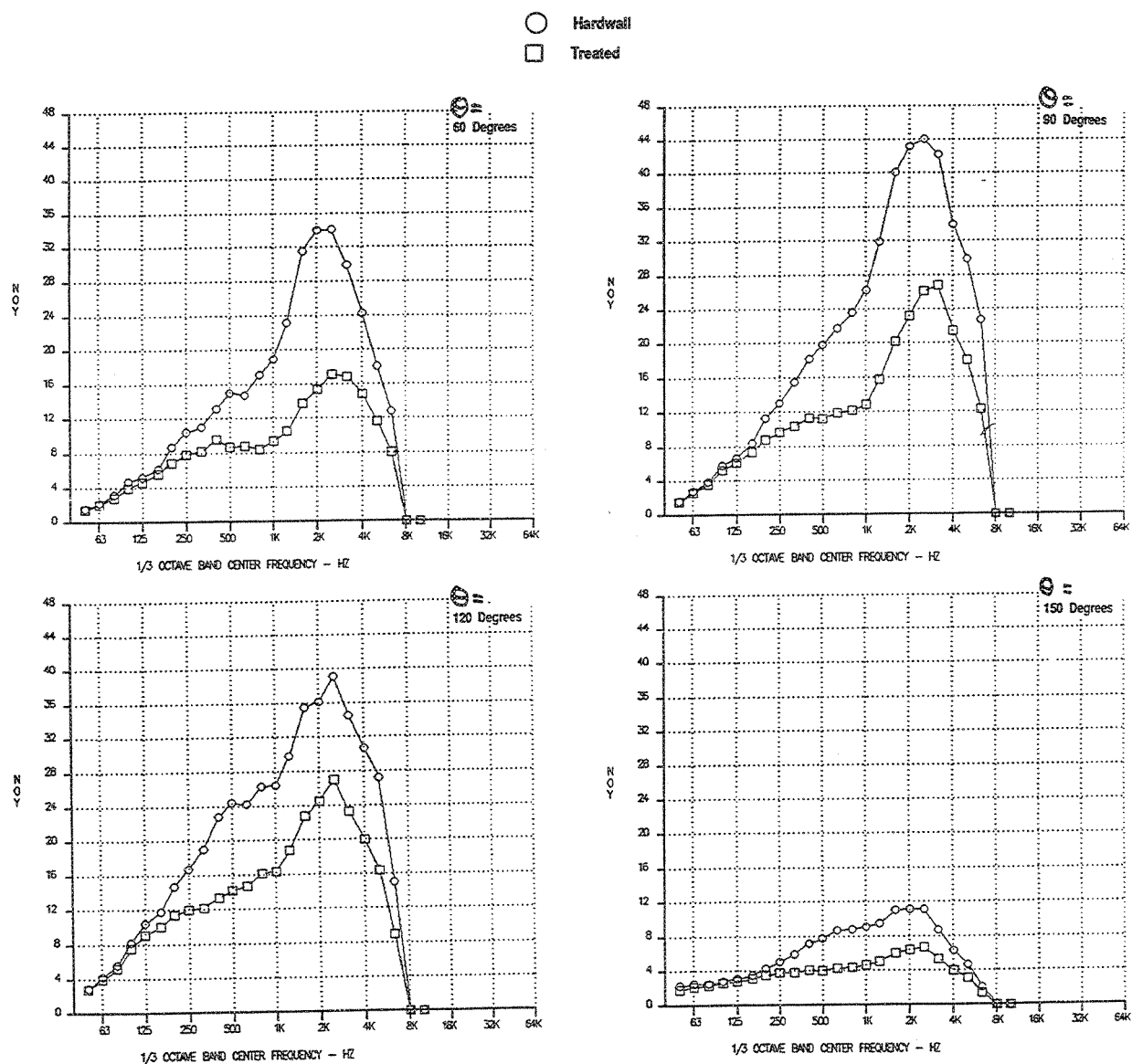


Figure 107. Liner Attenuation, NOY Versus Frequency — Ideal Unsuppressed Primary Jet Velocity=2384 ft/sec  
Vortical Mixer, Long Shroud  
(Sideline=1629 ft, SAR=4.4, MAR=0.97,  $A_{g*}=1086 \text{ in}^2$ ,  $M_n=0.32$ ,  $V_{fl}=357 \text{ ft/sec}$ )

○ Hardwall - Treated

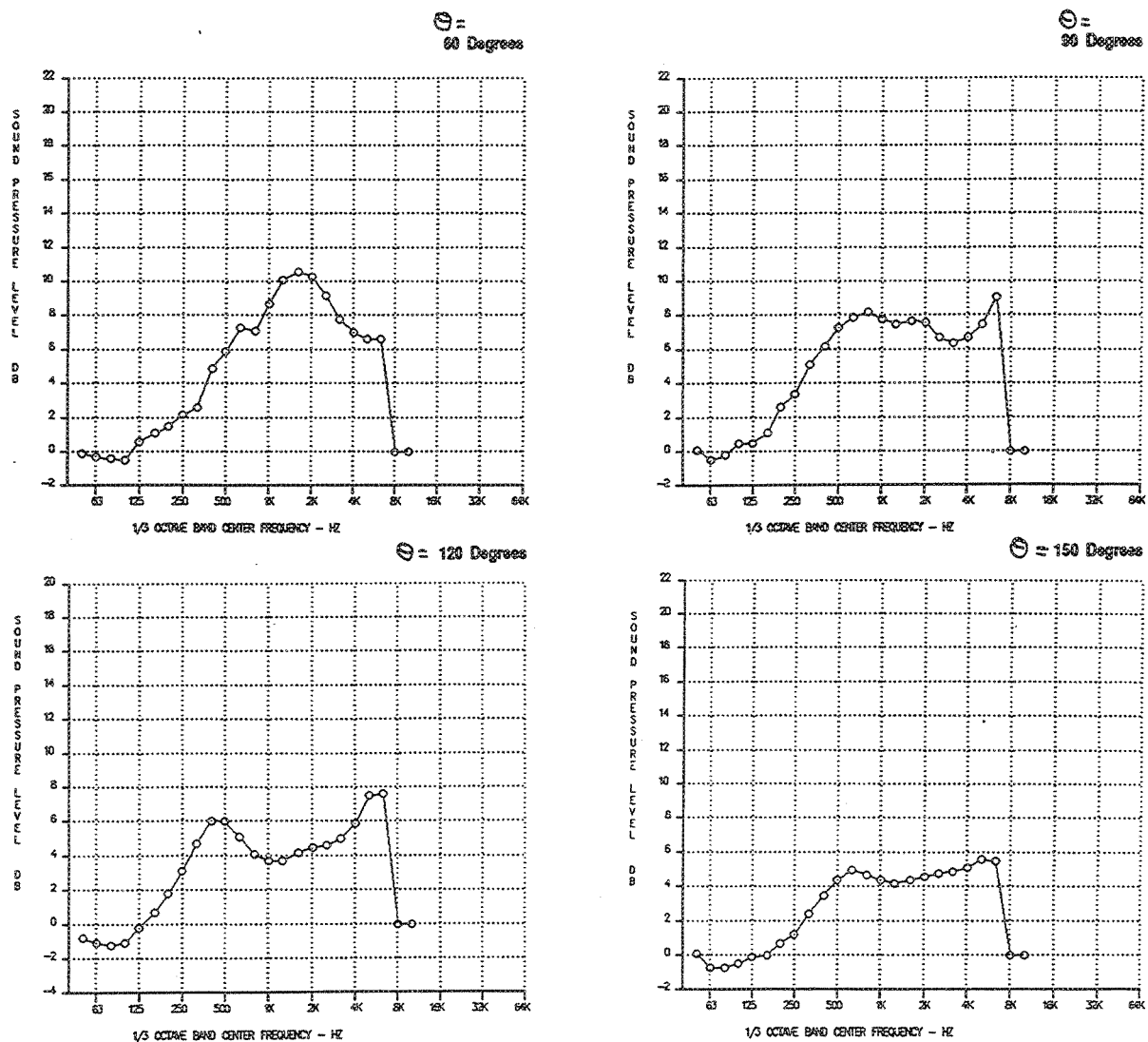


Figure 108. Liner Attenuation, SPL Versus Frequency — Ideal Unsuppressed Primary Jet Velocity=2384 ft/sec  
Axial Mixer, Long Shroud  
(Sideline=1629 ft, SAR=4.9, MAR=0.97,  $A_{g*}=1086 \text{ in}^2$ ,  $Mn=0.32$ ,  $V_{fl}=357 \text{ ft/sec}$ )

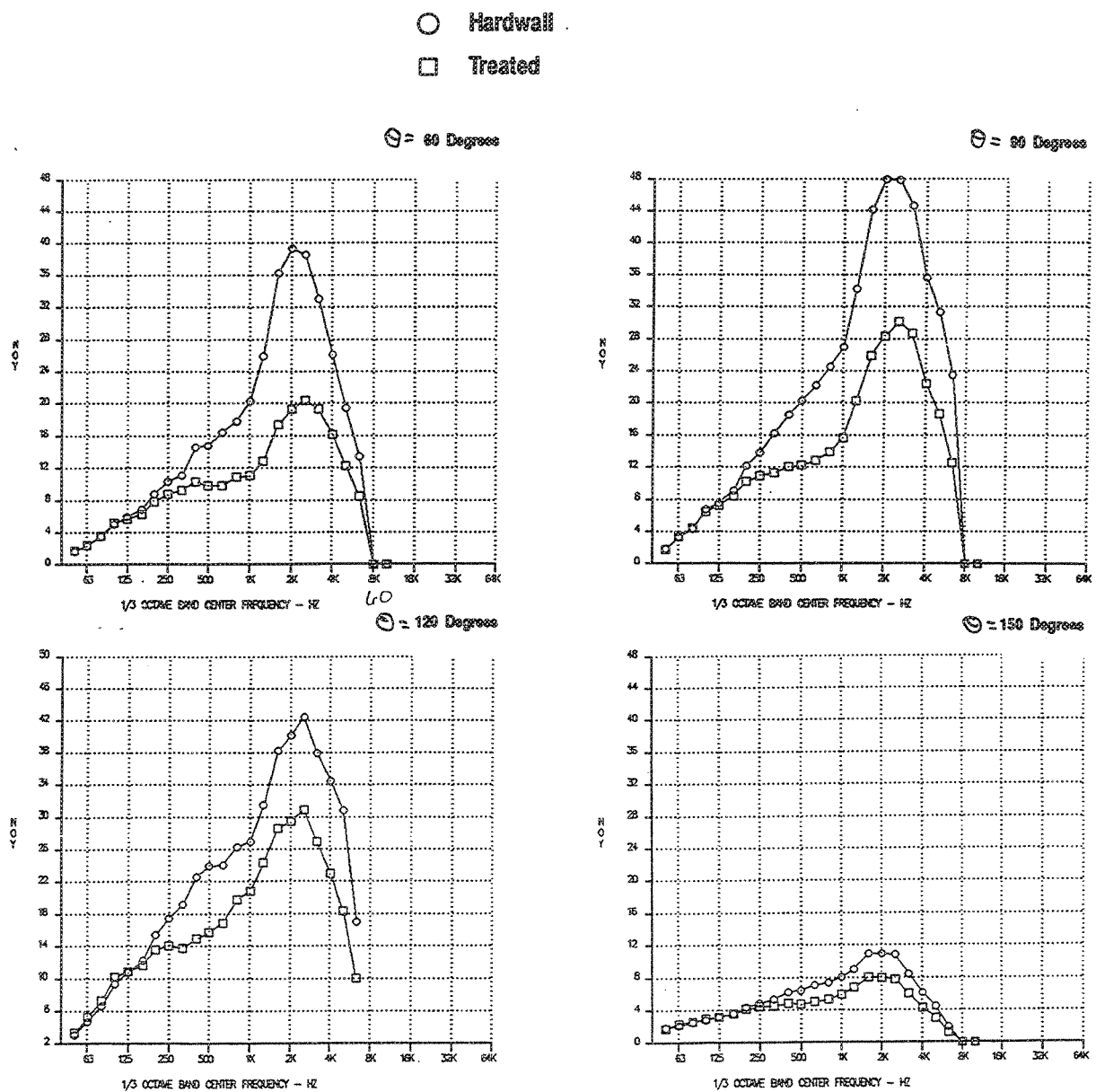
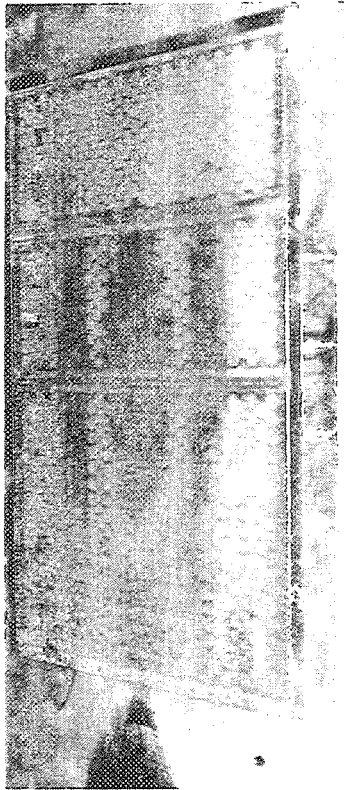
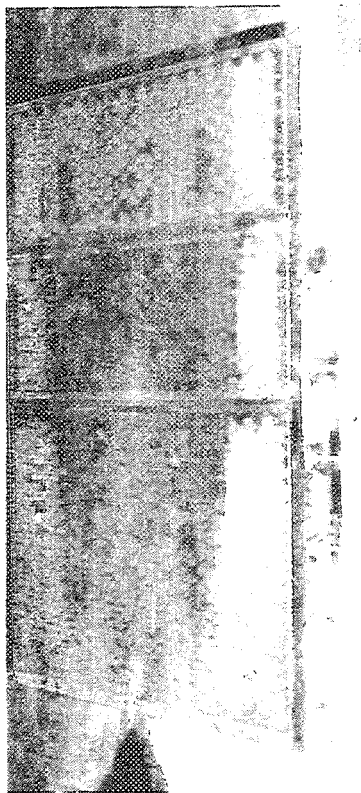


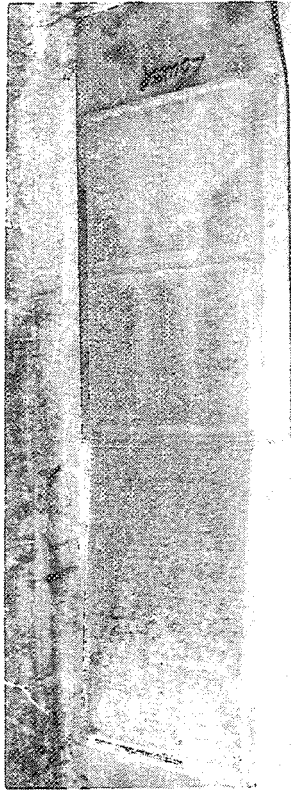
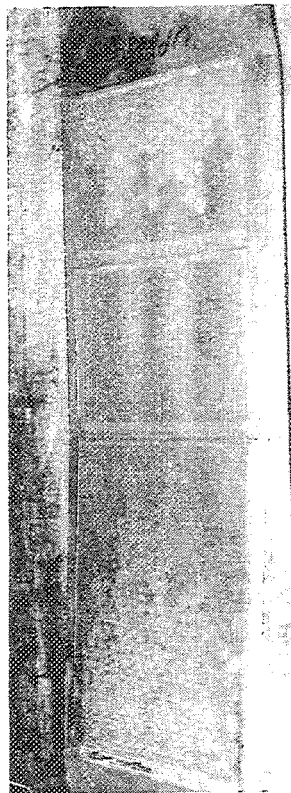
Figure 109. Liner Attenuation, NOY Versus Frequency — Ideal Unsuppressed Primary Jet Velocity=2384 ft/sec  
Axial Mixer, Long Shroud  
(Sideline=1629 ft, SAR=4.9, MAR=0.97,  $A_{g*}=1086 \text{ in}^2$ ,  $M_n=0.32$ ,  $V_{\Pi}=357 \text{ ft/sec}$ )

# PW 2D Model : Astroquartz Degradation

## Side Panels



## Upper/Lower Panels



Flow ⇒

*Figure 110. Degradation*

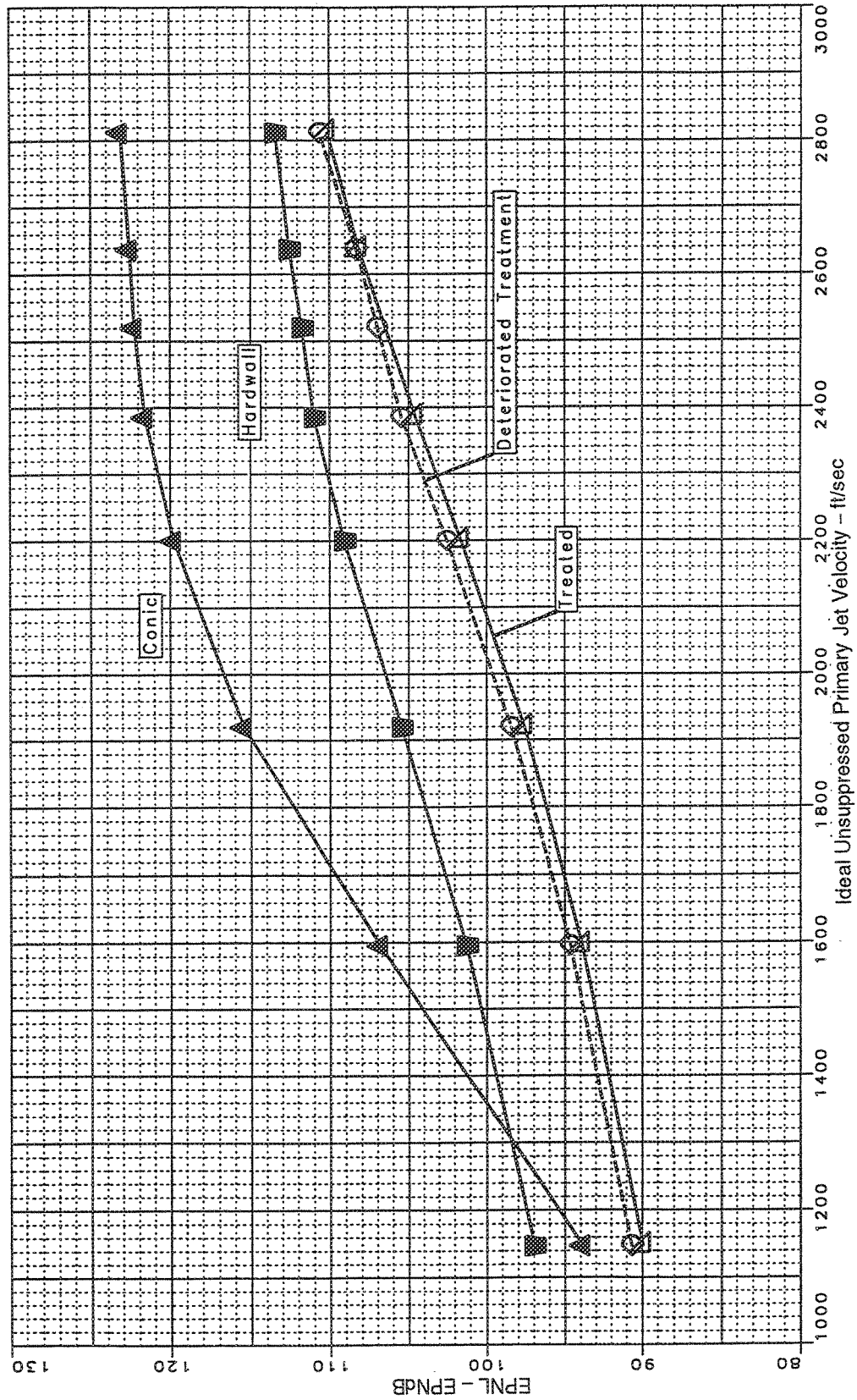


Figure 111. Effect of Treatment on Sideline Noise, Vortical Mixer, Long Shroud  
(Sideline=1629 ft, SAR=4.4, MAR=0.97,  $A_{g*}=1086 \text{ in}^2$ , Static)



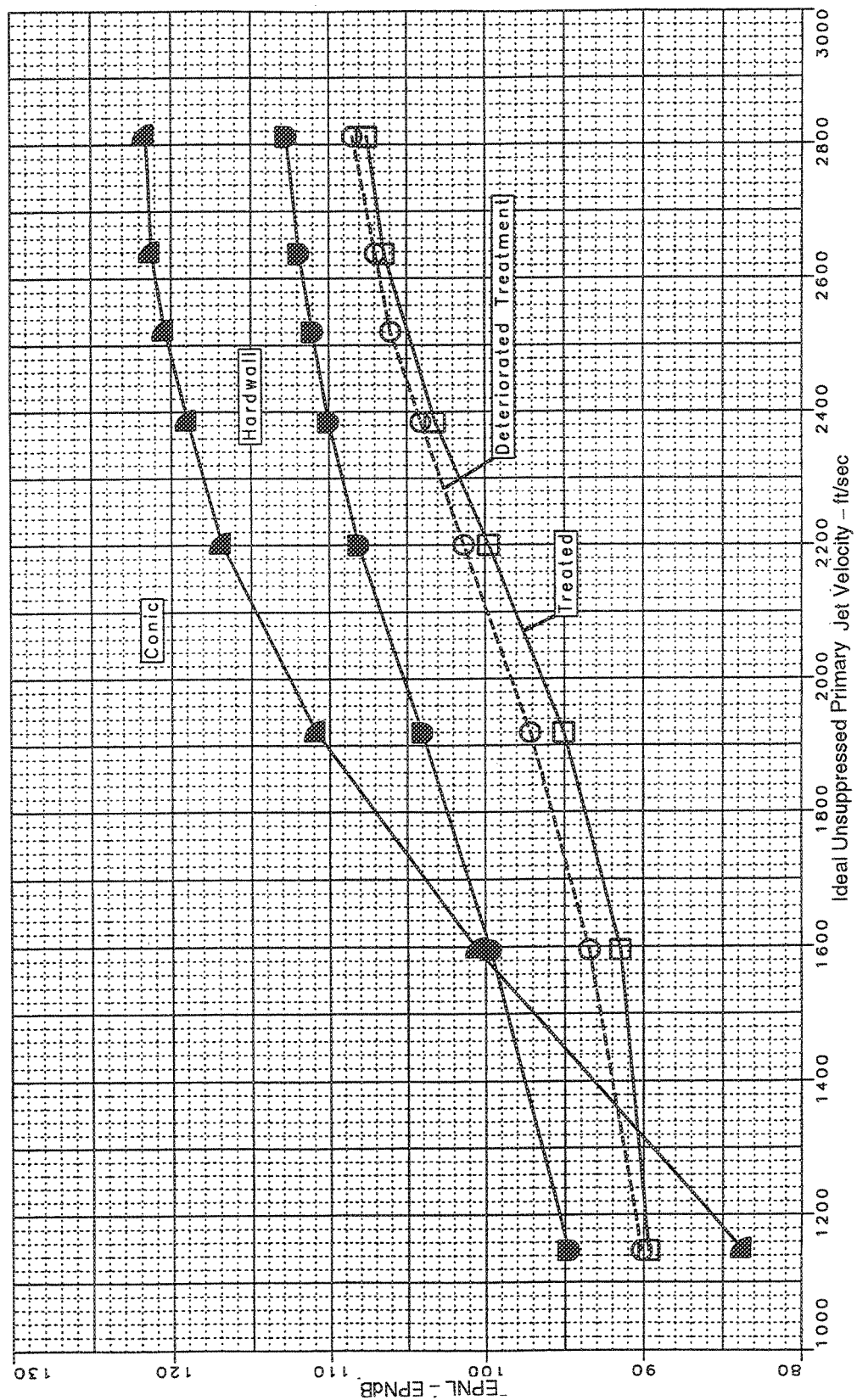


Figure 112. Effect of Treatment on Sideline Noise, Vortical Mixer, Long Shroud  
 (Sideline=1629 ft, SAR=4.4, MAR=0.97,  $A_{g*}=1086 \text{ in}^2$ ,  $M_n=0.32$ ,  $V_n=357 \text{ ft/sec}$ )

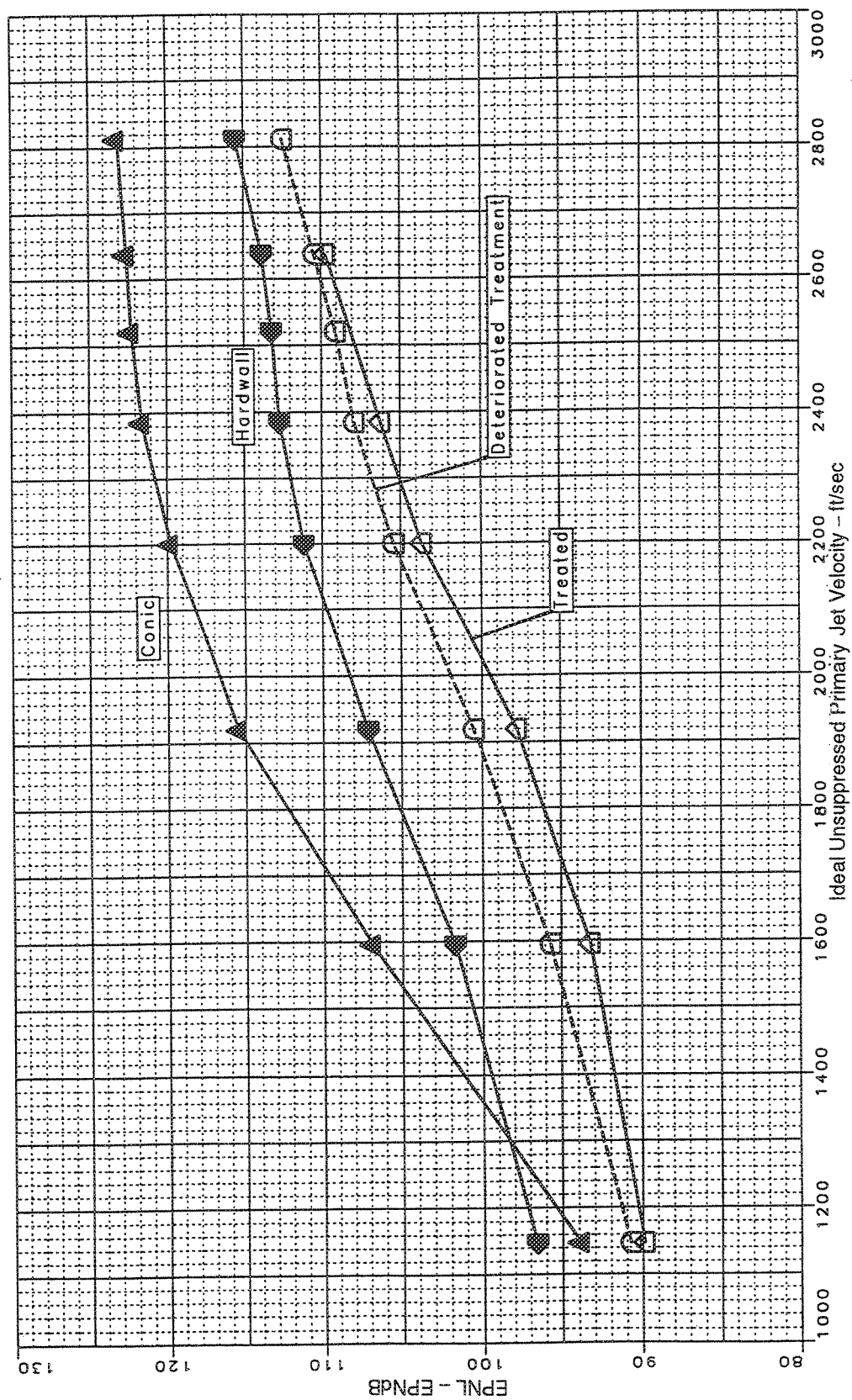


Figure 113. Effect of Treatment on Sideline Noise, Vortical Mixer, Long Shroud  
 (Sideline=1629 ft, SAR=4.4, MAR=1.19,  $A_{g*}=1086 \text{ in}^2$ , Static)

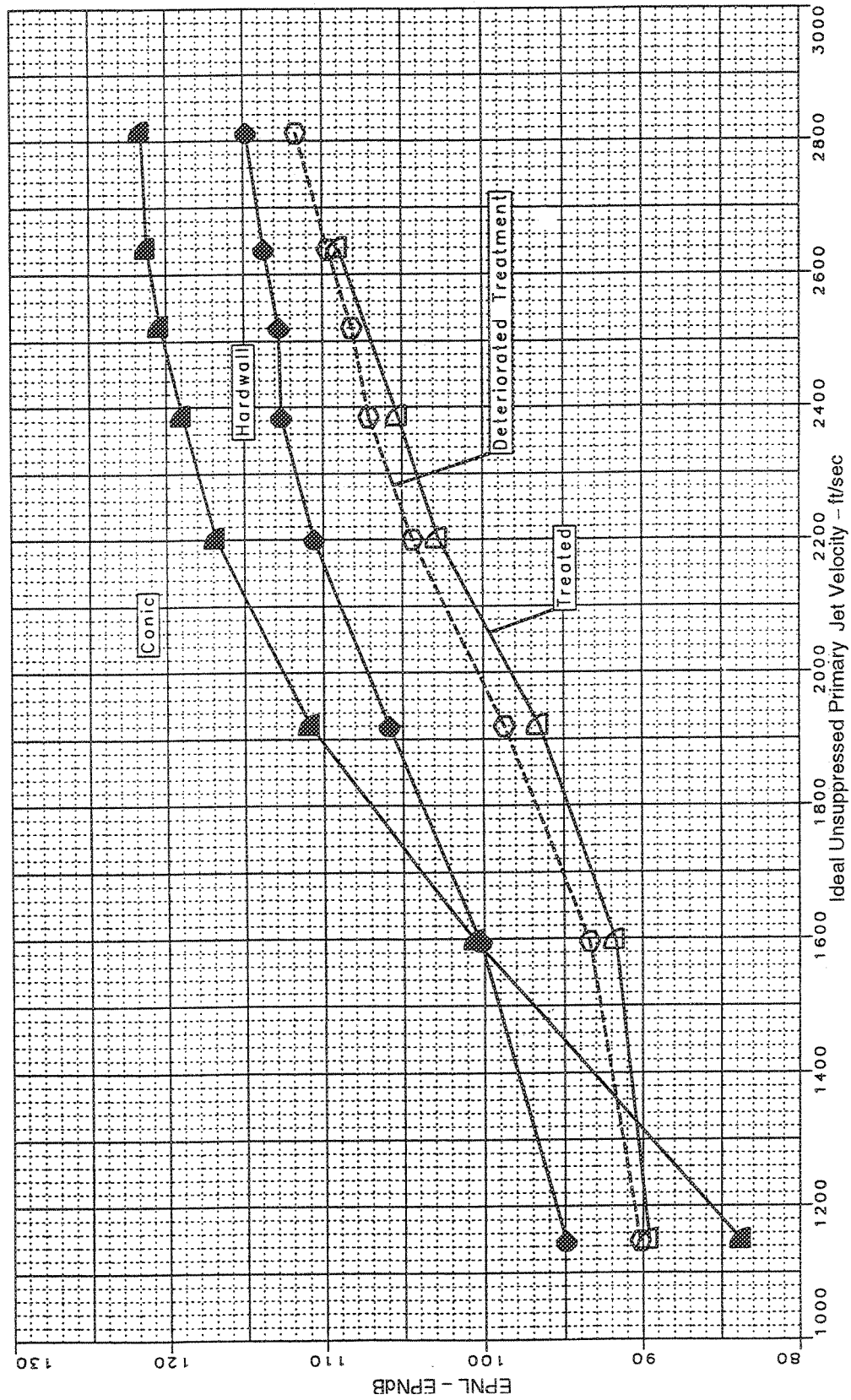


Figure 114. Effect of Treatment on Sideline Noise, Vortical Mixer, Long Shroud  
(Sideline=1629 ft, SAR=4.4, MAR=0.97,  $A_{g*}=1086 \text{ in}^2$ ,  $M_n=0.32$ ,  $V_{\eta}=357 \text{ ft/sec}$ )

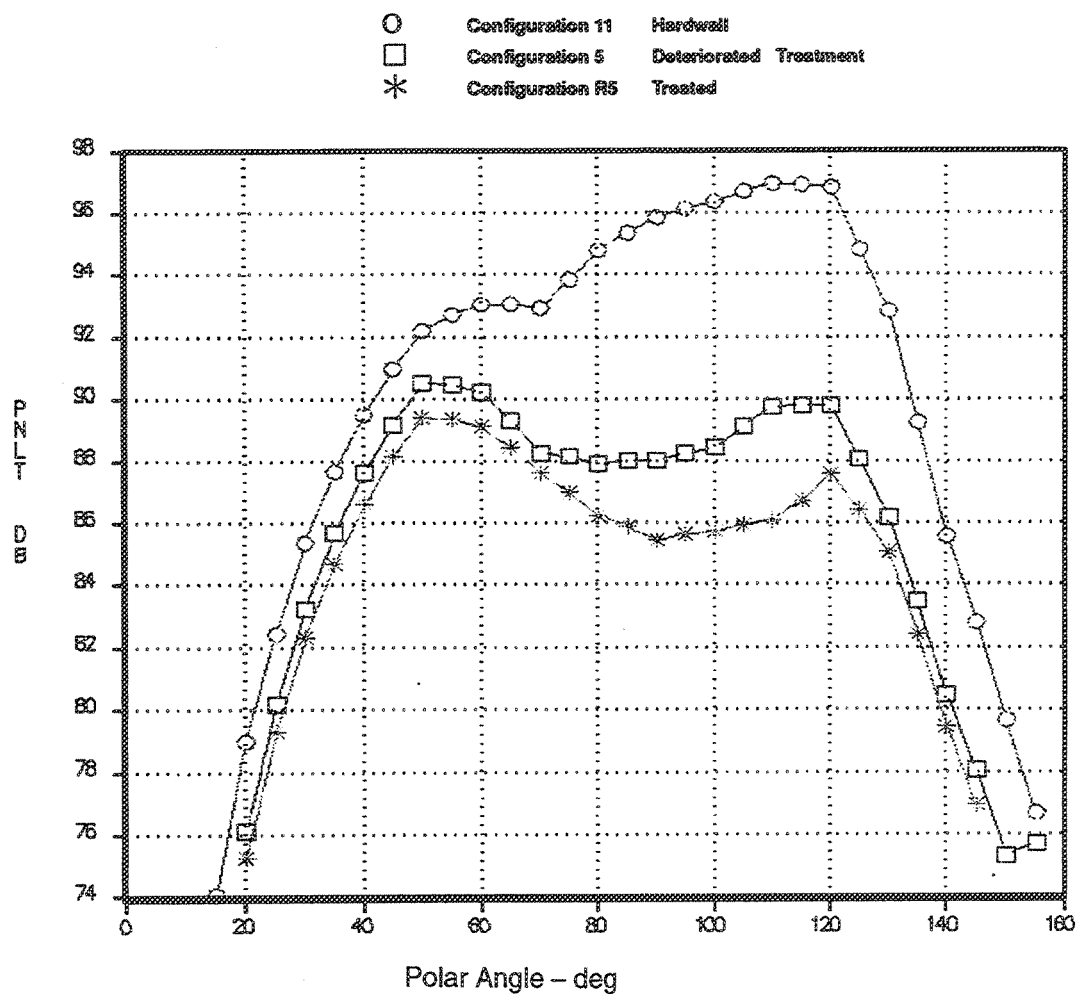


Figure 115. Effects of Deteriorated Treatment on Noise, PNLT Versus Angle  
 — Ideal Unsuppressed Primary Jet Velocity=1595 ft/sec, Vortical Mixer, Long Shroud  
 (Sideline=1629 ft, SAR=4.4, MAR=0.97,  $A_{g*}=1086 \text{ in}^2$ ,  $M_n=0.32$ ,  $V_{fl}=357 \text{ ft/sec}$ )

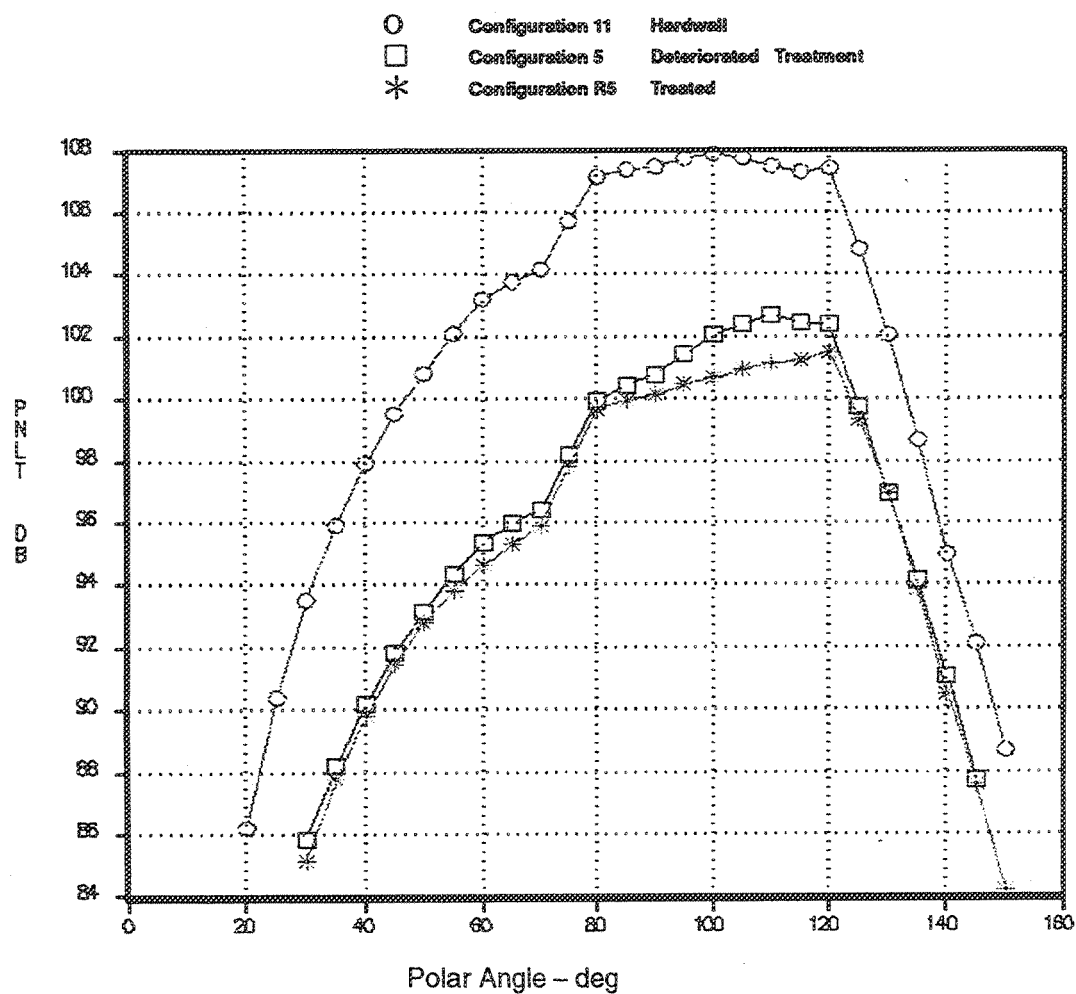


Figure 116. Effects of Deteriorated Treatment on Noise, PNLT Versus Angle  
 — Ideal Unsuppressed Primary Jet Velocity=2384 ft/sec, Vortical Mixer, Long Shroud  
 (Sideline=1629 ft, SAR=4.4, MAR=0.97,  $A_{g*}=1086 \text{ in}^2$ ,  $M_n=0.32$ ,  $V_{fl}=357 \text{ ft/sec}$ )

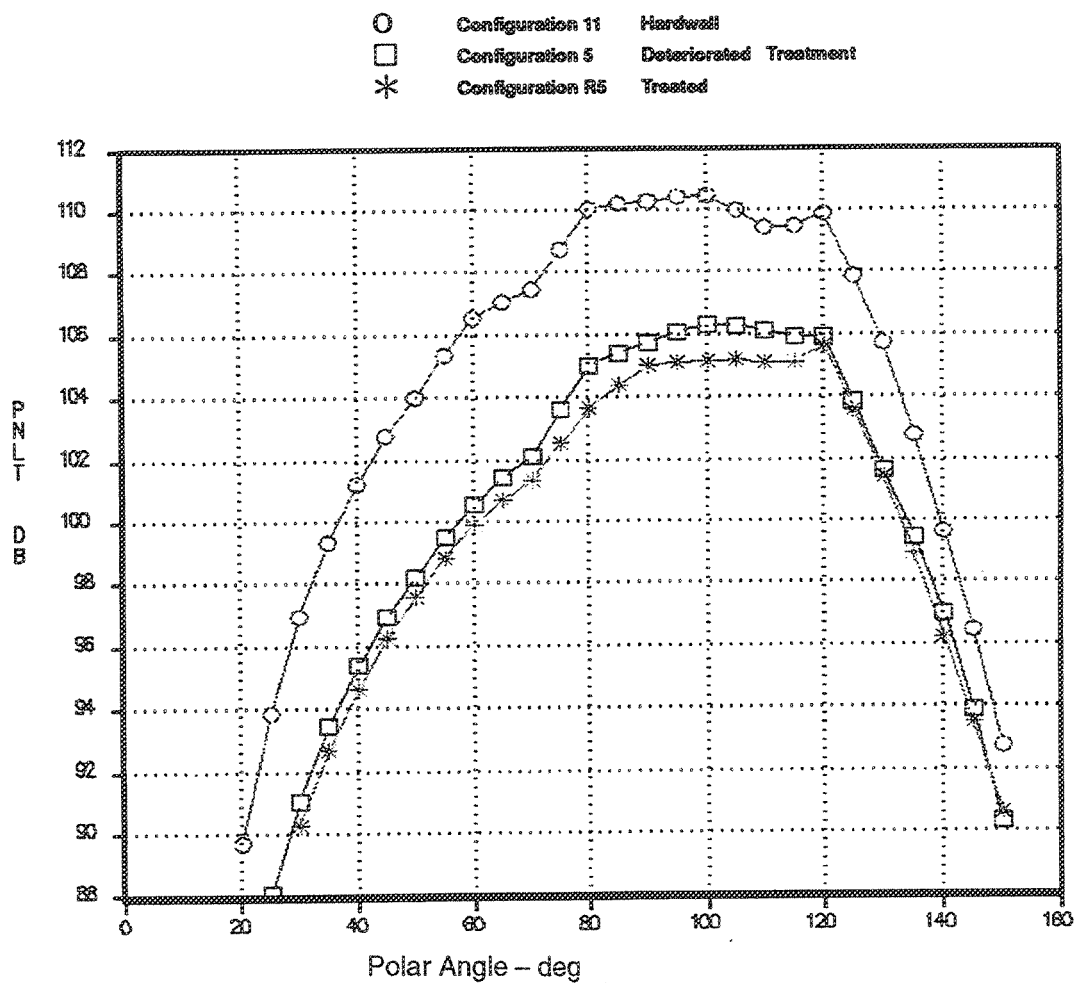


Figure 117. Effects of Deteriorated Treatment on Noise, PNL Versus Angle  
 — Ideal Unsuppressed Primary Jet Velocity=2812 ft/sec, Vortical Mixer, Long Shroud  
 (Sideline=1629 ft, SAR=4.4, MAR=0.97,  $A_{g*}=1086 \text{ in}^2$ ,  $M_n=0.32$ ,  $V_{\Pi}=357 \text{ ft/sec}$ )

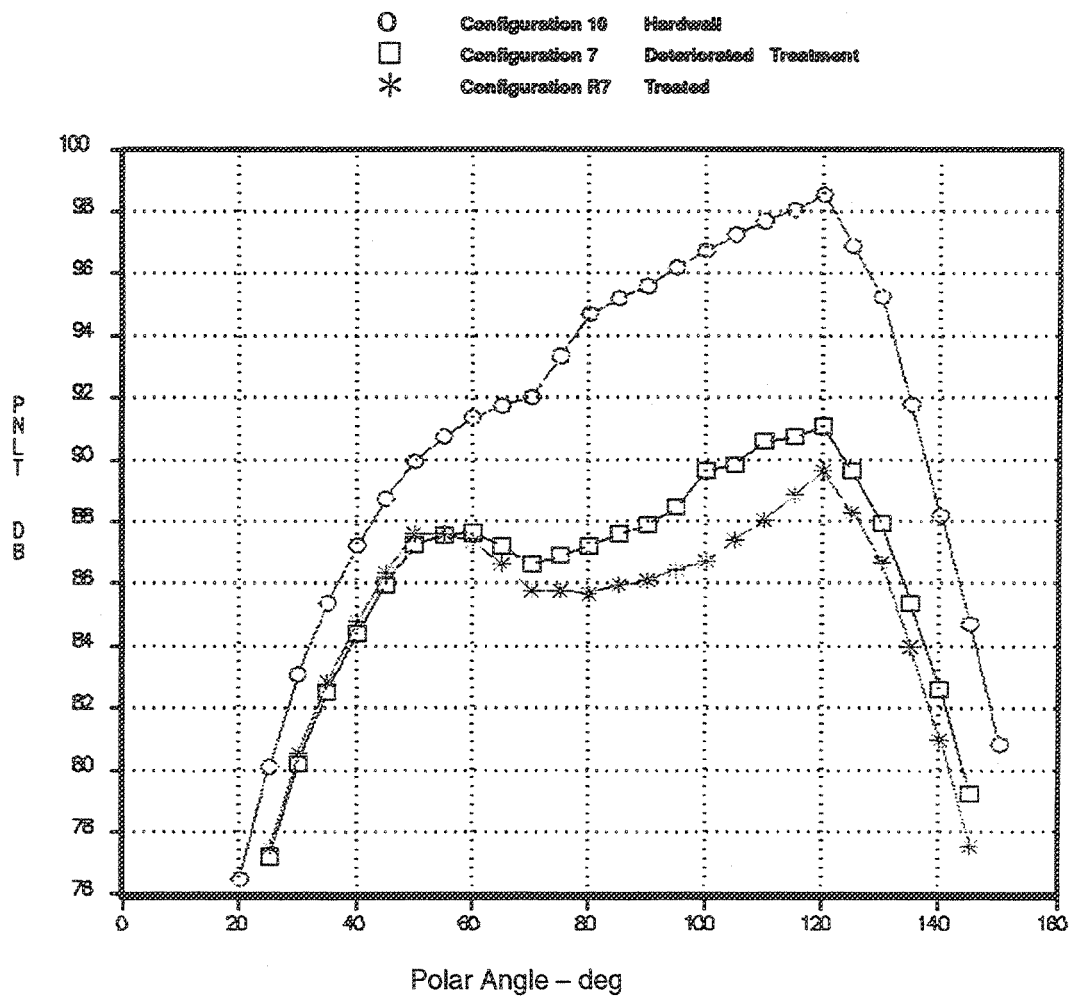


Figure 118. Effects of Deteriorated Treatment on Noise, PNLT Versus Angle  
 — Ideal Unsuppressed Primary Jet Velocity=1595 ft/sec, Vortical Mixer, Long Shroud  
 (Sideline=1629 ft, SAR=4.4, MAR=1.19,  $A_{g*}=1086 \text{ in}^2$ ,  $M_n=0.32$ ,  $V_{fl}=357 \text{ ft/sec}$ )

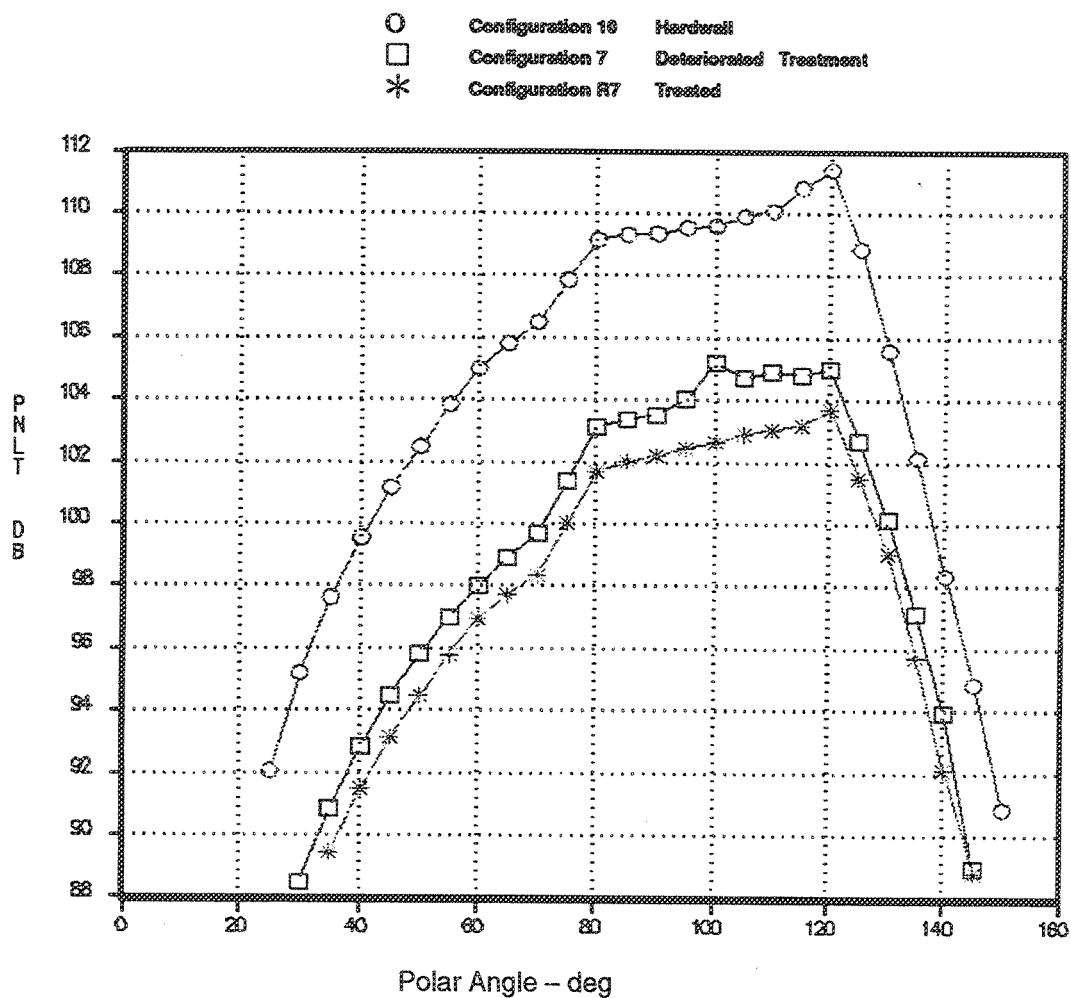


Figure 119. Effects of Deteriorated Treatment on Noise, PNLT Versus Angle  
 — Ideal Unsuppressed Primary Jet Velocity=2384 ft/sec, Vortical Mixer, Long Shroud  
 (Sideline=1629 ft, SAR=4.4, MAR=1.19,  $A_{g*}=1086 \text{ in}^2$ ,  $M_n=0.32$ ,  $V_{fl}=357 \text{ ft/sec}$ )



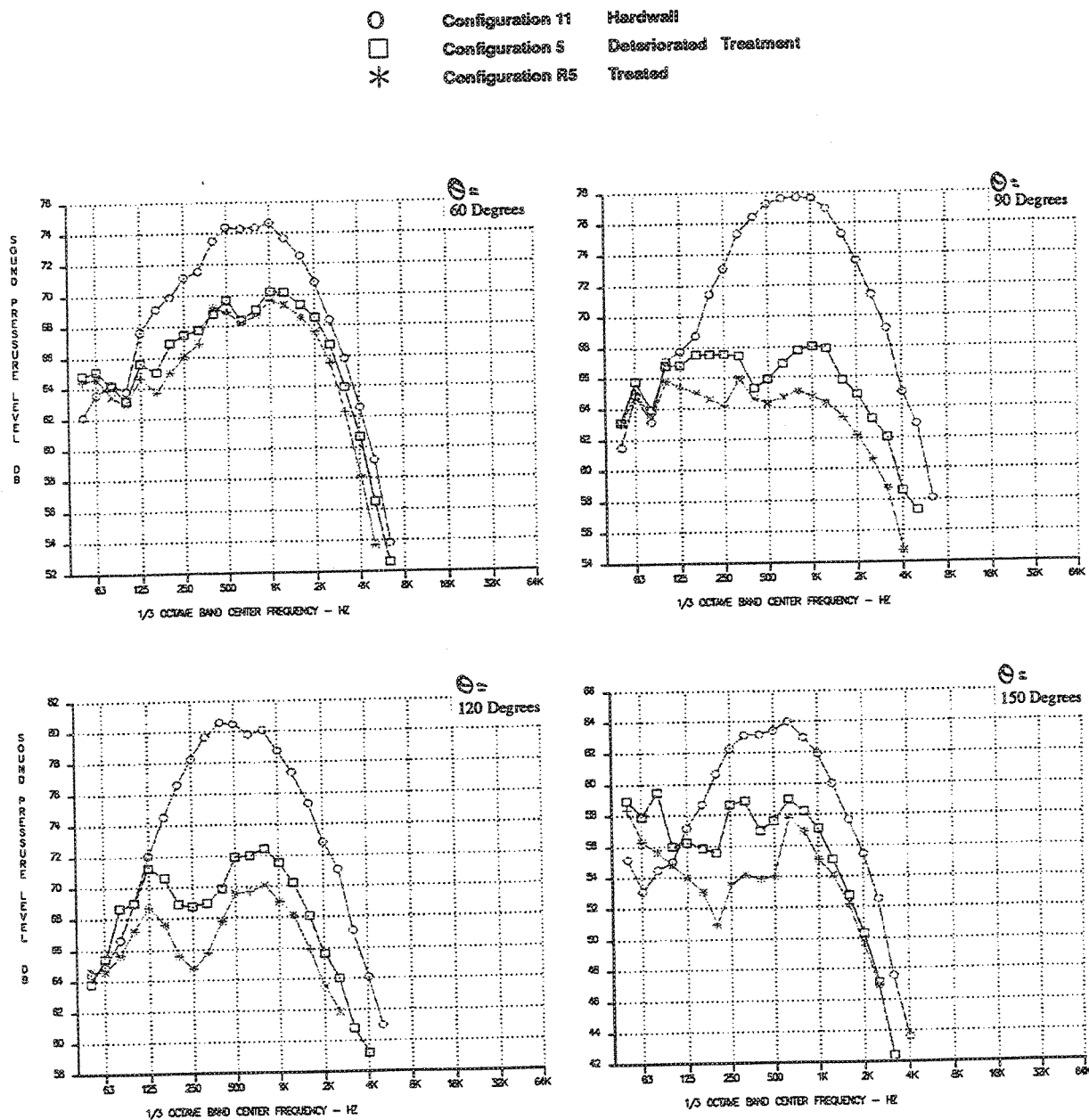


Figure 120. Effects of Deteriorated Treatment on Noise, SPL Versus Frequency  
 — Ideal Unsuppressed Primary Jet Velocity=1595 ft/sec, Vortical Mixer, Long Shroud  
 (Sideline=1629 ft, SAR=4.4, MAR=0.97,  $A_{g*}=1086 \text{ in}^2$ ,  $M_n=0.32$ ,  $V_{\Pi}=357 \text{ ft/sec}$ )

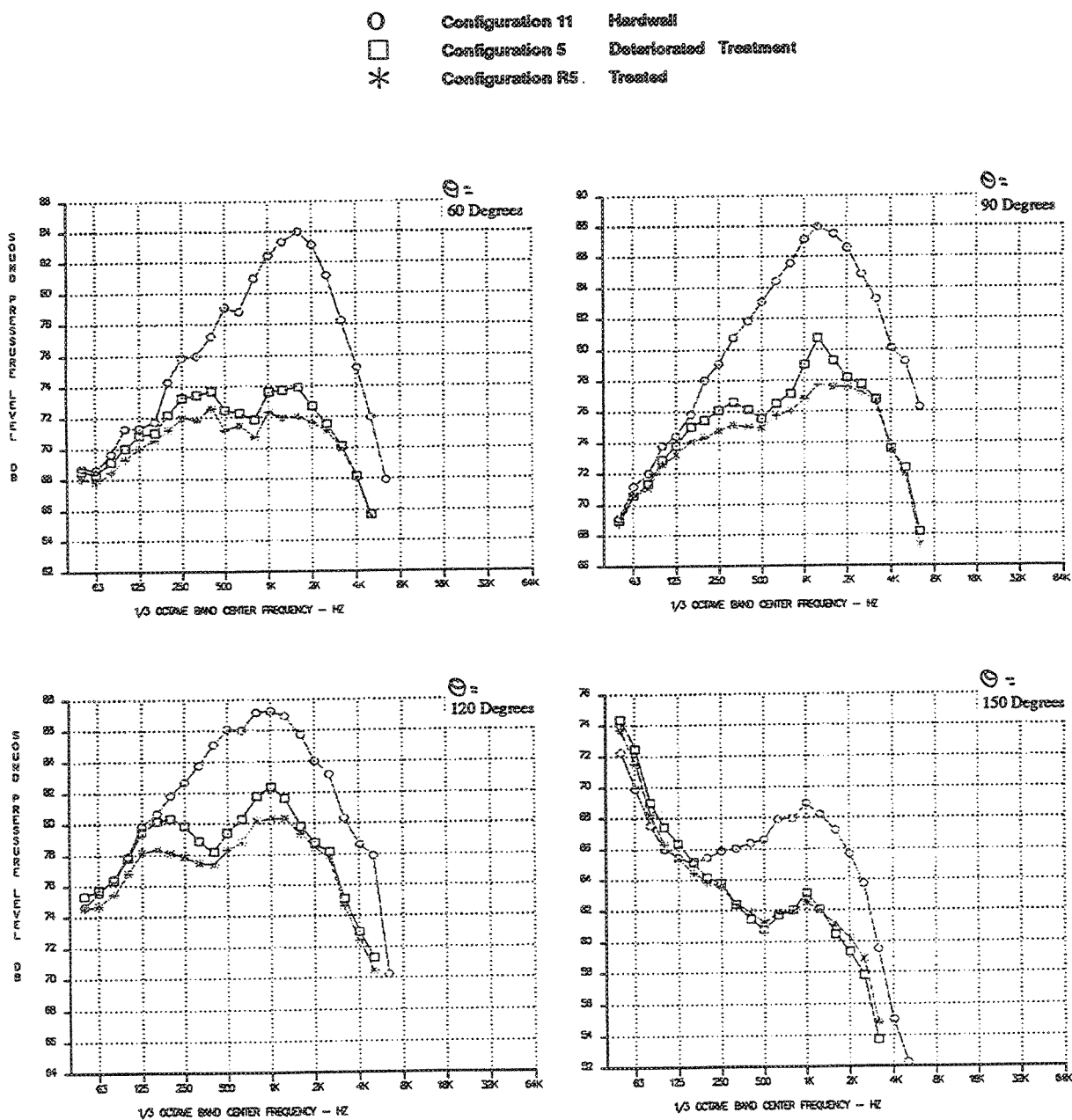


Figure 121. Effects of Deteriorated Treatment on Noise, SPL Versus Frequency  
 — Ideal Unsuppressed Primary Jet Velocity=2384 ft/sec, Vortical Mixer, Long Shroud  
 (Sideline=1629 ft, SAR=4.4, MAR=0.97,  $A_{g*}=1086 \text{ in}^2$ ,  $M_n=0.32$ ,  $V_{fl}=357 \text{ ft/sec}$ )

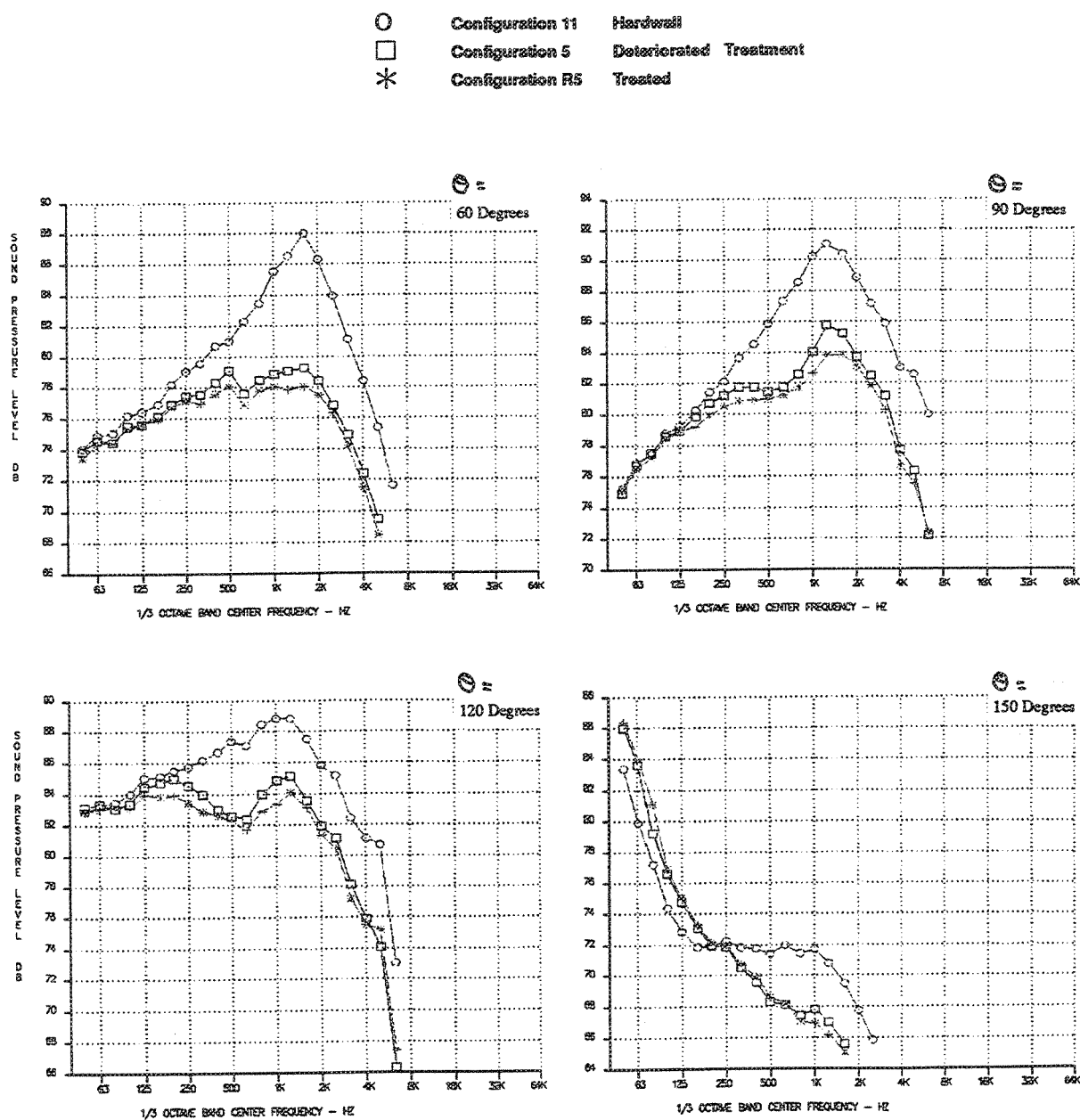


Figure 122. Effects of Deteriorated Treatment on Noise, SPL Versus Frequency  
 — Ideal Unsuppressed Primary Jet Velocity=2812 ft/sec, Vortical Mixer, Long Shroud  
 (Sideline=1629 ft, SAR=4.4, MAR=0.97,  $A_{g*}=1086 \text{ in}^2$ ,  $M_n=0.32$ ,  $V_{H}=357 \text{ ft/sec}$ )

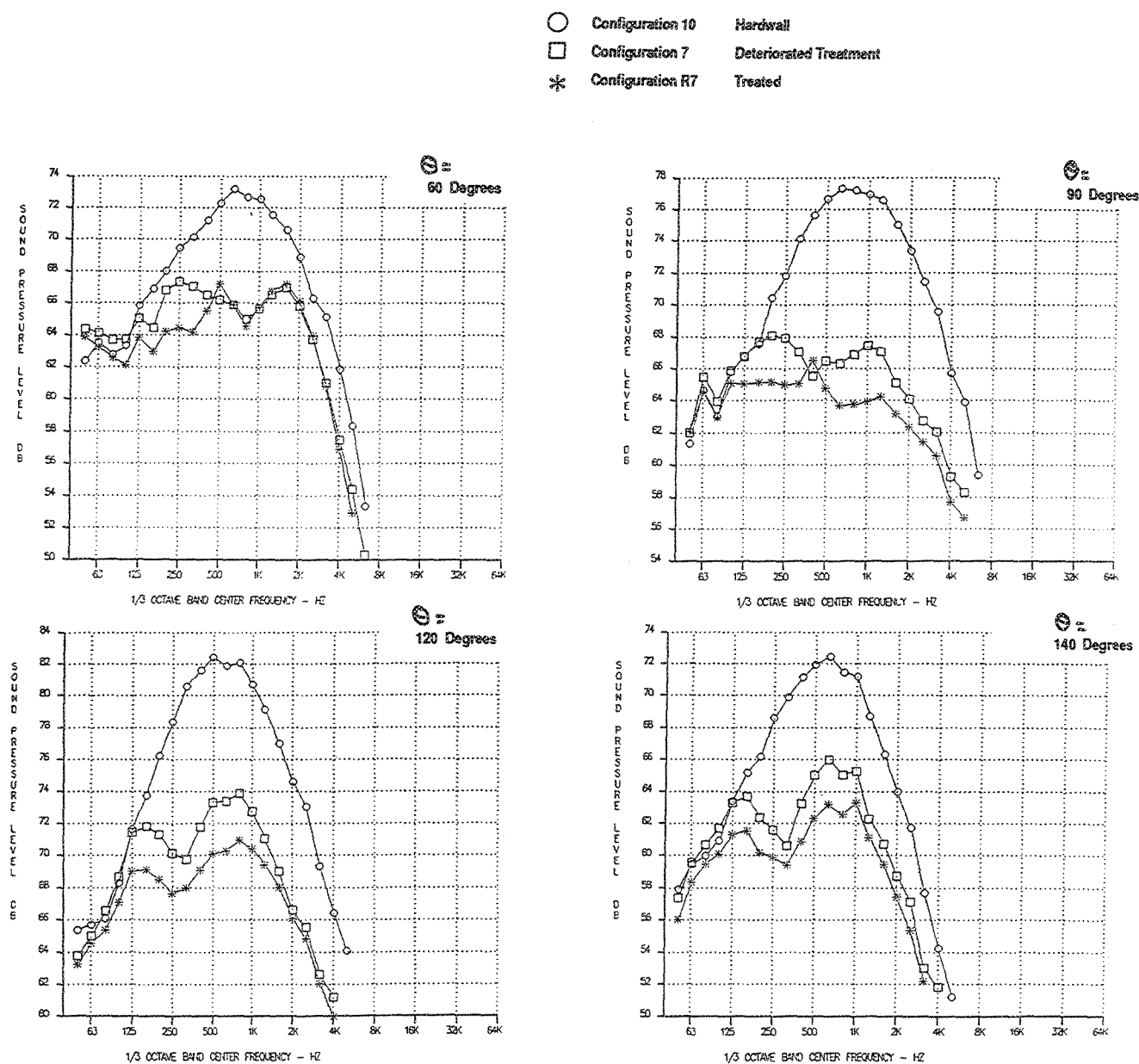


Figure 123. Effects of Deteriorated Treatment on Noise, SPL Versus Frequency  
 — Ideal Unsuppressed Primary Jet Velocity=1595 ft/sec, Vortical Mixer, Long Shroud  
 (Sideline=1629 ft, SAR=4.4, MAR=1.19,  $A_{g*}=1086 \text{ in}^2$ ,  $M_n=0.32$ ,  $V_{fl}=357 \text{ ft/sec}$ )

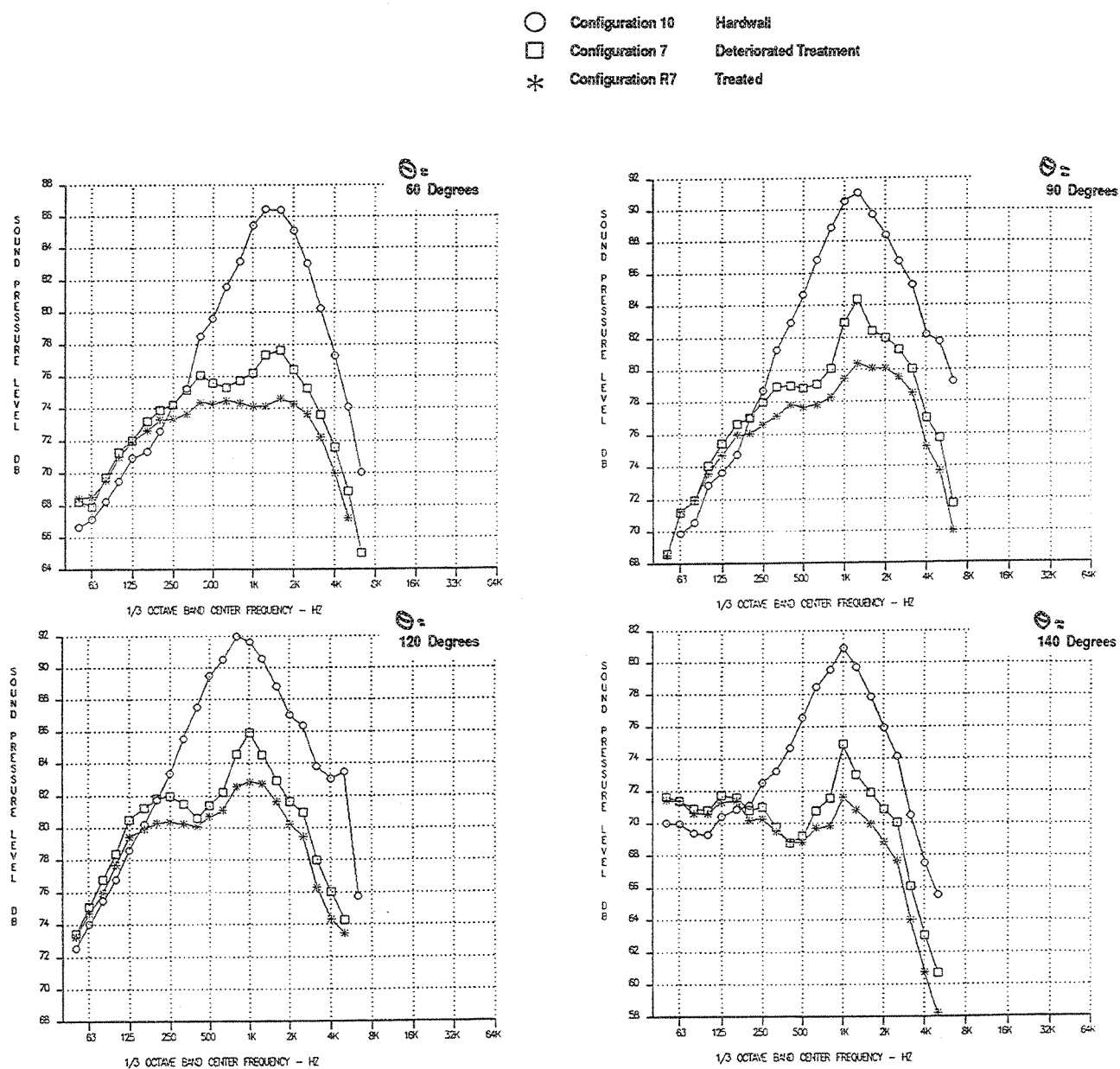


Figure 124. Effects of Deteriorated Treatment on Noise, SPL Versus Frequency  
 — Ideal Unsuppressed Primary Jet Velocity=2384 ft/sec, Vortical Mixer, Long Shroud  
 (Sideline=1629 ft, SAR=4.4, MAR=1.19,  $A_{g*}=1086 \text{ in}^2$ ,  $M_n=0.32$ ,  $V_{\bar{n}}=357 \text{ ft/sec}$ )

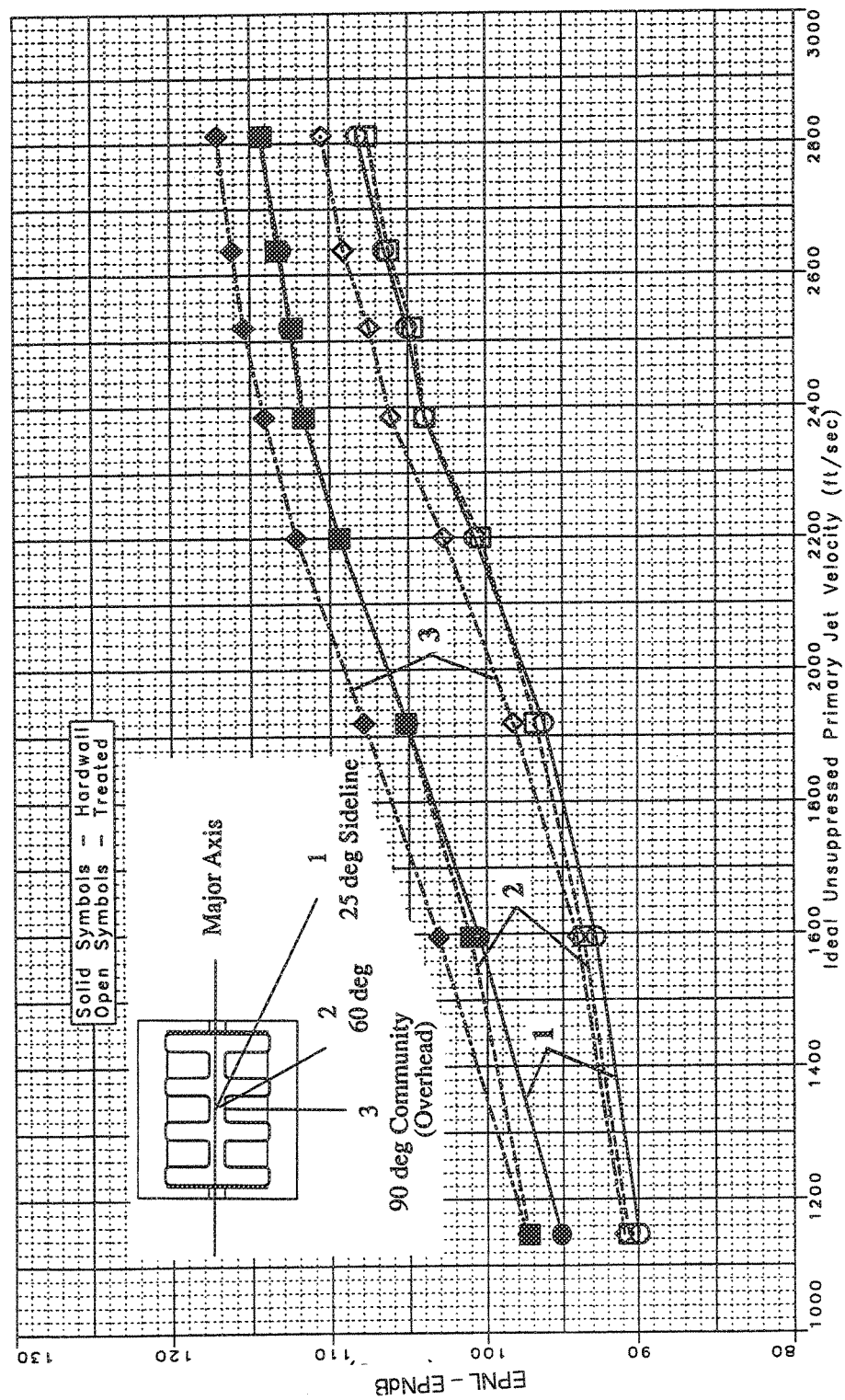


Figure 125. Noise Variation With Azimuthal Position, Vortical Mixer, Long Shroud  
( $SAR=4.9$ ,  $MAR=0.97$ ,  $A_{g*}=1086 \text{ in}^2$ ,  $Mn=0.32$ ,  $V_{\eta}=357 \text{ ft/sec}$ )

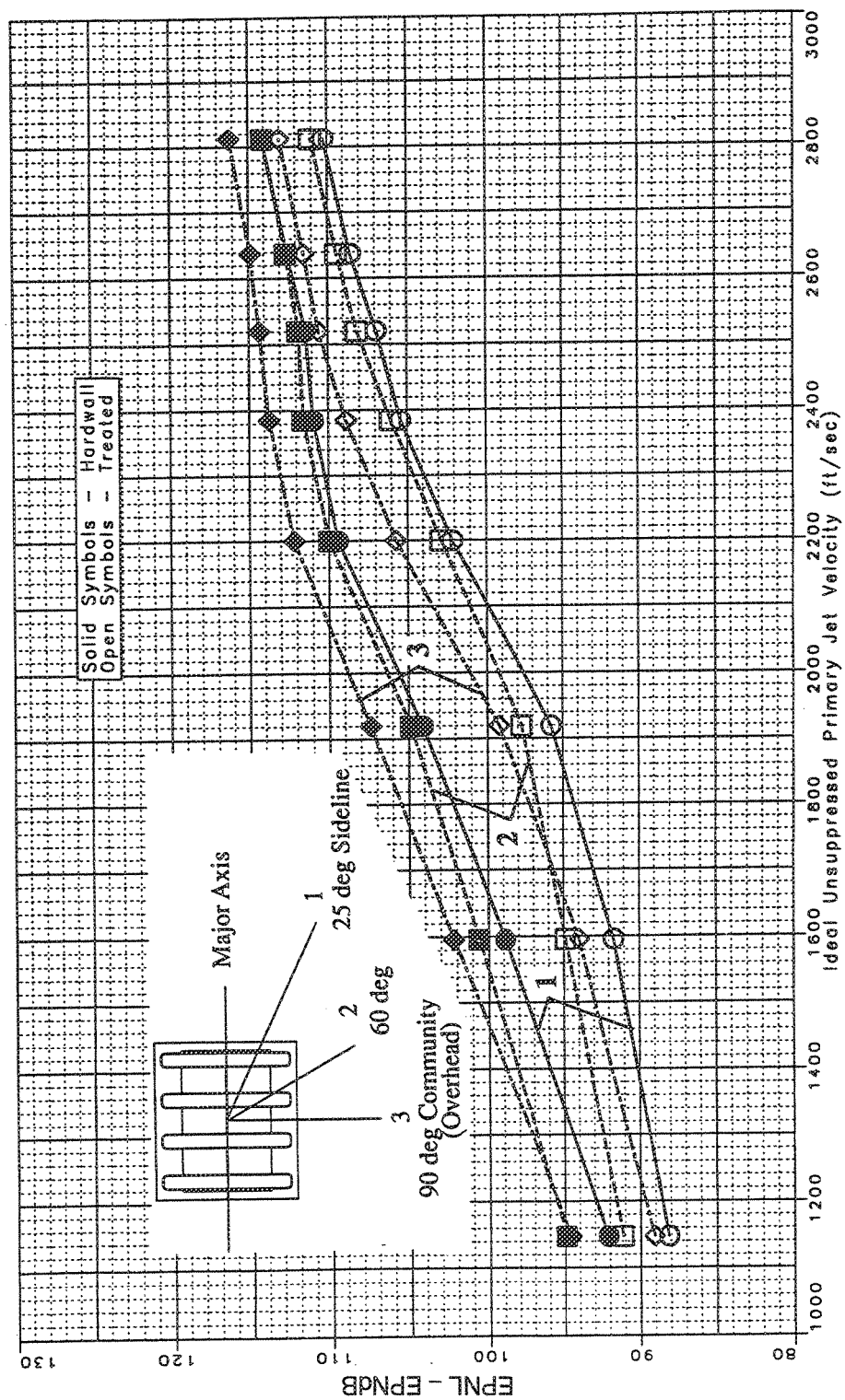


Figure 126. Noise Variation With Azimuthal Position, Axial Mixer, Long Shroud  
 (SAR=4.9, MAR=0.97,  $A_{g*}=1086 \text{ in}^2$ ,  $Mn=0.32$ ,  $V_{\eta}=357 \text{ ft/sec}$ )

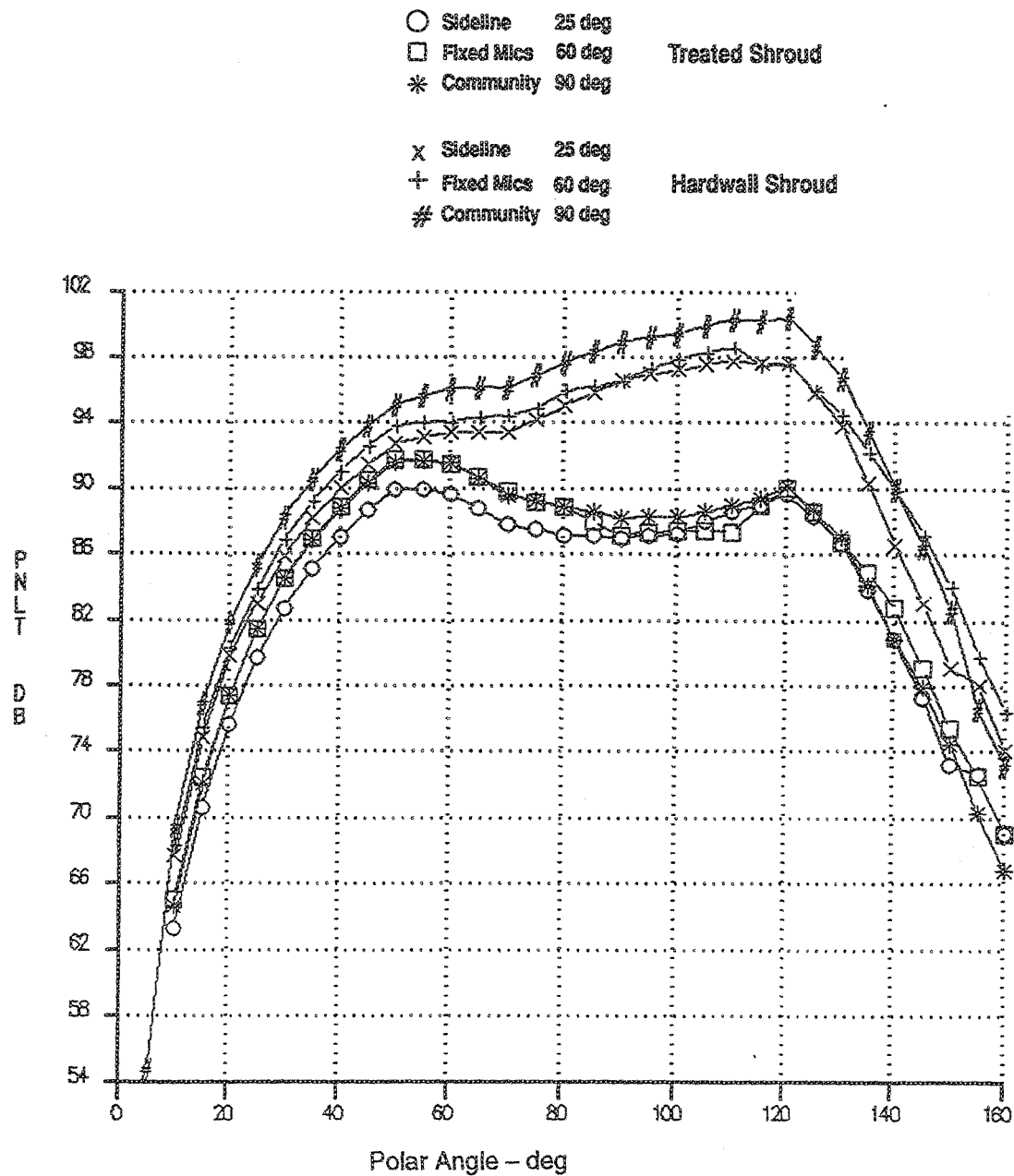


Figure 127. Azimuthal Variation of Noise Levels, PNL Versus Angle  
 — Ideal Unsuppressed Primary Jet Velocity=1595 ft/sec, Vortical Mixer  
 (Sideline=1629 ft, SAR=4.9, MAR=0.97,  $A_{g*}=1086 \text{ in}^2$ ,  $Mn=0.32$ ,  $V_{fl}=357 \text{ ft/sec}$ )



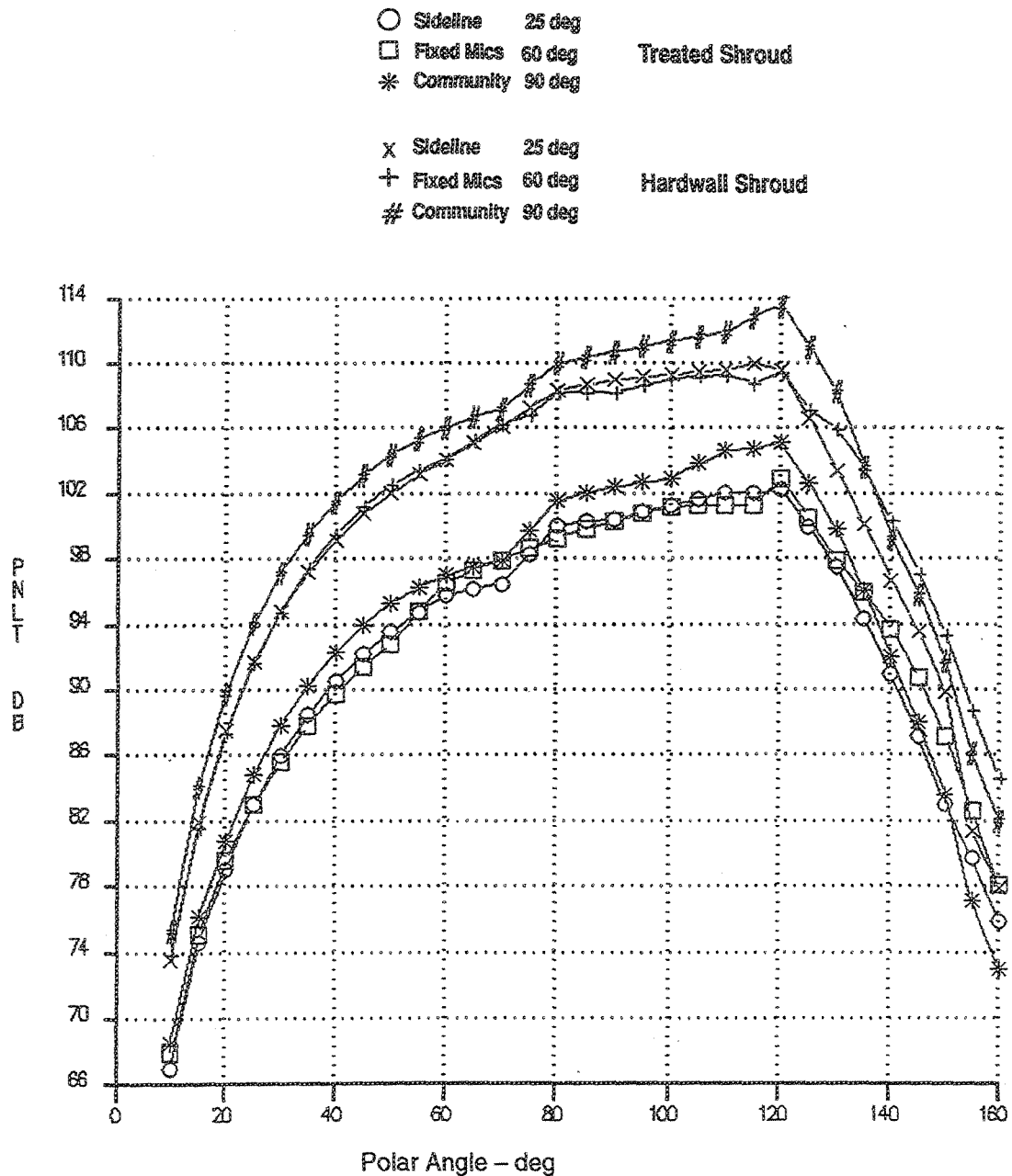


Figure 128. Azimuthal Variation of Noise Levels, PNLT Versus Angle  
 — Ideal Unsuppressed Primary Jet Velocity=2384 ft/sec, Vortical Mixer  
 (Sideline=1629 ft, SAR=4.9, MAR=0.97,  $A_{g*}=1086 \text{ in}^2$ ,  $M_n=0.32$ ,  $V_{\Pi}=357 \text{ ft/sec}$ )

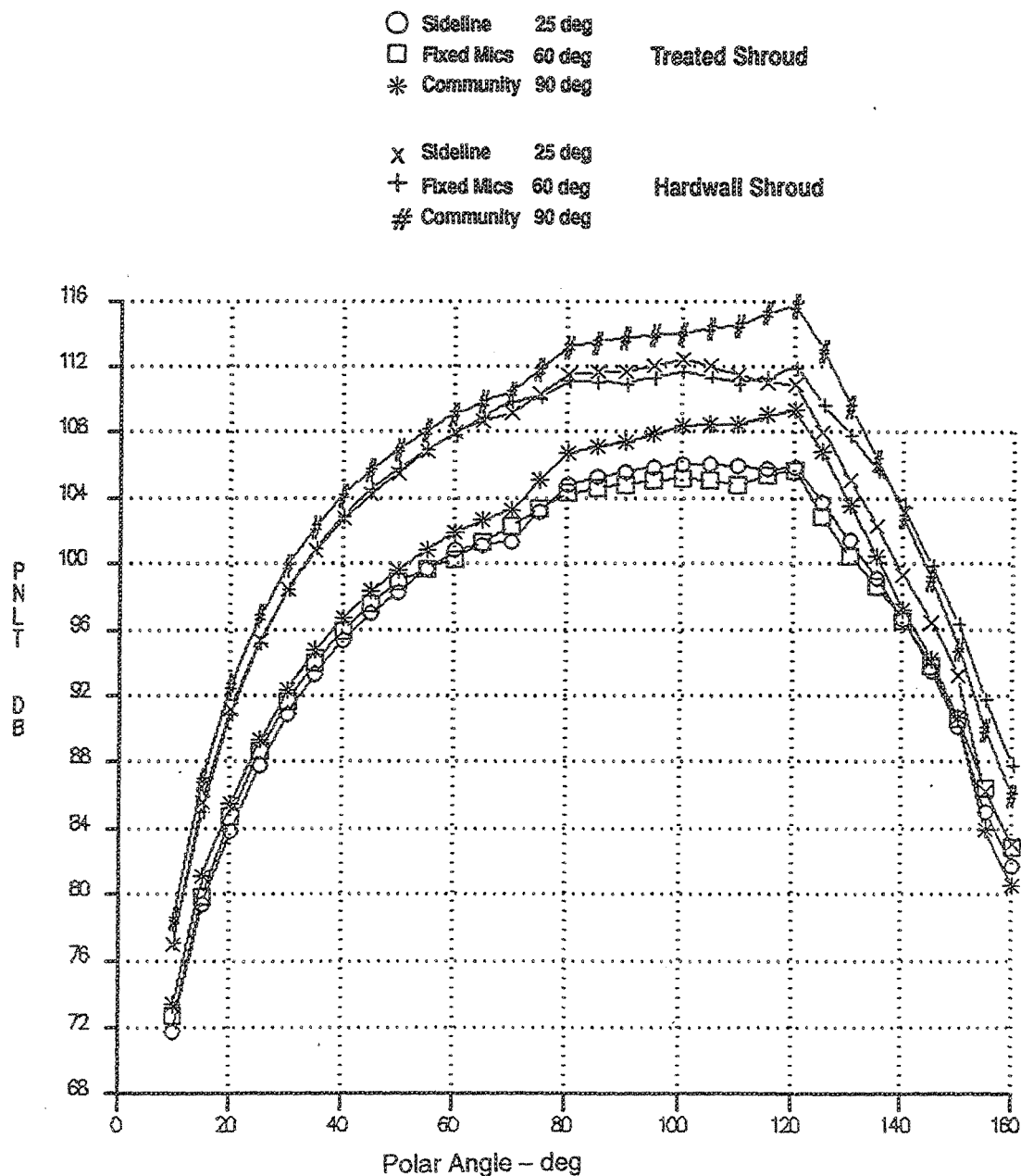


Figure 129. Azimuthal Variation of Noise Levels, PNLT Versus Angle  
 — Ideal Unsuppressed Primary Jet Velocity=2812 ft/sec, Vortical Mixer  
 (Sideline=1629 ft, SAR=4.9, MAR=0.97,  $A_{g*}=1086 \text{ in}^2$ ,  $Mn=0.32$ ,  $V_H=357 \text{ ft/sec}$ )

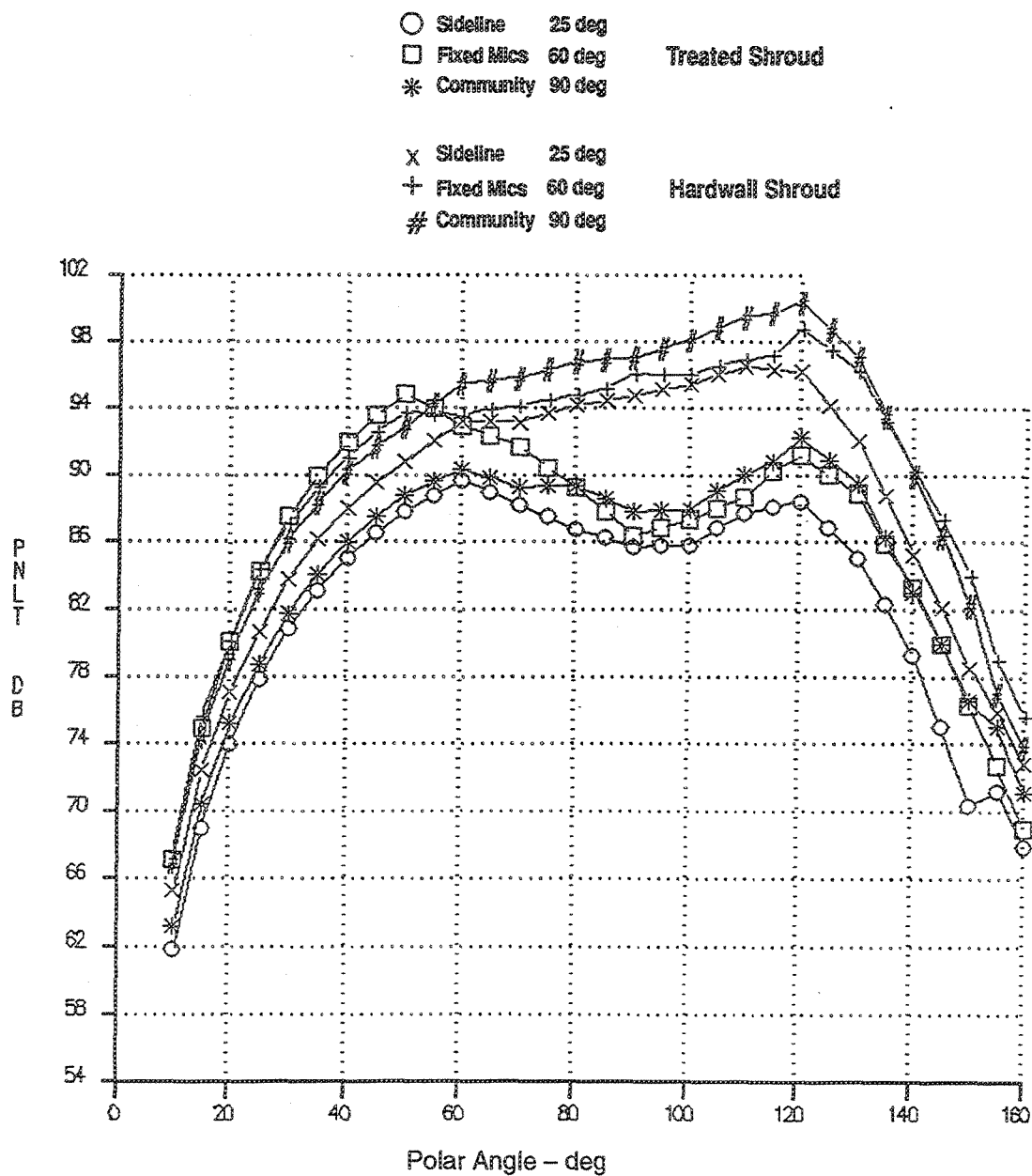


Figure 130. Azimuthal Variation of Noise Levels, PNLT Versus Angle  
 — Ideal Unsuppressed Primary Jet Velocity=1595 ft/sec, Axial Mixer  
 (Sideline=1629 ft, SAR=4.9, MAR=0.97,  $A_{g*}=1086 \text{ in}^2$ ,  $Mn=0.32$ ,  $V_{fl}=357 \text{ ft/sec}$ )

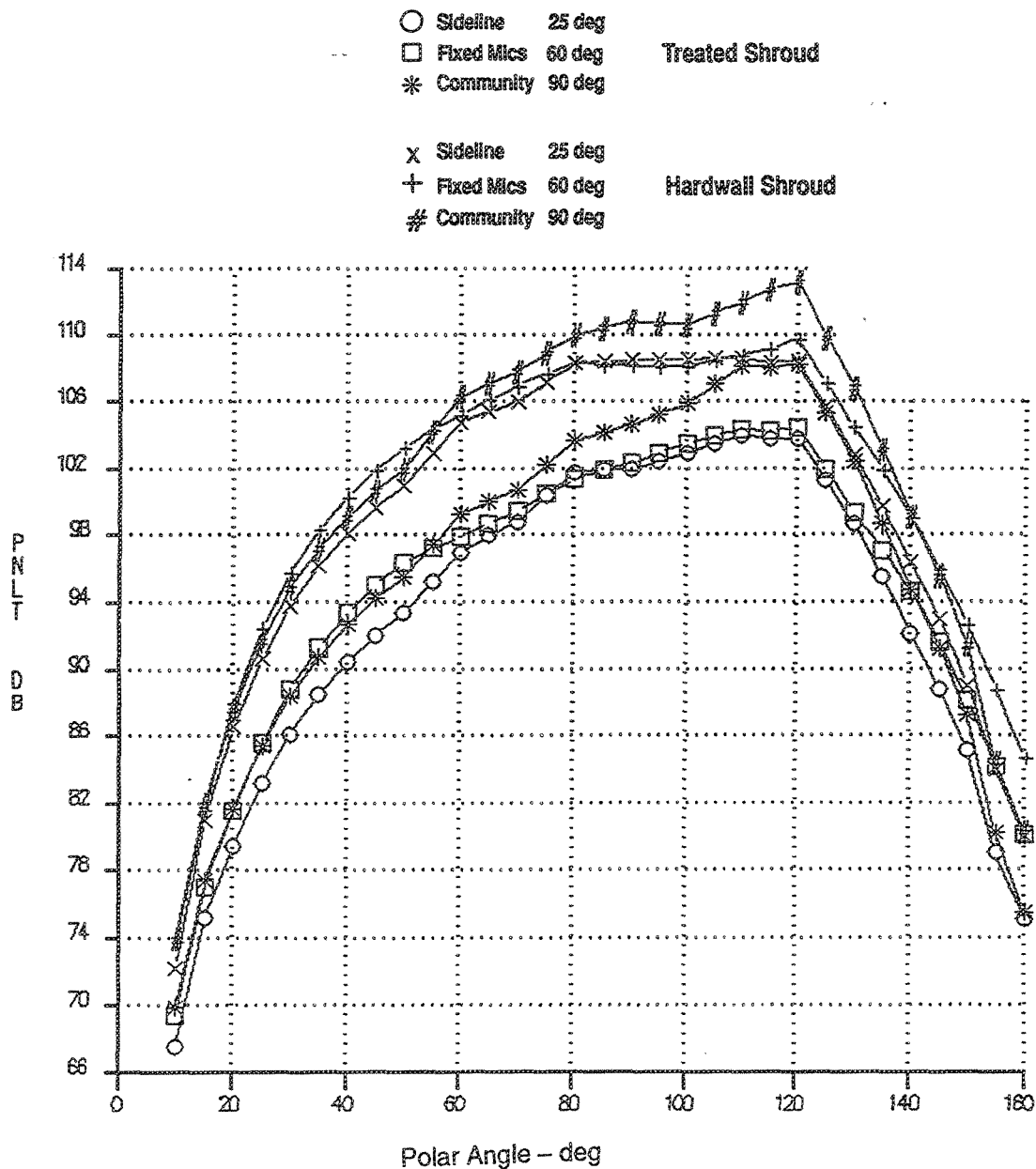


Figure 131. Azimuthal Variation of Noise Levels, PNLT Versus Angle  
 — Ideal Unsuppressed Primary Jet Velocity=2384 ft/sec, Axial Mixer  
 (Sideline=1629 ft, SAR=4.9, MAR=0.97,  $A_{g*}=1086 \text{ in}^2$ ,  $M_n=0.32$ ,  $V_{fl}=357 \text{ ft/sec}$ )

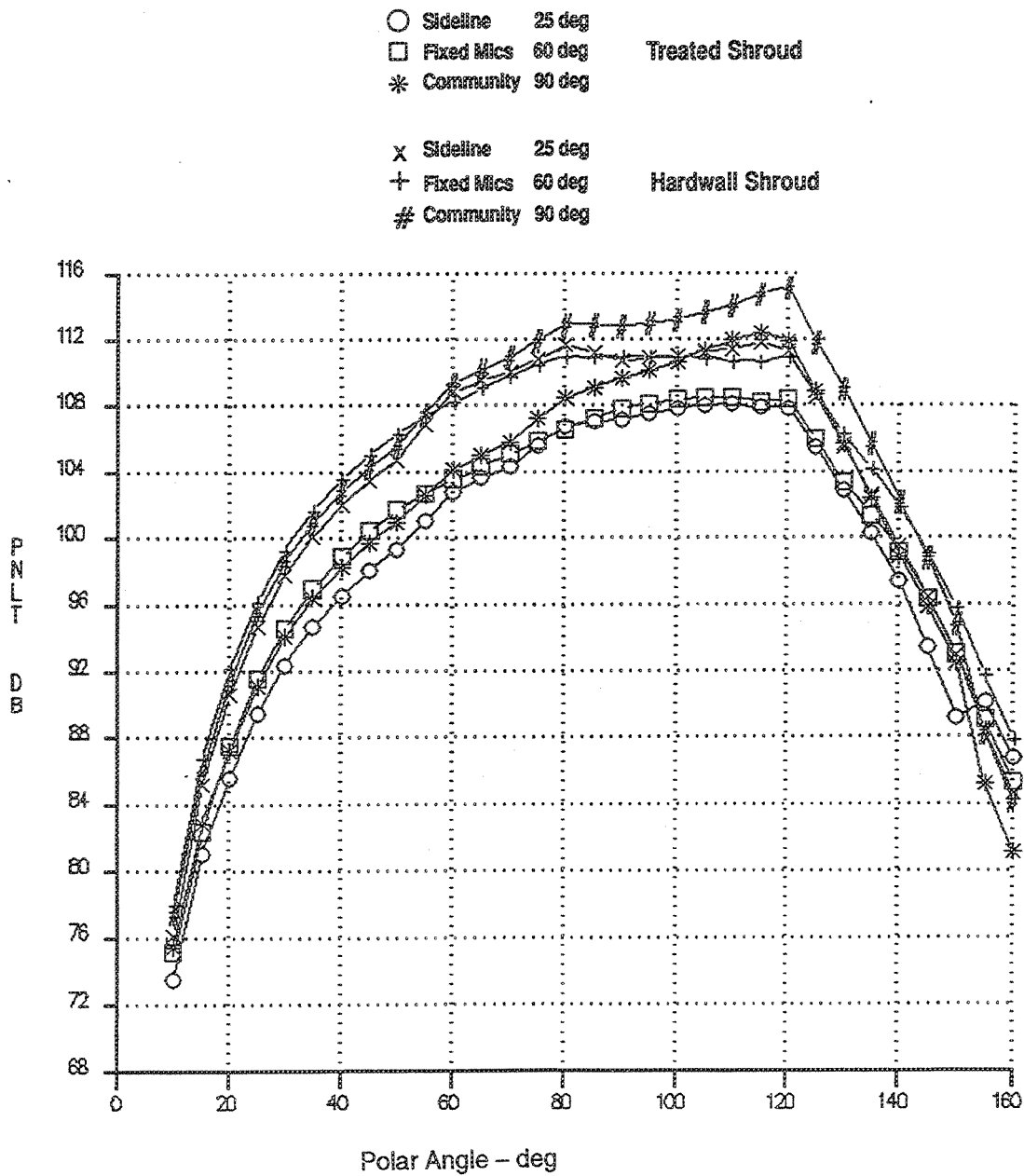


Figure 132. Azimuthal Variation of Noise Levels, PNLT Versus Angle  
 — Ideal Unsuppressed Primary Jet Velocity=2812 ft/sec, Axial Mixer  
 (Sideline=1629 ft, SAR=4.9, MAR=0.97,  $A_{g*}=1086 \text{ in}^2$ ,  $M_n=0.32$ ,  $V_{fl}=357 \text{ ft/sec}$ )

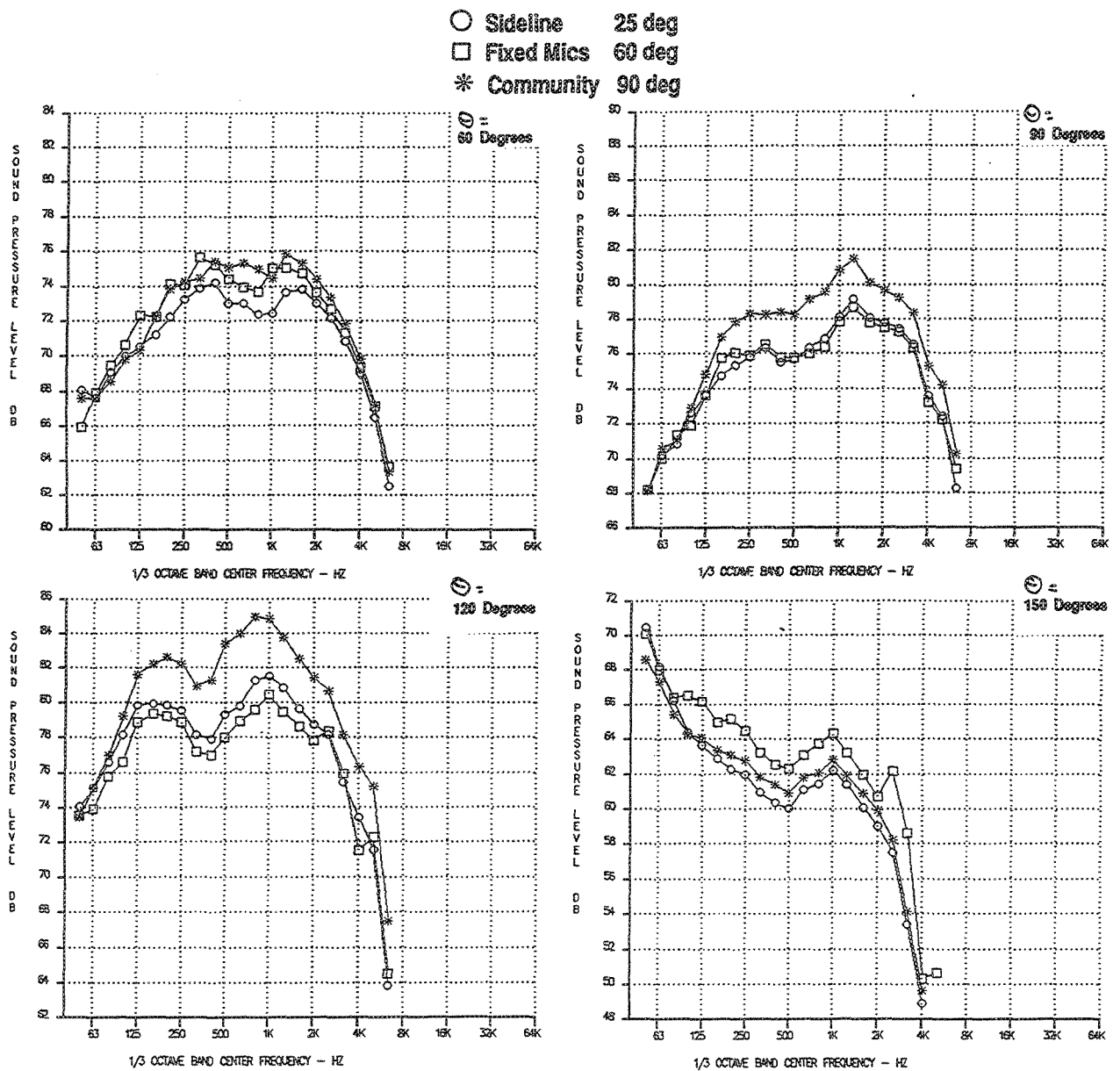


Figure 133. Azimuthal Variation of Noise Levels, SPL Versus Frequency  
 — Ideal Unsuppressed Primary Jet Velocity=2384 ft/sec, Vortical Mixer, Long Treated Shroud  
 (Sideline=1629 ft, SAR=4.9, MAR=0.97,  $A_{g*}=1086 \text{ in}^2$ ,  $M_n=0.32$ ,  $V_{fl}=357 \text{ ft/sec}$ )

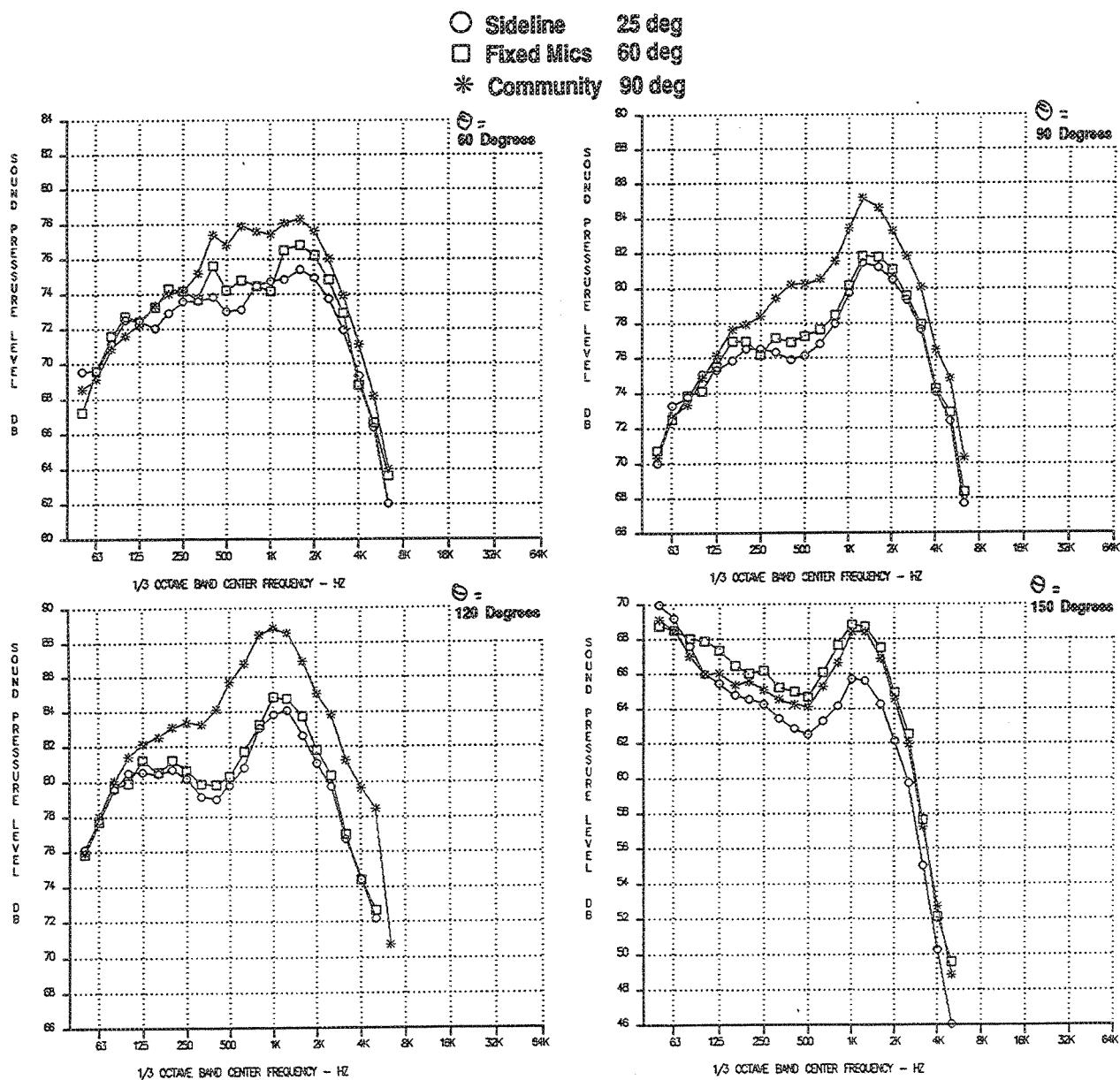


Figure 134. Azimuthal Variation of Noise Levels, SPL Versus Frequency  
 — Ideal Unsuppressed Primary Jet Velocity=2384 ft/sec, Axial Mixer, Long Treated Shroud  
 (Sideline=1629 ft, SAR=4.9, MAR=0.97,  $A_{g*}=1086 \text{ in}^2$ ,  $M_n=0.32$ ,  $V_{fl}=357 \text{ ft/sec}$ )

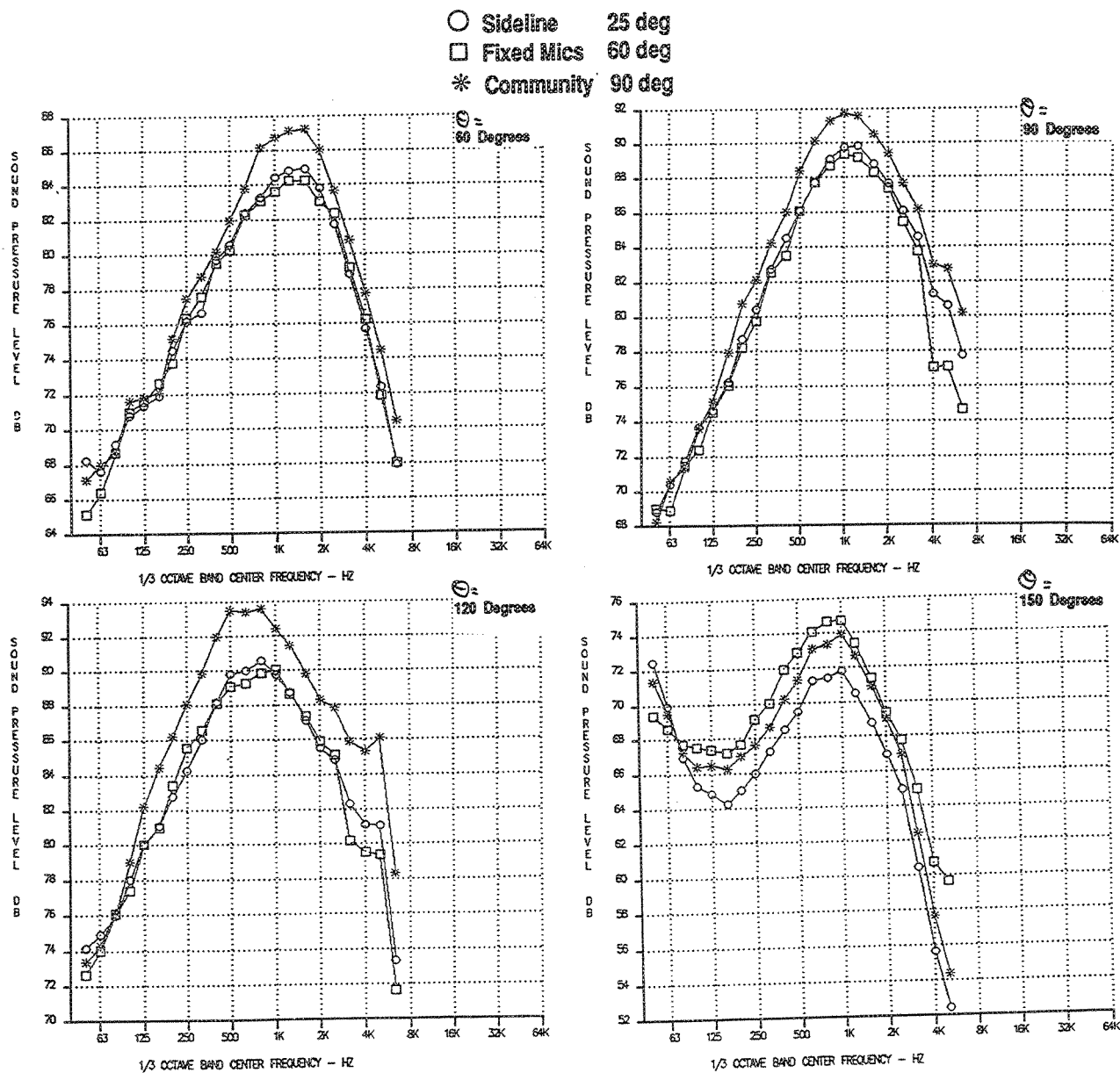


Figure 135. Azimuthal Variation of Noise Levels, SPL Versus Frequency  
 — Ideal Unsuppressed Primary Jet Velocity=2384 ft/sec, Vortical Mixer, Long Hardwall Shroud  
 (Sideline=1629 ft, SAR=4.9, MAR=0.97,  $A_{g*}=1086 \text{ in}^2$ ,  $M_n=0.32$ ,  $V_{fl}=357 \text{ ft/sec}$ )



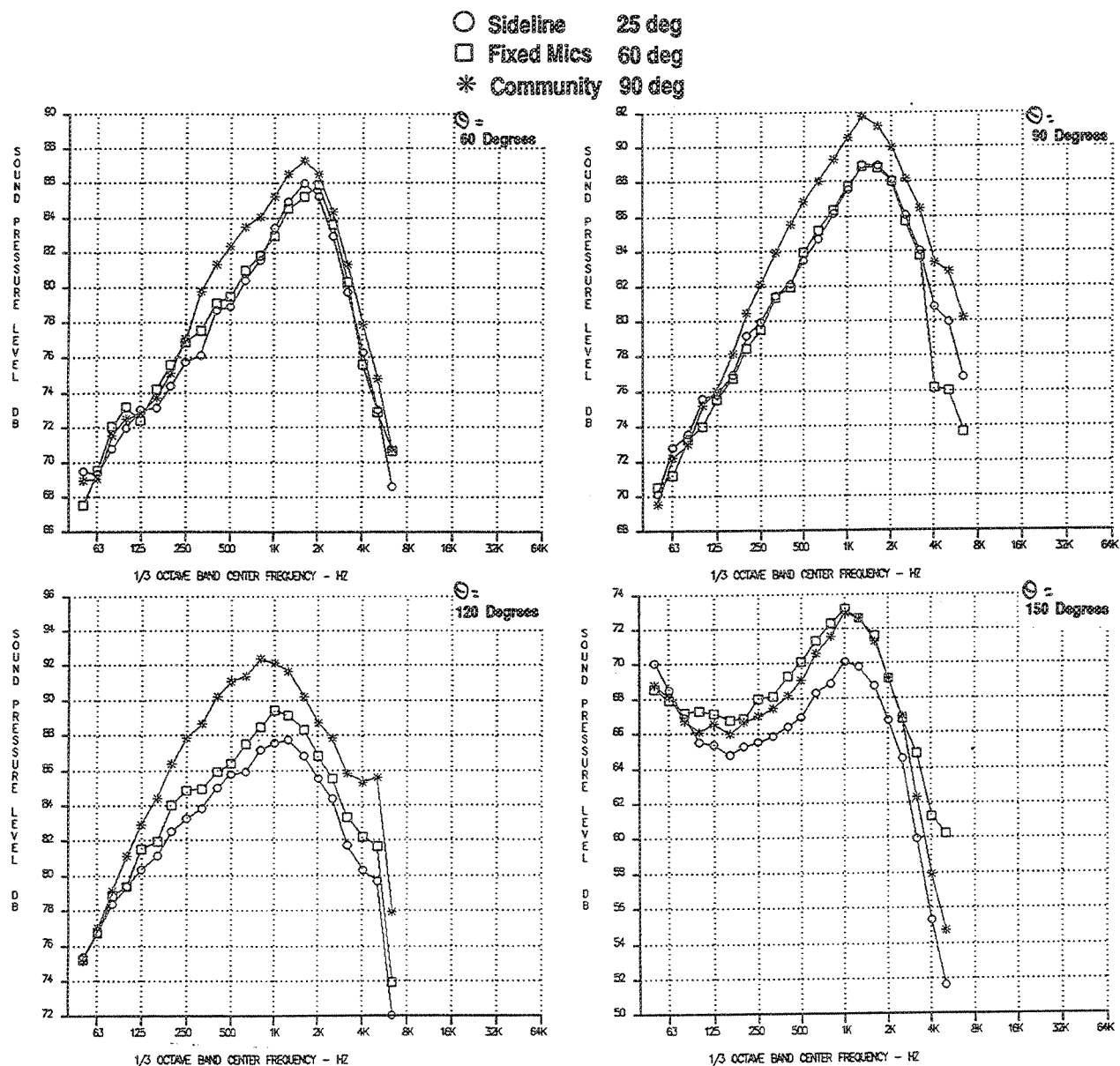


Figure 136. Azimuthal Variation of Noise Levels, SPL Versus Frequency  
 — Ideal Unsuppressed Primary Jet Velocity=2384 ft/sec, Axial Mixer, Long Hardwall Shroud  
 (Sideline=1629 ft, SAR=4.9, MAR=0.97,  $A_{g*}=1086 \text{ in}^2$ ,  $M_n=0.32$ ,  $V_{fl}=357 \text{ ft/sec}$ )

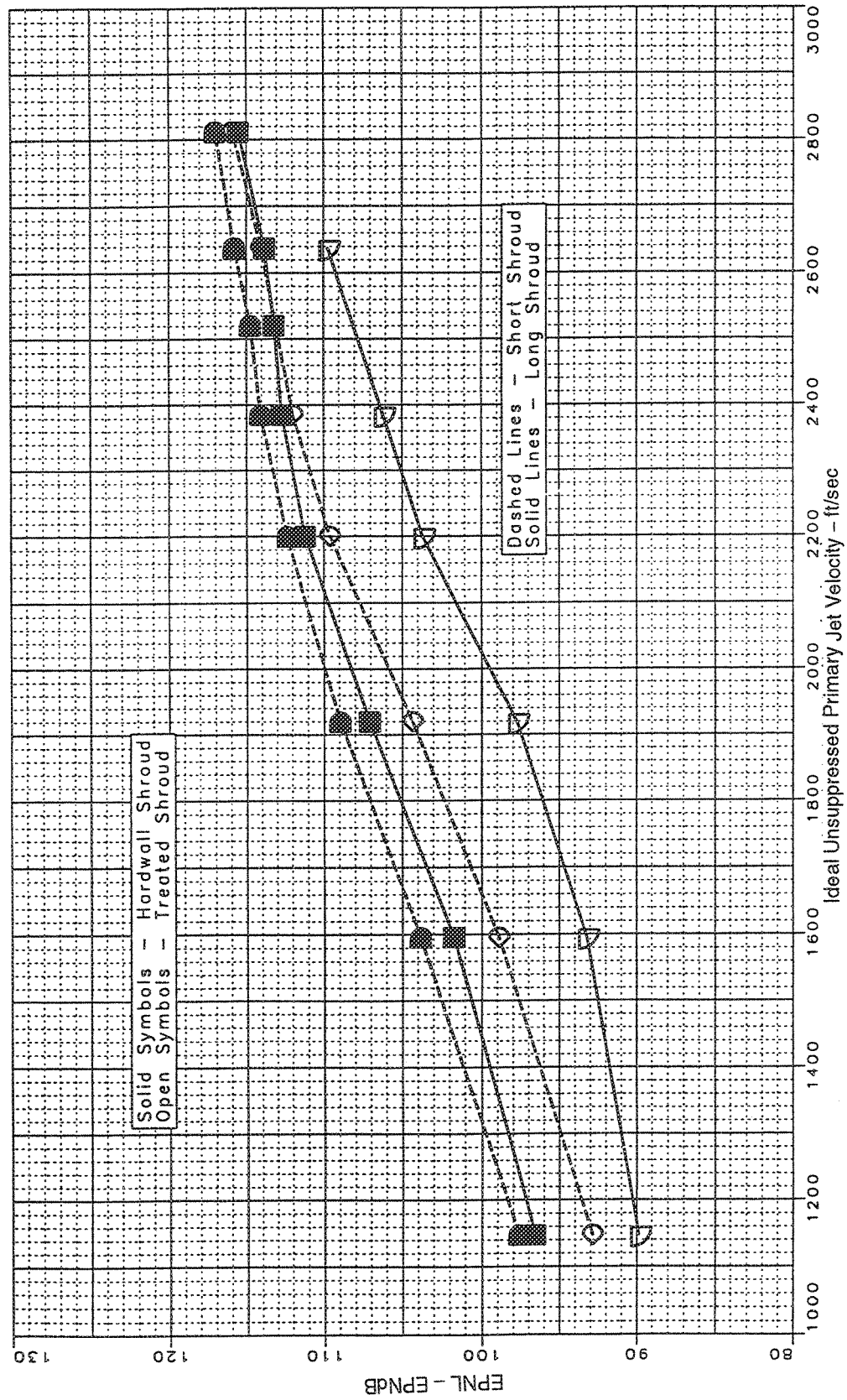


Figure 137. Effect of Shroud Length on Sideline Noise, Vortical Mixer, Hardwall Shroud  
(Sideline=1629 ft, SAR=4.4, MAR=1.19,  $A_{g*}=1086 \text{ in}^2$ , Static)

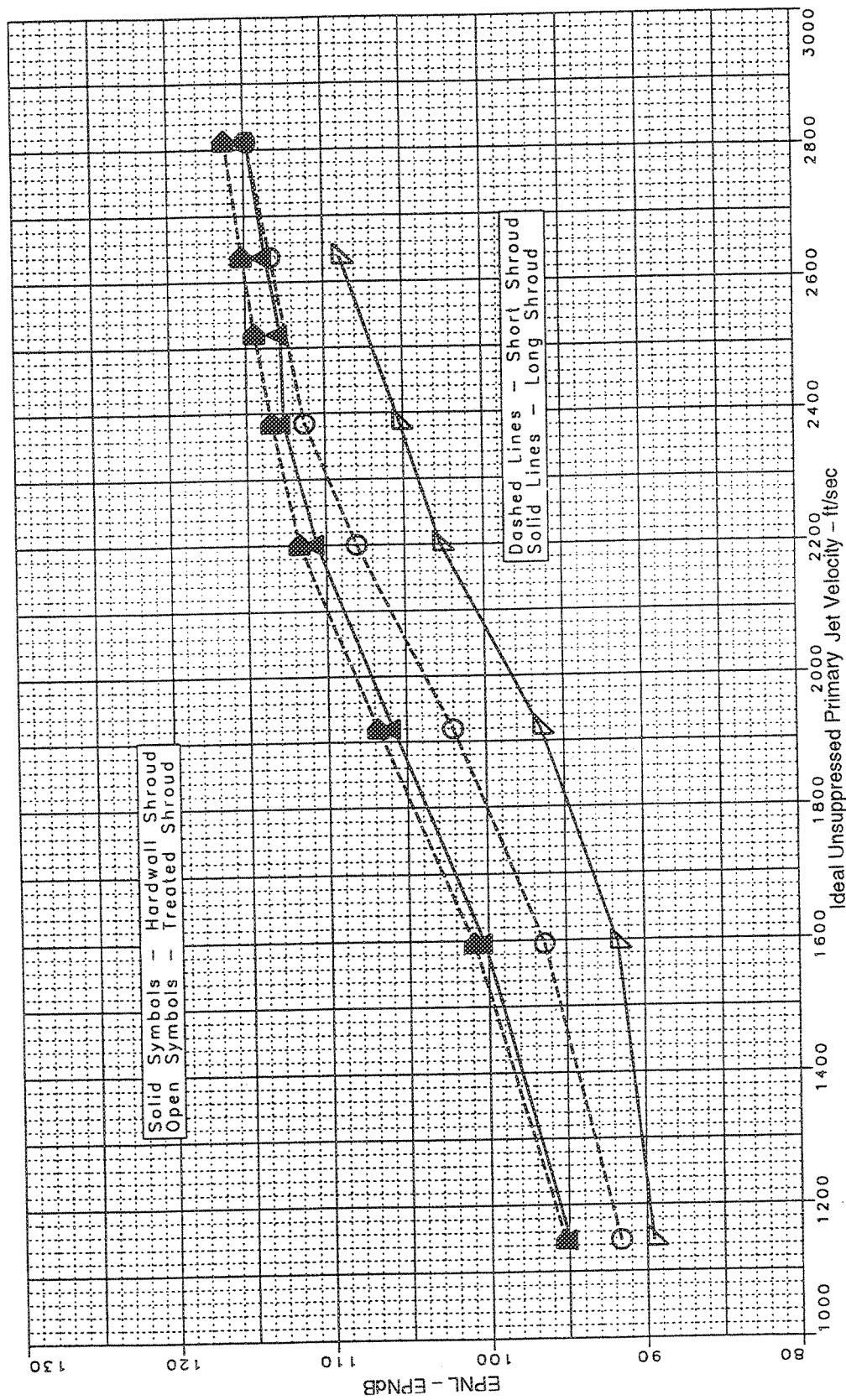


Figure 138. Effect of Shroud Length and Treatment on Sideline Noise Vortical Mixer  
 (Sideline=1629 ft, SAR=4.4, MAR=1.19,  $A_8=1086 \text{ in}^2$ ,  $M_n=0.32$ ,  $V_n=357 \text{ ft/sec}$ )

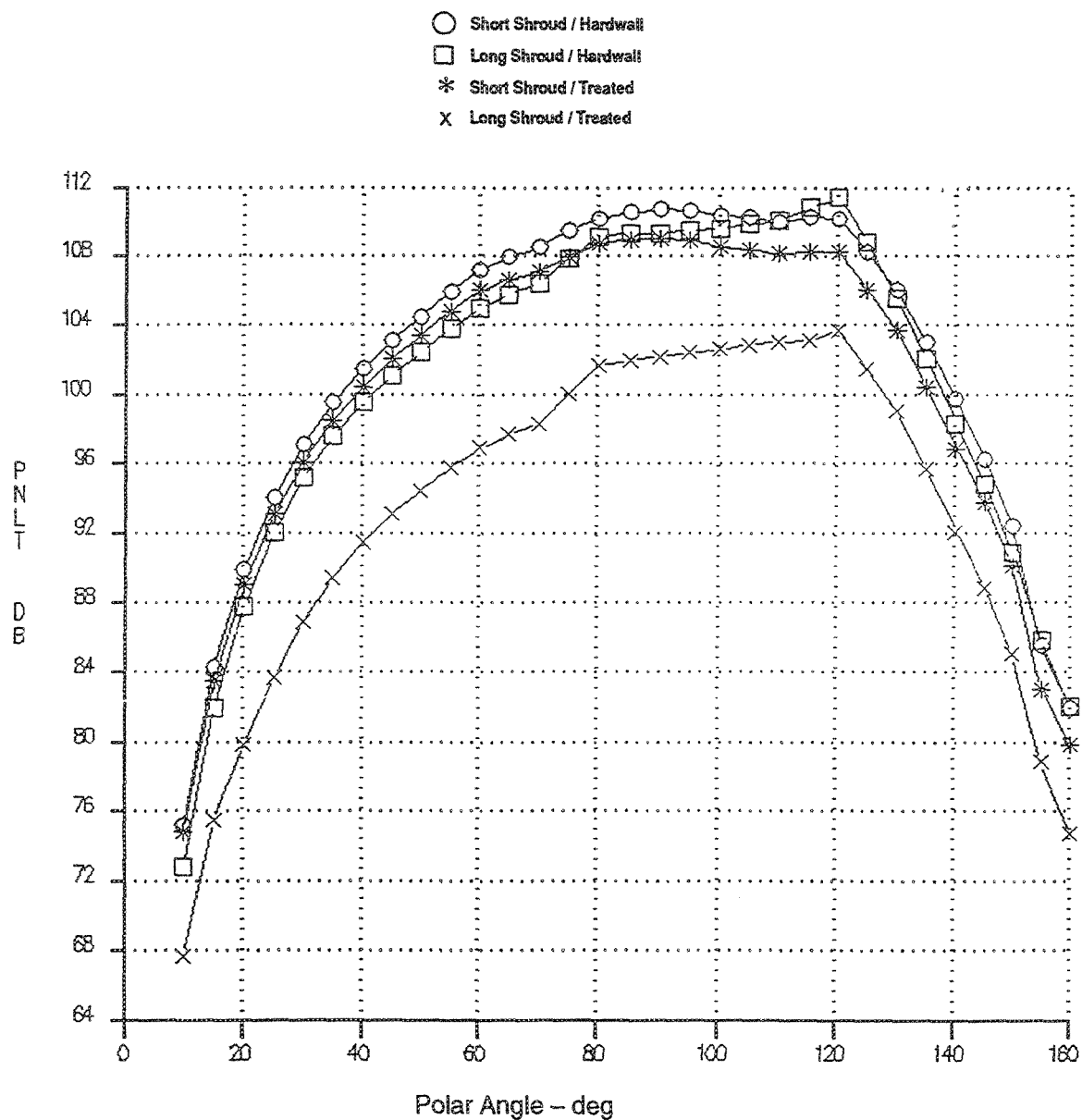


Figure 139. Effect of Shroud Length and Treatment, PNL vs. Angle  
 — Ideal Unsuppressed Primary Jet Velocity=2384 ft/sec, Vortical Mixer  
 (Sideline=1629 ft, SAR=4.4, MAR=1.19,  $A_{g*}=1086 \text{ in}^2$ ,  $M_n=0.32$ ,  $V_{fl}=357 \text{ ft/sec}$ )

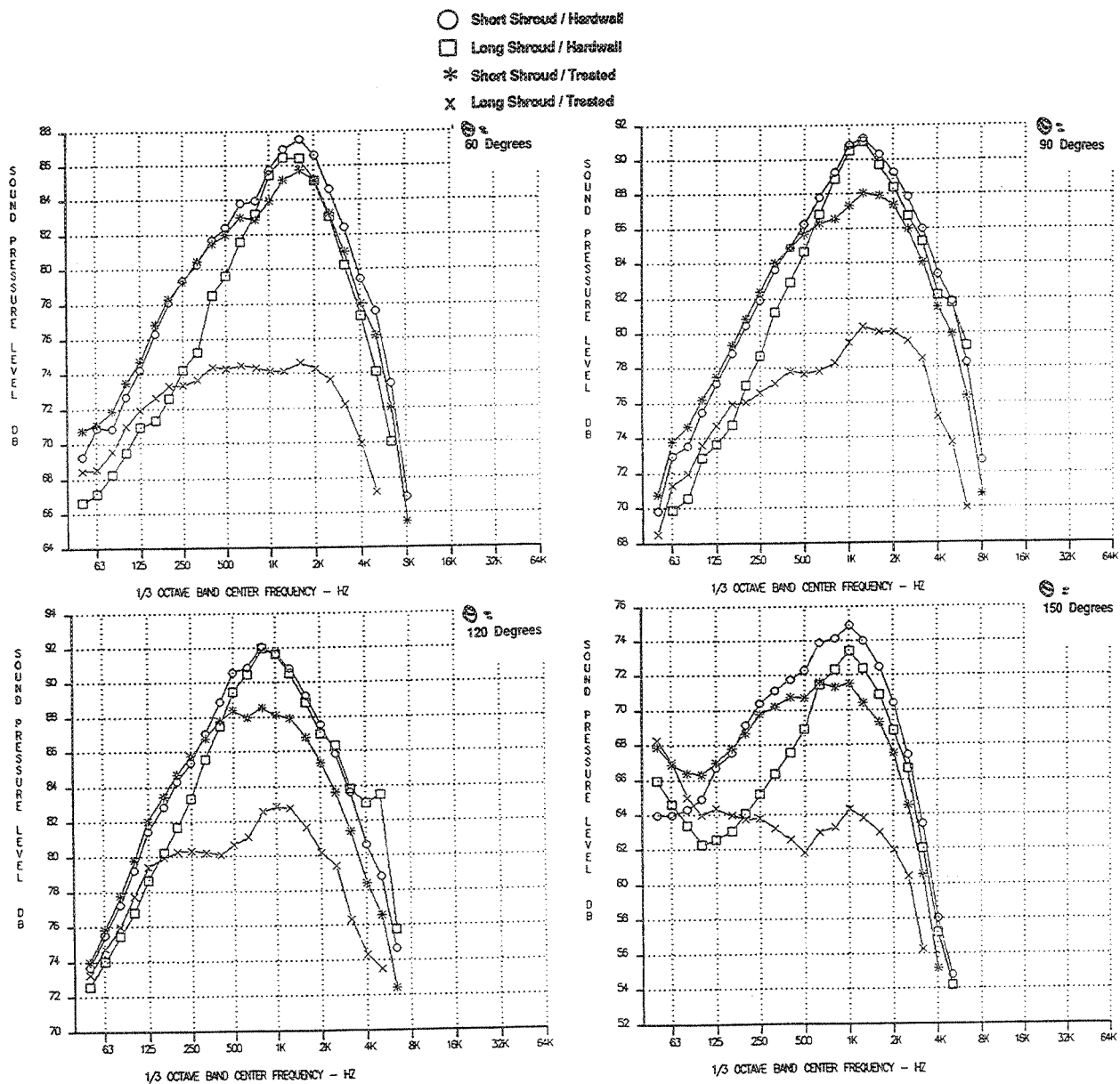


Figure 140. Effect of Shroud Length and Treatment, SPL Versus Frequency  
 — Ideal Unsuppressed Primary Jet Velocity=2384 ft/sec, Vortical Mixer  
 (Sideline=1629 ft, SAR=4.4, MAR=1.19,  $A_{g*}=1086 \text{ in}^2$ ,  $M_n=0.32$ ,  $V_{fl}=357 \text{ ft/sec}$ )

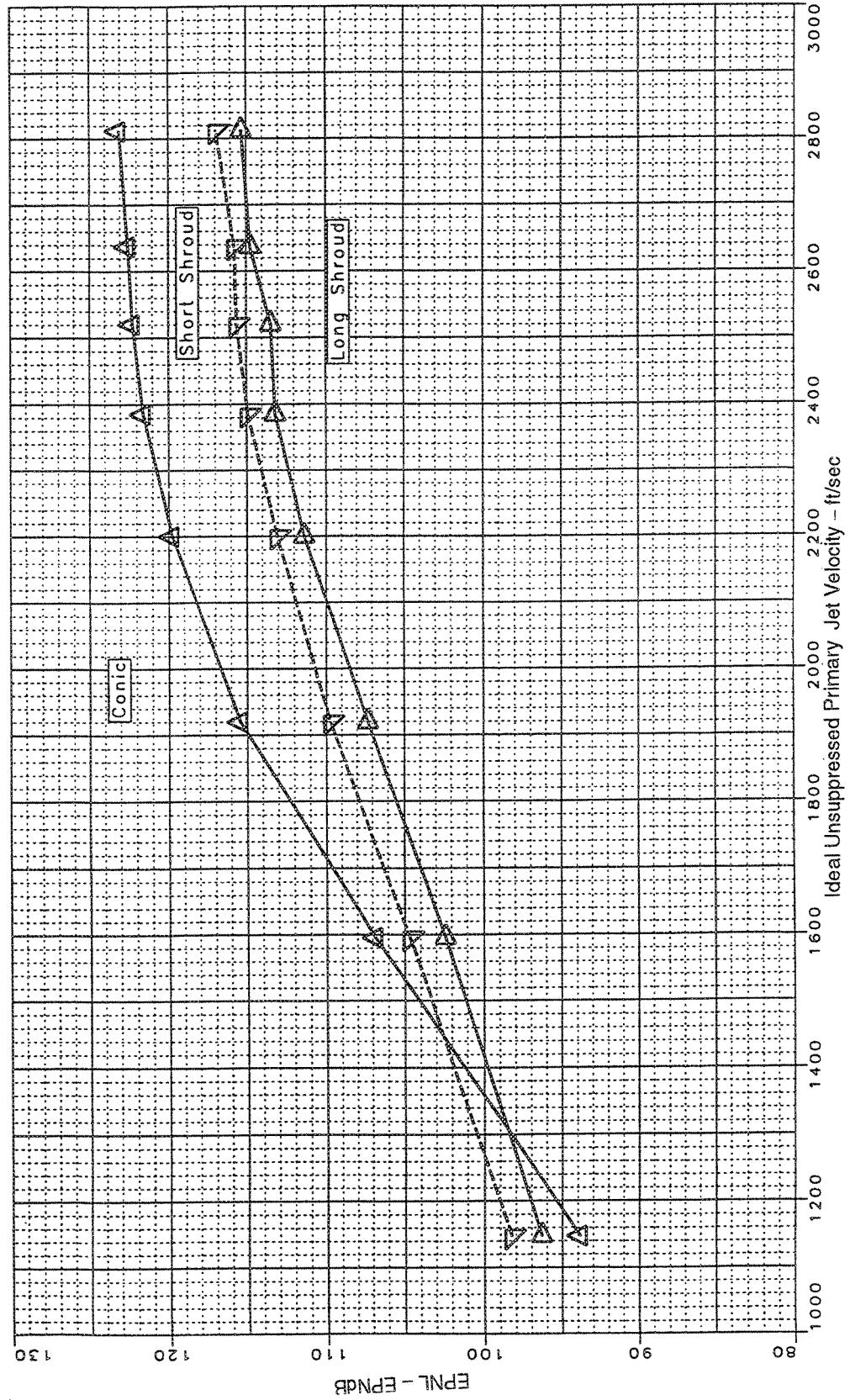


Figure 141. Effect of Shroud Length on Sideline Noise, Vortical Mixer, Hardwall Shroud  
(Sideline = 1629 ft, SAR = 4.9, MAR = 1.19,  $A_{g*} = 1086 \text{ in}^2$ , Static)

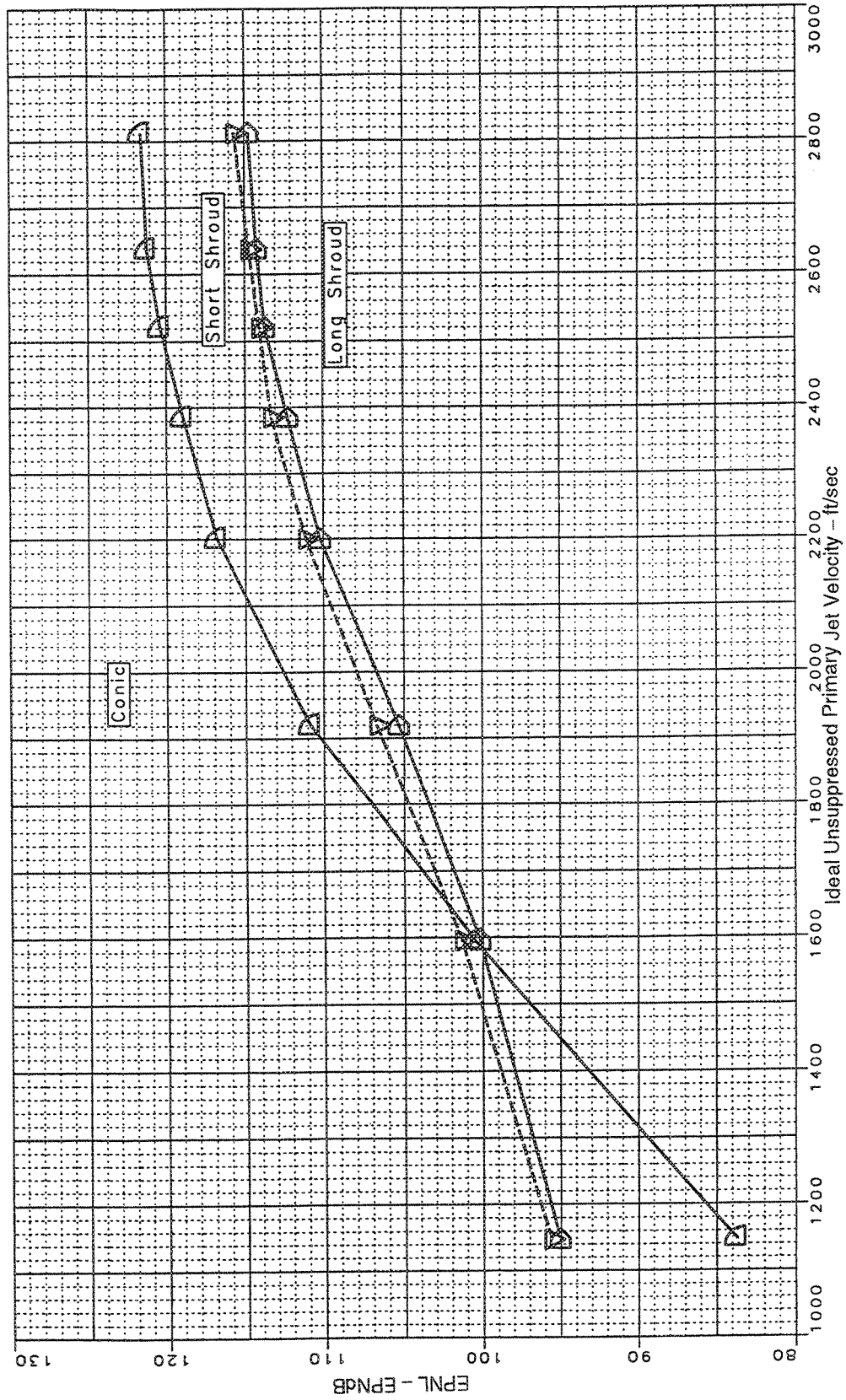


Figure 142. Effect of Shroud Length on Sideline Noise, Vortical Mixer, Hardwall Shroud  
(Sideline=1629 ft, SAR=4.9, MAR=1.19,  $A_{g*}=1086 \text{ in}^2$ ,  $Mn=0.32$ ,  $V_{\eta}=357 \text{ ft/sec}$ )

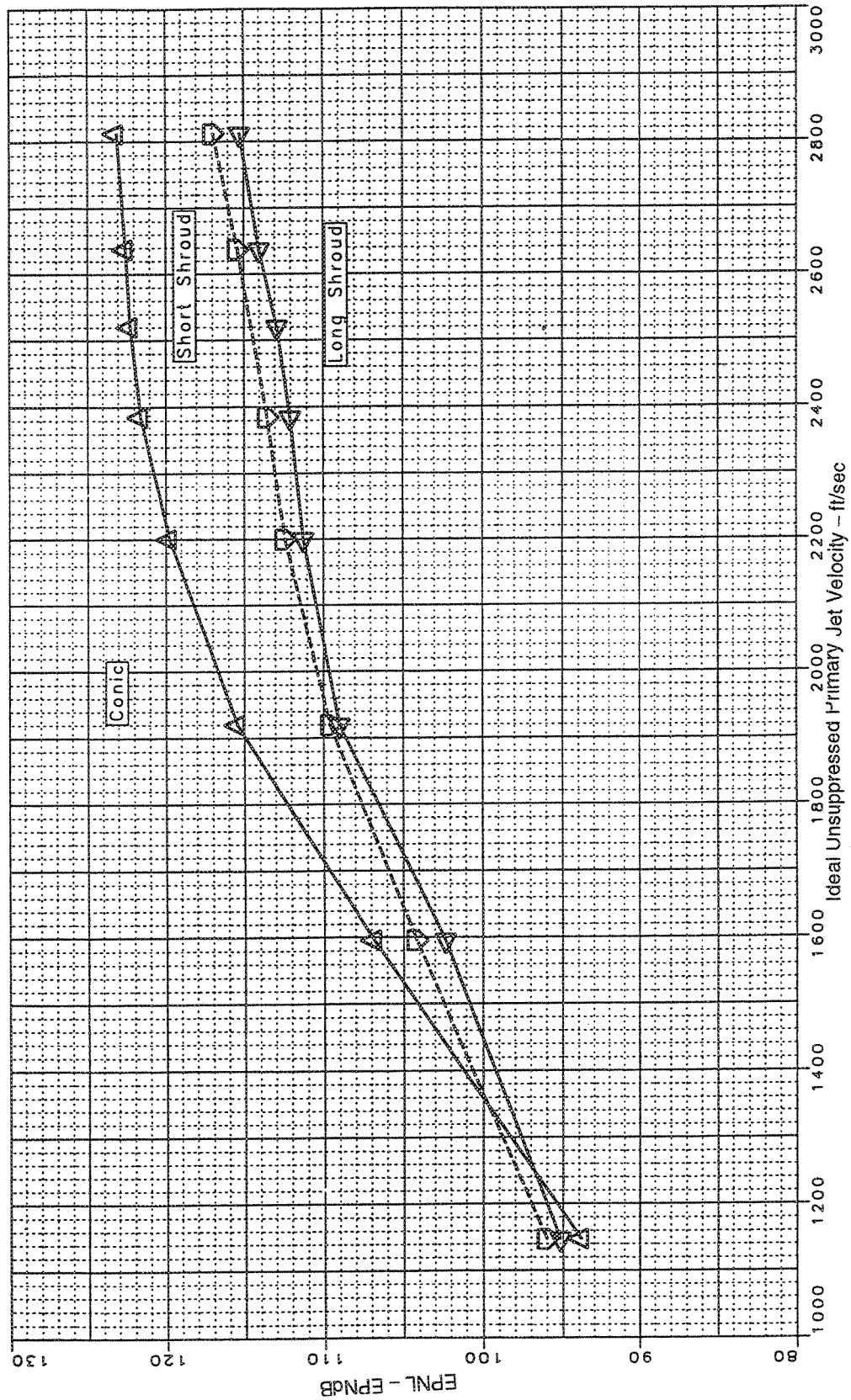


Figure 143. Effect of Shroud Length on Sideline Noise, Axial Mixer, Hardwall Shroud  
(Sideline=1629 ft, SAR=4.9, MAR=1.19,  $A_{g*}=1086 \text{ in}^2$ , Static)



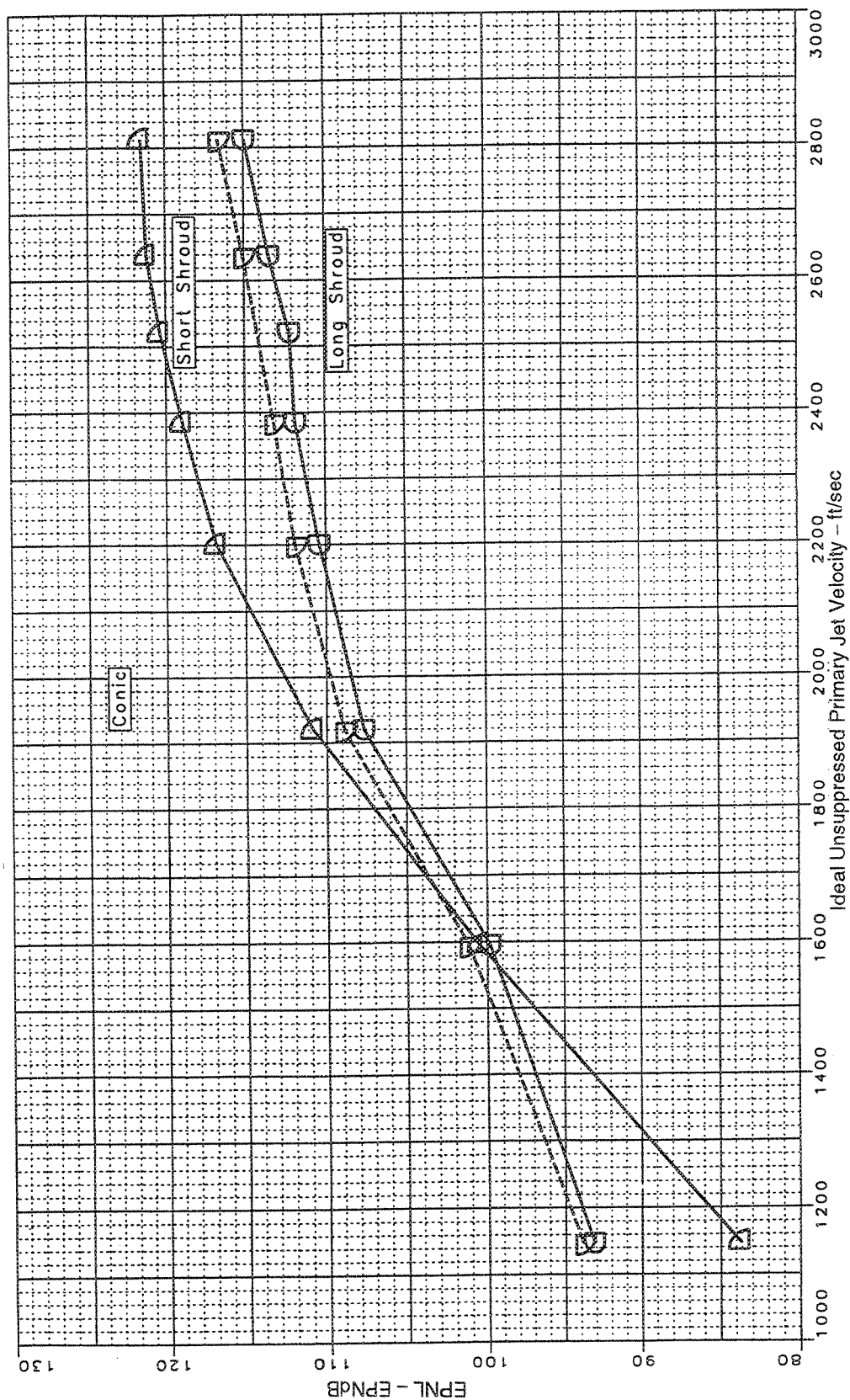
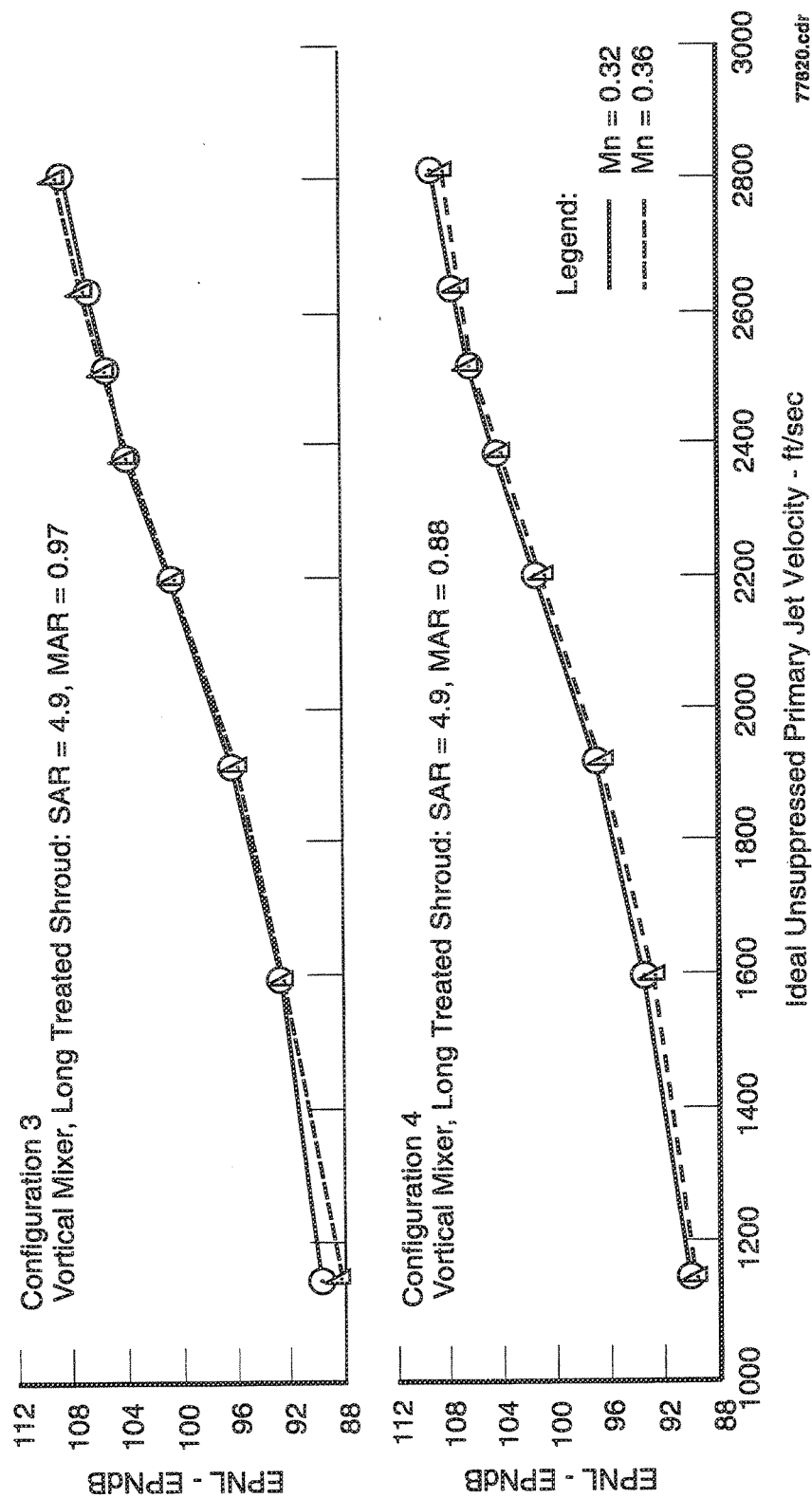


Figure 144. Effect of Shroud Length on Sideline Noise, Axial Mixer, Hardwall Shroud  
(Sideline=1629 ft, SAR=4.9, MAR=1.19,  $A_{g*}=1086 \text{ in}^2$ ,  $M_n=0.32$ ,  $V_{\eta}=357 \text{ ft/sec}$ )



77820.cdr

Figure 145. Effect of Flight Mach Number on Sideline Noise (Sideline=1629 ft,  $A_{g*}=1086 \text{ in}^2$ ,  $Mn=0.32$  and  $0.36$ )

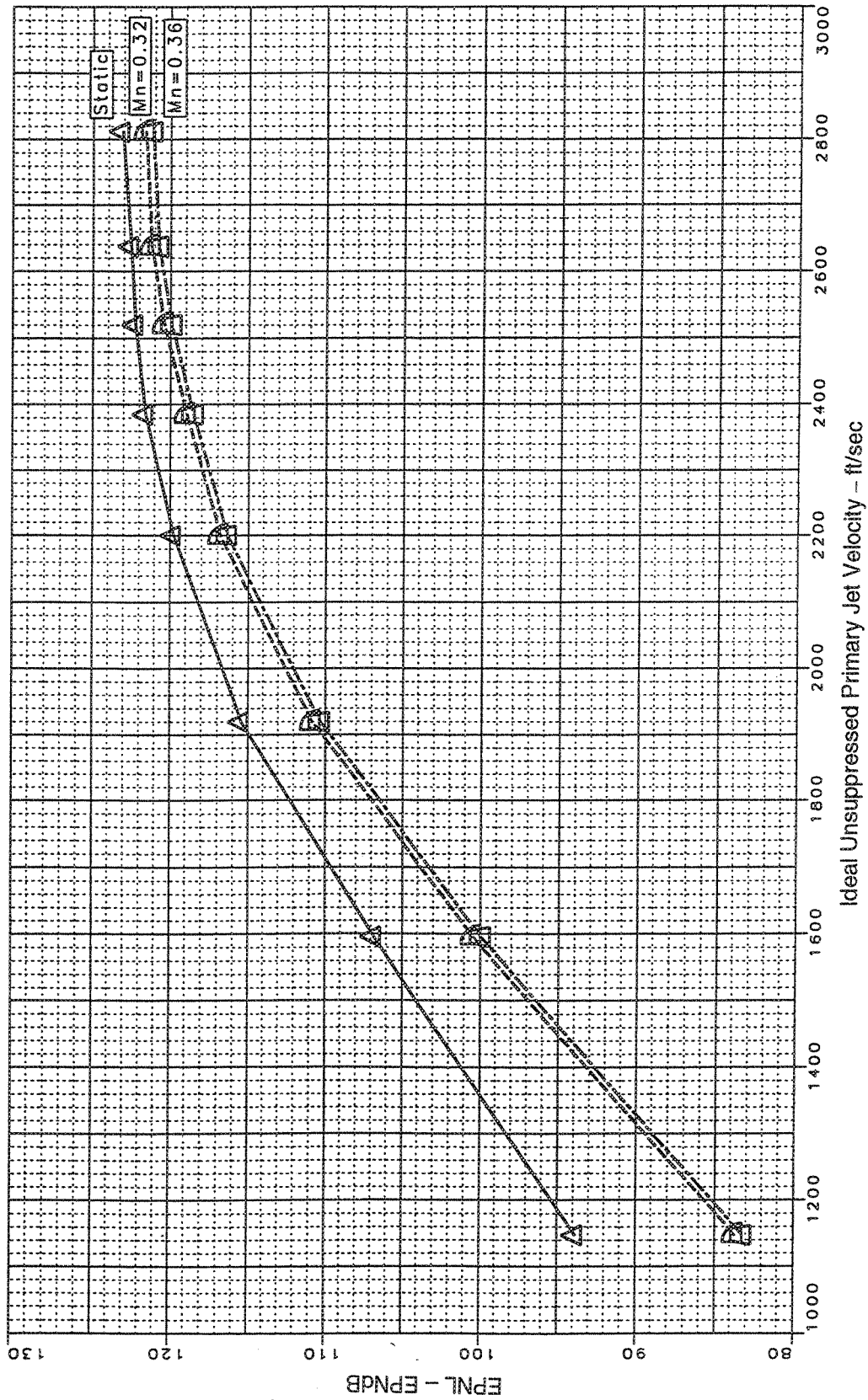


Figure 146. Effect of Flight Mach Number on Sideline Noise, Baseline Round Conic Nozzle  
(Sideline=1629 ft,  $A_{g*}=1086 \text{ in}^2$ ,  $Mn=0.0$ ,  $0.32$ , and  $0.36$ )

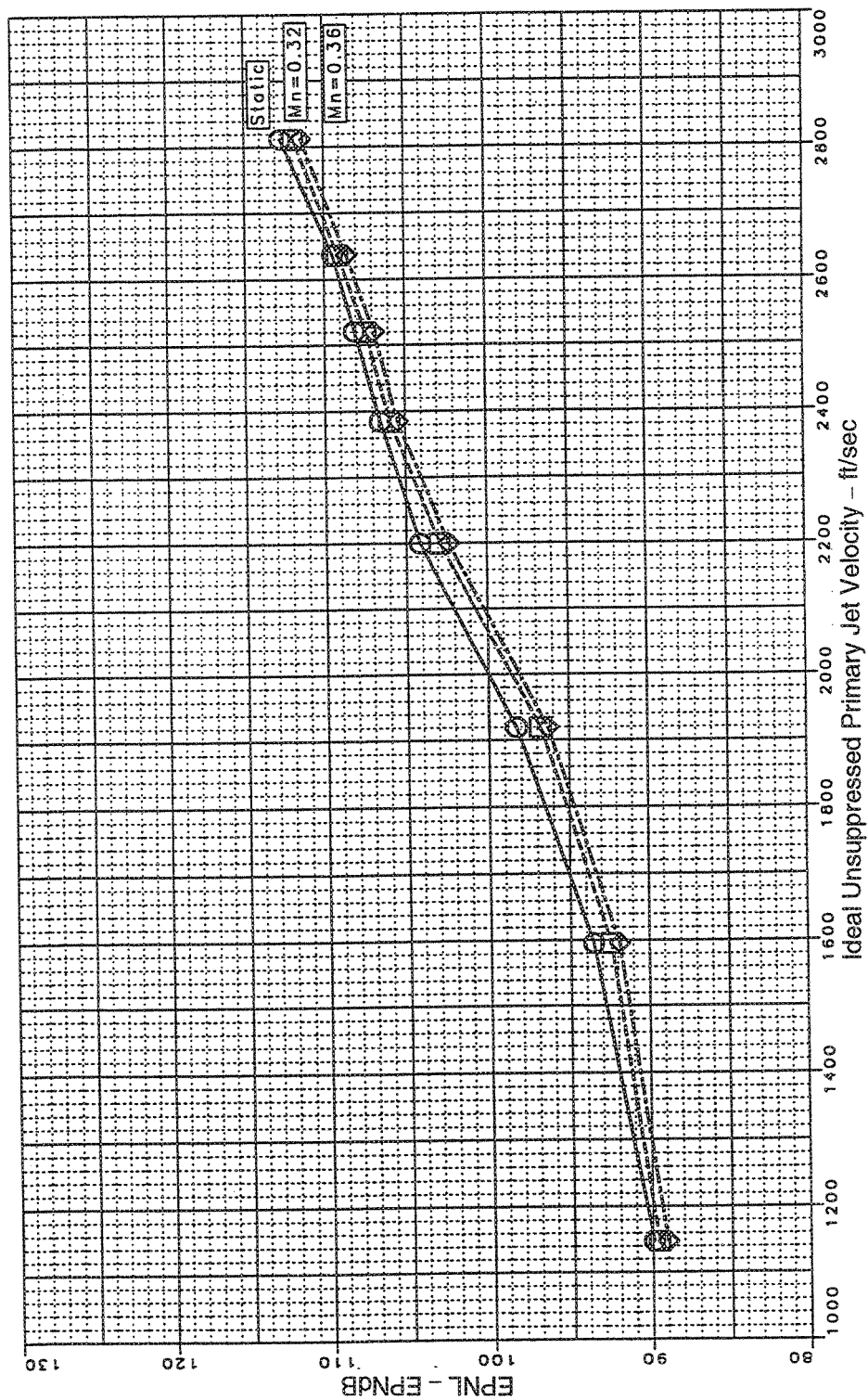


Figure 147. Effect of Flight Mach Number on Sideline Noise, Vortical Mixer, Long Treated Shroud  
(Sideline=1629 ft, SAR=4.9, MAR=1.19,  $A_{g*}=1086 \text{ in}^2$ ,  $M_n=0.0$ , 0.32, and 0.36)

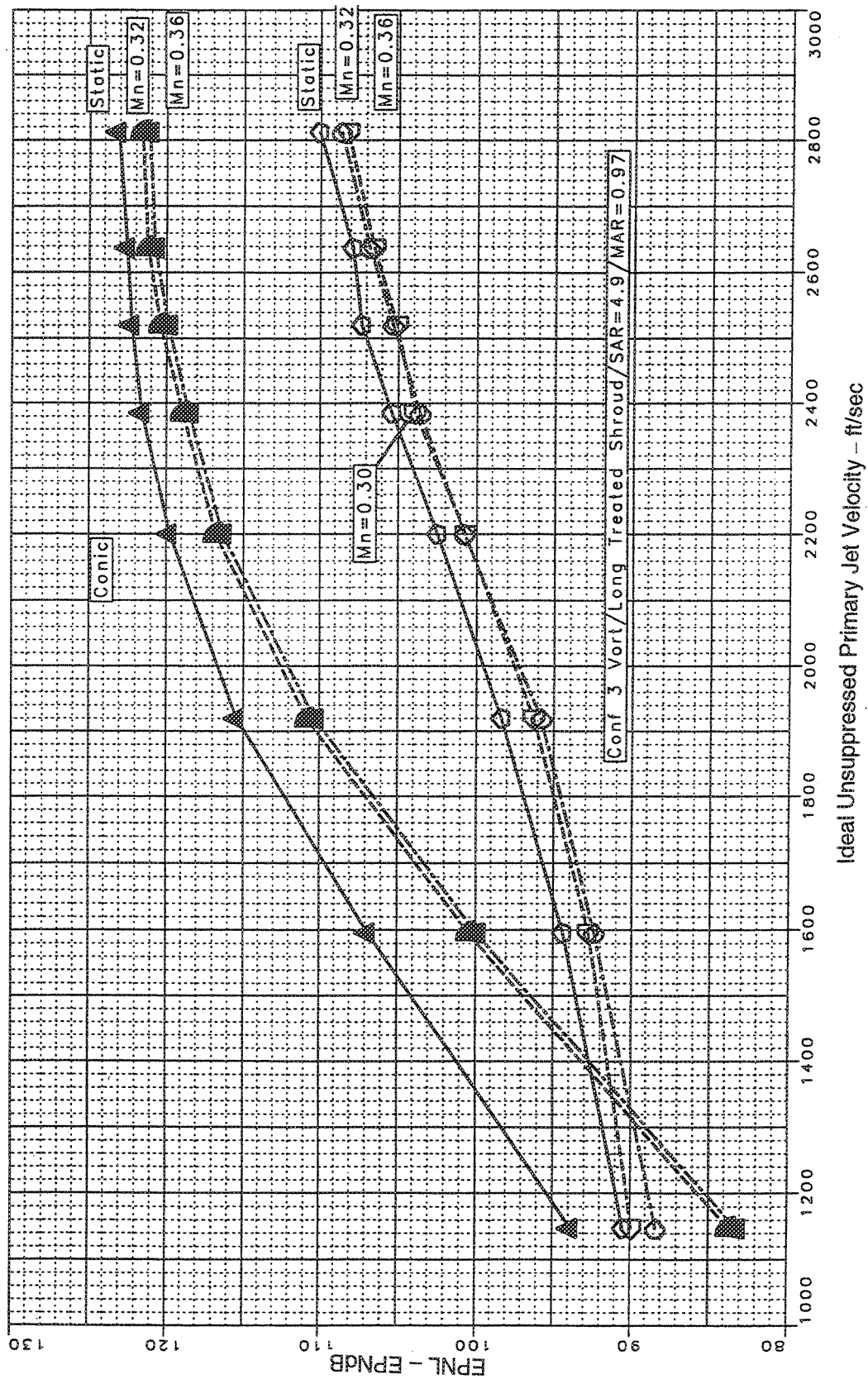


Figure 148. Effect of Flight Mach Number on Sideline Noise, Baseline Round Conic Nozzle, Vortical Mixer, Long Treated Shroud  
(Sideline=1629 ft, SAR=4.9, MAR=0.97,  $A_g=1086 \text{ in}^2$ ,  $M_n=0.0$ , 0.32, and 0.36)

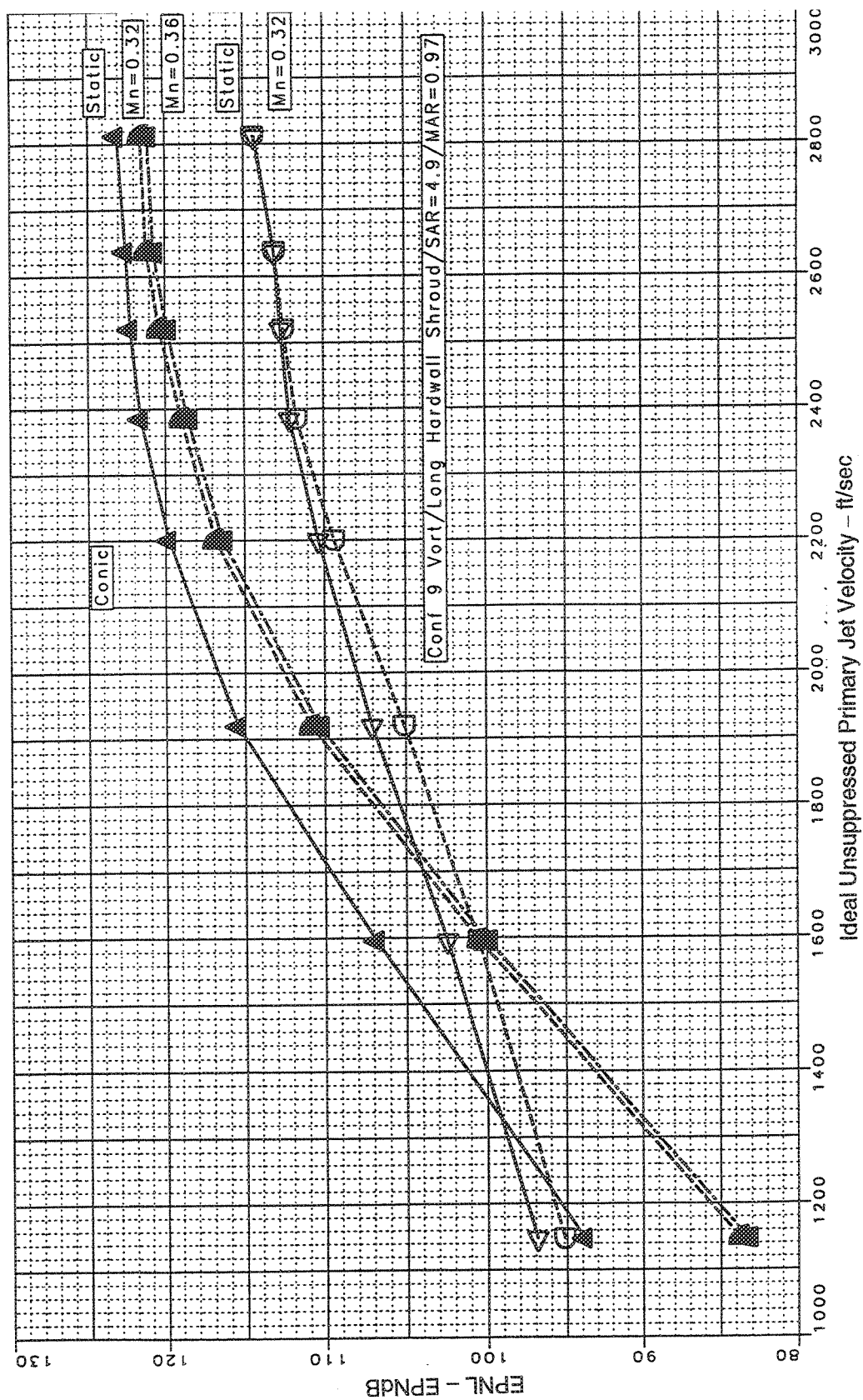


Figure 149. Effect of Flight Mach Number on Sideline Noise, Baseline Round Conic Nozzle, Vortical Mixer, Long Hardwall Shroud  
(Sideline=1629 ft, SAR=4.9, MAR=0.97,  $A_g=1086 \text{ in}^2$ ,  $M_n=0.0$ , 0.32, and 0.36)

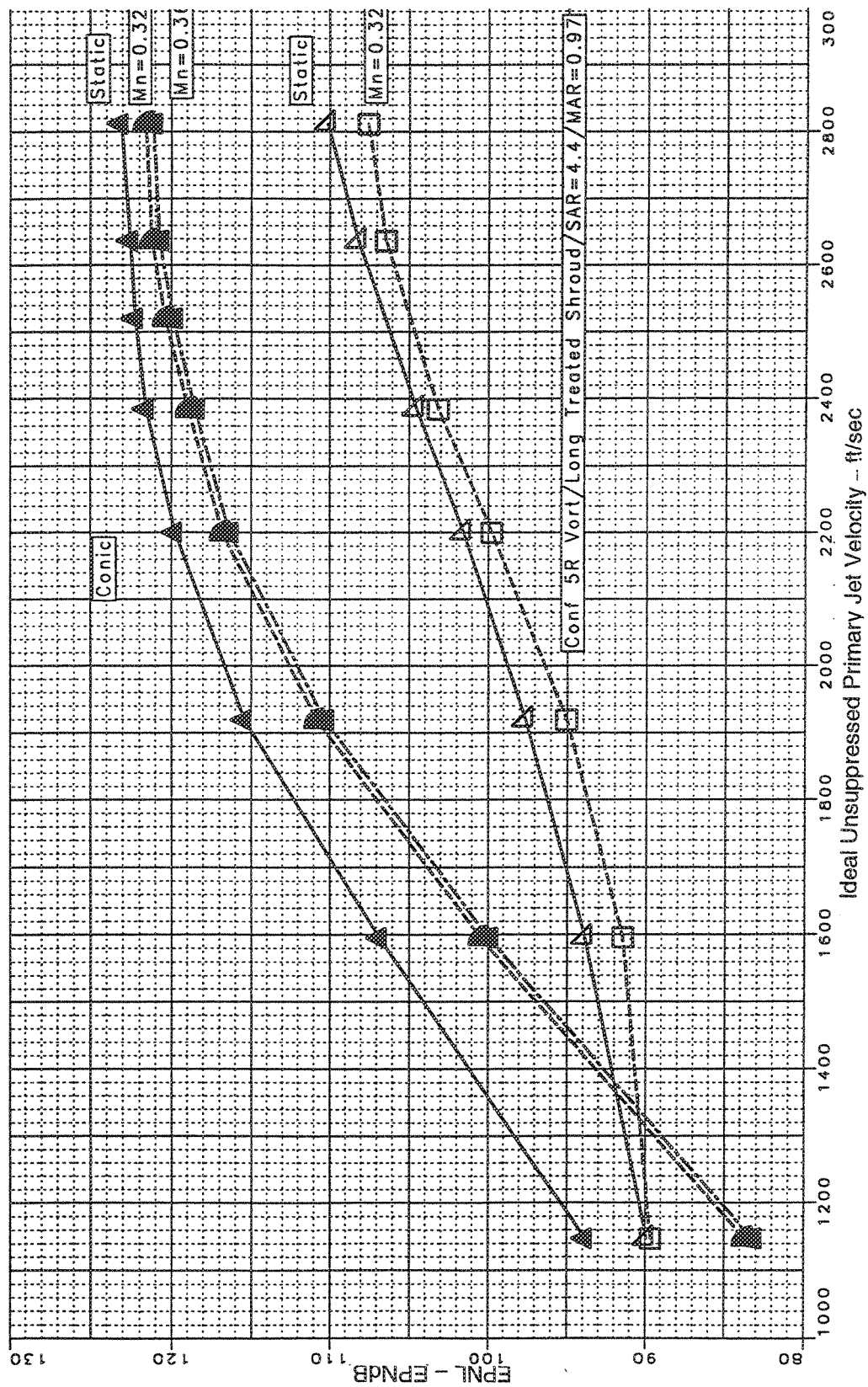


Figure 150. Effect of Flight Mach Number on Sideline Noise, Vortical Mixer, Long Treated Shroud  
(Sideline=1629 ft, SAR=4.4, MAR=0.97,  $A_{g*}=1086 \text{ in}^2$ ,  $Mn=0.0$ ,  $0.32$ , and  $0.36$ )

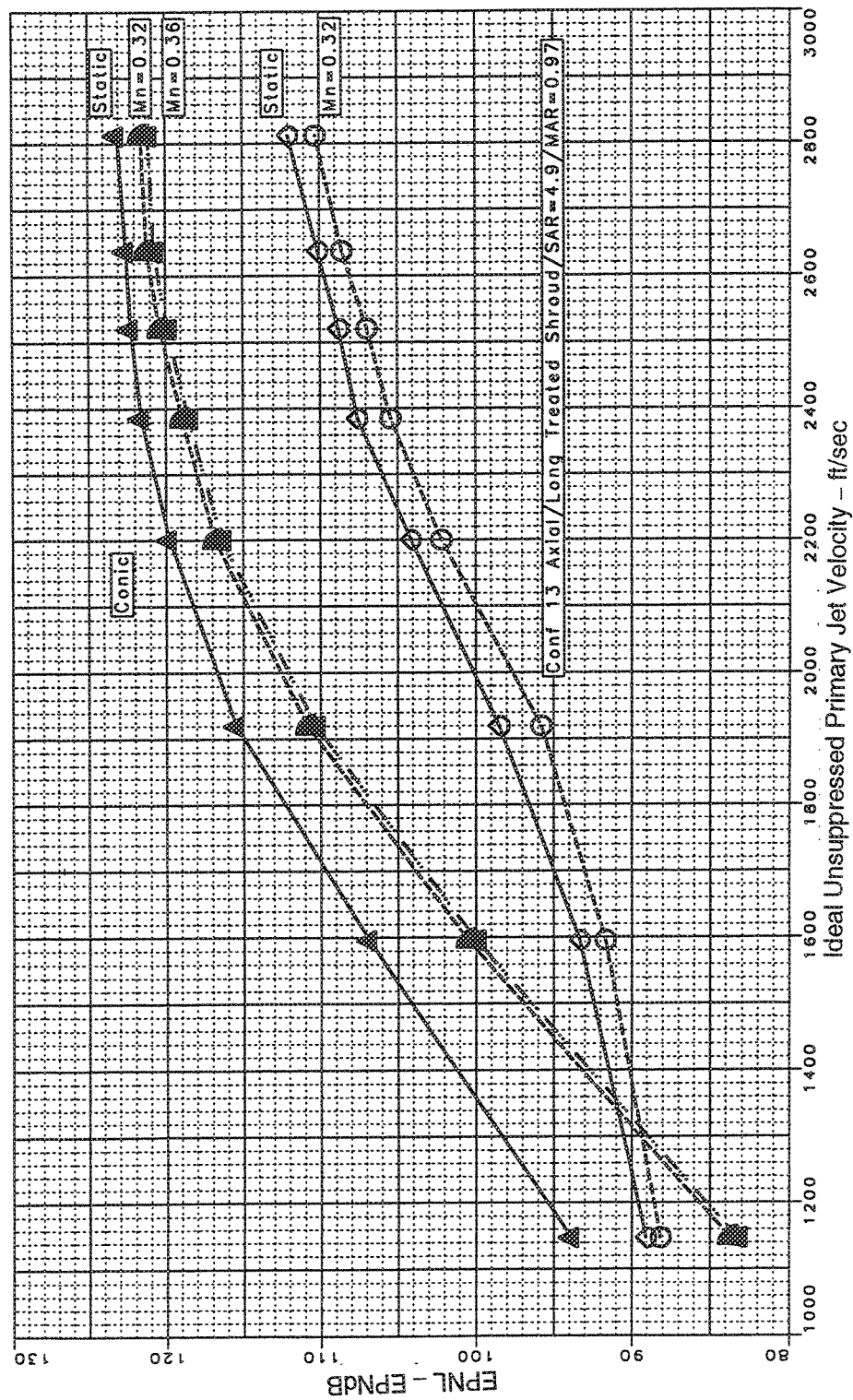


Figure 151. Effect of Flight Mach Number on Sideline Noise, Baseline Round Conic Nozzle, Axial Mixer, Long Treated Shroud  
(Sideline=1629 ft, SAR=4.9, MAR=0.97,  $A_{g*}=1086 \text{ in}^2$ ,  $Mn=0.0$ , 0.32, and 0.36)



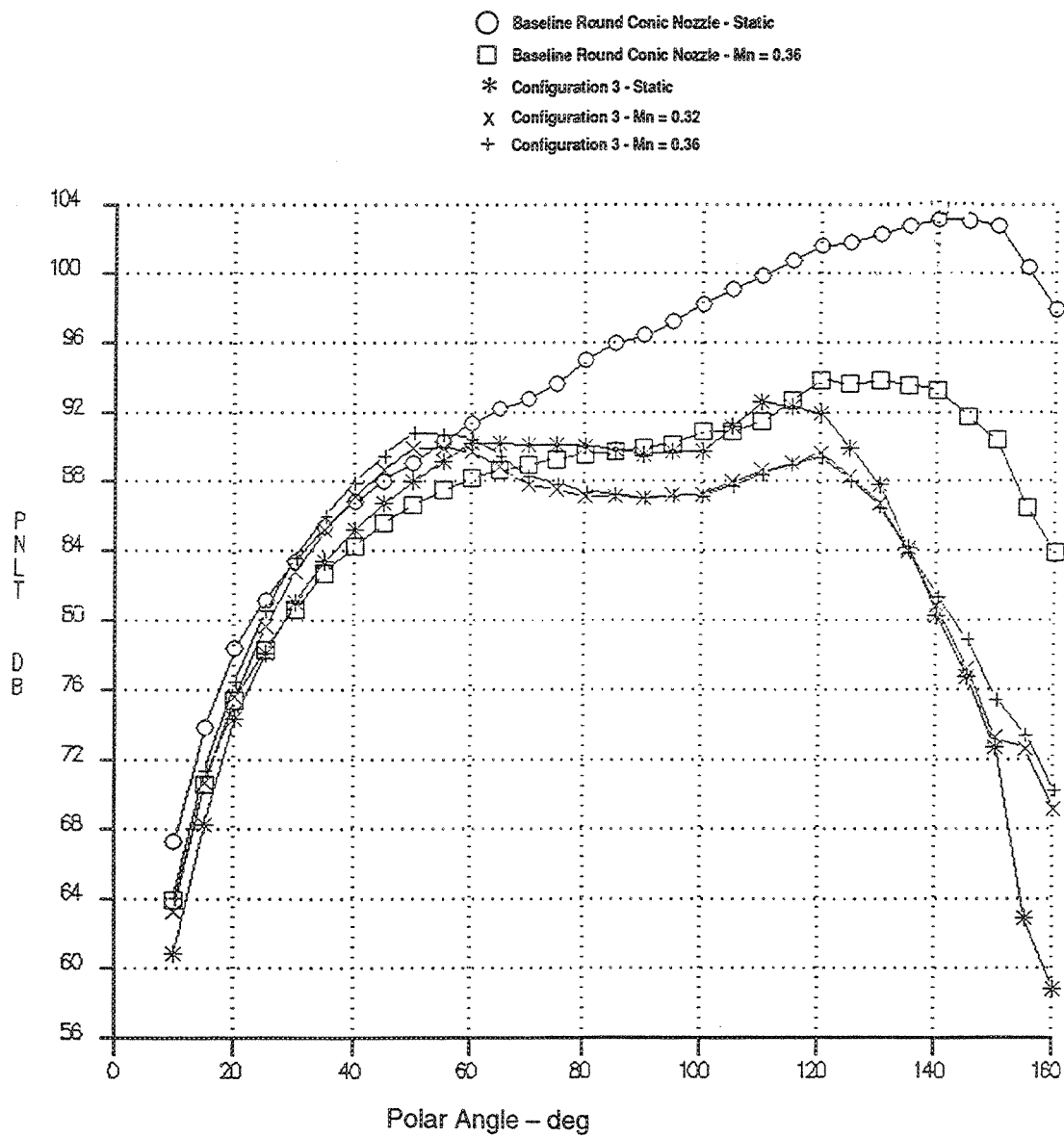


Figure 152. Effect of Flight Mach Number on Sideline Noise, PNL T Versus Angle  
 — Ideal Unsuppressed Primary Jet Velocity=1595 ft/sec, Baseline Round Conic Nozzle, Vortical Mixer,  
 Long Treated Shroud, (Sideline=1629 ft, SAR=4.9, MAR=0.97,  $A_{g*}=1086 \text{ in}^2$ )

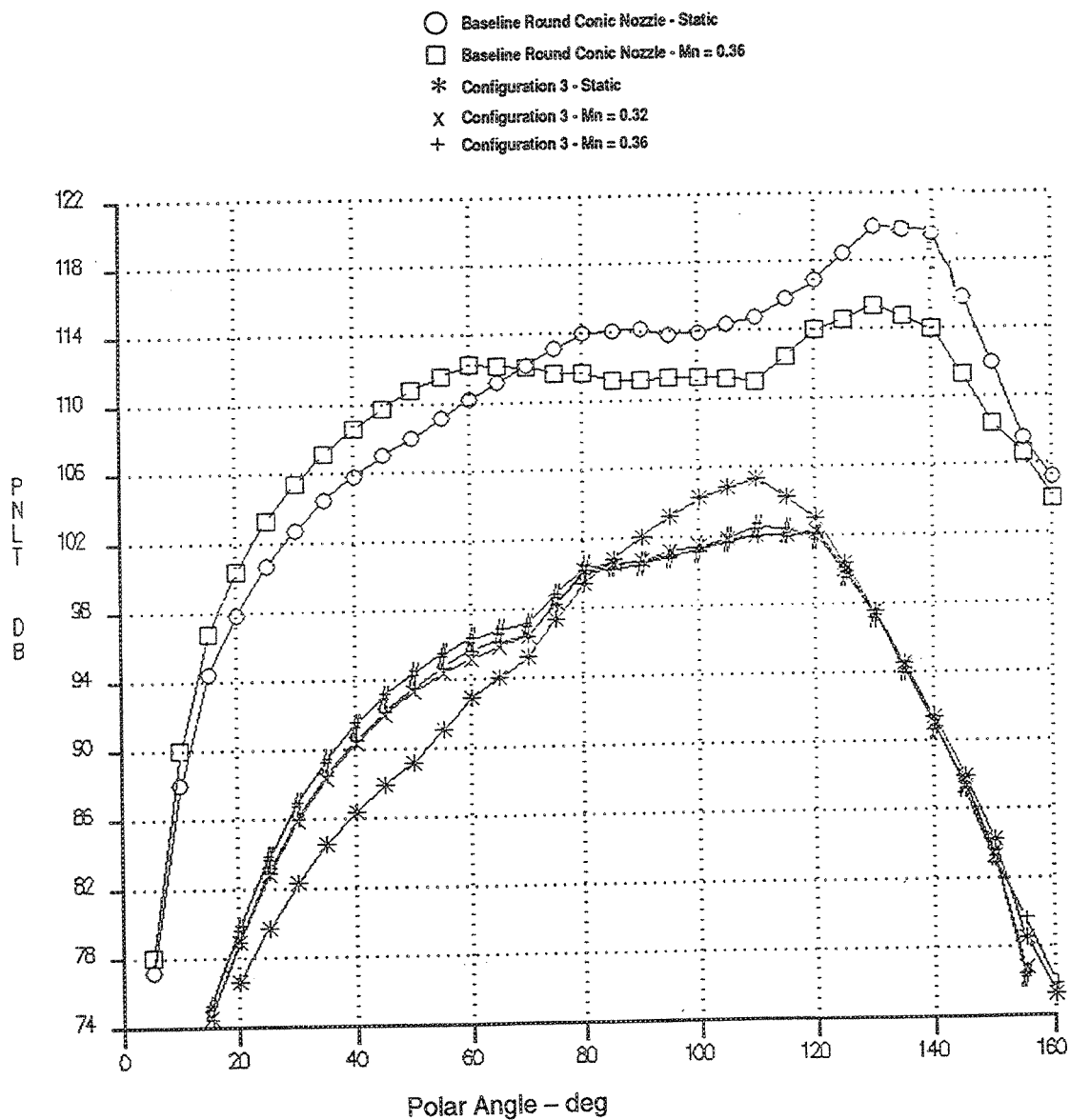


Figure 153. Effect of Flight Mach Number on Sideline Noise, PNL T Versus Angle  
 — Ideal Unsuppressed Primary Jet Velocity=2384 ft/sec, Baseline Round Conic Nozzle, Vortical Mixer,  
 Long Treated Shroud, (Sideline=1629 ft, SAR=4.9, MAR=0.97,  $A_{g*}=1086 \text{ in}^2$ )

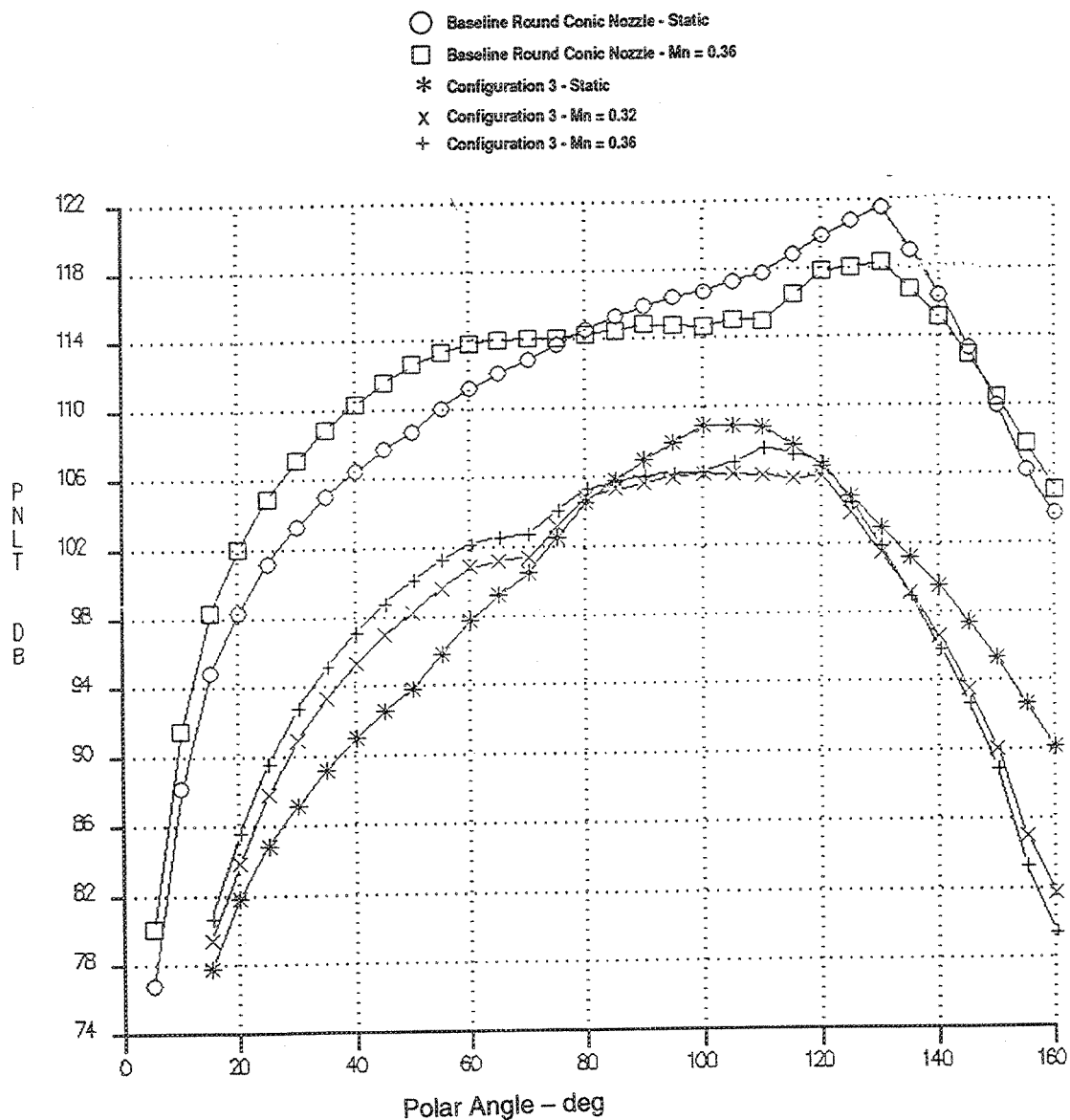


Figure 154. Effect of Flight Mach Number on Sideline Noise, PNL T Versus Angle  
 — Ideal Unsuppressed Primary Jet Velocity=2812 ft/sec, Baseline Round Conic Nozzle, Vortical Mixer,  
 Long Treated Shroud, (Sideline=1629 ft, SAR=4.9, MAR=0.97,  $A_{g*}=1086 \text{ in}^2$ )

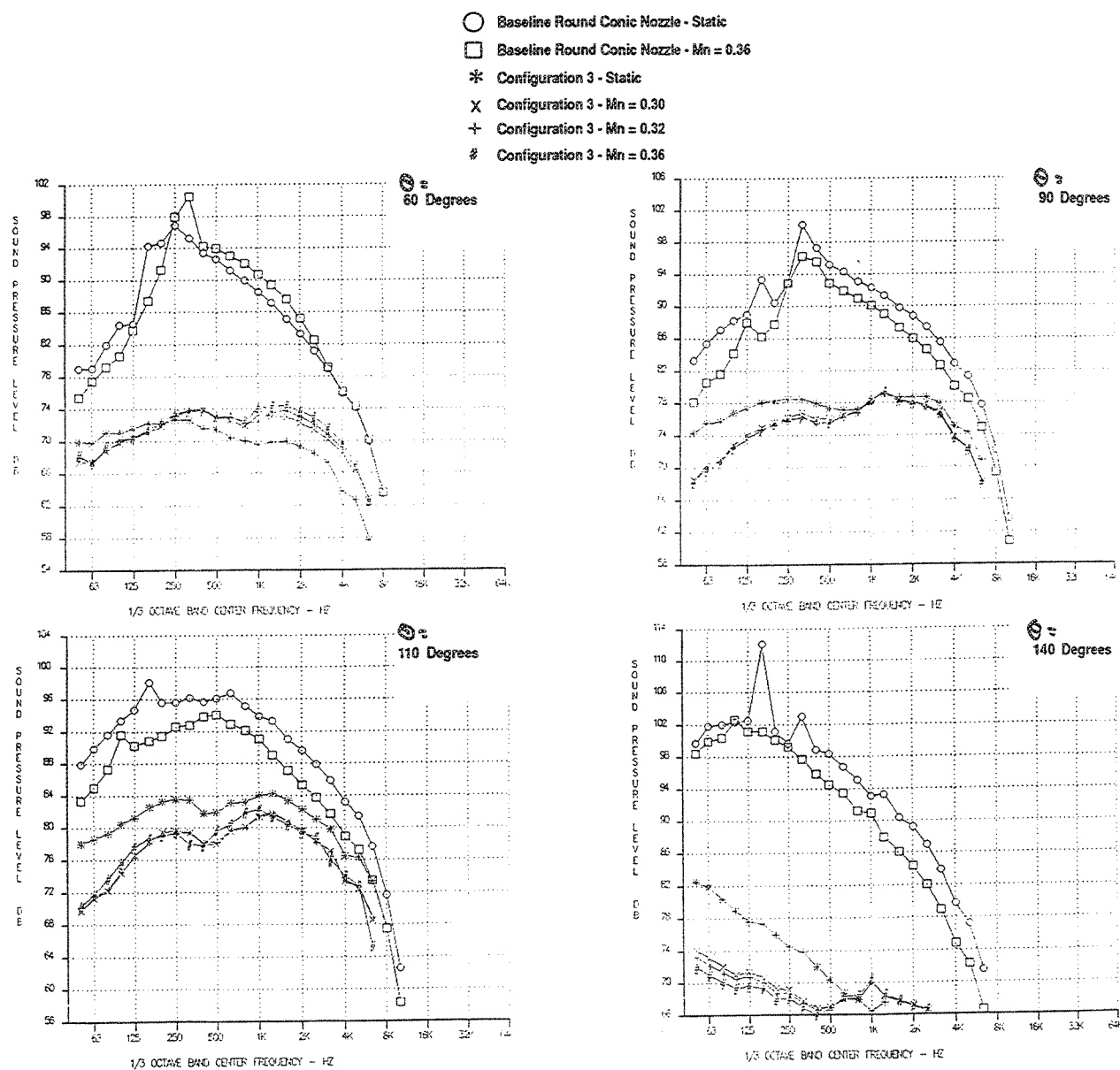


Figure 155. Effect of Flight Mach Number on Sideline Noise, SPL Versus Frequency  
 — Ideal Unsuppressed Primary Jet Velocity=2384 ft/sec, Baseline Round Conic Nozzle, Vortical Mixer,  
 Long Treated Shroud, (Sideline=1629 ft, SAR=4.9, MAR=0.97,  $A_{8*}=1086 \text{ in}^2$ )

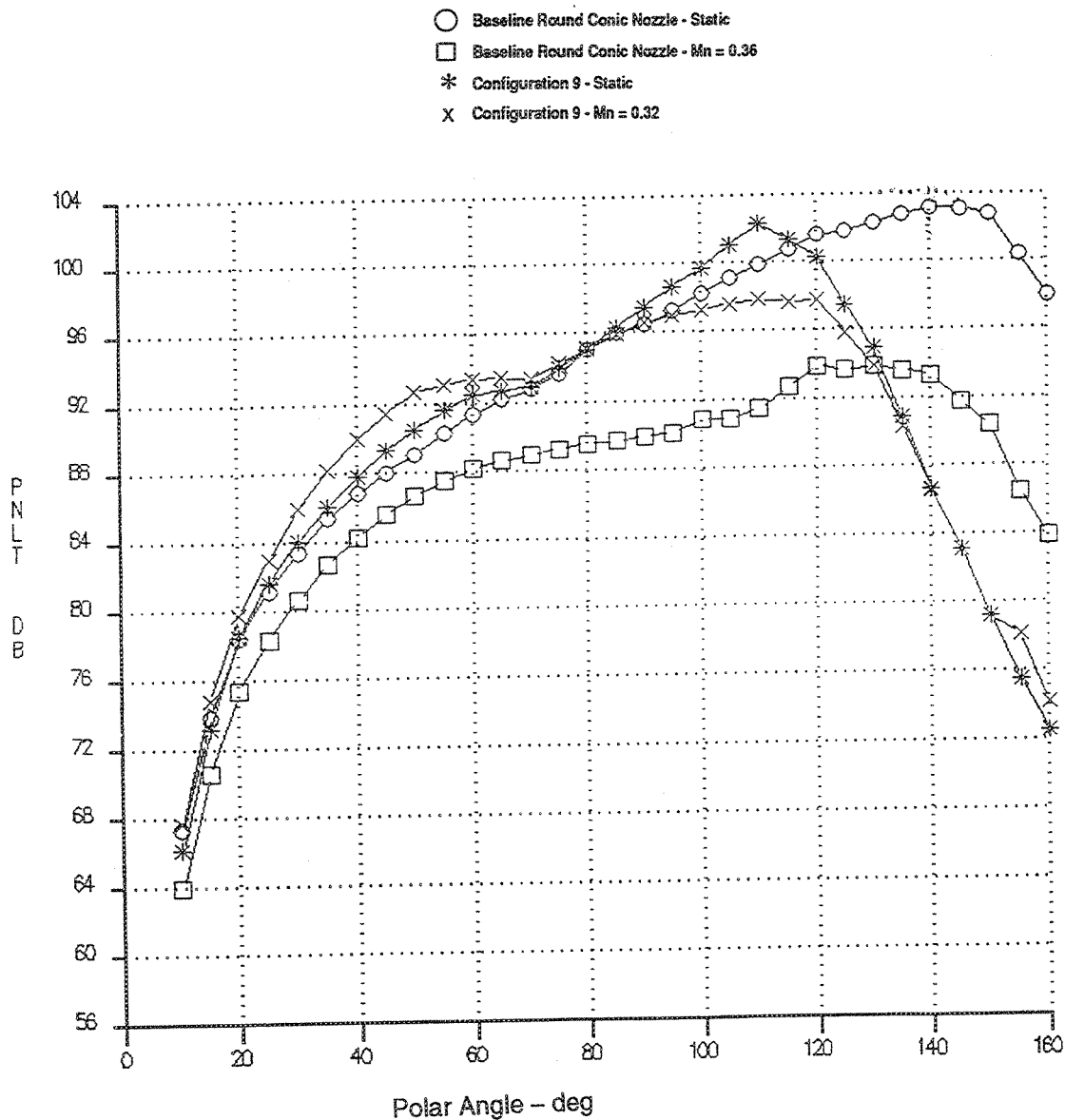


Figure 156. Effect of Flight Mach Number on Sideline Noise, PNL T Versus Angle  
 — Ideal Unsuppressed Primary Jet Velocity=1595 ft/sec, Baseline Round Conic Nozzle, Vortical Mixer,  
 Long Hardwall Shroud, (Sideline=1629 ft, SAR=4.9, MAR=0.97,  $A_{g*}=1086 \text{ in}^2$ )

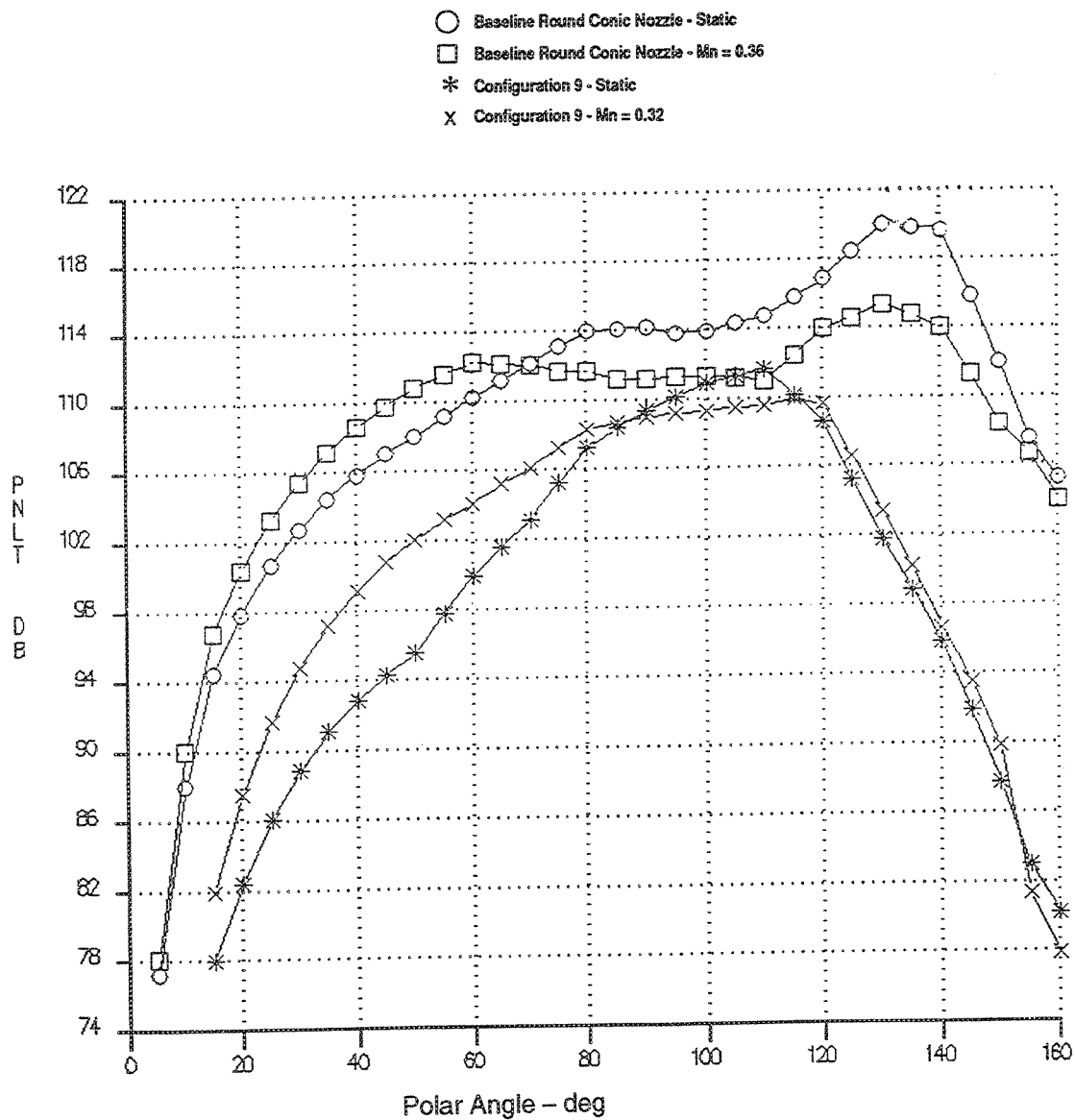


Figure 157. Effect of Flight Mach Number on Sideline Noise, PNL T Versus Angle  
 — Ideal Unsuppressed Primary Jet Velocity=2384 ft/sec, Baseline Round Conic Nozzle, Vortical Mixer,  
 Long Hardwall Shroud, (Sideline=1629 ft, SAR=4.9, MAR=0.97,  $A_{g*}=1086 \text{ in}^2$ )

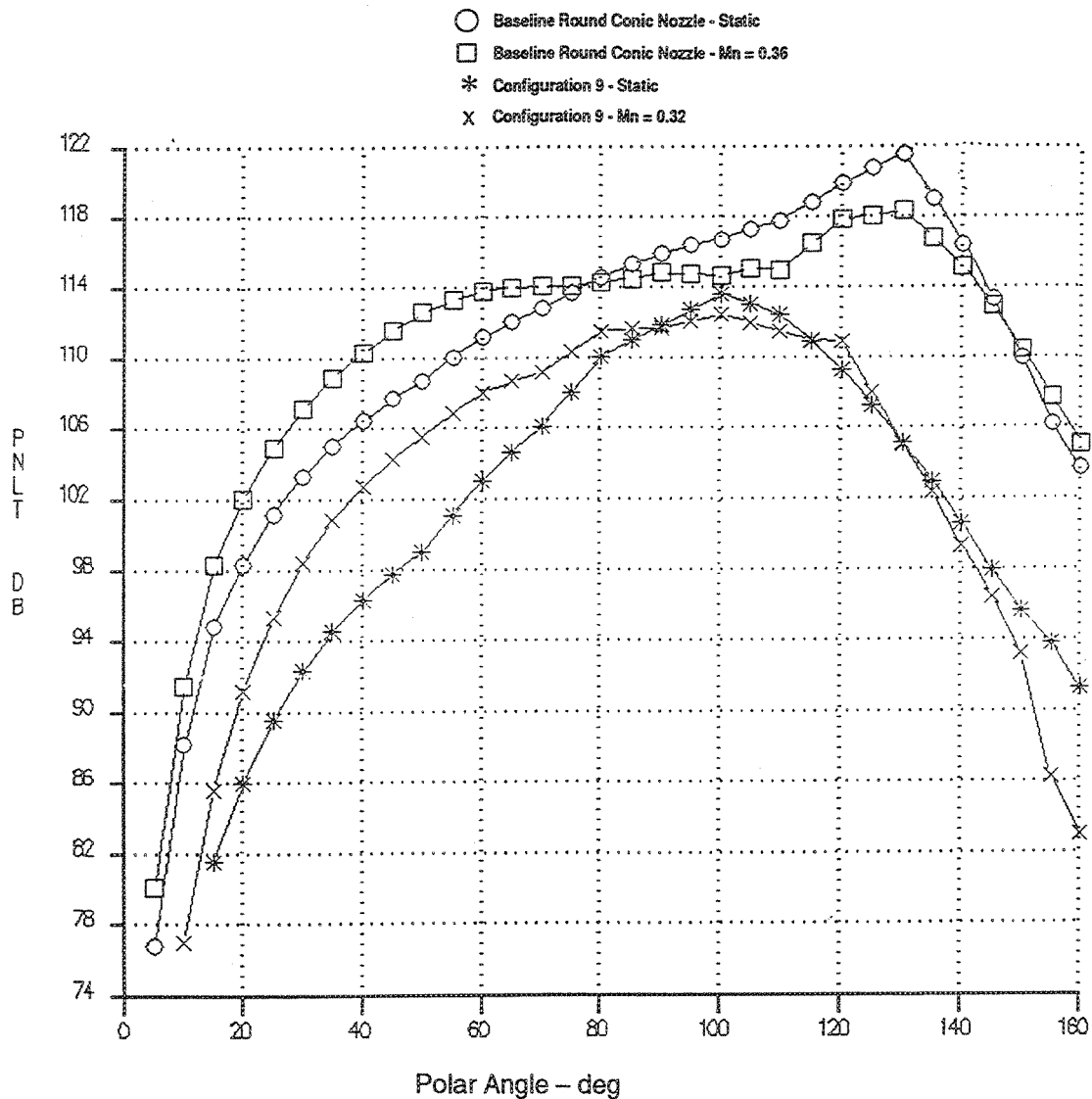


Figure 158. Effect of Flight Mach Number on Sideline Noise, PNL T Versus Angle  
 — Ideal Unsuppressed Primary Jet Velocity=2812 ft/sec, Baseline Round Conic Nozzle, Vortical Mixer,  
 Long Hardwall Shroud, (Sideline=1629 ft, SAR=4.9, MAR=0.97,  $A_{g*}=1086 \text{ in}^2$ )

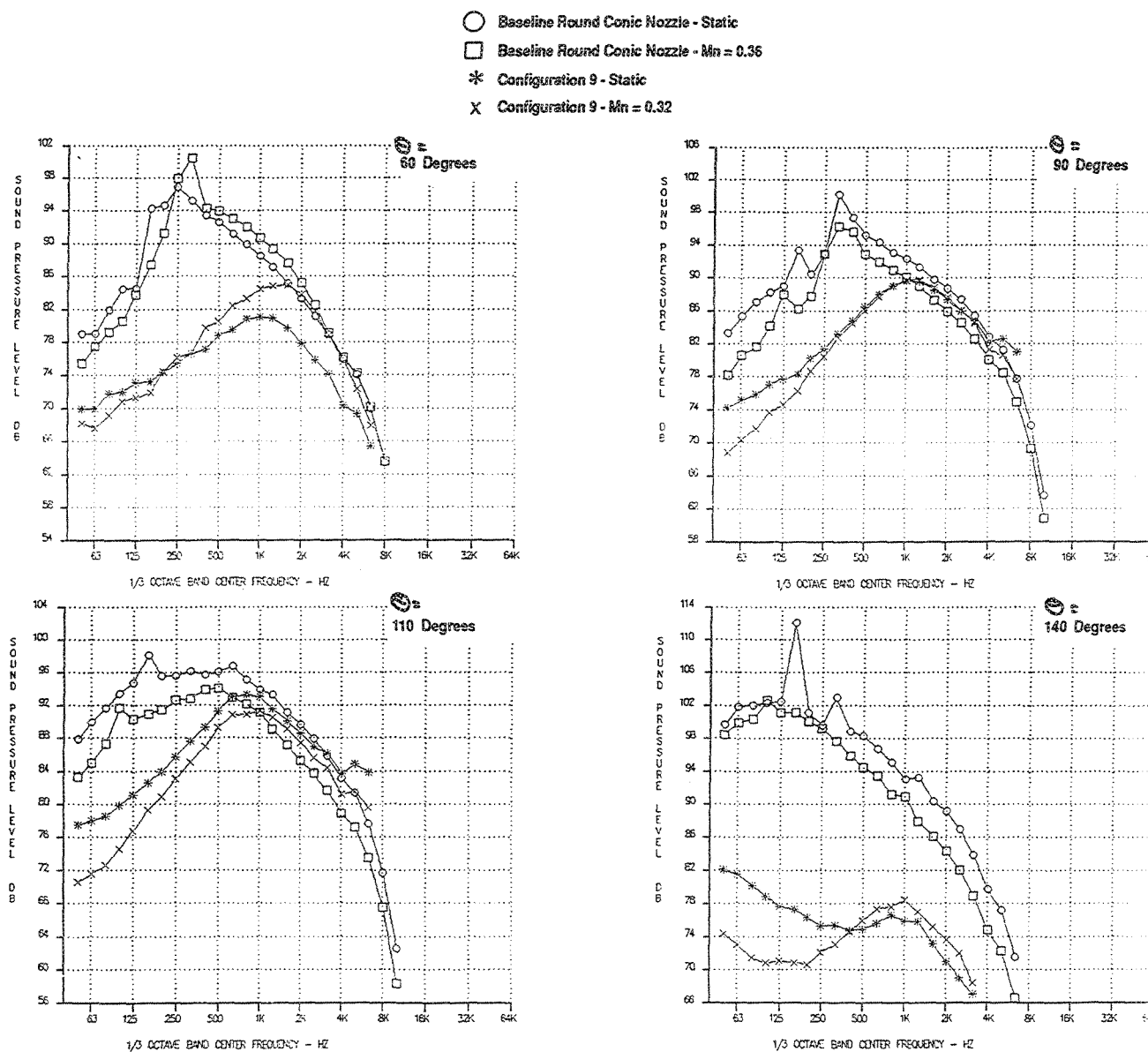


Figure 159. Effect of Flight Mach Number on Sideline Noise, SPL Versus Frequency  
 — Ideal Unsuppressed Primary Jet Velocity=2384ft/sec, Baseline Round Conic Nozzle, Vortical Mixer,  
 Long Hardwall Shroud, (Sideline=1629 ft, SAR=4.9, MAR=0.97,  $A_{g*}=1086 \text{ in}^2$ )



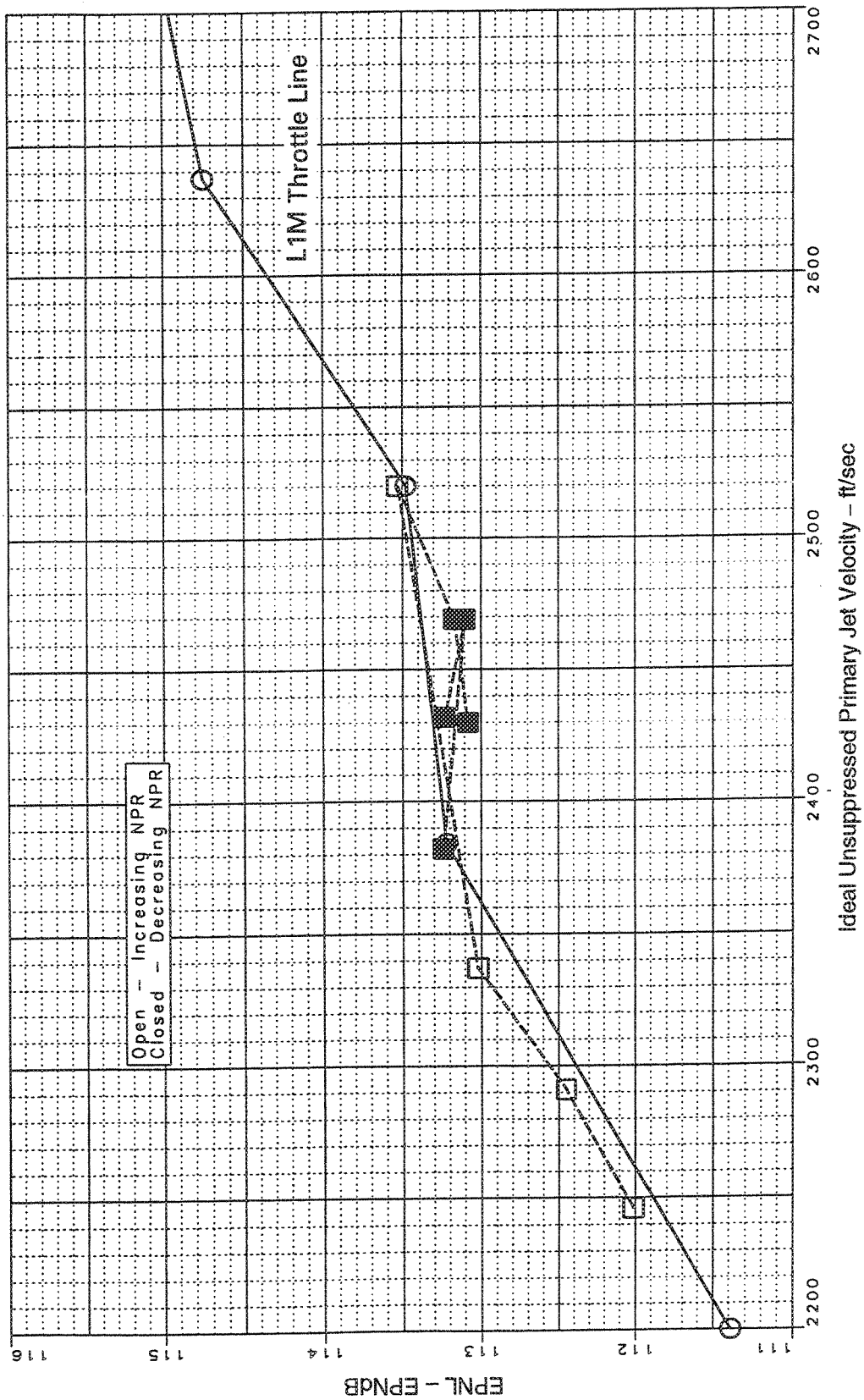


Figure 160. Sideline Noise Acoustic Hysteresis, Vortical Mixer, Long Hardwall Shroud  
(Sideline=1629 ft, SAR=4.9, MAR=1.19,  $A_{g*}=1086 \text{ in}^2$ , Static)

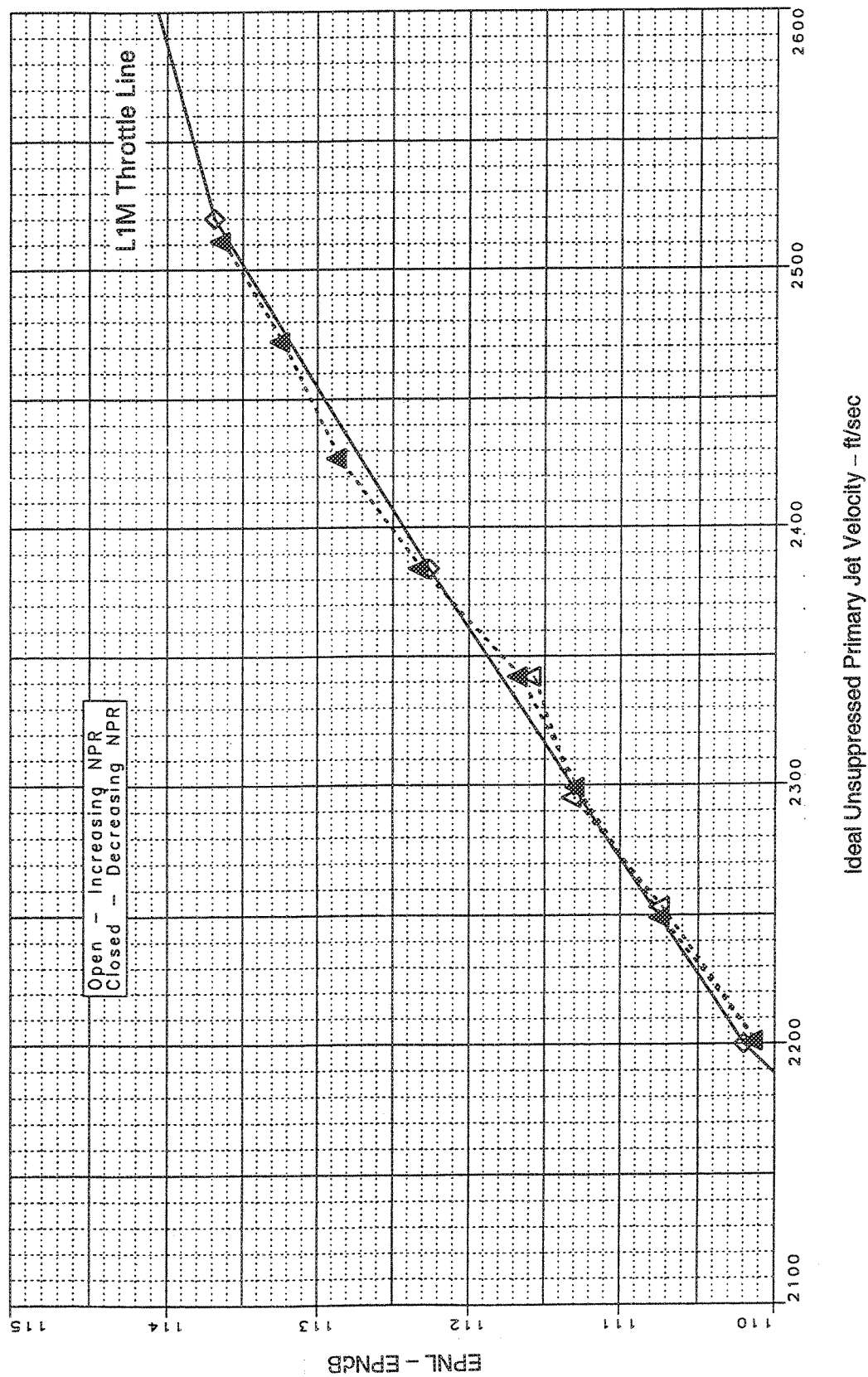


Figure 161. Sideline Noise Acoustic Hysteresis, Vortical Mixer, Long Hardwall Shroud  
(Sideline=1629 ft, SAR=4.9, MAR=1.19,  $A_{g*}=1086 \text{ in}^2$ ,  $M_n=0.32$ ,  $V_{\eta}=357 \text{ ft/sec}$ )

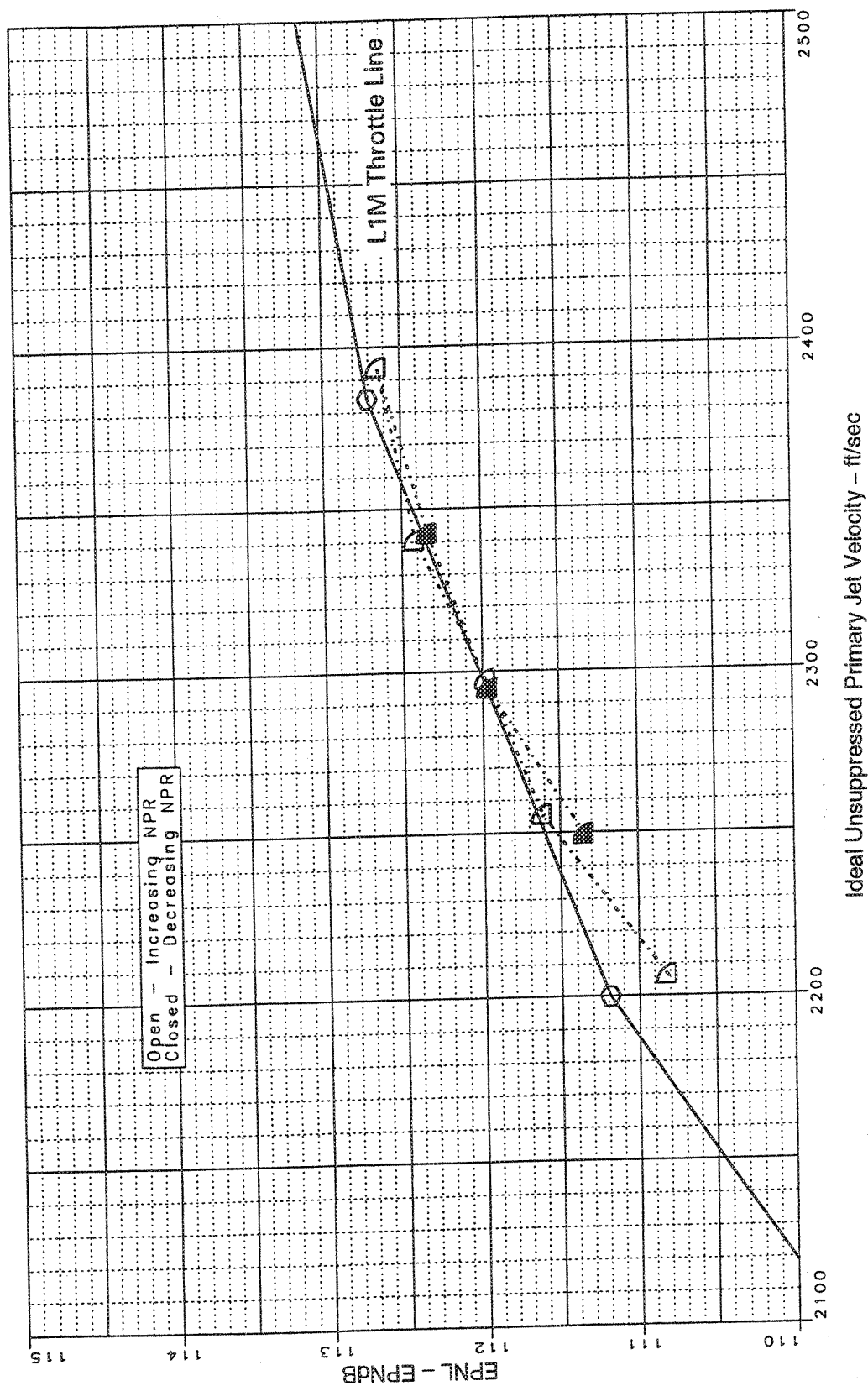


Figure 162. Sideline Noise Acoustic Hysteresis, Vortical Mixer, Long Hardwall Shroud  
(Sideline=1629 ft, SAR=4.4, MAR=1.19,  $A_{g*}=1086 \text{ in}^2$ , Static)

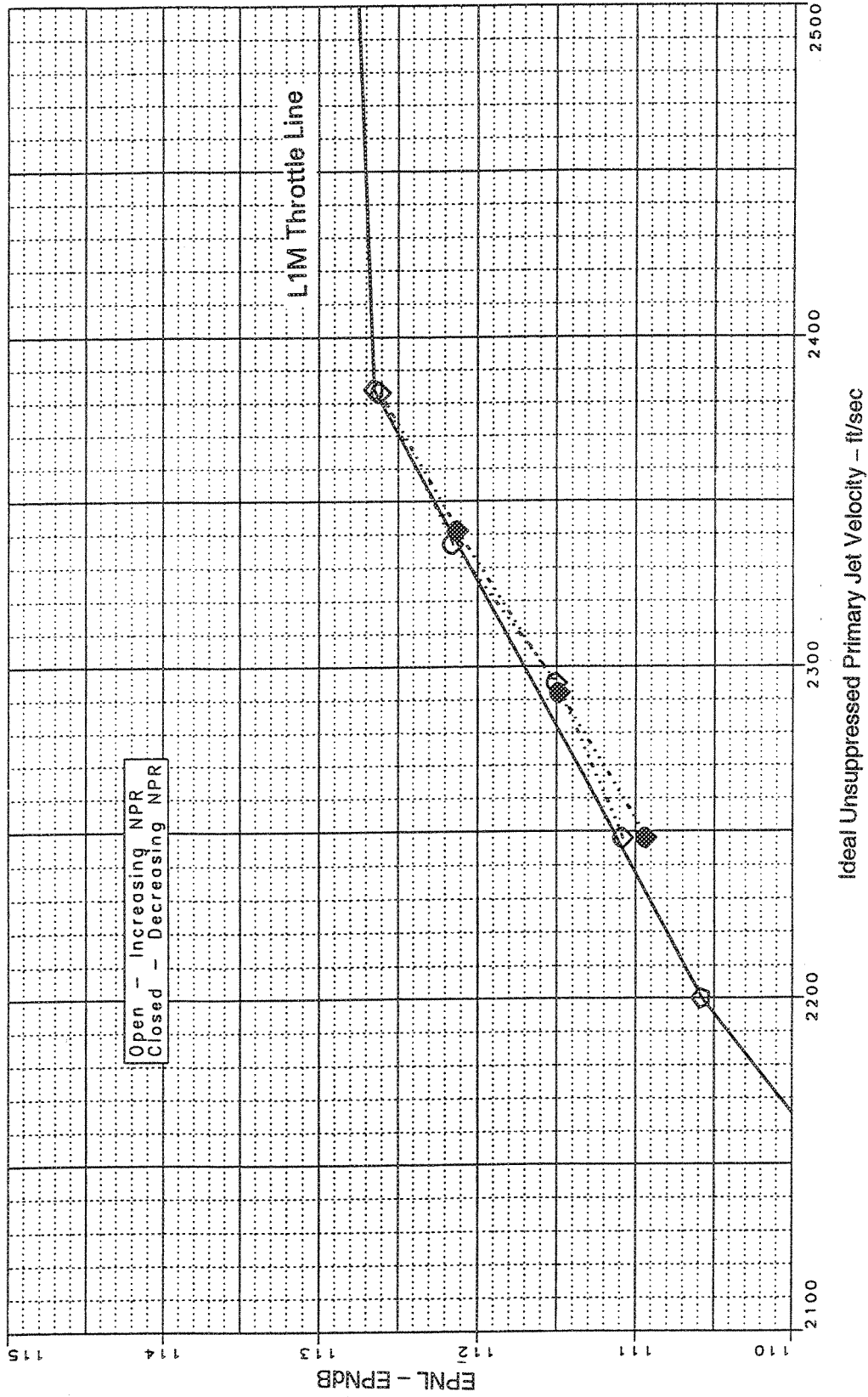


Figure 163. Sideline Noise Acoustic Hysteresis, Vortical Mixer, Long Hardwall Shroud  
(Sideline=1629 ft, SAR=4.4, MAR=1.19,  $A_{g*}=1086 \text{ in}^2$ ,  $Mn=0.32$ ,  $V_{\eta}=357 \text{ ft/sec}$ )

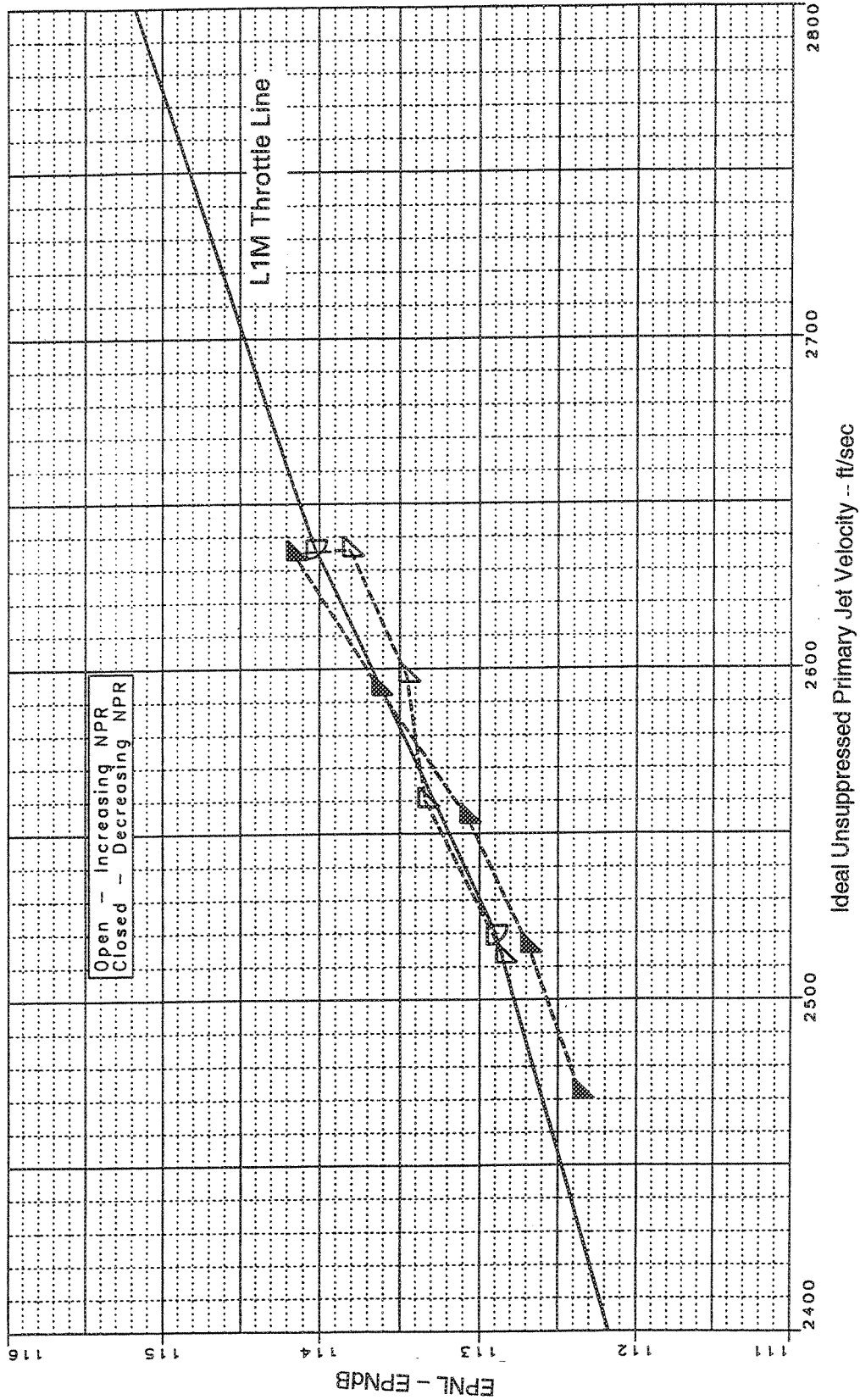


Figure 164. Sideline Noise Acoustic Hysteresis, Axial Mixer, Long Hardwall Shroud  
(Sideline=1629 ft, SAR=4.9, MAR=1.19,  $A_{g*}=1086 \text{ in}^2$ , Static)

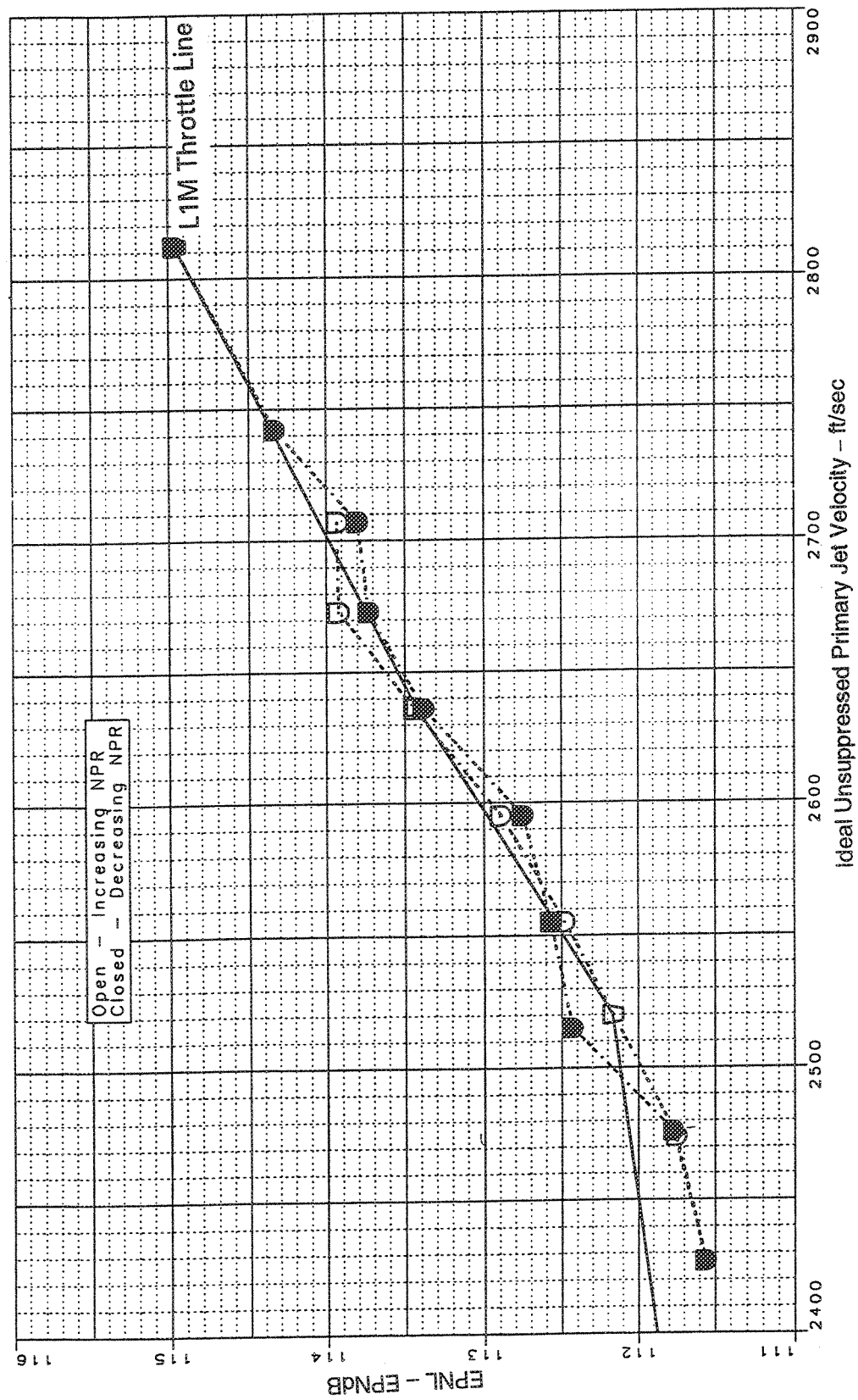


Figure 165. Sideline Noise Acoustic Hysteresis, Axial Mixer, Long Hardwall Shroud  
(Sideline=1629 ft, SAR=4.9, MAR=1.19,  $A_{g*}=1086 \text{ in}^2$ ,  $M_n=0.32$ ,  $V_{\eta}=357 \text{ ft/sec}$ )

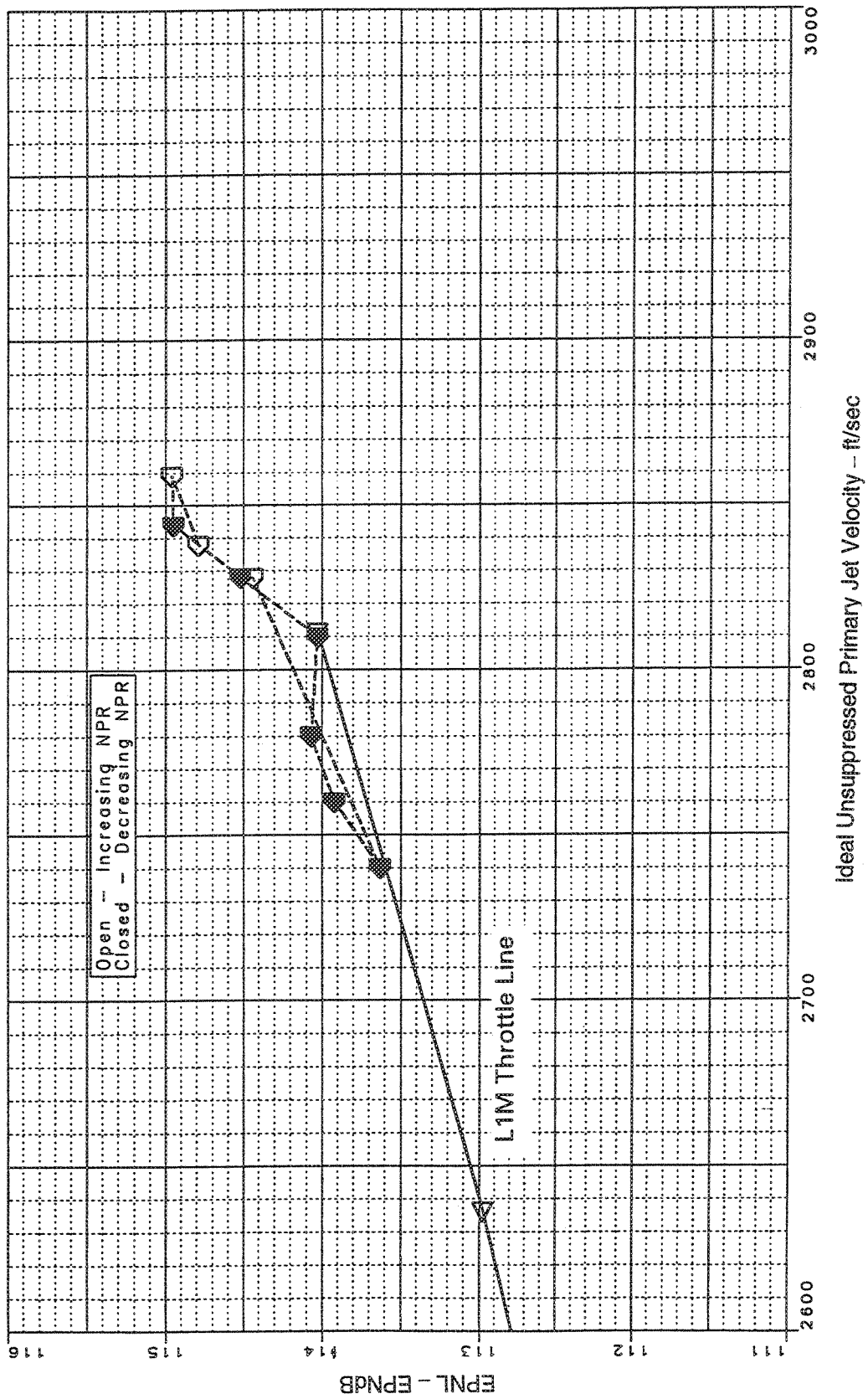


Figure 166. Sideline Noise Acoustic Hysteresis, Axial Mixer, Long Hardwall Shroud  
(Sideline=1629 ft, SAR=4.9, MAR=0.97,  $A_{g*}=1086 \text{ in}^2$ , Static)

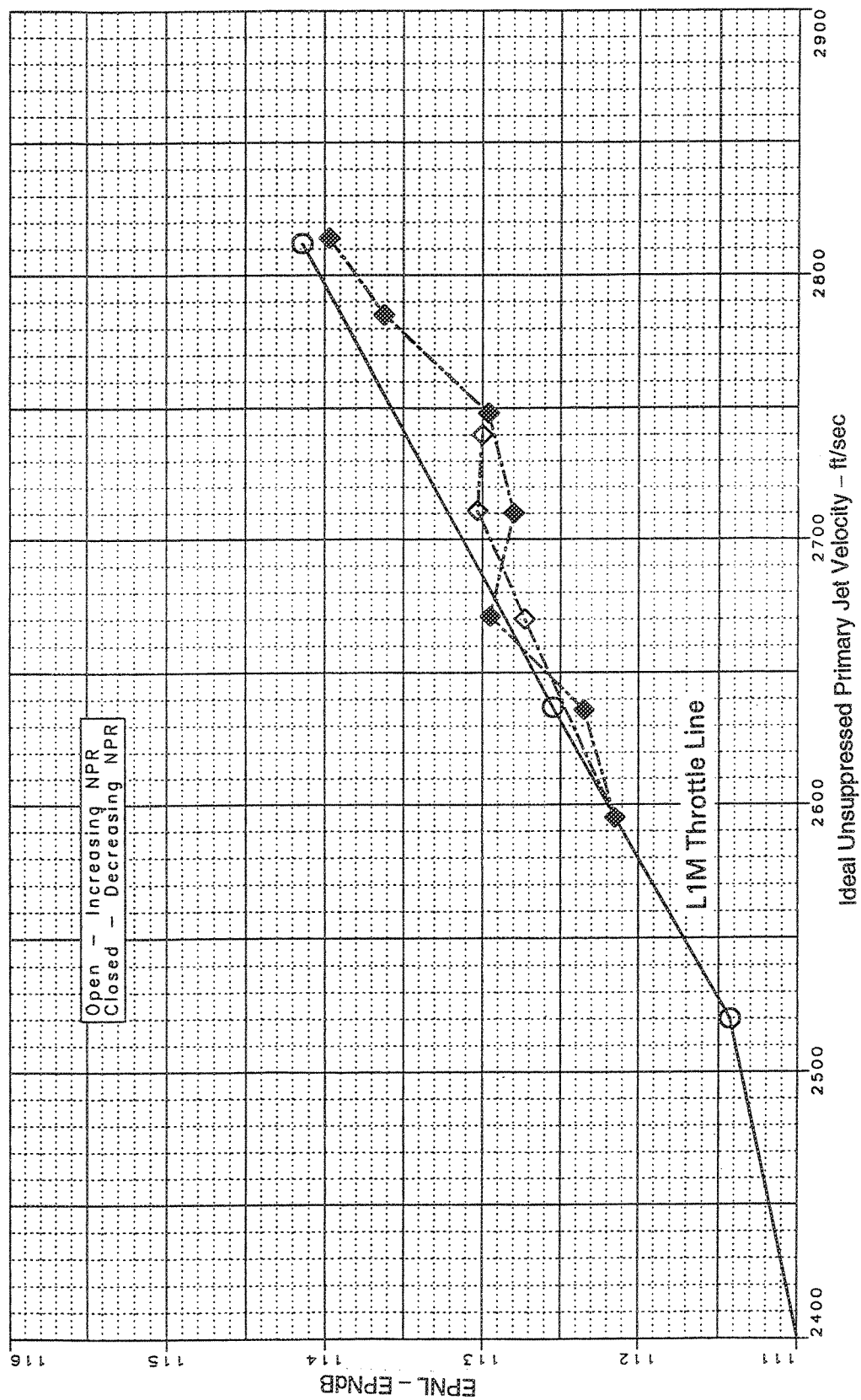


Figure 167. Sideline Noise Acoustic Hysteresis, Axial Mixer Long Hardwall Shroud  
(Sideline=1629 ft, SAR=4.9, MAR=0.97,  $A_{g*}=1086 \text{ in}^2$ ,  $M_n=0.32$ ,  $V_{\eta}=357 \text{ ft/sec}$ )



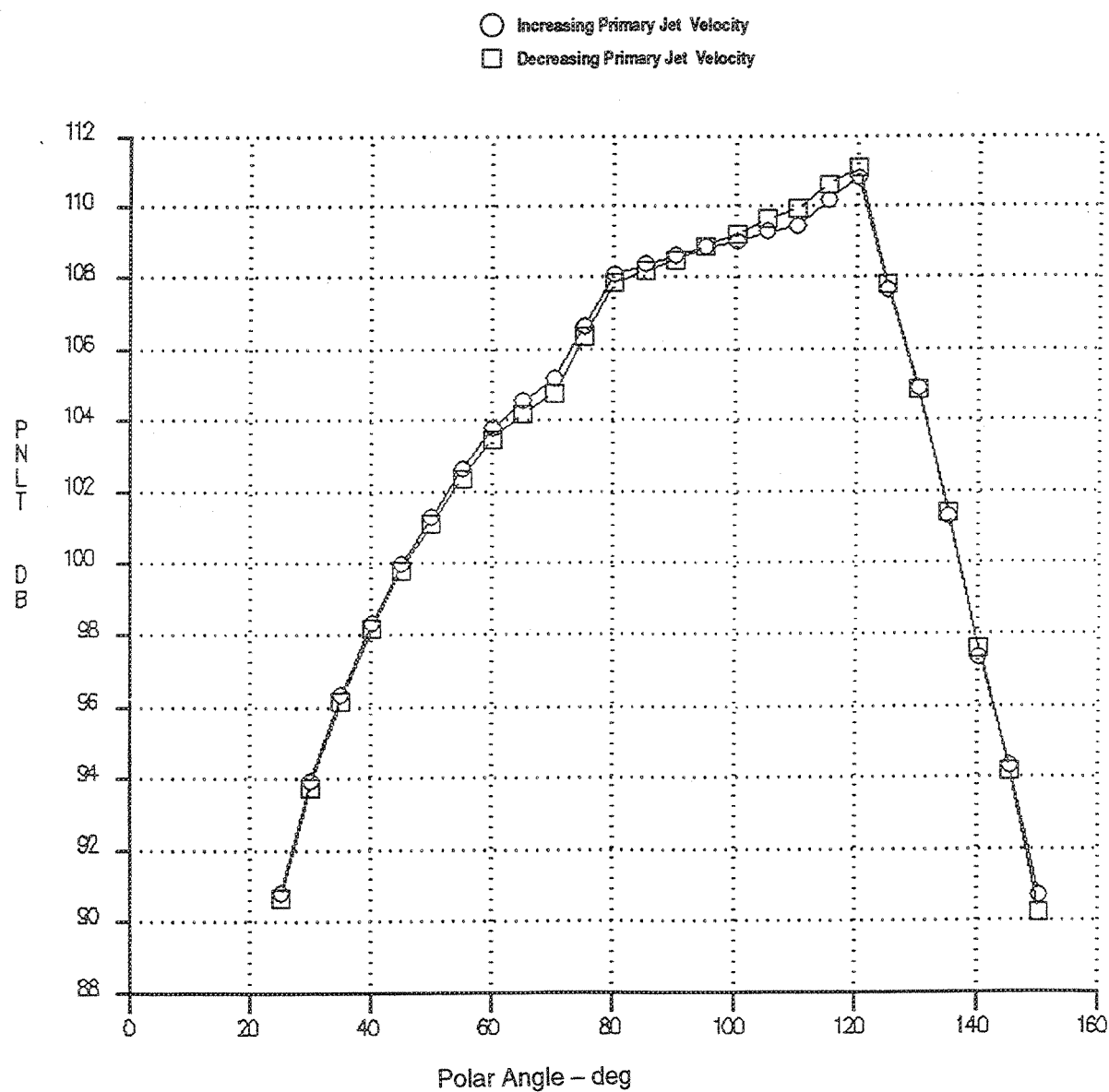


Figure 168. Sideline Noise Hysteresis, PNLT Versus Angle  
 — Ideal Unsuppressed Primary Jet Velocity=2340 ft/sec, Vortical Mixer, Long Hardwall Shroud  
 (Sideline=1629 ft, SAR=4.9, MAR=1.19,  $A_{g*}=1086 \text{ in}^2$ ,  $Mn=0.32$ ,  $V_{fl}=357 \text{ ft/sec}$ )

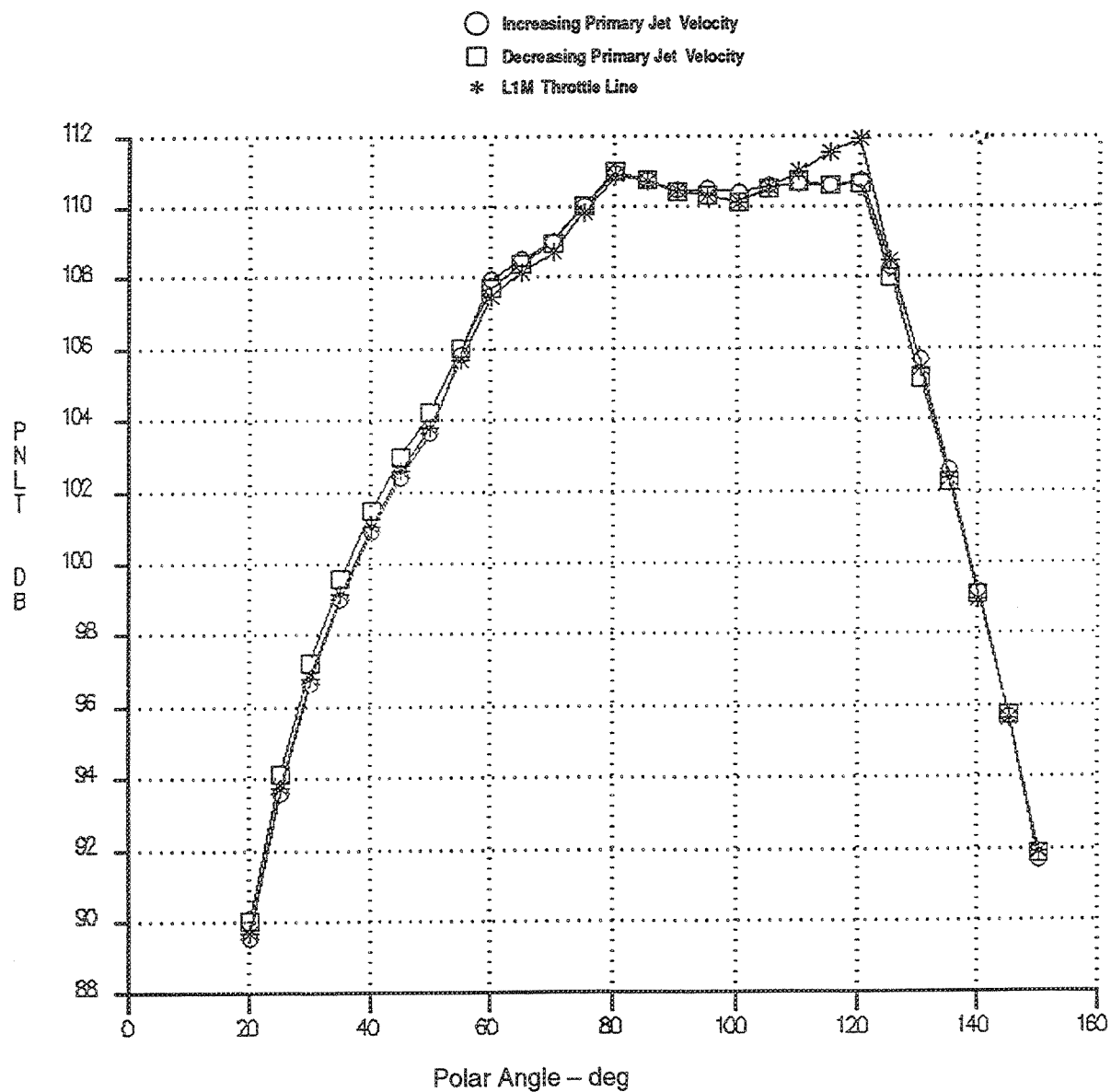


Figure 169. Sideline Noise Hysteresis, PNLT Versus Angle  
 — Ideal Unsuppressed Primary Jet Velocity=2637 ft/sec, Axial Mixer, Long Hardwall Shroud  
 (Sideline=1629 ft, SAR=4.9, MAR=1.19,  $A_{g*}=1086 \text{ in}^2$ ,  $M_n=0.32$ ,  $V_{fl}=357 \text{ ft/sec}$ )

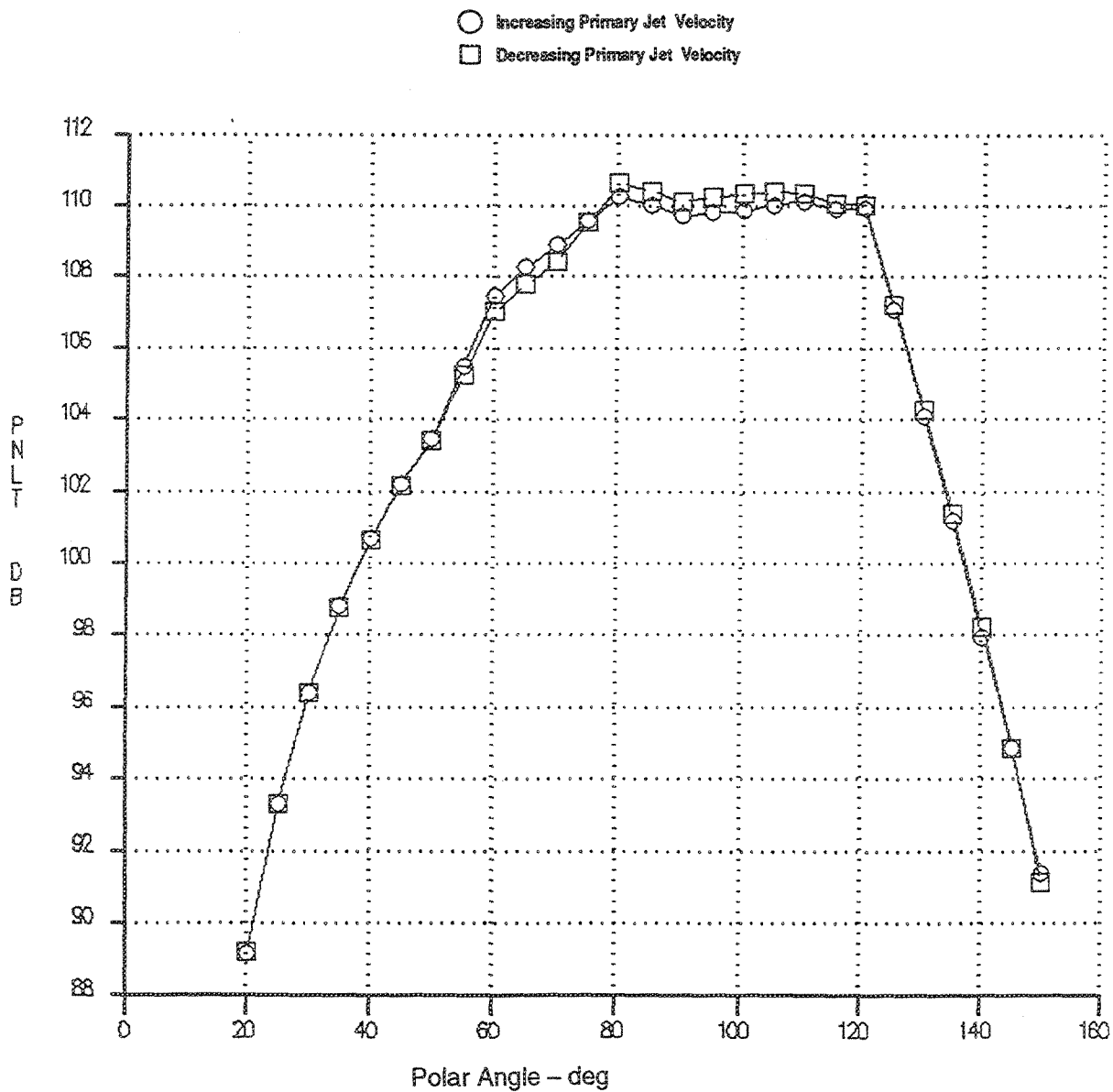
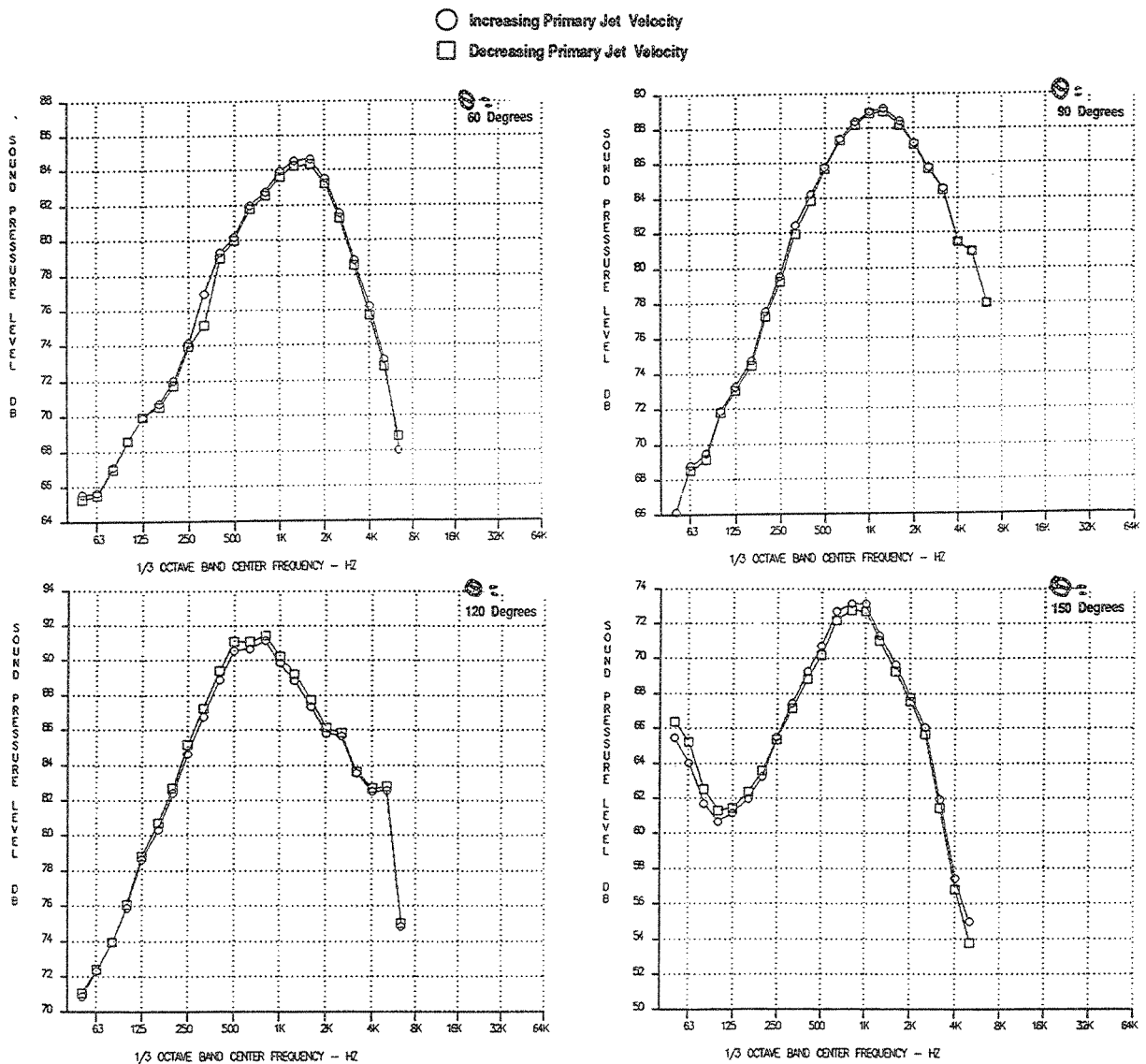


Figure 170. Sideline Noise Hysteresis, PNLT Versus Angle  
 — Ideal Unsuppressed Primary Jet Velocity=2670 ft/sec, Axial Mixer, Long Hardwall Shroud  
 (Sideline=1629 ft, SAR=4.9, MAR=0.97,  $A_{g*}=1086 \text{ in}^2$ ,  $M_n=0.32$ ,  $V_{fl}=357 \text{ ft/sec}$ )



*Figure 171. Sideline Noise Hysteresis, SPL vs. Frequency*  
 — Ideal Unsuppressed Primary Jet Velocity=2340 ft/sec, Vortical Mixer, Long Hardwall Shroud  
 (Sideline=1629 ft, SAR=4.9, MAR=1.19,  $A_{g*}=1086 \text{ in}^2$ ,  $M_n=0.32$ ,  $V_{H}=357 \text{ ft/sec}$ )

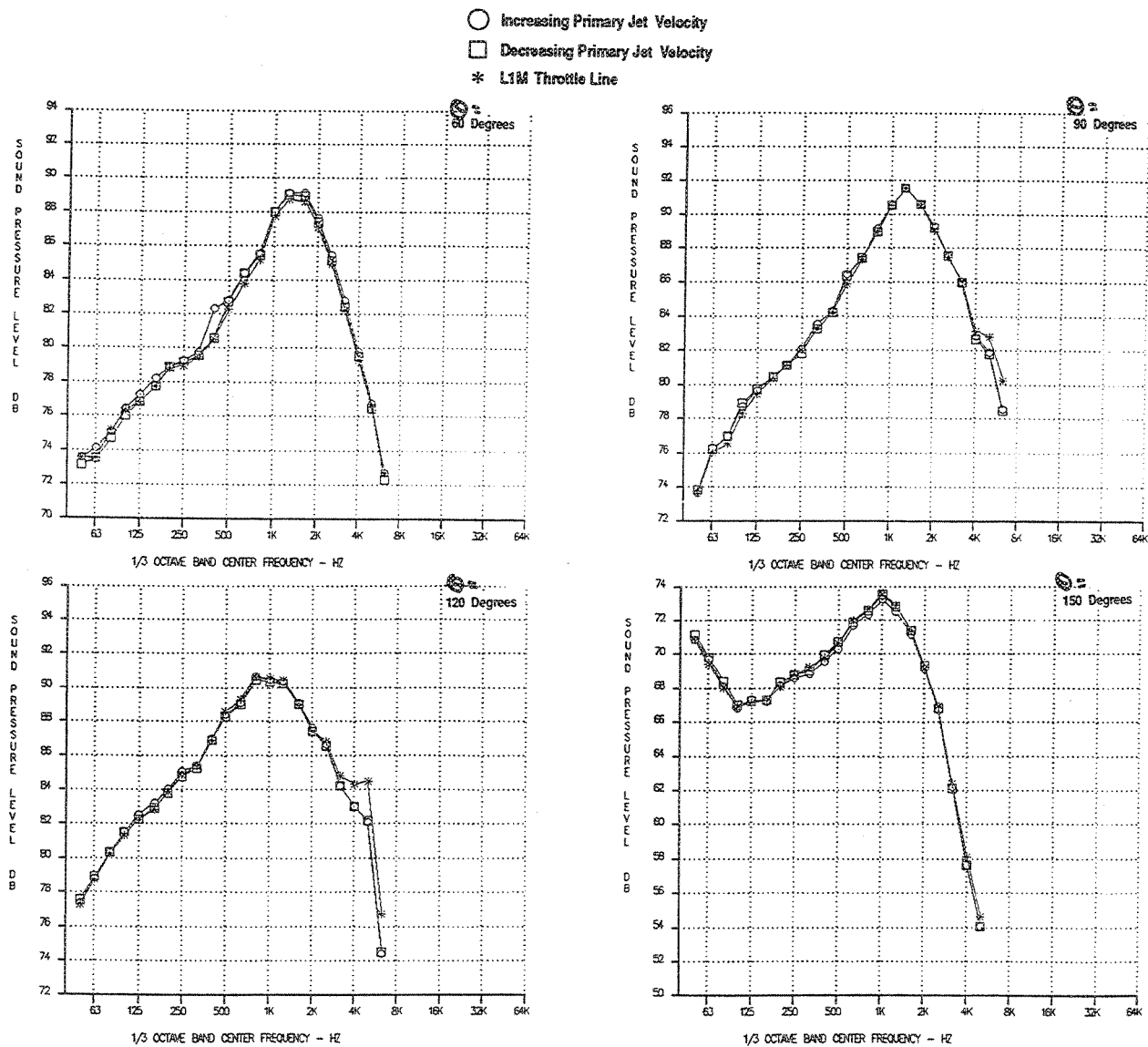


Figure 172. Sideline Noise Hysteresis, SPL vs. Frequency  
 — Ideal Unsuppressed Primary Jet Velocity=2637 ft/sec, Axial Mixer, Long Hardwall Shroud  
 (Sideline=1629 ft, SAR=4.9, MAR=1.19,  $A_{g*}=1086 \text{ in}^2$ ,  $M_n=0.32$ ,  $V_{fl}=357 \text{ ft/sec}$ )

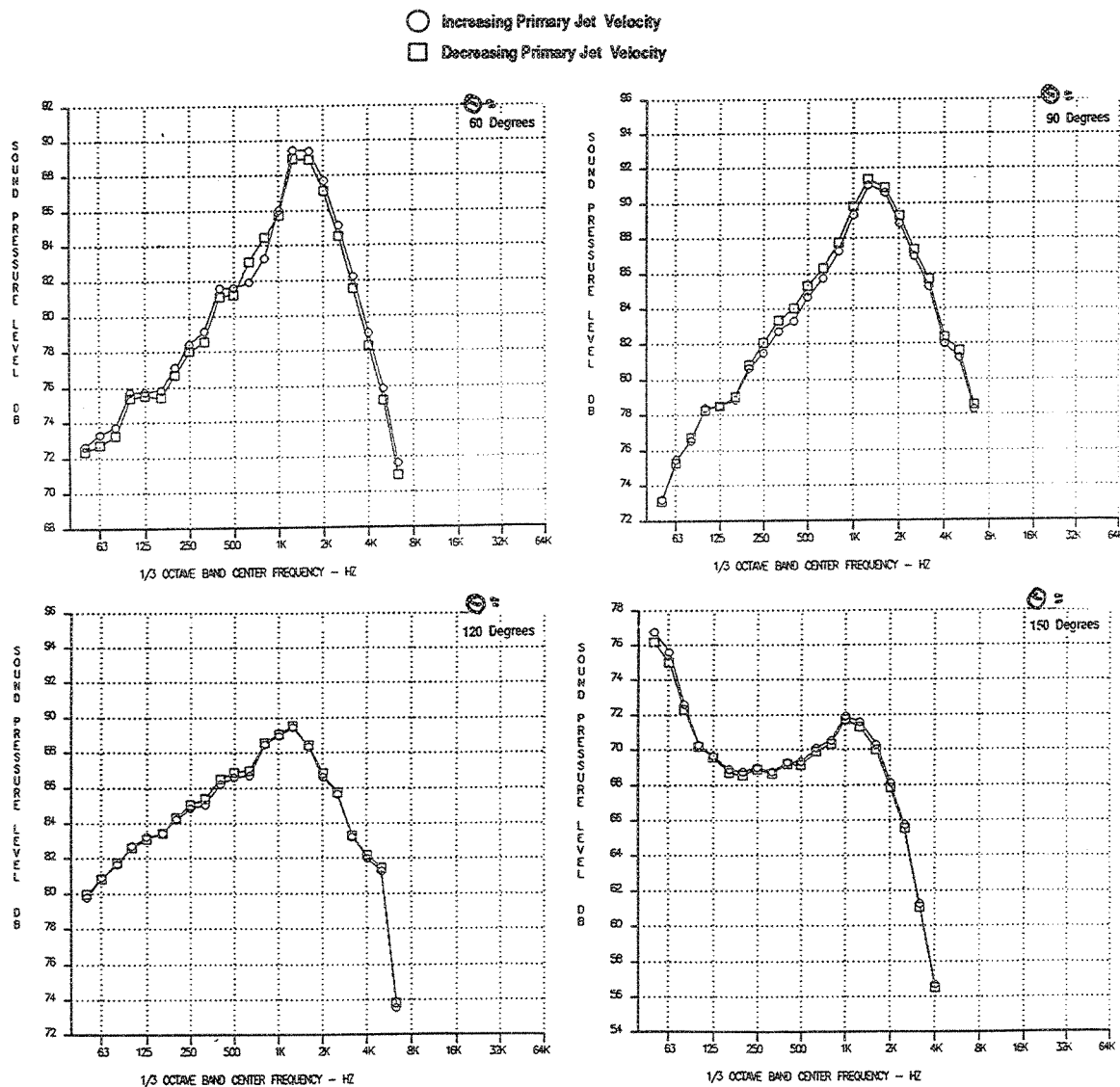


Figure 173. Sideline Noise Hysteresis, SPL vs. Frequency  
 — Ideal Unsuppressed Primary Jet Velocity=2670 ft/sec, Axial Mixer, Long Hardwall Shroud  
 (Sideline=1629 ft, SAR=4.9, MAR=0.97,  $A_8^*=1086 \text{ in}^2$ ,  $M_n=0.32$ ,  $V_{f1}=357 \text{ ft/sec}$ )

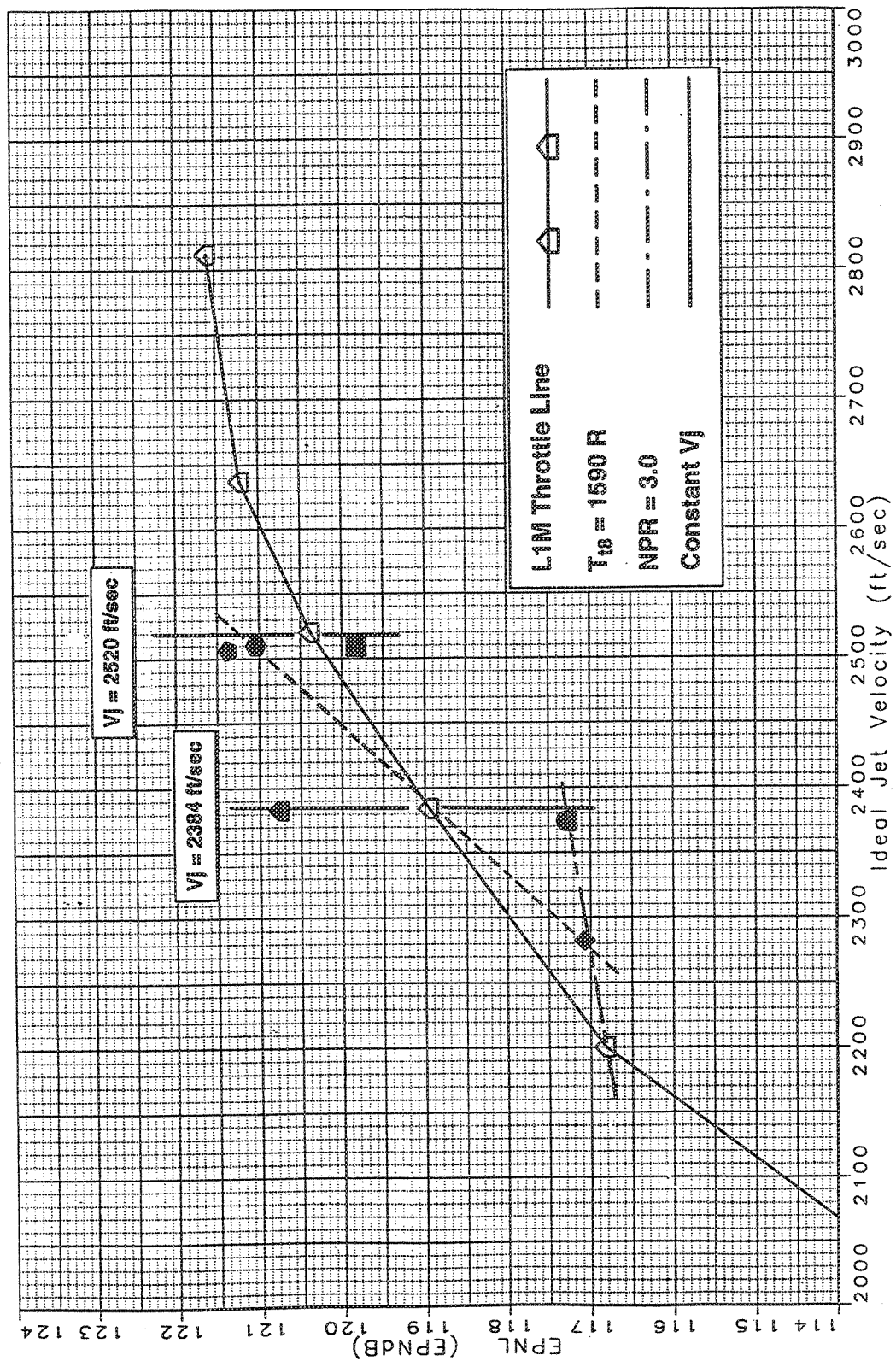


Figure 174. Sideline Noise Off the L1M Throttle Line, Baseline Round Conic Nozzle  
 (Sideline=1629 ft,  $A_g^*=1086 \text{ in}^2$ ,  $M_n=0.32$ ,  $V_{fl}=357 \text{ ft/sec}$ )

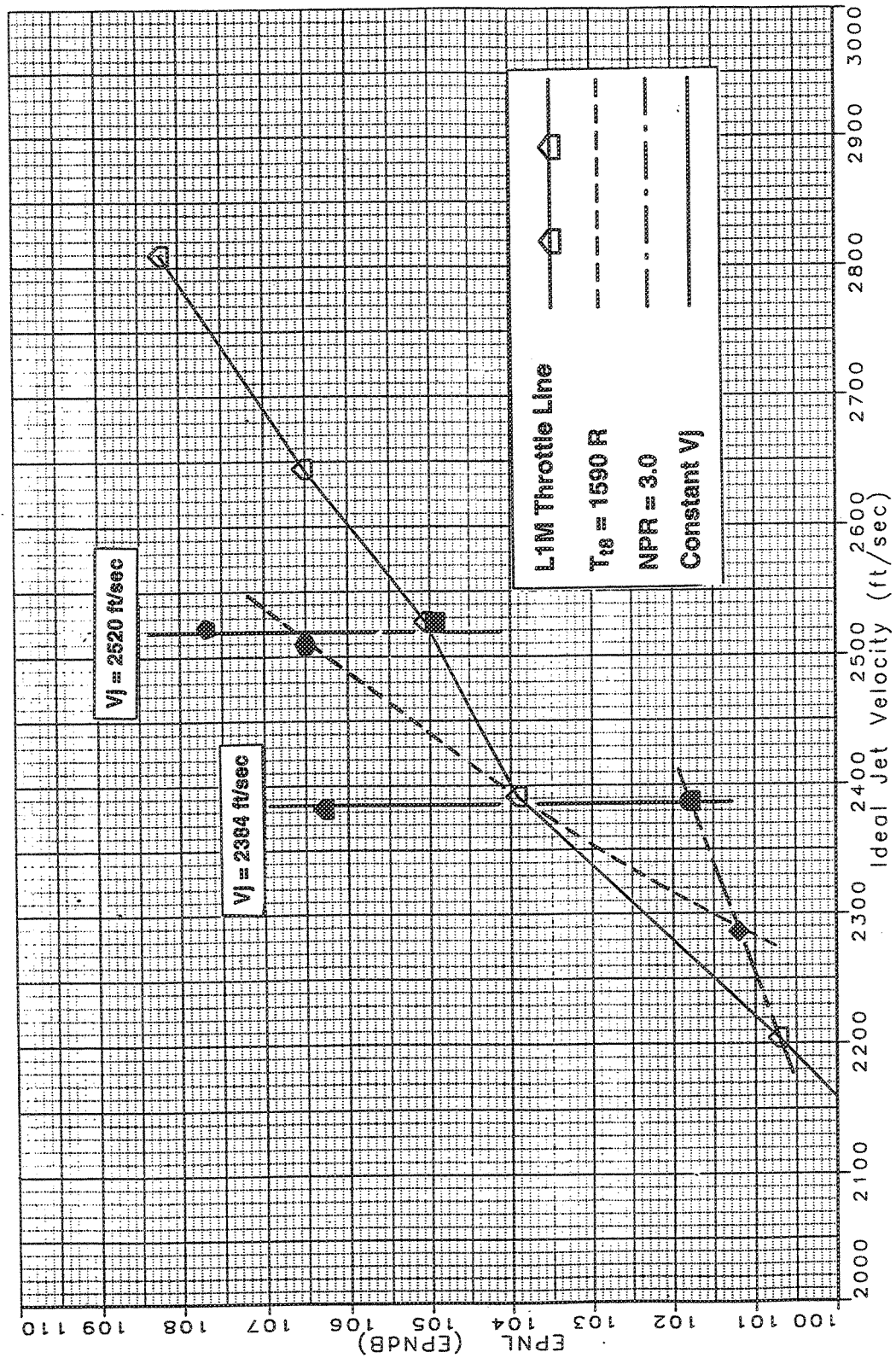


Figure 175. Sideline Noise Off the L1M Throttle Line, Vortical Mixer, Long Treated Shroud  
(Sideline=1629 ft, SAR=4.9, MAR=0.97,  $A_{g*}=1086$  in<sup>2</sup>,  $M_n=0.32$ ,  $V_{\eta}=357$  ft/sec)



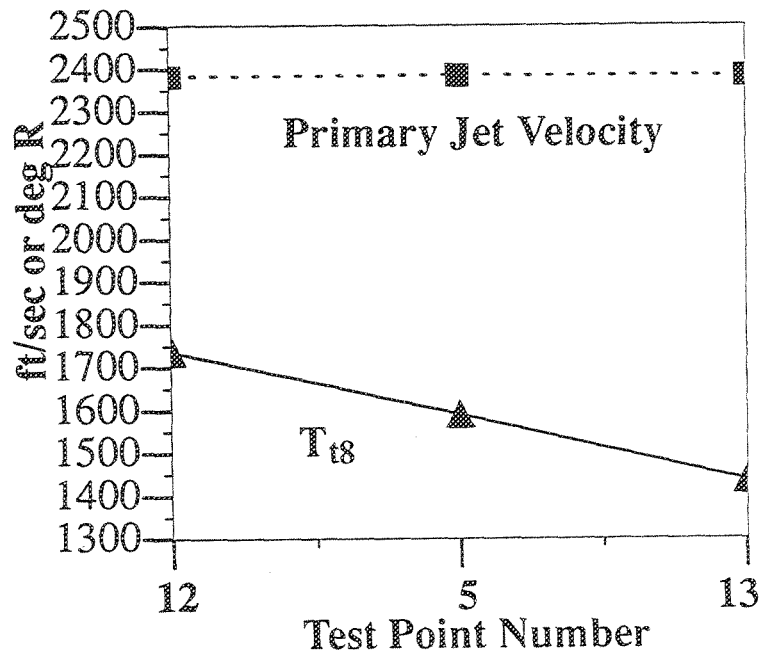


Figure 176. Constant Primary Jet Velocity (2384 ft/sec)

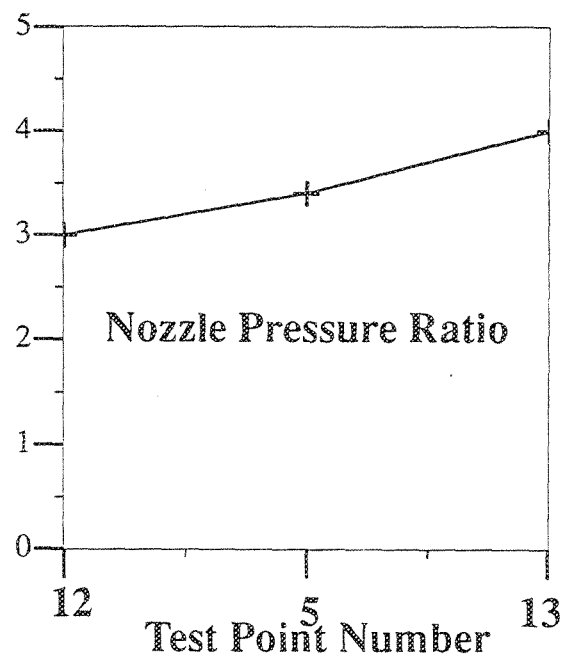


Figure 177. Constant Primary Jet Velocity (2384 ft/sec)

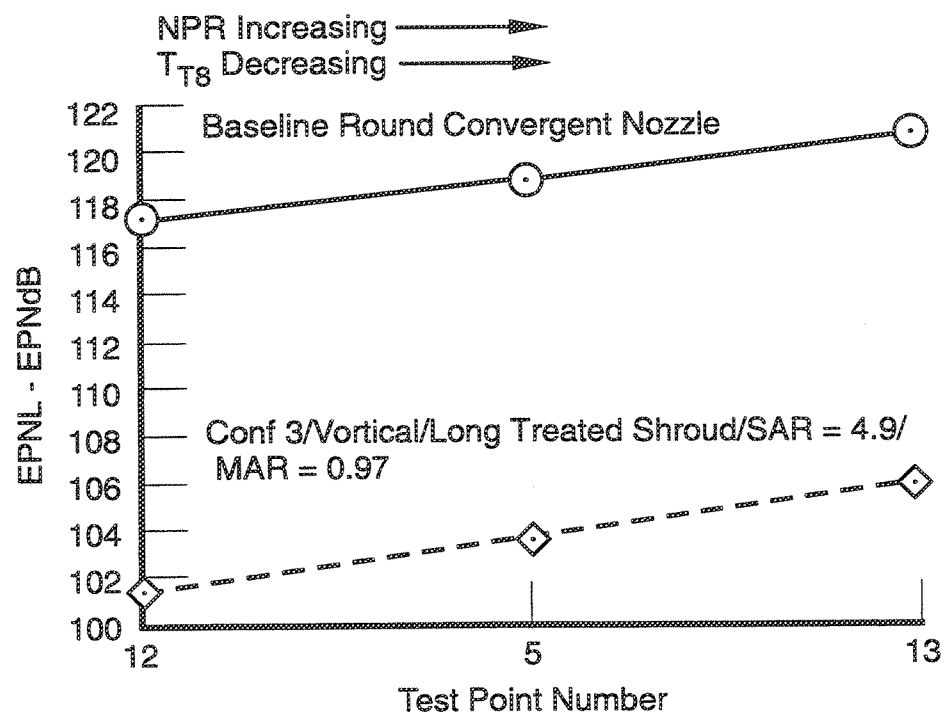


Figure 178. Sideline=1629 ft,  $A_{g*}=1086 \text{ in}^2$ ,  $Mn=0.32$ ,  $V_{\Pi}=357 \text{ ft/sec}$

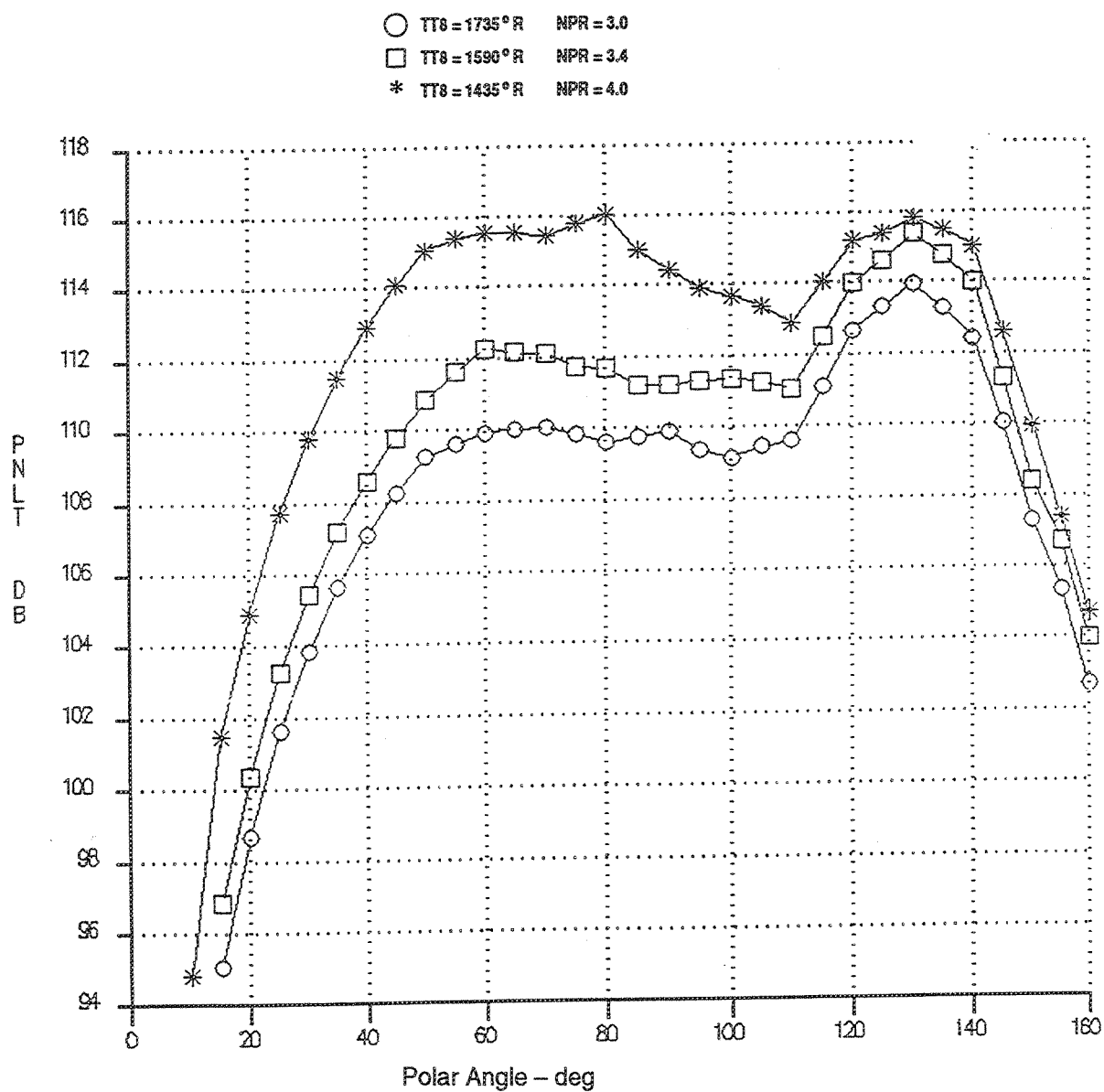


Figure 179. Off LIM Throttle Line Results, PNL T Versus Angle  
 — Ideal Unsuppressed Primary Jet Velocity=2384 ft/sec, Baseline Round Conic Nozzle,  
 (Sideline=1629 ft,  $A_{g*}=1086 \text{ in}^2$ ,  $M_n=0.32$ ,  $V_{\bar{n}}=357 \text{ ft/sec}$ )

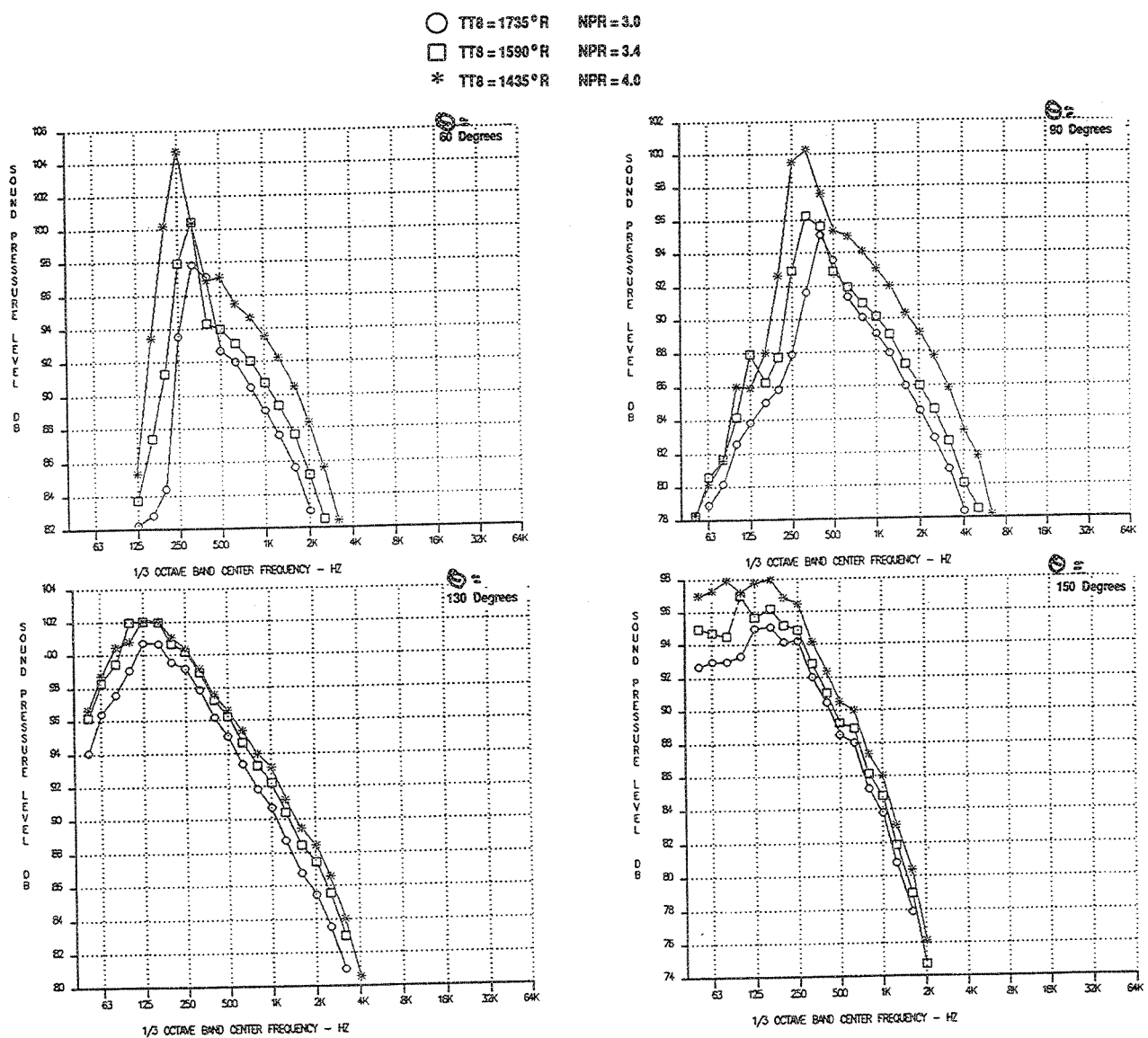


Figure 180. Off LIM Throttle Line Results, SPL Versus Frequency  
 — Ideal Unsuppressed Primary Jet Velocity=2384 ft/sec, Baseline Round Conic Nozzle  
 (Sideline=1629 ft,  $A_{g*}=1086 \text{ in}^2$ ,  $M_n=0.32$ ,  $V_{\bar{n}}=357 \text{ ft/sec}$ )

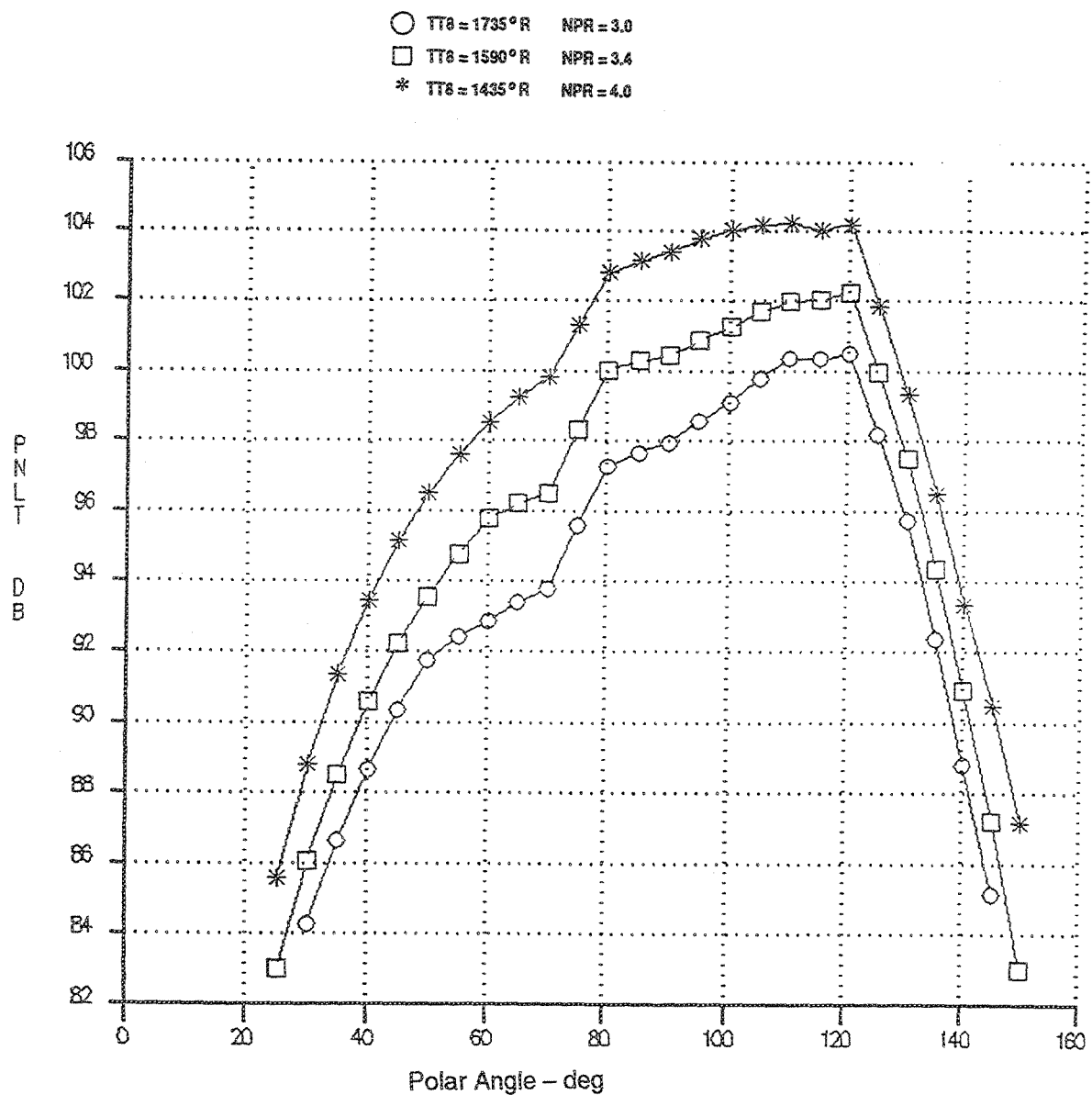


Figure 181. Off LIM Throttle Line Results, PNLT Versus Angle  
 — Ideal Unsuppressed Primary Jet Velocity=2384 ft/sec, Vortical Mixer, Long Treated Shroud  
 (Sideline=1629 ft, SAR=4.9, MAR=0.97,  $A_{g*}=1086 \text{ in}^2$ ,  $M_n=0.32$ ,  $V_{fl}=357 \text{ ft/sec}$ )

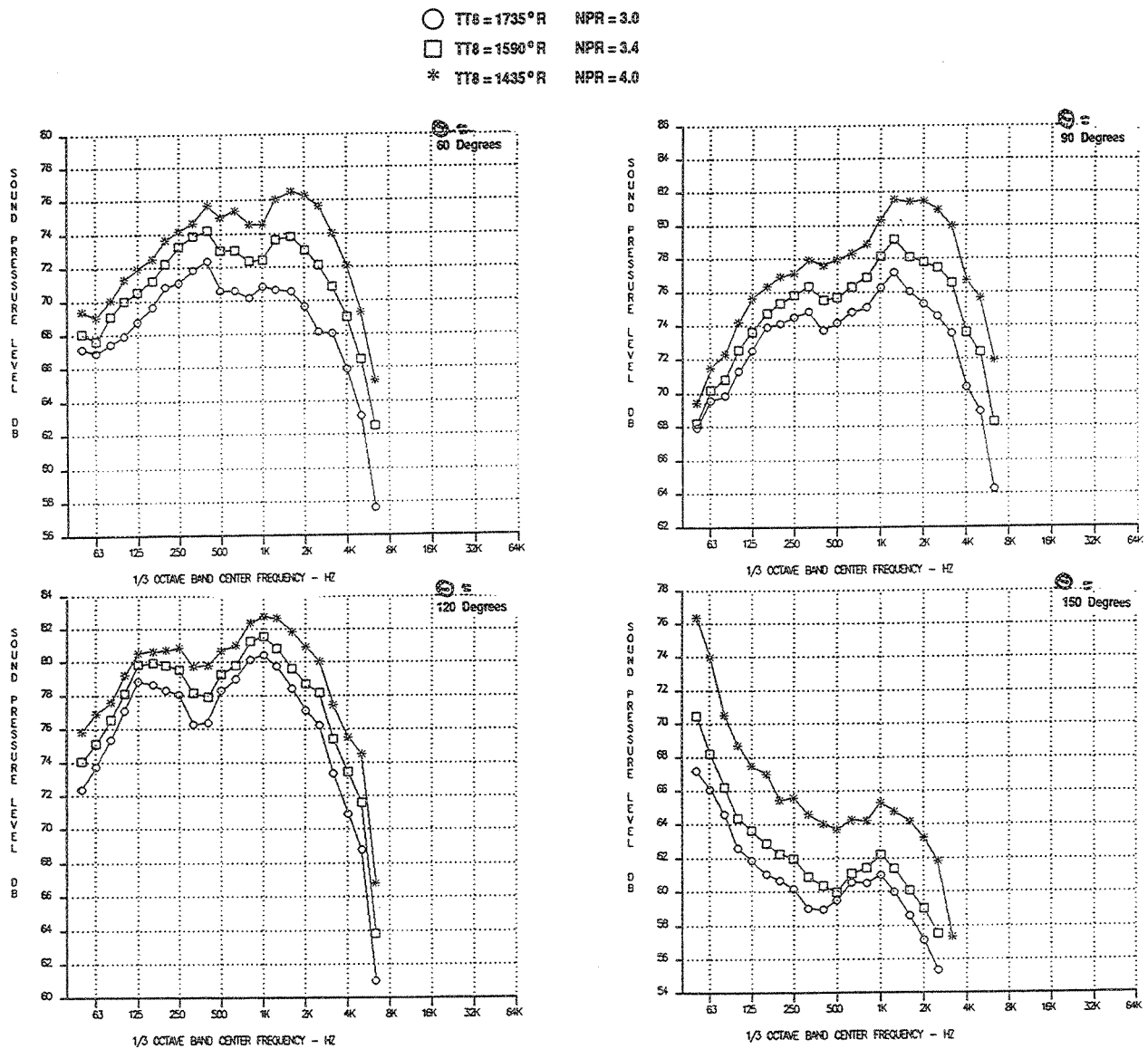


Figure 182. Off LIM Throttle Line Results, SPL Versus Frequency  
 — Ideal Unsuppressed Primary Jet Velocity=2384 ft/sec, Vortical Mixer, Long Treated Shroud  
 (Sideline=1629 ft, SAR=4.9, MAR=0.97,  $A_{g*}=1086 \text{ in}^2$ ,  $M_n=0.32$ ,  $V_{fl}=357 \text{ ft/sec}$ )

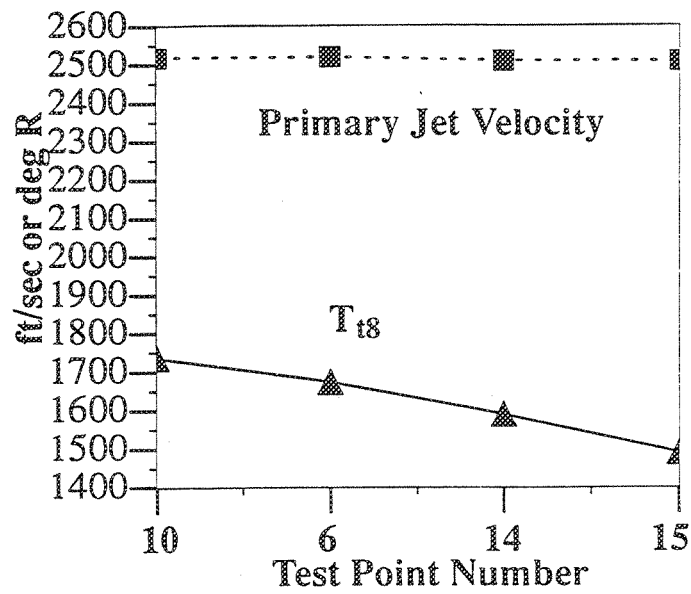


Figure 183. Constant Primary Jet Velocity (2520 ft/sec)

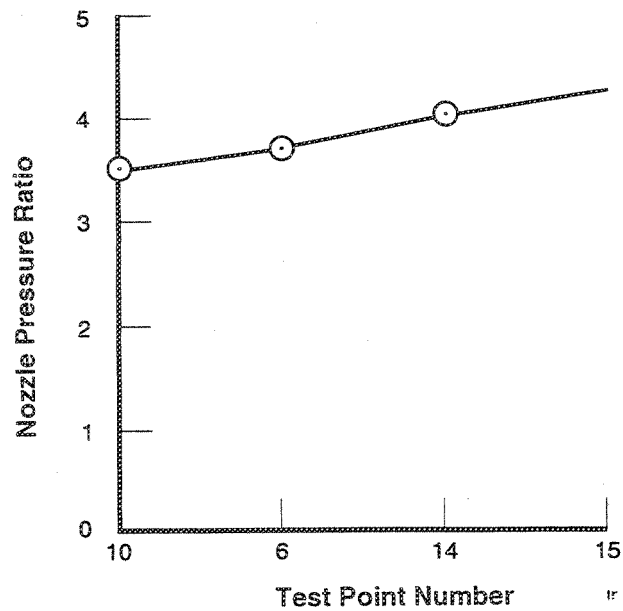


Figure 184. Constant Primary Jet Velocity (2520 ft/sec)

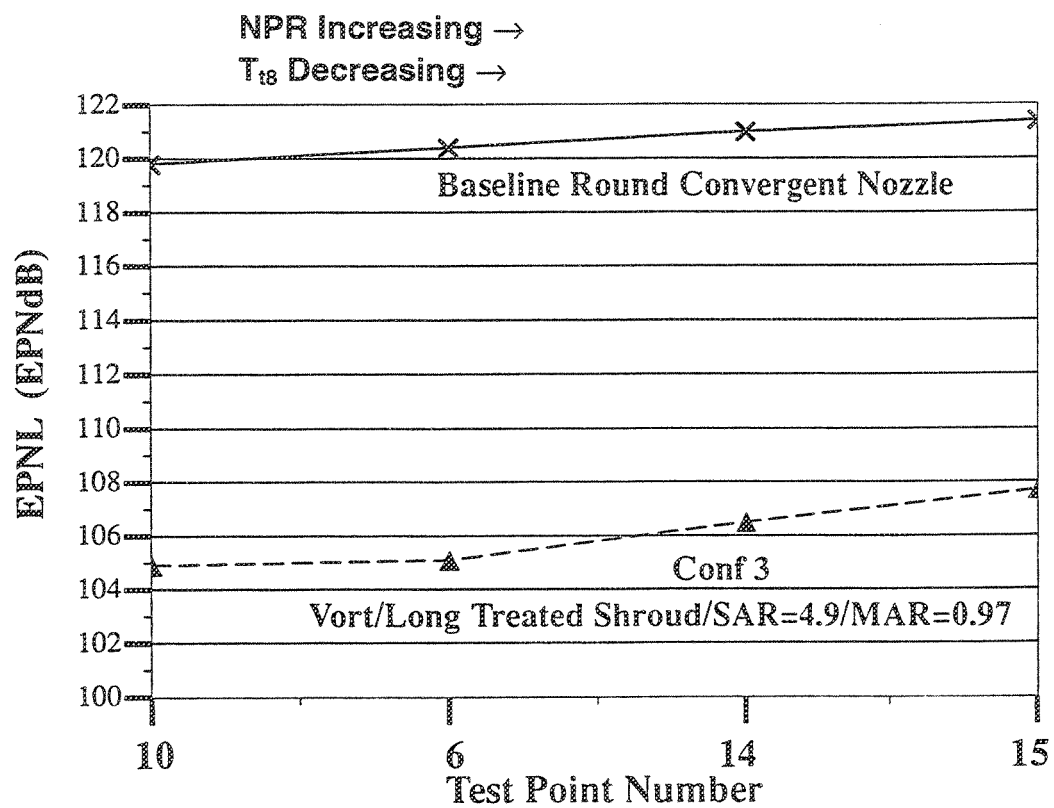


Figure 185. Sideline 1629 ft,  $A_{8*}=1086 \text{ in}^2$ ,  $V_{\Pi}=357 \text{ ft/sec}$



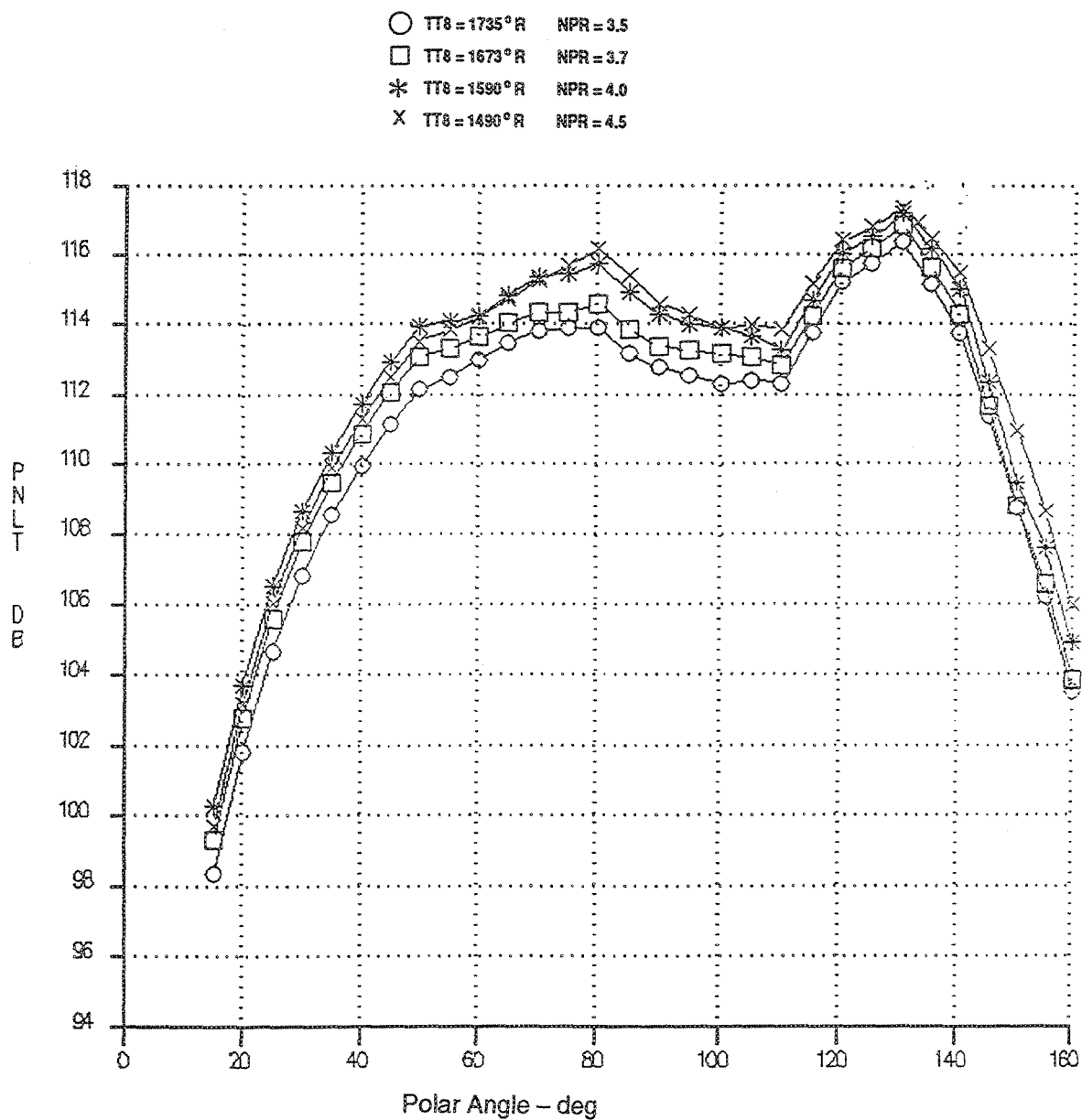


Figure 186. Off LIM Throttle Line Results, PNL T Versus Angle  
 — Ideal Unsuppressed Primary Jet Velocity=2520 ft/sec, Baseline Round Conic Nozzle  
 (Sideline=1629 ft,  $A_{g*}=1086 \text{ in}^2$ ,  $M_n=0.32$ ,  $V_{fl}=357 \text{ ft/sec}$ )

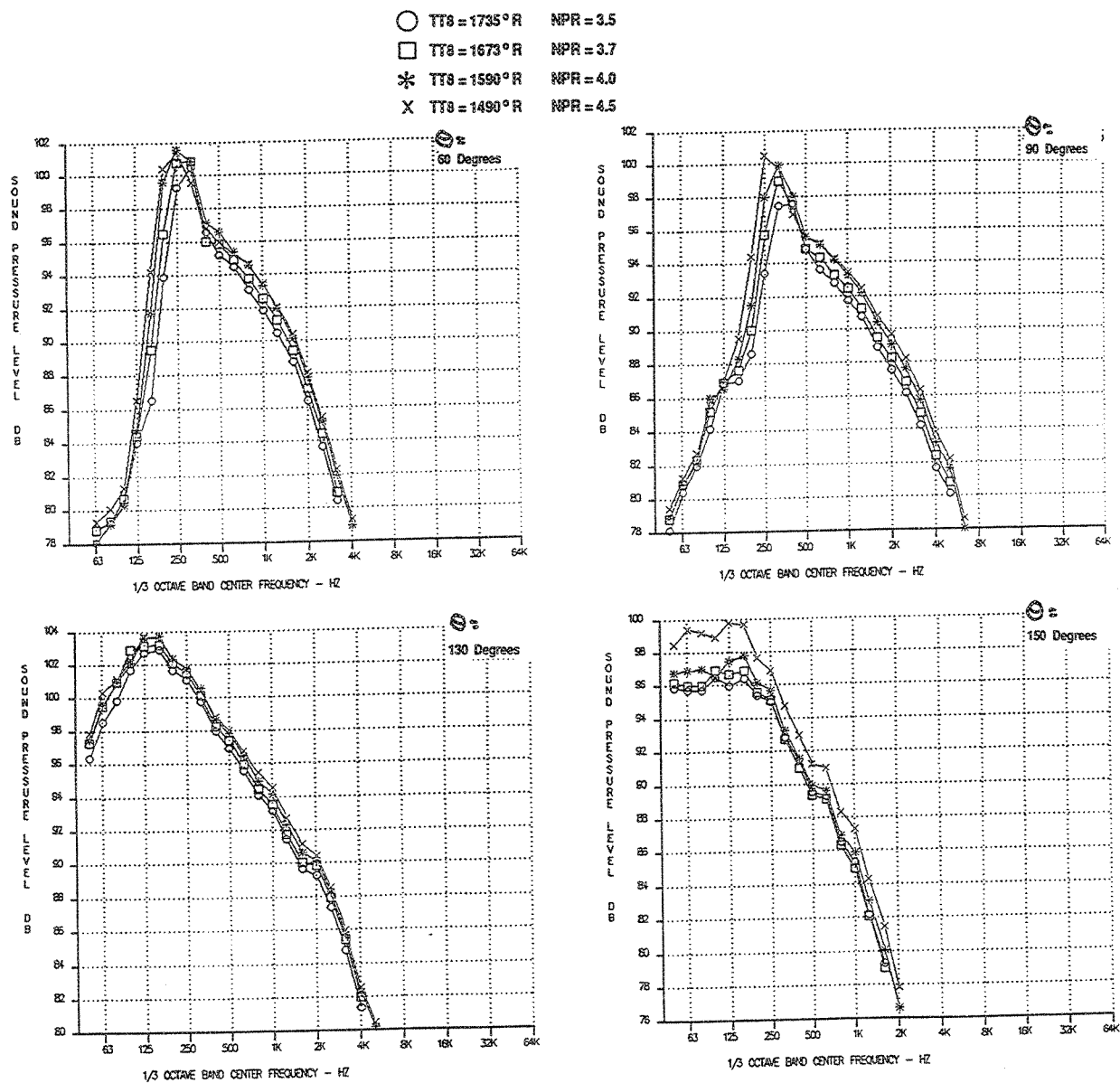


Figure 187. Off L1M Throttle Line Results, SPL vs. Frequency  
 — Ideal Unsuppressed Primary Jet Velocity=2520 ft/sec, Baseline Round Conic Nozzle  
 (Sideline=1629 ft,  $A_{8*}=1086 \text{ in}^2$ ,  $M_n=0.32$ ,  $V_{fl}=357 \text{ ft/sec}$ )

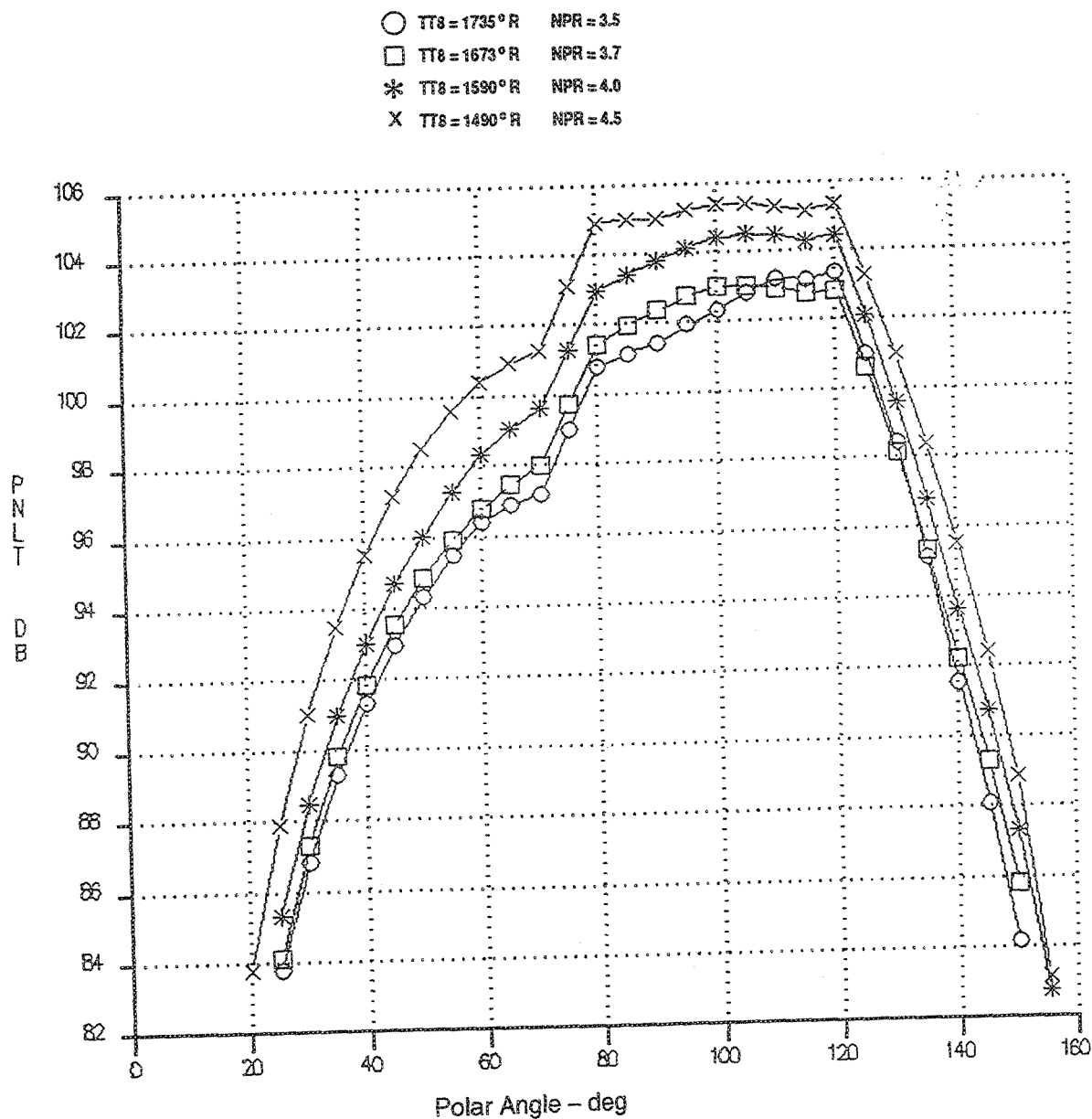


Figure 188. Off LIM Throttle Line Results, PNLT Versus Angle  
 — Ideal Unsuppressed Primary Jet Velocity=2520 ft/sec, Vortical Mixer, Long Treated Shroud  
 (Sideline=1629 ft, SAR=4.9, MAR=0.97,  $A_{g*}=1086 \text{ in}^2$ ,  $M_n=0.32$ ,  $V_{fl}=357 \text{ ft/sec}$ )

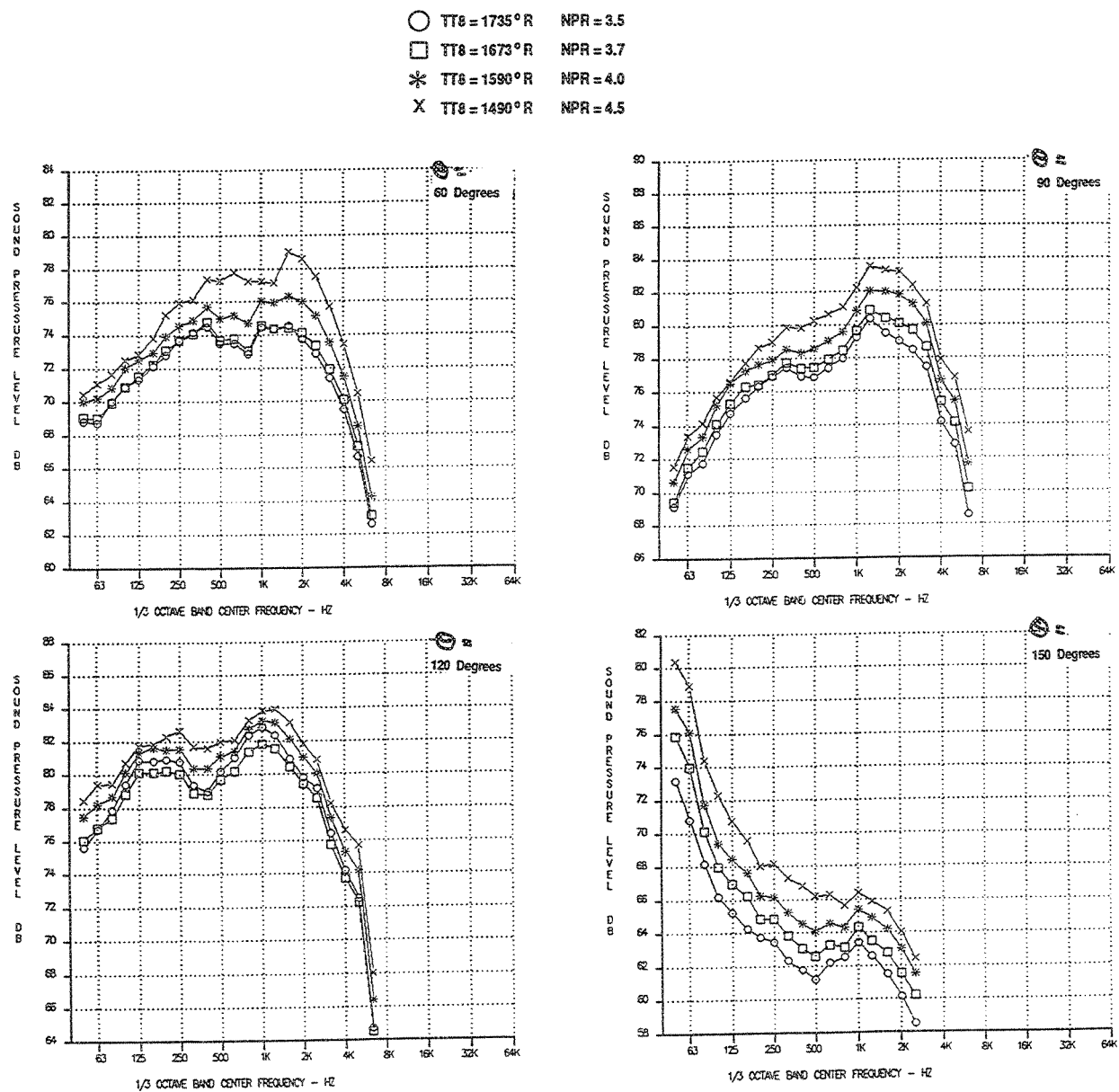


Figure 189. Off LIM Throttle Line Results, SPL vs. Frequency  
 — Ideal Unsuppressed Primary Jet Velocity=2520 ft/sec, Vortical Mixer, Long Treated Shroud  
 (Sideline=1629 ft, SAR=4.9, MAR=0.97,  $A_{8*}=1086 \text{ in}^2$ ,  $M_n=0.32$ ,  $V_{f1}=357 \text{ ft/sec}$ )

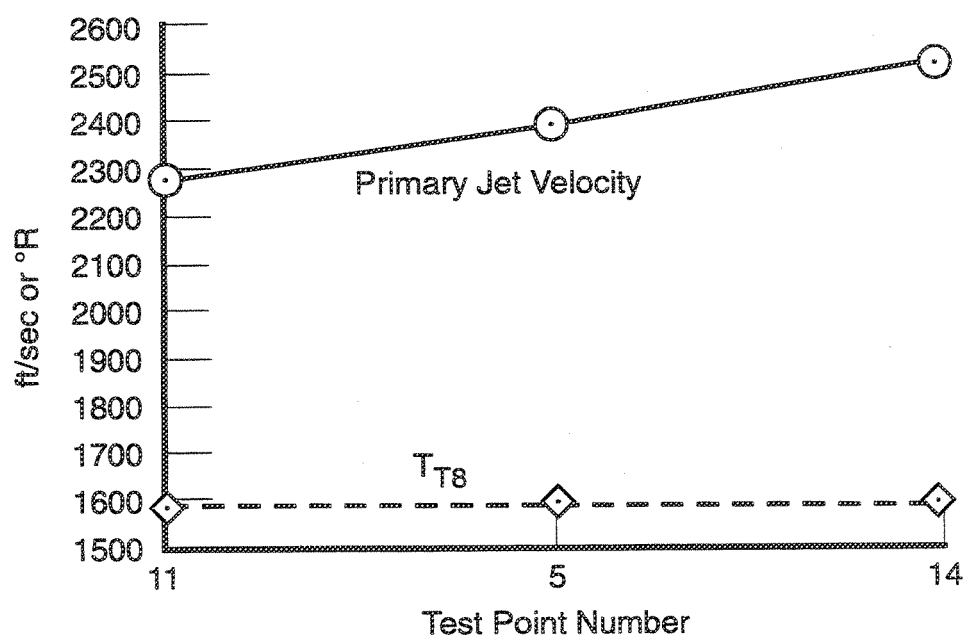


Figure 190. Constant Turbine Exit Total Temperature ( $T_{t8}=1590^{\circ}R$ )

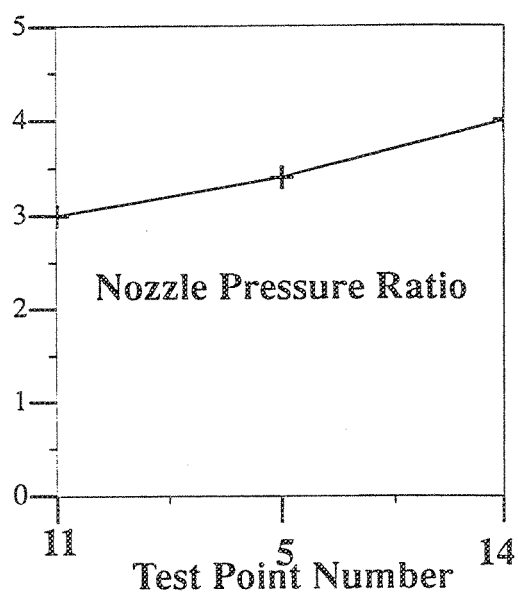


Figure 191. Constant Turbine Exit Total Temperature ( $T_{t8}=1590^{\circ}R$ )

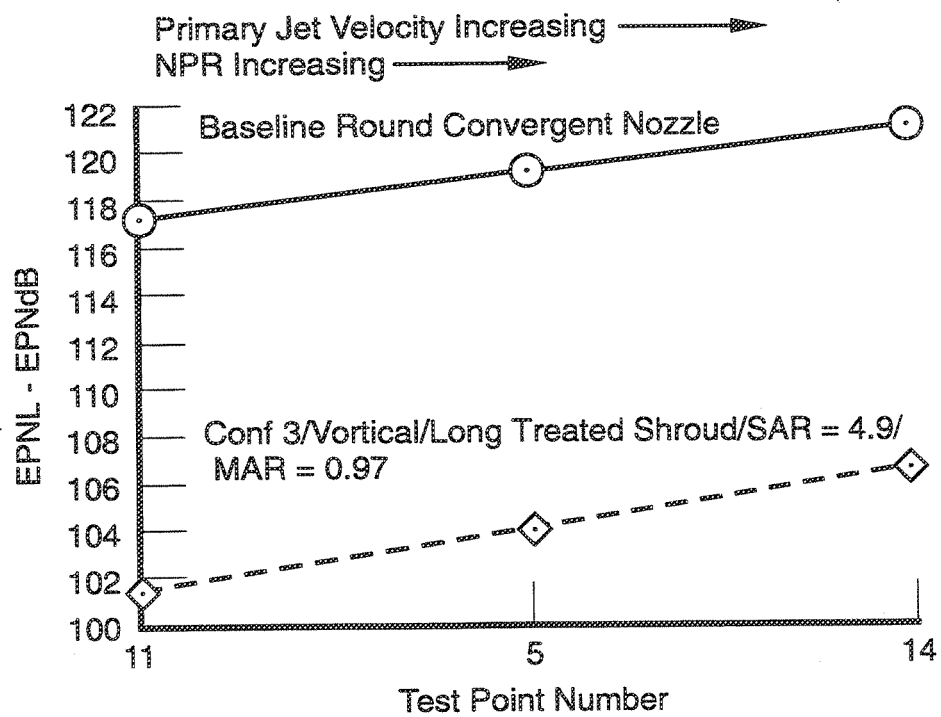


Figure 192. Sideline 1629 ft,  $A_{g*}=1086 \text{ in}^2$ ,  $V_{fl}=357 \text{ ft/sec}$

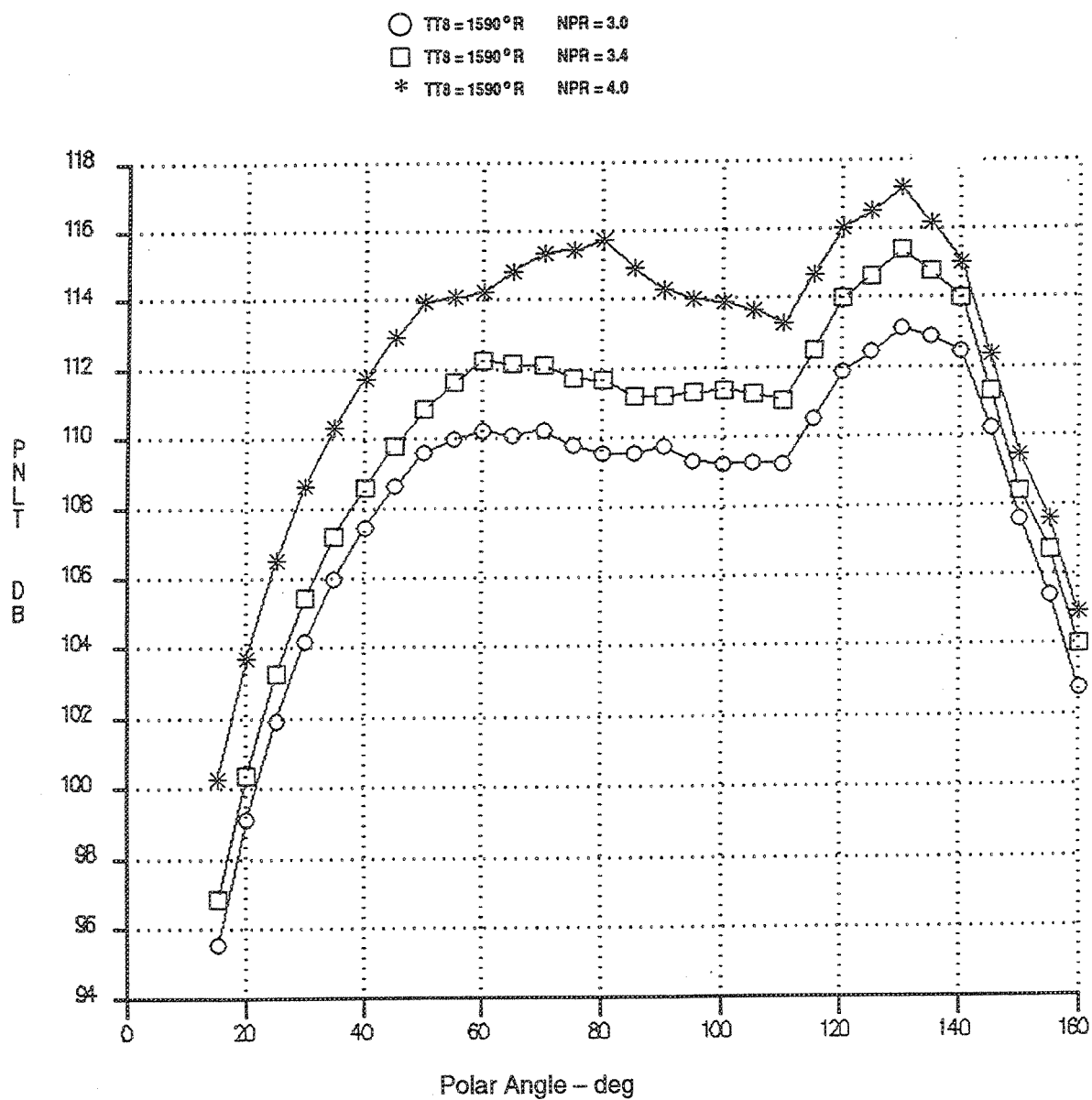


Figure 193. Off LIM Throttle Line Results, PNLT Versus Angle  
 —  $T_{t8} = 1590^{\circ}R$ , Baseline Round Conic Nozzle

(Sideline = 1629 ft,  $A_{g*} = 1086 \text{ in}^2$ ,  $M_n = 0.32$ ,  $V_{fl} = 357 \text{ ft/sec}$ )



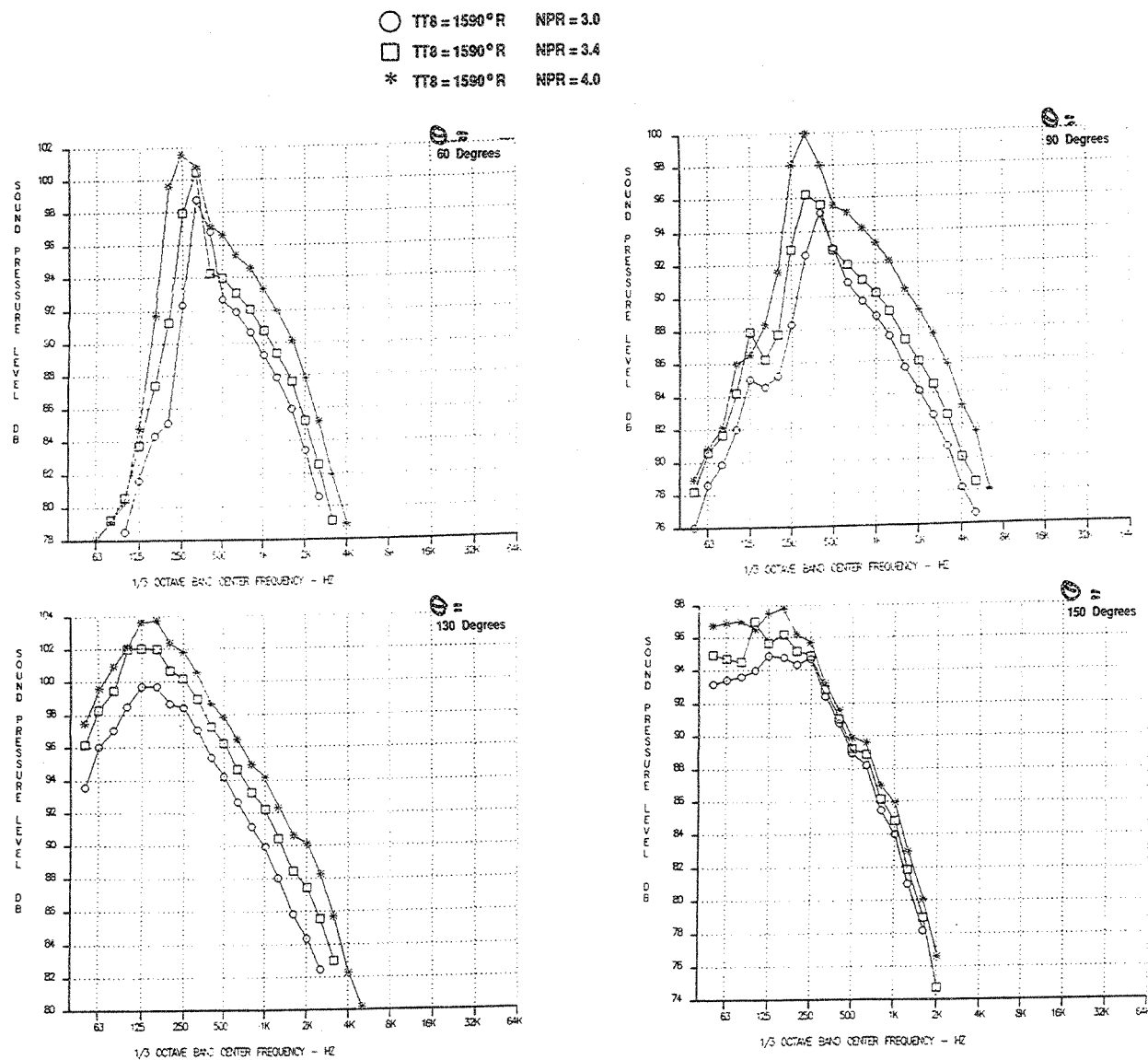


Figure 194. Off LIM Throttle Line Results, SPL vs. Frequency  
 —  $T_{t8} = 1590^\circ R$ , Baseline Round Conic Nozzle  
 (Sideline = 1629 ft,  $A_{g*} = 1086 \text{ in}^2$ ,  $M_n = 0.32$ ,  $V_{fl} = 357 \text{ ft/sec}$ )

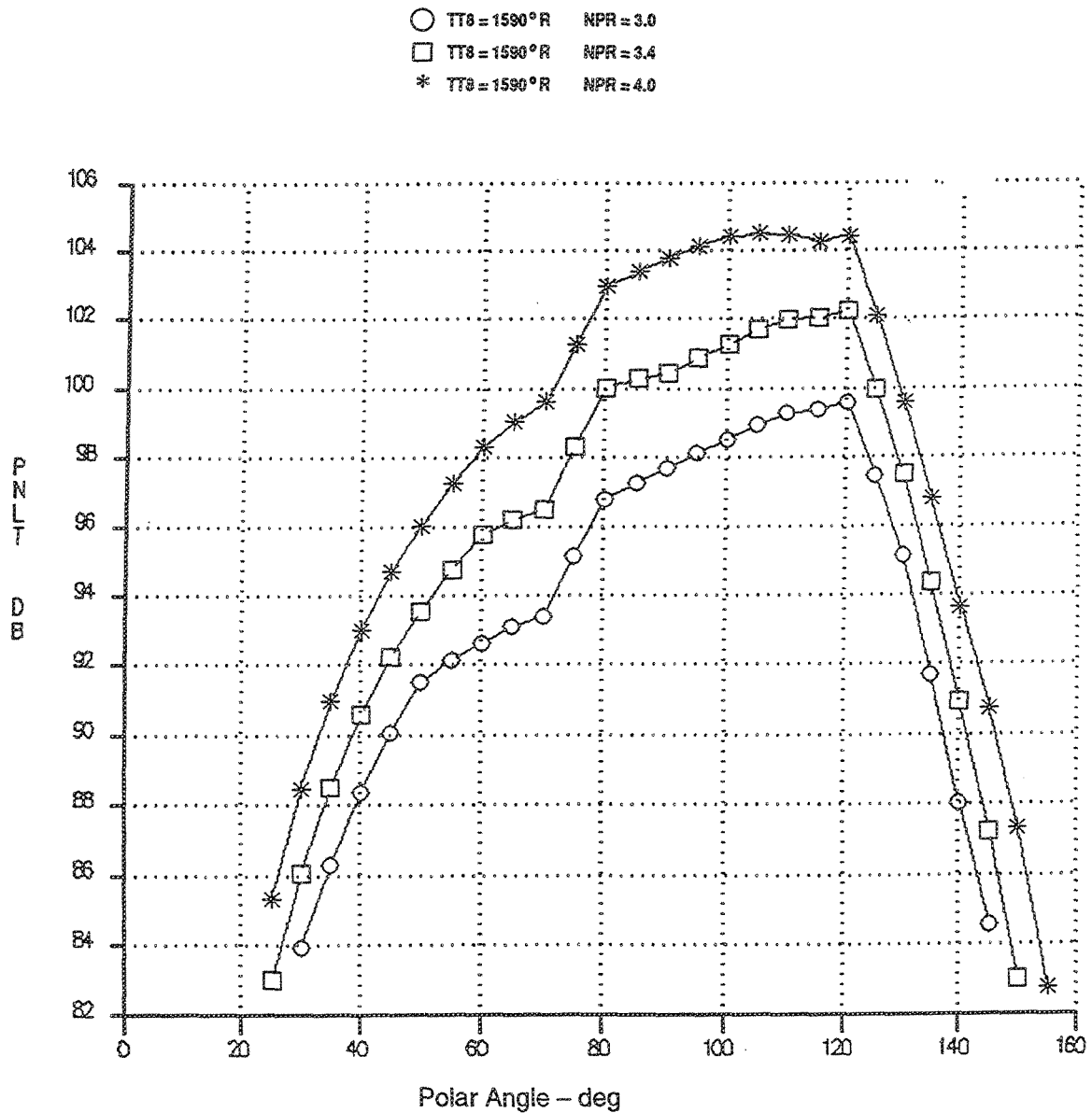


Figure 195. Off LIM Throttle Line Results, PNLT vs. Angle —  $T_{t8}=1590^\circ R$   
 Vortical Mixer, Long Treated Shroud  
 (Sideline=1629 ft, SAR=4.9, MAR=0.97,  $A_{g*}=1086 \text{ in}^2$ ,  $M_n=0.32$ ,  $V_{fl}=357 \text{ ft/sec}$ )

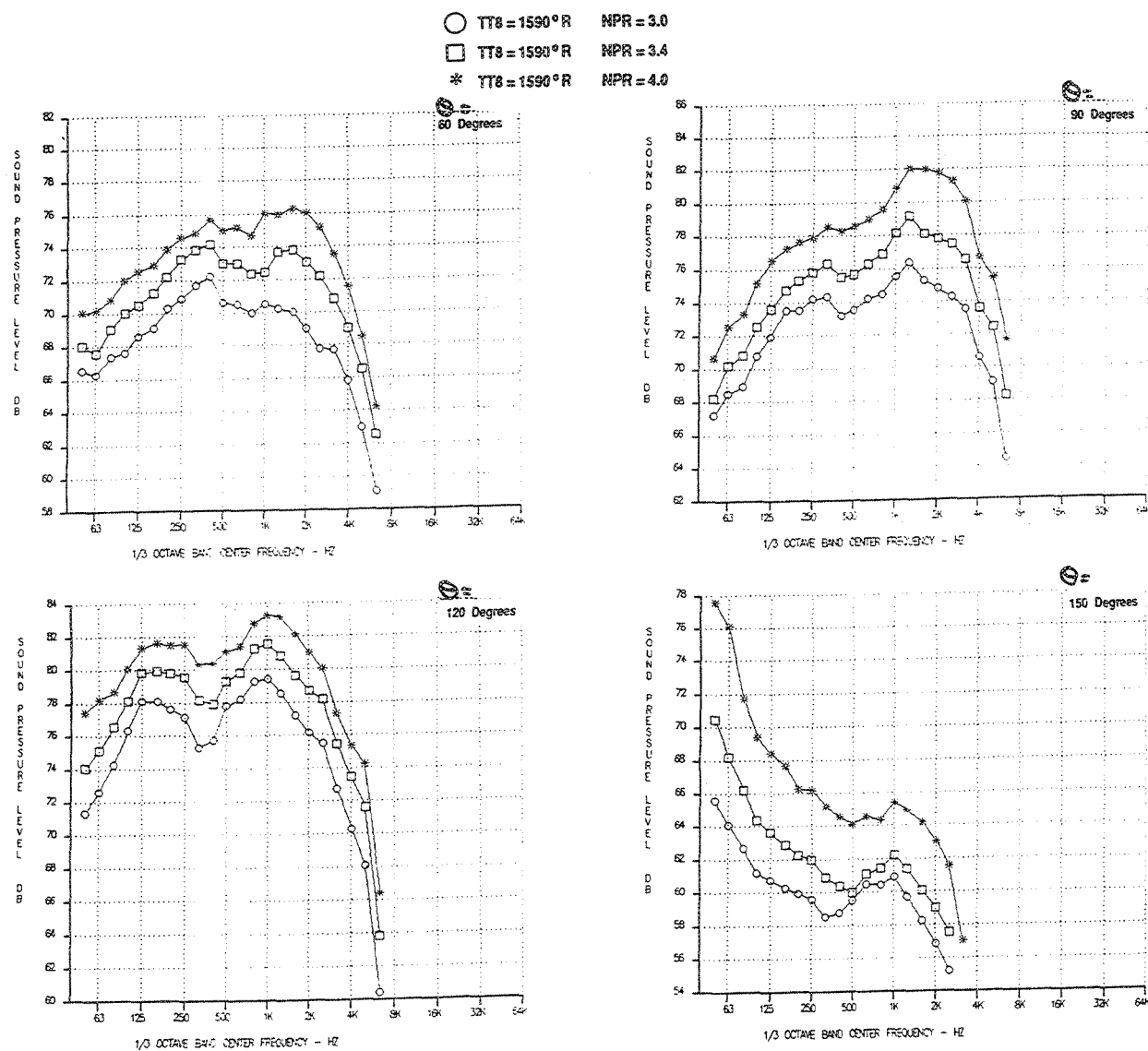


Figure 196. Off LIM Throttle Line Results, SPL vs. Frequency —  $T_{t8}=1590^\circ R$ ,  
 Vortical Mixer, Long Treated Shroud  
 (Sideline=1629 ft, SAR=4.9, MAR=0.97,  $A_8=1086 \text{ in}^2$ ,  $M_n=0.32$ ,  $V_{t8}=357 \text{ ft/sec}$ )

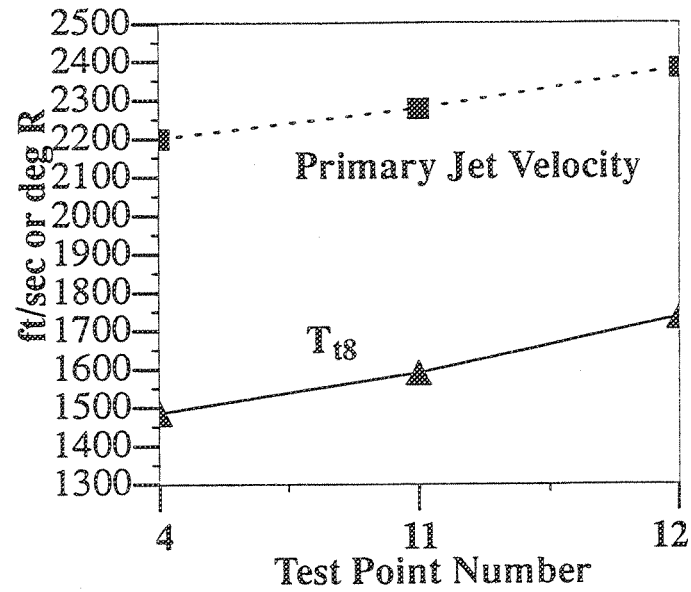


Figure 197. Constant Primary Nozzle Pressure Ratio (NPR=3.0)

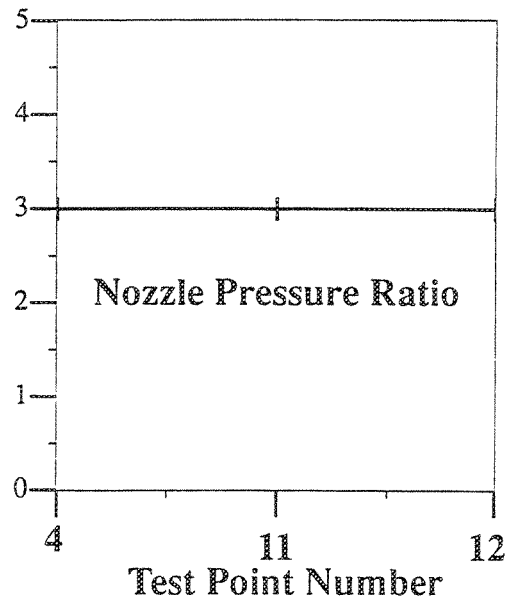


Figure 198. Constant Primary Nozzle Pressure Ratio (NPR=3.0)

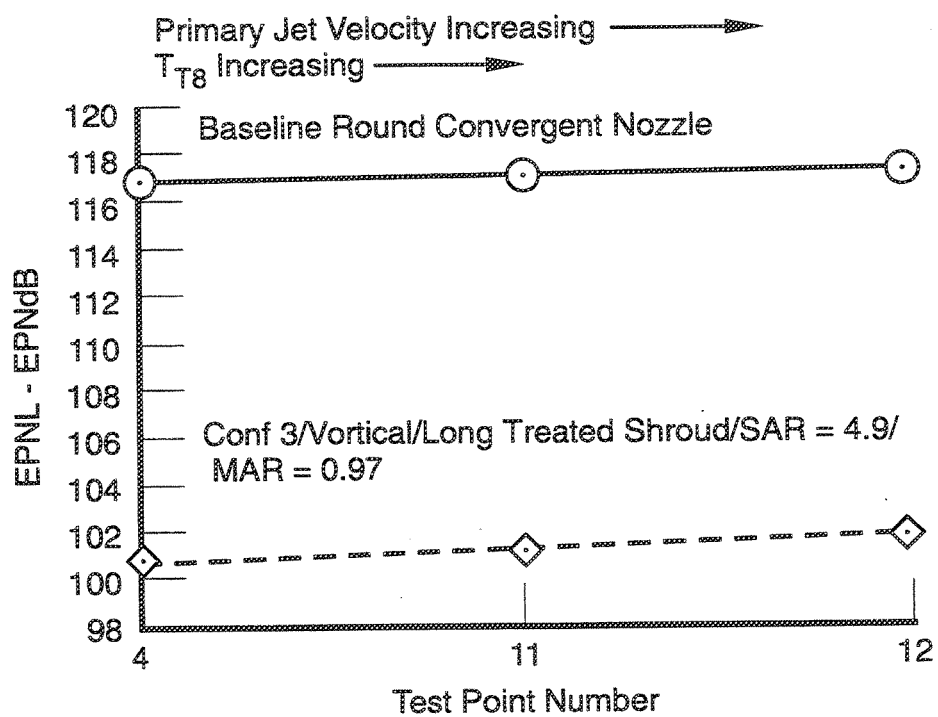


Figure 199. Sideline 1629 ft,  $A_{8*}=1086 \text{ in}^2$ ,  $V_{fl}=357 \text{ ft/sec}$

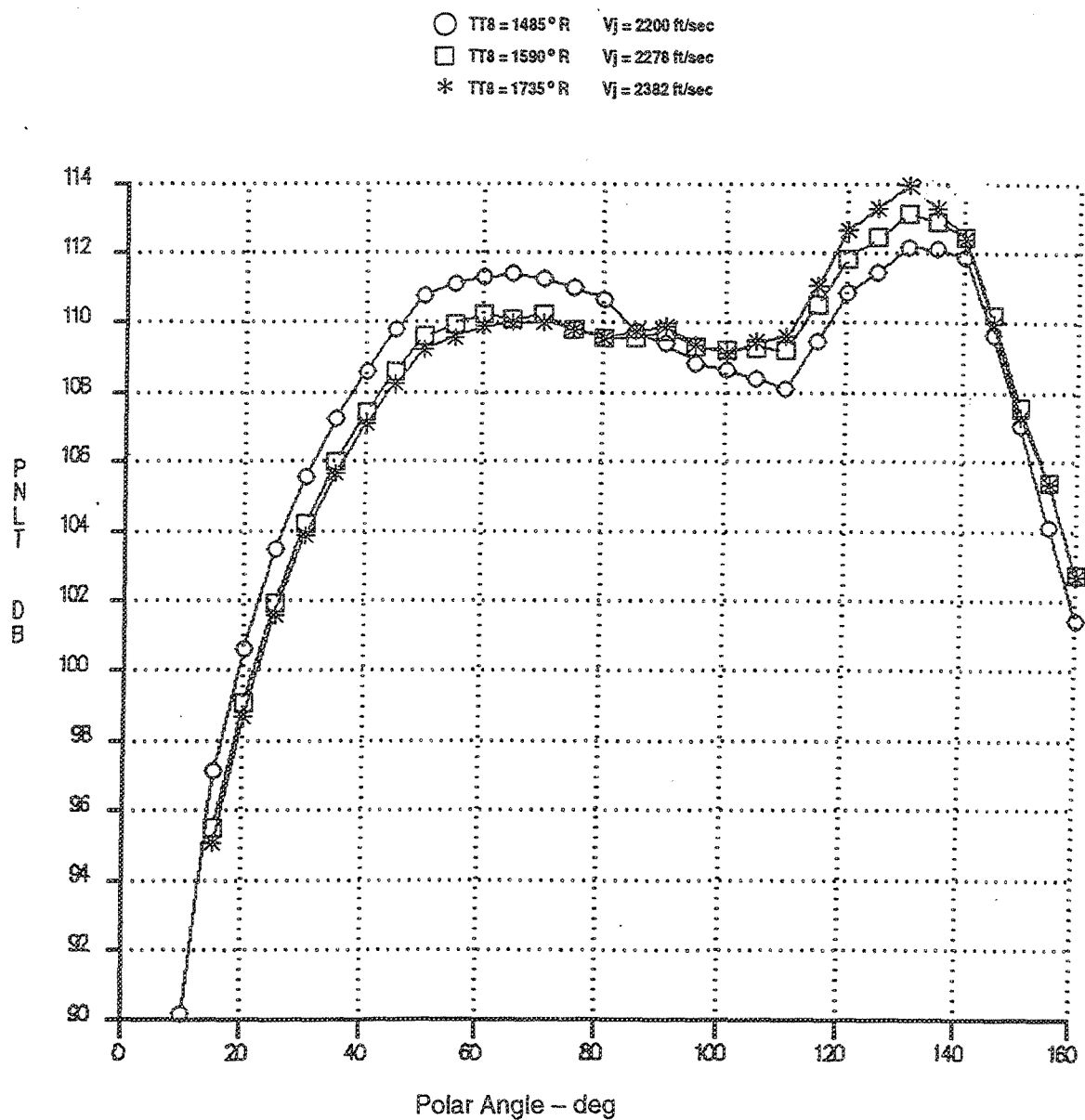


Figure 200. Off LIM Throttle Line Results, PNLT Versus Angle — NPR=3.0  
 Baseline Round Conic Nozzle  
 (Sideline=1629 ft,  $A_{g*}=1086$  in<sup>2</sup>,  $M_n=0.32$ ,  $V_{fl}=357$  ft/sec)

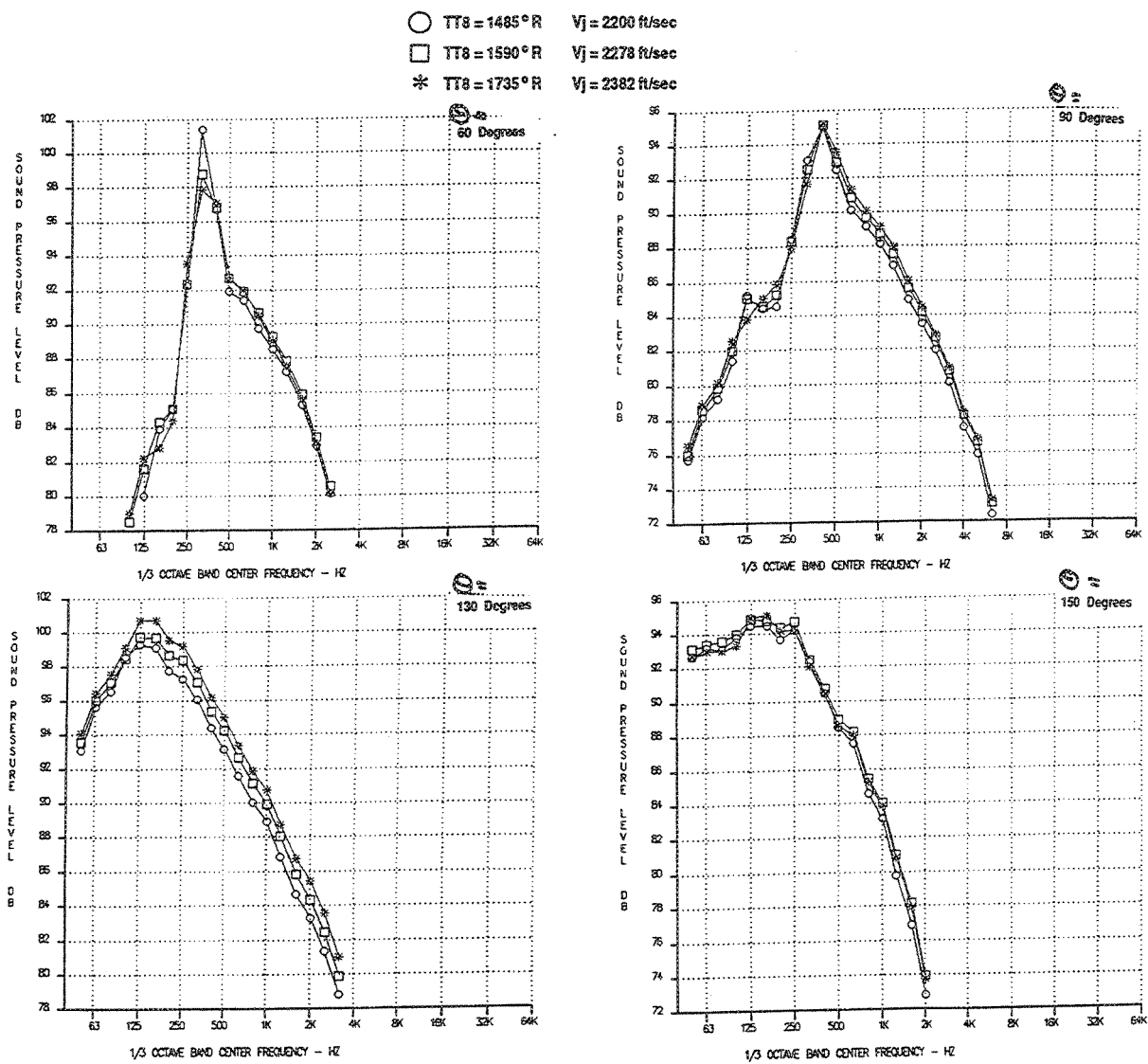


Figure 201. Off LIM Throttle Line Results, SPL vs. Frequency — NPR=3.0  
 Baseline Round Conic Nozzle  
 (Sideline=1629 ft,  $A_{g*}=1086 \text{ in}^2$ ,  $M_n=0.32$ ,  $V_{fl}=357 \text{ ft/sec}$ )

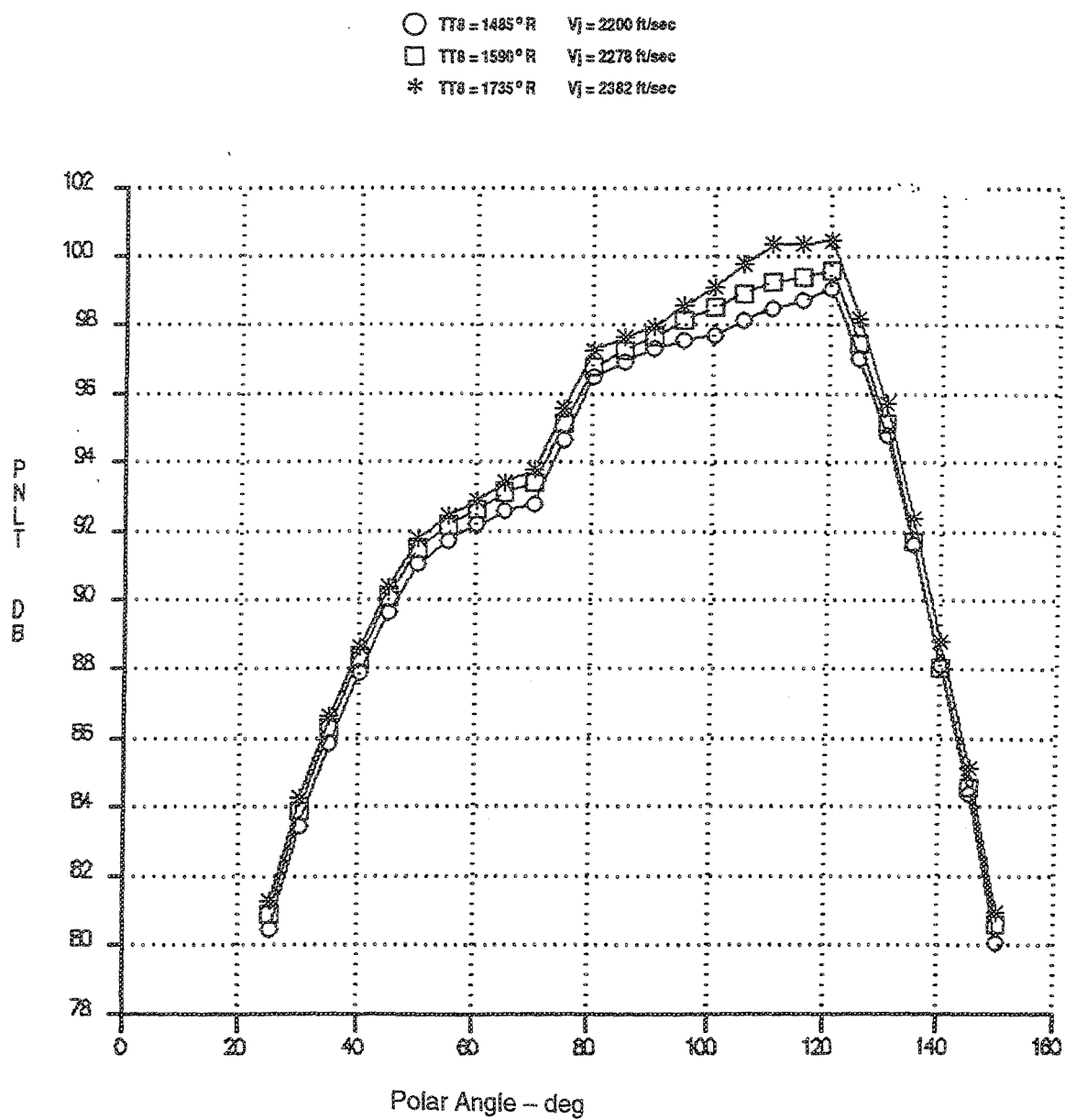


Figure 202. Off LIM Throttle Line Results, PNLT vs. Angle — NPR=3.0  
 Vortical Mixer, Long Treated Shroud  
 (Sideline=1629 ft, SAR=4.9, MAR=0.97,  $A_{g*}=1086$  in<sup>2</sup>,  $M_n=0.32$ ,  $V_{fl}=357$  ft/sec)



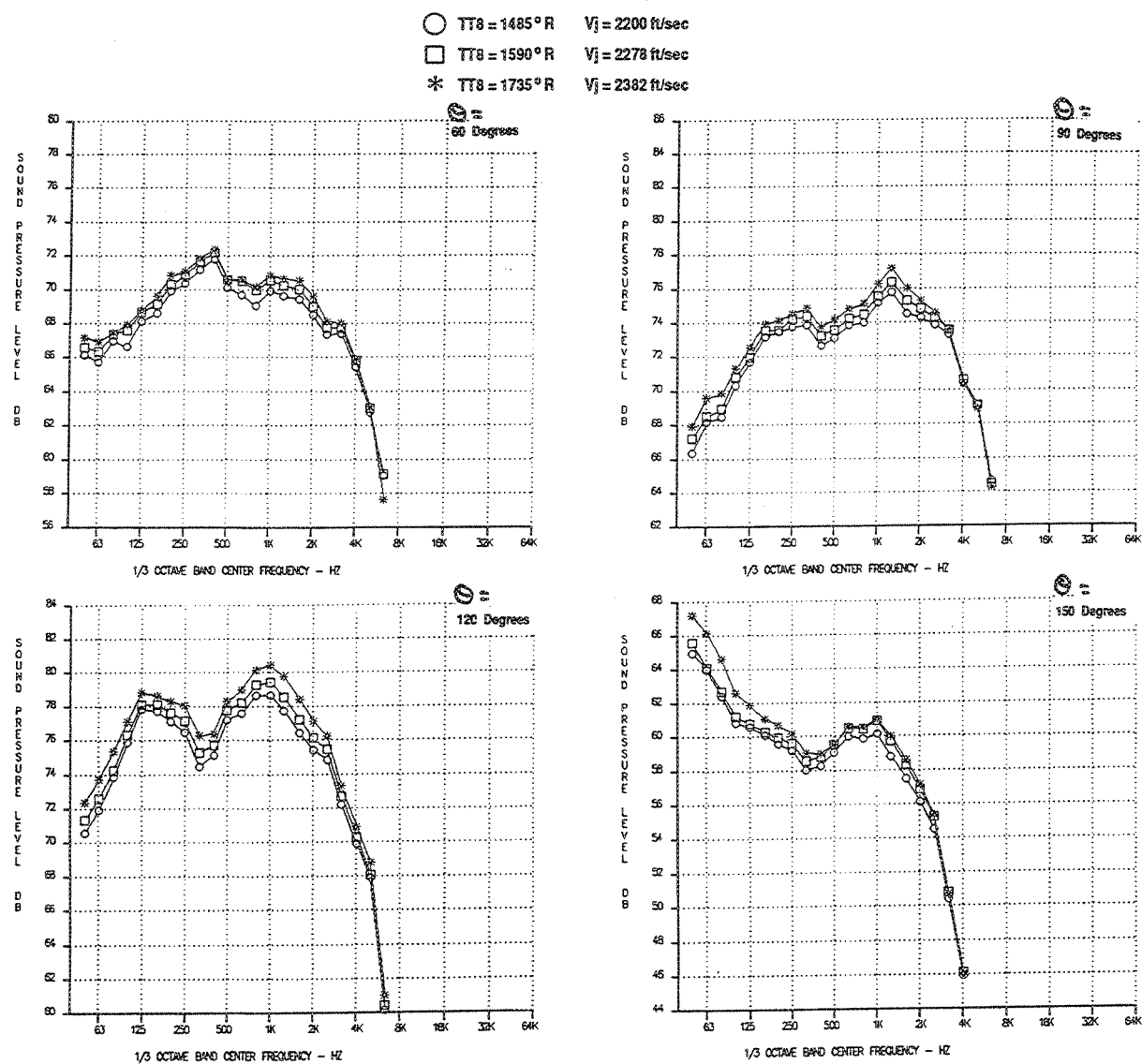


Figure 203. Off L1M Throttle Line Results, SPL vs. Frequency — NPR=3.0  
 Vortical Mixer, Long Treated Shroud  
 (Sideline=1629 ft, SAR=4.9, MAR=0.97,  $A_{8*}=1086$  in<sup>2</sup>,  $M_n=0.32$ ,  $V_{\bar{n}}=357$  ft/sec)

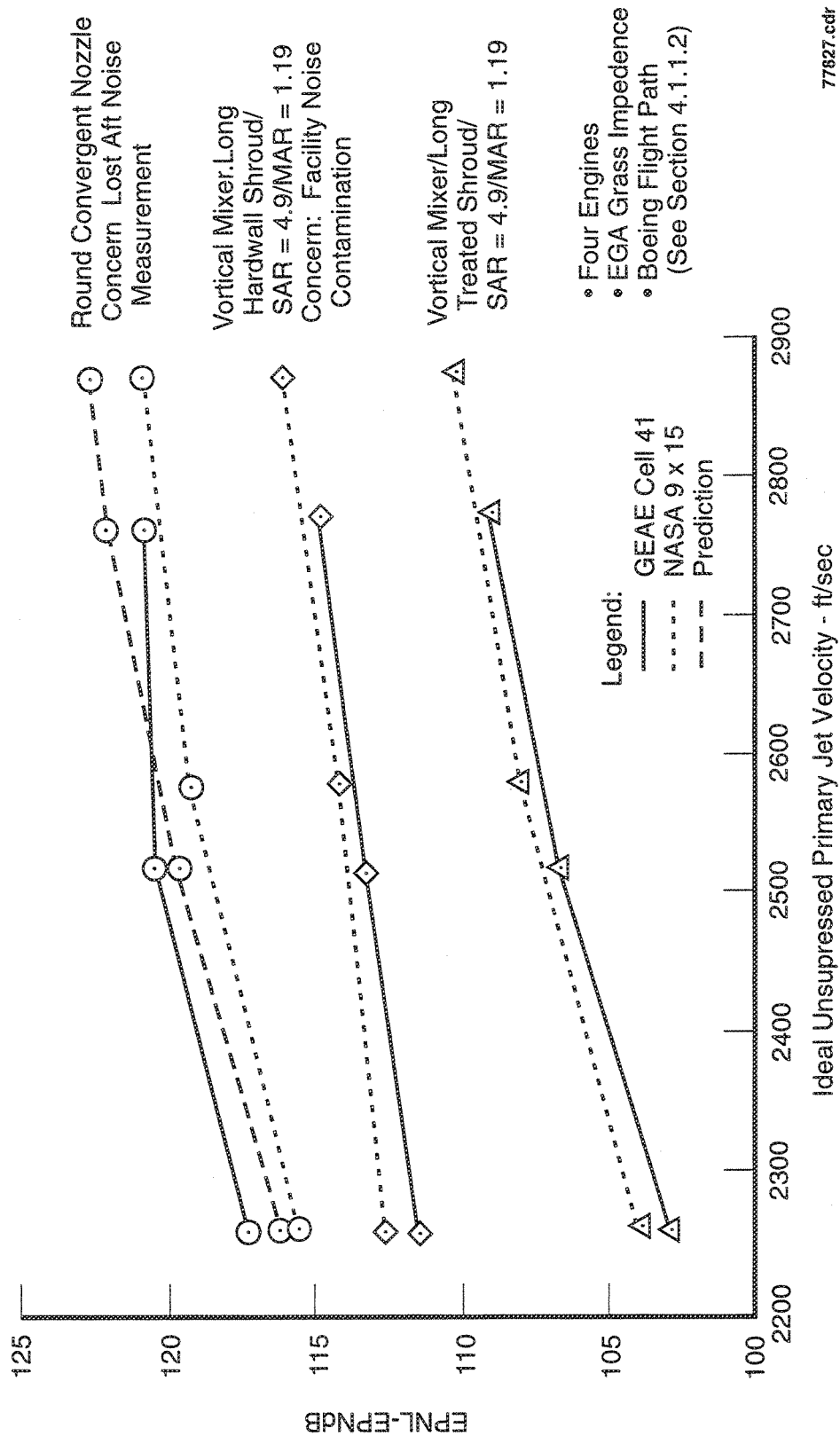


Figure 204. GEAE Cell 41 Test Results Support Concerns About NASA-LeRC 9 x 15 Data  
(Community, Sideline=1629 ft,  $A_8=1086 \text{ in}^2$ ,  $M_8=0.32$ ,  $V_8=406.4 \text{ ft/sec}$ )

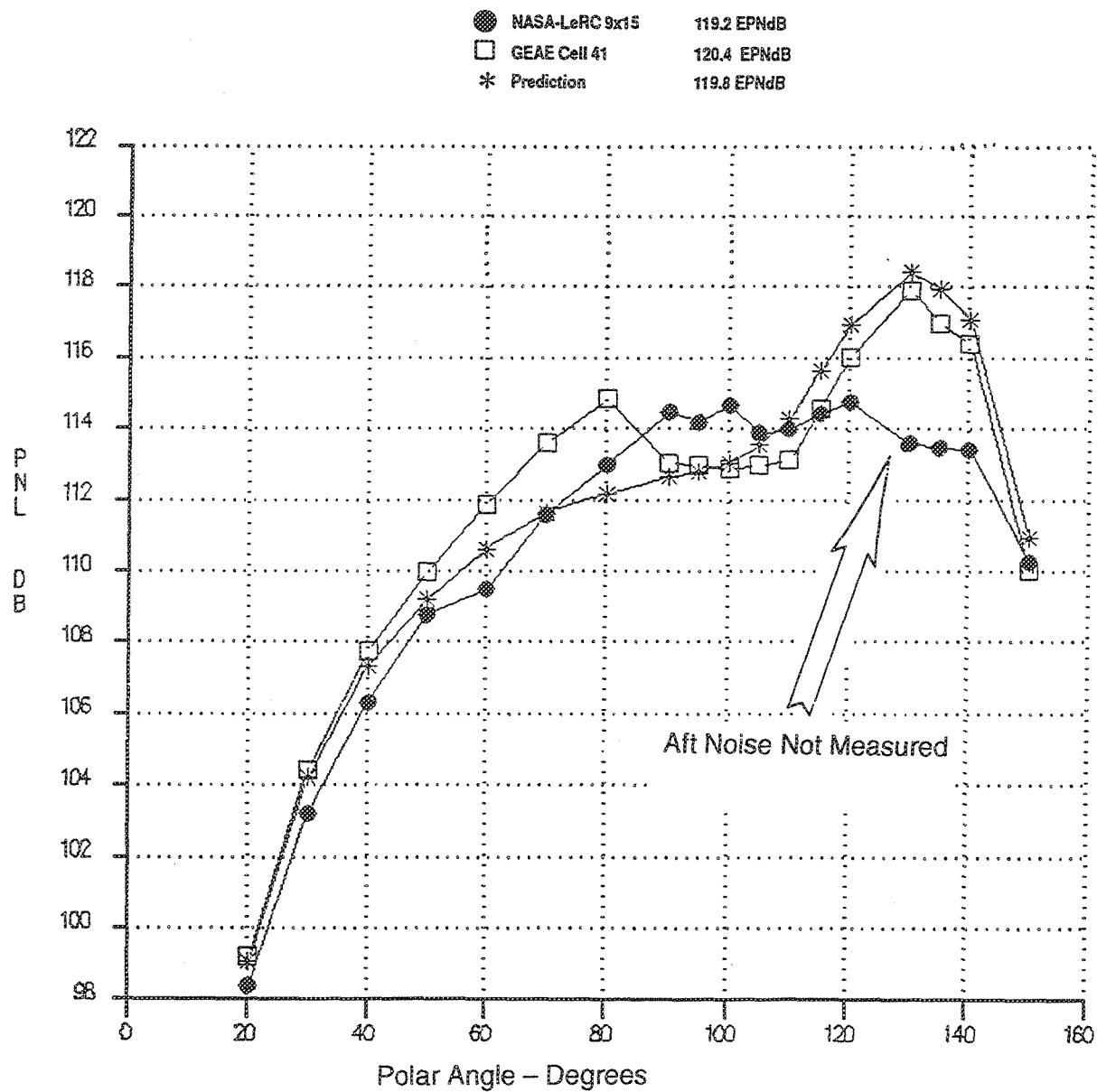


Figure 205. Comparison of NASA-LeRC 9x15 and GEAE Cell 41, PNL Versus Polar Angle  
 — Ideal Unsuppressed Primary Jet Velocity=2518 ft/sec, Baseline Round Conic Nozzle  
 (Sideline=1629 ft, NPR=3.5,  $T_{t8}=1735^{\circ}\text{R}$ ,  $A_{g*}=1086\text{ in}^2$ ,  $M_n=0.20$ )

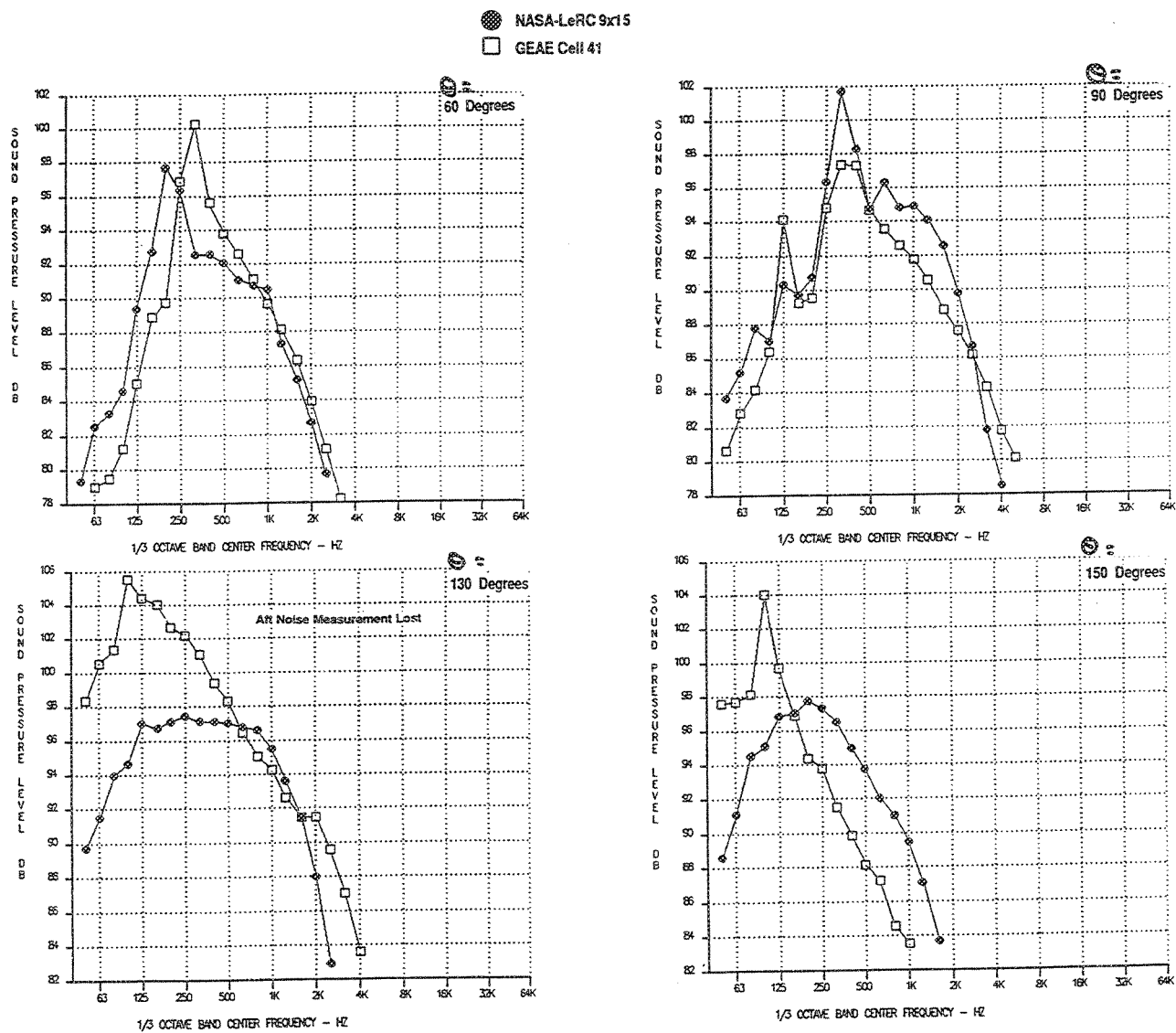


Figure 206. Comparison of NASA-LeRC 9x15 and GEAE Cell 41, SPL Versus Frequency  
— Ideal Unsuppressed Primary Jet Velocity=2518 ft/sec, Baseline Round Conic Nozzle  
(Sideline=1629 ft, NPR=3.5,  $T_{18}=1735^{\circ}\text{R}$ ,  $A_{8*}=1086\text{ in}^2$ ,  $M_n=0.20$ )

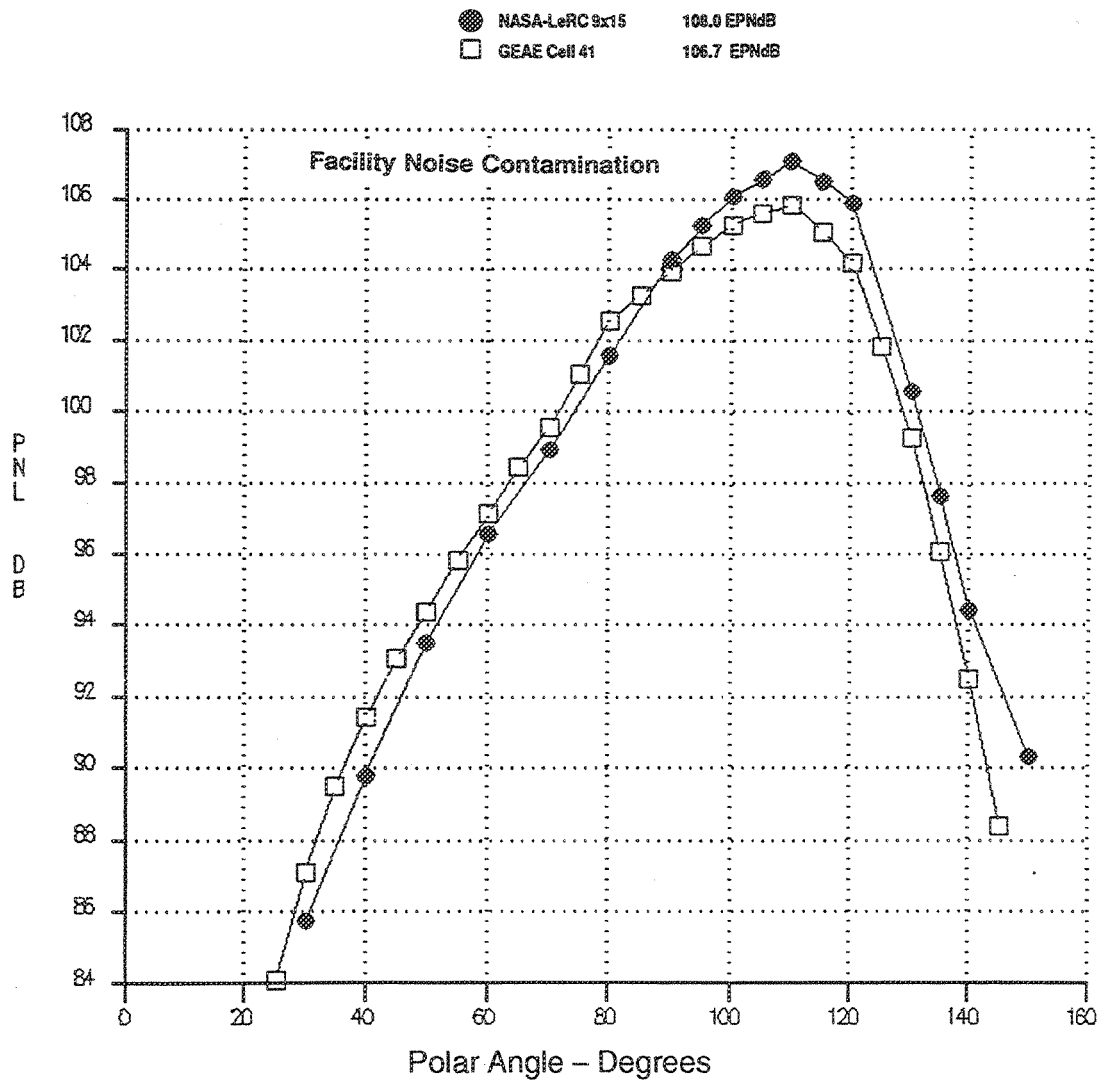


Figure 207. Comparison of NASA-LeRC 9x15 and GEAE Cell 41, PNL Versus Polar Angle  
— Ideal Unsuppressed Primary Jet Velocity=2518 ft/sec, Vortical Mixer, Fully-Treated Long Shroud  
(Overhead at 1629 ft, SAR=4.9, MAR=1.19,  $A_{8^*}=1086 \text{ in}^2$ ,  $M_n=0.20$ , NPR=3.5,  $T_{18}=1735^\circ\text{R}$ )

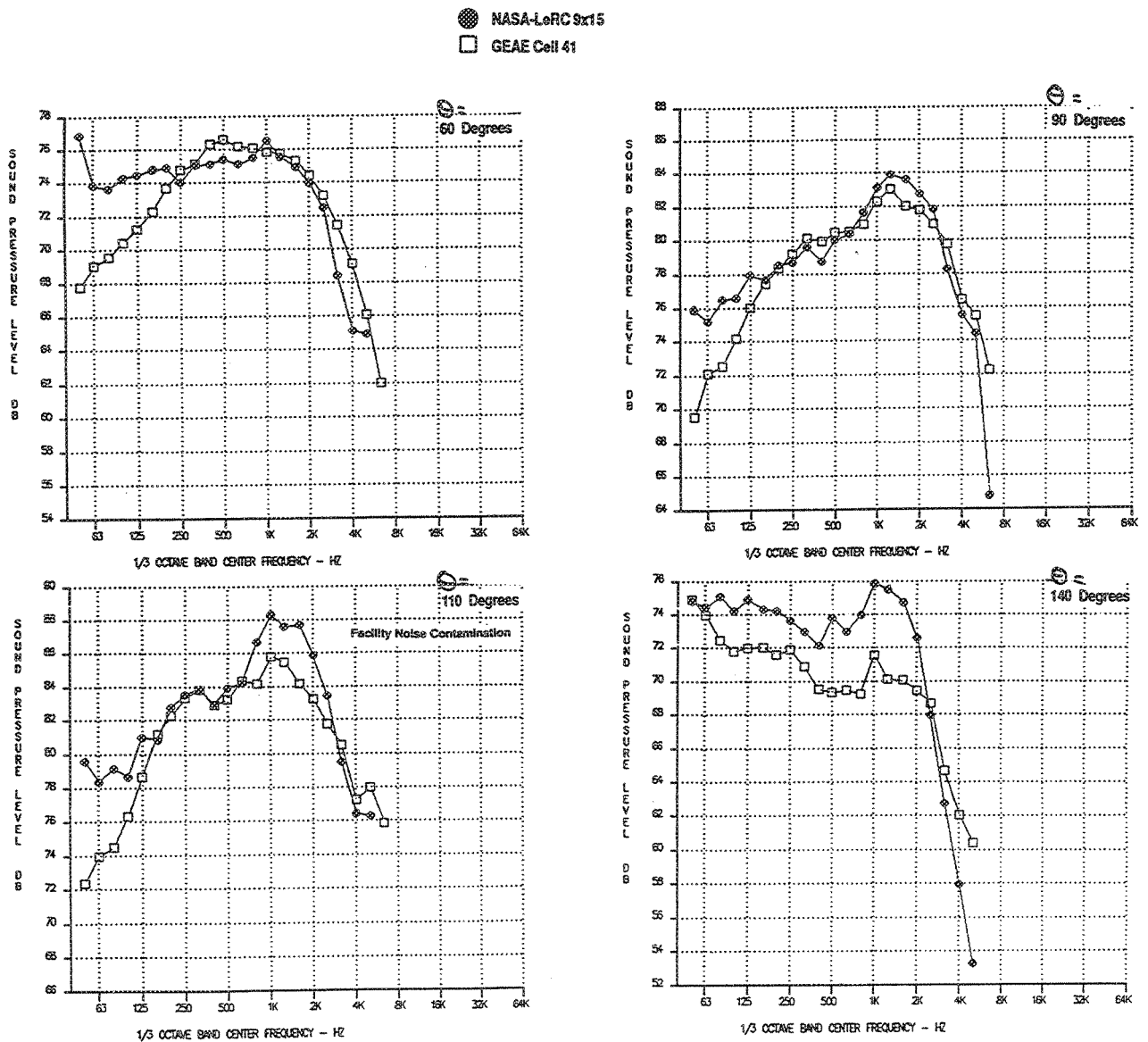


Figure 208. Comparison of NASA-LeRC 9x15 and GEAE Cell 41, SPL Versus Frequency  
 — Ideal Unsuppressed Primary Jet Velocity=2518 ft/sec, Vortical Mixer, Fully-Treated Long Shroud  
 (Overhead at 1629 ft, SAR=4.9, MAR=1.19,  $A_{g*}=1086 \text{ in}^2$ ,  $M_n=0.20$ , NPR=3.5,  $T_{t8}=1735^\circ\text{R}$ )

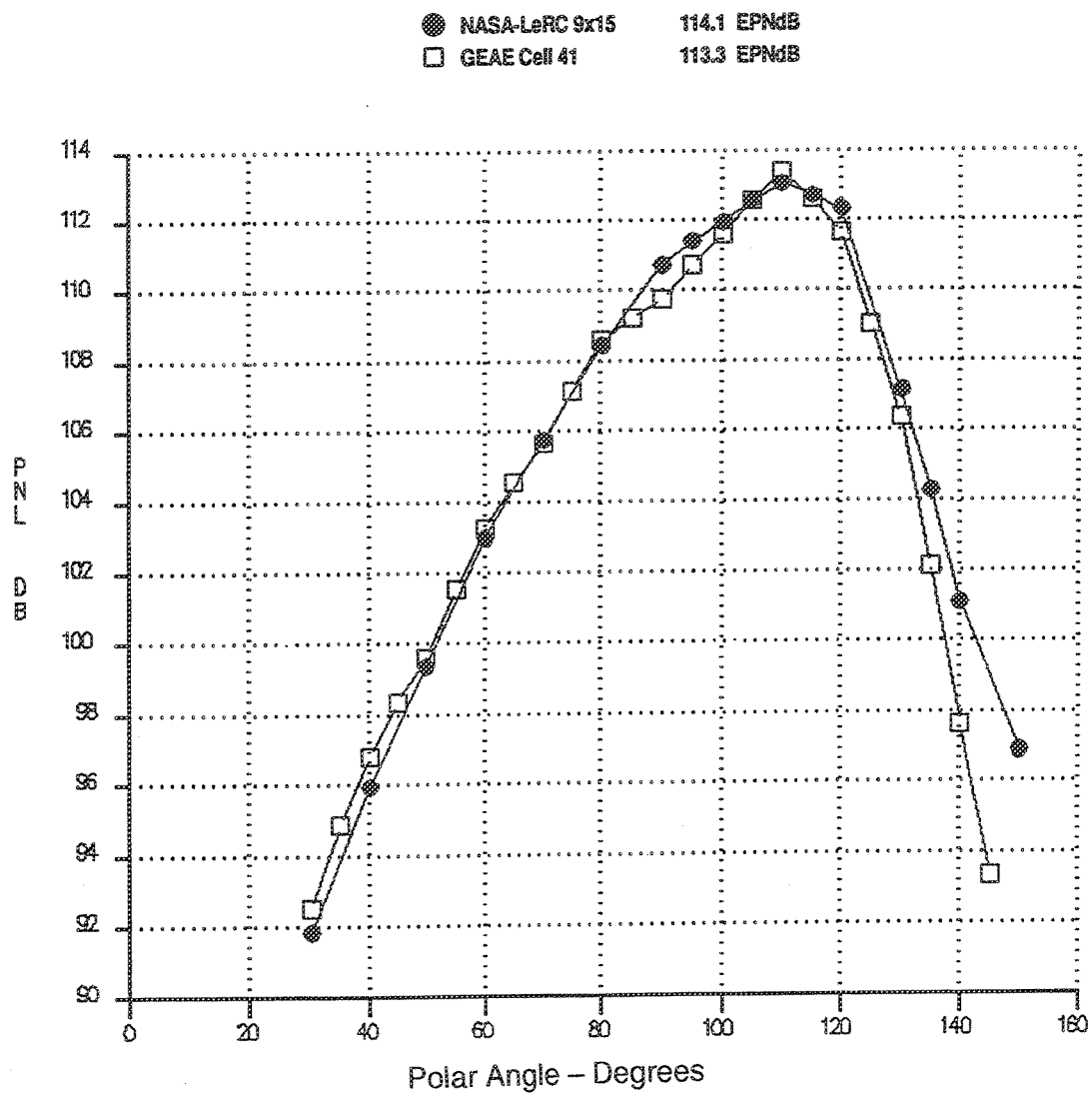


Figure 209. Comparison of NASA-LeRC 9x15 and GEAE Cell 41, PNL Versus Polar Angle  
 — Ideal Unsuppressed Primary Jet Velocity=2518 ft/sec, Vortical Mixer, Hardwall Long Shroud  
 (Overhead at 1629 ft, NPR=3.5,  $T_{t8}=1735^{\circ}\text{R}$ ,  $A_{g*}=1086\text{ in}^2$ ,  $M_n=0.20$ , SAR=4.9, MAR=1.19)

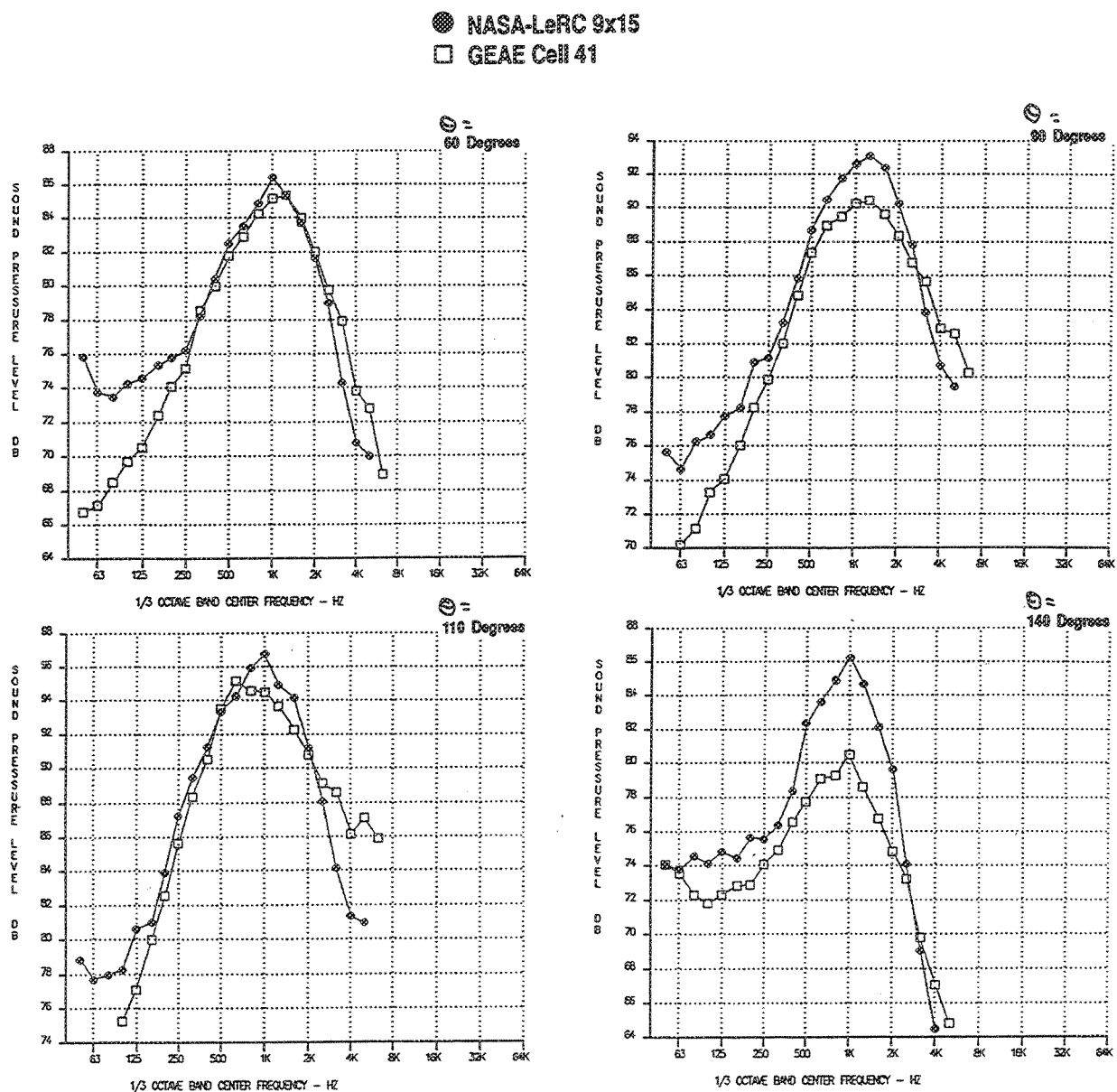


Figure 210. Comparison of NASA-LeRC 9x15 and GEAE Cell 41, SPL Versus. Frequency  
 — Ideal Unsuppressed Primary Jet Velocity=2518 ft/sec, Vortical Mixer, Hardwall Long Shroud  
 (Overhead at 1629 ft, SAR=4.9, MAR=1.19,  $A_8^*=1086 \text{ in}^2$ ,  $M_n=0.20$ , NPR=3.5,  $T_{t8}=1735^\circ\text{R}$ )



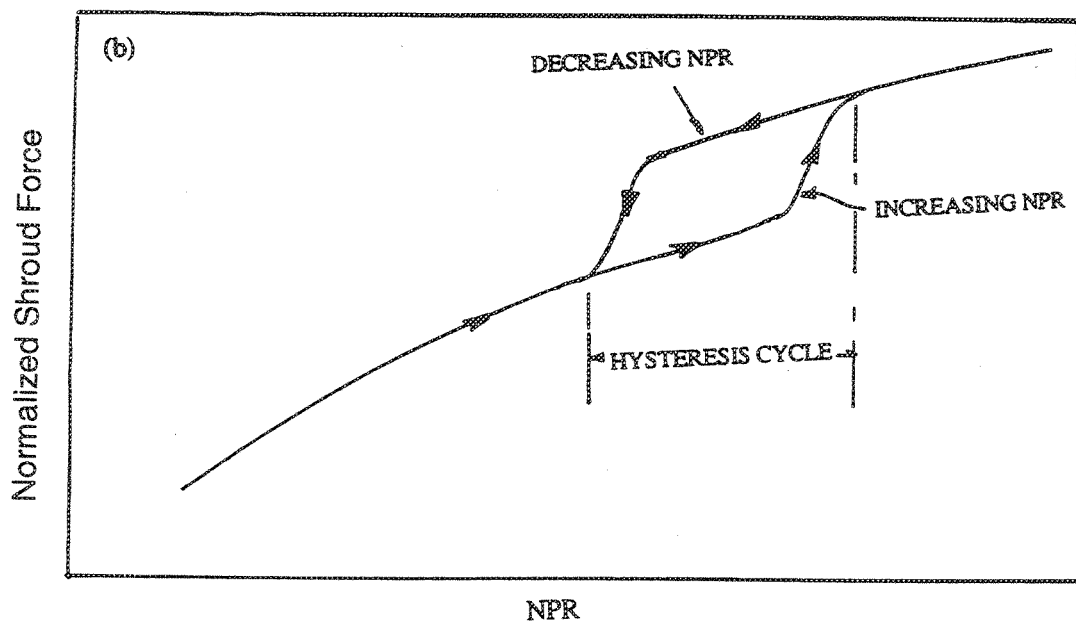
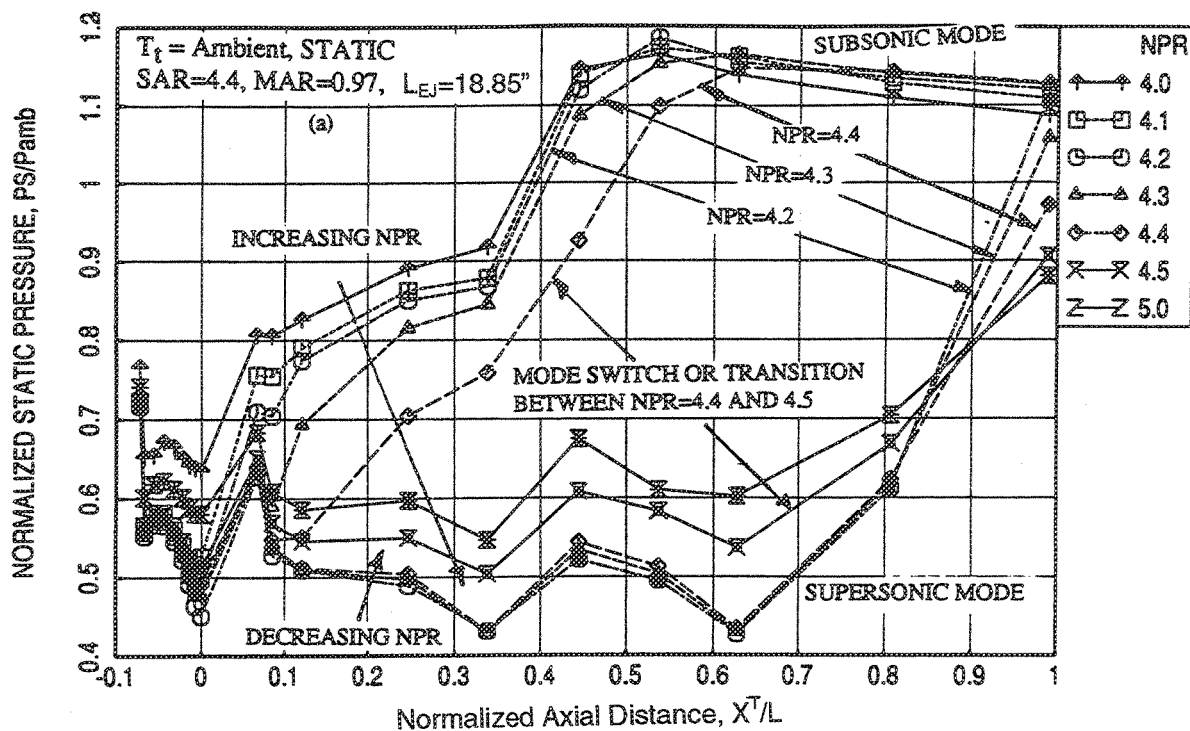


Figure 211.(a) Typical Static Pressure Distribution on the Internal Surface of the Ejector Shroud at Different Increasing and Decreasing NPR for a Vortical Mixer With Long Hardwall Shroud;  
(b) Typical Hysteresis Cycle

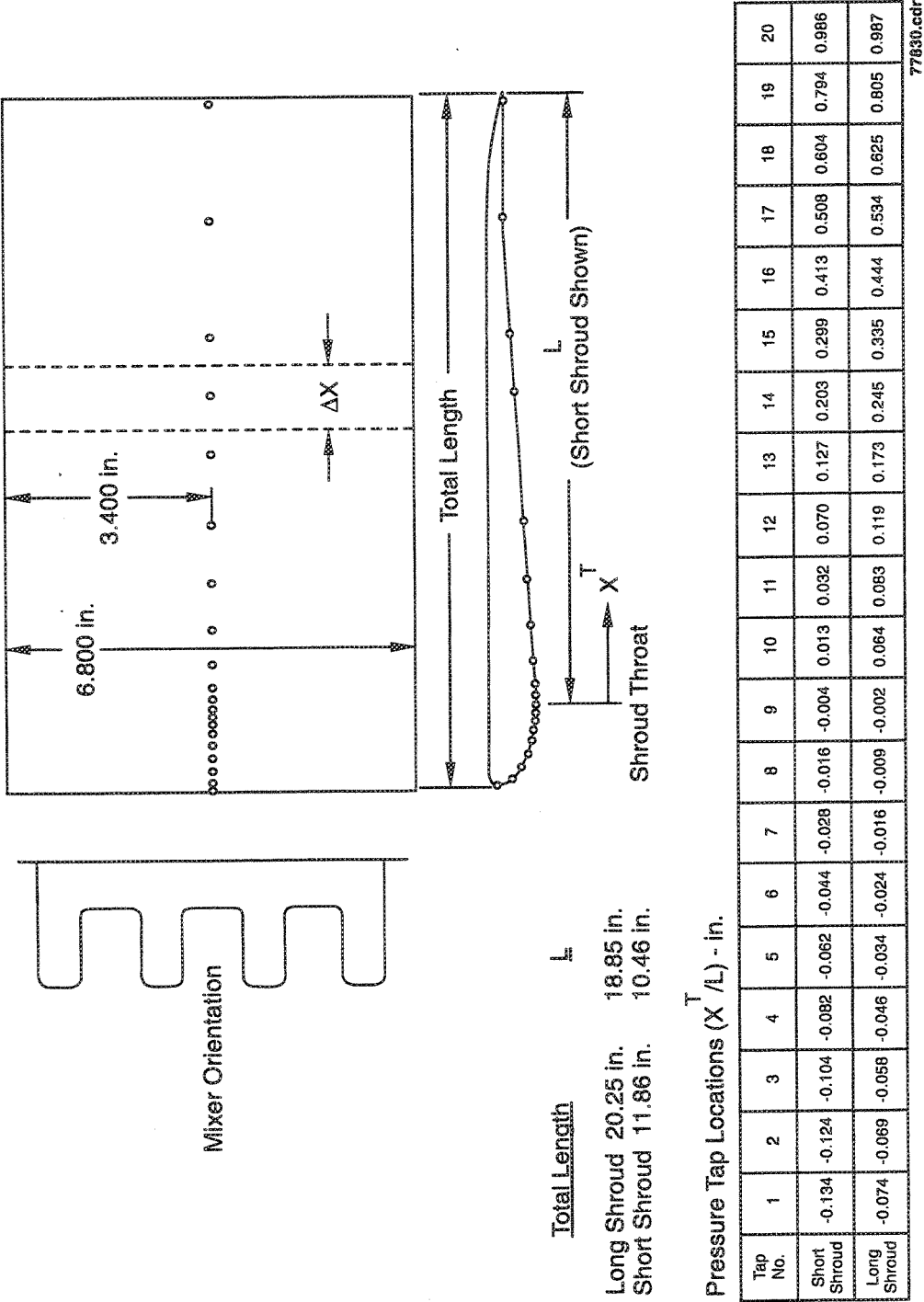


Figure 212. Static Pressure Instrumentation for P&W Two-Dimensional Hardwall Shrouds

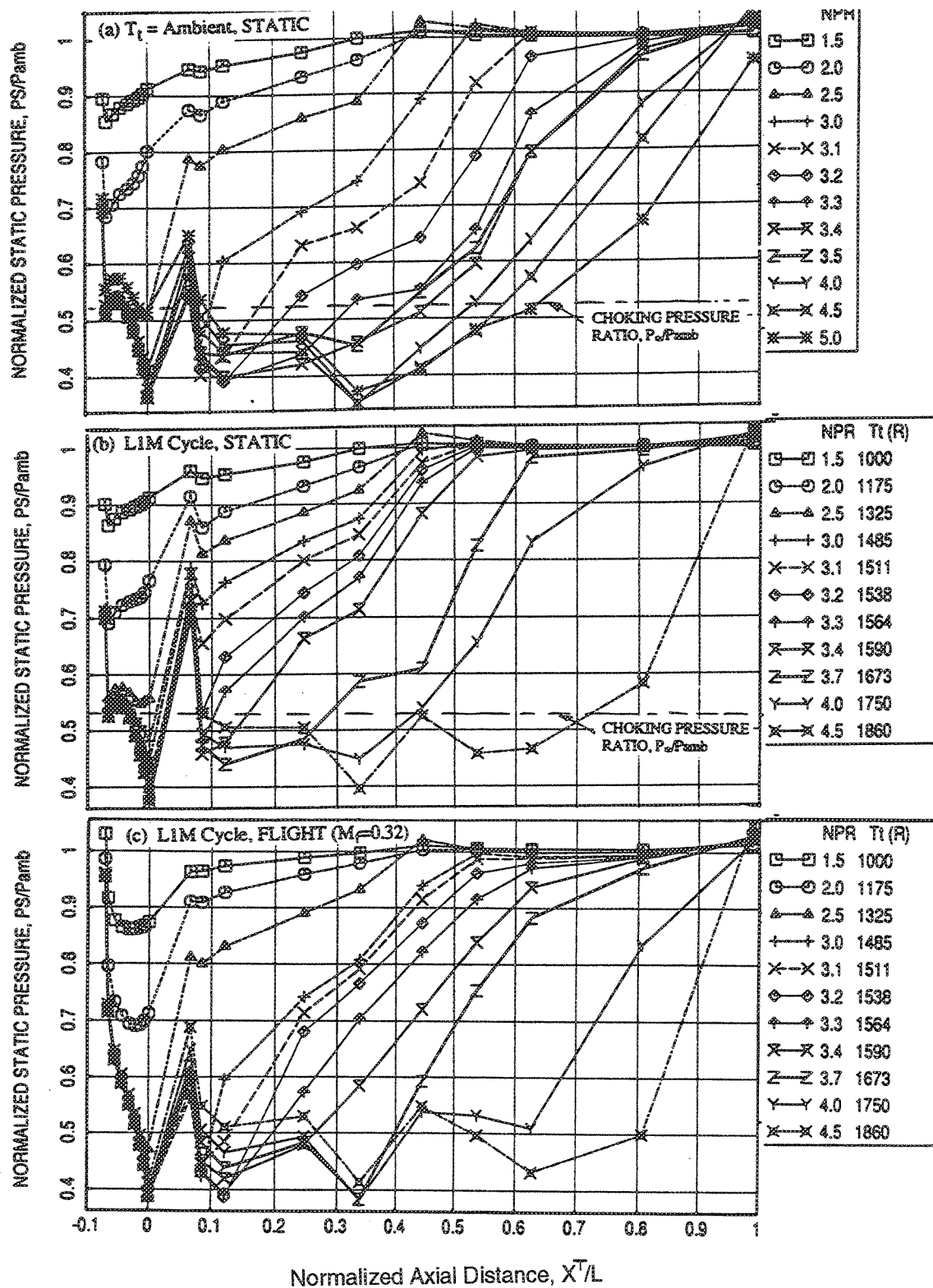


Figure 213. Axial Static Pressure Distribution on Shroud Surface for a Vortical Mixer-Ejector Configuration (SAR=4.4, MAR=1.18, Shroud Length=18.85 in.)

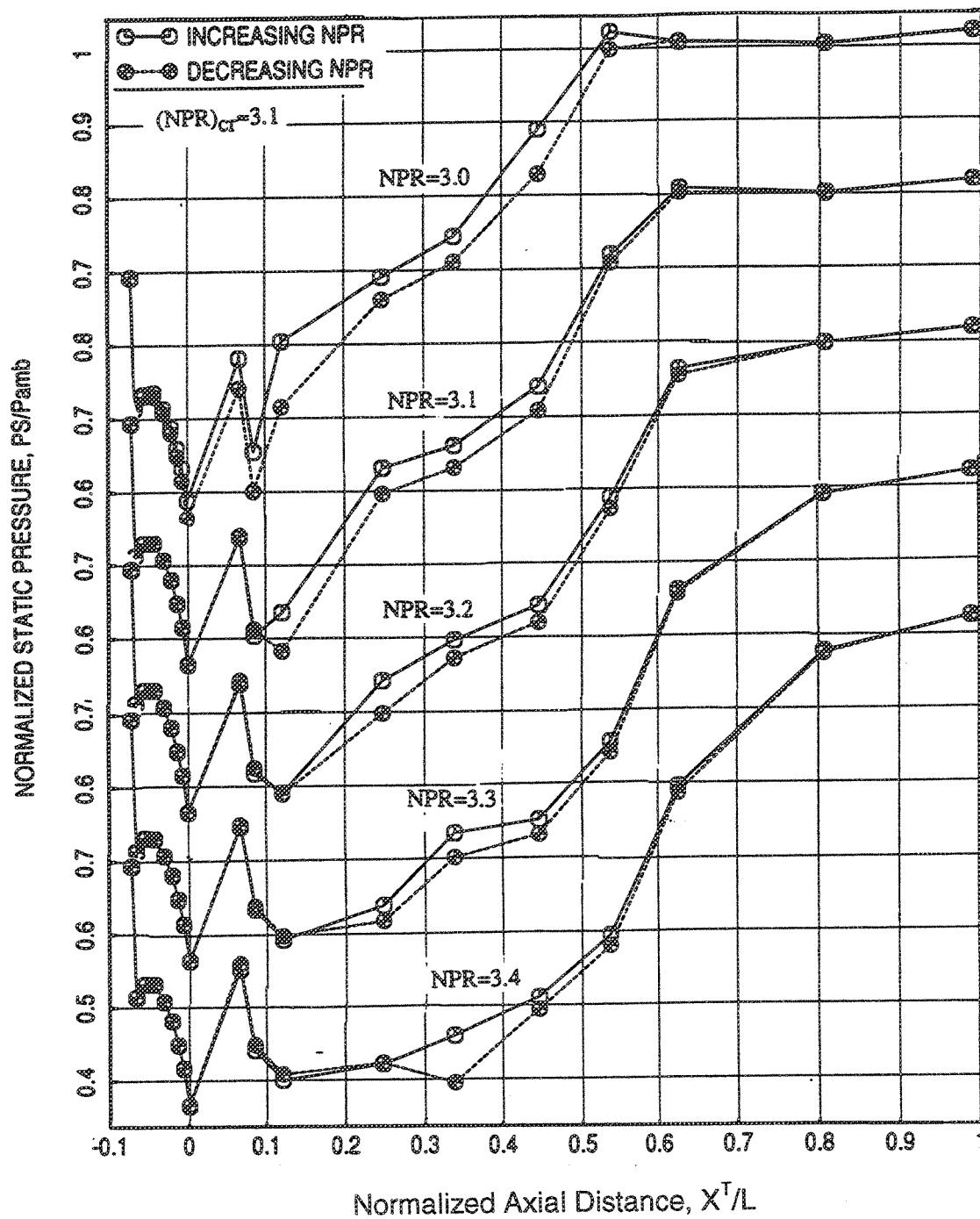


Figure 214. Effect of Increasing and Decreasing NPR on Axial Static Pressure Distribution on Shroud Surface for a Vortical Mixer-Ejector Configuration at Static Condition (SAR=4.4, MAR=1.18, Shroud Length=18.85 in.,  $T_t$ =Ambient)

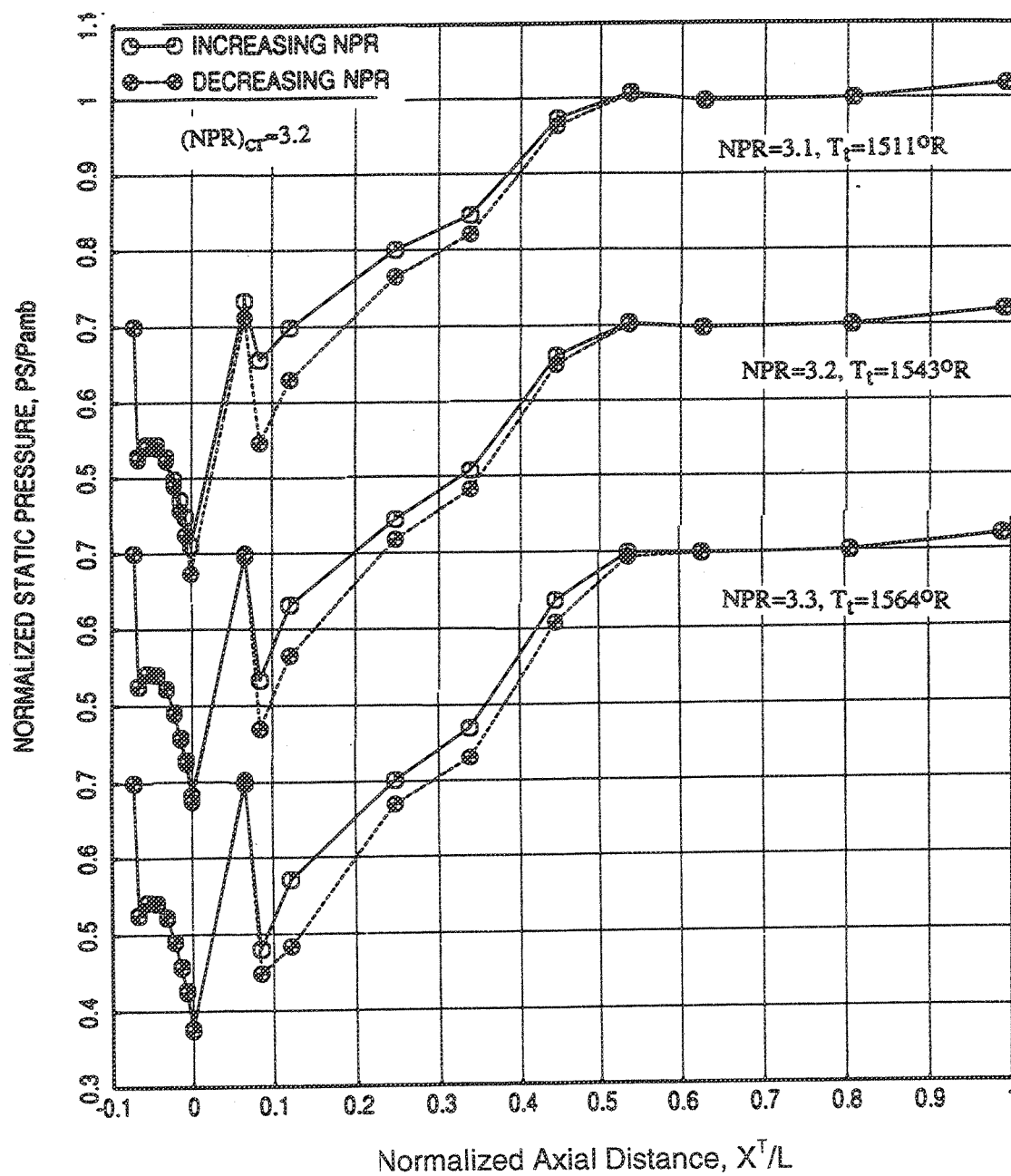


Figure 215. Effect of Increasing and Decreasing NPR on Axial Static Pressure Distribution on Shroud Surface for a Vortical Mixer-Ejector Configuration at Static Condition (SAR=4.4, MAR=1.18, Shroud Length=18.85 in., LIM Cycle)

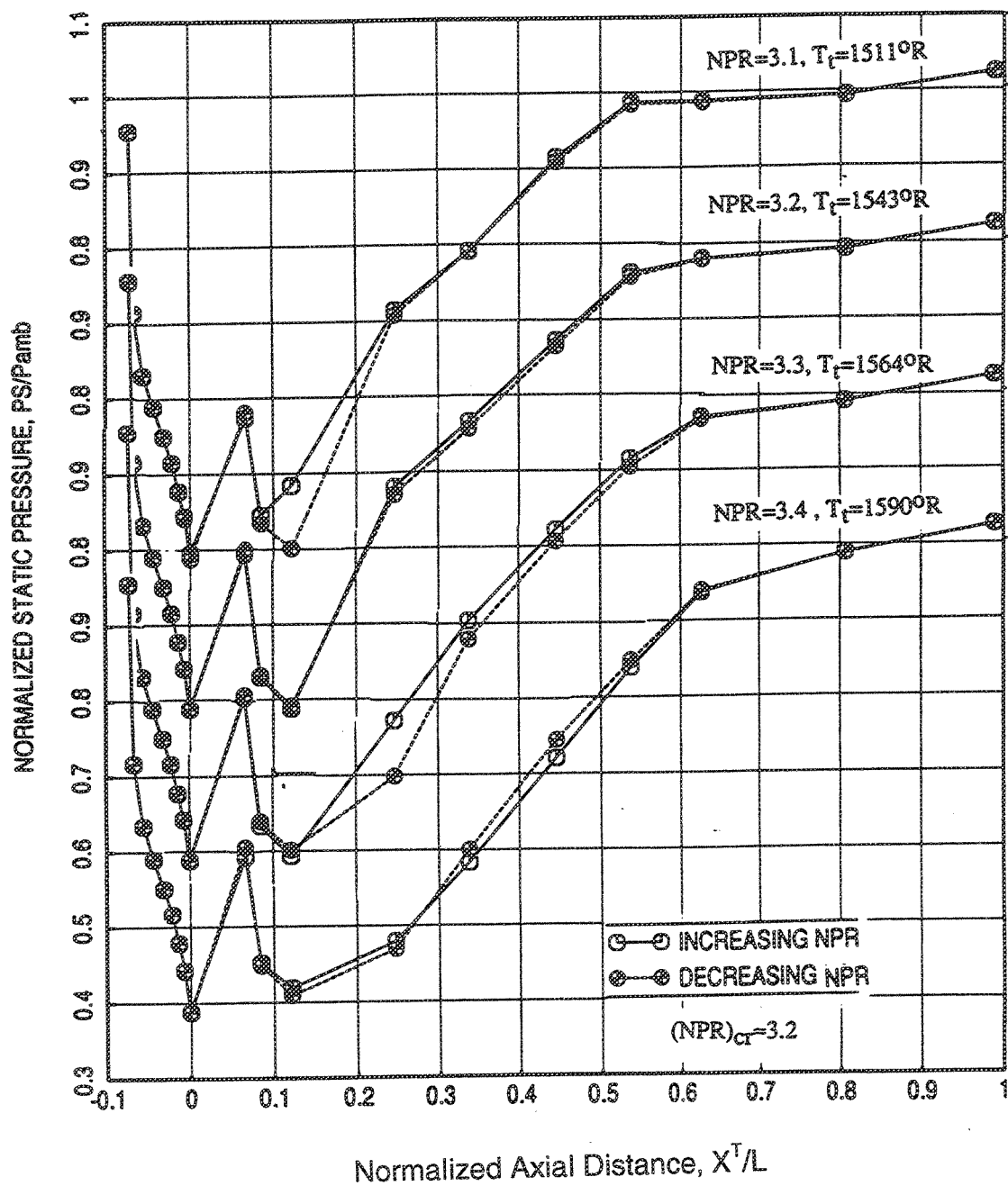


Figure 216. Effect of Increasing and Decreasing NPR on Axial Static Pressure Distribution on Shroud Surface for a Vortical Mixer-Ejector Configuration With Flight Simulation ( $Mn=0.32$ ) ( $SAR=4.4$ ,  $MAR=1.18$ , Shroud Length=18.85 in., LIM Cycle)

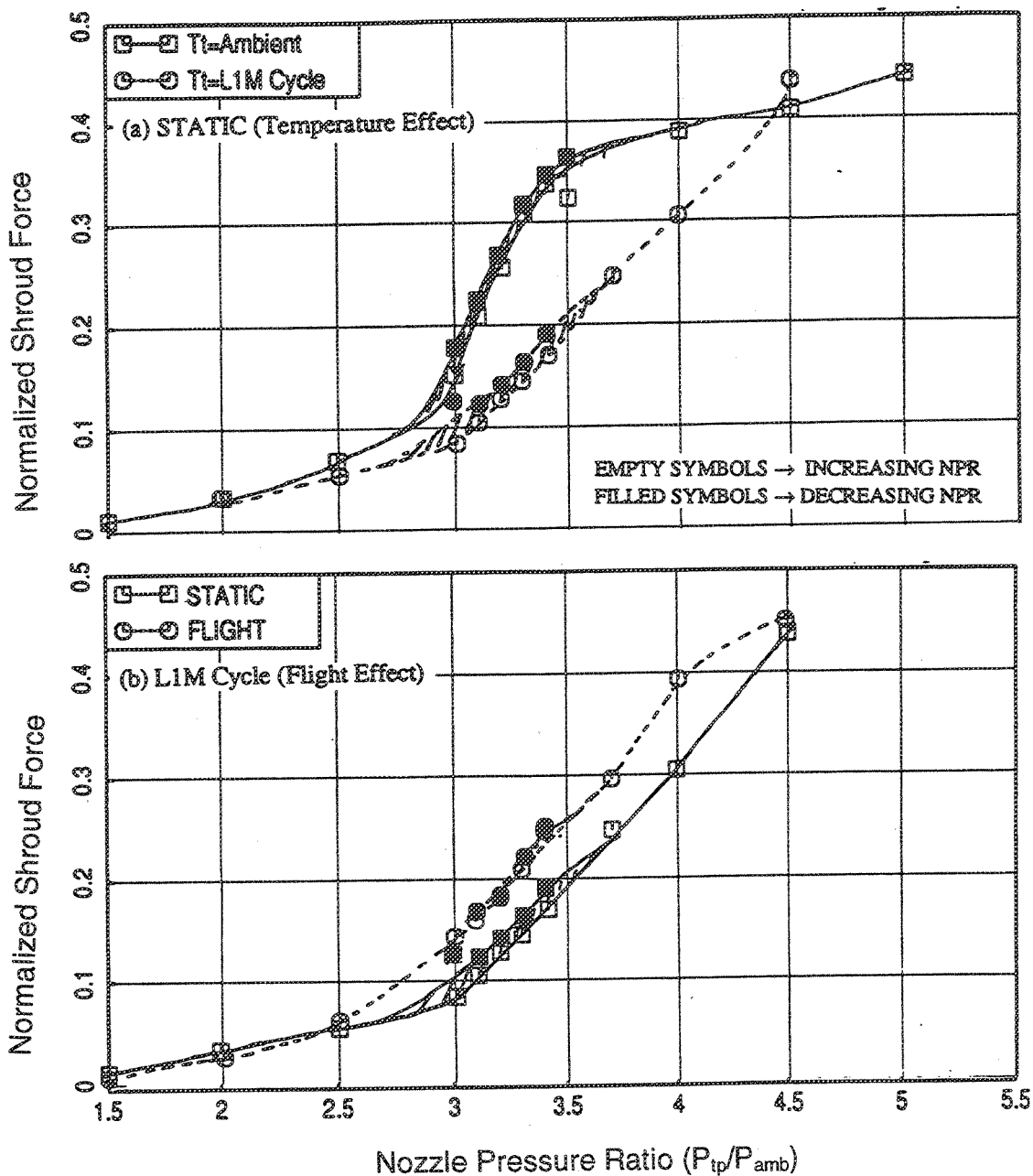


Figure 217. Variation of Normalized Shroud Force Due to: (a) Nozzle Total Temperature; (b) Flight Simulation ( $M_n=0.32$ ) for a Vortical Mixer-Ejector Configuration ( $SAR=4.4$ ,  $MAR=1.18$ , Shroud Length=18.85 in.)

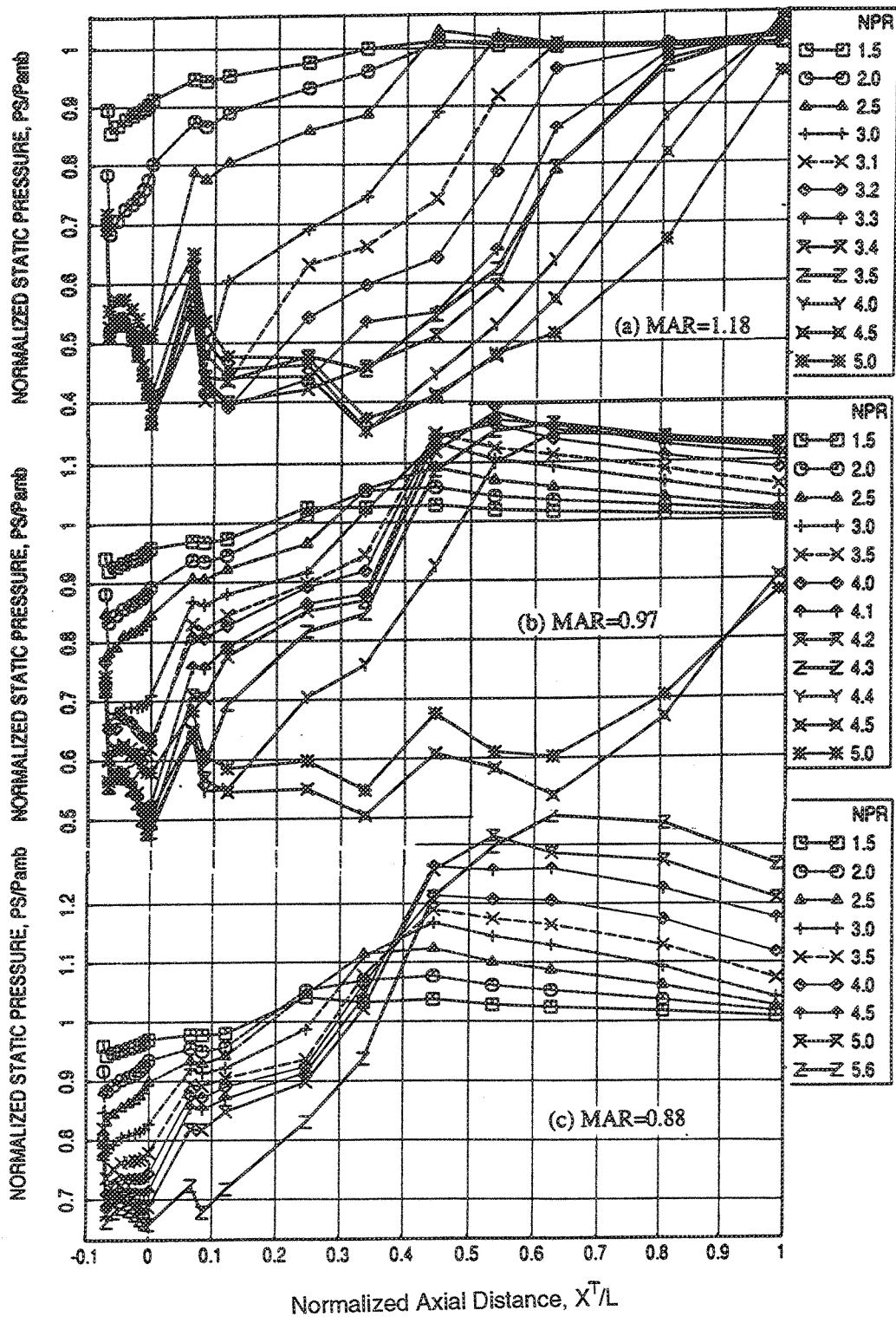


Figure 218. Effect of MAR on Axial Static Pressure Distribution on Shroud Surface for Vortical Mixer-Ejector Configurations at Static Condition: SAR=4.4, Shroud Length=18.85 in.,  $T_t$ =Ambient



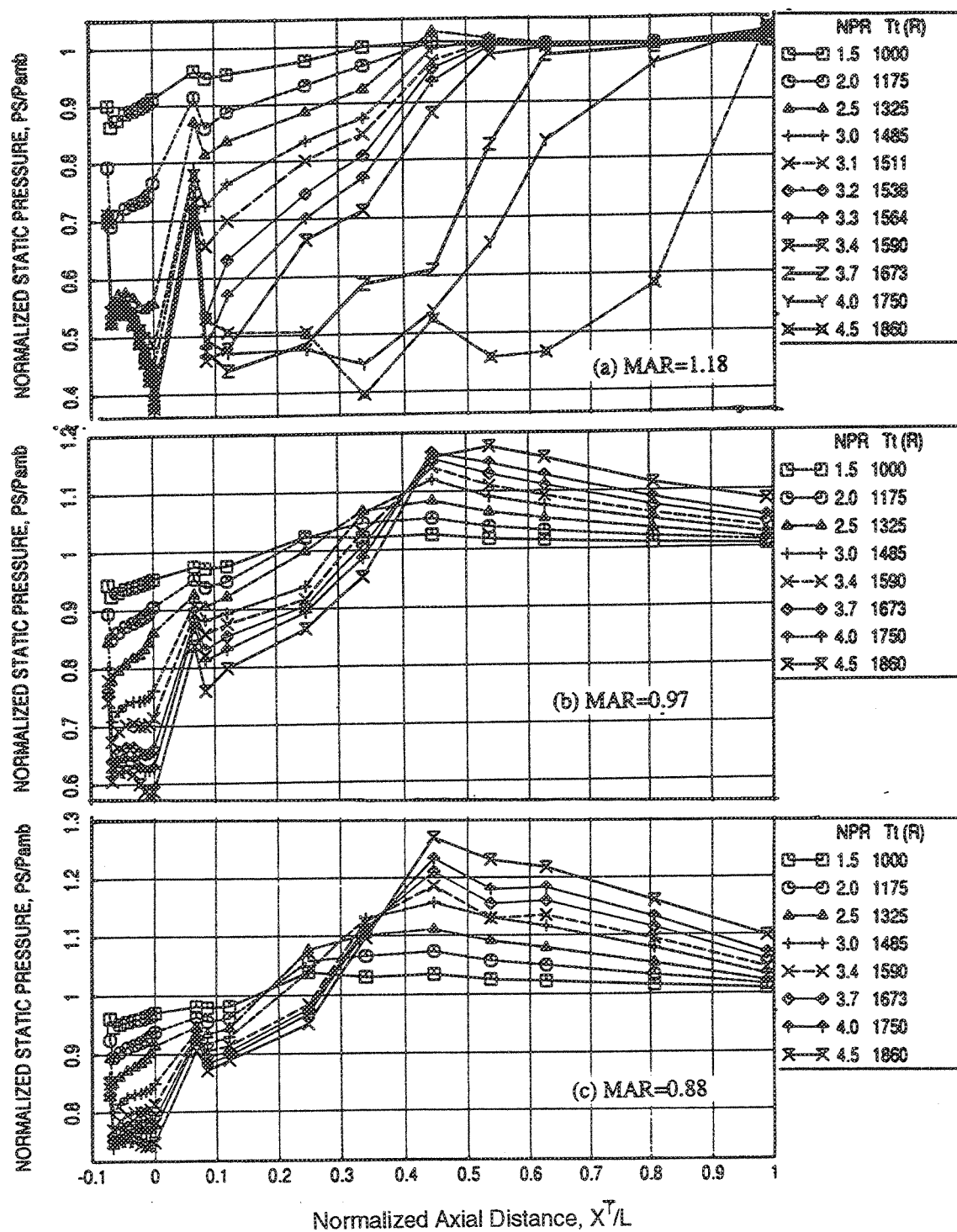


Figure 219. Effect of MAR on Axial Static Pressure Distribution on Shroud Surface for Vortical Mixer-Ejector Configurations at Static Conditions (SAR=4.4, Shroud Length=18.85 in., LIM Cycle)

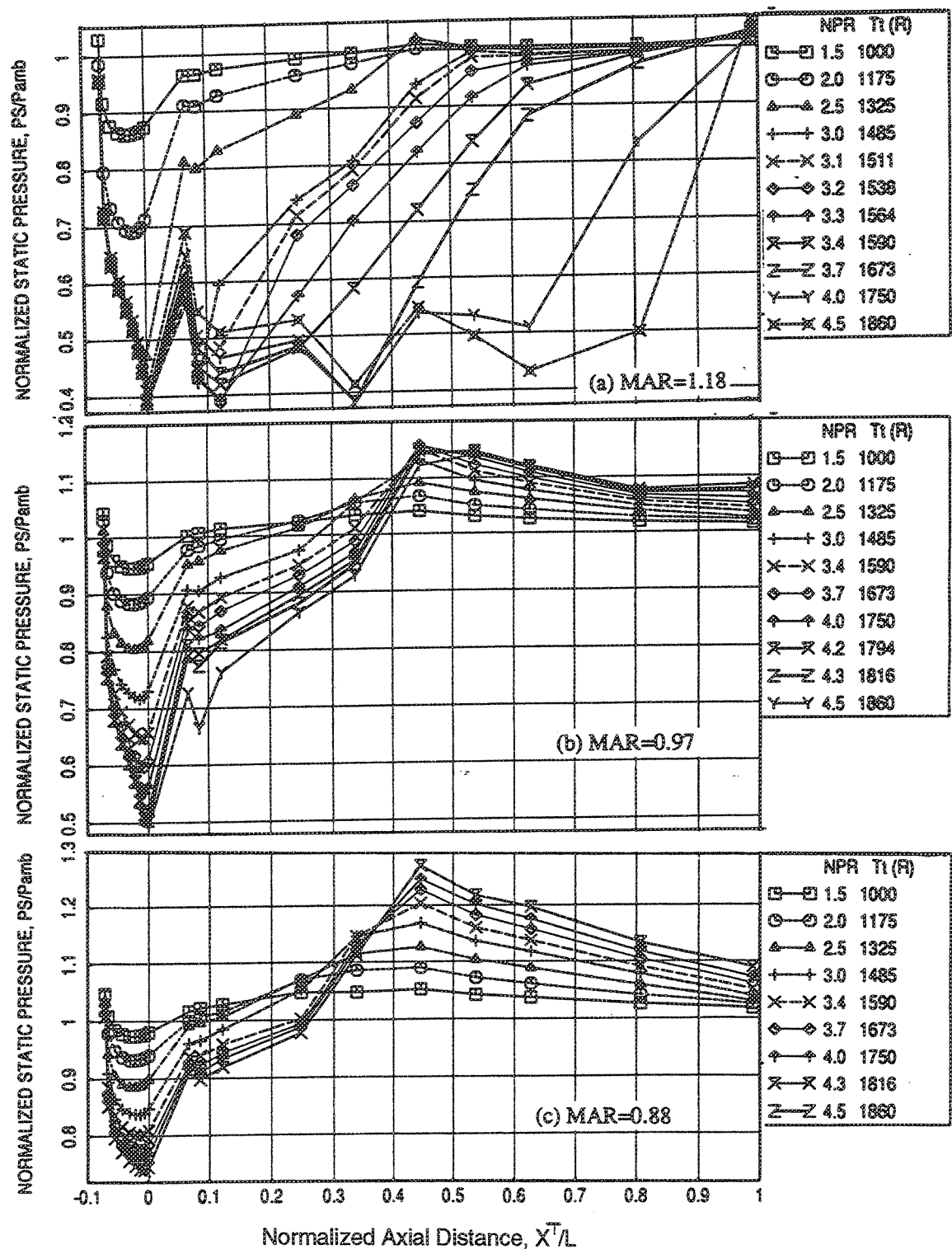


Figure 220. Effect of MAR on Axial Static Pressure Distribution on Shroud Surface for Vortical Mixer-Ejector Configurations With Flight Simulation ( $Mn=0.32$ ) ( $SAR=4.4$ , Shroud Length=18.85 in., LIM Cycle)

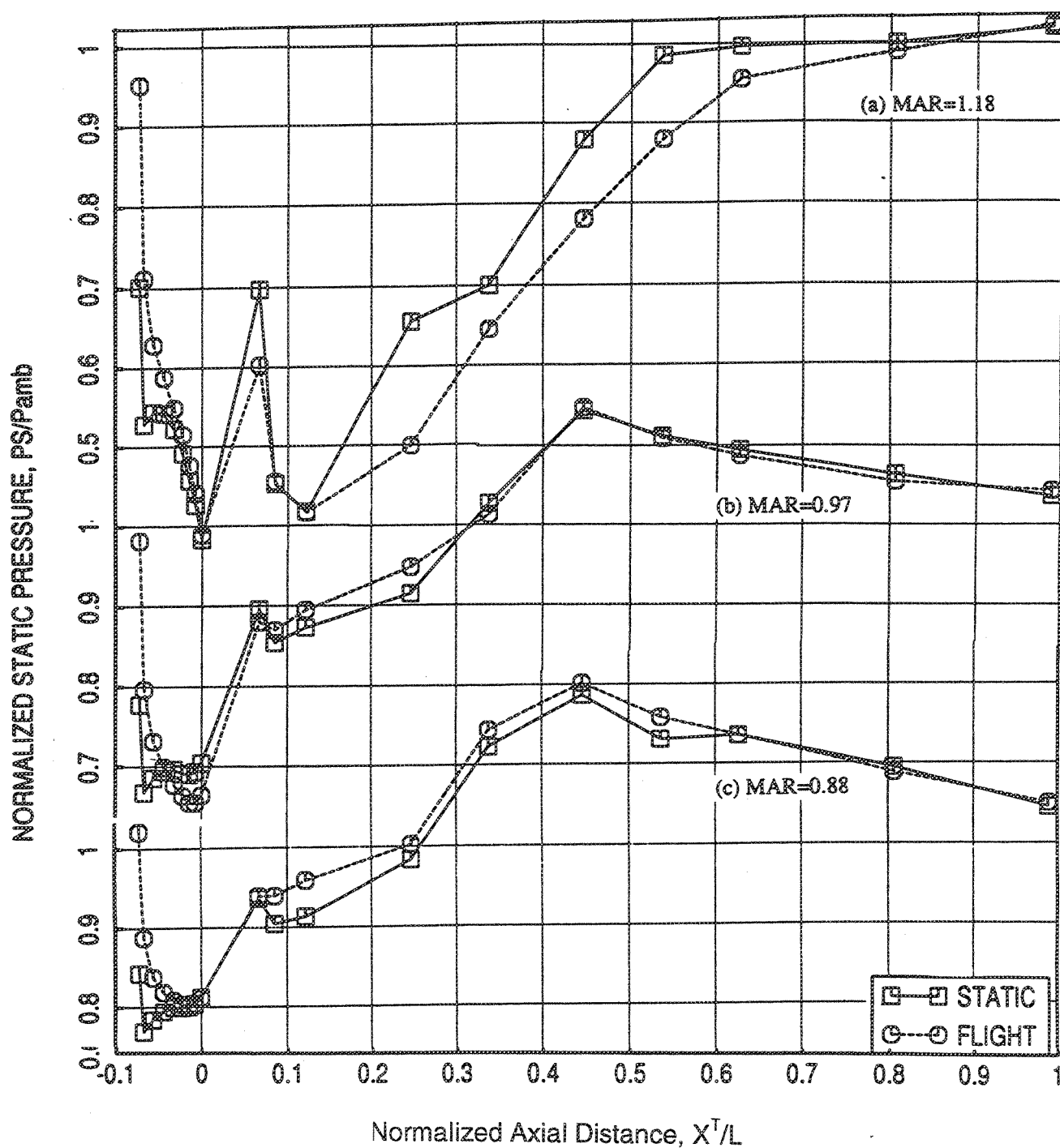


Figure 221. Effect of Flight on Axial Static Pressure Distribution on Shroud Surface for Vortical Mixer-Ejector Configurations on Different MAR (SAR=4.4, Shroud Length=18.85 in., NPR=3.4,  $T_1=1645^\circ\text{R}$ )

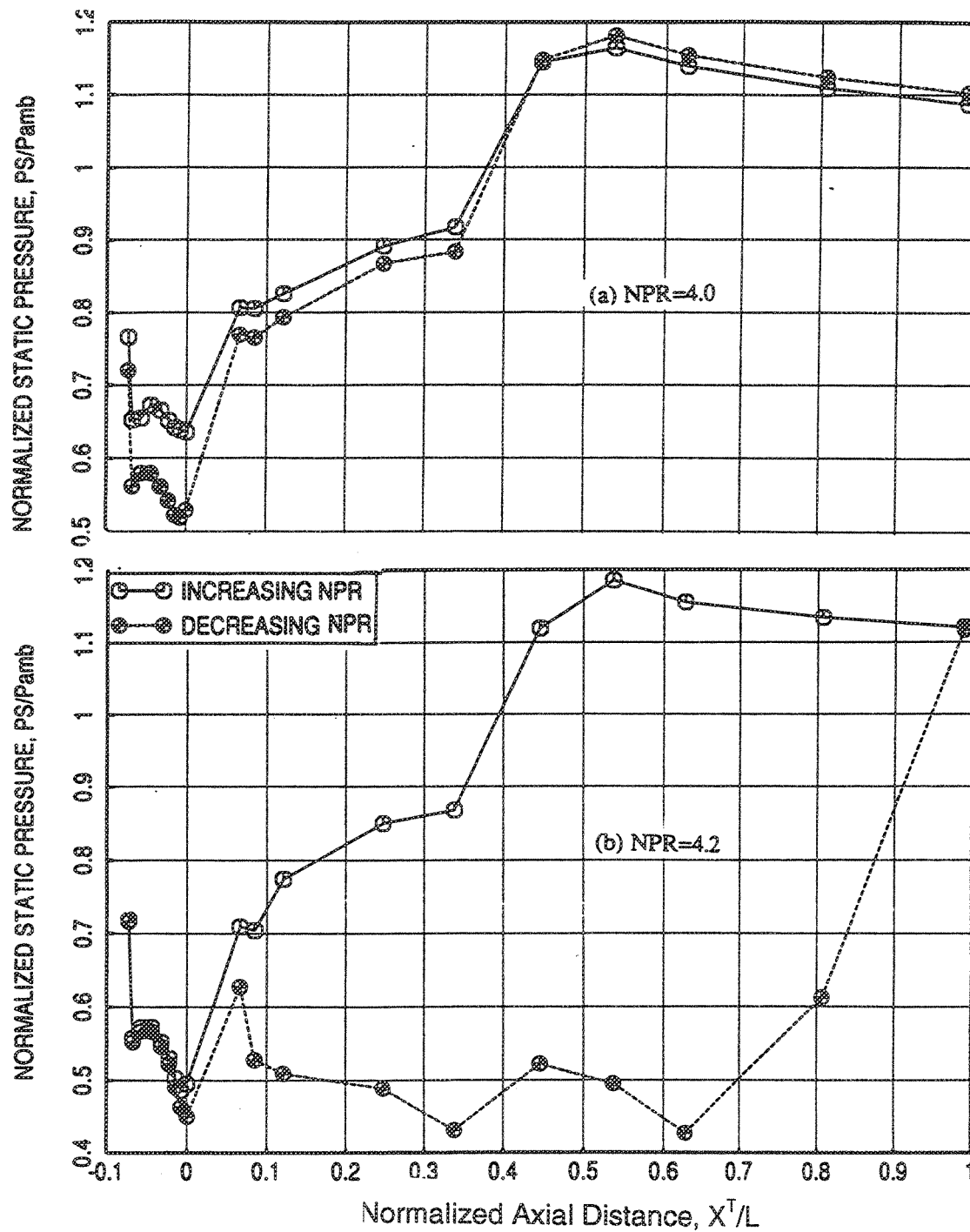


Figure 222. Effect of Increasing and Decreasing NPR on Axial Static Pressure Distribution on Shroud Surface for a Vortical Mixer-Ejector Configuration at Static Condition (SAR=4.4, MAR=0.97, Shroud Length=18.85 in.,  $T_t$ =Ambient)

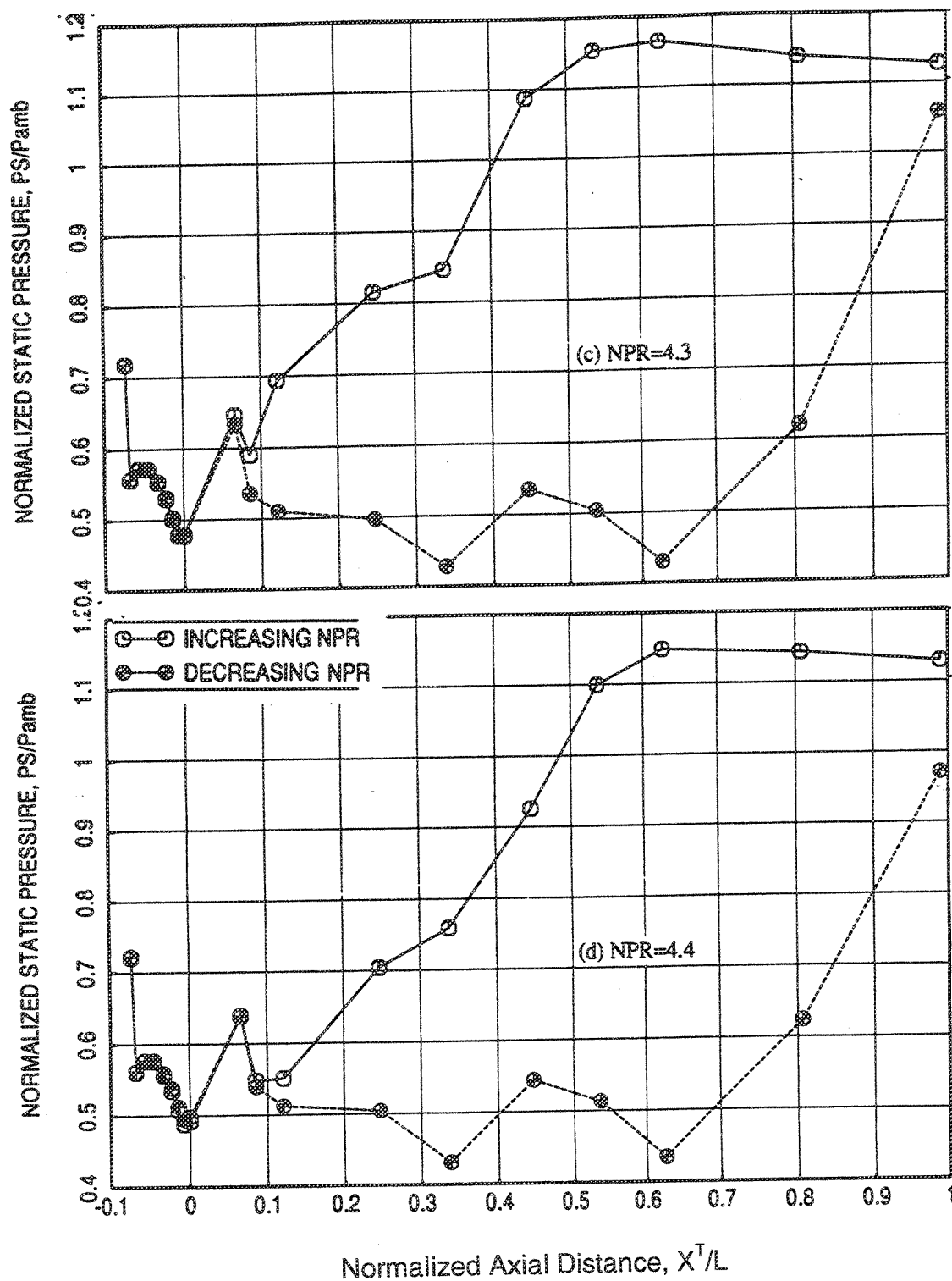


Figure 223. Effect of Increasing and Decreasing NPR on Axial Static Pressure Distribution on Shroud Surface for a Vortical Mixer-Ejector Configuration at Static Condition (SAR=4.4, MAR=0.97, Shroud Length=18.85 in.,  $T_t$ =Ambient)

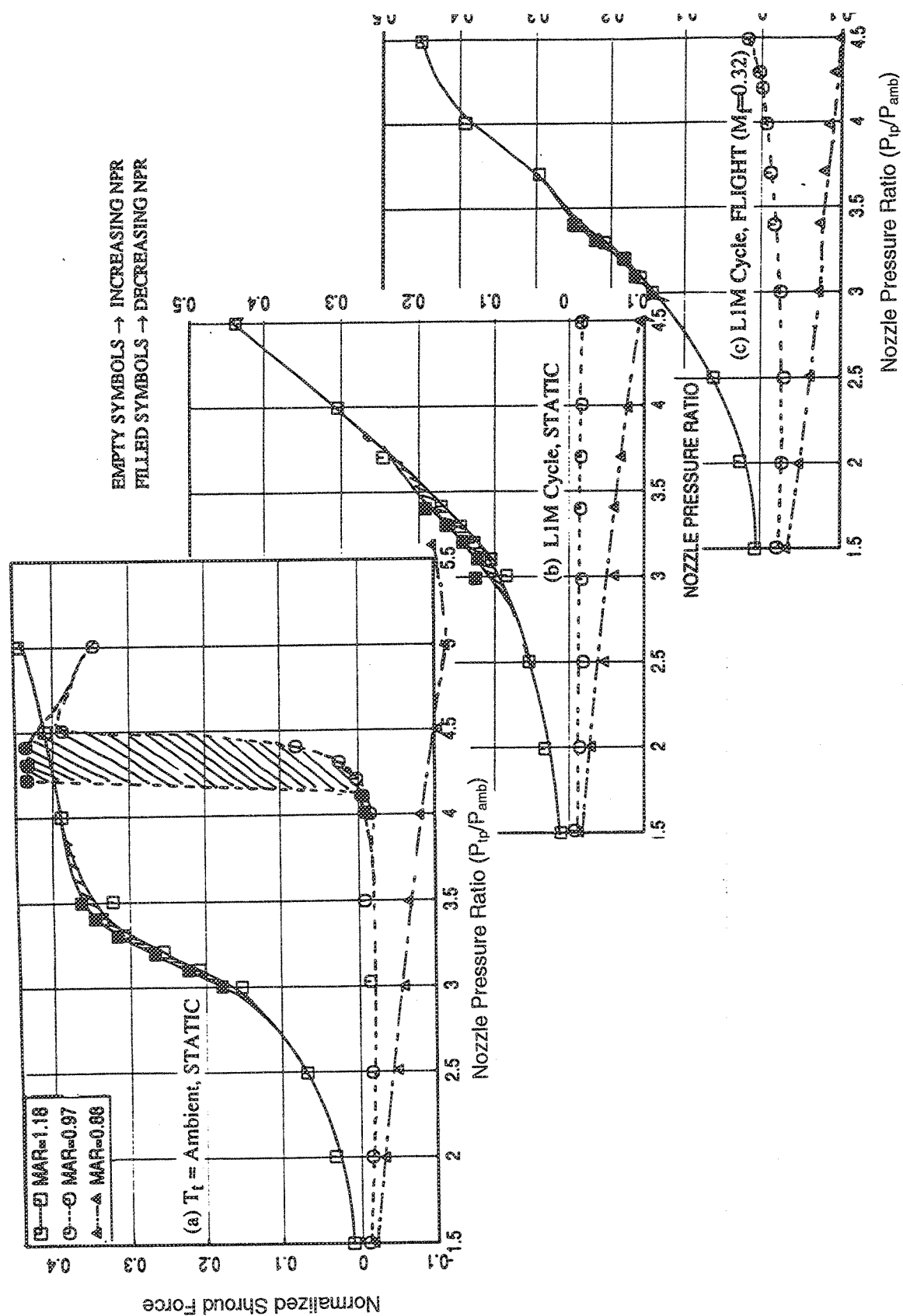


Figure 224. Variation of Normalized Shroud Force Due to MAR for Vortical Mixer-Ejector Configurations

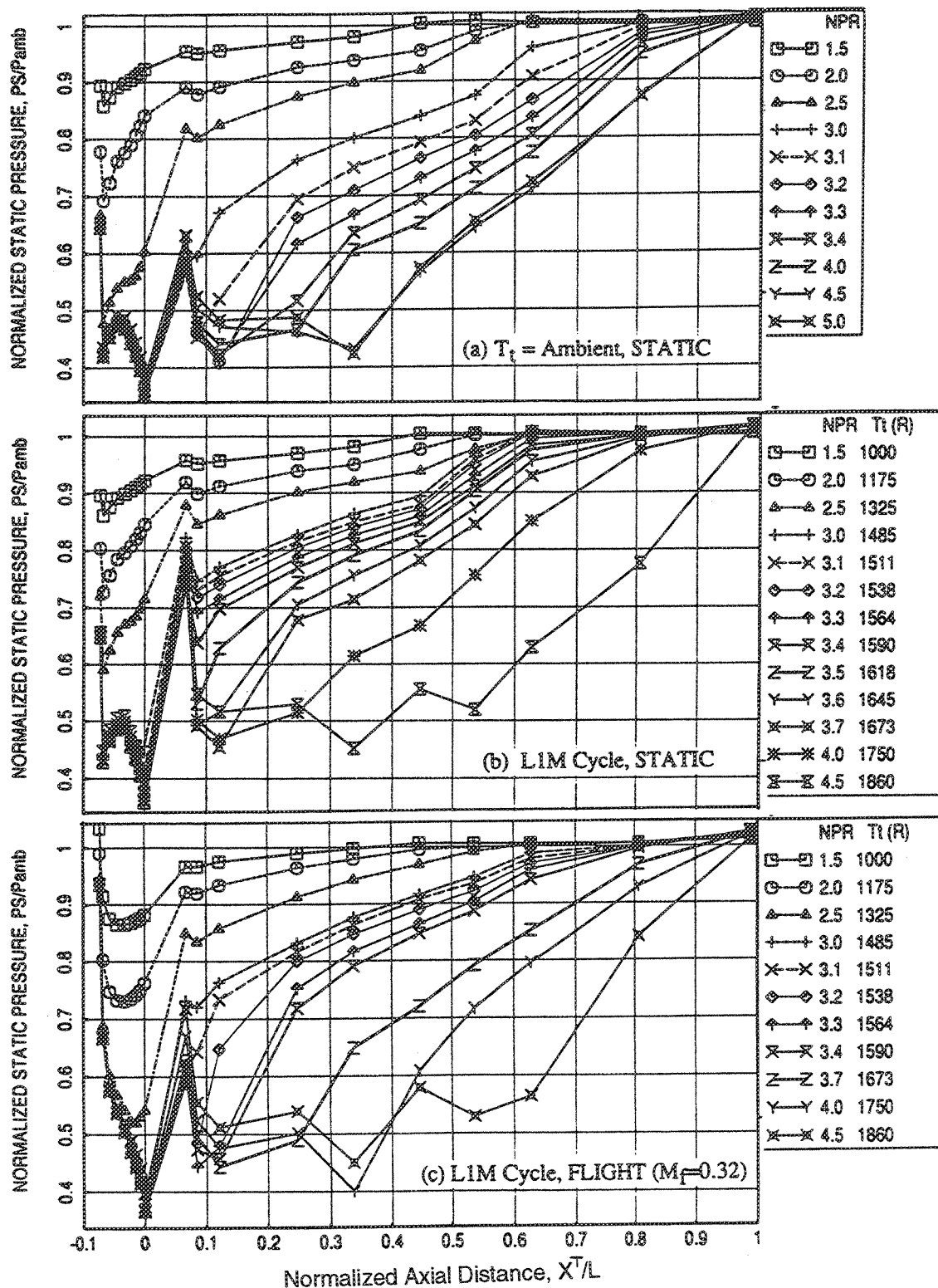


Figure 225. Axial Static Pressure Distribution on Shroud Surface for a Vortical Mixer-Ejector Configuration (SAR=4.9, MAR=1.18, Shroud Length=18.85 in.)

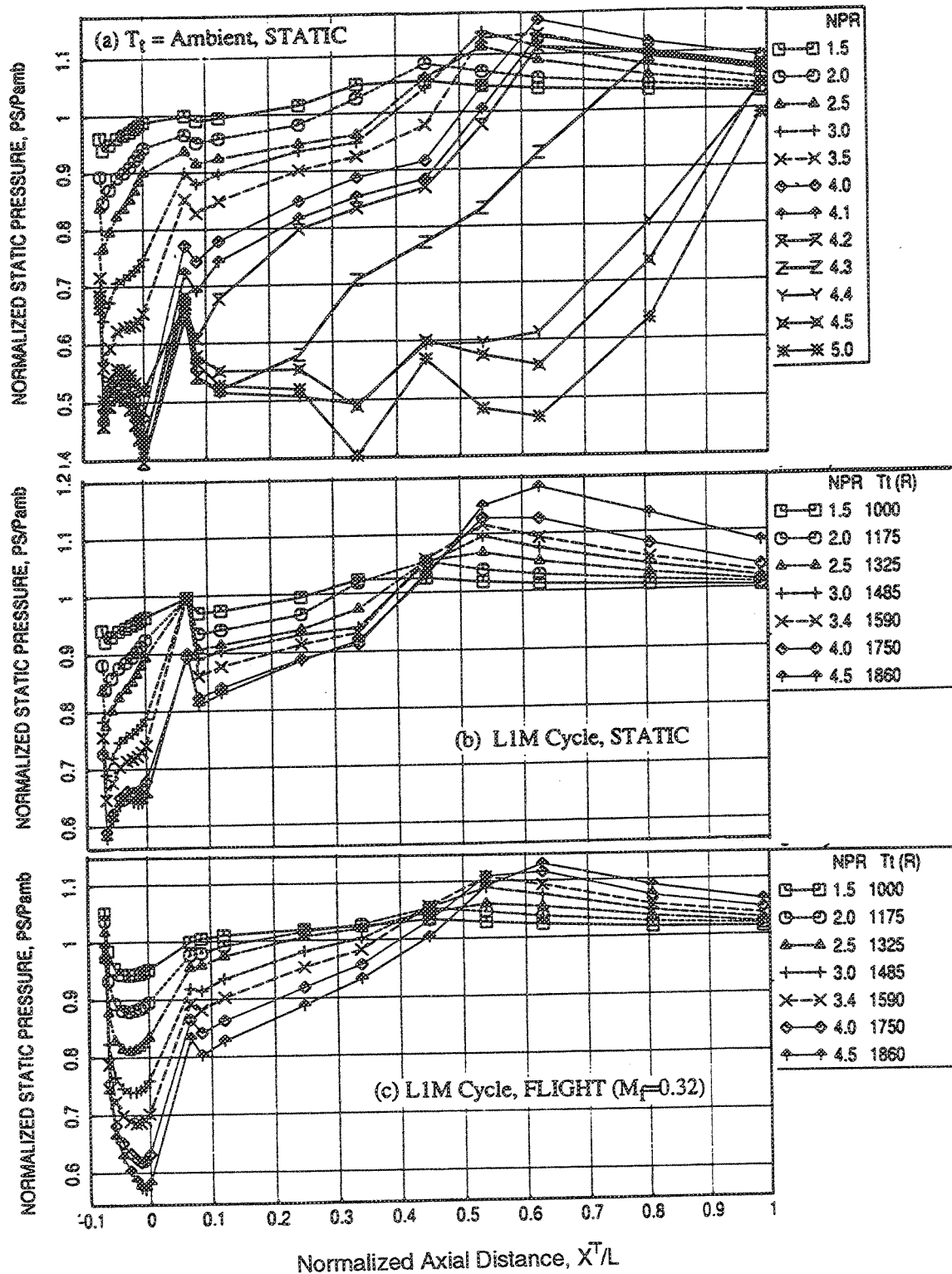


Figure 226. Axial Static Pressure Distribution on Shroud Surface for a Vortical Mixer-Ejector Configuration (SAR=4.9, MAR=0.97, Shroud Length=18.85 in.)



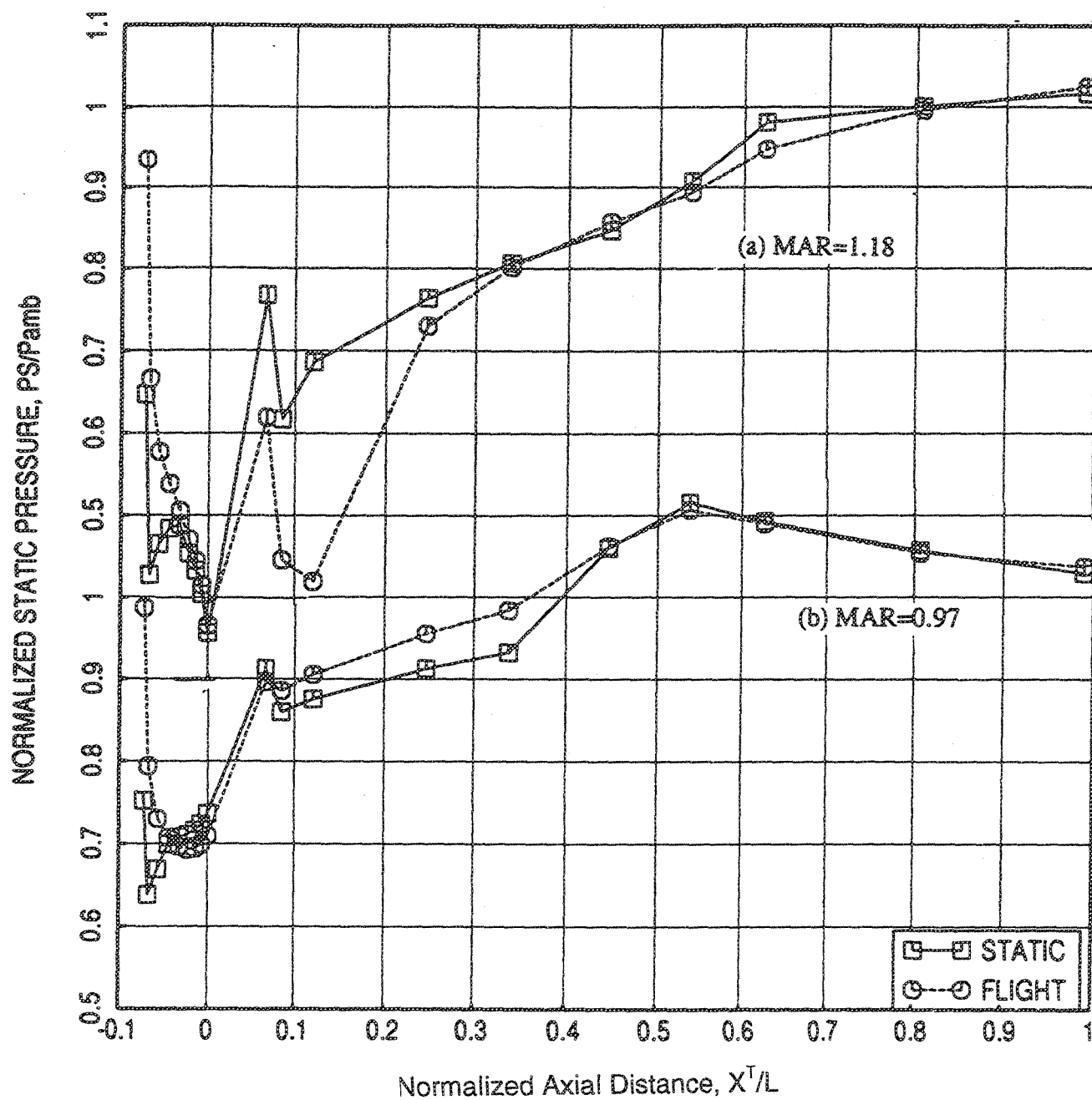


Figure 227. Effect of Flight on Axial Static Pressure Distribution on Shroud Surface for Vortical Mixer-Ejector Configurations of Different MAR (SAR=4.9, Shroud Length=18.85 in., NPR=3.4,  $T_t=1645^\circ R$ )

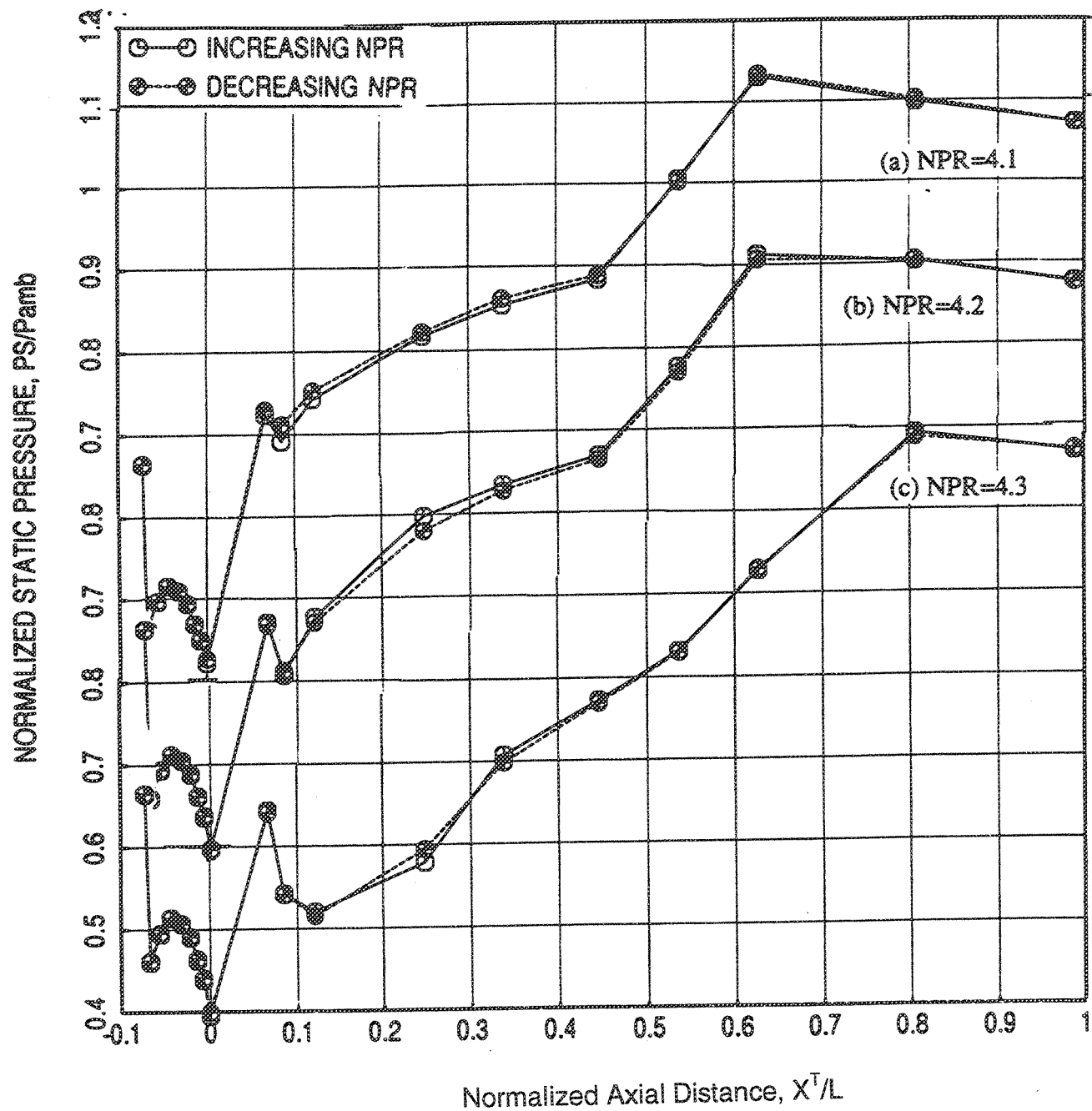


Figure 228. Effect of Increasing and Decreasing NPR on Axial Static Pressure Distribution on Shroud Surface for a Vortical Mixer-Ejector Configuration at Static Condition (SAR=4.9, MAR=0.97, Shroud Length=18.85 in.,  $T_t$ =Ambient)

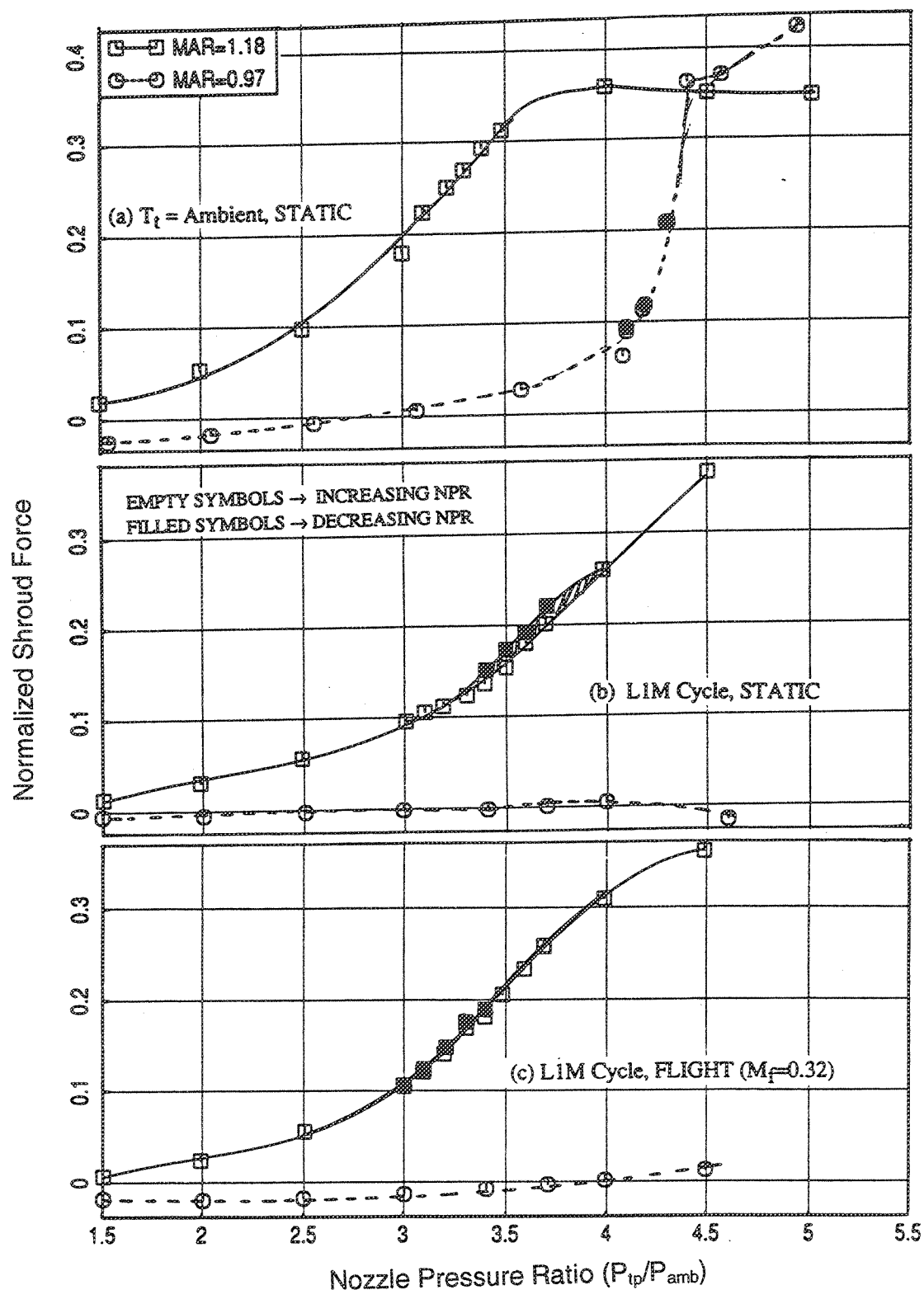


Figure 229. Variation of Normalized Shroud Force Due to MAR for Vortical Mixer-Ejector Configurations (SAR=4.9, Shroud Length=18.85 in.)

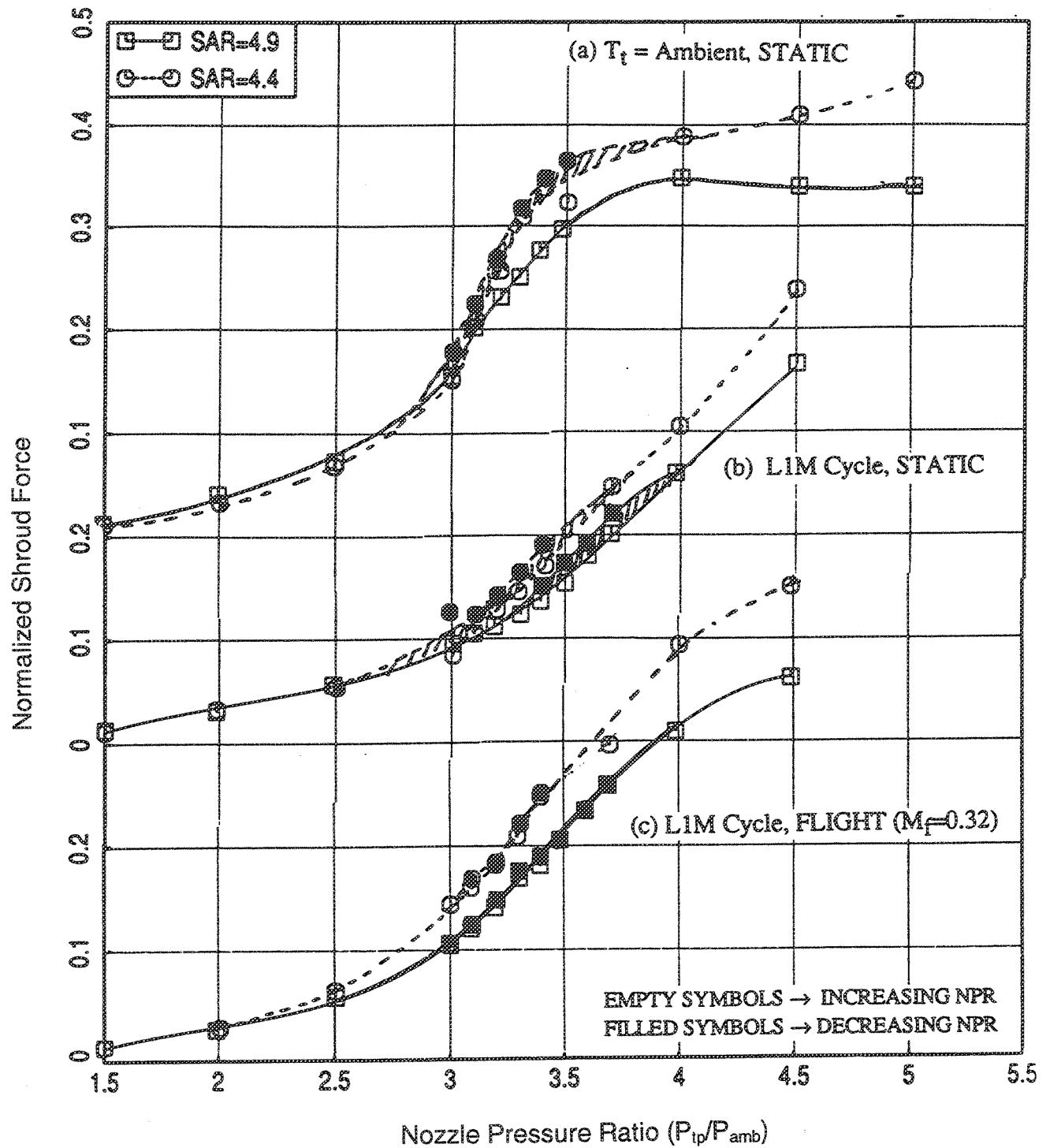


Figure 230. Variation of Normalized Shroud Force Due to SAR for Vortical Mixer-Ejector Configurations (MAR=1.18, Shroud Length=18.85 in.)

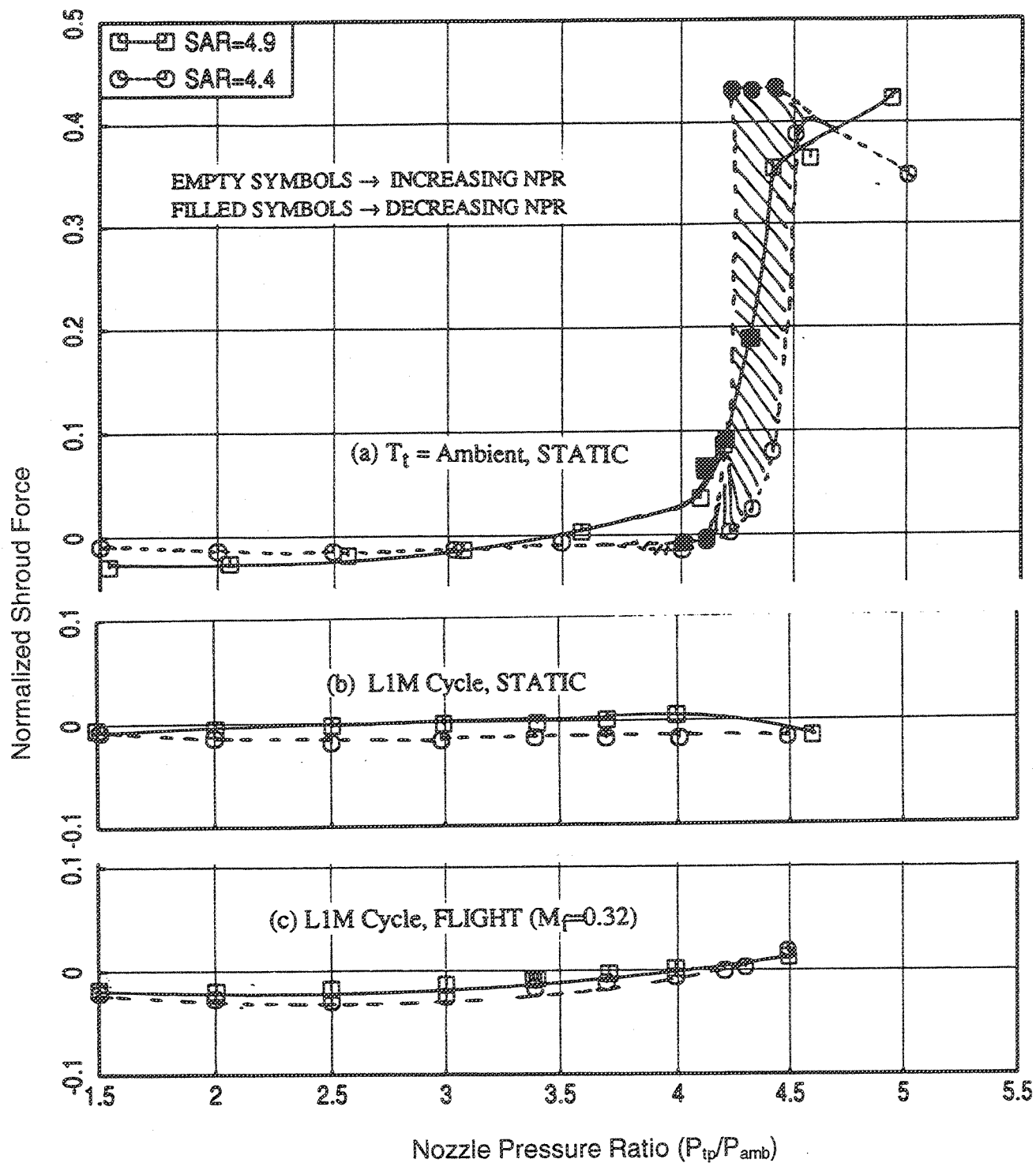


Figure 231. Variation of Normalized Shroud Force Due to SAR for Vortical Mixer-Ejector Configurations (MAR=0.97, Shroud Length=18.85 in.)

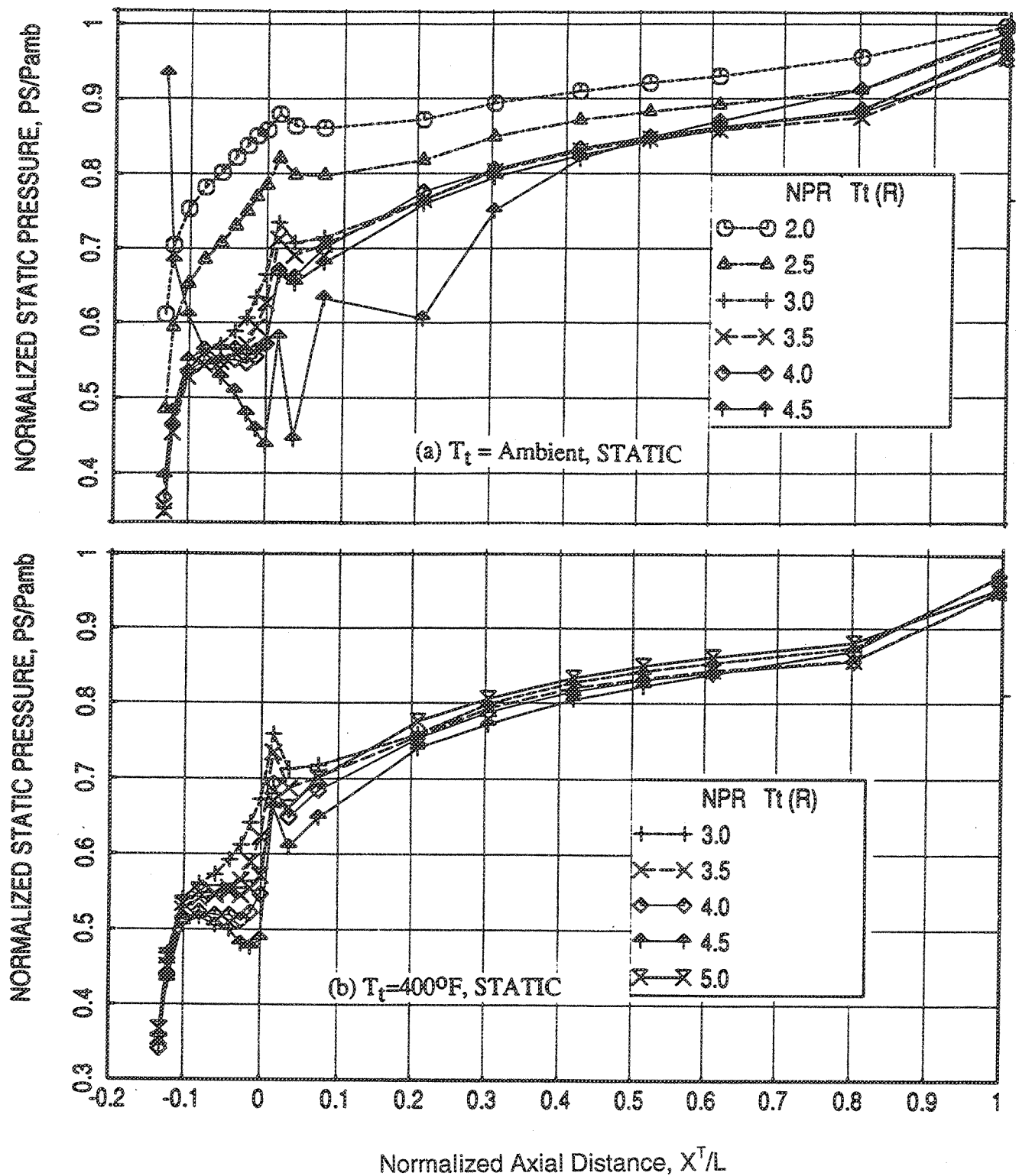


Figure 232. Axial Static Pressure Distribution on Shroud Surface for a Vortical Mixer-Ejector Configuration (SAR=4.9, MAR=1.18, Shroud Length=10.46 in.)

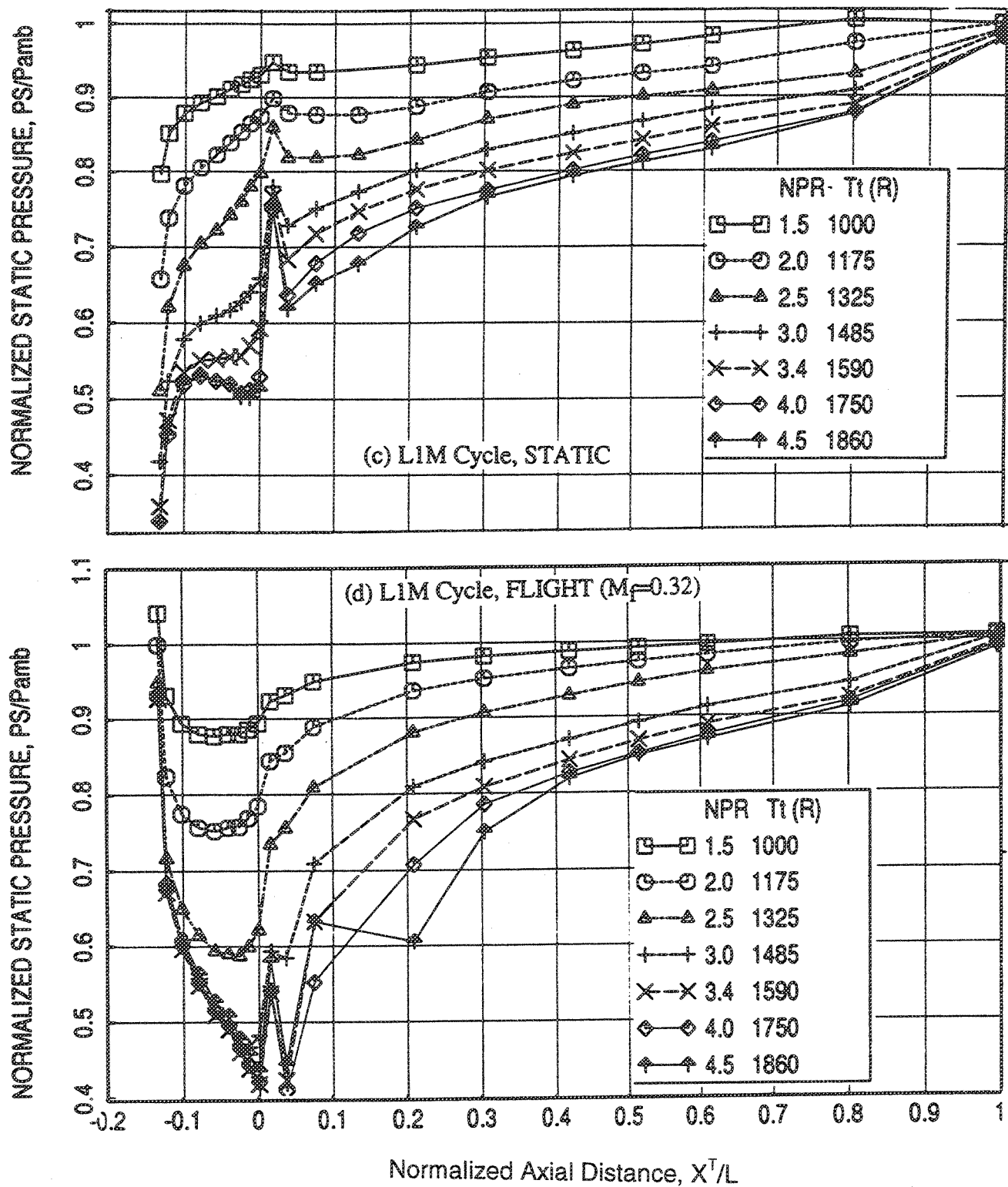


Figure 233. Axial Static Pressure Distribution on Shroud Surface for a Vortical Mixer-Ejector Configuration (SAR=4.9, MAR=1.18, Shroud Length=10.46 in.)

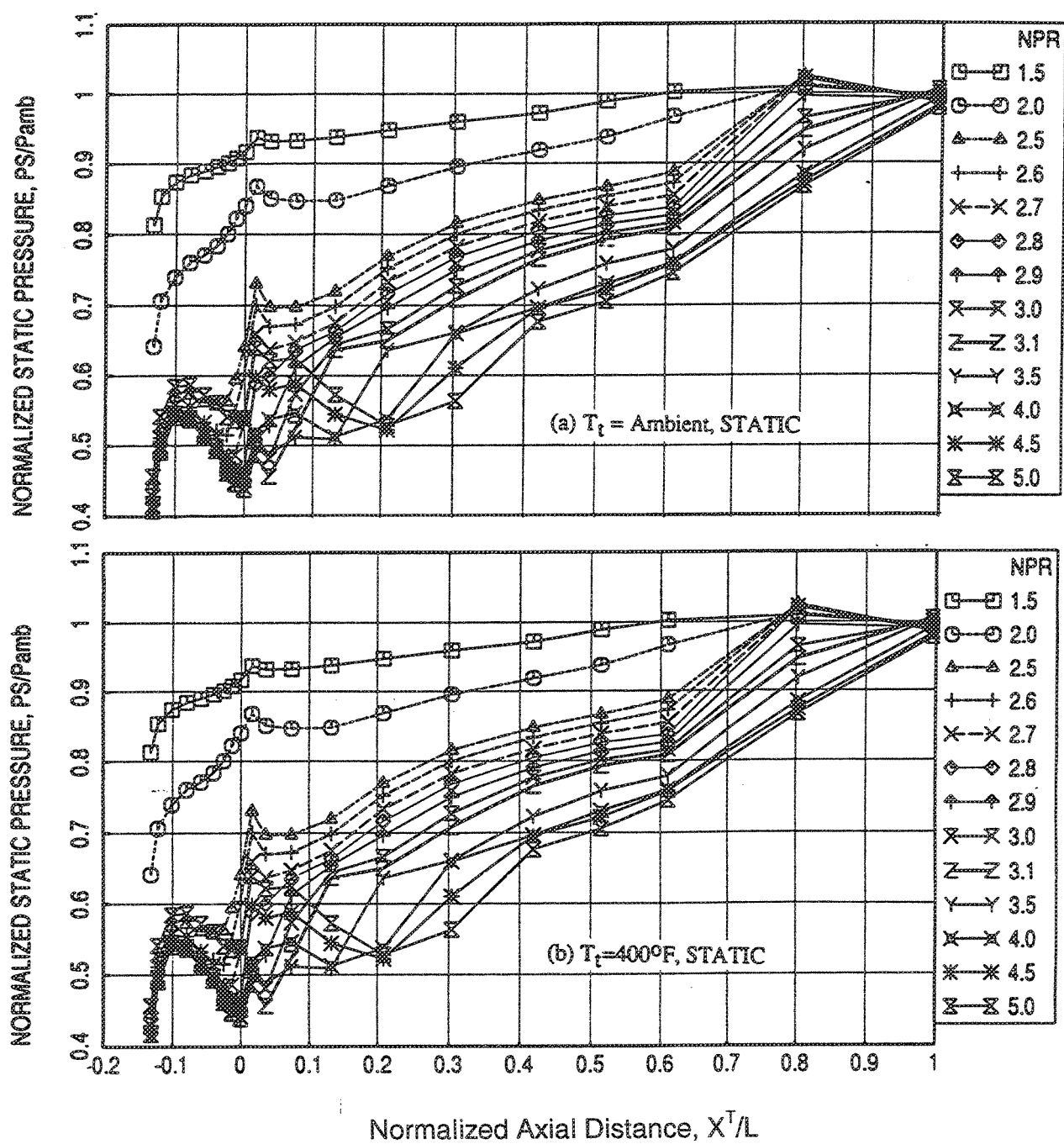


Figure 234. Axial Static Pressure Distribution on Shroud Surface for Vortical Mixer-Ejector Configuration (SAR=4.4, MAR=1.18, Shroud Length=10.46 in.)



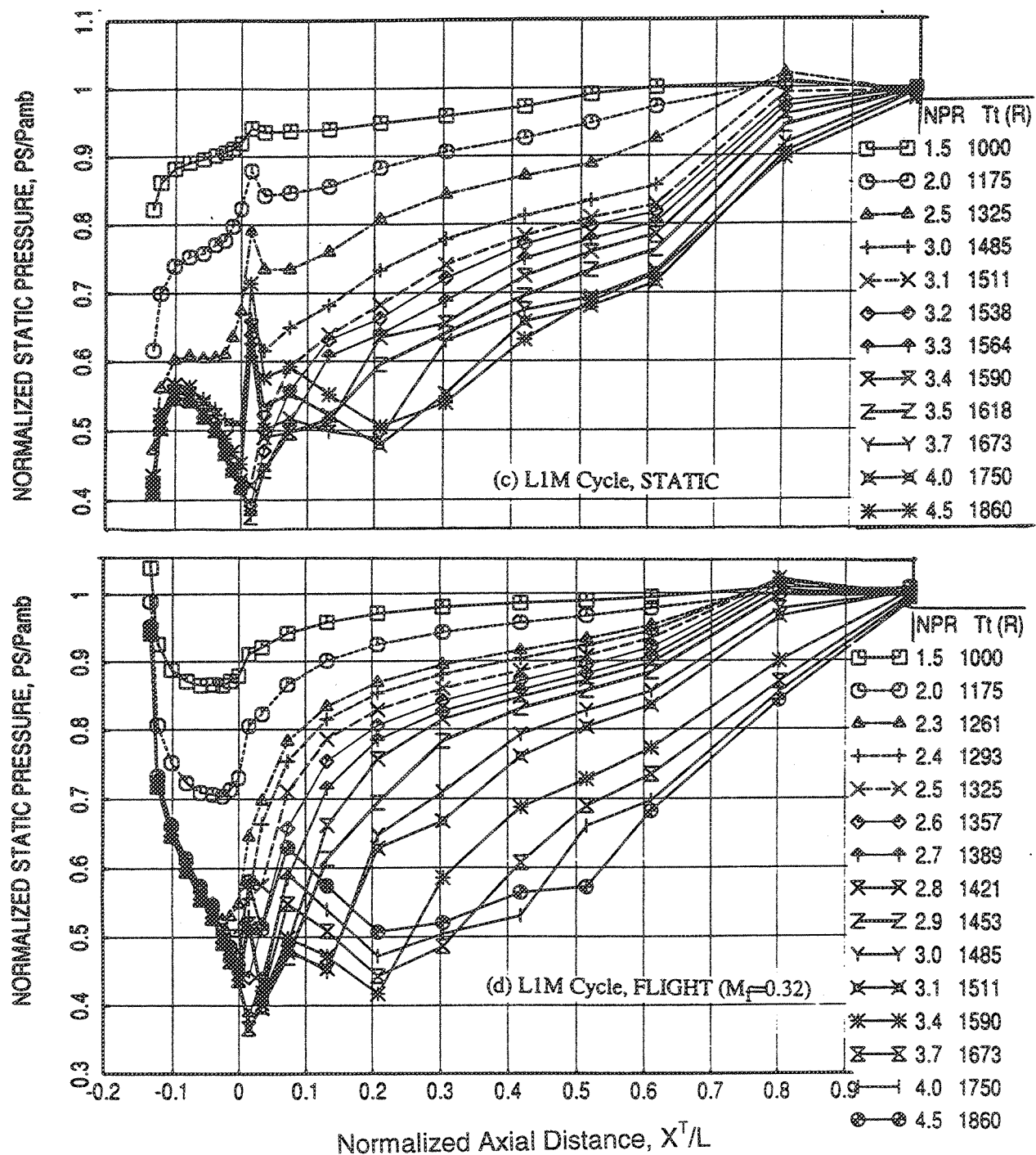


Figure 235. Axial Static Pressure Distribution on Shroud Surface for Vortical Mixer-Ejector Configuration (SAR=4.4, MAR=1.18, Shroud Length=10.46 in.)

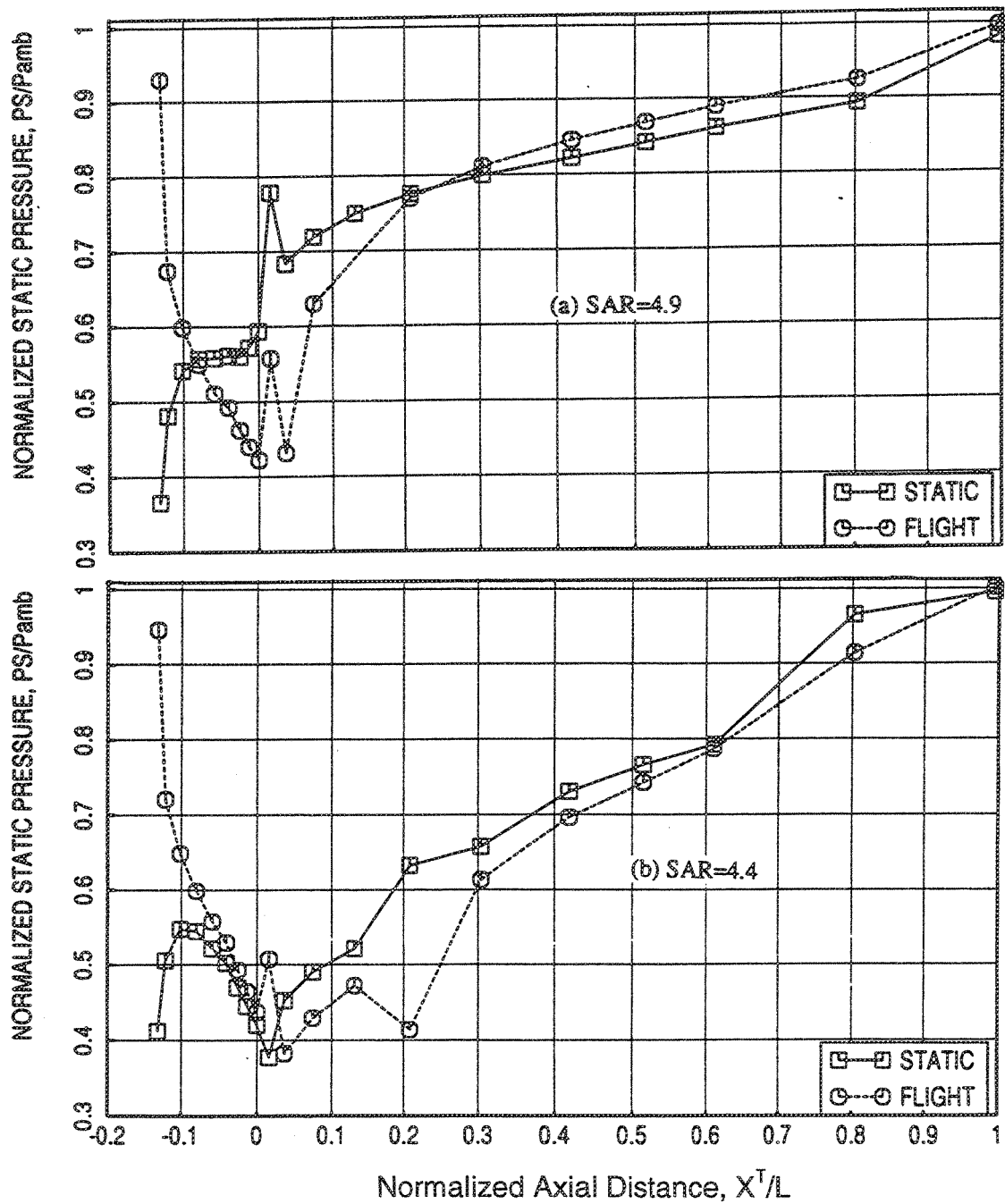


Figure 236. Effect of Flight on Axial Static Pressure Distribution on Shroud Surface for Vortical Mixer-Ejector Configurations of Different SAR (MAR=1.18, Shroud Length=10.46 in., NPR=3.4,  $T_t=1645^\circ\text{R}$ )

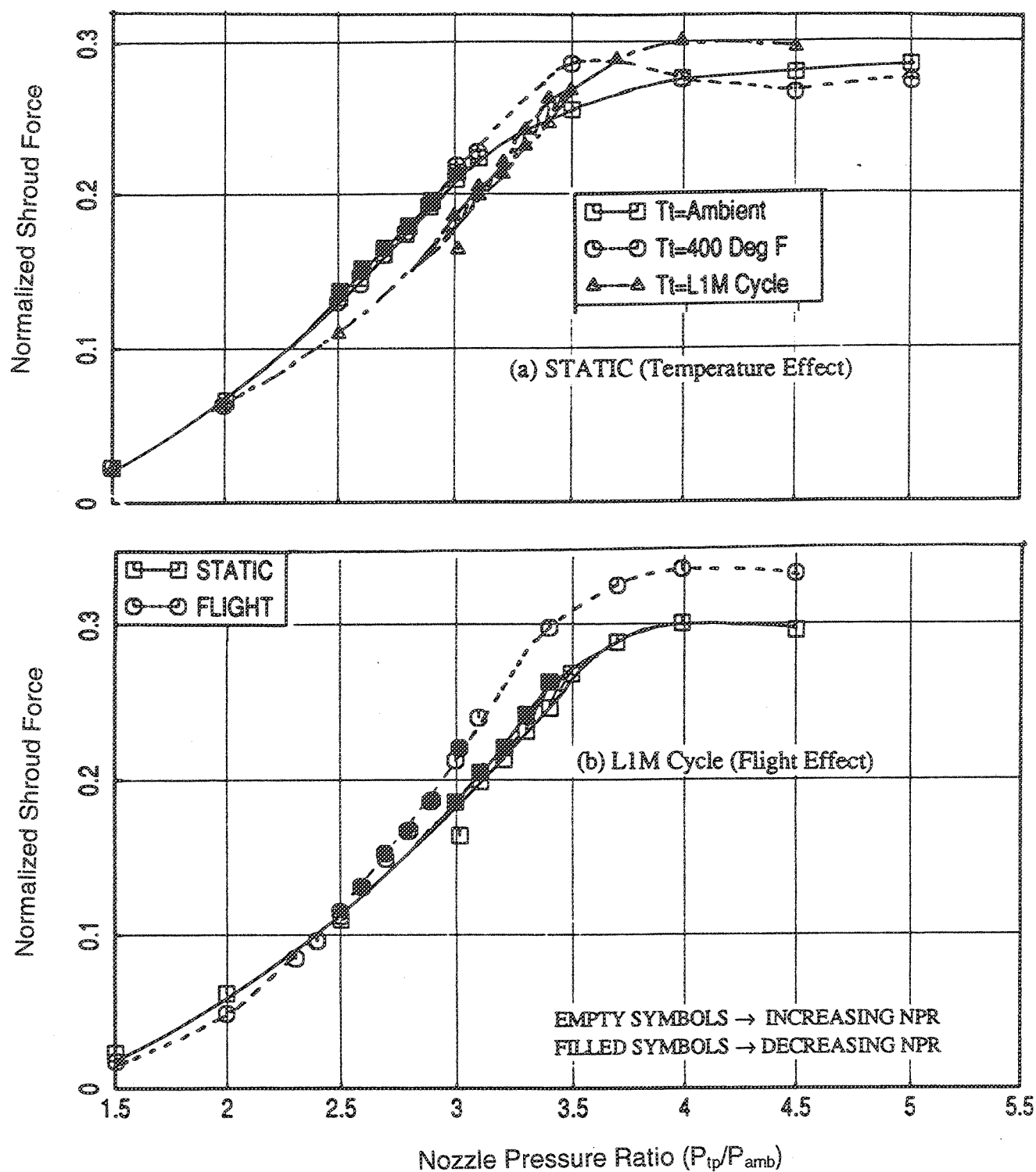


Figure 237. Variation of Normalized Shroud Force Due to: (a) Nozzle Total Temperature; (b) Flight Simulation ( $M_n=0.32$ ) for Vortical Mixer-Ejector Configuration ( $SAR=4.4$ ,  $MAR=1.18$ , Shroud Length=10.46 in.)

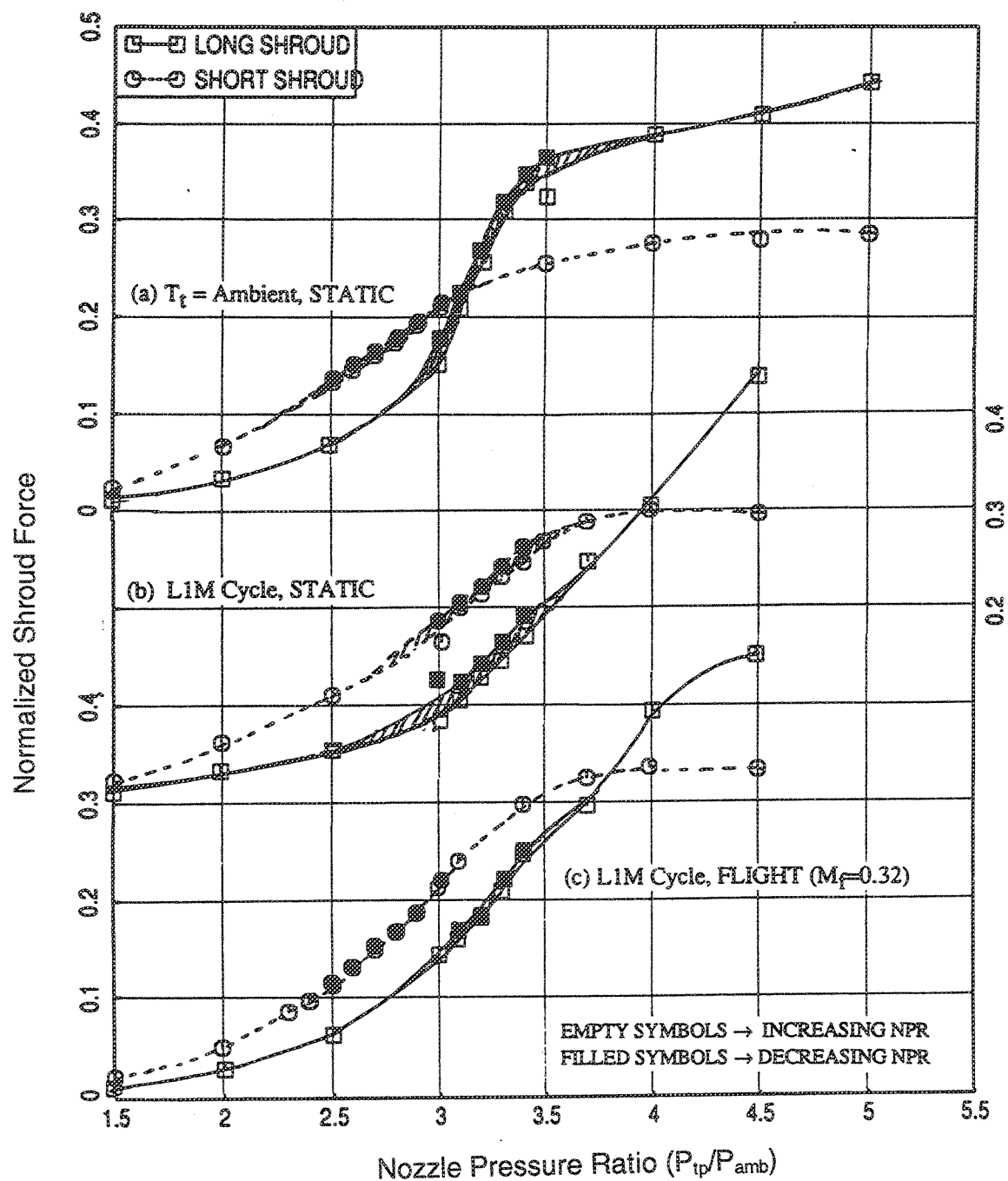


Figure 238. Variation of Normalized Shroud Force Due to Shroud Length for Vortical Mixer-Ejector Configurations ( $SAR=4.4$ ,  $MAR=1.18$ )

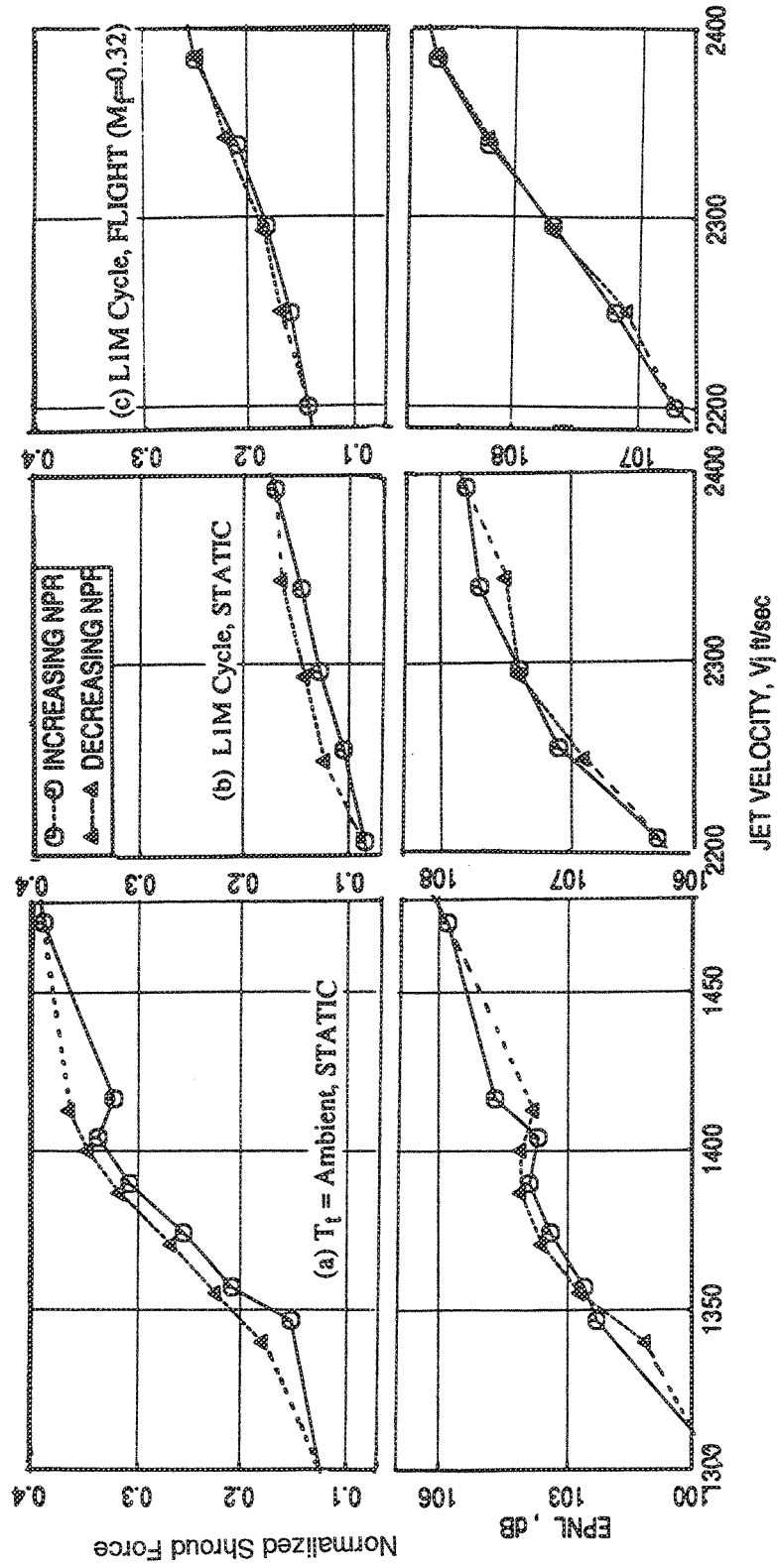


Figure 239. Normalized Shroud Force and Corresponding EPNL as Functions of Jet Velocity for Vortical Mixer-Ejector Configuration (SAR=4.4, MAR=1.18, Shroud Length=18.85 in.)

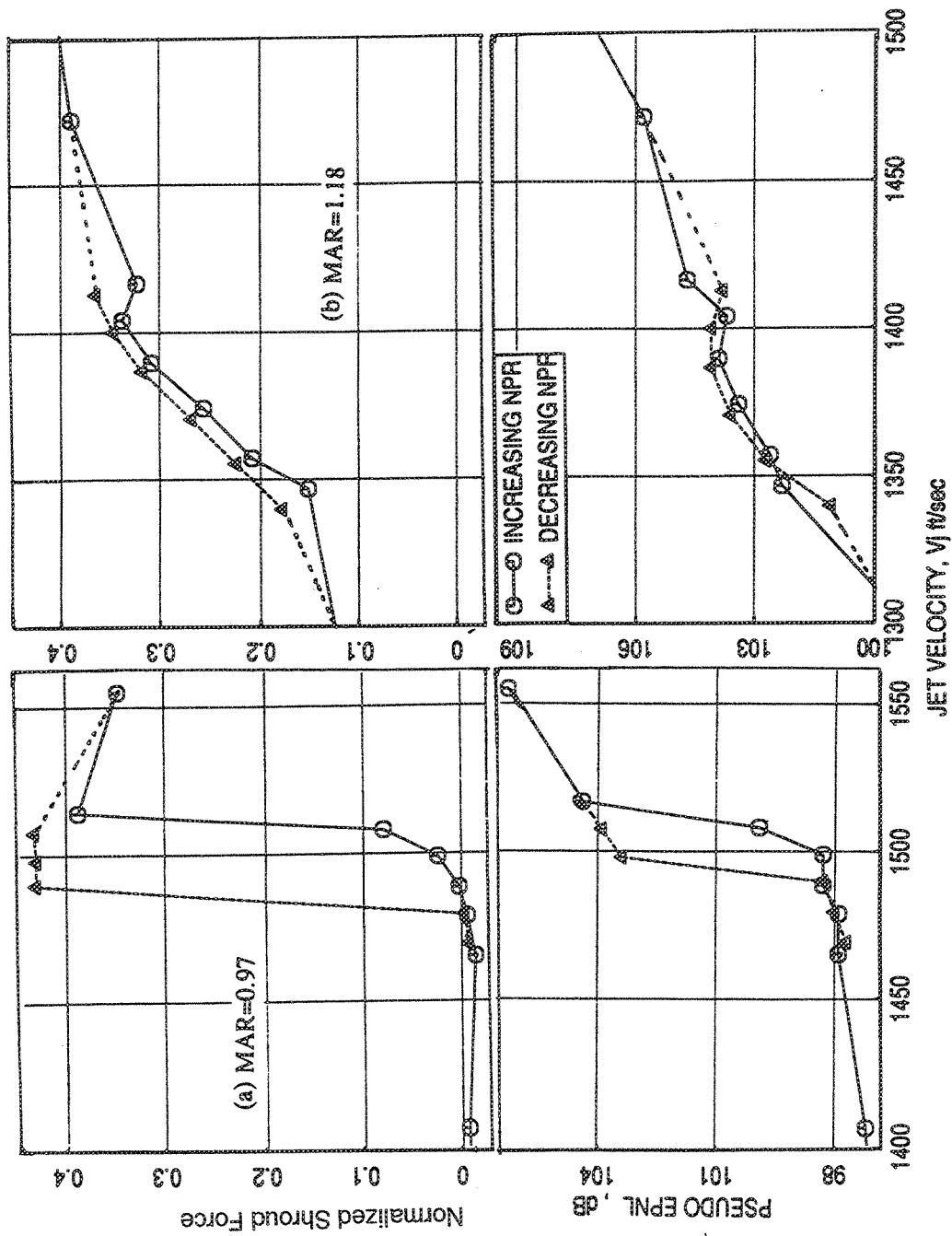


Figure 240. Normalized Shroud Force and Corresponding EPNL as Functions of Jet Velocity for Vortical Mixer-Ejector Configurations With Different MAR Settings at Ambient Temperature Condition (SAR=4.4, Shroud Length=18.85 in.)

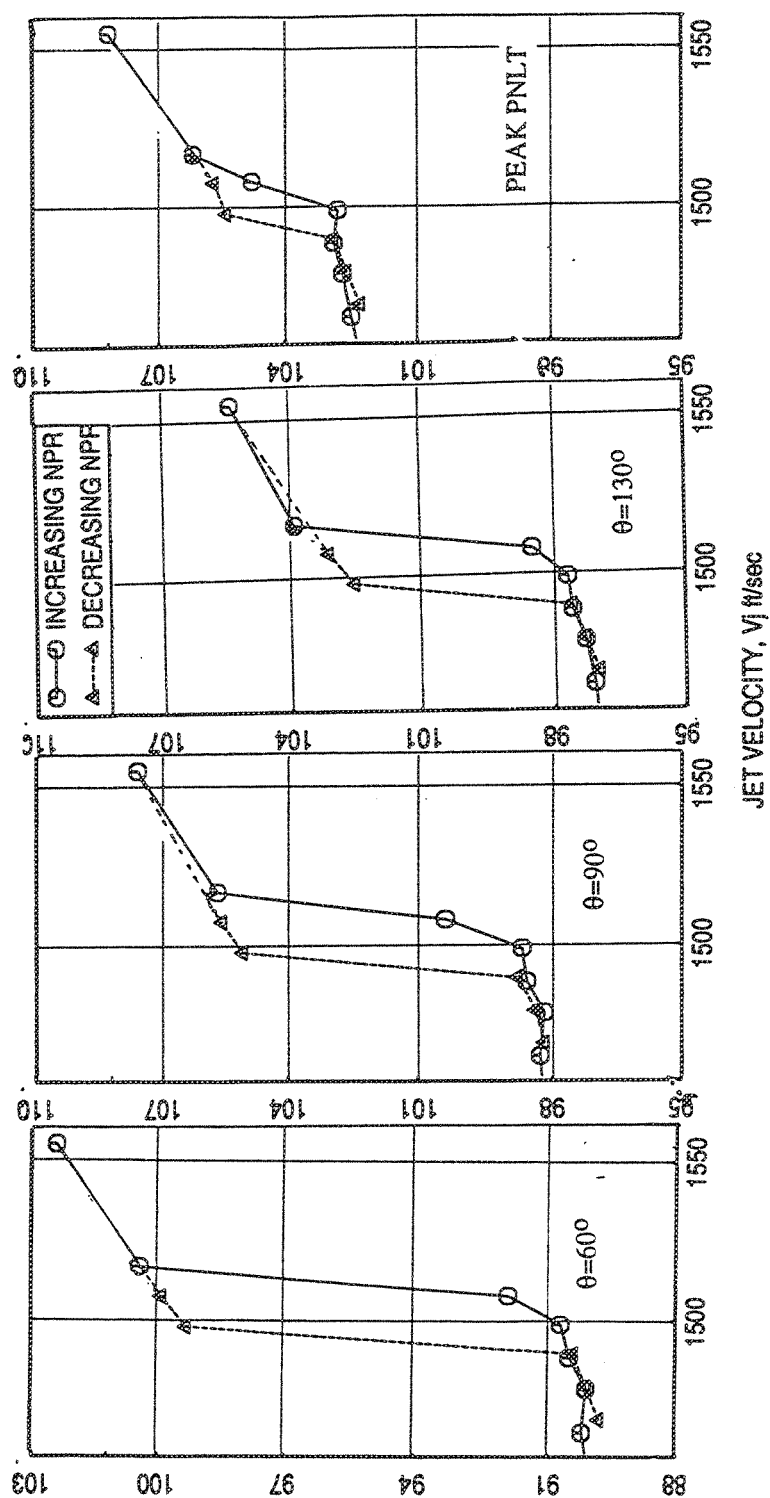


Figure 241. PNLT at Various Polar Angles and Peak PNLT as Functions of Jet Velocity for Vortical Mixer-Ejector Configuration at Ambient Temperature Condition (SAR=4.4, MAR=0.97, Shroud Length=18.85 in.)

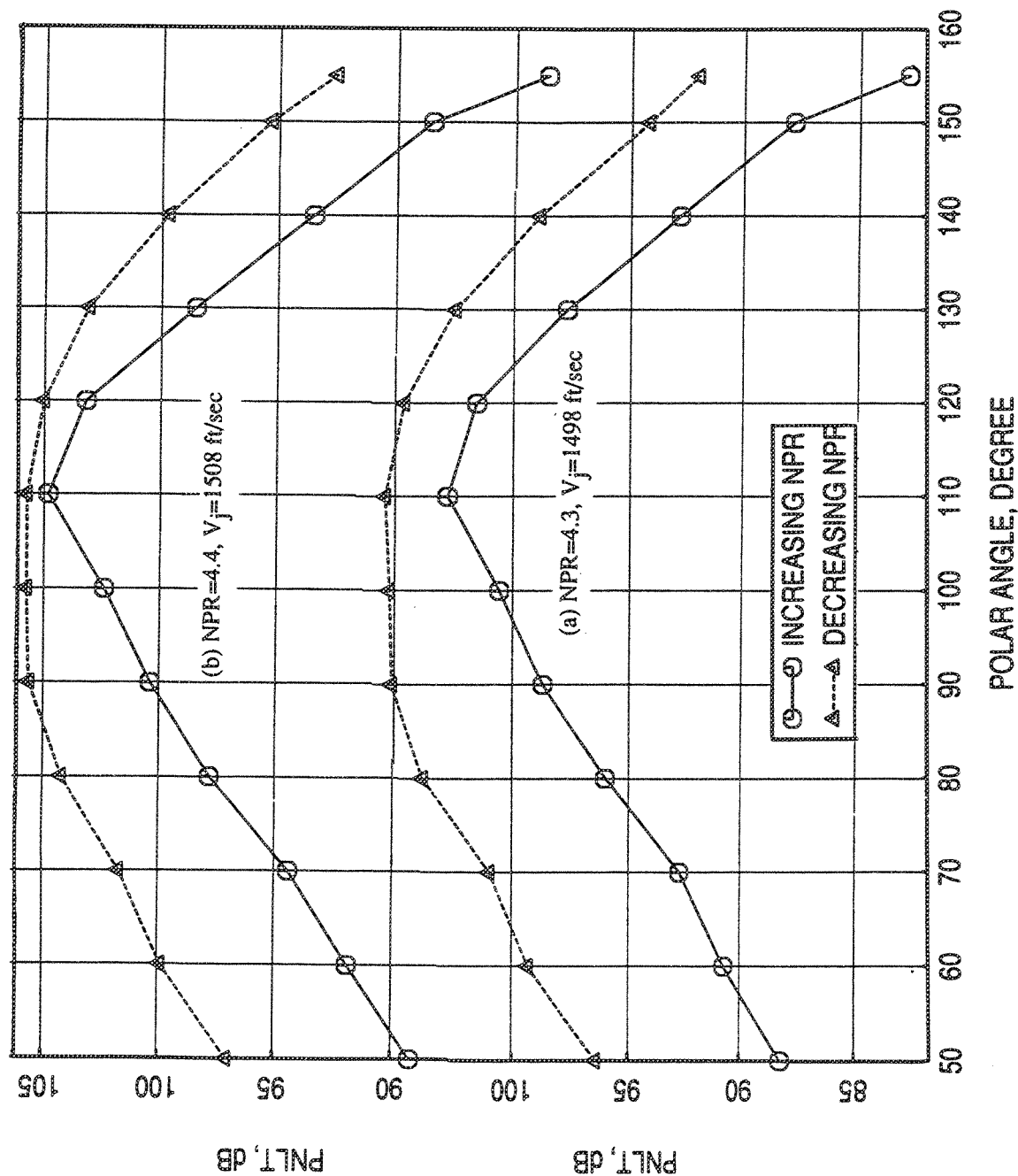


Figure 242. PNL Directivities at Two NPRs at Ambient Temperature Condition for Vortical Mixer-Ejector Configuration  
(SAR=4.4, MAR=0.97, Shroud Length=18.85 in.)



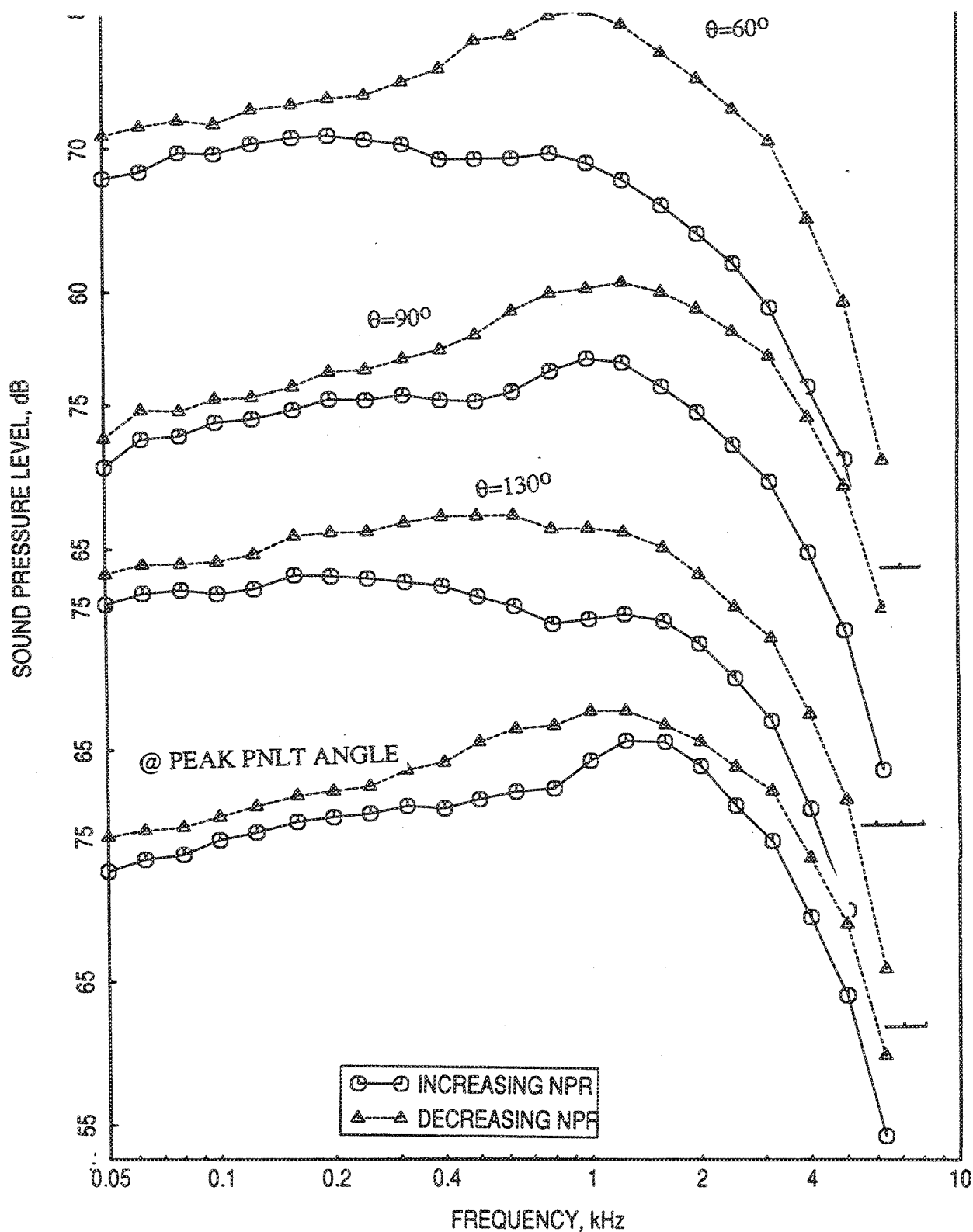


Figure 243. SPL Spectra at a Number of Polar Angles for NPR=4.3 and at Ambient Temperature Condition ( $V_j=1498$  ft/sec) for Vortical Mixer-Ejector Configuration (SAR=4.4, MAR=0.97, Shroud Length=18.85 in.)

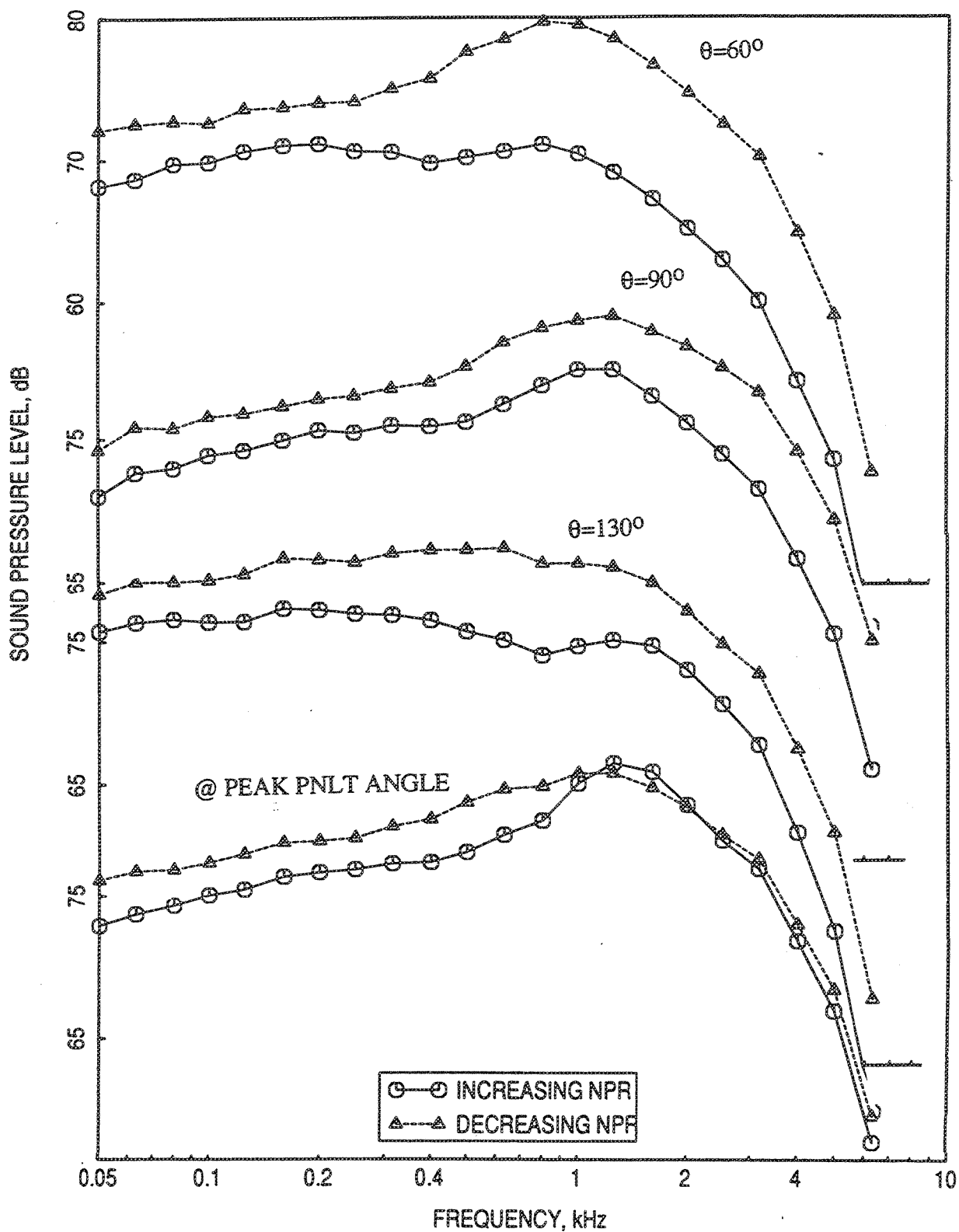


Figure 244. SPL Spectra At a Number of Polar Angles for  $NPR=4.4$  and At Ambient Temperature condition ( $V_j=1508$  ft/sec) For Vortical Mixer-Ejector Configuration ( $SAR=4.4$ ,  $MAR=0.97$ , Shroud Length=18.85 in.)

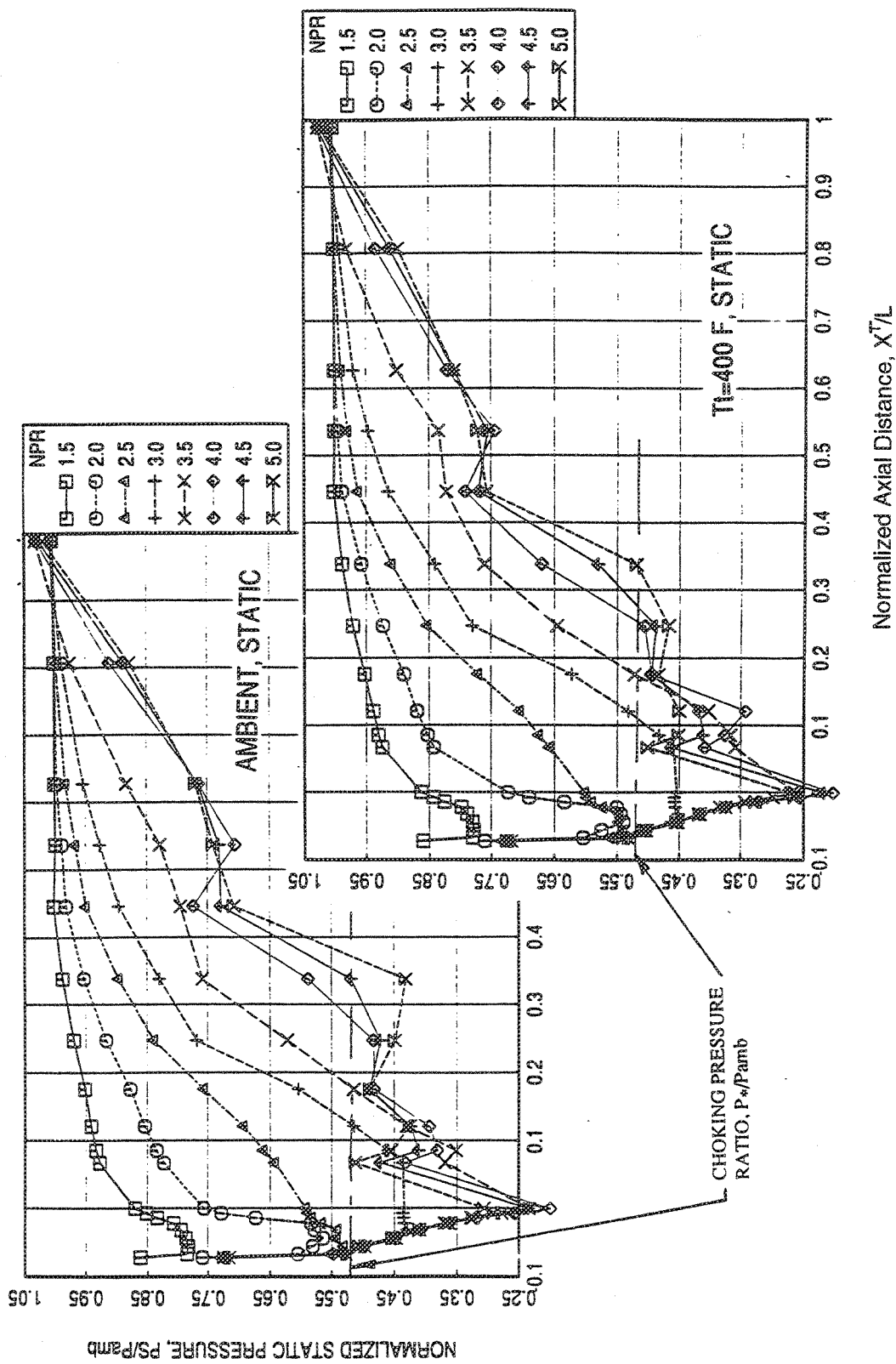


Figure 245. Axial Static Pressure Distribution on Shroud Surface For Axial Mixer-Ejector Configuration  
(SAR=4.9, MAR=1.18, Shroud Length=18.85 in.)

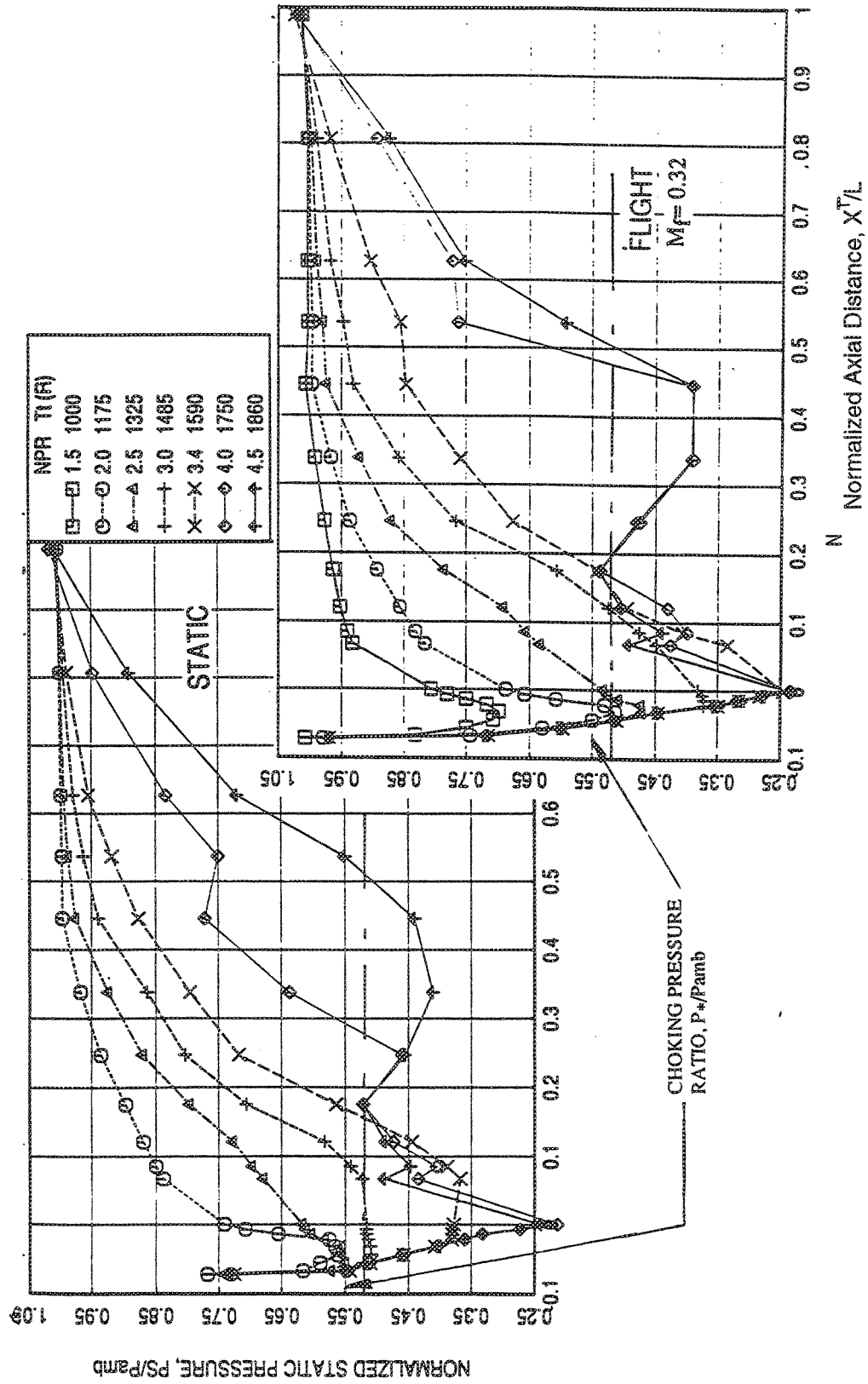


Figure 246. Axial Static Pressure Distribution on Shroud Surface For Axial Mixer-Ejector Configuration For LIM Cycle Condition  
(SAR=4.9, MAR=1.18, Shroud Length=18.85 in.)

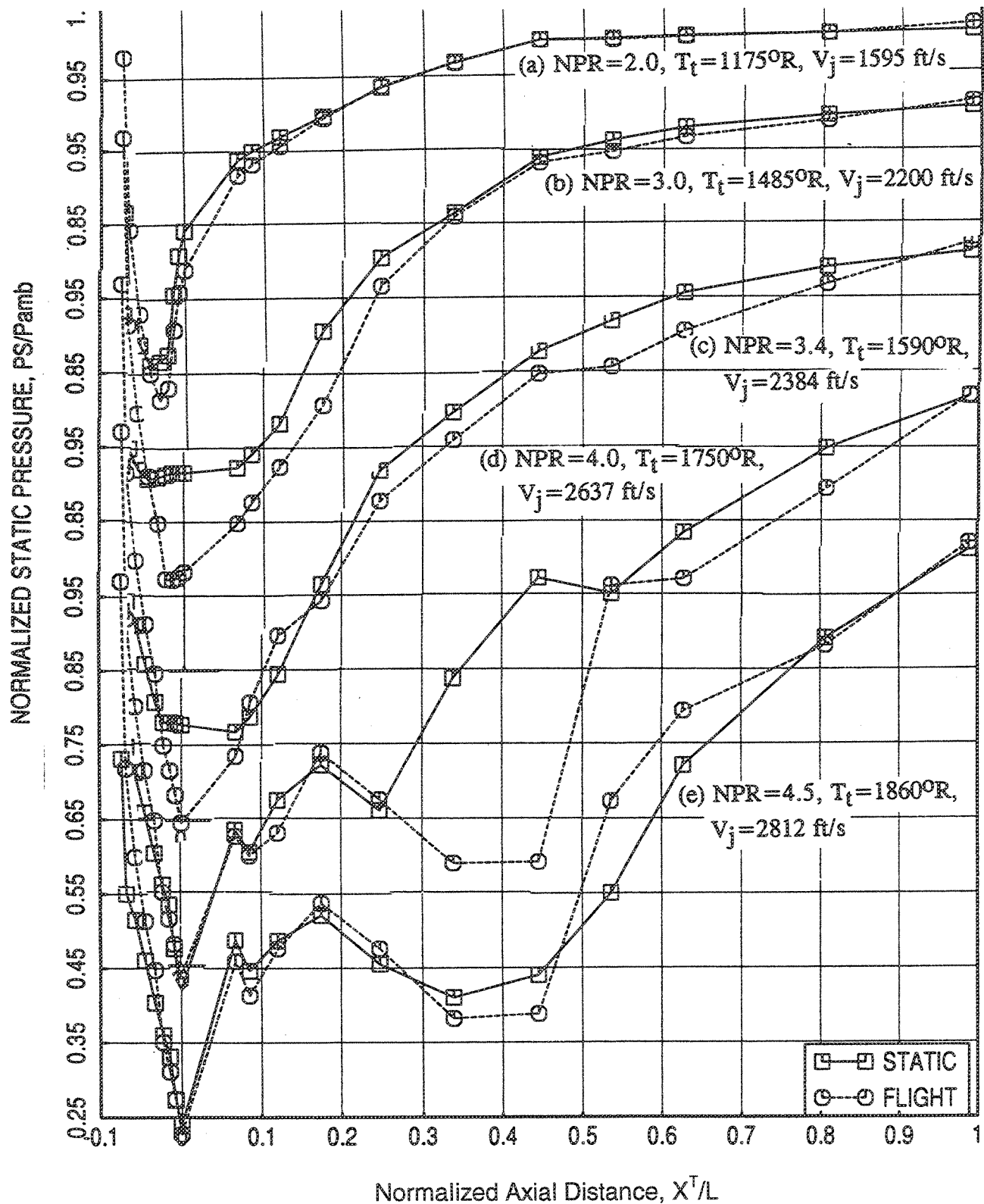


Figure 247. Effect of Flight on Axial Static Pressure Distribution on Shroud Surface for Axial Mixer-Ejector Configuration (MAR=1.18, SAR=4.9, Shroud Length=18.85 in.)

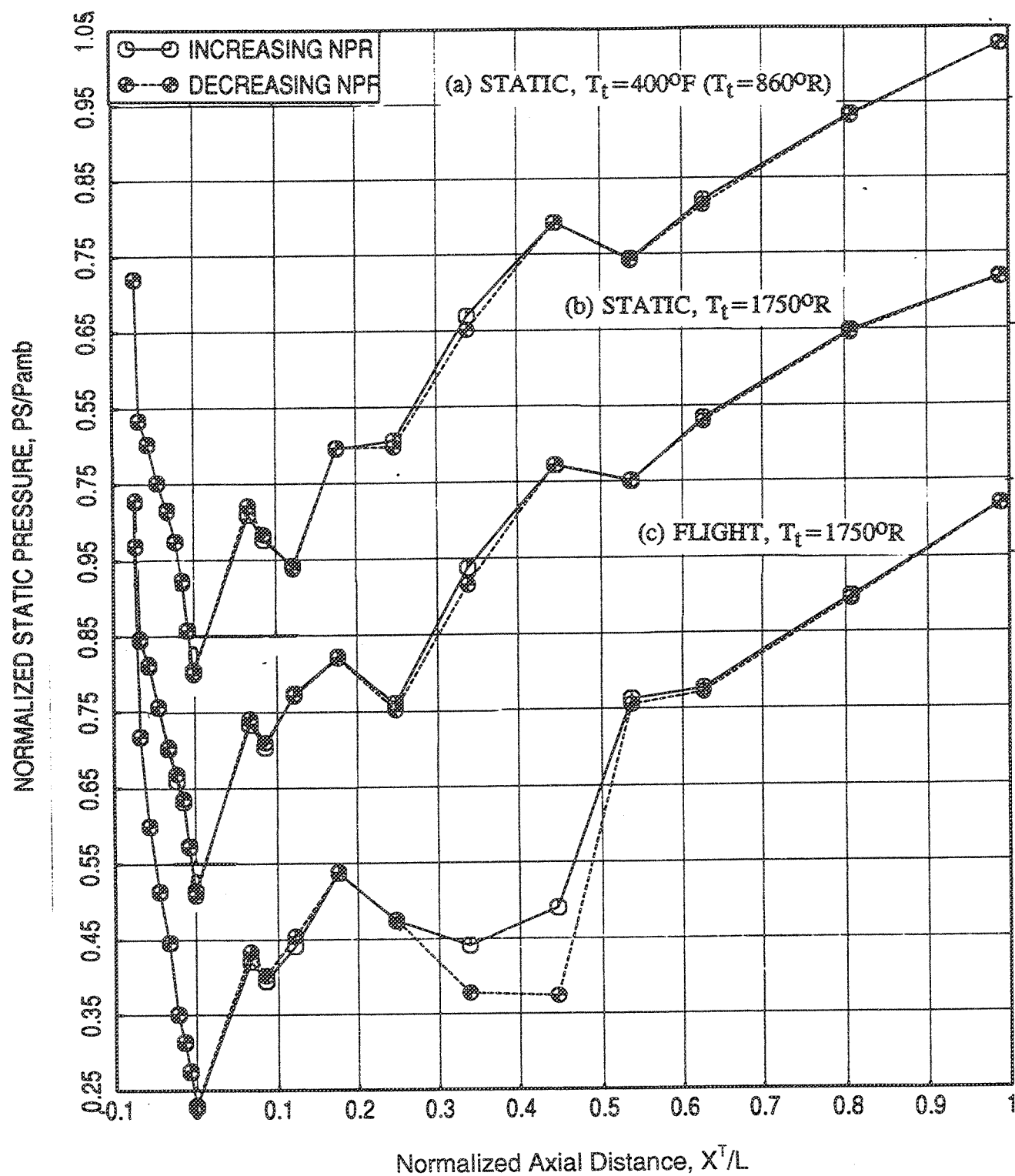


Figure 248. Effect of Increasing and Decreasing NPR on Axial Static Pressure Distribution on Shroud Surface For Axial Mixer-Ejector Configuration (NPR=4.0, SAR=4.9, MAR=1.18, Shroud Length=18.85 in.)

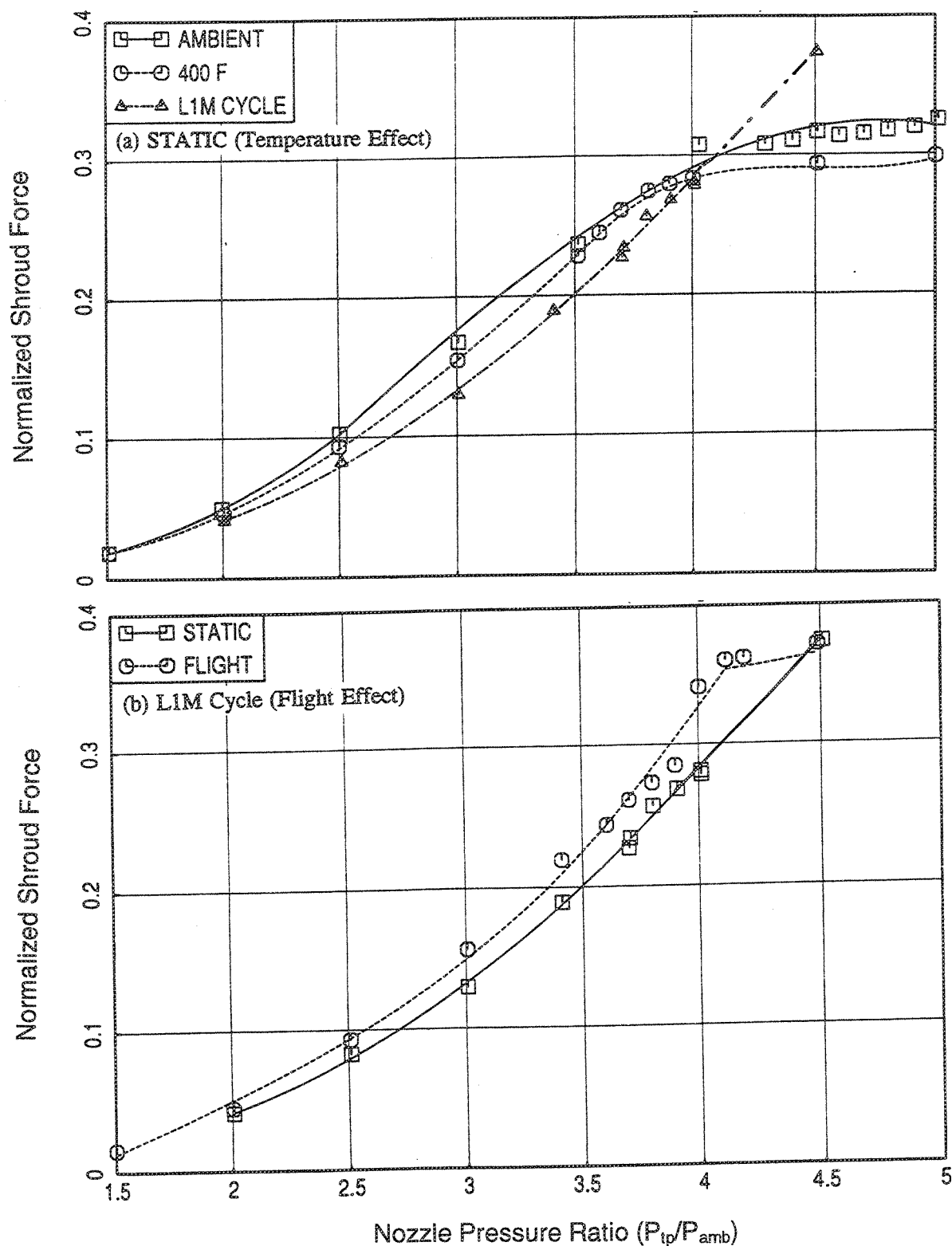


Figure 249. Variation of Normalized Shroud Force Due to: (a) Nozzle Total Temperature; (b) Flight Simulation ( $M_n=0.32$ ) For Axial Mixer-Ejector Configuration ( $SAR=4.9$ ,  $MAR=1.18$ , Shroud Length=18.85 in.)

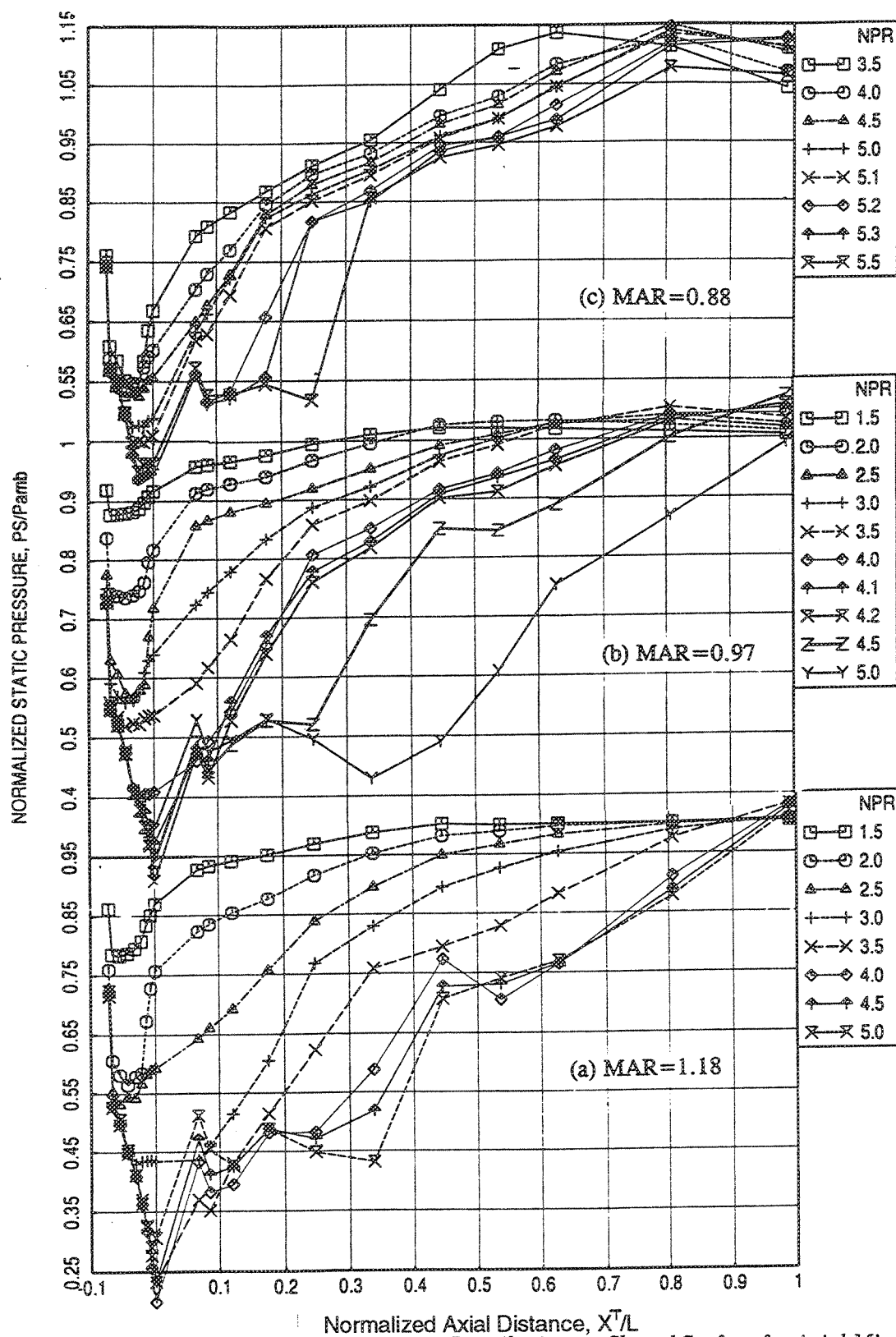


Figure 250. Effect of MAR on Axial Static Pressure Distribution on Shroud Surface for Axial Mixer-Ejector Configurations at Static Condition (SAR=4.9, Shroud Length=18.85 in.,  $T_t$ =Ambient)



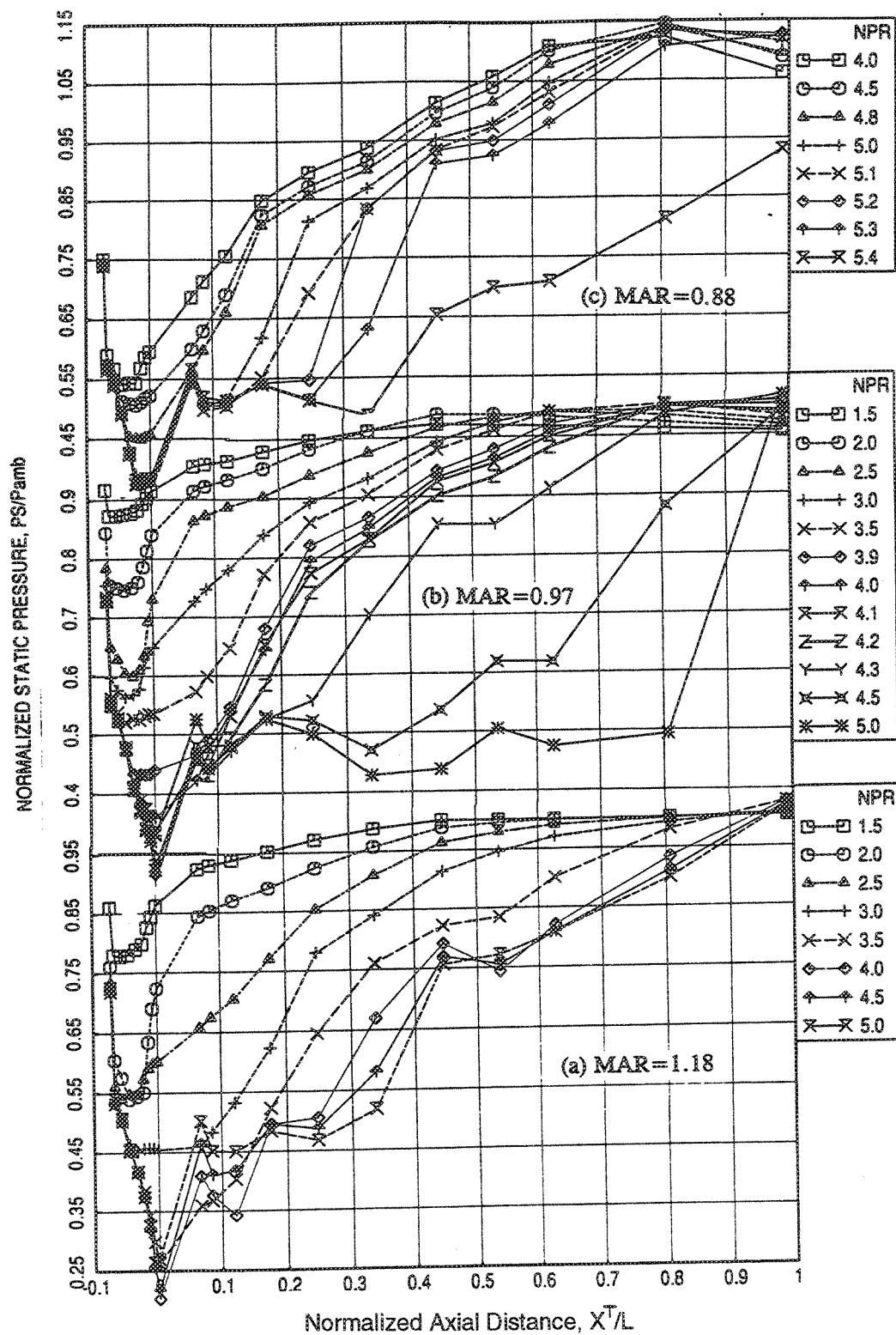


Figure 251. Effect of MAR on Axial Static Pressure Distribution on Shroud Surface for Axial Mixer-Ejector Configurations at Static Condition (SAR=4.9, Shroud Length=18.85 in.,  $T_t=400^\circ\text{F}$ )

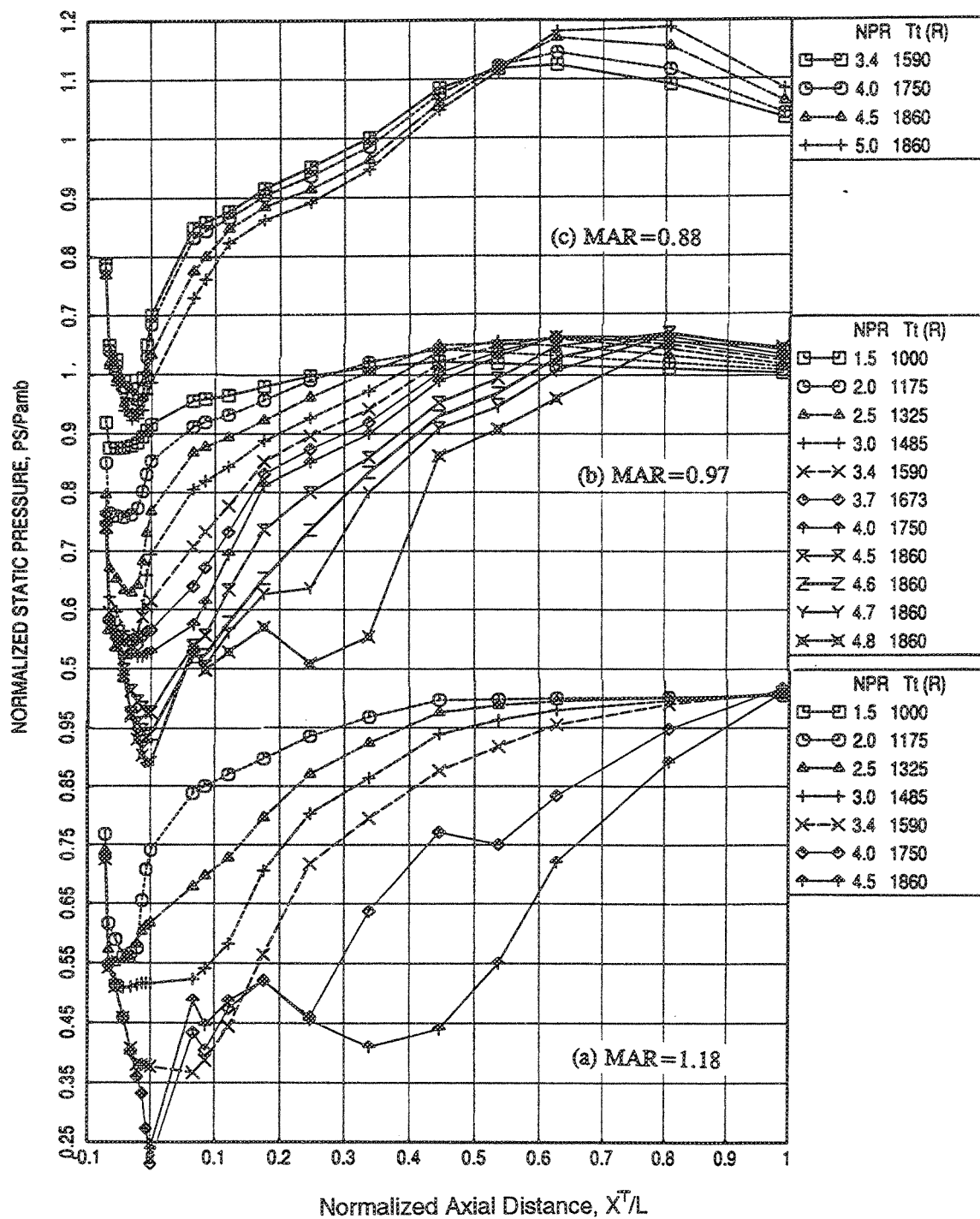


Figure 252. Effect of MAR on Axial Static Pressure Distribution on Shroud Surface for Axial Mixer-Ejector Configurations at Static Condition (SAR=4.9, Shroud Length=18.85 in., LIM Cycle)

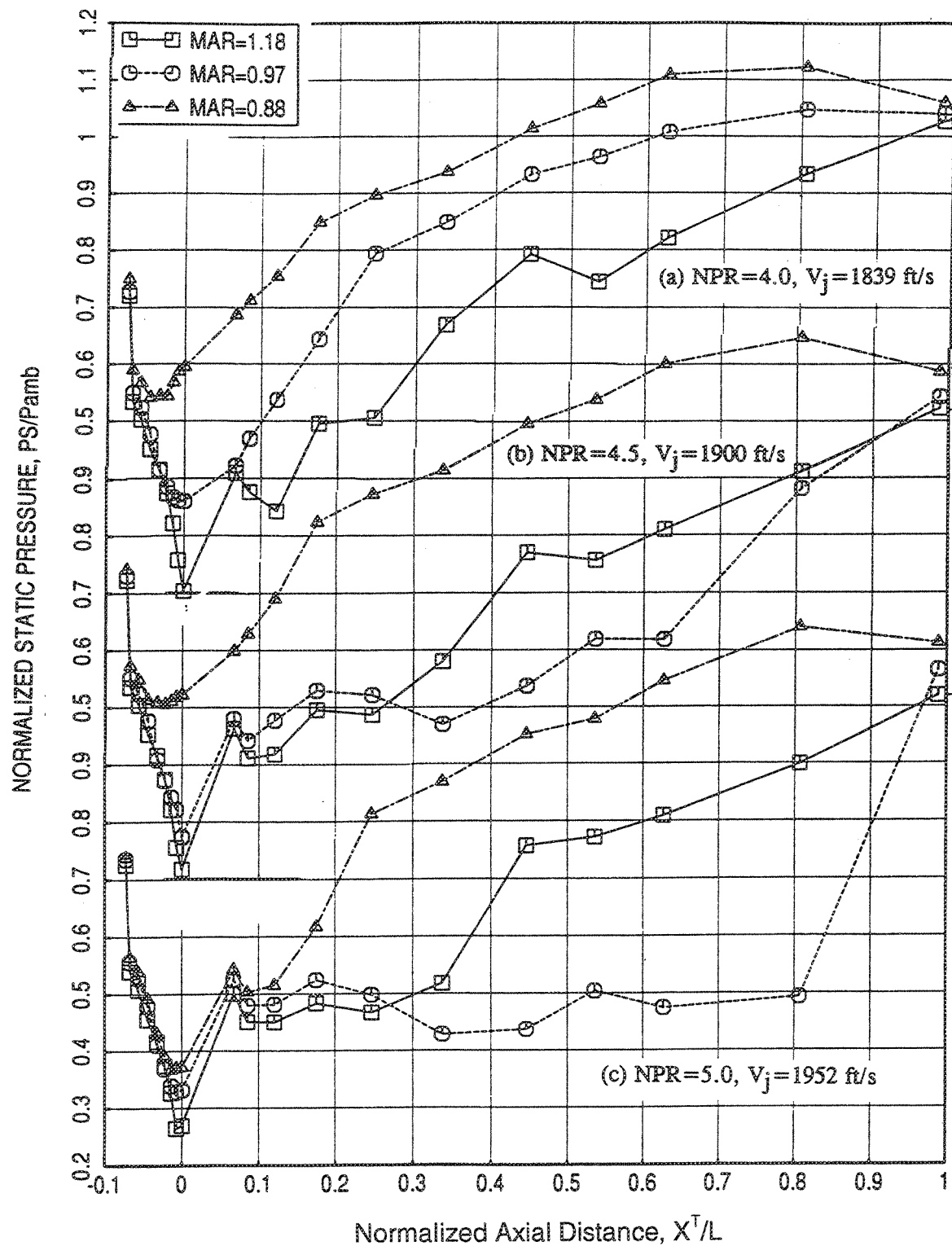


Figure 253. Effect of MAR on Axial Static Pressure Distribution on Shroud Surface For Axial Mixer-Ejector Configurations with Flight Simulation ( $Mn=0.32$ ) ( $SAR=4.9$ , Shroud Length=18.85 in., LIM Cycle)

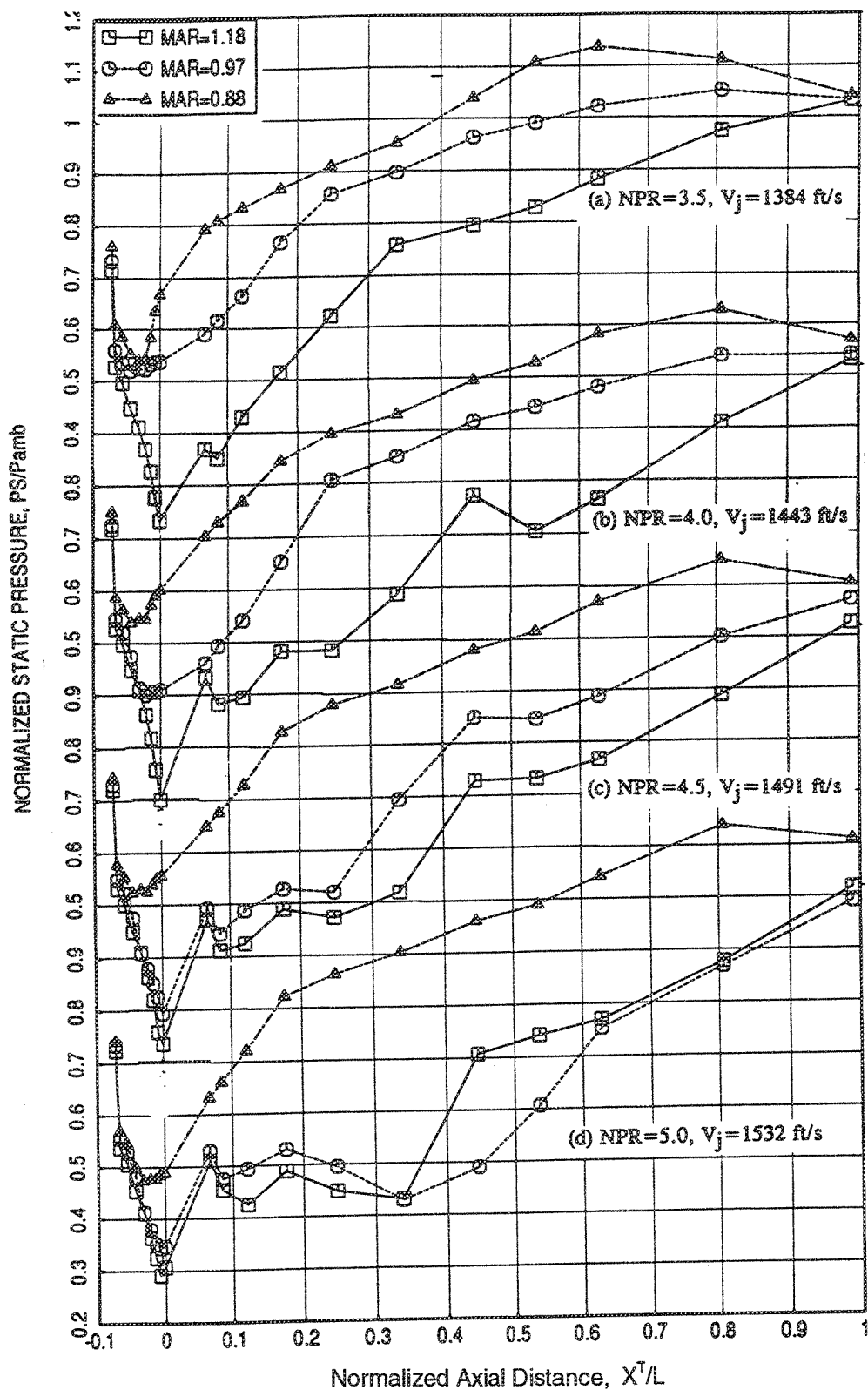


Figure 254. Effect of MAR on Axial Static Pressure Distribution on Shroud Surface for Axial Mixer-Ejector Configurations at Static Condition ( $SAR=4.9$ , Shroud Length=18.85 in.,  $T_t$ =Ambient)

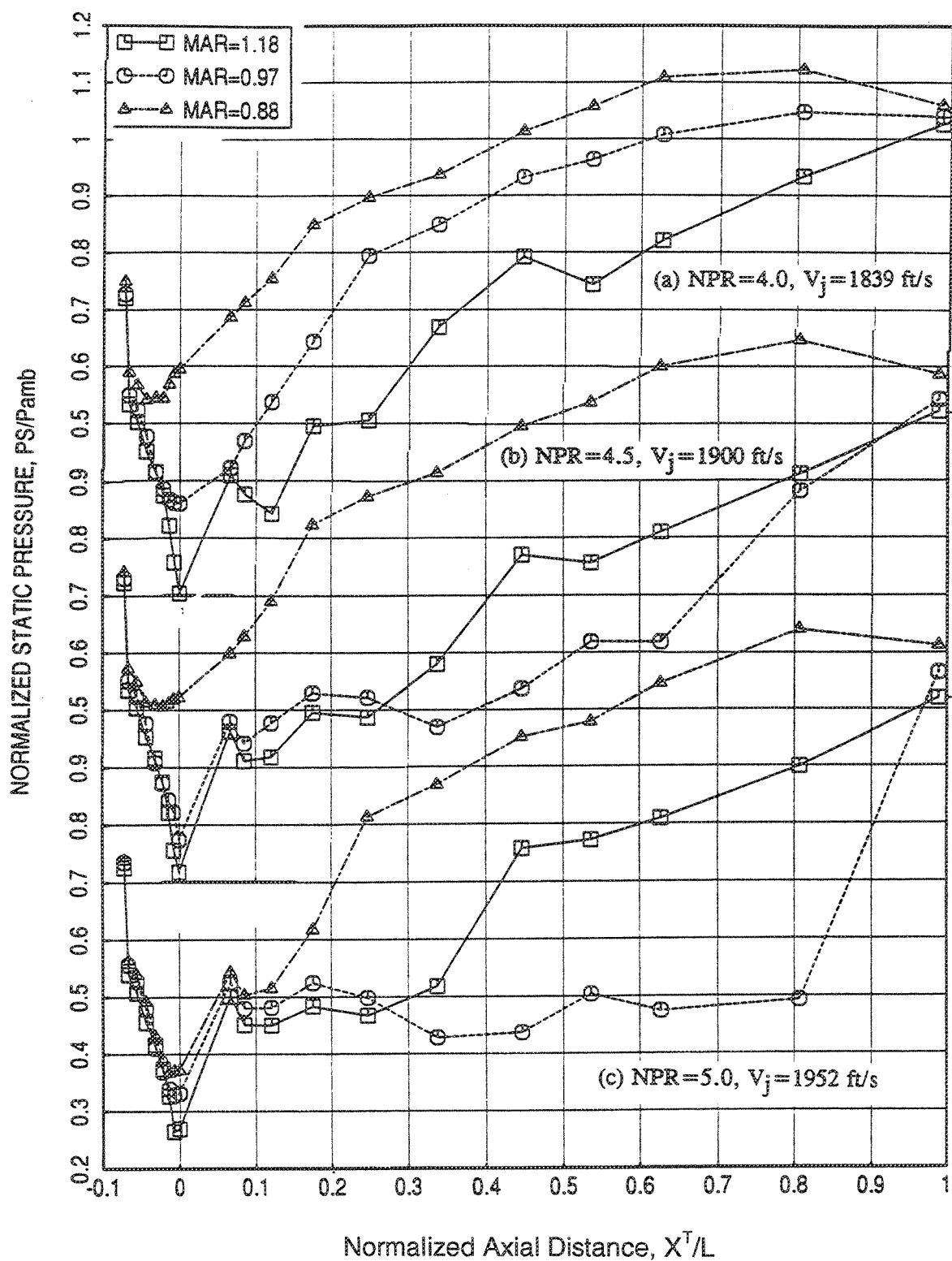


Figure 255. Effect of MAR on Axial Static Pressure Distribution on Shroud Surface for Axial Mixer-Ejector Configurations at Static Conditions ( $SAR=4.9$ , Shroud Length=18.85 in.,  $T_t=400^\circ F$ )

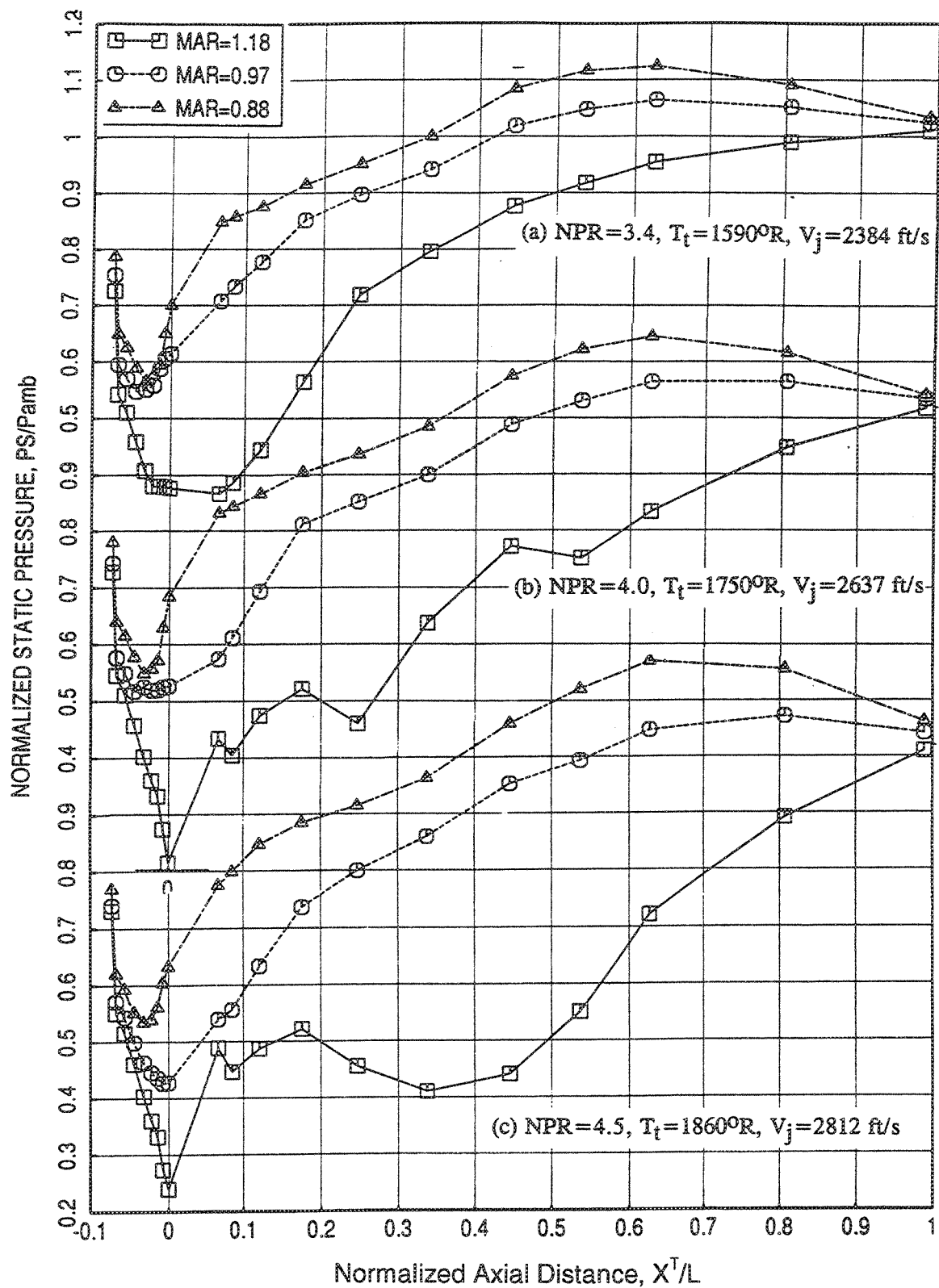


Figure 256. Effect of MAR on Axial Static Pressure Distribution on Shroud Surface for Axial Mixer-Ejector Configurations at Static Condition S (AR=4.9, Shroud Length=18.85 in., LIM Cycle)

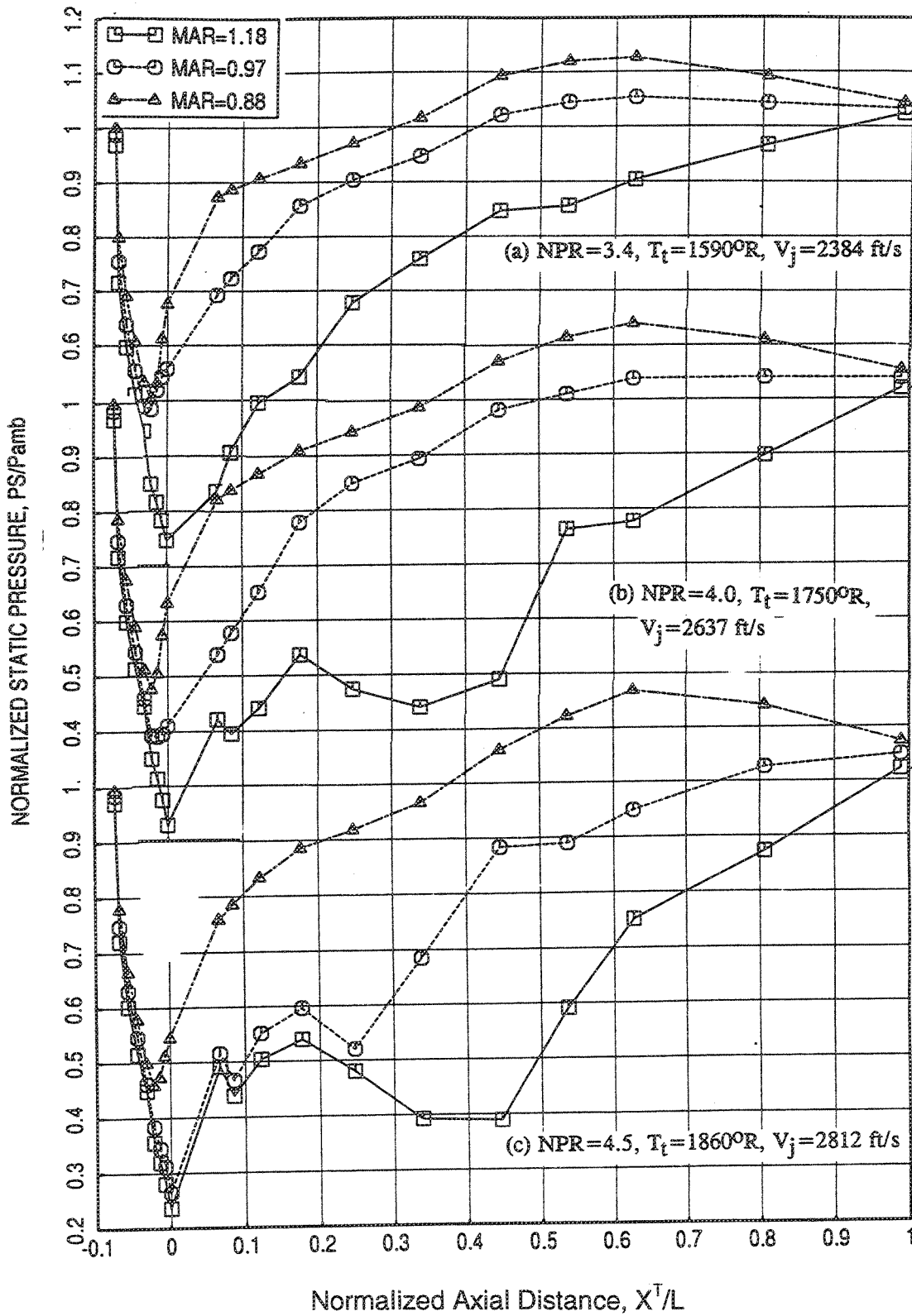


Figure 257. Effect of MAR on Axial Static Pressure Distribution on Shroud Surface for Axial Mixer-Ejector Configurations With Flight Simulation ( $Mn=0.32$ ) ( $SAR=4.9$ , Shroud Length=18.85 in., LIM Cycle)





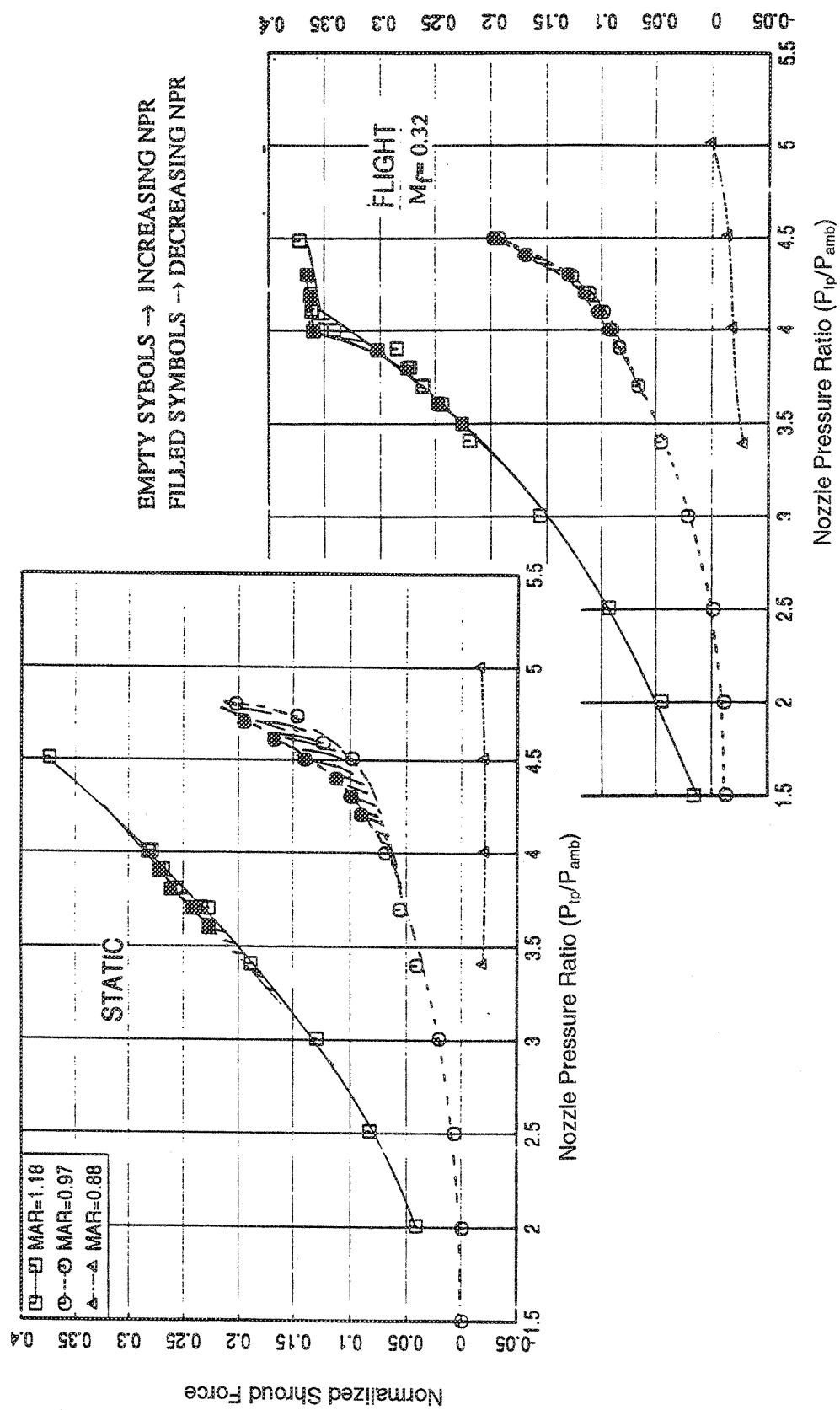


Figure 259. Effect of Ejector MAR on Normalized Shroud Force For Axial Mixer-Ejector Configurations for LIM Cycle Condition (SAR=4.9, Shroud Length=18.85 in.)

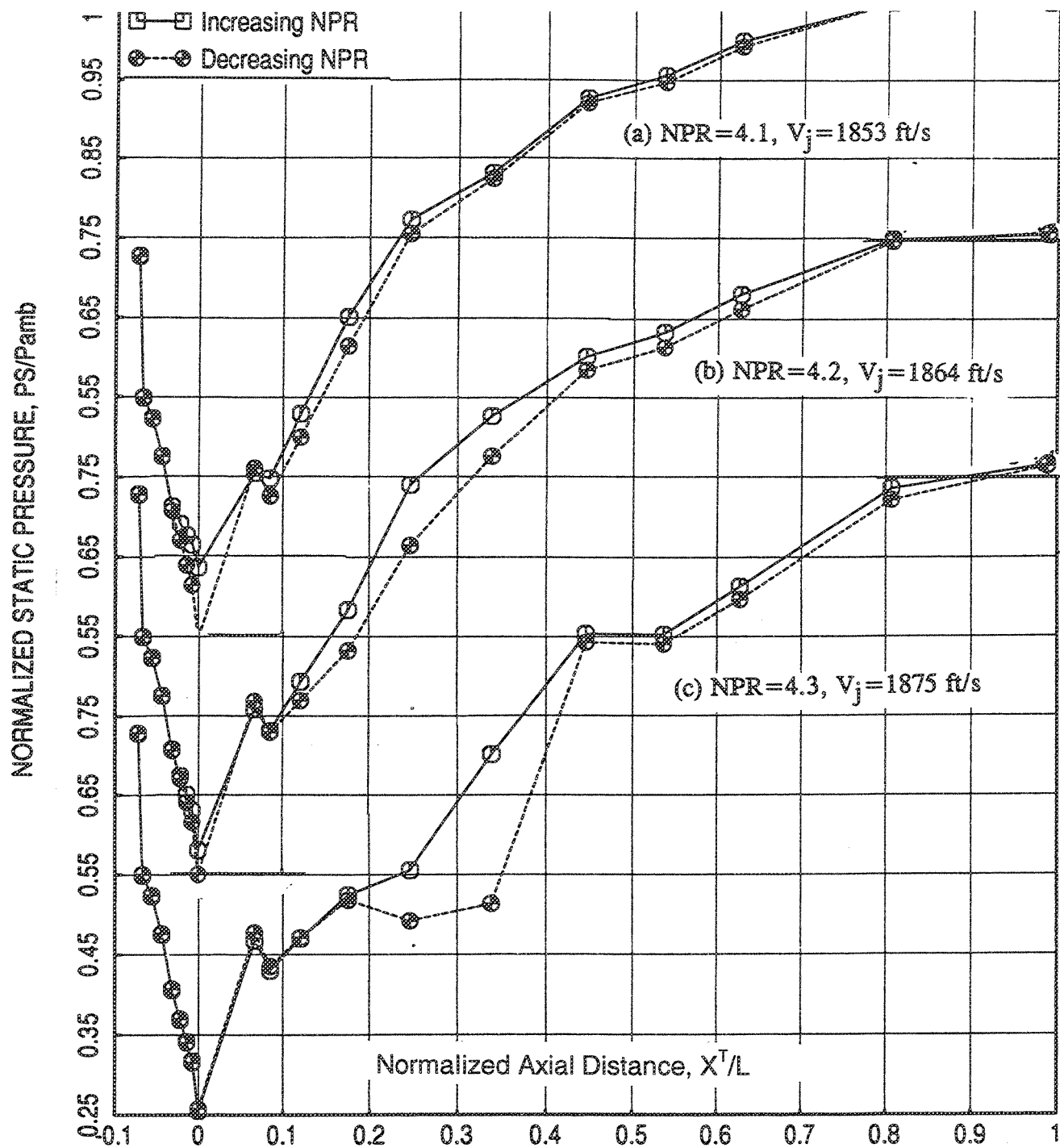


Figure 260. Effect of Increasing and Decreasing NPR on Axial Static Pressure Distribution on Shroud Surface for Axial Mixer-Ejector Configuration at Static Condition (SAR=4.9, MAR=0.97, Shroud Length=18.85 in.,  $T_t=400^\circ\text{F}$ )

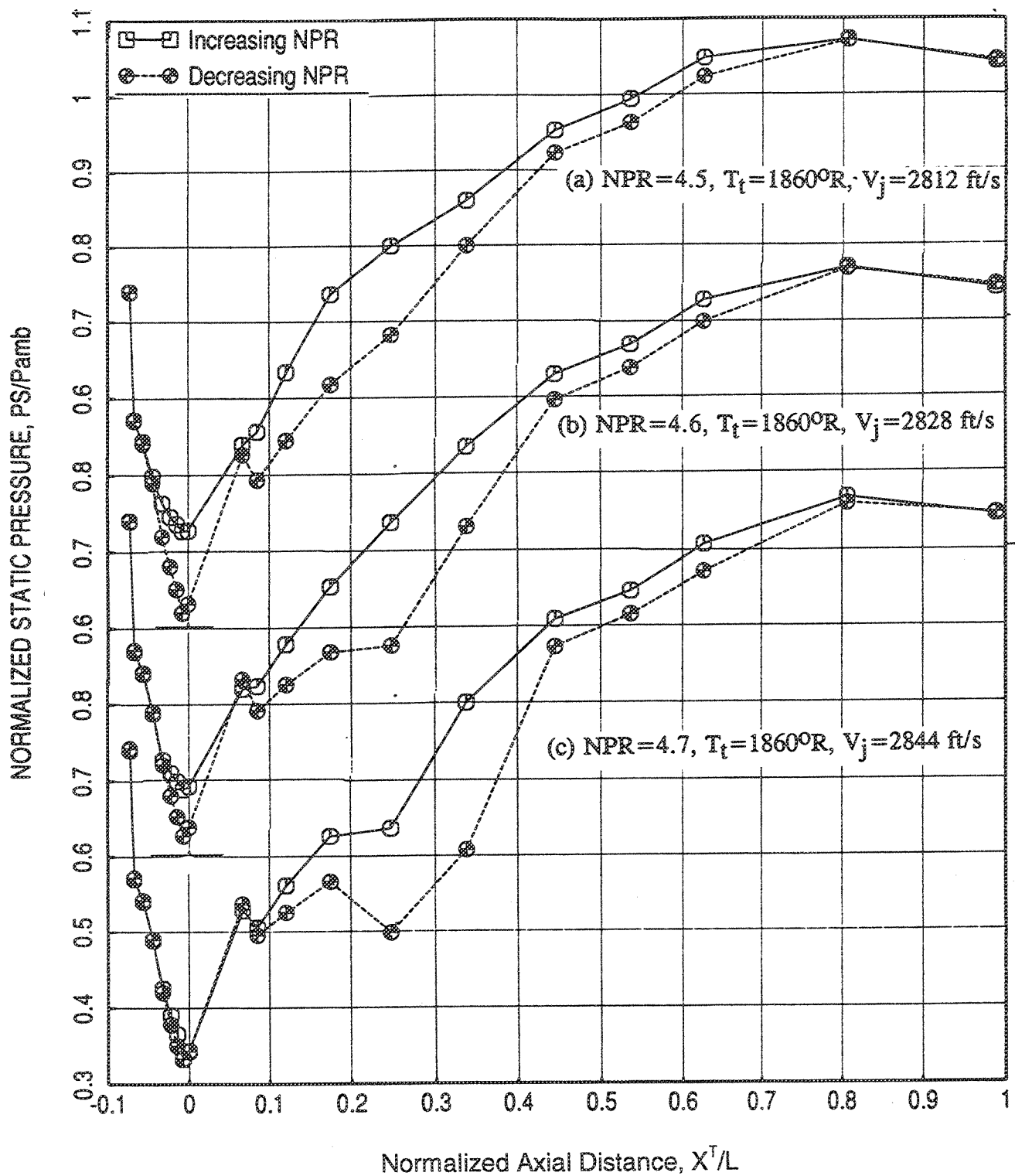


Figure 261. Effect of Increasing and Decreasing NPR on Axial Static Pressure Distribution on Shroud Surface for Axial Mixer-Ejector Configuration at Static Condition (SAR=4.9, MAR=0.97, Shroud Length=18.85 in., LIM Cycle)

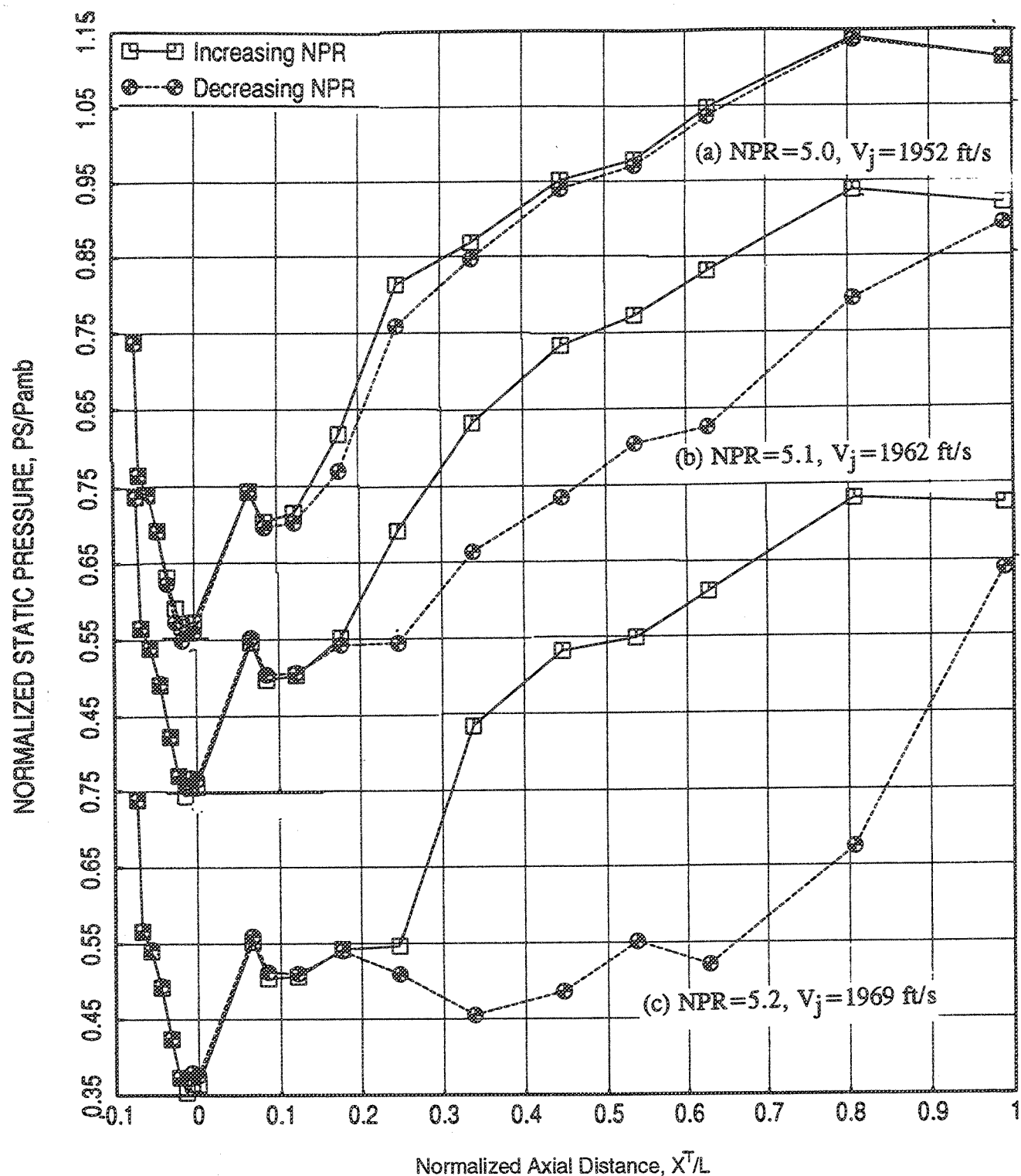


Figure 262. Effect of Increasing and Decreasing NPR on Axial Static Pressure Distribution on Shroud Surface for Axial Mixer-Ejector Configuration at Static Condition  
( $SAR=4.9$ ,  $MAR=0.88$ , Shroud Length=18.85 in.,  $T_t=400^\circ F$ )

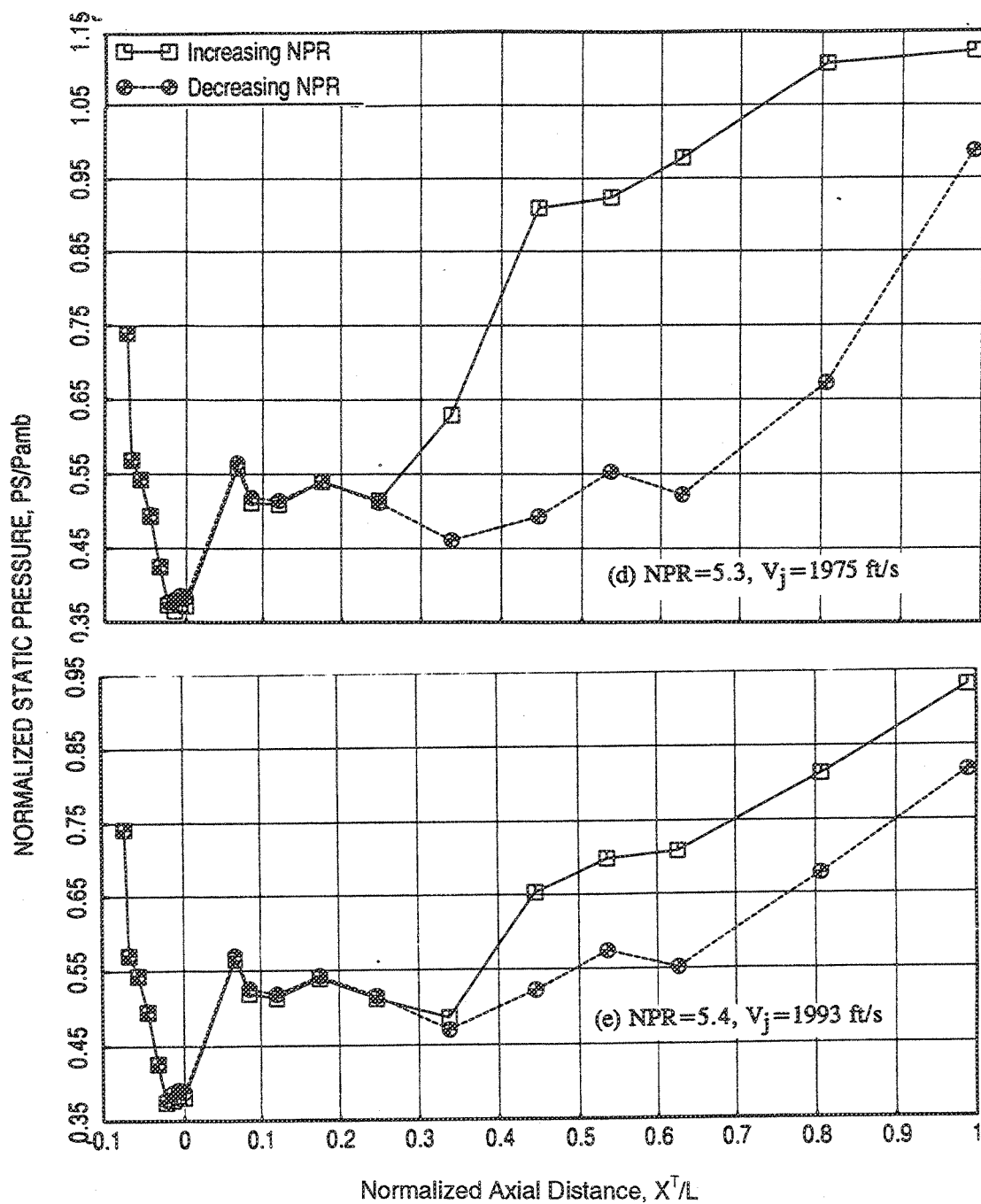


Figure 263. Effect of Increasing and Decreasing NPR on Axial Static Pressure Distribution on Shroud Surface for Axial Mixer-Ejector Configuration at Static Condition (SAR=4.9, MAR=0.88, Shroud Length=18.85 in.,  $T_t=400^\circ\text{F}$ )

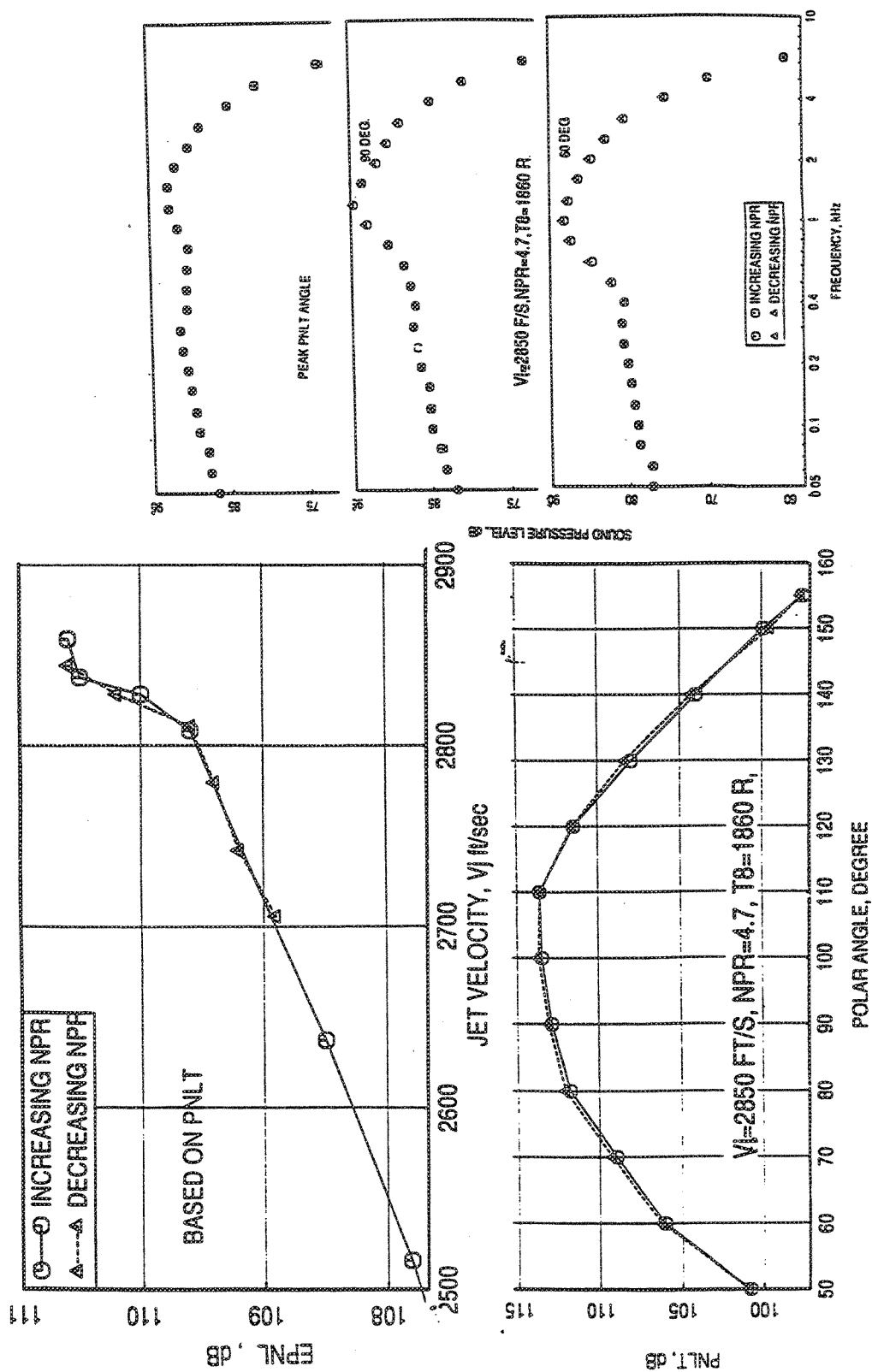


Figure 264. Effect of Hysteresis on Farfield Noise Characteristics of Axial Mixer-Ejector Nozzle at Static Condition (SAR=4.9, MAR=0.97, Shroud Length=18.85 in., Sideline=1629 ft.,  $A_8=1086 \text{ in}^2$ )

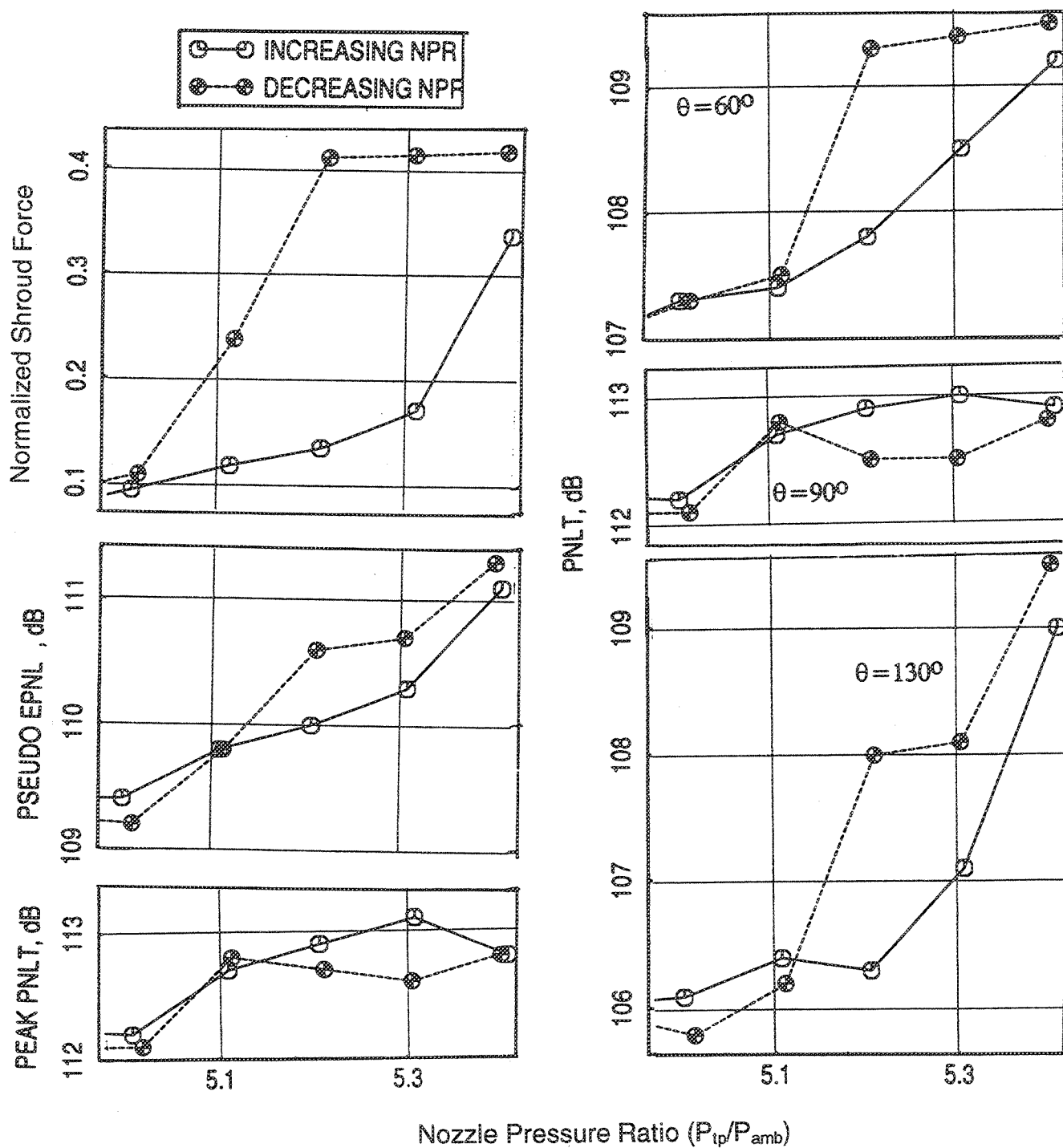


Figure 265. Normalized Shroud Force and Corresponding EPNL, Peak PNLT, and PNLT at Various Polar Angles as Functions of NPR for Axial Mixer-Ejector Configuration at 400°F (SAR=4.9, MAR=0.88, Shroud Length=18.85 in.)

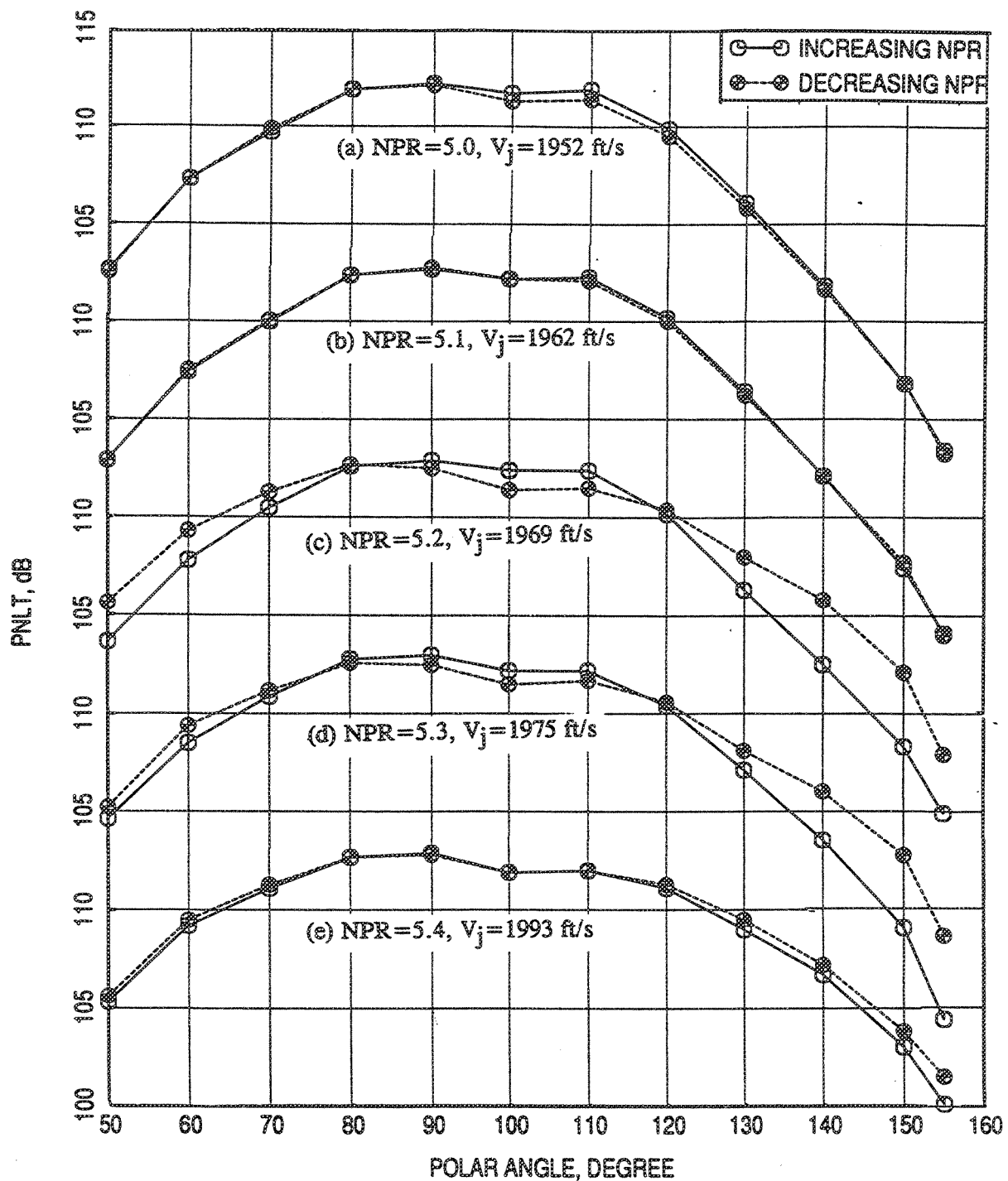


Figure 266. PNLT Directivities at Various NPRs at 400°F for Axial Mixer-Ejector Configuration (SAR=4.9, MAR=0.88, Shroud Length=18.85 in.)



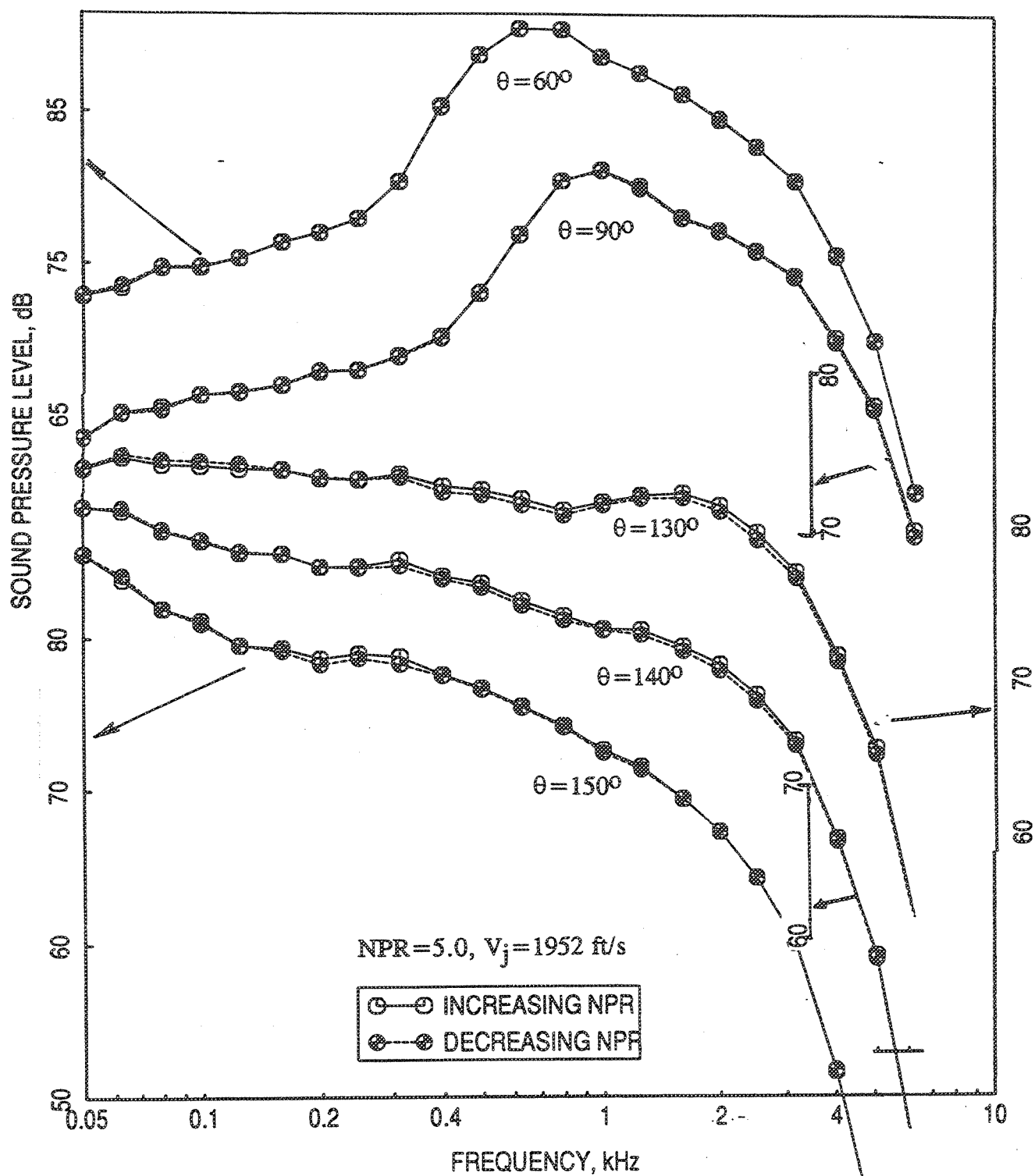


Figure 267. SPL Spectra at a Number of Polar Angles for  $NPR=5.0$  and  $400^\circ\text{F}$  for Axial Mixer-Ejector Configuration ( $SAR=4.9$ ,  $MAR=0.88$ , Shroud Length=18.85 in.)

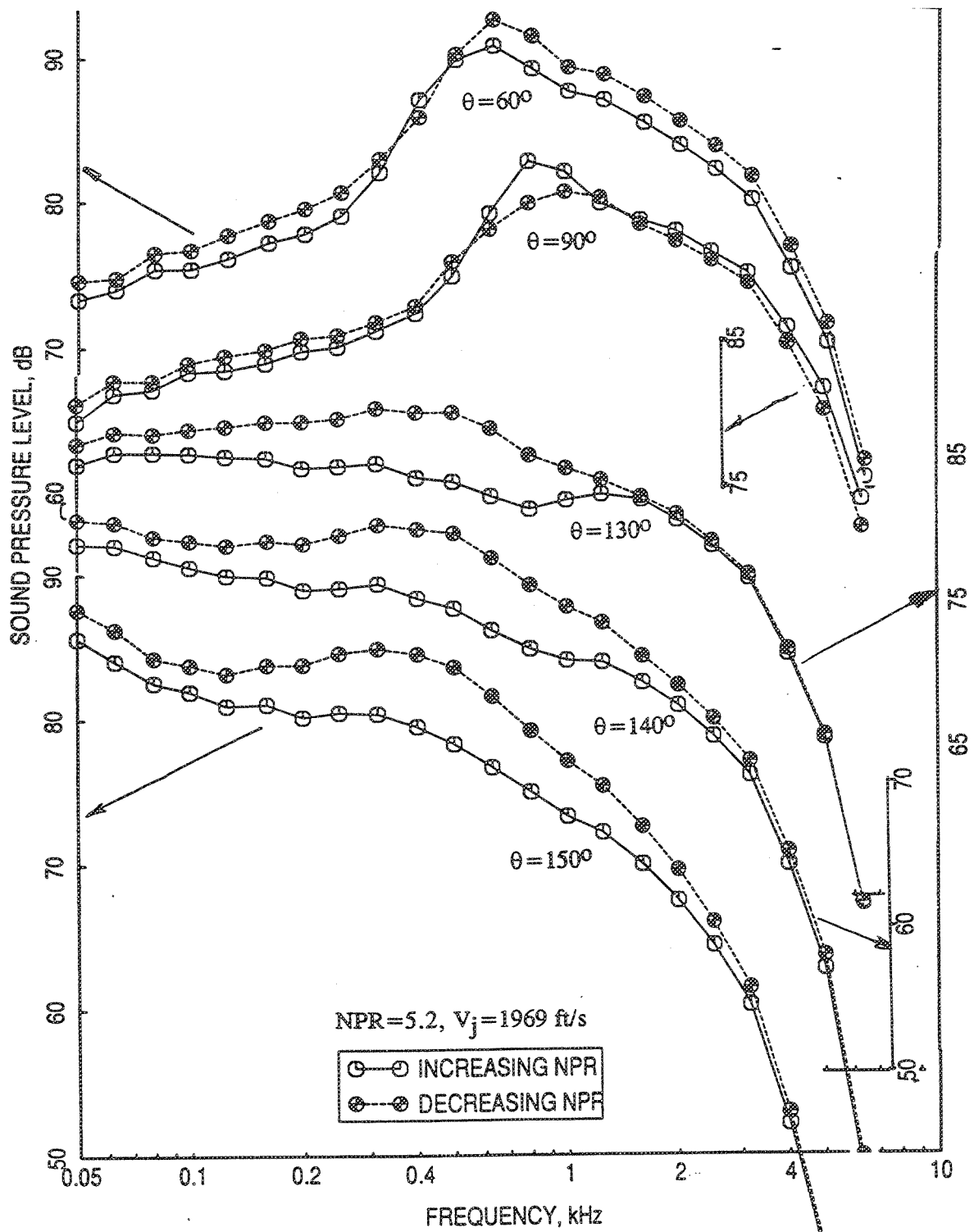


Figure 268. SPL Spectra at a Number of Polar Angles for NPR=5.2 and 400°F for Axial Mixer-Ejector Configuration (SAR=4.9, MAR=0.88, Shroud Length=18.85 in.)

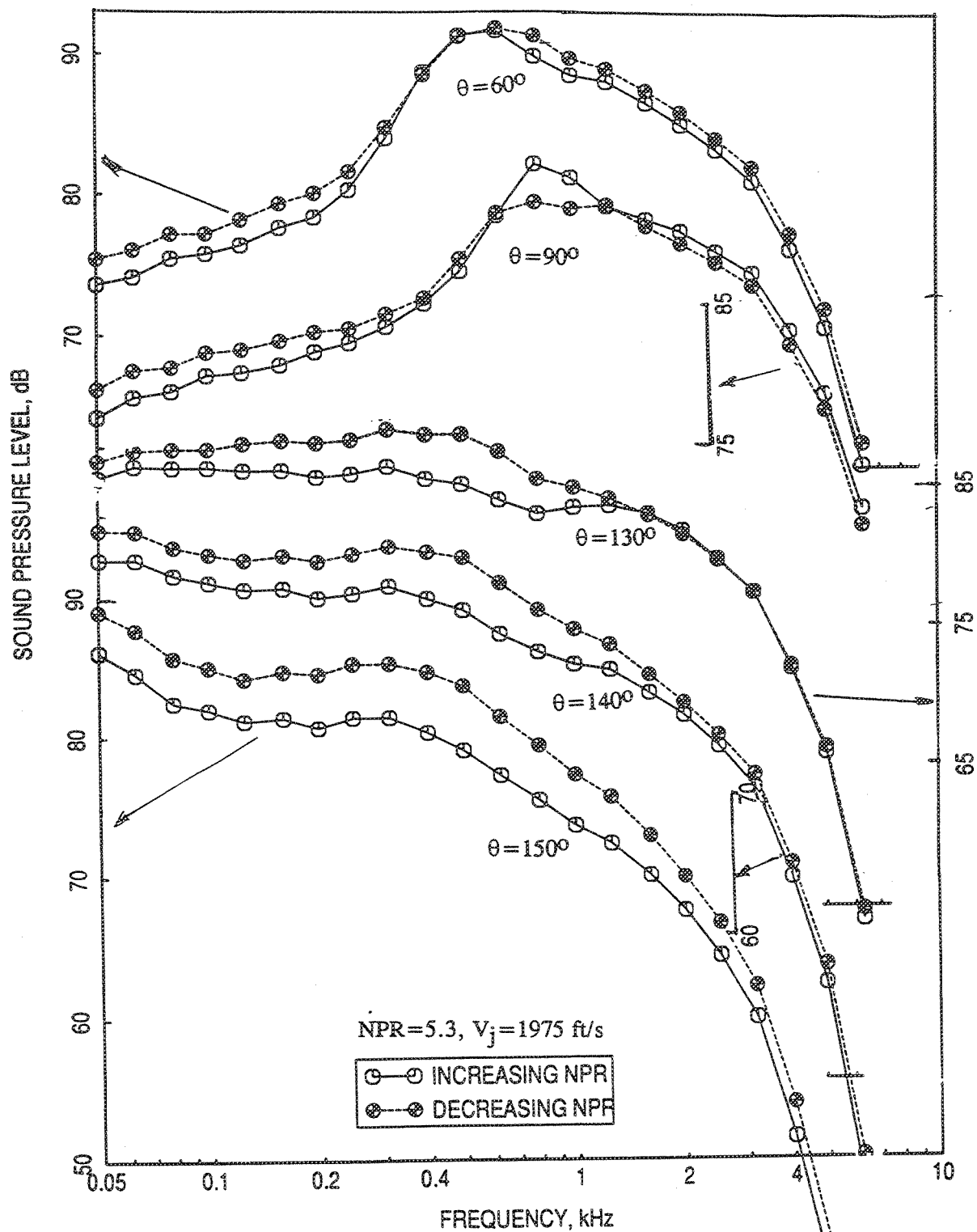


Figure 269. SPL Spectra at a Number of Polar Angles for  $NPR=5.3$  and  $400^\circ F$  for Axial Mixer-Ejector Configuration ( $SAR=4.9$ ,  $MAR=0.88$ , Shroud Length=18.85 in.)

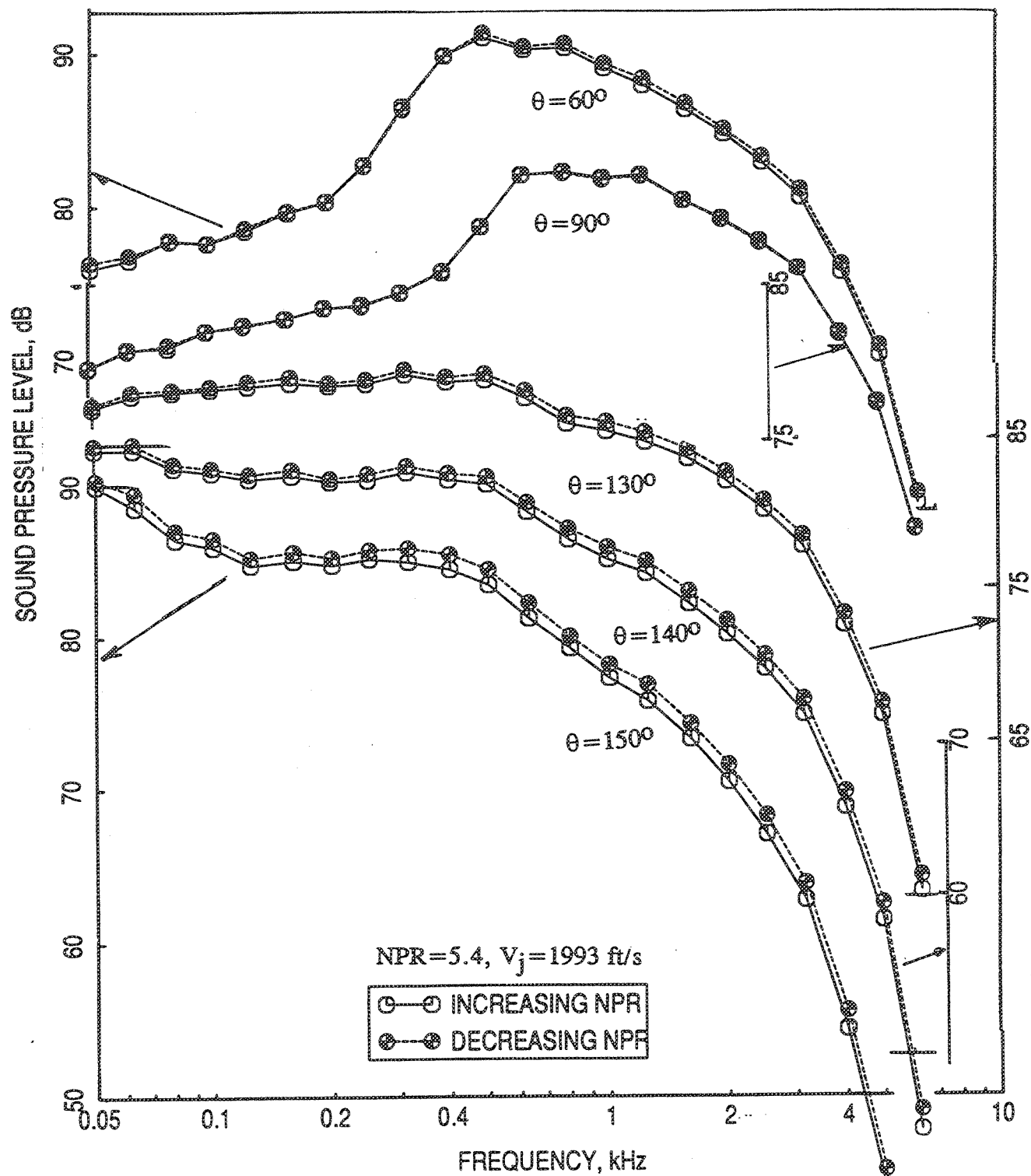


Figure 270. SPL Spectra at a Number of Polar Angles for NPR=5.4 and 400°F for Axial Mixer-Ejector Configuration (SAR=4.9, MAR=0.88, Shroud Length=18.85 in.)

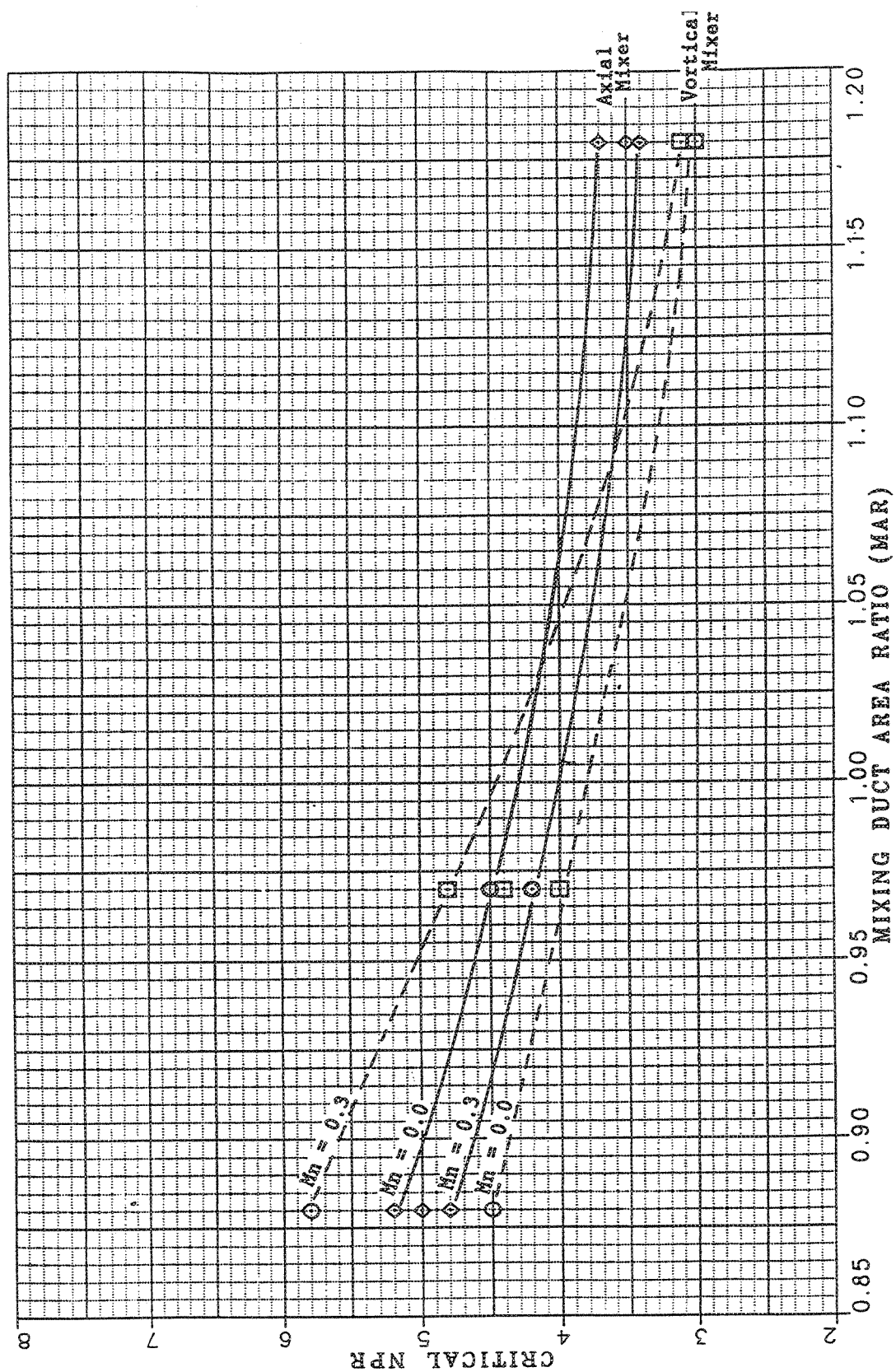
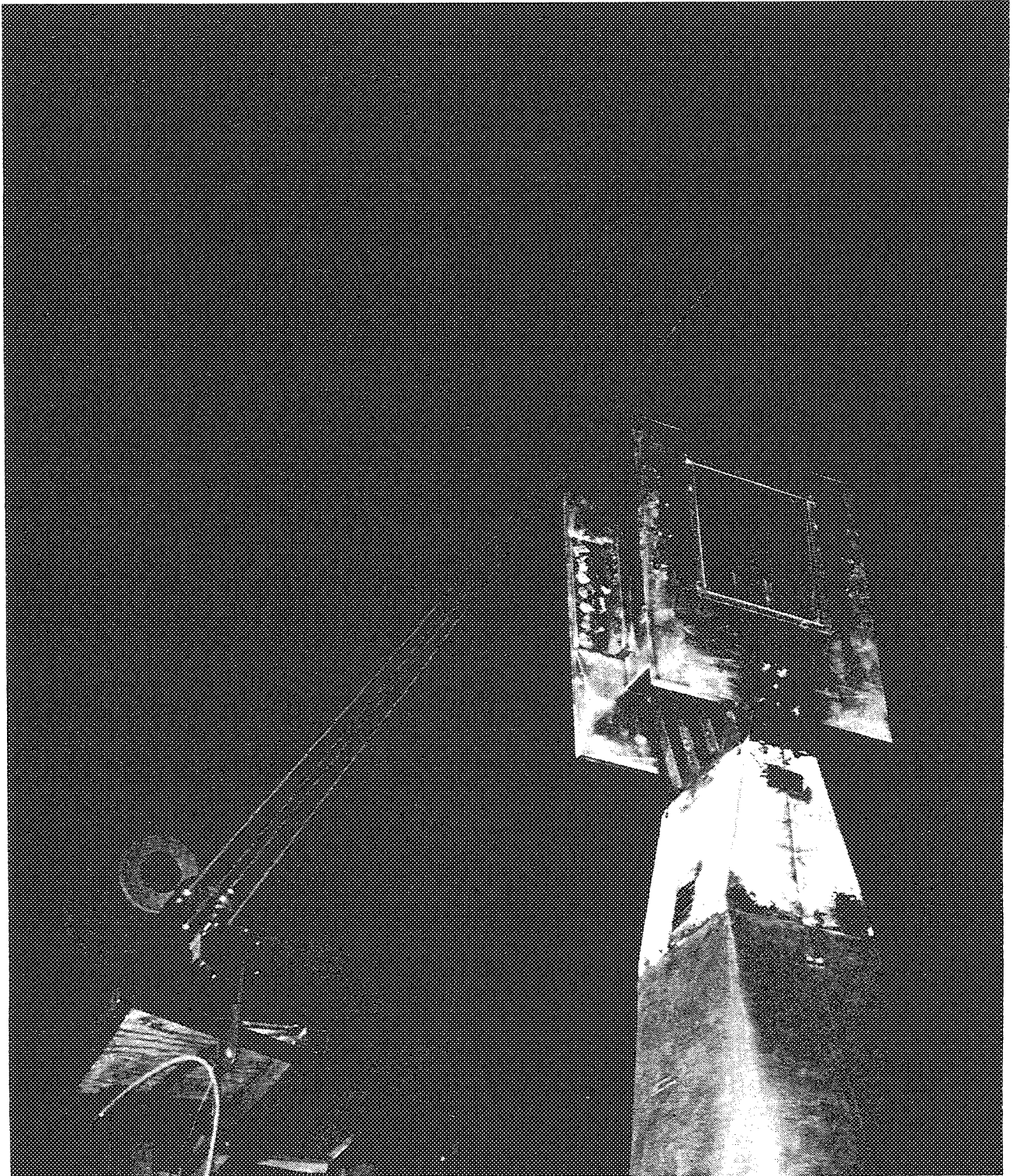


Figure 271. MAR is Key Determinant of NPRcr Where Mode Switch Occurs



*Figure 272. Laser Doppler Velocimetry System With Axial Mixer-Ejector Nozzle Configuration With Short Hardwall Shroud and Glass Windows on Sidewall — Mounted in Anechoic Chamber*

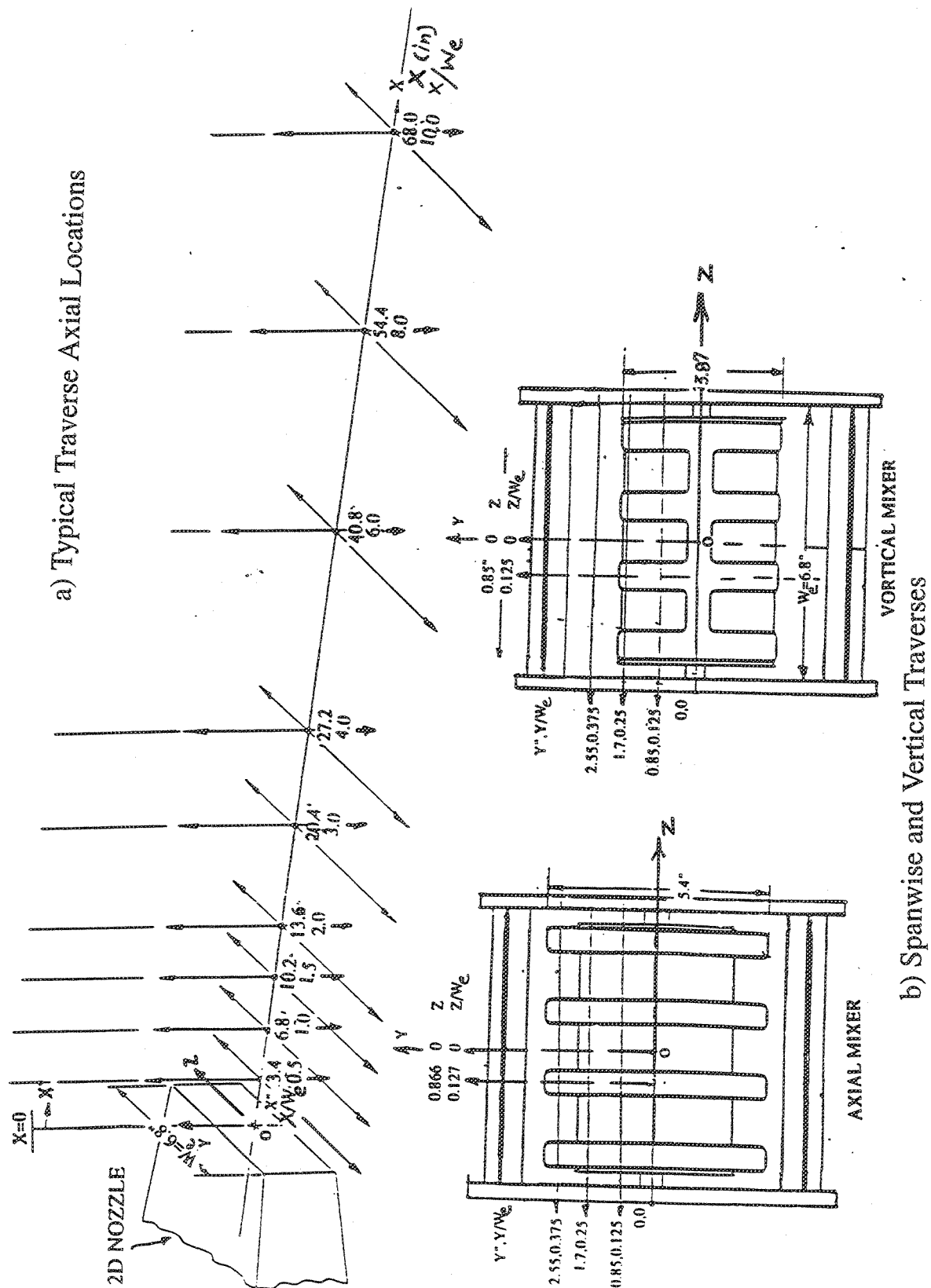


Figure 273. Laser Doppler Velocimetry Traverse Locations for External Plume Survey for P&W Mixer-Ejector Nozzles

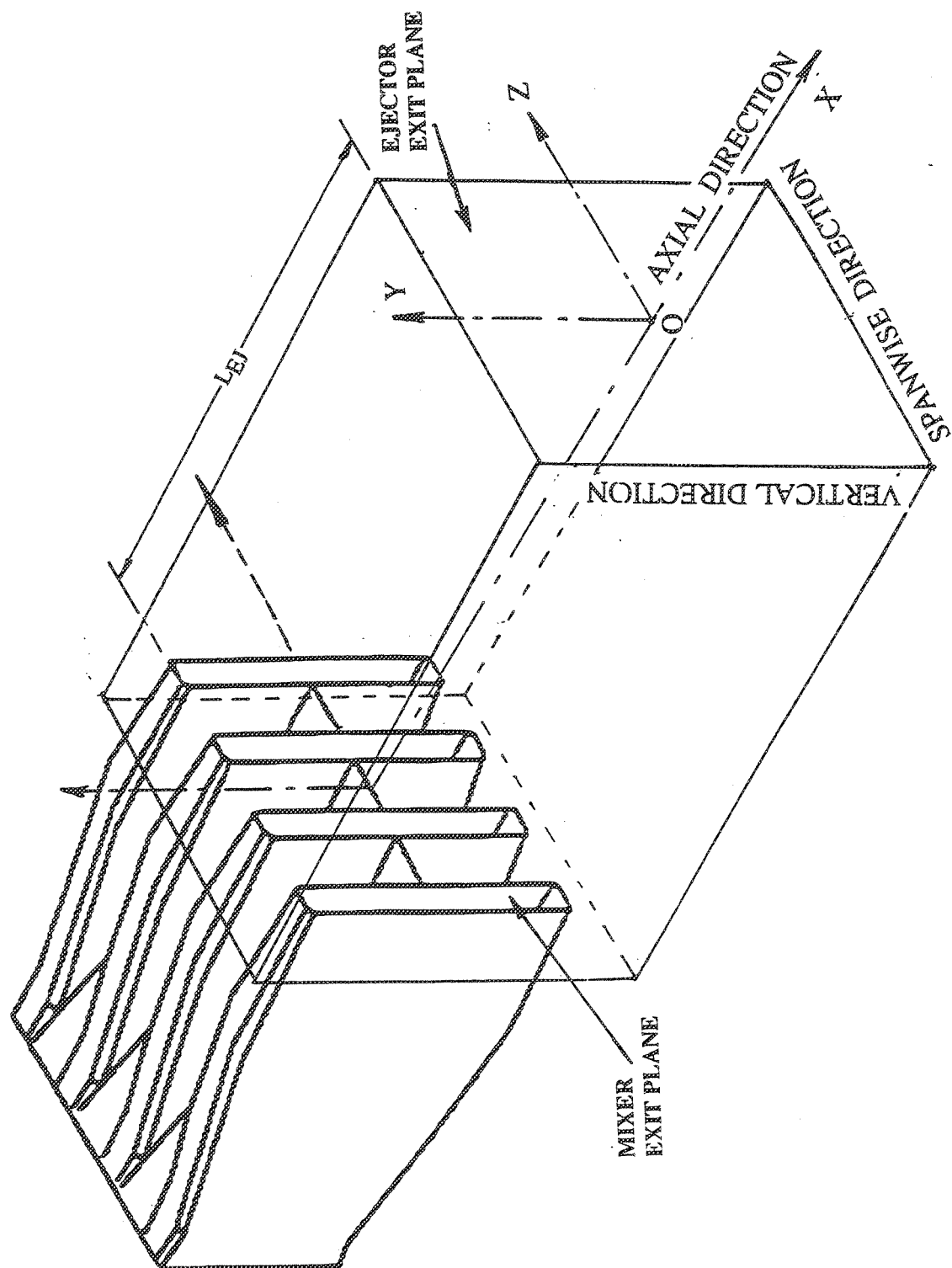


Figure 274. An Isometric View of an Axial Mixer-Ejector Nozzle Configuration



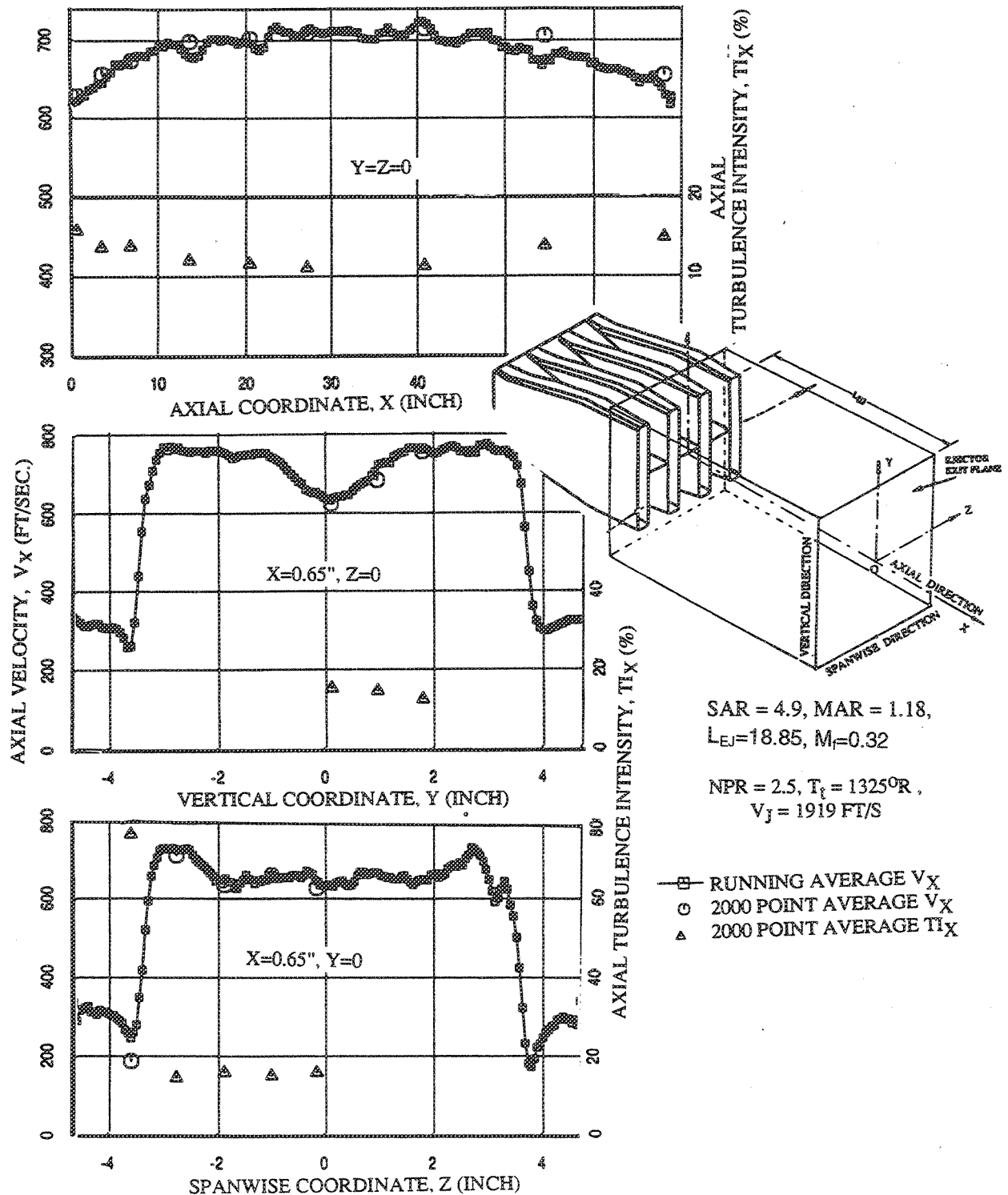


Figure 275. Comparison of Running Average Axial Velocity Components ( $V_X$ ) With Those Obtained From 2000 Data Points and the Axial Components of Turbulence Intensity ( $TI_X$ ) in the External Plume of the Axial Mixer-Ejector Nozzle With Long Hardwall Shroud

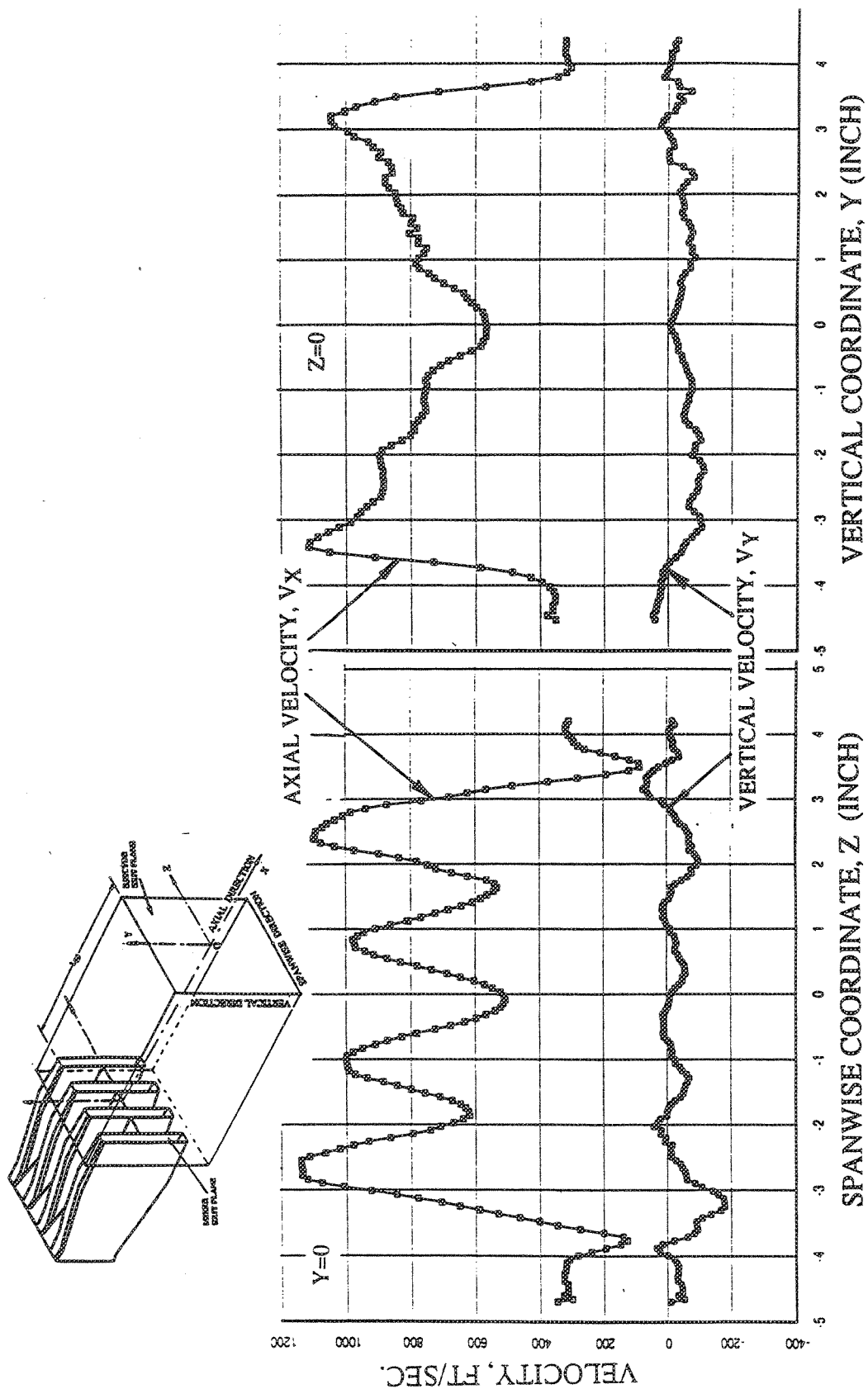


Figure 276. Axial and Vertical Velocity Distribution Close to Ejector Exit Planes of the Axial Mixer-Ejector Nozzle With Short Hardwall Shroud (SAR=4.9, MAR=1.18,  $L_{EJ}=10.46$  in.,  $X=0.65$  in.,  $Mn=0.32$ ,  $NPR=3.5$ ,  $T_t=1735^\circ R$ ,  $V_j=2518$  ft/sec.)

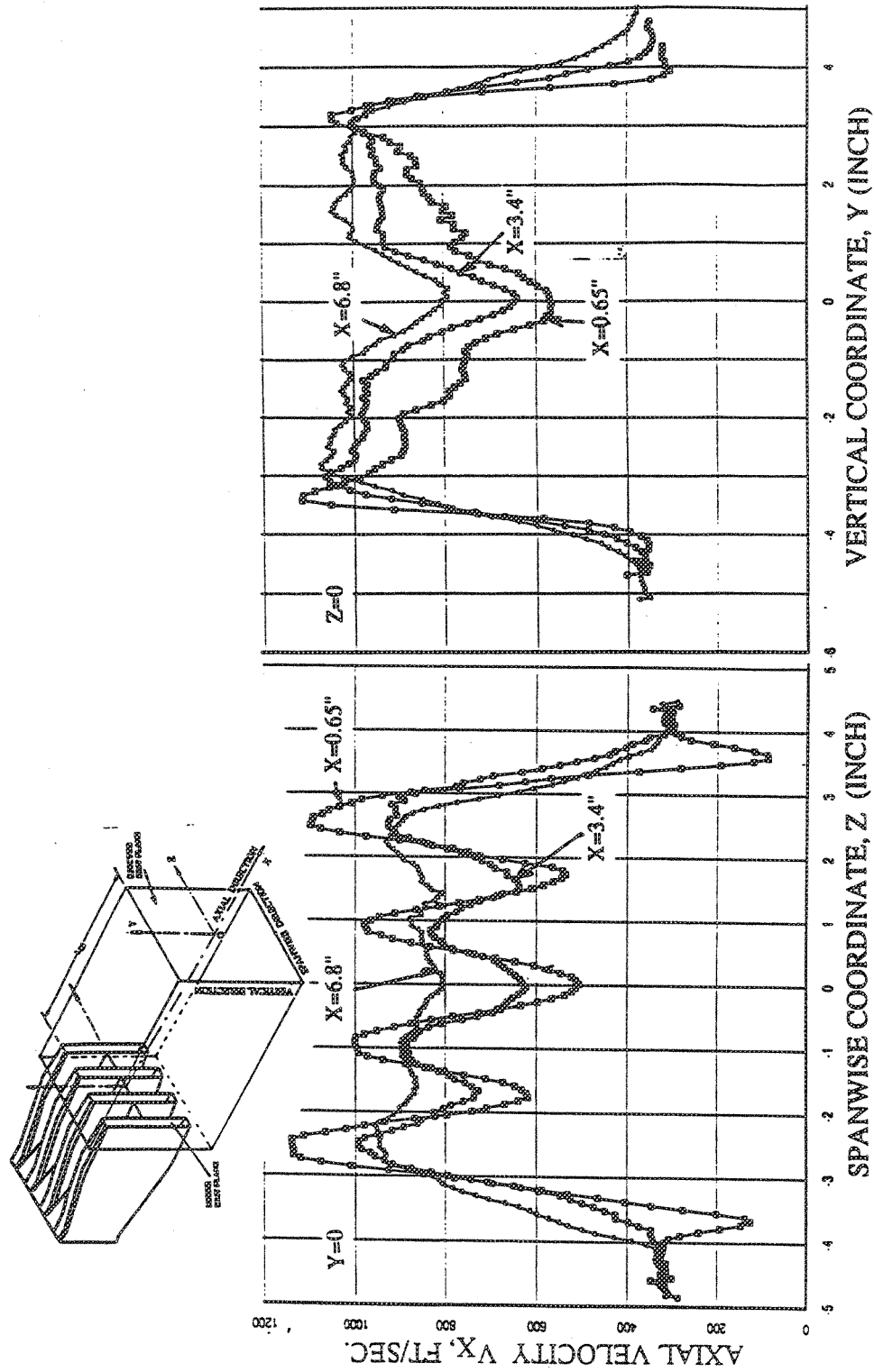


Figure 277. Axial Velocity Distributions at Various Locations Downstream From the Ejector Exit Plane of the Axial Mixer-Ejector Nozzle With Short Hardwall Shroud (SAR=4.9, MAR=1.18,  $L_{EJ}=10.46$  in.,  $Mn=0.32$ ,  $NPR=3.5$ ,  $T_t=1735^\circ R$ ,  $V_j=2518$  ft/sec.)

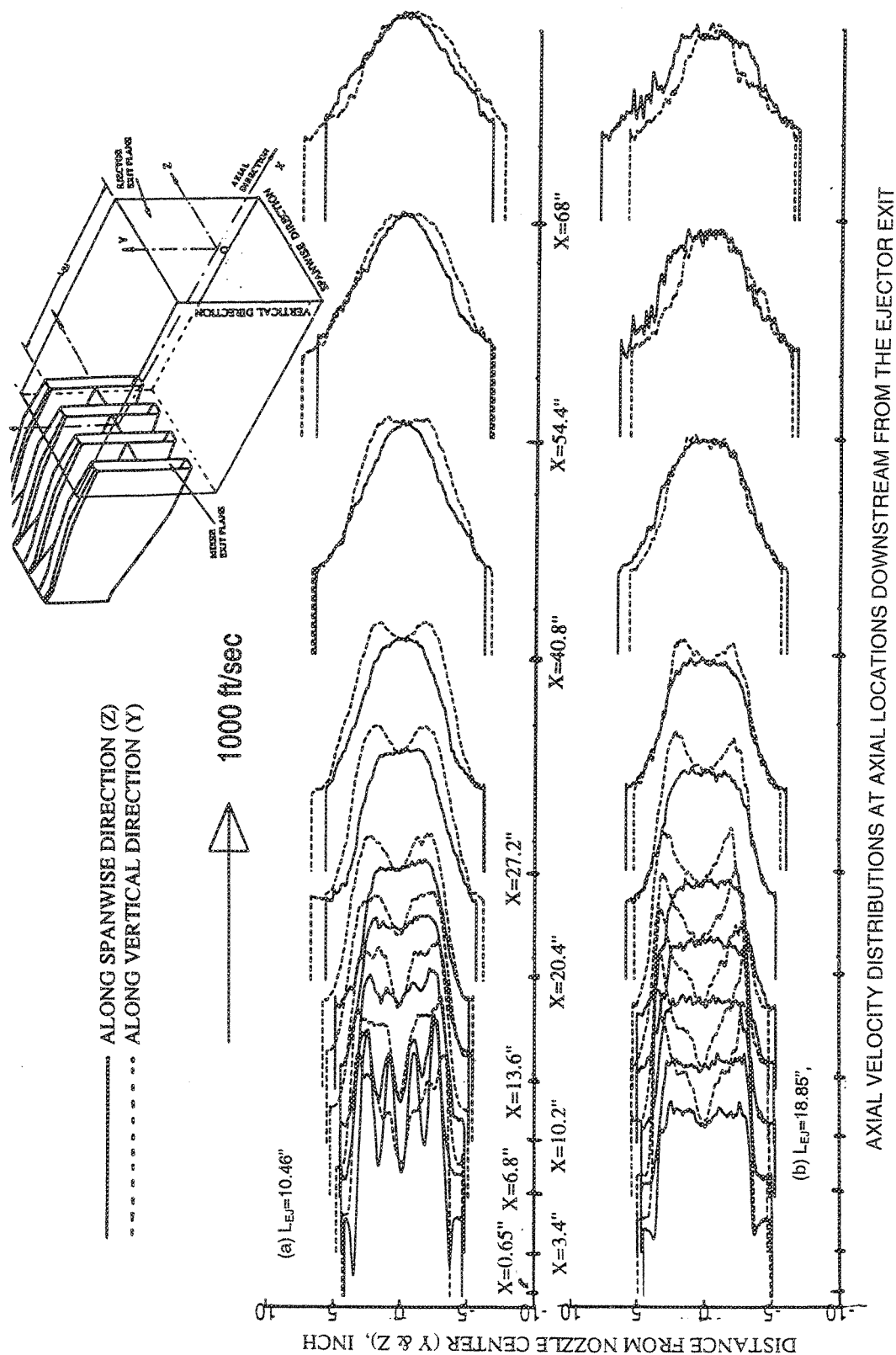


Figure 278. Comparison of Axial Velocity Distributions Between Spanwise (Z) and Vertical (Y) Directions at Various Axial Locations Downstream From the Ejector Exit Plane of Axial Mixer-Ejector Nozzles with Hardwall Shroud  
(SAR=4.9, MAR=1.18, Mn=0.32, NPR=3.5,  $T_t=1735^\circ R$ ,  $V_t=2518$  ft/sec): (a)  $L_{EJ}=10.46$  in., (b)  $L_{EJ}=18.85$  in.

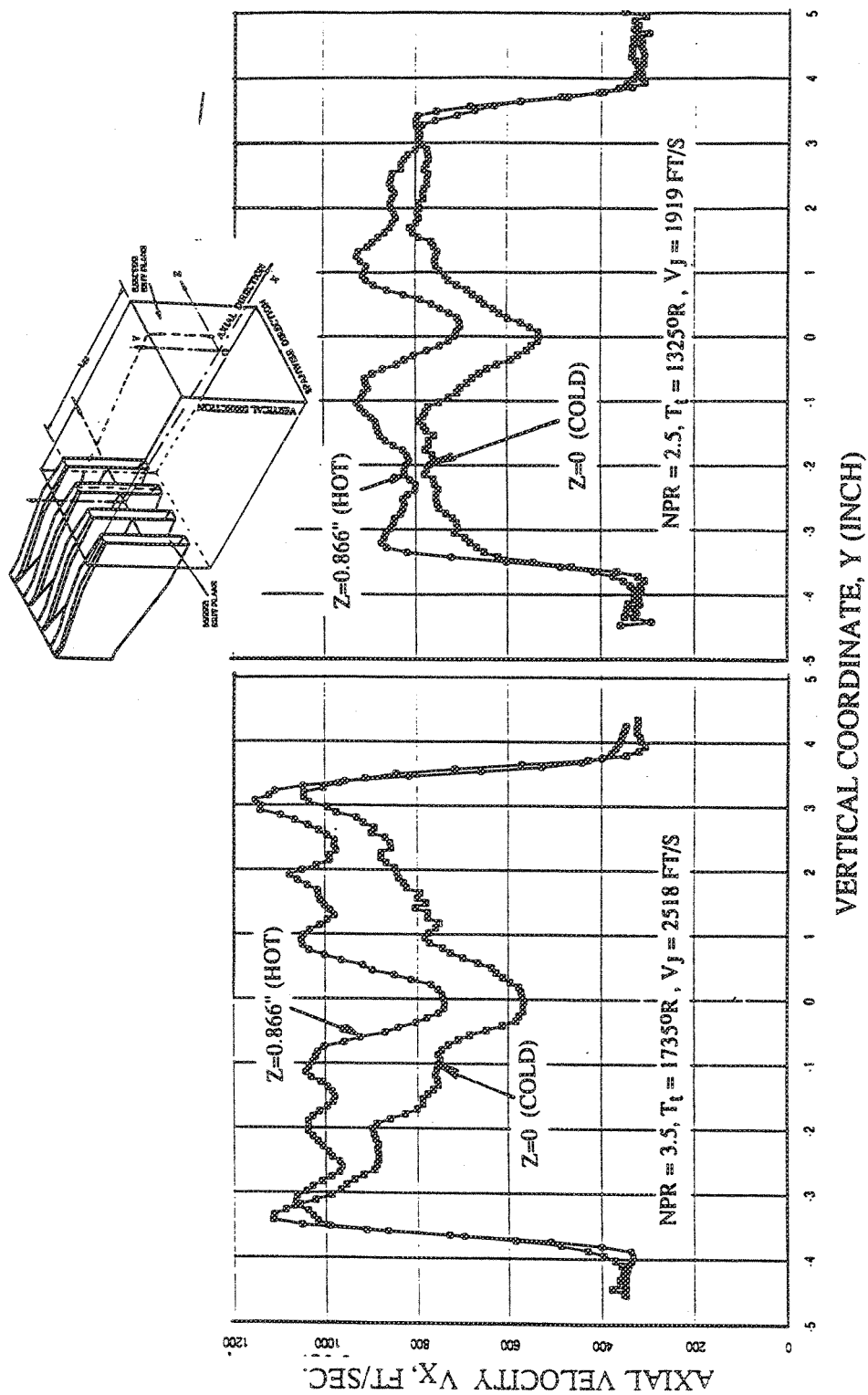


Figure 279. Axial Velocity Distributions Along the Chute Height at Hot and Cold Flow Regions Close to the Ejector Exit Plane of the Axial Mixer-Ejector Nozzle With Short Hardwall Shroud ( $SAR=4.9$ ,  $MAR=1.18$ ,  $L_{EJ}=10.46 \text{ in.}$ ,  $X=0.65 \text{ in.}$ ,  $Mn=0.32$ )

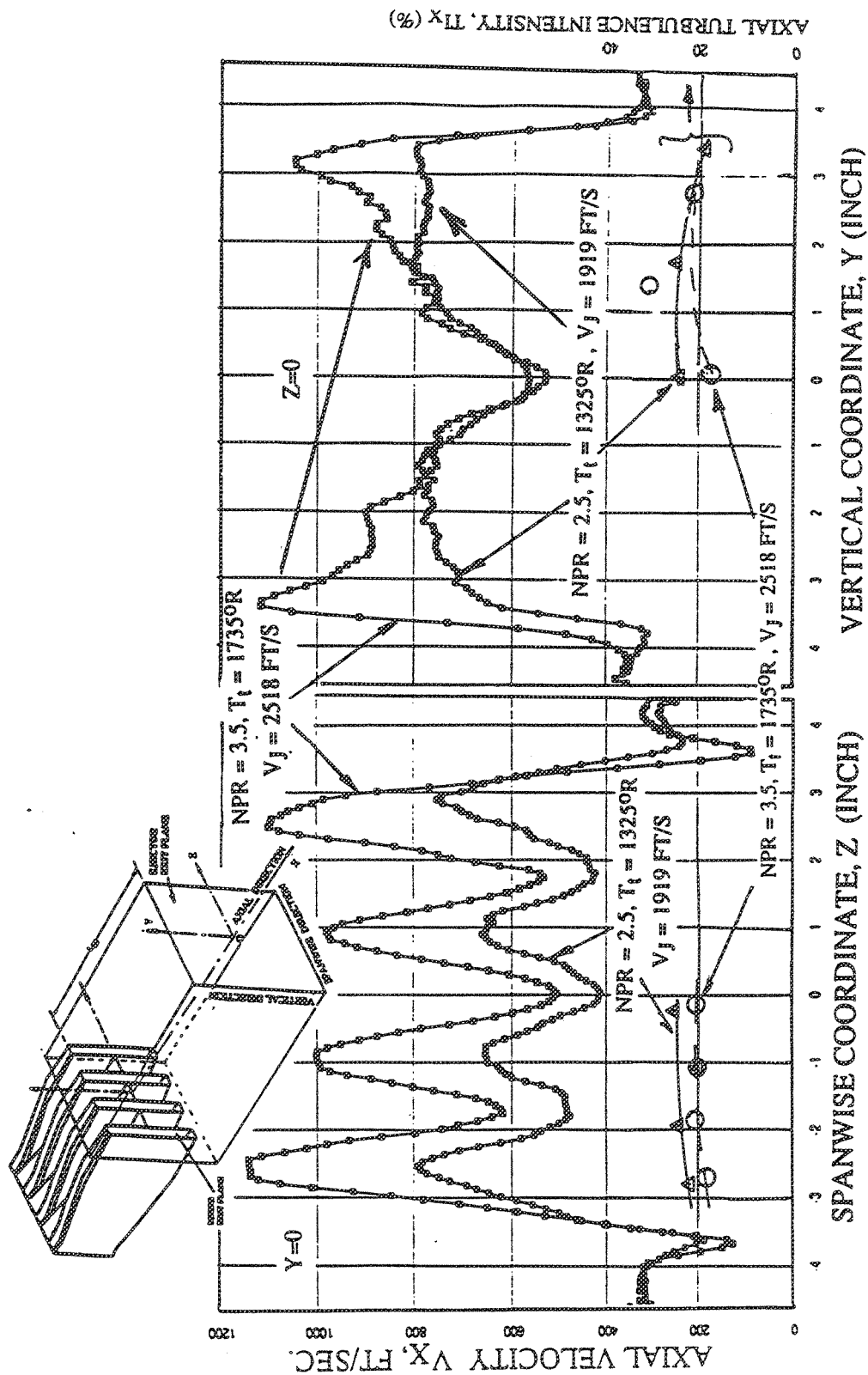


Figure 280. Effect of Nozzle Pressure Ratio on Axial Velocity and Turbulence Intensity Distributions Close to the Ejector Exit Plane of the Axial Mixer-Ejector Nozzle With Short Hardwall Shroud (SAR=4.9, MAR=1.18,  $L_{EJ}$ =10.46 in.,  $X$ =0.65 in.,  $Mn$ =0.32)

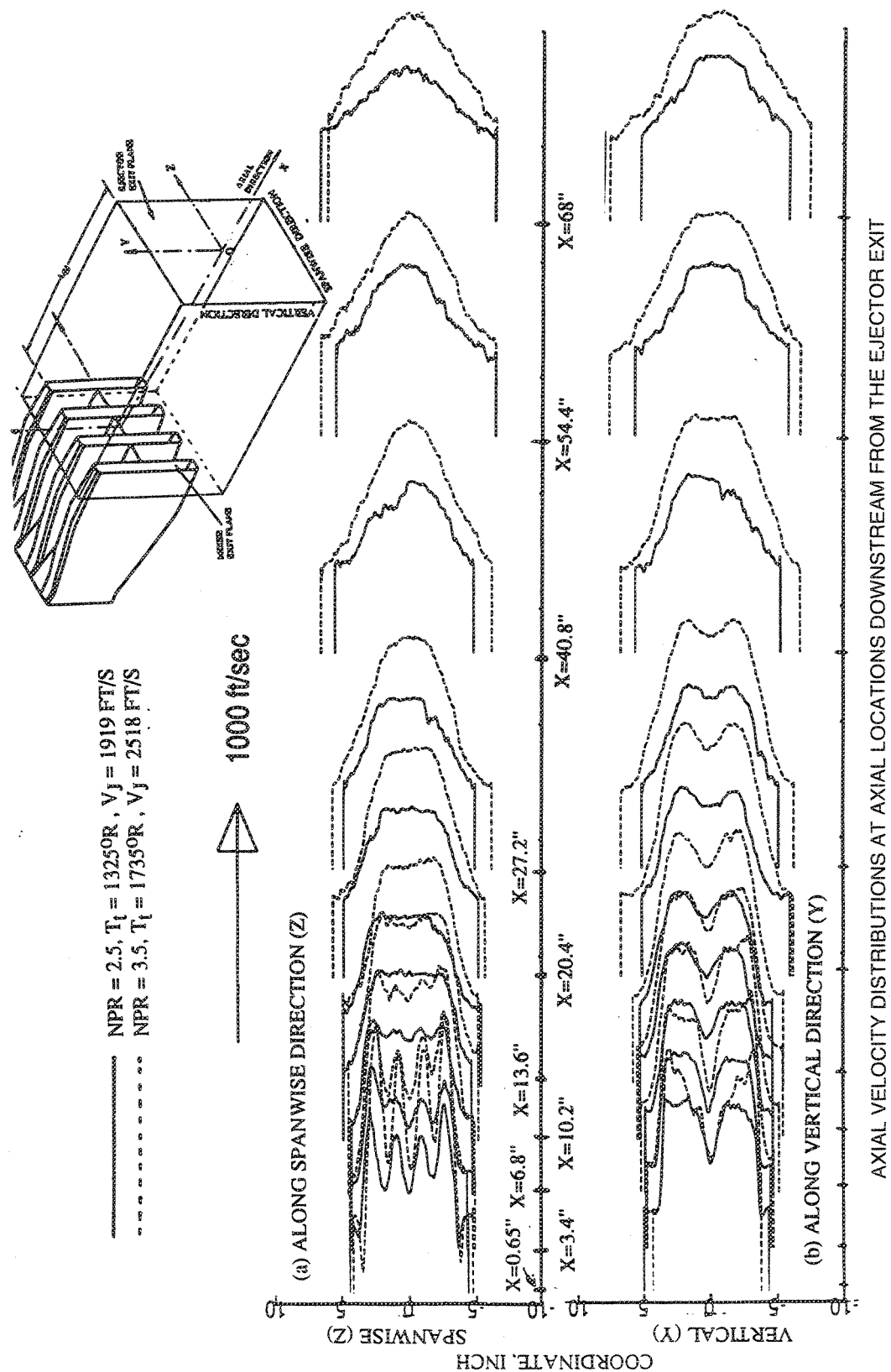


Figure 281. Comparison of Axial Velocity Distributions Between NPR=2.5,  $T_t=1325^\circ\text{R}$ ,  $V_j=1919 \text{ ft/sec}$ , and NPR=3.5,  $T_t=1735^\circ\text{R}$ ,  $V_j=2518 \text{ ft/sec}$  at Various Axial Locations Downstream From the Ejector Exit Plane of Axial Mixer-Ejector Nozzles With Hardwall Shroud (SAR=4.9, MAR=1.18,  $L_{EJ}=10.46 \text{ in.}$ ,  $Mn=0.32$ )

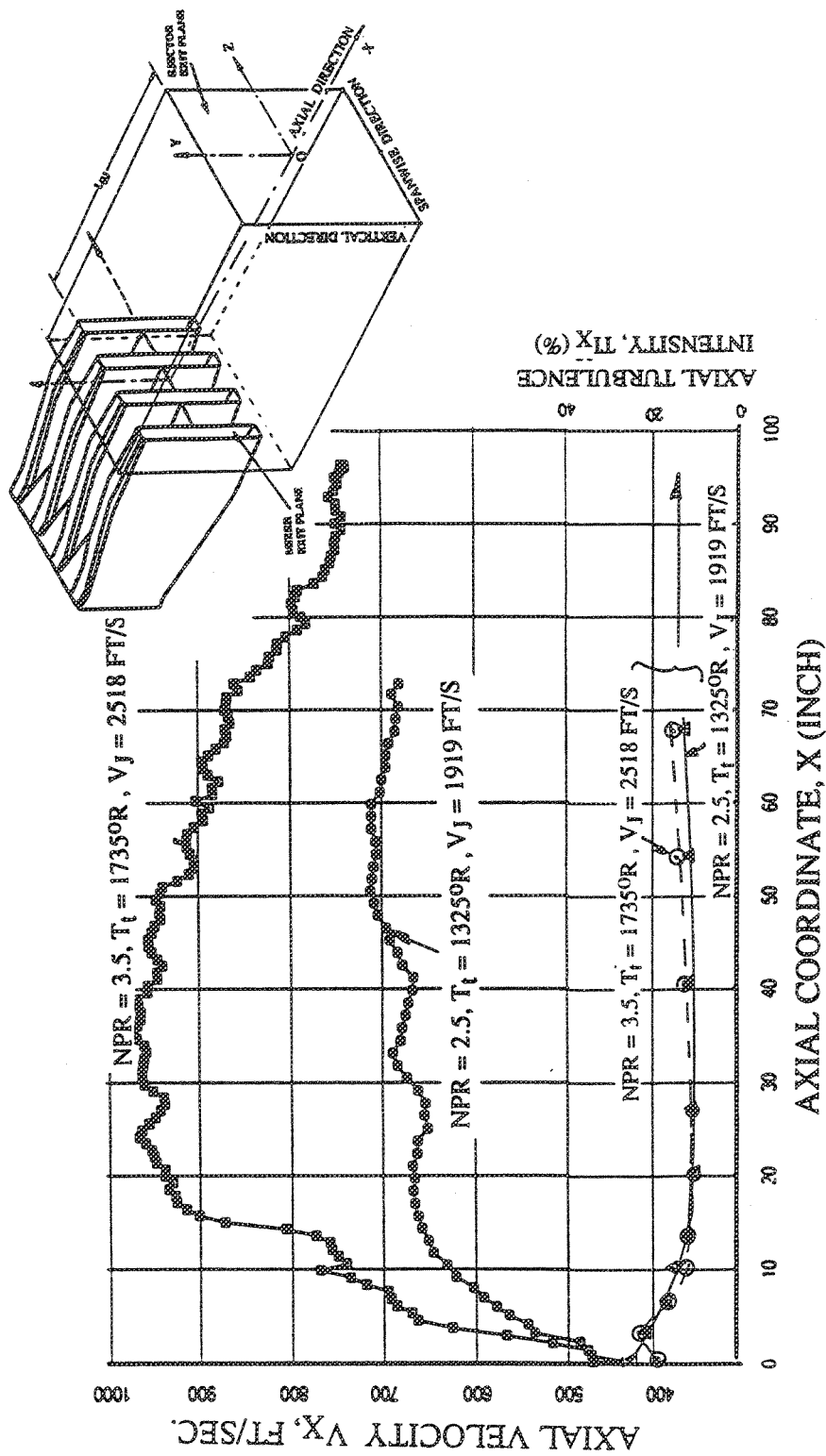


Figure 282. Effect of Nozzle Pressure Ratio on Axial Velocity and Turbulence Intensity Distribution Along X-Direction in External Plume of Axial Mixer-Ejector Nozzle With Short Hardwall Shroud (SAR=4.9, MAR=1.18,  $L_{EJ}=10.46$  in.,  $Y=Z=0$ ,  $Mn=0.32$ )



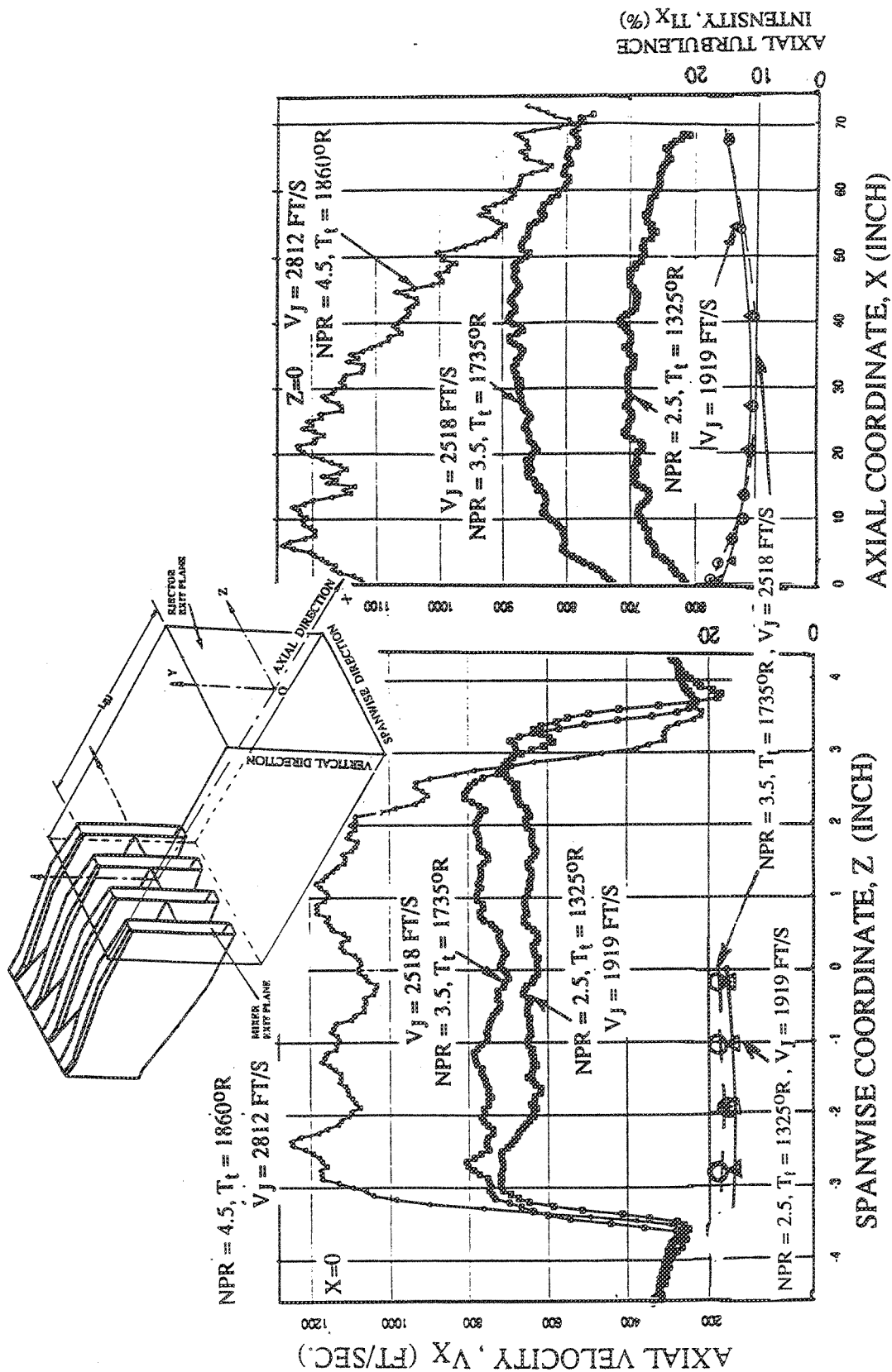


Figure 283. Effect of Nozzle Pressure Ratio on Axial Velocity and Turbulence Intensity Distribution in External Plume of Axial Mixer-Ejector Nozzle With Long Hardwall Shroud (SAR=4.9, MAR=1.18,  $L_{EJ}$ =18.85 in.,  $Mn$ =0.32)

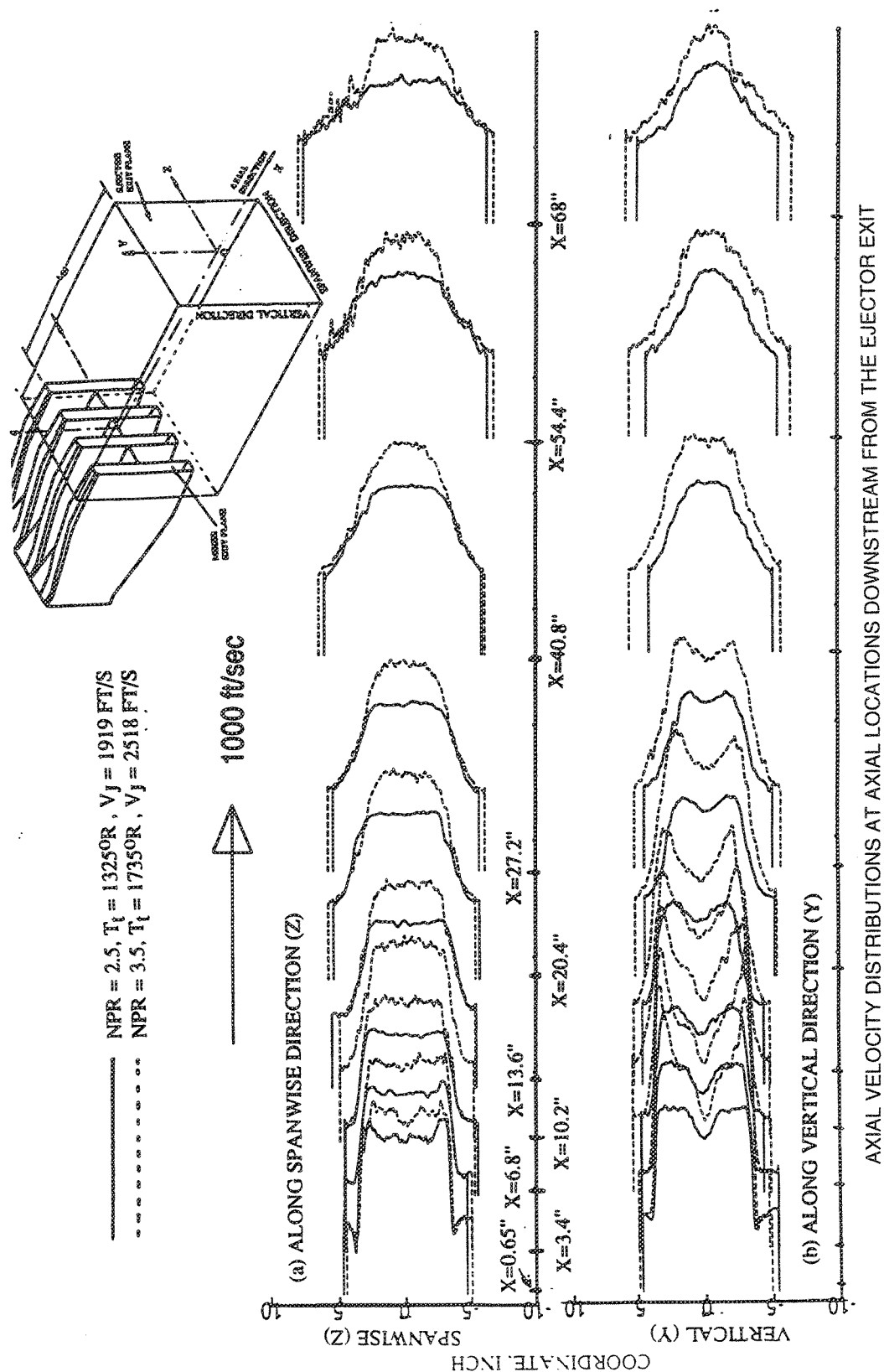


Figure 284. Comparison of Axial Velocity Distributions Between  $\text{NPR}=2.5$ ,  $T_t=1325^\circ\text{R}$ ,  $V_j=1919 \text{ ft/sec}$ , and  $\text{NPR}=3.5$ ,  $T_t=1735^\circ\text{R}$ ,  $V_j=2518 \text{ ft/sec}$  at Various Axial Locations Downstream From Ejector Exit Plane of Axial Mixer-Ejector Nozzles With Hardwall Shroud ( $\text{SAR}=4.9$ ,  $\text{MAR}=1.18$ ,  $L_{Ej}=18.85 \text{ in.}$ ,  $\text{Mn}=0.32$ )

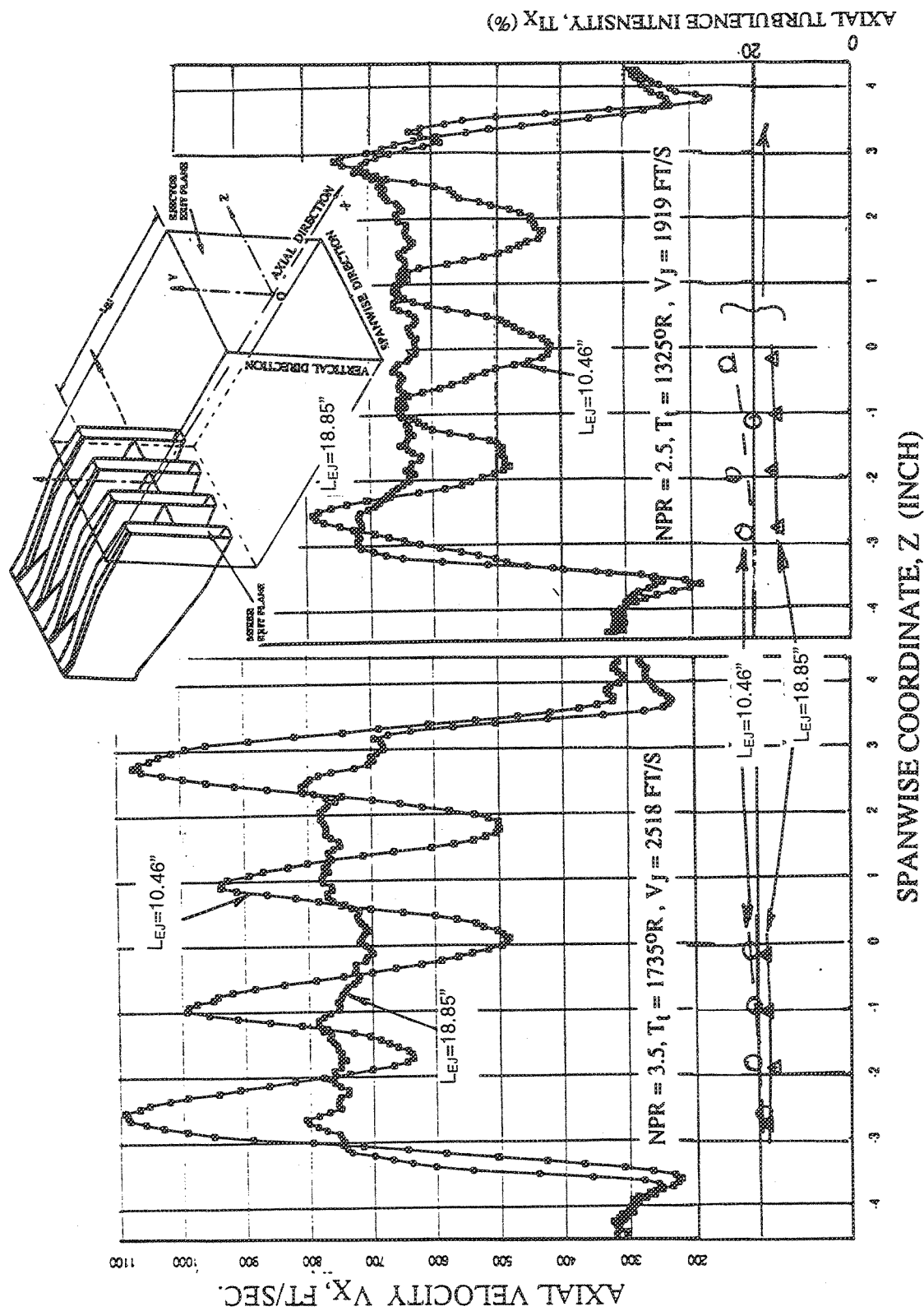


Figure 285. Effect of Shroud Length on Axial Velocity and Turbulence Intensity Distributions Close to Exit Plane of Hardwall Axial Mixer-Ejector Nozzle (SAR=4.9, MAR=1.18, X=0.65, Y=0, Mn=0.32)

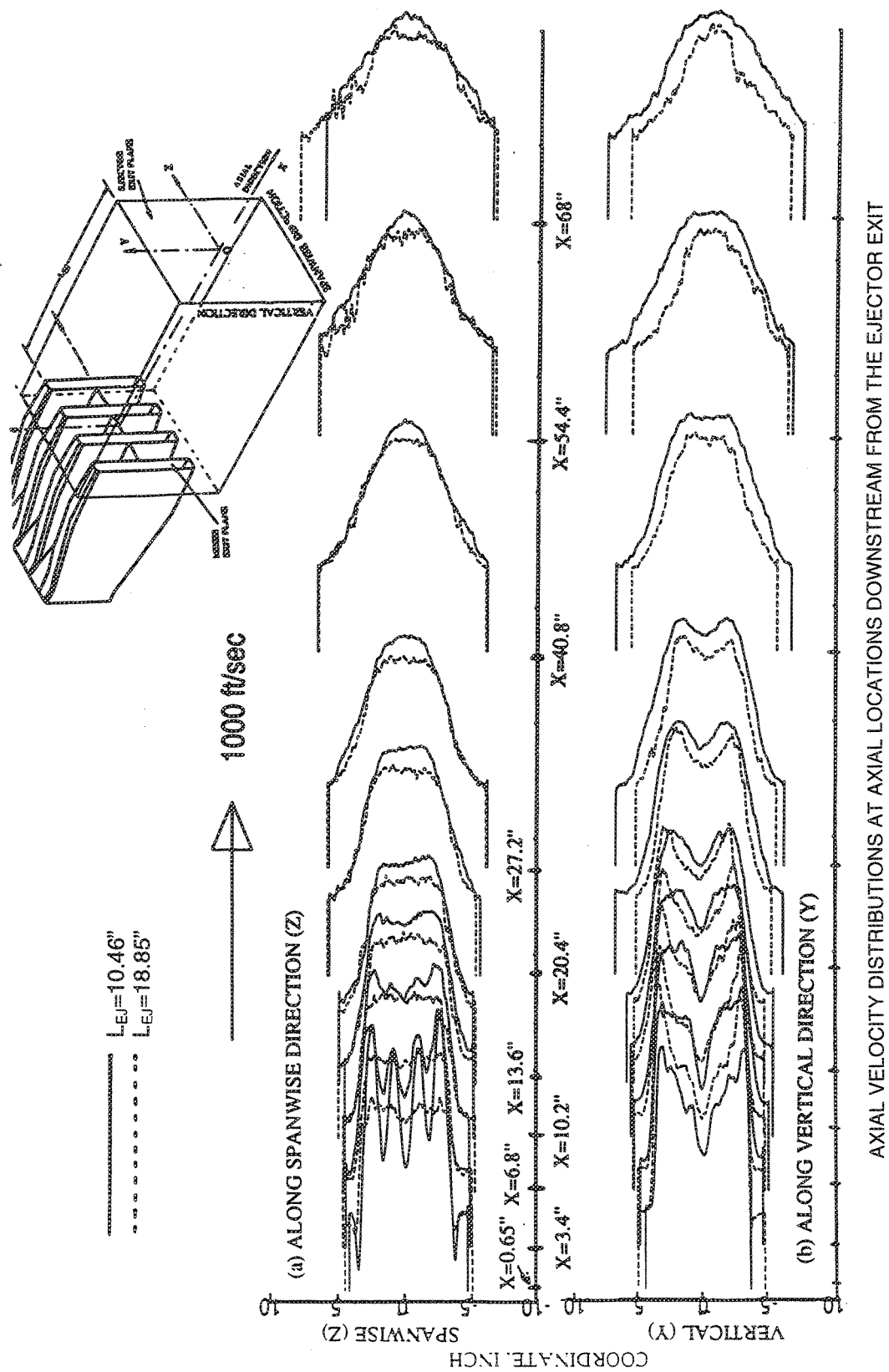


Figure 286. Comparison of Axial Velocity Distributions Between Short and Long Hardwall Shrouds at Various Axial Locations Downstream From Ejector Exit Plane of Axial Mixer-Ejector Nozzles  
(SAR=4.9, MAR=1.18, Mn=0.32, NPR=3.5,  $T_1=1735^\circ R$ ,  $V_1=2518$  ft/sec)

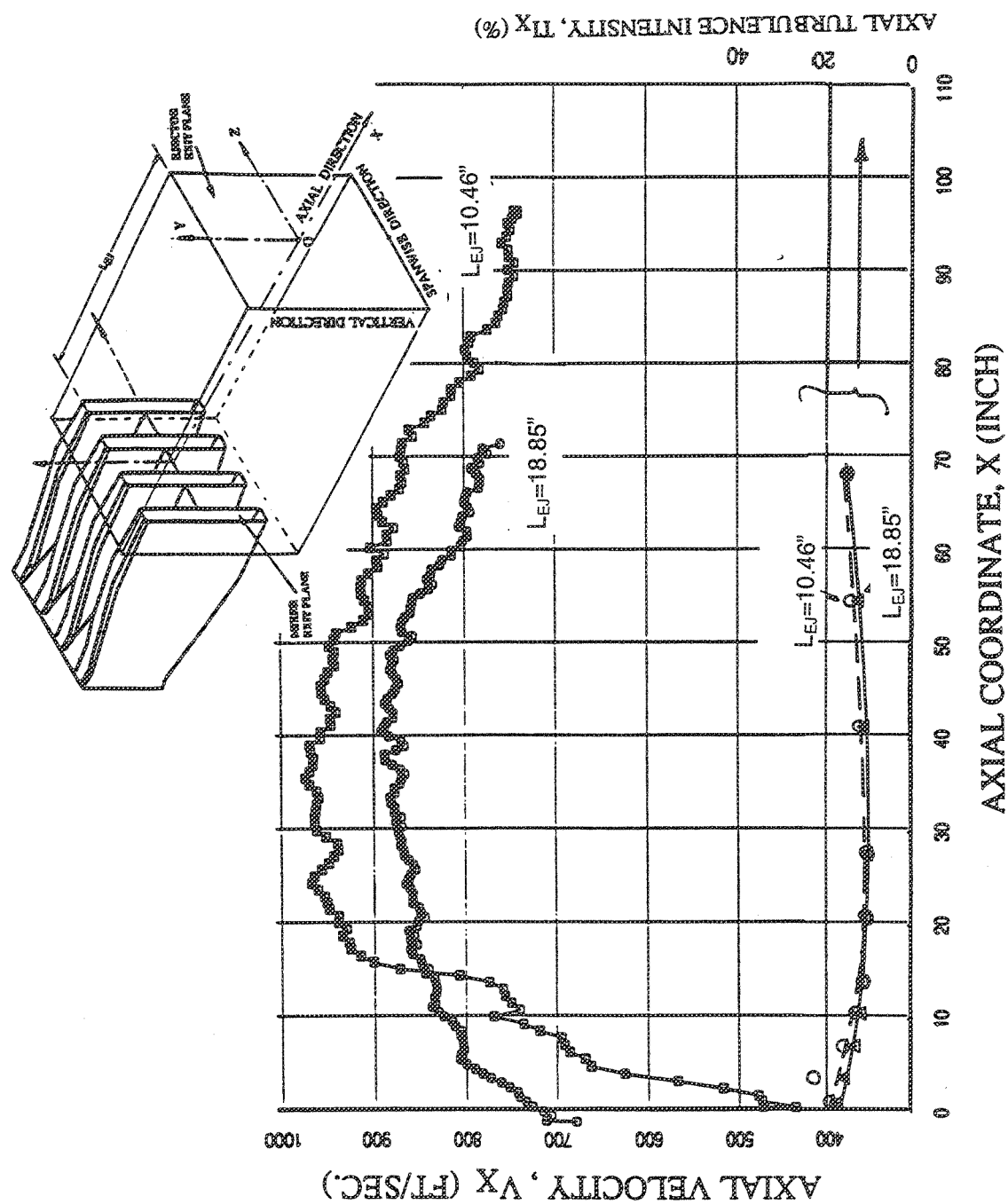


Figure 287. Effect of Shroud Length on Axial Velocity and Turbulence Intensity Distributions Along X-Direction in External Plume of Hardwall Axial Mixer-Ejector Nozzle (SAR=4.9, MAR=1.18,  $Y=Z=0$ ,  $Mn=0.32$ ,  $NPR=3.5$ ,  $T_t=1735^\circ R$ ,  $V_j=2518$  ft/sec)

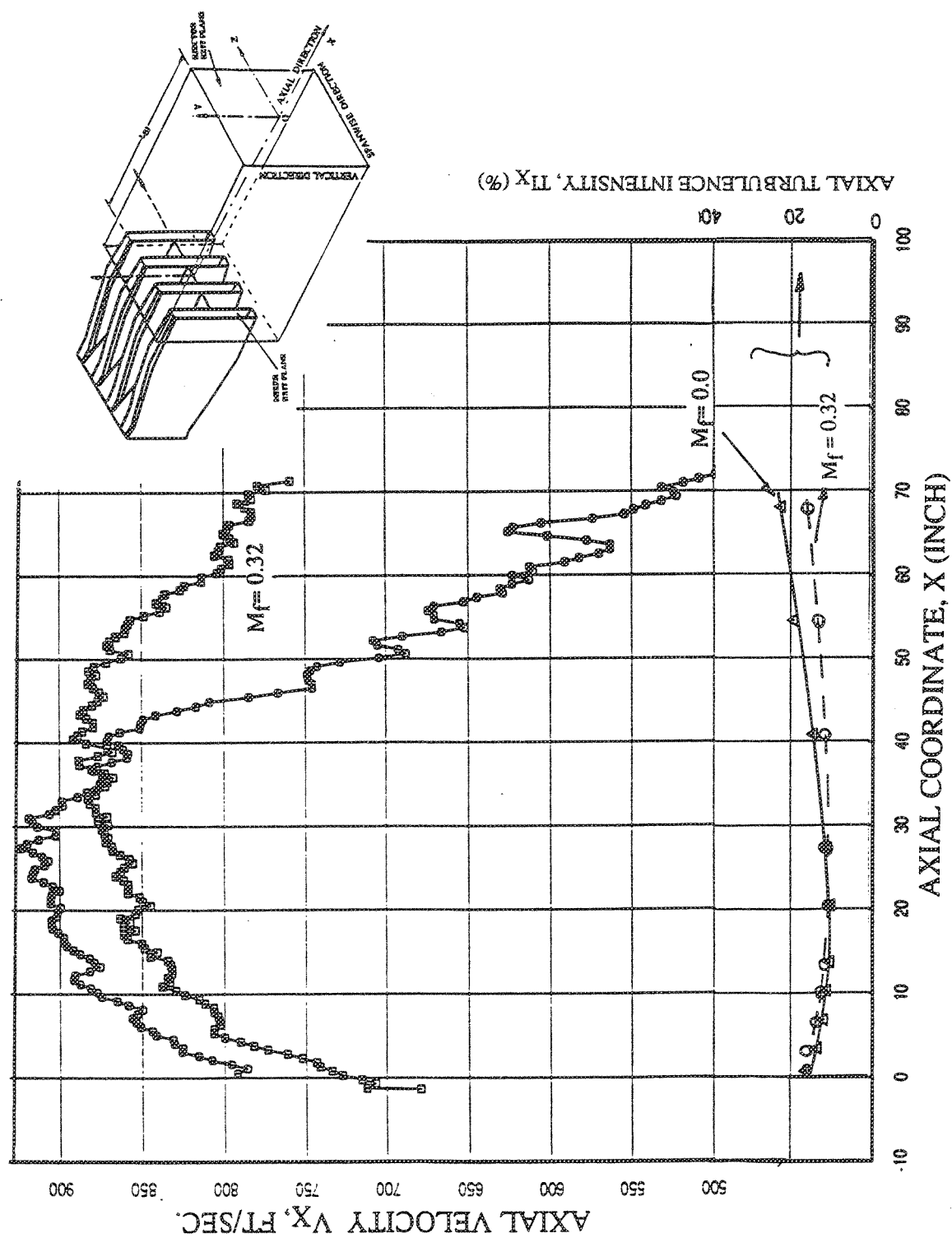


Figure 288. Effect of Flight on Axial Velocity and Turbulence Intensity Distributions Along X-Direction in External Plume of Axial Mixer-Ejector Nozzle With Long Hardwall Shroud (SAR=4.9, MAR=1.18,  $L_{EJ}=18.85$  in.,  $Y=Z=0$ , NPR=3.5,  $T_1=1735^\circ R$ ,  $V_j=2518$  ft/sec)

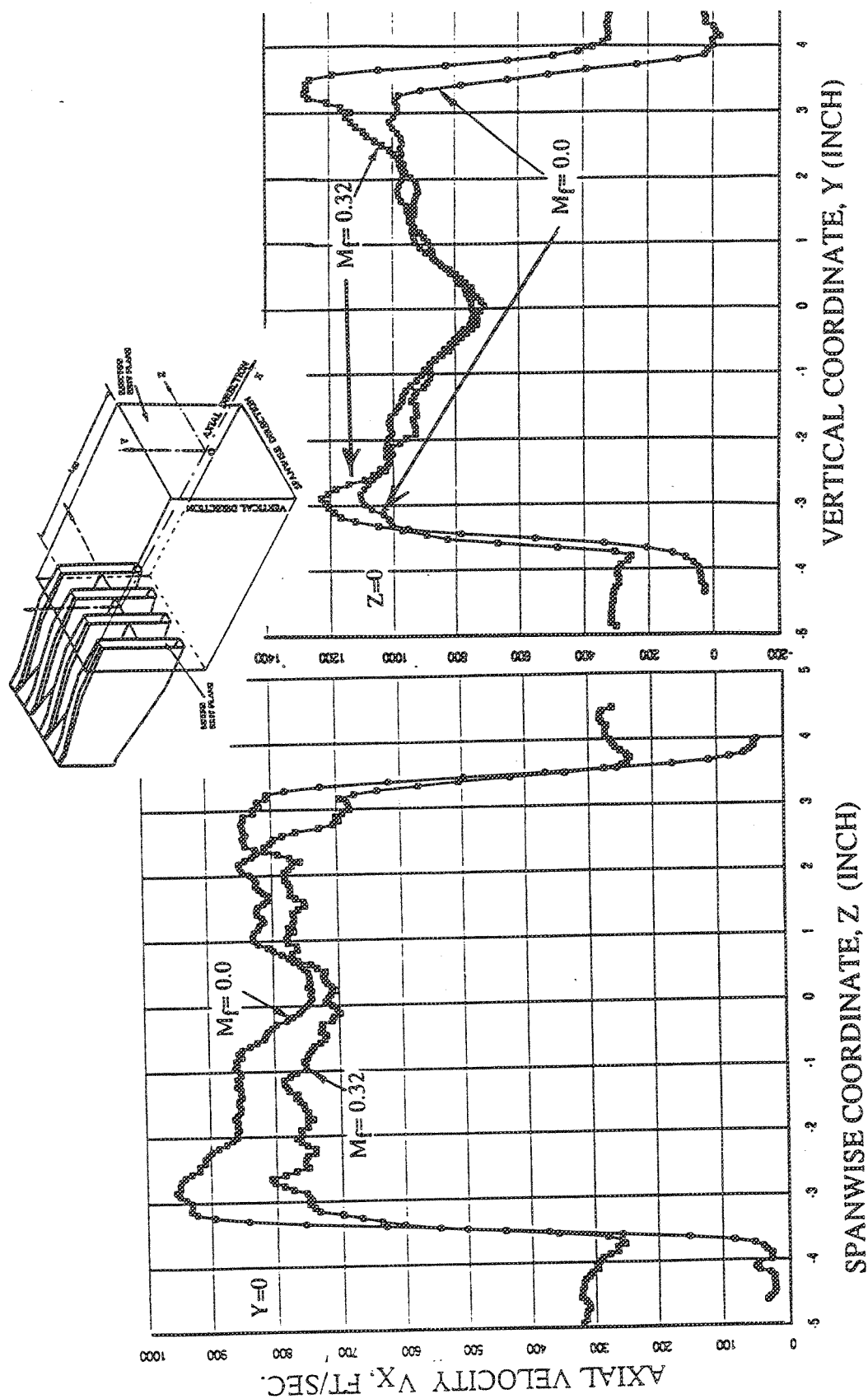


Figure 289. Effect of Flight on Axial Velocity Distribution Close to Exit Plane of Axial Mixer-Ejector Nozzle With Long Hardwall Shroud  
( $SAR=4.9$ ,  $MAR=1.18$ ,  $L_{EJ}=18.85$  in.,  $X=0.65$  in.,  $NPR=3.5$ ,  $T_t=1735^\circ R$ ,  $V_j=2518$  ft/sec)

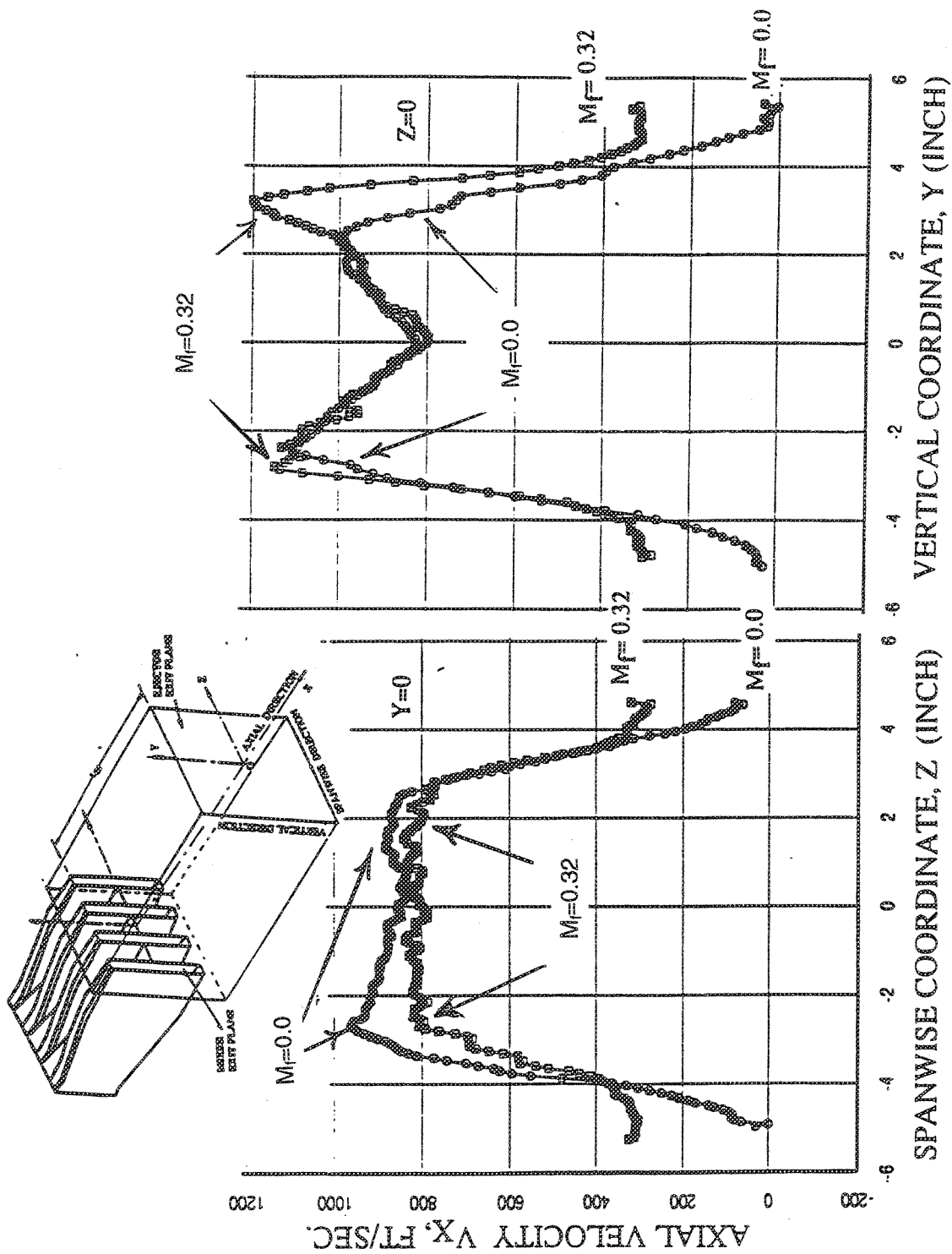


Figure 290. Effect of Flight on Axial Velocity Distribution At One Ejector Width ( $X=W=6.8$  in.) Downstream of Exit Plane of Axial Mixer-Ejector Nozzle With Long Hardwall Shroud ( $SAR=4.9$ ,  $MAR=1.18$ ,  $L_{EJ}=18.85$  in.,  $NPR=3.5$ ,  $T_i=1735^\circ R$ ,  $V_i=2518$  ft/sec)



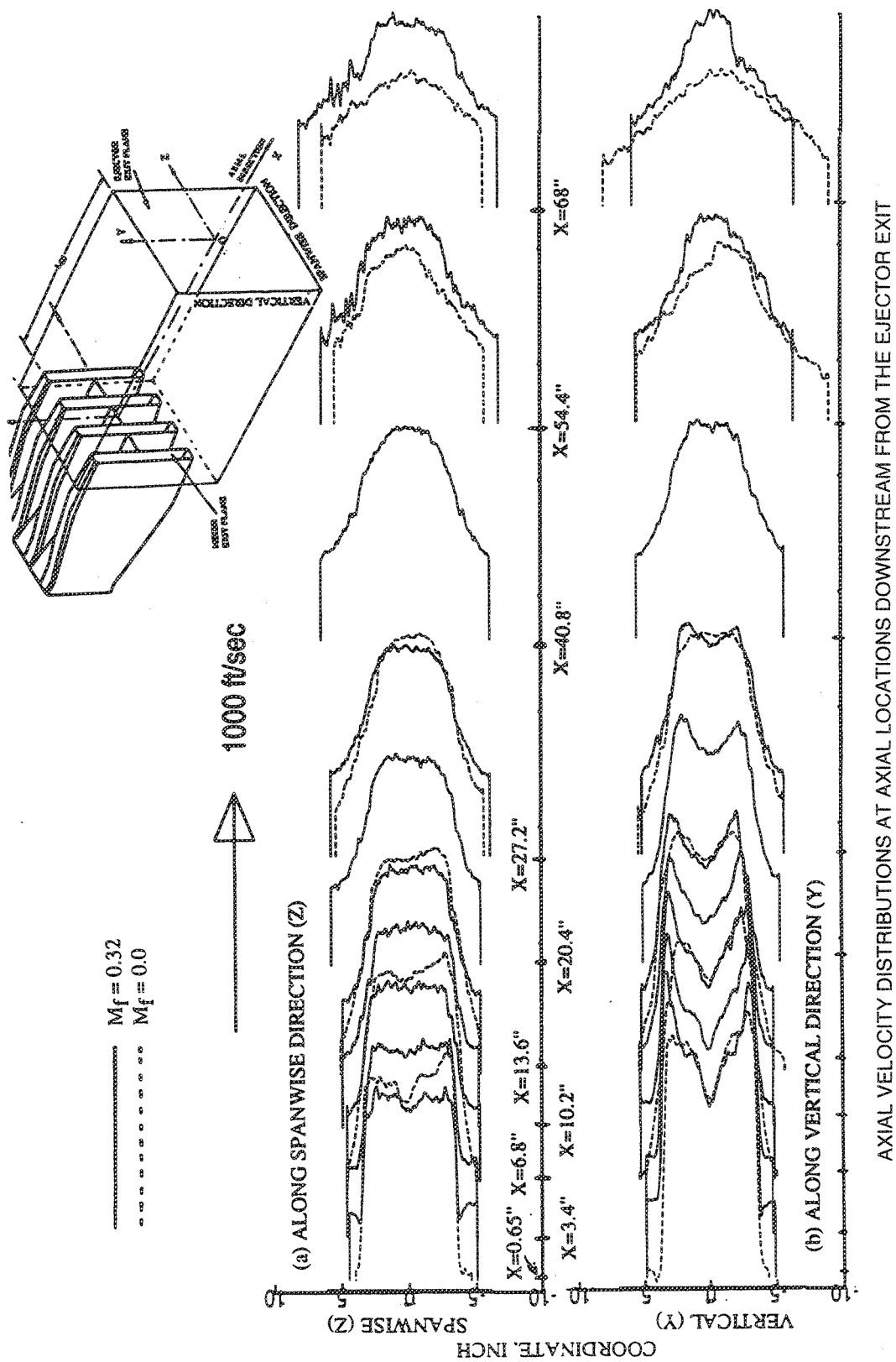


Figure 291. Comparison of Axial Velocity Distributions Between With/Without Flight Simulation at Various Axial Locations Downstream From Ejector Exit Plane of Axial Mixer-Ejector Nozzles With Hardwall Shroud  
(SAR=4.9, MAR=1.18,  $L_{EJ}=18.85$  in., NPR=3.5,  $T_1=1735^\circ R$ ,  $V_1=2518$  ft/sec)



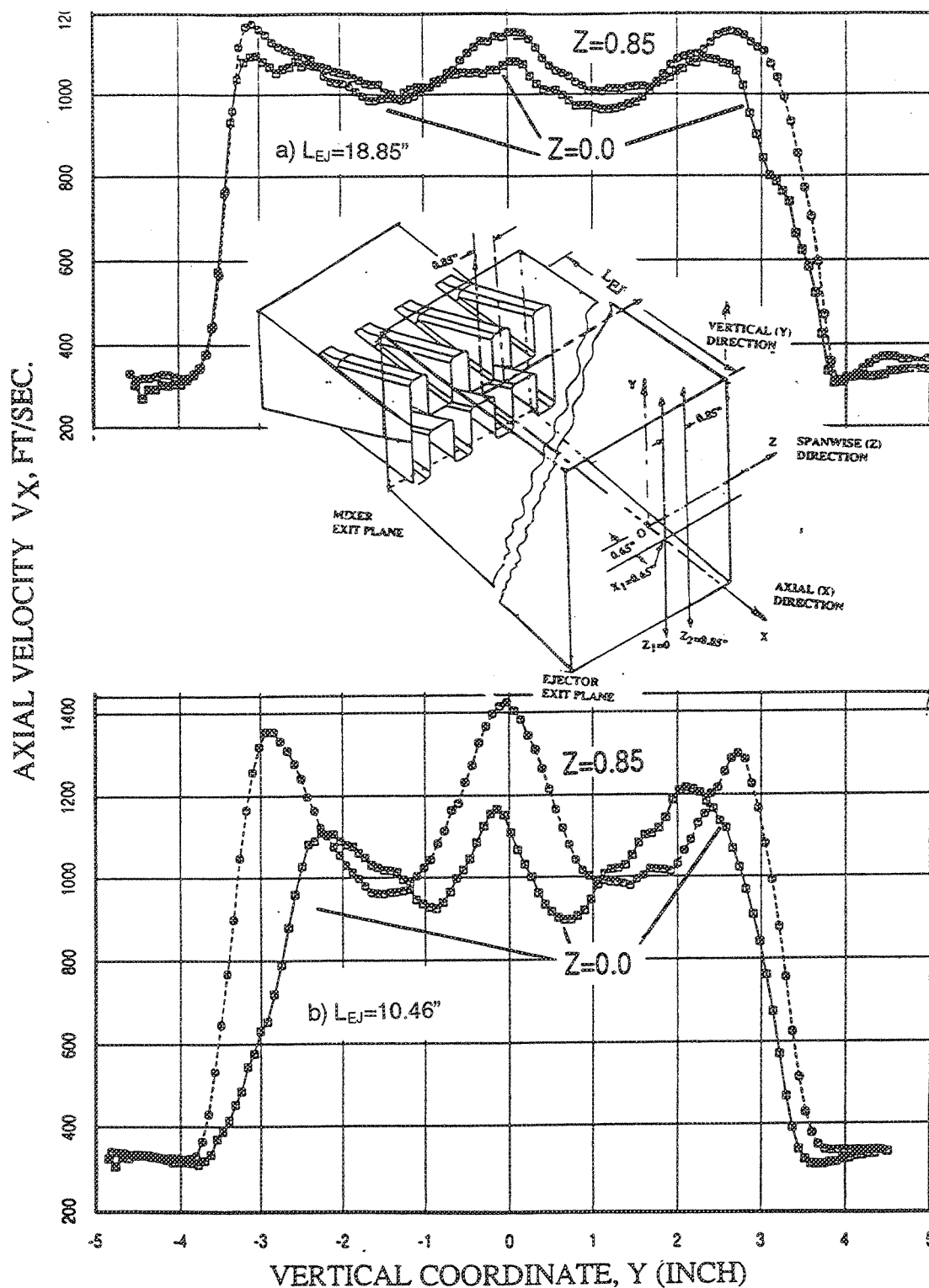


Figure 293. Axial Velocity Distributions Along Chute Height At Hot and Cold Flow Regions Close to Ejector Exit Plane of Vortical Mixer-Ejector Nozzle With Hardwall Shroud  
( $SAR=4.9$ ,  $MAR=1.18$ ,  $X=0.65$  in.,  $Mn=0.32$ ,  $NPR=3.5$ ,  $T_t=1735^\circ R$ ,  $V_j=2518$  ft/sec)

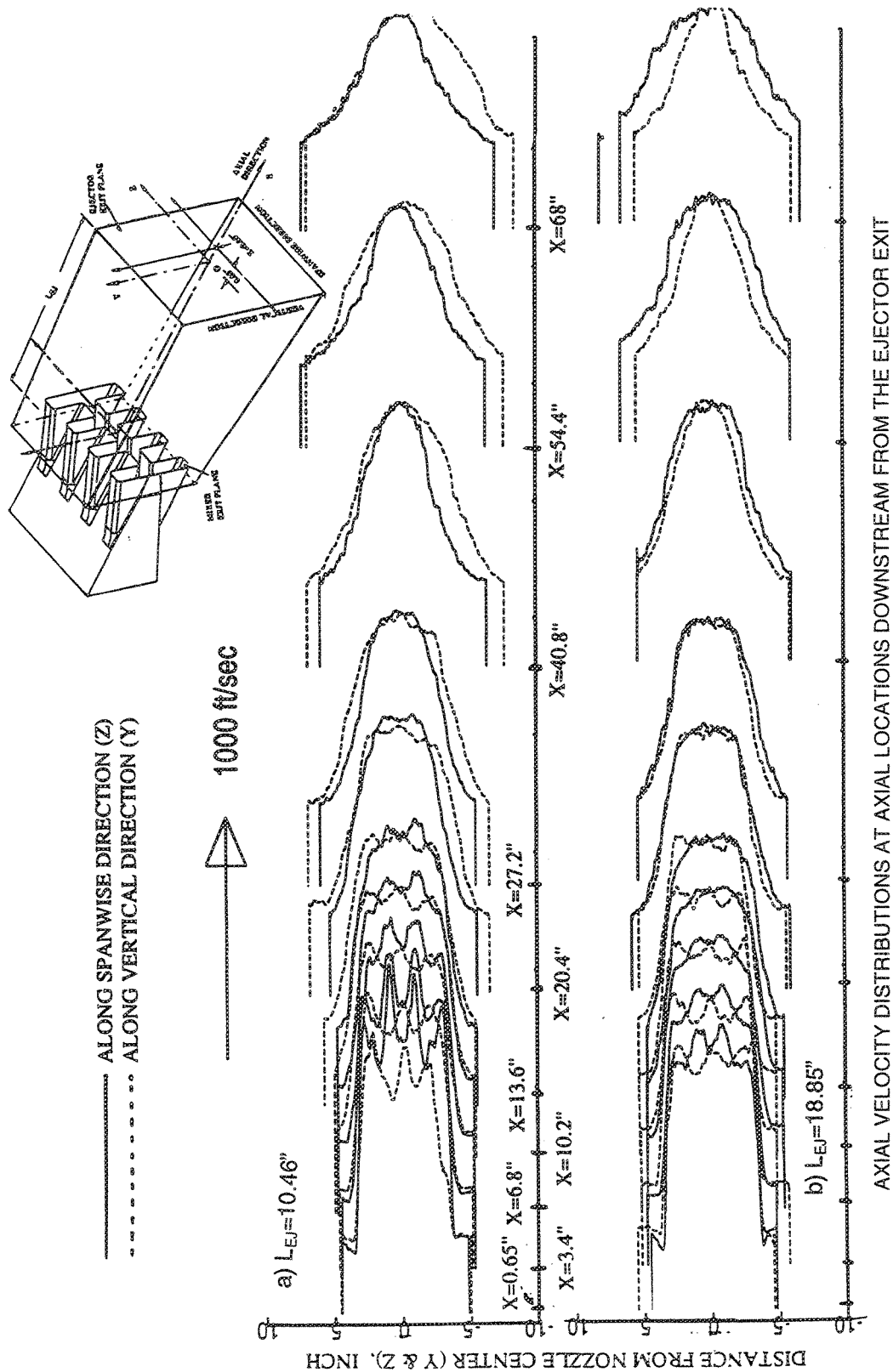


Figure 294. Comparison of Axial Velocity Distributions Between Spanwise (Z) and Vertical (Y) Directions at Various Axial Locations Downstream From Ejector Exit Plane of Vortical Mixer-Ejector Nozzles With Hardwall Shroud (SAR=4.9, MAR=1.18, Mn=0.32, NPR=3.5,  $T_t=1735^\circ\text{R}$ ,  $V_j=2518\text{ ft/sec}$ ) (a)  $L_{EJ}=10.46\text{ in.}$  (b)  $L_{EJ}=18.85\text{ in.}$

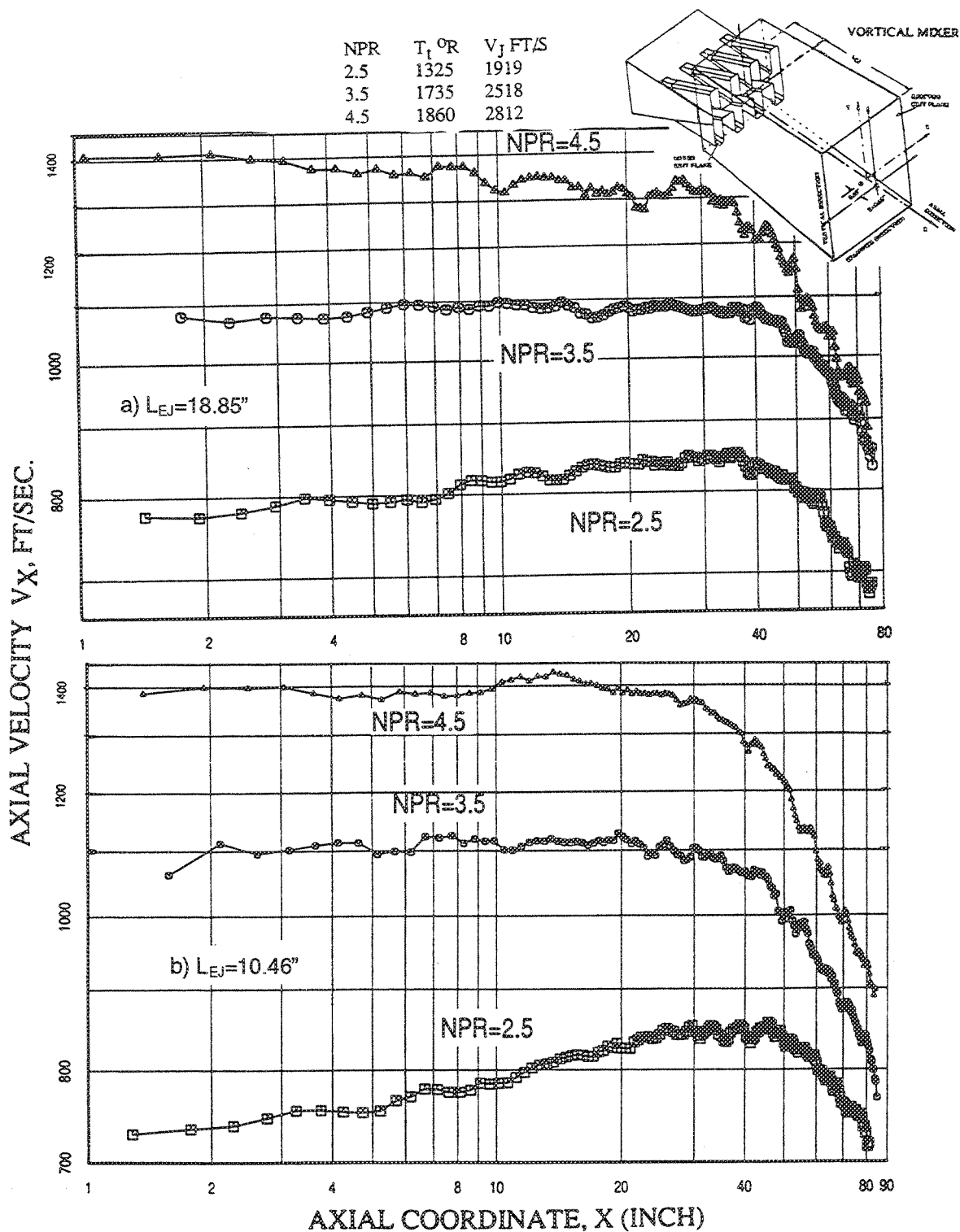


Figure 295. Effect of Nozzle Pressure Ratio on Axial Velocity Distributions Along Y-Direction in External Plume of Vortical Mixer-Ejector Nozzle With Hardwall Shroud ( $SAR=4.9$ ,  $MAR=1.18$ ,  $Z=0$ ,  $Mn=0.32$ )

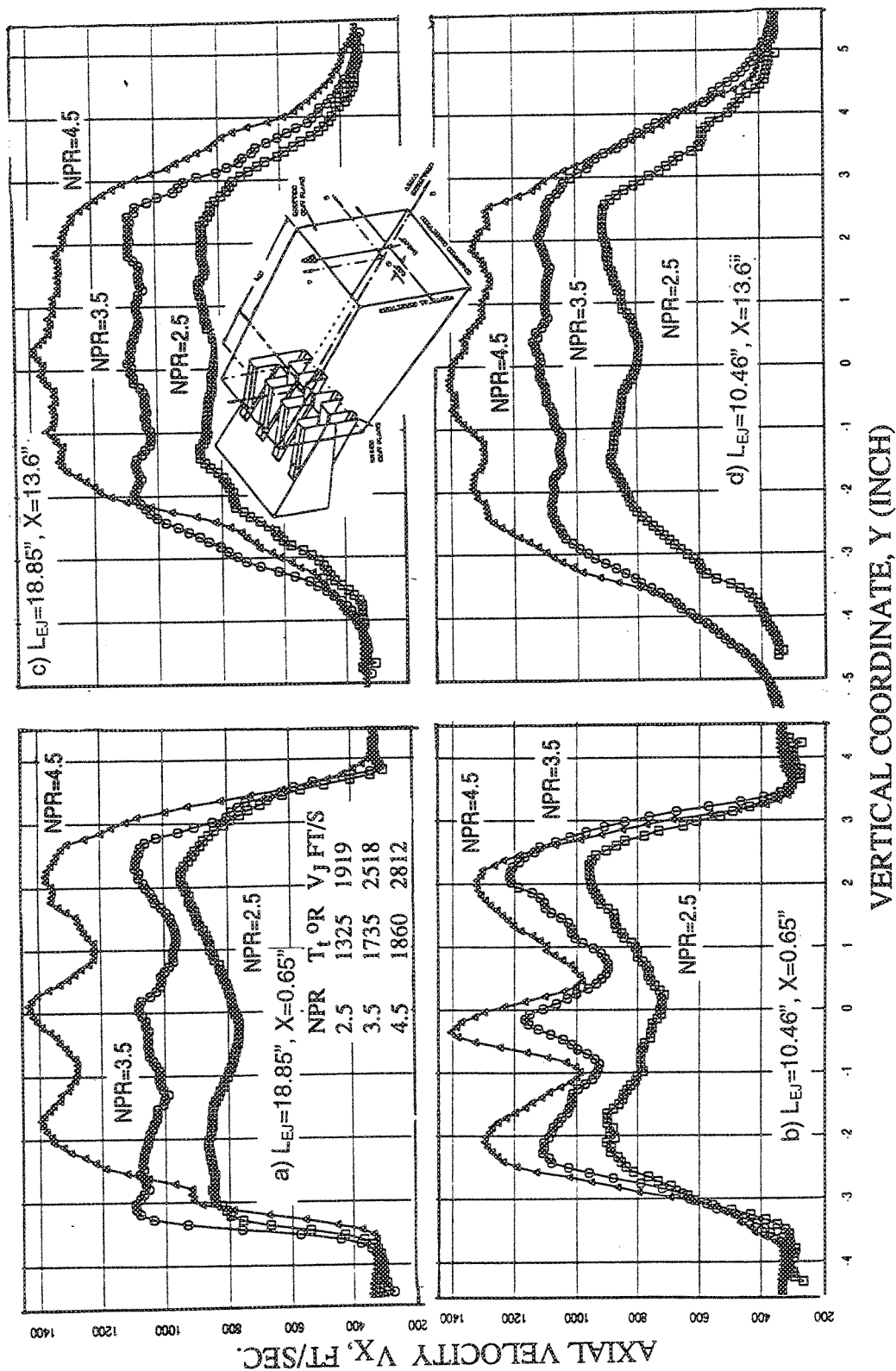


Figure 296. Effect of Nozzle Pressure Ratio on Axial Velocity Distributions Along Z-Direction in External Plume of Vortical Mixer-Ejector Nozzle With Hardwall Shroud (SAR=4.9, MAR=1.18, Y=0, Mn=0.32)

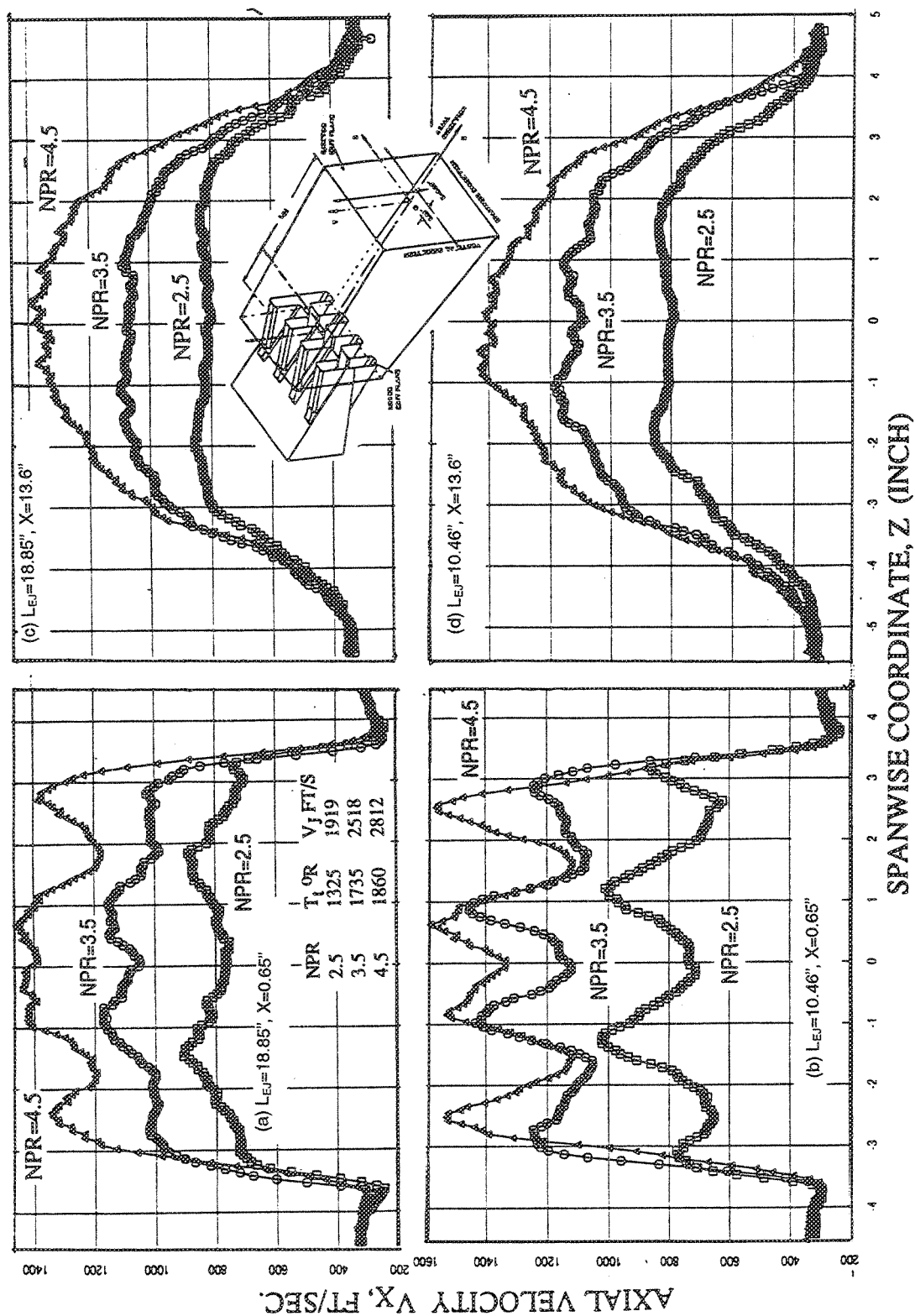


Figure 297. Comparison of Axial Velocity Distribution Between  $NPR=2.5$ ,  $T_1=1325^\circ R$ ,  $V_j=1919$  ft/sec, and  $NPR=3.5$ ,  $T_1=1735^\circ R$ ,  $V_j=2518$  ft/sec at Various Axial Locations Downstream From Ejector Exit Plane of Vortical Mixer-Ejector Nozzles With Hardwall Shroud ( $SAR=4.9$ ,  $MAR=1.18$ ,  $L_{EJ}=10.46$  in.,  $Mn=0.32$ )

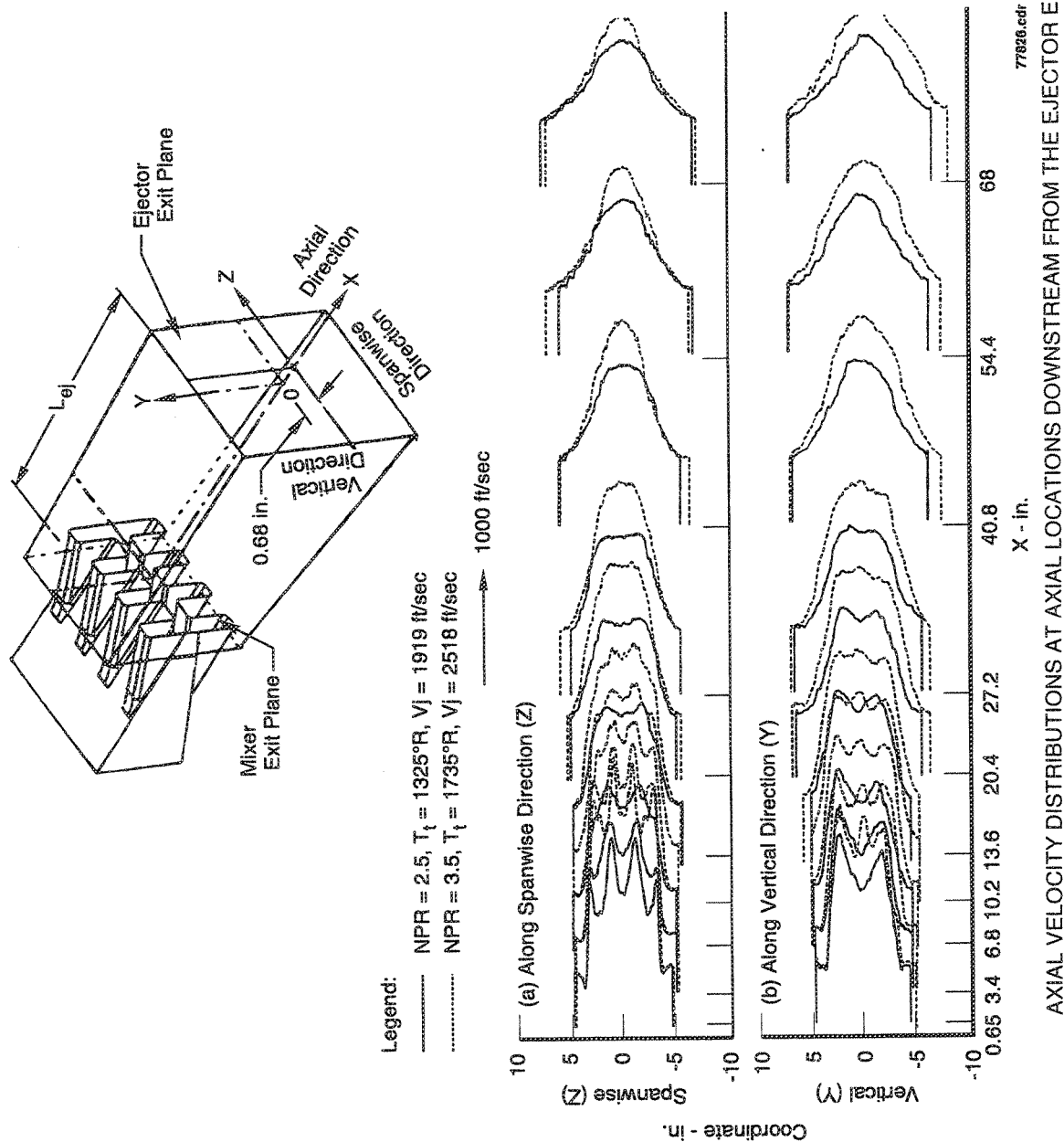


Figure 298. Comparison of Axial Velocity Distribution Between  $NPR=2.5$ ,  $T_t=1325^\circ R$ ,  $V_j=1919$  ft/sec, and  $NPR=3.5$ ,  $T_t=1735^\circ R$ ,  $V_j=2518$  ft/sec at Various Axial Locations Downstream From Ejector Exit Plane of Vortical Mixer-Ejector Nozzles With Hardwall Shroud ( $SAR=4.9$ ,  $MAR=1.18$ ,  $L_{ej}=10.46$  in.,  $Mn=0.32$ )



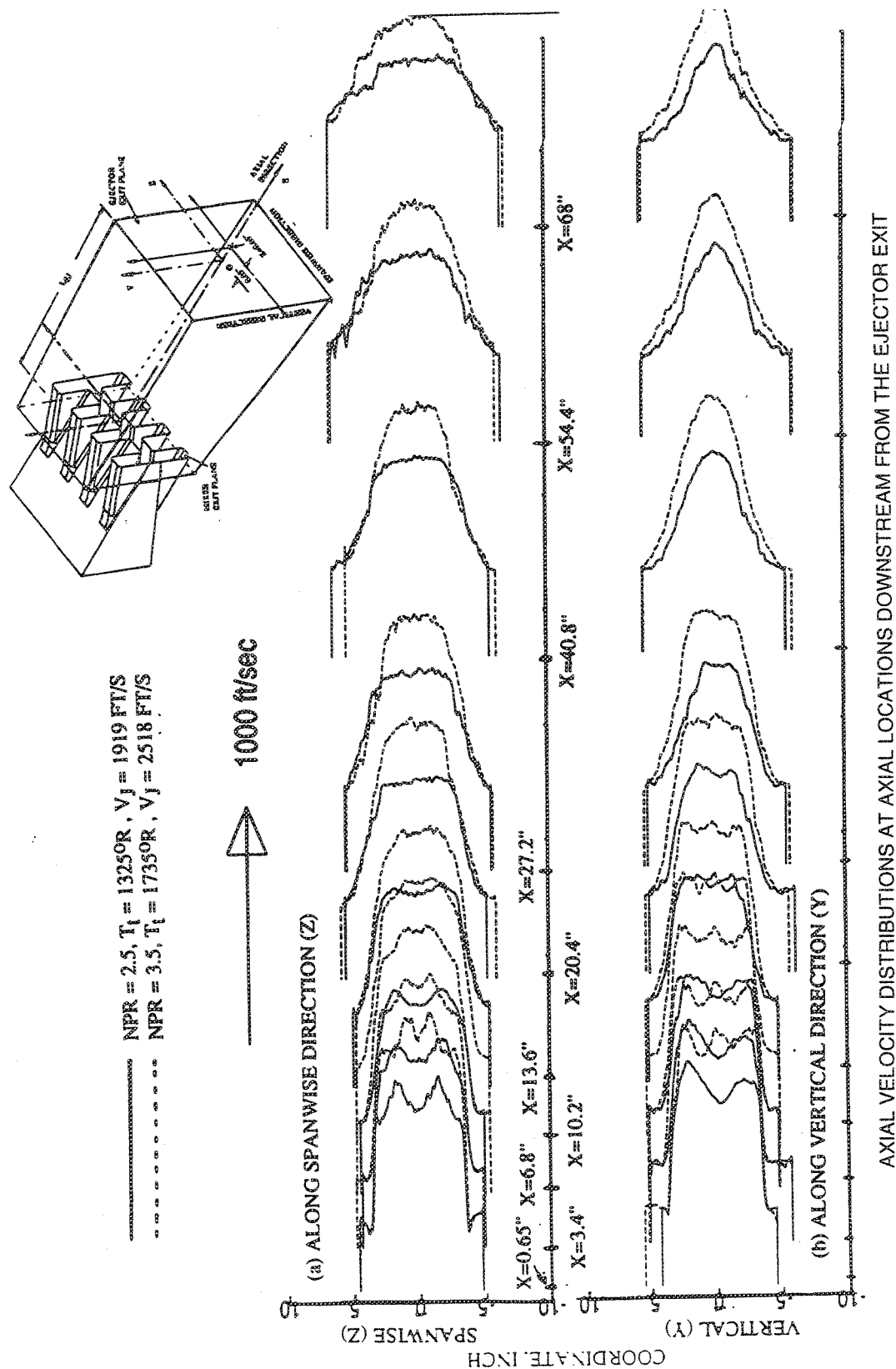


Figure 299. Comparison of Axial Velocity Distribution Between  $NPR=2.5$ ,  $T_t=1325^\circ R$ ,  $V_j=1919 \text{ ft/sec}$ , and  $NPR=3.5$ ,  $T_t=1735^\circ R$ ,  $V_j=2518 \text{ ft/sec}$  at Various Axial Locations Downstream From Ejector Exit Plane of Vortical Mixer-Ejector Nozzles With Hardwall Shroud ( $SAR=4.9$ ,  $MAR=1.18$ ,  $L_{EJ}=18.85 \text{ in.}$ ,  $Mn=0.32$ )

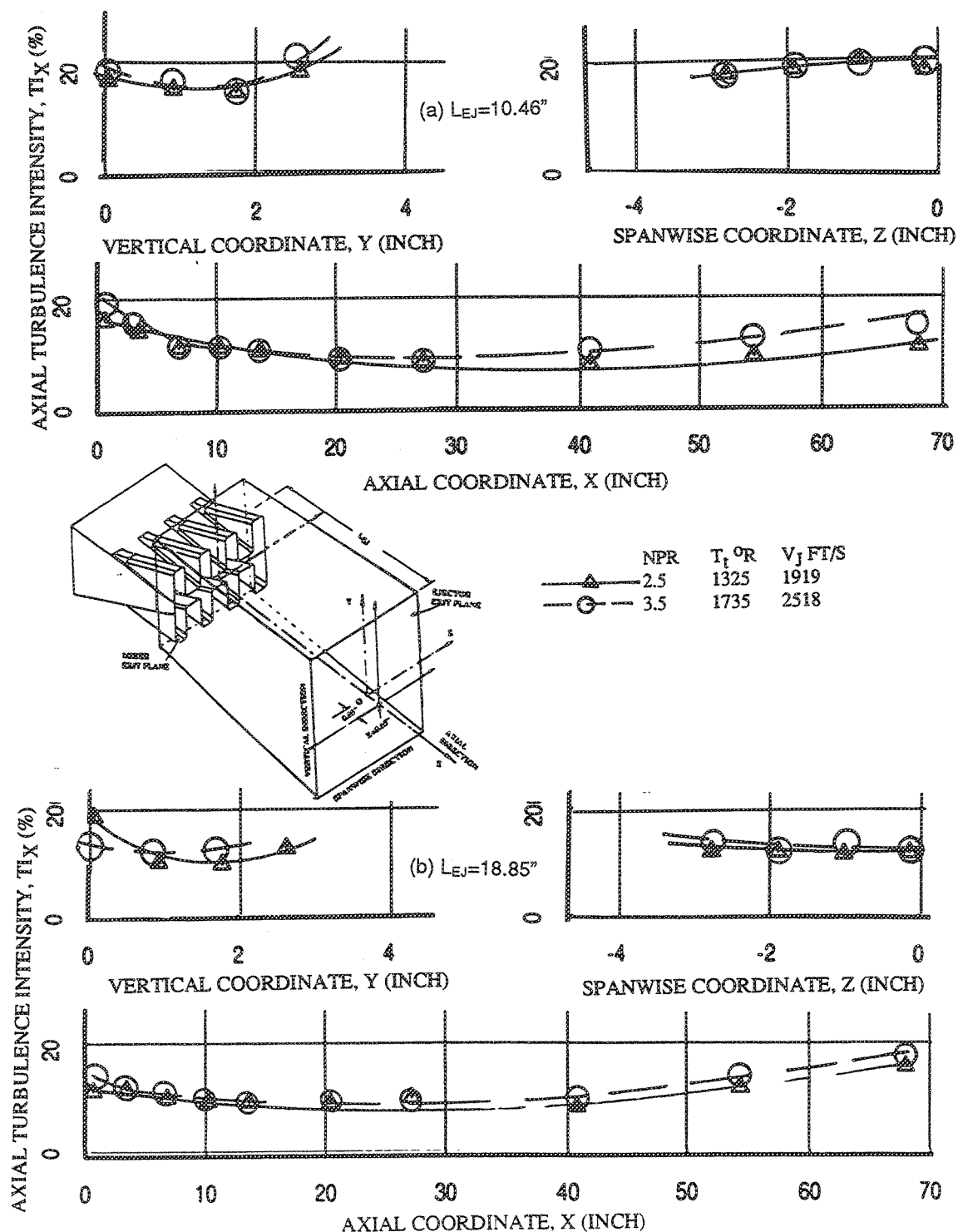


Figure 300. Effect of Nozzle Pressure Ratio on Axial Turbulence Intensity Distributions Along Vertical (Y), Spanwise (Z), and Axial (X) Directions in External Plume of Vortical Mixer-Ejector Nozzle With Hardwall Shroud ( $SAR=4.9$ ,  $MAR=1.18$ ,  $Mn=0.32$ )

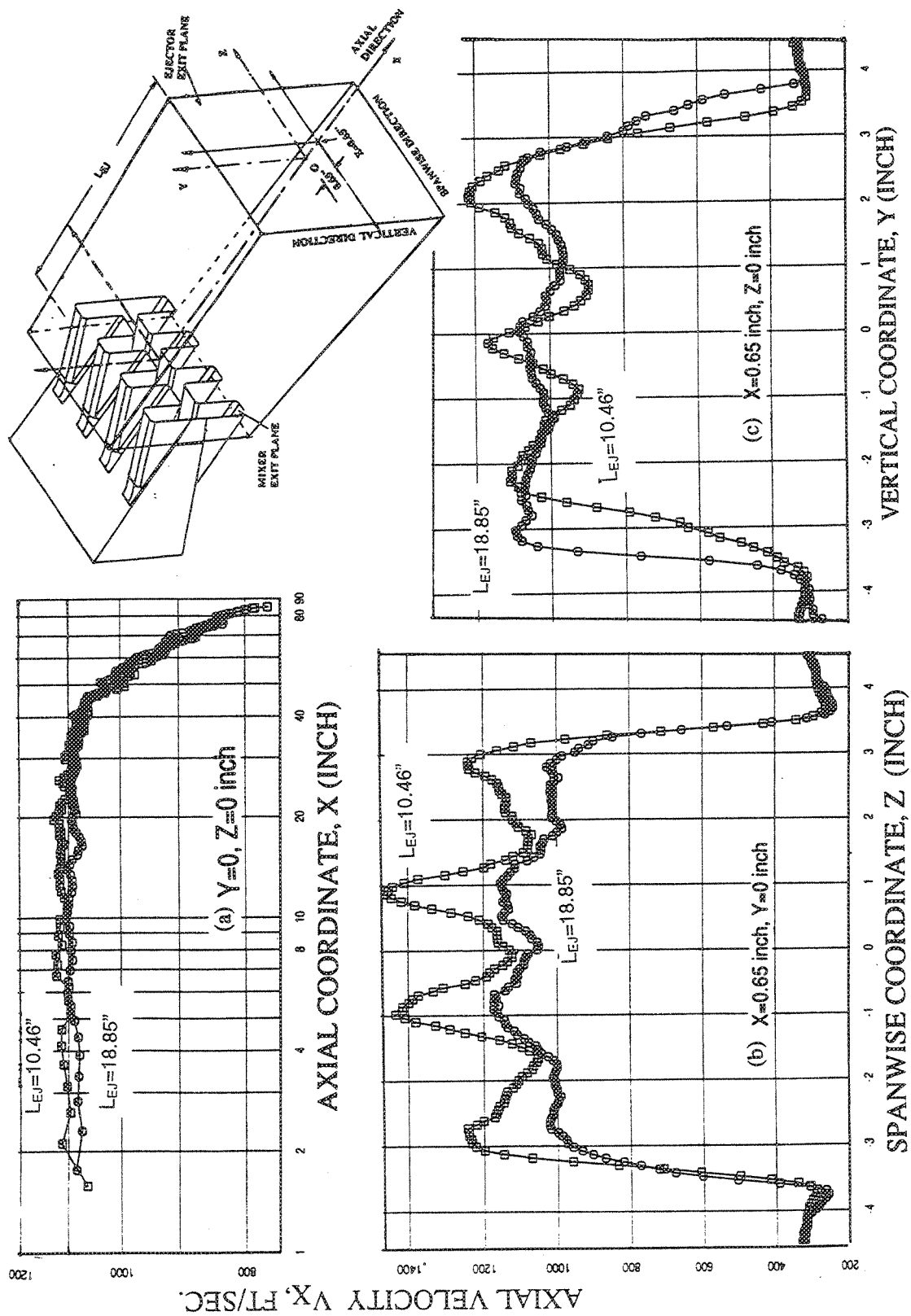


Figure 301. Effect of Shroud Length on Axial Velocity Distribution in External Plume of Hardwall Vortical Mixer-Ejector Nozzle  
( $SAR=4.9$ ,  $MAR=1.18$ ,  $Mn=0.32$ ,  $NPR=3.5$ ,  $T_t=1735^\circ R$ ,  $V_j=2518$  ft/sec)

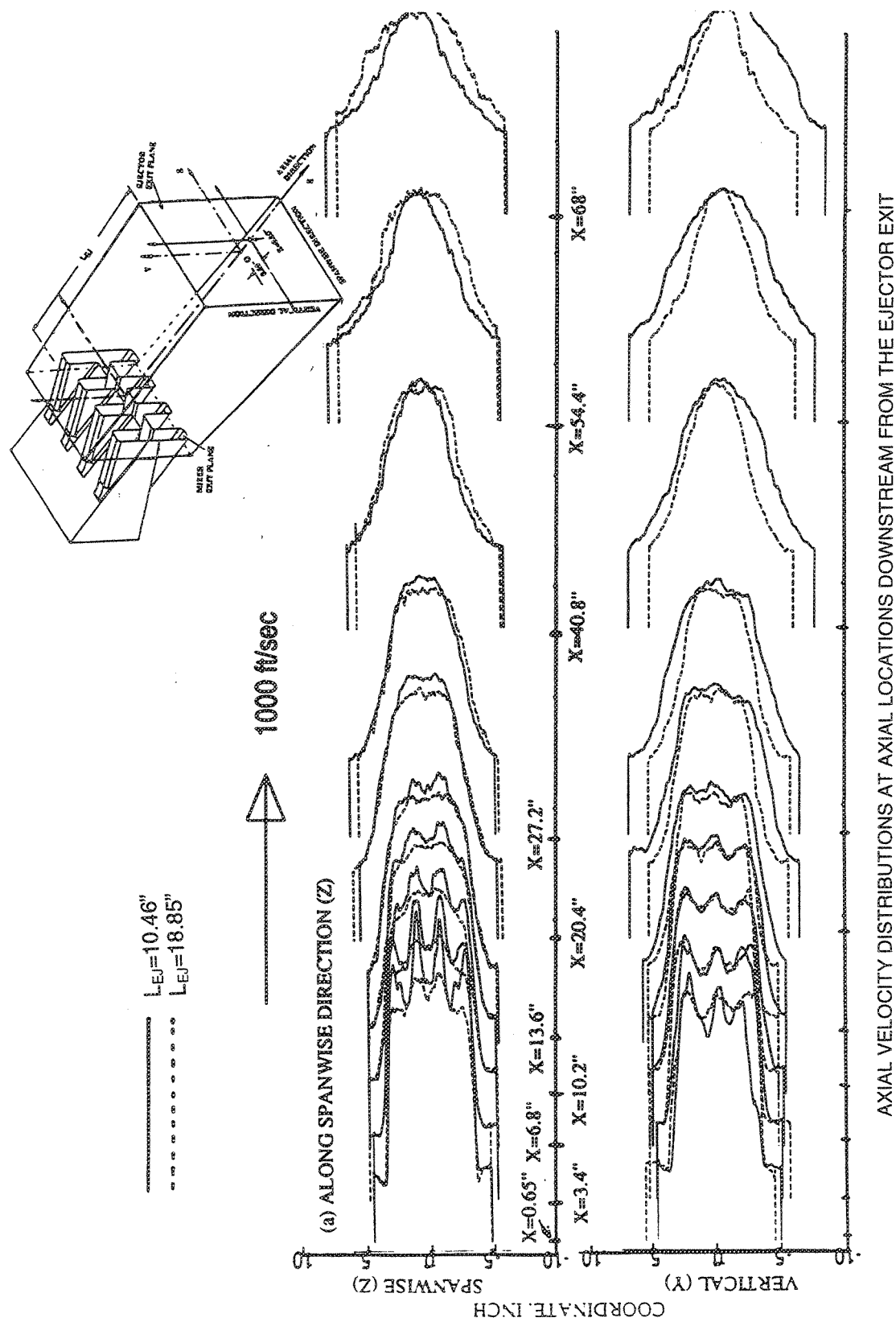


Figure 302. Comparison of Axial Velocity Distributions Between Short and Long Hardwall Shrouds at Various Locations Downstream From Ejector Exit Plane of Vortical Mixer-Ejector Nozzles (SAR=4.9, MAR=1.18, Mn=0.32, NPR=3.5,  $T_t=1735^\circ R$ ,  $V_j=2518$  ft/sec)

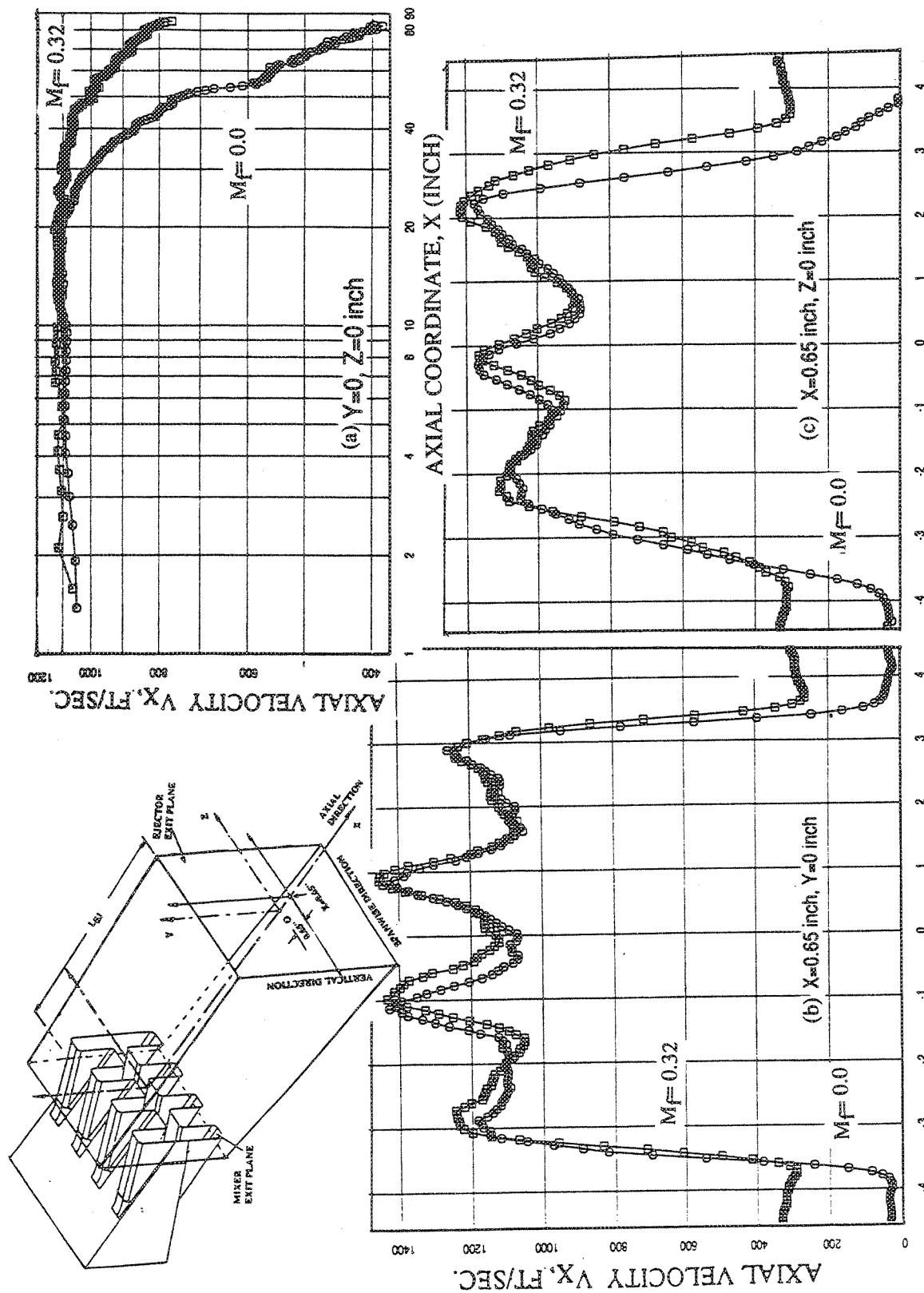


Figure 303. Effect of Flight on Axial Velocity Distribution in External Plume of Vortical Mixer-Ejector Nozzle With Short Hardwall Shroud  
(SAR=4.9, MAR=1.18,  $M_F=0.32$ ,  $L_{EJ}=10.46$  in., NPR=3.5,  $T_t=1735^\circ R$ ,  $V_j=2518$  ft/sec)

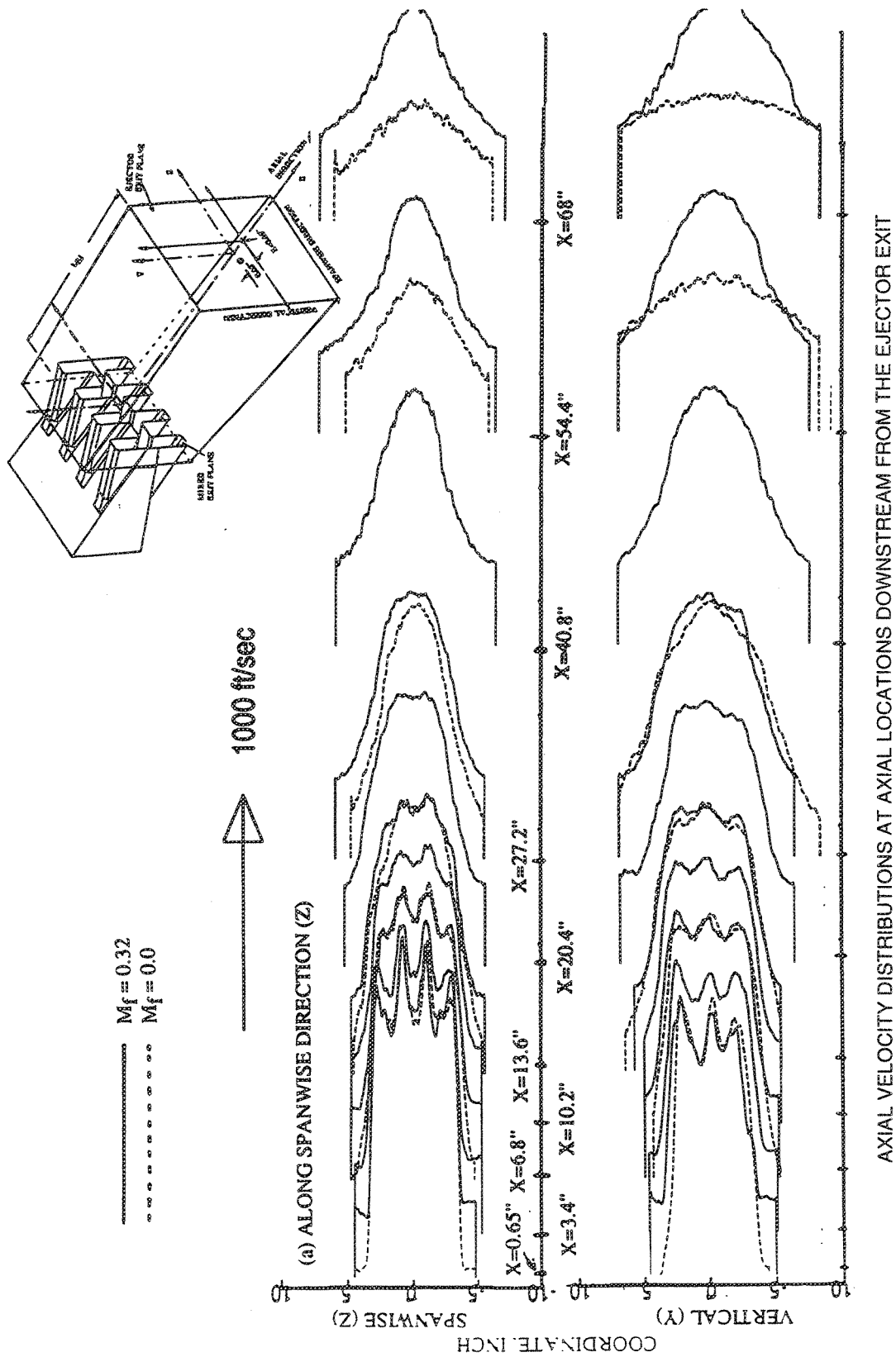


Figure 304. Comparison of Axial Velocity Distributions Between With/Without Flight Simulation at Various Axial Locations Downstream From Ejector Exit Plane of Vortical Mixer-Ejector Nozzles With Hardwall Shroud  
(SAR=4.9, MAR=1.18,  $L_{EJ}$ =10.46 in., NPR=3.5,  $T_t$ =1735°R,  $V_t$ =2518 ft/sec)

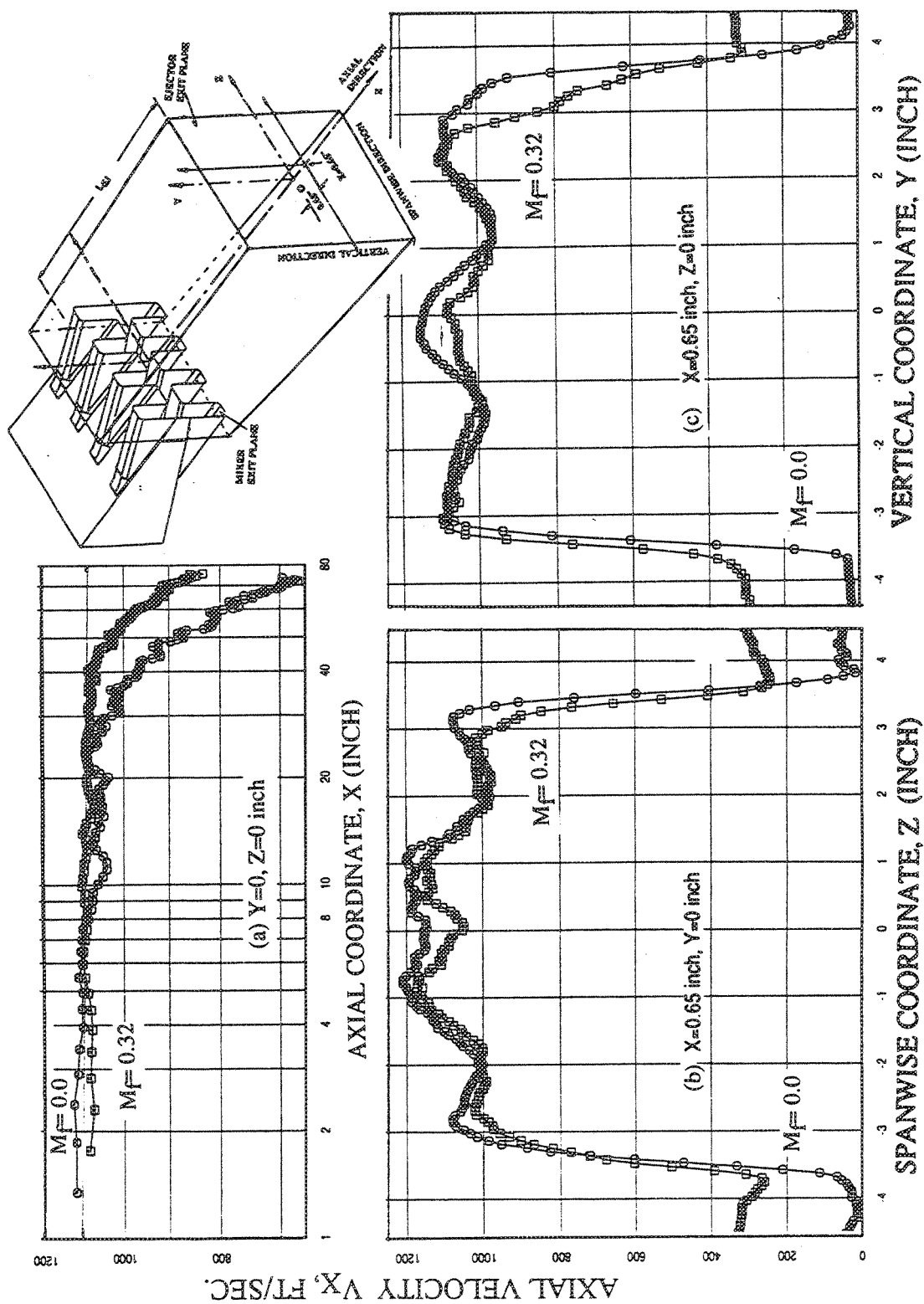


Figure 305. Effect of Flight on Axial Velocity Distribution in External Plume of Vortical Mixer-Ejector Nozzle With Long Hardwall Shroud  
(SAR=4.9, MAR=1.18,  $L_{EJ}$ =18.85 in., NPR=3.5,  $T_t$ =1735°R,  $V_j$ =2518 ft/sec)

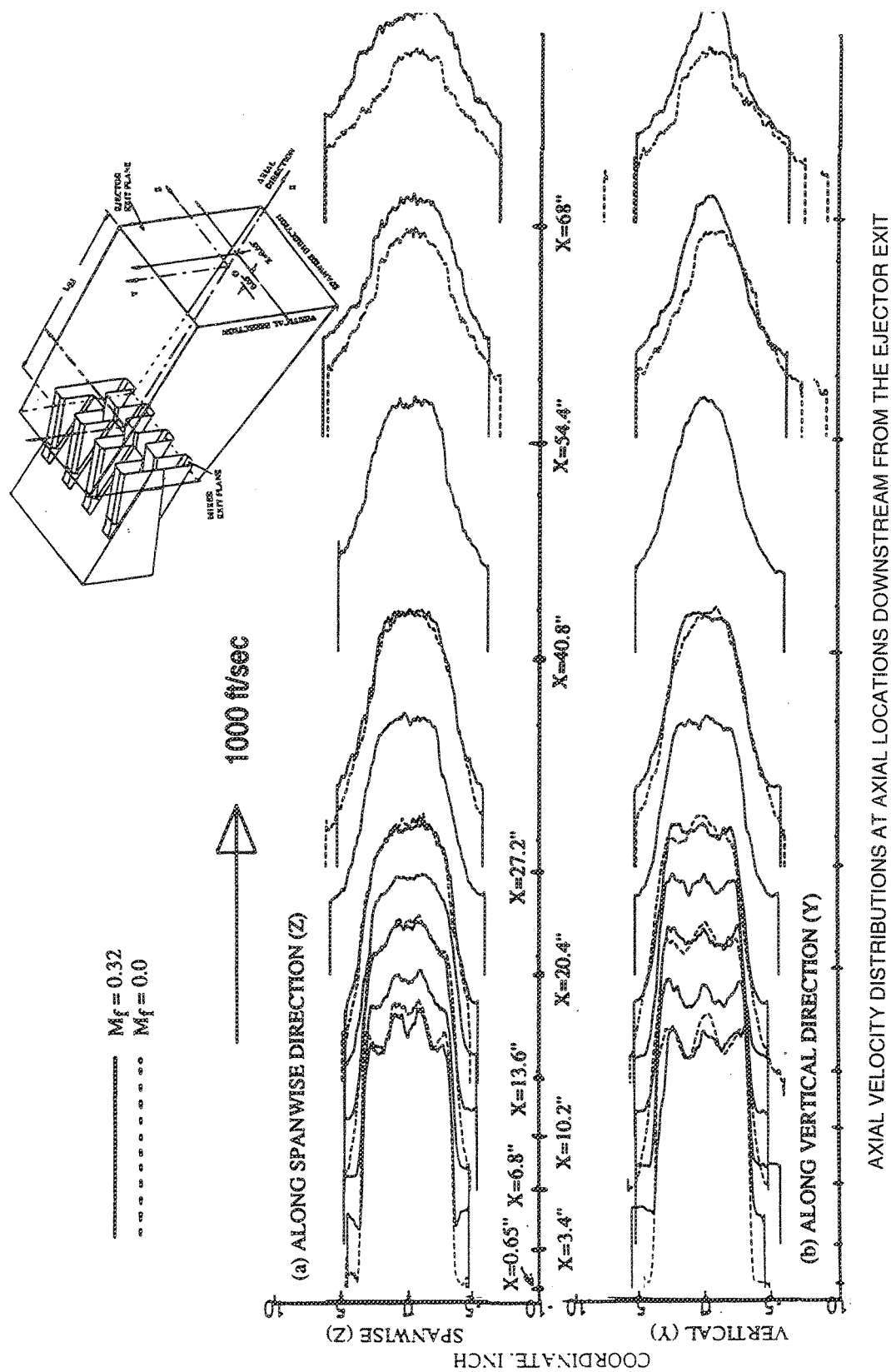


Figure 306. Comparison of Axial Velocity Distributions Between With/Without Flight Simulation at Various Axial Locations Downstream From Ejector Exit Plane of Vortical Mixer-Ejector Nozzles With Hardwall Shroud  
(SAR=4.9, MAR=1.18,  $L_{EJ}=18.85$  in., NPR=3.5,  $T_t=1735^\circ R$ ,  $V_t=2518$  ft/sec)



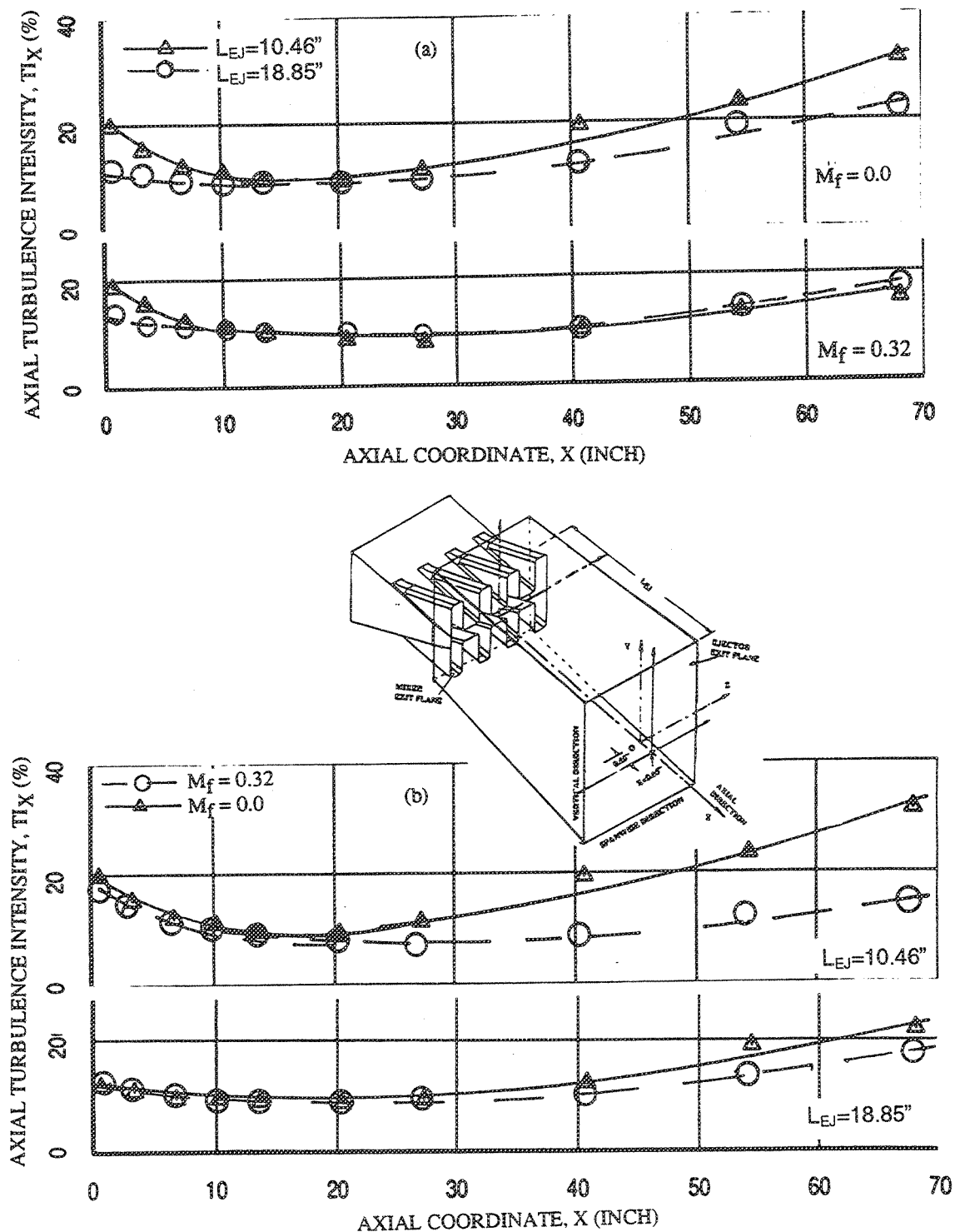


Figure 307. Effect of (a) Shroud Length, and (b) Flight Simulation on Axial Turbulence Intensity Distributions along X-Direction in External Plume of Vortical Mixer-Ejector Nozzle with Hardwall Shroud ( $SAR=4.9$ ,  $MAR=1.18$ ,  $Y=Z=0$ ,  $NPR=3.5$ ,  $T_t=1735^\circ R$ ,  $V_j=2518$  ft/sec)

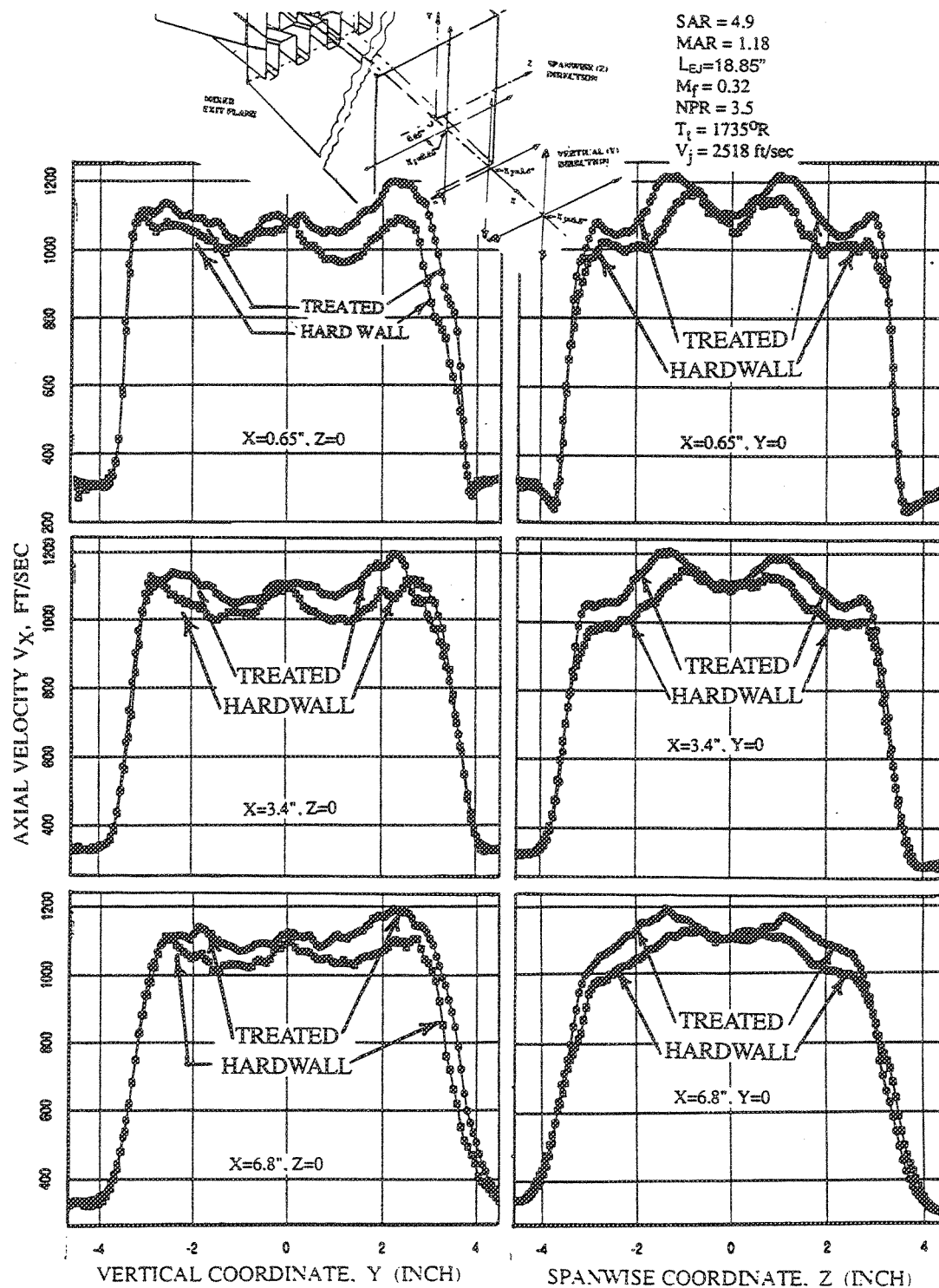


Figure 308. Effect of Acoustic Treatment on Axial Velocity Distributions Along Vertical (Y) and Spanwise (Z) Directions at Three Axial (X) Locations Downstream From Ejector Exit Plane of Vortical Mixer-Ejector Nozzle With Long Shroud

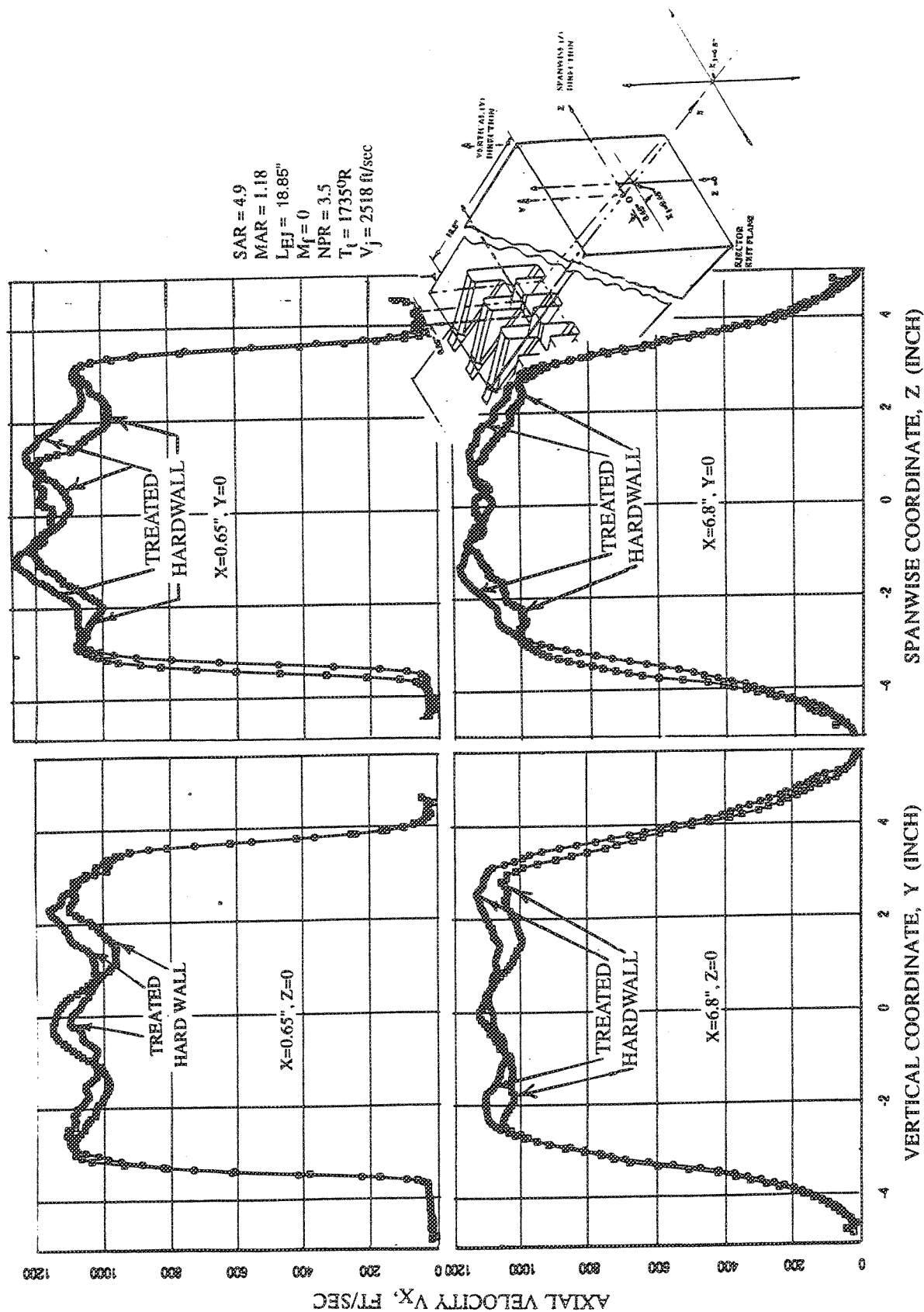


Figure 309. Effect of Acoustic Treatment on Axial Velocity Distributions along Vertical (Y) and Spanwise (Z) Directions At Two Axial (X) Locations Downstream From Ejector Exit Plane of Vortical mixer-Ejector Nozzle With Long Shroud

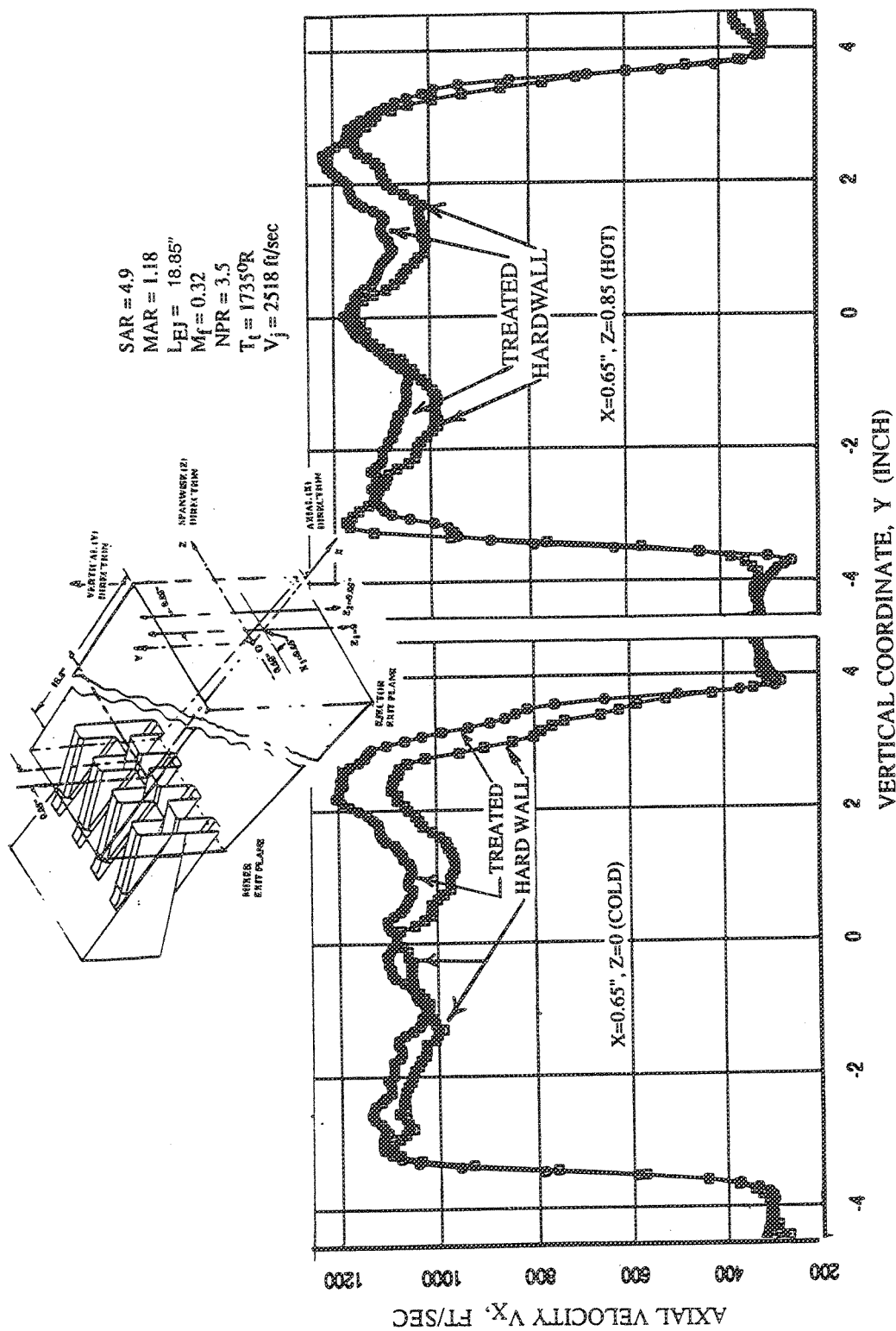


Figure 310. Effect of Acoustic Treatment on Axial Velocity Distributions Along Vertical (Y) Directions at Center of Hot ( $Z=0.85$  in.) and Cold ( $Z=0$  in.) Chute Flow Regions Close to Ejector Exit Plane of Vortical Mixer-Ejector Nozzle With Long Shroud

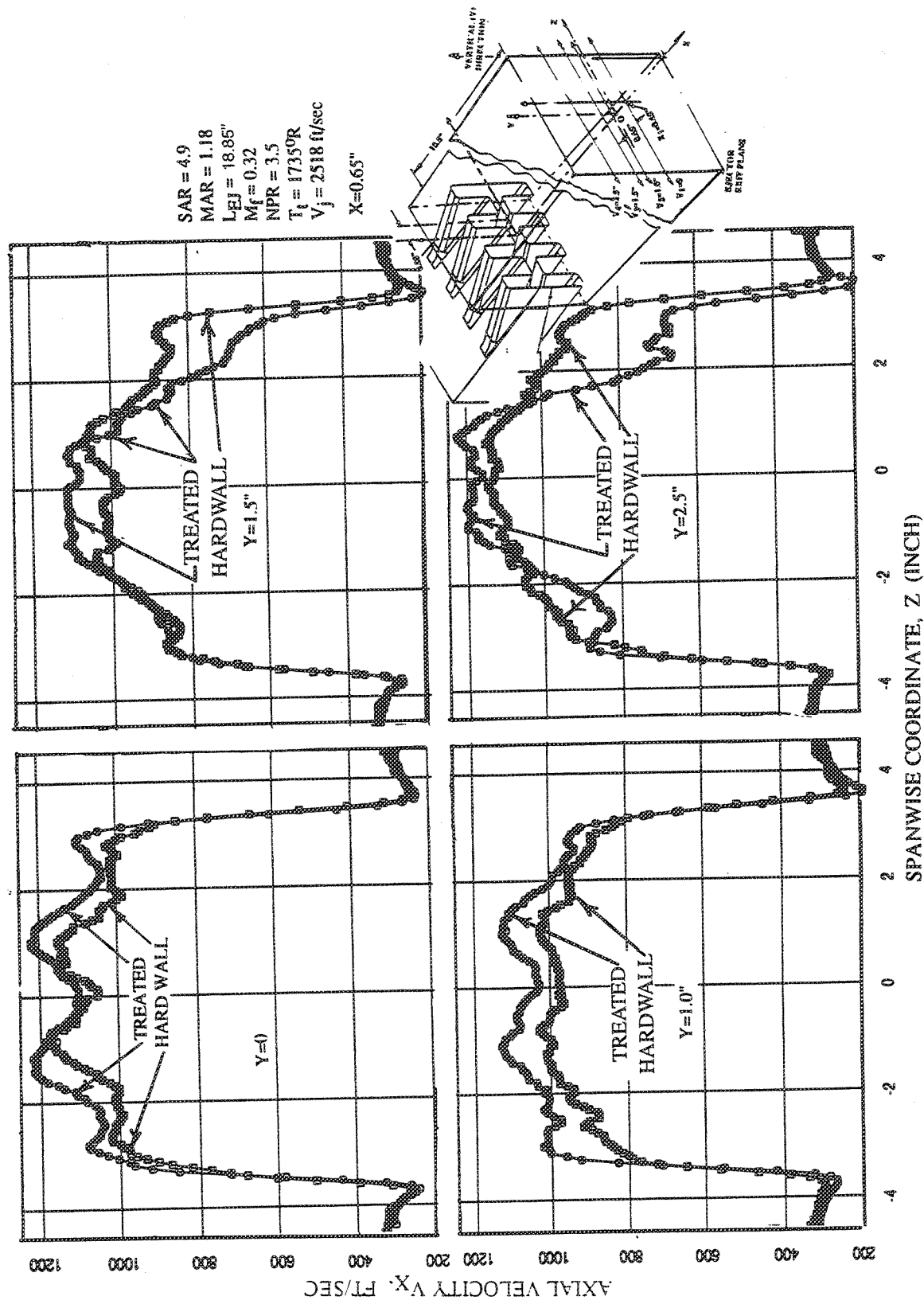


Figure 311. Effect of Acoustic Treatment on Axial Velocity Distributions Along Spanwise (Z) Direction at Four Vertical (Y) Locations Close to Ejector Exit Plane ( $X=0.65$  in.) of Vortical Mixer-Ejector Nozzle With Long Shroud

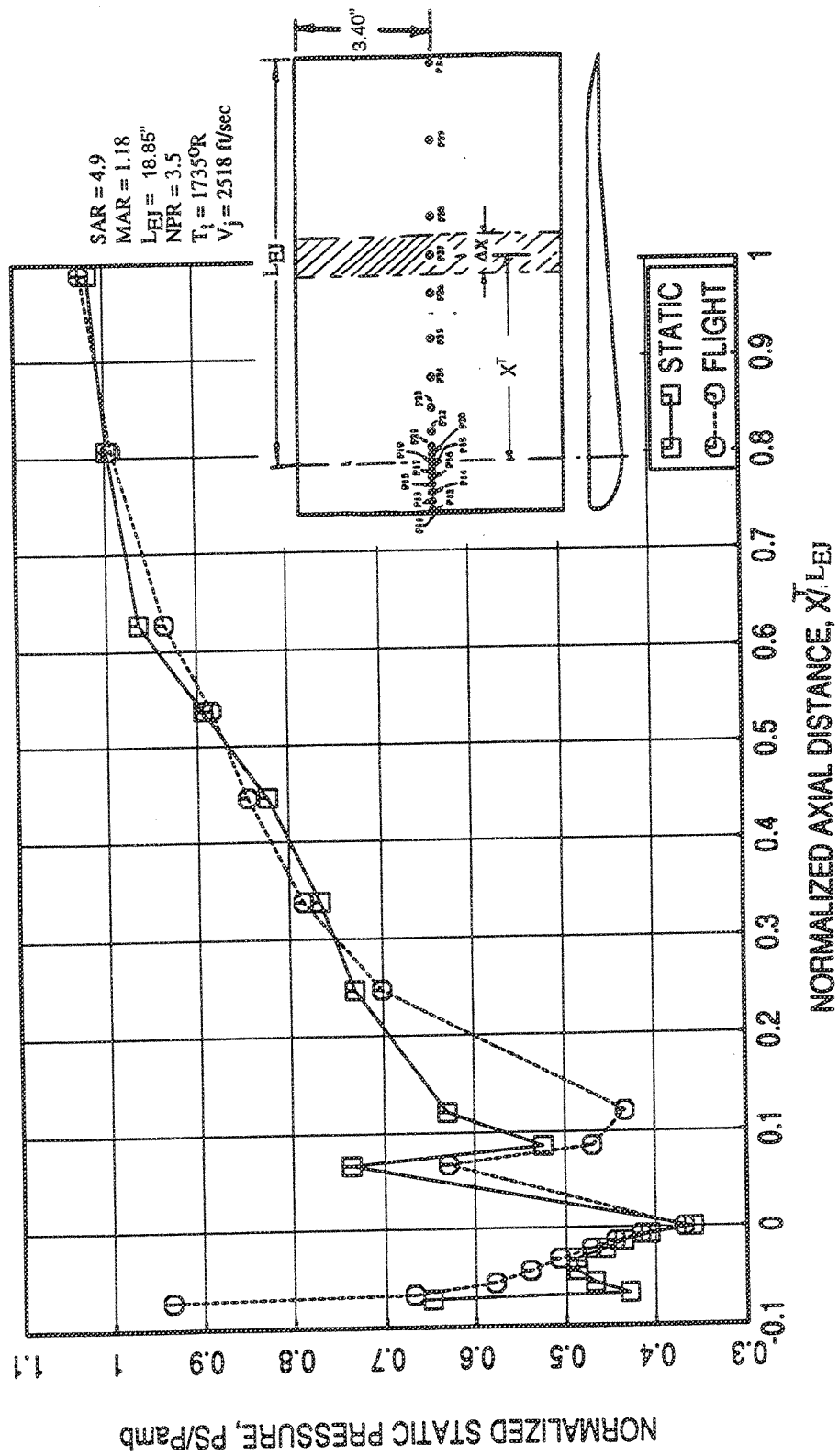


Figure 312. Effect of Flight on Axial Static Pressure Distribution on Internal Shroud Surface For Vortical Mixer-Ejector Nozzle With Long Hardwall Shroud

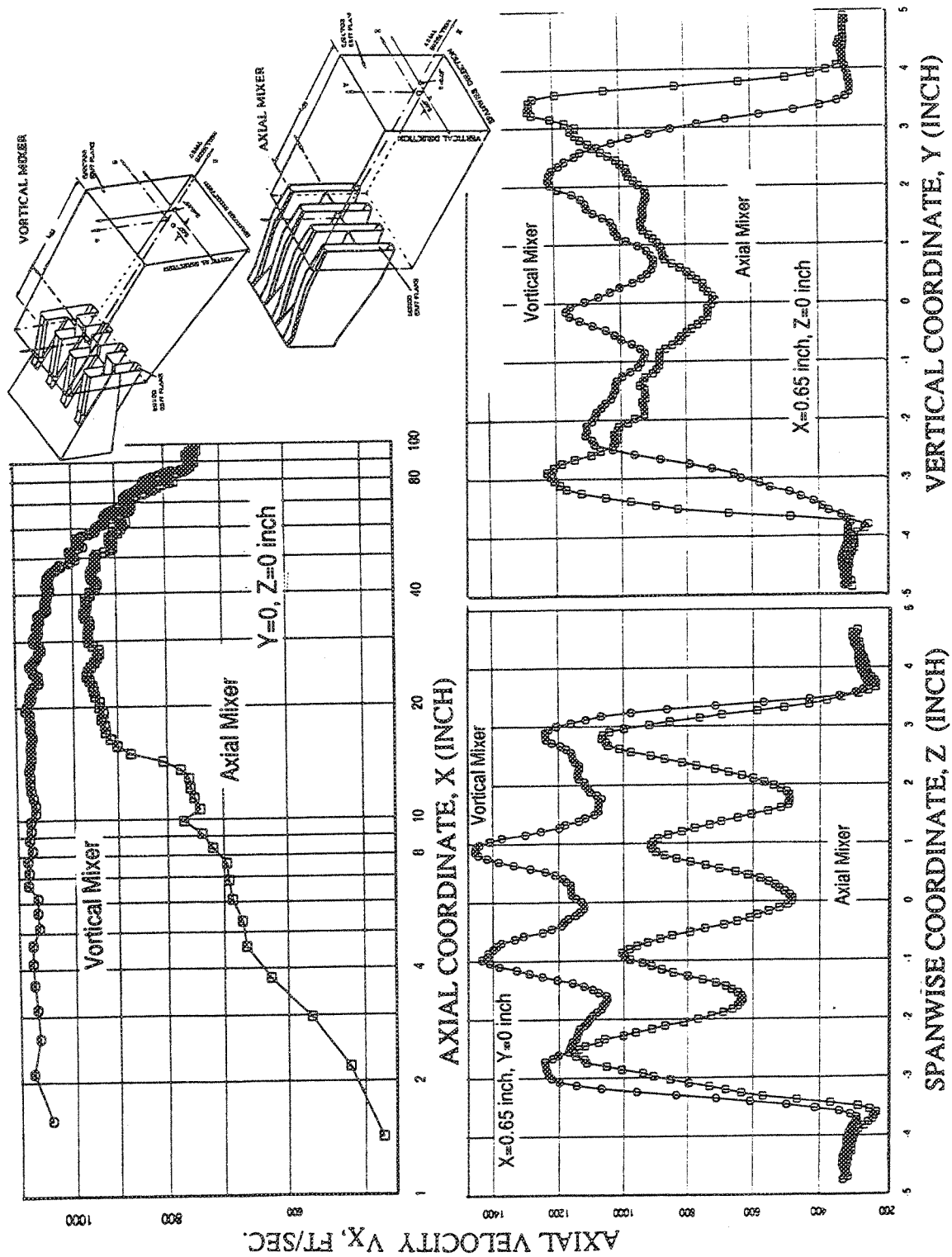


Figure 313. Effect of Mixer Design on Axial Velocity Distribution in External Plume of Hardwall Vortical Mixer-Ejector Nozzle  
 (SAR=4.9, MAR=1.18,  $L_{EJ}=10.46$  in.,  $Mn=0.32$ , NPR=3.5,  $T_t=1735^\circ R$ ,  $V_j=2518$  ft/sec)

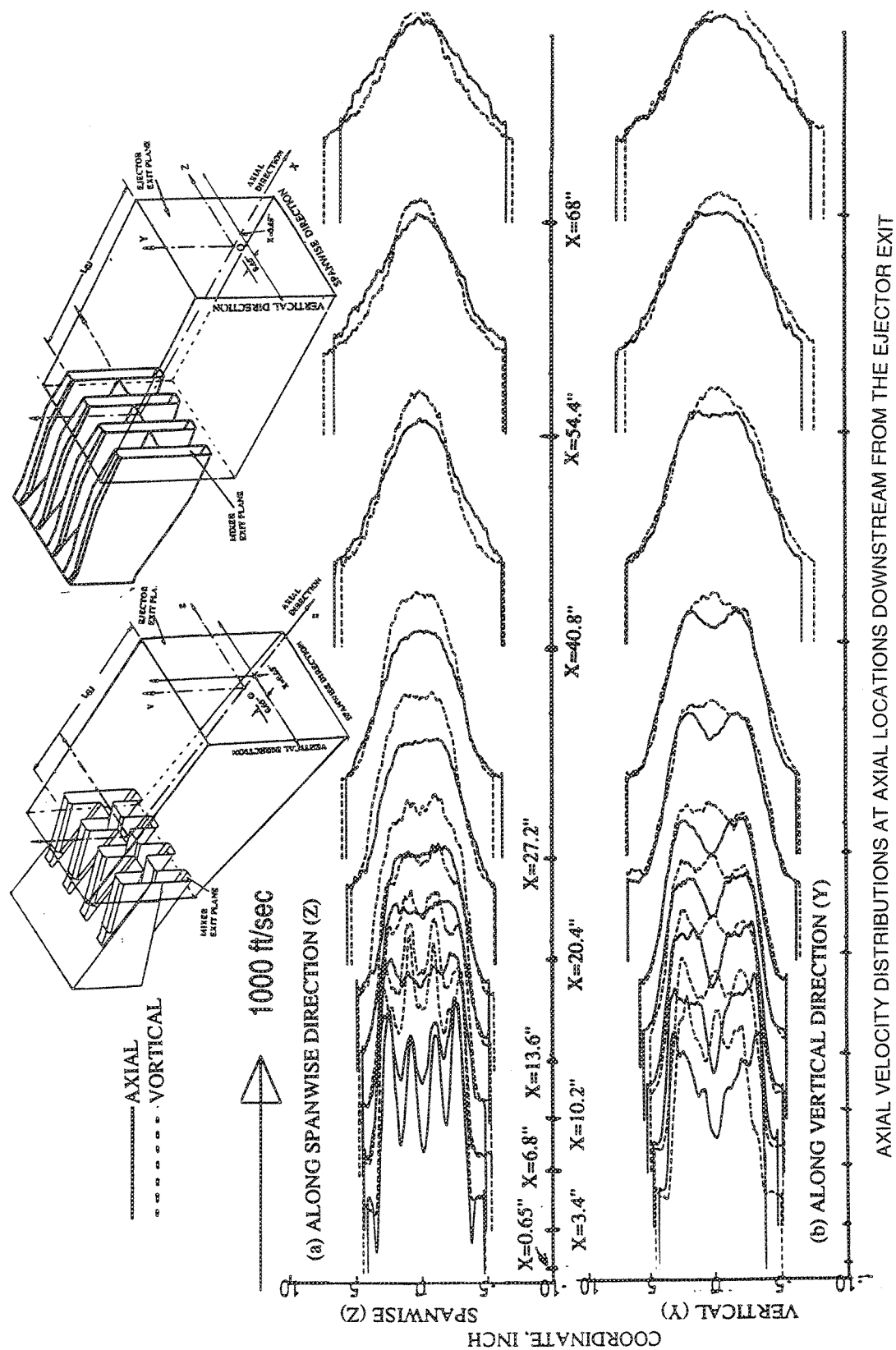
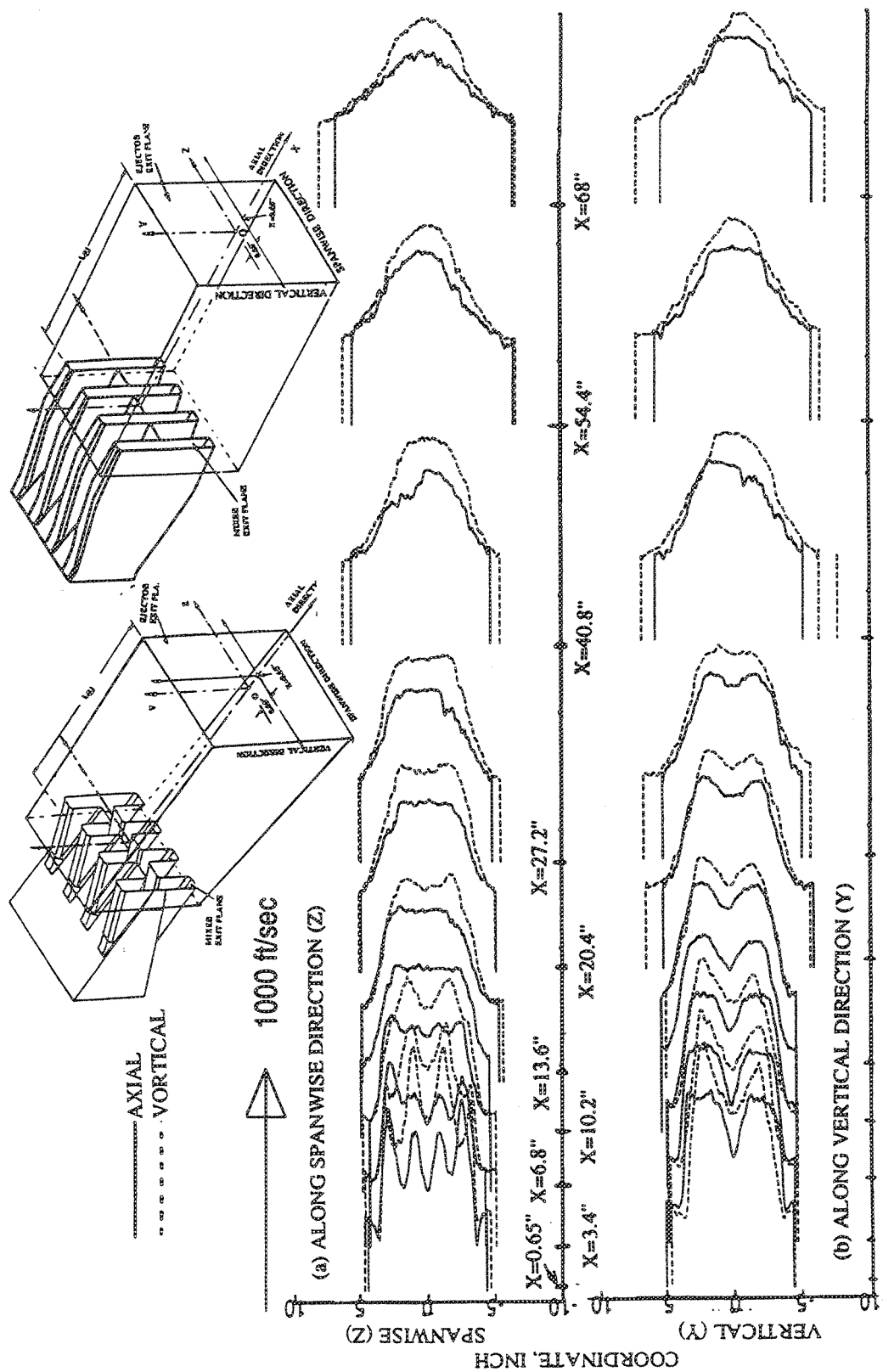


Figure 314. Comparison of Axial Velocity Distributions Between Axial and Vortical Mixer Designs With Hardwall Shroud at Various Axial Locations Downstream From Ejector Exit Plane  
 (SAR=4.9, MAR=1.18,  $L_{EJ}=10.46$  in.,  $Mn=0.32$ ,  $NPR=3.5$ ,  $T_t=1735^\circ R$ ,  $V_t=2518$  ft/sec)





AXIAL VELOCITY DISTRIBUTIONS AT AXIAL LOCATIONS DOWNSTREAM FROM THE EJECTOR EXIT

Figure 315. Comparison of Axial Velocity Distributions Between Axial and Vortical Mixer Designs With Hardwall Shroud at Various Axial Locations Downstream From Ejector Exit Plane  
(SAR=4.9, MAR=1.18,  $L_{EJ}=10.46$  in.,  $Mn=0.32$ ,  $NPR=2.5$ ,  $T_c=1325^\circ R$ ,  $V_i=1919$  ft/sec)

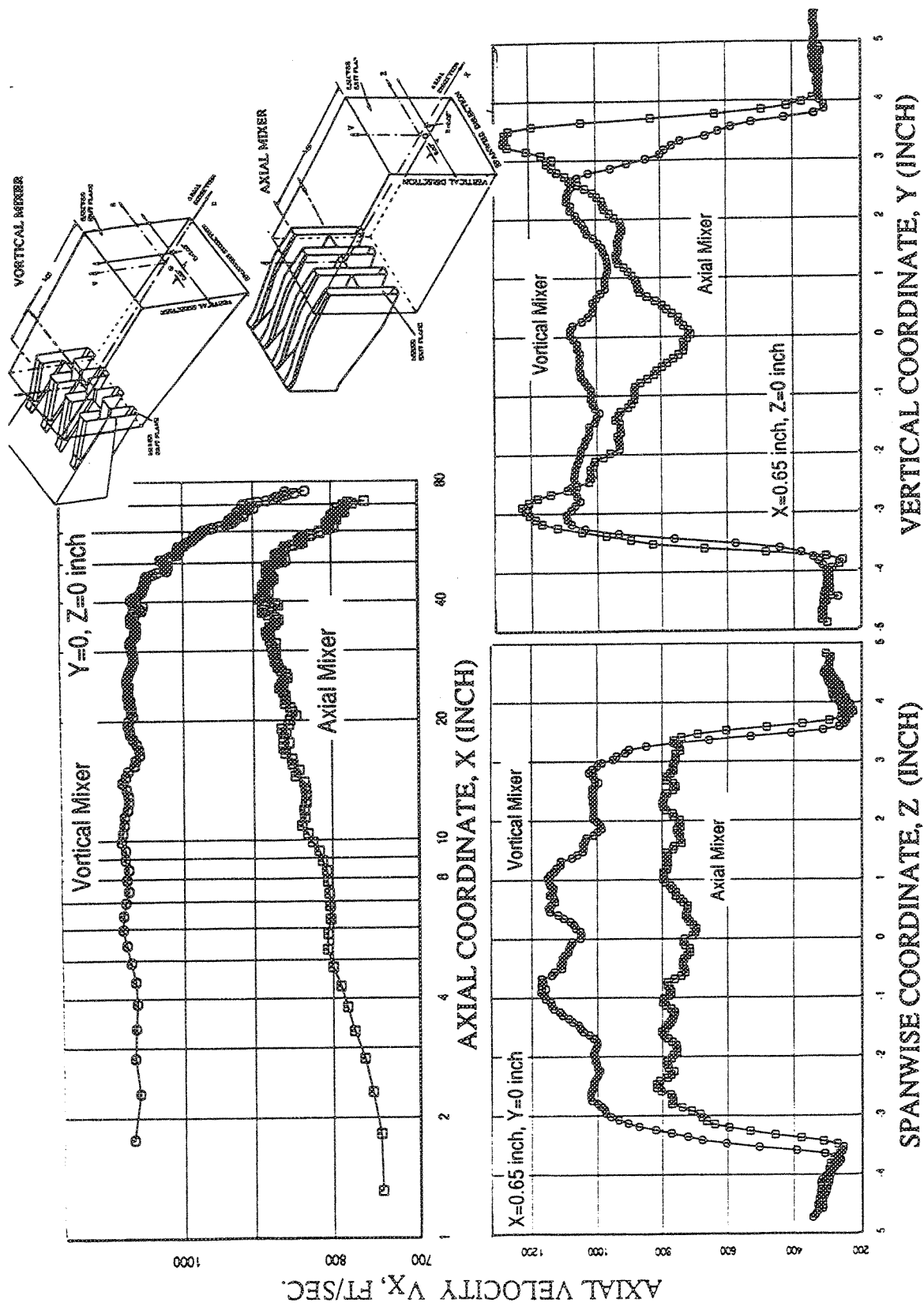
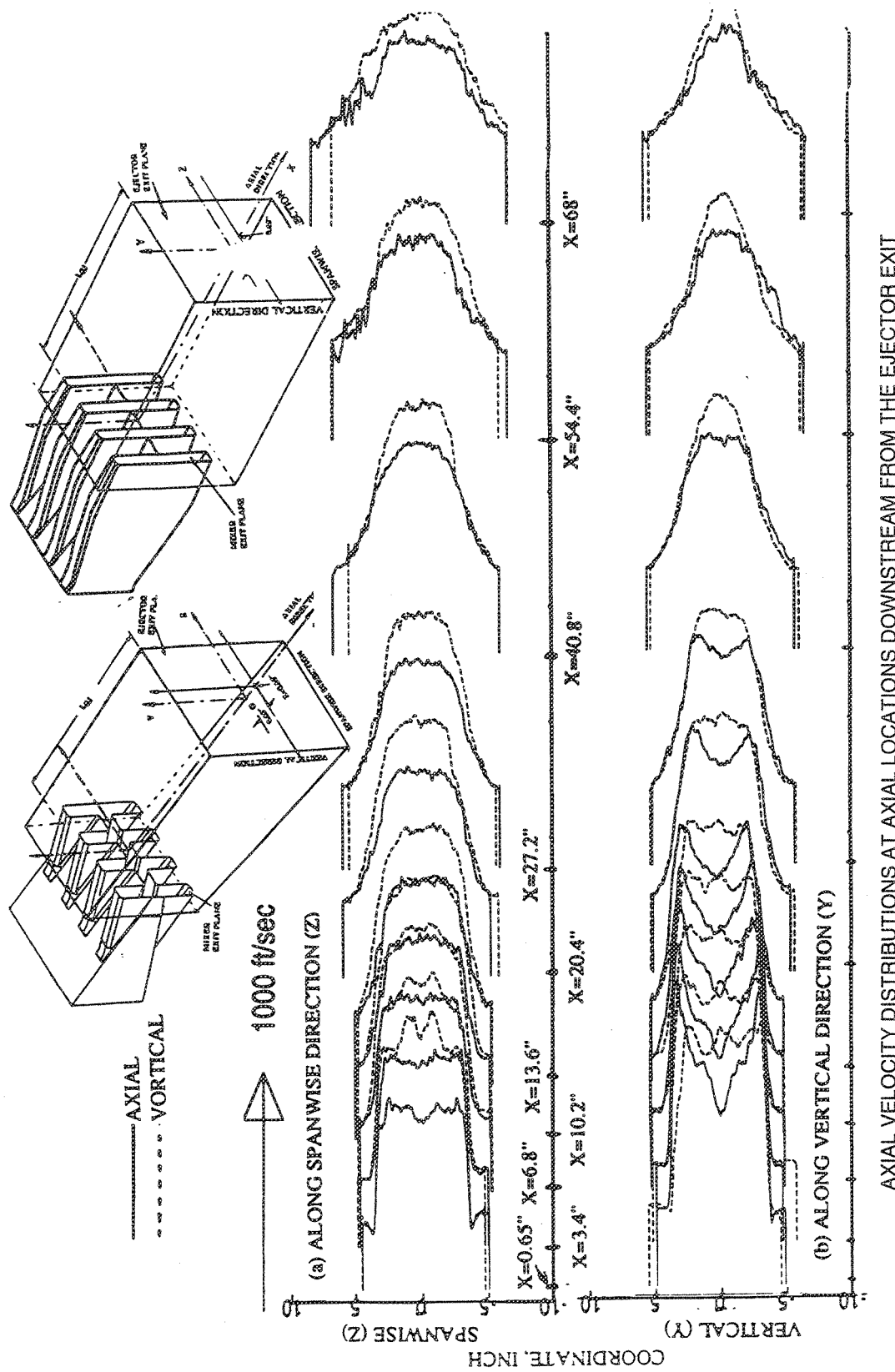


Figure 316. Effect of Mixer Design on Axial Velocity Distribution in External Plume of Hardwall Vortical Mixer-Ejector Nozzle  
 (SAR=4.9, MAR=1.18,  $L_{EJ}$ =18.85 in.,  $Mn$ =0.32, NPR=3.5,  $T_t$ =1735°R,  $V_j$ =2518 ft/sec)



AXIAL VELOCITY DISTRIBUTIONS AT AXIAL LOCATIONS DOWNSTREAM FROM THE EJECTOR EXIT

Figure 317. Comparison of Axial Velocity Distributions Between Axial and Vortical Mixer Designs With Hardwall Shroud at Various Axial Locations Downstream From Ejector Exit Plane  
(SAR=4.9, MAR=1.18,  $L_{EJ}=18.85$  in.,  $Mn=0.32$ ,  $NPR=3.5$ ,  $T_t=1735^\circ R$ ,  $V_t=2518$  ft/sec)

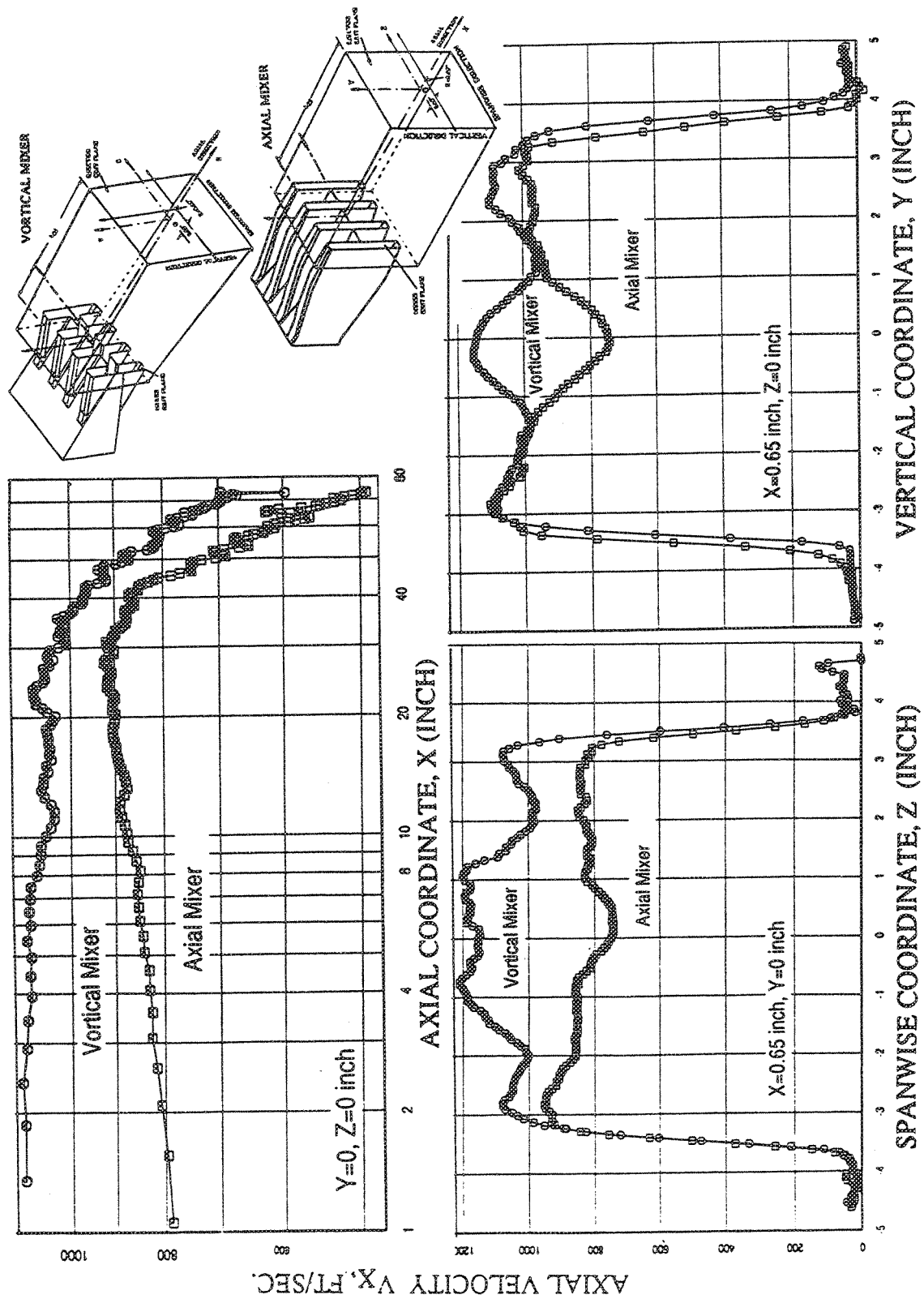


Figure 318. Effect of Mixer Design on Axial Velocity Distribution in External Plume of Hardwall Vortical Mixer-Ejector Nozzle  
( $SAR=4.9$ ,  $MAR=1.18$ ,  $L_{EJ}=18.85$  in.,  $Mn=0.0$ ,  $NPR=3.5$ ,  $T_1=1735^\circ R$ ,  $V_j=2518$  ft/sec)

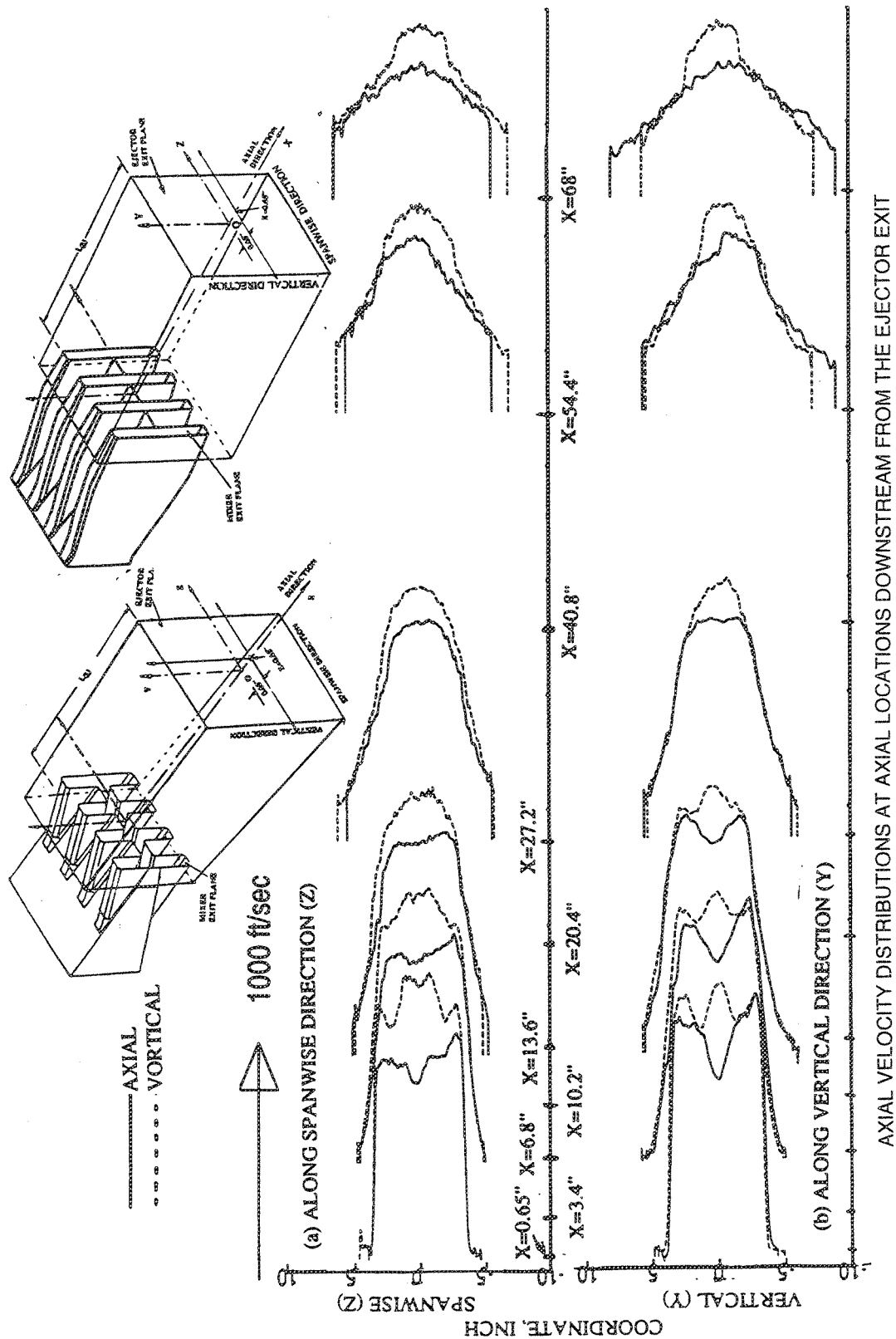


Figure 319. Comparison of Axial Velocity Distributions Between Axial and Vortical Mixer Designs With Hardwall Shroud at Various Axial Locations Downstream From Ejector Exit Plane  
(SAR=4.9, MAR=1.18,  $L_{EJ}=18.85$  in.,  $Mn=0.0$ ,  $NPR=3.5$ ,  $T_t=1735^\circ R$ ,  $V_t=2518$  ft/sec)

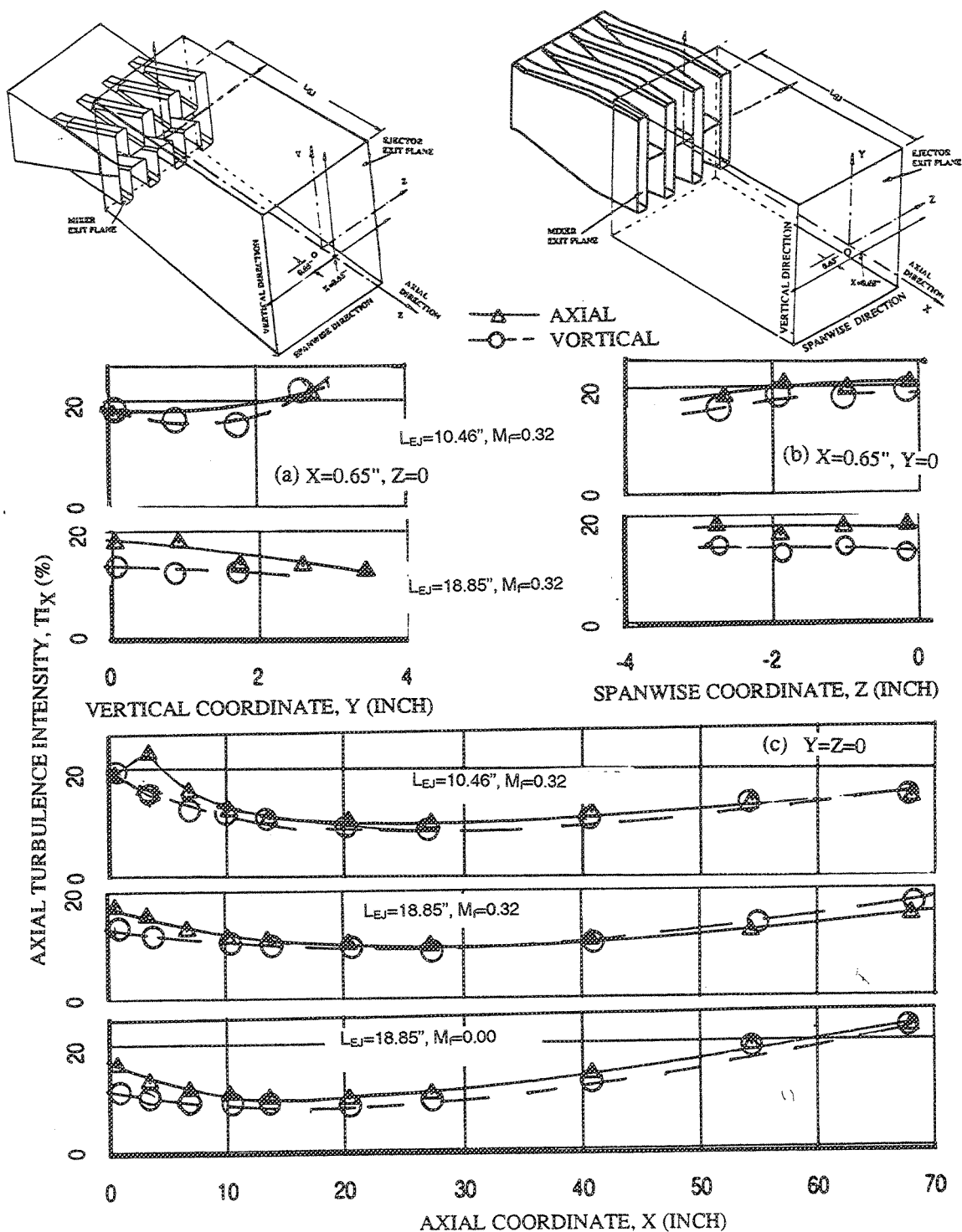


Figure 320. Effect of Mixer Designs With Hardwall Shroud on Axial Turbulence Intensity Distributions Along Axial (X), Vertical (Y), and Spanwise (Z) Directions in External Plume (SAR=4.9, MAR=1.18, NPR=3.5,  $T_t=1735^\circ R$ ,  $V_j=2518$  ft/sec)

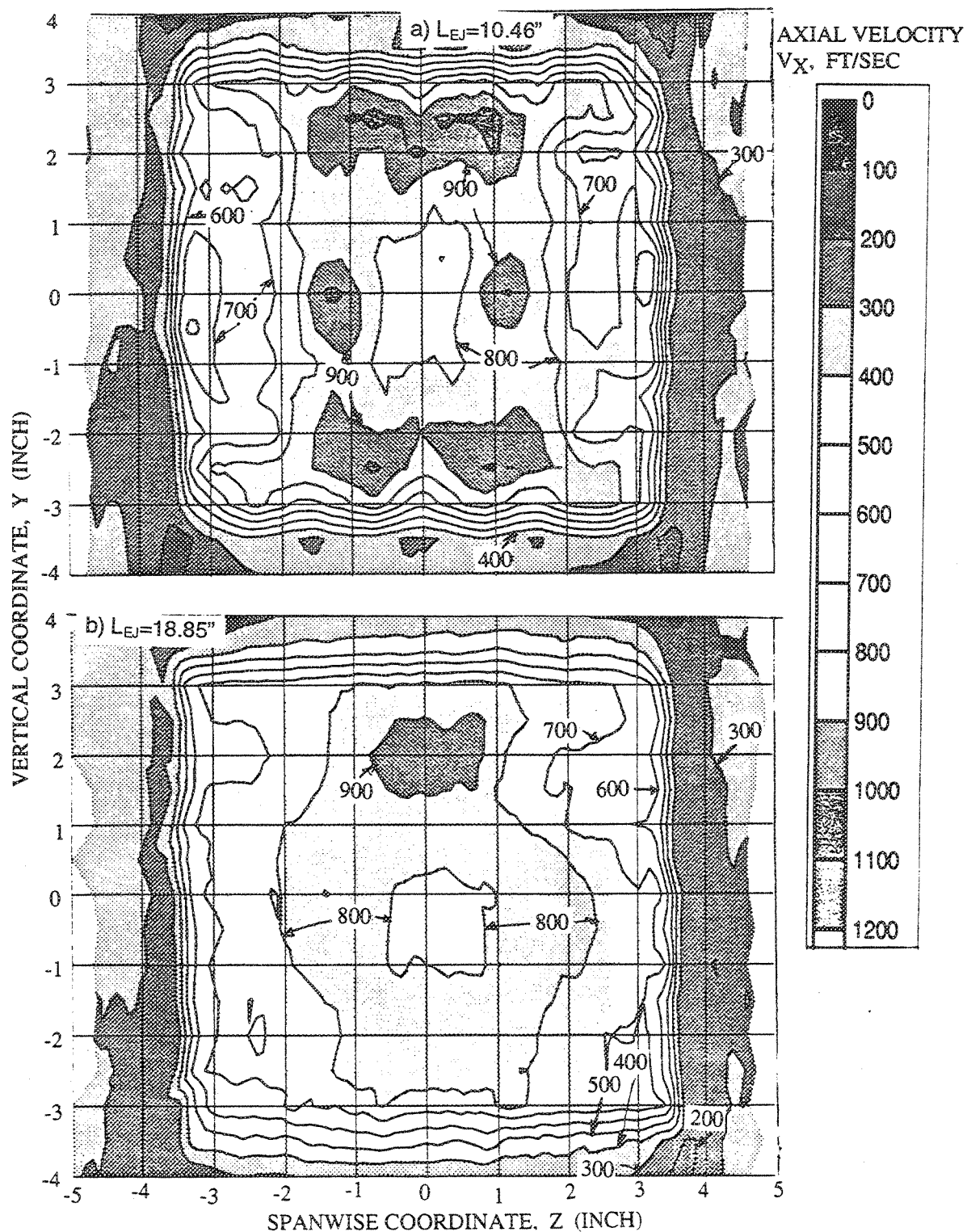


Figure 321. Effect of Shroud Length ( $L_{EJ}$ ) on Axial Velocity Distribution Close to Exit Plane of Hardwall Vortical Mixer-Ejector Nozzle ( $SAR=4.9$ ,  $MAR=1.18$ ,  $X=0.65$ ,  $Mn=0.32$ ,  $NPR=2.5$ ,  $T_t=1325^\circ R$ ,  $V_j=1919$  ft/sec)

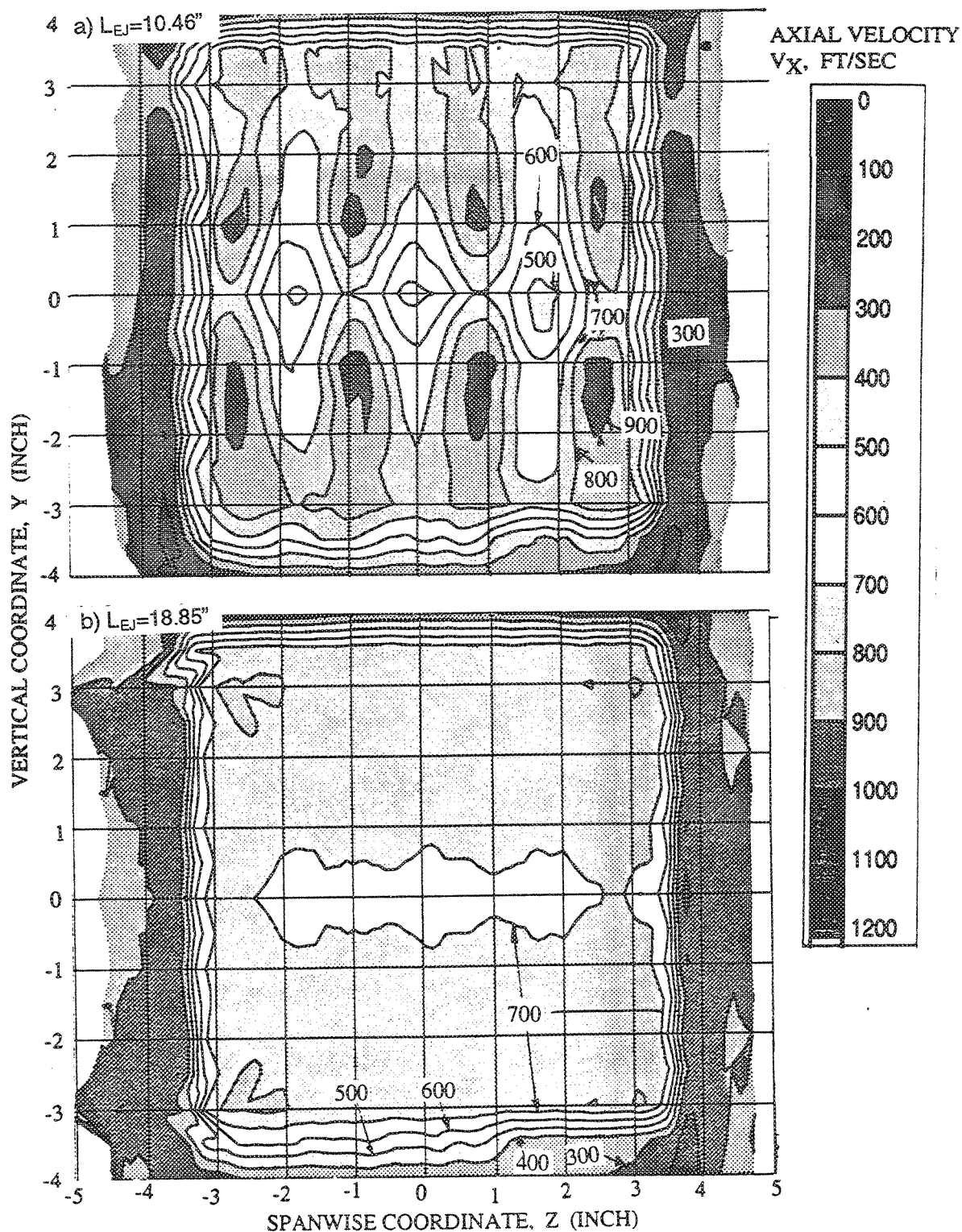


Figure 322. Effect of Shroud Length on Axial Velocity Distribution Close to Exit Plane of Hardwall Axial Mixer-Ejector Nozzle ( $SAR=4.9$ ,  $MAR=1.18$ ,  $X=0.65$ ,  $Mn=0.32$ ,  $NPR=2.5$ ,  $T_t=1325^\circ R$ ,  $V_j=1919$  ft/sec)



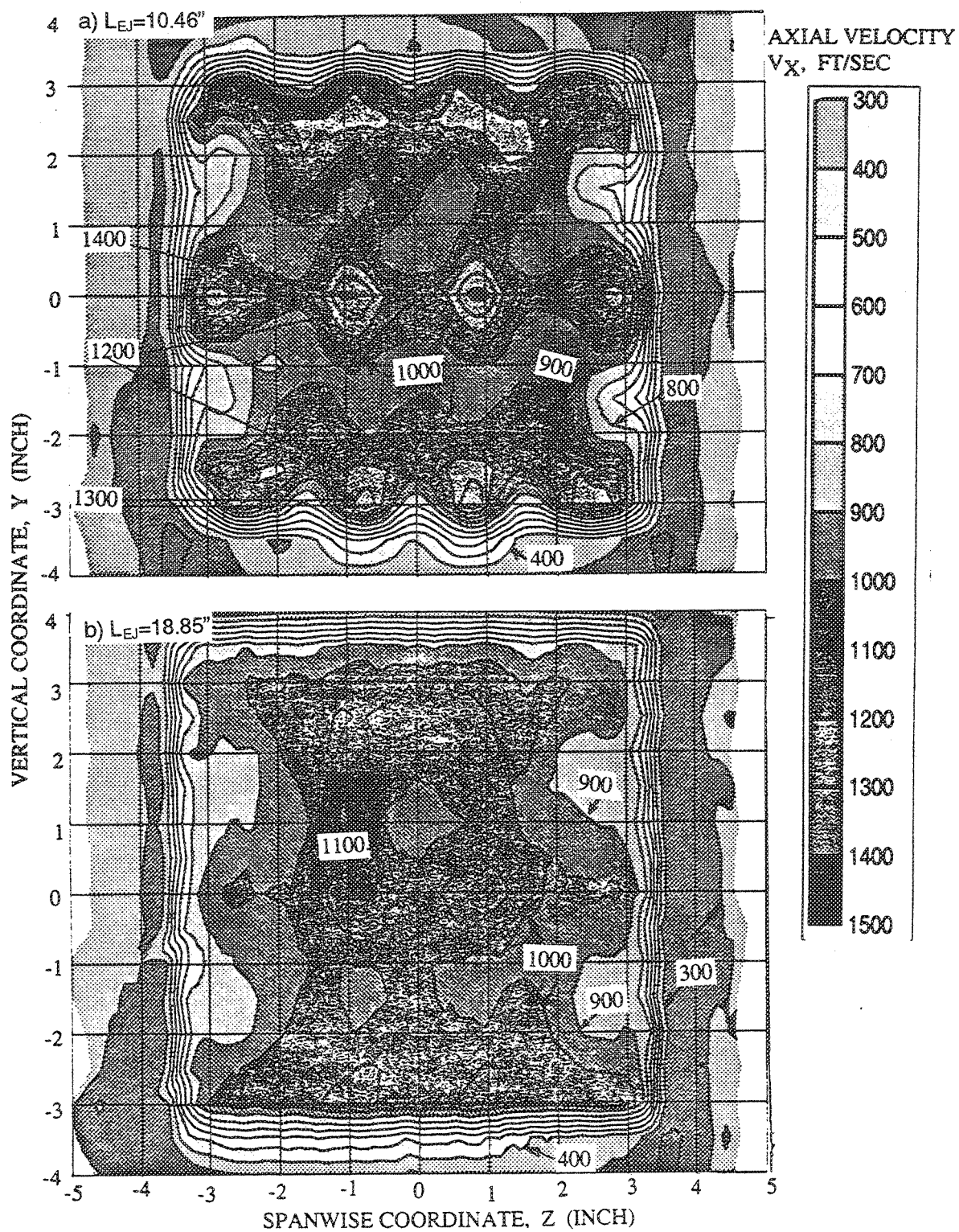


Figure 323. Effect of Shroud Length on Axial Velocity Distribution Close to Exit Plane of Hardwall Vortical Mixer-Ejector Nozzle (SAR=4.9, MAR=1.18,  $X=0.65$ ,  $Mn=0.32$ ,  $NPR=3.5$ ,  $T_t=1735^\circ R$ ,  $V_j=2518$  ft/sec)

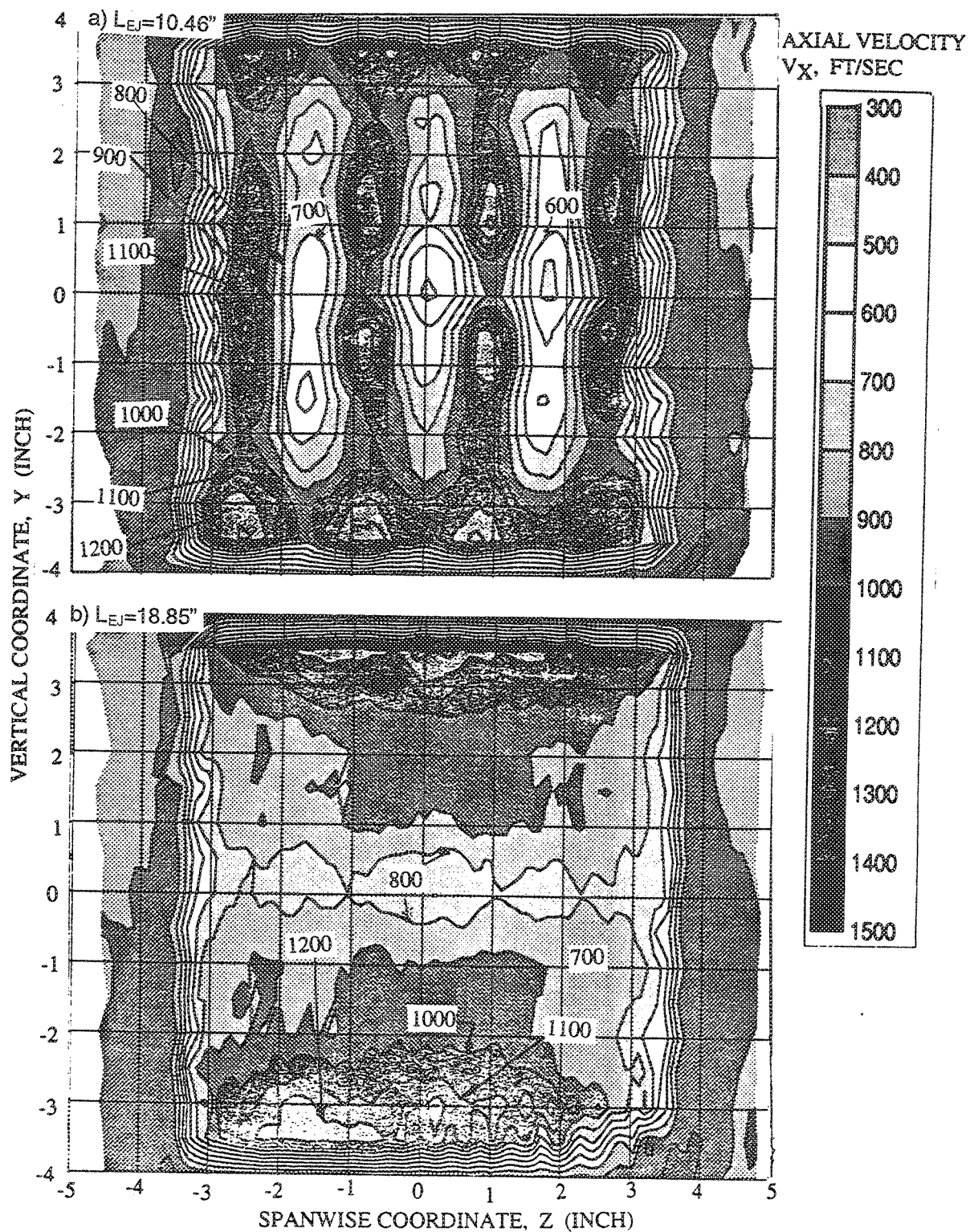
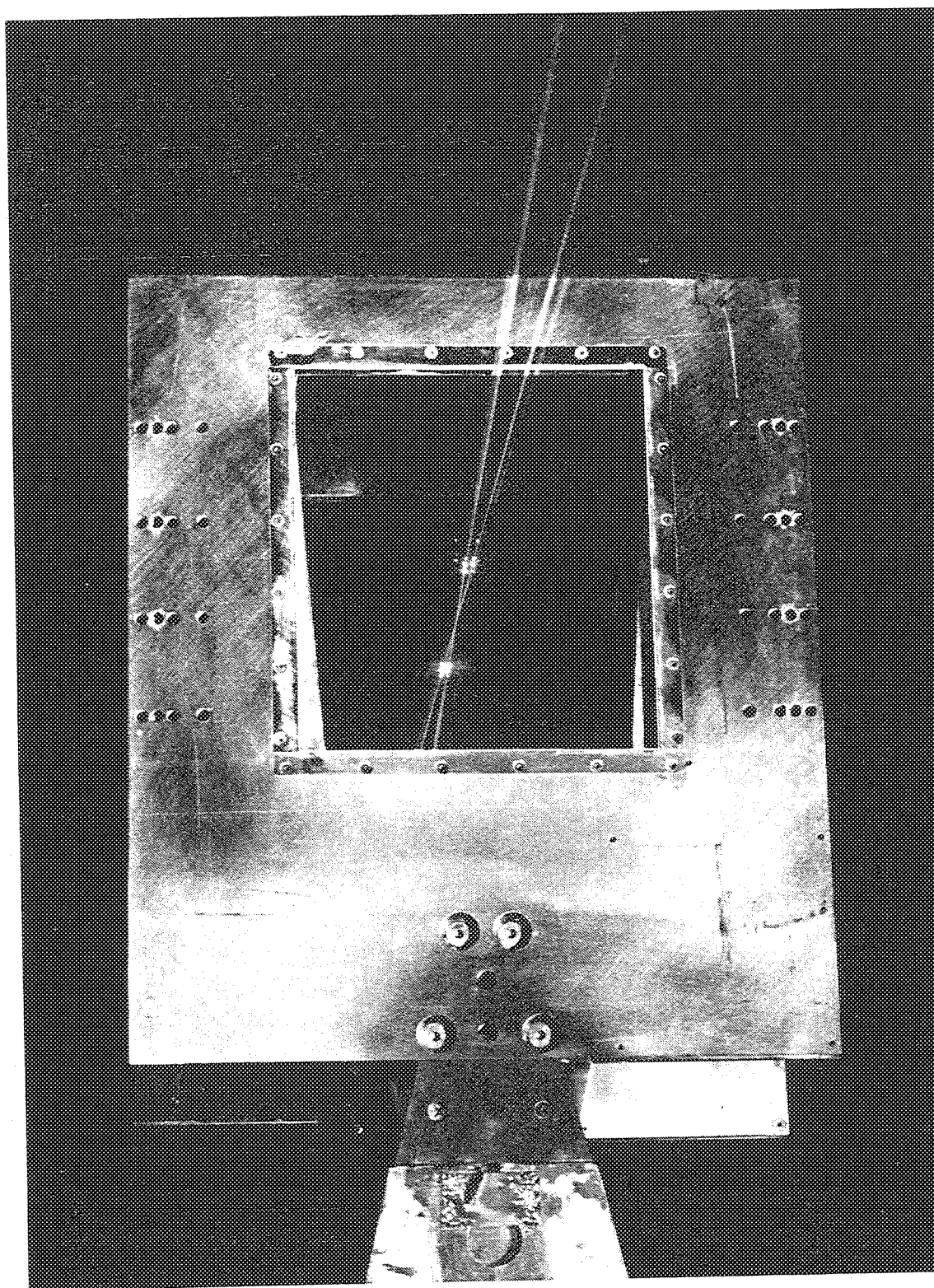


Figure 324. Effect of Shroud Length on Axial Velocity Distribution Close to Exit Plane of Hardwall Axial Mixer-Ejector Nozzle (SAR=4.9, MAR=1.18,  $X=0.65$ ,  $Mn=0.32$ , NPR=3.5,  $T_t=1735^\circ R$ ,  $V_j=2518$  ft/sec)



*Figure 325. Laser Beams Passing Through Sidewall Glass Windows of Mixer Ejector Nozzle Configuration With Short Hardwall Shroud, Mounted in Anechoic Chamber*

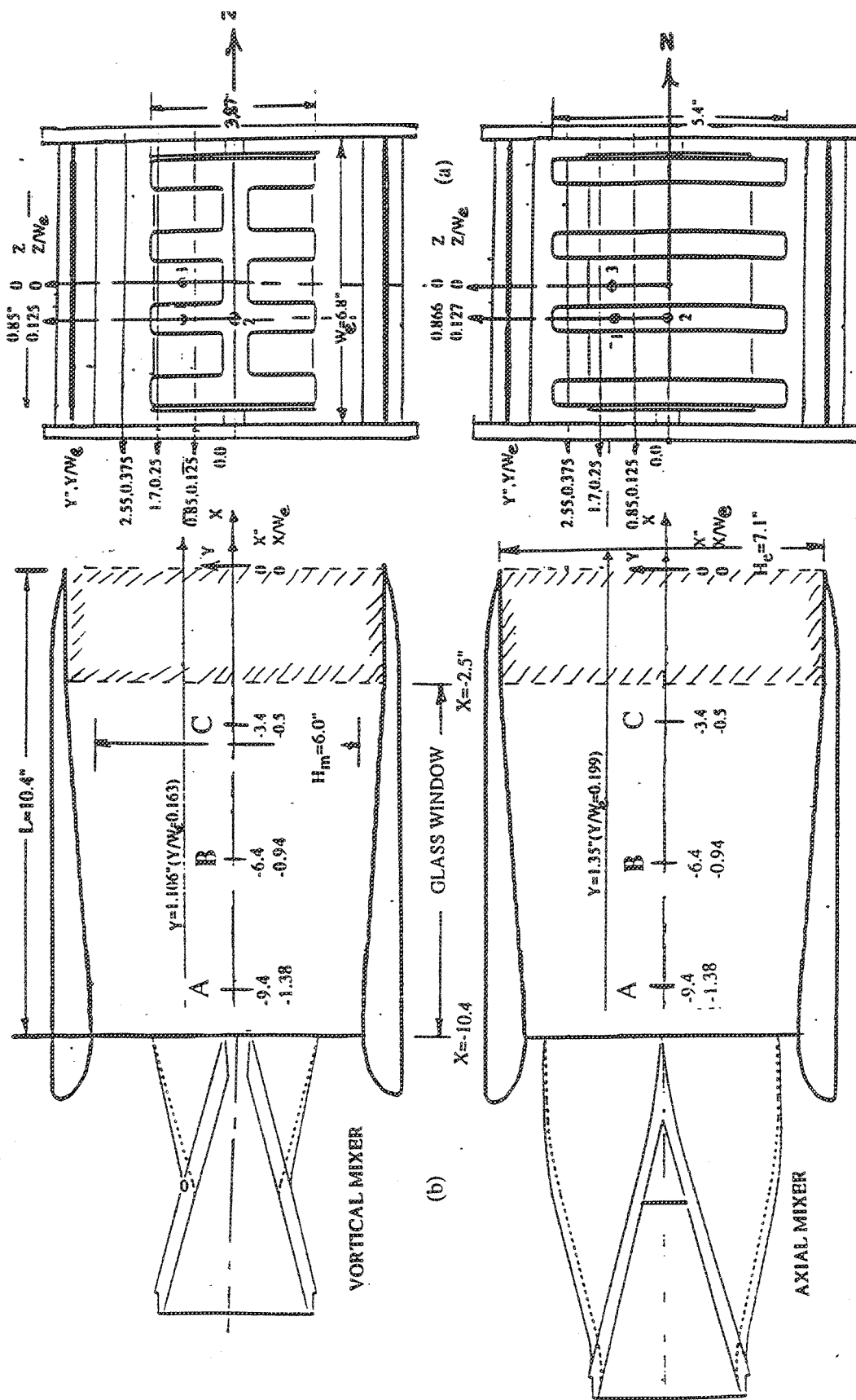


Figure 326. Laser Doppler Velocimetry Traverse Locations To Survey Flowfield Internal to Ejector

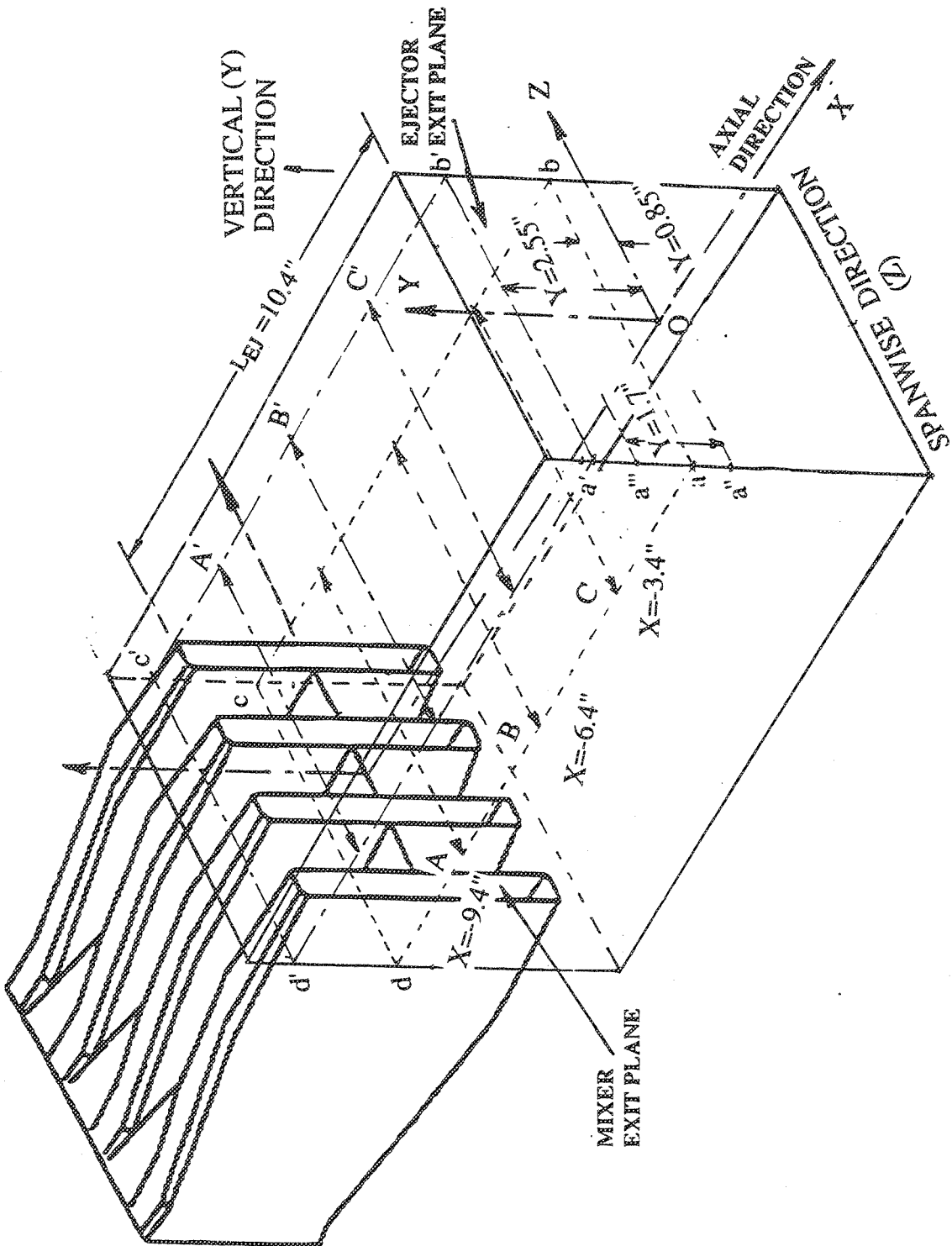


Figure 327. An Isometric View of Axial Mixer-Ejector Nozzle Configuration, Showing Spanwise (Z) LDV Traverse Locations at Two X-Y planes in Flowfield Internal to Ejector

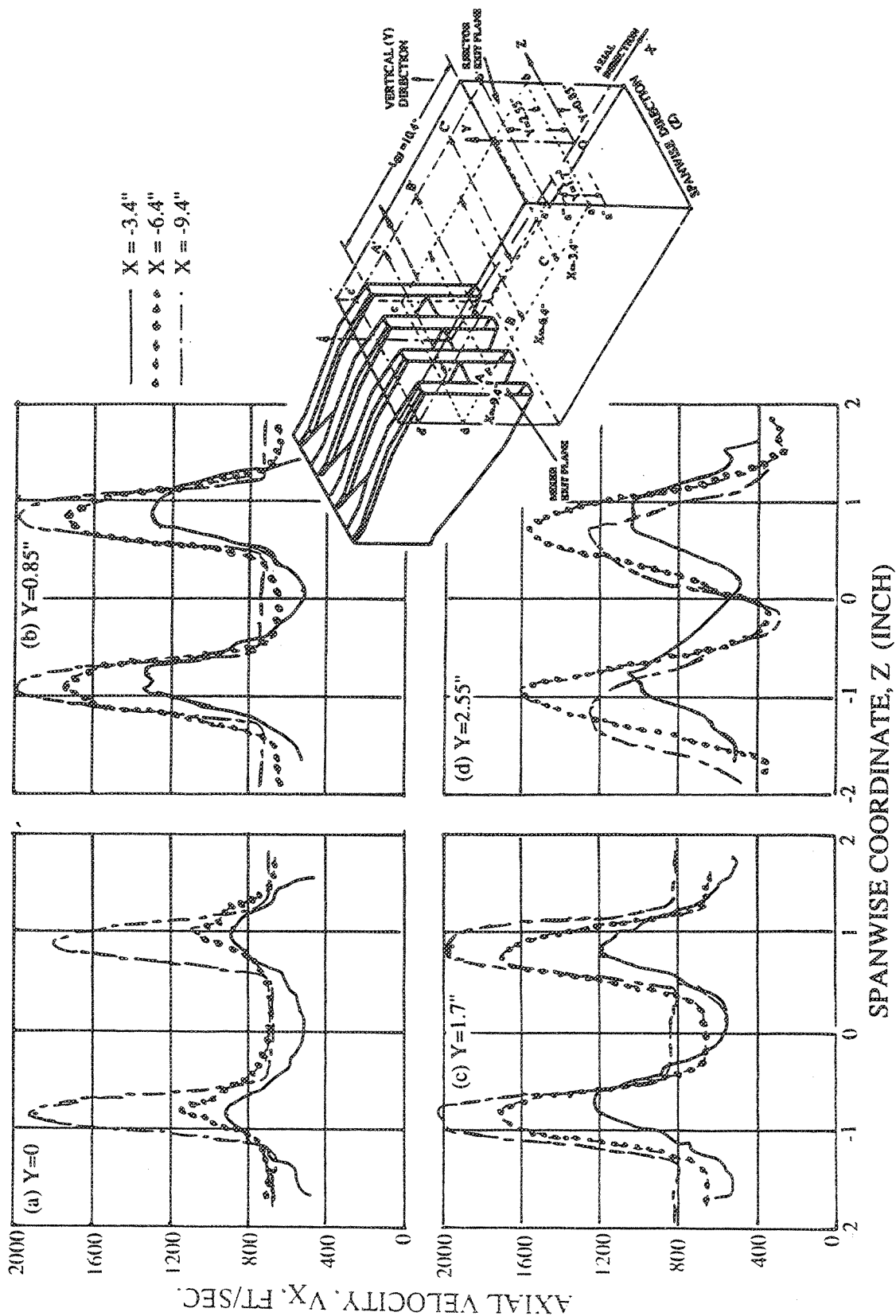


Figure 328. Variation of Axial Velocity Distributions Along Spanwise ( $Z$ ) Direction With Respect to Axial Locations at Four  $X$ - $Y$  Planes, Internal to Ejector of Axial Mixer-Ejector Nozzle With Short Hardwall Shroud  
( $SAR=4.9$ ,  $MAR=1.18$ ,  $L_{EJ}=10.46$  in.,  $Mn=0.32$ ,  $NPR=2.5$ ,  $T_t=1325^\circ R$ ,  $V_t=1919$  ft/sec)



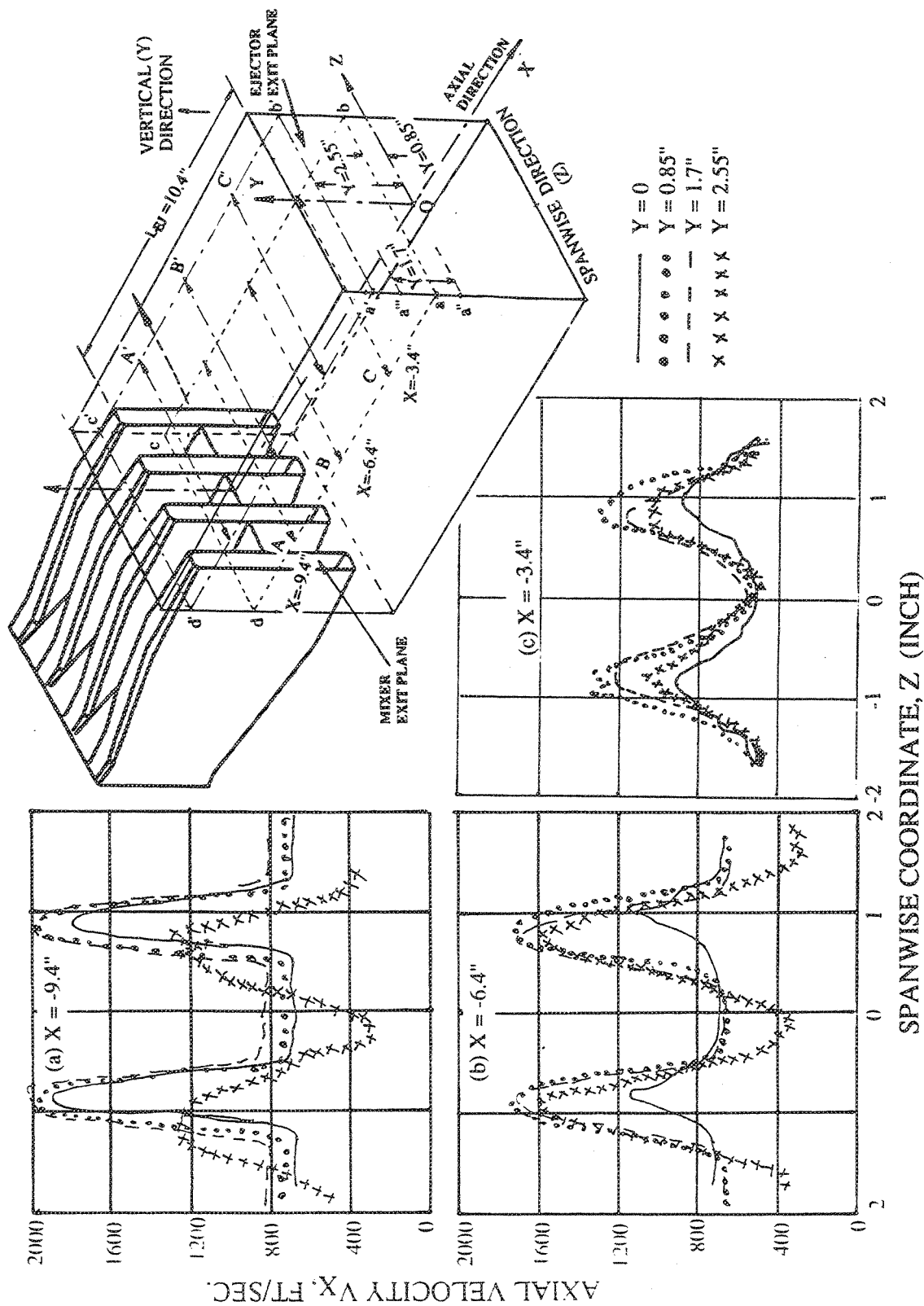


Figure 329. Variation of Axial Velocity Distributions Along Spanwise (Z) Direction With Respect to Y Direction at Three X-Y Planes, Internal to Ejector of Axial Mixer-Ejector Nozzle With Short Hardwall Shroud  
(SAR=4.9, MAR=1.18,  $L_{EJ}=10.46$  in.,  $Mn=0.32$ , NPR=2.5,  $T_1=1325^\circ R$ ,  $V_1=1919$  ft/sec)

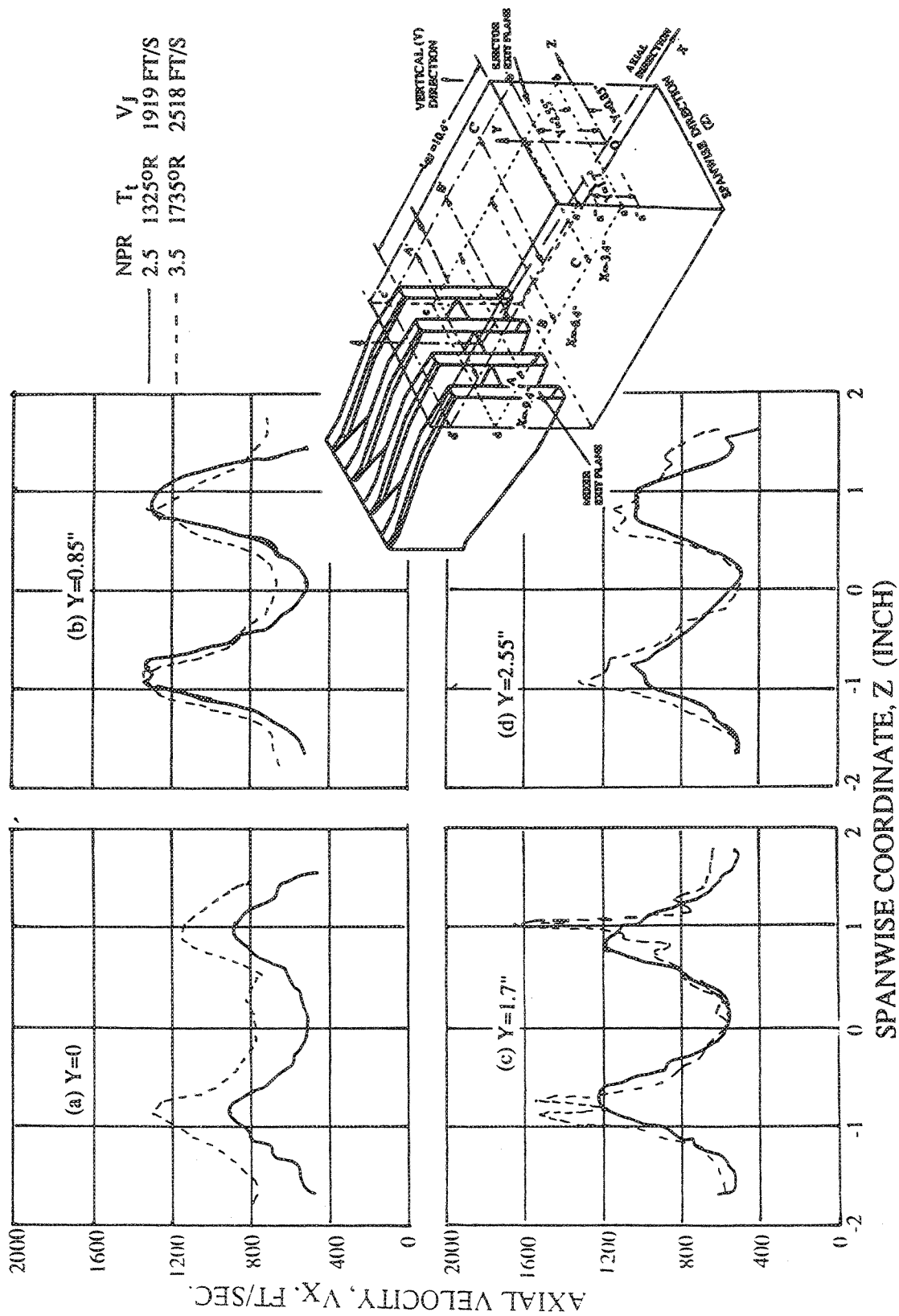


Figure 330. Effect of Nozzle Pressure Ratio on Axial Velocity Distributions Along Spanwise (Z) Direction at Four Y Locations With  $X=-3.4$  in., Internal to Ejector of Axial Mixer-Ejector Nozzle With Short Hardwall Shroud  
(SAR=4.9, MAR=1.18,  $L_{EJ}=10.46$  in.,  $Mn=0.32$ )





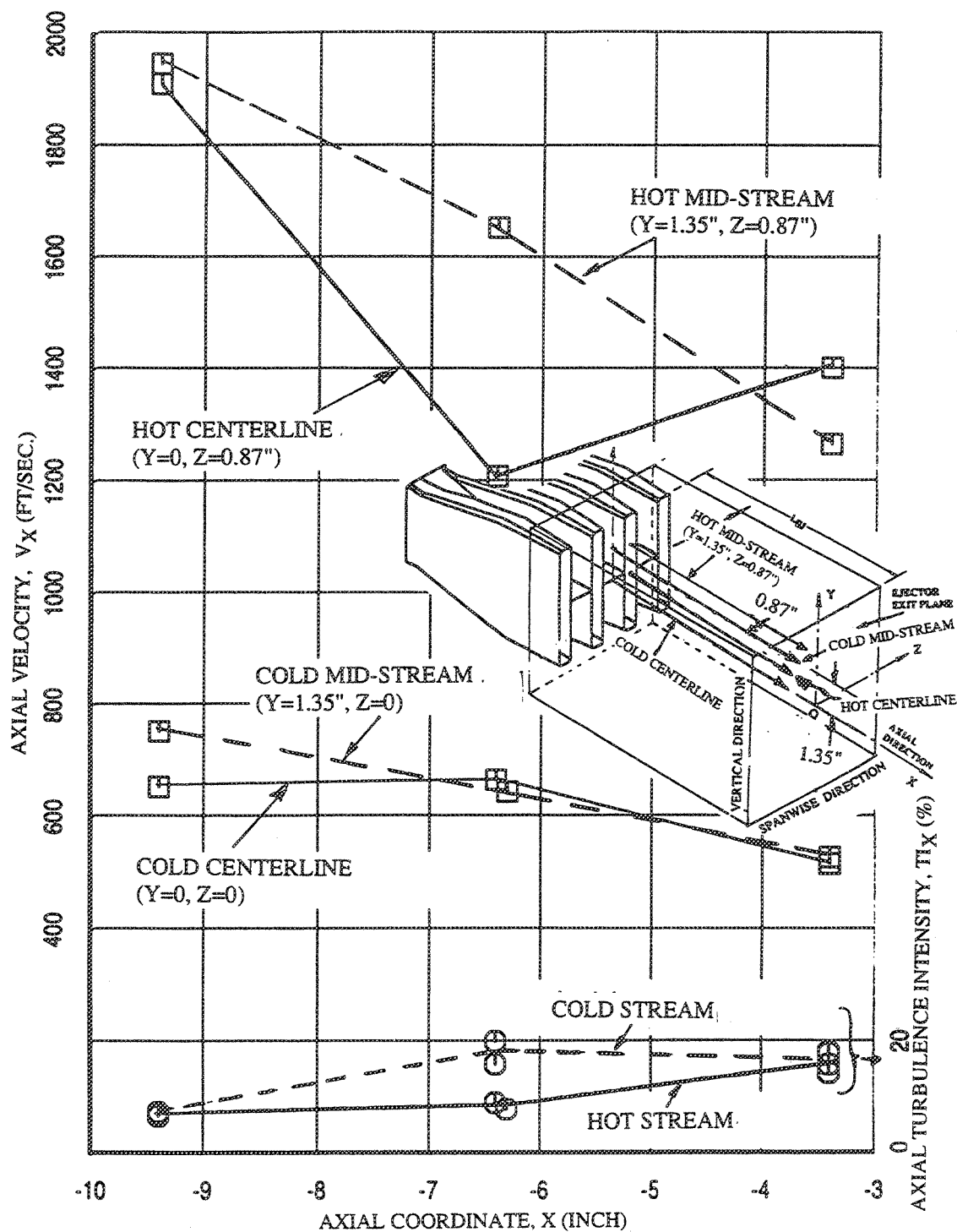


Figure 332. Axial Velocity and Turbulence Intensity Distributions Along X-Direction, Internal to Ejector of Axial Mixer-Ejector Nozzle With Short Hardwall Shroud  
( $SAR=4.9$ ,  $MAR=1.18$ ,  $L_{EJ}=10.46$  in.,  $NPR=2.5$ ,  $T_t=1325^\circ R$ ,  $V_j=1919$  ft/sec)

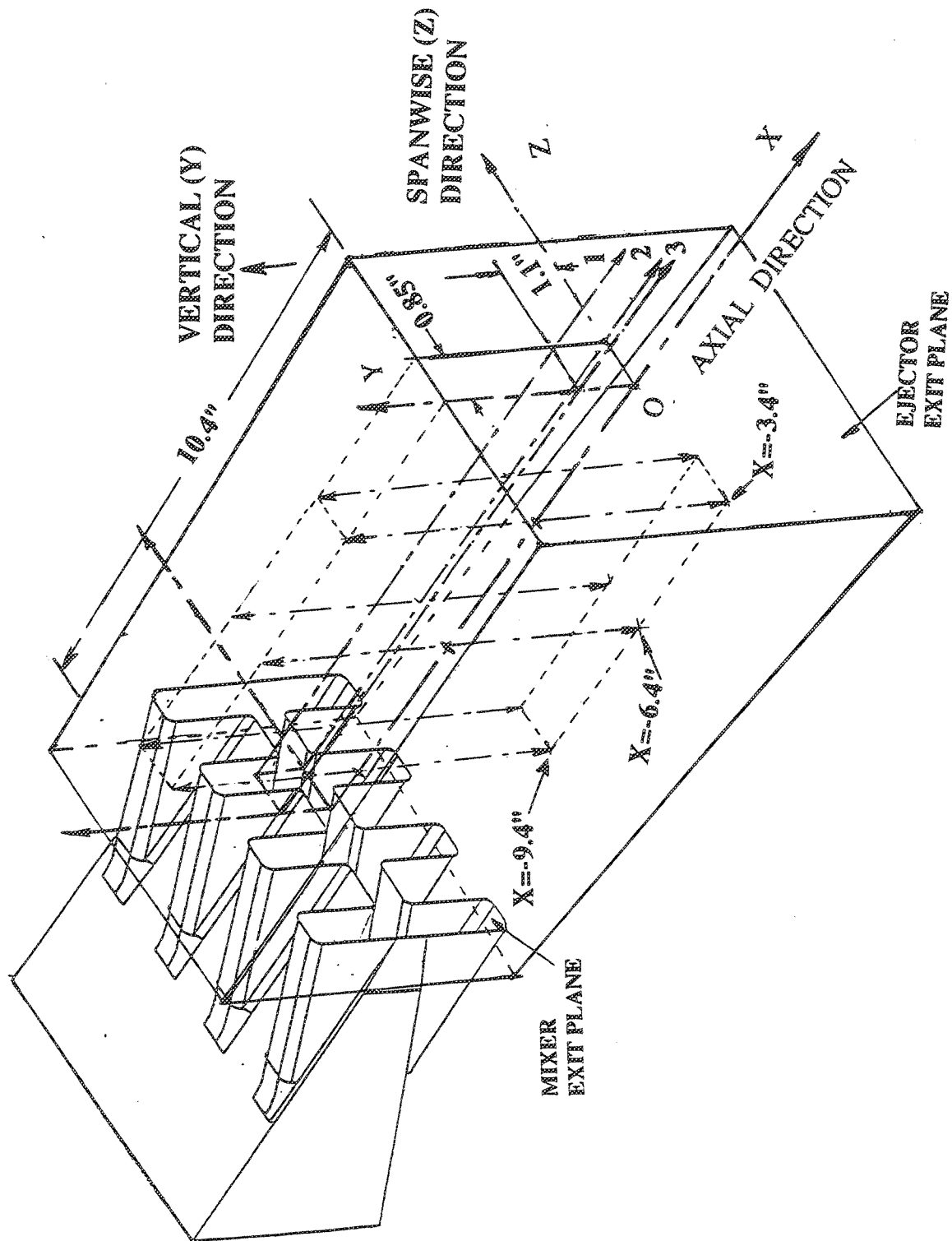


Figure 333. An Isometric View of a Vortical Mixer-Ejector Nozzle Configuration, Showing Axial (X) and Vertical (Y) Laser Doppler Velocimetry Traverse Locations in the Flowfield Internal to Ejector

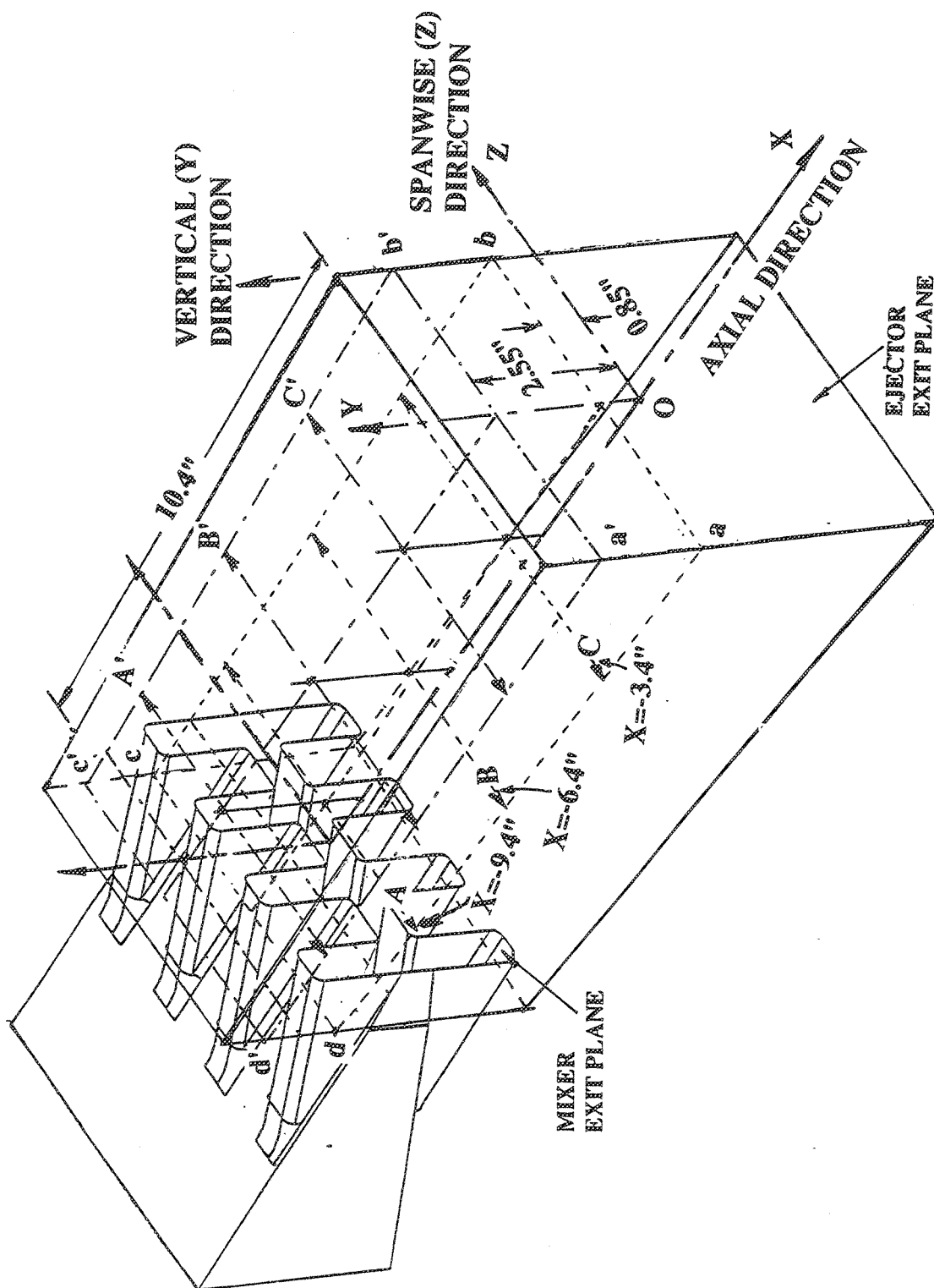


Figure 334. An Isometric View of a Vortical Mixer-Ejector Nozzle Configuration, Showing Spanwise (Z) Laser Doppler Velocimetry Traverse Locations at Two X-y Planes in the Flowfield Internal to Ejector

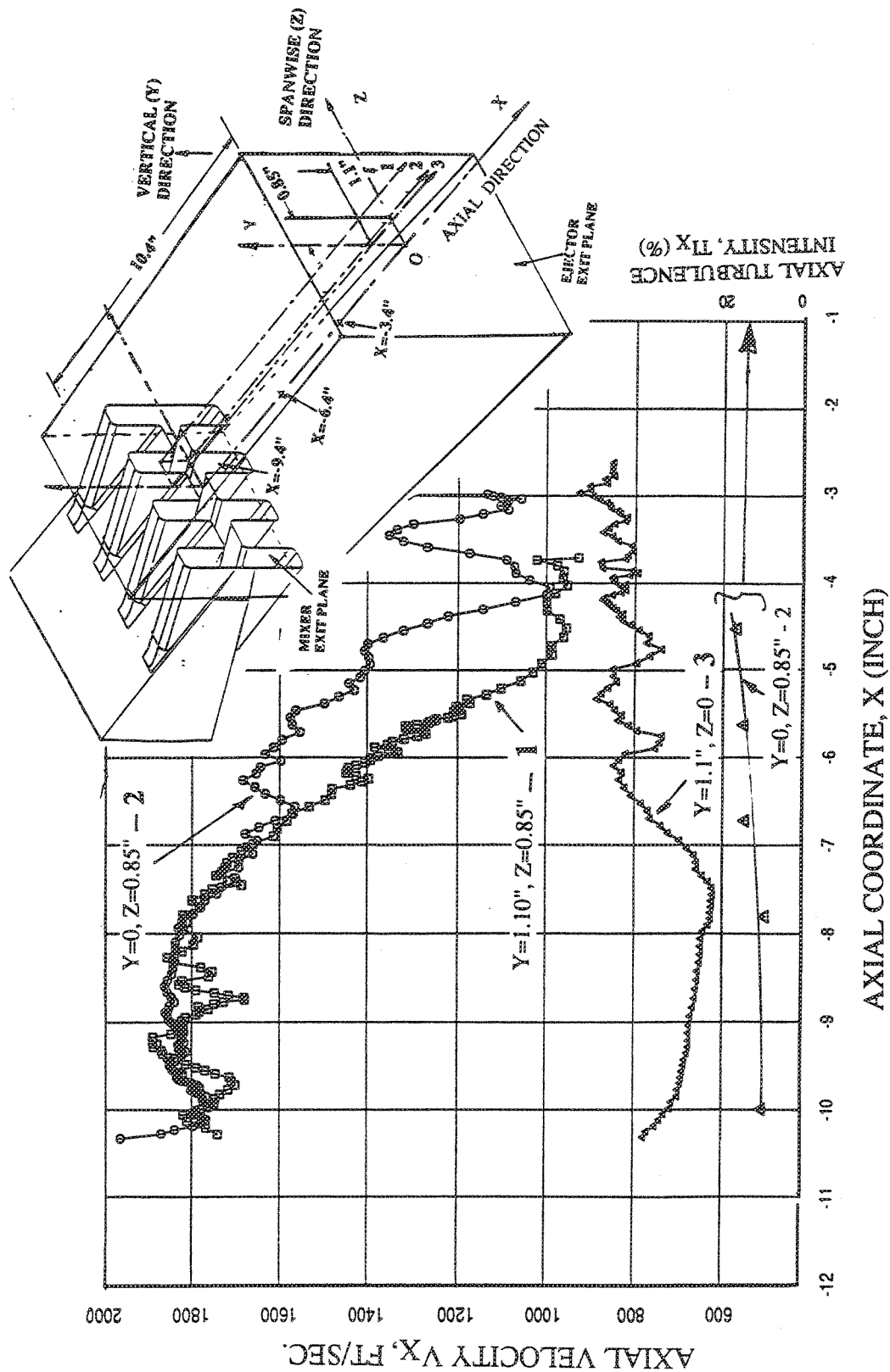


Figure 335. Axial Velocity and Turbulence Intensity Distributions Along X-Direction, Internal to Ejector of Vortical Mixer-Ejector Nozzle With Short Hardwall Shroud (SAR=4.9, MAR=1.18,  $L_{EJ}=10.46$  in.,  $Mn=0.32$ ,  $NPR=2.5$ ,  $T_t=1325^\circ R$ ,  $V_j=1919$  ft/sec)

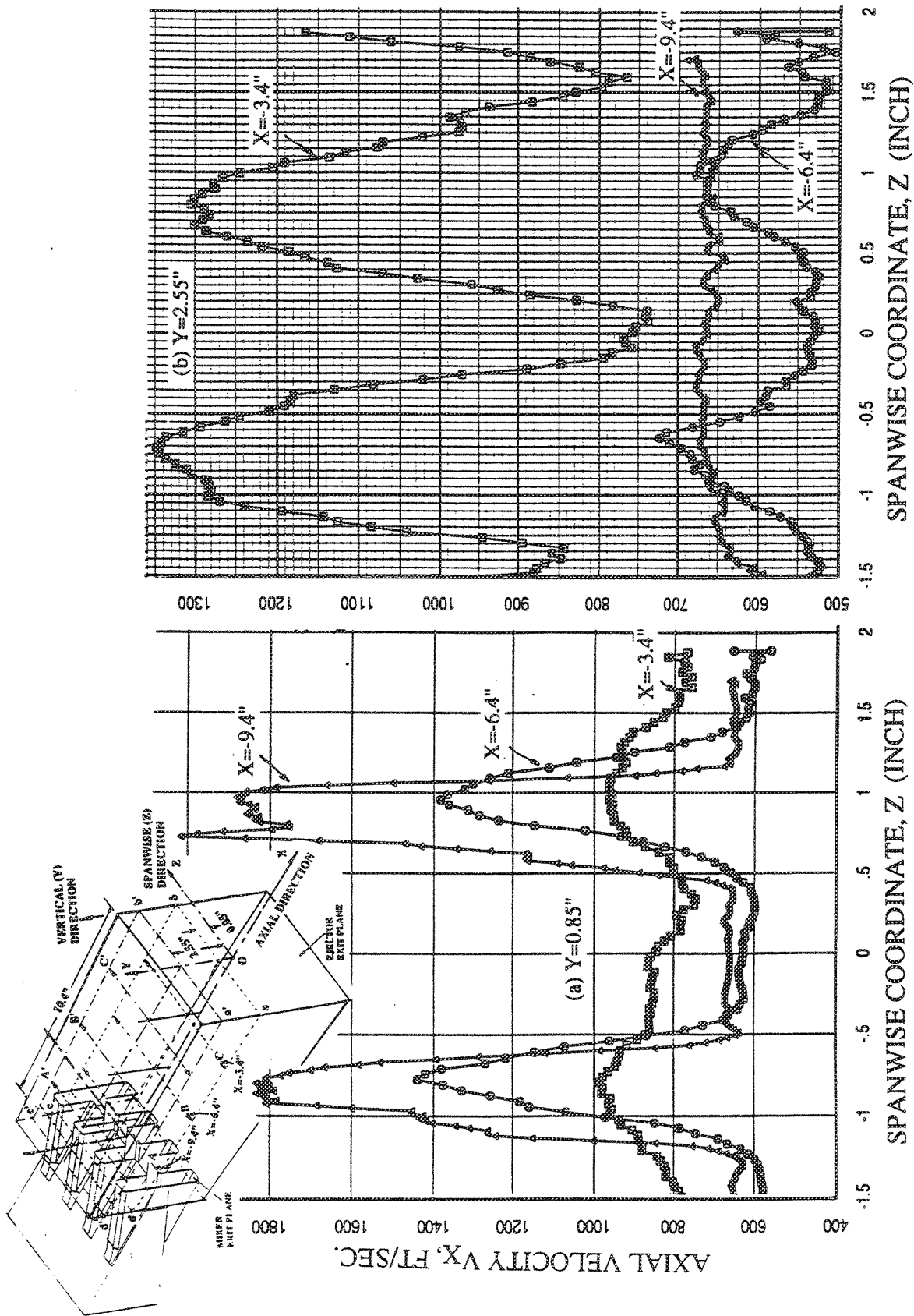


Figure 336. Axial Velocity Distributions Along Spanwise (Z) Direction at Two X-Y Planes, Internal to Ejector of Vortical Mixer-Ejector Nozzle With Short Hardwall Shroud (SAR=4.9, MAR=1.18,  $L_{EJ}=10.46$  in.,  $Mn=0.32$ ,  $NPR=2.5$ ,  $T_t=1325^\circ R$ ,  $V_j=1919$  ft/sec)

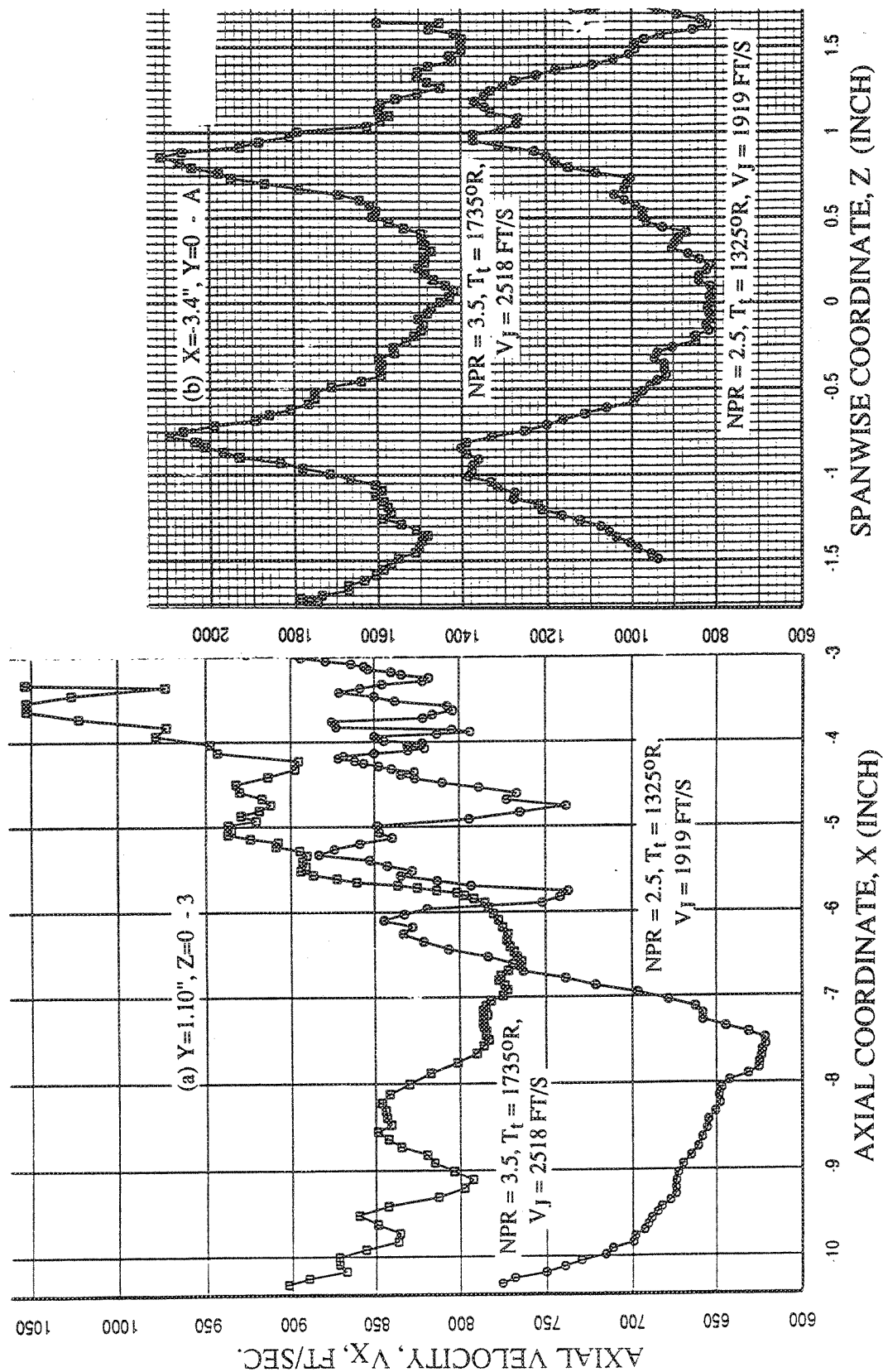


Figure 337. Axial Velocity Distributions Along Spanwise (Z) Direction at Two X-Y Planes, Internal to Ejector of Vortical Mixer-Ejector Nozzle With Short Hardwall Shroud (SAR=4.9, MAR=1.18,  $L_{EJ}=10.46$  in.,  $Mn=0.32$ , NPR=2.5,  $T_t=1325^\circ R$ ,  $V_J=1919$  ft/sec)

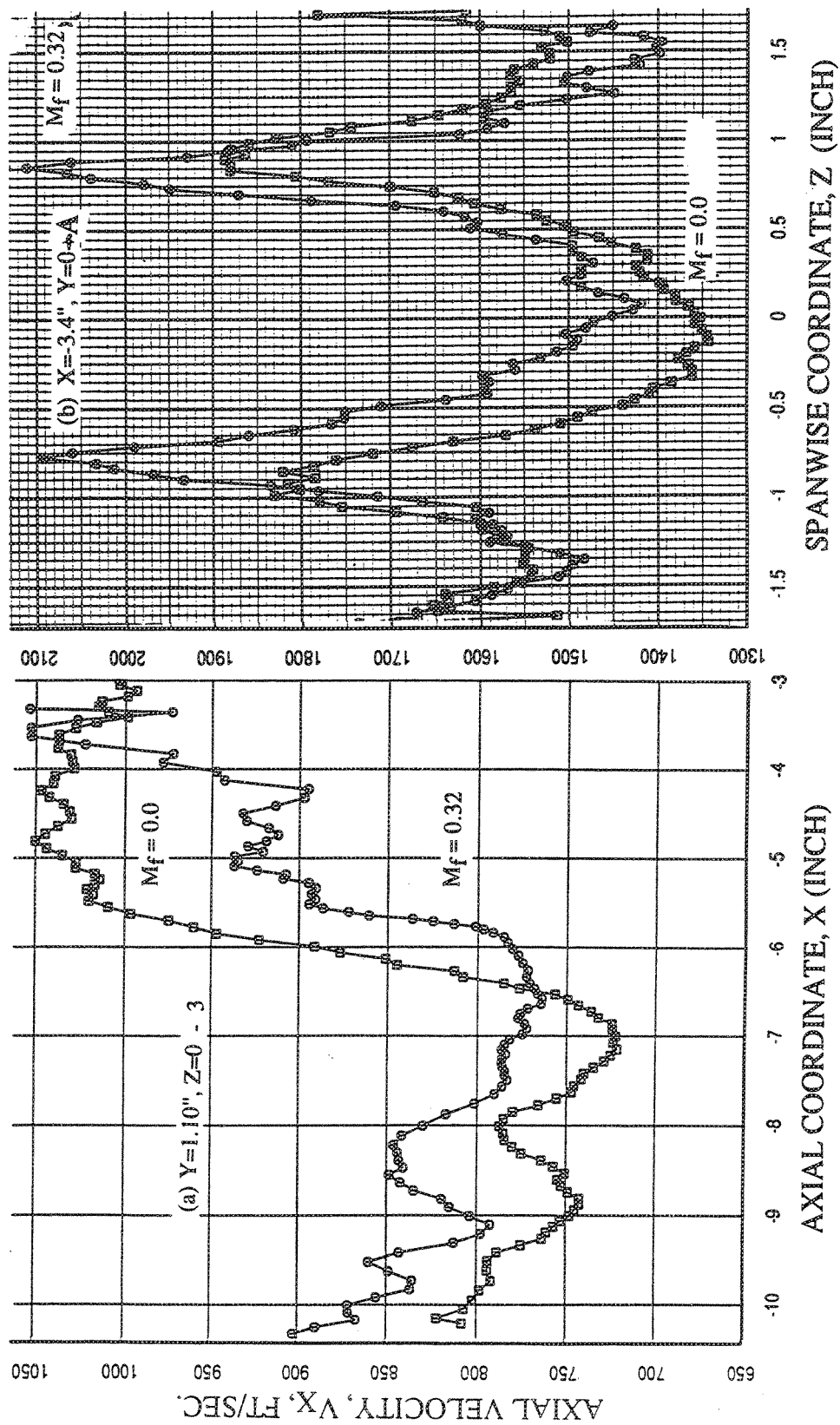


Figure 338. Effect of Flight on Axial Velocity Distributions Along Axial ( $X$ ) and Spanwise ( $Z$ ) Directions, Internal to Ejector of Vortical Mixer-Ejector Nozzle With Short Hardwall Shroud ( $SAR=4.9$ ,  $MAR=1.18$ ,  $L_{EJ}=10.46$  in.,  $NPR=3.5$ ,  $T_t=1735^\circ R$ ,  $V_t=2518$  ft/sec)





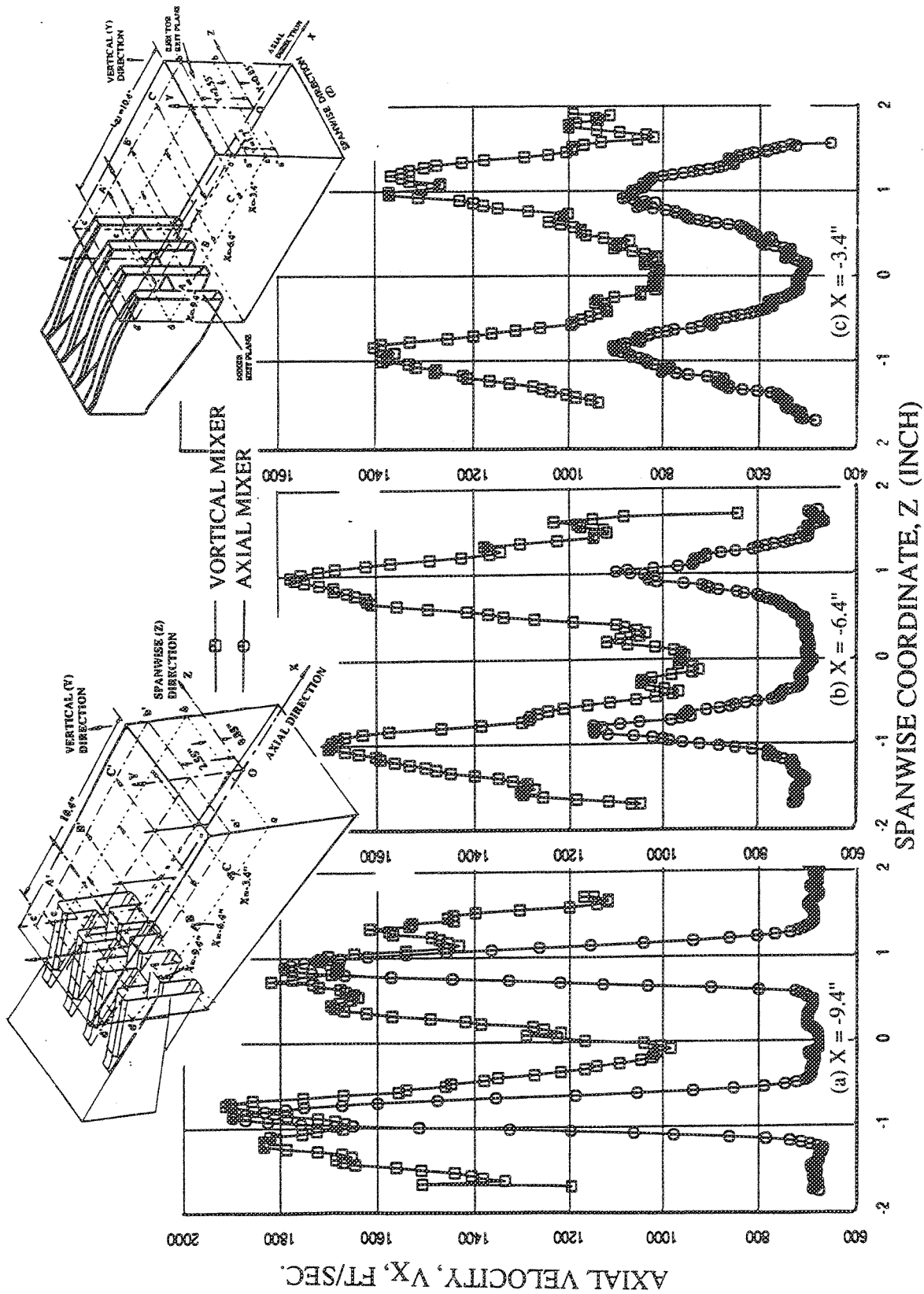


Figure 340. Comparison of Axial Velocity Distribution Along Spanwise (Z) Direction Between Vortical and Axial Mixers at Various Axial Locations Internal to Ejector With Short Hardwall Shroud at  $Y=1$   
 (SAR=4.9, MAR=1.18,  $L_{EJ}=10.46$  in.,  $Mn=0.32$ , NPR=2.5,  $T_t=1325^\circ R$ ,  $V_t=1919$  ft/sec)

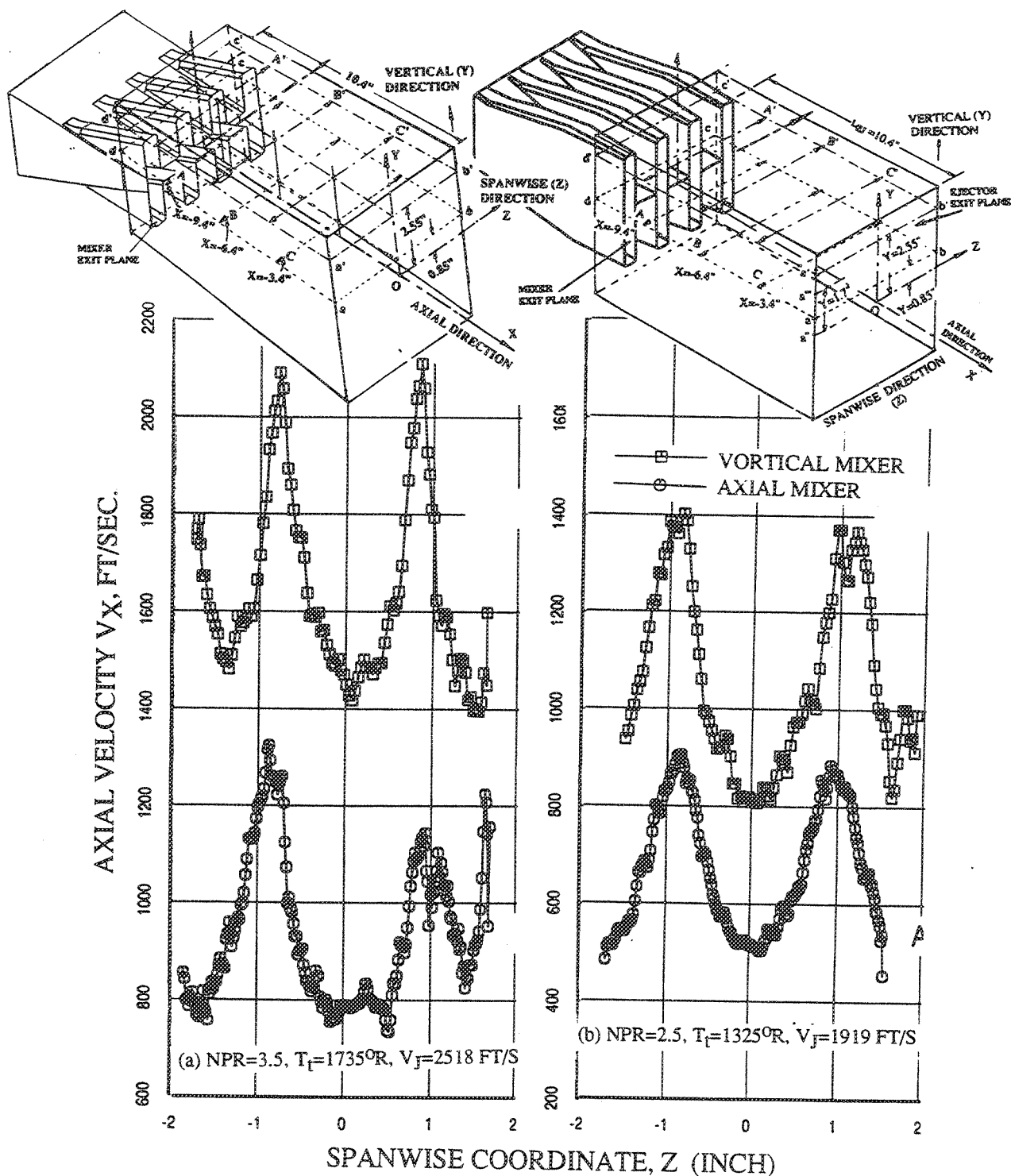
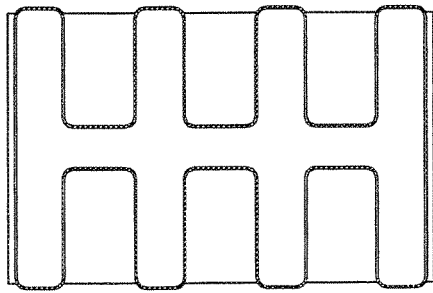
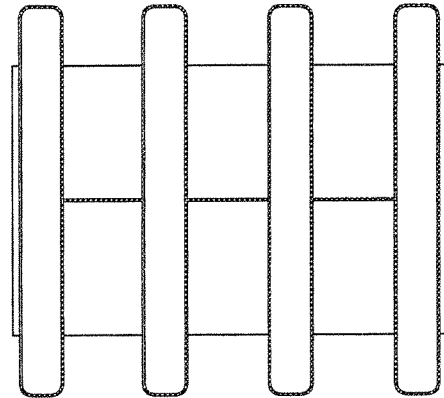


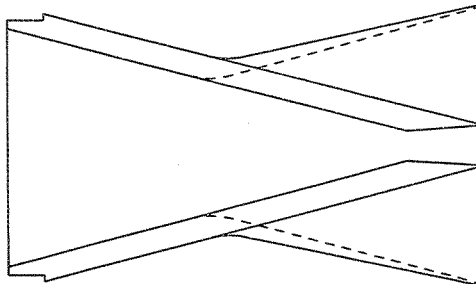
Figure 341. Comparison of Axial Velocity Distributions Along Spanwise (Z) Direction Between Vortical and Axial Mixers at  $X=-3.4$  in. and  $Y=0$  at Two Different Aerothermodynamic Conditions, Internal to Ejector With Short Hardwall Shroud ( $SAR=4.9$ ,  $MAR=1.18$ ,  $L_{EJ}=10.46$  in.,  $Mn=0.32$ )



Aft Looking Forward at Mixer Exit

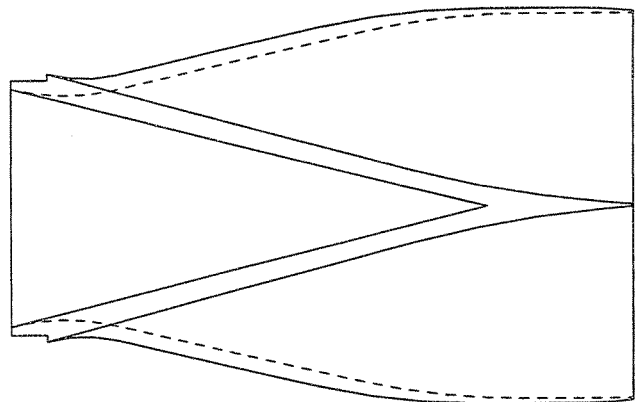


Aft Looking Forward at Mixer Exit



Side View (Cut Down Centerline of Primary Lobe)

(a) Vortical Mixer



Side View (Cut Down Centerline of Primary Lobe)

(b) Axial Mixer

*Figure 342. Geometry of Pratt & Whitney Mixers (Not to Scale)*

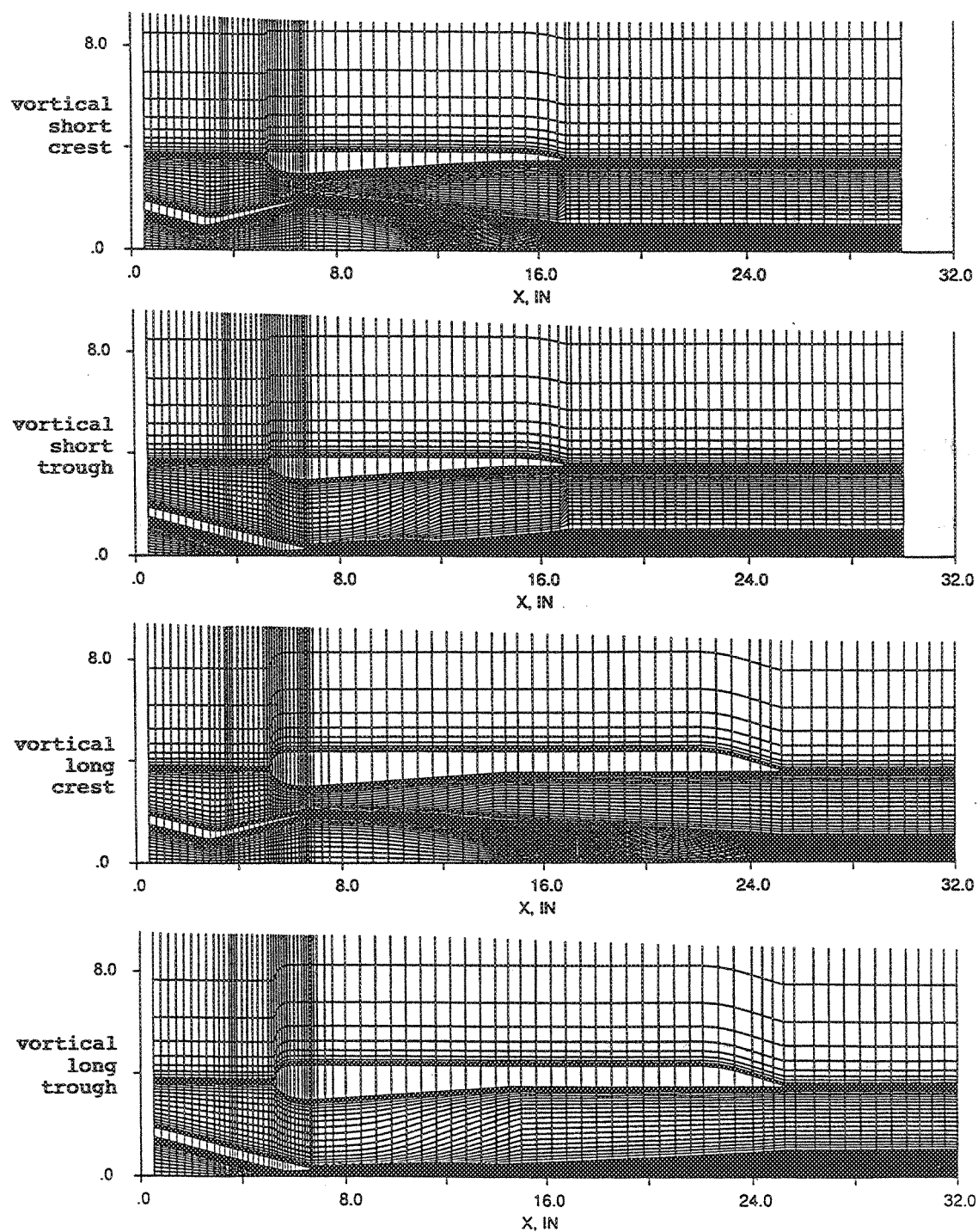


Figure 343. Axial Grid Cuts for Pratt & Whitney Vortical Mixer-Ejector

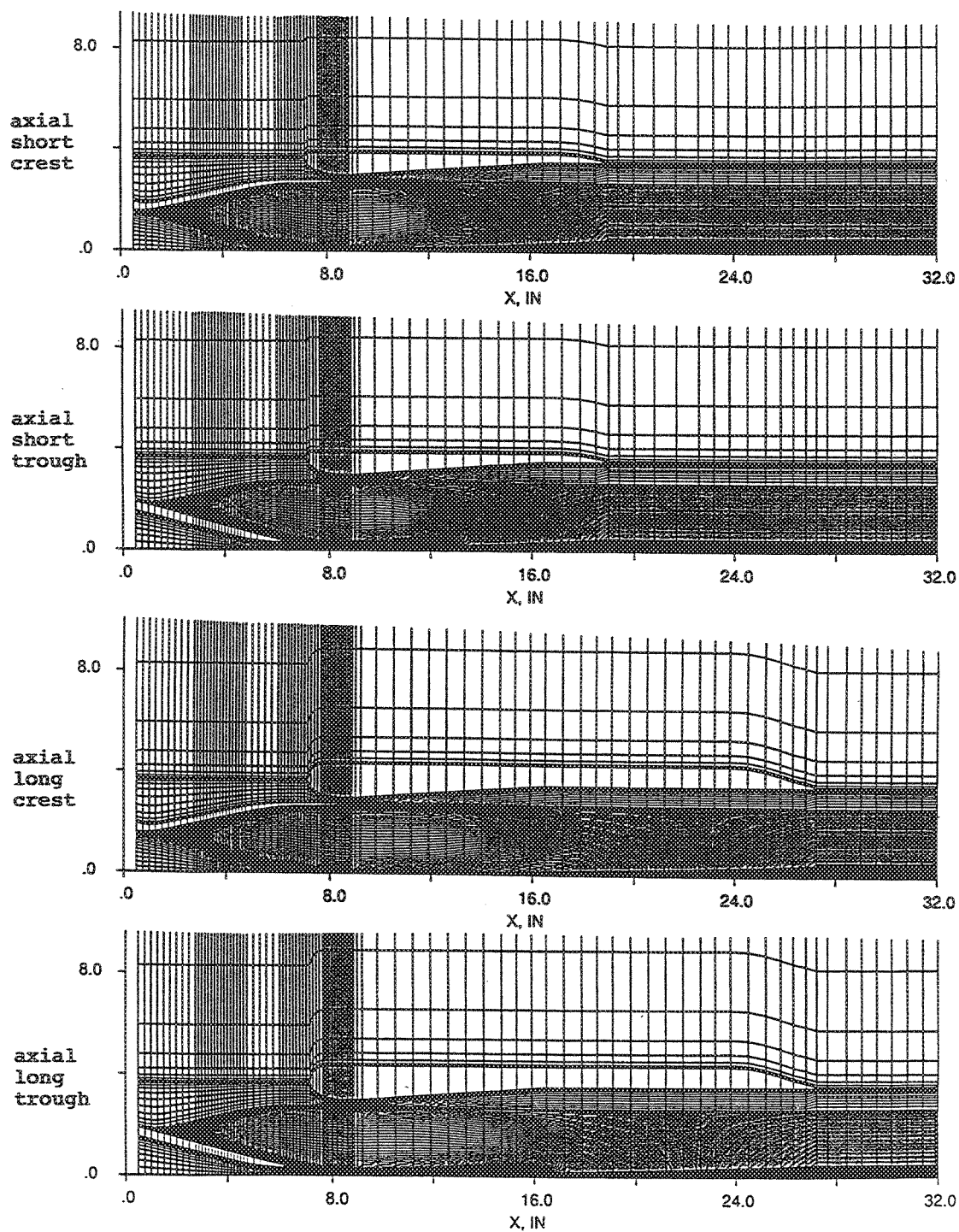


Figure 344. Axial Grid Cuts for Pratt & Whitney Axial Mixer-Ejector

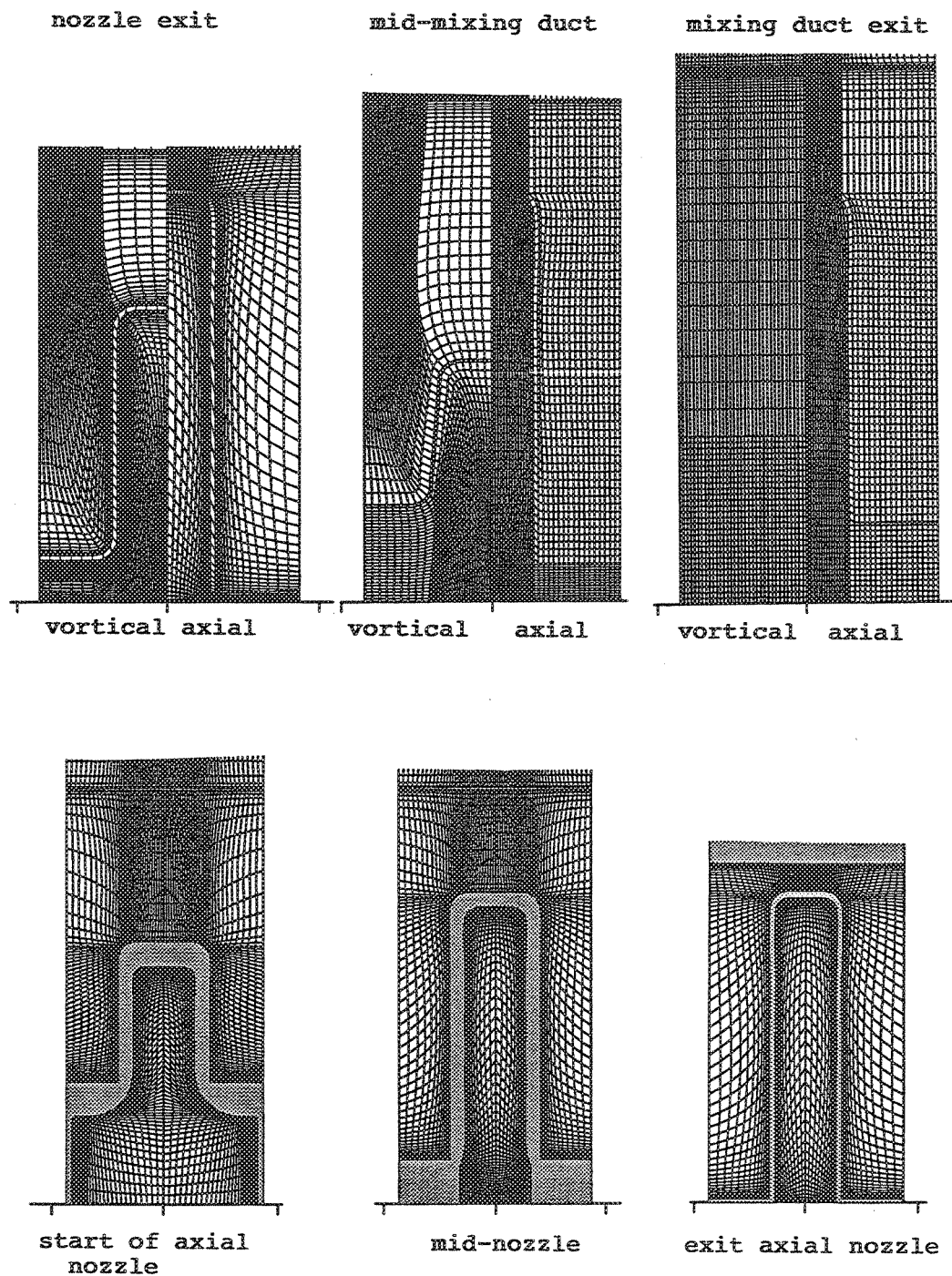


Figure 345. Cross-Sectional Grid Cuts for Pratt & Whitney Vortical and Axial Cases

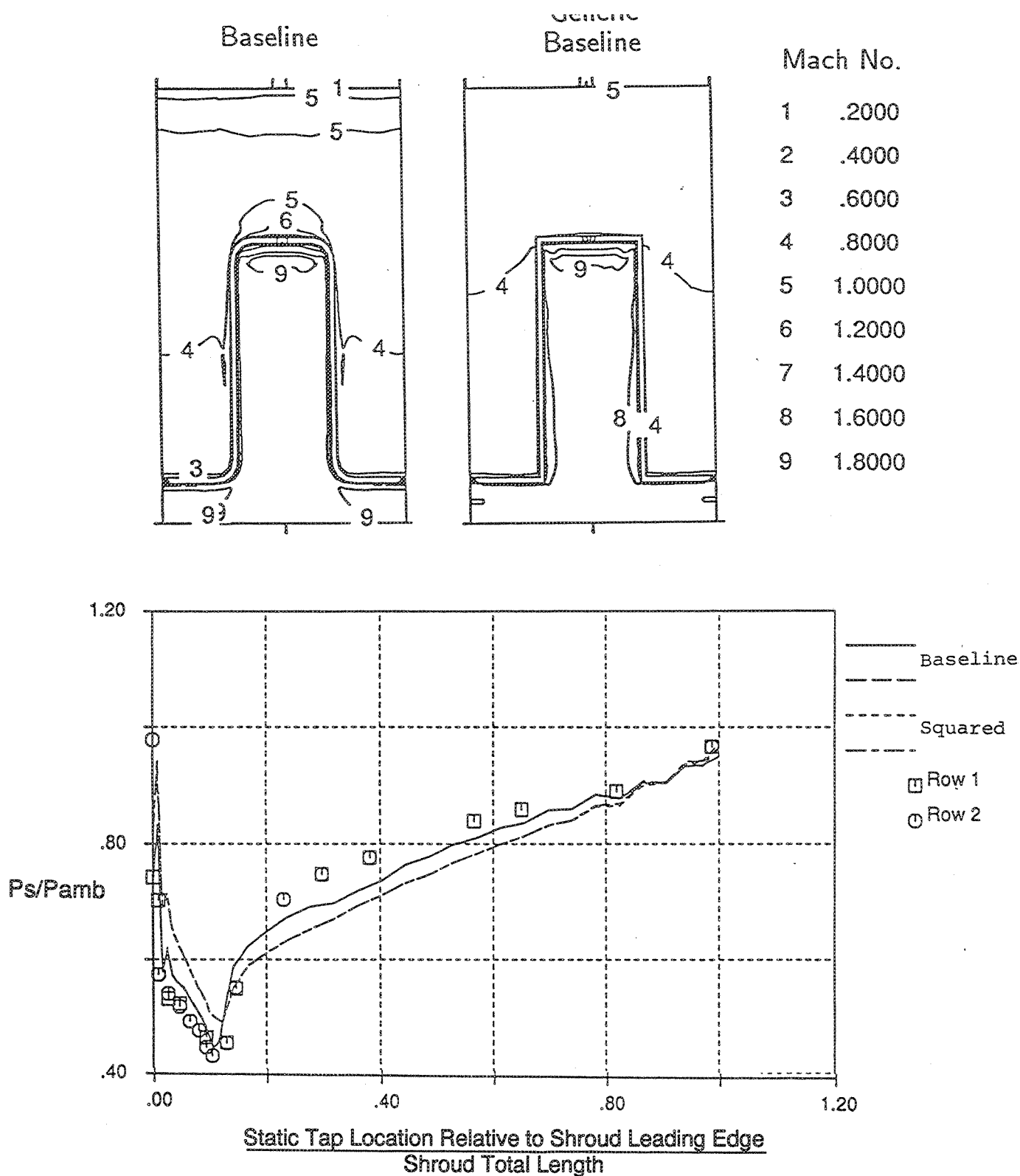


Figure 346. Effect of Lobe Squaring on Shroud Loading for Pratt & Whitney GEN 1 Mixer-Ejector



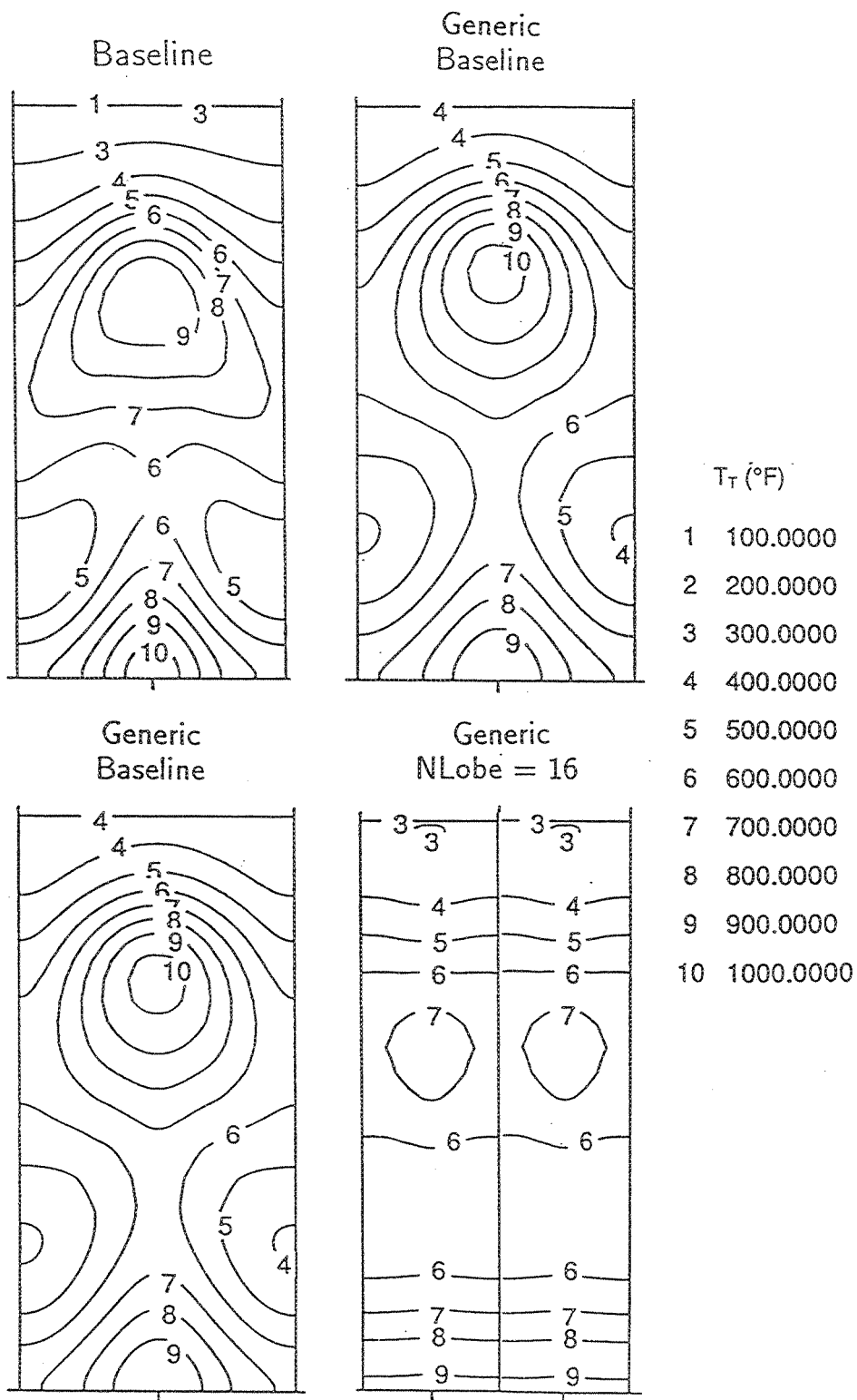


Figure 347. Effect of Parametrics on Ejector Exit Plane Total Temperature

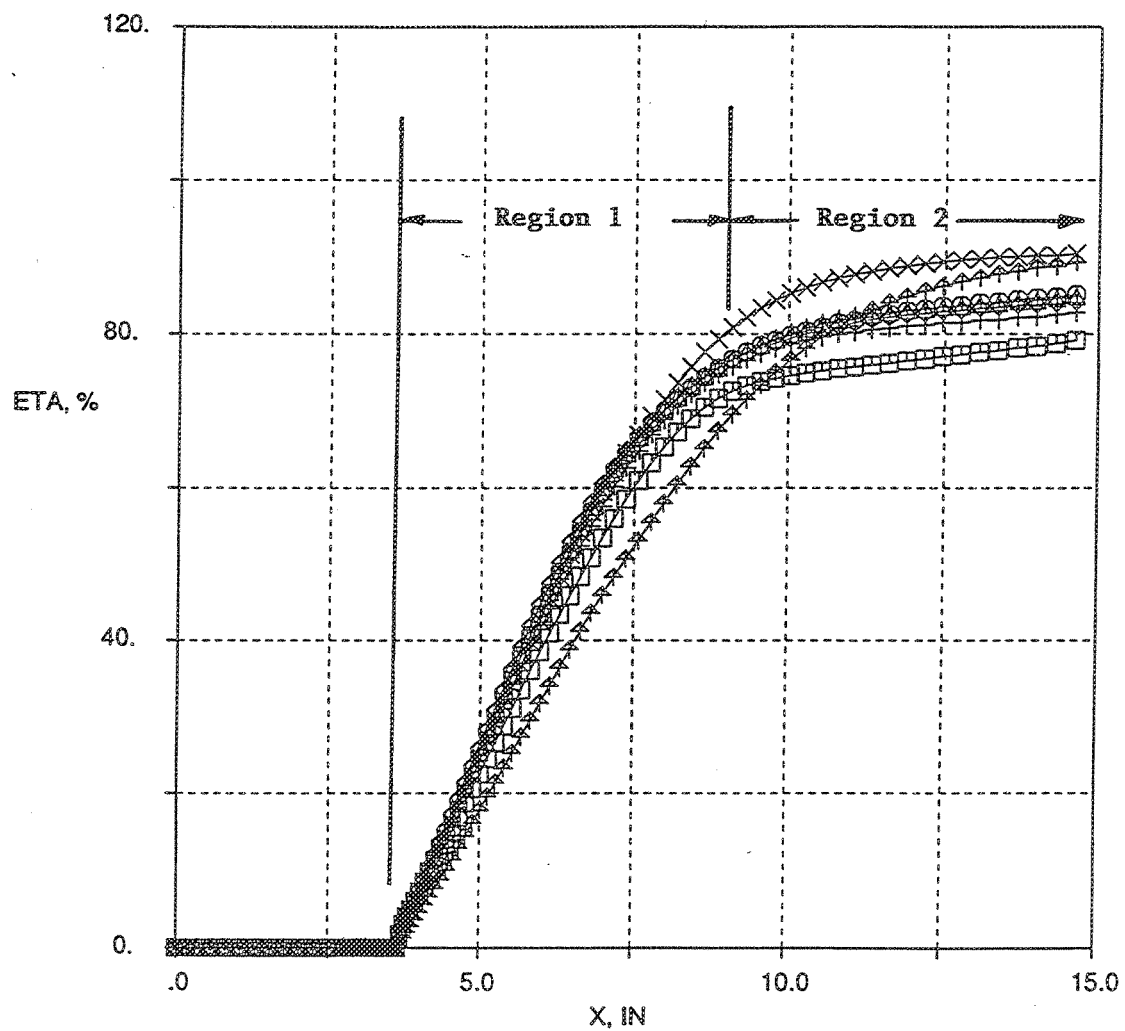


Figure 348. Mixing Efficiency of Parametric GEN 1.5 Mixer-Ejector Configurations

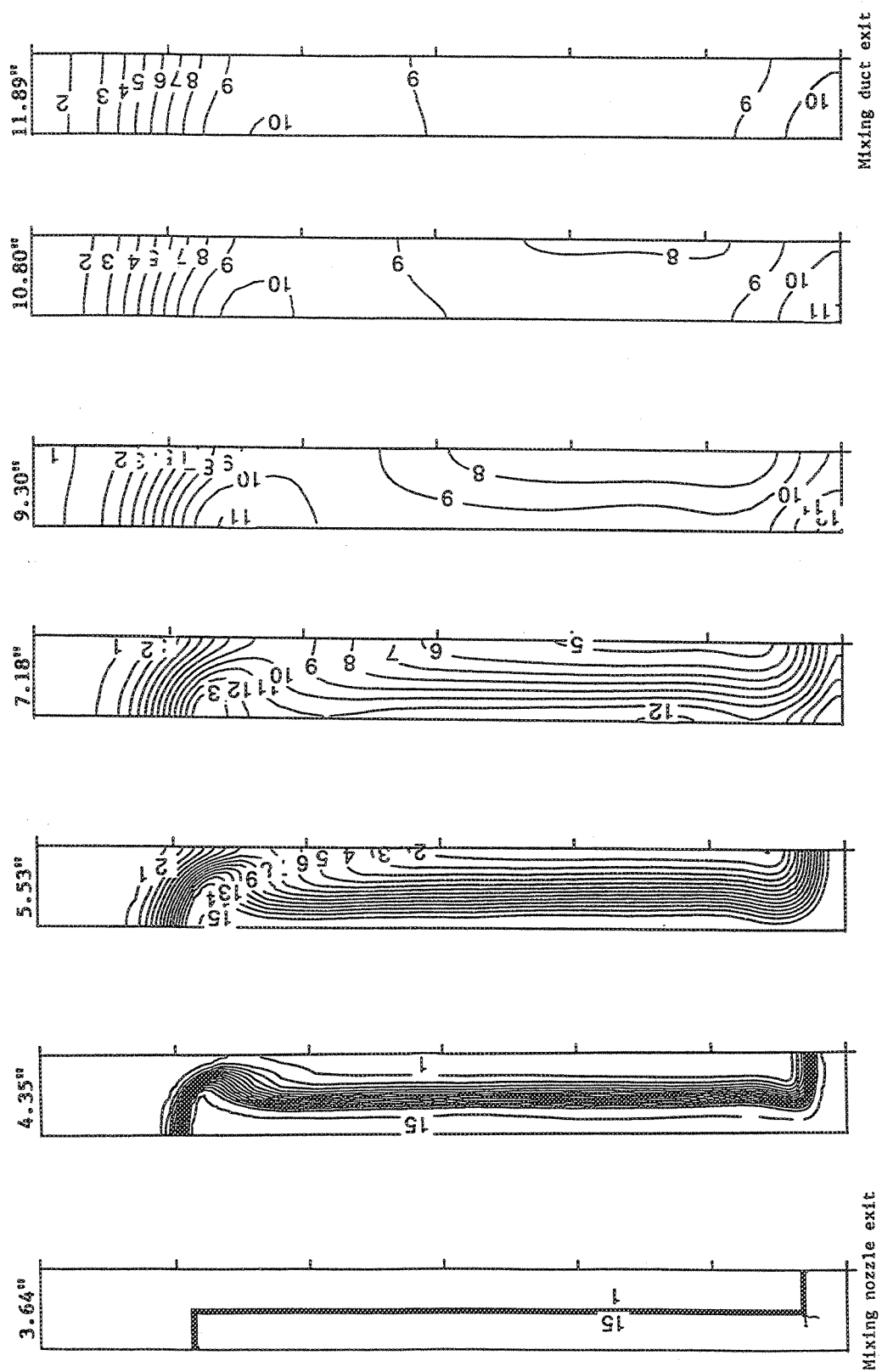


Figure 349. Isotherm Contour Plots for Typical GEN 1.5 Configuration

		<u>NPR</u>	<u>Top (°R)</u>	<u><math>\gamma\%</math></u>	<u><math>\omega</math></u>	<u><math>M_\infty</math></u>
————	Case 9301	3.5	1960	81	1.70	.20
-----	Case 9322	3.5	1735	80	1.60	.32
-----	Case 9405	3.5	1960	81	1.75	.32
□	□ Pt 868	3.5	1733			
○	○ Pt 871	3.5	1735			
△	△ Pt 858	4.0	1748			

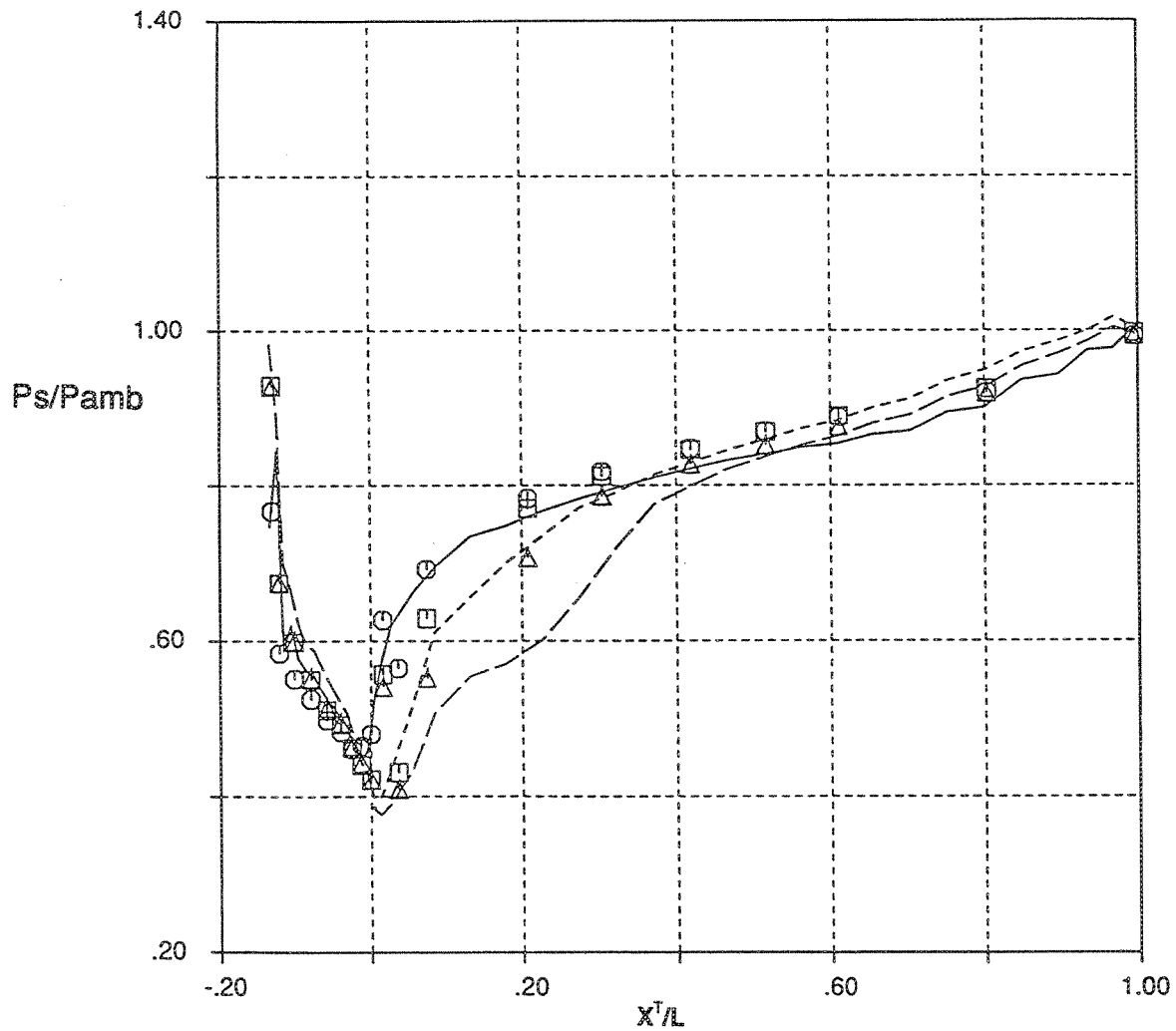


Figure 350. Comparison of Shroud Pressure Loading for Vortical Nozzle/Short Shroud Mixer-Ejector

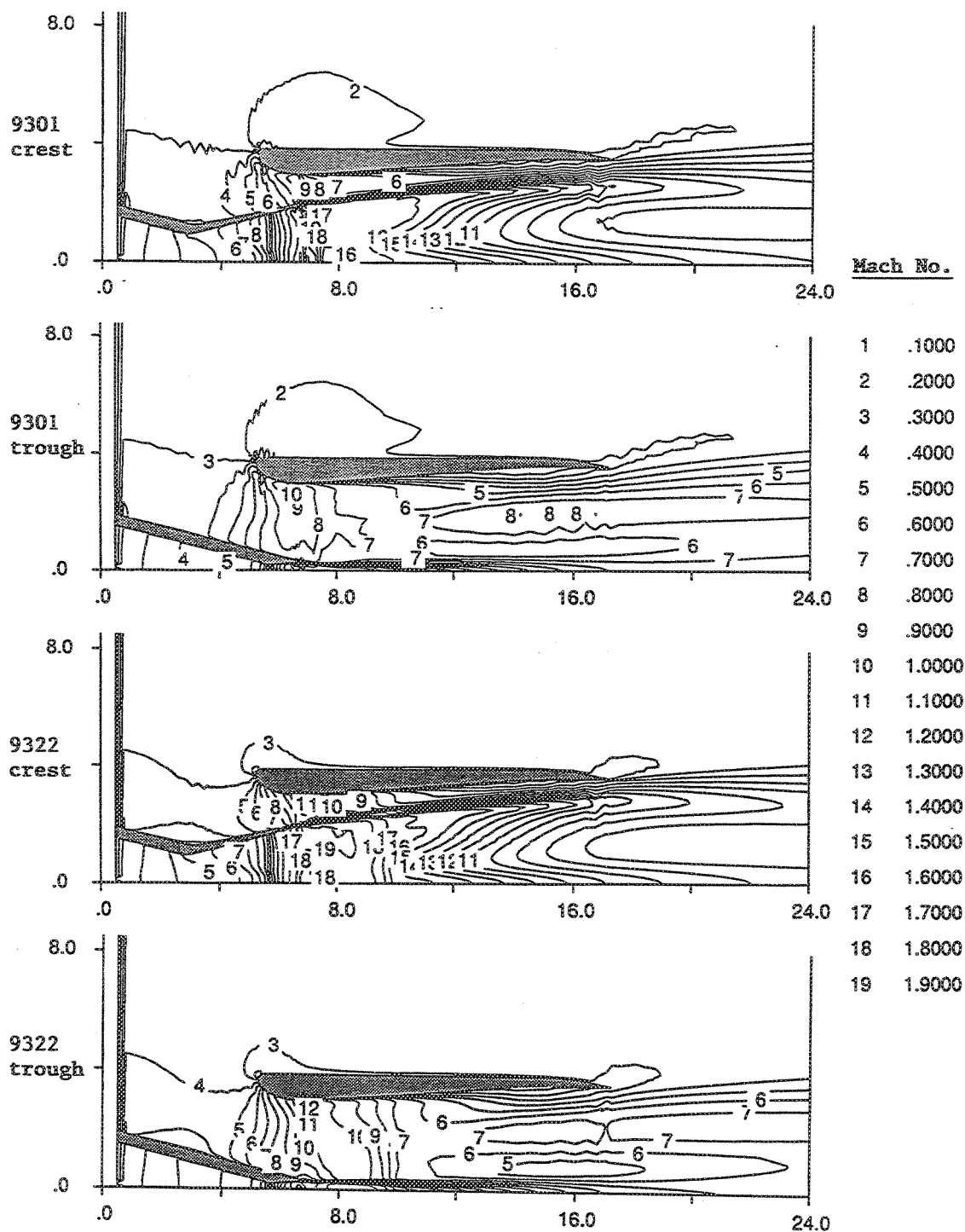


Figure 351. Axial Crest Mach Number Distributions for Vortical Nozzle/Short Shroud Mixer-Ejector

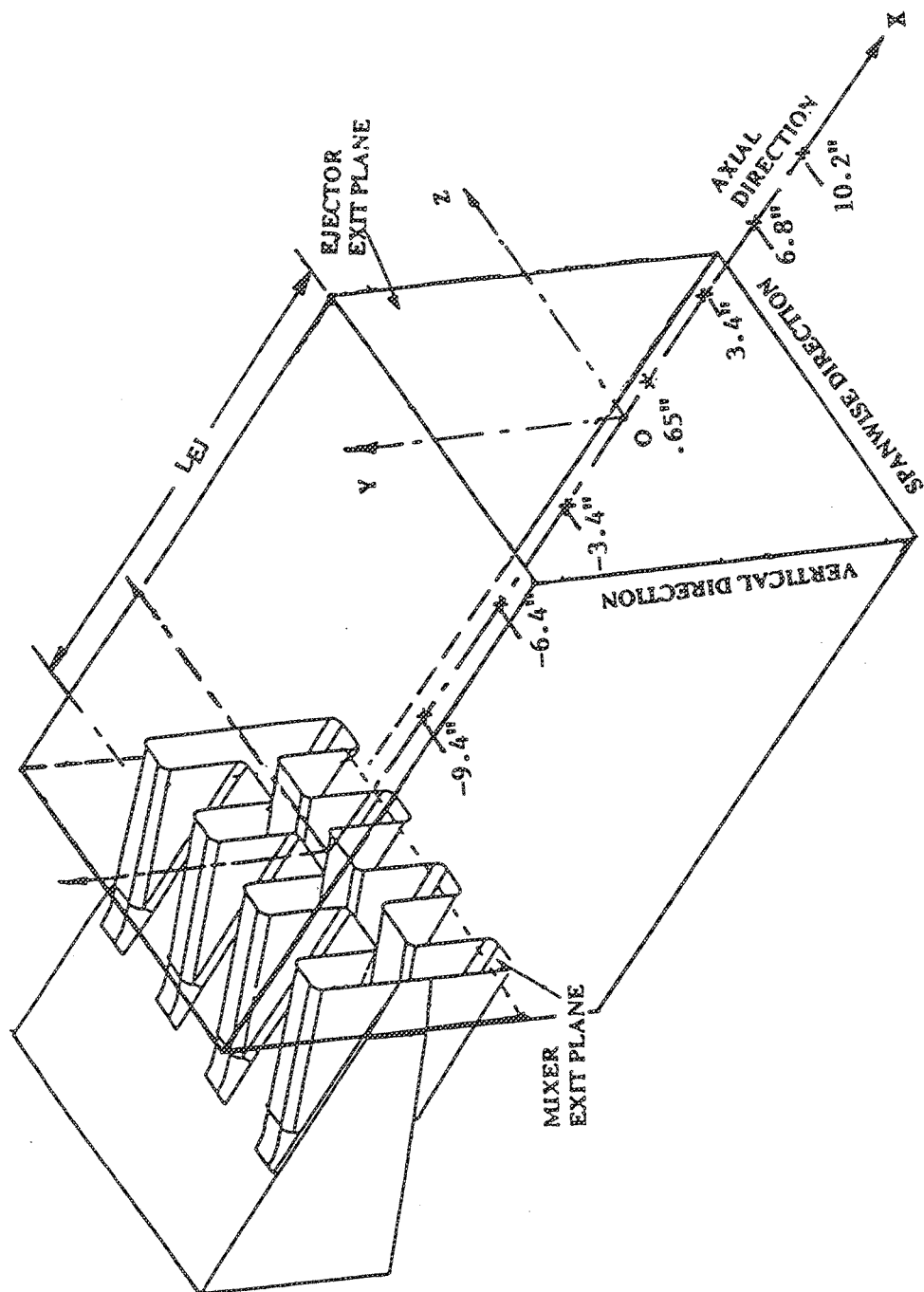


Figure 352. Schematic of Mixer-Ejector Geometry and Axial Location of Internal/External LDV Traverse Planes

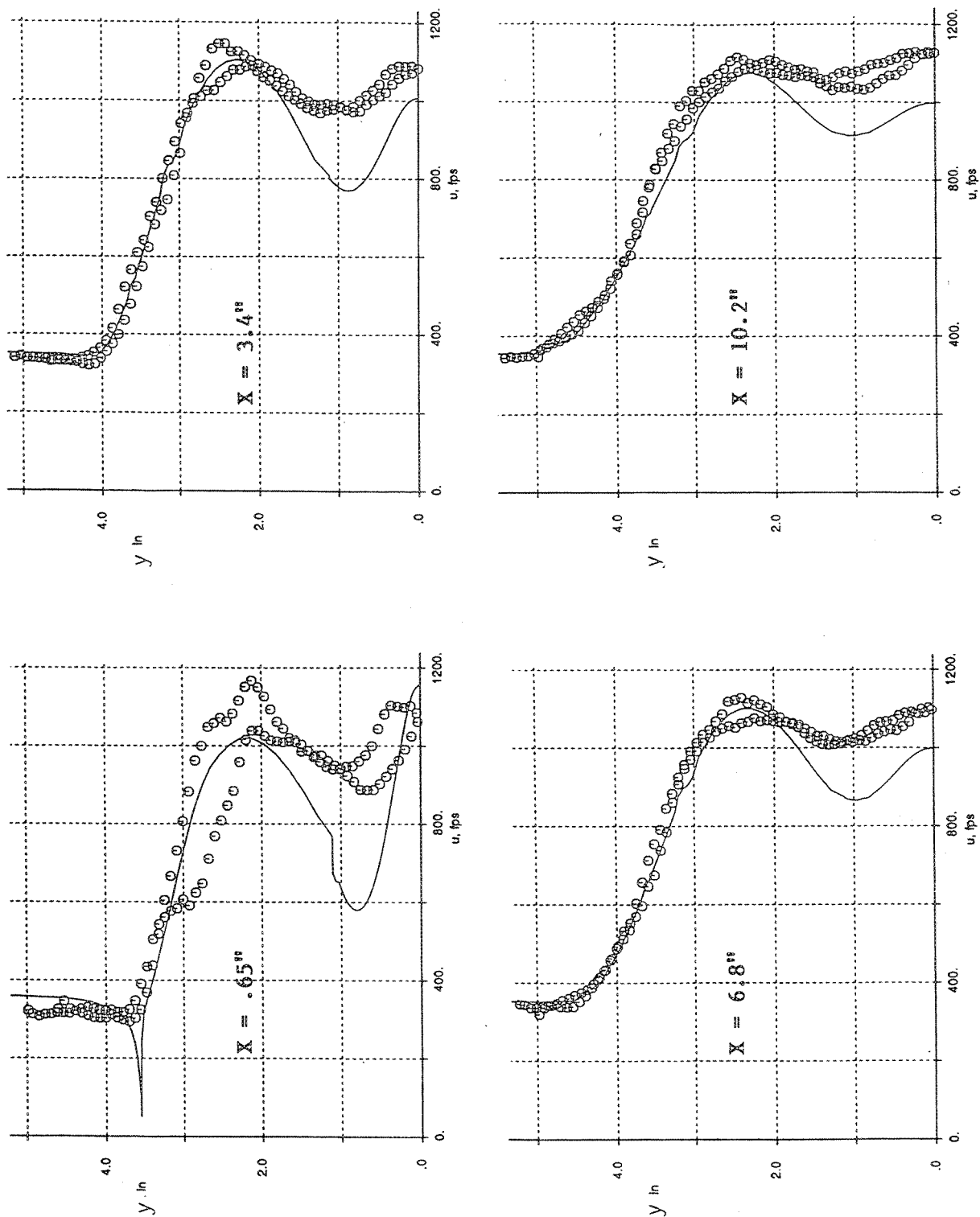


Figure 353. Comparison of Axial Velocity Profiles (Vortical, Trough Plane Cut) for Vortical/Short Shroud Mixer-Ejector

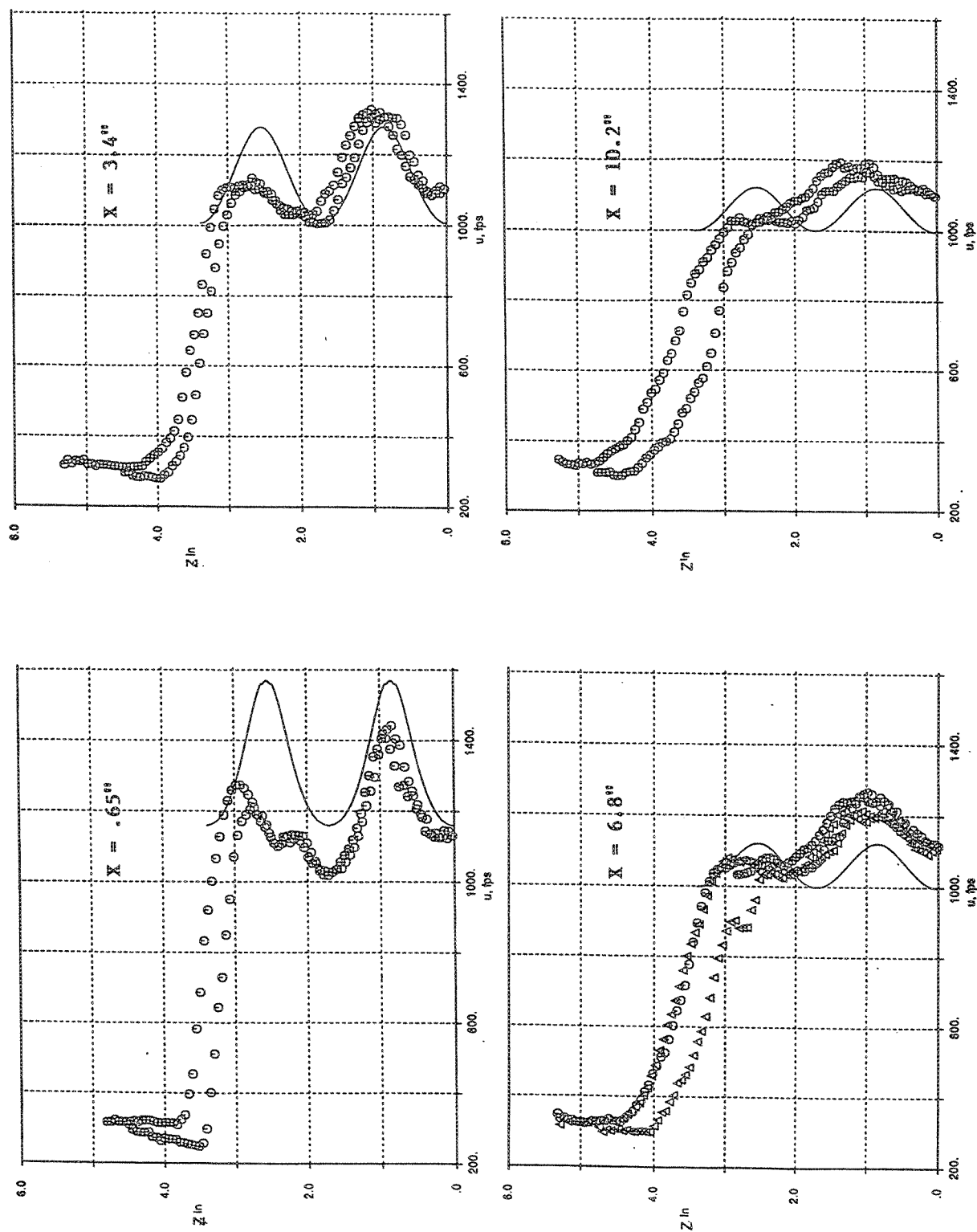
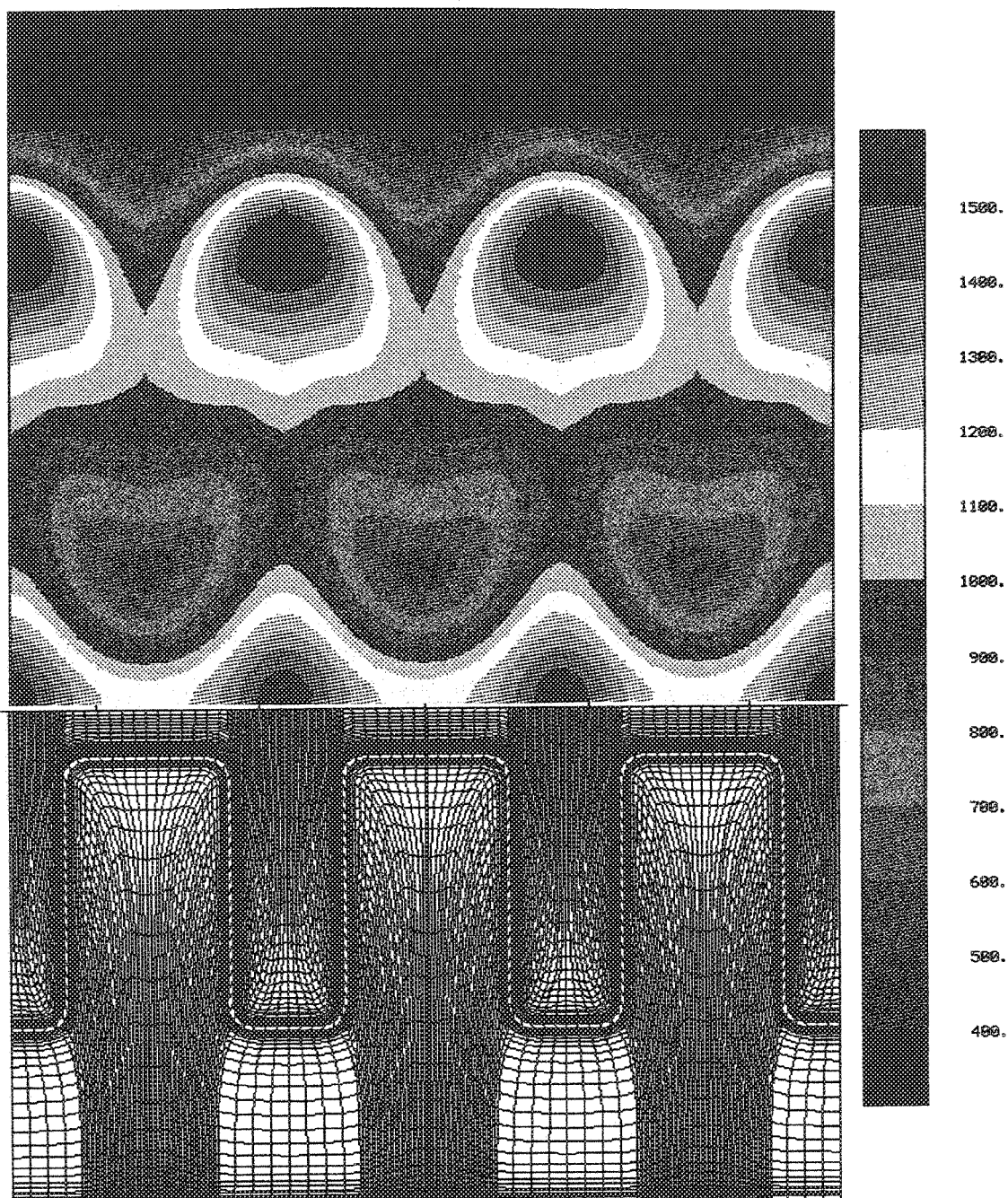


Figure 354. Comparison of Axial Velocity Profiles (Lateral, Symmetry Plane Cut) for Vortical/Short Shroud Mixer-Ejector





lobe9322 - baseline NPR=3.5  $T_t=1275F$   $M_{inf}=0.32$   
 Axial velocity, fps - TE of shroud

*Figure 355. Pratt & Whitney Vortical Nozzle With Short Shroud Axial Velocity at Ejector Exit Plane*

		NPR	Top (°R)	$\eta$ %	$\omega$
—	Case 9320	3.5	1735	91	1.61
- - -	Case 9402	3.8	1735	90	1.52
- - - -	Case 9403	3.5	1635	90	1.60
□	□ Pt 503	3.4	1589		
○	○ Pt 519	3.7	1679		

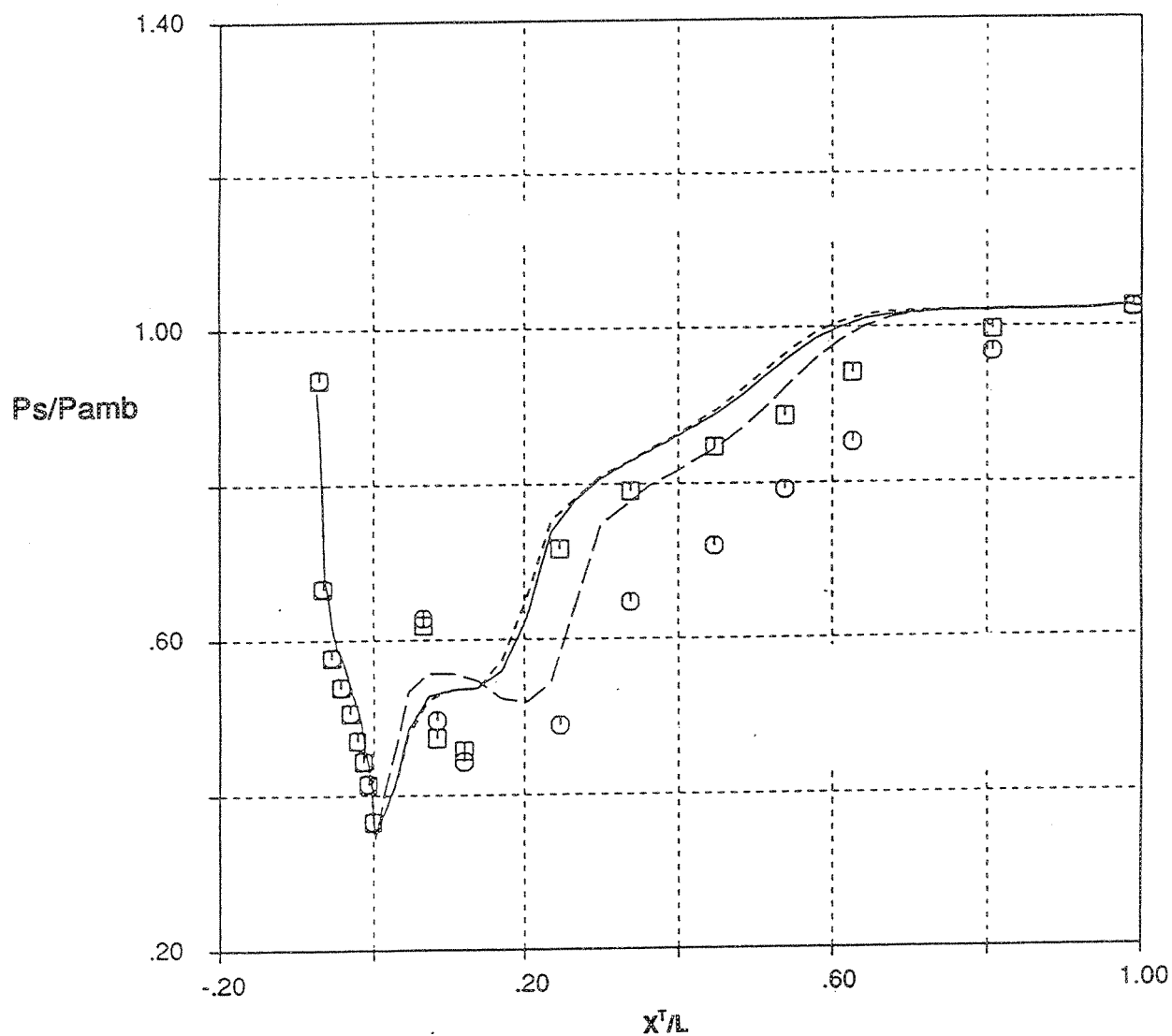


Figure 356. Comparison of Shroud Pressure Loading for Vortical Nozzle/Long Shroud Mixer-Ejector

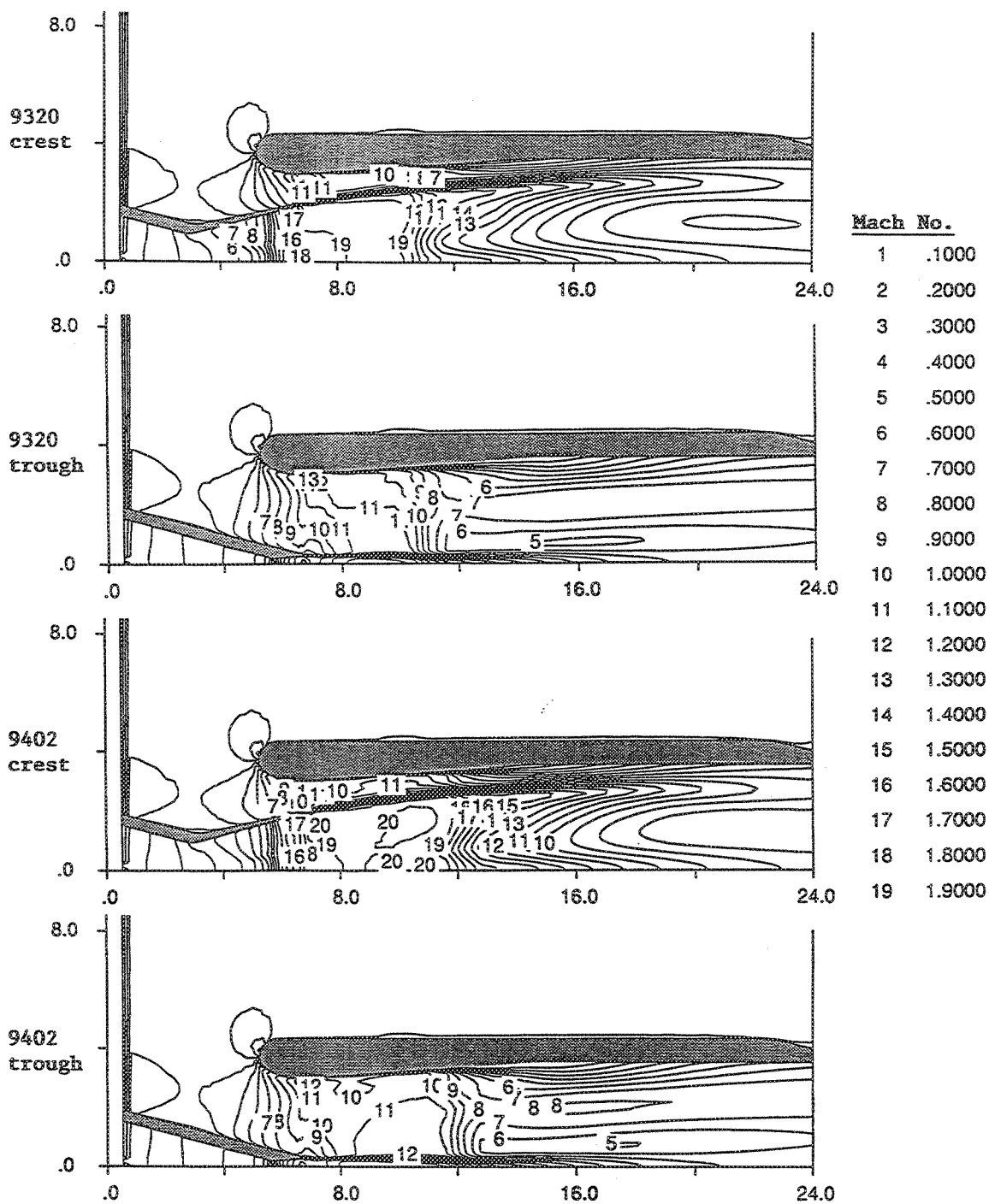


Figure 357. Axial Cut Mach Number Distributions for Vortical Nozzle/Short Shroud Cases

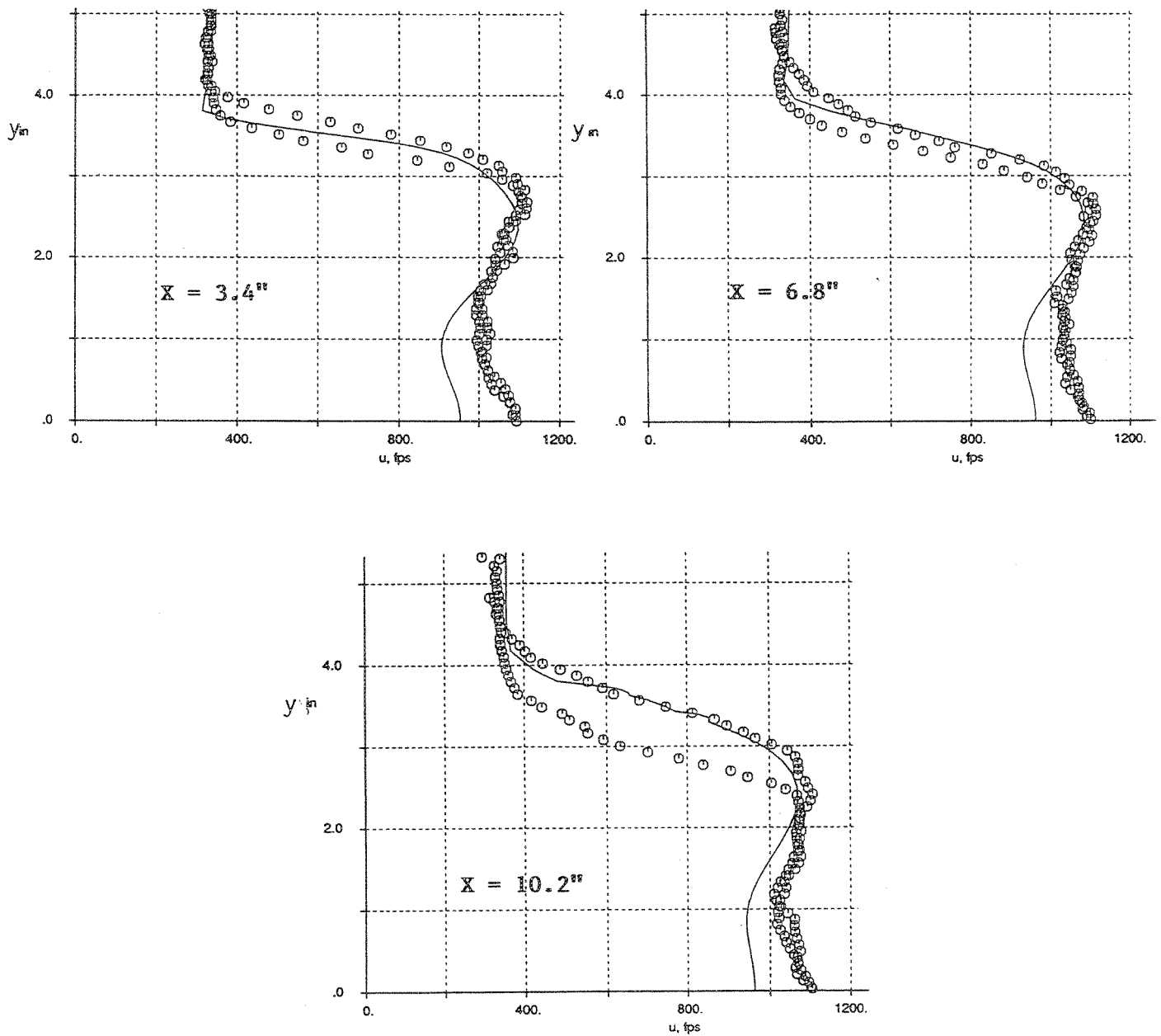
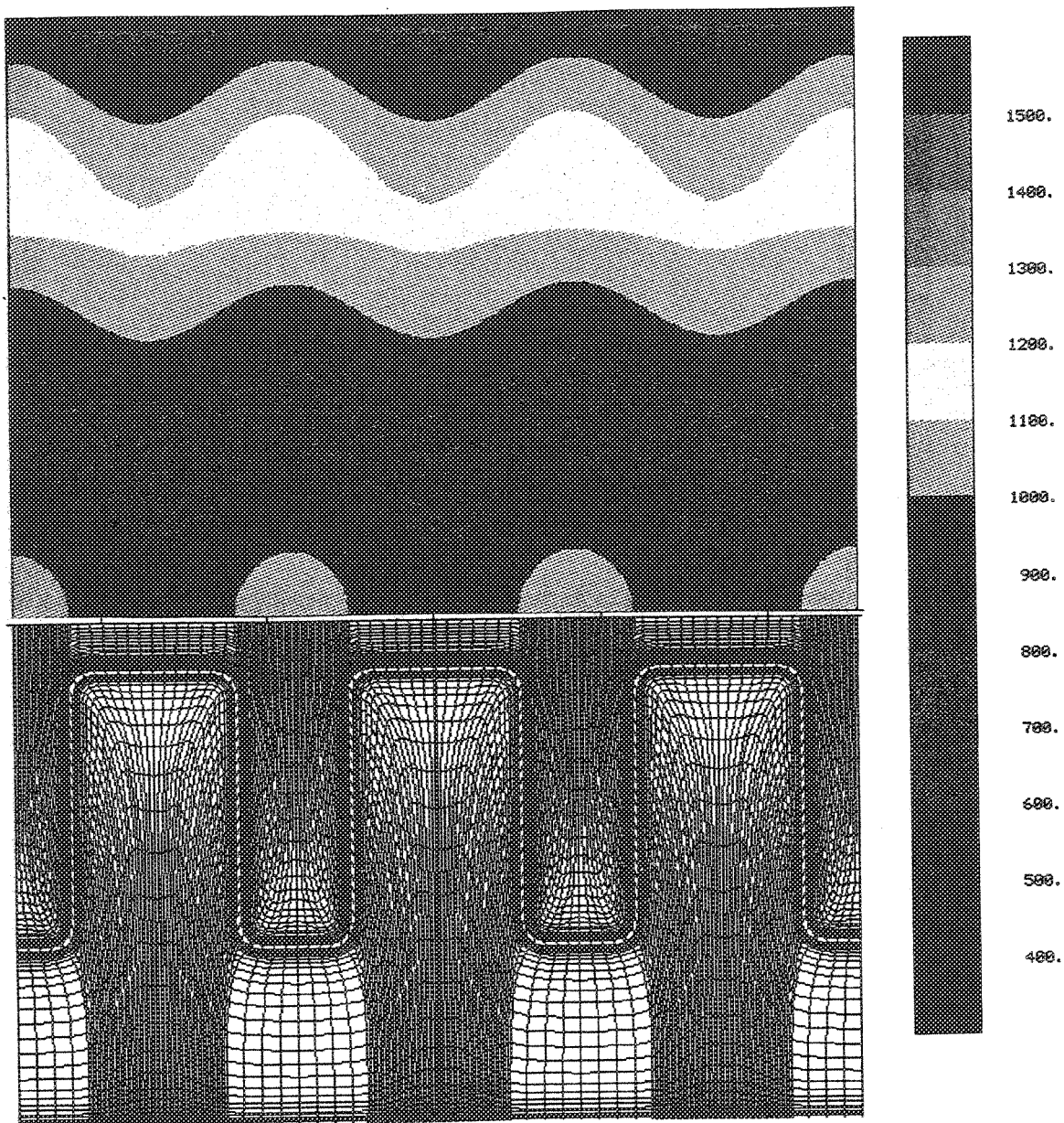


Figure 358. Comparison of Axial Velocity Profiles (Vortical, Trough Plane Cut) for Vortical/Long Shroud Mixer-Ejector



Lobe9320 - long shroud  $T_t=1735R$   $NPR=3.5$   $M_{inf}=0.32$   
Axial velocity, fps, shroud TE

*Figure 359. Pratt & Whitney Vortical Nozzle With Long Shroud, Axial Velocity at Ejector Exit Plane*

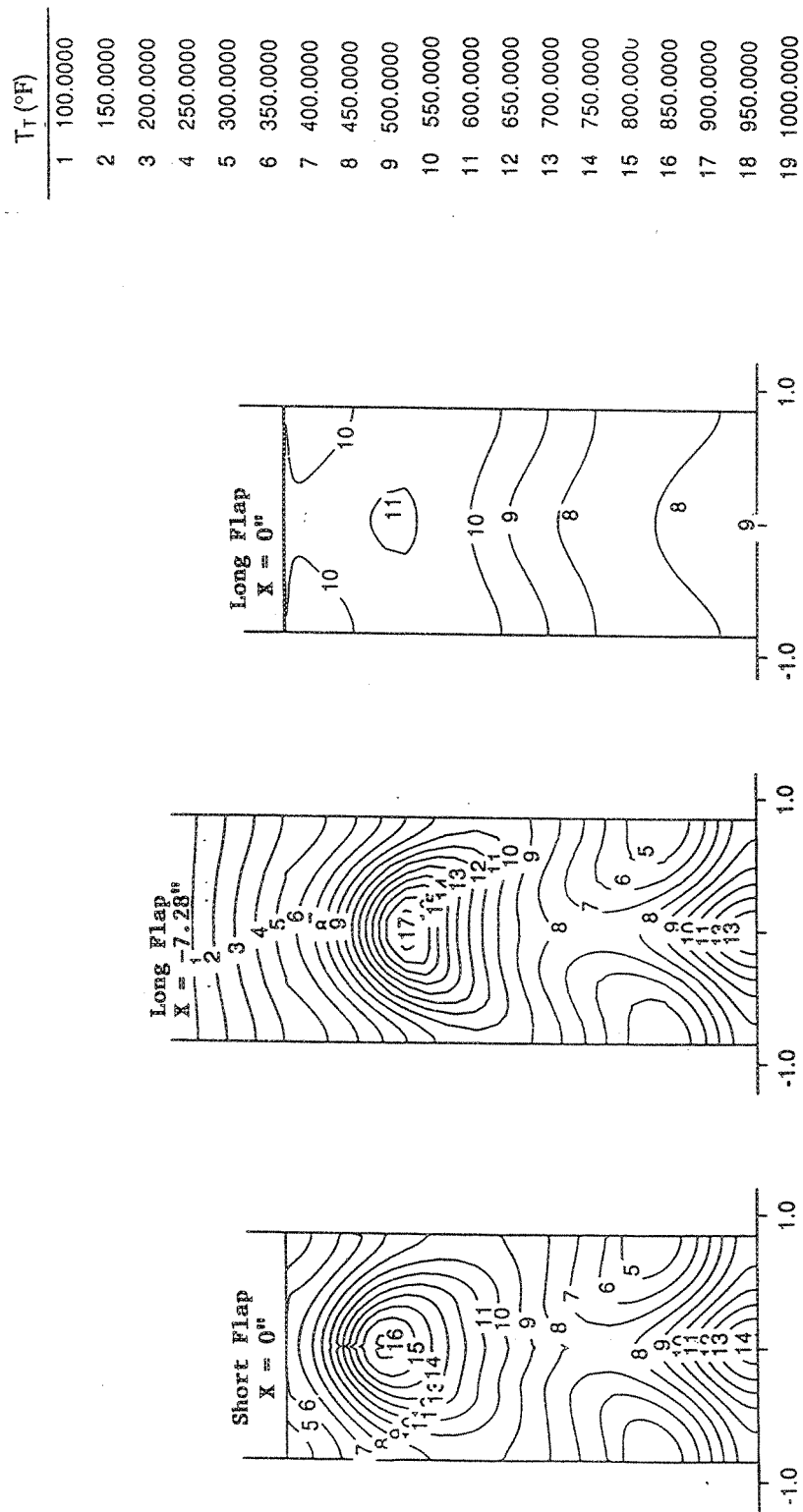


Figure 360. Comparison of Exit Plane Total Temperature Distributions for Vortical Nozzle Mixer-Ejector

		<u>NPR</u>	<u>Top (°R)</u>	<u><math>\eta\%</math></u>	<u><math>\omega</math></u>	<u><math>M_\infty</math></u>
—	Case 9401	3.5	1735	74	1.58	.32
- - -	Case 9312	3.5	1960	76	1.30	.20
□	□ Pt 1513	3.5	1735			
○	○ Pt 1512	3.4	1646			
△	△ Pt 1516	4.0	1752			

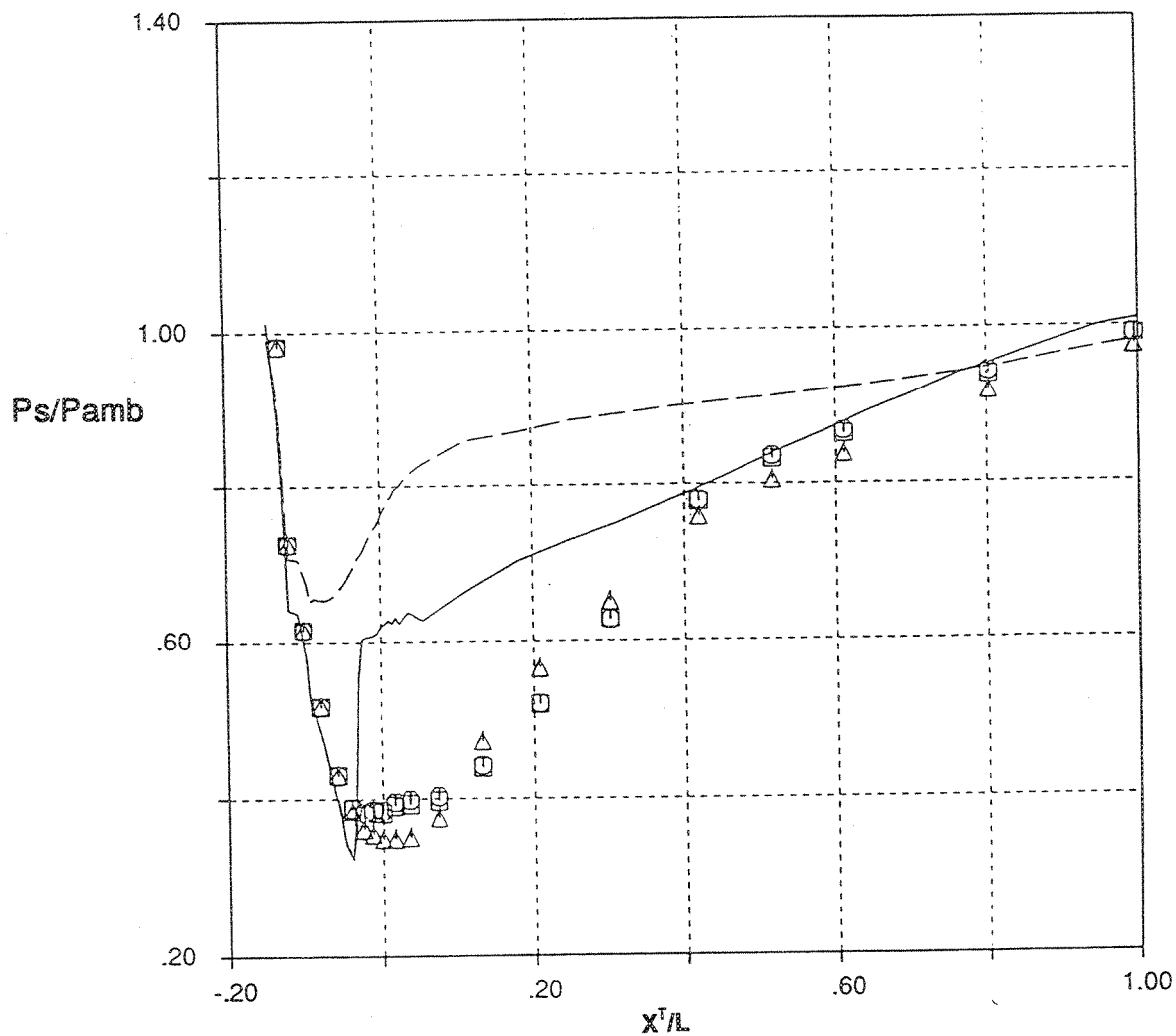


Figure 361. Comparison of Shroud Pressure Locking for Axial Nozzle/Short Shroud Mixer-Ejector

# NASTAR PW Axial Nozzle Calculations: Short Shroud

## Axial Velocity Contours

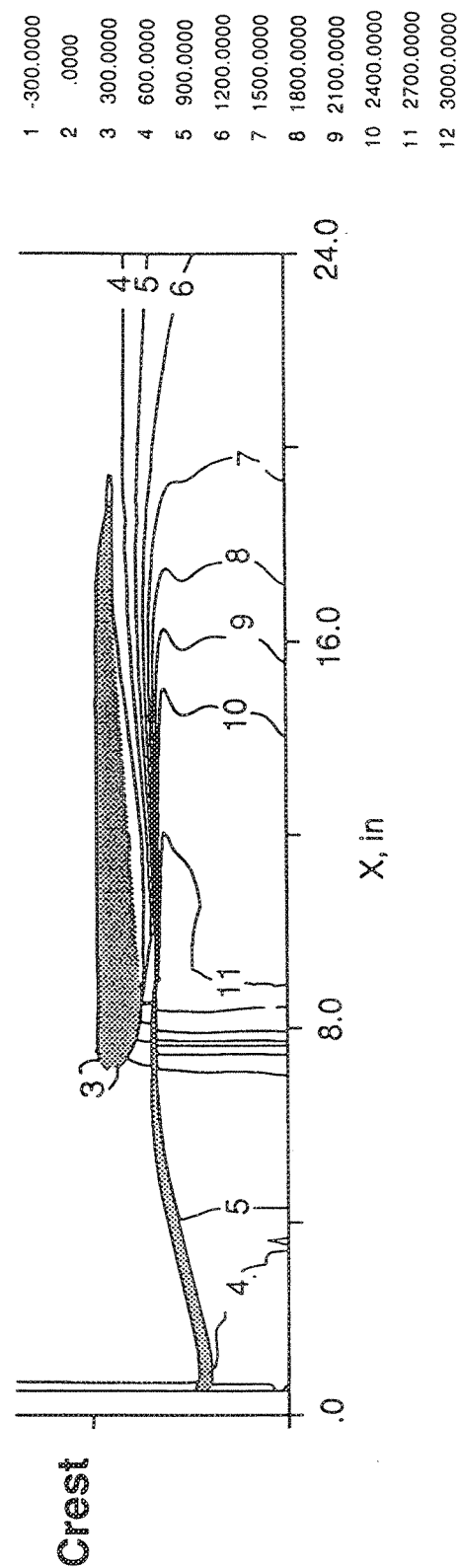
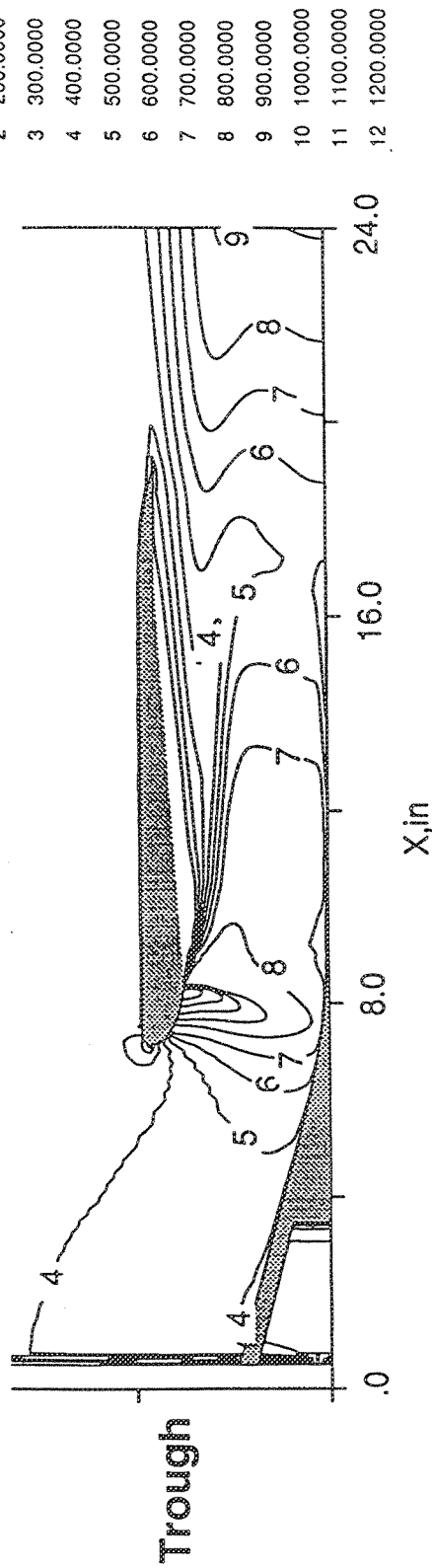


Figure 362. Axial Velocity Distributions for Axial Nozzle/Short Shroud Mixer-Ejector



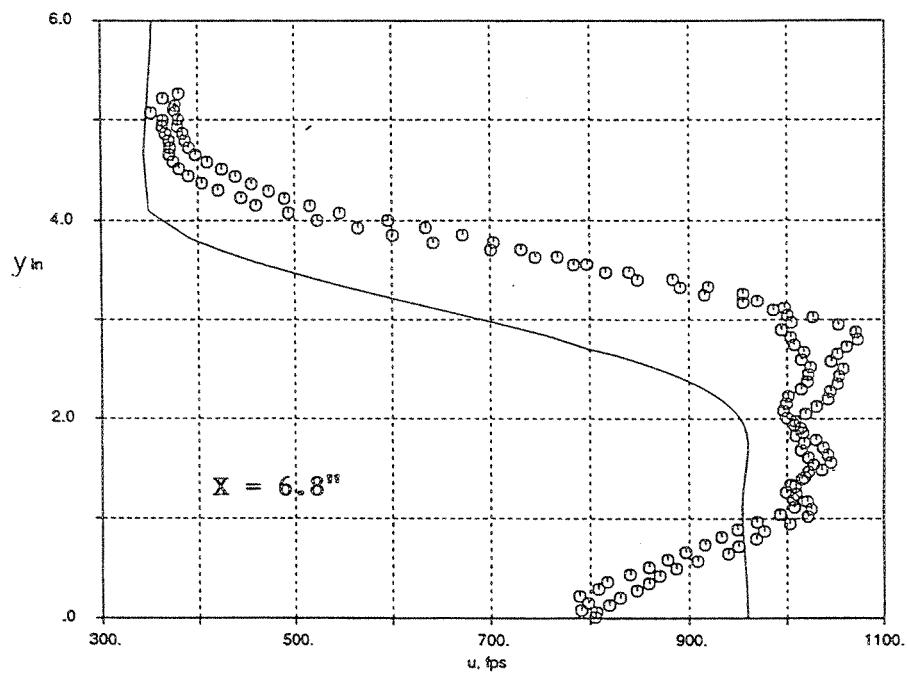
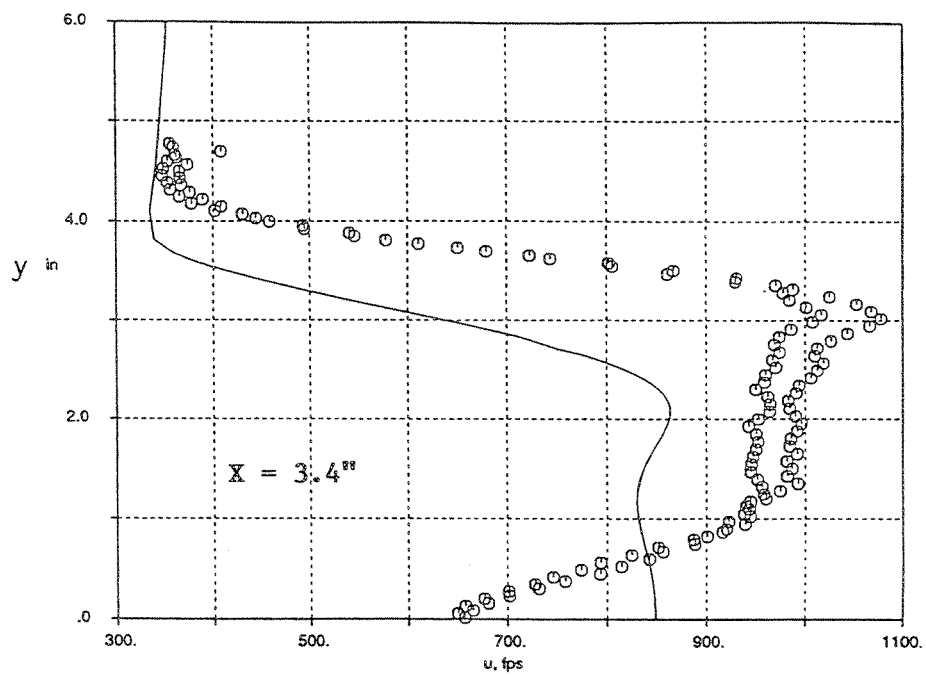


Figure 363. Comparison of Axial Velocity Profile (Vortical, Trough Plane Cut) for Axial, Short Shroud Mixer-Ejector

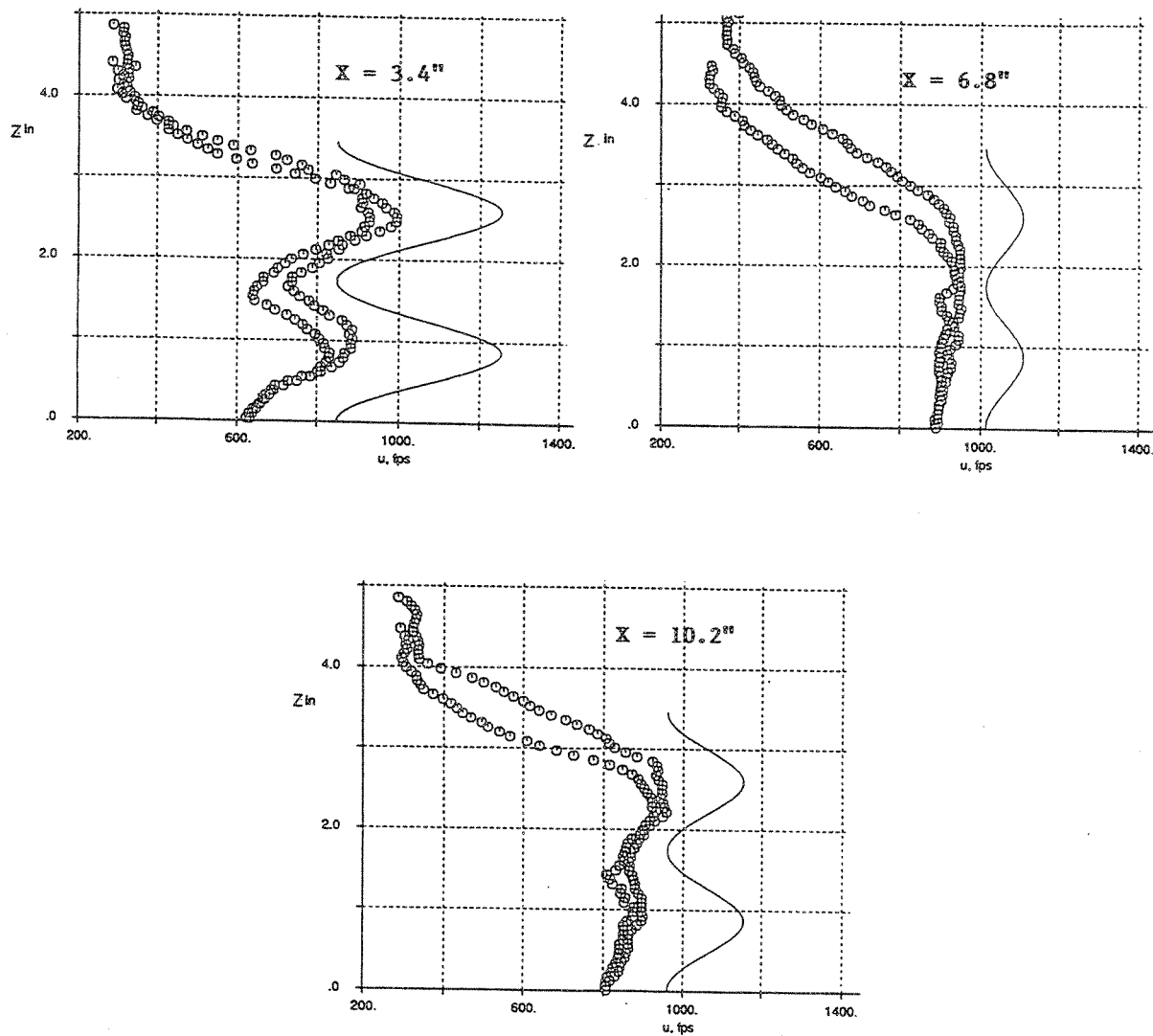


Figure 364. Comparison of Axial Velocity Profiles (Lateral, Symmetry Plane Cut) for Axial, Short Shroud Mixer-Ejector

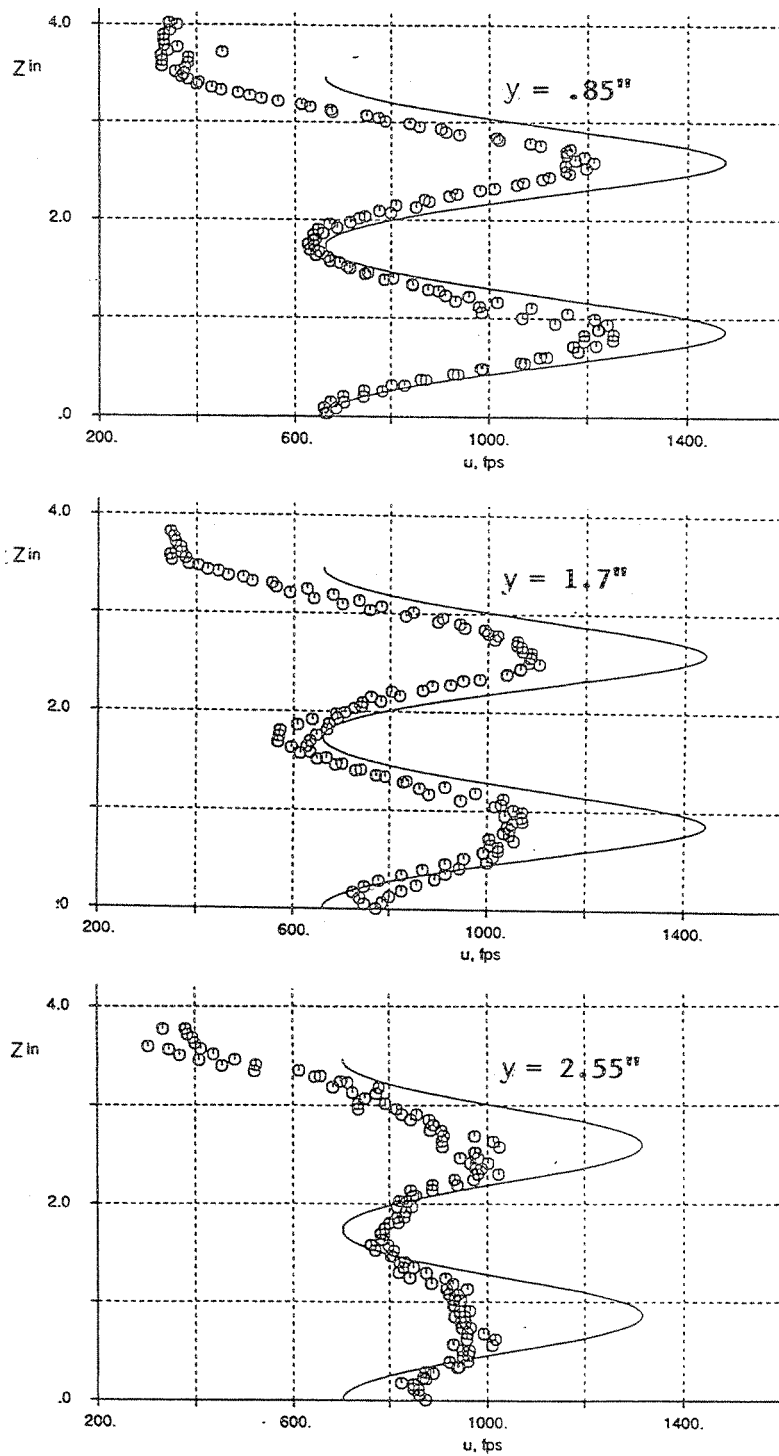


Figure 365. Comparison of Axial Velocity Profiles (Lateral Cuts,  $X=0.65$ ) for Axial, Short Shroud Mixer-Ejector

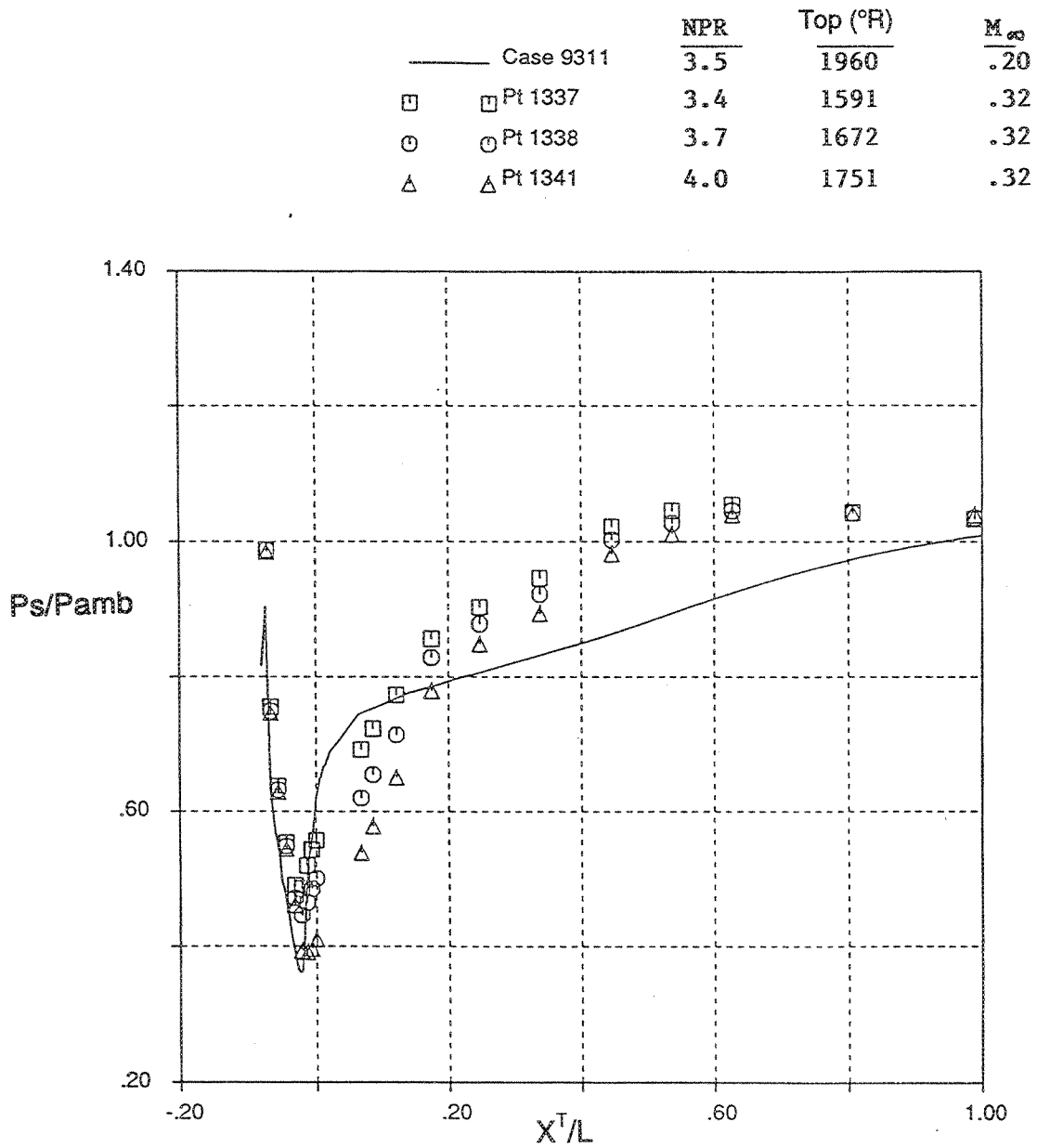


Figure 366. Comparison of Shroud Pressure Loading for Axial Nozzle, Long Shroud Mixer-Ejector

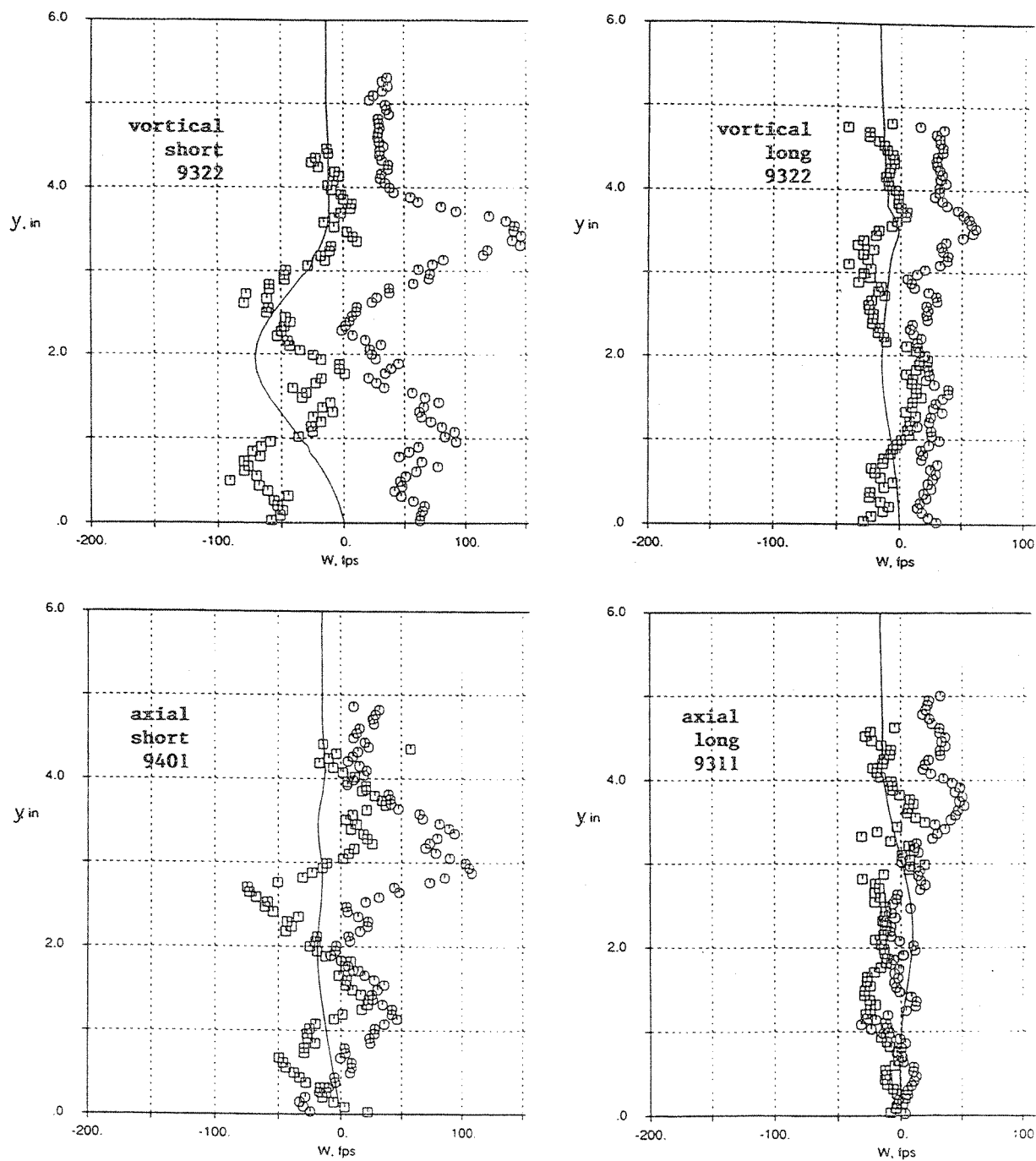


Figure 367. Comparison of Vertical Velocity Component at  $X=3.4$  in. Downstream of Mixer-Ejector Exit

This page intentionally left blank.

## APPENDIX A — LIST OF SYMBOLS

<i>Symbol</i>	<i>Definition</i>
$A$	Area (in <sup>2</sup> )
$A_8$	Area – Primary Nozzle Exit (in <sup>2</sup> )
$A_{8*}$	Area – Primary Nozzle Throat (in <sup>2</sup> )
$A_{8*ave}$	Area – Average Primary Nozzle Throat (in <sup>2</sup> )
$A_{Core}$	Area – Core Nozzle Exit (in <sup>2</sup> )
$A_{mix}$	Area – Internal Mixing Plane, $A_8 + A_s$ (in <sup>2</sup> )
$A_{exit}$	Area – Ejector-Shroud Exit (in <sup>2</sup> )
$A_{Fan}$	Area – Fan Nozzle Exit (in <sup>2</sup> )
$A_s$	Area – Secondary Flow at Internal Mixing Plane (in <sup>2</sup> )
$A_{treated}$	Area – Shroud Effective Acoustically Treated Surface (in <sup>2</sup> )
$A_{cross\ average}$	Area – Shroud Average Cross Sectional Flow (in <sup>2</sup> )
CER	Core Expansion Ratio, $A_8/A_{8*}$
Cvg	Gross Thrust Coefficient
	$Cvg = \frac{F - Drag}{m_p(V_{j,p})}$
	$F - Drag = \int_{\text{ejector exit}} V_x \rho \vec{V} \cdot \vec{n} dA + \int_{\text{ejector exit and shroud internal surface}} (P_s - P_{amb}) \vec{n} \cdot \vec{i} dA - \int_{\text{shroud internal surface}} \tau_w \cdot \vec{i} dA - m_s(V_{fl})$
	$V_{j,p} = \sqrt{\frac{2\gamma RT_{tp}}{\gamma - 1} \left[ 1 - \left( \frac{P_{tp}}{P_{amb}} \right)^{\frac{1-\gamma}{\gamma}} \right]}$
$dA$	Infinitesimally Small Portion of Area
EPNL	Effective Perceived Noise Level (EPNdB)
$F - Drag$	Nozzle Gross Thrust Minus Drag (lb)
He	Shroud Exit Height (in.)

<i>Symbol</i>	<i>Definition</i>
Hm	Shroud Throat Height (in.)
Hmxe	Maximum Mixer Exit Height (in.)
i	Unit Vector in Axial Direction
L, L <sub>EJ</sub>	Ejector-Shroud Length (Shroud Throat to Shroud Exit) (in.)
L/D	Normalized Treatment Parameter
m <sub>p</sub>	Primary Mass Flow Rate (lb/sec)
m <sub>s</sub>	Secondary Mass Flow Rate (lb/sec)
M <sub>n</sub> , M <sub>∞</sub> , M, M <sub>f</sub>	Mach Number
MAR	Mixing Area Ratio, A <sub>exit</sub> /A <sub>mix</sub>
n	Unit vector normal to surface
N	Number of samples
NOY	Unit of Perceived Noisiness
NPR	Primary Nozzle Pressure Ratio, P <sub>tp</sub> /P <sub>amb</sub>
NPR <sub>cr</sub>	Critical Primary Nozzle Pressure Ratio, P <sub>tp</sub> /P <sub>amb</sub>
OASPL	Overall Sound Pressure Level (dB)
P	Static Pressure (psia)
P <sub>amb</sub>	Ambient Pressure (psia or inHg)
P <sub>cr</sub> , P*	Critical Static Pressure (psia)
PEN	Mixer Penetration (%) = (Hmxe/Hm) x 100
PNL	Perceived Noise Level (PNdB)
PNLT	Tone Corrected Perceived Noise Level (PNTdB)
pps	Mass Flow Rate (lb/sec)
PRH	Percent Relative Humidity
PS, P <sub>s</sub>	Static Pressure, Secondary or Cold Flow Stream Pressure (psia)
P <sub>T</sub>	Total Pressure (psia)
P <sub>tp</sub> , P <sub>op</sub>	Primary or Hot Flow Stream Total Pressure (psia)
PWL	Acoustic Power Level (dB)
R	Gas Constant (ft-lb <sub>f</sub> /lb <sub>m</sub> -°R)
SAR	Shroud Area Ratio, A <sub>mix</sub> /A <sub>g*</sub>



<i>Symbol</i>	<i>Definition</i>
SL	Sideline Distance (ft)
SPL	Sound Pressure Level (dB)
T	Temperature (°R)
T <sub>amb</sub>	Ambient Temperature (°R)
TI <sub>x</sub>	Relative Axial Turbulence Intensity (percent)
	$TI_x = 100 \frac{\sqrt{\frac{\sum_{i=1}^N [V_{x,ave} - V_{x,i}]^2}{N}}}{V_{x,ave}}$
T <sub>0</sub>	Free Stream Total Temperature (°R)
T <sub>0i</sub>	Initial Axial Plane Total Temperature (°R)
T <sub>0m</sub>	Fully Mixed Total Temperature (°R)
T <sub>0x</sub>	Local Axial Plane total Temperature (°R)
T <sub>t8</sub> , T <sub>8</sub> , T <sub>tp</sub> , T <sub>op</sub> , T <sub>t</sub> , T <sub>T</sub>	Primary Total Temperature (°R or °F)
V	Velocity Vector
V <sub>fl</sub>	Flight Velocity (ft/sec)
V <sub>j,p</sub> , V <sub>jet</sub> , V <sub>j</sub>	Ideal Unsuppressed Primary Jet Velocity (ft/sec)
V <sub>x,ave</sub>	Average Axial Velocity (ft/sec)
V <sub>x,i</sub>	Instantaneous Axial Velocity (ft/sec)
V <sub>x</sub> , U, u	Axial Velocity (ft/sec)
V <sub>y</sub> , W	Vertical Velocity (ft/sec)
We	Shroud Exit Width (in.)
Wm	Shroud Throat Width (in.)
W <sub>p</sub>	Primary Nozzle Mass Flow
W <sub>s</sub>	Secondary Nozzle Mass Flow
X, x	Axial Cartesian Coordinate (in.)
X <sup>T</sup>	Distance downstream of shroud throat to static tap location (in.)

<i>Symbol</i>	<i>Definition</i>
$x^T/L$	Normalized Shroud Static Pressure Tap Axial Location
$Y, y$	Vertical Cartesian Coordinate (in.)
$Z, z$	Spanwise or Lateral Cartesian Coordinate (in.)
$\Delta X$	Incremental shroud length associated with shroud pressure tap (in.)
$\theta$	Polar Angle – Relative to Engine Inlet Axis (degrees)
$\psi$	Azimuthal Angle – Measured relative to the vertical plane of the fixed microphone array in the test facility (degrees)
$\eta$	Mixedness parameter based on the axial distribution of the mass averaged total temperature (%)
	$\eta = 100 \left[ 1.0 - \frac{\int \rho u  T_{0x} - T_{0m}  dA}{\int \rho u  T_{0i} - T_{0m}  dA} \right]$
$\rho$	Local Flow Density (lb <sub>m</sub> /ft <sup>3</sup> )
$\gamma$	Ratio of Specific Heats
$\omega$	Pumping or Aspiration Ratio, $m_s/m_p$
$\tau_\omega$	Shroud Internal Surface Shear Stress (lb/in <sup>2</sup> )

## APPENDIX B — ACOUSTIC TEST RUN SCHEDULE

### Configuration 1 – Baseline (3.241 in. diameter) Round Convergent Nozzle

<i>Run Number</i>	<i>Test Point Number Table 7</i>	<i>Mach Number</i>	<i>Microphone Position</i>	<i>Comments</i>
5		Static	Sideline	NPR = 1.8 $T_{t8} = 530^{\circ}\text{R}$
7-10 13 17 21 22 14 16 12 15 19 20 24 11 23	1-17	Static	Sideline	Pt 17 $T_{t8} = 1925^{\circ}\text{R}$
33		0.30	Sideline	NPR = 1.8 $T_{t8} = 530^{\circ}\text{R}$
34		0.20	Sideline	NPR = 1.8 $T_{t8} = 530^{\circ}\text{R}$
35		0.20	Sideline	NPR = 3.42 $T_{t8} = 530^{\circ}\text{R}$
36-39 51 45 55 56 53 46 52 54 43 44 42 40 58	1-17	0.36	Sideline	
47 41 57	10, 16, 17	0.20	Sideline	
50	5	0.30	Sideline	

### Configuration 2 – Vortical Mixer/Long Treated Shroud/SAR = 4.9/MAR = 1.19

<i>Run Number</i>	<i>Test Point Number Table 7</i>	<i>Mach Number</i>	<i>Microphone Position</i>	<i>Comments</i>
62 65 66 69 77 82 85 89 78 81 73 74 96 86 99 70 90	1-17	Static	Sideline	
63 64 67 68 76 83 84 88 79 80 72 75 97 87 98 71 91	1-17	Static	Community – Overhead	
116 119 120 123 139 111 108 104 143 112 140 144 103 107 100	1-15	0.36	Sideline	
136	5	0.30	Sideline	
137	5	0.30	Community – Overhead	
117 118 121 122 138 110 109 105 142 113 141 145 102 106 101	1-15	0.36	Community – Overhead	
115 124 93	10, 16, 17	0.20	Sideline	
114 125 92	10, 16, 17	0.20	Community – Overhead	

**Configuration 3 -- Vortical Mixer/Long Treated Shroud/SAR = 4.9/MAR = 0.97**

<i>Run Number</i>	<i>Test Point Number Table 7</i>	<i>Mach Number</i>	<i>Microphone Position</i>	<i>Comments</i>
149 175 199 198 179 178 171 169 266 267 258 270 259 263 262	1-15	Static	Sideline	
150 176 200 197 180 177 172 168 265 268 257 269 260 264 261	1-15	Static	Community – Overhead	
183	5	0.30	Sideline	
184	5	0.30	Community – Overhead	
153 215 203 194 182 162 165 166 186 187 191 190 157 161 158	1-15	0.32	Sideline	
155 216 204 193 181 163 164 167 185 188 192 189 156 160 159	1-15	0.32	Community – Overhead	
152 214 202 195 211 206 207 210	1-8	0.36	Sideline	
151 213 201 196 217 205 208 209	1-8	0.36	Community – Overhead	

**Configuration 4 -- Vortical Mixer/Long Treated Shroud/SAR = 4.9/MAR = 0.88**

<i>Run Number</i>	<i>Test Point Number Table 7</i>	<i>Mach Number</i>	<i>Microphone Position</i>	<i>Comments</i>
225 255 233 228 230 234 243 246 251 250 254 247 237 238 242	1-15	Static	Sideline	
226 256 232 227 231 235 244 245 252 249 253 248 236 239 240	1-15	Static	Community – Overhead	
323	5	0.30	Community – Overhead	
324	5	0.30	Sideline	
277 309 278 316 320 298 290 295 306 302 317 303 283 287 286	1-15	0.32	Sideline	
276 310 279 315 319 297 289 296 305 301 318 304 284 288 285	1-15	0.32	Community – Overhead	
274 312 281 313 321 299 291 294	1-8	0.36	Sideline	
275 311 280 314 322 300 292 293	1-8	0.36	Community – Overhead	

**Configuration 5 – Vortical Mixer/Long Treated Shroud/SAR = 4.4/MAR = 0.97**

<i>Run Number</i>	<i>Test Point Number Table 7</i>	<i>Mach Number</i>	<i>Microphone Position</i>	<i>Comments</i>
378 415 414 411 410 406 403 402 407	1-9	Static	Sideline	Deteriorated Treatment (All Runs)
379 416 413 412 409 405 404 401 408	1-9	Static	Community – Overhead	Deteriorated Treatment (All Runs)
391	5	0.30	Sideline	Deteriorated Treatment
392	5	0.30	Community – Overhead	Deteriorated Treatment
381 382 385 386 390 395 398 399 394	1-9	0.32	Sideline	Deteriorated Treatment (All Runs)
380 383 384 388 389 396 397 400 393	1-9	0.32	Community – Overhead	Deteriorated Treatment (All Runs)

**Configuration 5 – Vortical Mixer/Long Treated Shroud/SAR = 4.4/MAR = 0.97**

<i>Run Number</i>	<i>Test Point Number Table 7</i>	<i>Mach Number</i>	<i>Microphone Position</i>	<i>Comments</i>
1078 1081 1082 1085 1086 1090 1093 1089	1-5, 7-9	Static	Sideline	Restored Treatment
1079 1080 1083 1084 1087 1091 1092 1088	1-5, 7-9	Static	Community – Overhead	Restored Treatment
1109 1106 1105 1102 1101 1097 1094 1098	1-5, 7-9	0.32	Sideline	Restored Treatment
1108 1107 1104 1103 1100 1096 1095 1099	1-5, 7-9	0.32	Community – Overhead	Restored Treatment

**Configuration 6 -- Vortical Mixer/Long Treated Shroud/SAR = 4.4/MAR = 0.88**

<i>Run Number</i>	<i>Test Point Number Table 7</i>	<i>Mach Number</i>	<i>Microphone Position</i>	<i>Comments</i>
329 346 372 369 368 365 364 341 360	1-9	Static	Sideline	
330 347 371 370 367 366 363 343 361	1-9	Static	Community – Overhead	
354	5	0.30	Sideline	
355	5	0.30	Community – Overhead	
332 349 350 333 353 336 337 340 357	1-9	0.32	Sideline	
331 348 351 334 352 335 338 339 356	1-9	0.32	Community – Overhead	

**Configuration 7 -- Vortical Mixer/Long Treated Shroud/SAR = 4.4/MAR = 1.19**

<i>Run Number</i>	<i>Test Point Number Table 7</i>	<i>Mach Number</i>	<i>Microphone Position</i>	<i>Comments</i>
419 447 450 451 455 459 443 442 456	1-9	Static	Sideline	Deteriorated Treatment (All Runs)
420 448 449 452 453 458 444 441 457	1-9	Static	Community – Overhead	Deteriorated Treatment (All Runs)
431	5	0.30	Sideline	Deteriorated Treatment
432	5	0.30	Community – Overhead	Deteriorated Treatment
422 423 426 427 430 435 438 439 434	1-9	0.32	Sideline	Deteriorated Treatment (All Runs)
421 424 425 428 429 436 437 440 433	1-9	0.32	Community – Overhead	Deteriorated Treatment (All Runs)

**Configuration 7R – Vortical Mixer/Long Treated Shroud/SAR = 4.4/MAR = 1.19**

<i>Run Number</i>	<i>Test Point Number Table 7</i>	<i>Mach Number</i>	<i>Microphone Position</i>	<i>Comments</i>
1050 1074 1073 1070 1069 1066	1-5 and 7	Static	Sideline	Restored Treatment
1051 1075 1072 1071 1068 1067	1-5 and 7	Static	Community – Overhead	Restored Treatment
1053 1054 1057 1058 1061 1065 1062	1-5, 7 and 9	0.32	Sideline	Restored Treatment
1052 1055 1056 1059 1060 1064 1063	1-5, 7 and 9	0.32	Community – Overhead	Restored Treatment

**Configuration 8 – Vortical Mixer/Long Hardwall Shroud/SAR = 4.9/MAR = 1.19**

<i>Run Number</i>	<i>Test Point Number Table 7</i>	<i>Mach Number</i>	<i>Microphone Position</i>	<i>Comments</i>
480 483 484 487 542 545 546 569 554 565 557 566 561 562 558	1-15	Static	Sideline	
481 482 485 486 543 544 547 568 555 564 556 567 560 563 559	1-15	Static	Community – Overhead	
491 494 495 497 503 519 522 570 506 510 502 507 518 514 515	1-15	0.32	Sideline	
492 493 496 498 504 520 521 572 505 509 501 508 517 513 516	1-15	0.32	Community – Overhead	
511 499 574	10, 16, 17	0.20	Sideline	
512 500 573	10, 16, 17	0.20	Community – Overhead	

<i>Run Number</i>	<i>NPR</i>	<i>T<sub>18</sub> (°R)</i>	<i>Mach Number</i>	<i>Microphone Position</i>	<i>Comments</i>
468-475	1.5-5.0 (0.5 increment)	Ambient	Static	Sideline	Vjet Sweep
476-479	3.1-3.4 (0.1 increment)	Ambient	Static	Sideline	Vjet Sweep
523-532 (526 527 Void)	3.7-3.0 (0.1 increment)	Hot	0.32	Sideline	Vjet Sweep
533-535	3.1-3.3 (0.1 increment)	Hot	0.32	Sideline	Vjet Sweep
539-541	3.1-3.3 (0.1 increment)	Hot	Static	Sideline	Vjet Sweep

<i>Run Number</i>	<i>NPR</i>	<i>T<sub>18</sub></i> (°R)	<i>Mach Number</i>	<i>Microphone Position</i>	<i>Comments</i>
548-550	3.7-3.5 (0.1 increment)	Hot	Static	Sideline	Vjet Sweep
551-552	3.5-3.6 (0.1 increment)	Hot	Static	Sideline	Vjet Sweep
553	3.4	1130	Static	Sideline	

**Configuration 9 – Vortical Mixer/Long Hardwall Shroud/SAR = 4.9/MAR = 0.97**

<i>Run Number</i>	<i>Test Point Number</i> <i>Table 7</i>	<i>Mach Number</i>	<i>Microphone Position</i>	<i>Comments</i>
577 580 581 584 585 588 593 594 590	1-9	Static	Sideline	
578 579 582 583 586 587 592 595 591	1-9	Static	Community – Overhead	
606 609 610 613 614 619 622 623 618	1-9	0.32	Sideline	
607 608 611 612 615 620 621 624 617	1-9	0.32	Community – Overhead	

<i>Run Number</i>	<i>NPR</i>	<i>T<sub>18</sub></i> (°R)	<i>Mach Number</i>	<i>Microphone Position</i>	<i>Comments</i>
596-603	1.5-5.0 (0.5 increment)	Ambient	Static	Sideline	Vjet Sweep
625-628	4.1-4.4 (0.1 increment)	Ambient	Static	Sideline	Vjet Sweep
629-631	4.3-4.1 (0.1 increment)	Ambient	Static	Sideline	Vjet Sweep



Configuration 10 – Vortical Mixer/Long Hardwall Shroud/SAR = 4.4/MAR = 1.19

<i>Run Number</i>	<i>Test Point Number Table 7</i>	<i>Mach Number</i>	<i>Microphone Position</i>	<i>Comments</i>
669 666 657 654 645 649 650 653 646	1-9	Static	Sideline	
668 667 656 655 644 648 651 652 647	1-9	Static	Community – Overhead	
634 637 638 641 642 680 681 684 676	1-9	0.32	Sideline	
635 636 639 640 643 679 682 683 678	1-9	0.32	Community – Overhead	

<i>Run Number</i>	<i>NPR</i>	<i>T<sub>ts</sub> (°R)</i>	<i>Mach Number</i>	<i>Microphone Position</i>	<i>Comments</i>
673 674 675 694-698	1.5-5.0 (0.5 increment)	Ambient	Static	Sideline	Vjet Sweep
699-704	3.5-3.0 (0.1 increment)	Ambient	Static	Sideline	Vjet Sweep
705-708	3.1-3.4 (0.1 increment)	Ambient	Static	Sideline	Vjet Sweep
658-662	3.0-3.4 (0.1 increment)	Hot	Static	Sideline	Vjet Sweep
663-665	3.3-3.1 (0.1 increment)	Hot	Static	Sideline	Vjet Sweep
686-688	3.1-3.3 (0.1 increment)	Hot	0.32	Sideline	Vjet Sweep
690-693	3.4-3.1 (0.1 increment)	Hot	0.32	Sideline	Vjet Sweep

**Configuration 11 – Vortical Mixer/Long Hardwall Shroud/SAR = 4.4/MAR = 0.97**

<i>Run Number</i>	<i>Test Point Number Table 7</i>	<i>Mach Number</i>	<i>Microphone Position</i>	<i>Comments</i>
731 756 757 760 761 765 768 753 764	1-9	Static	Sideline	
732 755 758 759 762 766 767 754 763	1-9	Static	Community – Overhead	
734 735 738 739 742 746 747 750 743	1-9	0.32	Sideline	
733 736 737 740 741 745 748 749 744	1-9	0.32	Community – Overhead	
751		0.32	Sideline	NPR = 4.3 $T_{t8} = 1820^{\circ}\text{R}$
752		0.32	Sideline	NPR = 4.2 $T_{t8} = 1795^{\circ}\text{R}$

<i>Run Number</i>	<i>NPR</i>	<i><math>T_{t8}</math> (<math>^{\circ}\text{R}</math>)</i>	<i>Mach Number</i>	<i>Microphone Position</i>	<i>Comments</i>
711-718	1.5-5.0 (0.5 increment)	Ambient	Static	Sideline	Vjet Sweep
719-723	4.4-4.0 (0.1 increment)	Ambient	Static	Sideline	Vjet Sweep
724-728	4.1-4.5 (0.1 increment)	Ambient	Static	Sideline	Vjet Sweep

**Configuration 12 – Vortical Mixer/Long Hardwall Shroud/SAR = 4.4/MAR = 0.88**

<i>Run Number</i>	<i>Test Point Number Table 7</i>	<i>Mach Number</i>	<i>Microphone Position</i>	<i>Comments</i>
771 774 775 778 817 813 812 809 816	1-9	Static	Sideline	
772 773 776 777 818 814 811 810 815	1-9	Static	Community – Overhead	
790 793 794 797 798 802 805 806 801	1-9	0.32	Sideline	
791 792 795 796 799 803 804 807 800	1-9	0.32	Community – Overhead	
808		0.32	Sideline	NPR = 4.3 $T_{t8} = 1815^{\circ}\text{R}$

<i>Run Number</i>	<i>NPR</i>	<i>T<sub>18</sub></i> (°R)	<i>Mach Number</i>	<i>Microphone Position</i>	<i>Comments</i>
779-786	1.5-5.0 (0.5 increment)	Ambient	Static	Sideline	Vjet Sweep
787	5.6	Ambient	Static	Sideline	

**Configuration 13 – Axial Mixer/Long Treated Shroud/SAR = 4.9/MAR = 0.97**

<i>Run Number</i>	<i>Test Point Number</i> <i>Table 7</i>	<i>Mach Number</i>	<i>Microphone Position</i>	<i>Comments</i>
1418 1454 1451 1450 1447 1443 1442 1439 1446	1-9	Static	Sideline	
1420 1453 1452 1449 1448 1444 1441 1440 1445	1-9	Static	Community – Overhead	
1422 1423 1426 1427 1430 1434 1435 1438 1431	1-9	0.32	Sideline	
1421 1424 1425 1428 1429 1433 1436 1437 1432	1-9	0.32	Community – Overhead	

**Configuration 14 – Axial Mixer/Long Hardwall Shroud/SAR = 4.9/MAR = 1.19**

<i>Run Number</i>	<i>Test Point Number</i> <i>Table 7</i>	<i>Mach Number</i>	<i>Microphone Position</i>	<i>Comments</i>
1147 1181 1184 1185 1188 1189 1192 1193 1200 1201 1205 1204 1197 1168 1196	1-15	Static	Sideline	
1148 1182 1183 1186 1187 1190 1191 1194 1199 1202 1206 1203 1198 1169 1195	1-15	Static	Community – Overhead	
1151 1152 1155 1156 1159 1160 1163 1220 1213 1217 1164 1216 1209 1167 1212	1-15	0.32	Sideline	
1150 1153 1154 1157 1158 1161 1162 1219 1214 1218 1165 1215 1210 1166 1211	1-15	0.32	Community – Overhead	

<i>Run Number</i>	<i>NPR</i>	<i>T<sub>ts</sub></i> (°R)	<i>Mach Number</i>	<i>Microphone Position</i>	<i>Comments</i>
1172-1179	1.5-5.0 (0.5 increment)	Ambient	Static	Sideline	Vjet Sweep
1243-1249	4.3-5.0 (0.1 increment excluding 4.5)	Ambient	Static	Sideline	Vjet Sweep
1250-1252	4.9-4.7 (0.1 increment)	Ambient	Static	Sideline	Vjet Sweep
1180 1255-1261	1.5-5.0 (0.5 increment)	860	Static	Sideline	Vjet Sweep
1262-1266	3.6-4.0 (0.1 increment)	860	Static	Sideline	Vjet Sweep
1267-1271	3.9-3.5 (0.1 increment)	860	Static	Sideline	Vjet Sweep
1272-1275	3.7-4.0 (0.1 increment)	Hot	Static	Sideline	Vjet Sweep
1276-1280	4.0-3.6 (0.1 increment)	Hot	Static	Sideline	Vjet Sweep
1221-1229	4.3-3.5 (0.1 increment)	Hot	0.32	Sideline	Vjet Sweep
1230-1235	3.6-4.2 (0.1 increment) excluding 3.7	Hot	0.32	Sideline	Vjet Sweep

**Configuration 15 -- Vortical Mixer/Short Hardwall Shroud/SAR = 4.9/MAR = 1.19**

<i>Run Number</i>	<i>Test Point Number</i> <i>Table 7</i>	<i>Mach Number</i>	<i>Microphone Position</i>	<i>Comments</i>
843 889 892 893 896 897 900 901 913 912 908 909 877 904 905	1-15	Static	Sideline	
844 890 891 894 895 898 899 902 914 911 907 910 878 903 906	1-15	Static	Community – Overhead	
846 847 850 851 854 855 858 859 881 868 884 872 880 867 864	1-15	0.32	Sideline	
845 848 849 852 853 856 857 860 882 869 883 873 879 866 865	1-15	0.32	Community – Overhead	
871 885 862	10, 16, 17	0.20	Sideline	Pt 17 T <sub>ts</sub> = 1890°R
870 886 861	10, 16, 17	0.20	Community – Overhead	Pt 17 T <sub>ts</sub> = 1890°R

<i>Run Number</i>	<i>NPR</i>	<i>T<sub>18</sub></i> (°R)	<i>Mach Number</i>	<i>Microphone Position</i>	<i>Comments</i>
831-837	2.0-5.0 (0.5 increment)	Ambient	Static	Sideline	Vjet Sweep
838-842	3.0-5.0 (0.5 increment)	860	Static	Sideline	Vjet Sweep

**Configuration 16 – Axial Mixer/Short Hardwall Shroud/SAR = 4.9/MAR = 1.19**

<i>Run Number</i>	<i>Test Point Number Table 7</i>	<i>Mach Number</i>	<i>Microphone Position</i>	<i>Comments</i>
1497 1540 1537 1536 1532 1525 1524 1529 1528 1533 1521	1-5, 7-10, 16, 17	Static	Sideline	
1498 1539 1538 1535 1531 1526 1523 1530 1527 1534 1522	1-5, 7-10, 16, 17	Static	Community – Overhead	
1500 1501 1504 1505 1509 1516 1517 1512 1513 1508 1520	1-5, 7-10, 16, 17	0.32	Sideline	
1499 1502 1503 1506 1510 1515 1518 1511 1514 1507 1519	1-5, 7-10, 16, 17	0.32	Community – Overhead	

<i>Run Number</i>	<i>NPR</i>	<i>T<sub>18</sub></i> (°R)	<i>Mach Number</i>	<i>Microphone Position</i>	<i>Comments</i>
1491-1495	3.0-5.0 (0.5 increment)	Ambient	Static	Sideline	Vjet Sweep
1496	5.3	Ambient	Static	Sideline	

**Configuration 17 – Vortical Mixer/Short Hardwall Shroud/SAR = 4.4/MAR = 1.19**

<i>Run Number</i>	<i>Test Point Number Table 7</i>	<i>Mach Number</i>	<i>Microphone Position</i>	<i>Comments</i>
917 999 1002 1003 1006 1007 1010 1011 1032 1029 1025 1028 1036 1033 1037	1-15	Static	Sideline	
918 1000 1001 1004 1005 1008 1009 1012 1031 1030 1026 1027 1035 1034 1038	1-15	Static	Community – Overhead	
920 921 924 925 928 929 932 933 944 941 948 945 940 937 936	1-15	0.32	Sideline	
919 922 923 926 927 930 931 934 943 942 947 946 939 938 935	1-15	0.32	Community – Overhead	

<i>Run Number</i>	<i>NPR</i>	<i>T<sub>ts</sub></i> (°R)	<i>Mach Number</i>	<i>Microphone Position</i>	<i>Comments</i>
959-966	1.5-5.0 (0.5 increment)	Ambient	Static	Sideline	Vjet Sweep
967-973	3.1-2.5 (0.1 increment)	Ambient	Static	Sideline	Vjet Sweep
974-978	2.6-3.1 (0.1 increment) excluding 3.0	Ambient	Static	Sideline	Vjet Sweep
979-986	1.5-5.0 (0.5 increment)	860	Static	Sideline	Vjet Sweep
987-993	3.1-2.5 (0.1 increment)	860	Static	Sideline	Vjet Sweep
994-998	2.6-3.1 (0.1 increment) excluding 3.0	860	Static	Sideline	Vjet Sweep
1039-1043	3.4-3.0 (0.1 increment)	Hot	Static	Sideline	Vjet Sweep
1044-1047	3.1-3.5 (0.1 increment) excluding 3.4	Hot	Static	Sideline	Vjet Sweep
949-956	3.0-2.3 (0.1 increment)	Hot	0.32	Sideline	Vjet Sweep
1015	2.4	Hot	0.32	Sideline	
1020-1024	2.6-3.1 (0.1 increment) excluding 3.0	Hot	0.32	Sideline	Vjet Sweep

**Configuration 18 – Vortical Mixer/Short Treated Shroud/SAR = 4.4/MAR = 1.19**

<i>Run Number</i>	<i>Test Point Number</i> <i>Table 7</i>	<i>Mach Number</i>	<i>Microphone Position</i>	<i>Comments</i>
1112 1115 1116 1119 1120 1124 1127 1123	1-5, 7-9	Static	Sideline	
1113 1114 1117 1118 1121 1125 1126 1122	1-5, 7-9	Static	Community – Overhead	
1143 1140 1139 1136 1135 1131 1128 1132	1-5, 7-9	0.32	Sideline	
1142 1141 1138 1137 1134 1130 1129 1133	1-5, 7-9	0.32	Community – Overhead	

Configuration 19 -- Axial Mixer/Long Hardwall Shroud/SAR = 4.9/MAR = 0.97

<i>Run Number</i>	<i>Test Point Number Table 7</i>	<i>Mach Number</i>	<i>Microphone Position</i>	<i>Comments</i>
1326 1354 1357 1358 1361 1363 1366 1367	1-8	Static	Sideline	
1327 1355 1356 1359 1360 1364 1365 1368	1-8	Static	Community – Overhead	
1329 1330 1333 1334 1337 1338 1341 1342	1-8	0.32	Sideline	
1328 1331 1332 1335 1336 1339 1340 1343	1-8	0.32	Community – Overhead	

<i>Run Number</i>	<i>NPR</i>	<i>T<sub>ts</sub> (°R)</i>	<i>Mach Number</i>	<i>Microphone Position</i>	<i>Comments</i>
1283-1285 1288-1292	1.5-5.0 (0.5 increment)	Ambient	Static	Sideline	Vjet Sweep
1293-1301	4.7-3.9 (0.1 increment)	Ambient	Static	Sideline	Vjet Sweep
1302-1303	4.1-4.2 (0.1 increment)	Ambient	Static	Sideline	Vjet Sweep
1304 1306-1312	1.5-5.0 (0.5 increment)	860	Static	Sideline	Vjet Sweep
1313-1319	4.4-3.8 (0.1 increment)	860	Static	Sideline	Vjet Sweep
1320-1323	3.9-4.3 (0.1 increment) excluding 4.0	860	Static	Sideline	Vjet Sweep
1369	4.74	Hot	Static	Sideline	
1370-1376	4.8-4.2 (0.1 increment)	Hot	Static	Sideline	Vjet Sweep
1377	4.6	Hot	Static	Sideline	
1344-1350	4.5-3.9 (0.1 increment)	Hot	0.32	Sideline	Vjet Sweep
1351-1353	4.1-4.3 (0.1 increment)	Hot	0.32	Sideline	Vjet Sweep

**Configuration 20 – Axial Mixer/Long Hardwall Shroud/SAR = 4.9/MAR = 0.88**

<i>Run Number</i>	<i>Test Point Number Table 7</i>	<i>Mach Number</i>	<i>Microphone Position</i>	<i>Comments</i>
1407-1409	5, 7, 8	Static	Sideline	
1410		Static	Sideline	NPR = 5.0 $T_{t8} = 1845^{\circ}\text{R}$
1415 1414 1412	5, 7, 8	0.32	Sideline	
1411		0.32	Sideline	NPR = 5.0 $T_{t8} = 1860^{\circ}\text{R}$

<i>Run Number</i>	<i>NPR</i>	<i><math>T_{t8}</math> (<math>^{\circ}\text{R}</math>)</i>	<i>Mach Number</i>	<i>Microphone Position</i>	<i>Comments</i>
1380-1383	3.5-5.0 (0.5 increment)	Ambient	Static	Sideline	Vjet Sweep
1384-1389	5.5-5.0 (0.1 increment)	Ambient	Static	Sideline	Vjet Sweep
1390-1392	5.1-5.3 (0.1 increment)	Ambient	Static	Sideline	Vjet Sweep
1393-1395	4.0-5.0 (0.5 increment)	860	Static	Sideline	Vjet Sweep
1396-1399	5.1-5.4 (0.1 increment)	860	Static	Sideline	Vjet Sweep
1400-1405	5.4-4.8 (0.1 increment) excluding 4.9	860	Static	Sideline	Vjet Sweep
1406	4.8	860	Static	Sideline	

**Configuration 21 – Axial Mixer/Long Treated Shroud/SAR = 4.9/MAR = 0.88**

<i>Run Number</i>	<i>Test Point Number Table 7</i>	<i>Mach Number</i>	<i>Microphone Position</i>	<i>Comments</i>
1457 1488 1485 1484 1481 1477 1476 1480	1-5, 7-9	Static	Sideline	
1458 1487 1486 1483 1482 1478 1475 1479	1-5, 7-9	Static	Community – Overhead	
1460 1461 1464 1465 1468 1472 1473 1469	1-5, 7-9	0.32	Sideline	
1459 1462 1463 1466 1467 1471 1474 1470	1-5, 7-9	0.32	Community – Overhead	



## APPENDIX C — COMPARISON OF GEAE AND P&W EPNL RESULTS

Acoustic results, where noted, were processed by General Electric Aircraft Engines (GEAE). The remainder of the acoustic results were processed by Pratt & Whitney (P&W). Caution should be exercised when comparing P&W and GEAE derived results because of differences in the assumptions used for data reduction.

Table 16 defines the assumptions used by P&W in calculating the Effective Perceived Noise Level (EPNL) for all the test configurations. At three representative primary jet velocities, the table shows the cumulative effect of changing each P&W assumption to match those used by GEAE. The Boeing aircraft flight path of 5.5-degree climb angle with 13.2-degree aircraft pitch angle was changed to a flat flight path, the extra ground attenuation was removed, adjacent engine shielding was removed, conditions were converted to free field, one engine was assumed instead of four, and finally, a standard day was used instead of the hotter Federal Aviation Administration day. The total difference in calculated EPNL between P&W and GEAE was 3.6 to 3.9 EPNdB.

Acoustic results processed by P&W and GEAE with identical assumptions showed excellent agreement. Figure compares the static and flight-simulated acoustic results processed by P&W and GEAE from Configuration 3 (vortical mixer/long treated shroud/Shroud Area Ratio = 4.9/Mixing Area Ratio = 0.97). The common assumptions were one engine at free field, standard day conditions of 59F/70 percent relative humidity. A flat flight path was used at 689-ft altitude and 1476-ft sideline distance (1629-ft hypotenuse).

Table 16. Pratt & Whitney Acoustic Assumptions Effect on EPNL

PW EPNL (EPNdB)	Ideal Unsuppressed Primary Jet Velocity (ft/sec)			EPNL Change
	1919	2384	2812	
	NPR=2.5 $T_{t8}=1325^{\circ}R$	NPR=3.4 $T_{t8}=1590^{\circ}R$	NPR=4.5 $T_{t8}=1860^{\circ}R$	
Boeing Flight Path Extra Ground Attenuation (EGA) Grass Field 4 Engines with Shielding FAA Day (77°F, 70% r.h.)	96.3	103.9	108.2	Base
Flight Path	95.7	103.1	107.6	-0.6 to 0.8
EGA	98.2	105.3	109.9	+2.2 to 2.5
Shielding	99.3	106.5	110.9	+1.0 to 1.2
Free Field	98.0	105.3	109.8	-1.1 to 1.3
1 Engine	91.9	99.2	103.7	-6.1
Standard Day (59°F, 70% r.h.)	92.7	100.0	104.4	+0.7 to 0.8
Total Difference (EPNdB)	-3.6	-3.9	-3.8	
PW (EPNdB)	92.7	100.0	104.4	
GEAE (EPNdB) 1 engine Free Field Standard Day (59°F, 70% r.h.)	92.9	100.1	104.6	

Configuration 3 – Vortical Mixer/Long Treated Shroud; SAR = 4.9; MAR = 0.97

$A_{g*} = 1086 \text{ in}^2$ ; Sideline = 1629 ft;  $V_{fl} = 357 \text{ ft/sec}$ .

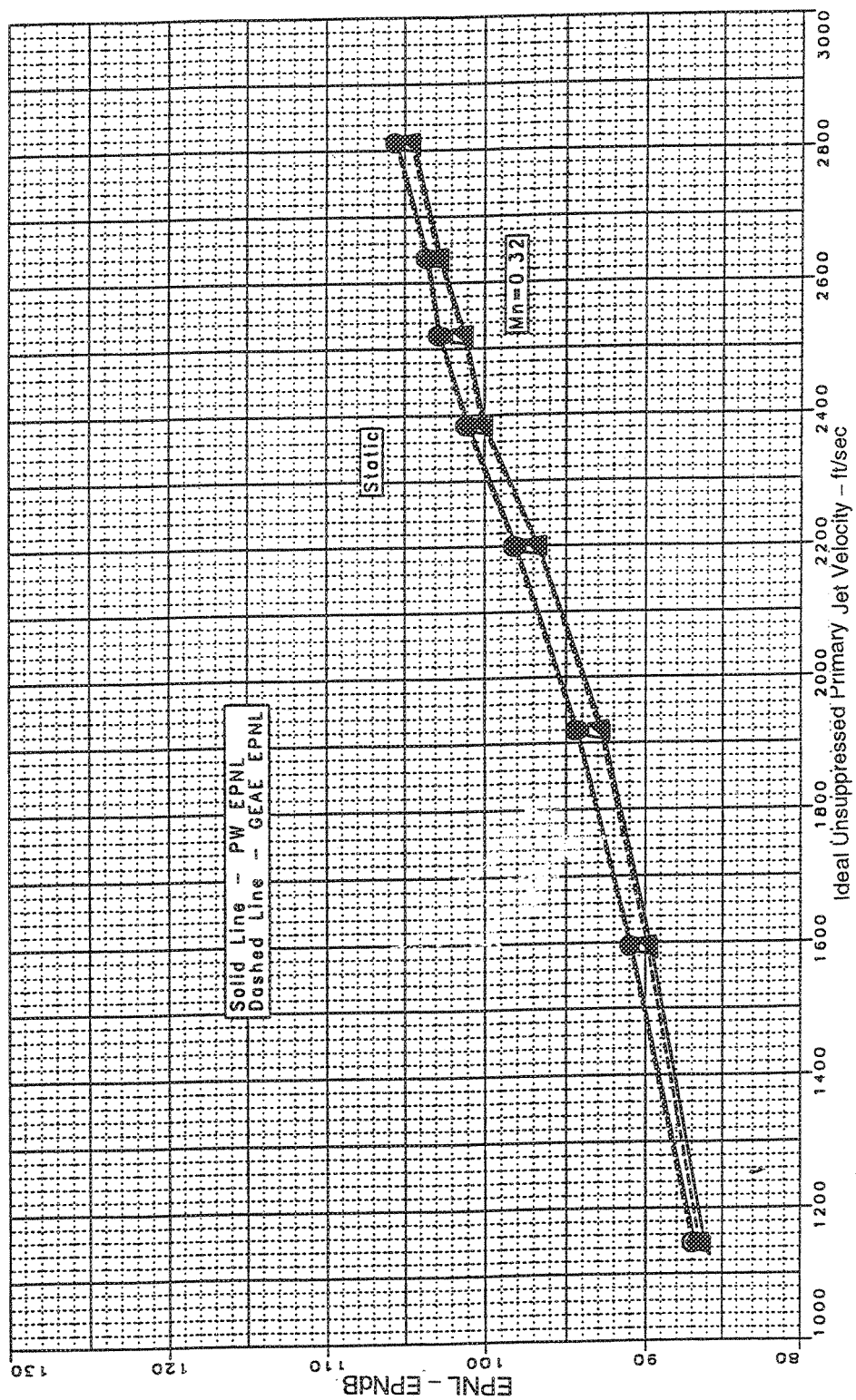


Figure 368. P & W and GEAC EPNL Calculations Agree Vortical Mixer Long Treated Shroud:  
(MAR = 0.97, SAR = 4.9, A8\* = 1086 in.2, Sideline = 1629 ft)

This page intentionally left blank.

## APPENDIX D — MODEL SCALE EFFECTS

Caution should be used when acoustic testing with scale models less than 1/10 scale because difficulties can arise with data reduction due to large atmospheric attenuation corrections.

After processing, some of the full-scale, 150-ft arc, noise spectra data exhibited a hook-up starting at approximately 2000 Hz. This result was a consequence of the small model scale (1:11.47) and the atmospheric attenuations used to correct the measured data. As an example, the full-scale spectral data at 4000 Hz comes from model spectral data at approximately 46,000 Hz. At those high frequencies, the atmospheric attenuation corrections are very large. As a result, the corrections for atmospheric attenuation within the test facility were over estimated, causing an overcompensation and hookup in the measured noise spectra typically starting at 2000 Hz full scale or approximately 23,000-Hz model scale. This was especially significant in the static and flight simulated data from the baseline round convergent nozzle and the short ejector configurations (15, 16, 17, and 18) where model high-frequency noise was most prevalent. Noise spectra from these five configurations that exhibited this hookup were corrected by holding the full-scale, 150-ft arc, 2000-Hz sound pressure level (SPL) constant from 2000 Hz to 10,000 Hz. If a minimum SPL existed between 2000 Hz and 10,000 Hz, the minimum SPL was held constant from the frequency at which the minimum occurred to 10,000 Hz. This correction was used because any other correction would impose an arbitrarily chosen rolloff rate to the noise spectra data, thus creating some ambiguity in the test results.

Figures 369 and 370 illustrate the full-scale, Federal Aviation Administration (FAA) standard day, 150-ft arc acoustic data hookup and correction for the baseline round convergent nozzle and Configuration 15 (vortical mixer/short hardwall shroud/Shroud Area Ratio [SAR] = 4.9/Mixing Area Ratio [MAR] = 1.185) at  $V_{jet} = 2384$  ft/sec. Figures 371 and 372 show the same spectra extrapolated to the sideline position at 1629 ft. The corresponding Tone-Corrected Perceived Noise Level (PNLT) directivity at  $V_{jet} = 2384$  ft/sec are shown in Figures 373 and 374. The reduction in measured aft noise is especially clear for the baseline round convergent nozzle, where the largest change to the noise data occurred at the polar angles of 110 to 130 degrees. Finally, Figures 375 and 376 illustrate the change in Effective Perceived Noise Level (EPNL), at static and flight simulated conditions, due to the data correction for the baseline round convergent nozzle and Configuration 15. The effect of the data correction on Configurations 16, 17, and 18 results were very similar in magnitude to that shown for Configuration 15.

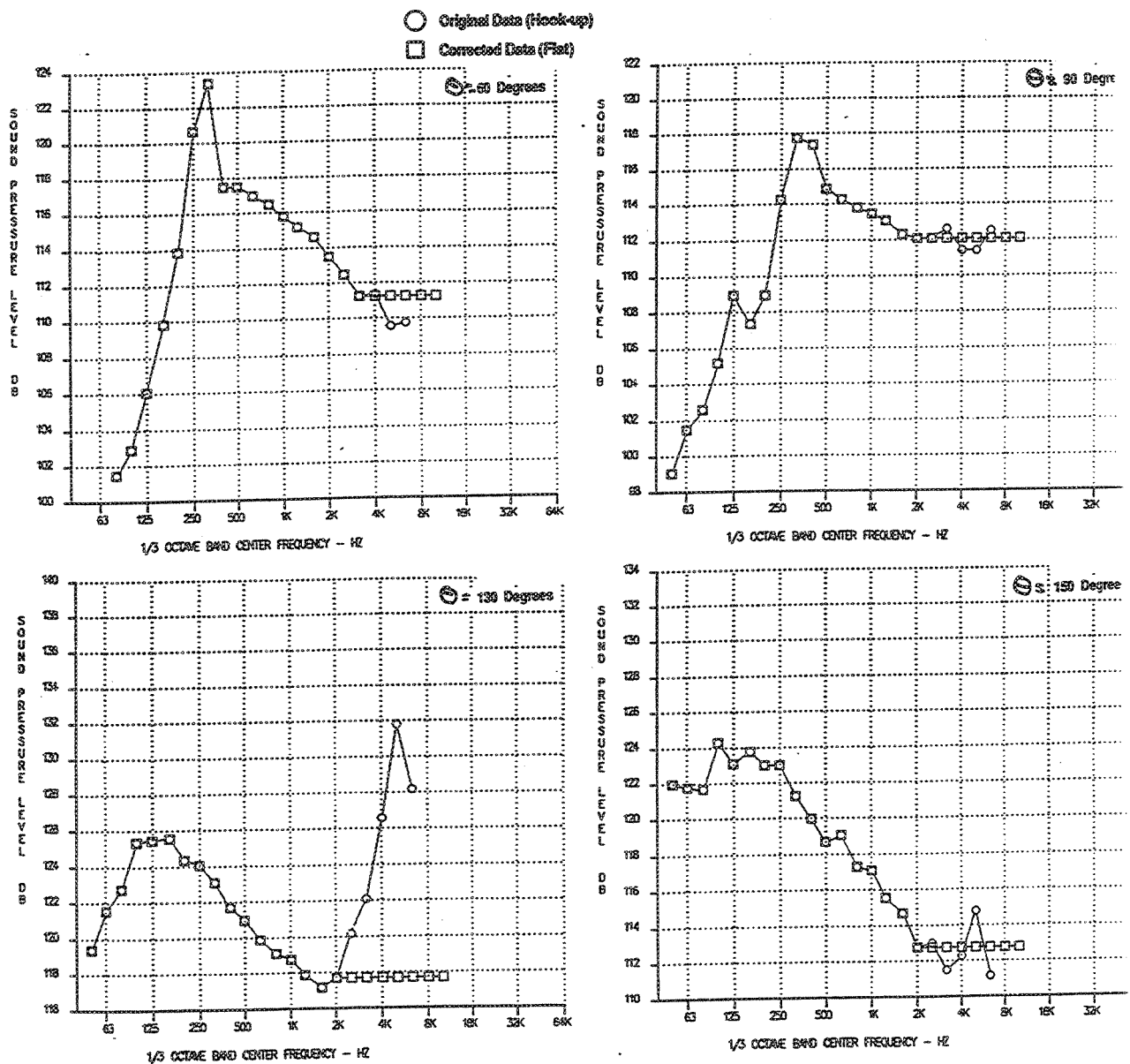


Figure 369. Noise Spectra Hookup and Correction – SPL Versus Frequency at 60, 90, 130, and 150 degrees  
 Baseline Round Conic Nozzle

(150-ft Arc,  $A_{g*}=1086 \text{ in}^2$ ,  $V_j=2384 \text{ ft/sec}$ ,  $M_n=0.32$ ,  $V_{fl}=357 \text{ ft/sec}$ )

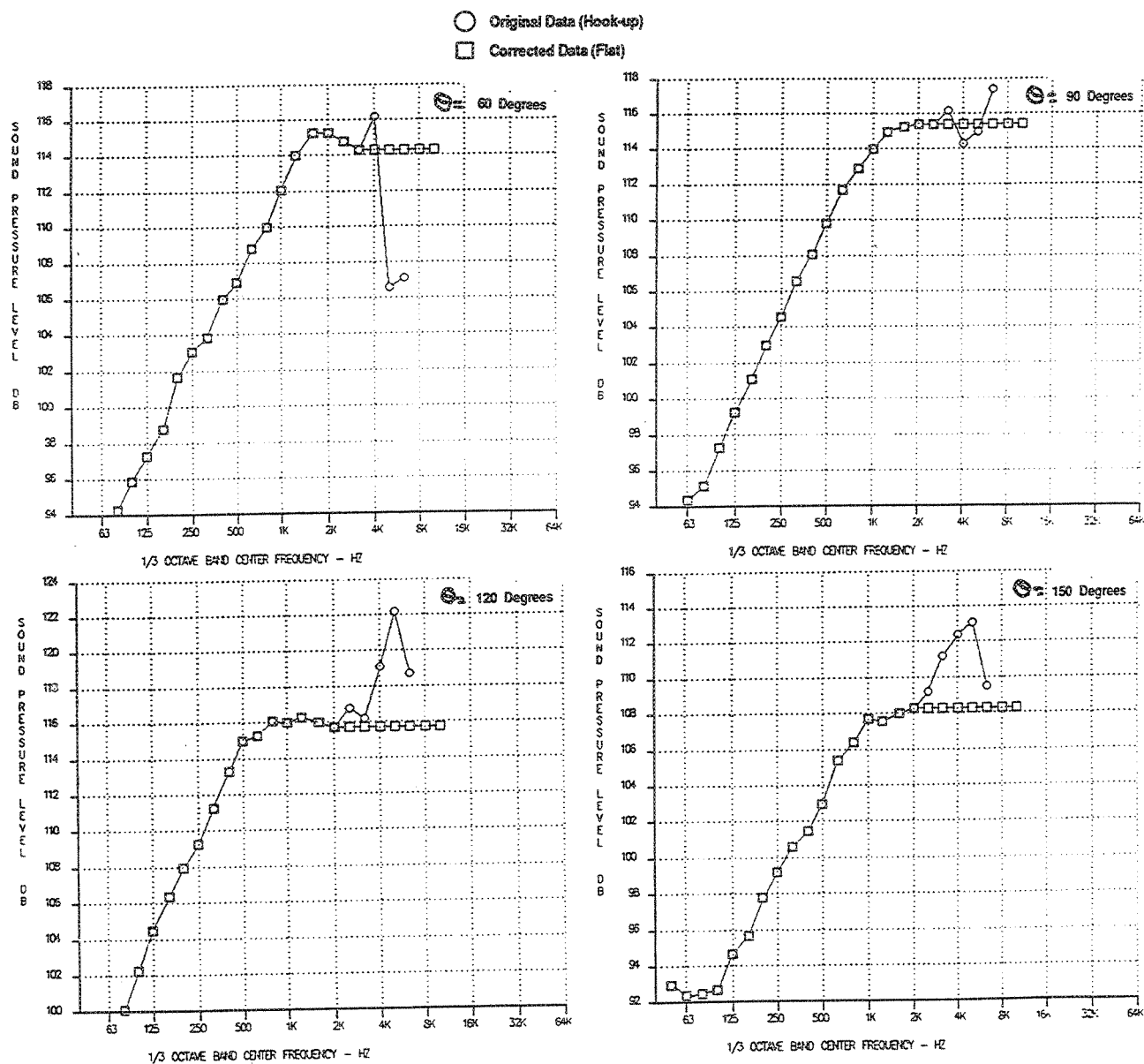


Figure 370. Noise Spectra Hookup and Correction – SPL Versus Frequency at 60, 90, 120, and 150 degrees  
 Vortical Mixer, Hardwall, Short Shroud  
 (SAR=4.9, MAR=1.185, 150-ft Arc,  $A_8^*=1086 \text{ in}^2$ ,  $V_j=2384 \text{ ft/sec}$ ,  $Mn=0.32$ ,  $V_{fl}=357 \text{ ft/sec}$ )

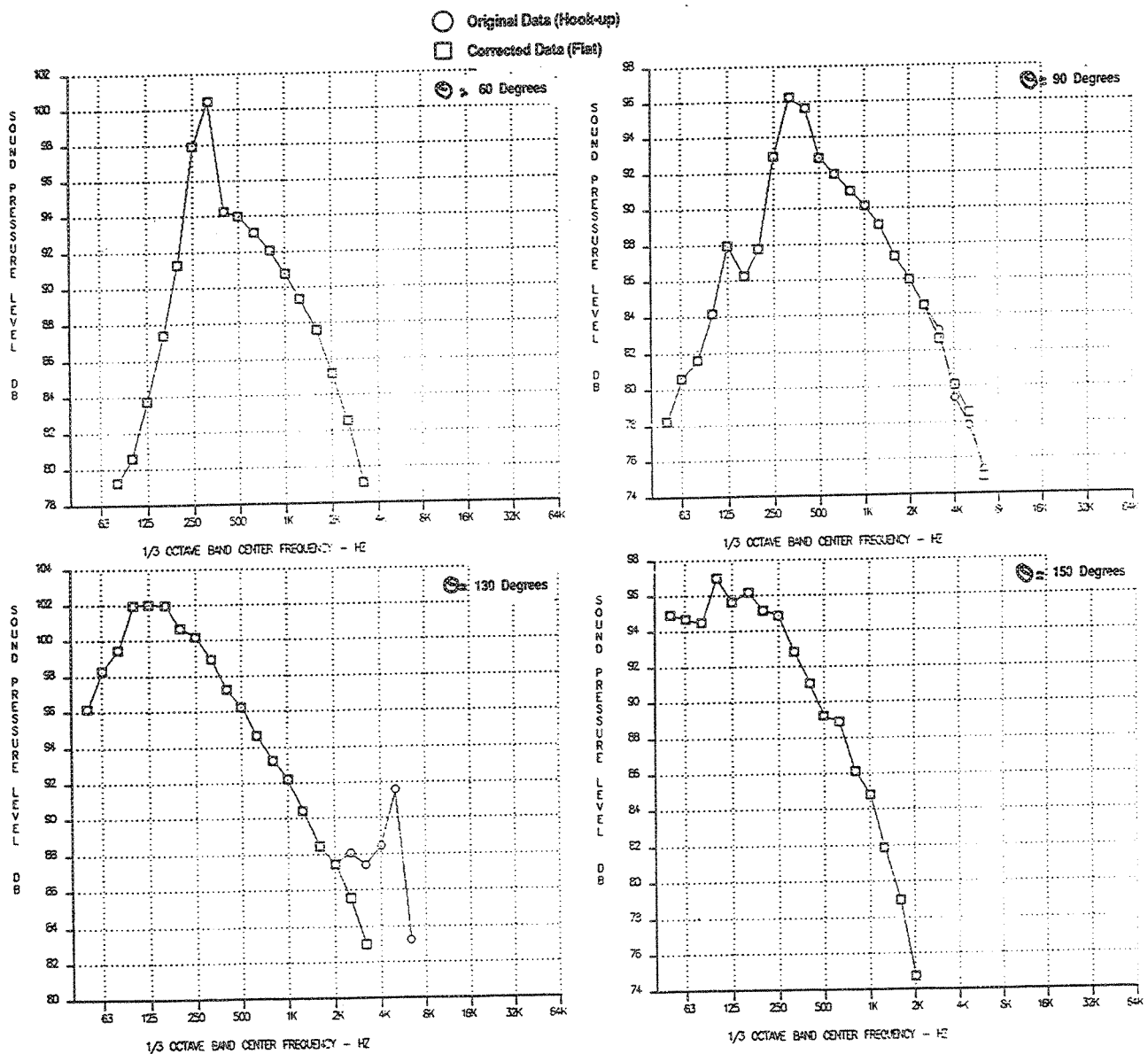


Figure 371. Noise Spectra Hookup and Correction – SPL Versus Frequency at 60, 90, 130, and 150 degrees  
 Baseline Round Conic Nozzle

(Sideline=1629 ft,  $A_{8*}=1086 \text{ in}^2$ ,  $V_j=2384 \text{ ft/sec}$ ,  $M_n=0.32$ ,  $V_{fl}=357 \text{ ft/sec}$ )



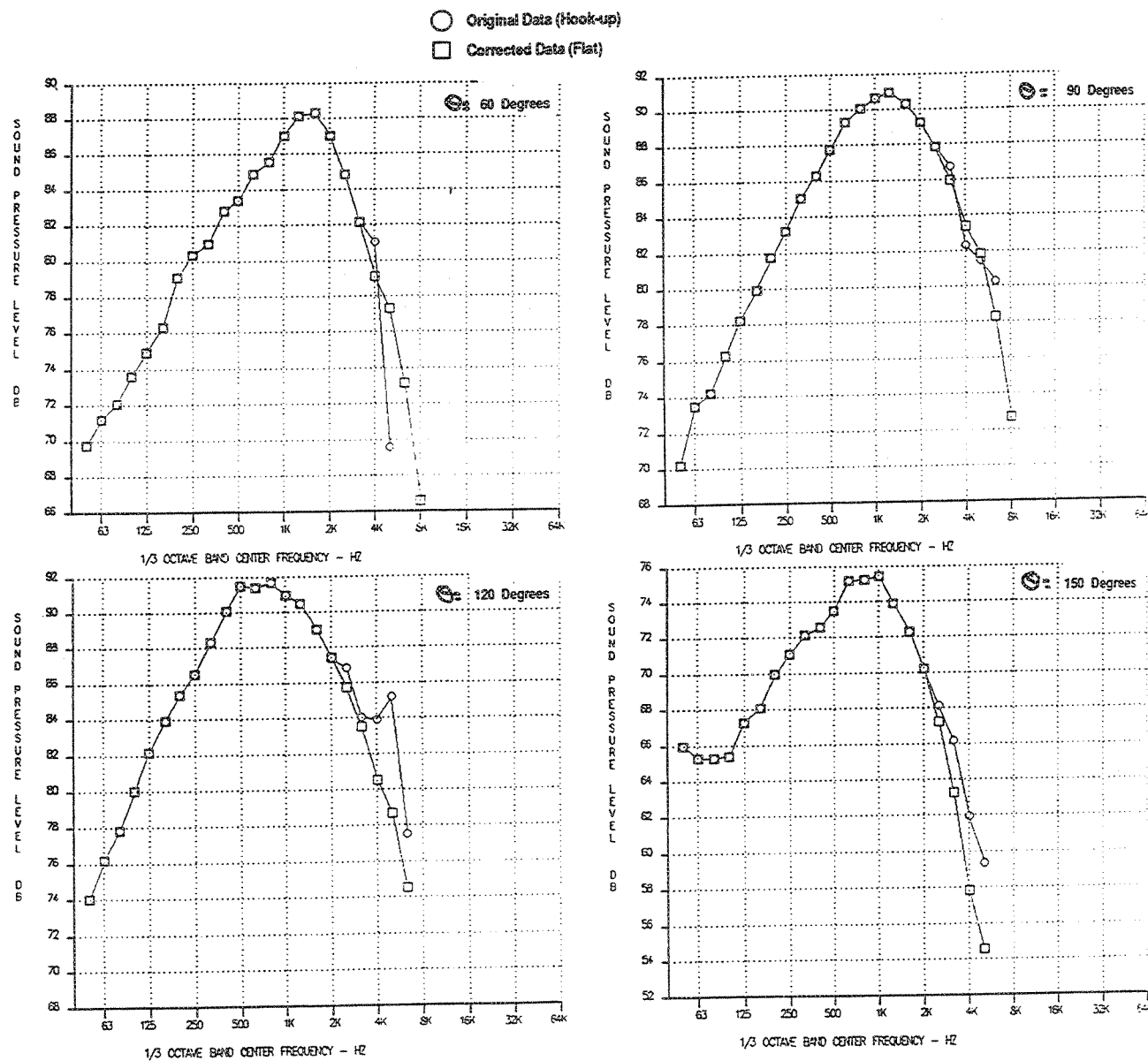


Figure 372. Noise Spectra Hookup and Correction – SPL Versus Frequency at 60, 90, 120, and 150 degrees  
 Vortical Mixer, Hardwall, Short Shroud  
 (SAR=4.9, MAR=1.185, Sideline=1629 ft,  $A_8^*=1086 \text{ in}^2$ ,  $V_j=2384 \text{ ft/sec}$ ,  $M_n=0.32$ ,  $V_{H}=357 \text{ ft/sec}$ )

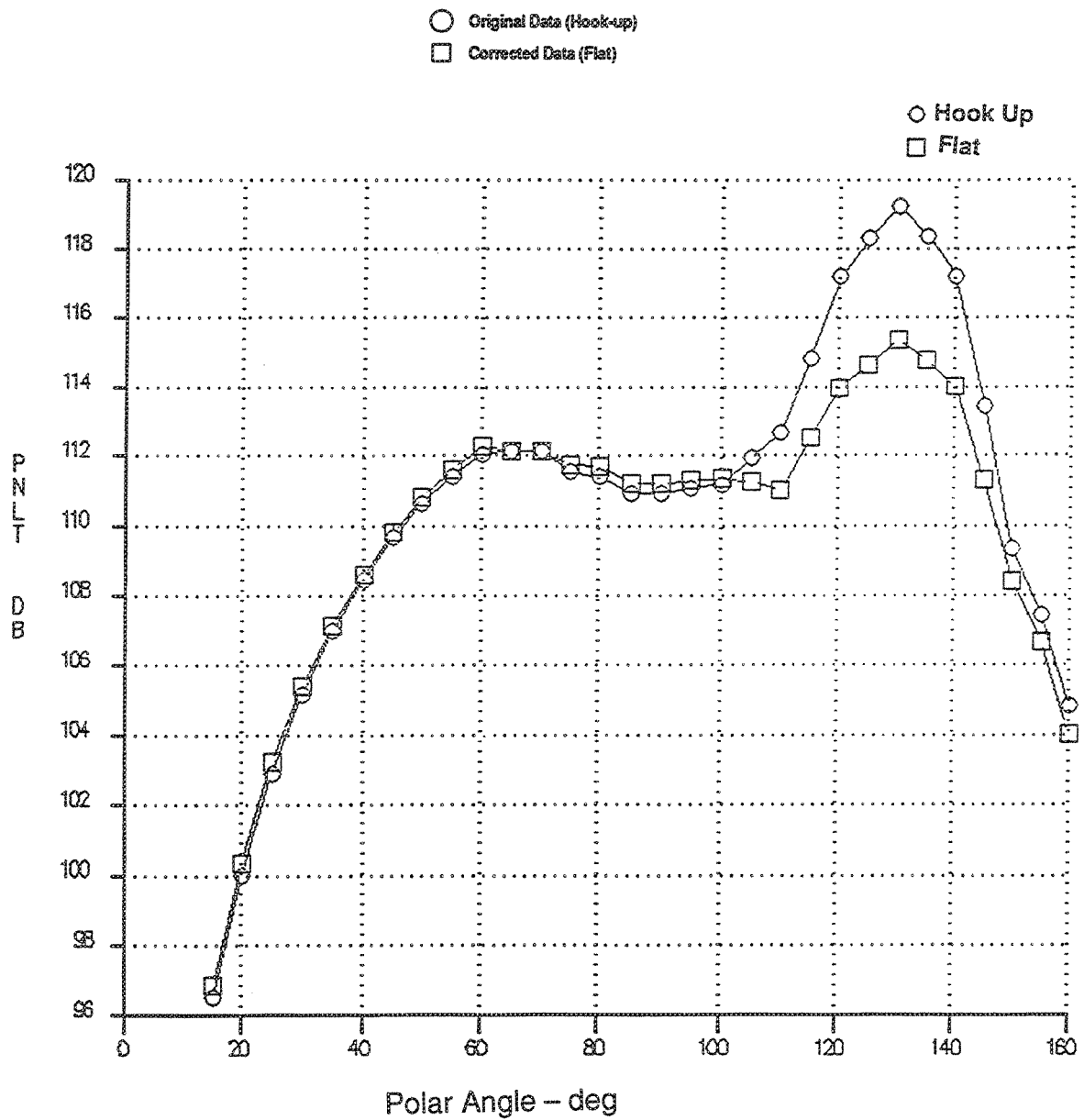


Figure 373. Noise Spectra Hookup and Correction – PNLT Versus Angle  
Baseline Round Conic Nozzle  
(Sideline=1629 ft,  $A_{8*}=1086 \text{ in}^2$ ,  $V_j=2384 \text{ ft/sec}$ ,  $M_n=0.32$ ,  $V_{fl}=357 \text{ ft/sec}$ )

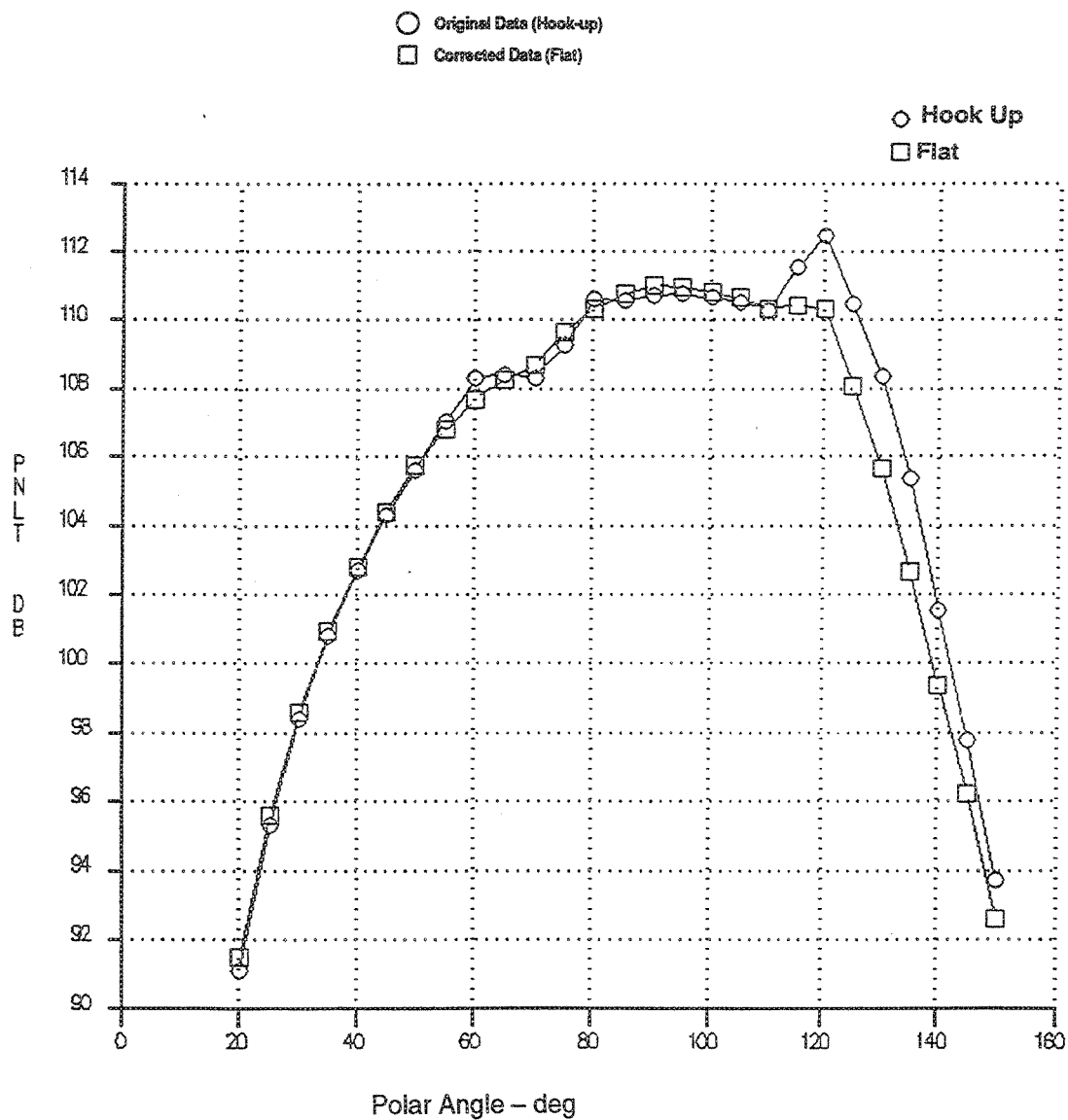


Figure 374. Noise Spectra Hook-Up and Correction - PNLT Versus Angle, Vortical Mixer, Hardwall, Short Shroud

(SAR = 4.9, MAR = 1.185,  $A_{g*} = 1086 \text{ in}^2$ , Sideline = 1629 ft,  $V_j = 2384 \text{ ft/sec}$ ,  $Mn = 0.32$ ,  $V_{fl} = 357 \text{ ft/sec}$ )

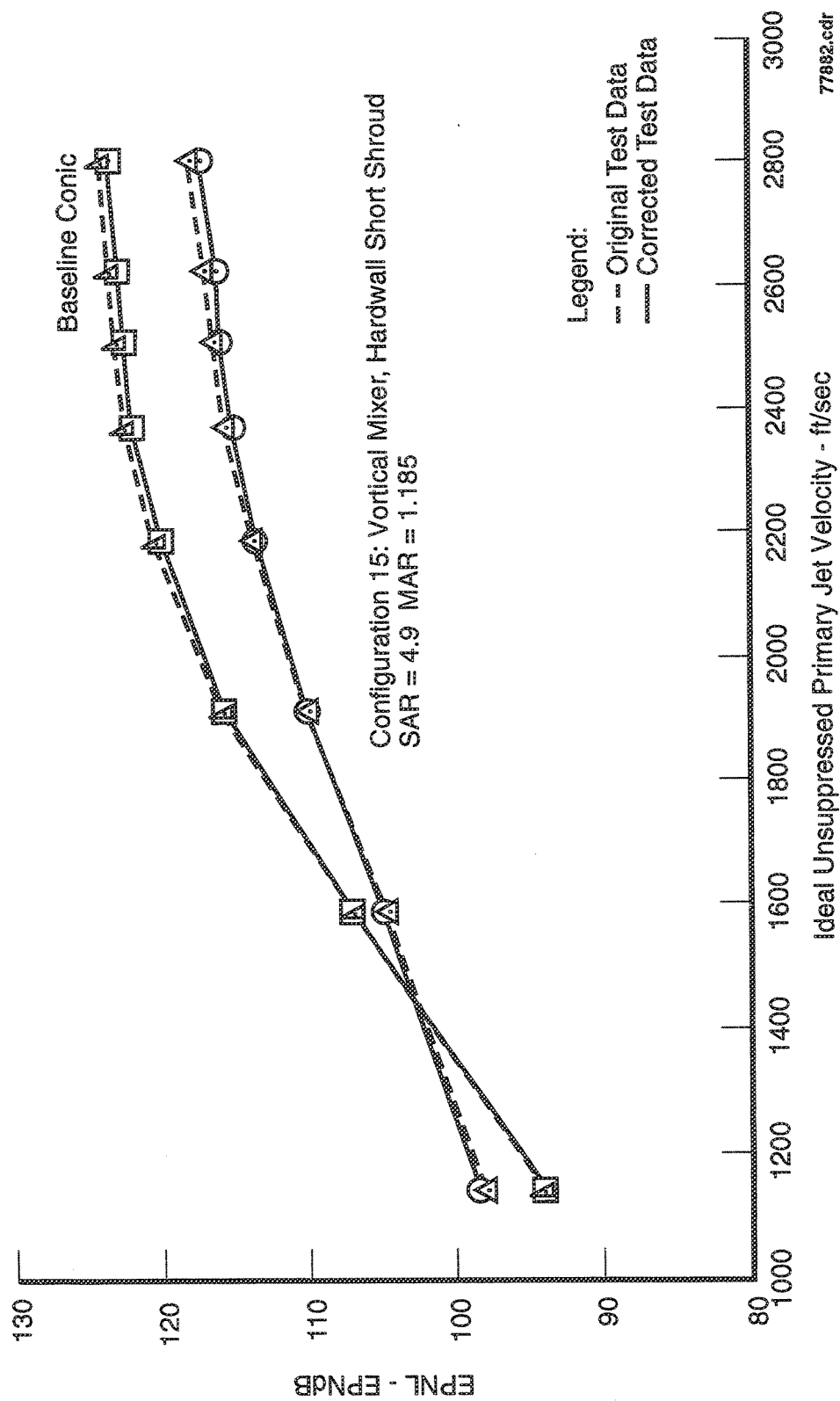


Figure 375. Effect of Data Correction on Sideline Noise – Baseline Round Conic Nozzle  
Vortical Mixer, Hardwall, Short Shroud  
(SAR = 4.9, MAR = 1.185,  $A_{g*} = 1086 \text{ in}^2$ , Sideline = 1629 ft, Static)

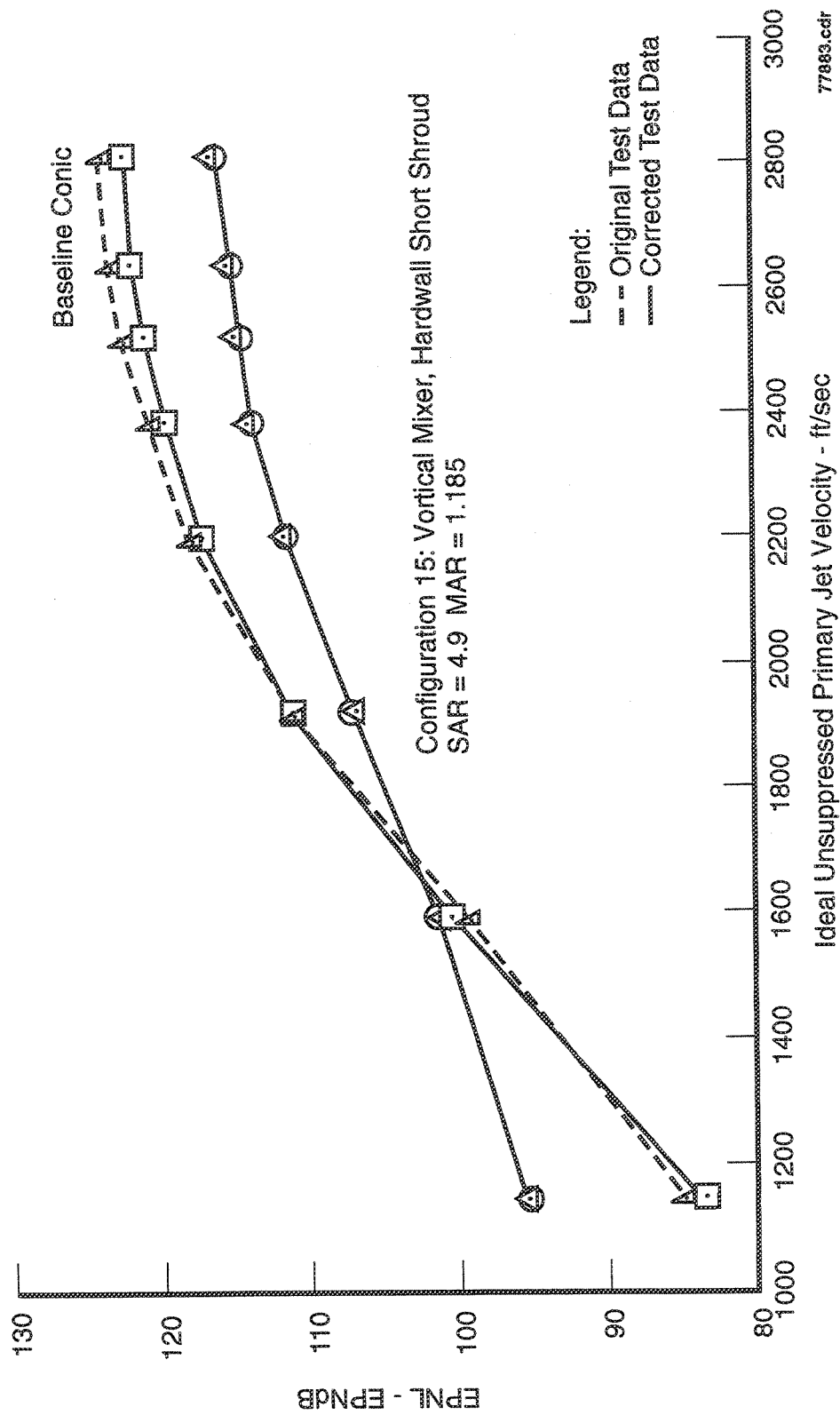


Figure 376. Effect of Data Correction on Sideline Noise – Baseline Round Conic Nozzle  
Vortical Mixer, Hardwall, Short Shroud

(SAR=4.9, MAR=1.185,  $A_{g*}=1086 \text{ in}^2$ , Sideline=1629 ft,  $Mn=0.32$ ,  $V_{\eta}=357 \text{ ft/sec}$ )

This page intentionally left blank.

## APPENDIX E — LIST OF TABLES

<i>Table</i>	<i>Page</i>
1. Microphone Positions.....	6
2. Acoustic Configurations --- Cold Inspected Model Dimensions .....	8
3. Hardwall Configurations --- Cold Inspected Model Dimensions .....	8
4. Cold-Inspected Mixer Areas .....	9
5. Pratt & Whitney 2D Mixer-Ejector L/D .....	10
6. Pratt & Whitney Two-Dimensional Mixer-Ejector Exhaust Nozzle Configurations .....	12
7. Test Point Definition .....	13
8. Laser Doppler Velocimeter Run Schedule.....	14
9. Nominal Velocities and Cycle Conditions.....	35
10. Conic Nozzle Test Conditions .....	36
11. High Speed Civil Transport Mixer-Ejector Exhaust Nozzle System Geometries .....	64
12. Baseline Flow Conditions for CFD Analysis.....	66
13. Squared Lobes Effect (Vortical Mixer, Short Shroud) .....	68
14. Parametrics with Squared Lobes (Vortical Mixer, Short Shroud) .....	69
15. Cell 41 Mixer Nozzle Analyses .....	70
16. P&W Acoustic Assumptions Effect on EPNL.....	444

This page intentionally left blank.



## APPENDIX F — LIST OF ILLUSTRATIONS

<i>Figure</i>	<i>Page</i>
1. Mixer-Ejector Model Mounted in Acoustic Test Facility .....	4
2. Side View of Cell 41 Anechoic Free-Jet Facility .....	15
3. Operating Domain of Cell 41 Anechoic Free Jet Facility .....	16
4. Plane View of Cell 41 Anechoic Free Jet Facility Showing 2D Nozzle Orientation for Acoustic and LV Tests .....	17
5. Laser Doppler Velocimeter System .....	18
6. P&W Baseline Round Convergent Nozzle .....	19
7. Assembly Drawing for P&W 2D Mixer-Ejector Nozzle .....	20
8. Mixer/Ejector Nomenclature .....	21
9. Lined Mixer-Ejector Configuration .....	22
10. Geometry of 2D Vortical Mixer Nozzle (All Dimensions in Inches) .....	23
11. Geometry of 2D Axial Mixer Nozzle (All Dimensions in Inches) .....	24
12. P&W 2D Model – Astroquartz Degradation .....	25
13. Static Pressure and Thermocouple Instrumentation for Vortical Mixer Nozzle .....	26
14. Static Pressure and Thermocouple Instrumentation for Axial Mixer Nozzle .....	27
15. Static Pressure Instrumentation for P&W Two-Dimensional Hardwall Shrouds .....	28
16. Comparison of Exhaust Nozzle Pressure Ratio and Total Temperature Versus Ideal Jet Velocity for Cycles Currently Under Consideration for HSCT Propulsion .....	29
17. Comparison of Exhaust Nozzle Pressure Ratio With Respect to Total Temperature for Cycles Currently Under Consideration for HSCT Propulsion .....	30
18. Acoustic Test Points for Pratt & Whitney Mixer-Ejector Nozzles in Terms of Nozzle Pressure Ratio Versus Total Temperature With Iso-Jet Velocity Lines .....	31
19. Acoustic Data Processing Flowchart .....	78
20. Cross-Sectional Views of Three Different Size Round Convergent Nozzles Tested in Cell 41 .....	79
21. Comparison of Pseudo-EPNL, PNLT at Various Polar Angles ( $\theta$ ) and Peak PNLT Data as a Function of Jet Velocity Between Three Different Size Conical Nozzles at Static Condition .....	80
22. Comparison of: (a) OASP, (b) PNL, and (c) PNLT Directivities at $V_j=1147$ ft/sec, $NPR=1.5$ , $T_g=1000^\circ R$ Between Three Different Size Conical Nozzles at Static Conditions .....	81
23. Comparison of PWL Spectra and SPL Spectra at Various Polar Angles ( $\theta$ ) at $V_j=1147$ ft/sec, $NPR=1.5$ , $T_g=1000^\circ R$ Between Three Different Size Conical Nozzles at Static Condition .....	82
24. Comparison of: (a) OASP, (b) PNL, and (c) PNLT Directivities at $V_j=1919$ ft/sec, $NPR=2.5$ , $T_g=1325^\circ R$ Between Three Different Size Conical Nozzles at Static Conditions .....	83
25. Comparison of PWL Spectra and SPL Spectra at Various Polar Angles ( $\theta$ ) at $V_j=1919$ ft/sec, $NPR=2.5$ , $T_g=1325^\circ R$ Between Three Different Size Conical Nozzles at Static Condition .....	84

26.	Comparison of: (a) OASP, (b) PNL, and (c) PNLT Directivities at $V_j=2384$ ft/sec, $NPR=3.4$ , $T_g=1590^\circ R$ Between Three Different Size Conical Nozzles at Static Conditions .....	85
27.	Comparison of PWL Spectra and SPL Spectra at Various Polar Angles ( $\theta$ ) at $V_j=2384$ ft/sec, $NPR=3.4$ , $T_g=1590^\circ R$ Between Three Different Size Conical Nozzles at Static Condition .....	86
28.	Comparison of: (a) OASP, (b) PNL, and (c) PNLT Directivities at $V_j=2812$ ft/sec, $NPR=4.5$ , $T_g=1860^\circ R$ Between Three Different Size Conical Nozzles at Static Conditions .....	87
29.	Comparison of PWL Spectra and SPL Spectra at Various Polar Angles ( $\theta$ ) at $V_j=2812$ ft/sec, $NPR=4.5$ , $T_g=1860^\circ R$ Between Three Different Size Conical Nozzles at Static Condition .....	88
30.	Comparison of Pseudo-EPNL, PNLT at Various Polar Angles ( $\theta$ ) and Peak PNLT Data as a Function of Jet Velocity Between Three Different Size Conical Nozzles With Flight Simulation ( $M_n=0.32$ ) .....	89
31.	Comparison of: (a) OASP, (b) PNL, and (c) PNLT Directivities at $V_j=1147$ ft/sec, $NPR=1.5$ , $T_g=1000^\circ R$ Between Three Different Size Conical Nozzles With Flight Simulation ( $M_n=0.32$ ) .....	90
32.	Comparison of PWL Spectra and SPL Spectra at Various Polar Angles ( $\theta$ ) at $V_j=1147$ ft/sec, $NPR=1.5$ , $T_g=1000^\circ R$ Between Three Different Size Conical Nozzles With Flight Simulation ( $M_n=0.32$ ) .....	91
33.	Comparison of: (a) OASP, (b) PNL, and (c) PNLT Directivities at $V_j=1919$ ft/sec, $NPR=2.5$ , $T_g=1325^\circ R$ Between Three Different Size Conical Nozzles With Flight Simulation ( $M_n=0.32$ ) .....	92
34.	Comparison of PWL Spectra and SPL Spectra at Various Polar Angles ( $\theta$ ) at $V_j=1919$ ft/sec, $NPR=2.5$ , $T_g=1325^\circ R$ Between Three Different Size Conical Nozzles With Flight Simulation ( $M_n=0.32$ ) .....	93
35.	Comparison of: (a) OASP, (b) PNL, and (c) PNLT Directivities at $V_j=2384$ ft/sec, $NPR=3.4$ , $T_g=1590^\circ R$ Between Three Different Size Conical Nozzles With Flight Simulation ( $M_n=0.32$ ) .....	94
36.	Comparison of PWL Spectra and SPL Spectra at Various Polar Angles ( $\theta$ ) at $V_j=2384$ ft/sec, $NPR=3.4$ , $T_g=1590^\circ R$ Between Three Different Size Conical Nozzles With Flight Simulation ( $M_n=0.32$ ) .....	95
37.	Comparison of: (a) OASP, (b) PNL, and (c) PNLT Directivities at $V_j=2812$ ft/sec, $NPR=4.5$ , $T_g=1860^\circ R$ Between Three Different Size Conical Nozzles With Flight Simulation ( $M_n=0.32$ ) .....	96
38.	Comparison of PWL Spectra and SPL Spectra at Various Polar Angles ( $\theta$ ) at $V_j=2812$ ft/sec, $NPR=4.5$ , $T_g=1860^\circ R$ Between Three Different Size Conical Nozzles With Flight Simulation ( $M_n=0.32$ ) .....	97
39.	Comparison of SPL Spectra at Polar Angle ( $\theta$ )= $60^\circ$ , $V_j=2812$ ft/sec, $NPR=4.5$ , and $T_g=1860^\circ R$ Between Three Different Size Conical Nozzles at Static Condition.....	98
40.	Comparison of SPL Spectra at Polar Angle ( $\theta$ )= $90^\circ$ , $V_j=2812$ ft/sec, $NPR=4.5$ , and $T_g=1860^\circ R$ Between Three Different Size Conical Nozzles at Static Condition.....	99
41.	Comparison of SPL Spectra at Polar Angle ( $\theta$ )= $130^\circ$ , $V_j=2812$ ft/sec, $NPR=4.5$ , and $T_g=1860^\circ R$ Between Three Different Size Conical Nozzles at Static Condition.....	100
42.	Ideal One-Dimensional Ejector Pumping Estimate ( $SAR=4.9$ , Altitude= $689$ ft, $M_n=0.32$ ) .....	101
43.	Effect of MAR ( $A_{exit}/A_{mix}$ ) on Sideline Noise, Vortical Mixer Long Treated Shroud ( $SAR=4.9$ , $A_{g*}=1086$ in <sup>2</sup> , $SL=1629$ ft, Static) .....	102
44.	Effect of MAR ( $A_{exit}/A_{mix}$ ) on Sideline Noise, Vortical Mixer Long Treated Shroud ( $SAR=4.9$ , $A_{g*}=1086$ in <sup>2</sup> , $SL=1629$ ft, $M_n=0.32$ , $V_{\Pi}=357$ ft/sec) .....	103
45.	Effect of MAR on PNLT vs. Angle — Ideal Unsuppressed Primary Jet Velocity= $1595$ ft/sec Vortical Mixer, Long Treated Shroud (Sideline= $1629$ ft, $A_{g*}=1086$ in <sup>2</sup> , $SAR=4.9$ , $V_{\Pi}=357$ ft/sec) .....	104
46.	Effect of MAR on PNLT vs. Angle — Ideal Unsuppressed Primary Jet Velocity= $2384$ ft/sec Vortical Mixer, Long Treated Shroud (Sideline= $1629$ ft, $A_{g*}=1086$ in <sup>2</sup> , $SAR=4.9$ , $V_{\Pi}=357$ ft/sec) .....	105

47.	Effect of MAR on PNLT vs. Angle — Ideal Unsuppressed Primary Jet Velocity=2812 ft/sec Vortical Mixer, Long Treated Shroud (Sideline=1629 ft, $A_{g*}=1086 \text{ in}^2$ , SAR=4.9, $V_{ff}=357 \text{ ft/sec}$ ) .....	106
48.	Effect of MAR on SPL Versus Frequency — Ideal Unsuppressed Primary Jet Velocity=1595 ft/sec Vortical Mixer, Long Treated Shroud (Sideline=1629 ft, $A_{g*}=1086 \text{ in}^2$ , SAR=4.9, Mn=0.32, $V_{ff}=357 \text{ ft/sec}$ ).....	107
49.	Effect of MAR on SPL Versus Frequency — Ideal Unsuppressed Primary Jet Velocity=2384 ft/sec Vortical Mixer, Long Treated Shroud (Sideline=1629 ft, $A_{g*}=1086 \text{ in}^2$ , SAR=4.9, Mn=0.32, $V_{ff}=357 \text{ ft/sec}$ ).....	108
50.	Effect of MAR on SPL Versus Frequency — Ideal Unsuppressed Primary Jet Velocity=2812 ft/sec Vortical Mixer, Long Treated Shroud (Sideline=1629 ft, $A_{g*}=1086 \text{ in}^2$ , SAR=4.9, Mn=0.32, $V_{ff}=357 \text{ ft/sec}$ ).....	109
51.	Effect of MAR ( $A_{exit}/A_{mix}$ ) on Sideline Noise, Vortical Mixer Long Treated Shroud (Sideline=1627 ft, SAR=4.4, $A_{g*}=1086 \text{ in}^2$ , Static) .....	110
52.	Effect of MAR ( $A_{exit}/A_{mix}$ ) on Sideline Noise, Vortical Mixer Long Treated Shroud (Sideline=1629 ft, SAR=4.4, $A_{g*}=1086 \text{ in}^2$ , Mn=0.32, $V_{ff}=357 \text{ ft/sec}$ ) .....	111
53.	Effect of MAR, PNLT Versus Angle — Ideal Unsuppressed Primary Jet Velocity=1595 ft/sec Vortical Mixer, Long Treated Shroud (Sideline=1629 ft, $A_{g*}=1086 \text{ in}^2$ , SAR=4.4, Mn=0.32, $V_{ff}=357 \text{ ft/sec}$ ).....	112
54.	Effect of MAR, PNLT Versus Angle — Ideal Unsuppressed Primary Jet Velocity=2384 ft/sec Vortical Mixer, Long Treated Shroud (Sideline=1629 ft, $A_{g*}=1086 \text{ in}^2$ , SAR=4.4, Mn=0.32, $V_{ff}=357 \text{ ft/sec}$ ).....	113
55.	Effect of MAR, PNLT Versus Angle — Ideal Unsuppressed Primary Jet Velocity=2812 ft/sec Vortical Mixer, Long Treated Shroud (Sideline=1629 ft, $A_{g*}=1086 \text{ in}^2$ , SAR=4.4, Mn=0.32, $V_{ff}=357 \text{ ft/sec}$ ).....	114
56.	Effect of MAR, SPL Versus Frequency — Ideal Unsuppressed Primary Jet Velocity=1595 ft/sec Vortical Mixer, Long Treated Shroud (Sideline=1629 ft, $A_{g*}=1086 \text{ in}^2$ , SAR=4.4, Mn=0.32, $V_{ff}=357 \text{ ft/sec}$ ).....	115
57.	Effect of MAR, SPL Versus Frequency — Ideal Unsuppressed Primary Jet Velocity=2384 ft/sec Vortical Mixer, Long Treated Shroud (Sideline=1629 ft, $A_{g*}=1086 \text{ in}^2$ , SAR=4.4, Mn=0.32, $V_{ff}=357 \text{ ft/sec}$ ).....	116
58.	Effect of MAR, SPL Versus Frequency — Ideal Unsuppressed Primary Jet Velocity=2812 ft/sec Vortical Mixer, Long Treated Shroud (Sideline=1629 ft, $A_{g*}=1086 \text{ in}^2$ , SAR=4.4, Mn=0.32, $V_{ff}=357 \text{ ft/sec}$ ).....	117
59.	Effect of MAR ( $A_{exit}/A_{mix}$ ) on Sideline Noise, Axial Mixer Long Treated Shroud (Sideline=1629 ft, SAR=4.9, $A_{g*}=1086 \text{ in}^2$ , Static) .....	118
60.	Effect of MAR ( $A_{exit}/A_{mix}$ ) on Sideline Noise, Axial Mixer Long Treated Shroud (Sideline=1629 ft, SAR=4.9, $A_{g*}=1086 \text{ in}^2$ , Mn=0.32, $V_{ff}=357 \text{ ft/sec}$ ).....	119

61.	Effect of MAR, PNLT Versus Angle — Ideal Unsuppressed Primary Jet Velocity=1595 ft/sec Axial Mixer, Long Treated Shroud (Sideline=1629 ft, $A_{g*}=1086 \text{ in}^2$ , SAR=4.9, Mn=0.32, $V_{fl}=357 \text{ ft/sec}$ ).....	120
62.	Effect of MAR, PNLT Versus Angle — Ideal Unsuppressed Primary Jet Velocity=2384 ft/sec Axial Mixer, Long Treated Shroud (Sideline=1629 ft, $A_{g*}=1086 \text{ in}^2$ , SAR=4.9, Mn=0.32, $V_{fl}=357 \text{ ft/sec}$ ).....	121
63.	Effect of MAR, PNLT Versus Angle — Ideal Unsuppressed Primary Jet Velocity=2812 ft/sec Axial Mixer, Long Treated Shroud (Sideline=1629 ft, $A_{g*}=1086 \text{ in}^2$ , SAR=4.9, Mn=0.32, $V_{fl}=357 \text{ ft/sec}$ ).....	122
64.	Effect of MAR, SPL Versus Frequency — Ideal Unsuppressed Primary Jet Velocity=1595 ft/sec Axial Mixer, Long Treated Shroud (Sideline=1629 ft, $A_{g*}=1086 \text{ in}^2$ , SAR=4.9, Mn=0.32, $V_{fl}=357 \text{ ft/sec}$ ).....	123
65.	Effect of MAR, SPL Versus Frequency — Ideal Unsuppressed Primary Jet Velocity=2384 ft/sec Axial Mixer, Long Treated Shroud (Sideline=1629 ft, $A_{g*}=1086 \text{ in}^2$ , SAR=4.9, Mn=0.32, $V_{fl}=357 \text{ ft/sec}$ ).....	124
66.	Effect of MAR, SPL Versus Frequency — Ideal Unsuppressed Primary Jet Velocity=2812 ft/sec Axial Mixer, Long Treated Shroud (Sideline=1629 ft, $A_{g*}=1086 \text{ in}^2$ , SAR=4.9, Mn=0.32, $V_{fl}=357 \text{ ft/sec}$ ).....	125
67.	Effect of SAR ( $A_{mix}/A_{g*}$ ) on Sideline Noise, Vortical Mixer, Long Treated Shroud (Sideline=1629 ft, MAR=0.97, $A_{g*}=1086 \text{ in}^2$ , Static).....	126
68.	Effect of SAR ( $A_{mix}/A_{g*}$ ) on Sideline Noise, Vortical Mixer, Long Treated Shroud (Sideline=1629 ft, MAR=0.97, $A_{g*}=1086 \text{ in}^2$ , Mn=0.32, $V_{fl}=357 \text{ ft/sec}$ ) .....	127
69.	Effect of SAR, PNLT Versus Angle — Ideal Unsuppressed Primary Jet Velocity=1595 ft/sec Vortical Mixer, Long Treated Shroud (Sideline=1629 ft, $A_{g*}=1086 \text{ in}^2$ , MAR=0.97, Mn=0.32, $V_{fl}=357 \text{ ft/sec}$ ) .....	128
70.	Effect of SAR, PNLT Versus Angle — Ideal Unsuppressed Primary Jet Velocity=2384 ft/sec Vortical Mixer, Long Treated Shroud (Sideline=1629 ft, $A_{g*}=1086 \text{ in}^2$ , MAR=0.97, Mn=0.32, $V_{fl}=357 \text{ ft/sec}$ ) .....	129
71.	Effect of SAR, PNLT Versus Angle — Ideal Unsuppressed Primary Jet Velocity=2812 ft/sec Vortical Mixer, Long Treated Shroud (Sideline=1629 ft, $A_{g*}=1086 \text{ in}^2$ , MAR=0.97, Mn=0.32, $V_{fl}=357 \text{ ft/sec}$ ) .....	130
72.	Effect of SAR, SPL Versus Frequency — Ideal Unsuppressed Primary Jet Velocity=1595 ft/sec Vortical Mixer, Long Treated Shroud (Sideline=1629 ft, $A_{g*}=1086 \text{ in}^2$ , MAR=0.97, Mn=0.32, $V_{fl}=357 \text{ ft/sec}$ ) .....	131
73.	Effect of SAR, SPL Versus Frequency — Ideal Unsuppressed Primary Jet Velocity=2384 ft/sec Vortical Mixer, Long Treated Shroud (Sideline=1629 ft, $A_{g*}=1086 \text{ in}^2$ , MAR=0.97, Mn=0.32, $V_{fl}=357 \text{ ft/sec}$ ) .....	132
74.	Effect of SAR, SPL Versus Frequency — Ideal Unsuppressed Primary Jet Velocity=2812 ft/sec Vortical Mixer, Long Treated Shroud (Sideline=1629 ft, $A_{g*}=1086 \text{ in}^2$ , MAR=0.97, Mn=0.32, $V_{fl}=357 \text{ ft/sec}$ ) .....	133

75.	Mixer Comparison Long Shroud (Sideline=1629 ft, SAR=4.9, MAR=0.97, $A_{g*}=1086 \text{ in}^2$ , Static) .....	134
76.	Mixer Comparison Long Shroud (Sideline=1629 ft, SAR=4.9, MAR=0.97, $A_{g*}=1086 \text{ in}^2$ , $Mn=0.32$ , $V_{fl}=357 \text{ ft/sec}$ ).....	135
77.	Mixer Comparison Long Shroud (Sideline=1629 ft, SAR=4.9, MAR=0.88, $A_{g*}=1086 \text{ in}^2$ , Static) .....	136
78.	Mixer Comparison Long Shroud (Sideline=1629 ft, SAR=4.9, MAR=0.88, $A_{g*}=1086 \text{ in}^2$ , $Mn=0.32$ , $V_{fl}=357 \text{ ft/sec}$ ).....	137
79.	Mixer Comparison, PNLT Versus Angle — Ideal Unsuppressed Primary Jet Velocity=1595 ft/sec Long Shroud (Sideline=1629 ft, SAR=4.9, MAR=0.97, $A_{g*}=1086 \text{ in}^2$ , $Mn=0.32$ , $V_{fl}=357 \text{ ft/sec}$ ) .....	138
80.	Mixer Comparison, PNLT Versus Angle — Ideal Unsuppressed Primary Jet Velocity=2384 ft/sec Long Shroud (Sideline=1629 ft, SAR=4.9, MAR=0.97, $A_{g*}=1086 \text{ in}^2$ , $Mn=0.32$ , $V_{fl}=357 \text{ ft/sec}$ ) .....	139
81.	Mixer Comparison, SPL Versus Frequency — Ideal Unsuppressed Primary Jet Velocity=1595 ft/sec Long Shroud (Sideline=1629 ft, SAR=4.9, MAR=0.97, $A_{g*}=1086 \text{ in}^2$ , $Mn=0.32$ , $V_{fl}=357 \text{ ft/sec}$ ) .....	140
82.	Mixer Comparison, SPL Versus Frequency — Ideal Unsuppressed Primary Jet Velocity=2384 ft/sec Long Shroud (Sideline=1629 ft, SAR=4.9, MAR=0.97, $A_{g*}=1086 \text{ in}^2$ , $Mn=0.32$ , $V_{fl}=357 \text{ ft/sec}$ ) .....	141
83.	Effect of Treatment on Sideline Noise, Vortical Mixer Long Shroud (Sideline=1629 ft, SAR=4.9, MAR=1.19, $A_{g*}=1086 \text{ in}^2$ , Static).....	142
84.	Effect of Treatment on Sideline Noise, Vortical Mixer Long Shroud (Sideline=1629 ft, SAR=4.9, MAR=1.19, $A_{g*}=1086 \text{ in}^2$ , $Mn=0.32$ , $V_{fl}=357 \text{ ft/sec}$ ) .....	143
85.	Effect of Treatment on Sideline Noise, Vortical Mixer Long Shroud (Sideline=1629 ft, SAR=4.9, MAR=0.97, $A_{g*}=1086 \text{ in}^2$ , Static).....	144
86.	Effect of Treatment on Sideline Noise, Vortical Mixer Long Shroud (Sideline=1629 ft, SAR=4.9, MAR=0.97, $A_{g*}=1086 \text{ in}^2$ , $Mn=0.32$ , $V_{fl}=357 \text{ ft/sec}$ ).....	145
87.	Effect of Treatment on Sideline Noise, Vortical Mixer Long Shroud (Sideline=1629 ft, SAR=4.4, MAR=0.88, $A_{g*}=1086 \text{ in}^2$ , Static).....	146
88.	Effect of Treatment on Sideline Noise, Vortical Mixer Long Shroud (Sideline=1629 ft, SAR=4.4, MAR=0.88, $A_{g*}=1086 \text{ in}^2$ , $Mn=0.32$ , $V_{fl}=357 \text{ ft/sec}$ ) .....	147
89.	Effect of Treatment on Noise, PNLT Versus Angle — Ideal Unsuppressed Primary Jet Velocity=1595 ft/sec, Vortical Mixer, Long Shroud (Sideline=1629 ft, SAR=4.9, MAR=0.97, $A_{g*}=1086 \text{ in}^2$ , $Mn=0.32$ , $V_{fl}=357 \text{ ft/sec}$ ) .....	148
90.	Effect of Treatment on Noise, PNLT Versus Angle — Ideal Unsuppressed Primary Jet Velocity=2394 ft/sec, Vortical Mixer, Long Shroud (Sideline=1629 ft, SAR=4.9, MAR=0.97, $A_{g*}=1086 \text{ in}^2$ , $Mn=0.32$ , $V_{fl}=357 \text{ ft/sec}$ ) .....	149
91.	Effect of Treatment on Noise, PNLT Versus Angle — Ideal Unsuppressed Primary Jet Velocity=2812 ft/sec, Vortical Mixer, Long Shroud (Sideline=1629 ft, SAR=4.9, MAR=0.97, $A_{g*}=1086 \text{ in}^2$ , $Mn=0.32$ , $V_{fl}=357 \text{ ft/sec}$ ) .....	150

92.	Effect of Treatment on Noise, SPL Versus Frequency — Ideal Unsuppressed Primary Jet Velocity=1595 ft/sec, Vortical Mixer, Long Shroud (Sideline=1629 ft, SAR=4.9, MAR=0.97, $A_g=1086 \text{ in}^2$ , $Mn=0.32$ , $V_{\text{fl}}=357 \text{ ft/sec}$ ) .....	151
93.	Effect of Treatment on Noise, SPL Versus Frequency — Ideal Unsuppressed Primary Jet Velocity=2384 ft/sec, Vortical Mixer, Long Shroud (Sideline=1629 ft, SAR=4.9, MAR=0.97, $A_g=1086 \text{ in}^2$ , $Mn=0.32$ , $V_{\text{fl}}=357 \text{ ft/sec}$ ) .....	152
94.	Effect of Treatment on Noise, PNLT Versus Angle — Ideal Unsuppressed Primary Jet Velocity=2812 ft/sec, Vortical Mixer, Long Shroud (Sideline=1629 ft, SAR=4.9, MAR=0.97, $A_g=1086 \text{ in}^2$ , $Mn=0.32$ , $V_{\text{fl}}=357 \text{ ft/sec}$ ) .....	153
95.	Effect of Treatment on Sideline Noise, Axial Mixer Long Shroud (Sideline=1629 ft, SAR=4.9, MAR=0.97, $A_g=1086 \text{ in}^2$ , Static) .....	154
96.	Effect of Treatment on Sideline Noise, Axial Mixer Long Shroud (Sideline=1629 ft, SAR=4.9, MAR=0.97, $A_g=1086 \text{ in}^2$ , $Mn=0.32$ , $V_{\text{fl}}=357 \text{ ft/sec}$ ) .....	155
97.	Effect of Treatment on Noise, PNLT Versus Angle — Ideal Unsuppressed Primary Jet Velocity=1595 ft/sec, Axial Mixer, Long Shroud (Sideline=1629 ft, SAR=4.9, MAR=0.97, $A_g=1086 \text{ in}^2$ , $Mn=0.32$ , $V_{\text{fl}}=357 \text{ ft/sec}$ ) .....	156
98.	Effect of Treatment on Noise, PNLT Versus Angle — Ideal Unsuppressed Primary Jet Velocity=2384 ft/sec, Axial Mixer, Long Shroud (Sideline=1629 ft, SAR=4.9, MAR=0.97, $A_g=1086 \text{ in}^2$ , $Mn=0.32$ , $V_{\text{fl}}=357 \text{ ft/sec}$ ) .....	157
99.	Effect of Treatment on Noise, PNLT Versus Angle — Ideal Unsuppressed Primary Jet Velocity=2812 ft/sec, Axial Mixer, Long Shroud (Sideline=1629 ft, SAR=4.9, MAR=0.97, $A_g=1086 \text{ in}^2$ , $Mn=0.32$ , $V_{\text{fl}}=357 \text{ ft/sec}$ ) .....	158
100.	Effect of Treatment on Noise, SPL Versus Angle — Ideal Unsuppressed Primary Jet Velocity=1595 ft/sec, Axial Mixer, Long Shroud (Sideline=1629 ft, SAR=4.9, MAR=0.97, $A_g=1086 \text{ in}^2$ , $Mn=0.32$ , $V_{\text{fl}}=357 \text{ ft/sec}$ ) .....	159
101.	Effect of Treatment on Noise, SPL Versus Angle — Ideal Unsuppressed Primary Jet Velocity=2384 ft/sec, Axial Mixer, Long Shroud (Sideline=1629 ft, SAR=4.9, MAR=0.97, $A_g=1086 \text{ in}^2$ , $Mn=0.32$ , $V_{\text{fl}}=357 \text{ ft/sec}$ ) .....	160
102.	Effect of Treatment on Noise, SPL Versus Angle — Ideal Unsuppressed Primary Jet Velocity=2812 ft/sec, Axial Mixer, Long Shroud (Sideline=1629 ft, SAR=4.9, MAR=0.97, $A_g=1086 \text{ in}^2$ , $Mn=0.32$ , $V_{\text{fl}}=357 \text{ ft/sec}$ ) .....	161
103.	Comparison of Liner Effectiveness – Hardwall-Treated Vortical and Axial Mixers, Long Shroud (Sideline=1629 ft, SAR=4.9, MAR=0.97, $A_g=1086 \text{ in}^2$ , $Mn=0.32$ , $V_{\text{fl}}=357 \text{ ft/sec}$ ) .....	162
104.	Liner Attenuation, SPL Versus Frequency — Ideal Unsuppressed Primary Jet Velocity=2384 ft/sec Vortical Mixer, Long Shroud (Sideline=1629 ft, SAR=4.9, MAR=0.97, $A_g=1086 \text{ in}^2$ , $Mn=0.32$ , $V_{\text{fl}}=357 \text{ ft/sec}$ ) .....	163
105.	Liner Attenuation, NOY Versus Frequency — Ideal Unsuppressed Primary Jet Velocity=2384 ft/sec Vortical Mixer, Long Shroud (Sideline=1629 ft, SAR=4.9, MAR=0.97, $A_g=1086 \text{ in}^2$ , $Mn=0.32$ , $V_{\text{fl}}=357 \text{ ft/sec}$ ) .....	164

106.	Liner Attenuation, SPL Versus Frequency — Ideal Unsuppressed Primary Jet Velocity=2384 ft/sec Vortical Mixer, Long Shroud (Sideline=1629 ft, SAR=4.4, MAR=0.97, $A_{g*}=1086 \text{ in}^2$ , $Mn=0.32$ , $V_{fl}=357 \text{ ft/sec}$ ) .....	165
107.	Liner Attenuation, NOY Versus Frequency — Ideal Unsuppressed Primary Jet Velocity=2384 ft/sec Vortical Mixer, Long Shroud (Sideline=1629 ft, SAR=4.4, MAR=0.97, $A_{g*}=1086 \text{ in}^2$ , $Mn=0.32$ , $V_{fl}=357 \text{ ft/sec}$ ) .....	166
108.	Liner Attenuation, SPL Versus Frequency — Ideal Unsuppressed Primary Jet Velocity=2384 ft/sec Axial Mixer, Long Shroud (Sideline=1629 ft, SAR=4.9, MAR=0.97, $A_{g*}=1086 \text{ in}^2$ , $Mn=0.32$ , $V_{fl}=357 \text{ ft/sec}$ ) .....	167
109.	Liner Attenuation, NOY Versus Frequency — Ideal Unsuppressed Primary Jet Velocity=2384 ft/sec Axial Mixer, Long Shroud (Sideline=1629 ft, SAR=4.9, MAR=0.97, $A_{g*}=1086 \text{ in}^2$ , $Mn=0.32$ , $V_{fl}=357 \text{ ft/sec}$ ) .....	168
110.	Degradation .....	169
111.	Effect of Treatment on Sideline Noise, Vortical Mixer, Long Shroud (Sideline=1629 ft, SAR=4.4, MAR=0.97, $A_{g*}=1086 \text{ in}^2$ , Static) .....	170
112.	Effect of Treatment on Sideline Noise, Vortical Mixer, Long Shroud (Sideline=1629 ft, SAR=4.4, MAR=0.97, $A_{g*}=1086 \text{ in}^2$ , $Mn=0.32$ , $V_{fl}=357 \text{ ft/sec}$ ) .....	171
113.	Effect of Treatment on Sideline Noise, Vortical Mixer, Long Shroud (Sideline=1629 ft, SAR=4.4, MAR=1.19, $A_{g*}=1086 \text{ in}^2$ , Static) .....	172
114.	Effect of Treatment on Sideline Noise, Vortical Mixer, Long Shroud (Sideline=1629 ft, SAR=4.4, MAR=0.97, $A_{g*}=1086 \text{ in}^2$ , $Mn=0.32$ , $V_{fl}=357 \text{ ft/sec}$ ) .....	173
115.	Effects of Deteriorated Treatment on Noise, PNLT Versus Angle — Ideal Unsuppressed Primary Jet Velocity=1595 ft/sec, Vortical Mixer, Long Shroud (Sideline=1629 ft, SAR=4.4, MAR=0.97, $A_{g*}=1086 \text{ in}^2$ , $Mn=0.32$ , $V_{fl}=357 \text{ ft/sec}$ ) .....	174
116.	Effects of Deteriorated Treatment on Noise, PNLT Versus Angle — Ideal Unsuppressed Primary Jet Velocity=2384 ft/sec, Vortical Mixer, Long Shroud (Sideline=1629 ft, SAR=4.4, MAR=0.97, $A_{g*}=1086 \text{ in}^2$ , $Mn=0.32$ , $V_{fl}=357 \text{ ft/sec}$ ) .....	175
117.	Effects of Deteriorated Treatment on Noise, PNLT Versus Angle — Ideal Unsuppressed Primary Jet Velocity=2812 ft/sec, Vortical Mixer, Long Shroud (Sideline=1629 ft, SAR=4.4, MAR=0.97, $A_{g*}=1086 \text{ in}^2$ , $Mn=0.32$ , $V_{fl}=357 \text{ ft/sec}$ ) .....	176
118.	Effects of Deteriorated Treatment on Noise, PNLT Versus Angle — Ideal Unsuppressed Primary Jet Velocity=1595 ft/sec, Vortical Mixer, Long Shroud (Sideline=1629 ft, SAR=4.4, MAR=1.19, $A_{g*}=1086 \text{ in}^2$ , $Mn=0.32$ , $V_{fl}=357 \text{ ft/sec}$ ) .....	177
119.	Effects of Deteriorated Treatment on Noise, PNLT Versus Angle — Ideal Unsuppressed Primary Jet Velocity=2384 ft/sec, Vortical Mixer, Long Shroud (Sideline=1629 ft, SAR=4.4, MAR=1.19, $A_{g*}=1086 \text{ in}^2$ , $Mn=0.32$ , $V_{fl}=357 \text{ ft/sec}$ ) .....	178
120.	Effects of Deteriorated Treatment on Noise, SPL Versus Frequency — Ideal Unsuppressed Primary Jet Velocity=1595 ft/sec, Vortical Mixer, Long Shroud (Sideline=1629 ft, SAR=4.4, MAR=0.97, $A_{g*}=1086 \text{ in}^2$ , $Mn=0.32$ , $V_{fl}=357 \text{ ft/sec}$ ) .....	179

121.	Effects of Deteriorated Treatment on Noise, SPL Versus Frequency — Ideal Unsuppressed Primary Jet Velocity=2384 ft/sec, Vortical Mixer, Long Shroud (Sideline=1629 ft, SAR=4.4, MAR=0.97, $A_{g*}=1086 \text{ in}^2$ , $M_n=0.32$ , $V_{\Pi}=357 \text{ ft/sec}$ ) .....	180
122.	Effects of Deteriorated Treatment on Noise, SPL Versus Frequency — Ideal Unsuppressed Primary Jet Velocity=2812 ft/sec, Vortical Mixer, Long Shroud (Sideline=1629 ft, SAR=4.4, MAR=0.97, $A_{g*}=1086 \text{ in}^2$ , $M_n=0.32$ , $V_{\Pi}=357 \text{ ft/sec}$ ) .....	181
123.	Effects of Deteriorated Treatment on Noise, SPL Versus Frequency — Ideal Unsuppressed Primary Jet Velocity=1595 ft/sec, Vortical Mixer, Long Shroud (Sideline=1629 ft, SAR=4.4, MAR=1.19, $A_{g*}=1086 \text{ in}^2$ , $M_n=0.32$ , $V_{\Pi}=357 \text{ ft/sec}$ ) .....	182
124.	Effects of Deteriorated Treatment on Noise, SPL Versus Frequency — Ideal Unsuppressed Primary Jet Velocity=2384 ft/sec, Vortical Mixer, Long Shroud (Sideline=1629 ft, SAR=4.4, MAR=1.19, $A_{g*}=1086 \text{ in}^2$ , $M_n=0.32$ , $V_{\Pi}=357 \text{ ft/sec}$ ) .....	183
125.	Noise Variation With Azimuthal Position, Vortical Mixer, Long Shroud (SAR=4.9, MAR=0.97, $A_{g*}=1086 \text{ in}^2$ , $M_n=0.32$ , $V_{\Pi}=357 \text{ ft/sec}$ ) .....	184
126.	Noise Variation With Azimuthal Position, Axial Mixer, Long Shroud (SAR=4.9, MAR=0.97, $A_{g*}=1086 \text{ in}^2$ , $M_n=0.32$ , $V_{\Pi}=357 \text{ ft/sec}$ ) .....	185
127.	Azimuthal Variation of Noise Levels, PNLT Versus Angle — Ideal Unsuppressed Primary Jet Velocity=1595 ft/sec, Vortical Mixer (Sideline=1629 ft, SAR=4.9, MAR=0.97, $A_{g*}=1086 \text{ in}^2$ , $M_n=0.32$ , $V_{\Pi}=357 \text{ ft/sec}$ ) .....	186
128.	Azimuthal Variation of Noise Levels, PNLT Versus Angle — Ideal Unsuppressed Primary Jet Velocity=2384 ft/sec, Vortical Mixer (Sideline=1629 ft, SAR=4.9, MAR=0.97, $A_{g*}=1086 \text{ in}^2$ , $M_n=0.32$ , $V_{\Pi}=357 \text{ ft/sec}$ ) .....	187
129.	Azimuthal Variation of Noise Levels, PNLT Versus Angle — Ideal Unsuppressed Primary Jet Velocity=2812 ft/sec, Vortical Mixer (Sideline=1629 ft, SAR=4.9, MAR=0.97, $A_{g*}=1086 \text{ in}^2$ , $M_n=0.32$ , $V_{\Pi}=357 \text{ ft/sec}$ ) .....	188
130.	Azimuthal Variation of Noise Levels, PNLT Versus Angle — Ideal Unsuppressed Primary Jet Velocity=1595 ft/sec, Axial Mixer (Sideline=1629 ft, SAR=4.9, MAR=0.97, $A_{g*}=1086 \text{ in}^2$ , $M_n=0.32$ , $V_{\Pi}=357 \text{ ft/sec}$ ) .....	189
131.	Azimuthal Variation of Noise Levels, PNLT Versus Angle — Ideal Unsuppressed Primary Jet Velocity=2384 ft/sec, Axial Mixer (Sideline=1629 ft, SAR=4.9, MAR=0.97, $A_{g*}=1086 \text{ in}^2$ , $M_n=0.32$ , $V_{\Pi}=357 \text{ ft/sec}$ ) .....	190
132.	Azimuthal Variation of Noise Levels, PNLT Versus Angle — Ideal Unsuppressed Primary Jet Velocity=2812 ft/sec, Axial Mixer (Sideline=1629 ft, SAR=4.9, MAR=0.97, $A_{g*}=1086 \text{ in}^2$ , $M_n=0.32$ , $V_{\Pi}=357 \text{ ft/sec}$ ) .....	191
133.	Azimuthal Variation of Noise Levels, SPL Versus Frequency — Ideal Unsuppressed Primary Jet Velocity=2384 ft/sec, Vortical Mixer, Long Treated Shroud (Sideline=1629 ft, SAR=4.9, MAR=0.97, $A_{g*}=1086 \text{ in}^2$ , $M_n=0.32$ , $V_{\Pi}=357 \text{ ft/sec}$ ) .....	192
134.	Azimuthal Variation of Noise Levels, SPL Versus Frequency — Ideal Unsuppressed Primary Jet Velocity=2384 ft/sec, Axial Mixer, Long Treated Shroud (Sideline=1629 ft, SAR=4.9, MAR=0.97, $A_{g*}=1086 \text{ in}^2$ , $M_n=0.32$ , $V_{\Pi}=357 \text{ ft/sec}$ ) .....	193



135.	Azimuthal Variation of Noise Levels, SPL Versus Frequency — Ideal Unsuppressed Primary Jet Velocity=2384 ft/sec, Vortical Mixer, Long Hardwall Shroud (Sideline=1629 ft, SAR=4.9, MAR=0.97, $A_{g*}=1086 \text{ in}^2$ , $Mn=0.32$ , $V_{fl}=357 \text{ ft/sec}$ ) .....	194
136.	Azimuthal Variation of Noise Levels, SPL Versus Frequency — Ideal Unsuppressed Primary Jet Velocity=2384 ft/sec, Axial Mixer, Long Hardwall Shroud (Sideline=1629 ft, SAR=4.9, MAR=0.97, $A_{g*}=1086 \text{ in}^2$ , $Mn=0.32$ , $V_{fl}=357 \text{ ft/sec}$ ) .....	195
137.	Effect of Shroud Length on Sideline Noise, Vortical Mixer, Hardwall Shroud (Sideline=1629 ft, SAR=4.4, MAR=1.19, $A_{g*}=1086 \text{ in}^2$ , Static).....	196
138.	Effect of Shroud Length and Treatment on Sideline Noise Vortical Mixer (Sideline=1629 ft, SAR=4.4, MAR=1.19, $A_{g*}=1086 \text{ in}^2$ , $Mn=0.32$ , $V_{fl}=357 \text{ ft/sec}$ ) .....	197
139.	Effect of Shroud Length and Treatment, PNLT vs. Angle — Ideal Unsuppressed Primary Jet Velocity=2384 ft/sec, Vortical Mixer (Sideline=1629 ft, SAR=4.4, MAR=1.19, $A_{g*}=1086 \text{ in}^2$ , $Mn=0.32$ , $V_{fl}=357 \text{ ft/sec}$ ) .....	198
140.	Effect of Shroud Length and Treatment, SPL Versus Frequency — Ideal Unsuppressed Primary Jet Velocity=2384 ft/sec, Vortical Mixer (Sideline=1629 ft, SAR=4.4, MAR=1.19, $A_{g*}=1086 \text{ in}^2$ , $Mn=0.32$ , $V_{fl}=357 \text{ ft/sec}$ ) .....	199
141.	Effect of Shroud Length on Sideline Noise, Vortical Mixer, Hardwall Shroud (Sideline=1629 ft, SAR=4.9, MAR=1.19, $A_{g*}=1086 \text{ in}^2$ , Static).....	200
142.	Effect of Shroud Length on Sideline Noise, Vortical Mixer Hardwall Shroud (Sideline=1629 ft, SAR=4.9, MAR=1.19, $A_{g*}=1086 \text{ in}^2$ , $Mn=0.32$ , $V_{fl}=357 \text{ ft/sec}$ ) .....	201
143.	Effect of Shroud Length on Sideline Noise, Axial Mixer Hardwall Shroud (Sideline=1629 ft, SAR=4.9, MAR=1.19, $A_{g*}=1086 \text{ in}^2$ , Static).....	202
144.	Effect of Shroud Length on Sideline Noise, Axial Mixer Hardwall Shroud (Sideline=1629 ft, SAR=4.9, MAR=1.19, $A_{g*}=1086 \text{ in}^2$ , $Mn=0.32$ , $V_{fl}=357 \text{ ft/sec}$ ).....	203
145.	Effect of Flight Mach Number on Sideline Noise (Sideline=1629 ft, $A_{g*}=1086 \text{ in}^2$ , $Mn=0.32$ and $0.36$ ).....	204
146.	Effect of Flight Mach Number on Sideline Noise, Baseline Round Conic Nozzle (Sideline=1629 ft, $A_{g*}=1086 \text{ in}^2$ , $Mn=0.0$ , $0.32$ , and $0.36$ ).....	205
147.	Effect of Flight Mach Number on Sideline Noise, Vortical Mixer, Long Treated Shroud (Sideline=1629 ft, SAR=4.9, MAR=1.19, $A_{g*}=1086 \text{ in}^2$ , $Mn=0.0$ , $0.32$ , and $0.36$ ) .....	206
148.	Effect of Flight Mach Number on Sideline Noise, Baseline Round Conic Nozzle, Vortical Mixer, Long Treated Shroud (Sideline=1629 ft, SAR=4.9, MAR=0.97, $A_{g*}=1086 \text{ in}^2$ , $Mn=0.0$ , $0.32$ , and $0.36$ ) .....	207
149.	Effect of Flight Mach Number on Sideline Noise, Baseline Round Conic Nozzle, Vortical Mixer, Long Hardwall Shroud (Sideline=1629 ft, SAR=4.9, MAR=0.97, $A_{g*}=1086 \text{ in}^2$ , $Mn=0.0$ , $0.32$ , and $0.36$ ) .....	208
150.	Effect of Flight Mach Number on Sideline Noise, Vortical Mixer, Long Treated Shroud (Sideline=1629 ft, SAR=4.4, MAR=0.97, $A_{g*}=1086 \text{ in}^2$ , $Mn=0.0$ , $0.32$ , and $0.36$ ) .....	209

151.	Effect of Flight Mach Number on Sideline Noise, Baseline Round Conic Nozzle, Axial Mixer, Long Treated Shroud (Sideline=1629 ft, SAR=4.9, MAR=0.97, $A_{g*}=1086 \text{ in}^2$ , Mn=0.0, 0.32, and 0.36) .....	210
152.	Effect of Flight Mach Number on Sideline Noise, PNLT Versus Angle — Ideal Unsuppressed Primary Jet Velocity=1595 ft/sec, Baseline Round Conic Nozzle, Vortical Mixer, Long Treated Shroud, (Sideline=1629 ft, SAR=4.9, MAR=0.97, $A_{g*}=1086 \text{ in}^2$ ).....	211
153.	Effect of Flight Mach Number on Sideline Noise, PNLT Versus Angle — Ideal Unsuppressed Primary Jet Velocity=2384 ft/sec, Baseline Round Conic Nozzle, Vortical Mixer, Long Treated Shroud, (Sideline=1629 ft, SAR=4.9, MAR=0.97, $A_{g*}=1086 \text{ in}^2$ ).....	212
154.	Effect of Flight Mach Number on Sideline Noise, PNLT Versus Angle — Ideal Unsuppressed Primary Jet Velocity=2812 ft/sec, Baseline Round Conic Nozzle, Vortical Mixer, Long Treated Shroud, (Sideline=1629 ft, SAR=4.9, MAR=0.97, $A_{g*}=1086 \text{ in}^2$ ).....	213
155.	Effect of Flight Mach Number on Sideline Noise, SPL Versus Frequency — Ideal Unsuppressed Primary Jet Velocity=2384 ft/sec, Baseline Round Conic Nozzle, Vortical Mixer, Long Treated Shroud, (Sideline=1629 ft, SAR=4.9, MAR=0.97, $A_{g*}=1086 \text{ in}^2$ ).....	214
156.	Effect of Flight Mach Number on Sideline Noise, PNLT Versus Angle — Ideal Unsuppressed Primary Jet Velocity=1595 ft/sec, Baseline Round Conic Nozzle, Vortical Mixer, Long Hardwall Shroud, (Sideline=1629 ft, SAR=4.9, MAR=0.97, $A_{g*}=1086 \text{ in}^2$ ).....	215
157.	Effect of Flight Mach Number on Sideline Noise, PNLT Versus Angle — Ideal Unsuppressed Primary Jet Velocity=2384 ft/sec, Baseline Round Conic Nozzle, Vortical Mixer, Long Hardwall Shroud, (Sideline=1629 ft, SAR=4.9, MAR=0.97, $A_{g*}=1086 \text{ in}^2$ ).....	216
158.	Effect of Flight Mach Number on Sideline Noise, PNLT Versus Angle — Ideal Unsuppressed Primary Jet Velocity=2812 ft/sec, Baseline Round Conic Nozzle, Vortical Mixer, Long Hardwall Shroud, (Sideline=1629 ft, SAR=4.9, MAR=0.97, $A_{g*}=1086 \text{ in}^2$ ).....	217
159.	Effect of Flight Mach Number on Sideline Noise, SPL Versus Frequency — Ideal Unsuppressed Primary Jet Velocity=2384ft/sec, Baseline Round Conic Nozzle, Vortical Mixer, Long Hardwall Shroud, (Sideline=1629 ft, SAR=4.9, MAR=0.97, $A_{g*}=1086 \text{ in}^2$ ).....	218
160.	Sideline Noise Acoustic Hysteresis, Vortical Mixer, Long Hardwall Shroud (Sideline=1629 ft, SAR=4.9, MAR=1.19, $A_{g*}=1086 \text{ in}^2$ , Static).....	219
161.	Sideline Noise Acoustic Hysteresis, Vortical Mixer, Long Hardwall Shroud (Sideline=1629 ft, SAR=4.9, MAR=1.19, $A_{g*}=1086 \text{ in}^2$ , Mn=0.32, $V_{fl}=357 \text{ ft/sec}$ ) .....	220
162.	Sideline Noise Acoustic Hysteresis, Vortical Mixer, Long Hardwall Shroud (SSideline=1629 ft, SAR=4.4, MAR=1.19, $A_{g*}=1086 \text{ in}^2$ , Static) .....	221
163.	Sideline Noise Acoustic Hysteresis, Vortical Mixer, Long Hardwall Shroud (Sideline=1629 ft, SAR=4.4, MAR=1.19, $A_{g*}=1086 \text{ in}^2$ , Mn=0.32, $V_{fl}=357 \text{ ft/sec}$ ) .....	222
164.	Sideline Noise Acoustic Hysteresis, Axial Mixer, Long Hardwall Shroud (Sideline=1629 ft, SAR=4.9, MAR=1.19, $A_{g*}=1086 \text{ in}^2$ , Static).....	223
165.	Sideline Noise Acoustic Hysteresis, Axial Mixer, Long Hardwall Shroud (Sideline=1629 ft, SAR=4.9, MAR=1.19, $A_{g*}=1086 \text{ in}^2$ , Mn=0.32, $V_{fl}=357 \text{ ft/sec}$ ) .....	224

166.	Sideline Noise Acoustic Hysteresis, Axial Mixer, Long Hardwall Shroud (Sideline=1629 ft, SAR=4.9, MAR=0.97, $A_{g*}=1086 \text{ in}^2$ , Static).....	225
167.	Sideline Noise Acoustic Hysteresis, Axial Mixer Long Hardwall Shroud (Sideline=1629 ft, SAR=4.9, MAR=0.97, $A_{g*}=1086 \text{ in}^2$ , $M_n=0.32$ , $V_{fl}=357 \text{ ft/sec}$ ) .....	226
168.	Sideline Noise Hysteresis, PNLT Versus Angle — Ideal Unsuppressed Primary Jet Velocity=2340 ft/sec, Vortical Mixer, Long Hardwall Shroud (Sideline=1629 ft, SAR=4.9, MAR=1.19, $A_{g*}=1086 \text{ in}^2$ , $M_n=0.32$ , $V_{fl}=357 \text{ ft/sec}$ ) .....	227
169.	Sideline Noise Hysteresis, PNLT Versus Angle — Ideal Unsuppressed Primary Jet Velocity=2637 ft/sec, Axial Mixer, Long Hardwall Shroud (Sideline=1629 ft, SAR=4.9, MAR=1.19, $A_{g*}=1086 \text{ in}^2$ , $M_n=0.32$ , $V_{fl}=357 \text{ ft/sec}$ ) .....	228
170.	Sideline Noise Hysteresis, PNLT Versus Angle — Ideal Unsuppressed Primary Jet Velocity=2670 ft/sec, Axial Mixer, Long Hardwall Shroud (Sideline=1629 ft, SAR=4.9, MAR=0.97, $A_{g*}=1086 \text{ in}^2$ , $M_n=0.32$ , $V_{fl}=357 \text{ ft/sec}$ ) .....	229
171.	Sideline Noise Hysteresis, SPL vs. Frequency — Ideal Unsuppressed Primary Jet Velocity=2340 ft/sec, Vortical Mixer, Long Hardwall Shroud (Sideline=1629 ft, SAR=4.9, MAR=1.19, $A_{g*}=1086 \text{ in}^2$ , $M_n=0.32$ , $V_{fl}=357 \text{ ft/sec}$ ) .....	230
172.	Sideline Noise Hysteresis, SPL vs. Frequency — Ideal Unsuppressed Primary Jet Velocity=2637 ft/sec, Axial Mixer, Long Hardwall Shroud (Sideline=1629 ft, SAR=4.9, MAR=1.19, $A_{g*}=1086 \text{ in}^2$ , $M_n=0.32$ , $V_{fl}=357 \text{ ft/sec}$ ) .....	231
173.	Sideline Noise Hysteresis, SPL vs. Frequency — Ideal Unsuppressed Primary Jet Velocity=2670 ft/sec, Axial Mixer, Long Hardwall Shroud (Sideline=1629 ft, SAR=4.9, MAR=0.97, $A_{g*}=1086 \text{ in}^2$ , $M_n=0.32$ , $V_{fl}=357 \text{ ft/sec}$ ) .....	232
174.	Sideline Noise Off the L1M Throttle Line, Baseline Round Conic Nozzle (Sideline=1629 ft, $A_{g*}=1086 \text{ in}^2$ , $M_n=0.32$ , $V_{fl}=357 \text{ ft/sec}$ ).....	233
175.	Sideline Noise Off the L1M Throttle Line, Vortical Mixer, Long Treated Shroud (Sideline=1629 ft, SAR=4.9, MAR=0.97, $A_{g*}=1086 \text{ in}^2$ , $M_n=0.32$ , $V_{fl}=357 \text{ ft/sec}$ ) .....	234
176.	Constant Primary Jet Velocity (2384 ft/sec) .....	235
177.	Constant Primary Jet Velocity (2384 ft/sec) .....	235
178.	Sideline=1629 ft, $A_{g*}=1086 \text{ in}^2$ , $M_n=0.32$ , $V_{fl}=357 \text{ ft/sec}$ .....	236
179.	Off L1M Throttle Line Results, PNLT Versus Angle — Ideal Unsuppressed Primary Jet Velocity=2384 ft/sec, Baseline Round Conic Nozzle, (Sideline=1629 ft, $A_{g*}=1086 \text{ in}^2$ , $M_n=0.32$ , $V_{fl}=357 \text{ ft/sec}$ ).....	237
180.	Off L1M Throttle Line Results, SPL Versus Frequency — Ideal Unsuppressed Primary Jet Velocity=2384 ft/sec, Baseline Round Conic Nozzle (Sideline=1629 ft, $A_{g*}=1086 \text{ in}^2$ , $M_n=0.32$ , $V_{fl}=357 \text{ ft/sec}$ ).....	238
181.	Off L1M Throttle Line Results, PNLT Versus Angle — Ideal Unsuppressed Primary Jet Velocity=2384 ft/sec, Vortical Mixer, Long Treated Shroud (Sideline=1629 ft, SAR=4.9, MAR=0.97, $A_{g*}=1086 \text{ in}^2$ , $M_n=0.32$ , $V_{fl}=357 \text{ ft/sec}$ ) .....	239

182.	Off L1M Throttle Line Results, SPL Versus Frequency — Ideal Unsuppressed Primary Jet Velocity=2384 ft/sec, Vortical Mixer, Long Treated Shroud (Sideline=1629 ft, SAR=4.9, MAR=0.97, $A_{g*}=1086 \text{ in}^2$ , $M_n=0.32$ , $V_{fl}=357 \text{ ft/sec}$ ) .....	240
183.	Constant Primary Jet Velocity (2520 ft/sec) .....	241
184.	Constant Primary Jet Velocity (2520 ft/sec) .....	241
185.	Sideline 1629 ft, $A_{g*}=1086 \text{ in}^2$ , $V_{fl}=357 \text{ ft/sec}$ .....	242
186.	Off L1M Throttle Line Results, PNLT Versus Angle — Ideal Unsuppressed Primary Jet Velocity=2520 ft/sec, Baseline Round Conic Nozzle (Sideline=1629 ft, $A_{g*}=1086 \text{ in}^2$ , $M_n=0.32$ , $V_{fl}=357 \text{ ft/sec}$ ).....	243
187.	Off L1M Throttle Line Results, SPL vs. Frequency — Ideal Unsuppressed Primary Jet Velocity=2520 ft/sec, Baseline Round Conic Nozzle (Sideline=1629 ft, $A_{g*}=1086 \text{ in}^2$ , $M_n=0.32$ , $V_{fl}=357 \text{ ft/sec}$ ).....	244
188.	Off L1M Throttle Line Results, PNLT Versus. Angle — Ideal Unsuppressed Primary Jet Velocity=2520 ft/sec, Vortical Mixer, Long Treated Shroud (Sideline=1629 ft, SAR=4.9, MAR=0.97, $A_{g*}=1086 \text{ in}^2$ , $M_n=0.32$ , $V_{fl}=357 \text{ ft/sec}$ ) .....	245
189.	Off L1M Throttle Line Results, SPL vs. Frequency — Ideal Unsuppressed Primary Jet Velocity=2520 ft/sec, Vortical Mixer, Long Treated Shroud (Sideline=1629 ft, SAR=4.9, MAR=0.97, $A_{g*}=1086 \text{ in}^2$ , $M_n=0.32$ , $V_{fl}=357 \text{ ft/sec}$ ) .....	246
190.	Constant Turbine Exit Total Temperature ( $T_{t8}=1590^\circ\text{R}$ ) .....	247
191.	Constant Turbine Exit Total Temperature ( $T_{t8}=1590^\circ\text{R}$ ) .....	248
192.	Sideline 1629 ft, $A_{g*}=1086 \text{ in}^2$ , $V_{fl}=357 \text{ ft/sec}$ .....	249
193.	Off L1M Throttle Line Results, PNLT Versus Angle — $T_{t8}=1590^\circ\text{R}$ , Baseline Round Conic Nozzle (Sideline=1629 ft, $A_{g*}=1086 \text{ in}^2$ , $M_n=0.32$ , $V_{fl}=357 \text{ ft/sec}$ ).....	250
194.	Off L1M Throttle Line Results, SPL vs. Frequency — $T_{t8}=1590^\circ\text{R}$ , Baseline Round Conic Nozzle (Sideline=1629 ft, $A_{g*}=1086 \text{ in}^2$ , $M_n=0.32$ , $V_{fl}=357 \text{ ft/sec}$ ).....	251
195.	Off L1M Throttle Line Results, PNLT vs. Angle — $T_{t8}=1590^\circ\text{R}$ , Vortical Mixer, Long Treated Shroud (Sideline=1629 ft, SAR=4.9, MAR=0.97, $A_{g*}=1086 \text{ in}^2$ , $M_n=0.32$ , $V_{fl}=357 \text{ ft/sec}$ ) .....	252
196.	Off L1M Throttle Line Results, SPL vs. Frequency — $T_{t8}=1590^\circ\text{R}$ , Vortical Mixer, Long Treated Shroud (Sideline=1629 ft, SAR=4.9, MAR=0.97, $A_{g*}=1086 \text{ in}^2$ , $M_n=0.32$ , $V_{fl}=357 \text{ ft/sec}$ ) .....	253
197.	Constant Primary Nozzle Pressure Ratio (NPR=3.0) .....	254
198.	Constant Primary Nozzle Pressure Ratio (NPR=3.0) .....	254
199.	Sideline 1629 ft, $A_{g*}=1086 \text{ in}^2$ , $V_{fl}=357 \text{ ft/sec}$ .....	255

200.	Off L1M Throttle Line Results, PNLT Versus Angle — NPR=3.0 Baseline Round Conic Nozzle (Sideline=1629 ft, $A_{g*}=1086 \text{ in}^2$ , $M_n=0.32$ , $V_{ff}=357 \text{ ft/sec}$ ).....	256
201.	Off L1M Throttle Line Results, SPL vs. Frequency — NPR=3.0 Baseline Round Conic Nozzle (Sideline=1629 ft, $A_{g*}=1086 \text{ in}^2$ , $M_n=0.32$ , $V_{ff}=357 \text{ ft/sec}$ ).....	257
202.	Off L1M Throttle Line Results, PNLT vs. Angle — NPR=3.0 Vortical Mixer, Long Treated Shroud (Sideline=1629 ft, SAR=4.9, MAR=0.97, $A_{g*}=1086 \text{ in}^2$ , $M_n=0.32$ , $V_{ff}=357 \text{ ft/sec}$ ) .....	258
203.	Off L1M Throttle Line Results, SPL vs. Frequency — NPR=3.0 Vortical Mixer, Long Treated Shroud (Sideline=1629 ft, SAR=4.9, MAR=0.97, $A_{g*}=1086 \text{ in}^2$ , $M_n=0.32$ , $V_{ff}=357 \text{ ft/sec}$ ) .....	259
204.	GEAE Cell 41 Test Results Support Concerns, About NASA-LeRC 9 x 15 Data (Community, Sideline=1629 ft, $A_{g*}=1086 \text{ in}^2$ , $M_n=0.32$ , $V_{ff}=406.4 \text{ ft/sec}$ ).....	260
205.	Comparison of NASA-LeRc 9x15 and GEAE Cell 41, PNL Versus Polar Angle — Ideal Unsuppressed Primary Jet Velocity=2518 ft/sec, Baseline Round Conic Nozzle (Sideline=1629 ft, NPR=3.5, $T_{t8}=1735^\circ\text{R}$ , $A_{g*}=1086 \text{ in}^2$ , $M_n=0.20$ ).....	261
206.	Comparison of NASA-LeRc 9x15 and GEAE Cell 41, SPL Versus Frequency — Ideal Unsuppressed Primary Jet Velocity=2518 ft/sec, Baseline Round Conic Nozzle (Sideline=1629 ft, NPR=3.5, $T_{t8}=1735^\circ\text{R}$ , $A_{g*}=1086 \text{ in}^2$ , $M_n=0.20$ ).....	262
207.	Comparison of NASA-LeRc 9x15 and GEAE Cell 41, PNL Versus Polar. Angle — Ideal Unsuppressed Primary Jet Velocity=2518 ft/sec, Vortical Mixer, Fully Treated Long Shroud (Overhead at 1629 ft, SAR=4.9, MAR=1.19, $A_{g*}=1086 \text{ in}^2$ , $M_n=0.20$ , NPR=3.5, $T_{t8}=1735^\circ\text{R}$ ) .....	263
208.	Comparison of NASA-LeRc 9x15 and GEAE Cell 41, SPL Versus Frequency — Ideal Unsuppressed Primary Jet Velocity=2518 ft/sec, Vortical Mixer, Fully Treated Long Shroud (Overhead at 1629 ft, SAR=4.9, MAR=1.19, $A_{g*}=1086 \text{ in}^2$ , $M_n=0.20$ , NPR=3.5, $T_{t8}=1735^\circ\text{R}$ ) .....	264
209.	Comparison of NASA-LeRc 9x15 and GEAE Cell 41, PNL Versus Polar. Angle — Ideal Unsuppressed Primary Jet Velocity=2518 ft/sec, Vortical Mixer, Hardwall Long Shroud (Overhead at 1629 ft, NPR=3.5, $T_{t8}=1735^\circ\text{R}$ , $A_{g*}=1086 \text{ in}^2$ , $M_n=0.20$ , SAR=4.9, MAR=1.19) .....	265
210.	Comparison of NASA-LeRc 9x15 and GEAE Cell 41, SPL Versus. Frequency — Ideal Unsuppressed Primary Jet Velocity=2518 ft/sec, Vortical Mixer, Hardwall Long Shroud (Overhead at 1629 ft, SAR=4.9, MAR=1.19, $A_{g*}=1086 \text{ in}^2$ , $M_n=0.20$ , NPR=3.5, $T_{t8}=1735^\circ\text{R}$ ) .....	266
211.	(a) Typical Static Pressure Distribution on the Internal Surface of the Ejector Shroud at Different Increasing and Decreasing NPR for a Vortical Mixer With Long Hardwall Shroud; (b) Typical Hysteresis Cycle.....	267
212.	Static Pressure Instrumentation for P&W Two-Dimensional Hardwall Shrouds.....	268
213.	Axial Static Pressure Distribution on Shroud Surface for a Vortical Mixer-Ejector Configuration: SAR=4.4, MAR=1.18, Shroud Length=18.85 in. ....	269
214.	Effect of Increasing and Decreasing NPR on Axial Static Pressure Distribution on Shroud Surface for a Vortical Mixer-Ejector Configuration at Static Condition: SAR=4.4, MAR=1.18, Shroud Length=18.85 in., $T_t=\text{Ambient}$ .....	270

215.	Effect of Increasing and Decreasing NPR on Axial Static Pressure Distribution on Shroud Surface for a Vortical Mixer-Ejector Configuration at Static Condition: SAR=4.4, MAR=1.18, Shroud Length=18.85 in., LIM Cycle.....	271
216.	Effect of Increasing and Decreasing NPR on Axial Static Pressure Distribution on Shroud Surface for a Vortical Mixer-Ejector Configuration With Flight Simulation ( $Mn=0.32$ ): SAR=4.4, MAR=1.18, Shroud Length=18.85 in., LIM Cycle.....	272
217.	Variation of Normalized Shroud Force Due to: (a) Nozzle Total Temperature; (b) Flight Simulation ( $Mn=0.32$ ) for a Vortical Mixer-Ejector Configuration: SAR=4.4, MAR=1.18, Shroud Length=18.85 in. ....	273
218.	Effect of MAR on Axial Static Pressure Distribution on Shroud Surface for Vortical Mixer-Ejector Configurations at Static Condition: SAR=4.4, Shroud Length=18.85 in., $T_t$ =Ambient.....	274
219.	Effect of MAR on Axial Static Pressure Distribution on Shroud Surface for Vortical Mixer-Ejector Configurations at Static Conditions: SAR=4.4, Shroud Length=18.85 in., LIM Cycle.....	275
220.	Effect of MAR on Axial Static Pressure Distribution on Shroud Surface for Vortical Mixer-Ejector Configurations With Flight Simulation ( $Mn=0.32$ ): SAR=4.4, Shroud Length=18.85 in., LIM Cycle.....	276
221.	Effect of Flight on Axial Static Pressure Distribution on Shroud Surface for Vortical Mixer-Ejector Configurations on Different MAR: SAR=4.4, Shroud Length=18.85 in., NPR=3.4, $T_t=1645^\circ R$ .....	277
222.	Effect of Increasing and Decreasing NPR on Axial Static Pressure Distribution on Shroud Surface for a Vortical Mixer-Ejector Configuration at Static Condition: SAR=4.4, MAR=0.97, Shroud Length=18.85 in., $T_t$ =Ambient .....	278
223.	Effect of Increasing and Decreasing NPR on Axial Static Pressure Distribution on Shroud Surface for a Vortical Mixer-Ejector Configuration at Static Condition: SAR=4.4, MAR=0.97, Shroud Length=18.85 in., $T_t$ =Ambient .....	279
224.	Variation of Normalized Shroud Force Due to MAR for Vortical Mixer-Ejector Configurations .....	280
225.	Axial Static Pressure Distribution on Shroud Surface for a Vortical Mixer-Ejector Configuration: SAR=4.9, MAR=1.18, Shroud Length=18.85 in. ....	281
226.	Axial Static Pressure Distribution on Shroud Surface for a Vortical Mixer-Ejector Configuration: SAR=4.9, MAR=0.97, Shroud Length=18.85 in. ....	282
227.	Effect of Flight on Axial Static Pressure Distribution on Shroud Surface for Vortical Mixer-Ejector Configurations of Different MAR: SAR=4.9, Shroud Length=18.85 in., NPR=3.4, $T_t=1645^\circ R$ .....	283
228.	Effect of Increasing and Decreasing NPR on Axial Static Pressure Distribution on Shroud Surface for a Vortical Mixer-Ejector Configuration at Static Condition: SAR=4.9, MAR=0.97, Shroud Length=18.85 in., $T_t$ =Ambient .....	284
229.	Variation of Normalized Shroud Force Due to MAR for Vortical Mixer-Ejector Configurations: SAR=4.9, Shroud Length=18.85 in. ....	285
230.	Variation of Normalized Shroud Force Due to SAR for Vortical Mixer-Ejector Configurations: MAR=1.18, Shroud Length=18.85 in. ....	286
231.	Variation of Normalized Shroud Force Due to SAR for Vortical Mixer-Ejector Configurations: MAR=0.97, Shroud Length=18.85 in. ....	287

232.	Axial Static Pressure Distribution on Shroud Surface for a Vortical Mixer-Ejector Configuration: SAR=4.9, MAR=1.18, Shroud Length=10.46 in. ....	288
233.	Axial Static Pressure Distribution on Shroud Surface for a Vortical Mixer-Ejector Configuration: SAR=4.9, MAR=1.18, Shroud Length=10.46 in. ....	289
234.	Axial Static Pressure Distribution on Shroud Surface for Vortical Mixer-Ejector Configuration: SAR=4.4, MAR=1.18, Shroud Length=10.46 in. ....	290
235.	Axial Static Pressure Distribution on Shroud Surface for Vortical Mixer-Ejector Configuration: SAR=4.4, MAR=1.18, Shroud Length=10.46 in. ....	291
236.	Effect of Flight on Axial Static Pressure Distribution on Shroud Surface for Vortical Mixer-Ejector Configurations of Different SAR: MAR=1.18, Shroud Length=10.46 in., NPR=3.4, $T_t=1645^\circ\text{R}$ .....	292
237.	Variation of Normalized Shroud Force Due to: (a) Nozzle Total Temperature; (b) Flight Simulation ( $M_n=0.32$ ) for Vortical Mixer-Ejector Configuration: SAR=4.4, MAR=1.18, Shroud Length=10.46in. ....	293
238.	Variation of Normalized Shroud Force Due to Shroud Length for Vortical Mixer-Ejector Configurations: SAR=4.4, MAR=1.18.....	294
239.	Normalized Shroud Force and Corresponding EPNL as Functions of Jet Velocity for Vortical Mixer-Ejector Configuration: SAR=4.4, MAR=1.18, Shroud Length=18.85 in.....	295
240.	Normalized Shroud Force and Corresponding EPNL as Functions of Jet Velocity for Vortical Mixer-Ejector Configurations With Different MAR Settings at Ambient Temperature Condition: SAR=4.4, Shroud Length=18.85 in. ....	296
241.	PNLT at Various Polar Angles and Peak PNL T as Functions of Jet Velocity for Vortical Mixer-Ejector Configuration at Ambient Temperature Condition: SAR=4.4, MAR=0.97, Shroud Length=18.85 in. ....	297
242.	PNLT Directivities at Two NPRs at Ambient Temperature Condition for Vortical Mixer-Ejector Configuration: SAR=4.4, MAR=0.97, Shroud Length=18.85 in. ....	298
243.	SPL Spectra at a Number of Polar Angles for NPR=4.3 and at Ambient Temperature Condition ( $V_j=1498$ ft/sec) for Vortical Mixer-Ejector Configuration: SAR=4.4, MAR=0.97, Shroud Length=18.85 in. ....	299
244.	SPL Spectra At a Number of Polar Angles for NPR=4.4 and At Ambient Temperature condition ( $V_j=1508$ ft/sec) For A Vortical Mixer-Ejector Configuration: SAR=4.4, MAR=0.97, Shroud Length=18.85 in. ...	300
245.	Axial Static Pressure Distribution on Shroud Surface For Axial Mixer-Ejector Configuration: SAR=4.9, MAR=1.18, Shroud Length=18.85 in. ....	301
246.	Axial Static Pressure Distribution on Shroud Surface For Axial Mixer-Ejector Configuration For LIM Cycle Condition: SAR=4.9, MAR=1.18, Shroud Length=18.85 in. ....	302
247.	Effect of Flight on Axial Static Pressure Distribution on Shroud Surface for Axial Mixer-Ejector Configuration: MAR=1.18, SAR=4.9, Shroud Length=18.85 in.....	303
248.	Effect of Increasing and Decreasing NPR on Axial Static Pressure Distribution on Shroud Surface For Axial Mixer-Ejector Configuration: NPR=4.0, SAR=4.9, MAR=1.18, Shroud Length=18.85 in. ....	304

249.	Variation of Normalized Shroud Force Due to: (a) Nozzle Total Temperature; (b) Flight Simulation (Mn=0.32) For Axial Mixer-Ejector Configuration: SAR=4.9, MAR=1.18, Shroud Length=18.85 in. ....	305
250.	Effect of MAR on Axial Static Pressure Distribution on Shroud Surface for Axial Mixer-Ejector Configurations at Static Condition: SAR=4.9, Shroud Length=18.85 in., $T_t$ =Ambient.....	306
251.	Effect of MAR on Axial Static Pressure Distribution on Shroud Surface for Axial Mixer-Ejector Configurations at Static Condition” SAR=4.9, Shroud Length=18.85 in., $T_t$ =400°F .....	307
252.	Effect of MAR on Axial Static Pressure Distribution on Shroud Surface for Axial Mixer-Ejector Configurations at Static Condition: SAR=4.9, Shroud Length=18.85 in., LIM Cycle .....	308
253.	Effect of MAR on Axial Static Pressure Distribution on Shroud Surface For Axial Mixer-Ejector Configurations with Flight Simulation (Mn=0.32): SAR=4.9, Shroud Length=18.85 in., LIM Cycle .....	309
254.	Effect of MAR on Axial Static Pressure Distribution on Shroud Surface for Axial Mixer-Ejector Configurations at Static Condition: SAR=4.9, Shroud Length=18.85 in., $T_t$ =Ambient.....	310
255.	Effect of MAR on Axial Static Pressure Distribution on Shroud Surface for Axial Mixer-Ejector Configurations at Static Conditions: SAR=4.9, Shroud Length=18.85 in., $T_t$ =400°F .....	311
256.	Effect of MAR on Axial Static Pressure Distribution on Shroud Surface for Axial Mixer-Ejector Configurations at Static Condition: SAR=4.9, Shroud Length=18.85 in., LIM Cycle .....	312
257.	Effect of MAR on Axial Static Pressure Distribution on Shroud Surface for Axial Mixer-Ejector Configurations With Flight Simulation (Mn=0.32): SAR=4.9, Shroud Length=18.85 in., LIM Cycle.....	313
258.	Effect of MAR on Normalized Shroud Force for Axial Mixer-Ejector Configurations: SAR=4.9, Shroud Length=18.85 in. ....	314
259.	Effect of Ejector MAR on Normalized Shroud Force For Axial Mixer-Ejector Configurations for LIM Cycle Condition: SAR=4.9, Shroud Length=18.85 in. ....	315
260.	Effect of Increasing and Decreasing NPR on Axial Static Pressure Distribution on Shroud Surface for Axial Mixer-Ejector Configuration at Static Condition: SAR=4.9, MAR=0.97, Shroud Length=18.85 in., $T_t$ =400°F.....	316
261.	Effect of Increasing and Decreasing NPR on Axial Static Pressure Distribution on Shroud Surface for Axial Mixer-Ejector Configuration at Static Condition: SAR=4.9, MAR=0.97, Shroud Length=18.85 in., LIM Cycle.....	317
262.	Effect of Increasing and Decreasing NPR on Axial Static Pressure Distribution on Shroud Surface for Axial Mixer-Ejector Configuration at Static Condition: SAR=4.9, MAR=0.88, Shroud Length=18.85 in., $T_t$ =400°F .....	318
263.	Effect of Increasing and Decreasing NPR on Axial Static Pressure Distribution on Shroud Surface for Axial Mixer-Ejector Configuration at Static Condition: SAR=4.9, MAR=0.88, Shroud Length=18.85 in., $T_t$ =400°F .....	319
264.	Effect of Hysteresis on Farfield Noise Characteristics of Axial Mixer-Ejector Nozzle at Static Condition: SAR=4.9, MAR=0.97, Shroud Length=18.85 in., Side Line=1629 ft., A8=1086 in <sup>2</sup> .....	320



265.	Normalized Shroud Force and Corresponding EPNL, Peak PNLT, and PNLT at Various Polar Angles as Functions of NPR for Axial Mixer-Ejector Configuration at 400°F SAR=4.9, MAR=0.88, Shroud Length=18.85 in. ....	321
266.	PNLT Directivities at Various NPRs at 400°F for Axial Mixer-Ejector Configuration: SAR=4.9, MAR=0.88, Shroud Length=18.85 in. ....	322
267.	SPL Spectra at a Number of Polar Angles for NPR=5.0 and 400°F for Axial Mixer-Ejector Configuration: SAR=4.9, MAR=0.88, Shroud Length=18.85 in. ....	323
268.	SPL Spectra at a Number of Polar Angles for NPR=5.2 and 400°F for Axial Mixer-Ejector Configuration: SAR=4.9, MAR=0.88, Shroud Length=18.85 in. ....	324
269.	SPL Spectra at a Number of Polar Angles for NPR=5.3 and 400°F for Axial Mixer-Ejector Configuration: SAR=4.9, MAR=0.88, Shroud Length=18.85 in. ....	325
270.	SPL Spectra at a Number of Polar Angles for NPR=5.4 and 400°F for Axial Mixer-Ejector Configuration: SAR=4.9, MAR=0.88, Shroud Length=18.85 in. ....	326
271.	MAR is Key Determinant of NPR <sub>cr</sub> Where Mode Switch Occurs.....	327
272.	Laser Doppler Velocimetry System With Axial Mixer-Ejector Nozzle Configuration With Short Hardwall Shroud and Glass Windows on Sidewall --- Mounted in Anechoic Chamber.....	328
273.	Laser Doppler Velocimetry Traverse Locations for External Plume Survey for P&W Mixer-Ejector Nozzles.....	329
274.	An Isometric View of an Axial Mixer-Ejector Nozzle Configuration.....	330
275.	Comparison of Running Average Axial Velocity Components ( $V_x$ ) With Those Obtained From 2000 Data Points and the Axial Components of Turbulence Intensity ( $TI_x$ ) in the External Plume of the Axial Mixer-Ejector Nozzle With Long Hardwall Shroud.....	331
276.	Axial and Vertical Velocity Distribution Close to Ejector Exit Planes of the Axial Mixer-Ejector Nozzle With Short Hardwall Shroud: SAR=4.9, MAR=1.18, $L_{EJ}$ =10.46 in., $X$ =0.65 in., $Mn$ =0.32, NPR=3.5, $T_t$ =1735°R, $V_j$ =2518 ft/sec. ....	332
277.	Axial Velocity Distributions at Various Locations Downstream From the Ejector Exit Plane of the Axial Mixer-Ejector Nozzle With Short Hardwall Shroud: SAR=4.9, MAR=1.18, $L_{EJ}$ =10.46 in., $Mn$ =0.32, NPR=3.5, $T_t$ =1735°R, $V_j$ =2518 ft/sec. ....	333
278.	Comparison of Axial Velocity Distributions Between Spanwise (Z) and Vertical (Y) Directions at Various Axial Locations Downstream From the Ejector Exit Plane of Axial Mixer-Ejector Nozzles with Hardwall Shroud: SAR=4.9, MAR=1.18, $Mn$ =0.32, NPR=3.5, $T_t$ =1735°R, $V_j$ =2518 ft/sec, (a) $L_{EJ}$ =10.46 in., (b) $L_{EJ}$ =18.85 in. ....	334
279.	Axial Velocity Distributions Along the Chute Height at Hot and Cold Flow Regions Close to the Ejector Exit Plane of the Axial Mixer-Ejector Nozzle With Short Hardwall Shroud: SAR=4.9, MAR=1.18, $L_{EJ}$ =10.46 in., $X$ =0.65 in., $Mn$ =0.32.....	335
280.	Effect of Nozzle Pressure Ratio on Axial Velocity and Turbulence Intensity Distributions Close to the Ejector Exit Plane of the Axial Mixer-Ejector Nozzle With Short Hardwall Shroud: SAR=4.9, MAR=1.18, $L_{EJ}$ =10.46 in., $X$ =0.65 in., $Mn$ =0.32.....	336

281.	Comparison of Axial Velocity Distributions Between $NPR=2.5$ , $T_t=1325^\circ R$ , $V_j=1919$ ft/sec, and $NPR=3.5$ , $T_t=1735^\circ R$ , $V_j=2518$ ft/sec at Various Axial Locations Downstream From the Ejector Exit Plane of Axial Mixer-Ejector Nozzles With Hardwall Shroud: $SAR=4.9$ , $MAR=1.18$ , $L_{EJ}=10.46$ in., $Mn=0.32$ .....	337
282.	Effect of Nozzle Pressure Ratio on Axial Velocity and Turbulence Intensity Distribution Along X-Direction in External Plume of Axial Mixer-Ejector Nozzle With Short Hardwall Shroud: $SAR=4.9$ , $MAR=1.18$ , $L_{EJ}=10.46$ in., $Y=Z=0$ , $Mn=0.32$ .....	338
283.	Effect of Nozzle Pressure Ratio on Axial Velocity and Turbulence Intensity Distribution in External Plume of Axial Mixer-Ejector Nozzle With Long Hardwall Shroud: $SAR=4.9$ , $MAR=1.18$ , $L_{EJ}=18.85$ in., $Mn=0.32$ .....	339
284.	Comparison of Axial Velocity Distributions Between $NPR=2.5$ , $T_t=1325^\circ R$ , $V_j=1919$ ft/sec, and $NPR=3.5$ , $T_t=1735^\circ R$ , $V_j=2518$ ft/sec at Various Axial Locations Downstream From Ejector Exit Plane of Axial Mixer-Ejector Nozzles With Hardwall Shroud: $SAR=4.9$ , $MAR=1.18$ , $L_{EJ}=18.85$ in., $Mn=0.32$ .....	340
285.	Effect of Shroud Length on Axial Velocity and Turbulence Intensity Distributions Close to Exit Plane of Hardwall Axial Mixer-Ejector Nozzle: $SAR=4.9$ , $MAR=1.18$ , $X=0.65$ , $Y=0$ , $Mn=0.32$ .....	341
286.	Comparison of Axial Velocity Distributions Between Short and Long Hardwall Shrouds at Various Axial Locations Downstream From Ejector Exit Plane of Axial Mixer-Ejector Nozzles: $SAR=4.9$ , $MAR=1.18$ , $Mn=0.32$ , $NPR=3.5$ , $T_t=1735^\circ R$ , $V_j=2518$ ft/sec .....	342
287.	Effect of Shroud Length on Axial Velocity and Turbulence Intensity Distributions Along X-Direction in External Plume of Hardwall Axial Mixer-Ejector Nozzle: $SAR=4.9$ , $MAR=1.18$ , $Y=Z=0$ , $Mn=0.32$ , $NPR=3.5$ , $T_t=1735^\circ R$ , $V_j=2518$ ft/sec .....	343
288.	Effect of Flight on Axial Velocity and Turbulence Intensity Distributions Along X-Direction in External Plume of Axial Mixer-Ejector Nozzle With Long Hardwall Shroud: $SAR=4.9$ , $MAR=1.18$ , $L_{EJ}=18.85$ in., $Y=Z=0$ , $NPR=3.5$ , $T_t=1735^\circ R$ , $V_j=2518$ ft/sec .....	344
289.	Effect of Flight on Axial Velocity Distribution Close to Exit Plane of Axial Mixer-Ejector Nozzle With Long Hardwall Shroud: $SAR=4.9$ , $MAR=1.18$ , $L_{EJ}=18.85$ in., $X=0.65$ in., $NPR=3.5$ , $T_t=1735^\circ R$ , $V_j=2518$ ft/sec .....	345
290.	Effect of Flight on Axial Velocity Distribution At One Ejector Width ( $X=W=6.8$ in.) Downstream of Exit Plane of Axial Mixer-Ejector Nozzle With Long Hardwall Shroud: $SAR=4.9$ , $MAR=1.18$ , $L_{EJ}=18.85$ in., $NPR=3.5$ , $T_t=1735^\circ R$ , $V_j=2518$ ft/sec .....	346
291.	Comparison of Axial Velocity Distributions Between With/Without Flight Simulation at Various Axial Locations Downstream From Ejector Exit Plane of Axial Mixer-Ejector Nozzles With Hardwall Shroud: $SAR=4.9$ , $MAR=1.18$ , $L_{EJ}=18.85$ in., $NPR=3.5$ , $T_t=1735^\circ R$ , $V_j=2518$ ft/sec .....	347
292.	An Isometric View of Vortical Mixer-Ejector Nozzle Configuration, Showing Axial (X), Vertical (Y), and Spanwise (Z) LDV Traverse Locations for External Plume Survey .....	348
293.	Axial Velocity Distributions Along Chute Height At Hot and Cold Flow Regions Close to Ejector Exit Plane of Vortical Mixer-Ejector Nozzle With Hardwall Shroud: $SAR=4.9$ , $MAR=1.18$ , $X=0.65$ in., $Mn=0.32$ , $NPR=3.5$ , $T_t=1735^\circ R$ , $V_j=2518$ ft/sec .....	349
294.	Comparison of Axial Velocity Distributions Between Spanwise (Z) and Vertical (Y) Directions at Various Axial Locations Downstream From Ejector Exit Plane of Vortical Mixer-Ejector Nozzles With Hardwall Shroud ( $SAR=4.9$ , $MAR=1.18$ , $Mn=0.32$ , $NPR=3.5$ , $T_t=1735^\circ R$ , $V_j=2518$ ft/sec) (a) $L_{EJ}=10.46$ in. (b) $L_{EJ}=18.85$ in. ....	350

295.	Effect of Nozzle Pressure Ratio on Axial Velocity Distributions Along Y-Direction in External Plume of Vortical Mixer-Ejector Nozzle With Hardwall Shroud (SAR=4.9, MAR=1.18, Z=0, Mn=0.32).....	351
296.	Effect of Nozzle Pressure Ratio on Axial Velocity Distributions Along Z-Direction in External Plume of Vortical Mixer-Ejector Nozzle With Hardwall Shroud (SAR=4.9, MAR=1.18, Y=0, Mn=0.32) .....	352
297.	Comparison of Axial Velocity Distribution Between NPR=2.5, $T_t=1325^\circ\text{R}$ , $V_j=1919$ ft/sec, and NPR=3.5, $T_t=1735^\circ\text{R}$ , $V_j=2518$ ft/sec at Various Axial Locations Downstream From Ejector Exit Plane of Vortical Mixer-Ejector Nozzles With Hardwall Shroud: SAR=4.9, MAR=1.18, $L_{EJ}=10.46$ in., Mn=0.32 .....	353
298.	Comparison of Axial Velocity Distribution Between NPR=2.5, $T_t=1325^\circ\text{R}$ , $V_j=1919$ ft/sec, and NPR=3.5, $T_t=1735^\circ\text{R}$ , $V_j=2518$ ft/sec at Various Axial Locations Downstream From Ejector Exit Plane of Vortical Mixer-Ejector Nozzles With Hardwall Shroud: SAR=4.9, MAR=1.18, $L_{EJ}=10.46$ in., Mn=0.32 .....	354
299.	Comparison of Axial Velocity Distribution Between NPR=2.5, $T_t=1325^\circ\text{R}$ , $V_j=1919$ ft/sec, and NPR=3.5, $T_t=1735^\circ\text{R}$ , $V_j=2518$ ft/sec at Various Axial Locations Downstream From Ejector Exit Plane of Vortical Mixer-Ejector Nozzles With Hardwall Shroud (SAR=4.9, MAR=1.18, $L_{EJ}=18.85$ in., Mn=0.32).....	355
300.	Effect of Nozzle Pressure Ratio on Axial Turbulence Intensity Distributions Along Vertical (Y), Spanwise (Z), and Axial (X) Directions in External Plume of Vortical Mixer-Ejector Nozzle With Hardwall Shroud (SAR=4.9, MAR=1.18, Mn=0.32).....	356
301.	Effect of Shroud Length on Axial Velocity Distribution in External Plume of Hardwall Vortical Mixer-Ejector Nozzle: SAR=4.9, MAR=1.18, Mn=0.32, NPR=3.5, $T_t=1735^\circ\text{R}$ , $V_j=2518$ ft/sec.....	357
302.	Comparison of Axial Velocity Distributions Between Short and Long Hardwall Shrouds at Various Locations Downstream From Ejector Exit Plane of Vortical Mixer-Ejector Nozzles (SAR=4.9, MAR=1.18, Mn=0.32, NPR=3.5, $T_t=1735^\circ\text{R}$ , $V_j=2518$ ft/sec).....	358
303.	Effect of Flight on Axial Velocity Distribution in External Plume of Vortical Mixer-Ejector Nozzle With Short Hardwall Shroud (SAR=4.9, MAR=1.18, Mn=0.32, $L_{EJ}=10.46$ in., NPR=3.5, $T_t=1735^\circ\text{R}$ , $V_j=2518$ ft/sec) .....	359
304.	Comparison of Axial Velocity Distributions Between With/Without Flight Simulation at Various Axial Locations Downstream From Ejector Exit Plane of Vortical Mixer-Ejector Nozzles With Hardwall Shroud: SAR=4.9, MAR=1.18, $L_{EJ}=10.46$ in., NPR=3.5, $T_t=1735^\circ\text{R}$ , $V_j=2518$ ft/sec.....	360
305.	Effect of Flight on Axial Velocity Distribution in External Plume of Vortical Mixer-Ejector Nozzle With Long Hardwall Shroud: SAR=4.9, MAR=1.18, $L_{EJ}=18.85$ in., NPR=3.5, $T_t=1735^\circ\text{R}$ , $V_j=2518$ ft/sec...361	
306.	Comparison of Axial Velocity Distributions Between With/Without Flight Simulation at Various Axial Locations Downstream From Ejector Exit Plane of Vortical Mixer-Ejector Nozzles With Hardwall Shroud: SAR=4.9, MAR=1.18, $L_{EJ}=18.85$ in., NPR=3.5, $T_t=1735^\circ\text{R}$ , $V_j=2518$ ft/sec.....	362
307.	Effect of (a) Shroud Length, and (b) Flight Simulation on Axial Turbulence Intensity Distributions along X-Direction in external plume of Vortical Mixer-Ejector Nozzle with Hardwall Shroud: SAR=4.9, MAR=1.18, Y=Z=0, NPR=3.5, $T_t=1735^\circ\text{R}$ , $V_j=2518$ ft/sec.....	363
308.	Effect of Acoustic Treatment on Axial Velocity Distributions Along Vertical (Y) and Spanwise (Z) Directions at Three Axial (X) Locations Downstream From Ejector Exit Plane of Vortical Mixer-Ejector Nozzle With Long Shroud.....	364
309.	Effect of Acoustic Treatment on Axial Velocity Distributions along Vertical (Y) and Spanwise (Z) Directions At Two Axial (X) Locations Downstream From Ejector Exit Plane of Vortical mixer-Ejector Nozzle With Long Shroud.....	365

310.	Effect of Acoustic Treatment on Axial Velocity Distributions Along Vertical (Y) Directions at Center of Hot ( $Z=0.85$ in.) and Cold ( $Z=0$ in.) Chute Flow Regions Close to Ejector Exit Plane of Vortical Mixer-Ejector Nozzle With Long Shroud.....	366
311.	Effect of Acoustic Treatment on Axial Velocity Distributions Along Spanwise (Z) Direction at Four Vertical (Y) Locations Close to Ejector Exit Plane ( $X=0.65$ in.) of Vortical Mixer-Ejector Nozzle With Long Shroud .....	367
312.	Effect of Flight on Axial Static Pressure Distribution on Internal Shroud Surface For Vortical Mixer-Ejector Nozzle With Long Hardwall Shroud.....	368
313.	Effect of Mixer Design on Axial Velocity Distribution in External Plume of Hardwall Vortical Mixer-Ejector Nozzle: SAR=4.9, MAR=1.18, $L_{EJ}=10.46$ in., $Mn=0.32$ , NPR=3.5, $T_t=1735^\circ R$ , $V_j=2518$ ft/sec.....	369
314.	Comparison of Axial Velocity Distributions Between Axial and Vortical Mixer Designs With Hardwall Shroud at Various Axial Locations Downstream From Ejector Exit Plane: SAR=4.9, MAR=1.18, $L_{EJ}=10.46$ in., $Mn=0.32$ , NPR=3.5, $T_t=1735^\circ R$ , $V_j=2518$ ft/sec.....	370
315.	Comparison of Axial Velocity Distributions Between Axial and Vortical Mixer Designs With Hardwall Shroud at Various Axial Locations Downstream From Ejector Exit Plane: SAR=4.9, MAR=1.18, $L_{EJ}=10.46$ in., $Mn=0.32$ , NPR=2.5, $T_t=1325^\circ R$ , $V_j=1919$ ft/sec.....	371
316.	Effect of Mixer Design on Axial Velocity Distribution in External Plume of Hardwall Vortical Mixer-Ejector Nozzle: SAR=4.9, MAR=1.18, $L_{EJ}=18.85$ in., $Mn=0.32$ , NPR=3.5, $T_t=1735^\circ R$ , $V_j=2518$ ft/sec.....	372
317.	Comparison of Axial Velocity Distributions Between Axial and Vortical Mixer Designs With Hardwall Shroud at Various Axial Locations Downstream From Ejector Exit Plane: SAR=4.9, MAR=1.18, $L_{EJ}=18.85$ in., $Mn=0.32$ , NPR=3.5, $T_t=1735^\circ R$ , $V_j=2518$ ft/sec.....	373
318.	Effect of Mixer Design on Axial Velocity Distribution in External Plume of Hardwall Vortical Mixer-Ejector Nozzle: SAR=4.9, MAR=1.18, $L_{EJ}=18.85$ in., $Mn=0.0$ , NPR=3.5, $T_t=1735^\circ R$ , $V_j=2518$ ft/sec.....	374
319.	Comparison of Axial Velocity Distributions Between Axial and Vortical Mixer Designs With Hardwall Shroud at Various Axial Locations Downstream From Ejector Exit Plane: SAR=4.9, MAR=1.18, $L_{EJ}=18.85$ in., $Mn=0.0$ , NPR=3.5, $T_t=1735^\circ R$ , $V_j=2518$ ft/sec.....	375
320.	Effect of Mixer Designs With Hardwall Shroud on Axial Turbulence Intensity Distributions Along Axial (X), Vertical (Y), and Spanwise (Z) Directions in External Plume: SAR=4.9, MAR=1.18, NPR=3.5, $T_t=1735^\circ R$ , $V_j=2518$ ft/sec.....	376
321.	Effect of Shroud Length ( $L_{EJ}$ ) on Axial Velocity Distribution Close to Exit Plane of Hardwall Vortical Mixer-Ejector Nozzle: SAR=4.9, MAR=1.18, $X=0.65$ , $Mn=0.32$ , NPR=2.5, $T_t=1325^\circ R$ , $V_j=1919$ ft/sec .....	377
322.	Effect of Shroud Length on Axial Velocity Distribution Close to Exit Plane of Hardwall Axial Mixer-Ejector Nozzle: SAR=4.9, MAR=1.18, $X=0.65$ , $Mn=0.32$ , NPR=2.5, $T_t=1325^\circ R$ , $V_j=1919$ ft/sec.....	378

323.	Effect of Shroud Length on Axial Velocity Distribution Close to Exit Plane of Hardwall Vortical Mixer-Ejector Nozzle: SAR=4.9, MAR=1.18, X=0.65, Mn=0.32, NPR=3.5, $T_t=1735^\circ\text{R}$ , $V_j=2518\text{ ft/sec}$ .....	379
324.	Effect of Shroud Length on Axial Velocity Distribution Close to Exit Plane of Hardwall Axial Mixer-Ejector Nozzle: SAR=4.9, MAR=1.18, X=0.65, Mn=0.32, NPR=3.5, $T_t=1735^\circ\text{R}$ , $V_j=2518\text{ ft/sec}$ .....	380
325.	Laser Beams Passing Through Sidewall Glass Windows of Mixer Ejector Nozzle Configuration With Short Hardwall Shroud: Mounted in Anechoic Chamber.....	381
326.	Laser Doppler Velocimetry Traverse Locations To Survey Flowfield Internal to Ejector.....	382
327.	An Isometric View of Axial Mixer-Ejector Nozzle Configuration, Showing Spanwise (Z) LDV Traverse Locations at Two X-Y planes in Flowfield Internal to Ejector .....	383
328.	Variation of Axial Velocity Distributions Along Spanwise (Z) Direction With Respect to Axial Locations at Four X-Y Planes, Internal to Ejector of Axial Mixer-Ejector Nozzle With Short Hardwall Shroud: SAR=4.9, MAR=1.18, $L_{EJ}=10.46\text{ in.}$ , Mn=0.32, NPR=2.5, $T_t=1325^\circ\text{R}$ , $V_j=1919\text{ ft/sec}$ .....	384
329.	Variation of Axial Velocity Distributions Along Spanwise (Z) Direction With Respect to Y Direction at Three X-Y Planes, Internal to Ejector of Axial Mixer-Ejector Nozzle With Short Hardwall Shroud: SAR=4.9, MAR=1.18, $L_{EJ}=10.46\text{ in.}$ , Mn=0.32, NPR=2.5, $T_t=1325^\circ\text{R}$ , $V_j=1919\text{ ft/sec}$ .....	385
330.	Effect of Nozzle Pressure Ratio on Axial Velocity Distributions Along Spanwise (Z) Direction at Four Y Locations With X=-3.4 in., Internal to Ejector of Axial Mixer-Ejector Nozzle With Short Hardwall Shroud: SAR=4.9, MAR=1.18, $L_{EJ}=10.46\text{ in.}$ , Mn=0.32.....	386
331.	Effect of Flight Simulation on Axial Velocity Distributions Along Spanwise (Z) Direction at Four Y Locations With X=-3.4 in., Internal to Ejector of Axial Mixer-Ejector Nozzle With Short Hardwall Shroud: SAR=4.9, MAR=1.18, $L_{EJ}=10.46\text{ in.}$ , NPR=3.5, $T_t=1735^\circ\text{R}$ , $V_j=2518\text{ ft/sec}$ .....	387
332.	Axial Velocity and Turbulence Intensity Distributions Along X-Direction, Internal to Ejector of Axial Mixer-Ejector Nozzle With Short Hardwall Shroud: SAR=4.9, MAR=1.18, $L_{EJ}=10.46\text{ in.}$ , NPR=2.5, $T_t=1325^\circ\text{R}$ , $V_j=1919\text{ ft/sec}$ .....	388
333.	An Isometric View of a Vortical Mixer-Ejector Nozzle Configuration, Showing Axial (X) and Vertical (Y) Laser Doppler Velocimetry Traverse Locations in the Flowfield Internal to Ejector .....	389
334.	An Isometric View of a Vortical Mixer-Ejector Nozzle Configuration, Showing Spanwise (Z) Laser Doppler Velocimetry Traverse Locations at Two X-y Planes in the Flowfield Internal to Ejector .....	390
335.	Axial Velocity and Turbulence Intensity Distributions Along X-Direction, Internal to Ejector of Vortical Mixer-Ejector Nozzle With Short Hardwall Shroud: SAR=4.9, MAR=1.18, $L_{EJ}=10.46\text{ in.}$ , Mn=0.32, NPR=2.5, $T_t=1325^\circ\text{R}$ , $V_j=1919\text{ ft/sec}$ .....	391
336.	Axial Velocity Distributions Along Spanwise (Z) Direction at Two X-Y Planes, Internal to Ejector of Vortical Mixer-Ejector Nozzle With Short Hardwall Shroud: SAR=4.9, MAR=1.18, $L_{EJ}=10.46\text{ in.}$ , Mn=0.32, NPR=2.5, $T_t=1325^\circ\text{R}$ , $V_j=1919\text{ ft/sec}$ .....	392
337.	Axial Velocity Distributions Along Spanwise (Z) Direction at Two X-Y Planes, Internal to Ejector of Vortical Mixer-Ejector Nozzle With Short Hardwall Shroud: SAR=4.9, MAR=1.18, $L_{EJ}=10.46\text{ in.}$ , Mn=0.32, NPR=2.5, $T_t=1325^\circ\text{R}$ , $V_j=1919\text{ ft/sec}$ .....	393

338.	Effect of Flight on Axial Velocity Distributions Along Axial (X) and Spanwise (Z) Directions, Internal to Ejector of Vortical Mixer-Ejector Nozzle With Short Hardwall Shroud: SAR=4.9, MAR=1.18, $L_{EJ}$ =10.46 in., NPR=3.5, $T_t$ =1735°R, $V_j$ =2518 ft/sec.....	394
339.	Comparison of Axial Velocity Distributions Along Spanwise (Z) Direction Between Vortical and Axial Mixers at Various Y locations at X=-9.4 in., Internal to Ejector With Short Hardwall Shroud: SAR=4.9, MAR=1.18, $L_{EJ}$ =10.46 in., Mn=0.32, NPR=2.5, $T_t$ =1325°R, $V_j$ =1919 ft/sec.....	395
340.	Comparison of Axial Velocity Distribution Along Spanwise (Z) Direction Between Vortical and Axial Mixers at Various Axial Locations Internal to Ejector With Short Hardwall Shroud at Y=1: SAR=4.9, MAR=1.18, $L_{EJ}$ =10.46 in., Mn=0.32, NPR=2.5, $T_t$ =1325°R, $V_j$ =1919 ft/sec.....	396
341.	Comparison of Axial Velocity Distributions Along Spanwise (Z) Direction Between Vortical and Axial Mixers at X=-3.4 in. and Y=0 at Two Different Aerothermodynamic Conditions, Internal to Ejector With Short Hardwall Shroud: SAR=4.9, MAR=1.18, $L_{EJ}$ =10.46 in., Mn=0.32.....	397
342.	Geometry of Pratt & Whitney Mixers (Not to Scale) .....	398
343.	Axial Grid Cuts for Pratt & Whitney Vortical Mixer-Ejector .....	399
344.	Axial Grid Cuts for Pratt & Whitney Axial Mixer-Ejector.....	400
345.	Cross-Sectional Grid Cuts for Pratt & Whitney Vortical and Axial Cases.....	401
346.	Effect of Lobe Squaring on Shroud Loading for Pratt & Whitney GEN 1 Mixer-Ejector .....	402
347.	Effect of Parametrics on Ejector Exit Plane Total Temperature.....	403
348.	Mixing Efficiency of Parametric GEN 1.5 Mixer-Ejector Configurations.....	404
349.	Isotherm Contour Plots for Typical GEN 1.5 Configuration.....	405
350.	Comparison of Shroud Pressure Loading for Vortical Nozzle/Short Shroud Mixer-Ejector .....	406
351.	Axial Crest Mach No. Distributions for Vortical Nozzle/Short Shroud Mixer-Ejector .....	407
352.	Schematic of Mixer-Ejector Geometry and Axial Location of Internal/External LV Traverse Planes .....	408
353.	Comparison of Axial Velocity Profiles (Vortical, Trough Plane Cut) for Vortical/Short Shroud Mixer-Ejector.....	409
354.	Comparison of Axial Velocity Profiles (Lateral, Symmetry Plane Cut) for Vortical/Short Shroud Mixer-Ejector.....	410
355.	Pratt & Whitney Vortical Nozzle With Short Shroud Axial Velocity at Ejector Exit Plane .....	411
356.	Comparison of Shroud Pressure Loading for Vortical Nozzle/Long Shroud Mixer-Ejector.....	412
357.	Axial Cut Mach No. Distributions for Vortical Nozzle/Short Shroud Cases .....	413
358.	Comparison of Axial Velocity Profiles (Vortical, Trough Plane Cut) for Vortical/Long Shroud Mixer-Ejector.....	414
359.	Pratt & Whitney Vortical Nozzle With Long Shroud, Axial Velocity at Ejector Exit Plane .....	415
360.	Comparison of Exit Plane Total Temperature Distributions for Vortical Nozzle Mixer-Ejector.....	416
361.	Comparison of Shroud Pressure Loading for Axial Nozzle/Short Shroud Mixer-Ejector.....	417
362.	Axial Velocity Distributions for Axial Nozzle/Short Shroud Mixer-Ejector .....	418

363.	Comparison of Axial Velocity Profile (Vortical, Trough Plane Cut) for Axial/Short Shroud Mixer-Ejector.....	419
364.	Comparison of Axial Velocity Profiles (Lateral, Symmetry Plane Cut) for Axial/Short Shroud Mixer-Ejector.....	420
365.	Comparison of Axial Velocity Profiles (Lateral Cuts, $X=0.65$ ) for Axial/Short Shroud Mixer-Ejector...	421
366.	Comparison of Shroud Pressure Loading for Axial Nozzle/Long Shroud Mixer-Ejector.....	422
367.	Comparison of Vertical Velocity Component at $X=3.4$ in. Downstream of Mixer-Ejector Exit .....	423
368.	P&W and GEAC EPNL Calculations Agree Vortical Mixer Long Treated Shroud: (MAR = 0.97, SAR = 4.9, $A_{g*} = 1086 \text{ in}^2$ , SL = 1629 ft) .....	445
369.	Noise Spectra Hookup and Correction – SPL Versus Frequency at 60, 90, 130, and 150 degrees Baseline Round Conic Nozzle (150-ft Arc, $A_{g*}=1086 \text{ in}^2$ , $V_j=2384 \text{ ft/sec}$ , $M_n=0.32$ , $V_{\Pi}=357 \text{ ft/sec}$ ).....	448
370.	Noise Spectra Hookup and Correction – SPL Versus Frequency at 60, 90, 120, and 150 degrees Vortical Mixer, Hardwall, Short Shroud (SAR=4.9, MAR=1.185, 150-ft Arc, $A_{g*}=1086 \text{ in}^2$ , $V_j=2384 \text{ ft/sec}$ , $M_n=0.32$ , $V_{\Pi}=357 \text{ ft/sec}$ ).....	449
371.	Noise Spectra Hookup and Correction – SPL Versus Frequency at 60, 90, 130, and 150 degrees Baseline Round Conic Nozzle (Sideline=1629 ft, $A_{g*}=1086 \text{ in}^2$ , $V_j=2384 \text{ ft/sec}$ , $M_n=0.32$ , $V_{\Pi}=357 \text{ ft/sec}$ ).....	450
372.	Noise Spectra Hookup and Correction – SPL Versus Frequency at 60, 90, 120, and 150 degrees Vortical Mixer, Hardwall, Short Shroud (SAR=4.9, MAR=1.185, Sideline=1629 ft, $A_{g*}=1086 \text{ in}^2$ , $V_j=2384 \text{ ft/sec}$ , $M_n=0.32$ , $V_{\Pi}=357 \text{ ft/sec}$ )....	451
373.	Noise Spectra Hookup and Correction – PNLT Versus Angle Baseline Round Conic Nozzle (Sideline=1629 ft, $A_{g*}=1086 \text{ in}^2$ , $V_j=2384 \text{ ft/sec}$ , $M_n=0.32$ , $V_{\Pi}=357 \text{ ft/sec}$ ).....	452
374.	Noise Spectra Hook-Up and Correction – PNLT Versus Angle, Vortical Mixer, Hardwall, Short Shroud (SAR = 4.9, MAR = 1.185, $A_{g*} = 1086 \text{ in}^2$ , Sideline = 1629 ft, $V_j=2384 \text{ ft/sec}$ , $M_n=0.32$ , $V_{\Pi} = 357 \text{ ft/sec}$ ) 453	
375.	Effect of Data Correction on Sideline Noise – Baseline Round Conic Nozzle Vortical Mixer, Hardwall, Short Shroud (SAR = 4.9, MAR = 1.185, $A_{g*} = 1086 \text{ in}^2$ , Sideline = 1629 ft, Static).....	454
376.	Effect of Data Correction on Sideline Noise – Baseline Round Conic Nozzle Vortical Mixer, Hardwall, Short Shroud (SAR=4.9, MAR=1.185, $A_{g*}=1086 \text{ in}^2$ , Sideline=1629 ft, $M_n=0.32$ , $V_{\Pi}=357 \text{ ft/sec}$ ) .....	455

REPORT DOCUMENTATION PAGE			Form Approved OMB No. 0704-0188	
Public reporting burden for this collection of information is estimated to average 1 hour per response, including the time for reviewing instructions, searching existing data sources, gathering and maintaining the data needed, and completing and reviewing the collection of information. Send comments regarding this burden estimate or any other aspect of this collection of information, including suggestions for reducing this burden, to Washington Headquarters Services, Directorate for Information Operations and Reports, 1215 Jefferson Davis Highway, Suite 1204, Arlington, VA 22202-4302, and to the Office of Management and Budget, Paperwork Reduction Project (0704-0188), Washington, DC 20503.				
1. AGENCY USE ONLY (Leave blank)		2. REPORT DATE February 2005		3. REPORT TYPE AND DATES COVERED Final Contractor Report
4. TITLE AND SUBTITLE  Results of Aero/Acoustic Tests and Analytical Studies of a Two-Dimensional Eight-Lobe Mixer-Ejector Exhaust Nozzle at Takeoff Conditions			5. FUNDING NUMBERS  WBS-22-714-09-46 NAS3-26618	
6. AUTHOR(S)  P. Schweiger, A. Stern, E. Gamble, T. Barber, L. Chiappetta, R. LaBarre, M. Salikuddin, H. Shin, and R. Majjigi				
7. PERFORMING ORGANIZATION NAME(S) AND ADDRESS(ES)  United Technologies Corporation Pratt & Whitney 400 Main Street East Hartford, Connecticut 06108			8. PERFORMING ORGANIZATION REPORT NUMBER  E-14784	
9. SPONSORING/MONITORING AGENCY NAME(S) AND ADDRESS(ES)  National Aeronautics and Space Administration Washington, DC 20546-0001			10. SPONSORING/MONITORING AGENCY REPORT NUMBER  NASA CR-2005-213324	
11. SUPPLEMENTARY NOTES This research was originally published internally as HSR042 in September 1996. P. Schweiger, A. Stern, and E. Gamble, Pratt & Whitney, East Hartford, Connecticut 06108; T. Barber, L. Chiappetta, and R. LaBarre, United Technologies Research Center, East Hartford, Connecticut 06108; M. Salikuddin, H. Shin, and R. Majjigi, General Electric Aircraft Engines, Cincinnati, Ohio 45125. Project Manager, Douglas Harrington (retired). Responsible person, Diane Chapman, Ultra-Efficient Engine Technology Program Office, NASA Glenn Research Center, organization code PA, 216-433-2309.				
12a. DISTRIBUTION/AVAILABILITY STATEMENT  Unclassified - Unlimited Subject Categories: 01, 02, 05, and 07 Available electronically at <a href="http://gltrs.grc.nasa.gov">http://gltrs.grc.nasa.gov</a> This publication is available from the NASA Center for AeroSpace Information, 301-621-0390.			12b. DISTRIBUTION CODE	
13. ABSTRACT (Maximum 200 words) Hot flow aero-acoustic tests were conducted with Pratt & Whitney's High-Speed Civil Transport (HSCT) Mixer-Ejector Exhaust Nozzles by General Electric Aircraft Engines (GEAE) in the GEAE Anechoic Freejet Noise Facility (Cell 41) located in Evendale, Ohio. The tests evaluated the impact of various geometric and design parameters on the noise generated by a two-dimensional (2-D) shrouded, 8-lobed, mixer-ejector exhaust nozzle. The shrouded mixer-ejector provides noise suppression by mixing relatively low energy ambient air with the hot, high-speed primary exhaust jet. Additional attenuation was obtained by lining the shroud internal walls with acoustic panels, which absorb acoustic energy generated during the mixing process. Two mixer designs were investigated, the high mixing "vortical" and aligned flow "axial", along with variations in the shroud internal mixing area ratios and shroud length. The shrouds were tested as hardwall or lined with acoustic panels packed with a bulk absorber. A total of 21 model configurations at 1:11.47 scale were tested. The models were tested over a range of primary nozzle pressure ratios and primary exhaust temperatures representative of typical HSCT aero thermodynamic cycles. Static as well as flight simulated data were acquired during testing. A round convergent unshrouded nozzle was tested to provide an acoustic baseline for comparison to the test configurations. Comparisons were made to previous test results obtained with this hardware at NASA Glenn's 9- by 15-foot low-speed wind tunnel (LSWT). Laser velocimetry was used to investigate external as well as ejector internal velocity profiles for comparison to computational predictions. Ejector interior wall static pressure data were also obtained. A significant reduction in exhaust system noise was demonstrated with the 2-D shrouded nozzle designs.				
14. SUBJECT TERMS  Jet noise; Flight effects; Mixer-ejector laser velocimetry; Computational fluid dynamics predictions			15. NUMBER OF PAGES 494	
			16. PRICE CODE	
17. SECURITY CLASSIFICATION OF REPORT Unclassified	18. SECURITY CLASSIFICATION OF THIS PAGE Unclassified	19. SECURITY CLASSIFICATION OF ABSTRACT Unclassified	20. LIMITATION OF ABSTRACT	





